The Synthesis, Structure and Properties of Anionic Metal–Tetraoxolene Coordination Polymers

Martin Peter van Koeverden

ORCID 0000-0002-7339-5168

Submitted in total fulfilment of the requirements of the degree of

Doctor of Philosophy

April 2021

SCHOOL OF CHEMISTRY

THE UNIVERSITY OF MELBOURNE

Copyright © 2021 Martin Peter van Koeverden

All right reserved. No part of this publication may be reproduced, stored or transmitted by print, photocopy, microfilm, electronic or any other means without the express written permission of the author.

"I've served this canon seven years and more,
Yet am no nearer science than before.
All that I ever had I've lost thereby,
And so, God knows, have many more than I.
Time was when I was fresh and fond of cheer,
Liked decent cloths and other handsome gear;
Now I might wear my hose upon my head,
And where my colour was a lively red,
My face is wan and wears a leaden look;
If you try science you'll be brought to book.
My eyes are bleared with work on preparations,
That's all the good you get from transmutations.
That slippery science stripped me down so bare
That I'm worth nothing, here or anywhere.
Added to that I am so deep in debt
From borrowing money, you can lay a bet
Long as I live I'll never pay it, never!
Let every man be warned by me for ever;
Whoever tries his hand at such behavings,
If he goes on I say will lose his savings,
What's more, so help me God, his only gains
Are empty money-bags and addled brains.
And by the time the man's gone raging mad
And risk and lost whatever goods he had,
He then eggs others on and off they run
To lose their goods, as he himself has done."

The Canon's Yeoman's Tale: The Canterbury Tales (ca. 1390s)
Geoffrey Chaucer, ca. 1340s–1400†
Translated by Nevill Coghill 1899–1980†

Abstract

Electrically conductive, magnetically ordered, and electrochemically active materials are important components for data processing technologies, energy conversion and storage devices, and sensors and optoelectronics. The synthesis of compounds with these properties is therefore an important scientific endeavour to meet the progressively more demanding sustainability and performance targets. Crystalline coordination polymers have recently been proposed as candidate materials to achieve these aims. Coordination polymers can exhibit synergy between electrical conductivity, magnetic ordering and electroactivity, coupled with porosity, flexibility, and tuneable architecture and functionality, not achievable using traditional inorganic materials. This thesis describes studies into anionic tetraoxolene coordination polymers constructed using ligands derived from 3,6-disubtitued-2,5-dihydroxy-1,4-benzoquinones (H_2Xan, X = F, Cl, Br; anilic acids), and redox-active viologen countercations. Despite the desirable properties of tetraoxolene coordination polymers previously described in literature, the impact that viologen countercations have upon the structure and properties of tetraoxolene coordination polymers has never been explored.

Chapter 2 first presents structural studies on a range of Mn^{II} and Cd^{II} coordination polymers synthesised using diamagnetic fluoranilate (Fan^{2-}) and chloranilate ($Clan^{2-}$) ligands and redox-active *N*,*N*′-dimethyl-4,4′-bipyridinium (MeV^{2+}) countercations. The structural disparity observed between Fan^{2-} and $Clan^{2-}$ compounds demonstrates the inherent sensitivity of reactions to supramolecular interactions between cations, metals, ligands, and solvents. It also highlights the structural unpredictability associated with the use of viologen cations, compared to redox-inactive alkylammonium countercations. Structural studies on mixed-valence Fe^{III}–tetraoxolene coordination polymers containing viologen countercations are subsequently presented, showing resultant anionic tetraoxolene network topology remains difficult to predict. However localisation of the tetraoxolene radical trianion ($Xan^{3-\bullet}$) state is consistently observed, caused by charge-transfer (CT) and Coulombic interactions between the π-electron deficient viologen cations, and the π-electron rich anionic networks. This reveals the potential for viologens to modulate the charge-state distribution in mixed-valence tetraoxolene coordination polymers.

In Chapter 3, 5,6-dihydropyrazino[1,2,3,4-*lmn*][1,10]-phenanthrolinediium ($PhenQ^{2+}$) countercations are incorporated into an isostructural family of mixed-valence 2D Fe^{III}–tetraoxolene frameworks (PhenQ)[$Fe_2(Xan)_3$] (X = F, Cl, Br). As for the mixed-valence networks obtained in Chapter 2, CT interactions between $PhenQ^{2+}$ cations and the anionic $[Fe_2(Xan)_3]^{2-}$ networks cause localisation of the $Xan^{3-\bullet}$ state and partial ligand charge-ordering. Spectroscopic studies on (PhenQ)[$Fe_2(Xan)_3$]·*y*DMF showed the network−cation interactions impact upon the electronic structure of the material. The inclusion of $PhenQ^{2+}$ gives rise to additional framework redox states and modifies the conductive and magnetic properties of the material, compared to tetraoxolene frameworks with only redox-inactive countercations.

Chapter 4 investigates a family of mixed-valence Fe–fluoranilate frameworks containing MeV^{2+} countercations, (MeV)[$Fe_2(Fan)_3$]·solvent (solvent = MeCN, DMF). X-ray diffraction studies reveal the compounds undergo a range of slight structural distortions upon changing the guest solvent. Remarkably, these guest-induced structure distortions cause partial switching of the Fe valence state, never before observed in Fe–tetraoxolene coordination polymers. The guest-induced Fe valence fluctuation in turn modifies the electronic spectra and structure of the frameworks, with resultant switching of the transport properties.

In Chapter 5, the mixed-valence Fe–tetraoxolene framework (MeV)[$Fe_2(Clan)_3$] undergoes a surprising structural transformation upon lattice solvent loss, causing the isolated compound to exhibit a previously unobserved cation–network packing arrangement. This dramatic structure transformation results in changes to the electronic spectrum of the compound, as well as the electrochemical response and transport properties of the material, compared to topologically similar Fe–tetraoxolene frameworks containing redox-inactive cations. These results demonstrate the impact of structure packing and supramolecular interactions on the network electronic structure. This provides encouragement that the physicochemical properties of the compounds may be tailored by controlling these supramolecular interactions.

Finally, Chapter 6 presents a summary of the results obtained in this thesis, highlights the overarching themes of this research, and puts forth possible future research directions for the field.

Declaration

This is to certify that:

i. *the thesis comprises only my original work towards the PhD except where indicated in the Preface;*
ii. *due acknowledgement has been made in the text to all other material used;*
iii. *the thesis is less than 100 000 words in length, exclusive of tables, maps, bibliographies and appendices.*

_____

Martin Peter van Koeverden

This page intentionally left blank

Preface

Unless as noted below, synthesis of all compounds presented, collection of experimental data, preparation of plots, and analysis and discussion of the results, was performed by the candidate.

In Chapter 2, Dr. Carol Hua collected synchrotron P-XRD data on **2.2b**. Processing and analysis of the data were undertaken by the candidate.

In Chapter 3, A/Prof. Deanna M. D'Alessandro from The University of Sydney undertook deconvolution of the UV-Vis-NIR spectrum of **3.1^{Cl}b**, and performed Hush analysis on the resultant deconvoluted spectrum. Interpretation of the results was undertaken by the candidate, under the supervision of A/Prof. Deanna M. D'Alessandro. Dr. Wasinee Phonsri measured and processed magnetic data on **3.1^{Cl}b** at Monash University, under the supervision of Prof. Keith S. Murray. Preparation of data plots and discussion of the magnetic data was undertaken by the candidate under the supervision of Dr. Wasinee Phonsri and Prof. Keith S. Murray.

Part of Chapter 3 has been published as:

> Martin P. van Koeverden, Brendan F. Abrahams, Deanna M. D'Alessandro, Patrick W. Doheny, Carol Hua, Timothy A. Hudson, Guy N. L. Jameson, Keith S. Murray, Wasinee Phonsri, Richard Robson, Ashley L. Sutton. "Tuning Charge-State Localization in a Semiconductive Iron(III)–Chloranilate Framework Magnet using a Redox-Active Cation." *Chem. Mater.*, **2020**, *32*(17), 7551–7563.

The experimental data was collected by the candidate unless as noted above. The initial draft of the manuscript was written substantially (80%) by the candidate, with subsequent drafts edited with the input of the candidates principle supervisor, Prof. Brendan F. Abrahams, as well as all other co-authors. The manuscript has been substantially rewritten and expanded by the candidate to form Chapter 3.

In Chapter 4, Dr. Carol Hua collected synchrotron P-XRD data on *mP* **4.1a**, *aP* **4.1a** and **4.1b**. Processing and analysis of the data were undertaken by the candidate. Dr. Patrick W. Doheny collected UV-Vis-NIR spectra of *aP* **4.1a** and **4.1b** at The University of Sydney, and Dr. Carol Hua undertook deconvolution of the UV-Vis-NIR spectra of *aP* **4.1a** and **4.1b** and performed Hush analysis on the resultant deconvoluted spectra. Preparation of data plots and interpretation of the results was

undertaken by the candidate, under the supervision of A/Prof. Deanna M. D'Alessandro and Dr. Carol Hua.

In Chapter 5, Dr. Carol Hua collected synchrotron P-XRD data on **5.1** and **5.2**. Processing and analysis of the data were undertaken by the candidate. Dr. Carol Hua also measured the UV-Vis-NIR spectrum of **5.2** at The University of Sydney and performed deconvolution and Hush analysis on the spectrum. The candidate prepared data plots and interpreted the results, under the supervision of A/Prof. Deanna M. D'Alessandro and Dr. Carol Hua.

In Chapters 3, 4 and 5, A/Prof. Guy N. L. Jameson measured ^{57}Fe Mössbauer spectra of **3.1^{Cl}b**, *aP* **4.1a**, **4.1b** and **5.1** at The University of Melbourne. A/Prof. Guy N. L. Jameson also performed fitting on the experimental spectra, and prepared data plots. Discussion of the results was undertaken by the candidate under the guidance of A/Prof. Guy N. L. Jameson.

In Chapters 3, 4 and 5, electrical conductivity measurements were undertaken using equipment, experimental procedures and software developed by Dr. Ashley L. Sutton within the candidate's research group. Assistance with electrical conductivity experiments was also provided to the candidate by Dr. Ashley L. Sutton.

Dr. Stephen P. Best furnished access to an inert atmosphere glovebox, and provided advice regarding handling of air-sensitive compounds prepared in Chapters 3, 4 and 5. A/Prof. Colette Boskovic furnished access to a potentiostat and associated equipment required to perform cyclic voltammetric experiments presented in Chapters 3, 4 and 5.

Synchrotron single-crystal X-ray diffraction used the MX1 and MX2 beamlines at the Australian Synchrotron, a part of ANSTO. Data collection on the MX2 beamline used the Australian Cancer Research Foundation (ACRF) detector. Synchrotron powder X-ray diffraction experiments were undertaken using the PD beamline of the Australian Synchrotron, a part of ANSTO.

The work presented herein was support by The University of Melbourne through a Melbourne Research Scholarship (MRS). Additional support was provided by the Australian Research Council (ARC) and the Australian Nuclear Science and Technology Organisation (ANSTO).

Publications

The following publication(s) arose from work presented in this thesis:

Martin P. van Koeverden, Brendan F. Abrahams, Deanna M. D'Alessandro, Patrick W. Doheny, Carol Hua, Timothy A. Hudson, Guy N. L. Jameson, Keith S. Murray, Wasinee Phonsri, Richard Robson, Ashley L. Sutton. "Tuning Charge-State Localization in a Semiconductive Iron(III)–Chloranilate Framework Magnet using a Redox-Active Cation." *Chem. Mater.*, **2020**, *32*(17), 7551–7563.

The following publication(s) arose during the PhD candidature but are not related to the work presented herein:

Thomas Fellowes, **Martin P. van Koeverden**, Jonathan M. White. "Thermal conversion of a pyridine solvate to a de-solvate facilitated by rearrangement of chalcogen bonds. The solvate and non-solvate structures of *N*-(2-nitro-4-(3-oxobenzo[*d*][1,2]selenazol-2(3*H*)-yl)phenyl)picolinamide." *CrystEngComm*, **2020**, (22), 4023–4029.

Presentations

The following oral presentations were given during the PhD candidature:

The Structure and Properties of Anionic Metal–Tetraoxolene Coordination Polymers. *PhD Completion Seminar*, **September 2020**, *The University of Melbourne*

Semiconductivity and Spontaneous Magnetisation in a Mixed-Valence Iron(III)-Chloranilate Framework – Awarded Don Stranks Prize. *Inorganic 19 (IC19) – RACI Inorganic Division Conference*, **December 2019**, *The University of Wollongong*

Mixed Valence Iron-Chloranilate Coordination Polymers Incorporating Redox Active Cations – Awarded Runner-Up for Best Oral Presentation. *RACI Victorian Inorganic Division Student Symposium*, **December 2018**, *Monash University*

The following poster presentations were given during the PhD candidature:

Semiconductivity and Spontaneous Magnetisation in a Mixed-Valence Iron(III)-Chloranilate Framework. *RACI Victorian Inorganic Division Student Symposium*, **December 2019**, *The University of Melbourne*

Mixed Valence Iron-Chloranilate Coordination Polymers Incorporating Redox Active Cations – Awarded Poster Prize. *Crystal32/AsCA18 – Joint SCANZ and Asian Crystallographic Association Conference*, **December 2018**, *The University of Auckland*

Acknowledgements

In reflecting over the course of my PhD candidature, and the writing process of this thesis, I am reminded of the adage that *"It takes a village to raise a child."* Much like a young child developing into an adult member of a society only by the guidance of multiple individuals, each with differing expertise and viewpoints, my development throughout the PhD candidature has been shaped by continued interactions with formative mentors, and supportive friends and colleagues. It would therefore be bordering on criminally remiss not to properly acknowledge their contribution in helping me through my candidature, and the writing process of this thesis.

Firstly, I am greatly indebted to my supervisor Prof. Brendan F. Abrahams, for his consistent encouragement, infectious enthusiasm, guidance, and patience over the last five-ish years. I am particularly grateful for his bold willingness to provide safe-haven to a recovering chemical engineer in his group of chemists and crystallographers. It is safe to say, I have thoroughly been converted to the field of coordination polymers. Profound thanks also go to my co-supervisor at The University of Sydney, A/Prof. Deanna M. D'Alessandro, for supporting my work and for her advice and wisdom in all things spectroscopic and voltammetric. I also owe Prof. Richard Robson a significant debt of gratitude. His un-wavering passion for chemistry and coordination polymers were, are, and will continue to be, truly inspiring. It has undoubtedly been a tremendous privilege to work alongside Richard every day, and to be exposed to his limitless ideas and chemical insights. I would also like to sincerely thank the members of my advisory panel, Dr. Lars Goerigk as panel chair, and Prof. Paul S. Donnelly as a panel member. Though I have perhaps not always appreciated it in the moment, their forthright guidance and insight have proved very helpful and motivating throughout my candidature.

I am very fortunate to have been able to work alongside great colleagues, past and present, within the Abrahams-Robson group: Dr. Ashley L. Sutton, Dr. A. David Dharma, Dr. Chris J. Kingsbury, Dr. Rob W. Elliott, Dr. Jess L. Holmes, Dr. Keith F. White, Dr. Tim A. Hudson, Dr. Chris J. Commons, Anna Ahveninen, Katelyn Clutterbuck, Robin W. Sanchez Arlt, Yang Liu, Hui Min Tay, Simon G. Hardin and Tara Shahani. Thanks for being a great group of people to hang around! In particular,

Dr. Keith F. White and Dr. Jess L. Holmes for their friendly welcome and making my entry to the Abrahams-Robson group smooth, and Dr. Tim A. Hudson for taking me on as yet another crystallographic Padawan! Dr. Ashley L. Sutton also warrants special mention, for helping me become acquainted with many of the measurements I have used throughout this work; his drive to develop new experimental techniques within the group is admirable. Thanks also go to the Boskovic and Hua groups for being great office and lab-mates, and being fantastic scientific soundboards: Dr. Elodie Rousset, Dr. Moya A. Hay, Dr. Gemma K. Gransbury, Maja A. Dunstan, Jett T. Janetzki, Aiden Aitkin, Will R. Reed, Vincent L. Nadurata, Katya Bondaruk, Shannon Thoonen and Tina Tezgerevska. In particular, A/Prof. Colette Boskovic for her scientific interest and professional advice, Dr. Carol Hua for her continuous scientific advice on many of the experiments performed throughout my candidature. In addition, Dr. Elodie Rousset and Dr. Moya A. Hay are thanked especially for help and advice with magnetic measurements. Dr. Elodie Rousset and Dr. Carol Hua also warrant special thanks for their helpful critiques regarding various chapters of this thesis.

Many thanks to my collaborators, without whom, complete vast sections of this work would not be possible: Prof. Keith S. Murray and Dr. Wasinee Phonsri at Monash University for magnetic measurements and friendly advice. A/Prof. Deanna M. D'Alessandro and her group at The University of Sydney, in particular Dr. Patrick W. Doheny, Dr. Pavel Usov and Dr. Marcello Solomon, for their advice on solid-state electrochemistry and spectroelectrochemistry. Within the School of Chemistry at The University of Melbourne, A/Prof. Guy N. L. Jameson for ^{57}Fe Mössbauer spectroscopy, and Dr. Stephen P. Best for his advice into air-sensitive techniques and furnishing access to a glovebox, as well as forthcoming insight into electrochemistry and EPR spectroscopy.

As is unfortunately par for the course when working in a university environment, one must often transit through the barren, unforgiving and hostile wastelands of bureaucracy. The skill with which some individuals can navigate through these bleak realms is frequently awe inspiring. Therefore, I owe a tremendous amount of gratitude to the administration staff within the School of Chemistry, in particular Liz Mills and Andrea Oliver, for deftly guiding me through the seemingly endless storms of paperwork, and for helping behind the scenes to keep the School of Chemistry

running smoothly. I would also like to thank the technical staff within the School of Chemistry, in particular Dr. Robert W. Gable for maintaining the X-ray diffraction equipment which was essential for the work in this thesis. Also thanks to the members of the Faculty of Science workshop, and in particular Les Gamel. The skill with which Les has been able to turn my vague ideas and crudely drawn line diagrams into beautiful and functional pieces of custom-made glassware has proven particularly uplifting, as have his fascinating and enlightening stories about the often-hidden sides of working in a university environment. The recent retirement of Les and the other workshop staff is a tremendous loss both for the Faculty of Science and the University.

I once heard it said that researchers are machines which turn coffee and money into ideas and discoveries, so without a source of funding (and coffee), none of the research within could have happened. With that in mind, I would like to thank the University of Melbourne, for financial support in the form of a Melbourne Research Scholarship, and the Australian Government and the Australian Research Council for funding projects in which I have been involved. Thanks also go to the Faculty of Science at The University of Melbourne, for travel funding in the form of a Science Abroad Travelling Scholarship. Additionally, the Inorganic Division of the Royal Australian Chemical Institute, for travel funding and awarding me the Don Stranks Prize at IC19. The Australian Synchrotron, a part of ANSTO is also gratefully acknowledged for providing access to critical research infrastructure used during my candidature.

To the great friends I have made within the School of Chemistry over the last five years, thank you being welcoming and accepting, despite me having committed the mortal sin of studying engineering in a former life. The Safety Conscious East Wing adjacent memes we shared over the years have helped me through the inevitable rough patches of any PhD candidature. In particular, cheers to Maja D, Caitlin H, Michael S, Nastasia B, Gemma G, Ben T, Elodie R, Moya H, Tom F, Dale L, Domi W, and Michael R, for sharing in scientific discussions and molecular banter, friendship, laughter and beverages at CPS Fridays (formerly/formally known as Friday Frothies) and The Old Folks Home, and the frequent extensions thereof at The Curtin, Naughtons, The Lincoln or many other fine drinking establishments.

My close friends outside of academia have also proven a shining light throughout my studies, in helping me escape the sometimes crushing embrace of research and PhD. Although our Saturday morning bike rides and coffees along Beach Road are no more, now that everyone has dispersed across the world, I truly value the friendship extended by Tim D, Tom S, Lachlan M, Pete R and Renee W over many years. I eagerly await the next Fitzroy pub crawl with you all!

Finally, I will be forever grateful for the support of my family – my Mum and Dad, Teresa and Josef, and my sisters, Anna and Pia. Mum warrants particular mention for possessing the fortitude and stamina to meticulously proofread this thesis; I think I probably owe her a few nice bottles of wine! Thank you all for the unconditional love, unwavering support and encouragement, and homecooked meals throughout both good and rough patches of my PhD. I could not have got this far without you!

Table of Contents

Abstract v

Declaration vii

Preface ix

Publications xi

Presentations xii

Acknowledgements xiii

Table of Contents xvii

List of Figures xxi

List of Schemes xxxvi

List of Tables xxxviii

Nomenclature xlii

Third Party Copyright Materials xlvii

Chapter 1 Literature Review 1

1.1 Introduction 3

1.2 Coordination Polymers 10

1.3 Tetraoxolene Coordination Polymers 42

1.4 Viologens and Viologen-Like Molecules 54

1.5 Thesis Scope 56

1.6 References 58

Chapter 2 Structural Diversity in Anionic Fluoranilate and Chloranilate Coordination Polymers Induced by Redox-Active Dications 71

2.1 Introduction 73

2.2 Results and Discussion 78

2.3 Conclusion 136

2.4 Experimental 137

2.5 References 162

Chapter 3 Structure and Properties of Mixed-Valence Anionic Iron–Tetraoxolene Frameworks Containing Phenanthrolinediium Cations .. 169

3.1 Introduction 171

3.2 Results and Discussion 174

3.3 Conclusion 222

3.4 Experimental 223

3.5 References 240

Chapter 4 Influence of Structural Transformations Upon the Properties of Mixed-Valence Iron–Fluoranilate Coordination Polymers 245

4.1 Introduction 247

4.2 Results and Discussion 250

4.3 Conclusion 309

4.4 Experimental.....311

4.5 References 322

Chapter 5 Structural Transformations and Properties of a Methyl Viologen Containing Mixed-Valence Iron–Chloranilate Framework..... 327

5.1 Introduction 329

5.2 Results and Discussion 332

5.3 Conclusion 377

5.4 Experimental.....379

5.5 References 387

Chapter 6 Conclusion..... 391

6.1 Thesis Summary 393

6.2 Future Work.....401

6.3 References 406

Chapter 7 Experimental Methods 409

7.1 Single-Crystal X-ray Diffraction (SC-XRD) 411

7.2 Powder X-ray Diffraction (P-XRD) 414

7.3 Elemental Analysis 414

7.4 Spectroscopic Methods 415

7.5 Thermogravimetric Analysis (TGA) 417

7.6 Electrochemistry 417

7.7 Magnetometry 417

7.8 Electrical Conductivity 418

7.9 References 420

Appendices

Appendix A Tetraoxolene Bond Length Analysis A1

Appendix B Electrical Conductivity Data B1

List of Figures

Chapter 1

Figure 1.1 The structures of common inorganic electroactive, magnetic or conductive materials.....5

Figure 1.2 The structures of organic metal (TTF)(TCNQ) and the molecular magnet ($Fe^{III}Cp^{*}_{2}$)(TCNE). 8

Figure 1.3 Coordination polymers.....11

Figure 1.4 Schematic of the uniform platonic (6,3) net topology. 13

Figure 1.5 Ball-and-stick representations of the (a) cubic (10,3)-*a* (**srs**) and (b) tetragonal (10,3)-*b* (**ths**) uniform platonic networks. .14

Figure 1.6 The defect-free structure and topology of of $(Fe^{III}_{4}[Fe^{II}(CN)_6]_3)\cdot xH_2O$ Prussian blue. 15

Figure 1.7 The structure of diamond and the diamondoid coordination polymer $[Cu(tcpm)]BF_4\cdot x PhNO_2$.....17

Figure 1.8 The structure of $Cu(Me_2DCNQI)_2$ coordination polymer.....20

Figure 1.9 The structure of the $Cu[Ni(pdt)_2]$ framework. 21

Figure 1.10 The structure of solvated $M_2(DEBDC)(DMF)_2\cdot x DMF$ (M = Mn, Fe; E = O, S) frameworks.....23

Figure 1.11 The structure and properties of $Fe_2(H_{0.67}BDT)_3$.....25

Figure 1.12 The structure of Zn_2(TTFTB) coordination polymer. 31

Figure 1.13 Structures of $Fe^{II}(TCNE)(C_4(CN)_8)$ (left) and $Mn(TCNE)_{1.5}(I_3)_{0.5}$ (right) coordination polymer magnets. 36

Figure 1.14 The structure and magnetic properties of the 2D layered coordination polymer $[\{Ru_2(O_2CCF_3)_4\}_2(F_4TCNQ)]$. 39

Figure 1.15 The structure and magnetic properties of the 3D coordination polymer $[\{Ru_2(O_2C{-}3\text{-}FPh)_4\}_2$(BTDA-TCNQ)]. 40

Figure 1.16 The structure and magnetic properties of 2D layered coordination polymers (^{n}Bu$_4$N)[Mn^{II}Cr^{III}(Xan)$_3$] (X = Cl, Br, I). 45

Figure 1.17 The switchable magnetic behaviour of a LIB cathode containing Li$_x$(^{n}Bu$_4$N)[Mn^{II}Cr^{III}(Clan^{2-})$_{(3-x)}$(Clan$^{3-\bullet}$)$_x$] (x = 0–3) in response to to electrochemical stimuli. 47

Figure 1.18 The structure and spectroscopic properties of the 3D (10,3)-*a* network in (^{n}Bu$_4$N)$_2$[Fe$_2$(dhbq)$_3$], and the structure and magnetic properies of the of the 2D layered coordination polymer (Me$_2$NH$_2$)$_2$[Fe$_2$(Clan)$_3$]·6DMF·2H2O..... 49

Figure 1.19 The temperature-dependance of the electrical conductivity of the 3D (10,3)-*a* framework (^{n}Bu$_4$N)$_2$[Fe$_2$(dhbq)$_3$], and the reduced compoound Na$_{0.9}$(^{n}Bu$_4$N)$_{1.8}$[Fe$_2$(dhbq)$_3$], and the 2D layered honeycomb framework (Me$_2$NH$_2$)[Fe$_2$(Clan)$_3$]. 52

Chapter 2

Figure 2.1 Diverse topologies of metal–tetraoxolene coordination polymers..... 75

Figure 2.2 P-XRD (λ = 1.54184 Å) pattern of **2.1$_{Mn}$** (red, T = 100 K) and calculated pattern from SC-XRD of **2.1$_{Mn}$** (black, T = 100 K). Tick marks (red) indicate the positions of the allowed reflections for the unit cell indexed from the experimental P-XRD pattern. 79

Figure 2.3 P-XRD (λ = 1.54184 Å) pattern of **2.1$_{Cd}$** synthesised using MeCN–H$_2$O (royal blue, T = 100 K) or acetone–H$_2$O (pale blue, T = 100 K) solvent systems, and calculated pattern from SC-XRD of **2.1$_{Cd}$** (black, T = 100 K). 80

Figure 2.4 (a) The 8-coordinate environment around Mn^{II} in **2.1$_{Mn}$.** (b) Ball-and-stick and (c) topological representations of the adamantane unit of the [Mn^{II}(Clan)$_2$]$^{2-}$ network in **2.1$_{Mn}$**. 81

Figure 2.5 Packing arrangement of MeV^{2+} cations (purple) within the anionic adamantane $[Mn(Clan)_2]^{2-}$ units in **2.1$_{Mn}$**. 82

Figure 2.6 Ball-and-stick (a, c, e) and spacefilling (b, d, f) representations of the interactions of the MeV^{2+} cation (purple) within the anionic $[Mn(Clan)_2]^{2-}$ adamantane unit in **2.1$_{Mn}$** (tan). 83

Figure 2.7 ATR FT-IR spectra of **2.1$_{Mn}$** (red) and **2.1$_{Cd}$** synthesised using either acetone–H_2O (pale blue) or MeCN–H_2O (royal blue) solvent systems, collected at room temperature in air. 84

Figure 2.8 Thermogravimetric analyses of (a) **2.1$_{Mn}$** (red) and **2.1$_{Cd}$** synthesised using either (b) acetone–H_2O (pale blue) or (c) MeCN–H_2O (royal blue) solvent systems at a scan rate of 5 °C min^{-1} in a flow of N_2.....85

Figure 2.9 The anionic $[Mn_2(Clan)_3]^{2-}$ (6,3) honeycomb sheets in **2.2a** viewed (a) along the crystallographic *a* axis and (b) along the plane of the anionic sheets oriented parallel to the crystallographic (111) plane.....87

Figure 2.10 Ball-and-stick (a, c, e) and spacefilling (b, d, f) representations of the interactions of the MeV^{2+} cations (purple) with the anionic $[Mn_2(Clan)_3]^{2-}$ sheets above (tan) and below (orange) in **2.2a**.....89

Figure 2.11 Alternating stacking of MeV^{2+} (purple) with $Clan^{2-}$ ligands in the anionic $[Mn_2(Clan)_3]^{2-}$ sheets (tan) in **2.2a**.....90

Figure 2.12 P-XRD (λ = 1.54184 Å) pattern of a MeCN slurry of bulk **2.2a** (green, T = 250 K) and calculated pattern from SC-XRD of **2.2a** (black, T = 100 K). 92

Figure 2.13 (a) ATR FT-IR spectrum of **2.2b** (isolated **2.2a**) conducted at ambient temperature in air. (b) Thermogravimetric analysis of **2.2b** (isolated **2.2b**) at a scan rate of 5 °C min^{-1} in a flow of N_2. 93

Figure 2.14 Synchrotron P-XRD (λ = 0.58835 Å) pattern of bulk **2.2b** (isolated **2.2a**, magenta, T = 100 K) and calculated patterns from SC-XRD of **2.1$_{Mn}$** (red, T = 100 K) and **2.2a** (green, T = 100 K)..... 94

Figure 2.15 (a) Coordination environment around Mn^{II} centres in **2.3$_{Mn}$** forming Mn_4 parallelograms. (b) Templating of Mn_4 parallelograms (tan) by ordered MeCN (teal) situated within the network void. (c) Anionic 1D $[Mn_2(Fan)_3(H_2O)_2]^{2-}$ ladders forming by edge-sharing Mn_4 parallelograms in **2.3$_{Mn}$**. 96

Figure 2.16 H-bonding interactions of the anionic 1D $[Mn_2(Fan)_3(H_2O)_2]^{2-}$ ladders, and the ladder-to-ladder packing and ligand symmetry relations in **2.3$_{Mn}$**..... 98

Figure 2.17 View just off the ladder axis showing packing of the MeV^{2+} cations (purple) with the 1D $[Mn_2(Fan)_3(H_2O)_2]^{2-}$ ladders in **2.3$_{Mn}$**. 99

Figure 2.18 Ball-and-stick (a, c, e) and spacefilling (b, d, f) representations of the interactions of the MeV^{2+} cations (purple) with the anionic $[Mn_2(Fan)_3(H_2O)_2]^{2-}$ ladders above (tan) and below (orange) in **2.3$_{Mn}$**..... 100

Figure 2.19 P-XRD (λ = 1.54184 Å) pattern of **2.3$_{Mn}$** (purple, T = 100 K) and calculated pattern from SC-XRD of **2.3$_{Mn}$** (black, T = 100 K)..... 102

Figure 2.20 P-XRD (λ = 1.54184 Å) pattern of bulk **2.3$_{Cd}$** (dark orange, T = 100 K) and calculated patterns from SC-XRD of **2.3$_{Cd}$** (black, T = 100 K) and **2.4** (light orange, T = 100 K)..... 103

Figure 2.21 ATR FT-IR spectra of **2.3$_{Mn}$** (purple) and **2.3$_{Cd}$** (orange) collected at room temperature in air. 106

Figure 2.22 Thermogravimetric (purple) and scanning differential thermal (red) analyses of **2.3$_{Mn}$** at a scan rate of 5 °C min^{-1} in a flow of N_2. 107

Figure 2.23 P-XRD (λ = 1.54184 Å) pattern of acetone slurry of bulk **2.5** (navy, T = 225 K) and calculated patterns from SC-XRD of **2.5** (black, T = 220 K). 108

Figure 2.24 (a) The high symmetry tetragonal (10,3)-*b* topology showing layers of orthogonal zig-zag chains. (b) The distorted (10,3)-*b* topology of **2.5**. The network is constructed from pseudo-1D $\{Fe–Clan^{n-}\}_\infty$ crankshaft chains (blue bonds) linked to other crankshaft chains by bridging $Clan^{n-}$ ligands (tan bonds). ... 109

Figure 2.25 The 1D $\{Fe–Clan^{n-}\}_\infty$ crankshaft chains in **2.5**. 110

Figure 2.26 Ball-and-stick (a, c, e) and spacefilling (b, d, f) representations of the interactions between $PDiQ^{m+}$ cations (purple) and $\{Fe–Clan^{n-}\}_\infty$ crankshaft chains (royal blue) and pillar $Clan^{n-}$ ligands (tan) in **2.5**. 112

Figure 2.27 Ball-and-stack (a, c) and spacefilling (b, d) representations of the packing of $PDiQ^{m+}$ cations (purple) with the anionic $[Fe_2(Clan)_3]^{x-}$ network (tan) in **2.5**. 113

Figure 2.28 Bond lengths of $PDiQ^{m+}$ cations in (a) $[PDiQ^{2+}](PF_6)_2$ and (b) **2.5**. Blue = N, black = C. Hydrogen omitted for clarity.. 114

Figure 2.29 Coordination environment and characteristic $Clan^{n-}$ bond lengths around Fe1 and Fe2 in **2.5** at T = 100 K. 117

Figure 2.30 Temperature dependence of the unit cell parameters (*a*, *b*, *c*, β and *V*) for **2.5** as measured by SC-XRD. 118

Figure 2.31 Temperature dependence of the characteristic ligand (a) $d_{C–O}$ and (b) $d_{C–C}$ values in **2.5** as measured by SC-XRD. 120

Figure 2.32 Ball-and-stick (a, c) and spacefilling (b, d) representations showing interactions of DiQ^{m+} cations (purple) with the anionic $[Fe_2(Clan)_3]^{x-}$ network in **2.6**. 124

Figure 2.33 Coordination environment and characteristic $Clan^{n-}$ bond lengths around Fe1 and Fe2 in **2.6** at T = 100 K. 126

Figure 2.34 The anionic $[Fe_2(Fan)_3]^{x-}$ (6,3) honeycomb sheets in **2.7** viewed (a) down the crystallographic (a) *b* axis and (b) *a* axis. 128

Figure 2.35 Geometric distortions of the anionic $[Fe_2(Fan)_3]^{x-}$ (6,3) honeycomb sheets in **2.7**. 129

Figure 2.36 Ball-and-stick (a, c, e) and spacefilling (b, d, f) representations of the interactions between $PDiQ^{m+}$ cations (purple) and the anionic $[Fe_2(Fan)_3]^{x-}$ sheets above (tan) and below (orange) in **2.7**. 131

Figure 2.37 Non-covalent interactions between $PDiQ^{m+}$ (purple) and the anionic $[Fe_2(Fan)_3]^{x-}$ network in **2.7**. 132

Figure 2.38 Packing of $PDiQ^{m+}$ cations (purple) and the anionic $[Fe_2(Fan)_3]^{x-}$ sheets in **2.7**. View down crystallographic (a) *b* axis showing cations lining the alternate walls of the spacious 1D hexagonal channels, and (b) *c* axis showing AA′AA′ stacking of anionic sheets. 133

Figure 2.39 Characteristic Fan^{n-} bonds lengths and coordination environment around Fe in **2.7**. 135

Chapter 3

Figure 3.1 The anionic $[Fe_2(Clan)_3]^{x-}$ (6,3) honeycomb sheets in $\mathbf{3.1^{Cl}a}$ viewed (a) along the crystallographic *c* axis and (b) *a* axis.. 177

Figure 3.2 Synchrotron P-XRD (λ = 0.77493 Å) pattern of an MeCN slurry of $\mathbf{3.1^{Cl}a}$ (red, *T* = 250 K) and calculated pattern (black, *T* = 240 K) from SC-XRD of $\mathbf{3.1^{Cl}a}$. 178

Figure 3.3 P-XRD (λ = 1.54184 Å) pattern of an MeCN slurry of **3.2** (dark green, *T* = 250 K), calculated pattern (pale green) from indexed experimental P-XRD and calculated pattern (black, *T* = 100 K) from SC-XRD of **3.2**. 179

Figure 3.4 Ball-and-stick (a, c, e) and spacefilling (b, d, f) representations of the interactions of the $PhenQ^{m+}$ cation (purple) with the anionic $[Fe_2(Clan)_3]^{x-}$ sheets above (tan) and below (orange) in **3.1^{Cl}a**. 180

Figure 3.5 Inclinations of the mean ligand and $PhenQ^{m+}$ planes in (a) **3.1^{Cl}a** and (b) **3.1^{F}** 181

Figure 3.6 Alternating stacking of $PhenQ^{m+}$ (purple) with ligands in the anionic $[Fe_2(Clan)_3]^{x-}$ sheets in **3.1^{Cl}a**. 182

Figure 3.7 Coordination environment and characteristic $Clan^{n-}$ bond lengths around (a) Fe in **3.1^{Cl}a** and (b) Zn in **3.2** at T = 100 K. 184

Figure 3.8 Bond lengths in $PhenQ^{m+}$ moieties in (a) $(PhenQ^{2+})Br_2$, (b) **3.1^{Cl}a** and (c) **3.2**. 185

Figure 3.9 Arrangement of $\mathbf{L_1}$ (blue, $Clan^{3-\bullet}$) and $\mathbf{L_2}$ (pink, $Clan^{2.5-}$) ligands giving $\{Fe^{III}–\mathbf{L_2}\}_\infty$ chains bridged by $\mathbf{L_1}$, which produces the anionic $[Fe_2(Clan)_3]^{2-}$ sheets in **3.1^{Cl}a**. 188

Figure 3.10 Temperature dependence of the cell parameters (a, b, c, β and V) as measured by SC-XRD for **3.1^{Cl}a**. 189

Figure 3.11 Temperature dependence of the ligand (a) $d_{C–O}$ and (b) characteristic $d_{C–C}$ values in **3.1^{Cl}a** as measured by SC-XRD. 191

Figure 3.12 Normalised ATR FT-IR spectra of **3.1^{Cl}a** (red), **3.1^{Cl}b** (blue) and **3.2** (green) collected under ambient conditions in air. ... 193

Figure 3.13 Distortion of the hexagonal channels and changes to the Fe···Fe···Fe angles for (a) **3.1^{Cl}a** and (b) **3.1^{Cl}b**. 194

Figure 3.14 Electron density difference ($F_O–F_C$) maps for (a, c, e) **3.1^{Cl}a** and (b, d, f) **3.1^{Cl}b**. 195

Figure 3.15 P-XRD (λ = 1.54184 Å) patterns of isolated **3.1^{Cl}b** at T = 240 K (navy) and T = 100 K (royal blue), calculated pattern (pale blue) from indexed experimental P-XRD pattern, and calculated pattern (black) from SC-XRD of **3.1^{Cl}b**. 196

Figure 3.16 Thermogravimetric analyses of (a, red) **3.1^{Cl}a**, (b, blue) **3.1^{Cl}b** and (c, green) **3.2** at a scan rate of 5 °C min^{-1} in a flow of N_2. 198

Figure 3.17 ^{57}Fe Mössbauer spectra of **3.1^{Cl}b** at T = 294 K (upper) and T = 5.8 K (lower). 200

Figure 3.18 Digital photograph of a sample of **3.1^{Cl}b** showing the dark-to-black colour of the crystals. 202

Figure 3.19 Normalised diffuse-reflectance UV-Vis-NIR spectra of **3.1^{Cl}b** (blue) and $(Et_4N)_2[Fe_2(Clan)_3]$ (orange).[14] 202

Figure 3.20 Tauc plot of the diffuse-reflectance UV-Vis-NIR data for **3.1^{Cl}b** showing the corresponding optical band gap (E_g). 203

Figure 3.21 Deconvolution of the diffuse-reflectance UV-Vis-NIR spectrum of **3.1^{Cl}b**..... 205

Figure 3.22 Cyclic voltammograms of solid **3.1^{Cl}b** in 0.1 M $(Et_4N)PF_6$/MeCN at various scan rates. 209

Figure 3.23 Temperature dependence of the dc magnetic susceptibility temperature product ($\chi_M T$) of **3.1^{Cl}b** collected in 1 kOe (dark blue) and 10 kOe (pale blue) applied dc field. 212

Figure 3.24 Inverse magnetic susceptibility ($1/\chi_M$) versus T for **3.1^{Cl}b** measured in an applied dc field (H_{dc}) of 1 kOe. Curie-Weiss fit (red) in the region T = 250–300 K, for calculation of the Weiss constant (Θ)..... 213

Figure 3.25 Variable-temperature field cooled (FC, closed circles) and zero-field cooled (ZFC, open circles) dc magnetic susceptibility for **3.1^{Cl}b** measured under an applied dc field (H_{dc}) of 0.1 kOe. 214

Figure 3.26 Temperature dependence of the in-phase (χ_M') and out-of-phase (χ_M'') ac susceptibility of **3.1^{Cl}b** collected in 0 Oe applied dc field over the range T = 1.8–80 K.....216

Figure 3.27 Temperature dependence of the in-phase (χ_M') and out-of-phase (χ_M'') ac susceptibility of **3.1^{Cl}b** collected in 0 Oe applied dc field over the range T = 15–37 K.....217

Figure 3.28 Magnetisation isotherms of **3.1^{Cl}b** measured in the range T = 2–20 K. 218

Figure 3.29 Field dependence of the magnetisation of **3.1^{Cl}b**. Inset shows expansion around the hysteresis loops. 219

Figure 3.30 Representative variable-temperature current-bias (*i*-*v*) plot for the premier two-point pressed pellet device of **3.1^{Cl}b** (Device 3).....221

Figure 3.31 Arrhenius plot of the temperature dependence for the electrical conductivity for the premier two-point pressed pellet device of **3.1^{Cl}b**.....222

Figure 3.32 Schlenk filtration procedure for isolation of **3.1^{Cl}b** under inert atmosphere conditions.....230

Chapter 4

Figure 4.1 The anionic $[Fe_2(Fan)_3]^{x-}$ (6,3) honeycomb sheet in *mP* **4.1a** viewed almost down the crystallographic *c* axis.....252

Figure 4.2 The Fe···Fe···Fe angles in the anionic $[Fe_2(Fan)_3]^{x-}$ (6,3) honeycomb sheets of *mP* 4.1a viewed along the crystallographic *c* axis.....253

Figure 4.3 ABAB stacking of the anionic $[Fe_2(Fan)_3]^{x-}$ A (tan) and B (orange) sheets in *mP* **4.1a**.....254

Figure 4.4 Ball-and-stick (a, c, e) and spacefilling (b, d, f) representations of the interactions of the MeV^{m+} cation (purple) with the anionic $[Fe_2(Fan)_3]^{x-}$ sheets above (tan) and below (orange) in *mP* **4.1a**. 255

Figure 4.5 Views of the stacking of the anionic $[Fe_2(Fan)_3]^{x-}$ sheets (orange) with MeV^{m+} cations (purple) in *mP* **4.1a**. 257

Figure 4.6 View along crystallographic (a) *a* axis and (b) *c* axis showing calculated solvent-accessible void space in *mP* **4.1a**..... 258

Figure 4.7 Coordination environment and characteristic Fan^{n-} bond lengths around Fe1 and Fe2 in *mP* **4.1a** at T = 100 K. 262

Figure 4.8 Arrangement of $\mathbf{L_1}$, $\mathbf{L_2}$ (pale blue, $Fan^{3-\bullet}$) and $\mathbf{L_3}$ (tan, Fan^{2-}) ligands giving paramagnetic pseudo-1D $\{Fe^{III}–Fan^{3-\bullet}\}_\infty$ chains, bridged by diamagnetic $\mathbf{L_3}$ ligands, forming the anionic $[Fe_2(Fan)_3]^{2-}$ sheets in *mP* **4.1a**. 263

Figure 4.9 Temperature dependence of the cell parameters (*a*, *b*, *c*, *β*, *V*) as measured by SC-XRD for *mP* **4.1a**. 264

Figure 4.10 Temperature dependence of the characteristic (a) $d_{C–O}$ and (b) $d_{C–C}$ values in *mP* **4.1a** as measured by SC-XRD. 266

Figure 4.11 Synchrotron P-XRD (λ = 0.58835 Å) pattern of an MeCN slurry of bulk *mP* **4.1a** (pale red, T = 250 K) and calculated pattern from SC-XRD of *mP* **4.1a** (black, T = 240 K)..... 267

Figure 4.12 Synchrotron P-XRD (λ = 0.58835 Å) pattern of isolated $(MeV)[Fe_2(Fan)_3]\cdot y$MeCN (**4.1a**, dark red, T = 100 K), an MeCN slurry of bulk *mP* **4.1a** (pale red, T = 250 K), and calculated pattern from SC-XRD of *mP* **4.1a** (black, T = 240 K)..... 269

Figure 4.13 Synchrotron P-XRD (λ = 0.58835 Å) pattern of isolated $(MeV)[Fe_2(Fan)_3]\cdot y$MeCN (**4.1a**, dark red, T = 100 K) and calculated pattern from SC-XRD of *aP* **4.1a** (black, T = 100 K)..... 270

Figure 4.14 Anionic $[Fe_2(Fan)_3]^{2-}$ sheet geometry and Fe···Fe···Fe angles in (a) *mP* **4.1a** and (b) *aP* **4.1a**. 272

Figure 4.15 ATR FT-IR spectra of (MeV)$[Fe_2(Fan)_3]\cdot y$MeCN (*aP* **4.1a**, red) and (MeV)$[Fe_2(Fan)_3]\cdot y$DMF (**4.1b**, blue) collected at room-temperature in air. 275

Figure 4.16 The anionic $[Fe_2(Fan)_3]^{x-}$ sheet geometry and Fe···Fe···Fe angles in **4.1b**. 277

Figure 4.17 Synchrotron P-XRD (λ = 0.58835 Å) pattern of isolated **4.1b** (blue, T = 100 K) and calculated pattern from SC-XRD of **4.1b** (black, T = 100 K). 279

Figure 4.18 Thermogravimetric analyses of (a, red) *aP* **4.1a**, (b, blue) **4.1b** and corresponding rates of mass loss (green) at a scan rate of 5 °C min^{-1} in a flow of N_2. 281

Figure 4.19 ^{57}Fe Mössbauer spectra of *aP* **4.1a** measured at T = 293 K (upper), T = 80 K (middle) and T = 6 K (lower). The fitted spectra correspond to Fe^{III} (blue) and Fe^{II} (red) sites. 283

Figure 4.20 ^{57}Fe Mössbauer spectra of **4.1b** in an eicosane matrix measured at T = 295 K (upper) and T = 5.8 K (lower). The experimental spectra (black) were fitted (blue) with a quadrupole doublet at 295 K and a sextet at 5.8 K. 287

Figure 4.21 Normalised diffuse-reflectance UV-Vis-NIR spectra of *aP* **4.1a** (red), **4.1b** (blue) and $(Et_4N)_2[Fe_2(Fan)_3]$ (teal). 290

Figure 4.22 Deconvolution of the diffuse-reflectance UV-Vis-NIR spectra of (a) *aP* **4.1a**, and (b) **4.1b**. 293

Figure 4.23 Tauc analysis on the experimental UV-Vis-NIR data of (a) *aP* **4.1a** (red) and (b) **4.1b** (blue) showing estimation of the corresponding optical band gaps (E_g, green) 296

Figure 4.24 Cyclic voltammograms of solid *aP* **4.1a** in 0.5 M $LiBF_4$/MeCN at (a) 20 mV s^{-1} (purple), (b) 50 mV s^{-1} (blue), (c) 100 mV s^{-1} (green), and (d) 200 mV s^{-1} (orange). 298

Figure 4.25 Cyclic voltammograms of solid *aP* **4.1a** in 0.1 M $(Et_4N)PF_6$/ MeCN at (a) 20 mV s^{-1} (purple), (b) 50 mV s^{-1} (blue), (c) 100 mV s^{-1} (green), (d) 200 mV s^{-1} (orange), and (e) 500 mV s^{-1} (red). 301

Figure 4.26 Representative variable-temperature current-bias plots for the premier two-point pressed pellet devices of (a) *aP* **4.1a** (Device 4) and (b) **4.1b** (Device 2). 307

Figure 4.27 Arrhenius plot of the temperature dependence of the electrical conductivity for the premier two-point devices of *aP* **4.1a** (red, Device 4) and **4.1b** (blue, Device 3). 308

Chapter 5

Figure 5.1 The anionic $[Fe_2(Clan)_3]^{x-}$ (6,3) honeycomb sheets in **5.1** viewed (a) down the crystallographic *a* axis and (b) along the plane of the anionic sheets parallel to the crystallographic (111) plane. 334

Figure 5.2 Ball-and-stick (a, c, e) and spacefilling (b, d, f) representations of the interactions of the MeV^{m+} cations (purple) with the anionic $[Fe_2(Clan)_3]^{x-}$ sheets above (tan) and below (orange) in **5.1**. 335

Figure 5.3 C–H···O interactions (dashed grey) between MeV^{m+} (purple) and $\mathbf{L_3}$ (yellow) in anionic $[Fe_2(Clan)_3]^{x-}$ sheets above and below. $\mathbf{L_1}$ and $\mathbf{L_2}$ shown in pale blue. 336

Figure 5.4 Alternating stacking of MeV^{m+} (purple) with $\mathbf{L_1}$ ligands in the anionic $[Fe_2(Clan)_3]^{x-}$ sheets (orange) in **5.1**. 337

Figure 5.5 Characteristic $Clan^{n-}$ bond lengths and coordination environment around Fe in **5.1** at T = 100 K. 339

Figure 5.6 Arrangement of $\mathbf{L_1}$, $\mathbf{L_2}$ (pale blue, $Clan^{3-\bullet}$) and $\mathbf{L_3}$ (tan, $Clan^{2-}$) ligands forming pseudo-1D $\{Fe^{III}–Clan^{3-\bullet}\}_\infty$ chains bridged by $\mathbf{L_3}$ producing the anionic $[Fe_2(Clan)_3]^{2-}$ sheets in **5.1**. 340

Figure 5.7 Temperature dependence of the unit cell parameters (*a*, *b*, *c*, *α*, *β*, *γ* and *V*) as measured by SC-XRD for **5.1**.....341

Figure 5.8 Temperature dependence of the characteristic ligand (a) $d_{C–O}$ and (b) $d_{C–C}$ values in **5.1** as measured by SC-XRD.....343

Figure 5.9 Synchrotron P-XRD (λ = 0.58835 Å) pattern of an MeCN slurry of bulk **5.1** (pale red, T = 250 K), and calculated pattern (black, T = 240 K) from SC-XRD of **5.1**. 345

Figure 5.10 Synchrotron P-XRD (λ = 0.58835 Å) pattern of isolated bulk **5.1** (**5.2**, red, T = 100 K), an MeCN slurry of bulk **5.1** (pale red, T = 250 K), and calculated pattern (black, T = 240 K) from SC-XRD of as-synthesised **5.1**.....346

Figure 5.11 Synchrotron P-XRD (λ = 0.58835 Å) pattern of **5.2** (isolated **5.1**) (red, T = 100 K), and calculated pattern (black, T = 100 K) from SC-XRD of **5.2**. 347

Figure 5.12 Ball-and-stick (a, c, e) and spacefilling (b, d, f) representations of the interactions of the MeV^{m+} cation (purple) with the Fe1 (tan) and Fe2 (orange) anionic $[Fe_2(Clan)_3]^{x-}$ layers in **5.2**.....350

Figure 5.13 Stacking of the Fe1 (tan) and Fe2 (orange) anionic $[Fe_2(Clan)_3]^{x-}$ sheets, and location of the MeV^{m+} (purple) cations in **5.2**. 351

Figure 5.14 ATR FT-IR spectrum of **5.2** collected at room-temperature in air. 353

Figure 5.15 ^{57}Fe Mössbauer spectra of **5.1** collected immediately following isolation from an MeCN slurry at T = 293 K(upper), T = 80 K (middle) and T = 6 K (lower). 357

Figure 5.16 Normalised diffuse reflectance UV-Vis-NIR spectra of **5.2** (red) and $(Et_4N)_2[Fe_2(Clan)_3]$·solvent (green). 359

Figure 5.17 Deconvolution of the diffuse-reflectance UV-Vis-NIR spectrum of **5.2**.....362

Figure 5.18 Tauc analysis on the experimental UV-Vis-NIR data of **5.2** (red) showing estimation of the optical band gap (E_g, green). 365

Figure 5.19 Cyclic voltammograms of solid **5.2** in 0.5 M $LiBF_4$/MeCN at (a) 20 mV s^{-1} (purple), (b) 50 mV s^{-1} (blue), (c) 100 mV s^{-1} (green), and (d) 200 mV s^{-1} (red). 367

Figure 5.20 Narrow-range cyclic voltammograms (ca. −1.4 to −0.2 V vs. Fc/Fc^+) of solid **5.2** in 0.5 M $LiBF_4$/MeCN at (a) 20 mV s^{-1} (purple), (b) 50 mV s^{-1} (blue), (c) 100 mV s^{-1} (green), and (d) 200 mV s^{-1} (red)..... 371

Figure 5.21 Representative variable-temperature current-bias (*i*-*v*) plot for the premier two-point pressed pellet device of **5.2** (Device 3). 374

Figure 5.22 Arrhenius plot of the temperature dependence of the electrical conductivity for the premier two-point pressed pellet device of **5.2** (Device 3). 375

Figure 5.23 Interlayer Coulombic interactions between cations (purple) and anionic $[Fe_2(Clan)_3]^{2-}$ sheets (tan and orange) in (a) $(^nPr_4N)_2[Fe_2(Clan)_3]$, and (b) **5.2**. 376

Chapter 7

Figure 7.1 (Top) components of two-electrode electrical conductivity screw cell. (Bottom) Assembled two electrode screw cell containing sample (black) pressed between copper dies, held in PLA cell holder..... 419

Appendix A

Figure A.1 Unfiltered distributions of unique crystallographic (a) $d_{C–O}$ (bin size 0.005 Å) and (b) diagnostic $d_{C–C}$ (bin size 0.01 Å) values for *M*–$Clan^{2-}$ reported to date. A6

Appendix B

Figure B.1 Arrhenius fits of the variable-temperature electrical conductivity for **3.1^{Cl}b** in four independent pressed pellet devices. B5

Figure B.2 Arrhenius fits of the variable-temperature electrical conductivity for *aP* **4.1a** in four independent pressed pellet devices. B6

Figure B.3 Arrhenius fits of the variable-temperature electrical conductivity for **4.1b** in four independent pressed pellet devices. B7

Figure B.4 Arrhenius fits of the variable-temperature electrical conductivity for **5.2** in four independent pressed pellet devices. B8

List of Schemes

Chapter 1

Scheme 1.1 The Creutz-Taube cation $[(NH_3)_5Ru(\mu\text{-pyz})Ru(NH_3)_5]^{5+}$ which exhibits electron delocalisation between the Ru^{II} and Ru^{III} states by IVCT. 9

Scheme 1.2 Schematics of 2D graphene-like layered coordination polymers synthesised using (a) hexasubstituted benzene (HEB) and (b) hexasubstituted triphenylene (HETP) ligands. 26

Scheme 1.3 Magnetic behaviour in extended frameworks in the absence of an applied field..... 33

Scheme 1.4 Electron transfer mechanisms in D_2A coordination polymers. Degenerate $D^0D^+A^{-\bullet}$ valence states can either be localised i.e. $D^0D^+A^{-\bullet}$ formulation or undergo IVCT i.e. delocalised $D^{+0.5}{}_2A^{-\bullet}$ formulation. 38

Scheme 1.5 Commonly observed valence states of tetraoxolene anions (anilates, X = H, F, Cl, Br, I, Me, NO_2, CN etc.)..... 43

Scheme 1.6 The reversible redox processes in 4,4′-bipyridyl- (upper) and 2,2′-bipyridyl-derived (lower) viologen cations. 55

Chapter 2

Scheme 2.1 Structures of the tetraoxolene ligand precursors and viologen or viologen-like cations used in Chapter 2. 77

Scheme 2.2 Bridging bis-bidentate coordination mode of Xan^{2-}, and bridging mono and bi-dentate coordination mode of Xan^{2-}..... 104

Chapter 3

Scheme 3.1 Structures of the tetraoxolene ligand precursors and viologen-like cation used in Chapter 3..... 174

Chapter 4

Scheme 4.1 Solvent exchange and isolation procedure performed upon as-synthesised (MeV)[$Fe_2(Fan)_3$]·5.3 (*mP* **4.1a**) yielding *aP* **4.1a** and **4.1b**.....268

Scheme 4.2 Proposed ion insertion processes operating during cyclic voltammetry of *aP* **4.1a** in 0.1 M (Et_4N)PF_6/MeCN.....304

Appendix A

Scheme A.1 (a) Bridging and (b) terminal coordination modes of Clan^{n-} ligands. Crystallographically unique (c) C–O, (d) diagnostic C–C, and (e) Fe–O bond used to determine mean $d_{C–O}$, $d_{C–C}$ and $d_{Fe–O}$ values for *M*–Clan^{n-} and Fe–Clan^{n-} compounds published within the CSD. A4

List of Tables

Chapter 2

Table 2.1 Analysis of the possible coordination geometries quantified using the CShM parameters for the two Fe sites in **2.5**. 115

Table 2.2 Fe–O bond lengths in **2.5** at T = 100 K as determined by SC-XRD. 116

Table 2.3 Analysis of the possible coordination geometries quantified using CShM parameters for the two Fe sites in **2.6**. 122

Table 2.4 Fe–O bond lengths in **2.6** at T = 100 K as determined by SC-XRD. 125

Table 2.5 Crystallographic data for $\mathbf{2.1_{Mn}}$, $\mathbf{2.1_{Cd}}$ and **2.2a**. 150

Table 2.6 Crystallographic data for $\mathbf{2.3_{Mn}}$, $\mathbf{2.3_{Cd}}$ and **2.4**. 153

Table 2.7 Crystallographic data of $(PDiQ)(PF_6)_2$ 155

Table 2.8 Crystallographic data of $(PDiQ)[Fe_2(Clan)_3]\cdot 4(acetone)$ (**2.5**) at various temperatures. 157

Table 2.9 Crystallographic data for **2.6** and **2.7**. 161

Chapter 3

Table 3.1 CShM analyses of the possible metal coordination geometries in $\mathbf{3.1^{Cl}a}$, $\mathbf{3.1^{F}}$, $\mathbf{3.1^{Br}}$ and **3.2**. 176

Table 3.2 Mean $d_{Fe–O}$ values in $\mathbf{3.1^{Cl}a}$, $\mathbf{3.1^{F}}$ and $\mathbf{3.1^{Br}}$ at T = 100 K as determined by SC-XRD. 186

Table 3.3 ^{57}Fe Mössbauer spectral parameters for $\mathbf{3.1^{Cl}b}$. 200

Table 3.4 Spectral data of the deconvoluted diffuse reflectance spectra of $\mathbf{3.1^{Cl}b}$ in comparison with the published data for $(Et_4N)_2[Fe_2(Clan)_3]$. 206

Table 3.5 Crystallographic data of $(PhenQ)[Fe_2(Clan)_3]\cdot 4.25MeCN\cdot 6.3H_2O$ ($\mathbf{3.1^{Cl}a}$) measured at several temperatures. 235

Table 3.6 Crystallographic data of **3.1^{F}**, **3.1^{Br}** and **3.1^{Cl}b**. 238

Table 3.7 Crystallographic data of **3.2** and [PhenQ]Br_2. 239

Chapter 4

Table 4.1 Analysis of the possible coordination geometries quantified using the CShM parameters for the two Fe sites in *mP* **4.1a**, and other Fe–fluoranilate frameworks reported in this thesis and literature. 259

Table 4.2 CShM analyses of the possible coordination geometries of the two Fe sites in the as-synthesised primitive monoclinic (*mP*) phase and isolated primitive triclinic (*aP*) phases of **4.1a**. ... 273

Table 4.3 CShM analyses of the possible coordination geometries of the two Fe sites in **4.1b**. 276

Table 4.4 Fitted ^{57}Fe Mössbauer spectral parameters for *aP* **4.1a**. 284

Table 4.5 Fitted ^{57}Fe Mössbauer spectral parameters for **4.1b**. 287

Table 4.6 Spectra data of the deconvolution diffuse-reflectance UV-Vis-NIR spectra of *aP* **4.1a** and **4.1b**. 294

Table 4.7 Disagreeable reflections omitted from the structure refinements of *mP* **4.1a** at various temperatures. 314

Table 4.8 Crystallographic data for the primitive monoclinic phase of (MeV)[Fe_2(Fan)$_3$]·5.3MeCN (*mP* **4.1a**) measured at several temperatures. 316

Table 4.9 Crystallographic data for *aP* **4.1a** and **4.1b**. 321

Chapter 5

Table 5.1 Analysis of the possible Fe coordination geometries in (MeV)[Fe_2(Clan)$_3$]·6MeCN (**5.1**) quantified using CShM parameters. 333

Table 5.2 CShM analyses of the possible coordination geometries of the Fe sites in **5.1** and **5.2**. 352

Table 5.3 ^{57}Fe Mössbauer spectral parameters for **5.1** measured immediately following isolation from a slurry in MeCN. 357

Table 5.4 Spectral data of the deconvoluted diffuse-reflectance UV-Vis-NIR spectrum of **5.2**, in comparison with the published data for **3.1^{Cl}b** (Section 3.2.5) and $(Et_4N)_2[Fe_2(Clan)_3]$. 363

Table 5.5 Crystallographic data for the $(MeV)[Fe_2(Clan)_3]\cdot 6MeCN$ (**5.1**) measured at several temperatures. 382

Table 5.6 Crystallographic data for **5.2**. 386

Chapter 6

Table 6.1 Inter-ring torsions exhibited by viologen cations, in selected salts reported in literature, and tetraoxolene coordination polymers this thesis..... 399

Table 6.2 Mixed-valence Fe–tetraoxolene coordination polymers reported in this thesis. 400

Appendix A

Table A.1 Average $d_{C–O}$ and diagnostic $d_{C–C}$ values of Clan$^{n–}$ moieties in *M*–Clan$^{2–}$ compounds reported to date. A7

Table A.2 Average $d_{C–O}$ and diagnostic $d_{C–C}$ values of Clan$^{n–}$ moieties in *M*–Clan$^{2.67–}$ and *M*–Clan$^{3–\bullet}$ compounds reported to date. ... A25

Table A.3 Average $d_{C–O}$ and diagnostic $d_{C–C}$ values of Clan$^{n–}$ moieties in *M*–Clan$^{4–}$ compounds reported to date. A27

Table A.4 Average $d_{Fe–O}$, and $d_{C–O}$ and diagnostic $d_{C–C}$ values of Clan$^{n–}$ moieties of Fe–Clan$^{n–}$ compounds reported to date..... A28

Table A.5 Ligand abbreviations used in Table A.1 through Table A.4. ..... A32

Appendix B

Table B.1 Pellet thickness and measured transport properties of four independent two-point pressed pellet devices of **3.1^{Cl}b**..... B3

Table B.2 Pellet thickness and measured transport properties of four independent two-point pressed pellet devices of *aP* **4.1a**. B3

Table B.3 Pellet thickness and measured transport properties of four independent two-point pressed pellet devices of **4.1b**. B4

Table B.4 Pellet thickness and measured transport properties of four independent two-point pressed pellet devices of **5.2**. B4

Nomenclature

Common Abbreviations

0D	0-dimensional
1D	1-dimensional
2D	2-dimensional
3D	3-dimensional
ac	alternating current
AFM	antiferromagnetic
ATR	attenuated total internal reflectance
CSD	Cambridge Crystallographic Database
CT	charge-transfer
D-A	donor-acceptor
dc	direct current
FC	field-cooled
Fc/Fc^+	ferrocene/ferrocenium
FiM	ferrimagnetic
FM	ferromagnetic
FT-IR	Fourier transform infrared
IVCT	intervalence charge-transfer
LIB	lithium-ion battery
MOF	metal-organic framework
NMR	nuclear magnetic resonance
P-XRD	powder X-ray diffraction
SCM	single-chain magnet
SC-XRD	single-crystal X-ray diffraction
TGA	thermogravimetric analysis
UV-Vis-NIR	ultraviolet-visible-near infrared
ZFC	zero field-cooled

Cations

DiQ^{m+}	6,7-dihydrodipyrido[1,2-*a*:2′,1′-*c*]pyrazinediium, where *m* = 0, 1, 2
MeV^{m+}	*N*,*N*′-dimethyl-4,4′-bipyridinium, where *m* = 0, 1, 2
$PDiQ^{m+}$	dipyrido[1,2-*a*:2′,1′-*c*]pyrazinediium, where *m* = 0, 1, 2
$PhenQ^{m+}$	5,6-dihydropyrazino[1,2,3,4-*lmn*][1,10]-phenanthrolinediium, where where *m* = 0, 1, 2
$^{n}Bu_4N^+$	tetra-*n*-butylammonium
Et_4N^+	tetraethylammonium
$^{n}Hx_4N$	tetra-*n*-hexylammonium
$Me_2NH_2^+$	dimethylammonium
Me_4N^+	tetramethylammonium
$^{n}Pr_4N^+$	tetra-*n*-propylammonium
TAG^+	tris(amino)guanidinium

Ligands, Donors and Acceptors

H_2dhbq	2,5-dihydroxy-1,4-benzoquinone
H_2Xan	3,6-disubstituted-2,5-dihydroxy-1,4-benzoquinone (X = F, Cl, Br, I, Me, CN, NO_2 etc.), anilic acid
H_4Xan	3,6-disubstituted-1,2,4,5-tetrahydroxybenzene (X = F, Cl, Br, I, Me, CN, NO_2 etc.)
$dhbq^{n-}$ or Xan^{n-}	tetraoxolene anion, where *n* = 2, 3 or 4 and X = F, Cl, Br, I, Me, CN, NO_2 etc.
2,2′-bpy	2,2′-bipyridine
4,4′-bpy	4,4′-bipyridine
$CNClan^{2-}$	3-chloro-6-cyano-2,5-dihydroxy-1,4-benzoquinone, cyanochloranilate
$[Ru_2^{II,II}]$	tetracarboxylate-bridged diruthenium(II,II) cluster ($Ru_2(O_2CR)_4$)
Cp	cyclopentadienyl
Cp^*	pentamethylcyclopentadienyl

DCNQI	*N*,*N*′-dicyanoquinodiimine
F_4TCNQ	2,3,5,6-tetrafluoro-7,7,8,8-quinodimethane
Me_2DCNQI	2,5-dimethyl-*N*,*N*′-dicyanoquinodiimine
Me_2TCNQ	2,5-dimethyl-7,7,8,8-tetracyanoquinodimethane
ox^{2-}	oxalate
pyz	pyrazine
TCNE	tetracyanoethylene
TCNQ	7,7,8,8-tetracyanoquinodimethane
TTF	tetrathiafulvalene

Solvents

$CDCl_3$	deuterochloroform
$CHCl_3$	chloroform
CH_2Cl_2	dichloromethane
DMF	*N*,*N*-dimethylformamide
EtOH	ethanol
MeCN	acetonitrile
MeOH	methanol
$PhNO_2$	nitrobenzene
THF	tetrahydrofuran

Parameters

$\langle u^2 \rangle$	mean-squared atomic displacement (Å^2)
a^*, b^*, c^*	reciprocal unit cell lengths (Å^{-1})
A_{cross}	cross-sectional area (cm^2)
D	diameter (mm)
E	electric field strength (V cm^{-1})
E_a	activation energy (eV)
E_A	acceptor electron affinity (eV)
F	structure factor (-)
f_{ADP}	anisotropic displacement parameter (-)

F_C	calculated structure factor (-)
f_{DW}	isotropic displacement parameter (-)
F_O	observed structure factor (-)
g	g-factor (-)
$GooF$	Goodness of fit defined by Equation (7.6) (-)
h, k, l	Miller indices (-)
H	magnetic field strength (Oe)
H_{ac}	ac magnetic field strength (Oe)
H_c	coercive magnetic field strength (Oe)
H_{dc}	dc magnetic field strength (Oe)
i	current (A)
I_D	donor ionisation potential (eV)
J	current density (A cm^2)
J_{AB}	coupling constant (Hz)
k_B	Boltzmann constant (8.6173×10^{-5} eV K^{-1})
L	length (cm)
m	viologen redox state (RV^{m+}), where m = 0, 1, 2
M	sample magnetisation ($N_A\mu_B$)
n	number of reflections (-)
N_A	Avogadro constant (6.0221×10^{23} mol^{-1})
p	number of parameters (-)
R	reflectance (-)
r	resistance (Ω)
R_{int}, R_1, R_2	agreement indices defined by Equations (7.1), (7.2) and (7.3) respectively (-)
S	spin (-)
S_L	ligand spin (-)
S_M	metal spin (-)
S_T	total spin (-)
T	temperature (K)

T_c	critical ordering temperature (K)
T_N	Néel temperature (K)
U_{ij}	components of the atomic displacement tensor, **U** (Å^2), where i = 1, 2, 3 and j = 1, 2, 3
v	voltage drop (V)
w, P, A, B	weighting factors defined by Equations (7.4) and (7.5) respectively (-)
x	tetraoxolene network $[M_2(Xan)_3]^{x-}$ charge state, where x = 0, 1, 2
Γ	$=1-\frac{\Delta\nu_{1/2}}{\Delta\nu_{1/2}^{\circ}}$, Gamma parameter
δ_C	carbon-13 chemical shift (ppm)
δ_H	proton chemical shift (ppm)
$\Delta\nu_{1/2}$	absorption bandwidth at half-height (cm^{-1})
$\Delta\nu_{1/2}^{\circ}$	theoretical absorption bandwidth at half-height (cm^{-1})
θ	scattering angle (°)
λ	wavelength (Å)
μ_B	Bohr magneton (9.2740 × 10^{-24} J T^{-1})
ν_{max}	energy of maximum absorption (cm^{-1})
ρ	electrical resistivity (Ω cm)
σ_0	conductivity Arrhenius pre-exponential (1 S cm^{-1})
σ_T	electrical conductivity at temperature T (S cm^{-1})
χ_M	molar magnetic susceptibility (cm^3 mol^{-1})
χ_M'	in-phase ac molar magnetic susceptibility (cm^3 mol^{-1})
χ_M''	out-of-phase ac magnetic susceptibility (cm^3 mol^{-1})
ω, φ, χ, κ	goniometer angles (°)

Third Party Copyright Materials

The following content has been adapted or reproduced from third party sources with the express permission of the copyright holder.

Citation Information for Third Party Copyright Material		Page
Figure 1.9	Adapted with permission from Y. Kobayashi *et al.*, *Chem. Mater.* **2010**, *22*, 4120-4122. Copyright © 2010 American Chemical Society	21
Figure 1.10	Adapted with permission from L. Sun *et al.*, *J. Am. Chem. Soc.* **2015**, *137*, 6164-6167. Copyright © 2015 American Chemical Society.	23
Figure 1.11	Adapted with permission from L. S. Xie *et al.*, *J. Am. Chem. Soc.* **2018**, *140*, 7411-7414. Copyright © 2018 American Chemical Society.	25
Scheme 1.2	Adapted with permission from L. S. Xie *et al.*, *Chem. Rev.* **2020**, *120*, 8536-8580. Copyright © 2018 American Chemical Society.	26
Figure 1.12	Adapted with permission from T. C. Narayan *et al.*, *J. Am. Chem. Soc.* **2012**, *134*, 12932-12935. Copyright © 2012 American Chemical Society.	31
Figure 1.14b	Adapted with permission from H. Miyasaka *et al.*, *J. Am. Chem. Soc.* **2006**, *128*, 11358-11359. Copyright © 2006 American Chemical Society.	39
Figure 1.15c & d	Adapted with permission from N. Motokawa *et al.*, *Angew. Chem. Int. Ed.* **2008**, *47*, 7760-7763. Copyright © 2008 WILEY-VCH Verlag GmbH & Co. KGaA.	40
Figure 1.16b	Adapted with permission from M. Atzori *et al.*, *Inorg. Chem.* **2013**, *52*, 10031-10040. Copyright © 2013 American Chemical Society.	45

Citation Information for Third Party Copyright Material		Page
Figure 1.17	Adapted with permission from K. Taniguchi *et al.*, *Chem. Mater.* **2017**, *29*, 10053-10059. Copyright © 2017 American Chemical Society.	47
Figure 1.18b	Adapted with permission from L. E. Darago *et al.*, *J. Am. Chem. Soc.* **2015**, *137*, 15703-15711. Copyright © 2015 American Chemical Society.	49
Figure 1.18d	Adapted with permission from J. A. DeGayner *et al.*, *J. Am. Chem. Soc.* **2017**, *139*, 4175-4184. Copyright © 2017 American Chemical Society.	49
Figure 1.19a	Adapted with permission from L. E. Darago *et al.*, *J. Am. Chem. Soc.* **2015**, *137*, 15703-15711. Copyright © 2015 American Chemical Society.	52
Figure 1.19b	Adapted with permission from J. A. DeGayner *et al.*, *J. Am. Chem. Soc.* **2017**, *139*, 4175-4184. Copyright © 2017 American Chemical Society.	52
Figure 7.1	Reproduced with permission from M. P. van Koeverden *et al.*, *Chem. Mater.* **2020**, *32*, 7551-7563. Copyright © 2020 American Chemical Society.	419

This page intentionally left blank

This page intentionally left blank

Chapter 1 Literature Review

1.1 Introduction 3

1.1.1 Functional Metal-based Materials 3
1.1.2 Designing Molecular Materials 6
1.1.3 Mixed Valency and Redox Activity 9

1.2 Coordination Polymers 10

1.2.1 Functional Coordination Polymers 10
1.2.2 Topology of Coordination Polymers 12
1.2.3 Net Approach to Coordination Polymers 14
1.2.4 Electrical Conductivity in Coordination Polymers 18
1.2.5 Magnetic Coordination Polymers 31

1.3 Tetraoxolene Coordination Polymers 42

1.3.1 Redox Activity of the Tetraoxolenes 42
1.3.2 Magnetic Tetraoxolene Coordination Polymers 43
1.3.3 Electrically Conductive Tetraoxolene Coordination Polymers 50

1.4 Viologens and Viologen-Like Molecules 54

1.5 Thesis Scope 56

1.6 References 58

This page intentionally left blank

1.1 Introduction

1.1.1 Functional Metal-based Materials

From the first brave forays into metallurgy during the Bronze Age, up to the present Technological Age, knowledge of how to process and manufacture metal-based materials has facilitated tremendous advances in human civilisation.[1, 2] Over the last two centuries, conductive, magnetic and electroactive materials have all emerged as essential in modern societies, as they form critical components of devices used in communication, energy storage and conversion, transportation and information processing.[3, 4] This has been driven home in 2020 (and still in 2021!), The Year(s) of Zoom, wherein magnetic, electroactive and conductive materials in batteries, computers, and telecommunication infrastructure have helped societies remain connected and functional, despite the need for physical distance. In addition, counteracting the existential challenges of climate change, and energy and water security among others, will require innovative energy storage and conversion, optoelectronic, sensing and separation devices.[5] Developing novel conducting, magnetic and electroactive materials is therefore an important component of this strategy, in order to achieve the performance and sustainability goals of such emerging technologies.

For many years, the available magnetic, conductive, or electroactive materials have been confined to inorganic compounds constructed from atomic building blocks (Figure 1.1). These compounds are broadly classified as either: bulk metallic or intermetallic compounds, or oxide and oxide-containing compounds.[3, 6] Examples of these include: $SmCo_5$ or $Nd_2Fe_{14}B$ magnets;[7-9] Cu in copper wires; Nb_3Sn superconductors;[10] $BaFe_{12}O_{19}$ in common ferrite magnets; $YBa_2Cu_3O_{7-x}$ or $La[O_{1-x}F_x]FeAs$ high-temperature superconductors;[11-14] layered $LiCoO_2$ in lithium-ion battery cathodes;[15, 16] and IrO_2 or RuO_2 oxygen evolution reaction electrocatalysts.[17, 18] Undoubtedly tremendous strides have been made towards improving the performance of these materials, so they will likely remain technologically important for years to come. However, atom-based inorganic compounds have inherent limitations which could limit future applications. This provides a significant impetus to produce new materials which either overcome the

limitations of existing inorganic compounds, or complement their properties allowing access to technologies not possible using conventional inorganic materials.[3]

For these atom-based inorganic materials, the metal centres are central to the desired properties. Metal centres carry unpaired electrons in either d- or f-orbitals, which when strongly interacting with each other, allow long-range magnetic ordering and permanent magnetism.[4, 19] Secondly, the metal species can exist in multiple redox states, which either facilitates catalytic activity, or provides free charge carriers allowing for long-range charge transport and electrical conductivity. The bonding in these atom-based compounds is either dominated by metal-metal interactions, or on the continuum between covalent and ionic bonding. The highly ionic or covalent bonding in these materials produces inflexible metal coordination geometries, so the network connectivity is extremely difficult to modify.[19, 20] This inflexibility limits the degree to which the structures can be modified, so that substitutional doping within narrow composition ranges is often the only method to vary the physical properties.[8, 14] In addition, the strong bonding present in these materials means that synthesis must occur using energy-intensive high temperature metallurgical-type processes.[21] The close metal-metal distances in these compounds facilitate effective spin exchange and long-range charge transport, required for the materials to have high magnetic ordering temperatures or electrical conductivity.[3] On the other hand, it also results in densely packed structures (Figure 1.1), so that any interaction of the material with the external environment is necessarily confined to the surface.

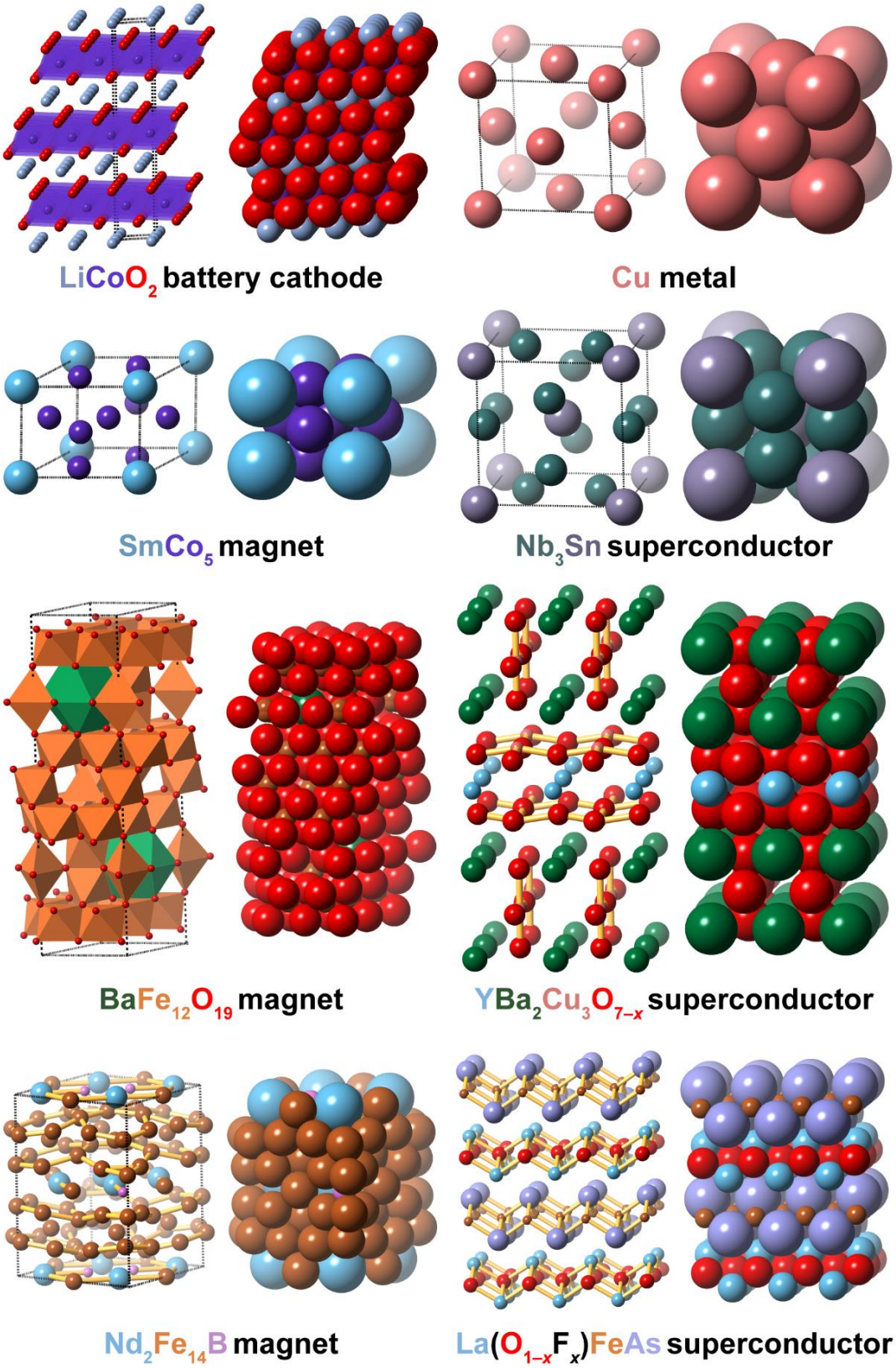


Figure 1.1 Ball-and-stick or polyhedral (left) and spacefilling (right) representations of the structures of common inorganic electroactive, magnetic or conductive materials.

1.1.2 Designing Molecular Materials

In the last four decades, molecular-based magnetic and conductive materials have been posited to replace or supplement dense, inorganic materials in some applications.[4, 21] In contrast to atom-based inorganic materials, molecular materials comprise any combination of organic, organometallic and inorganic molecular building blocks, which affords them several advantages.[21] A large diversity of organic components can be designed and incorporated, giving new materials with useful or even unique combinations of desirable physical properties. Using the vast and ever-expanding toolbox of organic chemical transformations available, parameters such as size and geometry, heteroelement composition or coordinating moieties of the organic components, can be systematically varied.[22, 23] Accurate structure-property relationships can therefore be developed,[24] so molecular materials with the desired conductive or magnetic properties can be reliably predicted and designed. Another advantage of molecular materials is the ease of processing compared to traditional inorganic compounds.[21, 25] For example, both solution-state reactions to synthesise bulk samples, or chemical vapour deposition techniques to produce thin films, can be achieved at mild to moderate temperatures, allowing formation of functional molecular materials on delicate substrates.

Charge-transfer (CT) complexes between electron-rich donors and electron-poor acceptors have featured heavily in the synthesis of conductive and magnetic molecular materials. The CT complex between the organic donor tetrathiafulvalene (TTF) and acceptor 7,7,8,8-tetracyanoquinodimethane (TCNQ) (Figure 1.2a, left), is among the most famous molecular materials. Single-crystal measurements on (TTF)(TCNQ) revealed electrical conductivity in the range ca. 200–600 S cm^{-1}. The electrical conductivity of (TTF)(TCNQ) also increases with decreasing temperature, indicative of metallic conductivity,[26] the discovery of which spurred the field of *'organic metals'*.[22] Structural studies revealed the compound consists of parallel segregated stacks of TTF and TCNQ moieties oriented parallel to the crystallographic *b* axis (Figure 1.2b),[27, 28] with the electrical conductivity highest in this direction. Using a polynitrile acceptor related to TCNQ, the first organic-based magnet was synthesised by co-crystallisation of tetracyanoethylene (TCNE) with the organometallic donor decamethylferrocene ($Fe^{II}Cp^{*}_{2}$) (Figure 1.2a, right), yielding the compound ($Fe^{III}Cp^{*}_{2}$)(TCNE).[29] Analysis of the structure is somewhat complicated by

temperature- and solvent-dependant disorder and polymorphism,[29-31] though broadly consists of 1-dimensional (1D) stacks of alternating $(Fe^{III}Cp^{*}_{2})^{+\bullet}$ cations and $(TCNE)^{-\bullet}$ radical anions (Figure 1.2c). At ca. 4 K, $(Fe^{III}Cp^{*}_{2})(TCNE)$ undergoes spontaneous ferromagnetic (FM) ordering, and is the first example of a permanent magnet containing *p*-orbital spins.[4, 29] Spontaneous ordering arises primarily from FM coupling between the $S = 1/2$ $(Fe^{III}Cp^{*}_{2})^{+\bullet}$ cations and $S = 1/2$ $(TCNE)^{-\bullet}$ radical anions in the 1D stacks.[29] Additional weaker interstack FM and antiferromagnetic (AFM) interactions also occur, giving an overall three-dimensional (3D) magnetic structure.[31] These examples serve to highlight the importance of incorporating radical (either metal- or organic-centred) and redox-active species into molecular materials to produce the desired magnetic and conductive properties.

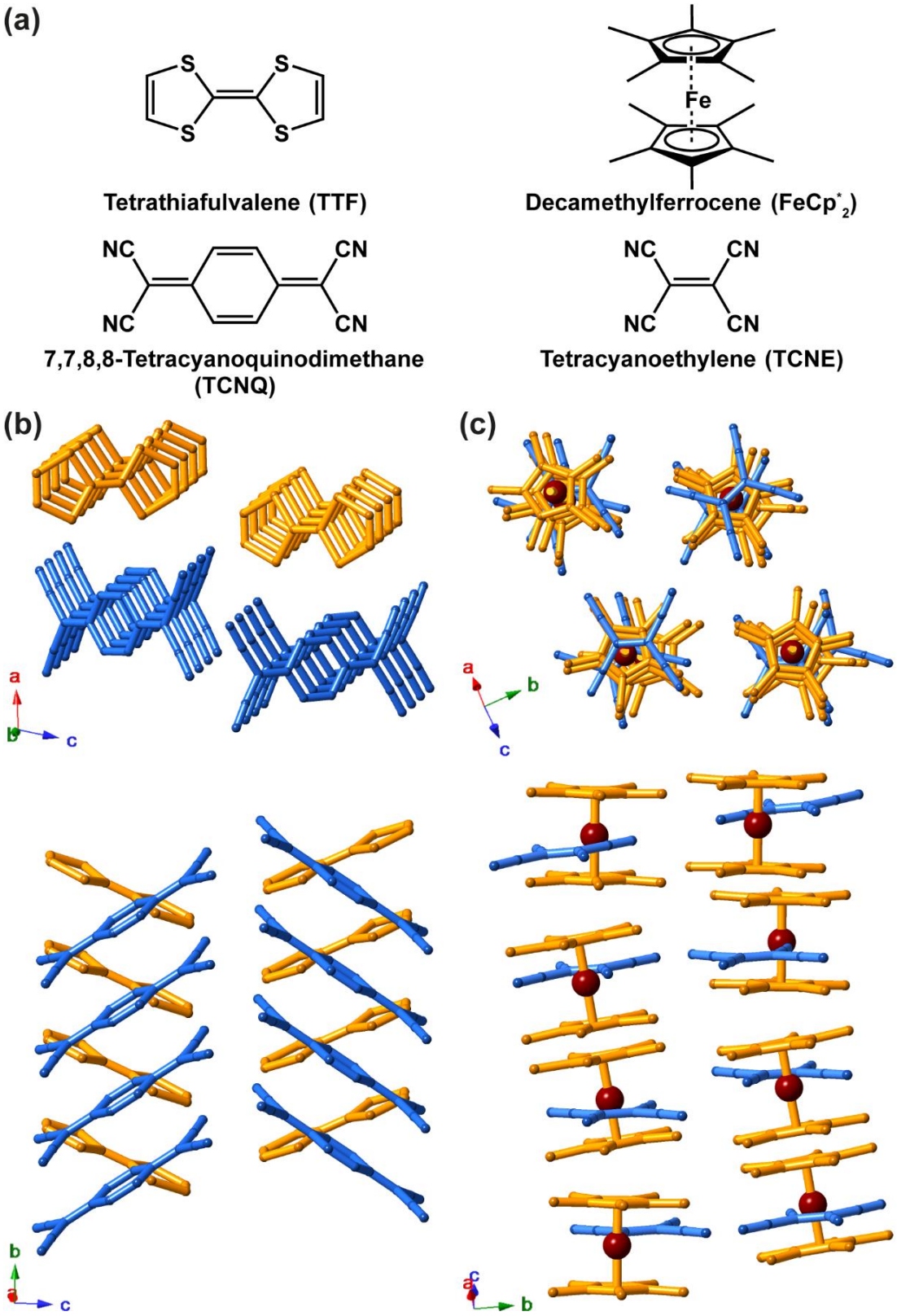
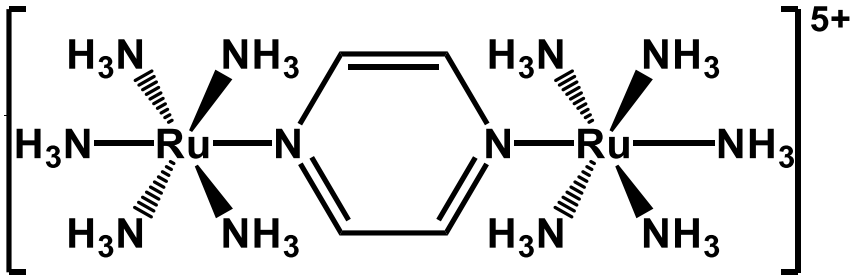


Figure 1.2 (a) The structures of the donors TTF and $Fe^{II}Cp^{*}_{2}$, and acceptors TCNQ and TCNE. (b) Segregated stacking of TTF (orange) and TCNQ (blue) in the organic metal (TTF)(TCNQ). (c) Alternating stacking of $(Fe^{III}Cp^{*}_{2})^{+\bullet}$ (orange) and $TCNE^{-\bullet}$ (blue) radicals in the molecular magnet $(Fe^{III}Cp^{*}_{2})(TCNE)$.

1.1.3 Mixed Valency and Redox Activity

Electrical conductivity in a material can only be achieved when mobile charge carriers are present. Incorporation of redox-active species in multiple valence states, termed *'mixed valency'*, into compounds is one method to introduce free charge carriers.[20, 32] In molecular i.e. zero-dimensional (0D) systems, mixed valency allows electron transfer between the different valence sites; this process is termed intervalence charge transfer (IVCT) and typically gives rise to characteristic absorption bands in the infrared (IR), mid-to-near infrared (NIR) or visible portions of the optical spectrum.[33] An illustrative example of this process in a 0D system is the Creutz-Taube cation $[(NH_3)_5Ru(\mu\text{-pyz})Ru(NH_3)_5]^{5+}$ (pyz = pyrazine) (Scheme 1.1).[34, 35] Though formally an Ru^{II}-Ru^{III} system, the barrier to electron transfer between Ru sites is sufficiently small and electron transfer sufficiently fast, that the electron is delocalised between the two sites. The complex therefore approaches a $[(NH_3)_5Ru^{2.5}(\mu\text{-pyz})Ru^{2.5}(NH_3)_5]^{5+}$ valence state distribution.[36]



Scheme 1.1 The Creutz-Taube cation $[(NH_3)_5Ru(\mu\text{-pyz})Ru(NH_3)_5]^{5+}$ which exhibits electron delocalisation between the Ru^{II} and Ru^{III} states by IVCT.

For the hypothetical mixed-valence system with sites A and B, R_A–R_B, Robin and Day defined the limiting degrees of electron delocalisation or valence trapping:[37] Class I, complete localisation with only integer valence-trapped oxidation states i.e. R_A^{n+}–$R_B^{(n+1)+}$; Class III, complete delocalisation and only valence detrapped non-integer oxidation states $R_A^{(n+0.5)+}$–$R_B^{(n+0.5)+}$. In the intermediate Class II regime, i.e. R_A^{n+}–$R_B^{(n+1)+} \leftrightarrow R_A^{(n+1)+}$–$R_B^{n+}$, distinct valences can be observed depending on the measurement time-scale, however there is a degree of electron delocalisation, subject to optical or thermal excitation.[37]

When mixed valency occurs in one-, two- and three-dimensional (1D, 2D, 3D respectively) systems, electron delocalisation provides a pathway for long-range charge transport and therefore electrical conductivity. For example, valence-pure $Mo^{VI}O_3$ or $W^{VI}O_3$ are insulating oxides, whereas the mixed-valence A_xMoO_3 or A_xWO_3 (A^+ = alkali metal) bronzes are electrically conductive.[37] Mixed valency is similarly important in affording conductive molecular materials. The organic metal (TTF)(TCNQ) cannot be described by a fully charge-transfer ionic $(TTF^{+\bullet})(TCNQ^{-\bullet})$ formulation.[38] Instead, only partial charge-transfer between donor (TTF) to acceptor occurs (TCNQ), giving a mixed-valence $(TTF^0)_{0.41}(TTF^{+\bullet})_{0.59}(TCNQ)_{0.41}(TCNQ^{-\bullet})_{0.59}$ charge distribution.[38] (TTF)(TCNQ) is classed as a one-dimensional (1D) metallic conductor as long-range charge-transport occurs due to efficient orbital overlap in both mixed-valence donors and acceptor stacks.[24, 38]

Mixed valency is not a necessary prerequisite for bulk magnetisation in a molecular material; the presence of spin carriers (metal or organic) and a strong interaction between the spins are the only requirements for magnetic ordering.[6] However, targeting mixed valency in molecular materials, can be a fruitful strategy to achieve magnetic ordering in a compound. For example, mixed-valence metal centres will have unequal S values e.g. S = 5/2 high-spin Fe^{III} and S = 2 high-spin Fe^{II}, so either FM or AFM coupling between them will afford a net magnetic moment. On the other hand, when the mixed valency involves organic-centred radical species bridging between metals, these organic radicals can act as relays to transmit spin exchange between paramagnetic metal centres.[39, 40] Consequently, targeting mixed valency in molecular materials is a particularly attractive strategy towards imparting conductivity and magnetic ordering.

1.2 Coordination Polymers

1.2.1 Functional Coordination Polymers

A class of molecular materials that has aroused attention for the synthesis of new (semi)conductive, magnetic or electroactive compounds are coordination polymers and the sub-class metal-organic frameworks (MOFs).[19, 39, 41-44] Crystalline coordination polymers are infinite arrays of metal atoms bridged by coordinating organic or inorganic ligands.[45] By varying the coordination number around the metal centre or metal cluster (e.g. 4-, 6- or 8- coordinate) and connectivity of the bridging

ligands (e.g. 2- or 3-connecting), a vast diversity of 1D, 2D and 3D networks can be designed and synthesised (Figure 1.3).

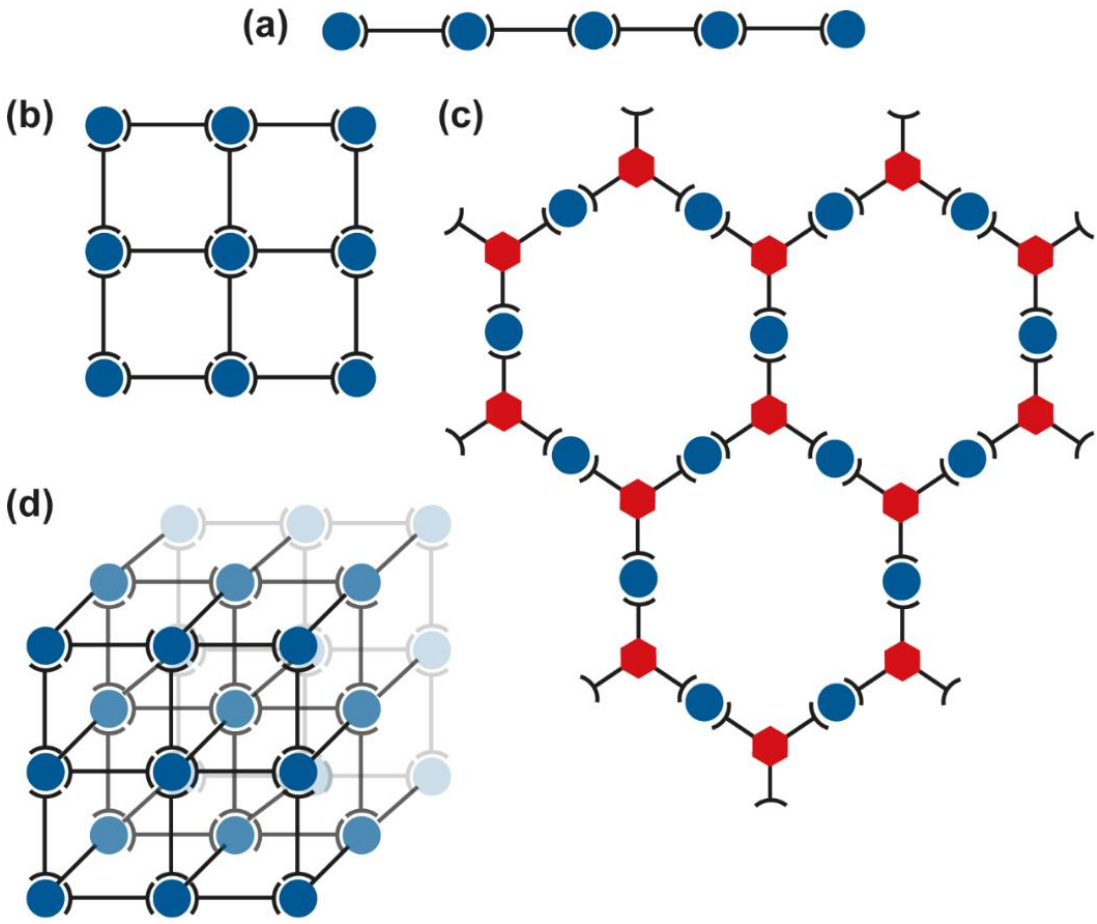


Figure 1.3 Coordination polymers. (a) 1D coordination polymer formed from 2-connecting ligands (black) and 2-connecting metal centres (blue). (b) 2D coordination polymer formed from 4-connecting metal centres (blue) and 2-connecting ligands (black). (c) 2D coordination polymer formed from 2-connecting metal centres (blue) and 3-connecting ligands (red hexagons). (d) 3D coordination polymer formed from 6-connecting metal centres (blue) and 2-connecting ligands (black).

An important feature of coordination polymers and MOFs is that by bridging metal centres with large organic ligands, materials with large void spaces can be produced. This is in stark contrast with traditional metallic and oxide-based inorganic compounds constructed from atomic building blocks, which are dense and have no void space. Critically, materials with combinations of properties not accessible in traditional

inorganic materials can be obtained, by introducing electroactive, conductive, and magnetic functionality alongside porosity in coordination polymers.[20, 39, 41, 43, 44] For example, guest species that can diffuse into the pores and interact with the framework can either vary the electrical conductivity,[46] or alternatively impart conductivity in a non-conductive framework.[47] A porous magnetic material could facilitate separation of paramagnetic guests from diamagnetic diluents, for example the non-cryogenic separation of oxygen from nitrogen.[19, 39] Consequently, these porous molecular materials have been posited as components in chemiresistive or magnetic sensors, lightweight magnets, (opto)electronic and energy conversion devices, and electrocatalysts.[48, 49] There is also significant fundamental interest in studying how these properties arise in these porous molecular materials,[43] which could facilitate better targeted synthesis of desirable porous compounds.

1.2.2 Topology of Coordination Polymers

In many cases, the connectivity, dimensionality, and geometry of coordination polymers influences their physical properties. Therefore, an understanding of the connectivity in these materials is essential to understand and predict their properties. A facile method to understand the structure of 2D and 3D coordination polymers is to simplify them to their underlying networks. Repeating units in the network which connect to three or more other points are termed *'nodes'*; these can be either metal centres, metal clusters, or ligands depending on connectivity.[45, 50] The bridges between nodes are 2-connecting and are termed *'links'*. Varying the connectivity and relative proportions of the nodes therefore affords a vast diversity of networks, of which a large number of theoretical networks were first described by A. F. Wells.[51] The underlying topology of the network is defined by the connectivity of each node, and the size of the smallest circuit of links around each node. If the size of all the unique circuits linking each node to itself are equal, the net is a *'uniform net'*, and if all the nodes also have an equivalent connectivity, the net is a *'uniform platonic net'*.[45] For such nets, the simple (*n*,*p*) notation introduced by Wells can be used to describe the network topology, where *n* is the size of the smallest circuit linking each node to itself, and *p* is the connectivity of each node. For example, the familiar hexagonal structure of honeycomb is a uniform platonic (6,3) net; all the smallest circuits around each node (the vertices of the hexagonal tessellation) contains six links, and each trigonal node is 3-connecting (Figure 1.4a). An additional complication can arise when

numerous topologically distinct networks possess the same (*n*,*p*) connectivity. Therefore, a more complete description of the coordination polymer structure is provided by reference to the geometry of the nodes. For example, replacing the trigonal nodes of the hexagonal tessellation with T-shaped 3-connecting nodes, gives the obviously geometrically distinct rectangular tessellation (Figure 1.4b), although both nets are topologically identical (6,3) nets.

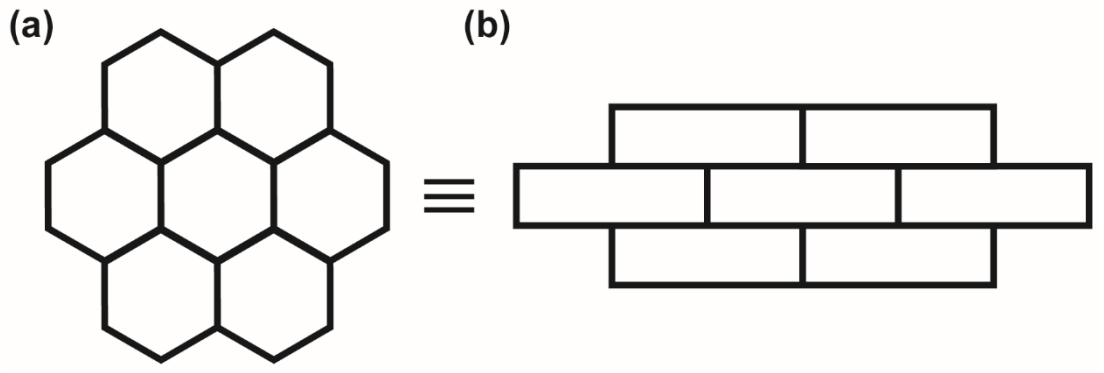


Figure 1.4 Schematic of the uniform platonic (6,3) net topology. Nodes occur at the vertexes of the polygons comprising the various nets. The two nets containing (a) trigonal and (b) T-shaped nodes are geometrically different but topologically identical.

The (10,3) series of 3D nets characterised by Wells are of special relevance in this thesis. Wells described seven distinct topologies of these (10,3) networks, namely (10,3)-*a* through (10,3)-*g*;[51] among extant coordination polymers, the (10,3)-*a* and (10,3)-*b* variants are the most prevalent (10,3) networks.[52-54] The highest symmetry variant is the cubic (10,3)-*a* network (Figure 1.5a). A key characteristic of the (10,3)-*a* net is the 4-fold helices oriented parallel to each of the unit cell axes; the handedness of each helix is equivalent, and thus the (10,3)-*a* topology is chiral.[45] When using chelating bridging ligands to link between 3-connecting octahedral metal centres, every metal node of a given configuration (Δ or Λ) is linked to three other nodes with the same configuration (Δ or Λ). The tetragonal (10,3)-*b* net is formed by connecting layers of zig-zag chains to orthogonal zig-zag chains in to the layers above and below; this arrangement also produces spacious hexagonal channels (Figure 1.5b).[45] Using chelating bridging ligands as the links between the octahedral metals, each node of a given handedness (Δ or Λ) is linked to one node with the same

handedness (Δ or Λ), and two of opposite handedness (Λ or Δ). The International Union of Pure and Applied Chemistry (IUPAC) now encourages[55] that the topology of new compounds is described using the three letter designation from the Reticular Chemistry Structure Resource (RCSR),[52, 56, 57] to avoid possible ambiguity when describing topologically and geometrically distinct nets with equivalent mathematical descriptions. For example, since the (10,3)-*a* and (10,3)-*b* nets have the same topology and connectivity as the silicon sublattices in $SrSi_2$ and α-$ThSi_2$ respectively, the RCSR symbols are **srs** and **ths**.

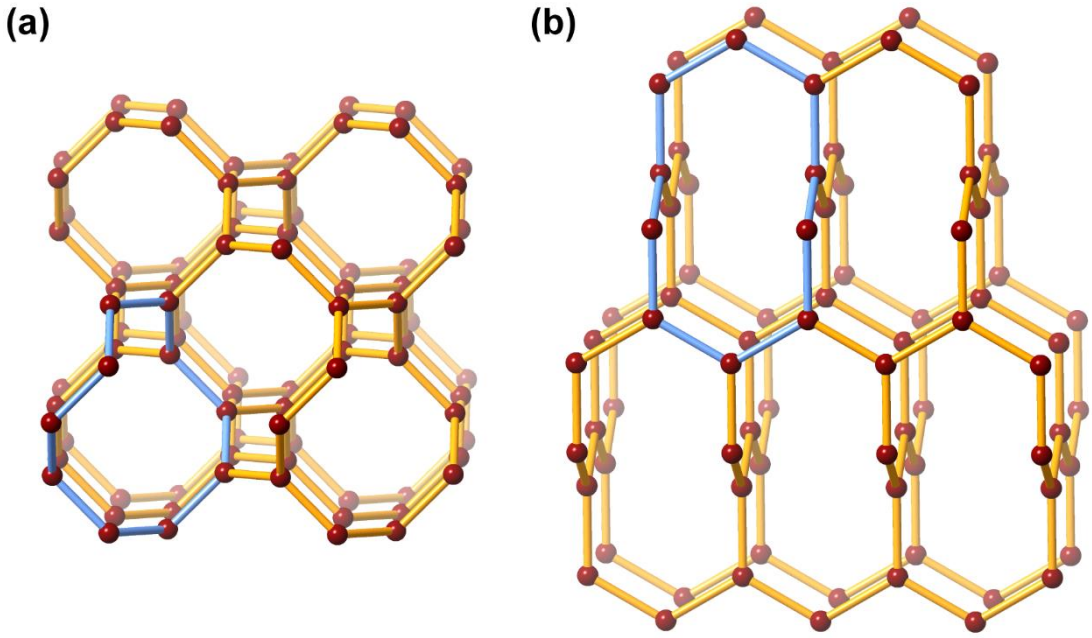


Figure 1.5 Ball-and-stick representations of the (a) cubic (10,3)-*a* (**srs**) and (b) tetragonal (10,3)-*b* (**ths**) uniform platonic networks. A 10-gon circuit in each structure is highlighted with blue connections. Maroon = nodes.

1.2.3 Net Approach to Coordination Polymers

Although not recognised as such when first synthesised by Diesbach in the 18th century, the brilliant blue pigment ($Fe^{III}_4[Fe^{II}(CN)_6]_3$), commonly termed Prussian blue, is considered the first coordination complex synthesised.[45] Arguably, it is also the first coordination polymer ever synthesised, although the precise structure eluded characterisation until 1977.[58] The structure consists of octahedral low-spin Fe^{II} (Fe^{II}_{LS}) centres linked to octahedral high-spin Fe^{III} (Fe^{III}_{HS}) centres via bridging linear

cyanide ligands (Figure 1.6a). Ignoring partial occupation of the $Fe^{II}(CN)_6$ sites, the Fe^{II} and Fe^{III} centres act as 6-connecting nodes, so the structure forms a 3D cubic network, equivalent to the primitive cubic (**pcu**) topology of rock salt (NaCl) or α-Po (Figure 1.6b). The intense blue colour of ($Fe^{III}_4[Fe^{II}(CN)_6]_3$) arises from IVCT between the Fe^{II} and Fe^{III} sites,[59] so that ($Fe^{III}_4[Fe^{II}(CN)_6]_3$) is also a mixed-valence coordination polymer. Cyanometallate chemistry has therefore been extensively investigated for the synthesis of coordination polymers,[60, 61] due to the fascinating (photo)magnetic and structural properties of these compounds.[62-67]

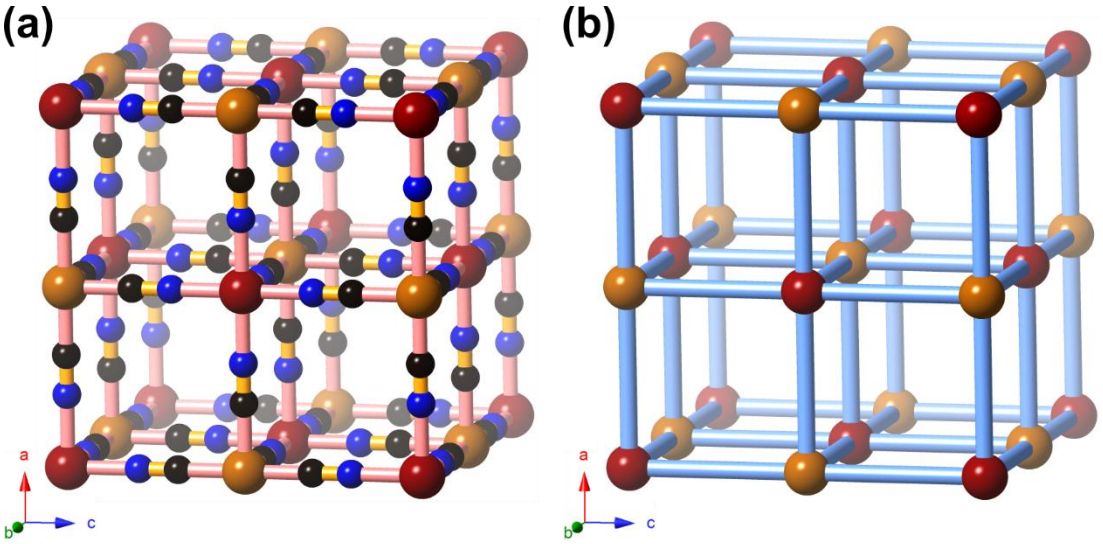


Figure 1.6 (a) The defect-free structure of $(Fe^{III}_4[Fe^{II}(CN)_6]_3)\cdot xH_2O$ Prussian blue showing coordination (pink bonds) of Fe centres by CN^- ligands. Interstitial water not shown for clarity. (b) The underlying topology (pale blue bonds) of $(Fe^{III}_4[Fe^{II}(CN)_6]_3)\cdot xH_2O$ Prussian blue showing α-Po or primitive cubic (**pcu**) structure. Maroon = high-spin Fe^{III} (Fe^{III}_{HS}), pale brown = low-spin Fe^{II} (Fe^{II}_{LS}), black = C, and blue = N.

Although cyanometallate building blocks exhibit predictable geometries and strong coordination bonding, the ability to produce porous materials is somewhat limited by the small length of cyanide ligands. Moreover, as additional chemical functionality cannot be appended to the cyanide ligands, the ability to finely design and tune the material properties is somewhat limited, requiring the use of ancillary organic ligands. The limitations of cyanide coordination can be overcome by using organic bridging ligands, which is a key tenet of the *'net approach'* to coordination polymers.[50, 68] This

strategy aims to replicate the topologies of known inorganic structures by replacing inorganic atomic nodes of given connectivity and geometry, with nodes and linkers comprised of metal centres and organic ligands linkers with equivalent connectivity and geometry.[50] This approach was heralded in the seminal works of Robson and Hoskins.[69, 70] The structure of diamond consists of tetrahedral C atoms connected with perfectly staggered bonds to give a 3D structure; a simple building unit apparent in the diamond (**dia**) topology is the adamantane unit (Figure 1.7a). The diamond topology was reproduced by reacting a 1:1 mixture of Cu^{I} and a tetranitrile ligand to yield the cationic coordination polymer $[Cu(tcpm)]BF_4 \cdot x PhNO_2$ (tcpm = 4,4′,4″,4‴-tetracyanophenylmethane, $PhNO_2$ = nitrobenzene). As desired, coordination between tetrahedral Cu^{I} centres and tetrahedral tcpm ligands afforded the intended 3D diamondoid (**dia**) network (Figure 1.7b). By extending the distance between tetrahedral nodes from ca. 1.5 Å in diamond, to ca. 8.9 Å in $[Cu(tcpm)]BF_4 \cdot x PhNO_2$, an open network structure with large adamantane cavities was produced (Figure 1.7c). These cavities occupy two-thirds of the crystal volume and are filled with highly disordered BF_4^- counteranions and $PhNO_2$ solvent, remarkably forming a solid structure largely comprising liquid solvent molecules. Although several works on polynitrile coordination polymers predate the report of $[Cu(tcpm)]BF_4$,[71-73] the works of Robson and Hoskins represent the first example of intentional replication of a known network topology by appropriate choice of the coordination polymer building blocks. Similar principles to the *'net approach'* have also been popularly termed *'reticular chemistry'*, in which multinuclear metal-carboxylate clusters form the nodes, which are linked by bridging organic ligands, to generate porous coordination polymers and MOFs.[74] Selecting ligands with equivalent coordination modes, but with larger dimensions or different pendant functionality then affords porous frameworks of increasingly higher surface area or varied pore surfaces, with the same topology as the parent framework, termed *'isoreticular synthesis'*.[75, 76]

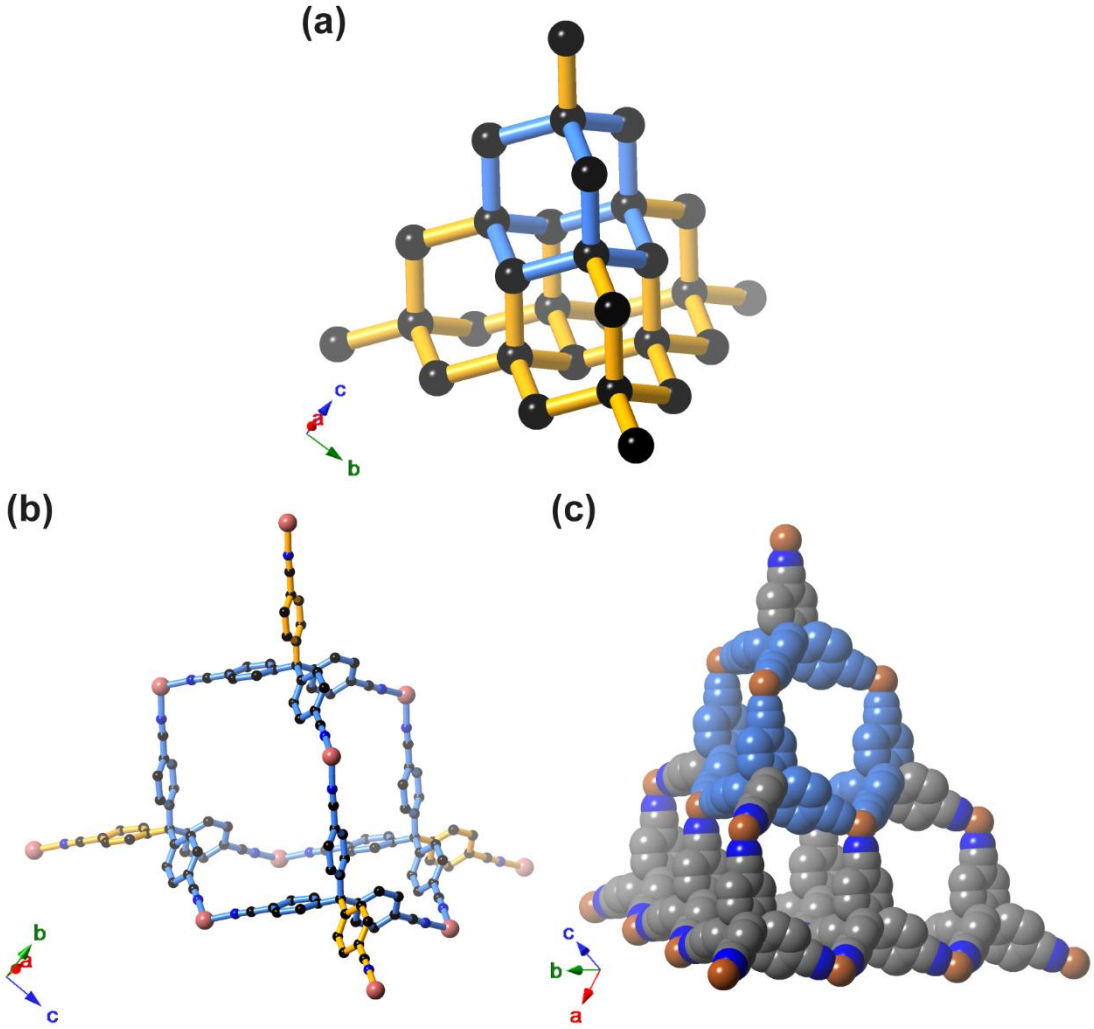


Figure 1.7 (a) Ball-and-stick representation of the structure of diamond, showing the tetrahedral geometry around each C atom and the adamantane unit (pale blue). (b) Ball-and-stick representation of the cationic diamondoid network of $[Cu(tcpm)]BF_4 \cdot x PhNO_2$, showing the adamantane unit (pale blue) formed by linking the ligand tetrahedral central C atom and tetrahedrally coordinated Cu^I nodes. (c) Spacefilling representation of the cationic network of $[Cu(tcpm)]BF_4 \cdot x PhNO_2$ showing an adamantane unit (pale blue atoms) and formation of spacious channels. Channels contain disordered BF_4^- and $PhNO_2$ not shown for clarity. Salmon = Cu, blue = N, and black = C.

1.2.4 Electrical Conductivity in Coordination Polymers

The potential of coordination polymers and MOFs to be synthesised containing large open pore spaces of tuneable shape and chemical functionality has made them obvious candidate materials in catalysis, gas storage and separation, similar to the application of inorganic zeolites.[77-80] Although interest has exploded in recent years, research efforts to use coordination polymers and MOFs as conductive materials with potential porosity have been relatively less intense.[20, 41, 44] This is despite the ability of coordination polymers to possess both porosity and conductivity in a single compound, in stark contrast to conventional inorganic materials. This probably arises because many of the principles used to design stable, porous coordination polymers are at odds with strategies to achieve conductivity in a material,[20] so that most coordination polymers are highly insulating or semiconducting at best. For example, the $Zr_6O_4(OH)_4$ and Zn_4O nodes of the prototypical stable MOFs, UiO-66 and MOF-5, are assembled from closed-shell metal centres coordinated to hard O donors, and therefore do not provide free charge carriers, limiting electrical conductivity.[41] Electrical conductivity still can be induced in frameworks assembled from closed-shell metal building blocks, however it requires the incorporation of redox-active ligands to provide charge transport pathways.[20] Moreover, many coordination polymers are designed with large metal-metal and ligand-ligand separation distances to achieve high porosity. However, this also limits orbital overlap between any potential redox active centres, also limiting long-range charge transport.[20]

Incorporation of mixed valency and open-shell species (metal or organic ligand radicals) into coordination polymers is a powerful route towards conductive porous frameworks.[32, 81] The unpaired electrons from either metal centres or radical ligands provide charge carriers, while the mixed valence sites (metal- or ligand-centred) provide a pathway for long-range charge transport.[20, 41] Broadly, charge-transport in coordination polymers can occur via either *'through bond'* or *'through space'* mechanisms. The *'through bond'* mechanism occurs when carrier migration is facilitated through bridging ligands. This mechanism of charge-transport is readily observed in the non-porous mixed-valence metal–halide (MX, $\{\cdots M^{II}\cdots X–M^{IV}–X\}_\infty$) and mixed-valence binuclear metal–halide (MMX, $\{–X–M^{II}–M^{III}–X–M^{II}–M^{III}\}_\infty$) 1D coordination polymer chains. For these compounds, the bridging halido ligands mediate electron transfer between the different valence metal sites (e.g. Pt^{II} and Pt^{IV})

for the MX chains, or between the mixed-valence binuclear $Pt^{II}Pt^{III}$ chain units.[82, 83] This results in 1D long-range change transport and either semiconductive or metallic behaviour.[84, 85] Alternatively, efficient π-d orbital admixing arising from redox matching between metal and organic ligands provides an extended conjugation pathway allowing carrier migration.[41, 44] The *'through space'* process relies upon close non-covalent interactions between π-conjugated organic species to promote efficient orbital overlap and long-range charge transport;[41, 44] this mechanism is similar to that operational in individual mixed-valence stacks in (TTF)(TCNQ).[26]

A salient example of the importance of both these charge transport mechanisms is the non-porous coordination polymer $Cu(Me_2DCNQI)_2$ (Me_2DCNQI = 2,5-dimethyl-*N*,*N*′-dicyanoquinodiimine) (Figure 1.8a).[72] The structure comprises tetrahedral Cu centres coordinated to four Me_2DCNQI bridging ligands, forming a 3D diamondoid network (Figure 1.8b). The overall structure comprises seven independent interpenetrating diamondoid $Cu(Me_2DCNQI)_2$ networks (Figure 1.8c & d); this also produces infinite co-facial stacks of mixed-valence $Me_2DCNQI^{0/-\bullet}$ ligands allowing *'though space'* charge transport. Remarkably, single crystals exhibit metallic conductivity, with a room temperature electrical conductivity of $\sigma_{295\ K}$ = 800 S cm^{-1}, rising to an impressive 5 × 10^5 S cm^{-1} at 3.5 K. Later structural and spectroscopic investigations revealed the presence of $Cu^{I/II}$ mixed valency (formally $Cu^{1.3+}$) and good π-d orbital overlap with the mixed-valence $Me_2DCNQI^{0/-\bullet}$ ligands, thereby providing an additional *'through bond'* charge-transport pathway resulting in quasi-3D metallicity.[86-89] The importance of both the charge-transport pathways in $Cu(Me_2DCNQI)_2$ is highlighted by comparison with the isostructural $Li(Me_2DCNQI)_2$ radical anion salt. In this case, charge transport only occurs in 1D *'through space'* via the mixed-valence co-facial $Me_2DCNQI^{0/-\bullet}$ stacks. $Li(Me_2DCNQI)_2$ therefore exhibits a lower room-temperature conductivity of $\sigma_{295\ K}$ = 300 S cm^{-1} and also undergoes a metal-semiconductor transition at ca. 200 K.[73]

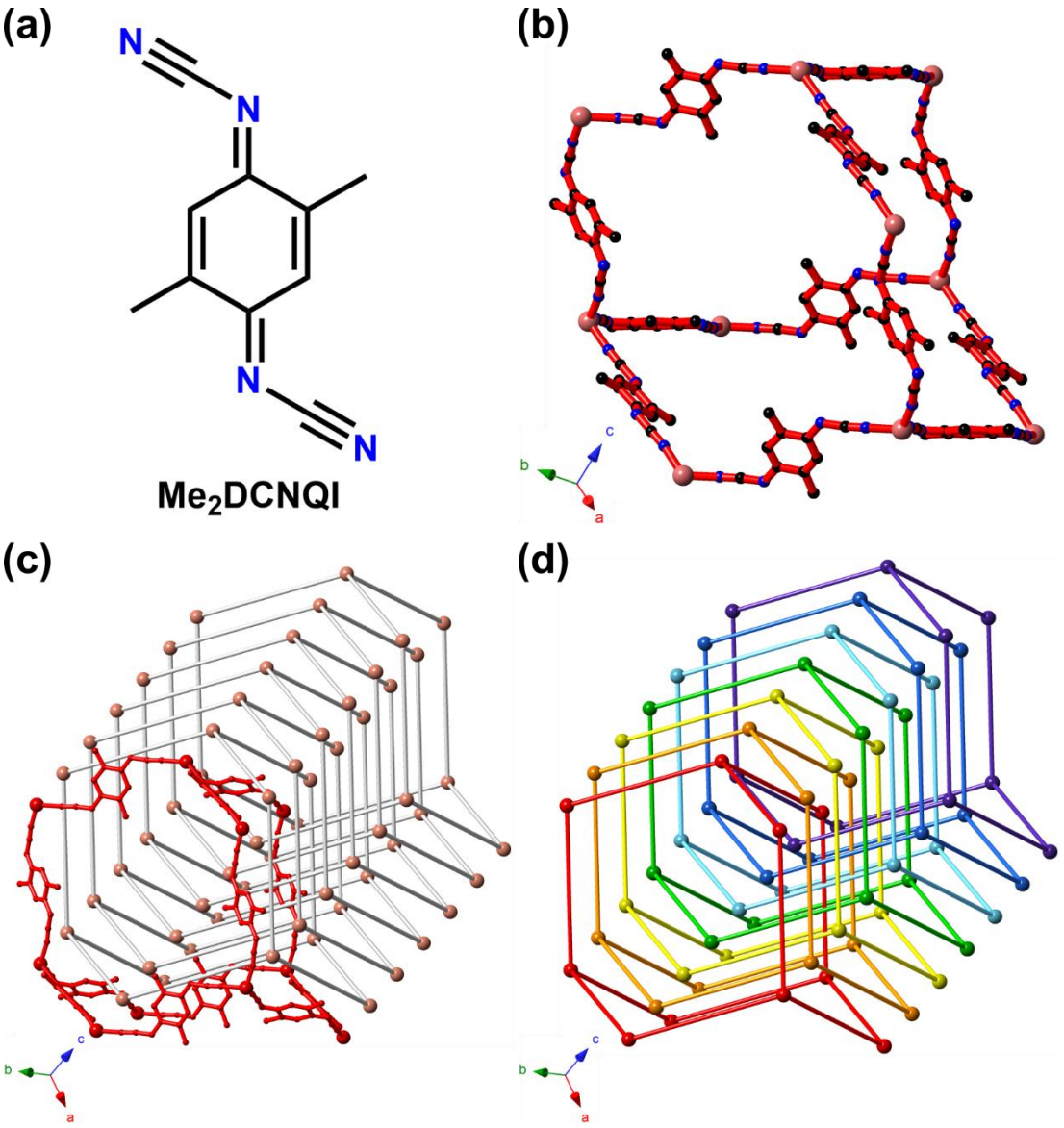


Figure 1.8 (a) The structure of 2,5-dimethyl-*N*,*N*′-dicyanoquinodiimine (Me_2DCNQI). (b) The adamantane unit (red bonds) of $Cu(Me_2DCNQI)_2$. Salmon = Cu, blue = N, and black = C. H atoms not shown for clarity. (c & d) The seven interpenetrating diamondoid networks of $Cu(Me_2DCNQI)_2$.

Despite the impressive metallic conductivity achieved using DCNQI-type ligands, interest in conductive porous coordination polymers did not eventuate until much later. An early example of a potentially porous coordination polymer designed using the *'though bond'* approach, was synthesised by reacting $Cu^{I}I$ and a Cu^{III} complex of pyrazine-2,3-dithiolate (pdt) ($[Cu^{III}(pdt)_2]^{-}$), yielding the 3D coordination polymer $Cu[Cu(pdt)_2]$.[90] The $[Cu(pdt)_2]^{x-}$ metalloligand acts as a 4-connecting node, linking

to square planar four-coordinate Cu centres via the pyrazine N donors, forming square 1D channels which run parallel to the tetragonal *c* axis. Because the $[Cu^{III}(pdt)_2]^-$ to $[Cu^{II}(pdt)_2]^{2-}$ redox couple occurs at relatively mild potentials (−0.33 V vs. Ag/AgCl), it was proposed Cu^I acted as an electron donor to the $[Cu^{III}(pdt)_2]^-$ metalloligand, giving a $Cu^{II}[Cu^{II}(pdt)_2]$ valence formulation. Semiconductivity, with a modest $\sigma_{300\,K} = 6 \times 10^{-4}$ S cm^{-1} was thought to arise from bistability between the Cu^I/Cu^{III} and Cu^{II}/Cu^{II} valence state distributions. Attempts to desolvate the $Cu[Cu(pdt)_2]$ framework lead to structure collapse, however the isostructural $Cu^{II}[Ni^{II}(pdt)_2]$ compound is a stable microporous material (Figure 1.9a).[91] In contrast to $Cu[Cu(pdt)_2]$, as-synthesised $Cu[Ni(pdt)_2]$ is a poor semiconductor, with room-temperature conductivity of only $\sigma_{RT} = 1 \times 10^{-8}$ S cm^{-1} and an activation energy $E_a = 0.49$ eV. Framework intercalation with I_2 vapour increased σ_{RT} ca. 10^4-fold and decreased E_a to 0.18 eV, suggestive of more facile charge transport. Improved charge-transport was thought to arise from partial oxidation of the $[Ni(pdt)_2]^{2-}$ sub-units to $[Ni(pdt)_2]^-$ (Figure 1.9b), thereby introducing mixed valency and facilitating hopping-type transport. More recently, the potential application of porous conductors in sensing applications was demonstrated by chemiresistive detection of various saturated and unsaturated hydrocarbons using $Cu[Ni(pdt)_2]$.[92]

REDACTED THIRD PARTY COPYRIGHT MATERIAL

Figure 1.9 (a) Ball-and-stick representation of the structure of the $Cu[Ni(pdt)_2]$ framework. Green = Ni, teal = Cu, yellow = S, blue = N, and grey = C. (b) Oxidation states of the $[Ni(pdt)_2]^{x-}$ metalloligand. Adapted with permission from Ref. [91]. Copyright © 2010 American Chemical Society.

The transport properties of porous frameworks isomorphous to $Zn_2(DOBDC)(DMF)_2$ ($DOBDC^{4-}$ = 2,5-dioxobenzene-1,4-dicarboxylate) commonly known as MOF-74,[93] have been studied extensively using a range of divalent metals, in addition to the thiophenoxide analogue ($DSBDC^{4-}$ 2,5-dithiobenzene-1,4-dicarboxylate).[94-96] Although there are slight variations in the structures and symmetry depending on the metal and chalcogen substitution, the compounds broadly consist of chains of edge-sharing ME_6 ($E_6 = O_6$ or O_4S_2) octahedra oriented parallel to the hexagonal *c* axis. Adjacent ME_6 chains then link via the bridging $DEBDC^{4-}$ (E = O, S) ligands producing a 3D framework with large 1D hexagonal pores (Figure 1.10a). Bridging μ^2-(thio)phenoxide coordination of the metal centres also gives infinite $\{M-E-\}_\infty$ chains (Figure 1.10b), so the structures were proposed as dimensionally reduced metal-chalcogenide compounds which typically exhibit electrical conductivity.[97] The compound $Mn_2(DSBDC)$ has a high intrinsic charge mobility comparable to organic semiconductors such as polythiophene.[94] Later studies however revealed both $Mn_2(DOBDC)(DMF)_2$ and $Mn_2(DSBDC)(DMF)_2$ exhibit low $\sigma_{RT} = 3.0 \times 10^{-13}$ S cm^{-1} and $\sigma_{RT} = 1.2 \times 10^{-12}$ S cm^{-1} respectively.[95] Replacing d^5 Mn^{II} with d^6 Fe^{II} during synthesis gave $Fe_2(DOBDC)(DMF)_2$ and $Fe_2(DSBDC)(DMF)_2$, which display ca. 10^6-fold higher electrical conductivity and significantly lower E_a values compared to the Mn^{II} analogues.[95] Electronic structure calculations revealed the dramatically higher conductivity of the Fe compounds stems from the lower band gap and higher energy valence band minimum in the Fe compounds, increasing the probability of thermally-activated electron transfer from valence to conduction bands. Interestingly, although ^{57}Fe Mössbauer spectroscopy suggested an absence of Fe^{III} content in $Fe_2(DOBDC)(DMF)_2$ and $Fe_2(DSBDC)(DMF)_2$,[95] later studies suggested trace amounts of Fe^{III} in the as-synthesised framework may still contribute to the conductivity of these materials.[96]

REDACTED THIRD PARTY COPYRIGHT MATERIAL



Figure 1.10 (a) Ball-and-stick representation of the structure of solvated $Fe_2(DSBDC)(DMF)_2 \cdot x$DMF. (b) The pseudo-1D $\{M{-}E{-}\}_\infty$ chains (purple bonds) in $M_2(DEBDC)(DMF)_2$ (M = Mn, Fe; E = O, S). (b) Blue = Fe, green = Mn, yellow = S, red = O, black = coordinated DMF O, and grey = C. Adapted with permission from Ref. [95]. Copyright © 2015 American Chemical Society.

Post-synthetic introduction of Fe-centred mixed valency in various Fe–azolate frameworks has recently been used to obtain porous, electrically conductive compounds. The porous 3D diamondoid framework $Fe(tri)_2$ (tri^- = 1,2,3-triazolate) was initially reported to be air-stable and intrinsically conductive, with a modest σ_{RT} = 7.7 × 10^{-5} S cm^{-1}.[98] The putative role of Fe-based mixed valency in the conductivity of $Fe(tri)_2$ was shown by I_2 doping, which increased σ_{RT} = 1.0 × 10^{-3} S cm^{-1}. More recent work has proven Fe-based mixed valency is critical in this system; valence-pure $Fe^{II}(tri)_2$ synthesised and handled under rigorously anaerobic conditions is insulating, showing an intrinsic conductivity of only 1 × 10^{-10} S cm^{-1}.[99] UV-Vis-NIR and ^{57}Fe Mössbauer spectroscopy showed tuneable post-synthetic oxidative doping to yield $Fe(tri)_2(BF_4)_x$ could be achieved, increasing the conductivity to 0.03(2) S cm^{-1} for x = 0.09, and up to 0.3(1) S cm^{-1} for x = 0.33. Similarly, single-crystal devices of the valence-pure 3D framework $Fe^{II}_2(H_{0.67}BDT)_3$ (H_2BDT = 5,5′-(1,4-phenylene)bis(1*H*-tetrazole)) exhibit modest ambient temperature conductivity of 6(2) × 10^{-5} S cm^{-1}.[100] In the structure, each bistetrazole ligand coordinates to four Fe^{II} centres, forming large square channels (Figure 1.11a). Psuedo-

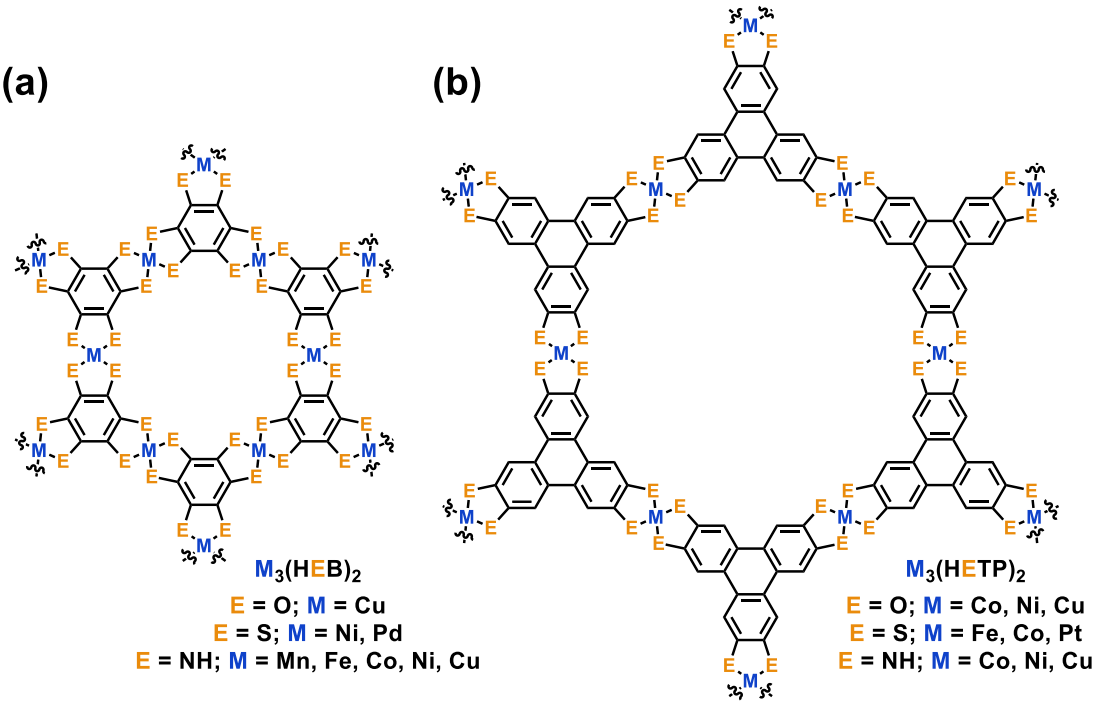
1D {Fe–N−N–}$_\infty$ chains that run parallel to the crystallographic *a* axis are formed by the μ^2-tetrazolate moieties bridging between Fe centres (Figure 1.11b). A *'through bond'* mechanism along these chains is the proposed pathway for charge transport, as the conductivity of single-crystal devices is highest in this direction. Introduction of Fe-based mixed valency via oxidative doping occurred upon exposure to ambient atmosphere. This was observed by UV-Vis-NIR spectroscopy and was indicated by the increasing absorption at λ = 690 nm ascribed to IVCT between Fe^{II} and Fe^{III} (Figure 1.11c). Tuneable doping depending on air exposure time was also achieved, such that single-crystal devices reached a conductivity of up to σ = 1.2(4) S cm^{-1} (Figure 1.11d), representing a 10^5-fold increase from the as-synthesised valence-pure compound. Alternatively, Long and co-workers used post-synthetic reductive doping on the valence-pure Fe–pyrazolate framework $Fe^{III}_2(BDP)_3$ (BDP^{2-} = 1,4-benzenedipyrazolate) to introduce Fe-based mixed valency giving $K_xFe_2(BDP)_3$.[101] The structure of $Fe_2(BDP)_3$ is similar to $Fe_2(H_{0.67}BDT)_3$, containing pseudo-1D {Fe–N−N–}$_\infty$ chains formed by octahedral coordination of Fe centres by μ^2-pyrazolate moieties. As in $Fe_2(H_{0.67}BDT)_3$, these chains are proposed as the major pathway for *'through bond'* charge transport as the conductivity was highest along this direct. Tuneable Fe-based mixed valency was evinced by ^{57}Fe Mössbauer and UV-Vis-NIR spectroscopy, with single-crystal devices of $K_xFe_2(BDP)_3$ exhibiting an up to ca. 10^4-fold increase in conductivity and ca. 400-fold increase in carrier mobility from the as-synthesised valence-pure $Fe^{III}_2(BDP)_3$ framework.

REDACTED THIRD PARTY COPYRIGHT MATERIAL



Figure 1.11 (a) The structure of $Fe_2(H_{0.67}BDT)_3$ viewed down the crystallographic *a* axis. (b) The 1D $\{Fe–N–N–\}_\infty$ chains in $Fe_2(H_{0.67}BDT)_3$ formed by the μ^2-tetrazolate moieties. Green = Fe, blue = N, and grey = C. (c) Diffuse reflectance UV-Vis-NIR spectrum of $Fe_2(H_{0.67}BDT)_3$ showing evolution of NIR absorbance ascribed to IVCT upon air exposure. (d) Electrical conductivity of single-crystal devices of $Fe_2(H_{0.67}BDT)_3$ showing evolution of conductivity upon exposure to ambient atmosphere. Adapted with permission from Ref. [100]. Copyright © 2018 American Chemical Society.

2D layered coordination polymers assembled from hexasubstituted triphenylene (HETP) or benzene (HEB) (E = O, S, NH) ligands are among the most conductive porous materials in literature.[44] Compounds in this group typically consist of trigonal 3-connecting organic ligands coordinated to square planar metal centres producing layered graphene-like materials with high in-layer conductivity (Scheme 1.2).[41, 44]



Scheme 1.2 Schematics of 2D graphene-like layered coordination polymers synthesised using (a) hexasubstituted benzene (HEB) and (b) hexasubstituted triphenylene (HETP) ligands. Adapted with permission from Ref. [44]. Copyright © 2020 American Chemical Society.

Several key factors make these planar ligands attractive for synthesis of conductive porous materials.[44] The ligands are particularly susceptible to oxidation to semiquinonoid radical species, which introduces free charge carriers into the 2D networks.[44] The extended π-conjugation in these ligands also stabilises and delocalises these radical species, facilitating efficient in-layer charge transport. Finally, by the use of relatively softer donor atoms (N or S), efficient overlap between metal d- and ligand π-orbitals results, producing an extended π-conjugated system throughout the layer, which promotes long-range charge transport.[44] While these materials are promising, there are several challenges associated with synthesis and analysis of these compounds. In these materials, relatively strong coordination bonding only occurs within the two dimensions of the layer plane, whereas the layer stacking is controlled by weaker, non-directional van der Waals interactions. Consequently, these layered compounds are prone to stacking faults and stacking disorder,[102] resulting in samples of variable crystallinity, conductivity and purity for

the same putative compounds.[44] Powder X-ray diffraction (P-XRD) or high-resolution transmission electron microscopy (HR-TEM) is typically the only route available to investigate the structure of these compounds, which hinders more rigorous determination of ligand and metal oxidation states by single-crystal X-ray diffraction (SC-XRD). In many cases, these slight structure distortions can have a significant impact on the observed conductivity, so that it is sometimes challenging to correlate the experimentally observed semiconductor behaviour, with the intrinsic metallic conductivity predicted spectroscopically or computationally.[103-105]

Through a reaction of 2,3,6,7,10,11-hexahydroxytriphenylene (H_6HOTP) with a Cu^{II} source, Hmadeh *et al.* synthesised the 2D layered $Cu_3(HOTP)_2$ coordination polymer.[106] The neutral layer formulation of $Cu_3(HOTP)_2$ suggests oxidation of the $HOTP^{6-}$ anion to a semiquinonoid radical $HOTP^{3-\bullet}$ state during synthesis. P-XRD studies revealed the compound was a layered 2D coordination polymer, with eclipsed stacking of the neutral sheets parallel to the hexagonal *c* axis. Single-crystal measurements on $Cu_3(HOTP)_2$ gave a $\sigma_{RT} \approx 0.2$ S cm^{-1}. Later HR-TEM investigations by Dincă and co-workers revealed the presence of slipped stacking of the neutral $Cu_3(HOTP)_2$ layers along the hexagonal *c* axis,[107] in contrast to the completely eclipsed layer stacking presumed in earlier studies.[106] Single-crystal and pellet measurements revealed comparable values of conductivity, suggesting the intralayer and interlayer conductivity are of similar magnitude. This suggests *'through space'* charge transport facilitated by co-facial stacking of the delocalised π-systems may also be an important contributor to the measured conductivity in these layered materials.

Substitution of the hard O donors in HOTP and HOB with softer S and N donors has proven an effective strategy to optimise d-π orbital overlap giving more highly conductive coordination polymers. Nishihara and co-workers extensively studied the structure, spectroscopy, and conductivity of the 2D layered coordination polymer $Ni_3(HSB)_2$ (H_6HSB = hexathiolbenzene).[103, 108] As expected, the network is formed by trigonal HSB nodes coordinated to square planar Ni centres, forming a hexagonal network. In contrast to $Cu_3(HOTP)_2$, P-XRD analysis on $Ni_3(HSB)_2$ indicated the layers engage in staggered stacking along the hexagonal *c* axis, with notable stacking disordered evinced by the broad diffraction peaks associated with the layer stacking periodicity. X-ray photoelectron spectroscopy (XPS) measurements indicated that as-synthesised $Ni_3(HSB)_2$ contains mixed-valence [Ni(dithiolene)$_3$] sub-units, with a ca.

1:3 ratio between the $[Ni(dithiolene)_3]^0$ and $[Ni(dithiolene)_3]^-$. This mixed valency is the proposed mechanism for charge transport, as the native $Ni_3(HSB)_2$ compound exhibits a room-temperature pellet conductivity of 0.15 S cm^{-1}, whereas reduced $Ni_3(HSB)_2$ has a much lower conductivity of 6.7×10^{-3} S cm^{-1}. Later four-point van der Pauw conductivity measurements designed to eliminate contact resistance, revealed thermally-activated semiconductor behaviour, with an intrinsic σ_{RT} = 2.8 S cm^{-1} and E_a = 26 meV.[103]. The semiconductor behaviour interestingly conflicts with electronic structure calculations and ultraviolet photoelectron spectroscopy (UPS) measurements, both of which indicate $Ni_3(HSB)_2$ should exhibit metallic conductivity. This discrepancy was attributed to structural disorder (probably layer stacking) in the real materials, leading to less efficient charge transport.

The non-porous 2D layered network $Cu_3(HSB)_2$ exhibits the highest known conductivity for a coordination polymer.[44] In contrast to $Ni_3(HSB)_2$, square planar Cu atoms in $Cu_3(HSB)_2$ link between 6-connecting HSB ligands due to μ^2-thiolate coordination, producing a dense layer with eclipsed stacking of the layers parallel to the hexagonal *c* axis.[109] The premier thin-film device of $Cu_3(HSB)_2$ exhibited an impressive σ_{RT} = 1580 S cm^{-1}, falling to 1360 S cm^{-1} at 2 K, consistent with thermally-activated semiconductor behaviour. Later work by the same group using improved synthetic conditions to produce more crystalline $Cu_3(HSB)_2$, showed the compound exhibits metallic conductivity between 300 K and 10 K, before undergoing a superconducting transition below 0.25 K.[110]

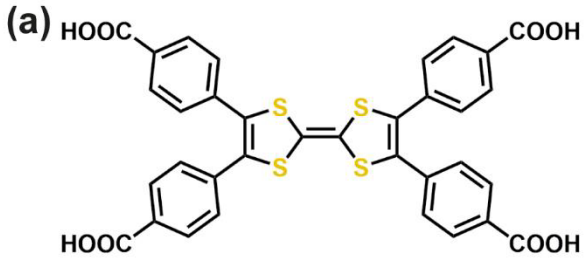
Marinescu and co-workers have recently shown 2D layered coordination polymers constructed with ligands derived from 2,3,6,7,10,11-hexathioltriphenylene (H_6HSTP) are promising porous, conductive materials. Eclipsed stacking of the layers in $Co_3(HSTP)_2$ produces spacious channels with run parallel to the hexagonal *c* axis, giving a material with a Brunauer-Emmett-Teller (BET) surface area of 370 m^2 g^{-1}.[111] Pressed pellet devices exhibited modest $\sigma_{300\ K} = 1.4 \times 10^{-3}$ S cm^{-1}, with thin-film devices showing a higher conductivity due to elimination of grain boundary resistance. Semiconductor behaviour with an E_a = 0.17 eV was observed down to 170 K, with a subsequent semiconductor-metal transition below 130 K. Time-resolved terahertz spectroscopy (TRTS) photoconductivity measurements on an ammonium counterion containing Fe analogue, $(H_4N)_3[Fe_3(HSTP)_2]$, revealed temperature independent band-like charge transport, though four-point conductivity measurements indicated

semiconductor behaviour with $\sigma_{300\ K}$ = 3.4 × 10^{-2} S cm^{-1} .[112] Later studies using ammonium-free material, $Fe_3(HSTP)_2$, revealed a $\sigma_{300\ K}$ = 0.2 S cm^{-1} with the compound also undergoing a semiconductor-metal transition below 100 K like $Co_3(HSTP)_2$. Subsequent oxidative doping of $Fe_3(HSTP)_2$ by ambient air exposure allowed the metallic transition temperature to be raised to 300 K, though with a concomitant reduction in conductivity to 1.4 × 10^{-3} S cm^{-1}. While promising, these results also demonstrate that understanding the intrinsic transport properties in these 2D graphene-like coordination polymers is often fraught with challenges, due to the complicated relationship between preparation, sample crystallinity and layer disorder and the observed electrical conductivity.

Coordination polymers derived from hexaaminobenzene (H_6HNB) and 2,3,6,7,10,11-hexaaminotriphenylene (H_6HNTP) ligands in combination with square planar metals are also promising conductive and porous materials.[44] Through solvothermal reaction between $H_6HNTP{\cdot}6HCl$ and ammoniacal $Ni^{II}Cl_2$, Sheberla *et al.* synthesised the coordination polymer $Ni_3(HITP)_2$ (HITP = 2,3,6,7,10,11-hexaiminotriphenylenesemiquinonate).[113] The neutral $Ni^{II}_3(HITP)_2$ formulation was demonstrated by a battery of analyses, indicating oxidation of the HNTP starting material to the semiquinonoid radical HITP occurred during synthesis, thus introducing charge carriers into the compound. Through a combination of P-XRD and Ni K-edge extended X-ray absorption fine structure (EXAFS) analyses, the compound was found to exhibit the intended 2D graphene-like structure. As with similar layered coordination polymers, slipped stacking of the neutral layers and relatively poor stacking order was observed. More recent HR-TEM studies revealed further intricacies in the stacking arrangement, indicative of short-range stacking order, but disorder over 100's of nanometre range.[107] Pressed pellet and thin-film devices of $Ni_3(HITP)_2$ exhibit σ_{RT} of 2 S cm^{-1} and 40 S cm^{-1} respectively, with thermally-activated transport observed for the thin-film device.[113] Single-crystal measurements revealed σ_{RT} up to an impressive 100 S cm^{-1} and low-temperature transport behaviour indicative of metallicity, though polycrystalline thin-films were semiconductive.[107] The Cu analogue, $Cu_3(HITP)_2$ while showing a lower σ_{RT} = 0.2 S cm^{-1} has recently been used for chemiresistive sensing of ammonia vapour.[114] More recently, band gap engineering of the $M_3(HITP)_2$ (M= Co, Ni, Cu) family was achieved by alloying

different proportions of the metal precursors, allowing the conductivity to be systematically tuned over a large range.[115]

In contrast to the *'through bond'* approach employed in the aforementioned compounds, the *'through space'* approach to conductivity can be advantageous, as redox-inactive but highly stable metals or metal clusters (e.g. Zn_4O) can be employed to synthesise the framework. Using redox-active tetrathiafulvalene-tetrabenzoic acid (H_4TTFTB) (Figure 1.12a), Dincă and co-workers synthesised the porous framework Zn_2(TTFTB).[97] The structure consists of infinite helices of co-facial TTF units locked in place by the infinite chains of ZnO_6 octahedra which run parallel to the TTF helices (Figure 1.12b & c). The π-orbital overlap engendered by the co-facial stacking of TTF units, along with partial oxidation of the TTF units during synthesis facilitated *'through space'* charge transport along the TTF helices, giving a porous material with carrier mobilities similar to that of conducting organic polymers.[97] Replacing Zn^{II} with redox-inactive Cd^{II}, produced a two-fold increase in single-crystal electrical conductivity, attributed to the larger ionic radius of Cd^{II} enforcing closer TTF stacking.[116] This in turn decreased the non-covalent S···S distance and improved π-orbital overlap improving charge transport.



Tetrathiafulvalene tetrabenzoic acid
(H_4TTFTB)

REDACTED THIRD PARTY COPYRIGHT MATERIAL

Figure 1.12 (a) Schematic of tetrathiafulvalene-tetrabenzoate (TTFTB). (b) The structure of Zn_2(TTFTB) viewed down crystallographic *c* axis showing 1D voids. (c) Side-on view of the helical co-facial TTF stacks showing close S···S contacts (dashed lines) and infinite chains of ZnO_6 octahedra (blue). Blue = Zn, gold = S, red = O, and grey = C. H atoms not shown for clarity. Adapted with permission from Ref. [97]. Copyright © 2012 American Chemical Society.

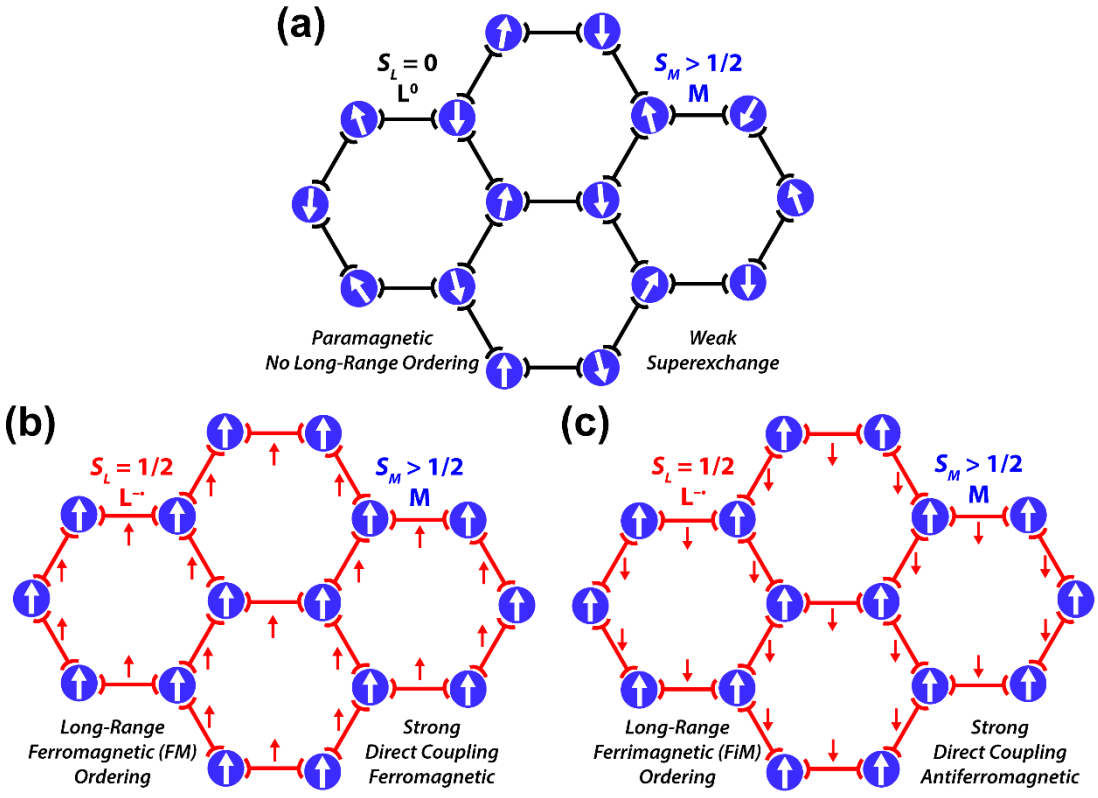
1.2.5 Magnetic Coordination Polymers

Many of the routes used for the synthesis of open, porous framework materials directly conflict with approaches that might be generally employed in producing a magnetic material. This dichotomy is much like that which exists for synthesis of porous, conducting materials, so there are notable parallels in the considerations used to achieve porous and magnetic compounds, as there are to achieve conductivity. Bulk FM or ferrimagnetic (FiM) ordering in a material requires both the presence of paramagnetic spin carriers and a strong interaction between these spins. If the interactions between spin carriers is only weak, the magnetic behaviour tends towards

paramagnetism (Scheme 1.3a). Paramagnetic compounds exhibit no remnant magnetisation in the absence of an applied field and are therefore not useful as permanent magnets.[39, 40] Two factors conspire against strong interactions in typical coordination polymers containing only diamagnetic ligands: diamagnetic atoms only transmit weak coupling between paramagnetic metal centres via a superexchange mechanism, preventing bulk magnetic ordering at useful temperatures.[19, 39] Secondly, the strength of magnetic coupling falls precipitously as the number of linking atoms between paramagnetic centres increases.[19, 117] The large diamagnetic carboxylate organic ligands e.g. terephthalate, often used to synthesise high surface-area frameworks, do not efficiently relay magnetic interactions between metal spin carriers, inhibiting long-range magnetic ordering. Although a large number of porous and non-porous coordination polymers exhibiting magnetic ordering have been synthesised using diamagnetic ligands, in particular oxalate,[118] the ordering temperatures of these compounds all remain below ca. 50 K due to the weak magnetic interactions present.[19]

An especially fruitful method to overcome the limitations of diamagnetic organic links, is by incorporating paramagnetic radical ligands into the framework.[19, 39, 40] These additional organic spin carriers function as a magnetic relay to which the paramagnetic metals can couple. If the coupling between paramagnetic metal and organic radical spins (S_M and S_L respectively) is FM, the organic spins both increase the total spin ($S_T = S_M + S_L$) of the framework, and provide a conduit for spin exchange leading to FM ordering (Scheme 1.3b).[39, 40] AFM coupling between metal centres and organic radicals is still advantageous, as AFM metal–radical coupling gives the desired ferromagnetic FM interaction between metals. While the total spin of the system ($S_T = S_M – S_L$) is reduced by AFM metal–radical coupling, the typically larger values of S_M compared to S_L (S_L = 1/2 for organic radicals) means a net FiM moment results (Scheme 1.3c). Another advantage of the metal–radical approach is that it affords the possibility to externally switch the magnetic ordering behaviour if the organic radical ligands are redox-active. Externally switching the redox state and therefore spin state of the relay ligand between diamagnetic and paramagnetic, by chemical[119, 120] or voltammetric[121-124] methods, allows the magnetic ordering behaviour to be reversibly modulated by external stimuli unlike conventional inorganic magnets. Moreover, since introducing organic radical ligands is an effective way to produce a mixed-valence

conductive coordination polymer, the review of magnetism in coordination polymers is heavily focussed on those incorporating radical ligands.



Scheme 1.3 Magnetic behaviour in extended frameworks in the absence of an applied field. (a) Paramagnetism due to weak metal-metal spin exchange mediated by superexchange through diamagnetic ligand. (b) Direct FM metal–radical coupling leading to long-range FM ordering, and (c) AFM metal–radical coupling leading to long-range FiM ordering.

Electron-poor polynitrile ligands have featured heavily in the synthesis of molecular magnetic materials such as $(FeCp^*_2)(TCNE)$, and magnetic coordination polymers,[19, 39] because they form stable organic radicals. The reaction between $V^0(C_6H_6)_2$ and $TCNE^0$ yields a pyrophoric, black solid $V(TCNE)_x{\cdot}yCH_2Cl_2$ ($x \approx 2$, $y \approx 0.5$) which exhibits magnetic ordering about 350 K.[125] Structural characterisation of the compound has been thwarted by the amorphous nature and slightly variable composition depending on the synthetic conditions. However the polymeric nature is suggested by XPS, EXAFS and X-ray absorption near edge structure (XANES) studies, which demonstrate the compound contains octahedral V^{II} coordinated to six

N atoms.[126] Models for $V(TCNE)_x{\cdot}yCH_2Cl_2$ have also been developed by comparison with the structurally characterised $Fe(TCNE)_2{\cdot}yCH_2Cl_2$ ($y \approx 0.3$) coordination polymer, which undergoes FiM ordering below 100 K.[127] The structure of $Fe(TCNE)_2{\cdot}yCH_2Cl_2$ comprises undulating 2D layers of octahedral $S = 2$ Fe^{II} centres coordinated to 4-connecting $S = ½$ $TCNE^{-\bullet}$ ligands (Figure 1.13a). The undulating layers are then linked by 4-connecting diamagnetic μ^4-$[C_4(CN)_8]^{2-}$ ligands, formed from two $TCNE^{-\bullet}$ units σ-dimerised by a covalent C–C bond, giving the $Fe^{II}(TCNE^{-\bullet})(C_4(CN)_8^{2-})_{0.5}$ formulation (Figure 1.13c & e). The structure of $V(TCNE)_x$ is more complex, with the valence formulation varying between $V^{II}(TCNE^{-\bullet})_z(TCNE^{2-})_{1-(z/2)}$ ($1 < z < 2$).[126] The structure model for limiting case with $z = 1$, consists of undulating sheets of V^{II} centres coordinated to four-connect paramagnetic $TCNE^{-\bullet}$ ligands, similar to the sheet structure of $Fe(TCNE)_2{\cdot}yCH_2Cl_2$. The axial V^{II} coordination sites are occupied by diamagnetic μ^4-$TCNE^{2-}$ ligands which link the sheets together. The presence of mixed-valence $TCNE^{2-/-\bullet}$ ligands may therefore explain the modest semiconductor behaviour observed, with pressed pellets of $V(TCNE)_x{\cdot}yCH_2Cl_2$ exhibiting $\sigma_{300\ K} \approx 10^{-3}$ S cm^{-1}.[128] For the $z = 2$ case, *trans*-μ^2-$TCNE^{-\bullet}$ ligands bridge the putative $V^{II}(TCNE^{-\bullet})$ sheets to give a 3D magnetic structure. Despite the amorphous and somewhat ambiguous structure of $V(TCNE)_x{\cdot}yCH_2Cl_2$, these results highlight the utility of the metal–radical approach to produce coordination polymer-based magnets with high ordering temperatures.

The reaction between $Mn^{II}I_2(thf)_3$ and $TCNE^0$ yields a 3D coordination polymer $Mn(TCNE)_{1.5}(I_3)_{0.5}{\cdot}0.5THF$ in addition to $Mn^{II}(TCNE)(C_4(CN)_8)_{0.5}$,[129] the latter is isostructural to $Fe^{II}(TCNE)(C_4(CN)_8)_{0.5}$. $Mn(TCNE)_{1.5}(I_3)_{0.5}{\cdot}0.5THF$ undergoes FiM ordering at $T_c = 171$ K,[129] representing the highest ordering temperature thus reported for a structurally characterised magnetic coordination polymer.[19] The structure of $Mn(TCNE)_{1.5}(I_3)_{0.5}$ comprises the familiar undulating layer motif, with octahedral $S = 5/2$ Mn^{II} centres coordinated to paramagnetic μ^4-$TCNE^{-\bullet}$ ligands (Figure 1.13b). The 3D network is formed by bridging the undulating layers by a second type of μ^4-$TCNE^{-\bullet}$ ligand, which occupies the axial Mn^{II} coordination sites. Due to the planar geometry and smaller size of bridging μ^4-$TCNE^{-\bullet}$ compared to μ^4-$[C_4(CN)_8]^{2-}$, the MnN_6 octahedra are more tilted compared to the FeN_6 octahedra and the sheets have a more pronounced corrugation (Figure 1.13b). This arrangement forms approximately square channels which run parallel to the crystallographic *a* axis, containing charge-

balancing I_3^- and disordered THF solvent (Figure 1.13d & f). Magnetic ordering in $Mn(TCNE)_{1.5}(I_3)_{0.5}\cdot 0.5THF$ at T_c = 171 K was evinced by the bifurcation of the field-cooled (FC) and zero field-cooled (ZFC) magnetisation data, in addition to peaks in the in-phase (χ_M') and out-of-phase (χ_M'') dynamic magnetic susceptibility. Long-range FiM ordering in $Mn(TCNE)_{1.5}(I_3)_{0.5}$ arises from strong direct AFM coupling between S = 5/2 Mn^{II} and S = 1/2 $TCNE^{-\bullet}$ in the undulating layers; the undulating FiM $Mn^{II}(TCNE^{-\bullet})$ layers then interact via AFM coupling with the bridging S = 1/2 μ^4-$TCNE^{-\bullet}$ ligands, producing an interlayer FM interaction and an overall FiM material. In contrast, $Mn^{II}(TCNE^{-\bullet})(C_4(CN)_8^{2-})$ undergoes AFM ordering at a Néel temperature T_N = 68 K, due to the presence of diamagnetic μ^4-$[C_4(CN)_8]^{2-}$ ligands linking the $Mn^{II}(TCNE^{-\bullet})$ layers, which leads to AFM coupling of the undulating $Mn^{II}(TCNE^{-\bullet})$ layers to each other.

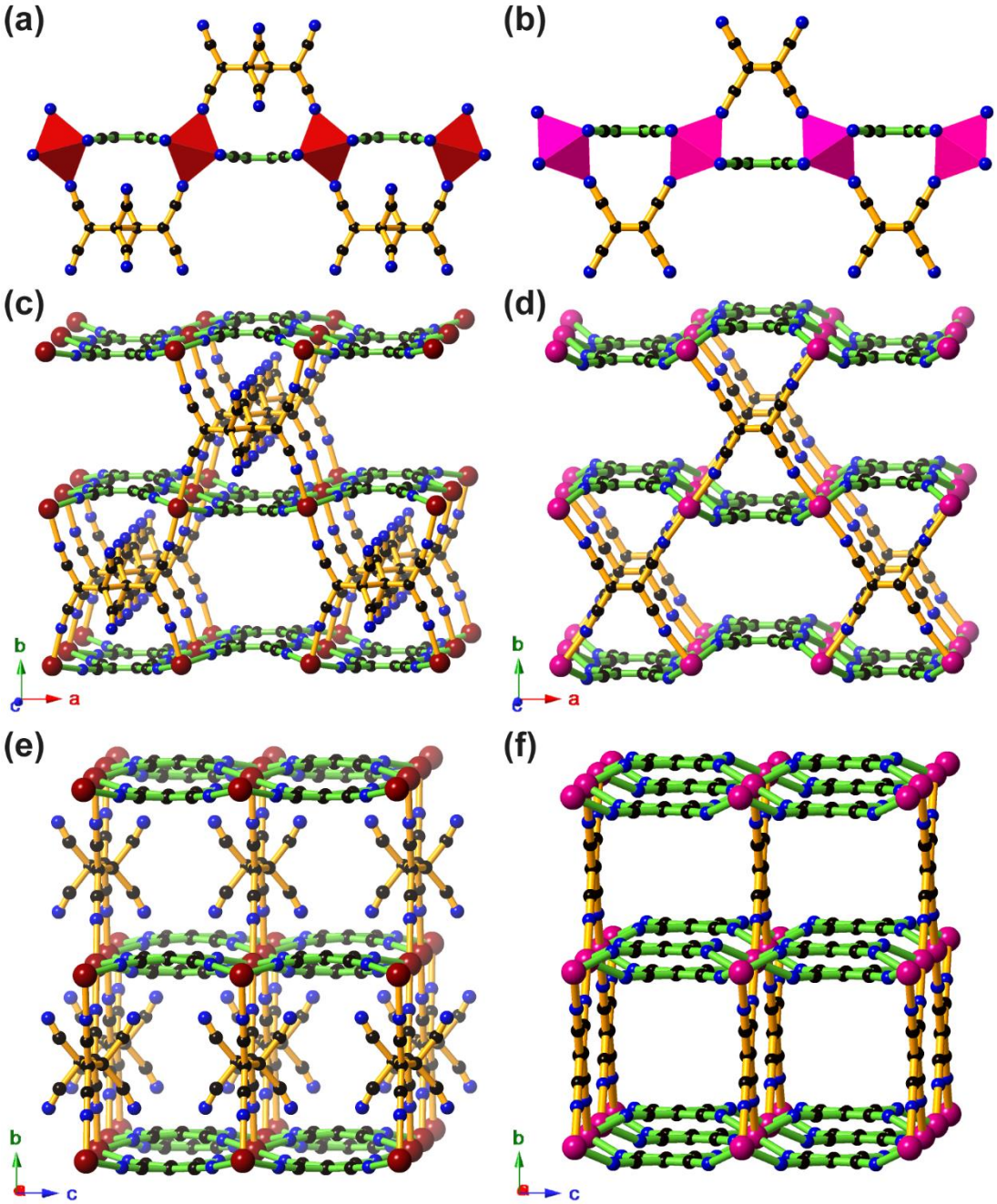
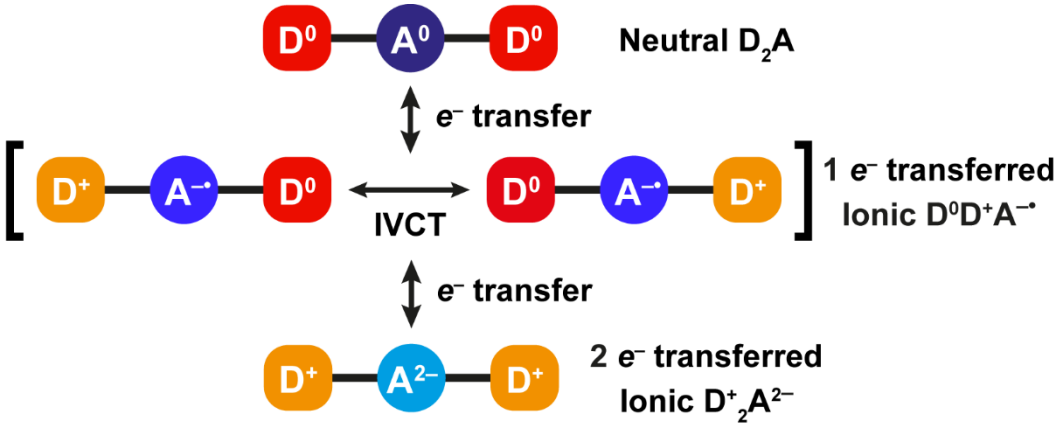


Figure 1.13 Structures of $Fe^{II}(TCNE)(C_4(CN)_8)$ (left) and $Mn(TCNE)_{1.5}(I_3)_{0.5}$ (right) coordination polymer magnets. (a & b) The undulating $M^{II}(TCNE^{-\bullet})$ sheets (pale green) and tilting of the $M^{II}N_6$ octahedral. Views down crystallographic (c & d) *c* and (e & f) *a* axes showing 3D networks formed by bridging undulating $M^{II}(TCNE^{-\bullet})$ sheets (pale green) with (c, e) diamagnetic μ^4-$[C_4(CN)_8]^{2-}$ (tan) or (d, f) paramagnetic μ^4-$TCNE^{-\bullet}$ ligands (tan). Maroon = Fe, magenta = Mn, blue = N, and black = C. I_3 (Mn only) and disordered solvents not shown for clarity. Only one orientation of the disordered $[C_4(CN)_8]^{2-}$ ligand shown for clarity.

Miyasaka and co-workers have extensively studied electron donor-acceptor (D-A) coordination polymer magnets assembled using polynitrile acceptor ligands.[130] The donors comprise tetracarboxylate-bridged diruthenium(II,II) paddlewheel clusters ($Ru_2(O_2CR)_4$) as electron rich donors (herein abbreviated as [Ru_2]), and electron-poor polynitrile (either R_xTCNQ or R_xDCNQI-type, where R denotes various substituents and *x* denotes the number) ligands as acceptors.[130] The two axial coordination sites of the [Ru_2] clusters are occupied by labile solvents, allowing coordination by the more strongly coordinating nitrile groups of the acceptor ligands. Varying the connectivity and geometry of the acceptor ligands allows 1-, 2- and 3D coordination polymers to be synthesised. These D-A systems have emerged as a powerful platform to generate conductive and magnetic coordination polymers. The ionisation potential (I_D) of the donor and electron affinity (E_A) of the acceptor can be finely and systematically tuned by varying the substituents on either the carboxylate ligands,[131] or the polynitrile acceptors respectively.[132-135] By carefully selecting donors and acceptors with appropriately matched I_D and E_A values, one can carefully tune along the continuum between neutral D^0A^0 to fully ionic $D^+A^{-\bullet}$ compounds, which form 1D coordination polymers. Using 4-connecting acceptor ligands i.e. R_xTCNQ, yields D_2A compounds which form 2D and 3D coordination polymers. Similarly, judicious choice of donor and acceptor with appropriate I_D and E_A, allows the valence state of the network to be tuned between neutral and either 1 or 2 electron transferred systems (Scheme 1.4).[130] For the paddlewheel [Ru_2] donors, one electron transfer from a S = 1 [$Ru_2^{II,II}$] unit generates an S = 3/2 [$Ru_2^{II,III}$] unit, both of which can engage in strong direct coupling with formed S = 1/2 $A^{-\bullet}$ ligands, allowing long-range magnetic ordering.[130]



Scheme 1.4 Electron transfer mechanisms in D_2A coordination polymers. Degenerate $D^0D^+A^{-\bullet}$ valence states can either be localised i.e. $D^0D^+A^{-\bullet}$ formulation or undergo IVCT i.e. delocalised $D^{+0.5}{}_2A^{-\bullet}$ formulation.

Reaction between TCNQ and $[Ru_2^{II,II}(O_2CCF_3)_4]$ yields a 2D coordination polymer in which tetracarboxylate $[Ru_2]$ units link between μ^4-TCNQ nodes.[136] However, as I_D and E_A in this system are not well matched, it is a neutral $D^0{}_2A^0$ $[\{Ru_2^{II,II}\}(TCNQ^0)\{Ru_2^{II,II}\}]$ system. The compound therefore only exhibits low temperature paramagnetism and no long-range ordering, due to insufficient spin exchange between the isolated $S = 1$ $[Ru_2^{II,II}]$ units.[136-138] Replacing TCNQ with the stronger acceptor F_4TCNQ gives the isostructural compound $[\{Ru_2(O_2CCF_3)_4\}_2(F_4TCNQ)]\cdot 3(p\text{-xylene})$ (F_4TCNQ = 2,3,5,6-tetrafluoro-7,7,8,8-quinodimethane) (Figure 1.14a), which has a one electron transferred delocalised $[\{Ru_2^{4.5+}\}(F_4TCNQ^{-\bullet})\{Ru_2^{4.5+}\}]$ charge distribution; the delocalised Ru^{II}/Ru^{III} mixed valency also leads to a modest electrical conductivity of $\sigma_{295\,K} = 4.4 \times 10^{-5}$ S cm^{-1}.[137] The $S = 1/2$ $F_4TCNQ^{-\bullet}$ ligand allows strong coupling between the $S = 1$ $[Ru_2^{II,II}]$ and $S = 3/2$ $[Ru_2^{II,III}]$ units, although bulk FiM or FM ordering at low temperature was not observed. Instead, AFM ordering between the 2D $[\{Ru_2\}_2(F_4TCNQ)]$ layers was observed, evidenced by the molar magnetic susceptibility (χ_M) decreasing below $T_N = 95$ K (Figure 1.14b) and the absence of a peak in χ_M'' data.[137, 138]

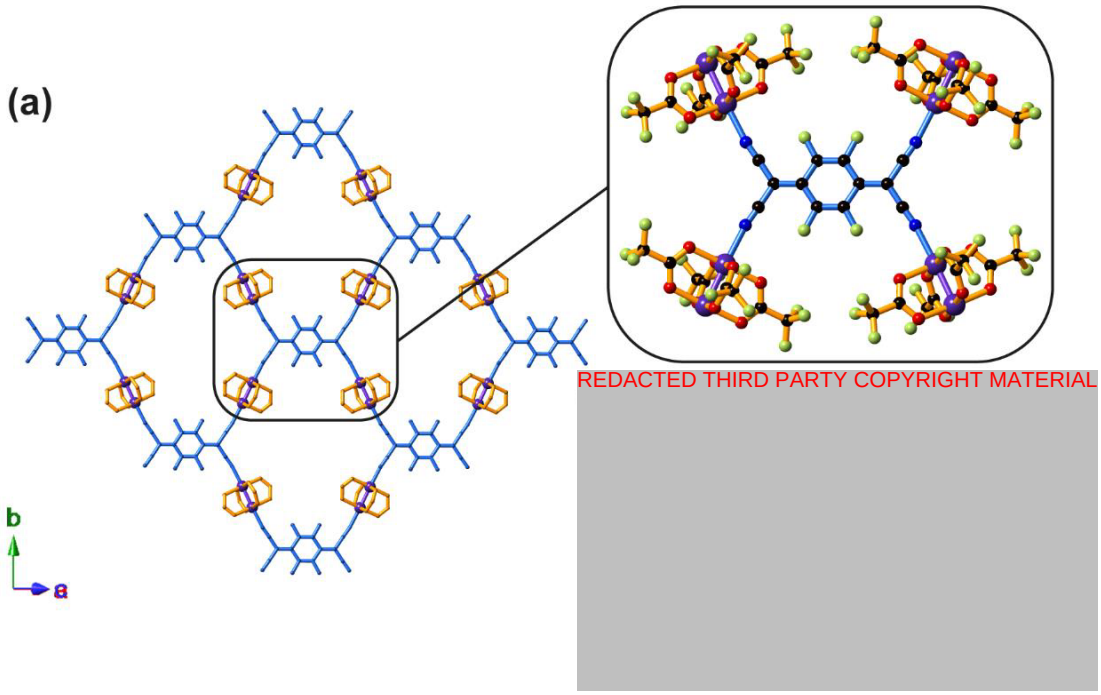
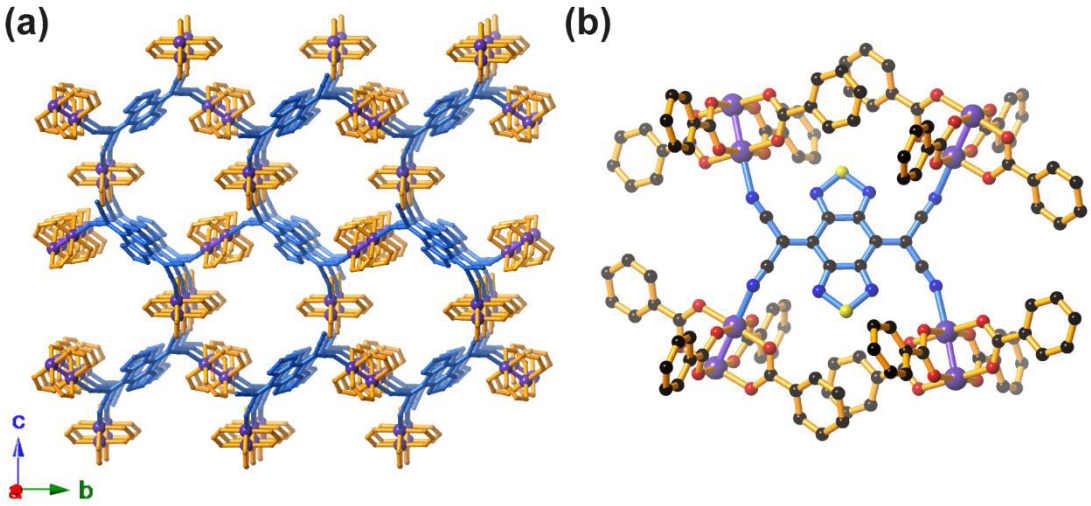


Figure 1.14 (a) 2D layer structure of [{$Ru_2(O_2CCF_3)_4$}$_2$(F_4TCNQ)] showing [Ru_2] donor units (orange) linking between acceptor F_4TCNQ ligands (pale blue). [Ru_2]-pendant CF_3 groups not shown for clarity. (Inset) Magnification of μ^4-F_4TCNQ coordination. Purple = Ru, pale green = F, red = O, blue = N, and black = C. (b) Temperature dependence of χ_M and $\chi_M T$ for [{$Ru_2(O_2CCF_3)_4$}$_2$(F_4TCNQ)] showing peak at T_N and decreasing χ_M below T_N suggesting AFM ordering. Adapted with permission from Ref. [137]. Copyright © 2006 American Chemical Society.

A similar reaction between [$Ru_2^{II,II}(O_2C$–3-FPh)$_4$] and BTDA-TCNQ yields a porous 3D coordination polymer in which [Ru_2] units link between slightly bent μ^4-BTDA-TCNQ ligands (3-F-$PhCO_2^-$ = 3-fluorobenzoate; BTDA-TCNQ = bis(1,2,5-thiadiazolo)tetracyanoquinodimethane) (Figure 1.15a & b).[139] A one electron transferred charge-ordered [{$Ru_2^{II,II}$}(BTDA-$TCNQ^{-\bullet}$){$Ru_2^{II,III}$}] formulation was assigned by examination of crystallographic Ru–O and BTDA-TCNQ C–C and C–N bond lengths. The higher than expected magnetic susceptibility-temperature product ($\chi_M T$) compared to that expected for two isolated S = 1 [$Ru_2^{II,II}$] units, suggested strong room-temperature coupling between the S = 1/2 BTDA-$TCNQ^{-\bullet}$ ligands the paramagnetic S = 1 [$Ru_2^{II,II}$] and S = 3/2 [$Ru_2^{II,III}$] units. Strong metal–radical coupling resulted in FM ordering at T_c = 107 K, indicated by the field-cooled dc susceptibility

measurements (χ_M), and as confirmed by the presence of peaks in χ_M' and χ_M'' data (Figure 1.15c & d).



REDACTED THIRD PARTY COPYRIGHT MATERIAL

Figure 1.15 (a) The 3D structure of [{Ru_2(O_2C–3-FPh)$_4$}$_2$(BTDA-TCNQ)] showing [Ru_2] donor units (orange) linking between BTDA-TCNQ acceptor ligands (pale blue). 3-Fluorophenyl groups not shown for clarity. (b) Bent geometry and μ^4-BTDA-TCNQ coordination. Purple = Ru, gold = S, red = O, blue = N, and black = C. F not shown for clarity. (c) Temperature dependence of χ_M and $\chi_M T$ (d) and χ_M' and χ_M'' for [{Ru_2(O_2C–3-FPh)$_4$}$_2$(BTDA-TCNQ)] showing long-range magnetic ordering at T_c = 107 K. Adapted with permission from Ref. [139]. Copyright © 2008 WILEY-VCH Verlag GmbH & Co. KGaA.

Due to the redox activity of the TCNQ ligands, the magnetic ordering in these [{Ru_2}$_2$(R_xTCNQ)] frameworks can also be reversibly switched externally. The 2D layered frameworks [{Ru_2(O_2C–F_4Ph)$_4$}$_2$(BTDA-TCNQ)] (F_4Ph–CO_2^- = 2,3,5,6-tetrafluorobenzoate) and [{Ru_2(O_2CF_3)$_4$}$_2$(BTDA-TCNQ)] are neutral $D^0{}_2A^0$

systems which behave as paramagnets, as the neutral BTDA-TCNQ ligands can only mediate weak superexchange between the $S = 1$ [$Ru_2^{II,II}$] units.[121, 122] Long-range FiM ordering could be turned on in these compounds by framework reduction in a lithium-ion battery (LIB) device giving ionic $D^0{}_2A^{-\bullet}$ systems. Magnetic ordering occurred due to the expected strong AFM coupling between the $S = 1$ [$Ru_2^{II,II}$] units and $S = 1/2$ BTDA-TCNQ$^{-\bullet}$ ligands. Further reduction to BTDA-TCNQ^{2-} decreased T_c as the diamagnetic BTDA-TCNQ^{2-} ligands causing progressively weaker coupling between the paramagnetic [$Ru_2^{II,II}$] units.

The porous nature of [{Ru_2}$_2$(R_xTCNQ)] frameworks also allow reversible guest-induced switching of magnetic ordering, a behaviour not accessible in conventional inorganic magnetic materials. The 2D framework [{$Ru_2(O_2C–Cl_3Ph)_4$}$_2$(Me_2TCNQ)]·$4CH_2Cl_2$ exhibits a charge-ordered [{$Ru_2^{II,II}$}(Me_2TCNQ$^{-\bullet}$){$Ru_2^{II,III}$}] valence distribution ($Cl_3Ph–CO_2^-$ = 2,3,5-trichlorobenzoate; Me_2TCNQ = 2,5-dimethyl-7,7,8,8-tetracyanoquinodimethane).[140] Due to strong AFM coupling between paramagnetic [Ru_2] units and Me_2TCNQ$^{-\bullet}$ ligands, the framework undergoes FiM ordering at T_c = 101 K. Loss of CH_2Cl_2 from the framework void space caused a valence state fluctuation, due to an additional electron transfer from a [$Ru_2^{II,II}$] unit, giving a putative intermediate [{Ru_2}$^{0.5+}$(Me_2TCNQ$^{1.5-}$){$Ru_2^{II,III}$}$^+$] formulation, representative of domains with [{$Ru_2^{II,II}$}(Me_2TCNQ$^{-\bullet}$){$Ru_2^{II,III}$}] and [{$Ru_2^{II,III}$}(Me_2TCNQ^{2-}){$Ru_2^{II,III}$}] charge distributions. The desolvated compound also underwent FiM ordering, though at a substantially lower T_c = 34 K, arising from the presence of domains containing diamagnetic Me_2TCNQ^{2-} ligands which did not effectively relay spin exchange. Reversible switching of T_c was achieved by repeated resolvation and desolvation of the compound, although slight differences in magnetic properties were observed between the pristine and resolvated compound, ascribed to structure disorder introduced by the solvation process.

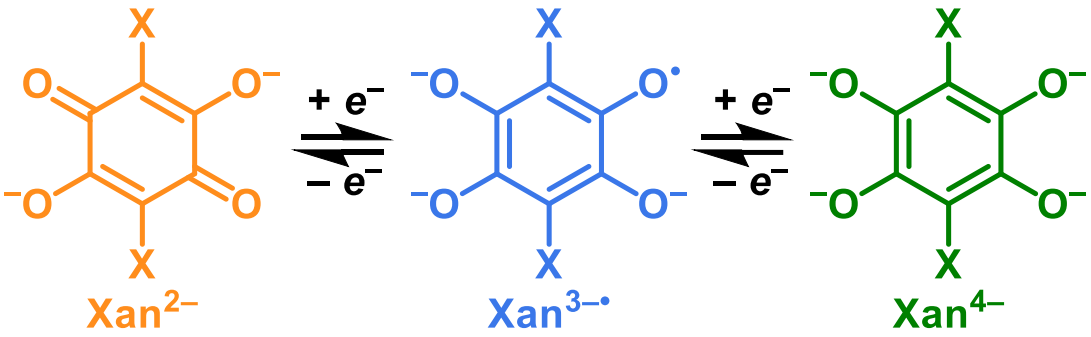
First reported in 2001,[141] single chain magnets (SCMs) are another class of coordination polymers which can exhibit ‘magnet-like’ behaviour i.e. freezing of the magnetisation in the absence of an applied field.[142] SCMs comprise 1D chains of strongly AFM or FM coupled spins, which are magnetically isolated from adjacent chains.[142, 143] In contrast to the magnetic coordination polymers described previously, in which hysteresis and slow magnetisation dynamics result from long-range ordering, these behaviours in SCMs arise due to the energy barrier associated with flipping an

individual spin state within the chains of coupled spins.[142, 143] Of particular relevance, SCM-like behaviour has recently been observed in 1- and 2D tetraoxolene coordination polymers (*vide infra*).[144, 145] An especially effective route to produce SCMs is by using radical ligands (S_L = 1/2) to bridge between paramagnetic metal centres of unequal spin ($S_M \neq S_L$), due to strong metal–radical coupling.[146] Stable bulky nitronyl-nitroxide bridging ligands have featured prominently in the synthesis of SCMs.[141, 146-150] However, due to the poor coordination ability of nitronyl-nitroxides, strongly electron-withdrawing ancillary ligands, such as hexafluoroacetylacetonate, are required around the paramagnetic metal centres to produce stable coordination polymers.[146]

1.3 Tetraoxolene Coordination Polymers

1.3.1 Redox Activity of the Tetraoxolenes

Following the pioneering studies of Robl and co-workers,[151-153] the ligands formed by deprotonating the tetraoxolenes, 2,5-dihydroxy-1,4-benzoquinone (H_2dhbq, X = H) and the 3,6-disubstituted analogues (termed anilic acids, H_2Xan, X = F, Cl, Br, I, CN, NO_2 etc.) have been extensively employed to synthesise a range of 1-, 2- and 3D coordination polymers.[154-158] Tetraoxolene ligands have several advantageous properties in the synthesis of magnetic and conductive coordination polymers. Variation of the 3,6-substituents, to either electron donating or electron withdrawing, allows tuning of the redox potential of the bridging ligand,[159] and to a lesser extent the degree of electronic coupling between paramagnetic metal centres.[160-162] Tetraoxolenes also exist in three accessible redox states: a quinonoid dianion (Xan^{2-}); a semiquinonoid radical trianion ($Xan^{3-\bullet}$); and an aromatic tetraanion (Xan^{4-}) (Scheme 1.5).[163-167]



Scheme 1.5 Commonly observed valence states of tetraoxolene anions (anilates, X = H, F, Cl, Br, I, Me, NO_2, CN etc.). NB: Single canonical form of semiquinonoid radical trianion shown.

Importantly, these redox states afford different degrees of electronic coupling between metal centres, with the closed-shell Xan^{2-} and Xan^{4-} states mediating only weak coupling via superexchange.[163, 166] In contrast, strong exchange between paramagnetic metal centres is afforded by the radical $Xan^{3-\bullet}$ state, due to strong coupling (typically AFM) between open-shell metals and the bridging radical ligand.[164, 165, 168, 169] The combination of readily switchable redox states and the ability of tetraoxolenes to afford effective magnetic communication between metal centres makes them highly attractive ligands in the synthesis of magnetic and conductive coordination polymers.

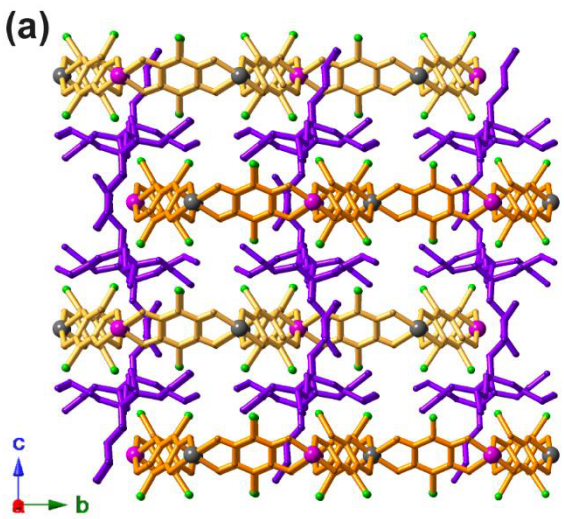
1.3.2 Magnetic Tetraoxolene Coordination Polymers

Interest in the use of tetraoxolene ligands to synthesise porous magnetic coordination polymers stems, to a great degree, from work in the early 1990's on multifunctional magnetic metal–oxalate coordination polymers.[158] In these compounds, the magnetic properties arise from coupling between metal centres in the $[M^{II}_2(ox)_3]^{2-}$ or $[M^{II}M^{III}(ox)_3]^{-}$ (ox^{2-} = oxalate) networks, with the topology and geometry of the network dictated by the charge-balancing countercations.[118] Additional properties such as spin-crossover, photochromism and electrical conductivity can be engendered by incorporating functional cations.[118] For example, Coronado and co-workers synthesised a FM and metallically conductive coordination polymer using mixed-valence BEDT-TTF (BEDT-TTF = bis(ethylenedithio)-tetrathiafulvalene) cations to charge balance a $[Mn^{II}Cr^{III}(ox)_3]^{-}$ network, forming the

compound $(BEDT\text{-}TTF)_3[Mn^{II}Cr^{III}(ox)_3]$.[170] The structure comprises alternating layers of hexagonal (6,3) $[Mn^{II}Cr^{III}(ox)_3]^-$ sheets, and layers of 1D stacks of mixed-valence BEDT-TTF cations. Long-range FM ordering was observed around 5.5 K, with the magnetic behaviour of the compound consistent with previously reported $[Mn^{II}Cr^{III}(ox)_3]^-$ networks. The authors therefore concluded magnetic ordering arose solely due to exchange interactions in the bimetallic network. The high $\sigma_{RT} \approx 250$ S cm^{-1} and metallic conductivity down to 2 K arose due to charge transport along the mixed-valence BEDT-TTF stacks in the organic layer, with no significant interaction between the conducting and FM components observed. A similar compound in which the BEDT-TTF was substituted with BEDT-TSF (BEDT-TSF = bis(ethylenedithio)tetraselenafulvalene) exhibited a combination of FiM ordering at 5.3 K, and metallic conductivity down to 150 K, arising exclusively from the inorganic and organic layers respectively.[171]

Despite these interesting multifunctional properties, which can be introduced using a range of cations, later studies demonstrated the magnetic ordering temperature in $[M_2(ox)_3]^{x-}$ networks was largely insensitive to the identity of the cation, as they did not efficiently modulate the exchange interactions between metal centres.[158] Moreover, while the short metal-metal distances in oxalate networks promotes effective magnetic coupling between metal centres, the small size of oxalate means these compounds are dense and non-porous compounds. Oxalate and tetraoxolene ligands exhibit similar coordination modes, which coupled with the increased size of tetraoxolene ligands, allows porous coordination polymers to potentially be synthesised by using tetraoxolene instead of oxalate ligands.[158] An additional advantage of tetraoxolenes over oxalate is the presence of 3,6-disubstitution, allowing the degree of magnetic coupling between metal centres to be varied. This provides a more effective mechanism of tuning the exchange interactions in the magnetic network, compared to cation substitution in oxalate networks.[158] This was elegantly demonstrated by Atzori *et al.*, who investigated the magnetic properties of a family of isostructural bimetallic (6,3) 2D networks of composition $(^nBu_4N)[Mn^{II}Cr^{III}(Xan)_3]\cdot$solvent ($^nBu_4N^+$ = tetra-*n*-butylammonium; X = H, Cl, Br, I) (Figure 1.16a).[172] At room temperature, all the compounds exhibited $\chi_M T$ values of ca. 6.2 cm^3 K mol^{-1}, close to the expected value of 6.25 cm^3 K mol^{-1} (g = 2.0) for two non-interacting Mn^{II} and Cr^{III} centres. At low temperature, the compounds exhibited

net FiM ordering, arising from AFM coupling between Mn^{II} (S = 5/2) and Cr^{III} (S = 3/2) centres. Importantly, T_c varied between 5.5–11.0 K and was correlated with the electronegativity of the ligand substituent; with the less electronegative X = H substituent affording the framework with the highest T_c, as shown by variation of the peak position in the χ_M' data (Figure 1.16b).



REDACTED THIRD PARTY COPYRIGHT MATERIAL

Figure 1.16 (a) Structure of the 2D layered (^{n}Bu$_4$N)[$Mn^{II}Cr^{III}$(Clan)$_3$] coordination polymer showing packing of anionic [$Mn^{II}Cr^{III}$(Clan)$_3$]$^-$ layers with disordered ^{n}Bu$_4$N$^+$ cations (purple). Magenta = Mn, grey = Cr, green = Cl. H atoms and solvents not shown for clarity. (b) Thermal variation of the in-phase ac magnetic susceptibility (χ_M') showing Xan^{2-} substituents influence the FiM T_c. Adapted with permission from Ref. [172]. Copyright © 2013 American Chemical Society.

While numerous studies have investigated the magnetic properties of metal–tetraoxolene coordination polymers, the earlier works largely reported only paramagnetic compounds.[155, 156, 158, 173, 174] Although these compounds were typically synthesised using paramagnetic divalent metals, they also used diamagnetic Xan^{2-} forms of tetraoxolenes to bridge between metal centres. Given that Xan^{2-} only mediates weak magnetic communication via superexchange, this typically results in weak AFM coupling between the metals, preventing long-range ordering.[155, 156, 173-176] As the redox activity of the tetraoxolene ligands is maintained when incorporated into coordination polymers,[177] it was later realised that incorporation of the radical

$Xan^{3-\bullet}$ into the frameworks could produce porous frameworks capable of long-range magnetic ordering. Moreover, the ability to reversibly alter the ligand redox state between Xan^{2-} and $Xan^{3-\bullet}$, allows external stimuli to switch the magnetic states, a behaviour which is not achievable in conventional inorganic magnets. Similar to their work on D_2A [Ru2] systems, Miyasaka and co-workers utilised a LIB system to switch the magnetic states in the aforementioned 2D (^{n}Bu$_4$N)[$Mn^{II}Cr^{III}$(Clan)$_3$] coordination polymer between paramagnetic and ferrimagnetic.[123] Framework reduction and concomitant Li^+ insertion, giving a $Li_x(^n Bu_4N)[Mn^{II}Cr^{III}(Clan^{2-})_{3-x}(Clan^{3-\bullet})_x]$ (x = 0–3) formulation, increased sample magnetisation at low temperature and increased T_c, due to stronger coupling between metals and paramagnetic ligands (Figure 1.17a). Given the reversibility of the Li^+ insertion process, the magnetic properties of the compound could be switched by charging and discharging the LIB over several cycles (Figure 1.17b). This work was later extended, by transforming the paramagnetic compound $[(H_3O)_2(phenazine)_3][Fe^{II}_2(Clan^{2-})_3]$, which did not exhibit long-range ordering at 5 K, into the FiM compound $Li_3[(H_3O)_2(phenazine)_3][Fe^{II}_2(Clan^{3-\bullet})_3]$ that underwent long-range ordering at T_c = 128 K.[124] More recently, Liu *et al.* showed redox switching of conductive and magnetic properties in the (6,3) coordination polymer, $(Me_4N)_2[Mn^{II}_2(Clan^{2-})_3]$ (Me_4N^+ = tetramethylammonium).[120] Low temperature magnetic susceptibility measurements demonstrated the pristine framework was paramagnetic down to 2 K, due to weak AFM coupling between the S = 5/2 Mn^{II} centres mediated by the diamagnetic $Clan^{2-}$ ligands. The compound also exhibited a low $\sigma_{295\ K}$ = 1.14(3) × 10^{-13} S cm^{-1}, due to the absence of ligand-centred mixed valency. Reduction of the framework to $Na_3(Me_4N)_2[Mn^{II}_2(Clan^{3-\bullet})_3]$ resulted in markedly different properties, namely significantly increased $\sigma_{295\ K}$ = 2.27(1) × 10^{-8} S cm^{-1}, and the introduction of long-range FiM ordering at T_c = 41 K. The change in magnetic state was evinced by ac susceptibility and low-temperature magnetisation experiments and was ascribed to direct AFM coupling between the two S = 5/2 Mn^{II} centres and three S = 1/2 $Clan^{3-\bullet}$ ligands.

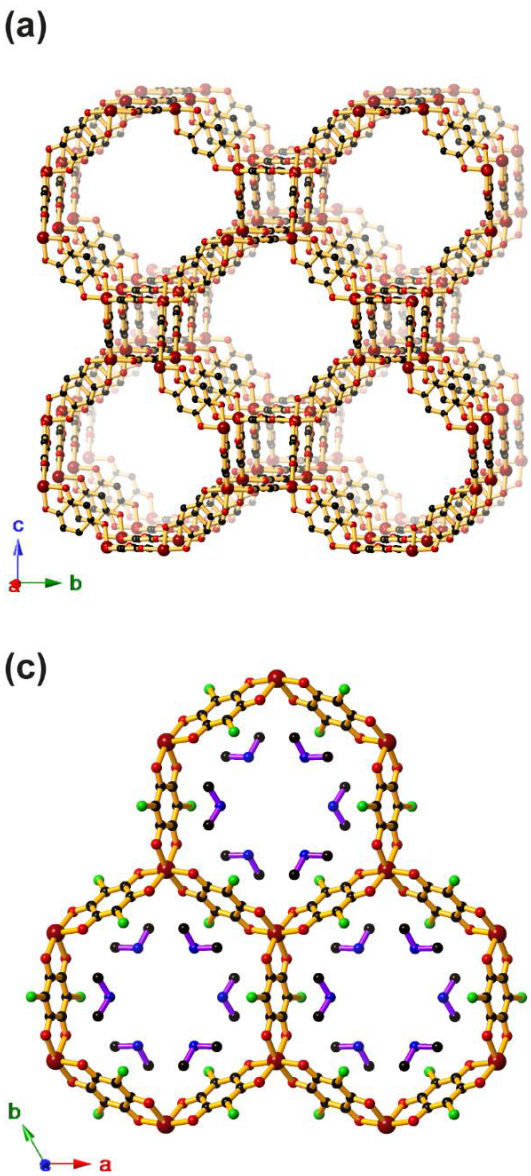
REDACTED THIRD PARTY COPYRIGHT MATERIAL

Figure 1.17 The magnetic response of a LIB cathode containing $Li_x(^nBu_4N)[Mn^{II}Cr^{III}(Clan^{2-})_{(3-x)}(Clan^{3-\bullet})_x]$ (x = 0–3) to electrochemical stimuli. (a) Variation of the temperature-dependant magnetisation with increasing Li^+ content i.e. degree of framework reduction, showing increasing low-temperature magnetisation due to conversion of diamagnetic $Clan^{2-}$ to radical $Clan^{3-\bullet}$ ligands. (b) Reversible switching of the FiM T_c (top) and magnetisation variation (ΔM, bottom) by LIB discharge (framework reduction, $Clan^{2-} \rightarrow Clan^{3-\bullet}$) and charge (framework oxidation, $Clan^{3-\bullet} \rightarrow Clan^{2-}$) cycles. Adapted with permission from Ref. [123]. Copyright © 2017 American Chemical Society.

An emerging class of metal–tetraoxolene frameworks of interest in the synthesis of porous magnetic materials is the Fe–tetraoxolene frameworks containing ligands in mixed-valence states. Upon the first synthesis of the 3D (10,3)-*a* $(^nBu_4N)_2[Fe_2(dhbq)_3]$ coordination polymer (Figure 1.18a) by Abrahams and co-workers, the valence state distribution was initially assigned as $(^nBu_4N)_2[Fe^{II}_2(dhbq^{2-})_3]$, by analogy with the isostructural $(^nBu_4N)_2[M_2(dhbq)_3]$ (M = Mn^{II}, Co^{II}, Ni^{II}, Zn^{II}, Cd^{II}) compounds.[178] However, ligand-centred mixed valency in the Fe compound was later recognised by Long and co-workers.[179] ^{57}Fe Mössbauer spectroscopy on $(^nBu_4N)_2[Fe_2(dhbq)_3]$ revealed isomer shift values consistent with Fe^{III}_{HS}, suggestive of spontaneous oxidation of putative Fe^{II} centres to Fe^{III} (Figure 1.18b). This was concomitant with partial reduction of the $(dhbq^{2-})_3$ ligands to $(dhbq^{2.67-})_3$ (formally $(dhbq^{2-})(dhbq^{3-\bullet})_2$) due to electron transfer from Fe^{II}. Similar ^{57}Fe Mössbauer spectroscopic analysis on

the 2D honeycomb framework $(Me_2NH_2)_2[Fe_2(Clan)_3]\cdot 6DMF\cdot 2H_2O$ ($Me_2NH_2^+$ = dimethyl-ammonium) (Figure 1.18c) by Harris and co-workers similarly revealed the presence of Fe^{III}_{HS}, again suggestive of mixed valence $(Me_2NH_2)_2[Fe^{III}_2(Clan^{2.67-})_3]$ charge distribution.[180] The spontaneous electron transfer from Fe^{II} donors to Xan^{2-} acceptors is analogous to the spontaneous CT observed in the aforementioned [Ru2] D_2A frameworks, though the Fe–tetraoxolene frameworks are better described as ionic D_2A_3 type systems due to the different stoichiometry.

These and other mixed-valence Fe–tetraoxolene coordination polymers are of interest for magnetic studies, as the as-synthesised frameworks intrinsically have paramagnetic metal centres with large *S* values bridged by radical ligands. This arrangement is predisposed towards long-range magnetic ordering. For example, $(Me_2NH_2)_2[Fe_2(Clan)_3]\cdot 6DMF\cdot 2H_2O$ undergoes long-range FiM ordering at T_c = 80 K, arising from AFM coupling between Fe^{III}_{HS} and $Clan^{3-\bullet}$ ligands.[180] Upon desolvation, magnetisation at low temperature was reduced, in addition to the ordering temperature decreasing to T_c = 26 K (Figure 1.18d). This was ascribed to framework distortions causing less favourable metal-ligand orbital overlap, and therefore less effective coupling between Fe^{III}_{HS} and $Clan^{3-\bullet}$. The ordering temperature was increased to T_c = 105 K by framework reduction with cobaltocene ($Co^{II}Cp_2$), to $(Co^{III}Cp_2)_{1.43}(Me_2NH_2)_{1.57}[Fe_2(Clan^{3-\bullet})_3]\cdot 4.9DMF$.[119] The increased T_c occurred due to enhanced coupling between Fe^{III}_{HS} and the three $Clan^{3-\bullet}$ ligands (Figure 1.18d), although the reduced compound could not be desolvated without losing crystallinity. Despite the presence of radical $dhbq^{3-\bullet}$ in $(^nBu_4N)_2[Fe_2(dhbq)_3]$, this compound only underwent long-range ordering at very low temperatures (< 8 K).[179] The isostructural mixed-valence fluoranilate coordination polymer $(^nBu_4N)_2[Fe_2(Fan)_3]$ similarly did not undergo long-range ordering at low temperature, experiencing only short-range ordering due to AFM Fe^{III}_{HS}–$Xan^{3-\bullet}$ coupling at low temperature.[181] In both cases, this behaviour was attributed to competing FM and AFM interactions at higher temperature, with the low temperature magnetic susceptibility governed by the AFM Fe^{III}_{HS}–$Xan^{3-\bullet}$ coupling. Overall, these results demonstrate the usefulness of tetraoxolene ligands in the assembly of magnetically interesting porous materials, particularly when incorporated into the networks in the radical $Xan^{3-\bullet}$ state.



REDACTED THIRD PARTY COPYRIGHT MATERIAL

Figure 1.18 (a) Ball-and-stick representation of a single anionic (10,3)-*a* network in $(^{n}Bu_4N)_2[Fe_2(dhbq)_3]$. Bu_4N^+ cations not shown for clarity. (b) ^{57}Fe Mössbauer spectra of $(^{n}Bu_4N)_2[Fe_2(dhbq)_3]$ and reduced $Na_{0.9}(^{n}Bu_4N)_{1.8}[Fe_2(dhbq)_3]$. Adapted with permission from Ref. [179]. Copyright © 2015 American Chemical Society. (c) The structure of the 2D $(Me_2NH_2)_2[Fe_2(Clan)_3]\cdot 6DMF\cdot 2H2O$ coordination polymer, showing packing between $Me_2NH_2^+$ cations (purple) and anionic $[Fe_2(Clan)_3]^{2-}$ honeycomb network. Maroon = Fe, green = Cl, red = O, blue = N, and black = C. H atoms and solvents not shown for clarity. (d) Field-cooled magnetisation data for $(Me_2NH_2)_2[Fe_2(Clan)_3]$ family indicating variation of ordering temperature with framework solvation and reduction state. Adapted with permission from Ref. [119]. Copyright © 2017 American Chemical Society.

Single-chain magnetism has also recently been demonstrated in Fe–tetraoxolene coordination polymers. However, in contrast to previously reported mixed-valence Fe–tetraoxolene compounds, in which the tetraoxolene $Xan^{3-\bullet}$ states are delocalised over equivalent crystallographic positions, the radical $Xan^{3-\bullet}$ states in these Fe–tetraoxolene SCMs are strictly localised. Single-chain magnetism was first realised in an Fe–tetraoxolene system by DeGayner *et al.*, in the 1D coordination polymer $(Me_4N)_2[Fe(Clan)Cl_2]$.[144] At low temperature, the structure comprises zig-zag chains of Fe^{III}_{HS} bridged by radical $Clan^{3-\bullet}$ ligands with ancillary *cis* chlorido ligands, whereas at high temperature, the compound exists in a valence tautomeric $(Me_4N)_2[Fe^{II}(Clan^{2-})Cl_2]$ form. Ac magnetic susceptibility measurements revealed that at low temperature, single-chain magnetism occurred, which was attributed to AFM coupling between $S = 5/2$ Fe^{III}_{HS} and $S = 1/2$ $Clan^{3-\bullet}$. Single-chain magnetism and valence tautomerism has also been observed in the mixed-valence 2D (6,3) coordination polymer $(^nPr_4N)_2[Fe_2(Clan)_3]\cdot$solvent ($^nPr_4N^+$ = tetra-*n*-propylammonium).[145] In contrast to previous reported mixed-valence Fe–tetraoxolene compounds, at low temperature the charge state distribution is strictly localised i.e. $(^nPr_4N)_2[Fe^{III}_2(Clan^{2-})(Clan^{3-\bullet})_2]\cdot$solvent. The (6,3) sheet structure is therefore comprised of zig-zag $\{Fe^{III}_{HS}–Clan^{3-\bullet}\}_\infty$ chains, bridged by $Clan^{2-}$ ligands, thus producing a quasi-1D magnetic chain even though the sheet topology is 2D. As in $(Me_4N)_2[Fe(Clan)Cl_2]$, Fe^{III}_{HS} and $Clan^{3-\bullet}$ undergo AFM coupling at low temperature, although the coupling was stronger in $(^nPr_4N)_2[Fe_2(Clan)_3]\cdot$solvent. Ac susceptibility measurements on the compound revealed a barrier height of $\Delta\tau = 67.3$ cm^{-1} and a relaxation time of $\tau_0 = 4.9 \times 10^{-11}$ s, both parameters consistent with single-chain magnetism.

1.3.3 Electrically Conductive Tetraoxolene Coordination Polymers

Compared to studies on the magnetic properties, the electrically conductive properties of tetraoxolene compounds have received relatively less attention until recently. Remarkably though, conductivity in a mixed-valence metal–tetraoxolene coordination polymer was first demonstrated in 1979 by Wrobleski and Brown.[182] In this work, the as-synthesised valence pure $[Fe^{II}(dhbq^{2-})(H_2O)_2]$ compound was oxidised using I_2 to a mixed-valence compound. ^{57}Fe Mössbauer spectroscopy demonstrated metal-centred mixed valency was introduced, giving a putative $[Fe^{II}_2Fe^{III}(dhbq^{2-})_3]I_3$ valence formulation. Partial Fe oxidation caused a significant

increase in conductivity from $\sigma_{300\,K} < 1 \times 10^{-10}$ S cm^{-1} to $\sigma_{300\,K} = 5 \times 10^{-5}$ S cm^{-1} in the mixed-valence compound. Despite this early work, interest in the use of metal–tetraoxolene coordination polymers as electrically conductive materials has only recently received significant attention, possibly arising from the lack of X-ray structural characterisation of the earlier reported [Fe(dhbq)(H_2O)$_2$] compound. Interest in these compounds was revived following the work of Long and co-workers[179] on the previously reported interpenetrating 3D (10,3)-*a* (^{n}Bu$_4$N)$_2$[Fe$_2$(dhbq)$_3$] coordination polymer.[178] Variable-temperature conductivity measurements revealed the as-synthesised compound exhibited $\sigma_{298\,K} = 1.6(1) \times 10^{-1}$ S cm^{-1}, in addition to semiconductor behaviour with an activation energy $E_a = 0.11$ eV.[179] This is consistent with thermally-activated intervalence charge transfer (IVCT) within the dhbq^{2-}/dhbq$^{3-\bullet}$ manifold. Further evidence of the electron hopping mechanism for charge transport was provided following chemical reduction to Na$_{0.9}$(^{n}Bu$_4$N)$_{1.8}$[Fe$_2$(dhbq)$_3$]. This process decreased the conductivity to $\sigma_{298\,K} = 6.2(1) \times 10^{-3}$ S cm^{-1} and increased the activation energy to $E_a = 0.18$ eV (Figure 1.19a), demonstrating the importance of mixed valency upon conductivity in tetraoxolene coordination polymers. Electrical conductivity was also reported in the isostructural fluoranilate analogue (^{n}Bu$_4$N)$_2$[Fe$_2$(Fan)$_3$], although it was more modest ($\sigma_{298\,K} = 1.77 \times 10^{-3}$ S cm^{-1}, $E_a = 0.124$ eV).[181] The reduced conductivity was partially attributed to the lower rhombohedral symmetry of (^{n}Bu$_4$N)$_2$[Fe$_2$(Fan)$_3$] relative to the cubic symmetry of (^{n}Bu$_4$N)$_2$[Fe$_2$(dhbq)$_3$], introducing anisotropy to the charge transport pathways in (^{n}Bu$_4$N)$_2$[Fe$_2$(Fan)$_3$].

Despite the high conductivity of (^{n}Bu$_4$N)$_2$[Fe$_2$(dhbq)$_3$] and (^{n}Bu$_4$N)$_2$[Fe$_2$(Fan)$_3$], these frameworks are not porous and have rather low magnetic ordering temperatures. Mixed-valence (6,3) networks have in recent years attracted significant attention due to the presence of large channels in their structure, affording magnetic and conductive porous materials. The 2D network (Me$_2$NH$_2$)$_2$[Fe$_2$(Clan$^{2.67-}$)$_3$]·6DMF·2H_2O also exhibits semiconductor behaviour with a high conductivity of $\sigma_{298\,K} = 1.4(7) \times 10^{-2}$ S cm^{-1}, $E_a = 0.26(1)$ eV.[119] Desolvation decreased the conductivity one order-of-magnitude, attributed to reduced metal-ligand orbital overlap, arising from the structural distortion upon desolvation. Chemical reduction to (Co^{III}Cp$_2$)$_{1.43}$(Me$_2$NH$_2$)$_{1.57}$[Fe$_2$(Clan$^{3-\bullet}$)$_3$] further decreased the conductivity to $\sigma_{298\,K} = 5.1(3) \times 10^{-4}$ S cm^{-1}, and increased $E_a = 0.34(1)$ eV (Figure 1.19b), reinforcing

the importance of mixed valency in providing a mechanism for charge transport. Extending this work, Long and co-workers synthesised the isostructural family $(Me_2NH_2)_x[M_2(Clan)_3]$ (M = Ti, V, x = 2; M = Cr, x = 1.5) to investigate how varying metal-ligand covalency impacted upon the magnetic and conductive properties of the frameworks.[183] The σ_{RT} increased with Cr < Ti < V, from $\sigma_{RT} = 1.2(1) \times 10^{-4}$ S cm^{-1} to $\sigma_{RT} = 4.5(3) \times 10^{-1}$ S cm^{-1}, which was reported as the highest value in a porous coordination polymer using O donors. The significantly higher conductivity of the V analogue was consistent with greater metal-ligand covalency, evinced by a broad, intense absorbance in the near- and mid-IR (NIR and MidIR respectively) region. This contrasted with the Cr and Ti analogues which displayed only very weak or moderate absorbances in the NIR, attributed to IVCT between ligand valence states, indicative of a lower degree of electron delocalisation.

REDACTED THIRD PARTY COPYRIGHT MATERIAL

Figure 1.19 (a) Temperature-dependant electrical conductivity of $(^nBu_4N)_2[Fe_2(dhbq)_3]$ and reduced compound $Na_{0.9}(^nBu_4N)_{1.8}[Fe_2(dhbq)_3]$ showing thermally-semiconductor behaviour. Adapted with permission from Ref. [179]. Copyright © 2015 American Chemical Society. (b) Arrhenius plots of the electrical conductivity of the $(Me_2NH_2)[Fe_2(Clan)_3]$ showing semiconductor behaviour and dependence of conductivity upon solvation and framework reduction. Adapted with permission from Ref. [119]. Copyright © 2017 American Chemical Society.

Metal-centred mixed valency in metal–tetraoxolene coordination polymers can also be utilised to produce conducting materials. Benmansour *et al.* synthesised the mixed-valence (6,3) networks $[(H_3O)(H_2O)(phenazine)_3][Fe_2(Xan)_3]\cdot 12H_2O$ (X = Cl, Br) and investigated the magnetic and conducting properties.[184] These coordination polymers contain Fe-centred mixed valency, described as a $[Fe^{II}Fe^{III}(Xan^{2-})_3]^-$ valence distribution, in contrast to the previously described mixed-valence Fe–tetraoxolene networks containing ligand-centred mixed valency. Similarly to ligand-centred mixed valency providing a pathway for long-range charge transport, Fe-centred mixed valency in these compounds gave rise to semiconductor behaviour. Measurement of the conductivity of single crystals either parallel (σ_{par}) and perpendicular (σ_{per}) to the anionic $[Fe^{II}Fe^{III}(Xan)_3]^-$ sheets demonstrated the significant anisotropy values ($\sigma_{par}/\sigma_{per}$) of ca. 300 and 500 for the $Clan^{2-}$ and $Bran^{2-}$ compounds respectively. These results suggest that charge transport occurs primarily within the plane of the mixed-valence 2D $[Fe^{II}Fe^{III}(Xan)_3]^-$ sheets. Temperature-dependant charge localisation has also been observed in the mixed-valence 2D coordination polymer $(TAG)[Fe^{II}Fe^{III}(CNClan)_3]$ (TAG^+ = tris(amino)guanidinium, $CNClan^{2-}$ = 3-chloro-6-cyano-2,5-dihydroxy-1,4-benzoquinone, cyanochloranilate).[185] The low temperature ^{57}Fe Mössbauer spectrum was consistent with localised Fe^{II} and Fe^{III} sites in a *ca.* 1:1 proportion. Upon warming, the spectrum collapses to a delocalised $Fe^{2.5+}$ state, confirming the temperature dependence of electron localisation in $[Fe^{II}Fe^{III}(Xan)_3]^-$ networks. A combination of metal- and ligand-centred mixed valency has very recently been observed in the 2D (6,3) coordination polymer $(Et_4N)_2[Fe_2(Fan)_3]\cdot$solvent by Murase *et al.*[186] While crystallographic studies were suggestive of purely ligand-centred mixed valency i.e. $(Et_4N)_2[Fe^{III}_2(Fan^{2.67-})_3]$ similarly to the isostructural Clan analogue,[187] ^{57}Fe Mössbauer spectroscopy revealed the presence of significant Fe^{II} character at 100 and 293 K in $(Et_4N)_2[Fe_2(Fan)_3]$. This discrepancy between crystallographic and spectroscopic experiments is not unexpected given the differing time scales for the measurements (ca. 10^{-8} s for relaxation of an ^{57}Fe nucleus, and hours for the measurement crystallographic data set). It highlights the importance of multiple experimental techniques to elucidate structure-property relationships in these materials. Importantly, the distinct Fe^{II} and Fe^{III} states at 293 K in $(Et_4N)_2[Fe_2(Fan)_3]\cdot$solvent, indicates less facile electron delocalisation compared to $(TAG)[Fe^{II}Fe^{III}(CNClan)_3]$. The differing magnetic properties in $(Et_4N)_2[Fe_2(Fan)_3]$ i.e. slow magnetisation relaxation, compared to similar trigonally

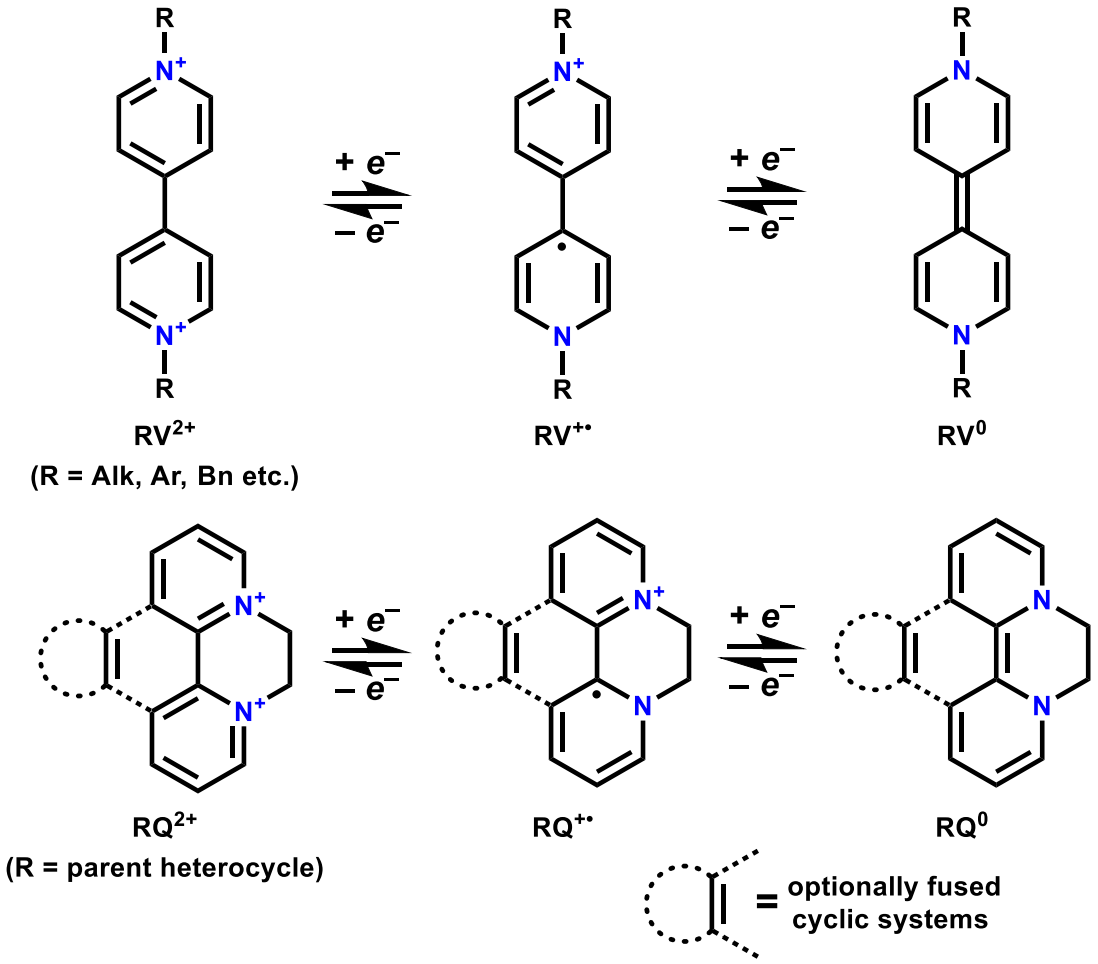
symmetric 2D $[Fe_2(Xan)_3]^{2-}$ networks was proposed to arise from the combination of Fe- and ligand-centred mixed valency.[186] The Fe-based mixed valency may also account for the higher conductivity of $(Et_4N)_2[Fe_2(Fan)_3]$ ($\sigma_{300\,K} = 1.8 \times 10^{-2}$ S cm^{-1}) compared to the isostructural $(Et_4N)_2[Fe_2(Clan)_3]$ network ($\sigma_{300\,K} = 2.2 \times 10^{-3}$ S cm^{-1}).

1.4 Viologens and Viologen-Like Molecules

Considering the similar coordination modes between oxalate and tetraoxolene ligands, it is unsurprising that countercations have a similar influence upon the network structure and topology in tetraoxolene frameworks as the role of countercations in oxalate networks.[118, 158] Moreover, incorporation of functional or redox-active cations into oxalate networks has been shown as an effective strategy to introduce properties not otherwise obtainable in these compounds.[118, 170, 171] Despite this, functional or redox-active cations have only infrequently served as counterions for anionic metal–tetraoxolene compounds.[188-192] Moreover, recent studies on mixed-valence metal–tetraoxolene frameworks have exclusively used redox-inactive cations (typically alkylammonium) to charge-balance and assist in templating the anionic networks.[119, 145, 179, 180, 183-187, 193-195] We therefore hypothesised that using redox-active cations could be a novel and fruitful strategy to obtain new tetraoxolene coordination polymer topologies, and perhaps also modulate the magnetic and conducting properties of mixed-valence frameworks due to the interactions between all redox-active components.

Quaternised bi- and poly-pyridinium cations, commonly termed viologens, are a major class of redox-active organic molecules of interest in supramolecular and materials chemistry.[196, 197] Tetraoxolenes and other acceptors like TCNQ and DCNQI, are Würster-type redox systems in which the oxidised state is quinonoid, and the reduced state is aromatic.[198] On the other hand, viologens are two-step Weitz-type redox systems, which exhibit complementary redox activity to Würster-type systems.[198] For viologens, the oxidised state (RV^{2+} for 4,4′-bipyridyl derived; RQ^{2+} for 2,2′-bipyridyl derived) is aromatic, which transforms to a highly-stable semiquinonoid radical cation ($RV^{+\bullet}$ or $RQ^{+\bullet}$) upon one electron reduction, and finally a neutral quinonoid species (RV^0 and RQ^0) following a subsequent one electron reduction (Scheme 1.6).[199] The first redox process from the aromatic dication to the semiquinonoid radical cation is highly reversible, whereas the second reduction (and

optionally subsequent reductions for polypyridinium systems) is often less reversible due to the low solubility of the neutral RV^0 species.[196, 199] Because their synthesis is relatively facile, an extraordinary diverse range of viologen and viologen-like systems have been synthesised, with the redox potentials of the compounds readily modulated by varying the: *N*-quaternary groups; the presence of conjugated spacers between the pyridinium rings; and addition of a range of fused (hetero)cyclic systems.[197, 199-207]



Scheme 1.6 The reversible redox processes in 4,4′-bipyridyl- (upper) and 2,2′-bipyridyl-derived (lower) viologen cations. NB: Single canonical forms of the semiquinonoid $RV^{+\bullet}$ and $RQ^{+\bullet}$ radical cations shown.

The programmable and reversible redox activity of viologens has therefore seen their application in electrochromic devices[208, 209] and organic batteries.[210, 211] Because viologens are π-conjugated systems and typically exhibit planar molecular geometries, they are predisposed to engage in supramolecular CT interactions with

other π-conjugated molecules.[196, 197] Critically the donor-acceptor character and strength of these CT interactions depends upon the redox state of the viologen moiety, so it is possible to reversibly switch the supramolecular interactions by external stimuli. The oxidised state RV^{2+} is π-electron poor and strongly interacts with π-electron rich species, for example polyaromatic hydrocarbons (PAHs) or TTF derivatives.[196, 197] In contrast, the radical cation $RV^{+\bullet}$ is weakly π-electron donating, and can interact with π-electron acceptors such as oxidised RV^{2+} species,[212] or other viologen radical cations via dimerisation,[213, 214] typical of π-electron radicals.[215-217] The switchable and reversible supramolecular interactions exhibited by viologens, termed *'affinity umpolung'* by Stoddart,[218] has therefore resulted in widespread use of viologen moieties into molecular switches and machines,[218-221] where external voltammetric or chemical stimuli can be used to produce predictable molecular movement. The richness of supramolecular interactions exhibited by viologen-like molecules, and redox activity complementary to tetraoxolenes, means they are ideal redox-active molecules to incorporate into redox-active metal−tetraoxolene systems.

1.5 Thesis Scope

This thesis is exclusively focussed on synthetic, structural, and physical property investigations of anionic metal–tetraoxolene coordination polymers containing viologen and viologen-like cations. There are two major aims to this work: understanding how the supramolecular interactions of viologens impacts upon the resultant topology and geometry of anionic tetraoxolene coordination polymers. Since in many cases, the electronic or magnetic properties are impacted by the coordination polymer structure, determining whether predictable network topologies can be synthesised by appropriate choice of templating viologen cation is an important goal. The second is to elucidate how the interplay of supramolecular and redox interactions between π-electron acceptor viologens, and π-electron rich mixed-valence tetraoxolene coordination polymers, could drive variations in the conductive, magnetic, and electroactive properties of these framework materials.

Chapter 2 concentrates exclusively on the first research goal and presents synthetic and X-ray structural studies on a range of novel 1-, 2- and 3D metal–tetraoxolene coordination polymers incorporating a range of viologen-like cations. This chapter is focused on understanding any possible templating effect of viologen cations on

framework topology and geometry. These studies are divided into investigations on frameworks containing divalent metals, and those that possess mixed-valence Fe–tetraoxolene frameworks. The latter compounds may form the basis of future electrochemical, magnetic, spectroscopic and conductivity studies.

Chapter 3 presents more focused X-ray structural studies on an isostructural family of anionic 2D mixed-valence Fe–tetraoxolene coordination polymers. These compounds all contain a viologen-like cation derived from 1,10-phenanthroline, namely 5,6-dihydropyrazino[1,2,3,4-*lmn*][1,10]-phenanthrolinediium ($PhenQ^{2+}$). These studies are aimed at determining how sensitive the CT interactions and templating effect of $PhenQ^{2+}$ cations are to the ligand halogen substituent. For the Fe–chloranilate compound, detailed structural, spectroscopic, magnetic and conductivity investigations where performed, to further uncover how the cation-network interactions influence the properties of the compound, by comparison with previously reported mixed-valence Fe–tetraoxolene frameworks which contain only redox-inactive cations.

Chapter 4 details how the properties a 2D mixed-valence Fe–fluoranilate coordination polymer containing *N*,*N*′-dimethyl-4,4′-bipyridinium (methyl viologen, MeV^{2+}) cations are impacted by changes in the guest species. Single-crystal and powder X-ray diffraction studies are first presented to elucidate the nature of the structural transformations which arise from guest exchange. ^{57}Fe Mössbauer and electronic spectroscopic, electrochemical and conductivity studies on the two compounds reveal significant changes in the properties arise from guest-induced structural transformations.

Chapter 5 provides an investigation of a 2D mixed-valence Fe–chloranilate coordination polymer containing MeV^{2+} cations. Single-crystal and powder X-ray diffraction studies are first presented, which reveal the compound exhibits a significant degree of structural plasticity. The structural flexibility of the compound results in unexpected physical properties, as revealed by spectroscopic, electrochemical and conductivity measurements.

Chapter 6 provides a summary of the findings of this thesis and puts forth overarching conclusions, allowing predictions about possible future directions and work for this field.

Chapter 7 details the general experimental methods utilised in this thesis. Supplementary Crystallographic Information Files (CIFs) and IUCr CheckCIF reports for all compounds characterised by SC-XRD are available from:

https://figshare.com/s/8b79b073c9a2a20312de

Other supplementary data and analyses which aid in interpretation of the results in this thesis is provided in Appendices A and B.

1.6 References

[1] T. A. Wertime, *Science* **1964**, *146*, 1257-1267.

[2] C. S. Smith, *Science* **1965**, *148*, 908-917.

[3] O. Gutfleisch, M. A. Willard, E. Brück, C. H. Chen, S. G. Sankar, J. P. Liu, *Adv. Mater.* **2011**, *23*, 821-842.

[4] J. S. Miller, *Chem. Soc. Rev.* **2011**, *40*, 3266-3296.

[5] D. Gielen, F. Boshell, D. Saygin, *Nat. Mater.* **2016**, *15*, 117-120.

[6] K. M. Krishnan, *Fundamentals and Applications of Magnetic Materials*, Oxford University Press, Oxford, UK, **2016**.

[7] D. Givord, H. S. Li, J. M. Moreau, *Solid State Commun.* **1984**, *50*, 497-499.

[8] J. F. Herbst, *Rev. Mod. Phys.* **1991**, *63*, 819-898.

[9] H. Kohlmann, T. C. Hansen, V. Nassif, *Inorg. Chem.* **2018**, *57*, 1702-1704.

[10] B. T. Matthias, T. H. Geballe, S. Geller, E. Corenzwit, *Phys. Rev.* **1954**, *95*, 1435-1435.

[11] M. K. Wu, J. R. Ashburn, C. J. Torng, P. H. Hor, R. L. Meng, L. Gao, Z. J. Huang, Y. Q. Wang, C. W. Chu, *Phys. Rev. Lett.* **1987**, *58*, 908-910.

[12] G. Calestani, C. Rizzoli, *Nature* **1987**, *328*, 606-607.

[13] W. I. F. David, W. T. A. Harrison, J. M. F. Gunn, O. Moze, A. K. Soper, P. Day, J. D. Jorgensen, D. G. Hinks, M. A. Beno, L. Soderholm, D. W. Capone Ii, I. K. Schuller, C. U. Segre, K. Zhang, J. D. Grace, *Nature* **1987**, *327*, 310-312.

[14] Y. Kamihara, T. Watanabe, M. Hirano, H. Hosono, *J. Am. Chem. Soc.* **2008**, *130*, 3296-3297.

[15] H. J. Orman, P. J. Wiseman, *Acta Crystallogr. C* **1984**, *40*, 12-14.

[16] Y. Shao-Horn, L. Croguennec, C. Delmas, E. C. Nelson, M. A. O'Keefe, *Nat. Mater.* **2003**, *2*, 464-467.

[17] S. Trasatti, *Electrochim. Acta* **1991**, *36*, 225-241.

[18] J. Rossmeisl, Z. W. Qu, H. Zhu, G. J. Kroes, J. K. Nørskov, *J. Electroanal. Chem.* **2007**, *607*, 83-89.

[19] A. E. Thorarinsdottir, T. D. Harris, *Chem. Rev.* **2020**, *120*, 8716-8789.

[20] D. M. D'Alessandro, J. R. R. Kanga, J. S. Caddy, *Aust. J. Chem.* **2011**, *64*, 718-722.

[21] J. S. Miller, A. J. Epstein, *Angew. Chem. Int. Ed. Engl.* **1994**, *33*, 385-415.

[22] M. R. Bryce, L. C. Murphy, *Nature* **1984**, *309*, 119-126.

[23] A. Caneschi, D. Gatteschi, R. Sessoli, P. Rey, *Acc. Chem. Res.* **1989**, *22*, 392-398.

[24] D. Jérome, *Chem. Rev.* **2004**, *104*, 5565-5592.

[25] J. S. Miller, *Dalton Trans.* **2006**, 2742-2749.

[26] J. Ferraris, D. O. Cowan, V. Walatka, J. H. Perlstein, *J. Am. Chem. Soc.* **1973**, *95*, 948-949.

[27] T. E. Phillips, T. J. Kistenmacher, J. P. Ferraris, D. O. Cowan, *J. Chem. Soc., Chem. Commun.* **1973**, 471-472.

[28] T. J. Kistenmacher, T. E. Phillips, D. O. Cowan, *Acta Crystallogr. B* **1974**, *30*, 763-768.

[29] J. S. Miller, J. C. Calabrese, H. Rommelmann, S. R. Chittipeddi, J. H. Zhang, W. M. Reiff, A. J. Epstein, *J. Am. Chem. Soc.* **1987**, *109*, 769-781.

[30] M. L. Taliaferro, T. D. Selby, J. S. Miller, *Chem. Mater.* **2003**, *15*, 3602-3606.

[31] J.-H. Her, P. W. Stephens, J. Ribas-Ariño, J. J. Novoa, W. W. Shum, J. S. Miller, *Inorg. Chem.* **2009**, *48*, 3296-3307.

[32] R. Murase, C. F. Leong, D. M. D'Alessandro, *Inorg. Chem.* **2017**, *56*, 14373-14382.

[33] N. S. Hush, in *Prog. Inorg. Chem., Vol. 8* (Ed.: F. A. Cotton), Interscience Publishers, New York, NY, **1967**.

[34] C. Creutz, H. Taube, *J. Am. Chem. Soc.* **1969**, *91*, 3988-3989.

[35] C. Creutz, H. Taube, *J. Am. Chem. Soc.* **1973**, *95*, 1086-1094.

[36] K. D. Demadis, C. M. Hartshorn, T. J. Meyer, *Chem. Rev.* **2001**, *101*, 2655-2686.

[37] M. B. Robin, P. Day, in *Advances in Inorganic Chemistry and Radiochemistry, Vol. 10* (Eds.: H. J. Emeléus, A. G. Sharpe), Academic Press, London, UK, **1968**.

[38] J. B. Torrance, *Acc. Chem. Res.* **1979**, *12*, 79-86.

[39] P. Dechambenoit, J. R. Long, *Chem. Soc. Rev.* **2011**, *40*, 3249-3265.

[40] T. B. Faust, D. M. D'Alessandro, *RSC Adv.* **2014**, *4*, 17498-17512.

[41] L. Sun, M. G. Campbell, M. Dincă, *Angew. Chem. Int. Ed.* **2016**, *55*, 3566-3579.

[42] G. Givaja, P. Amo-Ochoa, C. J. Gómez-García, F. Zamora, *Chem. Soc. Rev.* **2012**, *41*, 115-147.

[43] D. M. D'Alessandro, *Chem. Commun.* **2016**, *52*, 8957-8971.

[44] L. S. Xie, G. Skorupskii, M. Dincă, *Chem. Rev.* **2020**, *120*, 8536-8580.

[45] S. R. Batten, S. M. Neville, D. Turner, *Coordination Polymers: Design, Analysis and Applications*, The Royal Society of Chemistry, Cambridge, UK, **2009**.

[46] M. D. Allendorf, M. E. Foster, F. Léonard, V. Stavila, P. L. Feng, F. P. Doty, K. Leong, E. Y. Ma, S. R. Johnston, A. A. Talin, *J. Phys. Chem. Lett.* **2015**, *6*, 1182-1195.

[47] A. A. Talin, A. Centrone, A. C. Ford, M. E. Foster, V. Stavila, P. Haney, R. A. Kinney, V. Szalai, F. El Gabaly, H. P. Yoon, F. Léonard, M. D. Allendorf, *Science* **2014**, *343*, 66-69.

[48] M. D. Allendorf, A. Schwartzberg, V. Stavila, A. A. Talin, *Chem. Eur. J.* **2011**, *17*, 11372-11388.

[49] V. Stavila, A. A. Talin, M. D. Allendorf, *Chem. Soc. Rev.* **2014**, *43*, 5994-6010.

[50] R. Robson, *J. Chem. Soc., Dalton Trans.* **2000**, 3735-3744.

[51] A. F. Wells, *Three-Dimensional Nets and Polyhedra*, John Wiley & Sons, New York, NY, **1977**.

[52] N. W. Ockwig, O. Delgado-Friedrichs, M. O'Keeffe, O. M. Yaghi, *Acc. Chem. Res.* **2005**, *38*, 176-182.

[53] E. V. Alexandrov, V. A. Blatov, A. V. Kochetkov, D. M. Proserpio, *CrystEngComm* **2011**, *13*, 3947-3958.

[54] A. P. Shevchenko, E. V. Alexandrov, A. A. Golov, O. A. Blatova, A. S. Duyunova, V. A. Blatov, *Chem. Commun.* **2020**, *56*, 9616-9619.

[55] S. R. Batten, N. R. Champness, X.-M. Chen, J. Garcia-Martinez, S. Kitagawa, L. Öhrström, M. O'Keeffe, M. P. Suh, J. Reedijk, *Pure Appl. Chem.* **2013**, *85*, 1715-1724.

[56] M. O'Keeffe, M. A. Peskov, S. J. Ramsden, O. M. Yaghi, *Acc. Chem. Res.* **2008**, *41*, 1782-1789.

[57] Reticular Chemistry Structure Resource. http://rcsr.anu.edu.au/ Accessed: 08/02/2021

[58] H. J. Buser, D. Schwarzenbach, W. Petter, A. Ludi, *Inorg. Chem.* **1977**, *16*, 2704-2710.

[59] M. B. Robin, *Inorg. Chem.* **1962**, *1*, 337-342.

[60] K. R. Dunbar, R. A. Heintz, in *Prog. Inorg. Chem.*, *Vol. 45* (Ed.: K. D. Karlin), John Wiley & Sons, New York, NY, **1997**.

[61] E. V. Alexandrov, A. V. Virovets, V. A. Blatov, E. V. Peresypkina, *Chem. Rev.* **2015**, *115*, 12286-12319.

[62] M. Ohba, H. Ōkawa, *Coord. Chem. Rev.* **2000**, *198*, 313-328.

[63] P. Gütlich, Y. Garcia, T. Woike, *Coord. Chem. Rev.* **2001**, *219-221*, 839-879.

[64] S. Margadonna, K. Prassides, A. N. Fitch, *J. Am. Chem. Soc.* **2004**, *126*, 15390-15391.

[65] S.-i. Ohkoshi, H. Tokoro, *Acc. Chem. Res.* **2012**, *45*, 1749-1758.

[66] A. L. Goodwin, C. J. Kepert, *Phys. Rev. B* **2005**, *71*, 140301.

[67] K. W. Chapman, P. J. Chupas, C. J. Kepert, *J. Am. Chem. Soc.* **2006**, *128*, 7009-7014.

[68] R. Robson, *Dalton Trans.* **2008**, 5113-5131.

[69] B. F. Hoskins, R. Robson, *J. Am. Chem. Soc.* **1989**, *111*, 5962-5964.

[70] B. F. Hoskins, R. Robson, *J. Am. Chem. Soc.* **1990**, *112*, 1546-1554.

[71] K. Yukio, M. Ikuo, H. Taiichi, S. Yoshihiko, *Bull. Chem. Soc. Jpn.* **1959**, *32*, 1221-1226.

[72] A. Aumüller, P. Erk, G. Klebe, S. Hünig, J. U. von Schütz, H.-P. Werner, *Angew. Chem. Int. Ed. Engl.* **1986**, *25*, 740-741.

[73] R. Kato, H. Kobayashi, A. Kobayashi, T. Mori, H. Inokuchi, *Chem. Lett.* **1987**, *16*, 1579-1582.

[74] O. M. Yaghi, M. O'Keeffe, N. W. Ockwig, H. K. Chae, M. Eddaoudi, J. Kim, *Nature* **2003**, *423*, 705-714.

[75] M. Eddaoudi, J. Kim, N. Rosi, D. Vodak, J. Wachter, M. O'Keeffe, O. M. Yaghi, *Science* **2002**, *295*, 469-472.

[76] N. L. Rosi, J. Eckert, M. Eddaoudi, D. T. Vodak, J. Kim, M. O'Keeffe, O. M. Yaghi, *Science* **2003**, *300*, 1127-1129.

[77] K. Sumida, D. L. Rogow, J. A. Mason, T. M. McDonald, E. D. Bloch, Z. R. Herm, T.-H. Bae, J. R. Long, *Chem. Rev.* **2012**, *112*, 724-781.

[78] M. P. Suh, H. J. Park, T. K. Prasad, D.-W. Lim, *Chem. Rev.* **2012**, *112*, 782-835.

[79] J.-R. Li, J. Sculley, H.-C. Zhou, *Chem. Rev.* **2012**, *112*, 869-932.

[80] Q. Wang, D. Astruc, *Chem. Rev.* **2020**, *120*, 1438-1511.

[81] C. F. Leong, P. M. Usov, D. M. D'Alessandro, *MRS Bull.* **2016**, *41*, 858-864.

[82] C. Bellitto, A. Flamini, L. Gastaldi, L. Scaramuzza, *Inorg. Chem.* **1983**, *22*, 444-449.

[83] R. J. H. Clark, *Chem. Soc. Rev.* **1990**, *19*, 107-131.

[84] H. Kitagawa, N. Onodera, T. Sonoyama, M. Yamamoto, T. Fukawa, T. Mitani, M. Seto, Y. Maeda, *J. Am. Chem. Soc.* **1999**, *121*, 10068-10080.

[85] M. Mitsumi, T. Murase, H. Kishida, T. Yoshinari, Y. Ozawa, K. Toriumi, T. Sonoyama, H. Kitagawa, T. Mitani, *J. Am. Chem. Soc.* **2001**, *123*, 11179-11192.

[86] I. H. Inoue, A. Kakizaki, H. Namatame, A. Fujimori, A. Kobayashi, R. Kato, H. Kobayashi, *Phys. Rev. B* **1992**, *45*, 5828-5833.

[87] R. Kato, H. Kobayashi, A. Kobayashi, *J. Am. Chem. Soc.* **1989**, *111*, 5224-5232.

[88] A. Kobayashi, R. Kato, H. Kobayashi, T. Mori, H. Inokuchi, *Solid State Commun.* **1987**, *64*, 45-51.

[89] J. U. von Schütz, D. Bauer, S. Hünig, K. Sinzger, H. C. Wolf, *J. Phys. Chem.* **1993**, *97*, 12030-12033.

[90] S. Takaishi, M. Hosoda, T. Kajiwara, H. Miyasaka, M. Yamashita, Y. Nakanishi, Y. Kitagawa, K. Yamaguchi, A. Kobayashi, H. Kitagawa, *Inorg. Chem.* **2009**, *48*, 9048-9050.

[91] Y. Kobayashi, B. Jacobs, M. D. Allendorf, J. R. Long, *Chem. Mater.* **2010**, *22*, 4120-4122.

[92] M. L. Aubrey, M. T. Kapelewski, J. F. Melville, J. Oktawiec, D. Presti, L. Gagliardi, J. R. Long, *J. Am. Chem. Soc.* **2019**, *141*, 5005-5013.

[93] N. L. Rosi, J. Kim, M. Eddaoudi, B. Chen, M. O'Keeffe, O. M. Yaghi, *J. Am. Chem. Soc.* **2005**, *127*, 1504-1518.

[94] L. Sun, T. Miyakai, S. Seki, M. Dincă, *J. Am. Chem. Soc.* **2013**, *135*, 8185-8188.

[95] L. Sun, C. H. Hendon, M. A. Minier, A. Walsh, M. Dincă, *J. Am. Chem. Soc.* **2015**, *137*, 6164-6167.

[96] L. Sun, C. H. Hendon, S. S. Park, Y. Tulchinsky, R. Wan, F. Wang, A. Walsh, M. Dincă, *Chem. Sci.* **2017**, *8*, 4450-4457.

[97] T. C. Narayan, T. Miyakai, S. Seki, M. Dincă, *J. Am. Chem. Soc.* **2012**, *134*, 12932-12935.

[98] F. Gándara, F. J. Uribe-Romo, D. K. Britt, H. Furukawa, L. Lei, R. Cheng, X. Duan, M. O'Keeffe, O. M. Yaghi, *Chem. Eur. J.* **2012**, *18*, 10595-10601.

[99] J. G. Park, M. L. Aubrey, J. Oktawiec, K. Chakarawet, L. E. Darago, F. Grandjean, G. J. Long, J. R. Long, *J. Am. Chem. Soc.* **2018**, *140*, 8526-8534.

[100] L. S. Xie, L. Sun, R. Wan, S. S. Park, J. A. DeGayner, C. H. Hendon, M. Dincă, *J. Am. Chem. Soc.* **2018**, *140*, 7411-7414.

[101] M. L. Aubrey, B. M. Wiers, S. C. Andrews, T. Sakurai, S. E. Reyes-Lillo, S. M. Hamed, C.-J. Yu, L. E. Darago, J. A. Mason, J.-O. Baeg, F. Grandjean, G. J. Long, S. Seki, J. B. Neaton, P. Yang, J. R. Long, *Nat. Mater.* **2018**, *17*, 625-632.

[102] A. B. Cairns, A. L. Goodwin, *Chem. Soc. Rev.* **2013**, *42*, 4881-4893.

[103] T. Kambe, R. Sakamoto, T. Kusamoto, T. Pal, N. Fukui, K. Hoshiko, T. Shimojima, Z. Wang, T. Hirahara, K. Ishizaka, S. Hasegawa, F. Liu, H. Nishihara, *J. Am. Chem. Soc.* **2014**, *136*, 14357-14360.

[104] S. Chen, J. Dai, X. C. Zeng, *Phys. Chem. Chem. Phys.* **2015**, *17*, 5954-5958.

[105] M. E. Foster, K. Sohlberg, M. D. Allendorf, A. A. Talin, *J. Phys. Chem. Lett.* **2018**, *9*, 481-486.

[106] M. Hmadeh, Z. Lu, Z. Liu, F. Gándara, H. Furukawa, S. Wan, V. Augustyn, R. Chang, L. Liao, F. Zhou, E. Perre, V. Ozolins, K. Suenaga, X. Duan, B. Dunn, Y. Yamamto, O. Terasaki, O. M. Yaghi, *Chem. Mater.* **2012**, *24*, 3511-3513.

[107] R. W. Day, D. K. Bediako, M. Rezaee, L. R. Parent, G. Skorupskii, M. Q. Arguilla, C. H. Hendon, I. Stassen, N. C. Gianneschi, P. Kim, M. Dincă, *ACS Cent. Sci.* **2019**, *5*, 1959-1964.

[108] T. Kambe, R. Sakamoto, K. Hoshiko, K. Takada, M. Miyachi, J.-H. Ryu, S. Sasaki, J. Kim, K. Nakazato, M. Takata, H. Nishihara, *J. Am. Chem. Soc.* **2013**, *135*, 2462-2465.

[109] X. Huang, P. Sheng, Z. Tu, F. Zhang, J. Wang, H. Geng, Y. Zou, C.-a. Di, Y. Yi, Y. Sun, W. Xu, D. Zhu, *Nat. Comm.* **2015**, *6*, 7408.

[110] X. Huang, S. Zhang, L. Liu, L. Yu, G. Chen, W. Xu, D. Zhu, *Angew. Chem. Int. Ed.* **2018**, *57*, 146-150.

[111] A. J. Clough, J. M. Skelton, C. A. Downes, A. A. de la Rosa, J. W. Yoo, A. Walsh, B. C. Melot, S. C. Marinescu, *J. Am. Chem. Soc.* **2017**, *139*, 10863-10867.

[112] R. Dong, P. Han, H. Arora, M. Ballabio, M. Karakus, Z. Zhang, C. Shekhar, P. Adler, P. S. Petkov, A. Erbe, S. C. B. Mannsfeld, C. Felser, T. Heine, M. Bonn, X. Feng, E. Cánovas, *Nat. Mater.* **2018**, *17*, 1027-1032.

[113] D. Sheberla, L. Sun, M. A. Blood-Forsythe, S. Er, C. R. Wade, C. K. Brozek, A. Aspuru-Guzik, M. Dincă, *J. Am. Chem. Soc.* **2014**, *136*, 8859-8862.

[114] M. G. Campbell, D. Sheberla, S. F. Liu, T. M. Swager, M. Dincă, *Angew. Chem. Int. Ed.* **2015**, *54*, 4349-4352.

[115] T. Chen, J.-H. Dou, L. Yang, C. Sun, N. J. Libretto, G. Skorupskii, J. T. Miller, M. Dincă, *J. Am. Chem. Soc.* **2020**, *142*, 12367-12373.

[116] S. S. Park, E. R. Hontz, L. Sun, C. H. Hendon, A. Walsh, T. Van Voorhis, M. Dincă, *J. Am. Chem. Soc.* **2015**, *137*, 1774-1777.

[117] M. Kurmoo, *Chem. Soc. Rev.* **2009**, *38*, 1353-1379.

[118] M. Clemente-León, E. Coronado, C. Martí-Gastaldo, F. M. Romero, *Chem. Soc. Rev.* **2011**, *40*, 473-497.

[119] J. A. DeGayner, I.-R. Jeon, L. Sun, M. Dincă, T. D. Harris, *J. Am. Chem. Soc.* **2017**, *139*, 4175-4184.

[120] L. Liu, J. A. DeGayner, L. Sun, D. Z. Zee, T. D. Harris, *Chem. Sci.* **2019**, *10*, 4652-4661.

[121] K. Taniguchi, K. Narushima, J. Mahin, W. Kosaka, H. Miyasaka, *Angew. Chem. Int. Ed.* **2016**, *55*, 5238-5242.

[122] K. Taniguchi, K. Narushima, H. Sagayama, W. Kosaka, N. Shito, H. Miyasaka, *Adv. Funct. Mater.* **2017**, *27*, 1604990.

[123] K. Taniguchi, J. Chen, Y. Sekine, H. Miyasaka, *Chem. Mater.* **2017**, *29*, 10053-10059.

[124] J. Chen, K. Taniguchi, Y. Sekine, H. Miyasaka, *J. Magn. Magn. Mater.* **2020**, *494*, 165818.

[125] J. M. Manriquez, G. T. Yee, R. S. McLean, A. J. Epstein, J. S. Miller, *Science* **1991**, *252*, 1415-1417.

[126] J. S. Miller, *Polyhedron* **2009**, *28*, 1596-1605.

[127] J.-H. Her, P. W. Stephens, K. I. Pokhodnya, M. Bonner, J. S. Miller, *Angew. Chem. Int. Ed.* **2007**, *46*, 1521-1524.

[128] G. Du, J. Joo, A. J. Epstein, J. S. Miller, *J. Appl. Phys.* **1993**, *73*, 6566-6568.

[129] K. H. Stone, P. W. Stephens, A. C. McConnell, E. Shurdha, K. I. Pokhodnya, J. S. Miller, *Adv. Mater.* **2010**, *22*, 2514-2519.

[130] H. Miyasaka, *Acc. Chem. Res.* **2013**, *46*, 248-257.

[131] H. Miyasaka, N. Motokawa, R. Atsuumi, H. Kamo, Y. Asai, M. Yamashita, *Dalton Trans.* **2011**, *40*, 673-682.

[132] A. Aumüller, S. Hünig, *Liebigs Ann. Chem.* **1986**, *1986*, 165-176.

[133] N. Martín, J. L. Segura, C. Seoane, *J. Mater. Chem.* **1997**, *7*, 1661-1676.

[134] S. Hünig, *J. Mater. Chem.* **1995**, *5*, 1469-1479.

[135] S. Hünig, R. Bau, M. Kemmer, H. Meixner, T. Metzenthin, K. Peters, K. Sinzger, J. Gulbis, *Eur. J. Org. Chem.* **1998**, *1998*, 335-348.

[136] H. Miyasaka, C. S. Campos-Fernández, R. Clérac, K. R. Dunbar, *Angew. Chem. Int. Ed.* **2000**, *39*, 3831-3835.

[137] H. Miyasaka, T. Izawa, N. Takahashi, M. Yamashita, K. R. Dunbar, *J. Am. Chem. Soc.* **2006**, *128*, 11358-11359.

[138] H. Miyasaka, N. Motokawa, S. Matsunaga, M. Yamashita, K. Sugimoto, T. Mori, N. Toyota, K. R. Dunbar, *J. Am. Chem. Soc.* **2010**, *132*, 1532-1544.

[139] N. Motokawa, H. Miyasaka, M. Yamashita, K. R. Dunbar, *Angew. Chem. Int. Ed.* **2008**, *47*, 7760-7763.

[140] J. Zhang, W. Kosaka, K. Sugimoto, H. Miyasaka, *J. Am. Chem. Soc.* **2018**, *140*, 5644-5652.

[141] A. Caneschi, D. Gatteschi, N. Lalioti, C. Sangregorio, R. Sessoli, G. Venturi, A. Vindigni, A. Rettori, M. G. Pini, M. A. Novak, *Angew. Chem. Int. Ed.* **2001**, *40*, 1760-1763.

[142] H. Miyasaka, M. Julve, M. Yamashita, R. Clérac, *Inorg. Chem.* **2009**, *48*, 3420-3437.

[143] L. Bogani, A. Vindigni, R. Sessoli, D. Gatteschi, *J. Mater. Chem.* **2008**, *18*, 4750-4758.

[144] J. A. DeGayner, K. Wang, T. D. Harris, *J. Am. Chem. Soc.* **2018**, *140*, 6550-6553.

[145] J. Chen, Y. Sekine, Y. Komatsumaru, S. Hayami, H. Miyasaka, *Angew. Chem. Int. Ed.* **2018**, *57*, 12043-12047.

[146] X. Meng, W. Shi, P. Cheng, *Coord. Chem. Rev.* **2019**, *378*, 134-150.

[147] L. Bogani, C. Sangregorio, R. Sessoli, D. Gatteschi, *Angew. Chem. Int. Ed.* **2005**, *44*, 5817-5821.

[148] K. Bernot, L. Bogani, A. Caneschi, D. Gatteschi, R. Sessoli, *J. Am. Chem. Soc.* **2006**, *128*, 7947-7956.

[149] M. G. F. Vaz, R. A. A. Cassaro, H. Akpinar, J. A. Schlueter, P. M. Lahti, M. A. Novak, *Chem. Eur. J.* **2014**, *20*, 5460-5467.

[150] X. Liu, X. Feng, K. R. Meihaus, X. Meng, Y. Zhang, L. Li, J.-L. Liu, K. S. Pedersen, L. Keller, W. Shi, Y.-Q. Zhang, P. Cheng, J. R. Long, *Angew. Chem. Int. Ed.* **2020**, *59*, 10610-10618.

[151] A. Weiss, E. Riegler, C. Robl, *Z. Naturforsch., B: Chem. Sci.* **1986**, *41*, 1501.

[152] C. Robl, A. Weiss, *Mater. Res. Bull.* **1987**, *22*, 497-504.

[153] C. Robl, *Mater. Res. Bull.* **1987**, *22*, 1483-1491.

[154] S. Kitagawa, S. Kawata, *Coord. Chem. Rev.* **2002**, *224*, 11-34.

[155] S. Kawata, S. Kitagawa, M. Kondo, I. Furuchi, M. Munakata, *Angew. Chem. Int. Ed. Engl.* **1994**, *33*, 1759-1761.

[156] B. F. Abrahams, K. D. Lu, B. Moubaraki, K. S. Murray, R. Robson, *J. Chem. Soc., Dalton Trans.* **2000**, 1793-1797.

[157] B. F. Abrahams, J. Coleiro, K. Ha, B. F. Hoskins, S. D. Orchard, R. Robson, *J. Chem. Soc., Dalton Trans.* **2002**, 1586-1594.

[158] M. L. Mercuri, F. Congiu, G. Concas, S. A. Sahadevan, *Magnetochemistry* **2017**, *3*, 17.

[159] K. Heinze, G. Huttner, L. Zsolnai, A. Jacobi, P. Schober, *Chem. Eur. J.* **1997**, *3*, 732-743.

[160] F. Tinti, M. Verdaguer, O. Kahn, J. M. Savariault, *Inorg. Chem.* **1987**, *26*, 2380-2384.

[161] K. Heinze, G. Huttner, O. Walter, *Eur. J. Inorg. Chem.* **1999**, *1999*, 593-600.

[162] A. E. Thorarinsdottir, R. Bjornsson, T. D. Harris, *Inorg. Chem.* **2020**, *59*, 4634-4649.

[163] A. Dei, D. Gatteschi, L. Pardi, U. Russo, *Inorg. Chem.* **1991**, *30*, 2589-2594.

[164] K. S. Min, A. L. Rheingold, A. DiPasquale, J. S. Miller, *Inorg. Chem.* **2006**, *45*, 6135-6137.

[165] K. S. Min, A. G. DiPasquale, J. A. Golen, A. L. Rheingold, J. S. Miller, *J. Am. Chem. Soc.* **2007**, *129*, 2360-2368.

[166] D. Guo, J. K. McCusker, *Inorg. Chem.* **2007**, *46*, 3257-3274.

[167] K. Nakabayashi, S.-i. Ohkoshi, *Inorg. Chem.* **2009**, *48*, 8647-8649.

[168] P. Zhang, M. Perfetti, M. Kern, P. P. Hallmen, L. Ungur, S. Lenz, M. R. Ringenberg, W. Frey, H. Stoll, G. Rauhut, J. van Slageren, *Chem. Sci.* **2018**, *9*, 1221-1230.

[169] W. R. Reed, M. A. Dunstan, R. W. Gable, W. Phonsri, K. S. Murray, R. A. Mole, C. Boskovic, *Dalton Trans.* **2019**, *48*, 15635-15645.

[170] E. Coronado, J. R. Galán-Mascarós, C. J. Gómez-García, V. Laukhin, *Nature* **2000**, *408*, 447-449.

[171] A. Alberola, E. Coronado, J. R. Galán-Mascarós, C. Giménez-Saiz, C. J. Gómez-García, *J. Am. Chem. Soc.* **2003**, *125*, 10774-10775.

[172] M. Atzori, S. Benmansour, G. Mínguez Espallargas, M. Clemente-León, A. Abhervé, P. Gómez-Claramunt, E. Coronado, F. Artizzu, E. Sessini, P. Deplano, A. Serpe, M. L. Mercuri, C. J. Gómez García, *Inorg. Chem.* **2013**, *52*, 10031-10040.

[173] S. Kawata, S. Kitagawa, H. Kumagai, C. Kudo, H. Kamesaki, T. Ishiyama, R. Suzuki, M. Kondo, M. Katada, *Inorg. Chem.* **1996**, *35*, 4449-4461.

[174] T.-T. Luo, Y.-H. Liu, H.-L. Tsai, C.-C. Su, C.-H. Ueng, K.-L. Lu, *Eur. J. Inorg. Chem.* **2004**, *2004*, 4253-4258.

[175] J. T. Wrobleski, D. B. Brown, *Inorg. Chem.* **1979**, *18*, 498-504.

[176] S. Kawata, S. Kitagawa, H. Kumagai, T. Ishiyama, K. Honda, H. Tobita, K. Adachi, M. Katada, *Chem. Mater.* **1998**, *10*, 3902-3912.

[177] B. F. Abrahams, A. M. Bond, T. H. Le, L. J. McCormick, A. Nafady, R. Robson, N. Vo, *Chem. Commun.* **2012**, *48*, 11422-11424.

[178] B. F. Abrahams, T. A. Hudson, L. J. McCormick, R. Robson, *Cryst. Growth Des.* **2011**, *11*, 2717-2720.

[179] L. E. Darago, M. L. Aubrey, C. J. Yu, M. I. Gonzalez, J. R. Long, *J. Am. Chem. Soc.* **2015**, *137*, 15703-15711.

[180] I.-R. Jeon, B. Negru, R. P. Van Duyne, T. D. Harris, *J. Am. Chem. Soc.* **2015**, *137*, 15699-15702.

[181] R. Murase, B. F. Abrahams, D. M. D'Alessandro, C. G. Davies, T. A. Hudson, G. N. L. Jameson, B. Moubaraki, K. S. Murray, R. Robson, A. L. Sutton, *Inorg. Chem.* **2017**, *56*, 9025-9035.

[182] J. T. Wrobleski, D. B. Brown, *Inorg. Chem.* **1979**, *18*, 2738-2749.

[183] M. E. Ziebel, L. E. Darago, J. R. Long, *J. Am. Chem. Soc.* **2018**, *140*, 3040-3051.

[184] S. Benmansour, A. Abhervé, P. Gómez-Claramunt, C. Vallés-García, C. J. Gómez-García, *ACS Appl. Mater. Interfaces* **2017**, *9*, 26210-26218.

[185] S. A. Sahadevan, A. Abhervé, N. Monni, C. Sáenz de Pipaón, J. R. Galán-Mascarós, J. C. Waerenborgh, B. J. C. Vieira, P. Auban-Senzier, S. Pillet, E.-E. Bendeif, P. Alemany, E. Canadell, M. L. Mercuri, N. Avarvari, *J. Am. Chem. Soc.* **2018**, *140*, 12611-12621.

[186] R. Murase, C. J. Commons, T. A. Hudson, G. N. L. Jameson, C. D. Ling, K. S. Murray, W. Phonsri, R. Robson, Q. Xia, B. F. Abrahams, D. M. D'Alessandro, *Inorg. Chem.* **2020**, *59*, 3619-3630.

[187] C. J. Kingsbury, B. F. Abrahams, D. M. D'Alessandro, T. A. Hudson, R. Murase, R. Robson, K. F. White, *Cryst. Growth Des.* **2017**, *17*, 1465-1470.

[188] K. Nagayoshi, M. K. Kabir, H. Tobita, K. Honda, M. Kawahara, M. Katada, K. Adachi, H. Nishikawa, I. Ikemoto, H. Kumagai, Y. Hosokoshi, K. Inoue, S. Kitagawa, S. Kawata, *J. Am. Chem. Soc.* **2003**, *125*, 221-232.

[189] M. Atzori, F. Pop, P. Auban-Senzier, C. J. Gómez-García, E. Canadell, F. Artizzu, A. Serpe, P. Deplano, N. Avarvari, M. L. Mercuri, *Inorg. Chem.* **2014**, *53*, 7028-7039.

[190] M. Atzori, F. Pop, P. Auban-Senzier, R. Clérac, E. Canadell, M. L. Mercuri, N. Avarvari, *Inorg. Chem.* **2015**, *54*, 3643-3653.

[191] S. A. Sahadevan, A. Abhervé, N. Monni, P. Auban-Senzier, J. Cano, F. Lloret, M. Julve, H. Cui, R. Kato, E. Canadell, M. L. Mercuri, N. Avarvari, *Inorg. Chem.* **2019**, *58*, 15359-15370.

[192] S. A. Sahadevan, A. Abhervé, N. Monni, P. Auban-Senzier, H. Cui, R. Kato, M. L. Mercuri, N. Avarvari, *Cryst. Growth Des.* **2020**, *20*, 6777-6786.

[193] J. Chen, Y. Sekine, A. Okazawa, H. Sato, W. Kosaka, H. Miyasaka, *Chem. Sci.* **2020**, *11*, 3610-3618.

[194] M. E. Ziebel, C. A. Gaggioli, A. B. Turkiewicz, W. Ryu, L. Gagliardi, J. R. Long, *J. Am. Chem. Soc.* **2020**, *142*, 2653-2664.

[195] Y. Sekine, J. Chen, N. Eguchi, H. Miyasaka, *Chem. Commun.* **2020**.

[196] L. Striepe, T. Baumgartner, *Chem. Eur. J.* **2017**, *23*, 16924-16940.

[197] J. Ding, C. Zheng, L. Wang, C. Lu, B. Zhang, Y. Chen, M. Li, G. Zhai, X. Zhuang, *J. Mater. Chem. A* **2019**, *7*, 23337-23360.

[198] K. Deuchert, S. Hünig, *Angew. Chem. Int. Ed. Engl.* **1978**, *17*, 875-886.

[199] C. L. Bird, A. T. Kuhn, *Chem. Soc. Rev.* **1981**, *10*, 49-82.

[200] S. Hünig, J. Groβ, W. Schenk, *Liebigs Ann. Chem.* **1973**, *1973*, 324-338.

[201] S. Hünig, J. Groβ, E. F. Lier, H. Quast, *Liebigs Ann. Chem.* **1973**, *1973*, 339-358.

[202] S. Hünig, W. Schenk, *Liebigs Ann. Chem.* **1979**, *1979*, 1523-1533.

[203] K. Hiroyoshi, S. Tsuyoshi, *Bull. Chem. Soc. Jpn.* **1987**, *60*, 794-796.

[204] W.-K. Gries, E. Günther, S. Hünig, *Liebigs Ann. Chem.* **1991**, *1991*, 1021-1028.

[205] W. W. Porter, III, T. P. Vaid, A. L. Rheingold, *J. Am. Chem. Soc* **2005**, *127*, 16559-16566.

[206] A. N. Basuray, H.-P. Jacquot de Rouville, K. J. Hartlieb, T. Kikuchi, N. L. Strutt, C. J. Bruns, M. W. Ambrogio, A.-J. Avestro, S. T. Schneebeli, A. C. Fahrenbach, J. F. Stoddart, *Angew. Chem. Int. Ed.* **2012**, *51*, 11872-11877.

[207] A. N. Woodward, J. M. Kolesar, S. R. Hall, N.-A. Saleh, D. S. Jones, M. G. Walter, *J. Am. Chem. Soc.* **2017**, *139*, 8467-8473.

[208] K. Madasamy, D. Velayutham, V. Suryanarayanan, M. Kathiresan, K.-C. Ho, *J. Mater. Chem. C* **2019**, *7*, 4622-4637.

[209] R. J. Mortimer, *Electrochim. Acta* **1999**, *44*, 2971-2981.

[210] T. Liu, X. Wei, Z. Nie, V. Sprenkle, W. Wang, *Adv. Energy Mater.* **2016**, *6*, 1501449.

[211] J. Luo, B. Hu, C. Debruler, T. L. Liu, *Angew. Chem. Int. Ed.* **2018**, *57*, 231-235.

[212] N. Leblanc, N. Mercier, O. Toma, A. H. Kassiba, L. Zorina, P. Auban-Senzier, C. Pasquier, *Chem. Commun.* **2013**, *49*, 10272-10274.

[213] E. M. Kosower, J. L. Cotter, *J. Am. Chem. Soc.* **1964**, *86*, 5524-5527.

[214] M. R. Geraskina, A. S. Dutton, M. J. Juetten, S. A. Wood, A. H. Winter, *Angew. Chem. Int. Ed.* **2017**, *56*, 9435-9439.

[215] J.-M. Lü, S. V. Rosokha, J. K. Kochi, *J. Am. Chem. Soc.* **2003**, *125*, 12161-12171.

[216] D.-W. Zhang, J. Tian, L. Chen, L. Zhang, Z.-T. Li, *Chem. Asian J.* **2015**, *10*, 56-68.

[217] M. Kertesz, *Chem. Eur. J.* **2019**, *25*, 400-416.

[218] J. M. Spruell, A. Coskun, D. C. Friedman, R. S. Forgan, A. A. Sarjeant, A. Trabolsi, A. C. Fahrenbach, G. Barin, W. F. Paxton, S. K. Dey, M. A. Olson, D. Benítez, E. Tkatchouk, M. T. Colvin, R. Carmielli, S. T. Caldwell, G. M. Rosair, S. G. Hewage, F. Duclairoir, J. L. Seymour, A. M. Z. Slawin, W. A. Goddard, M. R. Wasielewski, G. Cooke, J. F. Stoddart, *Nat. Chem.* **2010**, *2*, 870-879.

[219] P. R. Ashton, V. Balzani, J. Becher, A. Credi, M. C. T. Fyfe, G. Mattersteig, S. Menzer, M. B. Nielsen, F. M. Raymo, J. F. Stoddart, M. Venturi, D. J. Williams, *J. Am. Chem. Soc.* **1999**, *121*, 3951-3957.

[220] J. Sun, Y. Wu, Y. Wang, Z. Liu, C. Cheng, K. J. Hartlieb, M. R. Wasielewski, J. F. Stoddart, *J. Am. Chem. Soc.* **2015**, *137*, 13484-13487.

[221] A. Trabolsi, N. Khashab, A. C. Fahrenbach, D. C. Friedman, M. T. Colvin, K. K. Cotí, D. Benítez, E. Tkatchouk, J.-C. Olsen, M. E. Belowich, R. Carmielli, H. A. Khatib, W. A. Goddard, M. R. Wasielewski, J. F. Stoddart, *Nat. Chem.* **2010**, *2*, 42-49.

This page intentionally left blank

Chapter 2 Structural Diversity in Anionic Fluoranilate and Chloranilate Coordination Polymers Induced by Redox-Active Dications

2.1 Introduction 73

2.1.1 Controlling Topology in Tetraoxolene Coordination Polymers 73

2.1.2 Chapter Aim 76

2.2 Results and Discussion 78

2.2.1 Divalent Metal Networks 78

2.2.2 Mixed-Valence Iron Networks 107

2.3 Conclusion 135

2.4 Experimental 136

2.4.1 General Considerations 136

2.4.2 Ligand Synthesis 137

2.4.3 Cation Synthesis 139

2.4.4 Coordination Polymer Synthesis 143

2.4.5 Single-Crystal X-ray Diffraction (SC-XRD) 148

2.4.6 Powder X-ray Diffraction (P-XRD) 161

2.5 References 161

This page intentionally left blank

2.1 Introduction

2.1.1 Controlling Topology in Tetraoxolene Coordination Polymers

Controlling the topological dimensionality (1, 2-, 3-dimensional, 1D, 2D and 3D respectively), connectivity and geometry of magnetic or electrically conductive coordination polymers is an important synthetic strategy. This is because the metal-metal interactions in the network can be affected by the network structure, which thereby influences the conductive or magnetic properties. The topology of magnetic bimetallic oxalate $[M^{II}M^{III}(ox)_3]^-$ (M^{II} = Mn, Fe, Co, Ni, Cu, Zn; M^{III} = Cr, Fe; ox^{2-} = oxalate) networks is readily modulated using charge-balancing countercations.[1, 2] Alkylammonium cations result in layered (6,3) networks,[3, 4] whereas bulkier $[Z^{II}(2,2'\text{-bpy})_3]^{2+}$ cations (Z = Fe, Co, Ni, Ru; 2,2′-bpy = 2,2′-bipyridine) or $[Z^{III}Cp^*_2]^+$ cations (Z = Fe, Co; Cp^* = pentamethylcyclopentadienyl) help template chiral (10,3)-*a* networks.[5-7] Superexchange between the M^{II} and M^{III} centres, mediated by the oxalate ligands, allows ferro- (FM) or antiferromagnetic (AFM) metal-metal coupling which facilitates long-range magnetic ordering. Interestingly, spontaneous ordering generally occurs at higher temperatures in the 2D oxalate networks (up to T_c = 48 K for $(^nHx_4N)[Fe^{II}Fe^{III}(ox)_3]$, $^nHx_4N^+$ = tetra-*n*-hexylammonium)[4] compared to similar 3D (10,3)-*a* counterparts (T_c = 6.6 K for $[Fe^{II}(2,2'\text{-bpy})_3][Co^{II}Cr^{III}(ox)_3](ClO_4)$).[7] This is despite the equivalent $[M^{II}M^{III}(ox)_3]^-$ network formulations, and therefore similar crystal-field environments, between the 2D and 3D networks.[8] The lower ordering temperature in the 3D networks was proposed to arise from tetrahedral and non-coaxial alignment of the magnetic anisotropy axes, compared to the coaxial alignment in the layered 2D networks.[8]

Given the similar coordination modes and structures of oxalate and tetraoxolene ligands,[2] the network topology of tetraoxolene coordination polymers may analogously influence the desired physicochemical properties. An illustration of this factor is the mixed-valence 3D (10,3)-*a* framework $(^nBu_4N)_2[Fe_2(dhbq)_3]$ ($^nBu_4N^+$ = tetra-*n*-butylammonium), which only undergoes ferrimagnetic (FiM) ordering at T_c = 8K.[9] On the other hand, the mixed-valence layered 2D framework $(Me_2NH_2)_2[Fe_2(Clan)_3]\cdot 6DMF\cdot 2H_2O$ ($Me_2NH_2^+$ = dimethylammonium) exhibits FiM ordering at T_c = 80 K.[10] This disparity occurs despite both compounds containing

delocalised radical trianion ($dhbq^{3-\bullet}$ or $Clan^{3-\bullet}$) ligands, which should facilitate strong metal-metal spin exchange leading to high ordering temperatures. These results reinforce the intimate connection between physical properties and network topology. Therefore, methods to predictably modulate the topology, dimensionality and geometry in coordination polymers could facilitate design of new materials with desirable physical properties. A survey of the Cambridge Crystallographic Database (CSD) reveals a myriad of diverse metal–tetraoxolene coordination polymers with a range of structures which have been characterised (see Appendix A for structural analysis concentrating on polymeric *M*–$Clan^{n-}$ compounds). These can be broadly classified as:

- 1D chains containing *trans* monodentate ancillary ligands giving linear strip polymers (Figure 2.1a)[11, 12]
- 1D chains containing *cis* ancillary ligands (either mono- or bidentate) giving either zig-zag chains (Figure 2.1b)[13, 14] or crankshaft chains (Figure 2.1c)[15] depending on the alternation of the absolution configuration around the metal centres ($\{\Delta–\Lambda–\Delta–\Lambda\}_\infty$ for the zig-zag chains, and $\{\Delta–\Delta–\Lambda–\Lambda\}_\infty$ for crankshaft chains)
- Ladder-like 1D chains (Figure 2.1d)[16]
- Neutral 2D sheets formed by weaving 1D chains together with ancillary bridging ligands (Figure 2.1e)[17, 18]
- 2D polymers formed by bridging metal centres with tetraoxolene ligands giving anionic (Figure 2.1f)[10, 19-31] or neutral sheets (Figure 2.1g)[30, 32-35] depending on the metal charge and metal-ligand stoichiometry
- Neutral and anionic 3D networks (Figure 2.1h)[9, 30, 33, 36-38]

Despite the compositional and structural diversity, the 2D (6,3) honeycomb and 3D (10,3)-*a* topologies are notably dominant in anionic tetraoxolene coordination polymers.[2]

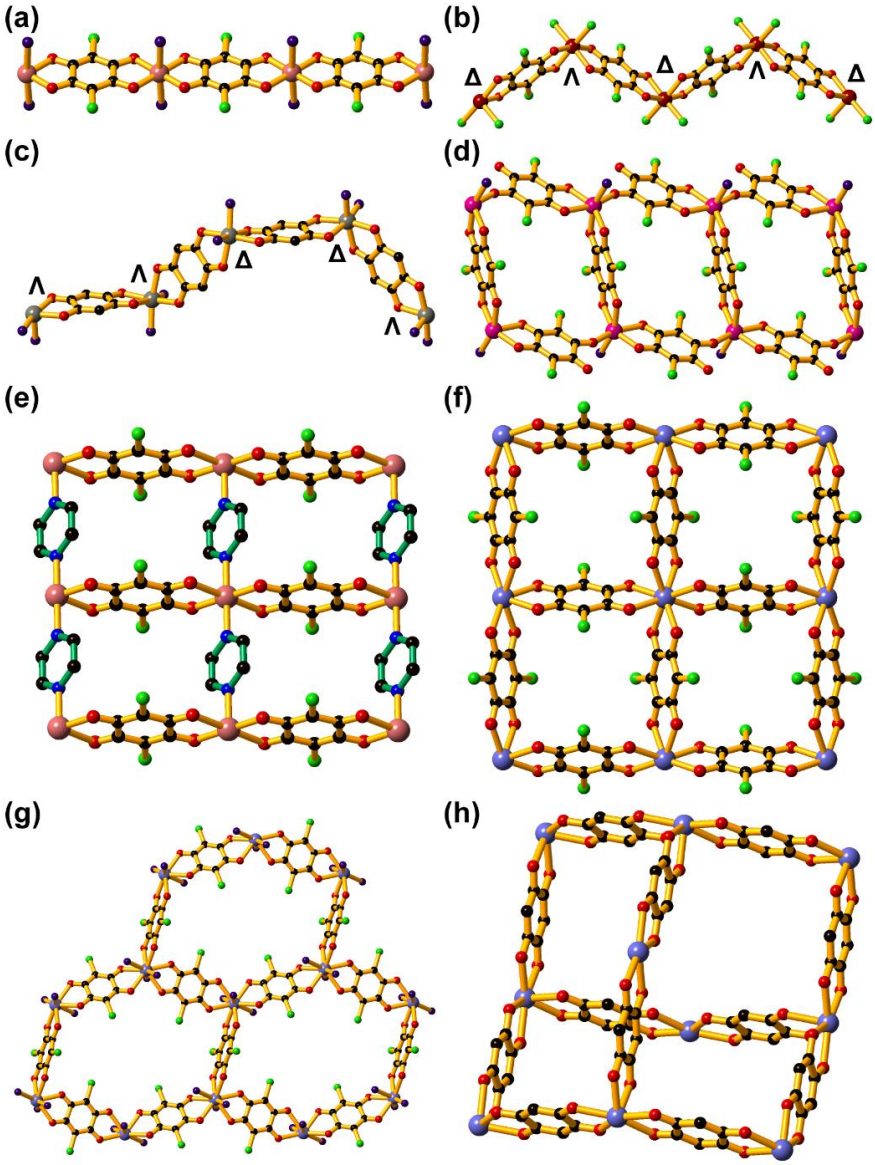


Figure 2.1 Diverse topologies of metal–tetraoxolene coordination polymers. (a) Neutral $[Cu^{II}(Clan)(H_2O)_2]$ 1D linear strips,[11] (b) anionic 1D zig-zag chains of $(Me_4N)_2[Fe^{III}(Clan)Cl_2]$,[14] (c) neutral $[Zn^{II}(dhbq)(H_2O)_2]$ crankshaft chains,[15] (d) anionic 1D ladder chains of (2,2′-bpyH)$[Mn^{II}_2(Clan)_3(H_2O)_2]$,[16] (e) neutral $[Cu^{II}(Clan)(pyz)]$ 2D sheets of woven from $\{Cu^{II}–Clan\}_\infty$ strips and bridging pyrazine (pyz, green bonds) ligands,[17] (f) anionic 2D sheets in $(Me_4N)[Sc^{III}(Clan)_2]$,[29] (g) neutral $[Er^{III}_2(Clan)_3(H_2O)_6]$ 2D layers,[34] and (h) an adamantane unit of the anionic 3D diamondoid network in $Na_5[Ho^{III}(thb)_2]$ (thb^{4-} = 1,2,4,5-tetrahydroxybenzene).[39] Salmon = Cu, maroon = Fe, grey = Zn, magenta = Mn, mauve = Sc, Er, Ho, green = Cl, red = O, blue = N, black = C, and purple = coordinated H_2O. H not shown for clarity.

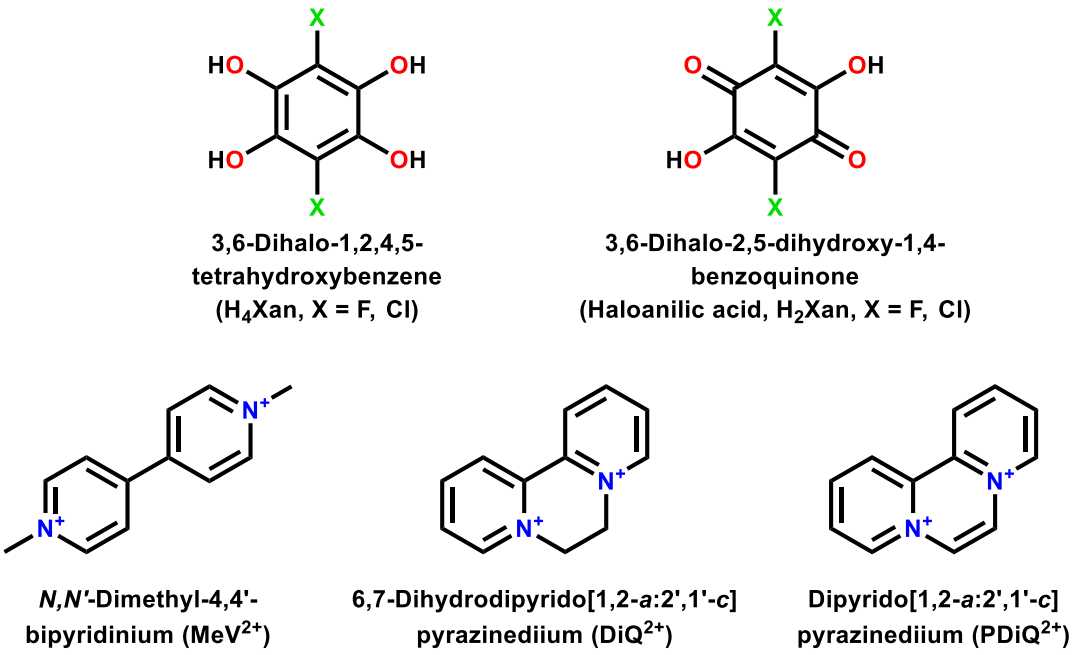
An extraordinarily diverse range of ‘inert’ templating or alternatively ‘functional’ templating cations (e.g. spin-crossover, electrically conductive, photochromism) have been introduced into anionic oxalate networks.[1] This has allowed synthesis of hybrid magnetic materials where the cations both help template the topology of the magnetic network, and also introduce additional functionality, for example such as electrical conductivity, spin crossover or photochromism.[1, 40, 41] An analogous strategy using ‘functional’ cations in anionic tetraoxolene frameworks has curiously been underexploited. Only a handful of functional cations have been used impart new properties into anionic tetraoxolene coordination polymers,[42, 43] with redox-inactive and non-functional ammonium or phosphonium cations predominating as charge-balancing cations.[9, 10, 21, 24, 28-30, 36, 38, 44, 45] Recent work by Bondaruk and Hua has shown even using redox-inactive cations not previously used as countercations for Ce^{III} or Er^{III}–chloranilate frameworks yields diverse network topologies.[30] Given the disparate size and shape of viologens compared to alkylammonium cations, and the possibility of charge-transfer (CT) interactions between viologens and π-electron donors, there is tremendous scope to explore the range of topologies and structures which could be accessed.

Additionally, compared to other tetraoxolene ligands, the supramolecular and coordination chemistry of fluoranilate is curiously underexplored. Of the ca. 600 metal–tetraoxolene compounds containing bridging tetraoxolene ligands reported in the CSD, only eight utilise fluoranilate ligands![28, 38, 45-48] The unique physicochemical properties of organofluorine compounds,[49, 50] therefore provide significant motivation to synthesise metal–fluoranilate coordination polymers isostructural to their chlor- and bromanilate congeners. Properties such as the magnetic ordering temperature or conductivity can depend on the halogen substituent,[25, 48, 51] so synthesis of complete isostructural families of metal–tetraoxolene frameworks could provide deeper structure-property insights that will aid design and synthesis of functional, porous materials.

2.1.2 Chapter Aim

This chapter details synthetic and structural investigations on a number of anionic fluor- and chloranilate coordination polymers incorporating a range of viologen and viologen-like cations (Scheme 2.1). This work is divided into two parts:

- Anionic Mn^{II} and Cd^{II}–tetraoxolene coordination polymers containing *N,N′*-dimethyl-4,4′-bipyridinium (methyl viologen, MeV^{2+}) cations.
- Anionic mixed-valence Fe–tetraoxolene coordination polymers containing viologen-like 2,2-bipyridine-derived cations.



Scheme 2.1 Structures of the tetraoxolene ligand precursors and viologen or viologen-like cations used in Chapter 2.

The first section is aimed towards producing an isostructural family of anionic fluor- and chloranilate coordination polymers, to better understand how sensitive the reaction outcomes are to the interactions between metals, cations, ligand substituents and solvent. Better understanding of these interactions could facilitate reliable prediction and design of a tetraoxolene coordination polymer with an intended network topology. The second part on mixed-valence Fe–tetraoxolene frameworks is similarly geared towards exploring the possible structures and topologies which result from incorporating viologen-like cations, with the structure templating effect primarily derived from the largely planar geometry of viologen-like cations. Additionally, we wished to explore whether the putative CT interactions between π-electron deficient viologen cations, and π-electron rich tetraoxolene radical cations ($Xan^{3-\bullet}$) in the mixed-valence Fe networks, could be a novel interaction to influence topology.

2.2 Results and Discussion

2.2.1 Divalent Metal Networks

2.2.1.1 Chloranilate Coordination Polymers

The Mn^{II} and Cd^{II} frameworks were synthesised by layering an aqueous solution of metal nitrate, methyl viologen ditosylate ($MeV(OTs)_2$) and LiOAc below solutions of the reduced form of fluoranilic acid, 3,6-difluoro-1,2,4,5-tetrahydroxybenzene (H_4Fan) or chloranilic acid, 3,6-dichloro-1,2,4,5-tetrahydroxybenzene (H_4Clan), in acetone or MeCN, with a 1:1 v/v buffer layer of the corresponding solvent and H_2O. Crystals appeared on the vial walls in addition to the vial bottom within two days, which were harvested after seven days. In accordance with our previous work,[28, 36] slow diffusion reactions, coupled with slow aerial oxidation of H_4Xan to the active H_2Xan form, was found to be a versatile method to yield single-crystal X-ray diffraction (SC-XRD) quality crystals. The structures obtained are classified in three groups: anionic 3D diamondoid (**dia**) networks, anionic 2D (6,3) (**hex**) networks, and anionic 1D coordination polymers.

Diamond Networks

For the acetone–H_2O solvent system, an aqueous solution of $Mn^{II}(NO_3)_2{\cdot}4H_2O$ or $Cd^{II}(NO_3)_2{\cdot}6H_2O$, $MeV(OTs)_2$ and LiOAc layered below an acetone solution of H_4Clan, yielded bright red elongated octahedral crystals of the 3D diamondoid (**dia**) coordination polymer $(MeV)[Mn(Clan)_2]$ (**2.1$_{Mn}$**), and the isostructural diamagnetic Cd analogue $(MeV)[Cd(Clan)_2]$ (**2.1$_{Cd}$**). For the Cd^{II} system, use of an MeCN–H_2O solvent system also leads to crystallisation of bulk phase-pure **2.1$_{Cd}$**, whereas with Mn^{II}, a different product results (*vide infra*). Phase purity of the bulk samples was confirmed by powder X-ray diffraction (P-XRD) (Figure 2.2 for **2.1$_{Mn}$**; Figure 2.3 for **2.1$_{Cd}$**). Using **2.1$_{Mn}$** as the archetype, a satisfactory structure refinement was found in the orthorhombic *Fddd* space group. The asymmetric unit comprises a chloranilate ($Clan^{n-}$) ligand residing on a centre of inversion, and a Mn centre and MeV^{m+} cation each sitting at the intersection of three orthogonal two-fold axes. Each Mn centre is coordinated to four crystallographically equivalent chelating $Clan^{n-}$ ligands through eight O donor atoms (Figure 2.4a). Notably, there is a marked asymmetry of the Mn–O bond lengths ($d_{Mn–O}$ = 2.168(1) and 2.587(1) Å) so that the coordination

geometry is a slightly distorted triangular dodecahedron. A similar asymmetry of Cd–O bond lengths is observed in **2.1$_{Cd}$** ($d_{Cd–O}$ = 2.273(2) and 2.512(2) Å), although not as pronounced as in **2.1$_{Mn}$**, resulting that the Cd coordination geometry lies closer to perfect triangular dodecahedron than in **2.1$_{Mn}$** (Continuous shape measure (CShM)[52, 53] parameter for triangular dodecahedron: 0.964 for **2.1$_{Mn}$**; 0.801 for **2.1$_{Cd}$**). In both, **2.1$_{Mn}$** and **2.1$_{Cd}$**, the $d_{M–O}$ values are consistent with the metal centres existing in the divalent state (Mn^{II} or Cd^{II}), requiring the $Clan^{n–}$ to exist in the dianionic form i.e. $Clan^{2–}$, giving an overall $(MeV^{2+})[M^{II}(Clan^{2–})_2]$ charge state distribution. The $Clan^{n–}$ oxidation state is also indicated by the mean ligand C–O ($d_{C–O}$) and diagnostic C–C (across the five-membered chelate ring, $d_{C–C}$) bond lengths. The average ligand $d_{C–O}$ (1.249(1) Å for **2.1$_{Mn}$**; 1.249(2) Å for **2.1$_{Cd}$**) and diagnostic $d_{C–C}$ (1.543(2) Å for **2.1$_{Mn}$**; 1.544(3) Å for **2.1$_{Cd}$**) values are both consistent with the $Clan^{2–}$, as they lie within the range expected for $Clan^{2–}$ ($d_{C–O}$ = 1.248–1.272 Å; $d_{C–C}$ = 1.506–1.551 Å, see Appendix A).

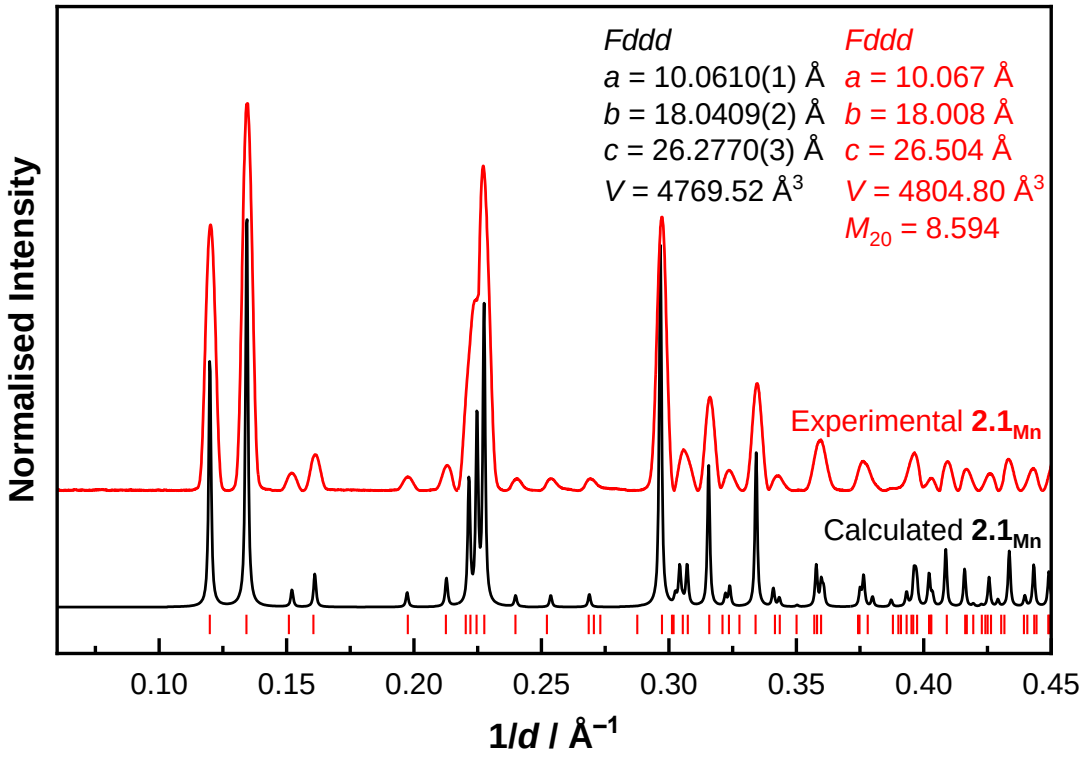


Figure 2.2 P-XRD (λ = 1.54184 Å) pattern of **2.1$_{Mn}$** (red, T = 100 K) and calculated pattern from SC-XRD of **2.1$_{Mn}$** (black, T = 100 K). Tick marks (red) indicate the positions of the allowed reflections for the unit cell indexed from the experimental P-XRD pattern.

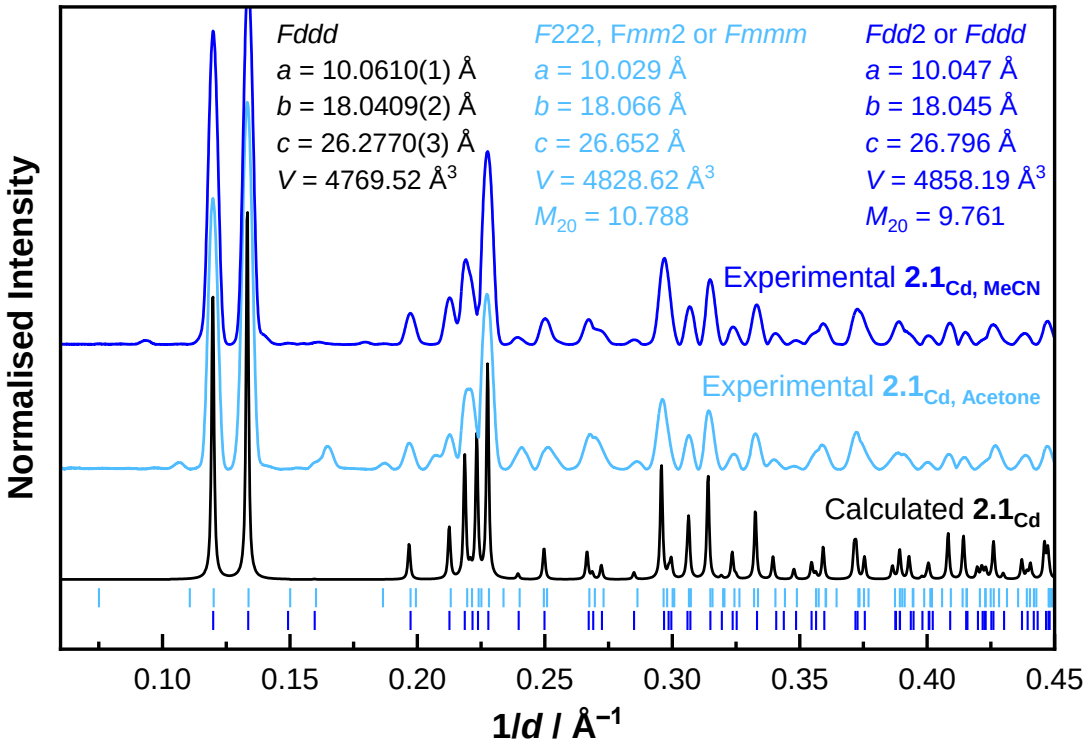


Figure 2.3 P-XRD (λ = 1.54184 Å) pattern of **2.1$_{Cd}$** synthesised using MeCN–H_2O (royal blue, T = 100 K) or acetone–H_2O (pale blue, T = 100 K) solvent systems, and calculated pattern from SC-XRD of **2.1$_{Cd}$** (black, T = 100 K). Tick marks (royal and pale blue) indicate the positions of the allowed reflections for the unit cells indexed from the experimental P-XRD patterns.

The diamondoid $[M^{II}(Clan^{2-})_2]^{2-}$ network is consequently formed by bridging every metal centre to four equivalent metal centres by the $Clan^{2-}$ ligands (Figure 2.4b & c). Although the 3D diamond topology is a relatively common 3D topology observed in coordination polymers,[54-56] analysis of the CSD reveals it is remarkably rare in metal–tetraoxolene coordination polymers. In tetraoxolene coordination polymers, the diamondoid topology has only been obtained using either lanthanoid (Y^{III}, Ho^{III}, Ce^{III} or Er^{III}),[30, 33, 39] actinoid (Th^{IV})[33] or post-transition metal (Bi^{III})[57] centres. This is likely due to the large ionic radii of these metal centres, affording higher coordination numbers and more flexible coordination geometry, both required to form the 4-connecting nodes of the diamondoid topology. The large ionic radii of Mn^{II} and Cd^{II} (0.97 Å and 1.09 Å respectively) compared to other first row transition

metals is consistent with the higher coordination number required to form the diamondoid network.

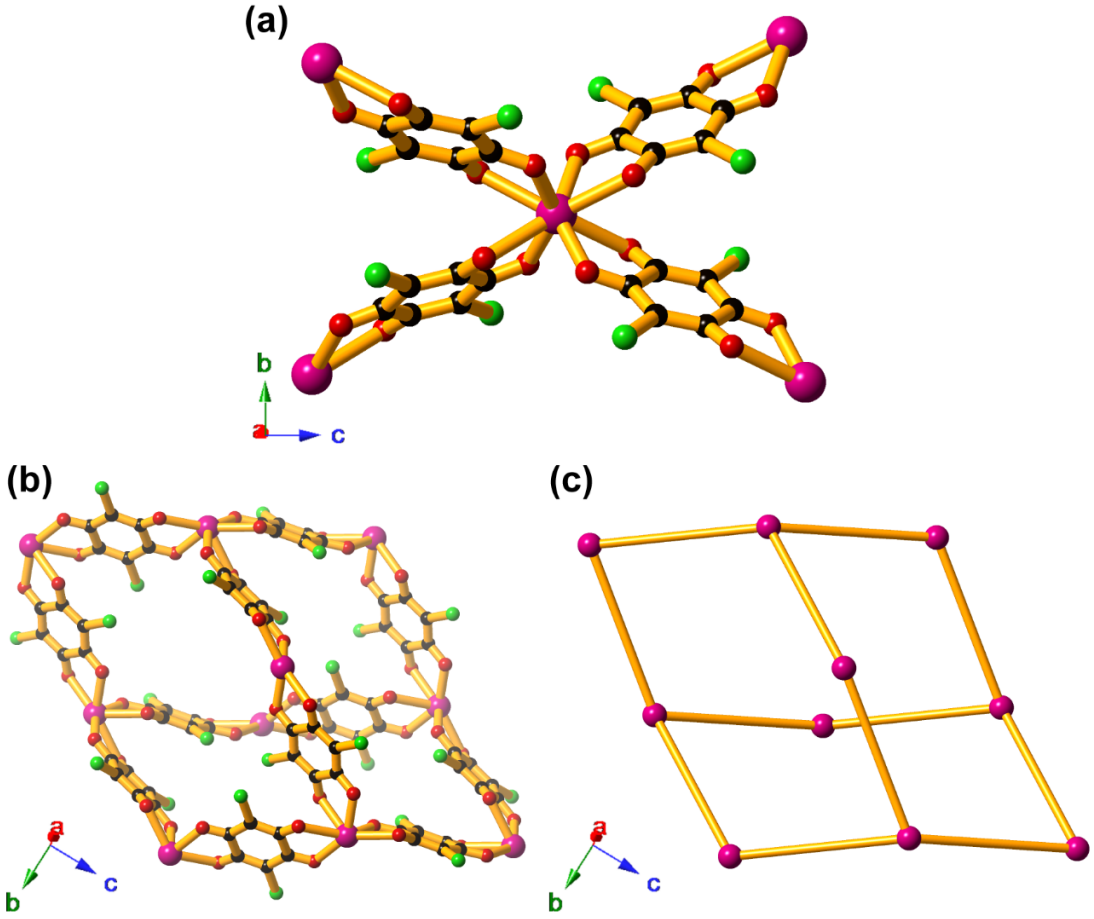


Figure 2.4 (a) The 8-coordinate environment around Mn^{II} in **2.1$_{Mn}$**. (b) Ball-and-stick and (c) topological representations of the adamantane unit of the $[Mn^{II}(Clan)_2]^{2-}$ network in **2.1$_{Mn}$**. Magenta = Mn, green = Cl, red = O, and black = C.

Charge-balancing MeV^{2+} cations are situated at the centre of adamantane unit of the $[M^{II}(Clan)_2]^{2-}$ network, with each MeV^{2+} protruding slightly into the adamantane windows of adjacent units (Figure 2.5). This arrangement gives a dense, non-porous coordination polymer. The central C–C bond of MeV^{2+} is oriented parallel to the crystallographic *c* axis and situated on the intersection of three orthogonal 2-fold axes. Each MeV^{2+} molecule is pinned within the adamantane cage by C–Cl$\cdots\pi$ interactions between the pyridinium rings of MeV^{2+} and Cl atoms of $Clan^{2-}$ ligands in the framework ($d_{C–Cl\cdots\pi}$ = 3.340 Å) (Figure 2.6). This interaction produces

significant torsion about the central C–C bond of MeV^{2+} (39.36 ° in **2.1$_{Mn}$**; 39.74 ° in **2.1$_{Cd}$**), typically seen by MeV^{2+}, whereas the radical cation $MeV^{+\bullet}$ exhibits a conformation which is closer to planar in the solid state.[58, 59] Additional, the C–C and C–N bond lengths ($d_{C–C}$ and $d_{C–N}$ respectively) in viologen-like molecules are diagnostic of oxidation state, due to introduction of semiquinonoid character following reduction from the aromatic dication to the radical monocation.[58-61] Comparing the $d_{C–C}$ and $d_{C–N}$ values for the MeV^{2+}cation in **2.1$_{Mn}$** and **2.1$_{Cd}$**, particularly the inter-ring C–C bond, to those of MeV^{2+},[62, 63] or $MeV^{+\bullet}$,[58, 59] confirms the cations in **2.1$_{Mn}$** and **2.1$_{Cd}$** are in the expected MeV^{2+} valence state.

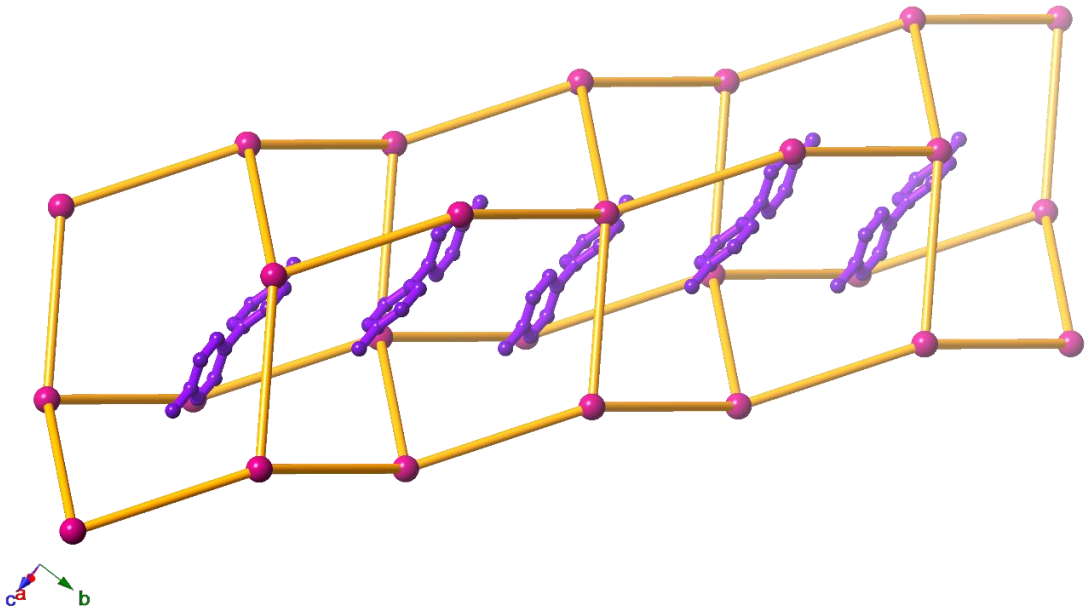


Figure 2.5 Packing arrangement of MeV^{2+} cations (purple) within the anionic adamantane $[Mn(Clan)_2]^{2-}$ units in **2.1$_{Mn}$**. Only the topological representation of the anionic $[Mn(Clan)_2]^{2-}$ network is shown for clarity. Magenta = Mn.

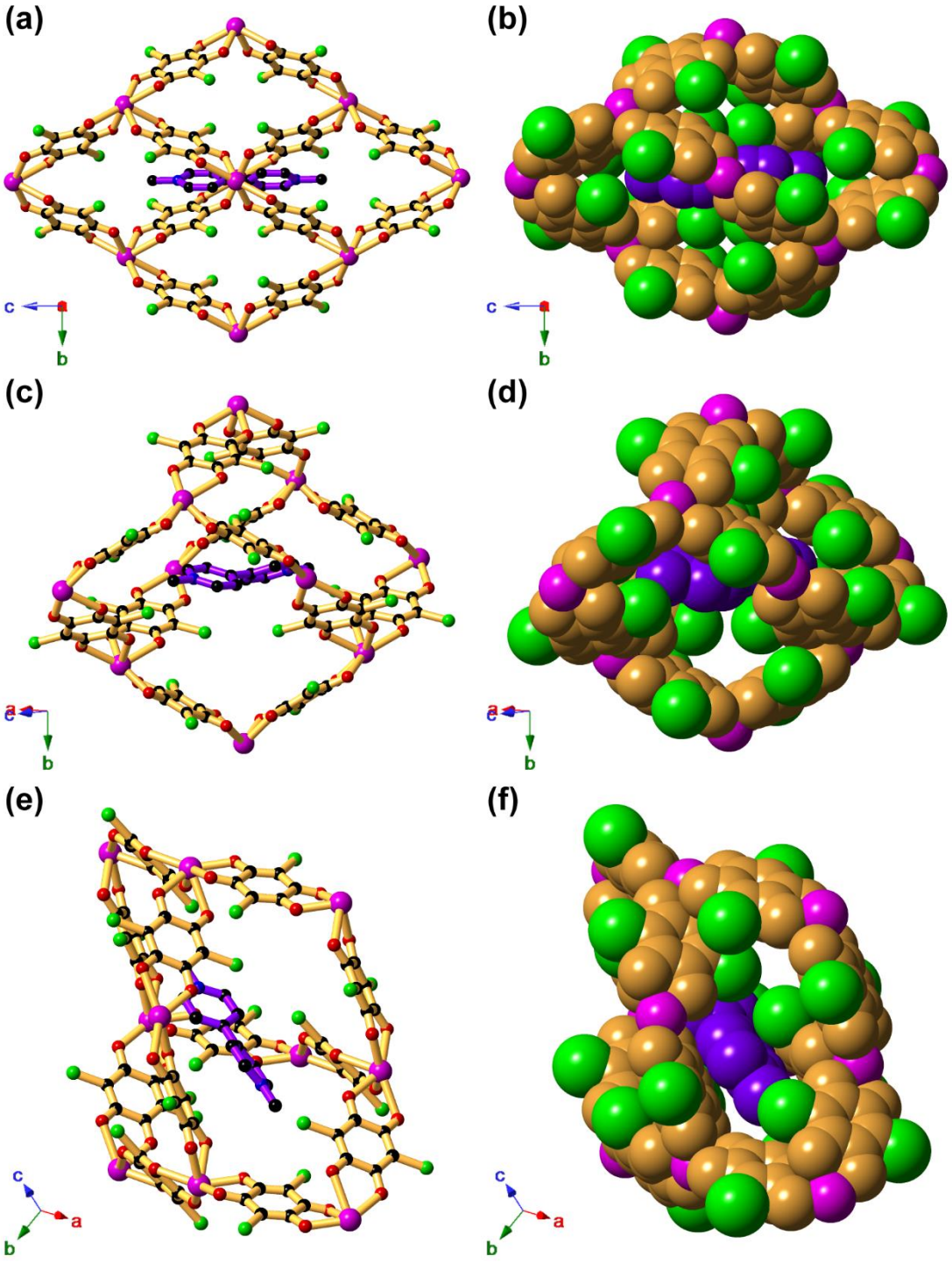


Figure 2.6 Ball-and-stick (a, c, e) and spacefilling (b, d, f) representations of the interactions of the MeV^{2+} cation (purple) within the anionic $[Mn(Clan)_2]^{2-}$ adamantane unit in **2.1$_{Mn}$** (tan). Magenta = Mn, green = Cl, red = O, blue = N, and black = C.

Further evidence of the chemically similar and dense, solvent-free nature of **2.1$_{Mn}$** and **2.1$_{Cd}$** is provided by Fourier-transform infrared (FT-IR) spectroscopy and

thermogravimetric analysis (TGA) of the bulk products. The FT-IR spectra of **2.1$_{Mn}$** (Figure 2.7, red), and **2.1$_{Cd}$** prepared using either an acetone–H_2O (Figure 2.7, pale blue) or MeCN–H_2O (Figure 2.7, royal blue) solvent system, show no absorptions that can be attributed to either water (ν_{O-H} ca. 3500 cm^{-1}) or MeCN ($\nu_{C\equiv N}$ ca. 2200 cm^{-1}) indicating an absence of guest solvent molecules in the bulk products. The absence of weight loss up to ca. 300 °C by TGA upon **2.1$_{Mn}$** and **2.1$_{Cd}$** synthesised using an MeCN–H_2O solvent systems also indicates the compounds do not contain guest solvent (Figure 2.8a & c). In the case of **2.1$_{Cd}$**, synthesised using an acetone–H_2O solvent system (Figure 2.8b), a slight weight loss corresponding to ca. 0.34 H_2O per formula unit is observed, indicative of partial solvation upon exposure to atmospheric moisture. The value of H_2O uptake by **2.1$_{Cd}$** suggested by TGA also agrees well with the solvation indicated by elemental analysis (0.4 H_2O per unit formula, see Section 2.4.4.2). The slightly discrepancy in H_2O uptake for **2.1$_{Cd}$** between TGA and FT-IR spectroscopy is possibly due to differences in atmospheric humidity at the times of measurement.

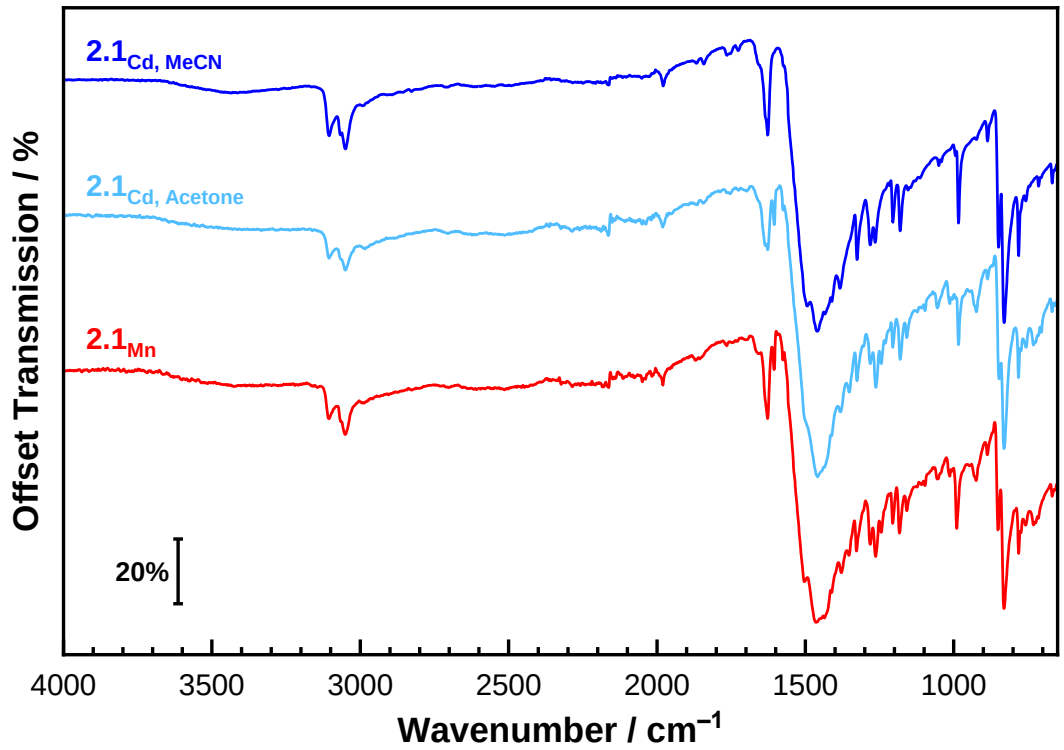


Figure 2.7 ATR FT-IR spectra of **2.1$_{Mn}$** (red) and **2.1$_{Cd}$** synthesised using either acetone–H_2O (pale blue) or MeCN–H_2O (royal blue) solvent systems, collected at room temperature in air.

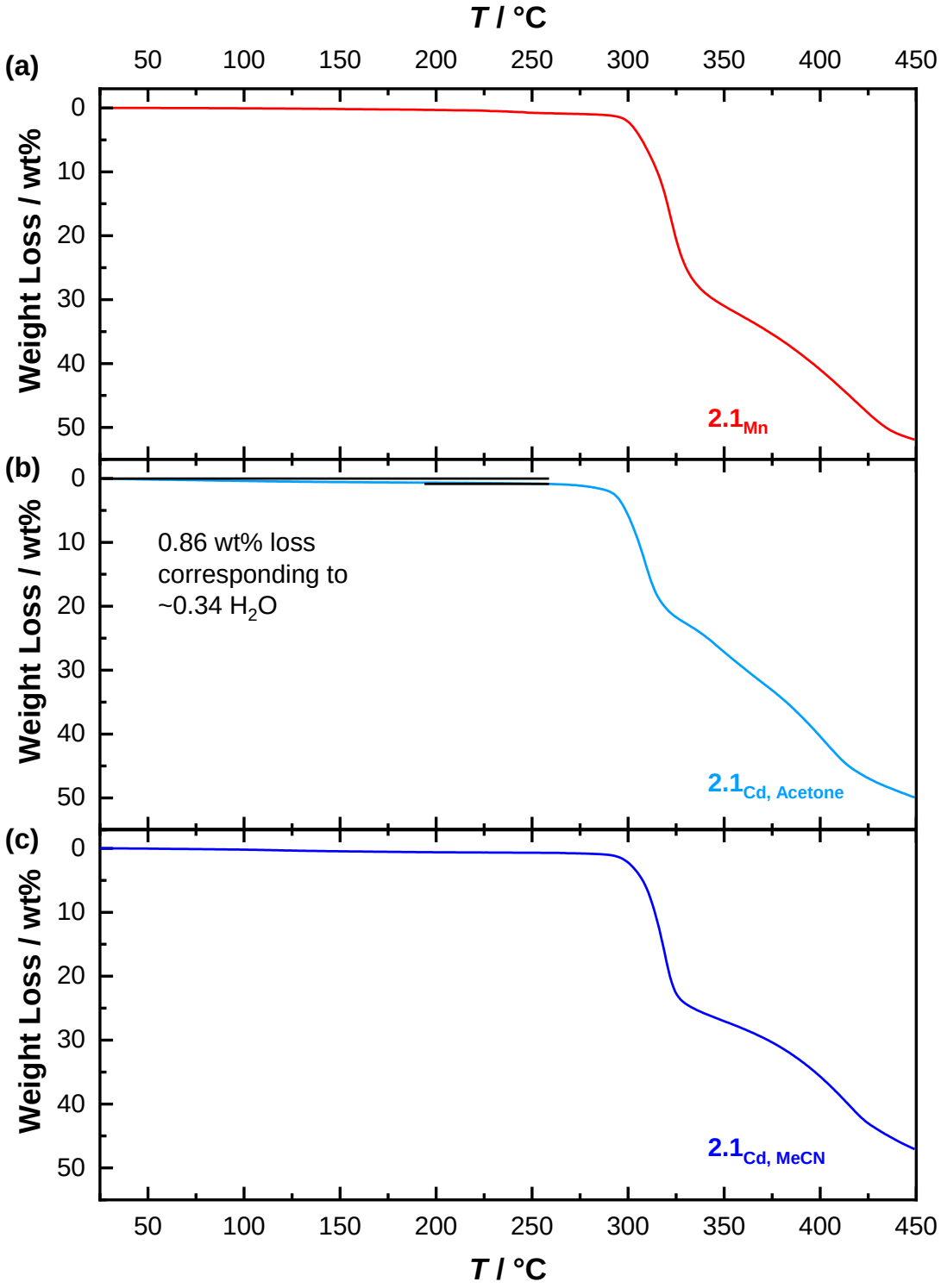


Figure 2.8 Thermogravimetric analyses of (a) **2.1$_{Mn}$** (red) and **2.1$_{Cd}$** synthesised using either (b) acetone–H_2O (pale blue) or (c) MeCN–H_2O (royal blue) solvent systems at a scan rate of 5 °C min^{-1} in a flow of N_2.

2D Networks

An analogous reaction for the synthesis of **2.1$_{Mn}$** but instead using a MeCN–H_2O solvent mixture affords reddish-brown plate single crystals of the 2D coordination polymer (MeV)[Mn_2(Clan)$_3$]·6MeCN (**2.2a**). A satisfactory structure solution for **2.2a** was found in the triclinic *P*−1 space group, with the asymmetric unit containing one Mn centre, three independent Clan^{n-} ligands (**L$_1$**, **L$_2$** and **L$_3$**) and a MeV^{m+} cation; the three Clan^{n-} ligands and MeV^{m+} cation all lie upon centres of inversion in the asymmetric unit. The Mn centre is in a slightly distorted octahedral environment produced by the six O donor atoms of three bridging bis-bidendate Clan^{n-} ligands. As with **2.1$_{Mn}$**, inspection of the average $d_{Mn–O}$ (2.174(1) Å), and mean ligand $d_{C–O}$ (1.256(1), 1.256(1) and 1.258(1) Å for **L$_1$**, **L$_2$** and **L$_3$** respectively) and $d_{C–C}$ (1.541(2), 1.541(2) and 1.537(2) Å for **L$_1$**, **L$_2$** and **L$_3$** respectively) values indicates the valence states are Mn^{II} and $Clan^{2-}$ respectively. The anionic [Mn^{II}_2(Clan^{2-})$_3$]$^{2-}$ sheets are therefore formed by linking Mn centres of a given configuration (either Δ or Λ) to three Mn centres of opposite configuration (either Λ or Δ) via the bridging bis-bidentate $Clan^{2-}$ ligands, producing a honeycomb (6,3) network (Figure 2.9a). In contrast to (6,3) networks with trigonal symmetry, such as $(Et_4N)_2[M_2(Xan)_3]$ (M = Zn, Mn, Fe; X = F, Cl),[28, 45] which exhibit a perfect hexagonal geometry of the (6,3) network i.e. 120° M···M···M angles, the hexagonal sheets in **2.2a** are sheared in one direction, so that the Mn···Mn···Mn angles change to 115.09°, 130.20° and 114.46°. The distorted sheet geometry likely results from several factors. Alkylammonium cations commonly exhibit threefold or pseudo-threefold symmetry, affording excellent packing compatibility with anionic $[M_2(Clan)_3]^{2-}$ sheets with regular hexagonal geometry. In contrast, the planar nature of the MeV^{2+} cations probably results in poorer steric compatibility with anionic $[M_2(Clan)_3]^{2-}$ sheets with trigonal or hexagonal symmetry. In constant to many (6,3) networks which contain large voids filled with highly disordered solvent, each hexagonal void in **2.2a** contains six highly ordered MeCN molecules, suggesting the MeCN also plays an important role in templating the structure. The mean plane of the anionic $[Mn_2(Clan)_3]^{2-}$ sheets (defined through the Mn centres) lies parallel to the crystallographic (111) plane, which is inclined 72.63° from the (001) plane; the corresponding inter-sheet spacing is 7.033 Å (Figure 2.9b).

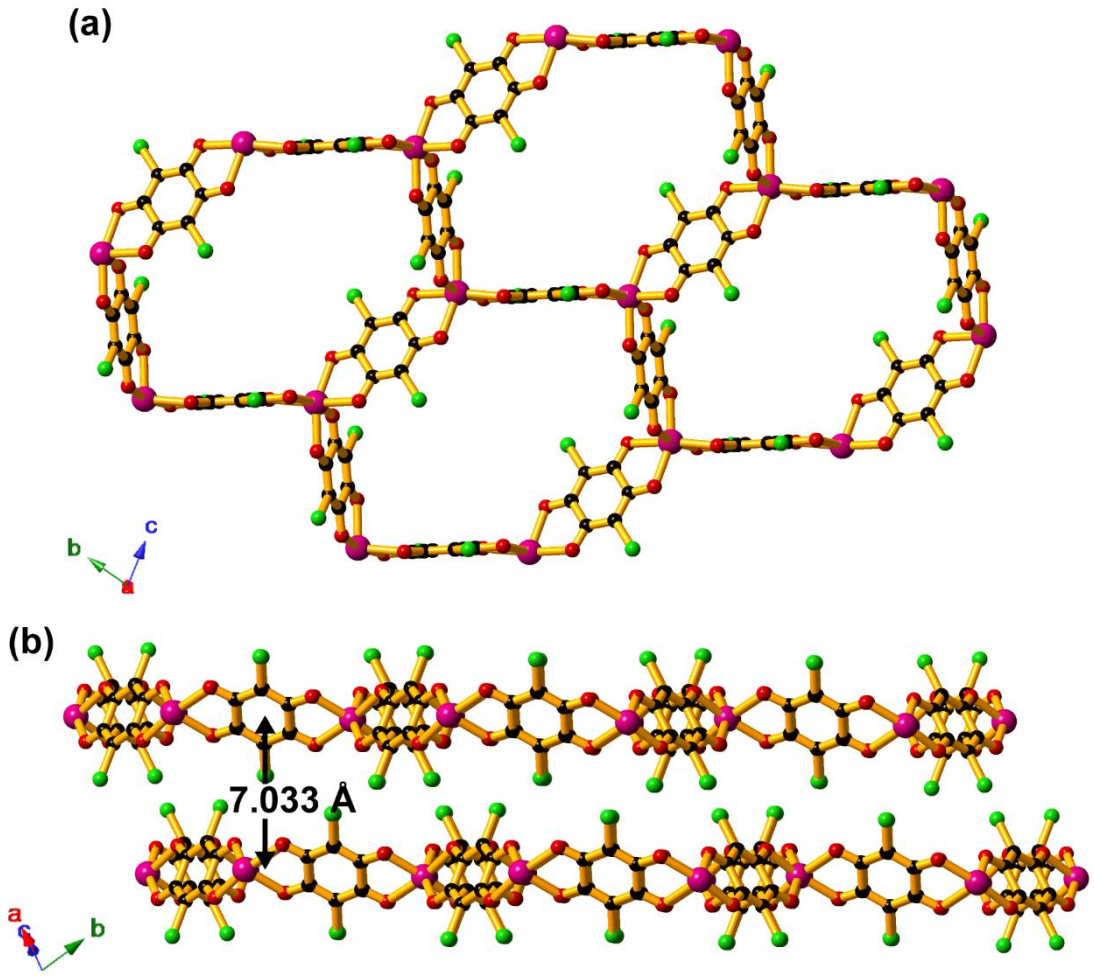


Figure 2.9 The anionic $[Mn_2(Clan)_3]^{2-}$ (6,3) honeycomb sheets in **2.2a** viewed (a) along the crystallographic *a* axis and (b) along the plane of the anionic sheets oriented parallel to the crystallographic (111) plane. Magenta = Mn, green = Cl, red = O, black = C.

Electrical neutrality of the compound is achieved through incorporation of MeV^{2+} cations located between the anionic $[Mn_2(Clan)_3]^{2-}$ sheets, sandwiched between two **L₁** $Clan^{2-}$ ligands from the sheet above and below (Figure 2.10). As the $Clan^{2-}$ is relatively π-electron poor, CT interactions are probably not a significant interaction between cation and the anionic $[Mn_2(Clan)_3]^{2-}$ network. This is evinced by the absence of close face-to-face contact between $Clan^{2-}$ and MeV^{2+}. Instead, MeV^{2+} cations are probably located at this position due to a combination of Coulombic interactions, and favourable shape complementarity locking the anionic sheets above and below together, in combination with C–H···O interactions between aryl H atoms of MeV^{2+} and O atoms in the sheets above and below ($d_{H\cdots O}$ = 2.381, 2.405 Å). Stacks of alternating stacks of $Clan^{2-}$ and MeV^{2+} moieties are formed along the crystallographic *a* axis (Figure 2.11). This arrangement leads to AAAA stacking of the $[Mn_2(Clan)_3]^{2-}$ sheets, in which the configurations of the Mn centres in a column, viewed along the crystallographic *a* axis, are either all Δ or all Λ. The large geometrically distorted hexagonal 1D channels formed by the sheet stacking are filled with six well-ordered MeCN molecules per formula unit, so the overall structure is dense. The MeCN molecules are readily lost upon removal of the crystals from the mother liquor (*vide infra*).

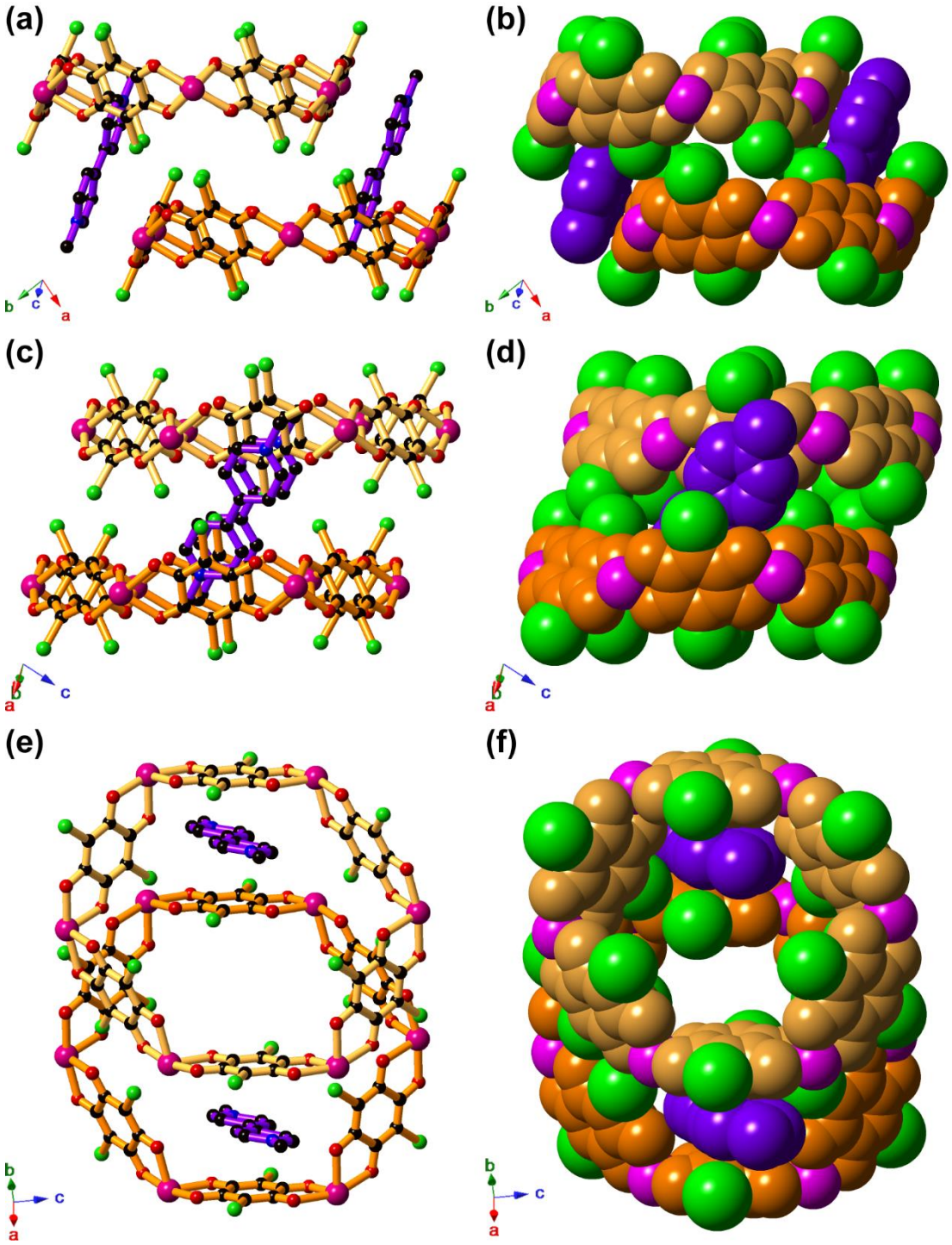


Figure 2.10 Ball-and-stick (a, c, e) and spacefilling (b, d, f) representations of the interactions of the MeV^{2+} cations (purple) with the anionic $[Mn_2(Clan)_3]^{2-}$ sheets above (tan) and below (orange) in **2.2a**. Views along (a–d) the plane of the anionic sheets and (e, f) along the one-dimensional channels. Magenta = Mn, green = Cl, red = O, blue = N, black = C. H atoms and ordered MeCN in channels not shown for clarity.

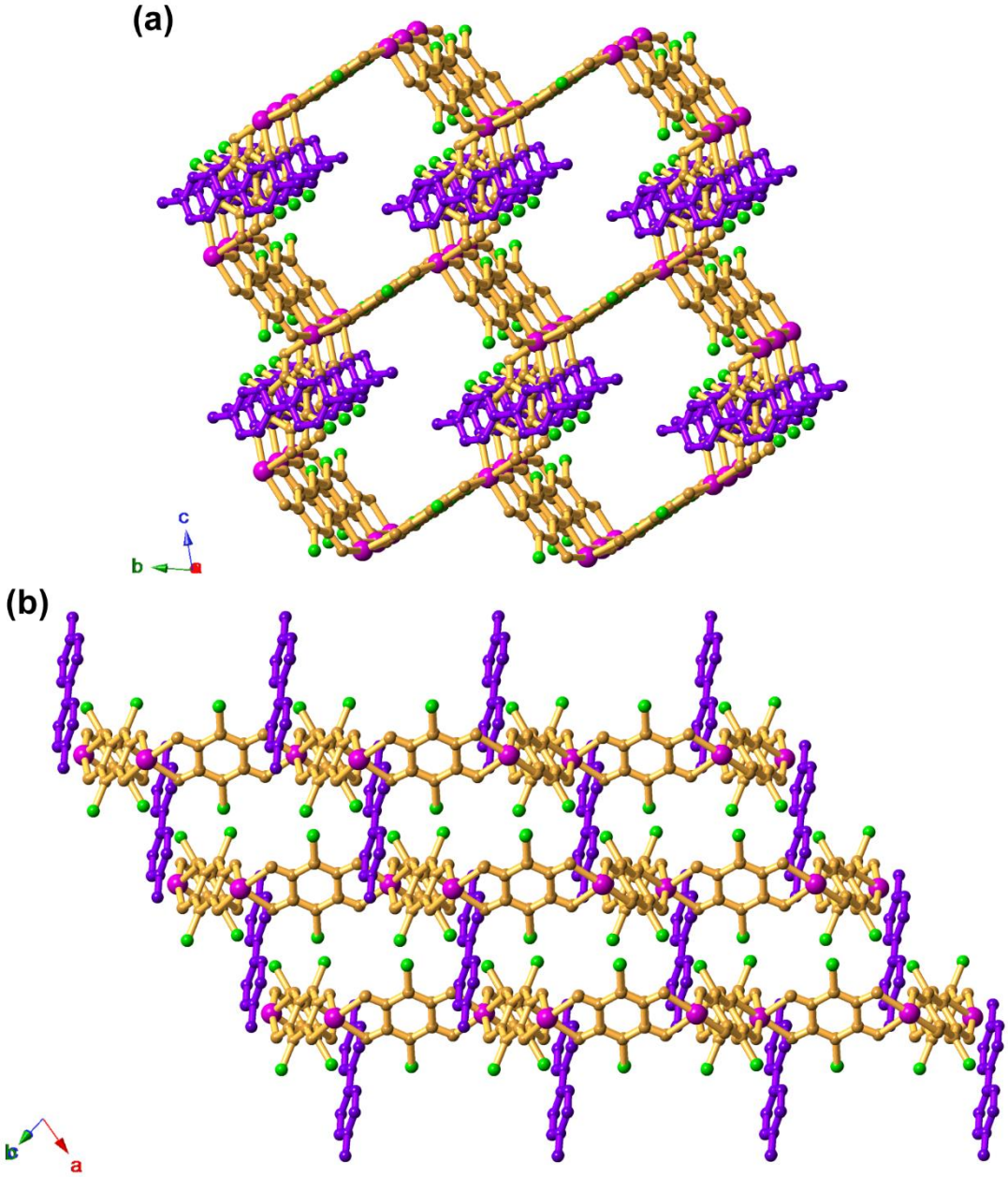


Figure 2.11 Alternating stacking of MeV^{2+} (purple) with $Clan^{2-}$ ligands in the anionic $[Mn_2(Clan)_3]^{2-}$ sheets (tan) in **2.2a**. Views along (a) the crystallographic *a* axis showing hexagonal channels and AAAA stacking, and (b) the plane of the anionic $[Mn_2(Clan)_3]^{2-}$ sheets. Ordered MeCN in channels not shown for clarity. Magenta = Mn, green = Cl. H atoms not shown for clarity.

Good agreement between the calculated P-XRD pattern, and the experimental pattern (as an MeCN slurry to preserve solvation) indicates that **2.2a** is the dominant phase in the product (Figure 2.12). The differences in cell parameters between the experimental and calculated patterns probably arise from thermal expansion of the unit cell. Notably, the unit cell parameters for an isomorphous (MeV)[Fe_2(Clan)$_3$]·6MeCN polymer measured at 240 K (see Section 5.2.3) match reasonably well to the cell parameters from the indexed P-XRD pattern of **2.2a**, measured at 250 K. Moreover, (MeV)[Fe_2(Clan)$_3$]·6MeCN exhibits similar thermal variation of cell parameters i.e. increase of *a*, *b*, *c* and *V*, and decrease of α, β, γ with increasing temperature. This supports the conclusion that the differences between the unit cell parameters determined by SC-XRD of **2.2a**, and those obtained from P-XRD on an MeCN slurry of **2.2a**, arise due to thermal expansion of the unit cell. Nevertheless, microscopic inspection of the crystalline product revealed a small number of bright-red octahedral crystals, which are the 3D diamondoid phase $\mathbf{2.1_{Mn}}$. Despite repeated attempts, co-crystallisation of a small amount of $\mathbf{2.1_{Mn}}$ with **2.2a** seemingly cannot be avoided. Generation of two distinct products possibly reflects a competition between kinetic and thermodynamic factors. Moreover, an analogous reaction between $Cd^{II}(NO_3)_2$ and MeV^{2+} with H_4Clan in MeCN–H_2O yields only the 3D diamondoid phase $\mathbf{2.1_{Cd}}$, instead of the hypothetical honeycomb compound (MeV)[Cd_2(Clan)$_3$]·6MeCN. This suggests that the 3D diamondoid phase may be favoured kinetically, whereas the 2D networks may be the thermodynamic product.

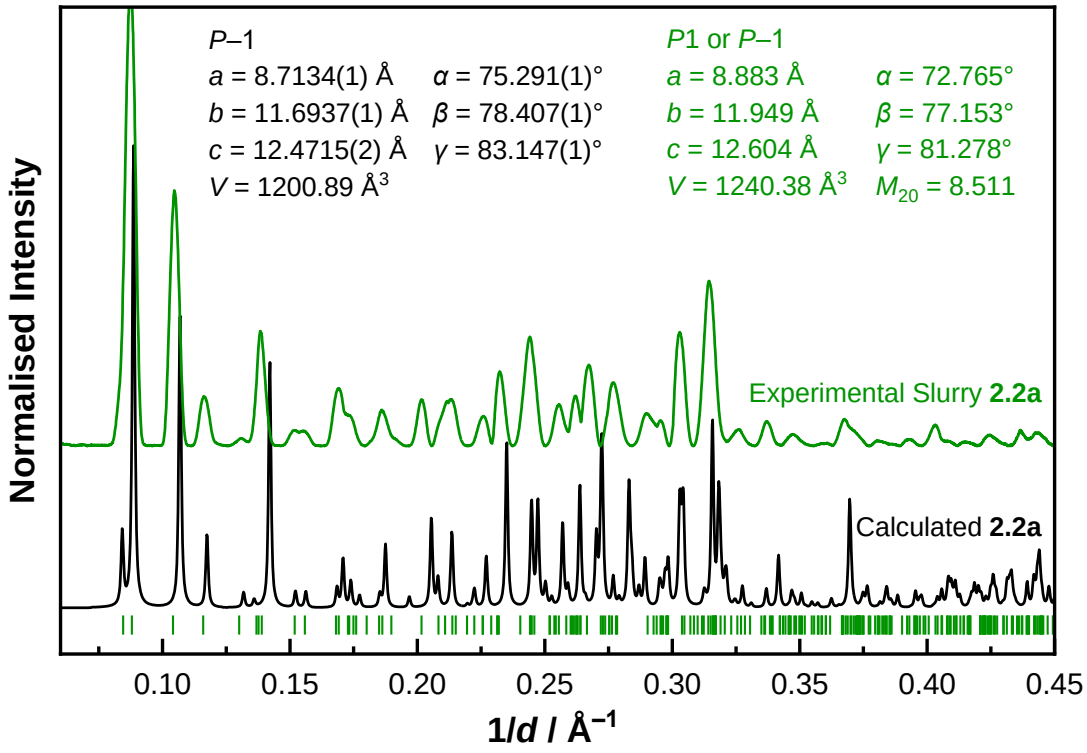


Figure 2.12 P-XRD (λ = 1.54184 Å) pattern of a MeCN slurry of bulk **2.2a** (green, T = 250 K) and calculated pattern from SC-XRD of **2.2a** (black, T = 100 K). Tick marks (green) indicate the positions of the allowed reflections for the unit cell indexed from the experimental P-XRD pattern.

An additional complication arises upon isolation of **2.2a**. Although **2.2a** crystallises with six MeCN per formula unit, this solvent is readily lost upon removal from the mother liquor and exposure to air during filtration. The MeCN lost is readily replaced by atmospheric H_2O, as shown by FT-IR spectroscopy (Figure 2.13a), forming the compound **2.2b**. This is evinced by the absence of $\nu_{C\equiv N}$ at ca. 2200 cm^{-1} which would be expected for the MeCN solvate, and instead appearance of a broad, intense absorbance around 3415 cm^{-1}, indicative of H_2O in **2.2b**. Additionally, TGA (Figure 2.13b) demonstrates a weight loss of 3.59% between 25 and 115 °C, with a second weight loss of 2.91% between 115 and 205 °C. The sum of these values is significantly lower than expected for six MeCN per unit formula (21.17%), and corresponds approximately to $3.5H_2O$ per unit formula. Loss of MeCN from the channels is further supported by elemental analysis of **2.2b**. This shows a significantly lower C and N content compared to that expected for

(MeV)[Mn_2(Clan)$_3$]·6MeCN, with the analyses indicating approximately 2.5H_2O per unit formula (see Section 2.4.4.3).

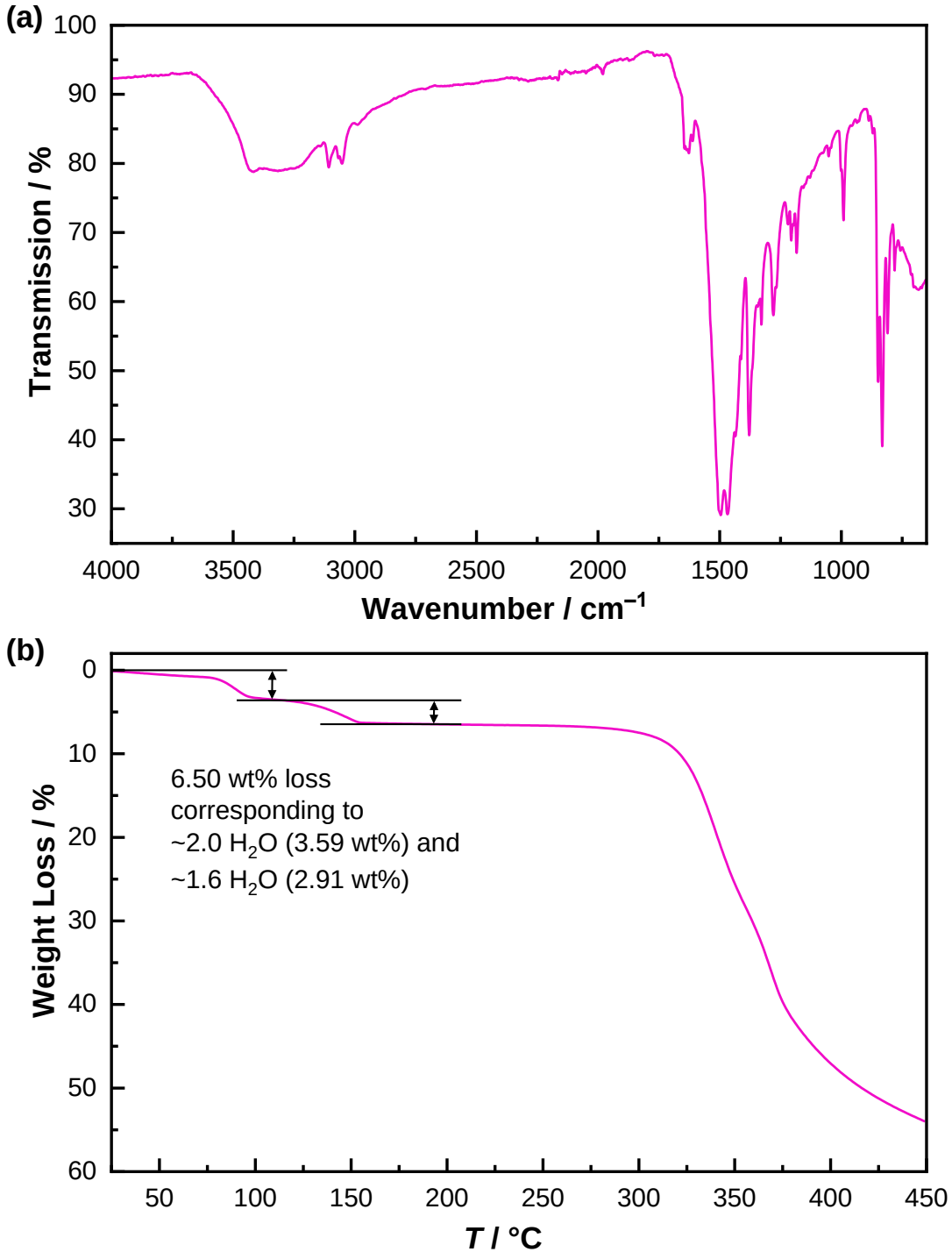


Figure 2.13 (a) ATR FT-IR spectrum of **2.2b** (isolated **2.2a**) conducted at ambient temperature in air. (b) Thermogravimetric analysis of **2.2b** (isolated **2.2b**) at a scan rate of 5 °C min^{-1} in a flow of N_2.

MeCN loss from **2.2a** also causes a significant structural transformation, as shown by P-XRD analyses (Figure 2.14). In contrast to the slurry sample, in which the presence of the diamondoid **2.1$_{Mn}$** phase is not apparent, good agreement between numerous peaks calculated for **2.1$_{Mn}$** and the bulk **2.2b** is observed. Moreover, the absence of reflections corresponding to **2.2a** indicate either complete loss of crystallinity of this product, or transformation to an unidentified third crystalline phase upon exposure to atmospheric moisture and loss of MeCN guest solvent. Due to the predominance of the reflections attributed to **2.1$_{Mn}$**, structure determination of the **2.2b** phase could not be performed.

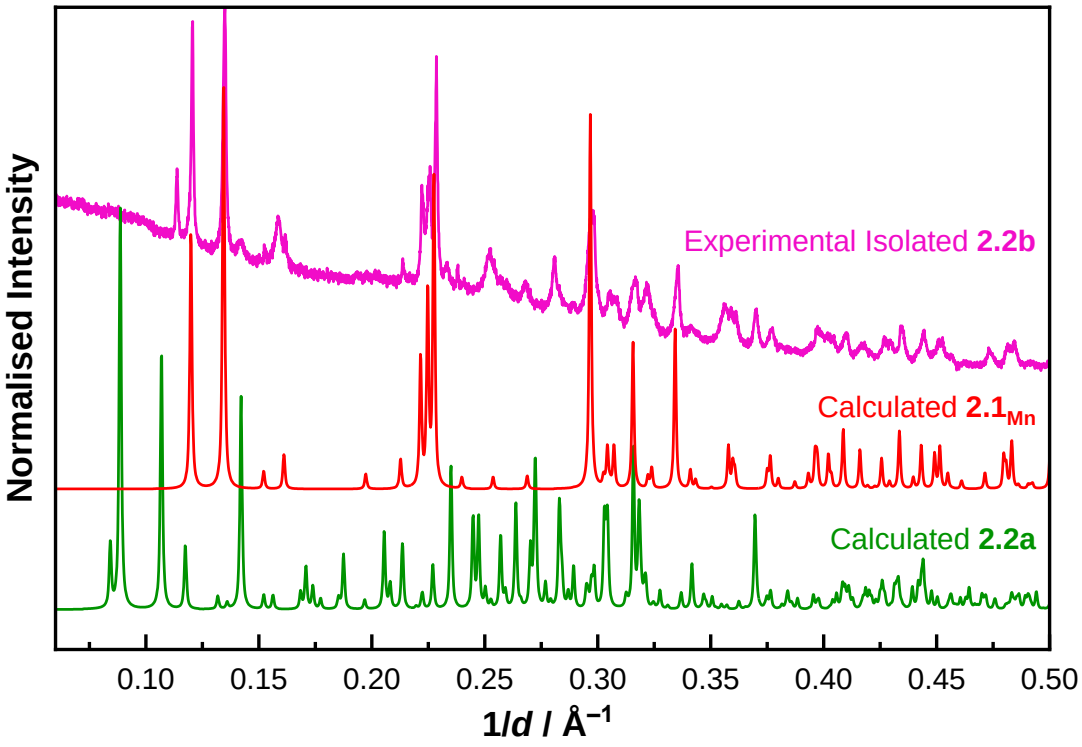


Figure 2.14 Synchrotron P-XRD (λ = 0.58835 Å) pattern of bulk **2.2b** (isolated **2.2a**, magenta, T = 100 K) and calculated patterns from SC-XRD of **2.1$_{Mn}$** (red, T = 100 K) and **2.2a** (green, T = 100 K).

2.2.1.2 Fluoranilate Coordination Polymers

Slow diffusion reactions using a MeCN–H_2O solvent system with $Mn^{II}(NO_3)_2$ or $Cd^{II}(NO_3)_2$, H_4Fan and MeV^{2+}, yields the one-dimensional (1D) ladder compound $(MeV)[Mn_2(Fan)_3(H_2O)_2]\cdot y$MeCN$\cdot z H_2O$ (**2.3$_{Mn}$**) and the isostructural diamagnetic Cd analogue $(MeV)[Cd_2(Fan)_3(H_2O)_2]\cdot y$MeCN$\cdot z H_2O$ (**2.3$_{Cd}$**). For both **2.3$_{Mn}$** and **2.3$_{Cd}$**, satisfactory structure refinements were found in the triclinic space group $P\bar{1}$, with further structure description for the archetype **2.3$_{Mn}$**. The asymmetric unit comprises two crystallographically unique metal centres (Mn1 and Mn2), and four unique Fan^{n-} ligands (**L$_1$** through **L$_4$**). The ligands **L$_1$** and **L$_3$** lie on inversion centres, whereas **L$_2$** and **L$_4$** reside on general positions. The asymmetric unit also contains one MeV^{m+} and two coordinated H_2O molecules, in addition to H_2O and MeCN molecules of solvation. The structures of **2.3$_{Mn}$** and **2.3$_{Cd}$** are somewhat unexpected. Each metal centre resides in a slightly distorted octahedral environment coordinated to six O donor atoms from a combination of one coordinating H_2O molecule, and five O donor atoms from three coordinating Fan^{n-} ligands (Figure 2.15a). The $d_{M–O}$ and mean ligand $d_{C–O}$ and diagnostic $d_{C–C}$ values indicate the metals are in the divalent state, and all ligands are in the Fan^{2-} form, giving a $(MeV^{2+})[M^{II}_2(Fan^{2-})_3(H_2O)_2]$ valence distribution. In contrast to the structures described previously in this work, in which the $Clan^{2-}$ ligands are always bridging bis-bidentate, the Fan^{2-} ligands in **2.3$_{Mn}$** are a combination of bridging bis-bidentate and bridging mono- and bi-dentate. Four Mn centres are arranged at the corners of a parallelogram (Mn_4), with the sides bridged by Fan^{n-} ligands; two of ligands, **L$_2$** and **L$_4$**, are monodentate on one side and bidentate on the other (Figure 2.15a). On the other hand, the other two ligands, **L$_1$** and **L$_3$**, are bridging bis-bidentate Fan^{2-} ligands. MeCN appears partly responsible for templating this arrangement, as the voids of the Mn_4 parallelograms contain a well ordered MeCN in **2.3$_{Mn}$**, and a slightly disordered MeCN in **2.3$_{Cd}$** (Figure 2.15b). Chains of edge-sharing Mn_4 parallelograms form the 1D ladders, with the ladder axis running parallel to the crystallographic (1$\bar{1}$0) plane; bridging bis-bidendate ligands (**L$_1$** and **L$_3$**) form the rungs of the ladders, and {Mn–**L$_2$**–Mn–**L$_4$**}$_\infty$ chains form the sides (Figure 2.15c).

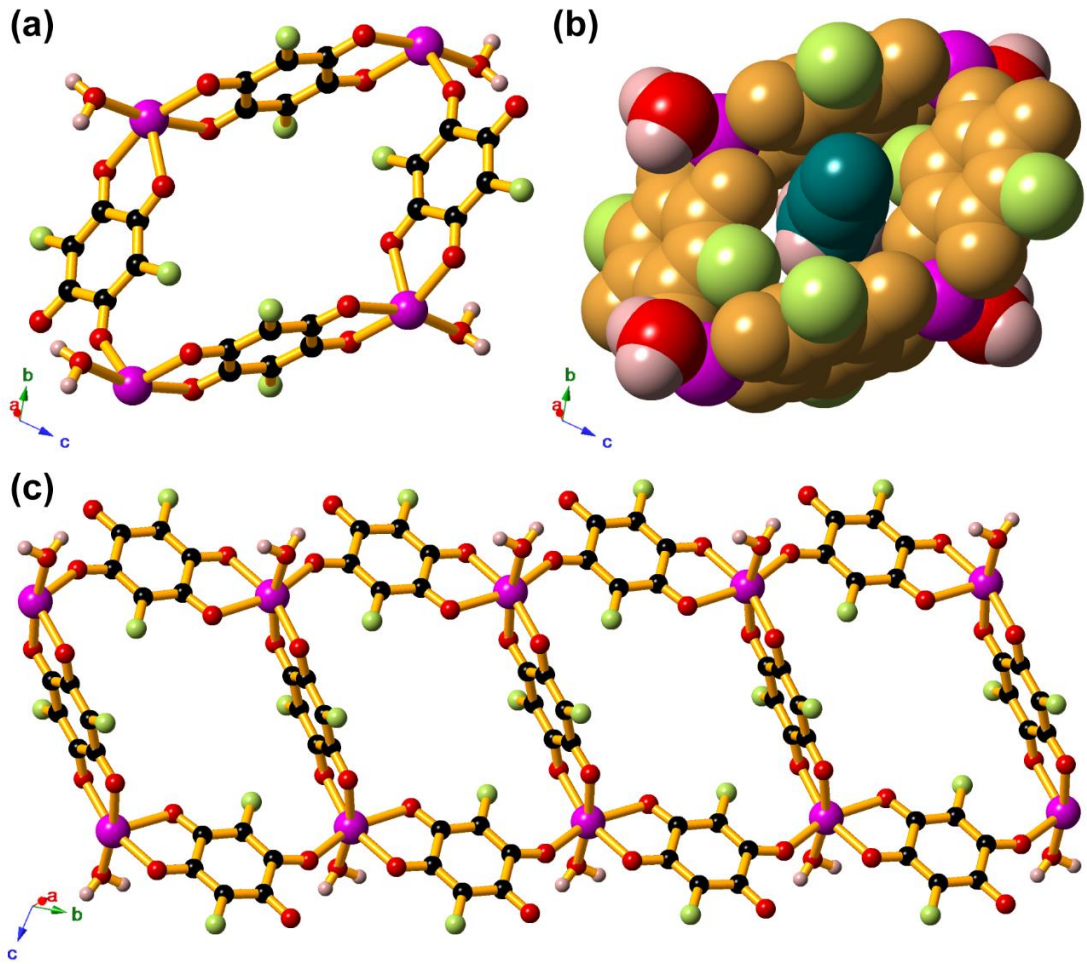


Figure 2.15 (a) Coordination environment around Mn^{II} centres in **2.3$_{Mn}$** forming Mn_4 parallelograms. (b) Templating of Mn_4 parallelograms (tan) by ordered MeCN (teal) situated within the network void. (c) Anionic 1D $[Mn_2(Fan)_3(H_2O)_2]^{2-}$ ladders forming by edge-sharing Mn4 parallelograms in **2.3$_{Mn}$**. Magenta = Mn, pale green = F, red = O, black = C, pale pink = H.

The coordinated H_2O molecules participate in H-bonding interactions with adjacent 1D ladders. Viewed down the axis of the ladder, Mn centres in adjacent ladders, and coordinated H_2O are situated approximately at corners of a parallelogram (Figure 2.16a & b). Two H-bonding interactions occur from each coordinated H_2O to H-bond acceptors in the adjacent ladder. One occurs from the H_2O molecule to a non-coordinating O atom at the monodentate end of **L$_2$** or **L$_4$** ($d_{O\cdots O}$ = 2.669(2) Å and 2.713(2)Å in **2.3$_{Mn}$**; $d_{O\cdots O}$ = 2.702(2) and 2.730(2) Å in **2.3$_{Cd}$**). The other occurs between the coordinated H_2O molecule and a coordinating O donor at the bidentate end of **L$_2$** or **L$_4$** ($d_{O\cdots O}$ = 2.720(2) and 2.777(2) Å in **2.3$_{Mn}$**;

$d_{O\cdots O}$ = 2.733(3) and 2.808(3) Å in **2.3$_{Cd}$**). An equivalent H-bonding interaction occurs from the coordinated H_2O in the adjacent ladder to O acceptor atoms in the first chain. The edge ligands (**L$_2$** and **L$_4$**) also participate in a weak face-to-face stacking interaction with the symmetrically equivalent edge ligand (**L$_2$** and **L$_4$**) in the adjacent chain (Figure 2.16c). This combination of H-bonding and weak face-to-face stacking occurs along the entire length and on both sides of the 1D anionic ladders, producing layers of H-bonded 1D ladders which sit parallel to the crystallographic (1−10) plane. A similar 1D ladder geometry and packing arrangement has been observed in the compound (2,2′-bpyH$^+$)$_2$[Mn$_2$(Clan)$_3$(H$_2$O)$_2$]·2H$_2$O.[16] Compared to this compound, the M_4 parallelogram voids in **2.3$_{Mn}$** and **2.3$_{Cd}$** are sheared by a slightly greater extent away from rectangular geometry in the direction of the rungs, with large changes in the M···M···M angles formed by the parallelograms (70.3° and 109.7 ° for **2.3$_{Mn}$**; 67.5° and 112.4° for **2.3$_{Cd}$**; 80.4° and 99.6° for (2,2′-bpyH$^+$)$_2$[Mn$_2$(Clan)$_3$(H$_2$O)$_2$]·2H$_2$O). In that compound, more significant shearing of the parallelograms is prevented by steric interactions between Cl atoms in the edge ligands and the Mn centres. By contrast, the smaller van der Waals radius of F in **2.3$_{Mn}$** and **2.3$_{Cd}$**, reduces steric interactions with the metal centres, which facilitates the greater shearing of the M_4 parallelograms. This also facilitates much closer C−F···C contacts between F atoms in the edge ligands and C atoms in the rung ligands ($d_{F\cdots C}$ = 2.980(3) and 2.988(3) Å in **2.3$_{Mn}$**; $d_{F\cdots C}$ = 2.992(3) and 3.022(3) Å in **2.3$_{Cd}$**), than the equivalent C−Cl···C contacts ($d_{Cl\cdots C}$ 3.402(3) Å) in (2,2′-bpyH$^+$)$_2$[Mn$_2$(Clan)$_3$(H$_2$O)$_2$]·2H$_2$O.

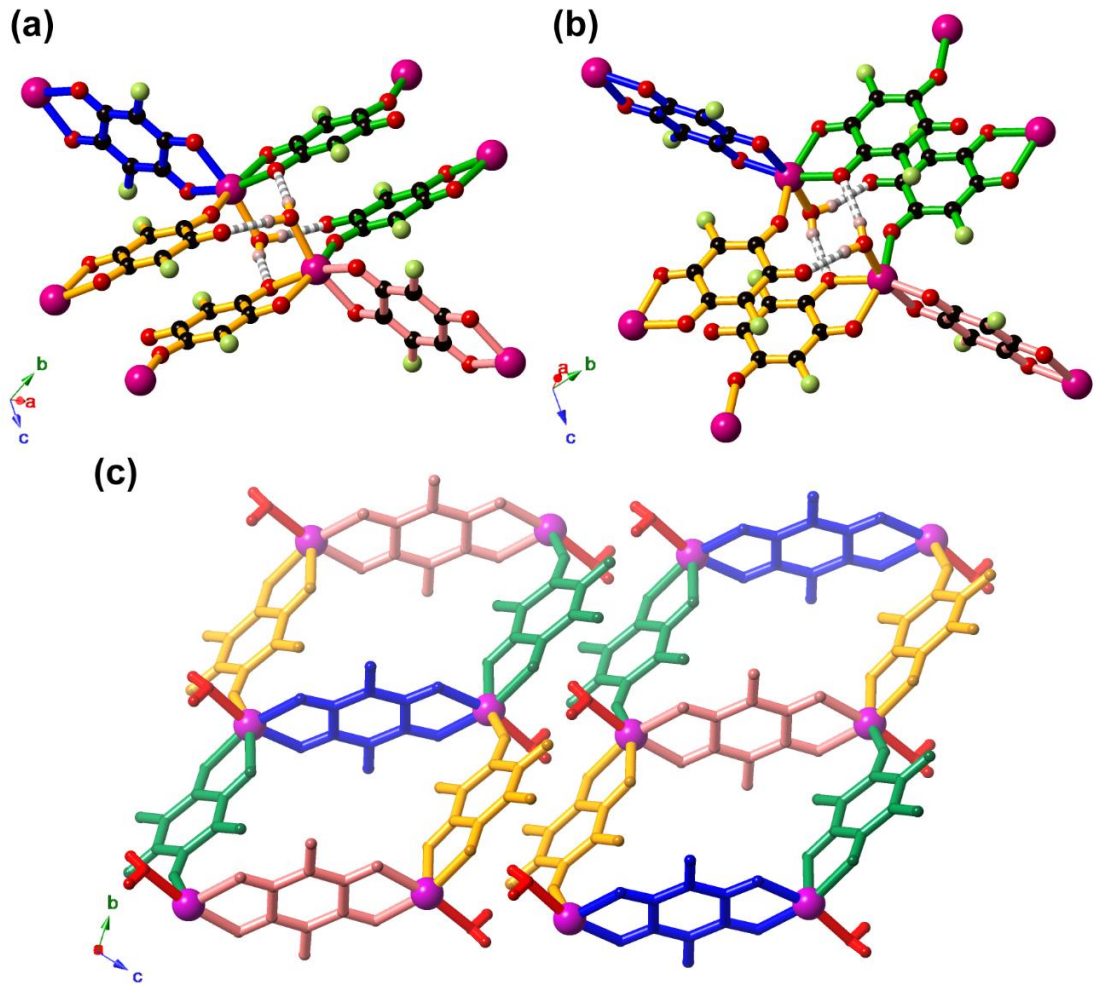


Figure 2.16 H-bonding interactions of the anionic 1D ladders in **2.3$_{Mn}$**. (a, b) Ball-and-stick representations of the H-bonding (dashed grey) between coordinated H_2O molecules and Fan^{2-} ligands in the 1D $[Mn_2(Fan)_3(H_2O)_2]^{2-}$ ladders. Crystallographically unique ligands **L$_1$** (royal blue), **L$_2$** (emerald green), **L$_3$** (light red), **L$_4$** (yellow). Magenta = Mn, pale green = F, red = O, black = C, pale pink = H. (c) Ladder-to-ladder packing and symmetry relations of **L$_1$** through **L$_4$** ligands in adjacent anionic ladder facilitated by coordinated H_2O molecules (red).

The voids between the H-bonded ladder layers are occupied by charge-balancing MeV^{2+} countercations and disordered MeCN and H_2O solvent molecules. The location of MeV^{2+} in **2.3$_{Mn}$** contrasts with that of 2,2′-bpyH$^+$ in (2,2′-bpyH)$_2$[Mn$_2$(Clan)$_3$(H$_2$O)$_2$]·2H$_2$O. In the latter case, 2,2′-bpyH$^+$ partly intrudes into the void of the Mn$_4$ parallelograms, and rests upon the ladder-edge $Clan^{2-}$ ligand via face-to-face interactions. In **2.3$_{Mn}$** and **2.3$_{Cd}$**, MeV^{2+} cations are situated exclusively in the voids between the H-bonded ladder layers, with the axis of the inter-ring C–C bond oriented roughly parallel to the long axis of the ladders (Figure 2.17). Intrusion of MeV^{2+} into the M$_4$ parallelograms is prevented by the MeCN molecule occupying the M$_4$ parallelogram voids. The faces of each MeV^{2+} cation rest slightly on the surface of the **L$_3$** edge ligand (Figure 2.18a & b), although there is no significant CT interaction, presumably because Fan^{2-} is a relatively poor π-electron donor. The MeV^{2+} cation is pinned in this location on one long edge by an approximate rectangle of F atoms from four rung ligands in ladders above and below (Figure 2.18). On the other edge, two coordinating H_2O molecules from the ladder above, as well as an edge-on F···π interaction from an edge **L$_2$** ligand in the adjacent layer above (Figure 2.18e & f), preventing the MeV^{2+} cation from slipping from its location.

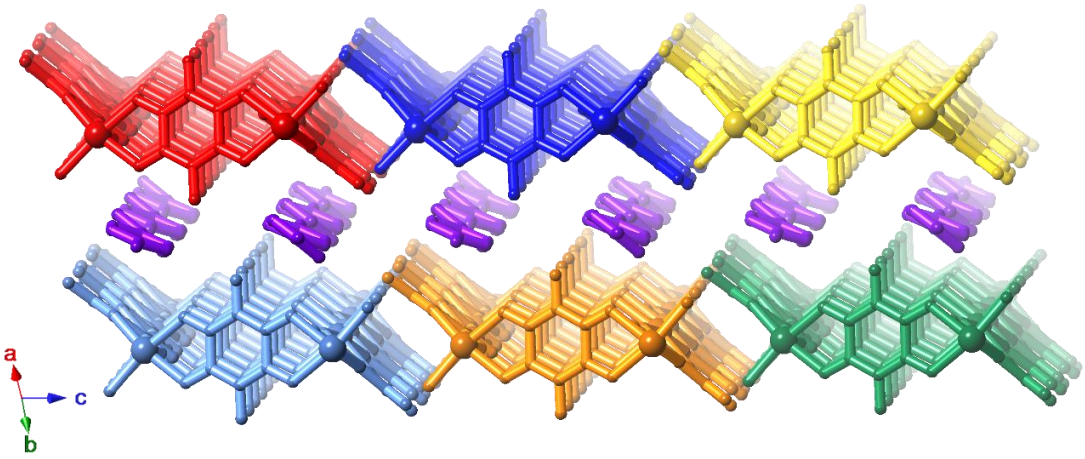


Figure 2.17 View just off the ladder axis showing packing of the MeV^{2+} cations (purple) with the 1D [Mn$_2$(Fan)$_3$(H$_2$O)$_2$]$^{2-}$ ladders in **2.3$_{Mn}$**.

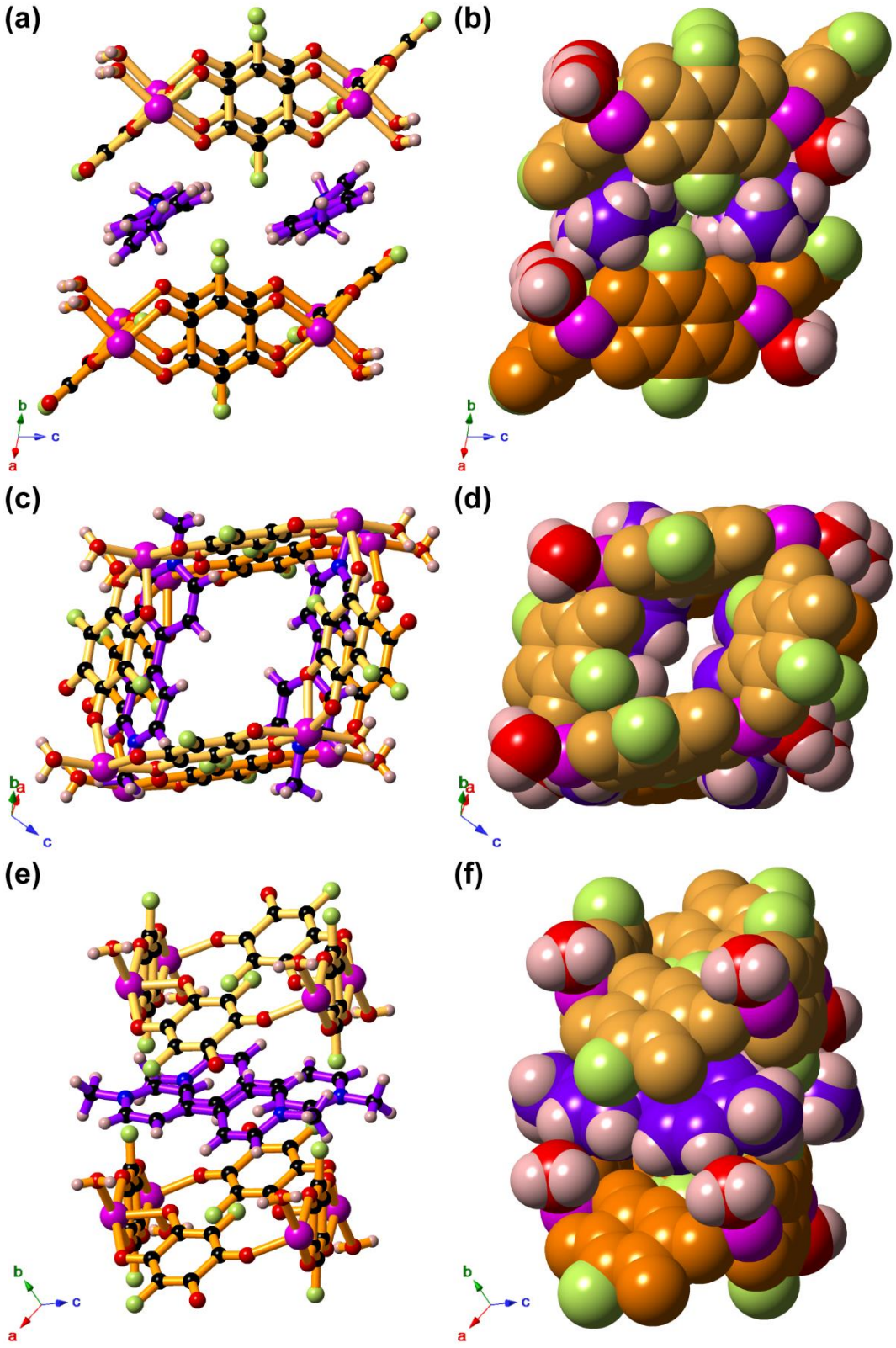


Figure 2.18 Ball-and-stick (a, c, e) and spacefilling (b, d, f) representations of the interactions of the MeV^{2+} cations (purple) with the anionic $[Mn_2(Fan)_3(H_2O)_2]^{2-}$ ladders above (tan) and below (orange) in **2.3$_{Mn}$**. Magenta = Mn, pale green = Cl, red = O, blue = N, black = C, pale pink = H.

P-XRD analysis indicates the 1D ladder **2.3$_{Mn}$** is the only product crystallising from bulk reactions, as there is excellent agreement between the experimental P-XRD pattern and that calculated from the SC-XRD structure of **2.3$_{Mn}$** (Figure 2.19). However, a similar analysis for bulk reactions targeting **2.3$_{Cd}$** revealed a second co-crystallised phase (Figure 2.20). Indeed, microscopic inspection of the bulk sample revealed the product from Cd reactions was an inseparable mixture of yellowish-brown plate crystals of the desired **2.3$_{Cd}$** phase, intermingled with tiny very pale-yellow blocks. The structure of the second phase was determined by SC-XRD at the Australian Synchrotron MX2 beamline. A structure solution found in the monoclinic *C*2/*m* space group, revealing the compound is a 1D coordination polymer [Cd(Fan)(H_2O)$_2$] (**2.4**). Comparison of the extraneous peaks in the experimental P-XRD pattern of **2.3$_{Cd}$** (Figure 2.20, dark orange) and the calculated P-XRD pattern from the SC-XRD structure of **2.4** (Figure 2.20, light orange) reveals good agreement between these peaks, confirming the bulk product contains an inseparable mixture of **2.3$_{Cd}$** and **2.4**.

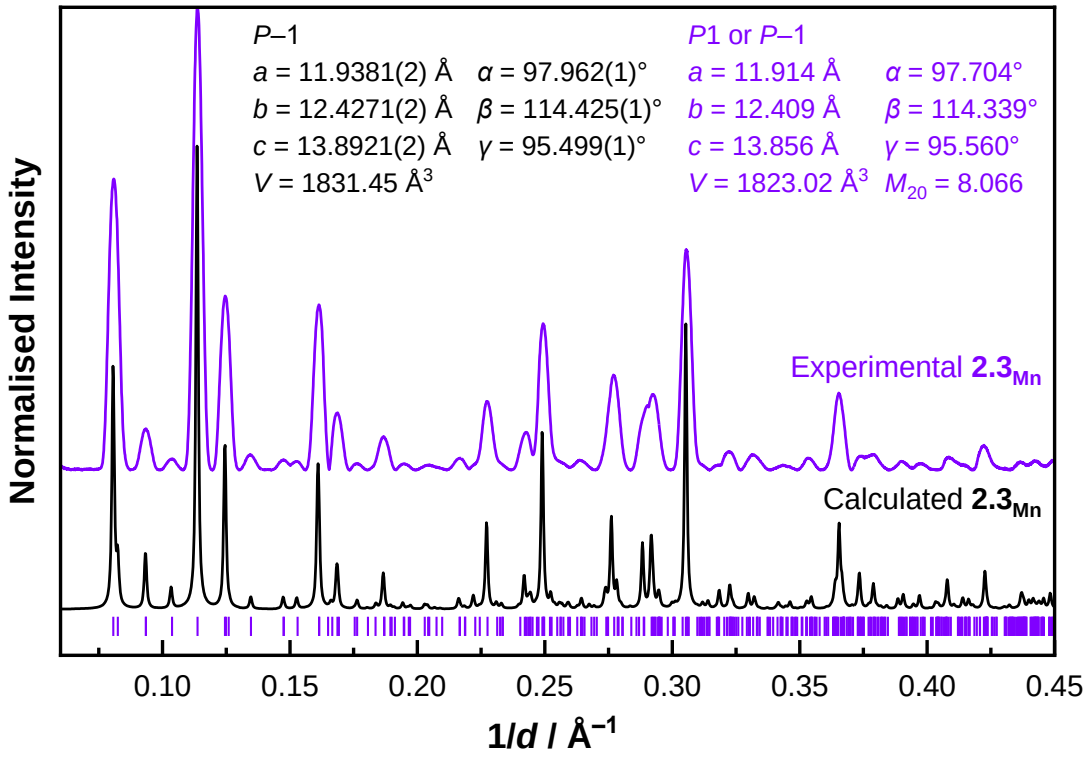


Figure 2.19 P-XRD (λ = 1.54184 Å) pattern of **2.3$_{Mn}$** (purple, T = 100 K) and calculated pattern from SC-XRD of **2.3$_{Mn}$** (black, T = 100 K). Tick marks (purple) indicate the positions of the allowed reflections for the unit cell indexed from the experimental P-XRD pattern.

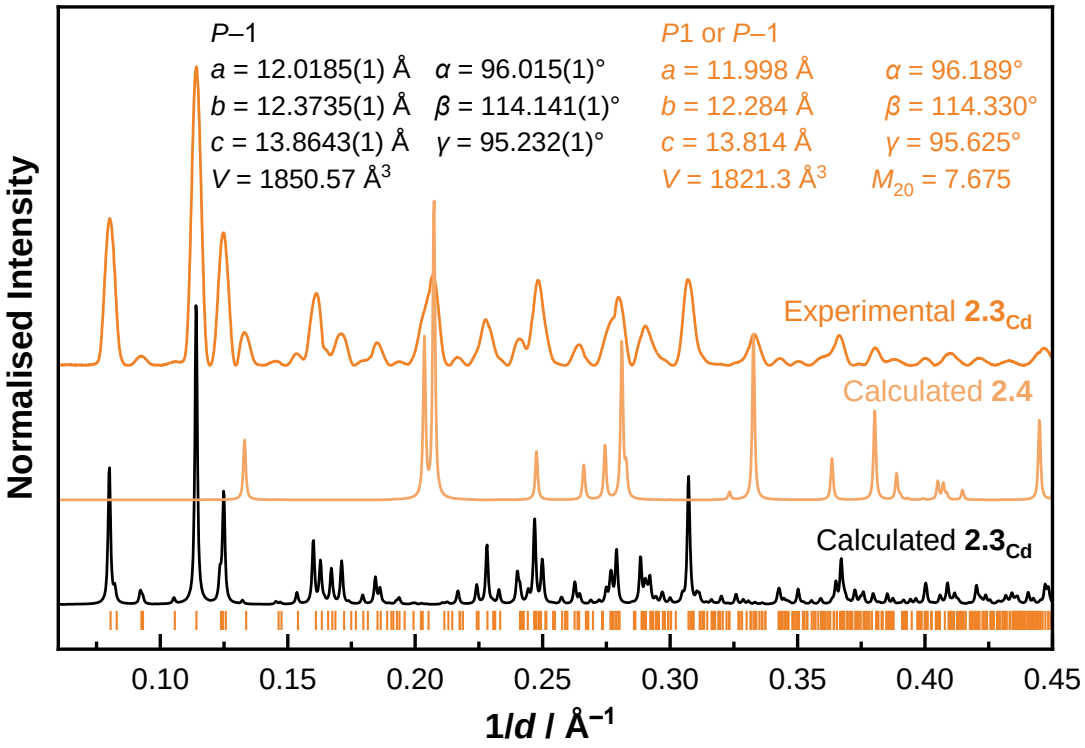
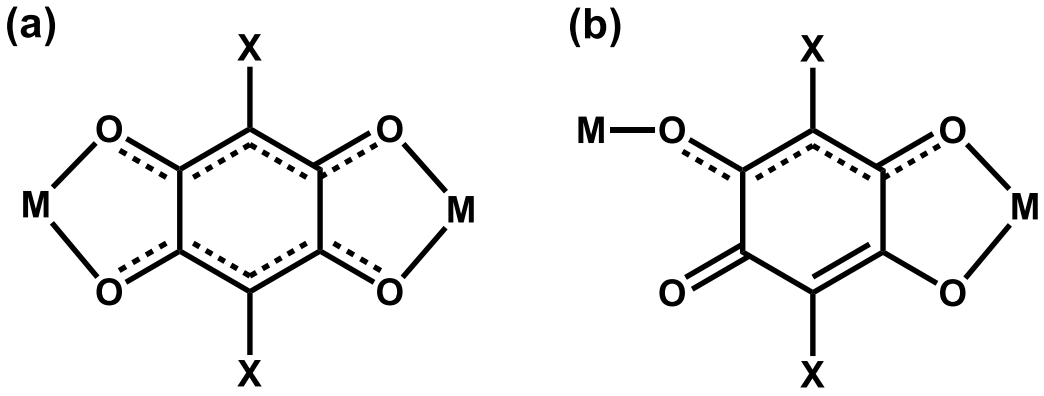


Figure 2.20 P-XRD (λ = 1.54184 Å) pattern of bulk **2.3$_{Cd}$** (dark orange, T = 100 K) and calculated patterns from SC-XRD of **2.3$_{Cd}$** (black, T = 100 K) and **2.4** (light orange, T = 100 K). Tick marks (dark orange) indicate the positions of the allowed reflections for the state unit cell indexed from the experimental P-XRD pattern. NB: Peaks in the experimental P-XRD attributed to the **2.4** phase have been excluded from the pattern indexing.

In **2.4**, four Cd^{II} coordination sites are occupied by the O donor atoms of two bridging bis-bidentate Fan^{2-} ligands, with two coordinating H_2O molecules occupying trans sites. Each 1D strip is surrounded by four strips, with the long axis of the strips and then Fan^{2-} planes both oriented parallel to the crystallographic (−101) plane. Each coordinated H_2O molecule participates in two H-bonding interactions (2.808 Å) with O acceptors from the Fan^{2-} ligands in two adjacent strips each, resulting in a densely packed structure. The structure of **2.4** is therefore essentially isostructural to the 1D strip coordination polymers $[M(dhbq)(H_2O)_2]$ (M = Mg, Mn, Zn),[12, 15] with a slight expansion of the unit cell, owing to the larger van der Waals radius of F versus H preventing closer packing in **2.4**. It is not immediately apparent why **2.4** co-crystallises with **2.3$_{Cd}$**, but an isostructural 1D

[Mn(Fan)(H_2O)$_2$] strip does not co-crystallise with **2.3$_{Mn}$**. Nielson *et. al* recently noted preferential crystallisation of the neutral 1D strips [Ni(dhbq)(H_2O)$_2$] in reactions targeting the anionic 3D (10,3)-*a* (^{n}Bu$_4$N)$_2$[Ni$_2$(dhbq)$_3$] coordination polymer.[64] The authors noted rapid mixing of the Ni(OAc)$_2$ and H_2dhbq formed only the 1D [Ni(dhbq)(H_2O)$_2$] strips, whereas slow addition of Ni(OAc)$_2$ to a refluxing H_2dhbq solution formed the desired (^{n}Bu$_4$N)$_2$[Ni$_2$(dhbq)$_3$] phase. This suggests the 1D strips are the kinetic product, whereas the anionic networks could be the thermodynamic product.

Despite unavoidable co-crystallisation of **2.4** with **2.3$_{Cd}$**, FT-IR spectroscopy (Figure 2.21) reveals the bulk sample is chemically similar to **2.3$_{Mn}$**, indicating the desired **2.3$_{Cd}$** phase is a major component of the mixed product. The FT-IR spectra of the two compounds also reveal interesting details about the electronic structure of the various coordination modes of the Fan^{2-} ligands in the structures. Depending on the coordination mode of the Xan^{2-} ligands, the carbon-oxygen bonds may be part of a delocalised O=C–C=C–O$^-$ ↔ $^-$O–C=C–C=O system (C⋯O, bond order 1.5, in bridging bis-bidendate Xan^{2-} (Scheme 2.2a), or alternatively localised C–O (bond order one) and C=O (bond order two) bonds for the mono- and bi-dentate mode (Scheme 2.2b). As the carbon-oxygen bond order changes between these Xan^{2-} forms, the vibrational stretching frequencies of these bonds provides insight into the electronic structure.[65-67]



Scheme 2.2 (a) Bridging bis-bidentate coordination mode of Xan^{2-}, showing delocalised C⋯O bonds. (b) Bridging mono and bi-dentate coordination mode of Xan^{2-}, showing localised C–O and C=O on one edge of the ligand and delocalised C⋯O bonds on the other edge.

In $(2,2'\text{-bpyH}^{+})_2[Mn_2(Clan)_3(H_2O)_2]\cdot 2H_2O$, which exhibits a similar ladder structure as **2.3$_{Mn}$** and **2.3$_{Cd}$**, the bridging mono- and bi-dentate coordination mode of $Clan^{2-}$ exhibits a combination of two delocalised C⋯O bonds on one edge of the molecule, and localised C–O and C=O bonds on the other edge (Scheme 2.2b).[16] In the FT-IR spectrum of **2.3$_{Mn}$**, the strong absorption at 1520 cm^{-1} and weaker shoulder at ca. 1380 cm^{-1} are ascribed to stretching of delocalised C⋯O bonds. These bonds are present in both the bridging bis-bidentate (**L$_1$** and **L$_3$**), and mono- and bi-dentate (**L$_2$** and **L$_4$**) Fan^{2-} ligands.[16, 67] The presence of a localised, uncoordinated C=O bonds in **L$_2$** and **L$_4$** is suggested by the intense absorption at 1644 cm^{-1}, which is absent in the FT-IR spectra of frameworks containing only bridging bis-bidentate Xan^{2-} ligands, such as **2.2b** (Figure 2.13a). However definitive assignment of this absorption as a localised $\nu_{C=O}$ is complicated as the FT-IR spectra of $MeV(OTs)_2$ or $(MeV)Cl_2$ also exhibit a strong absorption in this region, ascribed to aryl $\nu_{C=C}$ (see Section 2.4.3.1). The localised, coordinating C–O bond of **L$_2$** and **L$_4$** is indicated by the intense $\nu_{C–O}$ = 1348 cm^{-1}.[65-67] This feature is also absent in the spectra of compounds containing only bridging bis-bidentate Xan^{2-} ligands, indicative of the different electronic structure of Fan^{2-} in **2.3$_{Mn}$** and **2.3$_{Cd}$**, compared to typical metal–tetraoxolene coordination polymers.

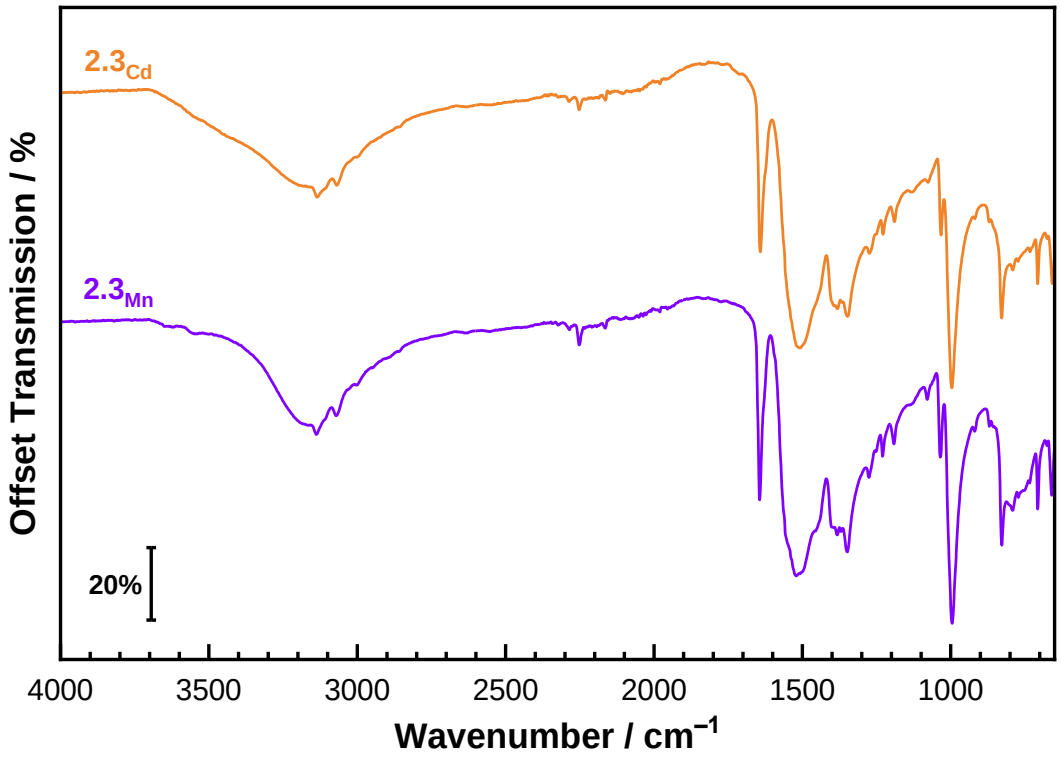


Figure 2.21 ATR FT-IR spectra of **2.3$_{Mn}$** (purple) and **2.3$_{Cd}$** (orange) collected at room temperature in air.

The FT-IR spectra of **2.3$_{Mn}$** and **2.3$_{Cd}$** also provide insight into the solvation of the compounds. The strong broad absorptions around 3200 cm^{-1} are due to the $\nu_{O–H}$ of H_2O molecules, either solvated in the network voids, or coordinated to the Mn^{II} or Cd^{II} centres. The presence of solvated MeCN in the crystal structure of **2.3$_{Mn}$** and **2.3$_{Cd}$** is indicated by the weak absorptions at ca. 2200 cm^{-1} due to the $\nu_{C\equiv N}$ of MeCN. Finally, TGA and scanning differential thermal analysis (SDTA) were used to confirm the degree of solvation in **2.3$_{Mn}$** (Figure 2.22). Co-crystallisation of an inseparable mixture of **2.3$_{Cd}$** and **2.4** precluded TGA of the Cd^{II} congener. Between 25–150 °C, **2.3$_{Mn}$** exhibits a weight loss of 12.0%, corresponding to two coordinated H_2O molecules, in addition to 1.6 MeCN and 0.5 H_2O of solvation per formula unit. The endothermic dip in the SDTA trace at ca. 90 °C confirms this weight loss is due to solvent loss not exothermic network decomposition. The solvation calculated by TGA is slightly lower than estimated by SC-XRD and is likely due to loss of volatile MeCN upon isolation of **2.3$_{Mn}$**. However the solvent content calculated by TGA

gratifyingly matches well with that calculated from elemental analysis (1.4 MeCN and 0.4 H_2O, see Section 2.4.4.4).

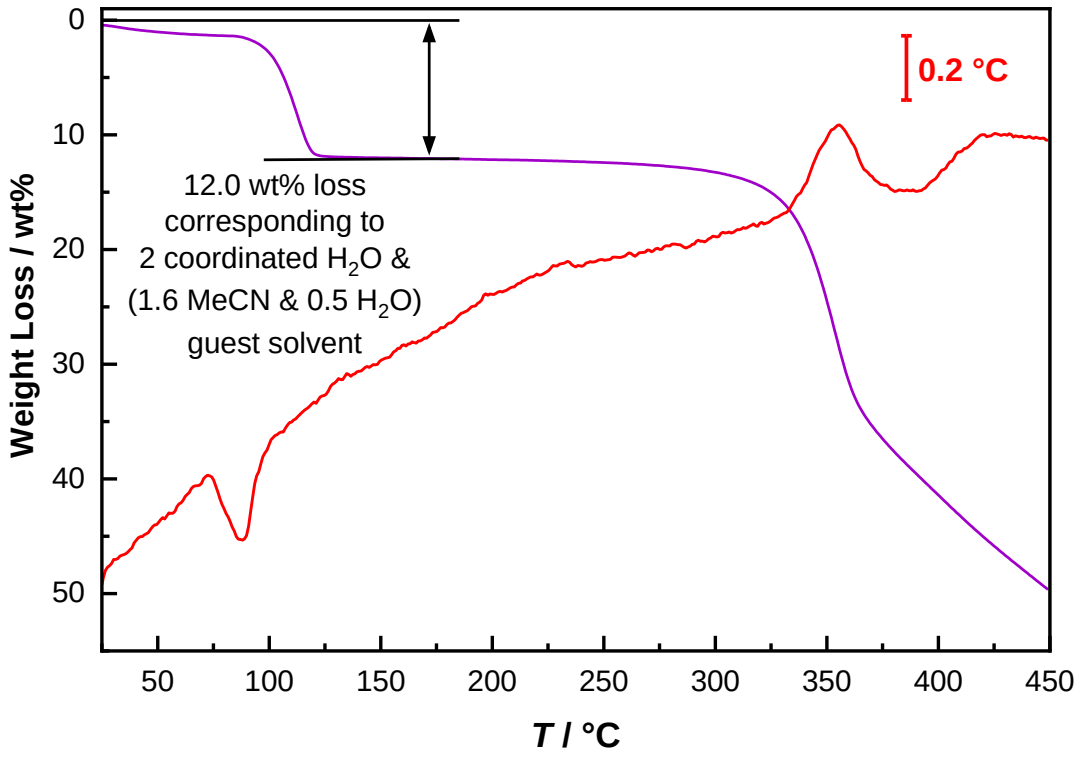


Figure 2.22 Thermogravimetric (purple) and scanning differential thermal (red) analyses of **2.3$_{Mn}$** at a scan rate of 5 °C min^{-1} in a flow of N_2.

2.2.2 Mixed-Valence Iron Networks

2.2.2.1 (PDiQ)[Fe$_2$(Clan)$_3$]·4(acetone)

The coordination polymer (PDiQ)[$Fe_2(Clan)_3$]·*y*(acetone)·*z*H_2O (**2.5**) was synthesised by layering an aqueous solution of $(NH_4)_2Fe^{II}(SO_4)_2·6H_2O$ and dipyrido[1,2-*a*:2′,1′-*c*]pyrazinediium ($PDiQ^{2+}$, as the dibromide salt) below an acetone solution of H_4Clan with a 1:1 v/v acetone–H_2O buffer layer. Following diffusion of the solutions over five days, irregular black plates with a metallic blue-green lustre were visible on the vial walls. The structure of **2.5** was determined using SC-XRD, with a satisfactory refinement achieved in the monoclinic $P2_1/n$ space group, demonstrating **2.5** is a 3D coordination polymer with a $[Fe_2(Clan)_3]^{x-}$ network structure (Table 2.8). For bulk synthesis of **2.5**, $Fe^{II}Cl_2·4H_2O$ and LiOAc were used in place of $(NH_4)_2Fe^{II}(SO_4)_2·6H_2O$ to afford a phase-pure product, albeit producing

smaller crystals precluding SC-XRD with samples synthesised under these conditions. P-XRD analysis on **2.5** was conducted as a slurry in acetone to maintain the solvation state of the compound. Reasonable agreement between the experimental P-XRD pattern of bulk **2.5** (Figure 2.23, navy) and that calculated from SC-XRD of **2.5** (Figure 2.23, black) is observed indicating the SC-XRD structure adequately represents the bulk sample; indexing of the experimental pattern however was not possible.

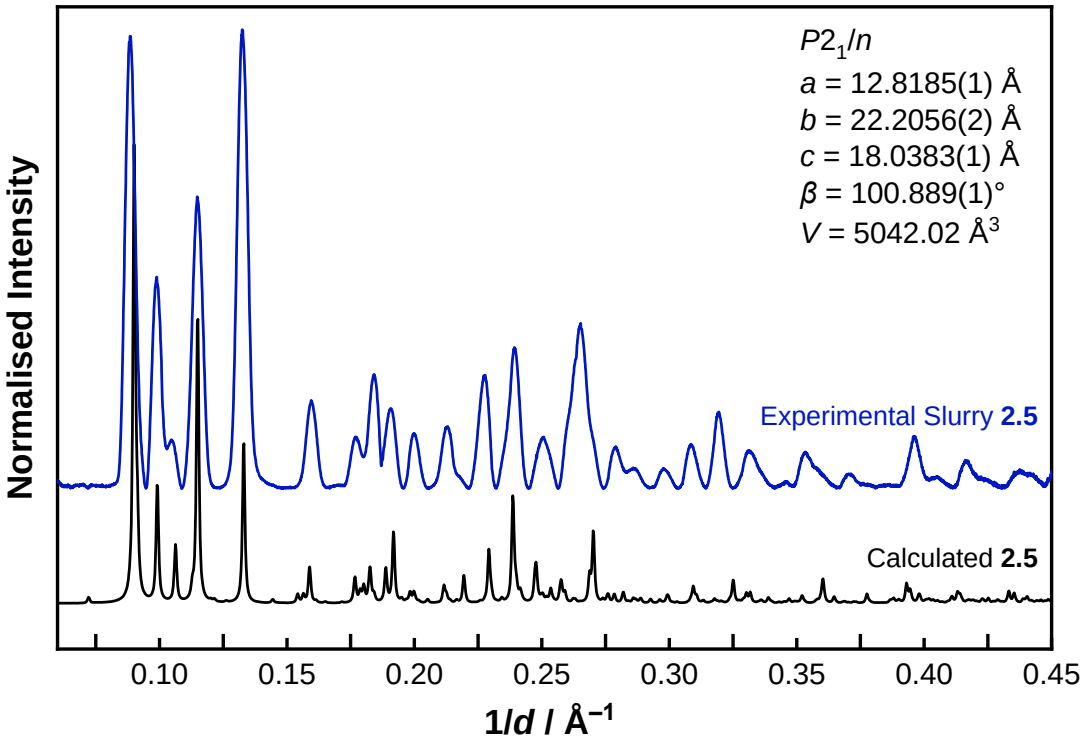


Figure 2.23 P-XRD (λ = 1.54184 Å) pattern of acetone slurry of bulk **2.5** (navy, T = 225 K) and calculated patterns from SC-XRD of **2.5** (black, T = 220 K).

The anionic $[Fe_2(Clan)_3]^{x-}$ network in **2.5** has the (10,3)-*b* or $ThSi_2$ (**ths**) topology, formed by linking every Fe centre (either Δ or Λ configuration) to one Fe centre with the same configuration (either Δ or Λ), and two Fe centres with opposite configuration (either Λ or Δ). In the highest symmetry tetragonal form, the (10,3)-*b* network comprises layers of orthogonal zig-zag chains linked to zig-zag chains in the layers above and below (Figure 2.24a).[68] The (10,3)-*b* topology of **2.5** is significantly distorted compared to the tetragonal (10,3)-*b* form (Figure 2.24b),

notably the hexagonal voids of **2.5** are sheared significantly, and the angles between zig-zag chains reduced from 90° in the tetragonal form to 44° in **2.5**. An alternate description of the (10,3)-*b* network provides further insight into the structure of **2.5**. In this model, the anionic (10,3)-*b* network of **2.5** is constructed from pseudo-1D {Fe–Clan^{n-}}$_\infty$ crankshaft chains (Figure 2.24b, blue) linked to other crankshaft chains by bridging Clan^{n-} ligands (Figure 2.24b, tan). Layers of these crankshaft chains are oriented parallel to the (010) plane with bridging Clan^{n-} ligands forming the pillars between these crankshaft layers (Figure 2.25a). Every crankshaft chain links to two crankshaft chains in the layer above, and two chains in the layer below (Figure 2.25b & c). To the best of the candidate's knowledge, a mixed-valence Fe–tetraoxolene coordination polymer with the (10,3)-*b* topology has not been reported in literature, giving considerable scope for future physical property investigations of this material.

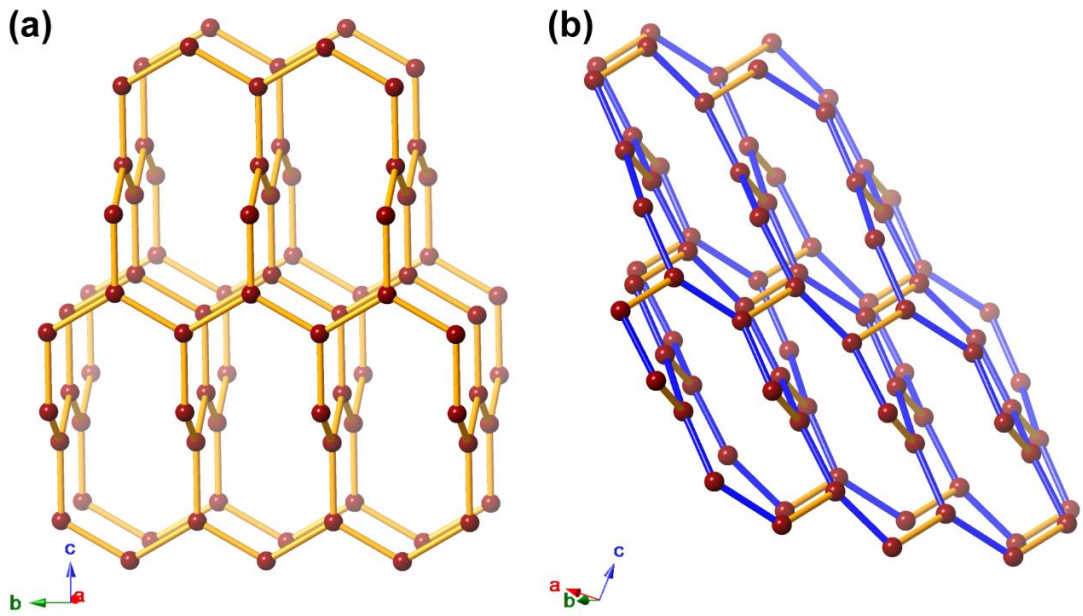


Figure 2.24 (a) The high symmetry tetragonal (10,3)-*b* topology showing layers of orthogonal zig-zag chains. (b) The distorted (10,3)-*b* topology of **2.5**. The network is constructed from pseudo-1D {Fe–Clan^{n-}}$_\infty$ crankshaft chains (blue bonds) linked to other crankshaft chains by bridging Clan^{n-} ligands (tan bonds).

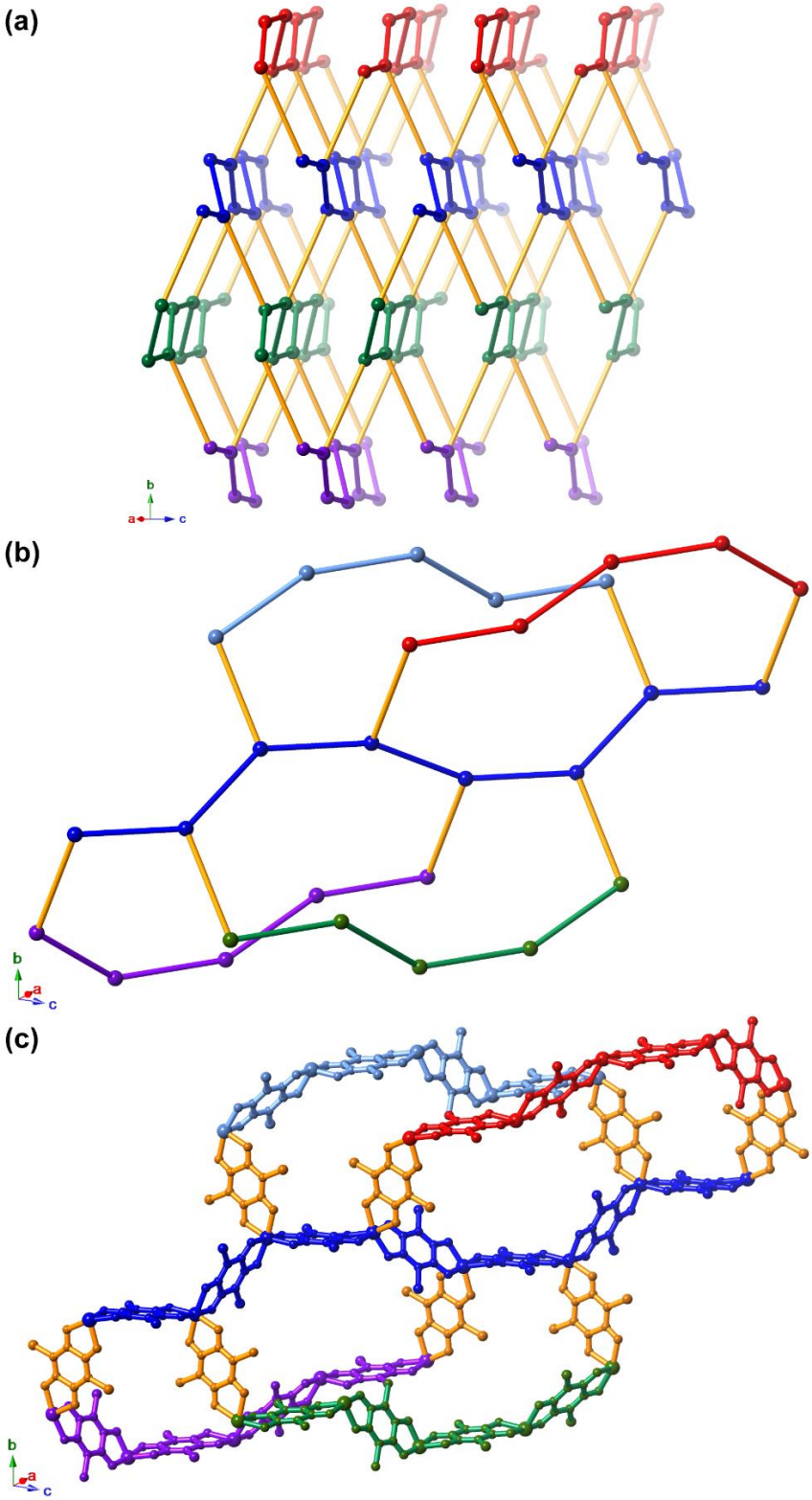


Figure 2.25 The 1D {Fe–Clan^{n-}}$_\infty$ crankshaft chains in **2.5**. (a) View along (010) plane showing layers of {Fe–Clan^{n-}}$_\infty$ crankshaft chains (red, blue, green and purple) linked to adjacent layers of crankshaft chains by pillaring Clan^{n-} ligands (tan bonds). (b, c) Bridging of a {Fe–Clan^{n-}}$_\infty$ crankshaft chain (blue) to four other crankshaft chains (pale blue, red, purple and green).

Charge-balancing $PDiQ^{m+}$ cations lie with one aromatic face snugly resting against a $Clan^{n-}$ ligand from the crankshaft chains (Figure 2.26); the other $PDiQ^{m+}$ face is exposed to a framework void. When viewed along the crystallographic *c* axis, these form approximately rectangular channels (Figure 2.27a & b). This arrangement likely arises from a combination of strong CT interactions between the π-electron deficient $PDiQ^{m+}$ cation and the anionic network, and Coulombic interactions between the dication and anionic network. These strong CT interactions are evinced by close C···C contacts ($d_{C\cdots C}$ = 3.244(4) and 3.265(4) Å). The cations are also wedged in place on their short edge by C–H···O interactions ($d_{H\cdots O}$ = 2.252–2.428 Å) between $Clan^{n-}$ ligands oriented co-planar to the $PDiQ^{m+}$ cations in adjacent crankshaft chains (Figure 2.26e & f).

As a result of the cation-network interaction, the channel floors are tiled with alternating $Clan^{n-}$ and $PDiQ^{m+}$ motifs (Figure 2.27). Inclined $Clan^{n-}$ ligands in the 1D crankshaft chains form an approximately triangular channel roof, with the direction of inclination alternating along the *c* axis. The floor tiling moieties ($Clan^{n-}$ and $PDiQ^{m+}$) also engage in close CT interactions with their complementary tiling moieties ($PDiQ^{m+}$ and $Clan^{n-}$) in the channel below. Finally, the channel walls are the pillar $Clan^{n-}$ ligands which link between the layers of crankshaft chains form the rectangular channel walls. Viewed down the crystallographic *c* axis, these ligands are alternately line the left and right side of each channel, producing windows in the channel walls. Each channel is therefore interconnected with adjacent channels left and right, forming a large interconnected gallery space in layers parallel to the (010) plane; smaller gaps in the channel roofs also connect each mirrored channel above, giving an overall 3D interconnected potential void space in the structure. As for **2.2a**, $\mathbf{2.3_{Mn}}$ and $\mathbf{2.3_{Cd}}$, the organic solvent used, appears to play an important role in templating the structure. This is suggested by occupation of the potential void spaces in **2.5** with three highly ordered and one slightly disordered acetone molecules per formula unit i.e. $(PDiQ)[Fe_2(Clan)_3]\cdot 4(acetone)$. Moreover, attempts to crystallise **2.5** using a MeCN–H_2O solvent system instead of acetone–H_2O led only to poorly crystalline products which could not be characterised.

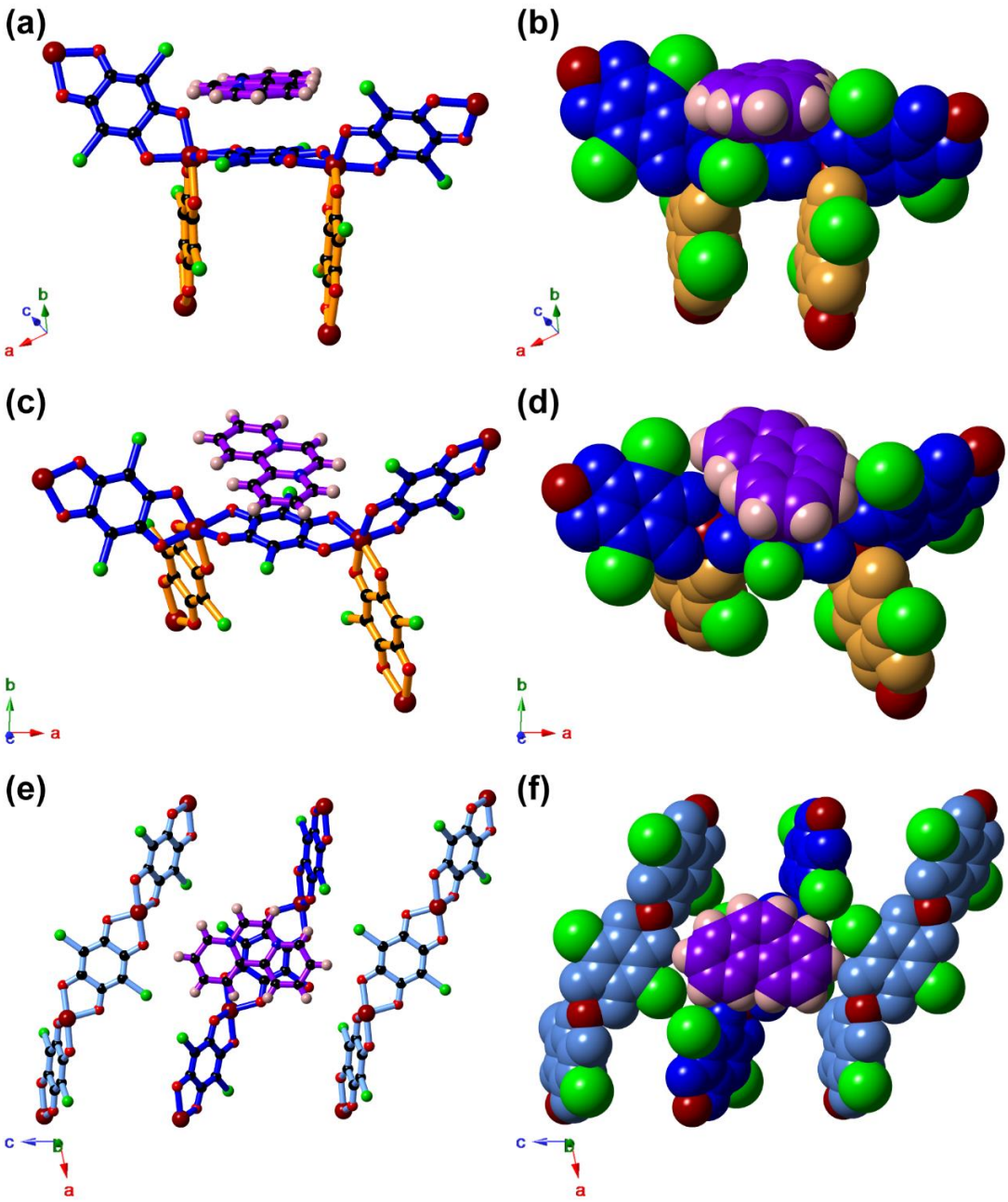


Figure 2.26 Ball-and-stick (a, c, e) and spacefilling (b, d, f) representations of the interactions between $PDiQ^{m+}$ cations (purple) and $\{Fe–Clan^{n-}\}_{\infty}$ crankshaft chains (royal blue) and pillar $Clan^{n-}$ ligands (tan) in **2.5**. (e, f) $PDiQ^{m+}$ molecules wedged between $\{Fe–Clan^{n-}\}_{\infty}$ crankshaft chain (royal blue) with adjacent $\{Fe–Clan^{n-}\}_{\infty}$ crankshaft chains (pale blue). No pillar $Clan^{n-}$ ligands and only one $PDiQ^{m+}$ molecule is shown for clarity. Maroon = Fe, green = Cl, red = O, blue = N, black = C, and pale pink = H.

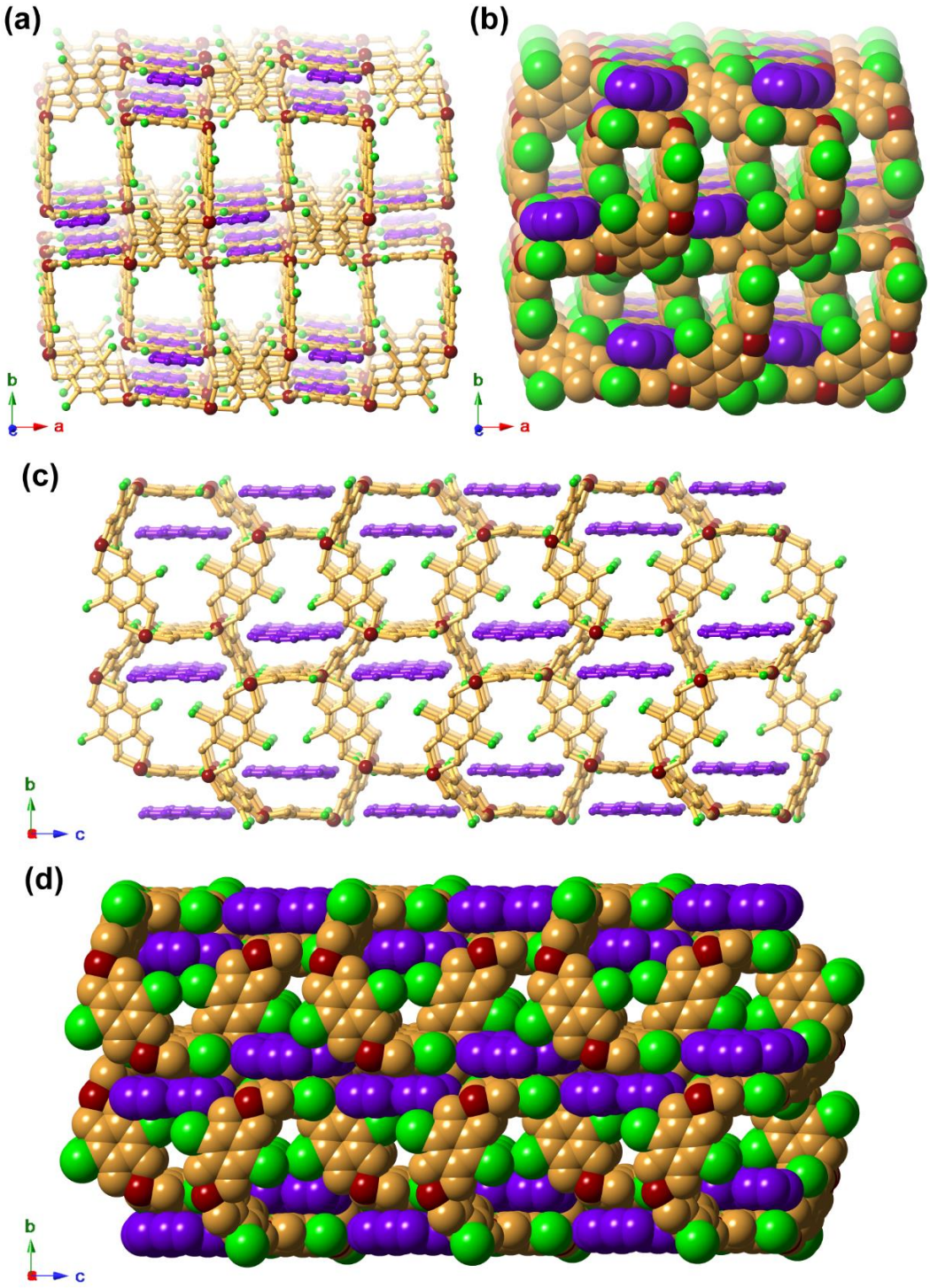


Figure 2.27 Ball-and-stack (a, c) and spacefilling (b, d) representations of the packing of $PDiQ^{m+}$ cations (purple) with the anionic $[Fe_2(Clan)_3]^{x-}$ network (tan) in **2.5**. View down the (a, b) crystallographic *c* axis showing formation of rectangular channels and tiling of channel floors. View down the (c, d) crystallographic *a* axis showing alternating tiling of channel floors with $PDiQ^{m+}$ and $Clan^{n-}$ and formation of channel walls from pillaring $Clan^{n-}$ ligands.

The crystallographic Fe, ligand and $PDiQ^{m+}$ oxidation states in **2.5** were determined by examination of the characteristic bond lengths in the structure. These analyses are indicative of a ligand charge-ordered $(PDiQ^{2+})[Fe^{III}_2(Clan^{2-})(Clan^{3-\bullet})_2]$ formulation for **2.5**. Crystallographic C−C ($d_{C–C}$) and C−N ($d_{C–N}$) bond lengths in viologens are well known to be diagnostic of oxidation state,[58, 60, 61] arising from conversion of the oxidised aromatic dication to a semiquinonoid radical cation upon one electron reduction. Comparison of $d_{C–C}$ and $d_{C–N}$ values for the $PDiQ^{m+}$ cations in $[PDiQ^{2+}](PF_6)_2$ and **2.5** do not reveal significant differences (Figure 2.28), indicating $PDiQ^{m+}$ in **2.5** exists in the $PDiQ^{2+}$ state, and the network charge is therefore $[Fe_2(Clan)_3]^{2-}$.

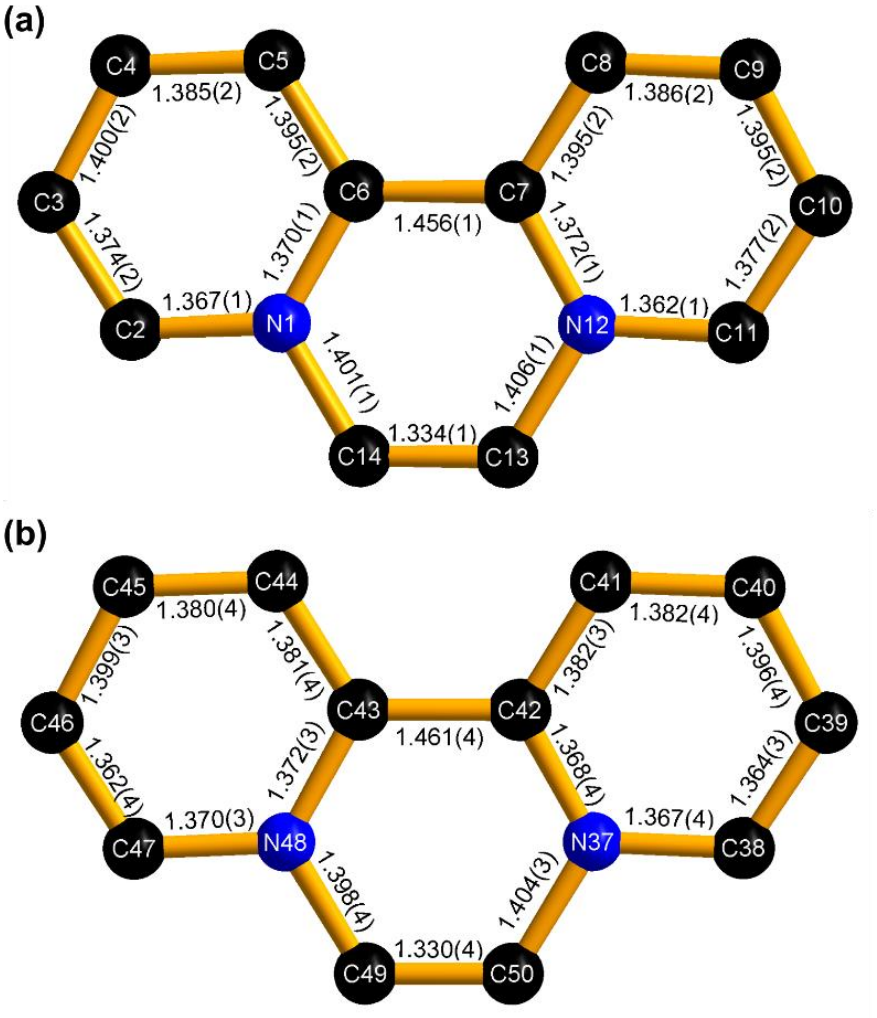


Figure 2.28 Bond lengths of $PDiQ^{m+}$ cations in (a) $[PDiQ^{2+}](PF_6)_2$ and (b) **2.5**. Blue = N, black = C. Hydrogen omitted for clarity.

The asymmetric unit of **2.5** contains two crystallographically unique Fe centres (Fe1 and Fe2) and four unique bridging Clan^{n-} ligands (**L$_1$**, **L$_2$**, **L$_3$** and **L$_4$**); **L$_1$** and **L$_4$** lie upon centres of inversion whereas **L$_2$** and **L$_3$** reside on general positions. Fe1 and Fe2 are in slightly distorted octahedral environments (Table 2.1), coordinated to six O atoms from three bridging bis-bidentate Clan^{n-} ligands. The pseudo-1D {Fe–Clan^{n-}}$_\infty$ crankshaft chains are formed by {Fe1–**L$_1$**–Fe1–**L$_2$**–Fe2–**L$_4$**–Fe2–**L$_2$**}$_\infty$ chains, with **L$_3$** as the linking pillar ligands between each crankshaft chain and four other crankshaft chains in the layers above and below.

Table 2.1 Analysis of the possible coordination geometries quantified using the CShM parameters for the two Fe sites in **2.5**.

Site	Coordination Geometry (Symmetry)				
	HP-6 (***D*$_{6h}$**)	**PPY-6** (***C*$_{5v}$**)	**OC-6** (***O*$_h$**)	**TPR-6** (***D*$_{3h}$**)	**JPPY-6** (***C*$_{5v}$**)
Fe1	30.774	23.386	**1.222**	12.411	27.176
Fe2	32.443	23.681	**1.437**	11.202	27.169

HP-6: Hexagon; PPY-6: Pentagonal pyramid; OC-6: Octahedron; TPR-6: Trigonal prism; JPPY-6: Johnson pentagonal pyramid J2

The Fe–O bond lengths ($d_{Fe–O}$) are given in Table 2.2, with average $d_{Fe–O}$ values of 2.019(16) and 2.012(18) Å for Fe1 and Fe2 respectively. These values are consistent with those expected for high-spin Fe^{III} (Fe$^{III}_{HS}$) and closely match values reported for other mixed valence Fe–tetraoxolene coordination polymers which contain Fe$^{III}_{HS}$ as determined by SC-XRD and ^{57}Fe Mössbauer spectroscopy (Table A.4).[9, 10, 31, 45, 69, 70]

Table 2.2 Fe–O bond lengths in **2.5** at T = 100 K as determined by SC-XRD.

Ligand	$d_{Fe1–O}$ / Å	$d_{Fe2–O}$ / Å
L_1	1.989(2), 1.993(2)	N/A
L_2	2.009(2), 1.978(2)	1.978(2), 2.018(2)
L_3	2.076(2), 2.070(2)	2.103(2), 2.077(2)
L_4	N/A	1.984(2), 1.980(2)
Average	2.019(16)	2.012(18)

The presence of Fe^{III}_{HS} in **2.5** suggests spontaneous electron transfer from Fe^{II} to the bridging ligands, forming $Clan^{3-\bullet}$ and Fe^{III} species in the network. Analysis of literature metal-chloranilate compounds demonstrates the expected values $d_{C–O}$ lie in the range 1.248–1.272 Å for $Clan^{2-}$, and 1.291–1.316 Å for $Clan^{3-\bullet}$ (see Appendix A for full details). There is a similar variation in diagnostic $d_{C–C}$ values (across the five-membered OCCO chelate ring), with 1.506–1.551 Å expected for $Clan^{2-}$ and 1.431–1.473 Å expected for $Clan^{3-\bullet}$. For **L_1**, **L_2** and **L_4**, the average $d_{C–O}$ values are 1.295(3), 1.292(2) and 1.292(4) Å, with diagnostic mean $d_{C–C}$ values of 1.471(4) (C2–C4′), 1.475(3) (C8–C9 & C11–C12) and 1.475(4) (C32–C34′) Å respectively (Figure 2.29), which all closely match those expected for the $Clan^{3-\bullet}$ state. By contrast, **L_3** exhibits mean $d_{C–O}$ and $d_{C–C}$ (C20–C21 & C23–C24) values of 1.257(2) and 1.535(3) Å respectively, which are consistent with the $Clan^{2-}$ state. As a result of the ratio of ligands, the tentative valence formulation of **2.5** is $(PDiQ^{2+})[Fe^{III}_2(\mathbf{L_1}^{3-\bullet})_{0.5}(\mathbf{L_2}^{3-\bullet})(\mathbf{L_3}^{2-})(\mathbf{L_4}^{3-\bullet})_{0.5}]$ i.e. a ligand charge-ordered $(PDiQ^{2+})[Fe^{III}_2(Clan^{2-})(Clan^{3-\bullet})_2]$ formulation. The (10,3)-*b* topology of **2.5** is therefore formed from paramagnetic $\{Fe^{III}–Clan^{3-\bullet}\}_\infty$ crankshaft chains linked to other crankshaft chains by $Clan^{2-}$ (**L_3**) ligands. The elongated Fe–O bonds to **L_3** likely results from reduced Coulombic interaction between Fe^{III} and $Clan^{2-}$ compared to Fe^{III} and $Clan^{3-\bullet}$. A similar elongation of Fe–O bonds between Fe^{III} and $Clan^{2-}$ relative to Fe^{III} and $Clan^{3-\bullet}$ was observed by Miyasaka and co-workers in honeycomb (6,3) networks exhibiting an analogous ligand charge-ordered

(^{n}Pr$_4$N)$_2$[Fe$^{III}_2$(Clan^{2-})(Clan$^{3-\bullet}$)$_2$] formulation.[31, 71] Considering that PDiQ^{2+} in **2.5** engages in a close (3.242 Å) face-to-face interaction with **L$_2$**, localisation of the Clan$^{3-\bullet}$ state at this site likely arises from a combination of: CT between the π-electron deficient cation, and the relatively electron rich **L$_2$** (as Clan$^{3-\bullet}$); in addition to an attractive Coulombic interaction between the 3− and 2+ components. However, the rationale for localisation of Clan^{2-} or Clan$^{3-\bullet}$ at the remaining (**L$_1$**, **L$_3$** and **L$_4$**) sites is less obvious. We hypothesise it arises from different Coulombic interaction strengths between cations and the three ligand sites. The O donor atoms of Clan^{2-} and Clan$^{3-\bullet}$ are both locations of significant electron density,[72, 73] and are therefore likely the most significant positions for Coulombic interaction with cations. The closest O atom of **L$_3$** is 5.850 Å distant from the centroid of PDiQ^{2+}, compared to the closest O atom approaches of 5.132 Å and 4.884 Å for **L$_1$** and **L$_4$** respectively. Consequently, localisation of Clan$^{3-\bullet}$ at **L$_1$** and **L$_4$** may be slightly favoured energetically, due to the higher Madelung stabilisation resulting from the closer 2+/3− interaction, relative to a 2+/2− interaction if Clan^{2-} was localised at either **L$_1$** or **L$_4$** sites.

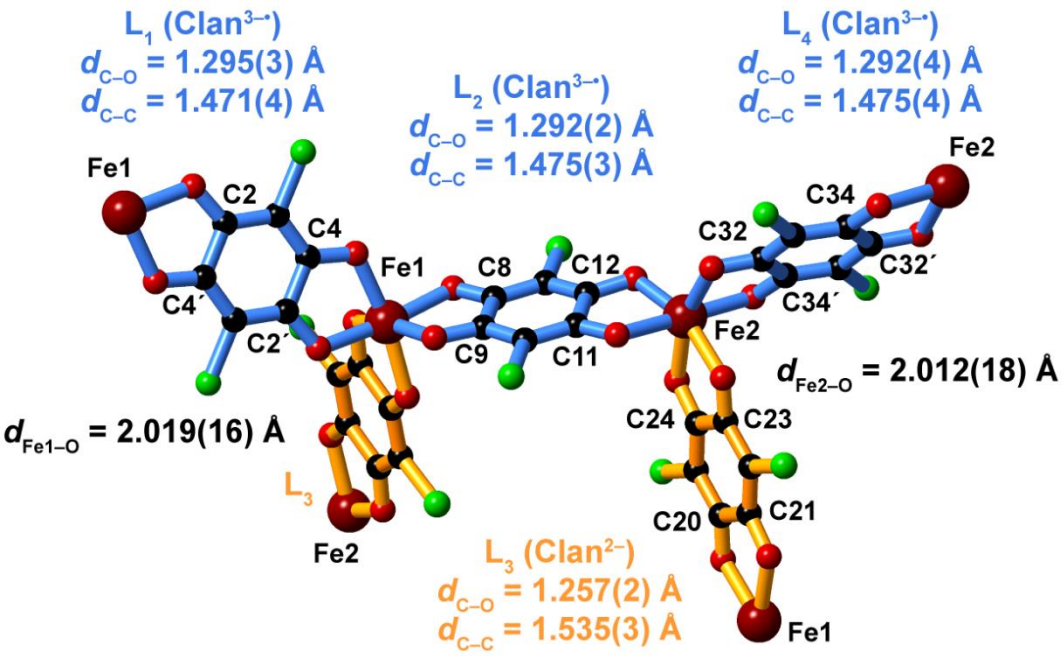


Figure 2.29 Coordination environment and characteristic Clan^{n-} bond lengths around Fe1 and Fe2 in **2.5** at T = 100 K. The stated characteristic $d_{C–O}$ and $d_{C–C}$ values are the mean of the crystallographically unique bond lengths i.e. $d_{C–C}$ for **L$_1$**: C2–C4′; for **L$_2$**: C8–C9 and C11–C12; for **L$_3$**: C20–C21 and C23–C24; for **L$_4$**: C32–C34′.

The charge-ordered structure of **2.5** raises two interesting possibilities. The $\{Fe^{III}–Clan^{3-\bullet}\}_\infty$ chain structure consisting of $S = 5/2$ Fe^{III}_{HS} centre bridged by $S = 1/2$ $Clan^{3-\bullet}$ ligands offers promise that **2.5** could exhibit slow magnetisation relaxation, analogously to $(^nPr_4N)_2[Fe_2(Clan)_3]\cdot 2(acetone)\cdot H_2O$ and $(Me_4N)_2[Fe(Clan)Cl_2]$,[14, 31] due to the pseudo-1D chain structure of **2.5**. Due to time-constraints, this possibility was not examined, though magnetic studies on **2.5** could form the basis of future investigations. Secondly, both $(Me_4N)_2[Fe(Clan)Cl_2]$ and $(^nPr_4N)_2[Fe_2(Clan)_3]$ (which contain charge-ordered zig-zag $\{Fe^{III}–Clan^{3-\bullet}\}_\infty$ chains) exhibit thermally-induced valence tautomerism. These compounds exist with $(Me_4N)_2[Fe^{III}(Clan^{3-\bullet})Cl_2]$ and $(^nPr_4N)_2[Fe^{III}_2(Clan^{2-})(Clan^{3-\bullet})_2]$ valence state distributions at low temperature, and transform to $(Me_4N)_2[Fe^{II}(Clan^{2-})Cl_2]$ and $(^nPr_4N)_2[Fe^{II}Fe^{III}(Clan^{2-})_2(Clan^{3-\bullet})]$ states above 213 K and 236K respectively. Given the pseudo-1D $\{Fe^{III}–Clan^{3-\bullet}\}_\infty$ chain structure (albeit as a crankshaft chain) present in **2.5**, the temperature dependence of ligand charge ordering in **2.5** was investigated by SC-XRD by warming the sample from 100 K to 260 K. The unit cell exhibits the expected thermal expansion upon warming (Figure 2.30).

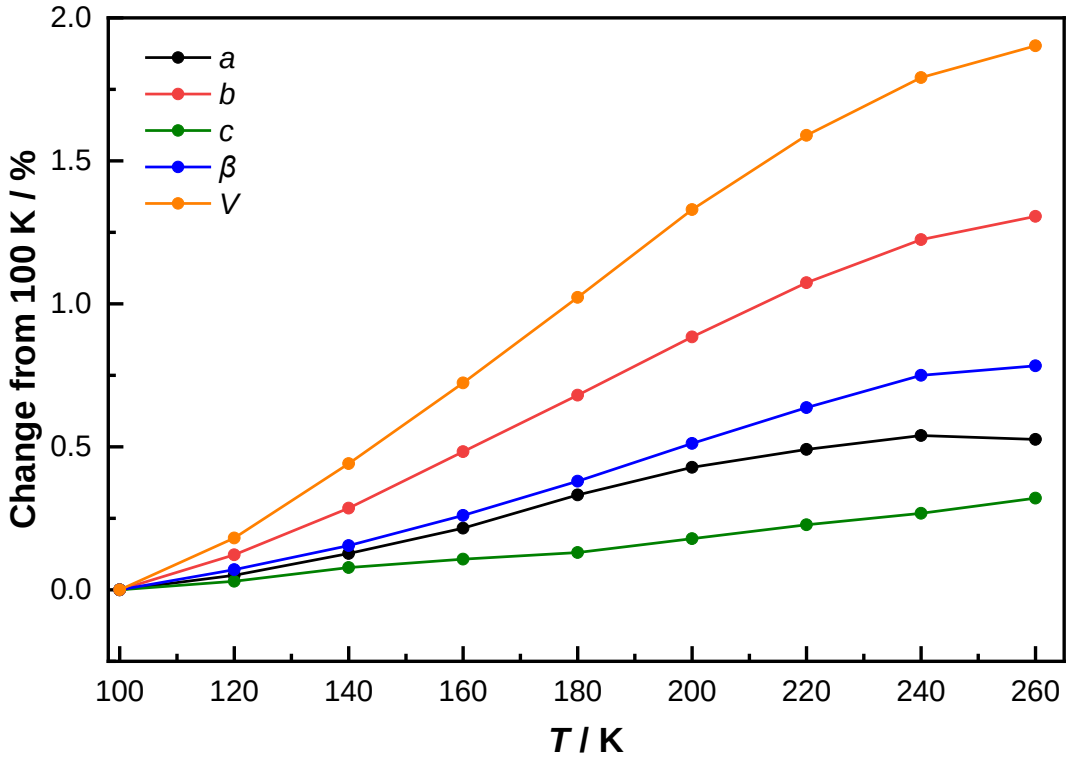


Figure 2.30 Temperature dependence of the unit cell parameters (*a*, *b*, *c*, *β* and *V*) for **2.5** as measured by SC-XRD. All values are normalised to those observed at $T = 100$ K.

Over the temperature range of the experiment (100–260 K), the $d_{C–O}$ values varied between 1.283–1.295 Å for **L_1**, **L_2** and **L_4**, and 1.255–1.260 Å for **L_3** (Figure 2.31a). These lie largely with range expected for the $Clan^{3-\bullet}$ (1.291–1.316 Å) state for **L_1**, **L_2** and **L_4**, and within the range expected for $Clan^{2-}$ (1.248–1.272 Å) for **L_3**. In addition, there is no significant thermal variation of diagnostic ligand $d_{C–C}$ values, varying between 1.470–1.482 Å for **L_1**, **L_2** and **L_4**, and between 1.529–1.537 Å for **L_3** (Figure 2.31b). Again, these values reside close to that expected for $Clan^{3-\bullet}$ (1.408–1.473 Å) and $Clan^{2-}$ (1.505–1.559 Å) respectively. Finally, the $d_{Fe–O}$ values vary between 2.019–2.026 Å for Fe1 and Fe2, indicating the two metal sites remain Fe^{III}_{HS} over the temperature range of the experiment. In combination, these results suggest that **2.5** maintains a charged-ordered $(PDiQ^{2+})[Fe^{III}_2(Clan^{2-})(Clan^{3-\bullet})_2]$ state over the temperature range 100–260 K and therefore does not possess a thermally-induced valence tautomeric transition in this region.

The absence of thermally-induced valence tautomerism in **2.5** contrasts with $(Me_4N)_2[Fe(Clan)Cl_2]$ and $(^nPr_4N)_2[Fe_2(Clan)_3]\cdot 2(acetone)\cdot H_2O$ which undergo valence tautomerism at 213 K and 236K respectively. The contrasting behaviour of **2.5** probably reflects a combination of Coulombic and CT interactions between $PDiQ^{2+}$ and the anionic $[Fe^2(Clan)_3]^{2-}$ network, stabilising the $Clan^{3-\bullet}$ at **L_1**, **L_2** and **L_4** sites. Interestingly for $(^nPr_4N)_2[Fe_2(Clan)_3]\cdot 2(acetone)\cdot H_2O$, the valence transition temperature was significantly increased from 236 K to ca. 317 K, by desolvation of the as-synthesised coordination polymer.[71] Desolvation induced a significant structural transformation, causing the two inequivalent cation-ligand electrostatic interaction distances to collapse to a single distance. The authors proposed that the inequivalent distance in the pristine compound facilitated thermally-induced electron transfer from the weakly interacting $Clan^{3-\bullet}$ ligand to Fe^{III}_{HS}. In contrast, the equivalent cation-ligand distances in the desolvated phase stabilised the charge-ordered $(^nPr_4N)_2[Fe^{III}_2(Clan^{2-})(Clan^{3-\bullet})_2]$ state at high temperature, due to the equivalent Coulombic interaction experienced by the two crystallographically inequivalent $Clan^{3-\bullet}$ ligands. This therefore demonstrates that valence tautomerism in Fe–tetraoxolene coordination polymers is sensitive to Coulombic interactions stabilising a particular charge-state distribution. There is likely a significant electrostatic interaction between $PDiQ^{2+}$ and **L_2** ($Clan^{3-\bullet}$), considering the location of the cation snugly resting on the ligand. Coupled with CT interaction between the π-

electron deficient $PDiQ^{2+}$ cation and the relatively electron-rich $Clan^{3-\bullet}$, electron transfer from **L₂** to Fe^{III}_{HS} (generating $Clan^{2-}$ and Fe^{II}) would seem energetically unfavourable.

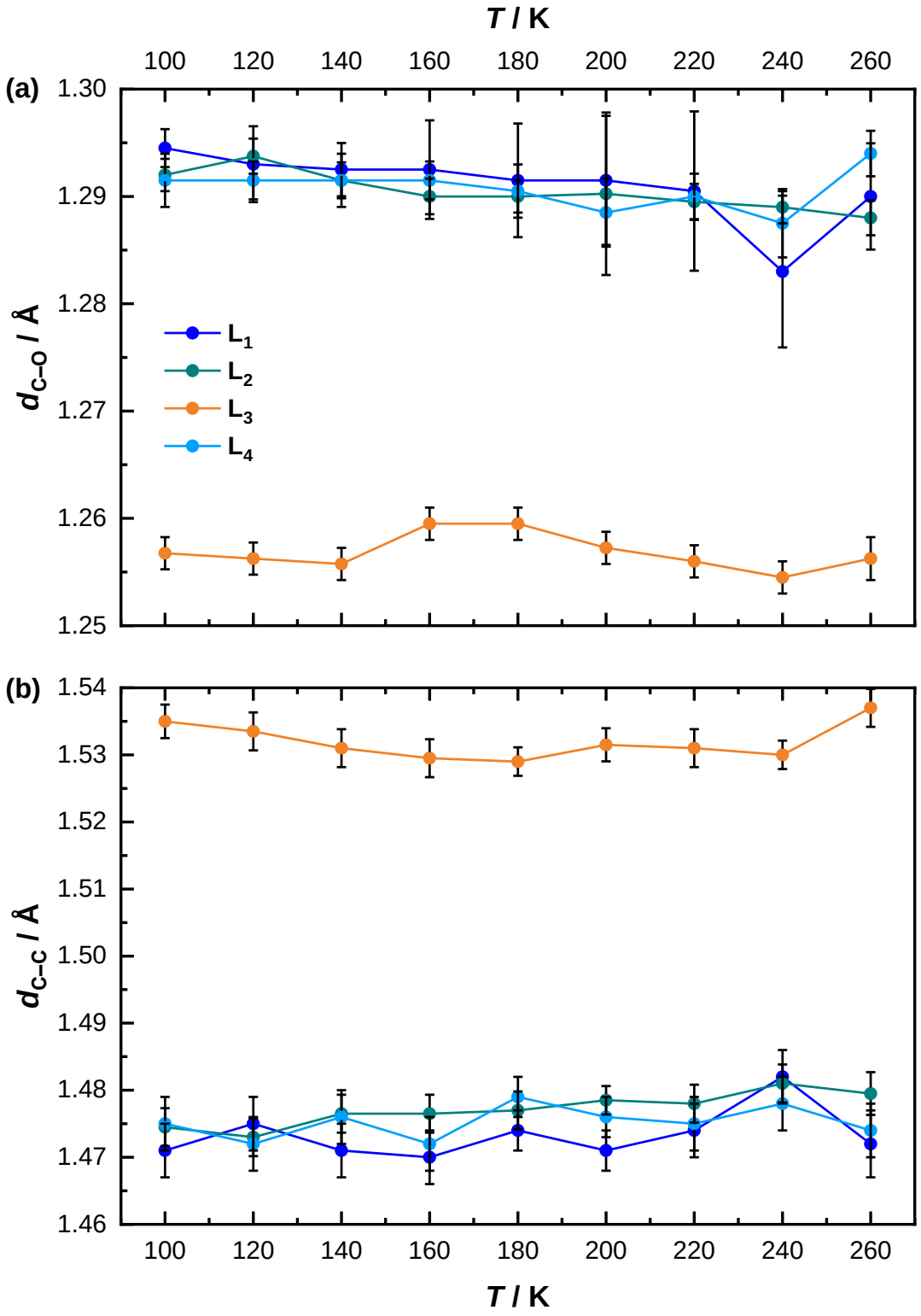


Figure 2.31 Temperature dependence of the characteristic ligand (a) $d_{C–O}$ and (b) $d_{C–C}$ values in **2.5** as measured by SC-XRD. Error bars are ± s.u.

2.2.2.2 (DiQ)[Fe$_2$(Clan)$_3$]·4(acetone)·1.5H$_2$O

An reaction using the dihydro analogue of PDiQ^{2+}, 6,7-dihydrodipyrido[1,2-*a*:2′,1′-*c*]pyrazinediium dibromide ([DiQ]Br$_2$) in place of (PDiQ)Br$_2$ yielded the coordination polymer (DiQ)[Fe$_2$(Clan)$_3$]·*y*(acetone)·*z*H$_2$O (**2.6**). Attempts to produce a bulk phase-pure product have been unsuccessful, precluding physical property analyses. SC-XRD analysis gave a satisfactory structure refinement in the triclinic *P*−1 space group (Table 2.9), revealing that **2.6** is a 3D coordination polymer with a (10,3)-*b* network topology. Although it crystallises in a lower symmetry triclinic space group, **2.6** is structurally to **2.5** because it exhibits the same network topology and cation packing as **2.5**. Slight differences in the structure of **2.6** arise from the non-planar geometry of DiQ^{m+} compared to PDiQ^{2+}. As with **2.5**, the asymmetric unit in **2.6** contains two unique Fe centres (Fe1 and Fe2) situated in slightly distorted octahedral environments, coordinated to six O donors from the bridging bis-bidentate Clan^{n-} ligands. The degree of distortion to the coordination environment was quantified using CShM parameters[52, 53] (Table 2.3). Compared to the Fe2 site in **2.5**, the environment around Fe2 in **2.6** is slightly more distorted from ideal octahedral geometry towards trigonal pyramidal. This is possibly due to the less efficient face-to-face packing of non-planar DiQ^{m+} with Clan^{n-} ligands in the network leading to changes in the ligand arrangement about Fe2. Layers of pseudo-1D {Fe–Clan}$_\infty$ crankshaft chains in **2.6** are oriented parallel to the (010) plane, as in **2.5**, with each crankshaft chain linked to four other crankshaft chains by pillaring Clan^{n-} ligands.

Table 2.3 Analysis of the possible coordination geometries quantified using CShM parameters for the two Fe sites in **2.6**.

Site	Coordination Geometry (Symmetry)				
	HP-6 (***D*$_{6h}$**)	**PPY-6** (***C*$_{5v}$**)	**OC-6** (***O*$_h$**)	**TPR-6** (***D*$_{3h}$**)	**JPPY-6** (***C*$_{5v}$**)
Fe1	31.105	23.677	**1.199**	11.955	27.555
Fe2	32.898	22.626	**1.752**	9.825	26.361

HP-6: Hexagon; PPY-6: Pentagonal pyramid; OC-6: Octahedron; TPR-6: Trigonal prism; JPPY-6: Johnson pentagonal pyramid J2

Charge-balancing DiQ^{m+} cations in **2.6** are in a similar position to $PDiQ^{2+}$ cations in **2.5**, resting against the face of a $Clan^{n-}$ ligand in the crankshaft chain (Figure 2.32a & b). However, due to the notable torsion (18.87°) of the pyridinium rings about the central C–C bond of DiQ^{m+}, and presence of non-coplanar methylene H atoms, the DiQ^{m+} cations in **2.6** do not make as close a face-to-face interaction with the $Clan^{n-}$ ligands, as $PDiQ^{2+}$ does with $Clan^{3-\bullet}$ in **2.5**. Therefore, only one close C···C contact (3.292(2) Å) exists between DiQ^{m+} cations and the facing $Clan^{n-}$ ligand. As in **2.5**, a combination of CT and Coulombic interactions are likely responsible for positioning electron-poor DiQ^{m+} cations against the relatively electron-rich anionic $Clan^{n-}$ ligands in the network for **2.6**. However, this CT interaction is weaker between DiQ^{m+} and $Clan^{n-}$ in **2.6**, as evidenced by fewer C···C close contacts, compared to the CT interaction between $PDiQ^{2+}$ and $Clan^{3-\bullet}$ in **2.5**. DiQ^{m+} may therefore have less impact on the electronic structure of the anionic $[Fe_2(Clan)_3]^{x-}$ network in **2.6**, compared to the influence $PDiQ^{2+}$ may exert over the electronic structure the anionic $[Fe_2(Clan)_3]^{2-}$ network in **2.5**. Torsion between the two pyridinium rings in DiQ^{m+} also facilitates a C–H···O interaction ($d_{H\cdots O}$ = 2.605 Å) between H6 of DiQ^{2+} and an O atom of an adjacent $Clan^{n-}$ ligand (Figure 2.32c & d). This also appears to cause the Fe···Fe···Fe angle along the crankshaft chain at Fe2 to decrease from 155.25(1)° in **2.5** to 149.42(1)° in **2.6**. In addition, the O donor atoms of the facing $Clan^{n-}$ ligands are slightly distorted out of the mean C_6 plane of the ligand, which coupled with the change of Fe···Fe···Fe angles, is the possible reason for the greater trigonal distortion to the Fe2 coordination geometry. As with **2.5**, 1D rectangular channels are visible viewed down the crystallographic *c* axis, with the channel floors tiled by alternating DiQ^{m+} and $Clan^{n-}$ motifs. As expected based upon the structural similarity with **2.5**, the combination of the 2,2′-bipyridinium-derived cation and acetone appear responsible for templating the (10,3)-*b* network. This is suggested by the presence of one well-ordered acetone, and three disordered acetone molecules per formula unit, in addition to one highly disordered partially occupied water. The scattering contribution of the disordered solvents was accounted for using the SQUEEZE[74] routine of PLATON,[75] affording an estimated solvation of $(DiQ)[Fe_2(Clan)_3]\cdot(1+3)(acetone)\cdot 1.5H_2O$ i.e. $(DiQ)[Fe_2(Clan)_3]\cdot 4(acetone)\cdot 1.5H_2O$. Inclusion of additional solvent probably arises as the solvent accessible volume is slightly larger in **2.6** (45.9%) compared to that of **2.5** (42.5%).

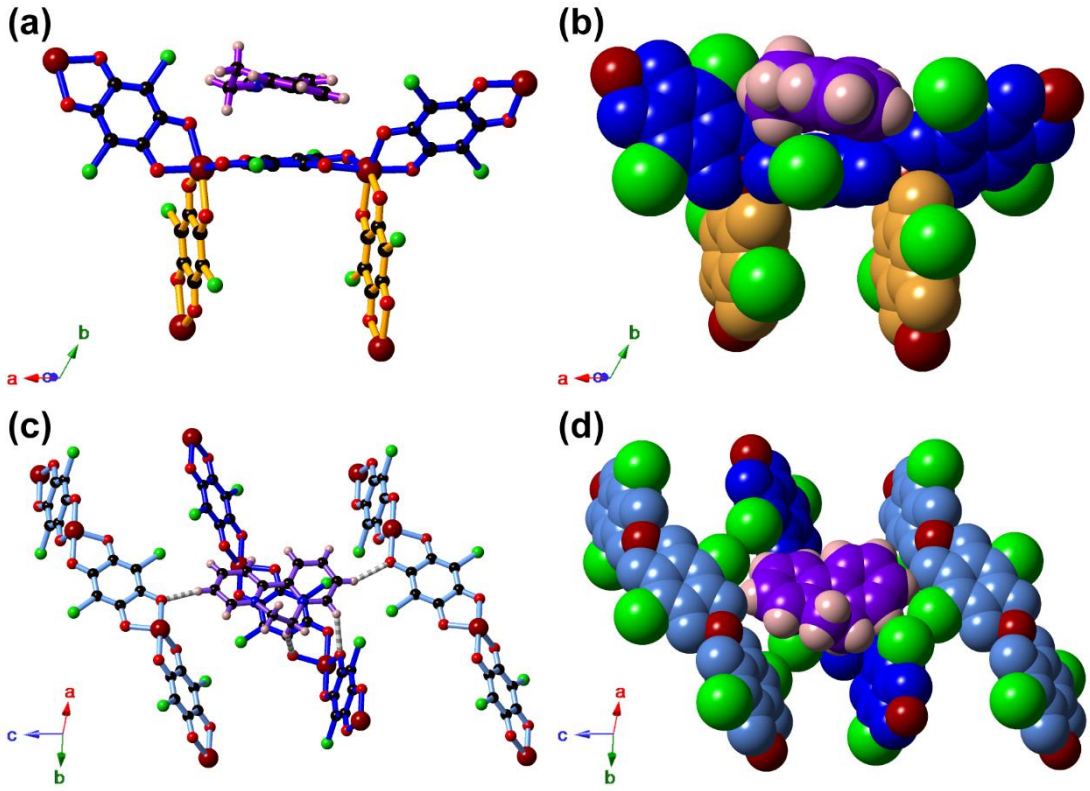


Figure 2.32 Ball-and-stick (a, c) and spacefilling (b, d) representations showing interactions of DiQ^{m+} cations (purple) with the anionic $[Fe_2(Clan)_3]^{x-}$ network in **2.6**. (a & b) DiQ^{m+} cations nestled against $\{Fe–Clan^{n-}\}_\infty$ crankshaft chain (royal blue) and pillar $Clan^{n-}$ ligands (tan). (c & d) C–H···O interactions (dashed bonds) of DiQ^{m+} cations wedged between $\{Fe–Clan^{n-}\}_\infty$ crankshaft chain (royal blue) with adjacent $\{Fe–Clan^{n-}\}_\infty$ crankshaft chains (pale blue). No pillar $Clan^{n-}$ ligands and only one DiQ^{m+} molecule is shown for clarity. Maroon = Fe, green = Cl, red = O, blue = N, black = C, and pale pink = H.

The crystallographic diagnostic bond lengths for Fe–O, $Clan^{n-}$ ligands and DiQ^{m+} cations all support a charge-ordered $(DiQ^{2+})[Fe^{III}_2(Clan^{2-})(Clan^{3-\bullet})_2]$ formulation for **2.6**. As expected, this is analogous to the charge-ordered $(PDiQ^{2+})[Fe^{III}_2(Clan^{2-})(Clan^{3-\bullet})_2]$ formulation of **2.5**. As with other viologen-like cations in this work, the $d_{C–C}$ and $d_{C–N}$ values for DiQ^{m+} cations in **2.6** were compared to the corresponding values for DiQ^{2+} in known dication salts i.e. $DiQ(PF_6)_2$,[76] to evaluate the cation oxidation state. These analyses revealed no significant differences, in particular the central C–C bond. The DiQ^{m+} cations in **2.6** were therefore assigned as in the DiQ^{2+} valence state, with a corresponding network

charge of $[Fe_2(Clan)_3]^{2-}$. Due to the lower triclinic symmetry of **2.6** compared to the monoclinic symmetry of **2.5**, the asymmetric unit contains five crystallographically unique $Clan^{n-}$ ligands, $\mathbf{L_1}$, $\mathbf{L_2}$, $\mathbf{L_3}$, $\mathbf{L_4}$ and $\mathbf{L_5}$ in a 0.5:0.5:1:0.5:0.5 ratio, because $\mathbf{L_1}$, $\mathbf{L_2}$, $\mathbf{L_4}$ and $\mathbf{L_5}$ lie upon centres of inversion, while $\mathbf{L_3}$ resides on a general position. The pseudo-1D {Fe–Clan}$_\infty$ crankshaft chains consists of {Fe1–$\mathbf{L_1}$–Fe1–$\mathbf{L_3}$–Fe2–$\mathbf{L_4}$–Fe2–$\mathbf{L_2}$}$_\infty$ repeat units, with $\mathbf{L_3}$ and $\mathbf{L_5}$ as the pillaring ligands which link each {Fe–Clan}$_\infty$ crankshaft chain to four adjacent crankshaft chains. For the Fe1 and Fe2 sites, the average $d_{Fe–O}$ values are 2.023(16) and 2.024(21) Å respectively (Table 2.4), with corresponding BVS values of 2.96 and 2.96. These BVS and $d_{Fe–O}$ values match closely to Fe^{III}_{HS} in an octahedral environment, also matching closely to Fe^{III}_{HS} observed in other mixed-valence Fe–tetraoxolene coordination polymers (Table A.4).[9, 10, 28, 31, 38, 45, 69, 70] The disparity in $d_{Fe–O}$ values between $\mathbf{L_1}$, $\mathbf{L_3}$, $\mathbf{L_4}$, compared to $\mathbf{L_2}$ and $\mathbf{L_5}$ is ascribed to differences in the ligand valence state (*vide infra*).

Table 2.4 Fe–O bond lengths in **2.6** at T = 100 K as determined by SC-XRD.

Ligand	$\boldsymbol{d_{Fe1–O}}$ **/ Å**	$\boldsymbol{d_{Fe2–O}}$ **/ Å**
$\mathbf{L_1}$	1.999(1), 1.993(1)	N/A
$\mathbf{L_2}$	2.077(1), 2.078(1)	N/A
$\mathbf{L_3}$	1.982(1), 2.007(1)	1.987(1), 2.002(1)
$\mathbf{L_4}$	N/A	1.987(1), 1.981(1)
$\mathbf{L_5}$	N/A	2.114(1), 2.073(1)
Average	2.023(16)	2.024(21)

Due to the dianionic $[Fe_2(Clan)_3]^{2-}$ network charge and Fe^{III}_{HS} formulation, the sum $Clan^{n-}$ ligand charge must be −8, to give an electrically neutral (DiQ)$[Fe_2(Clan)_3]$ framework. This therefore is suggestive of ligand-centred mixed valency formed by 1:2 proportion of $Clan^{2-}$:$Clan^{3-\bullet}$ in the network. By analogy with similar mixed-valence Fe–tetraoxolene frameworks, this likely arises from spontaneous electron transfer between Fe^{II} and $Clan^{2-}$, affording a network

containing Fe^{III}_{HS} and $Clan^{3-\bullet}$. Comparing the average ligand $d_{C–O}$ and diagnostic $d_{C–C}$ values to the corresponding ranges expected for $Clan^{2-}$ and $Clan^{3-\bullet}$ (Appendix A), reveals that **L**$_1$, **L**$_3$ and **L**$_4$ are $Clan^{3-\bullet}$, and **L**$_2$ and **L**$_5$ are $Clan^{2-}$ (Figure 2.33). The shortened Fe–O bonds for **L**$_1$, **L**$_3$, and **L**$_4$, compared to **L**$_2$ and **L**$_5$, is probably due to a stronger Coulombic interaction between Fe^{III}_{HS} and $Clan^{3-\bullet}$ compared to Fe^{III}_{HS} and $Clan^{2-}$, as observed in **2.5**. From the ratio of ligands in the asymmetric unit of **2.6**, the valence distribution is assigned as $(DiQ^{2+})[Fe^{III}_2(\mathbf{L_1}^{3-\bullet})_{0.5}(\mathbf{L_2}^{2-})_{0.5}(\mathbf{L_3}^{3-\bullet})(\mathbf{L_4}^{3-\bullet})_{0.5}(\mathbf{L_5}^{2-})_{0.5}]$, simplifying to a charge-ordered $(DiQ^{2+})[Fe^{III}_2(Clan^{2-})(Clan^{3-\bullet})_2]$ formulation. As with **2.5**, the crankshaft chains in **2.6**, which are the building blocks of the (10,3)-*b* network, are paramagnetic pseudo-1D $\{Fe^{III}_{HS}–Clan^{3-\bullet}\}_\infty$ chains. Each crankshaft $\{Fe^{III}_{HS}–Clan^{3-\bullet}\}_\infty$ chain is then linked to four other $\{Fe^{III}_{HS}–Clan^{3-\bullet}\}_\infty$ crankshaft chains by diamagnetic $Clan^{2-}$ pillar ligands (**L**$_2$ and **L**$_5$) which form the walls of the 1D channels, giving the overall (10,3)-*b* network topology.

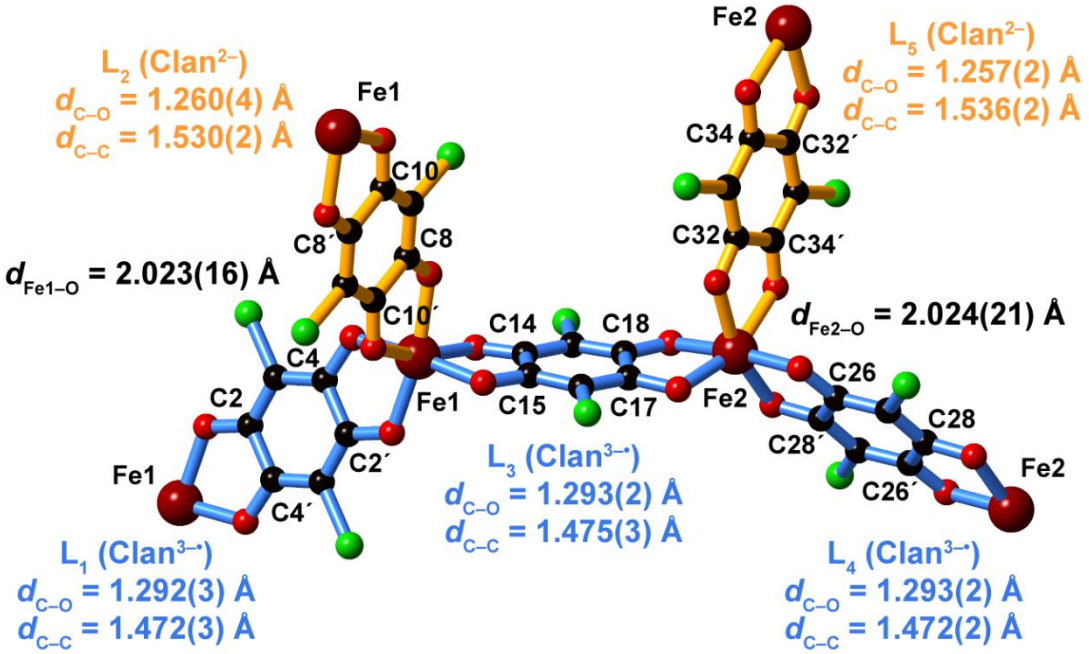


Figure 2.33 Coordination environment and characteristic $Clan^{n-}$ bond lengths around Fe1 and Fe2 in **2.6** at T = 100 K. The stated $d_{C–O}$ and characteristic $d_{C–C}$ values are the mean of the crystallographically unique bond lengths i.e. $d_{C–C}$ for **L**$_1$: C2–C4′; for **L**$_2$: C8–C10′; for **L**$_3$: C14–C15 and C17–C18; for **L**$_4$: C26–C28′; for **L**$_5$: C32–C34′.

*2.2.2.3 (PDiQ)[Fe$_2$(Fan)$_3$]·y*MeCN

Following synthesis and structure solution of **2.5** and **2.6**, attempts were made to synthesise isostructural (10,3)-*b* fluoranilate analogues, to lay the groundwork for future studies comparing the dependence of physical properties such as magnetic ordering temperature and conductivity upon ligand substituents. Slow diffusion reactions were trialled by layering an aqueous solution of $Fe^{II}Cl_2{\cdot}4H_2O$, $(PDiQ)Br_2$ and LiOAc below an acetone solution of H_4Fan with a 1:1 v/v acetone–H_2O buffer layer. Thin, flaky black crystals with an intense bluish metallic lustre were visible on the vial walls after four days. Structure solution was attempted using the MX1 beamline of the Australian Synchrotron, but owing to very weak diffraction, a satisfactory structure solution could not be obtained. While acetone appears to play an important role in templating the structure of **2.5** and **2.6**, we were curious if changing the synthetic solvent system could still afford the desired (10,3)-*b* network topology owing solely to the structure directing effect of $PDiQ^{2+}$. Layering an aqueous solution of $Fe^{II}Cl_2{\cdot}4H_2O$, $(PDiQ)Br_2$ and LiOAc below a MeCN solution of H_4Fan, with a buffer layer of 1:1 v/v MeCN–H_2O yielded black trapezoidal plate crystals with an intense blue metallic lustre. The crystals grew on the vial walls and were harvested after four days. Using SC-XRD analyses at the MX1 beamline of the Australian Synchrotron, a satisfactory structure refinement was found in the orthorhombic *Pnma* space group. The compound has the composition $(PDiQ)[Fe_2(Fan)_3]{\cdot}y$MeCN$\cdot z$$H_2O$ (**2.7**), with the $[Fe_2(Fan)_3]^{x-}$ network exhibiting the 2D honeycomb (6,3) topology. The successful synthesis of a highly crystalline product was somewhat surprising, given that attempts using Fe^{II}, $PDiQ^{2+}$ and $Clan^{n-}$ in an MeCN–H_2O solvent system yielded only amorphous or poorly crystalline material. However, it serves to highlight the delicate interplay between all components in the synthesis, such that slight changes, such as ligand substituent electronegativity can have dramatic effects on the nature of the products generated.

The asymmetric unit of **2.7** contains two crystallographically unique Fan^{n-} ligands, $\mathbf{L_1}$ and $\mathbf{L_2}$ in a 1:2 ratio and a single crystallographically unique Fe centre. The Fe centre resides in a slightly distorted octahedral environment, formed by six O donor atoms from three bridging Fan^{n-} ligands. The anionic honeycomb (6,3) sheets are formed by linking every Fe centre of a given configuration (either Δ or Λ) to three other centres of opposite configuration (either Λ or Δ) (Figure 2.34a). The anionic $[Fe_2(Fan)_3]^{x-}$ sheets stack parallel to the crystallographic *b* axis, with the sheet-to-sheet spacing (7.680 Å) corresponding to half the length of the crystallographic *b* axis (Figure 2.34b).

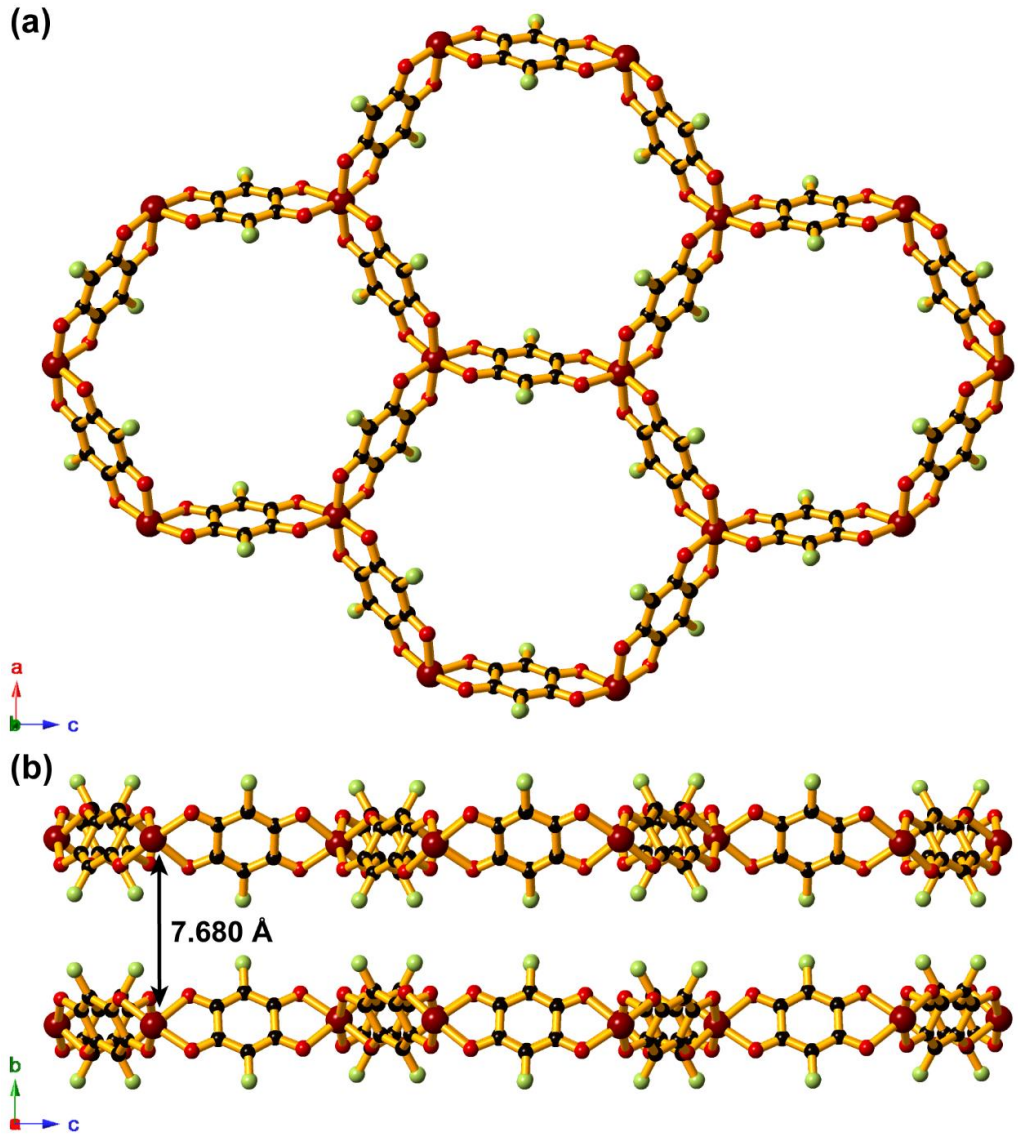


Figure 2.34 The anionic $[Fe_2(Fan)_3]^{x-}$ (6,3) honeycomb sheets in **2.7** viewed (a) down the crystallographic (a) *b* axis and (b) *a* axis. Maroon = Fe, pale green = F, red = O, black = C.

The lower orthorhombic symmetry of **2.7** compared to other honeycomb Fe–tetraoxolene frameworks with trigonal symmetry,[10, 24, 26-28, 45, 69] results because the Fe···Fe···Fe angles within the anionic $[Fe_2(Fan)_3]^{x-}$ sheets of **2.7** are distorted slightly from 120° to 116.97(1)°, 118.20(1)° and 124.80(1)°. The anionic $[Fe_2(Fan)_3]^{x-}$ sheets therefore appear slightly compressed in the crystallographic (010) plane. For each row of hexagonal voids oriented parallel to the crystallographic *a* axis, the two adjacent rows of hexagonal voids appear sheared in the opposite direction (Figure 2.35a). Additionally, when viewed parallel to the (010) plane, a slight corrugation of the anionic sheets is apparent (Figure 2.35b).

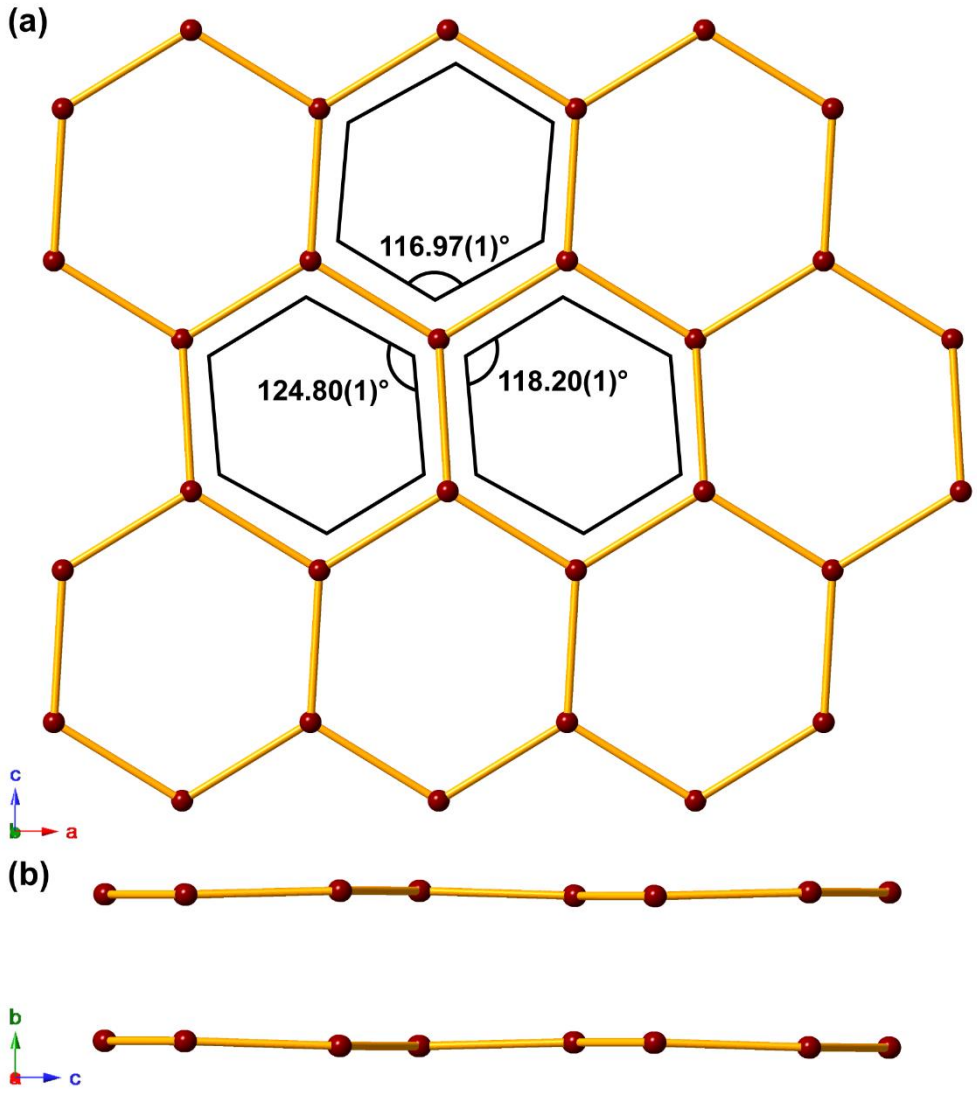


Figure 2.35 Geometric distortions of the anionic $[Fe_2(Fan)_3]^{x-}$ (6,3) honeycomb sheets in **2.7**. (a) The Fe···Fe···Fe angles in the anionic sheets viewed down the crystallographic *b* axis, and (b) corrugation of anionic sheets viewed down the crystallographic *a* axis.

Charge-balancing $PDiQ^{m+}$ cations reside in a surprising position, considering their π-electron poor nature compared to the relatively electron rich nature of the anionic $[Fe_2(Fan)_3]^{x-}$ network. In contrast to **2.5** and **2.6**, in which the $PDiQ^{2+}$ and DiQ^{2+} cations engage in face-to-face interactions with electron-rich $Clan^{3-\bullet}$ ligands in the anionic network, $PDiQ^{m+}$ cations in **2.7** lie entirely within the hexagonal voids, with the plane of the cation oriented parallel to the crystallographic *b* axis and perpendicular to the plane of the anionic $[Fe_2(Fan)_3]^{x-}$ sheets (Figure 2.36). Viewed down the *b* axis, one face to the $PDiQ^{m+}$ cations tile the walls of the hexagonal channels formed by stacking of the anionic $[Fe_2(Fan)_3]^{x-}$ sheets. The other face of the $PDiQ^{m+}$ cations are oriented towards the network, though curiously do not engage in a face-to-face CT interaction with the anionic $[Fe_2(Fan)_3]^{x-}$ network. The location of cations relative to the anionic network appears to be influenced significantly by attractive C−H···O interactions, and to a lesser extent Coulombic interactions and steric constraints. On one long edge of each $PDiQ^{m+}$ cation, 6H, 6H′ and methine H atoms form two pincers which engage in C−H···O interactions ($d_{H\cdots O}$ = 2.230 and 2.567 Å) with O donor atoms of $\mathbf{L_2}$ ligands in the sheets above and below (Figure 2.37a). This interaction also causes the positive N atoms of $PDiQ^{m+}$ to be only 3.750 Å away from these O donor atoms, probably helping to lock $PDiQ^{m+}$ cations in this position by a Coulombic interaction. This C−H···O interaction also causes $\mathbf{L_2}$ ligands to tilt slightly towards the cations, so the mean ligand plane is 59.42° from the mean anionic sheet plane, compared to 62.19° between the mean planes of $\mathbf{L_1}$ ligands and the anionic sheets. On the other long edge of the $PDiQ^{m+}$ cations, yawing of the cations relative to the crystallographic *b* axis on the C−H···O 'hinge' is limited by the 3H and 3H′ atoms of $PDiQ^{m+}$ impinging on a line of two F atoms from $\mathbf{L_1}$ ligands in the sheets above and below in close contact ($d_{F\cdots F}$ = 2.720(3) Å) (Figure 2.37b).

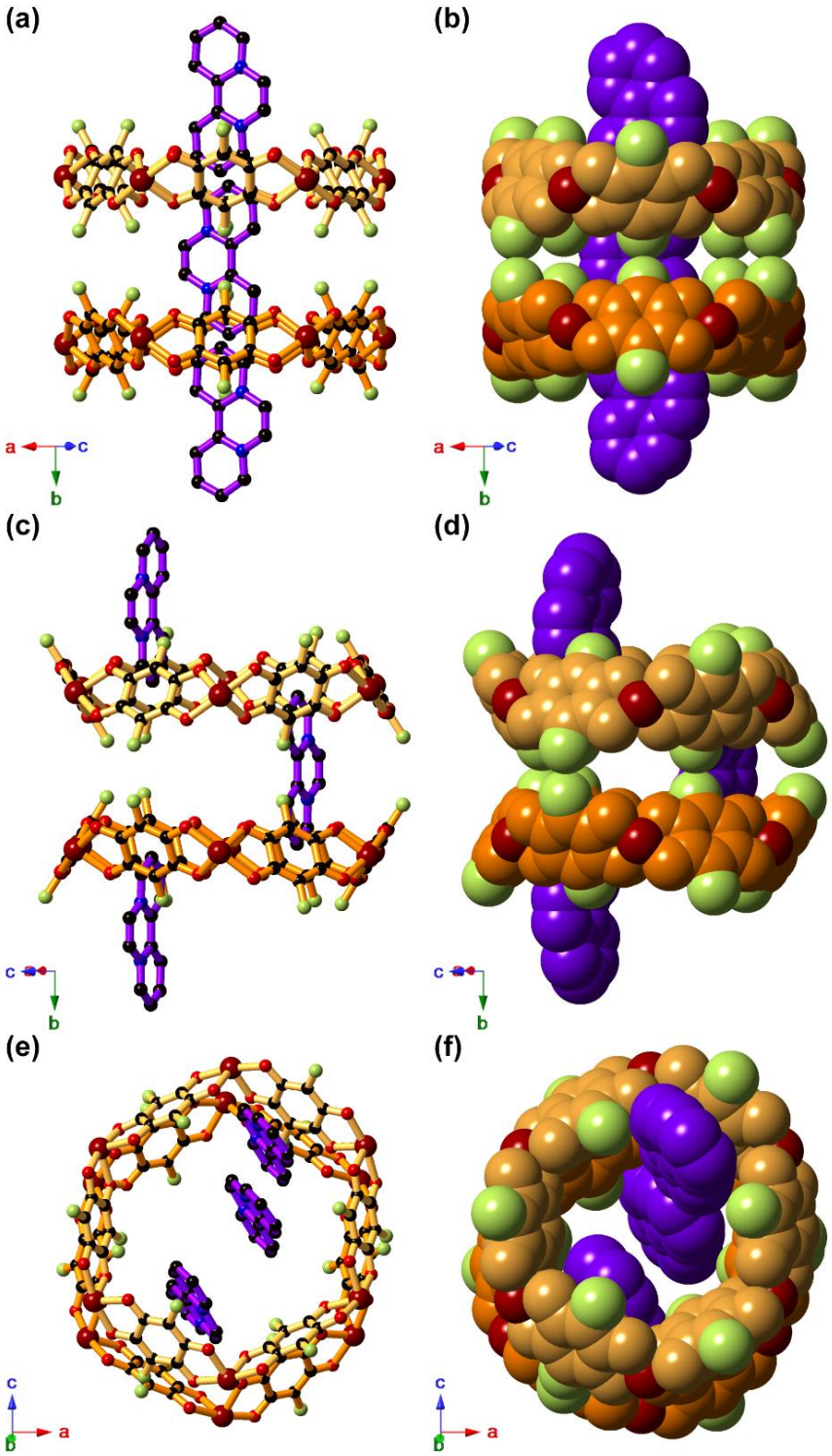


Figure 2.36 Ball-and-stick (a, c, e) and spacefilling (b, d, f) representations of the interactions between $PDiQ^{m+}$ cations (purple) and the anionic $[Fe_2(Fan)_3]^{x-}$ sheets above (tan) and below (orange) in **2.7**. Views (a–d) parallel to the crystallographic (010) plane, and (e, f) along the crystallographic *b* axis. Ordered and disordered MeCN in channels not shown for clarity. Maroon = Fe, pale green = F, red = O, blue = N and black = C.

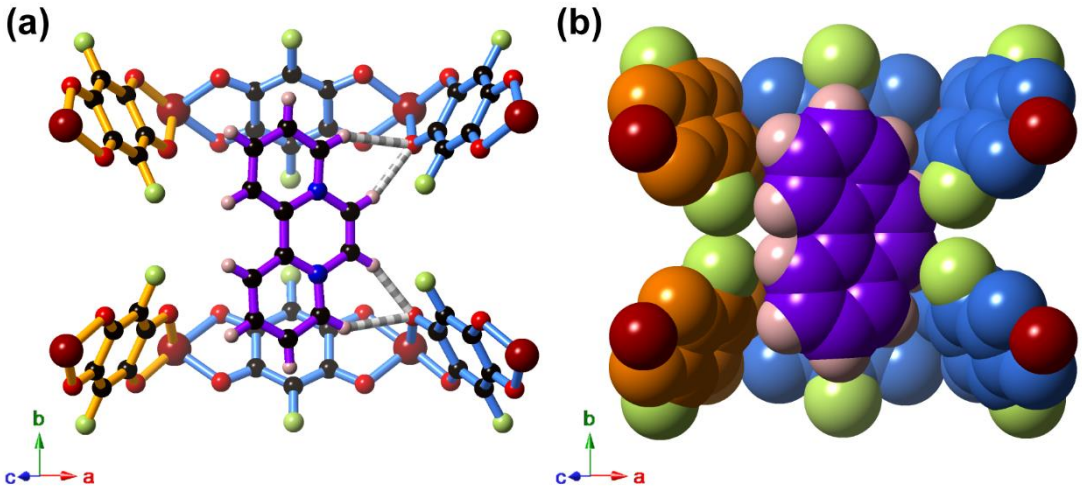


Figure 2.37 Non-covalent interactions between $PDiQ^{m+}$ (purple) and the anionic $[Fe_2(Fan)_3]^{x-}$ network in **2.7**. (a) C–H···O interactions (dashed grey) between $PDiQ^{m+}$ (purple) and O donor atoms of $\mathbf{L_2}$ (pale blue) ligands in sheets above and below. (b) Steric interaction between $PDiQ^{m+}$ (purple) and F atoms of $\mathbf{L_1}$ (orange) ligands in sheets above and below. Maroon = Fe, pale green = F, red = O, blue = N, black = C, and pale pink = H.

Although $PDiQ^{m+}$ cations within the hexagonal network voids do occupy some of the channel volume, the channels which run parallel to the crystallographic *b* axis are still quite spacious, comprising ca. 43% of the unit cell volume. Because the planar $PDiQ^{m+}$ cations line the channel walls, the channel opening is more rectangular, and undulates along the *b* axis, to accommodate the alternating positions of the cations along the channel walls (Figure 2.38a). The anionic $[Fe_2(Fan)_3]^{x-}$ honeycomb sheets in **2.7** stack in an AA′AA′ arrangement (Figure 2.38b), in contrast to the AAAA $[Mn_2(Clan)_3]^{2-}$ sheet stacking observed in the honeycomb framework **2.2a**. For a column of Fe centres in **2.7**, formed when viewed down the sheet stacking axis (*b* axis for **2.7**), the configuration alternates between Δ and Λ, compared to all Δ or all Λ for AAAA stacking. This AA′AA′ stacking is favourable in **2.7** because the $PDiQ^{m+}$ cations are not sandwiched between ligands in the anionic $[Fe_2(Fan)_3]^{x-}$ sheets, so the orientation of stacks of ligands (pointing into or out of a hexagonal channel) are less influenced by steric constraints imposed by interaction with a cation. Additionally, the C–H···O interactions between $PDiQ^{m+}$ and $\mathbf{L_2}$ ligands in sheets above and below probably also influence the relative orientation of the

ligands. On the other hand, MeV^{2+} cations sandwiched between $\mathbf{L_1}$ ligands in **2.2a**, producing alternating stacks of MeV^{2+} and $\mathbf{L_1}$ ligands, enforces AAAA stacking of the $[Mn_2(Clan)_3]^{2-}$ sheets, because the relative orientation of all ligands in a stack must be the same, due to steric interaction with the sandwiched MeV^{2+} cations. The 1D channels in **2.7** are filled with a combination of one well-ordered MeCN molecule per formula unit, as well as MeCN molecules severely disordered over special positions in the unit cell. As a satisfactory solvent model could not be obtained for the disordered solvent, the scattering contribution of the disordered solvent was accounted for using the SQUEEZE[74] routine of PLATON,[75] allowing the total solvation to be estimated as $(PDiQ)[Fe_2(Fan)_3]\cdot(1+7.3)MeCN$ i.e. $(PDiQ)[Fe_2(Fan)_3]\cdot 8.3MeCN$.

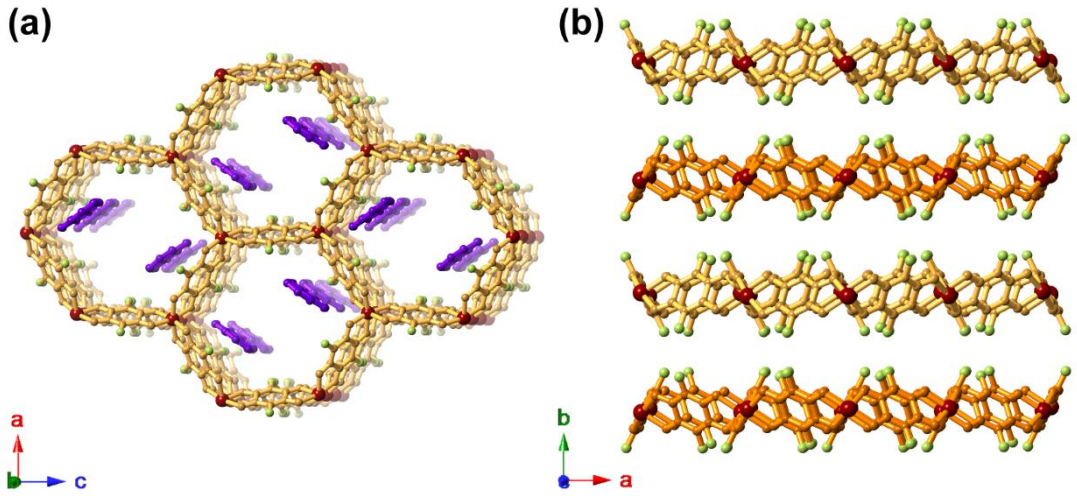


Figure 2.38 Packing of $PDiQ^{m+}$ cations (purple) and the anionic $[Fe_2(Fan)_3]^{x-}$ sheets in **2.7**. View down crystallographic (a) *b* axis showing cations lining the alternate walls of the spacious 1D hexagonal channels, and (b) *c* axis showing AA′AA′ stacking of anionic sheets. $PDiQ^{2+}$ cations not shown for clarity. Maroon = Fe and pale green = F.

Examination of d_{Fe-O}, and diagnostic d_{C-C}, and d_{C-O} (for Fan^{n-}) and d_{C-N} (for $PDiQ^{m+}$) values supports a ligand charged-ordered $(PDiQ^{2+})[Fe^{III}_2(Fan^{2-})(Fan^{3-\bullet})_2]$ formulation for **2.7**. Comparison of the cation d_{C-C} and d_{C-N} values between $PDiQ^{2+}$ in $PDiQ(PF_6)_2$ and $PDiQ^{m+}$ in **2.7** reveals no significant differences in bond lengths between the two moieties. This therefore indicates the cations are in the $PDiQ^{2+}$ valence state in **2.7**, and therefore the network charge is $[Fe_2(Fan)_3]^{2-}$. For the Fe

site, average $d_{Fe–O}$ value is 2.020(11) Å with a corresponding BVS value of 2.97, both of which are consistent with Fe^{III}_{HS} in an octahedral environment. The average $d_{Fe–O}$ value also correlates well to average $d_{Fe–O}$ measured in other Fe^{III}–tetraoxolene frameworks,[9, 10, 28, 38, 45, 69] (Table A.4) providing a strong indication that **2.7** is an Fe^{III}–tetraoxolene framework. Fewer metal–fluoranilate compounds have been reported compared to metal–chloranilate compounds, so it is more difficult to definitively assign $Fan^{n–}$ oxidation states by comparison with literature. Nevertheless, the similar redox behaviour across the family of tetraoxolene ligands,[2] means that the diagnostic changes in bond length with oxidation state will follow the same trends for $Fan^{n–}$ as $Clan^{n–}$.

The two crystallographically unique ligands in **2.7**, $\mathbf{L_1}$ and $\mathbf{L_2}$, are in a 1:2 ratio in the network formula i.e. $[Fe^{III}_2(\mathbf{L_1})(\mathbf{L_2})_2]^{2–}$, therefore the total ligand charge must also be −8. For $\mathbf{L_1}$, the mean $d_{C–O}$ and diagnostic (across the five-membered chelate ring, C2–C4′) $d_{C–C}$ values are 1.276(5) Å and 1.512(6) Å respectively (Figure 2.39). These values match reasonably well to those expected for $Clan^{2–}$ ($d_{C–O}$ = 1.248–1.272 Å; $d_{C–C}$ = 1.506–1.551 Å, Appendix A), and also correspond closely to $d_{C–O}$ and $d_{C–C}$ values exhibited by $Fan^{2–}$ in the diamagnetic coordination polymers $(^nBu_4N)_2[Zn_2(Fan)_3]$ and $(Et_4N)_2[Zn_2(Fan)_3]$,[28, 38] strongly indicating $\mathbf{L_1}$ exists as $Fan^{2–}$. On the other hand, the mean $d_{C–O}$ and diagnostic $d_{C–C}$ values for $\mathbf{L_2}$ are 1.292(3) Å and 1.483(4) Å respectively (Figure 2.39). Elongation of the $\mathbf{L_2}$ C–O bonds and commensurate shortening of diagnostic C–C bonds clearly demonstrates this ligand exists in a more reduced valence state than $\mathbf{L_1}$, due to introduction of partial aromatic character upon tetraoxolene reduction.[2] The observed values also correspond reasonably well to the ranges expected for $Clan^{3–\bullet}$ ($d_{C–O}$ = 1.291–1.316 Å; $d_{C–C}$ = 1.408–1.473 Å, Appendix A), suggestive of the $Fan^{3–\bullet}$ state for $\mathbf{L_2}$. In addition, the $d_{C–O}$ and $d_{C–C}$ values for $\mathbf{L_2}$ are longer and shorter respectively, than the equivalent bond lengths observed for the intermediate $Fan^{2.67–}$ state observed in mixed-valence $(^nBu_4N)_2[Fe_2(Fan)_3]$ and $(Et_4N)_2[Fe_2(Fan)_3]$.[38, 45] These factors indicate that $\mathbf{L_2}$ is more reduced compared to $Fan^{2.67–}$ in these compounds, and is therefore in the $Fan^{3–\bullet}$ state. This, combination with the analyses for cation and $\mathbf{L_1}$ all support a ligand charge-ordered $(PDiQ^{2+})[Fe^{III}_2(Fan^{2–})(Fan^{3–\bullet})_2]$ distribution for **2.7**. Analogously to **2.5** and **2.6**, the average $d_{Fe–O}$ values between Fe and each ligand valence state differs, with the value for $\mathbf{L_1}$ of 2.053(6) Å slightly

longer than the 2.003(6) Å average $d_{Fe–O}$ value calculated for **L₂**. Unsurprisingly, the Fe–Fe distance across **L₁** (7.892(2) Å) is also slightly elongated relative to the Fe–Fe distance across **L₂** (7.795(2) Å). The disparity between $d_{Fe–O}$ and Fe–Fe distances for **L₁** and **L₂** is ascribed to the weaker Coulombic interaction between Fe^{III}_{HS} and localised $Fan^{2–}$ (**L₁**), compared to the interaction between Fe^{III}_{HS} and localised $Fan^{3–\bullet}$ (**L₂**). Similar behaviour has also been observed in **2.5** and **2.7**, and the charge-ordered alloyed $(^{n}Pr_4N)_2[Fe_2(Fan)_{3q}(Clan)_{3–3q}]$ (q = 0–0.42) family of frameworks,[31, 48, 71] suggesting that this is a potentially diagnostic feature in ligand charged-ordered tetraoxolene frameworks.

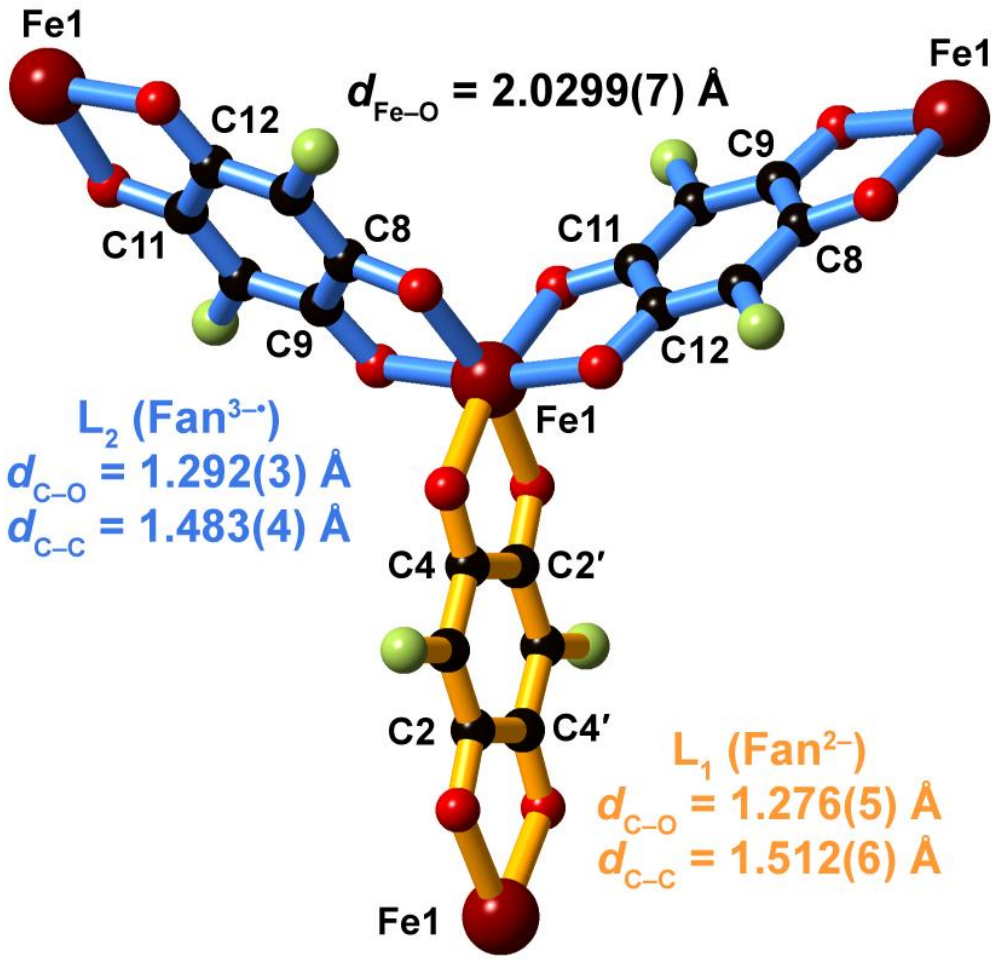


Figure 2.39 Characteristic $Fan^{n–}$ bond lengths and coordination environment around Fe in **2.7**. The indicated $d_{C–O}$ and characteristic $d_{C–C}$ values are the mean of the crystallographically unique bond lengths i.e. $d_{C–C}$ for **L₁**: C2–C4′, and for **L₂**: C8–C9 and C11–C12.

2.3 Conclusion

In this Chapter, three charge-balancing viologen cations were used to synthesise eight novel 1-, 2- and 3D anionic fluoranilate and chloranilate coordination polymers. With regards to the structural chemistry, these results first demonstrate that redox-active viologen-like cations can be successfully incorporated into metal–tetraoxolene coordination polymers. Secondly, the range of structures obtained afforded using only three different cations clearly validates our initial hypothesis that the disparate geometries and steric volumes of viologen cations, compared to alkyl-ammonium or -phosphonium cations, can induce anionic tetraoxolene networks to adopt previously uncommon topologies. Indeed, 3D diamondoid nets have rarely been reported for tetraoxolene coordination polymers, and 3D (10,3)-*b* tetraoxolene nets have never previously been reported.

Contrary to our initial aim of synthesising isostructural families of tetraoxolene coordination polymers by varying metals and ligand substituents, predicting the topologies templated by viologens is more difficult compared to previously employed cations. This is notably evident for the $Clan^{2-}$/MeV^{2+} system, where the topology, either 2D honeycomb or 3D diamondoid, depends upon the metal and solvents utilised. Until a more through survey is completed to afford greater insight into all the delicate supramolecular interactions between metals, ligands, viologens and solvent, *a priori* design of such tetraoxolene coordination polymers incorporating viologens is not yet achievable. This point is particularly salient regarding fluoranilate-viologen systems, as the $[M_2(Fan)_3]^{2-}$ networks obtained were not isostructural to their $[M_2(Clan)_3]^{2-}$ counterparts. However, since the supramolecular and coordination chemistry of fluoranilate remains underexplored, these findings highlight that there is significant promise in obtaining novel fluoranilate coordination polymers which could exhibit interesting topologies and properties.

Regarding the Fe^{III}–tetraoxolene frameworks, additional conclusions can be drawn. As expected, spontaneous electron transfer from the Fe^{II} to the bridging Xan^{2-} ligands yielded the mixed-valence frameworks containing Fe^{III} and the $Xan^{3-\bullet}$ form of the ligand. Much like the M^{II}–tetraoxolene coordination polymers, it appears difficult to reliably predict how each viologen will influence the topology and

geometry adopted by the anionic $[Fe^{III}_2(Xan)_3]^{2-}$ network. On the other hand, the high charge of viologens, and possibility of CT interactions seems to strongly influence the ligand charge-state distribution in the network. Previously reported mixed-valence Fe–tetraoxolene frameworks containing redox-inactive cations predominantly exhibit delocalised $[Fe^{III}_2(Clan^{2.67-})_3]^{2-}$ charge-state distributions. Because viologens are highly charged and π-electron poor, close-contact and CT interaction with the anionic network in **2.5** and **2.6**, appears to be an important factor in localising the relatively π-electron rich $Clan^{3-\bullet}$ ligand charge state, giving a charge-ordered $[Fe^{III}_2(Clan^{2-})(Clan^{3-\bullet})_2]^{2-}$ formulation. Although the network geometry and topology adopted may be less predictable, using viologens as countercations in mixed-valence Fe–tetraoxolene frameworks could prove a fruitful method to induce ligand charge-state localisation. Interestingly, ligand charge-ordering is also observed in **2.7** although no CT interactions occur between the viologen and the framework, with C–H···O interactions apparently playing a more important structure directing role. The structural disparity between these fluoranilate and chloranilate frameworks somewhat inhibits the idea of finely varying physical properties in an isostructural family by variation of ligand substituents. On the other hand, it reinforces the impetus to examine the coordination chemistry of fluoranilate more thoroughly, as interesting and dissimilar coordination polymers could be obtained.

2.4 Experimental

2.4.1 General Considerations

For crystallisations and synthesis, acetone, acetonitrile (MeCN) and diethyl ether (Et_2O) were obtained from commercial sources and used without further purification. Anhydrous MeCN was obtained by drying MeCN twice sequentially over activated 3 Å molecular sieves, which was then stored under at atmosphere of dry N_2. General spectroscopic and physical characterisation was performed as described in Chapter 7.

2.4.2 Ligand Synthesis

2.4.2.1 Fluoranilic acid (H_2Fan)

H_2Fan was synthesised using a modified literature procedure[77] in two steps from commercially available 2,3,5,6-tetrafluorohydroquinone, via the intermediate 2,3,5,6-tetrafluoro-1,4-benzoquinone (F_4BQ), also obtained using a modified literature procedure.[78] In brief, $(NH_4)_2Ce^{IV}(NO_3)_6$ (145.1 g, 220 mmol) was dissolved with stirring in H_2O (700 mL). 2,3,5,6-Tetrafluorohydroquinone (18.21 g, 100 mmol) was added portion wise to the stirring Ce^{IV} solution, causing an immediate colour change from a transparent orange solution to a pale-yellow suspension. The reaction was stirred 1 hr at rt., then extracted with Et_2O (3 × 200 mL) until the organic extract was colourless. The combined organic phase was washed with H_2O acidified with 2 drops conc. HCl (2 × 150 mL), brine acidified with 1 drop conc. HCl (150 mL), dried over $MgSO_4$ then concentrated to dryness at reduced pressure, yielding F_4BQ as a pale yellow scaly solid (15.63 g, 86.8%), which was used without further purification. FT-IR (KBr, cm^{-1}): 3442 (br s), 1702 (s), 1690 (s), 1677 (s), 1384 (m), 1335 (m), 1266 (w), 1004 (m), 542 (br w).

NaOH (9.5582 g, 734 mmol) was dissolved in H_2O (190 mL) and cooled in an ice-water bath to <10 °C. F_4BQ (9.5582 g, 53.1 mmol) dissolved in 1,4-dioxane (75 mL) was added dropwise over 30 min to the vigorously stirring NaOH solution. The reaction was then stirred 30 min at 10 °C, then warmed to 60 °C and stirred 1 hr. The chocolate brown suspension was cooled to rt., then the solids isolated by suction filtration (Por. 3 frit). The product was washed on the frit with 10% w/w NaOH solution (2 × 75 mL), 1:1 v/v EtOH/H_2O (100 mL) then EtOH (100 mL). The chocolate brown solid was then dried 24 hrs at 100 °C yielding an olive-green crude of Na_2Fan (10.51 g). The crude Na_2Fan (10.51 g) was suspended in H_2O (300 mL) and heated to 60 °C with stirring. Conc. HCl (100 mL) was added dropwise to the stirring suspension, causing precipitation of a dark red crystalline product. The reaction was cooled to rt., then the precipitated solids isolated by suction filtration (Por. 3 frit), then dried by suction yielding an orange-red crude (6.4468 g). The crude was dissolved in the minimum of boiling AcOH (120 mL), hot filtered to remove trace brown residue, then concentrated by boiling to ca. 80 mL. The intense cherry-red solution was then cooled slowly to rt. The crystallised orange-red rods were

isolated by suction filtration (Por. 3 frit), dried by suction then washed with *n*-hexane (2 × 100 mL), then dried *in vacuo* (0.3 mbar, 80 °C) over KOH yielding the title compound as a bright orange powder (4.88 g, 52.2% from F_4BQ). FT-IR (KBr, cm^{-1}): 3585 (br s), 3477 (br s), 1673 (m), 1631 (s), 1452 (w), 1384 (w), 1303 (m), 998 (m), 606 (br w).

2.4.2.2 3,6-Difluoro-1,2,4,5-tetrahydroxybenzene (H_4Fan)

3,6-Difluoro-1,2,4,5-tetrahydroxybenzene (H_4Fan) was synthesised according to a modified literature procedure.[28] In air, H_2Fan (4.2420 g, 24.1 mmol) was suspended in conc. HCl (100 mL) then heated to 100 °C with stirring. Mossy tin (3.433 g, 28.9 mg-atom) was added portion wise over 5 minutes to the stirring orange-red suspension, causing gas evolution and gradual bleaching of the solution. After 30 min., the clear pale-yellow solution was hot filtered through glass fibre paper to remove traces of insoluble tan residue and unreacted Sn. The clear filtrate was cooled slowly to rt., then 4 °C overnight. The crystallised pale-tan needles were isolated by suction filtration (Por. 3 frit) under an N_2 stream, then washed on the frit with conc. HCl (2 × 30 mL), dried by suction in a brisk N_2 stream, then washed on the frit with ice-cold $CHCl_3$ (2 × 30 mL). The product was then dried *in vacuo* over KOH then P_2O_5, yielding the title compound as pale-tan needles (3.77 g, 87.9%). The product is stable over several months when stored under N_2 at 4 °C. FT-IR (ATR, cm^{-1}): 3525 (br m), 3373 (br m), 3211 (br m), 1648 (m), 1546 (w), 1532 (w), 1498 (s), 1405 (w), 1327 (m), 1294 (w), 1235 (w), 1207 (m), 988 (m), 955 (s), 703 (w), 635 (w), 608 (w).

2.4.2.3 3,6-Dichloro-1,2,4,5-tetrahydroxybenzene (H_4Clan)

H_4Clan was synthesised using a modified literature procedure.[28] In air, chloranilic acid (H_2Clan, 6.270 g, 30 mmol) was suspended in conc. HCl (150 mL) then heated to 100 °C with stirring. Mossy tin (4.271 g, 36 mg-atom) was added portion wise over 5 minutes to the stirring red-orange suspension, causing gas evolution, and gradual bleaching of the solution. After 20 min., the clear pale-yellow reaction solution was hot filtered through glass fibre paper to remove traces of an insoluble tan residue and unreacted Sn, rinsing the reaction flask with additional hot concentrated HCl (2 × 20 mL). The clear filtrate was transferred to a flask fitted with

a septum, purged with N_2 then cooled to rt. then to 4 °C overnight. The product crystallised as white needles, which were isolated by suction filtration (Por. 3 frit) under an N_2 stream. The product was washed with ice-cold concentrated HCl (3 × 25 mL), then dried by suction in a brisk N_2 stream, then washed with ice-cold $CHCl_3$ (2 × 25 mL). The solid was dried *in vacuo* over KOH then P_2O_5, yielding the title compound as white to pale-tan needles (3.85 g, 61.1%). The product is stable over several months when stored under dry N_2 at 4 °C. $^{13}C\{^1H\}$-NMR (100 MHz, d_6-Acetone): δ_C 137.3, 110.5. FT-IR (ATR, cm^{-1}): 3281 (s, br), 1632 (w), 1541 (w), 1466 (s), 1327 (m), 1288 (m), 1148 (s), 961 (s), 920 (m), 861 (m), 821 (s), 713 (m), 608 (m).

2.4.3 Cation Synthesis

2.4.3.1 N,N'-Dimethyl-4,4'-bipyridinium di(4-toluenesulfonate) [MeV(OTs)$_2$]

4,4′-Bipyridine (4,4′-bpy, 9.371 g, 60 mmol) and methyl-4-toluenesulfonate (27.00 g, 145 mmol) were added to an oven-dried 500 mL round-bottom flask fitted with a reflux condenser topped with a $CaCl_2$ guard tube. MeCN (350 mL) was added, then the reaction placed in a thermostated oil bath (90 °C) and stirred 12 hrs. The pale-yellow reaction suspension was then cooled to rt., and the precipitated pale-yellow solid isolated by suction filtration (Por. 3 frit), rinsing the reaction flask with additional MeCN (2 × 50 mL). The product was washed on the frit with acetone (2 × 200 mL) then Et_2O (100 mL), then dried *in vacuo* over P_2O_5, yielding the title compound as a pale-yellow powder (26.6 g, 83.9%). ^1H-NMR (400 MHz, D_2O): δ_H 8.98 (d, J_{AB} = 6.7 Hz, 4H, Py^+-***H***2,2′,6,6′), 8.42 (d, J_{AB} = 6.7 Hz, 4H, Py^+-***H***3,3′,5,5′), 7.61 (d, J_{AB} = 8.1 Hz, 4H, Ar-***H***2,6), 7.30 (d, J_{AB} = 8.1 Hz, 4H, Ar-***H***3,5), 4.46 (s, 6H, N^+–C***H***$_3$), 2.35 (s, 6H, Ar–C***H***$_3$). FT-IR (KBr, cm^{-1}): 3443 (br m), 3052 (m), 1642 (m), 1567 (w), 1511 (w), 1452 (w), 1358 (w), 1177 (s), 1119 (s), 1030 (m), 1006 (m), 835 (m), 820 (m), 683 (s), 567 (s), 474 (w).

2.4.3.2 6,7-Dihydrodipyrido[1,2-a:2',1'-c]pyrazinediium dibromide ([DiQ]Br$_2$)

2,2′-Bipyridine (2,2′-bpy, 9.371 g, 60 mmol) was added to an oven-dried round-bottom flask fitted with a reflux condenser topped with a $CaCl_2$ guard tube.

1,2-Dibromoethane (250 mL) was added then the reaction was placed in a thermostated oil bath (135 °C) and stirred 15 hrs. The pale-yellow reaction suspension was cooled to rt., and the precipitated solids isolated by suction filtration (Por. 3 frit). The solid was washed on the frit with acetone (2 × 250 mL) until the filtrate was colourless, yielding a yellow crude (8.107 g). The solids were dissolved in boiling MeOH (150 mL), forming a yellow-brown solution, which was treated with decolourising charcoal then hot filtered. The filtrate was concentrated by boiling to ca. 80 mL then boiling acetone (ca. 120 mL) was added slowly, causing precipitation of fine microcrystalline solid. The mixture was cooled slowly to rt., then −20 °C overnight. The microcrystalline solid was isolated by suction filtration (Por. 3 frit), washed on the frit with acetone (2 × 100 mL) and Et_2O (100 mL), then dried *in vacuo* over P_2O_5 yielding the title compound as microcrystalline canary-yellow needles (7.38 g, 35.7%). ^{1}H-NMR (400 MHz, D_2O): δ_H 9.23 (d, J_{AB} = 6.0 Hz, 2H, Py$^+$-***H***6,6′), 9.00 (d, J_{AB} = 7.6 Hz, 2H, Py+-***H***3,3′), 8.96–8.89 (m, 2H, Py$^+$-***H***4,4′), 8.43–8.36 (m, 2H, Ar-***H***5,5′), 5.37 (s, 4H, C***H***$_2$). FT-IR (KBr, cm^{-1}): 3433 (s), 3390 (w), 3061 (m), 3043 (m), 3004 (w), 2951 (m), 2866 (w), 1612 (m), 1578 (m), 1497 (s), 1463 (m), 1463 (w), 1418 (w), 1375 (w), 1321 (w), 1286 (m), 1242 (w), 1226 (w), 1192 (m), 1172 (m), 1154 (m), 1136 (w), 940 (w), 792 (s), 713 (m), 612 (w), 587 (br m), 468 (m).

2.4.3.3 Dipyrido[1,2-a:2′,1′-c]pyrazinediium dibromide ([PDiQ]Br$_2$)

[PDiQ]Br_2 was synthesised in two steps from 2,2′-bpy, using a modified procedure from Corr and Glover[79] for the synthesis of the intermediate 6-hydroxy-6,7-dihydrodipyrido[1,2-*a*:2', l'-*c*]pyrazinediium dibromide ([HO-DiQ]Br_2) and a modified procedure according to Calder and Sasse[80] to affect the dehydration of [HO-DiQ]Br_2 to yield the desired [PDiQ]Br_2. Use of the combined procedures was advantageous, as removal of the 2,4-dinitrophenylhydrazine by-product from the HBr-catalysed cyclisation to yield [HO-DiQ]Br_2 according to Calder and Sasse[80] proved exceedingly difficult.

Crude bromoacetaldoxime was synthesised according to a modified literature procedure,[79, 81] yielding a strongly lachrymatory pale-yellow oil which solidified when stored at −20 °C under dry N_2. While ^{1}H-NMR spectroscopy indicated the crude product contained multiple compounds, it was sufficiently pure for subsequent

steps. Further purification was not attempted due to the known tendency of haloacetaldoximes to decompose violently upon distillation.[79, 82] FT-IR (neat, cm^{-1}): 3263 (s br), 2979 (w), 2897 (w), 1621 (w), 1431 (s), 1296 (m), 1252 (m), 1210 (w), 1182 (w), 1091 (w), 1045 (w), 990 (s), 936 (s), 860 (m), 716 (s).

An oven-dried two-neck round-bottom flask was fitted with a septum and reflux condenser topped with a gas inlet tube, then cooled under an atmosphere of dry N_2. 2,2′-bpy (7.809 g, 50 mmol) and anhydrous MeCN (100 mL) were then added. The solution was degassed by N_2 bubbling (20 min.), then the reaction was placed in a thermostated oil bath (60 °C) and stirred. A degassed solution of crude bromoacetaldoxime (7.59 g, 55 mmol) in dry MeCN (15 mL) was added dropwise to the stirring reaction solution by cannula transfer. The reaction was heated 2 hrs. with stirring under N_2, then cooled to rt. and stirred overnight. The clear yellow reaction solution was concentrated at reduced pressure in a fumehood to a yellow-brown oil. Et_2O (100 mL) was added slowly, precipitating a gummy yellow-brown solid. Then supernatant was decanted, and the residue triturated with additional boiling Et_2O (100 mL). The residue was dried *in vacuo* yielding a brown tacky gum (6.10 g). The residue was dissolved in conc. HBr (30 mL), and the reaction placed in a thermostated oil bath (100 °C) and stirred 15 min. Boiling acetone (150 mL) was cautiously added forming a homogenous brown solution which was cooled slowly to rt., causing crystallisation of a canary-yellow solid. The suspension was diluted with additional acetone to ca. 250 mL, then cooled to 4 °C overnight. The solids were isolated by suction filtration (Por. 3 frit), then washed on the frit with acetone (4 × 50 mL) and Et_2O (50 mL), then dried *in vacuo* over P_2O_5 yielding a microcrystalline yellow crude (6.05 g). The crude was dissolved in boiling 95% MeOH (ca. 250 mL), and the solution treated with decolourising charcoal and hot filtered. The filtrate was concentrated by boiling to ca. 80 mL, then boiling acetone (ca. 220 mL) was slowly added. The suspension was cooled slowly to rt., then 4 °C. The product was isolated by suction filtration (Por. 3 frit) then washed on the frit with acetone (4 × 25 mL) and Et_2O (25 mL) then dried *in vacuo* over P_2O_5, yielding [HO-DiQ]Br_2 as a lemon-yellow microcrystalline solid (4.47 g, 24.8% from 2,2′-bpy). ^{1}H-NMR (400 MHz, D_2O): δ_H 9.42 (d, J_{AB} = 6.1 Hz, 1H, Py^+-***H***6), 9.25 (d, J_{AB} = 6.0 Hz, 1H, Py^+-***H***6′), 9.08–8.91 (m, 4H, Py^+-***H***), 8.53–8.38 (m, 2 H, Py^+-***H***), 6.86 (t, J_{AB} = 3.70 Hz, 1H, C***H***OH), 5.42 (d, J_{AB} = 3.70 Hz, 2H, C$\boldsymbol{H}_2$).

An oven-dried two-neck round-bottom flask was fitted with a septum and a condenser topped with a gas inlet tube was cooled under an atmosphere of dry N_2. [HO-DiQ]Br_2 (4.4589 g, 12.4 mmol) was added, followed by thionyl chloride (40 mL, excess). The reaction was placed in a thermostated oil bath (75 °C) and stirred 2 hrs. under N_2. The reaction was then cooled overnight to rt. then diluted with anhydrous 1,4-dioxane (30 mL) and stirred 30 min. under N_2. The volatiles were then removed by distillation under N_2 (130 °C max bath temperature). The residue was suspended in acetone (75 mL) and the yellow crude solid isolated by suction filtration (Por. 3 frit). The product was washed on the frit with acetone (3 × 25 mL) and Et_2O (2 × 25 mL), then dried *in vacuo* over P_2O_5 yielding a mustard-yellow crude (3.66 g). The crude was dissolved in boiling MeOH (75 mL), the solution treated with decolourising charcoal then hot filtered. The filtrate was concentrated by boiling to ca. 20 mL, then boiling acetone (ca. 80 mL) was slowly added, causing crystallisation of a pale-yellow solid. The suspension was cooled slowly to rt., then −20 °C overnight. The product was isolated by suction filtration (Por. 3 frit), washed on the frit with ice-cold acetone (2 × 20 mL) and Et_2O (20 mL), then dried *in vacuo* over P_2O_5, yielding the title compound as a pale-yellow microcrystalline solid (3.34 g, 81.5%). ^{1}H-NMR (400 MHz, D_2O): δ_H 9.74 (d, J_{AB} = 8.5 Hz, 2H, Py^+-***H***6,6′), 9.69 (d, J_{AB} = 6.3 Hz, 2H, Py^+-***H***3,3′), 9.21–9.15 (m, 4H, Py^+-***H***4,4′ and C***H***=C***H***), 8.75–8.70 (m, 2H, Py^+-***H***5,5′). FT-IR (KBr, cm^{-1}): 3374 (br s), 3124 (m), 3065 (m), 3011 (m), 2967 (m), 2894 (w), 1689 (m), 1617 (m), 1494 (s), 1465 (m), 1421 (m), 1325 (m), 1300 (s), 1171 (m), 1147 (m), 977 (w), 815 (s), 767 (m), 698 (m), 626 (br m), 460 (m), 421 (m).

For crystal structure determination, [PDiQ]Br_2 was converted to PDiQ$(PF_6)_2$. [PDiQ]Br_2 (67.9 mg, 0.19 mmol) dissolved in H_2O (3 mL) was added dropwise to a solution of NH_4PF_6 (330 mg, 2.02 mmol) in H_2O (10 mL). The precipitated pale-yellow solid was isolated by centrifugation, washed by resuspension in MeOH (2 × 10 mL) and re-centrifugation, then dried *in vacuo* over P_2O_5. Crystals suitable for SC-XRD were obtained by slow vapour diffusion of Et_2O into a solution of PDiQ$(PF_6)_2$ in acetone. Single crystals suitable for X-ray diffraction were transferred immediately from the mother liquor to a cryoprotective oil to prevent putative solvent loss from the crystal lattice.

2.4.4 Coordination Polymer Synthesis

2.4.4.1 (MeV)[Mn(Clan)$_2$] (2.1$_{Mn}$)

In air, a solution of $Mn^{II}(NO_3)_2{\cdot}4H_2O$ (50.2 mg, 0.2 mmol), $MeV(OTs)_2$ (211.5 mg, 0.4 mmol) and $LiOAc{\cdot}2H_2O$ (26.4 mg, 0.2 mmol) in H_2O (4 mL) was carefully layered below a solution of H_4Clan (63.3 mg, 0.3 mmol) in acetone (10 mL) in a soda glass vial (OD = 25 mm), with a buffer layer of 1:1 v/v acetone/H_2O (4 mL). To obtain bulk product, four diffusion reactions were conducted in parallel. Bright-red elongated octahedra suitable for X-ray diffraction were visible on the vial walls within two days. After 7 days, the crystalline product was isolated by gravimetric separation. The crystalline product was dislodged from the vial walls, and the reactions mixed. The crystalline product was settled, and the turbid mother liquor removed. The crystalline product was resuspended in 2:1 v/v acetone/H_2O (10 mL) and the products from the parallel reactions combined. The supernatant liquid was decanted, then the crystalline product was washed with fresh 2:1 v/v acetone/H_2O (3 × 50 mL) by resuspension of the crystalline product, sedimentation of the crystalline product and decantation of the supernatant. The crystalline product was then washed with acetone (3 × 50 mL) as above, then isolated by suction filtration (Por. 3 frit), washing with additional acetone (3 × 10 mL), then dried by suction to a free flowing solid to yield **2.1$_{Mn}$** as a reddish-maroon crystalline powder (119.5 mg, 30.5%). FT-IR (ATR, cm^{-1}): 3051 (w), 1627 (w), 1464 (s), 1379 (w), 1328 (w), 1281 (w), 1263 (w), 1206 (w), 1183(w), 1158(w), 989 (m), 851 (w), 831 (s), 781 (w), 731 (w). Anal. Calcd. for $(C_{12}H_{14}N_2)(Mn_2Cl_4O_8C_{12})$: C, 44.0%; H, 2.15%; N, 4.28%. Found: C, 44.0%; H, 1.51%; N, 4.02%.

2.4.4.2 (MeV)[Cd(Clan)$_2$] (2.1$_{Cd}$)

In air, a solution of $Cd^{II}(NO_3)_2{\cdot}4H_2O$ (61.7 mg, 0.2 mmol), $MeV(OTs)_2$ (211.5 mg, 0.4 mmol) and $LiOAc{\cdot}2H_2O$ (26.4 mg, 0.2 mmol) in H_2O (4 mL) was carefully layered below a solution of H_4Clan (63.3 mg, 0.3 mmol) in acetone (10 mL) in a soda glass vial (OD = 25 mm), with a buffer layer of 1:1 v/v acetone/H_2O (4 mL). For synthesis of bulk product, four diffusion reactions were conducted in parallel. Bright-red feathery crystals suitable for X-ray diffraction were visible on the vial walls within two days. After seven days, the crystalline product

was isolated by gravimetric separation. The crystalline product was dislodged from the vial walls, and the reactions mixed. The crystalline product was settled, and the turbid supernatant removed. The crystalline product was resuspended in 2:1 v/v acetone/H_2O (10 mL) and the separate reactions combined. The supernatant liquid was decanted, then the crystalline product was washed 2:1 v/v acetone/H_2O (3 × 50 mL) by resuspension of the crystalline product, sedimentation of the crystalline product and decantation of the supernatant. The crystalline product was then washed with acetone (3 × 50 mL) as above, then isolated by suction filtration (Por. 3 frit), washing with additional acetone (3 × 10 mL), then dried by suction to a free-flowing solid to yield **2.1$_{Cd}$** as a bright-red crystalline powder (77.5 mg, 18.1%). FT-IR (ATR, cm^{-1}): 3103 (w), 3050 (w), 1627 (w), 1459 (s), 1326 (w), 1263 (w), 1181 (w), 984 (w), 924 (w), 847 (w), 830 (s), 782 (w), 731 (w). Upon prolonged standing in air, conversion to a partial hydrate occurred. Anal. Calcd. for $(C_{12}H_{14}N_2)(Cd_2Cl_4O_8C_{12})\cdot 0.4H_2O$: C, 40.04%; H, 2.07%; N, 3.89%. Found: C, 40.04%; H, 1.56%; N, 3.84%.

An analogous reaction and workup except replacing acetone with equivalent volumes of MeCN at all steps and using slightly higher quantities of $Cd^{II}(NO_3)_2\cdot 4H_2O$ (92.5 mg, 0.3 mmol) and $LiOAc\cdot 2H_2O$ (30.6 mg, 0.3 mmol) yielded **2.1$_{Cd}$** as a bright-red microcrystalline powder (137.8 mg, 32.2%). FT-IR (ATR, cm^{-1}): 3105 (w), 3050 (w), 1627 (w), 1460 (s), 1384 (w), 1326 (w), 1281 (w), 1265 (w), 1205 (w), 1181 (w), 984 (m), 849 (w), 830 (s), 781 (m), 714 (w), 668 (w). Upon prolonged standing in air, conversion to a partial hydrate occurred: Anal. Calcd. for $(C_{12}H_{14}N_2)(Cd_2Cl_4O_8C_{12})\cdot 0.9H_2O$: C, 39.55%; H, 2.19%; N, 3.84%. Found: C, 39.57%; H, 1.82%; N, 3.93%.

2.4.4.3 (MeV)[Mn$_2$(Clan)$_3$]·6MeCN (2.2a) and (MeV)[Mn$_2$(Clan)$_3$]·yH$_2$O (2.2b)

In air, a solution of $Mn^{II}(NO_3)_2\cdot 4H_2O$ (75.3 mg, 0.3 mmol), $MeV(OTs)_2$ (211.5 mg, 0.4 mmol) and $LiOAc\cdot 2H_2O$ (30.6 mg, 0.3 mmol) in H_2O (4 mL) was carefully layered below a solution of H_4Clan (63.3 mg, 0.3 mmol) in MeCN (10 mL) in a soda glass vial (OD = 25 mm), with a buffer layer of 1:1 v/v MeCN/H_2O (4 mL). For synthesis of bulk product, four reactions were conducted in parallel. Maroon parallelepiped plates were visible on the vial walls within two days. For **2.2a**, single

crystals were transferred immediately from the mother liquid to a cryoprotective oil (see Section 2.4.5.3); attempted isolation leads to replacement of solvated MeCN with H_2O and conversion to the hydrate (MeV)[Mn_2(Clan)$_3$]·$y$$H_2O$ (**2.2b**). After seven days, the crystalline product was isolated by gravimetric separation. The crystalline product was dislodged from the vial walls, and the reactions mixed. The crystalline product was settled, and the turbid supernatant removed. The crystalline product was resuspended in 2:1 v/v MeCN/H_2O (10 mL) and the separate reactions combined. The supernatant liquid was decanted, then the crystalline product was washed 2:1 v/v MeCN/H_2O (3 × 50 mL) by resuspension of the crystalline product, sedimentation of the crystalline product and decantation of the supernatant. The crystalline product was then washed with MeCN (3 × 50 mL) as above, then isolated by suction filtration (Por. 3 frit), washed with additional MeCN (3 × 10 mL), then dried by suction to a free-flowing solid to yield **2.2b** as a maroon powder (137.7 mg, 35.8%). FT-IR (ATR, cm^{-1}): 3416 (br m), 3107 (w), 3052 (w), 1627 (w), 1496 (s), 1460 (s), 1379 (m), 1329 (w), 1280 w), 1219 (w), 1206 (w), 1184 (w), 991 (w), 849 (w), 832 (m), 810 (w), 781 (w), 683 (w). Upon exposure to air, conversion to hydrate solvate occurred: Anal. Calcd. for ($C_{12}H_{14}N_2$)($Mn_2Cl_6O_{12}C_{18}$)·2.5H_2O: C, 37.45%; H, 1.99%; N, 2.91%. Found: C, 37.46%; H, 1.66%; N, 2.80%.

*2.4.4.4 (MeV)[Mn_2(Fan)$_3$(H_2O)$_2$]·yMeCN·$z$$H_2O$ (**2.3$_{Mn}$**)*

In air, a solution of $Mn^{II}(NO_3)_2$·4H_2O (75.3 mg, 0.3 mmol), MeV(OTs)$_2$ (211.5 mg, 0.4 mmol) and LiOAc·2H_2O (30.6 mg, 0.3 mmol) in H_2O (4 mL) was carefully layered below a solution of H_4Fan (53.4 mg, 0.3 mmol) in MeCN (10 mL) in a soda glass vial (OD = 25 mm), with a buffer layer of 1:1 v/v MeCN/H_2O (4 mL). Yellowish-brown plate crystals suitable for X-ray diffraction were visible on the vial walls within two days. The crystalline product was isolated by gravimetric separation after seven days of reaction. The crystalline product was dislodged from the vial walls, and the reaction mixed. The crystalline product was settled, and the turbid supernatant removed. The crystalline product was washed 2:1 v/v MeCN/H_2O (3 × 10 mL) by resuspension of the crystalline product, re-sedimentation of the crystalline product and decantation of the supernatant. The crystalline product was then washed with MeCN (3 × 10 mL) as above, then isolated by suction filtration (Por. 3 frit), washed with additional MeCN (3 × 5 mL), then dried by suction to a free-flowing solid to yield **2.3$_{Mn}$** as a dark-brown crystalline powder (30.3 mg,

33.0%). FT-IR (ATR, cm^{-1}): 3138 (br m), 2252 (w), 1644 (m), 1520 (s), 1382 (w), 1349 (m), 1276 (w), 1230 (w), 1191 (w), 1079 (w), 1035 (w), 995 (s), 828 (m), 792 (w), 707 (w), 660 (w). Upon exposure to air, partial solvent loss occurred: Anal. Calcd. for $(C_{12}H_{14}N_2)(Mn_2F_6O_{14}C_{18}H_4)\cdot 1.4(C_2H_3N)\cdot 0.4(H_2O)$: C, 42.87%; H, 2.52%; N, 5.18%. Found: C, 42.86%; H, 1.53%; N, 5.19%.

*2.4.4.5 (MeV)[Cd_2(Fan)$_3$(H_2O)$_2$]·y*MeCN·zH2O (2.3$_{Cd}$) and [Cd(Fan)(H_2O)$_2$] (2.4)*

In air, a solution of $Cd^{II}(NO_3)_2\cdot 4H_2O$ (92.5 mg, 0.3 mmol), $MeV(OTs)_2$ (211.5 mg, 0.4 mmol) and $LiOAc\cdot 2H_2O$ (30.6 mg, 0.3 mmol) in H_2O (4 mL) was carefully layered below a solution of H_4Fan (53.4 mg, 0.3 mmol) in MeCN (10 mL) in a soda glass vial (OD = 25 mm), with a buffer layer of 1:1 v/v MeCN/H_2O (4 mL). Yellowish-brown plate crystals suitable for X-ray diffraction were visible on the vial walls within two days. The crystalline product was isolated by gravimetric separation after seven days of reaction. The crystalline product was dislodged from the vial walls, and the reaction mixed. The crystalline product was settled, and the turbid supernatant removed. The crystalline product was washed 2:1 v/v MeCN/H_2O (3 × 10 mL) by resuspension of the crystalline product, re-sedimentation of the crystalline product and decantation of the supernatant. The crystalline product was then washed with MeCN (3 × 10 mL) as above, then isolated by suction filtration (Por. 3 frit), washed with additional MeCN (3 × 5 mL), then dried by suction to a free-flowing solid to yield an inseparable mixture of **2.3$_{Cd}$** and **2.4** as a dark-brown crystalline powder (43.3 mg). FT-IR (ATR, cm^{-1}): 3135 (br m), 2253 (w), 1642 (m), 1507 (s), 1382 (w), 1347 (m), 1228 (w), 1190 (w), 1033 (w), 996 (s), 829 (m), 707 (w), 658 (w). Satisfactory analyses could not be obtained as the product contains an inseparable mixture of **2.3$_{Cd}$** and **2.4**.

2.4.4.6 (PDiQ)[Fe_2(Clan)$_3$]·4(acetone) (2.5)

In air, a solution of $(NH_4)_2Fe^{II}(SO_4)_2\cdot 6H_2O$ (78.4 mg, 0.2 mmol) and $[PDiQ]Br_2$ (136.8 mg, 0.4 mmol) in H_2O (4 mL) was carefully layered below a solution of H_4Clan (84.4 mg, 0.4 mmol) in acetone (10 mL) in a soda glass vial (OD = 25 mm), with a buffer layer of 1:1 v/v acetone/H_2O (4 mL). Black plate crystals with a metallic blue-green lustre were visible on the vial walls within two days. Single

crystals were transferred immediately from the mother liquid to a cryoprotective oil (see Section 2.4.5.1). No yield was determined due to the presence of multiple crystalline phases in the reaction.

For synthesis of bulk product for slurry P-XRD, modified conditions were used to produce a phase-pure product. A solution of $Fe^{II}Cl_2 \cdot 4H_2O$ (59.6 mg, 0.3 mmol), $[PDiQ]Br_2$ (136.8 mg, 0.4 mmol) and $LiOAc \cdot 2H_2O$ (20.4 mg, 0.2 mmol) in H_2O (4 mL) was carefully layered below a solution of H_4Clan (63.3 mg, 0.3 mmol) in acetone (10 mL) in a soda glass vial (OD = 25 mm), with a buffer layer of 1:1 v/v acetone/H_2O (4 mL). Black plate crystals visible on the vial walls within two days, in addition to a greenish-brown powder on the vial bottom. The crystalline product was isolated by gravimetric separation after five days of reaction. The brown powder was aspirated from the vials in ca. 4 mL mother liquor, then the crystalline product was resuspended in the mother liquor. The crystalline product was settled, and the turbid supernatant removed. The crystalline product was washed 2:1 v/v acetone/H_2O (3 × 10 mL) by resuspension of the crystalline product, re-sedimentation of the crystalline product and decantation of the supernatant. The crystalline product was then washed with acetone as above (3 × 10 mL), and finally resuspended in fresh acetone (10 mL) for storage. No yield was determined due to storage of the product under solvent to prevent desolvation.

2.4.4.7 (DiQ)[Fe$_2$(Clan)$_3$]·y(acetone)·zH$_2$O (2.6)

In air, a solution of $(NH_4)_2Fe^{II}(SO_4)_2 \cdot 6H_2O$ (19.6 mg, 0.05 mmol) and $[DiQ]Br_2$ (17.2 mg, 0.1 mmol) in H_2O (2 mL) was carefully layered below a solution of H_4Clan (21.0 mg, 0.1 mmol) in acetone (5 mL) in a soda glass vial (OD = 20 mm), with a buffer layer of 1:1 v/v acetone/H_2O (2 mL). Black parallelepiped crystals with a metallic blue-green lustre were visible on the vial walls in two days. After five days reaction, single crystals were transferred immediately from the mother liquid to a cryoprotective oil (see Section 2.4.5.1). No yield was determined due to the presence of multiple crystalline phases in the reaction.

2.4.4.8 (PDiQ)[Fe$_2$(Fan)$_3$]·yMeCN·zH2O (2.7)

In air, a solution of $Fe^{II}Cl_2 \cdot 4H_2O$ (19.9 mg, 0.1 mmol), $[PDiQ]Br_2$ (68.4 mg, 0.2 mmol) and $LiOAc \cdot 2H_2O$ (10.2 mg, 0.1 mmol) in H_2O (2 mL) was layered below a solution of H_4Fan (26.7 mg, 0.15 mmol) in MeCN (5 mL) in a soda glass vial (OD = 20 mm), with a buffer layer of 1:1 v/v MeCN/H_2O (2 mL). Black block crystals with an intense metallic blue lustre were visible on the vial walls in two days. After four days, single crystals were transferred immediately from the mother liquid to a cryoprotective oil (see Section 2.4.5.1). No yield was determined due to the presence of multiple crystalline phases in the reaction.

2.4.5 Single-Crystal X-ray Diffraction (SC-XRD)

2.4.5.1 General Considerations

Unless otherwise noted, crystals were transferred directly from the crystallisation mother liquor into an oil-based cryoprotectant to prevent solvent loss. The crystals were then transferred to either MiTeGen mounts or nylon loops for measurement of crystallographic data. Crystallographic data collection and processing from laboratory and synchrotron sources was performed as described in Chapter 7.

2.4.5.2 (MeV)[Mn(Clan)$_2$] (2.1$_{Mn}$) and (MeV)[Cd(Clan)$_2$] (2.1$_{Cd}$)

Crystallographic data were measured at 100 K (**2.1$_{Mn}$**) or 120 K (**2.1$_{Cd}$**) using a Rigaku XtaLAB Synergy-S diffractometer (Table 2.5). For both **2.1$_{Mn}$** and **2.1$_{Cd}$**, data beyond d = 0.8 Å was excluded from the refinement using the SHEL instructions. In **2.1$_{Mn}$**, rigid bond restraints were applied to non-hydrogen atoms (excluding Mn) in the structure using the RIGU instruction.

2.4.5.3 (MeV)[Mn$_2$(Clan)$_3$]·6MeCN (2.2a)

Crystallographic data for **2.2a** were measured at 100 K (Table 2.5) using a Rigaku XtaLAB Synergy-S diffractometer. Rigid bond restraints were applied to all non-hydrogen atoms (excluding Mn) in the structure using the RIGU instruction.

Table 2.5 Crystallographic data for **2.1$_{Mn}$**, **2.1$_{Cd}$** and **2.2a**.

Compound	(MeV)[Mn(Clan)$_2$] (**2.1$_{Mn}$**)	(MeV)[Cd(Clan)$_2$] (**2.1$_{Cd}$**)	(MeV)[Mn$_2$(Clan)$_3$]·6MeCN (**2.2a**)
Empirical formula	$C_{24}H_{14}N_2O_8Cl_4Mn$	$C_{24}H_{14}N_2O_8Cl_4Cd$	$C_{21}H_{16}N_4O_6Cl_3Mn$
Formula weight	655.11	712.57	581.67
Habit	Octahedron	Irregular	Plate
T / K	99.9(4)	121(2)	100.0(5)
Crystal system	Orthorhombic	Orthorhomic	Triclinic
Space group	*Fddd*	*Fddd*	*P−1*
a / Å	10.06100(10)	10.0460(2)	8.71340(10)
b / Å	18.0409(2)	18.1043(2)	11.69370(10)
c / Å	26.2770(3)	26.7761(4)	12.4715(2)
α / °	90	90	75.2910(10)
β / °	90	90	78.4070(10)
γ / °	90	90	83.1470(10)
V / Å^3	4769.53(9)	4869.92(13)	1200.89(3)
Z	8	8	2
ρ_{calc} / g cm^{-3}	1.825	1.944	1.609
μ / mm^{-1}	9.142	11.730	7.950
F_{000}	2632.0	2816.0	588.0
Crystal size / mm^3	0.269 × 0.202 × 0.056	0.159 × 0.07 × 0.054	0.267 × 0.17 × 0.031
Radiation	Cu Kα (λ = 1.54184 Å)	Cu Kα (λ = 1.54184 Å)	Cu Kα (λ = 1.54184 Å)
2θ range / °	10.616 to 149.004	10.6 to 148.808	7.448 to 148.96
Index ranges	$-12 \le h \le 11$ $-22 \le k \le 19$ $-32 \le l \le 17$	$-12 \le h \le 12$ $-22 \le k \le 16$ $-32 \le l \le 33$	$-10 \le h \le 10$ $-14 \le k \le 14$ $-15 \le l \le 15$
Total/independent reflections	5125/1210 [R_{int} = 0.0268, R_{sigma} = 0.0164]	6587/1242 [R_{int} = 0.0307, R_{sigma} = 0.0189]	40457/4893 [R_{int} = 0.0405, R_{sigma} = 0.0181]
Data/restraints/ parameters	1210/48/92	1242/0/92	4893/153/320
Goodness-of-fit on F^2	1.083	1.085	1.029
Final R indexes [$I \ge 2\sigma$ (I)]	R_1 = 0.0301, wR_2 = 0.0853	R_1 = 0.0244, wR_2 = 0.0659	R_1 = 0.0253, wR_2 = 0.0661
Final R indexes [all data]	R_1 = 0.0305, wR_2 = 0.0856	R_1 = 0.0249, wR_2 = 0.0663	R_1 = 0.0258, wR_2 = 0.0664
Largest diff. peak/hole/ e Å^{-3}	0.35/−0.35	0.52/−0.58	0.31/−0.30

2.4.5.4 (MeV)[Mn$_2$(Fan)$_3$(H$_2$O)$_2$]·2MeCN·0.5H$_2$O (2.3$_{Mn}$) and (MeV)[Cd$_2$(Fan)$_3$(H$_2$O)$_2$]·2MeCN·0.6H$_2$O (2.3$_{Cd}$)

Crystallographic data for **2.3$_{Mn}$** and **2.3$_{Cd}$** were measured at 100 K using Rigaku XtaLAB Synergy-S diffractometer (Table 2.6). For both **2.3$_{Mn}$** and **2.3$_{Cd}$**, rigid bond restraints were applied to all non-hydrogen atoms in the MeV^{2+} cations using the RIGU instruction; in **2.3$_{Cd}$**, similar distance restraints were also applied to all non-hydrogen atoms of the MeV^{2+} cations using the SIMU instruction. For the coordinated H_2O molecules in **2.3$_{Mn}$** and **2.3$_{Cd}$**, the H atom positions were determined by examining the F_C–F_O map, with interatomic distance restraints of 0.84 Å (O–H 1,2 distance) and 1.34 Å (H···H 1,3 distance) applied using the DFIX instruction.

In **2.3$_{Mn}$**, rigid bond and similar distance restraints were applied to the well-ordered MeCN molecule contained in the network void formed by the Mn_4 parallelogram, using the RIGU and SIMU instructions. Modelling of the remaining solvent was attempted, but the disorder was too severe to give a satisfactory solvent model. The scattering contribution of this disordered solvent was therefore accounted for using the SQUEEZE[74] routine of PLATON.[75] The content of disordered solvent in the compound was estimated from the electron count estimated by SQUEEZE as one MeCN and 0.5 H_2O per formula unit. The total estimated solvation is therefore (MeV)[Mn$_2$(Fan)$_3$(H$_2$O)$_2$]·(1+1)MeCN·0.5H$_2$O i.e. (MeV)[Mn$_2$(Fan)$_3$(H$_2$O)$_2$]·2MeCN·0.5H$_2$O. The slight discrepancy between solvation estimated by SC-XRD and that calculated by TGA and elemental analysis is due to partial solvent loss upon isolation of **2.3$_{Mn}$**.

In **2.3$_{Cd}$**, additional restraints were necessary for the solvent model. The thermal ellipsoids the MeCN molecule residing in the network void formed by the Cd_4 parallelogram, were unacceptably large when modelled at a single position. This solvent was therefore modelled as disordered over two positions, with the total occupancy fixed at one, and the occupancy of each site allowed to refine against each other. The thermal displacement parameters of equivalent atoms at the two positions were constrained to be equal using the EADP instruction. Rigid bond and similar distance restraints were applied to all non-hydrogen atoms in MeCN using the RIGU and SIMU instructions. Additional interatomic distance restraints of 1.137 Å

(C≡N 1,2 distance), 1.456 Å (C–CH_3 1,2 distance) and 2.593 Å (N···CH_3 1,3 distance) were applied using the DFIX instruction for all MeCN molecules. Modelling of the remaining residual electron density attributed to solvent was attempted, but the disorder was too severe to give a satisfactory structure refinement. The scattering contribution of the disordered solvent was therefore accounted for using the SQUEEZE[74] routine of PLATON.[75] The content of disordered solvent in the compound was estimated from the electron count estimated by SQUEEZE as one MeCN and 0.6 H_2O per formula unit. The total estimated solvation is therefore (MeV)[$Cd_2(Fan)_3(H_2O)_2$]·(1+1)MeCN·0.6H_2O i.e. (MeV)[$Cd_2(Fan)_3(H_2O)_2$]·2MeCN·0.6H_2O.

2.4.5.5 [Cd(Fan)(H_2O)$_2$] (2.4)

Crystallographic data for **2.4** were collected at 100 K using the MX2 beamline of the Australian Synchrotron at λ = 0.71073 Å (Table 2.6). For the coordinated H_2O molecules, the H atom positions were determined by examining the F_C–F_O map with interatomic distance restraints of 0.84 Å (O–H 1,2 distance) and 1.34 Å (H···H 1,3 distance) applied using the DFIX instruction. The data completeness to θ is low (87.6%) due to the low triclinic symmetry of **2.4** and because the MX2 beamline only allows crystal rotation about one axis (φ).

Table 2.6 Crystallographic data for **2.3$_{Mn}$**, **2.3$_{Cd}$** and **2.4**.

Compound	(MeV)[Mn_2(Fan)$_3$(H_2O)$_2$]·2MeCN·0.5H_2O (**2.3$_{Mn}$**)	(MeV)[Cd_2(Fan)$_3$(H_2O)$_2$]·2MeCN·0.6H_2O (**2.3$_{Cd}$**)	[Cd(Fan)(H_2O)$_2$] (**2.4**)
Empirical formula	$C_{34}H_{25}N_4O_{14.5}F_6Mn_2$[a]	$C_{34}H_{25.2}N_4O_{14.6}F_6Cd_2$[b]	$C_6H_4CdF_2O_6$
Formula weight	945.46[a]	1062.18[b]	322.49
Habit	Plate	Plate	Plate
T / K	100.00(1)	100.00(10)	100.15
Crystal system	Triclinic	Triclinic	Monoclinic
Space group	$P\bar{1}$	$P\bar{1}$	$C2/m$
a / Å	11.9381(2)	12.01850(10)	6.6686(13)
b / Å	12.4271(2)	12.37350(10)	8.0832(16)
c / Å	13.8921(2)	13.86430(10)	8.1130(16)
α / °	97.9620(10)	96.0150(10)	90
β / °	114.4250(10)	114.1410(10)	112.03(3)
γ / °	95.4990(10)	95.2320(10)	90
V / Å^3	1831.45(5)	1850.57(3)	405.40(16)
Z	2	2	2
ρ_{calc} / g cm^{-3}	1.714	1.906	2.642
μ / mm^{-1}	6.592	10.180	2.738
F_{000}	954.0[a]	1048.0[b]	308.0
Crystal size / mm^3	0.194 × 0.085 × 0.022	0.252 × 0.14 × 0.035	0.05 × 0.05 × 0.01
Radiation	Cu Kα (λ = 1.54184 Å)	Cu Kα (λ = 1.54184 Å)	Synchrotron (λ = 0.71073 Å)
2θ range / °	7.128 to 155.914	7.074 to 156.264	5.416 to 63.014
Index ranges	$-15 \le h \le 14$ $-15 \le k \le 15$ $-15 \le l \le 17$	$-14 \le h \le 15$ $-15 \le k \le 15$ $-17 \le l \le 17$	$-9 \le h \le 9$ $-11 \le k \le 11$ $-10 \le l \le 10$
Total/independent reflections	28688/7660 [R_{int} = 0.0390, R_{sigma} = 0.0368]	28800/7747 [R_{int} = 0.0340, R_{sigma} = 0.0296]	3614/629 [R_{int} = 0.0622, R_{sigma} = 0.0312]
Data/restraints/ parameters	7660/132/533	7747/252/544	629/2/43
Goodness-of-fit on F^2	1.038	1.080	1.149
Final R indexes [$I \ge 2\sigma(I)$]	R_1 = 0.0359, wR_2 = 0.0977	R_1 = 0.0251, wR_2 = 0.0674	R_1 = 0.0306, wR_2 = 0.0809
Final R indexes [all data]	R_1 = 0.0437, wR_2 = 0.1039	R_1 = 0.0270, wR_2 = 0.0686	R_1 = 0.306, wR_2 = 0.089
Largest diff. peak/hole/ e Å^{-3}	0.35/−0.44	0.44/−0.84	2.02/−1.41

Includes contribution of [a]: one MeCN and 0.5 H_2O (**2.3$_{Mn}$**); [b]: and one MeCN and 0.6 H_2O (**2.3$_{Cd}$**) disordered molecules per formula unit. The scattering contribution was accounted using the SQUEEZE[74] routine in PLATON.[75]

2.4.5.6 Dipyrido[1,2-a:2',1'-c]pyrazinediium dibromide (PDiQ(PF_6)$_2$)

Crystallographic data for PDiQ(PF_6)$_2$ were measured using Cu-Kα (λ = 1.54184 Å) and Mo-Kα (λ = 0.71073 Å) radiation using two independent crystals (Table 2.7). The initial structure solution from the Mo-Kα dataset indicated the structure was best refined in the non-centrosymmetric space group $P2_1$. To correctly assign putative stereochemistry, Cu-Kα radiation was also used to obtain higher anomalous completeness, with data reduction performed by treating Friedel mates as inequivalent using CrysAlis PRO. In both structure solutions, rigid bond restraints to all P and F atoms in the structure were applied using the RIGU instruction; for the structure measured using Cu-Kα radiation, rigid bonds were applied to all non-hydrogen atoms. In both structure solutions, severe disorder of one PF_6^- anion was observed, as indicated by the elongated thermal ellipsoids of the F atoms. This anion was modelled as disordered over three positions, with the total occupancy fixed at one, and the occupancy of each site refined against each other using the SUMP instruction. This yielded an occupancy for the three sites as 0.58, 0.21 and 0.20 for the Cu-Kα structure, and 0.59, 0.20 and 0.21 for the Mo-Kα structure. The atomic displacement parameters for the equivalent P and F atoms in the three parts were also constrained to be equal using the EADP instruction.

Checks for missed additional symmetry using the ADDSYM routine of PLATON[75] suggested the correct space group was $P2_1/m$. An attempted structure refinement in this space group revealed a non-physically sensible structure. The structure was refined as racemic twin using a TWIN −1 0 0 0 −1 0 0 0 −1 2 instruction, with the contribution of each enantiomer refined using the batch scale factor BASF instruction. Refinement of the Flack parameter to 0.48(2) and 0.39(5) for the Cu-Kα and Mo-Kα datasets indicates structure is correctly refined as a racemic twin in the non-centrosymmetric $P2_1$ space group. The structure solution for the 6,7-dihydro analogue, DiQ(PF_6)$_2$ also exhibits similar behaviour, with the structure refined using similar unit cell parameters and in the same $P2_1$ space group as PDiQ(PF_6)$_2$.[76] As with PDiQ(PF_6)$_2$, the presence of a racemic twin in the structure of DiQ(PF_6)$_2$ was indicated by the refined Flack parameter between 0 and 1. Racemic twins in the analogous compounds evidently arises from torsion about the central C–C bond (C6–C7 in PDiQ(PF_6)$_2$) which produces axial chirality in the molecule.

Table 2.7 Crystallographic data of $(PDiQ)(PF_6)_2$

Compound	$(PDiQ)(PF_6)_2$	$(PDiQ)(PF_6)_2$
Empirical formula	$C_{12}H_{10}F_{12}N_2P_2$	$C_{12}H_{10}F_{12}N_2P_2$
Formula weight	472.16	472.16
Habit	Rod	Block
T / K	100.00(10)	100.00(10)
Crystal system	Monoclinic	Monoclinic
Space group	$P2_1$	$P2_1$
a / Å	6.47198(3)	6.47480(10)
b / Å	15.12128(7)	15.12670(10)
c / Å	8.24233(4)	8.24540(10)
α / °	90	90
β / °	103.4544(5)	103.4430(1)
γ / °	90	90
V / Å^3	784.494(7)	785.448(17)
Z	2	2
ρ_{calc} / g cm^{-3}	1.994	1.993
μ / mm^{-1}	3.853	0.412
F_{000}	468.0	468.0
Crystal size / mm^3	0.18 × 0.043 × 0.017	0.327 × 0.174 × 0.104
Radiation	Cu Kα (λ = 1.54184 Å)	Mo Kα (λ = 0.71073 Å)
2θ range / °	11.038 to 155.546	5.08 to 76.058
Index ranges	$-8 \le h \le 8$ $-19 \le k \le 19$ $-8 \le l \le 10$	$-11 \le h \le 11$ $-26 \le k \le 25$ $-14 \le l \le 13$
Total/independent reflections	19092/3306 [R_{int} = 0.0380, R_{sigma} = 0.0163]	62693/8216 [R_{int} = 0.0289, R_{sigma} = 0.0173]
Data/restraints/ parameters	3306/368/299	8216/254/299
Goodness-of-fit on F^2	1.081	1.056
Final R indexes [$I \ge 2\sigma$ (I)]	R_1 = 0.0228, wR_2 = 0.0594	R_1 = 0.0257, wR_2 = 0.0686
Final R indexes [all data]	R_1 = 0.0228, wR_2 = 0.0594	R_1 = 0.0272, wR_2 = 0.0694
Largest diff. peak/hole/ e Å^{-3}	0.22/−0.37	0.46/−0.23
Flack parameter	0.481(18)	0.39(5)

2.4.5.7 (PDiQ)[Fe_2(Clan)$_3$]·4(acetone) (2.5)

Crystallographic data for **2.5** were measured between 100–260 K (Table 2.8). The asymmetric unit of **2.5** contains four crystallographically inequivalent acetone solvent molecules. Between 100–260 K, rigid bond and similarity restraints were applied to all non-hydrogen atoms of all modelled acetone solvent molecules in the structure, using the RIGU and SIMU instructions respectively. Between 100–260 K, one molecule was modelled as ordered, with one molecule modelled as disordered over two positions. The total occupancy of the two disorder sites was fixed at one, and the occupancy of the two sites allowed to refine against each other. For the disordered acetone molecule, additional restraints and constraints were applied as follows. For the two positions, the chemically equivalent 1,2 and 1,3 interatomic distances (C to C and C to O) were refined against each other by restraining them using the similar distance SADI instruction. The C and O atoms were restrained to be coplanar using the FLAT instruction for both partially occupied sites of the disordered solvent molecule.

Between 100–160 K, the two remaining acetone molecules per formula unit were modelled as ordered. Above 180 K, the thermal ellipsoids of these solvent molecules became unacceptability large, suggesting either static or dynamic disorder. Modelling of these molecules as disordered over multiple positions was attempted, however a satisfactory solvent model could not be obtained. Severe disorder of these solvents possibly results as they sit within the framework voids, and only participate in weak C–H···O interactions with the anionic network and cation. Therefore the scattering contribution of these disordered molecules was accounted for using the SQUEEZE[74] routine of PLATON,[75] with the solvation of **2.5** assumed as four acetone per formula unit i.e. equivalent to the solvation at 100 K at which all solvent molecules were well ordered. Critically, the electron count of this disordered solvent estimated by SQUEEZE (70–80 e^- per formula unit depending on temperature) matches reasonably well to that expected for two disordered acetone molecules (64 e^- per formula unit). At 200 K and above, additional similar distance restraints to the 1,2 and 1,3 interatomic distances (C to C and C to O) for chemically equivalent atoms were applied to the well-ordered acetone molecule, using the SADI instruction, as described for the disordered solvent above. The C and O atoms of this molecule were also restrained to be coplanar using the FLAT instruction.

Table 2.8 Crystallographic data of (PDiQ)[Fe_2(Clan)$_3$]·4(acetone) (**2.5**) at various temperatures.

***T* / K**	**100.00(10)**	**120.00(10)**	**140.00(10)**
Empirical formula	$C_{42}H_{34}Cl_6Fe_2N_2O_{16}$	$C_{42}H_{34}Cl_6Fe_2N_2O_{16}$	$C_{42}H_{34}Cl_6Fe_2N_2O_{16}$
Formula weight	1147.11	1147.11	1147.11
Habit	Plate	Plate	Plate
Crystal system	Monoclinic	Monoclinic	Monoclinic
Space group	$P2_1/n$	$P2_1/n$	$P2_1/n$
a / Å	12.75590(10)	12.76240(10)	12.77210(10)
b / Å	21.9697(2)	21.9966(2)	22.0324(2)
c / Å	17.99740(10)	18.00280(10)	18.01140(10)
α / °	90	90	90
β / °	100.2500(1)	100.3210(1)	100.4050(1)
γ / °	90	90	90
V / Å^3	4963.16(7)	4972.14(7)	4985.06(7)
Z	4	4	4
ρ_{calc} / g cm^{-3}	1.535	1.532	1.528
μ / mm^{-1}	8.257	8.242	8.220
F_{000}	2328.0	2328.0	2328.0
Crystal size / mm^3	0.228 × 0.191 × 0.041	0.228 × 0.191 × 0.041	0.228 × 0.191 × 0.041
Radiation	Cu Kα (λ = 1.54184 Å)	Cu Kα (λ = 1.54184 Å)	Cu Kα (λ = 1.54184 Å)
2θ range / °	6.41 to 156.026	6.408 to 155.914	6.402 to 156.044
Index ranges	$-12 \le h \le 15$ $-27 \le k \le 27$ $-22 \le l \le 22$	$-15 \le h \le 12$ $-27 \le k \le 27$ $-22 \le l \le 22$	$-15 \le h \le 12$ $-27 \le k \le 27$ $-22 \le l \le 22$
Total/independent reflections	54228/10429 [R_{int} = 0.0526, R_{sigma} = 0.0367]	54632/10460 [R_{int} = 0.0484, R_{sigma} = 0.0345]	55109/10495 [R_{int} = 0.0489, R_{sigma} = 0.0352]
Data/restraints/ parameters	10429/195/636	10460/195/636	10495/180/636
Goodness-of-fit on F^2	1.072	1.059	1.066
Final R indexes [$I \ge 2\sigma$ (I)]	R_1 = 0.0496, wR_2 = 0.1375	R_1 = 0.0487, wR_2 = 0.1347	R_1 = 0.0488, wR_2 = 0.1365
Final R indexes [all data]	R_1 = 0.0537, wR_2 = 0.1410	R_1 = 0.0533, wR_2 = 0.1386	R_1 = 0.0536, wR_2 = 0.1402
Largest diff. peak/hole/ e Å^{-3}	0.84/−0.72	0.76/−0.68	0.72/−0.63

Table 2.8(cont.) Crystallographic data of (PDiQ)[Fe_2(Clan)$_3$]·4(acetone) (**2.5**) at various temperatures.

***T* / K**	**160.00(10)**	**180.00(10)**	**200.00(10)**
Empirical formula	$C_{42}H_{34}Cl_6Fe_2N_2O_{16}$	$C_{42}H_{34}Cl_6Fe_2N_2O_{16}$[a]	$C_{42}H_{34}Cl_6Fe_2N_2O_{16}$[a]
Formula weight	1147.11	1147.11[a]	1147.11[a]
Habit	Plate	Plate	Plate
Crystal system	Monoclinic	Monoclinic	Monoclinic
Space group	$P2_1/n$	$P2_1/n$	$P2_1/n$
a / Å	12.78340(10)	12.79820(10)	12.81053(12)
b / Å	22.0758(2)	22.1192(2)	22.1640(2)
c / Å	18.01670(10)	18.02090(10)	18.02964(15)
α / °	90	90	90
β / °	100.5110(1)	100.6310(1)	100.7632(8)
γ / °	90	90	90
V / Å^3	4999.06(7)	5013.90(7)	5029.15(8)
Z	4	4	4
ρ_{calc} / g cm^{-3}	1.524	1.520	1.515
μ / mm^{-1}	8.197	8.173	8.148
F_{000}	2328.0	2328.0[a]	2328.0[a]
Crystal size / mm^3	0.228 × 0.191 × 0.041	0.228 × 0.191 × 0.041	0.228 × 0.191 × 0.041
Radiation	Cu Kα (λ = 1.54184 Å)	Cu Kα (λ = 1.54184 Å)	Cu Kα (λ = 1.54184 Å)
2θ range / °	6.398 to 156.096	6.394 to 155.818	6.388 to 155.894
Index ranges	$-12 \le h \le 15$ $-27 \le k \le 27$ $-22 \le l \le 22$	$-16 \le h \le 12$ $-27 \le k \le 27$ $-22 \le l \le 22$	$-16 \le h \le 12$ $-27 \le k \le 27$ $-22 \le l \le 22$
Total/independent reflections	55416/10529 [R_{int} = 0.0533, R_{sigma} = 0.0374]	55867/10558 [R_{int} = 0.0559, R_{sigma} = 0.0406]	56306/10575 [R_{int} = 0.0509, R_{sigma} = 0.0363]
Data/restraints/ parameters	10529/195/636	10558/87/560	10575/147/560
Goodness-of-fit on F^2	1.058	1.047	1.059
Final R indexes [$I \ge 2\sigma(I)$]	R_1 = 0.0501, wR_2 = 0.1402	R_1 = 0.0455, wR_2 = 0.1249	R_1 = 0.0421, wR_2 = 0.1171
Final R indexes [all data]	R_1 = 0.0551, wR_2 = 0.1445	R_1 = 0.0506, wR_2 = 0.1288	R_1 = 0.0476, wR_2 = 0.1211
Largest diff. peak/hole/ e Å^{-3}	0.67/−0.64	0.53/−0.61	0.63/−0.46

[a]: Includes contribution of two severely disordered acetone molecules per formula unit. The scattering contribution was accounted using the SQUEEZE[74] routine in PLATON.[75]

Table 2.8(cont.) Crystallographic data of (PDiQ)[$Fe_2(Clan)_3$]·4(acetone) (**2.5**) at various temperatures.

***T* / K**	**220.00(10)**	**240.00(10)**	**260.00(10)**
Empirical formula	$C_{42}H_{34}Cl_6Fe_2N_2O_{16}$[a]	$C_{42}H_{34}Cl_6Fe_2N_2O_{16}$[a]	$C_{42}H_{34}Cl_6Fe_2N_2O_{16}$[a]
Formula weight	1147.11[a]	1147.11[a]	1147.11[a]
Habit	Plate	Plate	Plate
Crystal system	Monoclinic	Monoclinic	Monoclinic
Space group	$P2_1/n$	$P2_1/n$	$P2_1/n$
a / Å	12.81850(10)	12.82470(10)	12.8230(2)
b / Å	22.2056(2)	22.2387(2)	22.2566(5)
c / Å	18.03830(10)	18.04550(10)	18.0551(2)
α / °	90	90	90
β / °	100.8890(1)	101.0020(10)	101.035(2)
γ / °	90	90	90
V / Å^3	5042.02(7)	5052.07(7)	5057.59(15)
Z	4	4	4
ρ_{calc} / g cm^{-3}	1.511	1.508	1.507
μ / mm^{-1}	8.128	8.111	8.103
F_{000}	2328.0[a]	2328.0[a]	2328.0[a]
Crystal size / mm^3	0.228 × 0.191 × 0.041	0.228 × 0.191 × 0.041	0.228 × 0.191 × 0.041
Radiation	Cu Kα (λ = 1.54184 Å)	Cu Kα (λ = 1.54184 Å)	Cu Kα (λ = 1.54184 Å)
2θ range / °	6.382 to 155.768	6.38 to 156.204	6.376 to 156.506
Index ranges	$-16 \le h \le 12$ $-27 \le k \le 28$ $-22 \le l \le 22$	$-12 \le h \le 16$ $-27 \le k \le 28$ $-22 \le l \le 22$	$-12 \le h \le 16$ $-27 \le k \le 28$ $-22 \le l \le 22$
Total/independent reflections	56381/10590 [R_{int} = 0.0542, R_{sigma} = 0.0408]	56557/10621 [R_{int} = 0.0603, R_{sigma} = 0.0438]	56488/10626 [R_{int} = 0.0678, R_{sigma} = 0.0495]
Data/restraints/ parameters	10590/145/560	10621/147/556	10626/147/556
Goodness-of-fit on F^2	1.045	1.062	1.046
Final R indexes [$I \ge 2\sigma(I)$]	R_1 =0.0451, wR_2 = 0.1236	R_1 = 0.0478, wR_2 = 0.1322	R_1 = 0.0583, wR_2 = 0.1602
Final R indexes [all data]	R_1 = 0.0520, wR_2 = 0.1284	R_1 = 0.0561, wR_2 = 0.1384	R_1 = 0.0718, wR_2 = 0.1709
Largest diff. peak/hole/ e Å^{-3}	0.54/−0.53	0.68/−0.50	1.20/−0.67

[a]: Includes contribution of two severely disordered acetone molecules per formula unit. The scattering contribution was accounted using the SQUEEZE[74] routine in PLATON.[75]

2.4.5.8 (DiQ)[Fe$_2$(Clan)$_3$]·4(acetone)·1.5H$_2$O (2.6)

Crystallographic data for **2.6** were measured at 100 K (Table 2.9). The initial structure solution revealed the presence of one well-ordered and three severely disordered acetone molecules in the asymmetric unit. A model for these disordered solvent molecules could not be obtained, due to the residual positive electron density around the disordered solvent molecules within the framework voids. Assignment of this electron density as additional partial occupancy sites of acetone was not successful, as the arrangements of the peaks of residual peaks were not consistent with the molecular geometry of acetone, instead being ascribed to partial occupancy H_2O molecules. The scattering contribution of the severely disordered solvent was accounted for using the SQUEEZE[74] routine of PLATON.[75] The content of disordered solvent in the compound was estimated from the electron count estimated by SQUEEZE as three acetone and 1.5 H_2O per formula unit. The total estimated solvation is therefore (DiQ)[Fe$_2$(Clan)$_3$]·4(acetone)·1.5H$_2$O.

2.4.5.9 (PDiQ)[Fe$_2$(Fan)$_3$]·8.2MeCN (2.7)

Crystallographic data for **2.7** were measured using the MX1 beamline of the Australian Synchrotron at λ = 0.71073 Å. Data beyond d = 0.8 Å was excluded from the refinement using the SHEL instructions, due to the closest approach of the detector to the Smargon diffractometer preventing high completeness beyond d = 0.8 Å. Rigid bond restraints were applied to all non-hydrogen atoms (excluding Fe) in the structure using the RIGU instruction. The electron density difference (F_O–F_C) map revealed significant residual positive electron density in the network void space. Assignment of this electron density as MeCN solvent molecules was attempted, however only one MeCN molecule per asymmetric unit could be modelled satisfactorily, due to severe disorder of the remaining MeCN about multiple special positions. The structure refinement of **2.7** therefore only models one well-ordered MeCN molecule. The scattering contribution of the remaining disordered solvent was account for using the SQUEEZE[74] routine of PLATON.[75] The content of disordered solvent in the compound was estimated from the electron count estimated by SQUEEZE as 7.2 MeCN per formula unit. The total estimated solvation is therefore (PDiQ)[Fe$_2$(Fan)$_3$]·(1+7.2)MeCN i.e. (PDiQ)[Fe$_2$(Fan)$_3$]·8.2MeCN.

Table 2.9 Crystallographic data for **2.6** and **2.7**.

Compound	(DiQ)[Fe_2(Clan)$_3$]·4(acetone)·1.5H_2O (**2.6**)	(PDiQ)[Fe_2(Fan)$_3$]·8.2MeCN (**2.7**)
Empirical formula	$C_{41}H_{39}N_2O_{17.5}Cl_6Fe_2$[a]	$C_{23.2}F_3FeH_{17.3}N_{5.1}O_6$[b]
Formula weight	1164.14[a]	576.37[b]
Habit	Plank	Plate
T / K	100.00(10)	100.15(10)
Crystal system	Triclinic	Orthorhombic
Space group	$P\bar{1}$	*Pnma*
a / Å	12.77320(10)	13.290(3)
b / Å	12.91310(10)	15.360(3)
c / Å	18.00580(10)	23.900(5)
α / °	90.3170(10)	90
β / °	102.1440(10)	90
γ / °	116.6370(10)	90
V / Å^3	2578.29(4)	4878.8(18)
Z	2	8
ρ_{calc} / g cm^{-3}	1.500	1.569
μ / mm^{-1}	7.976	0.691
F_{000}	1186.00[a]	2346.0[b]
Crystal size / mm^3	0.342 × 0.123 × 0.049	0.3 × 0.2 × 0.1
Radiation	Cu Kα (λ = 1.54184 Å)	Synchrotron (λ = 0.710874 Å)
2θ range / °	5.054 to 156.094	3.152 to 52.744
Index ranges	$-16 \le h \le 15$ $-16 \le k \le 16$ $-16 \le l \le 22$	$-16 \le h \le 16$ $-19 \le k \le 19$ $-29 \le l \le 29$
Total/independent reflections	45643/10848 [R_{int} = 0.0313, R_{sigma} = 0.0253]	175604/5186 [R_{int} = 0.0312, R_{sigma} = 0.0074]
Data/restraints/ parameters	10848/0/507	5186/174/254
Goodness-of-fit on F^2	1.034	1.115
Final R indexes [$I \ge 2\sigma(I)$]	R_1 =0.0299, wR_2 = 0.0789	R_1 =0.0689, wR_2 = 0.1632
Final R indexes [all data]	R_1 =0.0308, wR_2 = 0.0795	R_1 =0.0692, wR_2 = 0.1633
Largest diff. peak/hole/ e Å^{-3}	0.56/−0.45	0.64/−0.56

Includes the contribution of [a]: three acetone and 1.5 H2O (**2.6**); [b]: 7.2 MeCN (**2.7**) disordered solvent molecules per formula unit. The scattering contribution was accounted using the SQUEEZE[74] routine in PLATON.[75].

2.4.6 Powder X-ray Diffraction (P-XRD)

P-XRD measurements were performed using laboratory (**2.1$_{Mn}$**, **2.1$_{Cd}$**, **2.2**, **2.3$_{Mn}$** and **2.3$_{Cd}$**, **2.5**) or synchrotron (**2.2b**) instrumentation as described in Chapter 7. For **2.2a** and **2.5**, the solvated crystalline products were gently ground under solvent (MeCN and acetone respectively) to prevent solvent loss, then transferred as slurries to borosilicate capillaries (OD = 0.7 mm) before being flame-sealed. For isolated samples (**2.1$_{Mn}$**, **2.1$_{Cd}$**, **2.2b**, **2.3$_{Mn}$** and **2.3$_{Cd}$**), the compounds were gently ground in air, then transferred to borosilicate capillaries (OD = 0.5 mm), before being flame-sealed.

2.5 References

[1] M. Clemente-León, E. Coronado, C. Martí-Gastaldo, F. M. Romero, *Chem. Soc. Rev.* **2011**, *40*, 473-497.

[2] M. L. Mercuri, F. Congiu, G. Concas, S. A. Sahadevan, *Magnetochemistry* **2017**, *3*, 17.

[3] H. Tamaki, Z. J. Zhong, N. Matsumoto, S. Kida, M. Koikawa, N. Achiwa, Y. Hashimoto, H. Okawa, *J. Am. Chem. Soc.* **1992**, *114*, 6974-6979.

[4] C. Mathonière, C. J. Nuttall, S. G. Carling, P. Day, *Inorg. Chem.* **1996**, *35*, 1201-1206.

[5] S. Decurtins, H. W. Schmalle, P. Schneuwly, H. R. Oswald, *Inorg. Chem.* **1993**, *32*, 1888-1892.

[6] R. Andrés, M. Brissard, M. Gruselle, C. Train, J. Vaissermann, B. Malézieux, J.-P. Jamet, M. Verdaguer, *Inorg. Chem.* **2001**, *40*, 4633-4640.

[7] E. Coronado, J. R. Galán-Mascarós, C. J. Gómez-García, J. M. Martínez-Agudo, *Inorg. Chem.* **2001**, *40*, 113-120.

[8] R. S. Fishman, M. Clemente-León, E. Coronado, *Inorg. Chem.* **2009**, *48*, 3039-3046.

[9] L. E. Darago, M. L. Aubrey, C. J. Yu, M. I. Gonzalez, J. R. Long, *J. Am. Chem. Soc.* **2015**, *137*, 15703-15711.

[10] I.-R. Jeon, B. Negru, R. P. Van Duyne, T. D. Harris, *J. Am. Chem. Soc.* **2015**, *137*, 15699-15702.

[11] S. Kawata, S. Kitagawa, H. Kumagai, C. Kudo, H. Kamesaki, T. Ishiyama, R. Suzuki, M. Kondo, M. Katada, *Inorg. Chem.* **1996**, *35*, 4449-4461.

[12] M. Shota, Y. Teppei, K. Hiroshi, *Chem. Lett.* **2009**, *38*, 654-655.

[13] B. F. Abrahams, K. D. Lu, B. Moubaraki, K. S. Murray, R. Robson, *J. Chem. Soc., Dalton Trans.* **2000**, 1793-1797.

[14] J. A. DeGayner, K. Wang, T. D. Harris, *J. Am. Chem. Soc.* **2018**, *140*, 6550-6553.

[15] B. F. Abrahams, A. D. Dharma, B. Dyett, T. A. Hudson, H. Maynard-Casely, C. J. Kingsbury, L. J. McCormick, R. Robson, A. L. Sutton, K. F. White, *Dalton Trans.* **2016**, *45*, 1339-1344.

[16] L. Androš Dubraja, K. Molčanov, D. Žilić, B. Kojić-Prodić, E. Wenger, *New J. Chem.* **2017**, *41*, 6785-6794.

[17] S. Kawata, S. Kitagawa, M. Kondo, I. Furuchi, M. Munakata, *Angew. Chem. Int. Ed. Engl.* **1994**, *33*, 1759-1761.

[18] H. Kumagai, S. Kawata, S. Kitagawa, *Inorg. Chim. Acta* **2002**, *337*, 387-392.

[19] C. Robl, A. Weiss, *Mater. Res. Bull.* **1987**, *22*, 497-504.

[20] C. Robl, *Mater. Res. Bull.* **1987**, *22*, 1483-1491.

[21] B. F. Abrahams, M. J. Grannas, T. A. Hudson, S. A. Hughes, N. H. Pranoto, R. Robson, *Dalton Trans.* **2011**, *40*, 12242-12247.

[22] T.-T. Luo, Y.-H. Liu, H.-L. Tsai, C.-C. Su, C.-H. Ueng, K.-L. Lu, *Eur. J. Inorg. Chem.* **2004**, *2004*, 4253-4258.

[23] G. V. Shilov, Z. K. Nikitina, N. S. Ovanesyan, S. M. Aldoshin, V. D. Makhaev, *Russ. Chem. Bull.* **2011**, *60*, 1209-1219.

[24] M. E. Ziebel, L. E. Darago, J. R. Long, *J. Am. Chem. Soc.* **2018**, *140*, 3040-3051.

[25] S. Benmansour, A. Abhervé, P. Gómez-Claramunt, C. Vallés-García, C. J. Gómez-García, *ACS Appl. Mater. Interfaces* **2017**, *9*, 26210-26218.

[26] L. Liu, J. A. DeGayner, L. Sun, D. Z. Zee, T. D. Harris, *Chem. Sci.* **2019**, *10*, 4652-4661.

[27] L. Liu, L. Li, J. A. DeGayner, P. H. Winegar, Y. Fang, T. D. Harris, *J. Am. Chem. Soc.* **2018**, *140*, 11444-11453.

[28] C. J. Kingsbury, B. F. Abrahams, D. M. D'Alessandro, T. A. Hudson, R. Murase, R. Robson, K. F. White, *Cryst. Growth Des.* **2017**, *17*, 1465-1470.

[29] C. J. Kingsbury, B. F. Abrahams, J. E. Auckett, H. Chevreau, A. D. Dharma, S. Duyker, Q. He, C. Hua, T. A. Hudson, K. S. Murray, W. Phonsri, V. K. Peterson, R. Robson, K. F. White, *Chem. Eur. J.* **2019**, *25*, 5222-5234.

[30] K. Bondaruk, C. Hua, *Cryst. Growth Des.* **2019**, *19*, 3338-3347.

[31] J. Chen, Y. Sekine, Y. Komatsumaru, S. Hayami, H. Miyasaka, *Angew. Chem. Int. Ed.* **2018**, *57*, 12043-12047.

[32] P. E. Riley, S. F. Haddad, K. N. Raymond, *Inorg. Chem.* **1983**, *22*, 3090-3096.

[33] B. F. Abrahams, J. Coleiro, K. Ha, B. F. Hoskins, S. D. Orchard, R. Robson, *J. Chem. Soc., Dalton Trans.* **2002**, 1586-1594.

[34] S. Benmansour, I. Pérez-Herráez, C. Cerezo-Navarrete, G. López-Martínez, C. Martínez Hernández, C. J. Gómez-García, *Dalton Trans.* **2018**, *47*, 6729-6741.

[35] M. E. Ziebel, J. C. Ondry, J. R. Long, *Chem. Sci.* **2020**, *11*, 6690-6700.

[36] B. F. Abrahams, T. A. Hudson, L. J. McCormick, R. Robson, *Cryst. Growth Des.* **2011**, *11*, 2717-2720.

[37] S. Benmansour, C. Vallés-García, P. Gómez-Claramunt, G. Mínguez Espallargas, C. J. Gómez-García, *Inorg. Chem.* **2015**, *54*, 5410-5418.

[38] R. Murase, B. F. Abrahams, D. M. D'Alessandro, C. G. Davies, T. A. Hudson, G. N. L. Jameson, B. Moubaraki, K. S. Murray, R. Robson, A. L. Sutton, *Inorg. Chem.* **2017**, *56*, 9025-9035.

[39] K. Nakabayashi, S.-i. Ohkoshi, *Inorg. Chem.* **2009**, *48*, 8647-8649.

[40] E. Coronado, J. R. Galán-Mascarós, C. J. Gómez-García, V. Laukhin, *Nature* **2000**, *408*, 447-449.

[41] A. Alberola, E. Coronado, J. R. Galán-Mascarós, C. Giménez-Saiz, C. J. Gómez-García, *J. Am. Chem. Soc.* **2003**, *125*, 10774-10775.

[42] A. Abhervé, M. Clemente-León, E. Coronado, C. J. Gómez-García, M. Verneret, *Inorg. Chem.* **2014**, *53*, 12014-12026.

[43] A. Abhervé, S. Mañas-Valero, M. Clemente-León, E. Coronado, *Chem. Sci.* **2015**, *6*, 4665-4673.

[44] B. F. Abrahams, A. M. Bond, T. H. Le, L. J. McCormick, A. Nafady, R. Robson, N. Vo, *Chem. Commun.* **2012**, *48*, 11422-11424.

[45] R. Murase, C. J. Commons, T. A. Hudson, G. N. L. Jameson, C. D. Ling, K. S. Murray, W. Phonsri, R. Robson, Q. Xia, B. F. Abrahams, D. M. D'Alessandro, *Inorg. Chem.* **2020**, *59*, 3619-3630.

[46] H.-N. Zhang, Y. Lu, W.-X. Gao, Y.-J. Lin, G.-X. Jin, *Chem. Eur. J.* **2018**, *24*, 18913-18921.

[47] W. R. Reed, M. A. Dunstan, R. W. Gable, W. Phonsri, K. S. Murray, R. A. Mole, C. Boskovic, *Dalton Trans.* **2019**, *48*, 15635-15645.

[48] Y. Sekine, J. Chen, N. Eguchi, H. Miyasaka, *Chem. Commun.* **2020**.

[49] L. Shimoni, J. P. Glusker, *Struct. Chem.* **1994**, *5*, 383-397.

[50] W. R. Dolbier, *J. Fluorine Chem.* **2005**, *126*, 157-163.

[51] M. Atzori, S. Benmansour, G. Mínguez Espallargas, M. Clemente-León, A. Abhervé, P. Gómez-Claramunt, E. Coronado, F. Artizzu, E. Sessini, P. Deplano, A. Serpe, M. L. Mercuri, C. J. Gómez García, *Inorg. Chem.* **2013**, *52*, 10031-10040.

[52] S. Alvarez, *Chem. Rev.* **2015**, *115*, 13447-13483.

[53] S. Alvarez, D. Avnir, M. Llunell, M. Pinsky, *New J. Chem.* **2002**, *26*, 996-1009.

[54] N. W. Ockwig, O. Delgado-Friedrichs, M. O'Keeffe, O. M. Yaghi, *Acc. Chem. Res.* **2005**, *38*, 176-182.

[55] E. V. Alexandrov, V. A. Blatov, A. V. Kochetkov, D. M. Proserpio, *CrystEngComm* **2011**, *13*, 3947-3958.

[56] A. P. Shevchenko, E. V. Alexandrov, A. A. Golov, O. A. Blatova, A. S. Duyunova, V. A. Blatov, *Chem. Commun.* **2020**, *56*, 9616-9619.

[57] H. Gao, X.-M. Zhang, *Dalton Trans.* **2012**, *41*, 1562-1567.

[58] T. M. Bockman, J. K. Kochi, *J. Org. Chem.* **1990**, *55*, 4127-4135.

[59] N. Leblanc, N. Mercier, O. Toma, A. H. Kassiba, L. Zorina, P. Auban-Senzier, C. Pasquier, *Chem. Commun.* **2013**, *49*, 10272-10274.

[60] W. W. Porter, III, T. P. Vaid, *J. Org. Chem.* **2005**, *70*, 5028-5035.

[61] W. W. Porter, III, T. P. Vaid, A. L. Rheingold, *J. Am. Chem. Soc* **2005**, *127*, 16559-16566.

[62] F. Huang, K. A. Switek, L. N. Zakharov, F. R. Fronczek, C. Slebodnick, M. Lam, J. A. Golen, W. S. Bryant, P. E. Mason, A. L. Rheingold, M. Ashraf-Khorassani, H. W. Gibson, *J. Org. Chem.* **2005**, *70*, 3231-3241.

[63] F. Yang, J.-C. Deng, Z.-G. Li, J.-W. Xu, *Acta Crystallogr. E* **2008**, *64*, o253.

[64] K. V. Nielson, L. Zhang, Q. Zhang, T. L. Liu, *Inorg. Chem.* **2019**, *58*, 10756-10760.

[65] K. Molčanov, M. Jurić, B. Kojić-Prodić, *Dalton Trans.* **2013**, *42*, 15756-15765.

[66] K. Molčanov, M. Jurić, B. Kojić-Prodić, *Dalton Trans.* **2014**, *43*, 7208-7218.

[67] M. Jurić, K. Molčanov, D. Žilić, B. Kojić-Prodić, *RSC Adv.* **2016**, *6*, 62785-62796.

[68] S. R. Batten, S. M. Neville, D. Turner, *Coordination Polymers: Design, Analysis and Applications*, The Royal Society of Chemistry, Cambridge, UK, **2009**.

[69] J. A. DeGayner, I.-R. Jeon, L. Sun, M. Dincă, T. D. Harris, *J. Am. Chem. Soc.* **2017**, *139*, 4175-4184.

[70] M. P. van Koeverden, B. F. Abrahams, D. M. D'Alessandro, P. W. Doheny, C. Hua, T. A. Hudson, G. N. L. Jameson, K. S. Murray, W. Phonsri, R. Robson, A. L. Sutton, *Chem. Mater.* **2020**, *32*, 7551-7563.

[71] J. Chen, Y. Sekine, A. Okazawa, H. Sato, W. Kosaka, H. Miyasaka, *Chem. Sci.* **2020**, *11*, 3610-3618.

[72] V. Vuković, K. Molčanov, C. Jelsch, E. Wenger, A. Krawczuk, M. Jurić, L. Androš Dubraja, B. Kojić-Prodić, *Cryst. Growth Des.* **2019**, *19*, 2802-2810.

[73] K. A. Collins, R. J. Saballos, M. S. Fataftah, D. Puggioni, J. M. Rondinelli, D. E. Freedman, *Chem. Sci.* **2020**, *11*, 5922-5928.

[74] A. L. Spek, *Acta Crystallogr. C* **2015**, *71*, 9-18.

[75] A. L. Spek, *Acta Crystallogr. D* **2009**, *65*, 148-155.

[76] F. Huang, C. Slebodnick, K. A. Switek, H. W. Gibson, *Tetrahedron* **2007**, *63*, 2829-2839.

[77] K. Wallenfels, K. Friedrich, *Chem. Ber.* **1960**, *93*, 3070-3082.

[78] M. Essers, G. Haufe, *J. Chem. Soc., Perkin Trans. 1* **2002**, 2719-2728.

[79] D. H. Corr, E. E. Glover, *J. Chem. Soc.* **1965**, 5816-5819.

[80] I. C. Calder, W. H. F. Sasse, *Tetrahedron Lett.* **1965**, *6*, 1465-1469.

[81] R. W. L. Kimber, J. C. Parham, *J. Org. Chem.* **1963**, *28*, 3205-3206.

[82] H. Brintzinger, R. Titzmann, *Chem. Ber.* **1952**, *85*, 344-345.

This page intentionally left blank

This page intentionally left blank

Chapter 3 Structure and Properties of Mixed-Valence Anionic Iron–Tetraoxolene Frameworks Containing Phenanthrolinediium Cations

3.1 Introduction 171

3.1.1 Mixed-Valence Tetraoxolene Coordination Polymers 171

3.1.2 Chapter Aim 173

3.2 Results and Discussion 174

3.2.1 Synthesis and Structure Description 174

3.2.2 Variable-Temperature Single-Crystal X-ray Diffraction 189

3.2.3 Solvent Exchange 192

3.2.4 ^{57}Fe Mössbauer Spectroscopy 199

3.2.5 Electronic Spectroscopy 201

3.2.6 Electrochemistry 206

3.2.7 Magnetism 210

3.2.8 Electrical Conductivity 219

3.3 Conclusion 222

3.4 Experimental 223

3.4.1 General Considerations 223

3.4.2 Ligand Synthesis 224

3.4.3 Cation Synthesis 226

3.4.4 Coordination Polymer Synthesis 227

3.4.5 Single-Crystal X-ray Diffraction (SC-XRD) 233

3.4.6 Powder X-ray Diffraction (P-XRD) 240

3.5 References 240

This page intentionally left blank

3.1 Introduction

3.1.1 Mixed-Valence Tetraoxolene Coordination Polymers

Mixed valency is an important characteristic that can facilitate long-range charge transport, and strong magnetic coupling between paramagnetic metal centres in 1-, 2- and 3-dimensional (1D, 2D and 3D respectively) coordination polymers.[1, 2] Frameworks with intrinsic mixed valency are therefore especially attractive synthetic targets towards porous conductive and magnetic materials.[1-5] Tetraoxolene ligands are well-suited to the role as bridging ligands in mixed-valence coordination polymers because they can coordinate to metals either in the quinonoid dianion state ($dhbq^{2-}$ or Xan^{2-}), semiquinonoid radical trianion state ($dhbq^{3-\bullet}$ or $Xan^{3-\bullet}$), or the aromatic tetraanion state (thb^{4-} or Xan^{4-}).[6] Because the electroactivity of tetraoxolene ligands is maintained within coordination polymers, reversible switching of the magnetic or conductive states can therefore be externally triggered.[7-9] Metal–tetraoxolene coordination polymers with intrinsic mixed valency can be synthesised using suitably reducing M^{II} species, whose electrochemical potential coincides with the $Xan^{2-}/Xan^{3-\bullet}$ redox couple, for example Fe^{II}, V^{II}, Ti^{II}.[10-15] Spontaneous electron transfer from the M^{II} species to the Xan^{2-} state, then gives rise to ligand-centred mixed valency, comprising either $\{M^{III}–Xan^{2-}/Xan^{3-\bullet}\}$ or $\{M^{IV}–Xan^{3-\bullet}/Xan^{4-}\}$ manifolds, depending on the potentials of the $M^{II/III}$ and $M^{III/IV}$ couples relative to the $Xan^{2-/3-\bullet}$ and $Xan^{3-\bullet/4-}$ couples.[15] Alternatively, metal-centred mixed valency is afforded by reacting M^{II} species with tris-anilate $[M^{III}(Xan^{2-})_3]^{3-}$ complexes in the complex-as-a-ligand approach, affording compounds with $\{M^{II}/M^{III}–Xan^{2-}\}$ valence manifolds.[16-18]

When tetraoxolene ligands in multiple oxidation states exist in the framework, intervalence charge-transfer (IVCT) between the ligand states can give rise to long-range charge transport and therefore electrical conductivity. Additionally, the $Xan^{3-\bullet}$ state provides an effective conduit for spin exchange between paramagnetic metal centres via direct metal-radical coupling,[19-23] which greatly facilitates long-range magnetic ordering.[3, 24] Unsurprisingly, the conductive and magnetic properties of mixed-valence tetraoxolene frameworks are impacted by the degree of electron delocalisation in these materials. The presence of 3,6-substituents on tetraoxolene ligands allows variation of these sites to be used as a ‘molecular set screw’ to adjust the degree of electronic communication between metal sites provided by the ligands.[6]

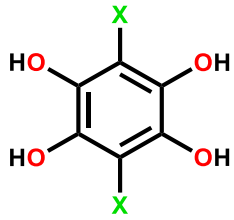
For example, Benmansour *et al.* demonstrated in the mixed-valence 2D honeycomb $[(H_3O)(H_2O)(phz)_3][Fe^{II}Fe^{III}(Xan)_3]$ frameworks (phz = phenazine; X= Cl, Br), the degree of electron localisation is influenced by the ligand substituents.[17] At room temperature both compounds are EPR silent, consistent with a valence averaged $Fe^{2.5+}$ state that is delocalised on the EPR spectroscopic timescale. Electron localisation i.e. distinct Fe^{II}-Fe^{III} sites, in the bromanilate compound was observed upon cooling to 40 K, indicated by the increasing EPR signal attributed to high-spin Fe^{III} (Fe^{III}_{HS}). In contrast, a Fe^{III}_{HS} signal was not observed in the chloranilate compound until cooled to 20 K, indicative of more facile electron transfer. This was the proposed rationale for the 10-fold higher electrical conductivity of the chloranilate compound, relative to the bromanilate analogue. The degree of ligand charge localisation also has a strong impact on the physical properties of mixed-valence tetraoxolene coordination polymers. A high degree of charge delocalisation over chemically equivalent sites e.g. $[M^{III}_2(Xan^{2.67-})_3]^{2-}$ or $[M^{2.5}_2(Xan^{2-})_3]^{-}$ valence formulations, typically results in higher electrical conductivity as long-range charge transport is energetically favourable in multiple directions.[10, 12, 13, 17, 18, 25] In contrast, localisation of valence states leads to decreased electrical conductivity, as charge-carrier hopping between sites becomes energetically more costly. However, the limit of completely localised of valence states e.g. a charge-ordered $[Fe^{III}_2(Xan^{2-})(Xan^{3-\bullet})_2]^{2-}$ formulation, can still give rise to interesting properties such as thermally-induced valence tautomerism or single-chain magnetism,[26-29] which are not observed in compounds with delocalised valence states. Elucidating strategies to precisely modulate the degree of valence localisation is therefore an important goal which could aid the design of new tetraoxolene frameworks with desirable properties.

To date, the vast majority of mixed-valence tetraoxolene frameworks fall into the first category comprising delocalised valence formulations. Mixed-valence frameworks with ligand charge-ordered formulations, such as $(^nPr_4N)_2[Fe_2(Xan)_3]$ (X = F, Cl, Br),[27-29] have proven rarer and their synthesis is arguably more serendipitous, with no clear strategy yet developed to predictably modulate the degree of charge ordering in mixed-valence tetraoxolene frameworks. In Chapter 1, the striking observation was made that strongly interacting or redox-active cations have rarely been incorporated into anionic metal–tetraoxolene materials,[30-33] with exclusive use of redox-inactive alkylammonium cations in conductive and magnetic

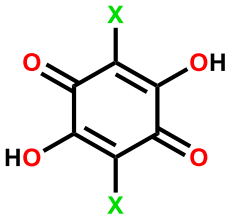
mixed-valence tetraoxolene coordination polymers.[10-12, 14, 15, 17, 18, 25, 27, 28, 34] By virtue of the rich electrochemistry and supramolecular interactions, viologen and viologen-like cations were deemed as ideal candidates to act as countercations in anionic metal–tetraoxolene coordination polymers. Chapter 2 demonstrated firstly that viologen and viologen-like cations facilitate diverse structural chemistry, producing a wide array of 1-, 2- and 3D metal–tetraoxolene coordination polymers. Secondly, viologen cations consistently induced localisation of the $Xan^{3-\bullet}$ valence state in mixed-valence Fe–tetraoxolene frameworks, giving ligand charge-ordered $[Fe^{III}_2(Xan^{2-})(Xan^{3-\bullet})_2]^{2-}$ formulations. It was proposed the combination of charge-transfer (CT) and strong Coulombic interactions between the π-electron deficient cations and the more electron-rich $Xan^{3-\bullet}$ form in the anionic mixed-valence networks was the driving force behind ligand charge ordering.

3.1.2 Chapter Aim

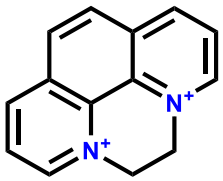
This chapter aims to extend the conclusions drawn in Chapter 2, with a particular focus on probing in greater detail, the physical properties of novel Fe–tetraoxolene frameworks which use viologen-like molecules as countercations. First, this chapter describes structural investigations of a family of mixed-valence Fe–tetraoxolene coordination polymers $(PhenQ)[Fe_2(Xan)_3]\cdot solvent$ (X = F, Cl, Br) containing the viologen-like 5,6-dihydropyrazino[1,2,3,4-*lmn*][1,10]-phenanthrolinediium ($PhenQ^{2+}$) cation (Scheme 3.1), in addition to an isostructural diamagnetic Zn analogue $(PhenQ)[Zn_2(Clan)_3]\cdot solvent$. Given the less predictable coordination chemistry of fluoranilate (Fan^{n-}) revealed in Chapter 2, the focus was initially to determine if an isostructural family of mixed-valence Fe–tetraoxolene coordination polymers could be obtained when viologens are employed as countercations. This was expected to provide further insight into the sensitivity of network structure and topology to the cation-framework interactions modulated by ligand substituents. This work was also intended to form the basis for future studies to systemically determine the impact of ligand substituents on the resultant conductive and magnetic properties.



3,6-Dihalo-1,2,4,5-tetrahydroxybenzene (H_4Xan, X = F, Cl, Br)



3,6-Dihalo-2,5-dihydroxy-1,4-benzoquinone (H_2Xan, X = F, Cl, Br)



5,6-Dihydropyrazino [1,2,3,4-*lmn*] phenanthrolindiium ($PhenQ^{2+}$)

Scheme 3.1 Structures of the tetraoxolene ligand precursors and viologen-like cation used in Chapter 3.

Considering the predictable viologen-framework interactions exhibited in mixed-valence Fe–tetraoxolene frameworks as revealed in Chapter 2, a second aim of this chapter was to understand how putative CT interactions between $PhenQ^{2+}$ and the anionic $[Fe_2(Xan)_3]^{2-}$ networks could impact the properties of the mixed-valence frameworks. For the Fe–chloranilate compound, $(PhenQ)[Fe_2(Clan)_3]\cdot$solvent, a combination of crystallographic, spectroscopic, magnetic, electrochemical and electrical conductivity experiments were undertaken to explore how cation-framework interactions modulated the physical properties of the compound, compared to similar mixed-valence Fe–chloranilate coordination polymers containing only redox-inactive cations.

3.2 Results and Discussion

3.2.1 Synthesis and Structure Description

As with all previous coordination polymers described in this thesis, a sample of the coordination polymer $(PhenQ)[Fe_2(Clan)_3]\cdot y MeCN\cdot z H_2O$ (**3.1^{Cl}a**) was synthesised using a slow diffusion reaction, by carefully layering a solution of $(NH_4)_2Fe^{II}(SO_4)_2\cdot 6H_2O$ and $(PhenQ)Br_2$ in H_2O below an MeCN solution of 3,6-dichloro-1,2,4,5-tetrahydroxybenzene (H_4Clan), with a buffer layer of 1:1 v/v MeCN–H_2O containing LiOAc. Following this procedure, black block crystals with a metallic blue-green lustre were visible on the vial walls within two days, in addition to a brownish-green flocculant powder on the vial bottoms. As with previous work conducted by the Abrahams-Robson group,[14, 35] slow diffusion reactions in

combination with slow aerial oxidation of the reduced H_4Clan form to the active H_2Clan form, were found to most readily yield crystals suitable for single-crystal X-ray diffraction (SC-XRD) analyses. A bulk sample for **3.1^{Cl}a** was readily synthesised by performing multiple diffusion reactions in parallel and combining the collected crystalline products during workup. The isostructural Zn^{II} compound, (PhenQ)[Zn_2(Clan)$_3$]·*y*MeCN·zH_2O (**3.2**) was synthesised in a similar reaction using $Zn^{II}(NO_3)_2$·6H_2O and PhenQ$(NO_3)_2$ in place of $(NH_4)_2Fe^{II}(SO_4)_2$·6H_2O and (PhenQ)Br_2. Although single crystals of **3.2** could be produced using (PhenQ)Br_2, the reactions were contaminated with a copious white precipitate which was presumably a tetrabromidozincate(II) species, which could not be separated from the desired coordination polymer during workup.

Single crystals of the isostructural Fe–fluoranilate and Fe–bromanilate compounds, namely (PhenQ)[Fe_2(Fan)$_3$] *y*Acetone·zH_2O (**3.1^{F}**) and (PhenQ)[Fe_2(Bran)$_3$] *y*MeCN·zH_2O (**3.1^{Br}**), were producing by slight variations to the aforementioned conditions. Bulk samples of **3.1^{F}** and **3.1^{Br}** for analyses could not be isolated due to difficulties obtaining phase pure materials despite repeated attempts. Reactions targeting **3.1^{Br}** were contaminated with a trisbromanilatoferrate(III) salt ((PhenQ)$_3$[Fe(bran)$_3$]$_2$·*y*H_2O, **3.3**), which grew concurrently with the desired **3.1^{Br}** phase. Co-crystallisation of **3.3** was possibly due to the lower solubility of the trisbromanilatoferrate(III) complex compared to the trischloranilatoferrate(III) complex. The structures of **3.1^{Cl}a**, **3.1^{F}**, **3.1^{Br}** and **3.2** were determined by SC-XRD with satisfactory refinements obtained in the monoclinic *C*2/*m* space group (Table 3.5, Table 3.6 & Table 3.7). The **3.1^{Cl}a** compound is archetypal of the family and described in detail below. Crystallographic analyses revealed the compounds are 2D anionic coordination polymers with a network composition of $[M_2(Xan)_3]^{x-}$. Each metal centre lies upon a two-fold axis and resides in a slightly distorted octahedral coordination environment, bound to six O donor atoms of three bridging Xan^{n-} ligands. The distortion away from ideal octahedral coordination geometry was quantified using Continuous Shape Measure (CShM) parameters,[36, 37] confirming very little distortion away from ideal octahedral metal coordination geometry (Table 3.1).

Table 3.1 CShM analyses of the possible metal coordination geometries in **3.1^{Cl}a**, **3.1^{F}**, **3.1^{Br}** and **3.2**.

Compound	Coordination Geometry (Symmetry)				
	HP-6 (D_{6h})	**PPY-6** (C_{5v})	**OC-6** (O_h)	**TPR-6** (D_{3h})	**JPPY-6** (C_{5v})
3.1^{Cl}a	31.881	23.345	**1.370**	11.016	27.270
3.1^{F}	32.641	24.888	**1.185**	10.641	28.738
3.1^{Br}	31.368	23.724	**1.282**	11.454	27.655
3.2	30.753	23.932	**1.352**	11.491	27.788

HP-6: Hexagon; PPY-6: Pentagonal pyramid; OC-6: Octahedron; TPR-6: Trigonal prism; JPPY-6: Johnson pentagonal pyramid J2

Every Fe centre (either Δ or Λ configuration) is linked via the bridging Clan^{n-} ligands to three Fe centres of opposite configuration, resulting in a two-dimensional (6,3) honeycomb sheet (Figure 3.1). The anionic sheets are stacked parallel to the crystallographic *c* axis, with the sheet-to-sheet spacing corresponding to the length of the *c* axis (Fig. 1b: 8.4943(2) Å for **3.1^{Cl}a**, 8.78110(10) for **3.1^{F}**, 8.7395(13) for **3.1^{Br}** and 8.49560(1) for **3.2**). The phase purity of bulk samples of **3.1^{Cl}a** and **3.2** was confirmed by P-XRD analyses, measured as slurries of the samples in MeCN to prevent desolvation (Figure 3.2 & Figure 3.3). Slight differences between the unit cell parameters were observed between bulk and single-crystal samples, notably lengthening of the *c* axis (corresponding to the sheet-to-sheet spacing), as indicated by shifting of the (001) reflection to lower 1/*d* values. This may arise from slight disorder in the sheet-to-sheet spacing, due to changes in the solvation state between SC- and P-XRD samples, was has also been observed in $(Me_2NH_2)_2[Fe_2(Clan)_3]$.[34]. The slight sheet geometry changes which occur in $(Me_2NH_2)_2[Fe_2(Clan)_3]$ upon desolvation,[11] and **3.1^{Cl}a** upon solvent exchange (see Section 0) provide further evidence of the structural sensitivity to solvation in these 2D networks, supporting the assessment that bulk **3.1^{Cl}a** and **3.2** are phase pure despite some mismatch between the experimental P-XRD patterns and those predicted from SC-XRD.

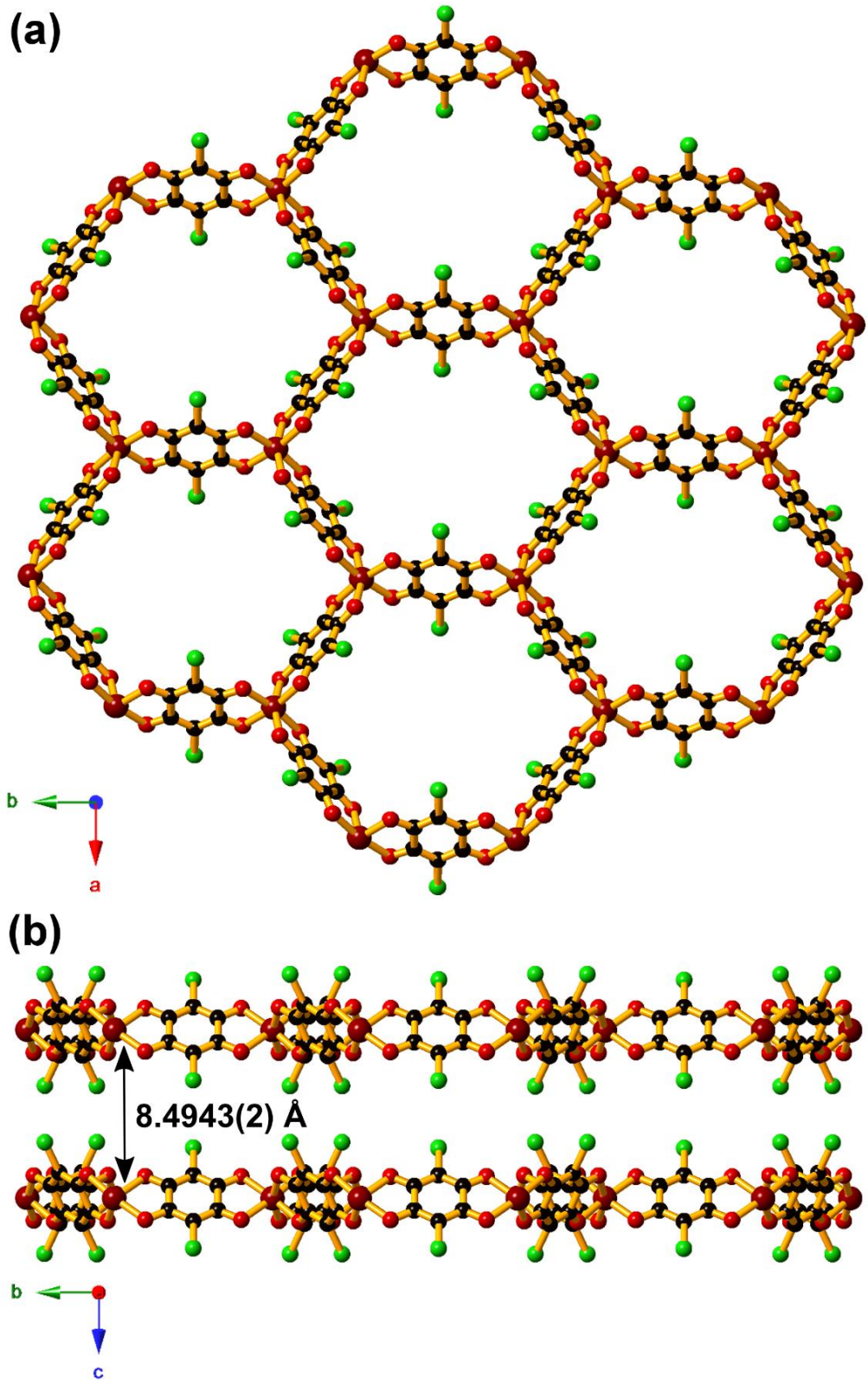


Figure 3.1 The anionic $[Fe_2(Clan)_3]^{x-}$ (6,3) honeycomb sheets in **3.1^{Cl}a** viewed (a) along the crystallographic *c* axis and (b) *a* axis. Maroon = Fe, green = Cl, red = O, black = C.

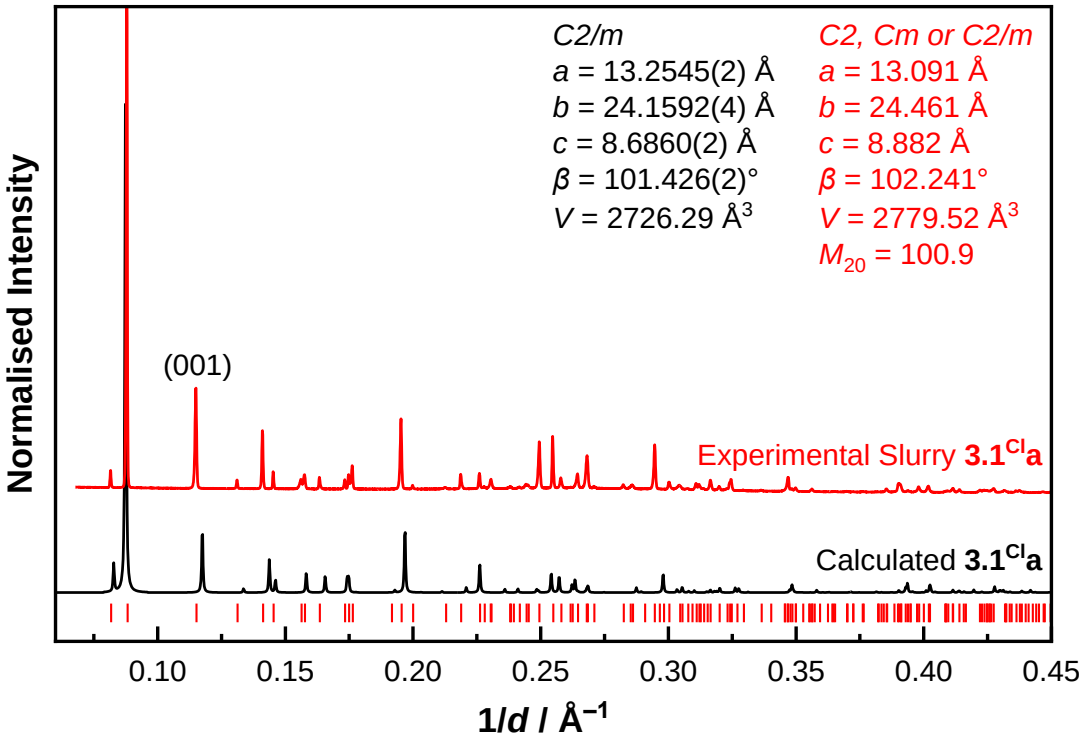


Figure 3.2 Synchrotron P-XRD (λ = 0.77493 Å) pattern of an MeCN slurry of **3.1^{Cl}a** (red, T = 250 K) and calculated pattern (black, T = 240 K) from SC-XRD of **3.1^{Cl}a**. Tick marks (red) show the positions of the calculated reflections.

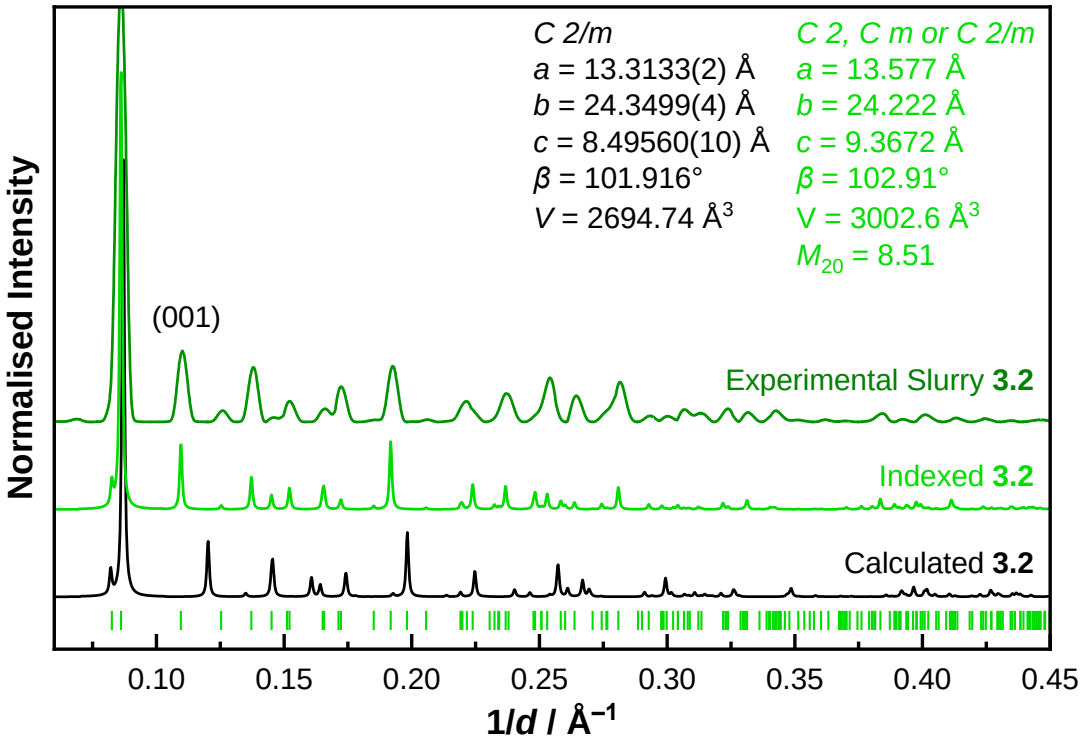


Figure 3.3 P-XRD (λ = 1.54184 Å) pattern of an MeCN slurry of **3.2** (dark green, T = 250 K), calculated pattern (pale green) from indexed experimental P-XRD and calculated pattern (black, T = 100 K) from SC-XRD of **3.2**. Tick marks show the positions of the calculated reflections from the indexed patterned (pale green).

The charge-balancing PhenQ^{m+} cations are snugly sandwiched between two Clan^{n-} ligands from the sheets above and below (Figure 3.4), which probably arises from the favourable shape complementarity, and strong π–π interaction between the planar electron-deficient PhenQ^{m+} cation and anionic network. This is evinced by the short interatomic contacts between cation and ligand, as close as 3.22 Å in **3.1^{Cl}a** (for C···Cl). Due to their location on a site of 2/*m* symmetry, the PhenQ^{m+} cations exhibit 2-fold disorder over crystallographically equivalent positions; these two equivalent orientations are shown in Figure 3.4.

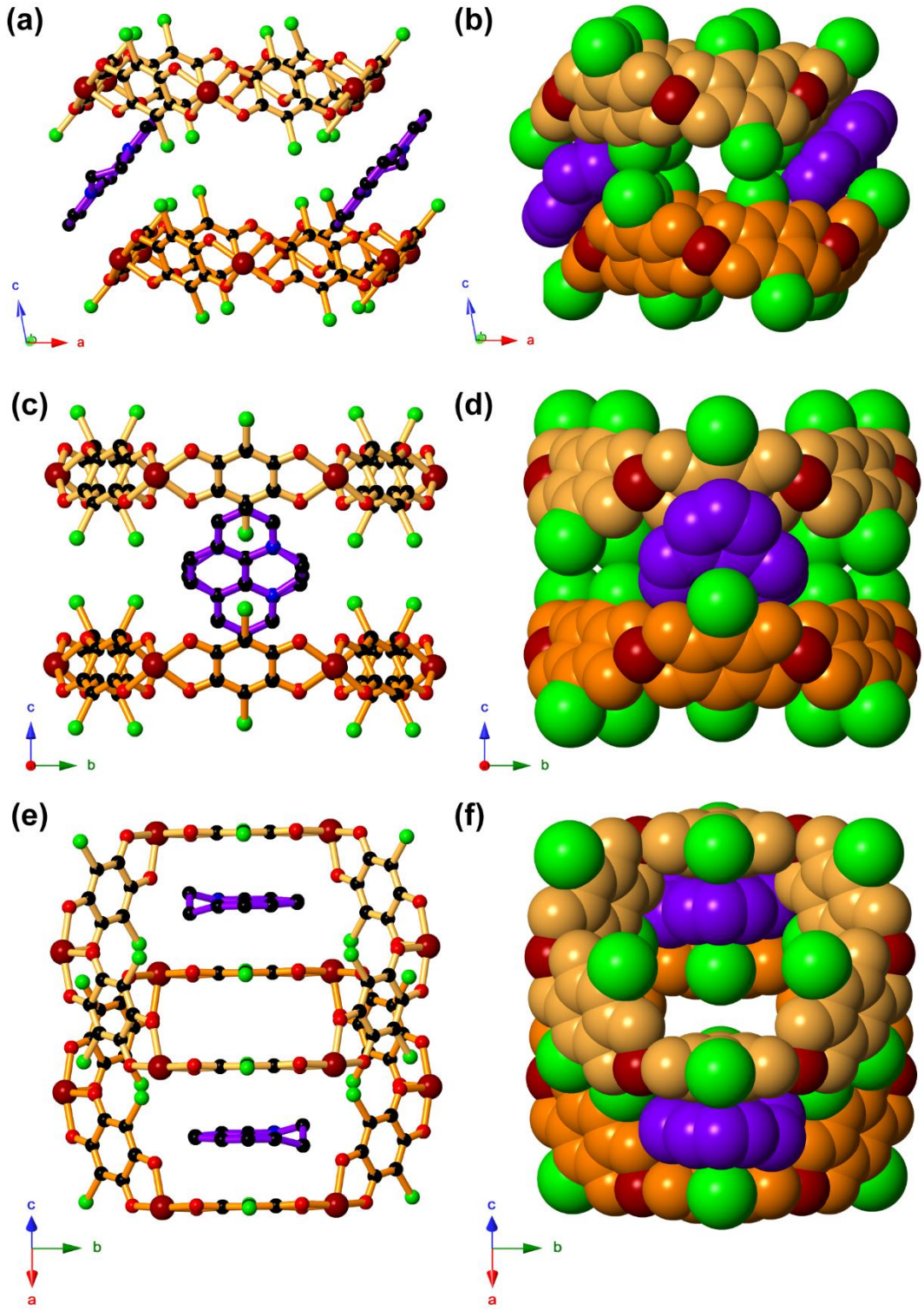


Figure 3.4 Ball-and-stick (a, c, e) and spacefilling (b, d, f) representations of the interactions of the $PhenQ^{m+}$ cation (purple) with the anionic $[Fe_2(Clan)_3]^{x-}$ sheets above (tan) and below (orange) in **3.1^{Cl}a**. View along the crystallographic (a, b) *b* and (c, d) *a* axes, and (e, f) along one-dimensional channels. Maroon = Fe, green = Cl, red = O, blue = N, and black = C.

Interestingly, the stacking geometry of $PhenQ^{m+}$ and Fan^{n-} in **3.1^{F}** stands out amongst the series. **3.1^{Cl}a**, **3.1^{Br}** and **3.2** all exhibit a similar inclination (54.58°, 53.85° and 54.17° respectively) of the mean plane of the ligand which interacts with $PhenQ^{m+}$, and the *ab* plane (intrasheet Fe–Fe plane). There is correspondingly only a slight inclination (2.73–4.07°) of the mean plane of $PhenQ^{m+}$ out of this mean ligand plane (Figure 3.5a). These factors cause essentially parallel stacking of $Clan^{n-}$ or $Bran^{n-}$ and $PhenQ^{m+}$. In contrast, the mean Fan^{n-} ligand plane is inclined 60.60° from the intrasheet Fe–Fe plane, with a concomitant inclination of the mean $PhenQ^{m+}$ plane 8.11° from the ligand plane. Interestingly the $PhenQ^{m+}$ plane remains similarly inclined from the Fe–Fe plane across the family (Figure 3.5b). This significant movement of Fan^{n-} ligands may arise from an attractive interaction between the highly polarised F atom and electropositive cationic π–surface of $PhenQ^{m+}$. Attractive F···π interactions have also been observed in the solid state between aryl fluorides tethered to extended pyridinium heterocycle acceptors, and is largely electrostatic in nature.[38] The short F···π distance of 2.993 Å, consistent with previously reported close F···π contacts, provides evidence for this attractive interaction.[39] The anomalous increase in sheet-to-sheet spacing in **3.1^{F}** compared to **3.1^{Cl}a** probably also arises from this attractive interaction, by slipping of the Fan^{n-} surfaces on $PhenQ^{m+}$ causing the anionic $[Fe_2(Fan)_3]^{x-}$ sheets in **3.1^{F}** to separate relative to those in **3.1^{Cl}a**.

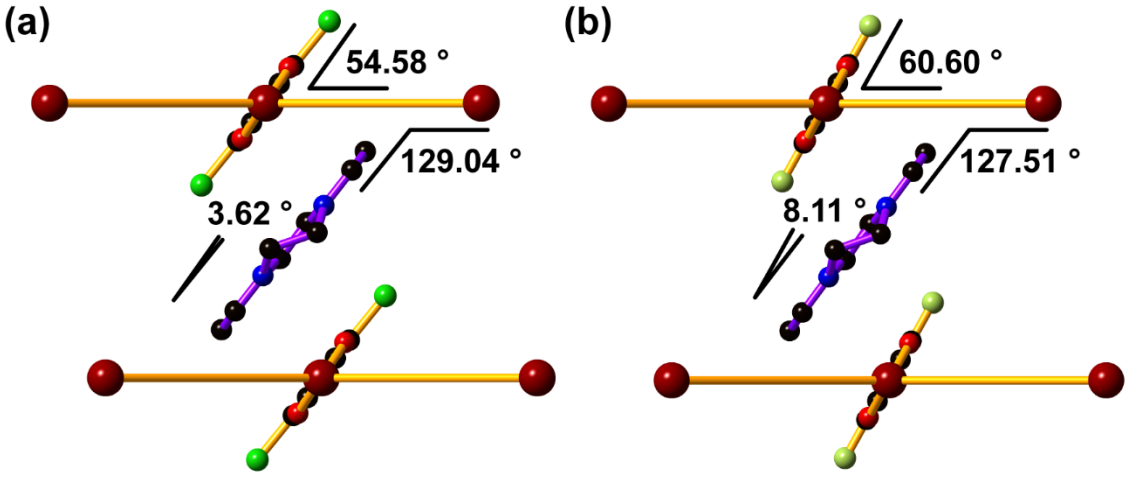


Figure 3.5 Inclinations of the mean ligand and $PhenQ^{m+}$ planes in (a) **3.1^{Cl}a** and (b) **3.1^{F}**. Maroon = Fe, green = Cl, pale green = F, red = O, blue = N, and black = C. H atoms and other non-interacting ligands omitted for clarity.

The alternation of $PhenQ^{m+}$ and $Clan^{n-}$ drives the AAAA stacking arrangement of the anionic sheets parallel to the *c* axis, such that within a column of Fe centres along the crystallographic *c* axis, the configuration around the Fe centres is either all Δ or all Λ (Figure 3.6). Spacious one-dimensional channels oriented along the *c* axis and inclined ca. 11° from the normal to the *ab* plane also result from this the sheet stacking arrangement. Despite the large size of the $PhenQ^{m+}$ cations, their location between the anionic sheets allows the compounds to maintain a highly porous character, with the one-dimensional channels occupying greater than 40% of the crystal volume. These channels are filled with highly disordered solvent molecules which could not be satisfactorily modelled. The scattering contribution of the disordered solvents was accounted for using the SQUEEZE[40] routine of PLATON[41], which allowed the solvation in **3.1^{Cl}a** to be tentatively estimated as (PhenQ)[$Fe_2(Clan)_3$]·4.25MeCN·6.3H_2O assuming an equivalent molar composition of guest solvent as that present during the crystallisation. Similar analyses for the other compounds in the family afforded estimated degrees of solvation of: **3.1^{F}** as (PhenQ)[$Fe_2(Fan)_3$]·4.25(acetone)·8.75H_2O; **3.1^{Br}** as (PhenQ)[$Fe_2(Bran)_3$]·4.5MeCN·5.85H_2O; and **3.2** as (PhenQ)[$Zn_2(Clan)_3$]·4.5MeCN·6.5H_2O.

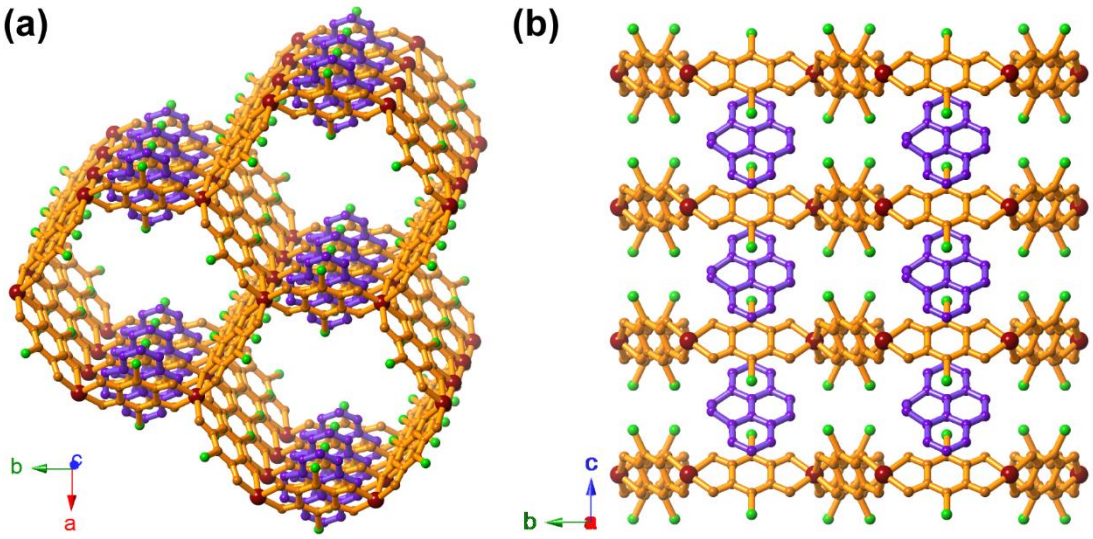


Figure 3.6 Alternating stacking of $PhenQ^{m+}$ (purple) with ligands in the anionic $[Fe_2(Clan)_3]^{x-}$ sheets in **3.1^{Cl}a**. View along the crystallographic (a) *c* axis, showing formation of spacious one-dimensional channels. (b) View along the crystallographic *a* axis showing AAAA stacking. Maroon = Fe, green = Cl.

The oxidation states of Fe, ligands and PhenQ^{m+} in the Fe compounds were determined by examining the characteristic bond lengths in the structure, using **3.2** as a reference in which the ligands and cations are unambiguously in the Clan^{2-} and PhenQ^{2+} oxidation states (*vide infra*). Excluding the PhenQ^{m+} cation, the asymmetric units of the compounds contain a single metal centre (Fe for **3.1^{Cl}a**, **3.1^{F}** and **3.1^{Br}**; Zn for **3.2**) and two crystallographically unique ligands in a 1:2 ratio (**L$_1$** and **L$_2$** respectively) (Figure 3.7). Analysis of *M*–chloranilate compounds reported in the Cambridge Structural Database (see Appendix A) reveals expected bond length ranges for the Clan^{2-} oxidation state of 1.248–1.272 Å for C–O and 1.506–1.551 Å for C–C. At 100 K in **3.2**, the mean ligand C–O bond lengths ($d_{C–O}$) were 1.256(4) Å and 1.253(6) Å for **L$_1$** and **L$_2$** respectively, with C–C bond lengths across the five-membered chelate ring ($d_{C–C}$; C8–C8′ for **L$_1$** and C2–C4′ for **L$_2$**) of 1.533(4) Å and 1.547(6) Å for **L$_1$** and **L$_2$** respectively. Thus **L$_1$** and **L$_2$** exist in **3.2** in the Clan^{2-} state, allowing the anionic sheets to be unambiguously formulated as [Zn^{II}(Clan^{2-})$_3$]$^{2-}$. Charge neutrality in **3.2** consequently requires PhenQ^{m+} to exist in the oxidised dicationic state (PhenQ^{2+}), so that the overall formulation is (PhenQ^{2+})[Zn$^{II}_2$(Clan^{2-})$_3$]. Crystallographic C–C and C–N bond lengths in viologens are known to be diagnostic of oxidation state, due to transformation from an aromatic to semiquinonoid structure upon one electron reduction.[42, 43] Comparison of the C−C and C−N bond lengths between [PhenQ]Br$_2$ and PhenQ^{m+} in **3.2**, particularly the central C−C bond (C6–C9 in [PhenQ]Br$_2$, C14–C14′ in **3.2**) reveals no significant differences, supporting assignment of the PhenQ^{m+} oxidation state in **3.2** as PhenQ^{2+} (Figure 3.8). A similar comparison of PhenQ^{m+} C–C and C–N bond lengths between compound **3.2** and **3.1^{Cl}a** (Figure 3.8), again indicates PhenQ^{m+} exists in **3.1^{Cl}a** in the dicationic aromatic valence state. Consequently, the framework in **3.1^{Cl}a** is also formulated as [Fe$_2$(Clan)$_3$]$^{2-}$. The Fe−O bond lengths ($d_{Fe–O}$) in **3.1^{Cl}a**, **3.1^{F}** and **3.1^{Br}** are given in Table 3.2.

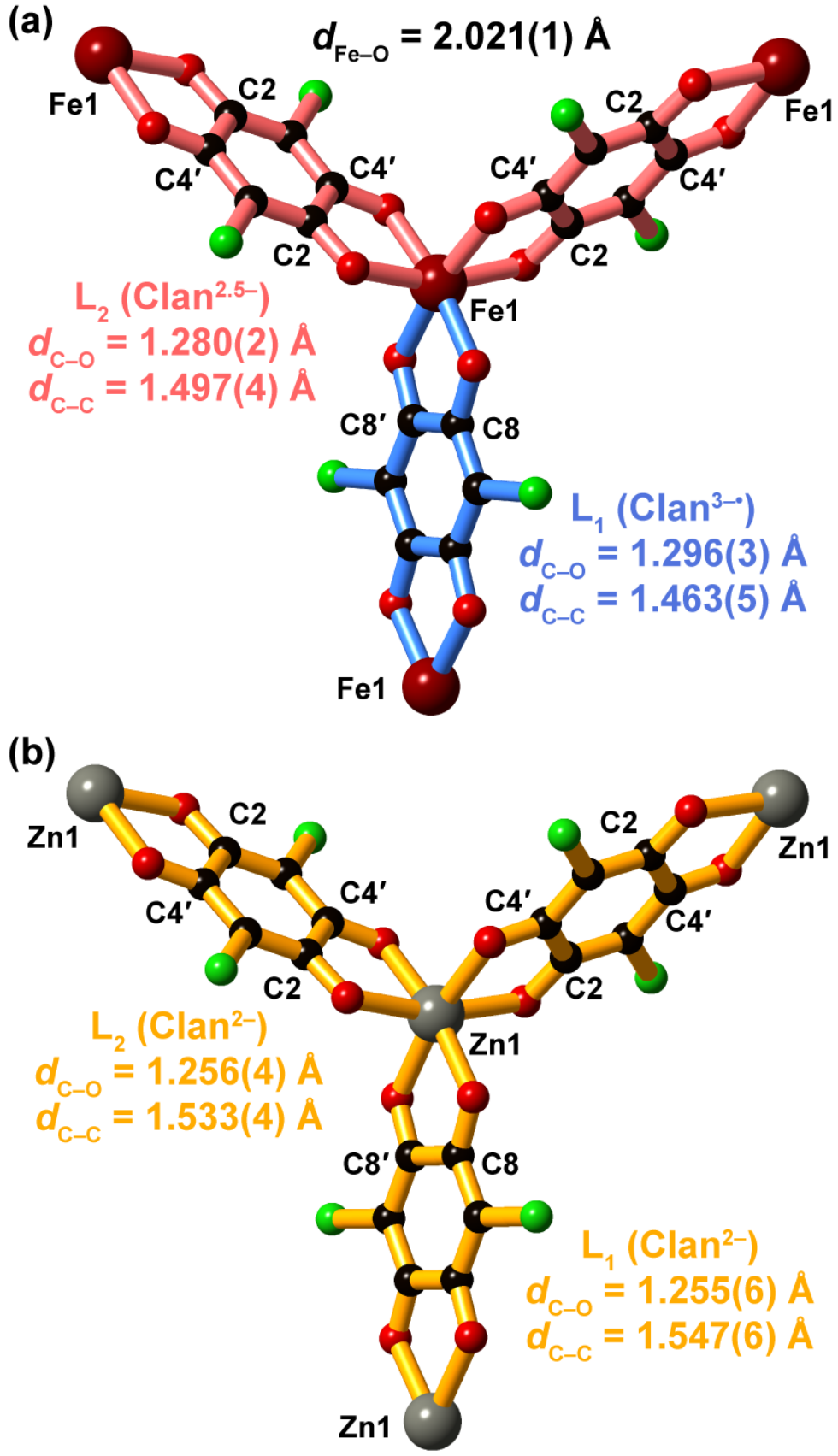


Figure 3.7 Coordination environment and characteristic Clan$^{n–}$ bond lengths around (a) Fe in **3.1^{Cl}a** and (b) Zn in **3.2** at T = 100 K.

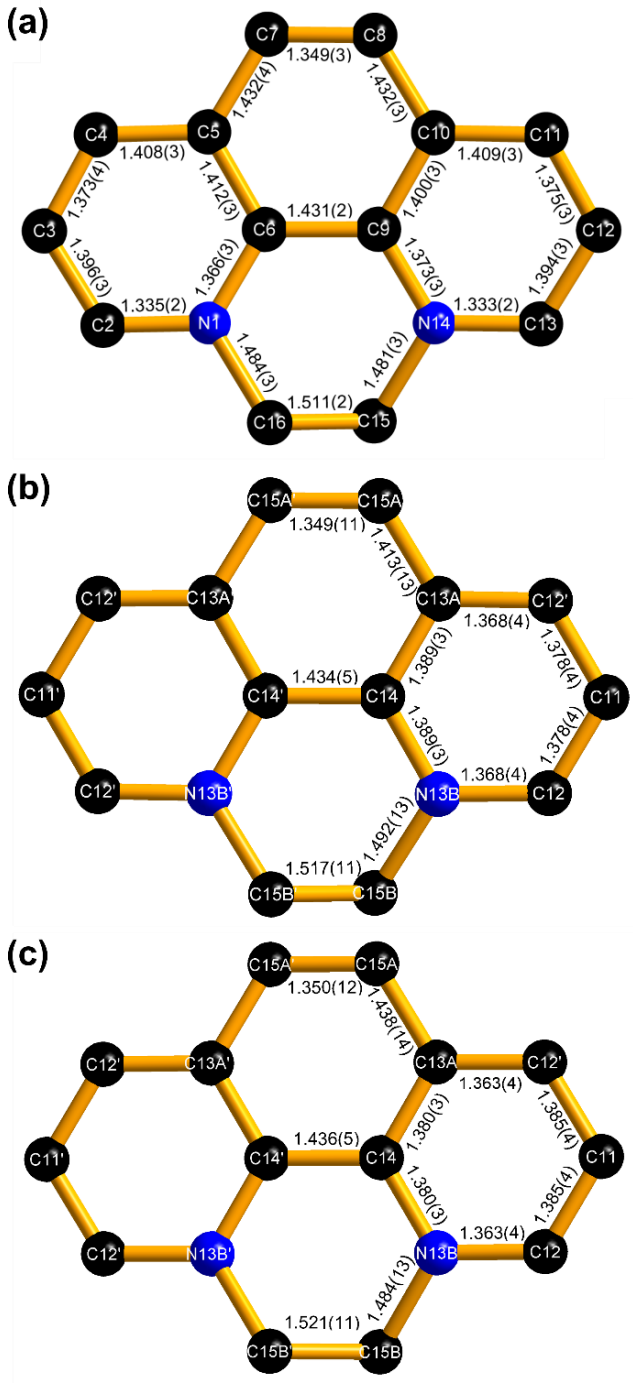


Figure 3.8 Bond lengths in PhenQ^{m+} moieties in (a) (PhenQ^{2+})Br$_2$, (b) **3.1^{Cl}a** and (c) **3.2**. NB: The location of PhenQ^{2+} on two special positions (inversion center on the C14–C14′ bond, and mirror plane bisecting the molecule) results in two-fold disorder of PhenQ^{m+} in **3.1^{Cl}a** and **3.2**. Consequently, the C13A and N13B positions have 50% occupancy by C13A and N13B respectively. The observed C–C and C–N bonds to these atoms are the average of the crystallographically unique C–C and C–N bonds observed in (PhenQ^{2+})Br$_2$. Blue = N, and black = C. H atoms not shown for clarity.

Table 3.2 Mean $d_{Fe–O}$ values in **3.1^{Cl}a**, **3.1^{F}** and **3.1^{Br}** at T = 100 K as determined by SC-XRD.

Compound	L_1 $d_{Fe–O}$ / Å	L_2 $d_{Fe–O}$ / Å
3.1^{Cl}a	2.006(2)	2.025(2), 2.030(2)
3.1^{F}	2.016(2)	2.019(2), 2.026(2)
3.1^{Br}	2.013(4)	2.032(4), 2.034(4)

These values are consistent with bond lengths reported in other mixed-valence Fe–tetraoxolene coordination polymers which were determined to contain high-spin Fe^{III} (Fe^{III}_{HS}), as determined by crystallography (Table A.4) and ^{57}Fe Mössbauer spectroscopy. In a similar manner to previously reported Fe–tetraoxolene frameworks which contain Fe^{III}_{HS} not Fe^{II}, the observation of a higher Fe oxidation state suggests the presence of radical ligands in the framework, due to electron transfer from Fe^{II} to the oxidised ligands, *in situ* generating Fe^{III}_{HS} centres and radical trianion forms of the bridging ligands. This conclusion is supported by comparison of C–O and C–C bond lengths between the diamagnetic Zn^{II} compound **3.2** and the Fe compounds, which reveals noticeable differences strongly indicating the presence of ligand-centred mixed valency in the Fe compounds. By analysis of metal–chloranilate compounds reported in the CSD (see Appendix A), the expected C–O and C–C (across the 5-membered chelate ring) bond lengths for Clan$^{3-\bullet}$ were determined as $d_{C–O}$ = 1.291–1.316 Å and $d_{C–C}$ = 1.431–1.473 Å respectively (Table A.2). In **3.1^{Cl}a**, the mean $d_{C–O}$ value in $\mathbf{L_1}$ is 1.296(3) Å, with a mean $d_{C–C}$ (C8–C8') value of 1.463(5) Å, which are within the range expected for Clan$^{3-\bullet}$ ligands. In contrast, the mean $d_{C–O}$ and $d_{C–C}$ values in $\mathbf{L_2}$ are 1.280(2) Å and 1.497(4) Å respectively. Interestingly, these values lie between the ranges expected for either the Clan^{2-} ($d_{C–O}$ = 1.248–1.272 Å; $d_{C–C}$ = 1.506–1.551 Å) or Clan$^{3-\bullet}$ valence states, suggestive of a non-integer oxidation state of $\mathbf{L_2}$. Given that **3.1^{Cl}a** contains Fe^{III}_{HS}, $\mathbf{L_1}$ in the Clan$^{3-\bullet}$ state, and PhenQ^{m+} in the dicationic state, maintenance of charge neutrality in **3.1^{Cl}a** requires $\mathbf{L_2}$ to have an average 2.5− charge per ligand, due to the 1:2 ratio of $\mathbf{L_1}$:$\mathbf{L_2}$, so that the suggested charge formulation is (PhenQ^{2+})[Fe^{III}_2($\mathbf{L_2}^{2.5-}$)$_2$($\mathbf{L_1}^{3-\bullet}$)].

The significance of these observation is understood by comparison of other mixed-valence Fe–tetraoxolene coordination polymers based upon the apparent crystallographic ligand oxidation states and the extent of delocalisation of any radical ligands. The two extremes consist of fully crystallographically localised ligand oxidation states, and the other is full delocalisation of ligand oxidation states. The mixed-valence 2D (^{n}Pr$_4$N)$_2$[Fe$_2$(Clan)$_3$]·2acetone framework exhibits localisation of ligand and Fe valence states, with a (^{n}Pr$_4$N)$_2$[Fe^{II}Fe^{III}(Clan^{2-})$_2$(Clan$^{3-\bullet}$)]·2(acetone) formulation at 250 K and the valence tautomeric (^{n}Pr$_4$N)$_2$[Fe$^{III}_2$(Clan^{2-})(Clan$^{3-\bullet}$)$_2$]·2(acetone) state at 100 K. At the other extreme, the mixed-valence frameworks (Me$_2$NH$_2$)$_2$[Fe$^{III}_2$(Clan)$_3$]·6DMF·2H$_2$O[11], (Et$_4$N)$_2$[Fe$^{III}_2$(Clan)$_3$]·20H$_2$O and (Bu$_4$N)$_2$[Fe$^{III}_2$(dhbq)$_3$][10] all display d_{Fe-O} values consistent with Fe$^{III}_{HS}$, and d_{C-O} values between the Clan^{2-} and Clan$^{3-\bullet}$ forms (1.280(5) Å for (Me$_2$NH$_2$)$_2$[Fe$^{III}_2$(Clan)$_3$]·6DMF·2H$_2$O, and 1.280(3) Å for (Et$_4$N)$_2$[Fe$^{III}_2$(Clan)$_3$]·solvent). Charge neutrality requires the networks in these compounds to be dianionic, so the network formulation is formally [Fe$^{III}_2$(Xan^{2-})(Xan$^{3-\bullet}$)$_2$]$^{2-}$. Interestingly, these compounds all exhibit high crystallographic symmetry; trigonal for (Me$_2$NH$_2$)$_2$[Fe$^{III}_2$(Clan)$_3$]·6DMF·2H$_2$O and (Et$_4$N)$_2$[Fe$^{III}_2$(Clan)$_3$]·20H$_2$O, and cubic for (Bu$_4$N)$_2$[Fe$^{III}_2$(dhbq)$_3$]. This high symmetry arises because the three ligand sites are chemically equivalent, indicative of delocalisation of the two radical dhbq$^{3-\bullet}$ or Xan$^{3-\bullet}$ ligands over the three equivalent sites, affording average ligand valences of dhbq$^{2.67-}$ or Xan$^{2.67-}$. Intermediate between these two extremes, **3.1^{Cl}a**, **3.1^{F}** and **3.1^{Br}** are examples which contain both crystallographically localised (**L$_1$**, Xan$^{3-\bullet}$) and delocalised (**L$_2$**, Xan$^{2.5-}$) radical ligands. This arrangement produces anionic [Fe$_2$(Xan)$_3$]$^{2-}$ sheets formed from {Fe^{III}–**L$_2$**}$_\infty$ chains knitted together with **L$_1$** ligands (Figure 3.9). A similar non-integer Clan^{n-} oxidation state has been observed recently in a high temperature phase of (^{n}Pr$_4$N)$_2$[Fe$_2$(Clan)$_3$], and was ascribed to layer-to-layer positional disorder of the (^{n}Pr$_4$N)$_2$[Fe^{II}Fe^{III}(Clan^{2-})$_2$(Clan$^{3-\bullet}$)] layers rather than a disordered (^{n}Pr$_4$N)$_2$[Fe$^{2.5}_2$(Clan^{2-})(Clan$^{2.5-}$)$_2$] state, as evidenced by distinct Fe^{II} and Fe^{III} sites by ^{57}Fe Mössbauer spectroscopy. In contrast, the partial localisation of the Xan$^{3-\bullet}$ ligands in **3.1^{Cl}a**, **3.1^{F}** and **3.1^{Br}** likely arises due to strong CT interactions between the π-electron poor PhenQ^{2+} cation, and the relatively electron rich **L$_1$** Xan$^{3-\bullet}$ ligands with which PhenQ^{2+} stacks. This intermediate case of radical ligand delocalisation, compared to previously reported compounds, may result in novel electrical or

magnetic properties, between the high conductivity and spontaneous magnetic ordering observed in $(Me_2NH_2)_2[Fe^{III}_2(Clan^{2.67-})_3]\cdot 6DMF\cdot 2H_2O$, and slow magnetisation relaxation and thermally induced valence-tautomerism observed for $(^nPr_4N)_2[Fe^{III}_2(Clan^{2-})(Clan^{3-\bullet})_2]\cdot 2$acetone.

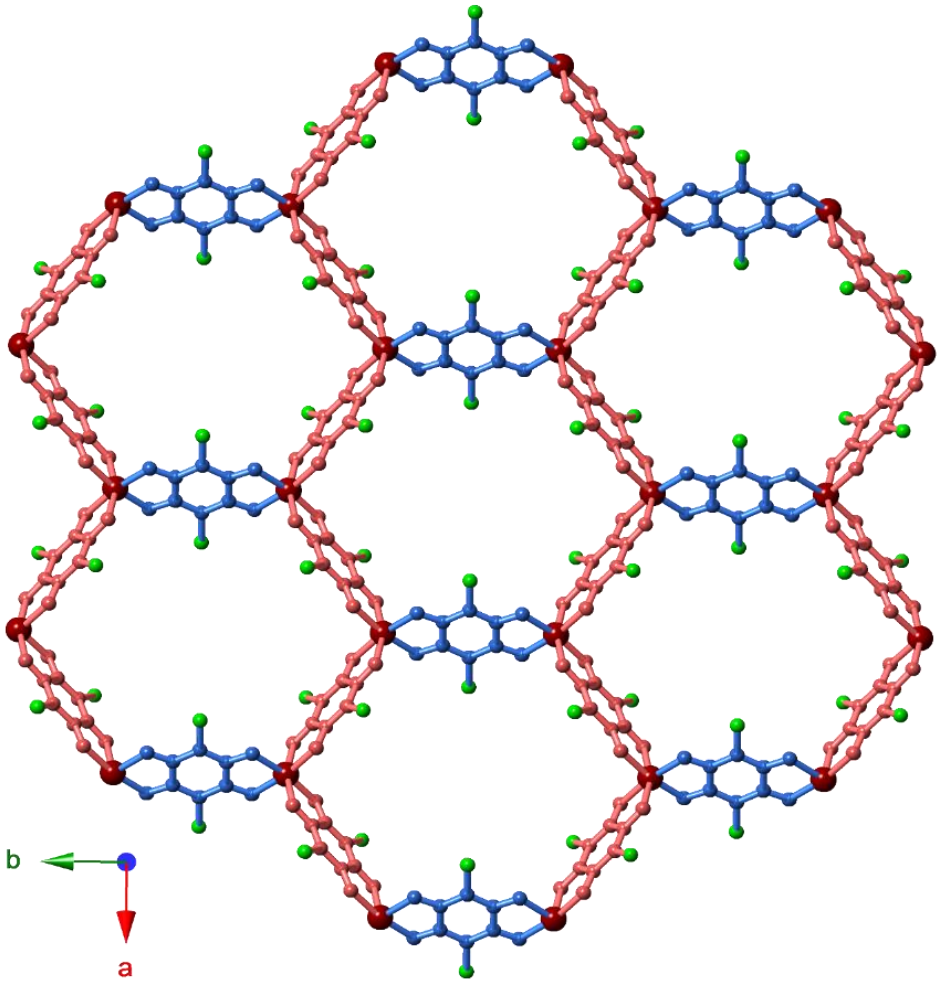


Figure 3.9 Arrangement of $\mathbf{L_1}$ (blue, $Clan^{3-\bullet}$) and $\mathbf{L_2}$ (pink, $Clan^{2.5-}$) ligands giving $\{Fe^{III}–\mathbf{L_2}\}_\infty$ chains bridged by $\mathbf{L_1}$, which produces the anionic $[Fe_2(Clan)_3]^{2-}$ sheets in $\mathbf{3.1^{Cl}a}$. Maroon = Fe, green = Cl. An equivalent arrangement of $\mathbf{L_1}$ and $\mathbf{L_2}$ is replicated in **3.2**, however both $\mathbf{L_1}$ and $\mathbf{L_2}$ are in the $Clan^{2-}$ valence state in **3.2**.

3.2.2 Variable-Temperature Single-Crystal X-ray Diffraction

As previously mentioned, thermally induced valence-tautomerism has been observed in the $(Me_4N)_2[Fe(Clan)Cl_2]$ and $(^nPr_4N)_2[Fe_2(Clan)_3]\cdot 2$acetone compounds. This process consists of a transition from a $\{Fe^{III}–Clan^{3-\bullet}\}$ state at $T < T_{1/2}$ to the $\{Fe^{II}–Clan^{2-}\}$ form at $T > T_{1/2}$. The valence-tautomeric transition was shown by changes in $d_{Fe–O}$ and ligand $d_{C–O}$ values, supported by ^{57}Fe Mössbauer spectroscopy for the Fe oxidation state, and either Raman or IR spectroscopy for the ligand oxidation state. Although, the origin of this phenomenon was not investigated in detail, it is striking to note that both these compounds contain localised $Clan^{3-\bullet}$ states, raising the possibility of thermally induced valence tautomerism in **3.1^{Cl}a**. Variable-temperature SC-XRD was conducted by warming the sample from 100 K to 260 K. The thermal variation of the cell parameters shows the expected thermal expansion of the unit cell with increasing temperature (Figure 3.10).

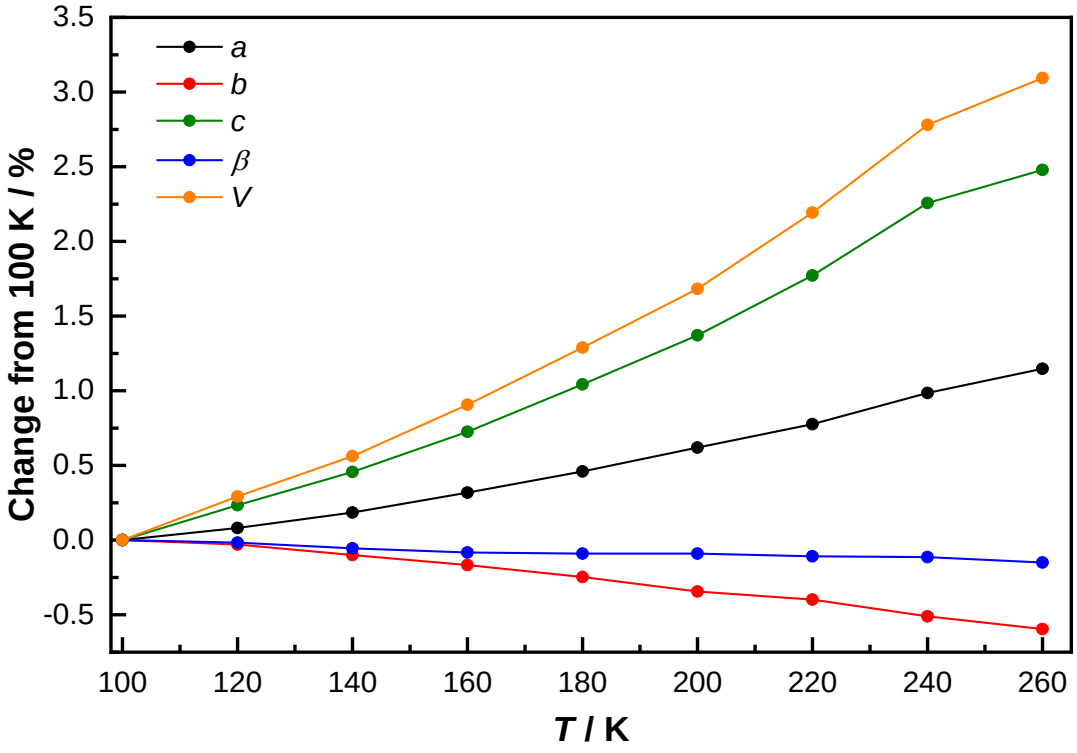


Figure 3.10 Temperature dependence of the cell parameters (*a*, *b*, *c*, *β* and *V*) as measured by SC-XRD for **3.1^{Cl}a**, where all values are normalised to those observed at T = 100 K.

Over the temperature range studied, the $d_{C–O}$ values for $\mathbf{L_1}$ and $\mathbf{L_2}$ varied from 1.292–1.298 Å and 1.275–1.280 Å respectively, which lie within the ranges expected for the $Clan^{3-\bullet}$ (1.291–1.316 Å) state and just above the range expected for $Clan^{2-}$ (1.248–1.272 Å) state (Figure 3.11). No significant variation in diagnostic ligand $d_{C–C}$ value (C8–C8' for $\mathbf{L_1}$, C2–C4' for $\mathbf{L_2}$) was observed, commensurate with the absence of C–O bond length variation. Over the course of the experiment, a minor increase in average $d_{Fe–O}$ values was observed (2.021(1) Å at 100 K to 2.033(1) at 260 K), however these values remain consistent with a Fe^{III}_{HS} state. The variable-temperature SC-XRD results therefore strongly indicate an absence of thermally-induced valence tautomerism in $\mathbf{3.1^{Cl}a}$, so that the partially charge ordered $(PhenQ^{2+})[Fe^{III}_2(Clan^{2.5-})_2(Clan^{3-\bullet})]$ state is maintained over the temperature range of study. The contrasting behaviour to $(^nPr_4N)_2[Fe_2(Clan)_3]\cdot 2acetone$) and $(Me_4N)_2[Fe(Clan)Cl_2]$ may arise from the differing cations in $\mathbf{3.1^{Cl}a}$. The electron-poor $PhenQ^{2+}$ is sandwiched between electron-rich $Clan^{3-\bullet}$ ligands ($\mathbf{L_1}$) in $\mathbf{3.1^{Cl}a}$, resulting in a significant CT interaction, which likely increases the barrier to electron transfer from $\mathbf{L_1}$ to Fe^{III}. This CT interaction is possibly also supplemented by increased Coulombic stabilisation of the $PhenQ^{2+}/Clan^{3-\bullet}$ pair, relative to a $PhenQ^{2+}/Clan^{2-}$ state. Moreover, valence tautomerism between Fe^{III} and the two $\mathbf{L_2}$ ligands, formally $[(Clan^{2-})(Clan^{3-\bullet})]$ is likely prevented by the low energy barrier to IVCT between the two ligands, as evidenced by the delocalisation indicated by the crystallography.

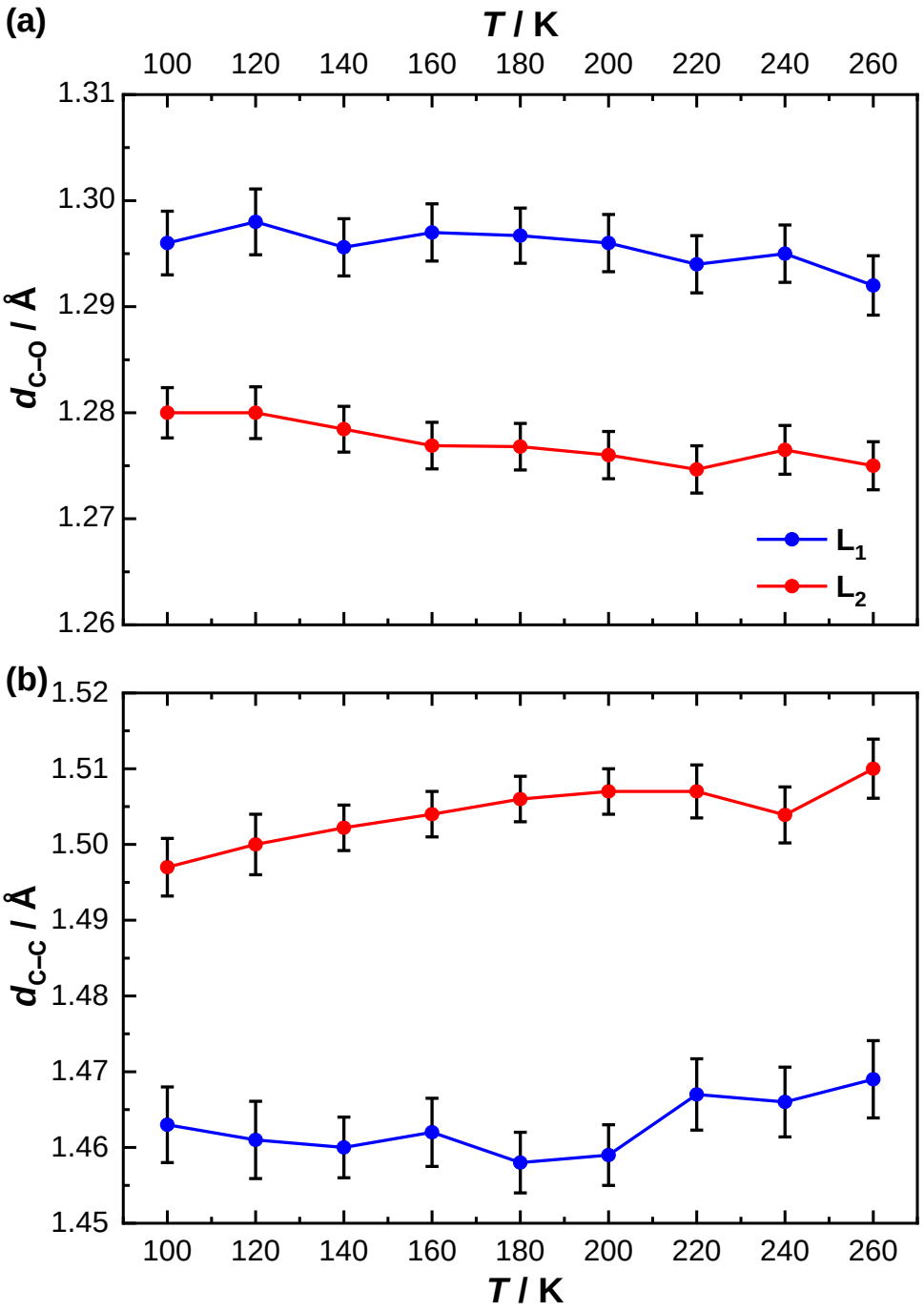


Figure 3.11 Temperature dependence of the ligand (a) $d_{C–O}$ and (b) characteristic $d_{C–C}$ values in **3.1^{Cl}a** as measured by SC-XRD. Error bars are ±s.u.

3.2.3 Solvent Exchange

Like many coordination polymers containing large framework voids filled with disordered volatile solvents, removing the crystals of **3.1^{Cl}a** from the mother liquor caused facile solvent loss from the compound, which might be expected to cause structural distortions or 'breathing' as has been commonly observed in many coordination polymers and frameworks.[44] Significant decreases in conductivity and magnetic ordering temperature are observed in $(Me_2NH_2)_2[Fe_2(Clan)_3]\cdot 6DMF\cdot 2H_2O$ upon desolvation.[12] This behaviour was ascribed to distortion of the hexagonal network,[11] causing less favourable metal-ligand orbital overlap and thus less efficient electronic communication within the network. Analogously, significant differences in the magnetic properties of $(Et_4N)_2[Fe_2(Fan)_3]$ were observed between the acetone and H_2O solvates.[25] Additionally, electrical conductivity studies were initially attempted using as-synthesised **3.1^{Cl}a**. However, during the experiment, anomalous time-dependence of the conductivity was observed over times scales as short as minutes. This behaviour was attributed to slight changes in solvation even during the measurement, causing continuous variation in framework geometry. Due to the design of the experimental apparatus, it was not feasible to monitor *in situ* any change in structure along with conductivity. Therefore, it would be impossible to deconvolute changes in conductivity arising from changes in solvation, from variation arising from the thermally-activated semiconductor behaviour. To prevent possible complications arising from an unknown solvation state in **3.1^{Cl}a**, exchange of volatile MeCN and H_2O guest solvents in **3.1^{Cl}a** with relatively involatile DMF was considered desirable. The guest solvent exchange process also provides a facile demonstration that **3.1^{Cl}a** is both robust and porous, opening the door for future studies using redox-active guest species.

Solvent exchange in **3.1^{Cl}a** was readily achieved by soaking a bulk sample of **3.1^{Cl}a** first in anhydrous, deoxygenated MeCN, to remove guest H_2O, followed by extensive soaking and washing with anhydrous, deoxygenated DMF. Conversion of bulk **3.1^{Cl}a** into the DMF solvate ($(PhenQ)[Fe_2(Clan)_3]\cdot y$DMF, **3.1^{Cl}b**) was evidenced using a combination of X-ray diffraction, FT-IR spectroscopy, and thermogravimetric analysis (TGA). The FT-IR spectra of **3.1^{Cl}a**, **3.1^{Cl}b** and **3.2** are presented in Figure 3.12. Appearance of an intense sharp absorbance at 1649 cm^{-1}, in addition to a weaker absorbance at 1089 cm^{-1} in the FT-IR spectrum of **3.1^{Cl}b**, attributed to $\nu_{C=O}$ and in-

plane CH_3 rocking of DMF respectively, provided an initial indication that the guest solvent was successfully changed from MeCN to DMF. The $\nu_{C\equiv N}$ of MeCN could not be observed in **3.1^{Cl}a** due to use of a diamond ATR crystal, which has intense diamond phonon absorption bands in the region 2600–1600 cm^{-1}.

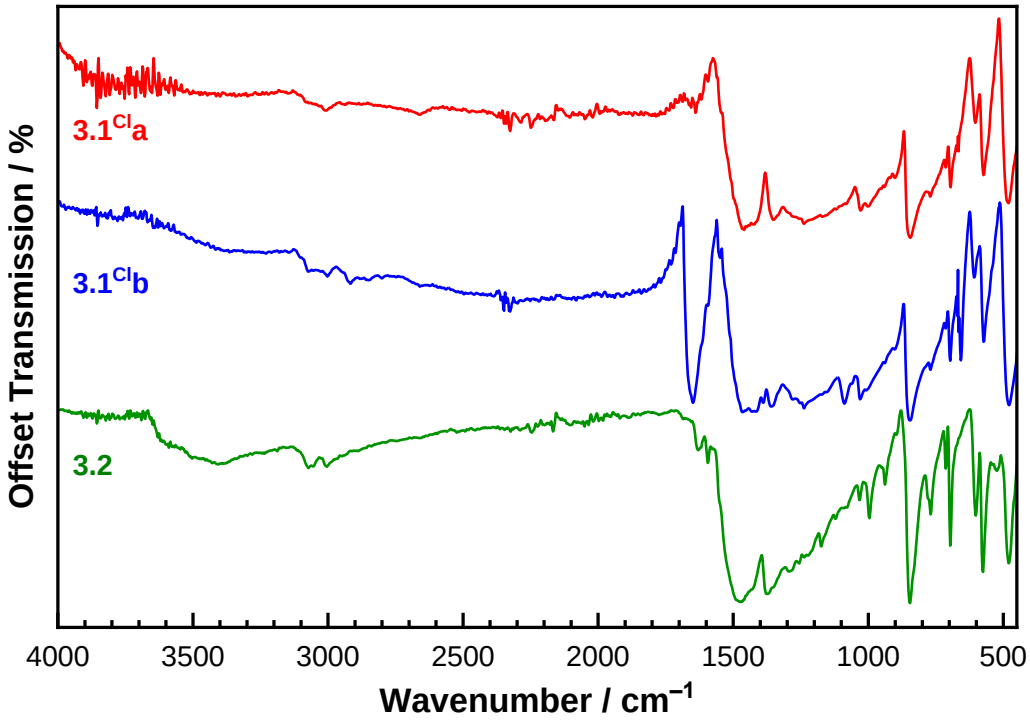


Figure 3.12 Normalised ATR FT-IR spectra of **3.1^{Cl}a** (red), **3.1^{Cl}b** (blue) and **3.2** (green) collected under ambient conditions in air.

Gratifyingly, a sample of **3.1^{Cl}b** following solvent exchange from as-synthesised **3.1^{Cl}a** still contained crystals suitable for SC-XRD analysis. The diffraction intensity however was significantly reduced compared to pristine **3.1^{Cl}a**, precluding timely collection of a variable-temperature dataset using laboratory instrumentation. Moreover, a variable-temperature collection was not attempted using synchrotron radiation due to the experimental setups on the MX1 and MX2 beamlines at the Australian Synchrotron, which prevent collection of complete datasets from low symmetry crystals arising from inadequate coverage of reciprocal space. A satisfactory structure determination for **3.1^{Cl}b** was achieved in the monoclinic *C*2/*m* space group, as for **3.1^{Cl}a**, with slight changes in the unit cell parameters (see Table 3.5 and Table 3.6). The most significant is the increased length of the crystallographic *c* axis,

corresponding to the interlayer sheet-to-sheet spacing (at T = 240 K: 8.6860(2) Å in **3.1^{Cl}a**; 8.7982(2) Å in **3.1^{Cl}b**). The increased sheet spacing was also coupled with distortion of the hexagonal channel geometry in **3.1^{Cl}b** towards a perfect hexagon (Figure 3.13). A similar distortion or 'breathing' of the sheet geometry was previously observed for $(Me_2NH_2)_2[Fe_2(Clan)_3]\cdot 6DMF\cdot 2H_2O$ upon desolvation.[11]

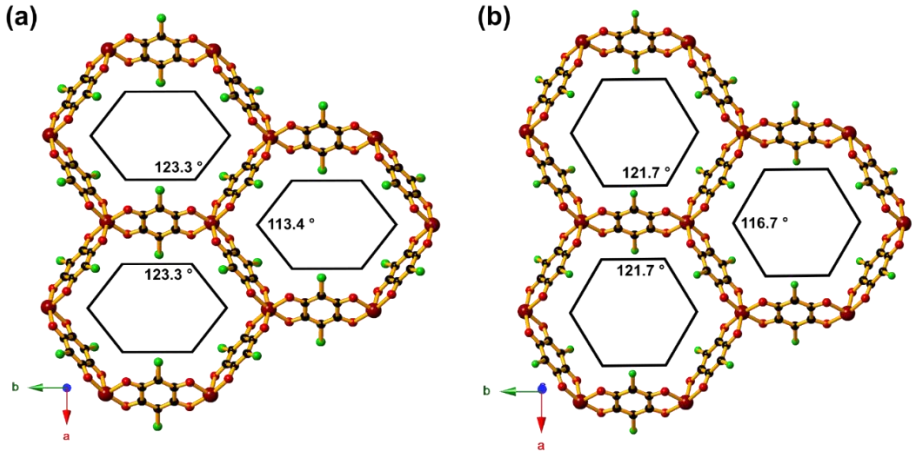


Figure 3.13 Distortion of the hexagonal channels and changes to the Fe···Fe···Fe angles for (a) **3.1^{Cl}a** and (b) **3.1^{Cl}b**.

Comparison of the electron density difference (F_O–F_C, where F_O and F_C are the observed and calculated structure factors for the model) maps between **3.1^{Cl}a** and **3.1^{Cl}b** also reveals significant differences between the two solvates (Figure 3.14). For **3.1^{Cl}a**, the 1D channels contain large regions of residual electron density, ascribed to disordered MeCN and H_2O which could not readily be modelled (Figure 3.14a, c, e). In contrast, the 1D channels in **3.1^{Cl}b** are occupied by large regions of electron density whose shape closely corresponds with that expected for DMF molecules (Figure 3.14b, d, f). Modelling of these regions of residual electron density yielded a formula consistent with 4 DMF molecules per formula unit i.e. $(PhenQ)[Fe_2(Clan)_3]\cdot 4DMF$. Complete modelling of the guest DMF solvent was not possible due to remaining electron density peaks located close to the DMF molecules, large anisotropic displacement parameters of the modelled solvents, and remaining regions of unassigned electron density, which were not readily assigned as DMF. Thus the SQUEEZE[40] routine of PLATON[41] was used to account for the scattering contribution of the ordered and disordered solvent, affording an estimated solvation for **3.1^{Cl}b** of $(PhenQ)[Fe_2(Clan)_3]\cdot 4.4DMF$.

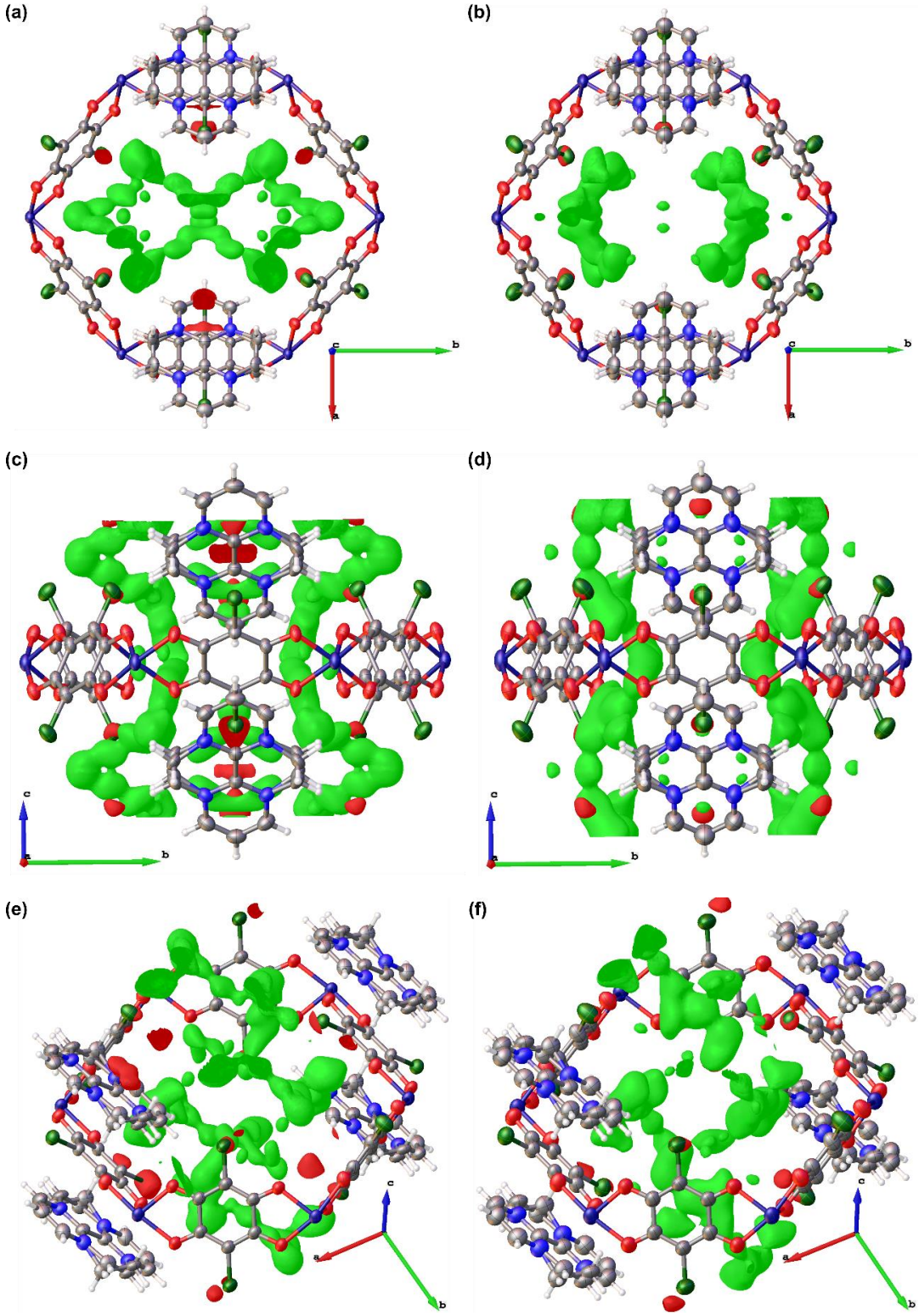


Figure 3.14 Electron density difference (F_O–F_C) maps for (a, c, e) **3.1^{Cl}a** and (b, d, f) **3.1^{Cl}b**. Maps plotted at a level of 1.4 e Å^{-3} and a resolution of 0.1 Å using the *OLEX2* graphical user interface.[45]

The phase purity of **3.1^{Cl}b** was confirmed by P-XRD. In a similar manner to bulk **3.1^{Cl}a** measured as an MeCN slurry, the pattern calculated from the SC-XRD structure of **3.1^{Cl}b** (Figure 3.15, black) and the experimental patterns (Figure 3.15, royal blue and navy) from isolated bulk samples reveal some differences, although they are not as pronounced as for **3.1^{Cl}a** or **3.2**. Shifting of the (001) reflection to lower 1/*d* value i.e. higher *d*-spacing, due to increased sheet-to-sheet spacing, is observed in the P-XRD pattern of an isolated sample of **3.1^{Cl}b**. Indexing the experimental patterns (pale blue) reveals slight changes to the unit cell parameters, which is probably due to slight changes in solvation upon vacuum filtration and transfer of the sample of **3.1^{Cl}b** into an inert atmosphere glovebox *in vacuo* in a Schlenk frit. Large differences in reflection intensity between calculated and experimental patterns are also observed, ascribed to preferred orientation effects, and slight sheet stacking disorder, as has been previously observed for $(Me_2NH_2)_2[Fe_2(Clan)_3]$.[34]

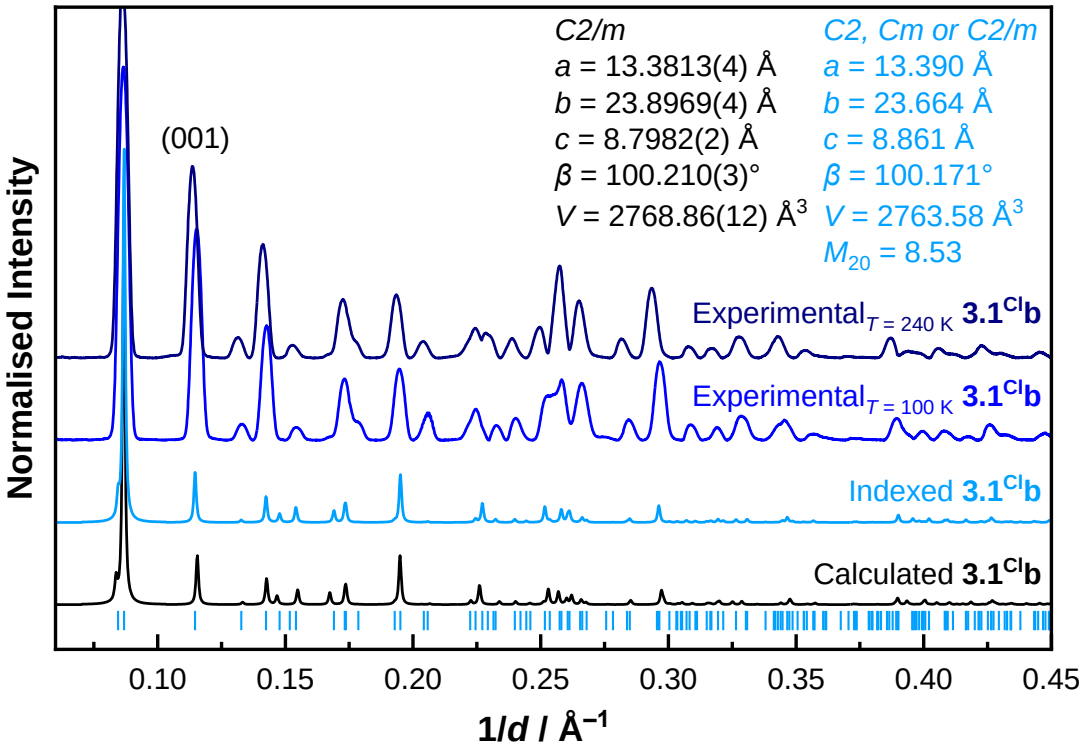


Figure 3.15 P-XRD (λ = 1.54184 Å) patterns of isolated **3.1^{Cl}b** at T = 240 K (navy) and T = 100 K (royal blue), calculated pattern (pale blue) from indexed experimental P-XRD pattern, and calculated pattern (black) from SC-XRD of **3.1^{Cl}b**. Tick marks (pale blue) indicate the positions of the allowed reflections for the unit cell indexed from the experimental P-XRD pattern (T = 100 K).

TGA and combustion analysis also confirmed **3.1^{Cl}a** was successfully transformed into **3.1^{Cl}b**, indicated by the differences in solvent content (Figure 3.16). There was however some discrepancy between the degree of solvation calculated by TGA and elemental analysis. This is ascribed to batch-to-batch variation in the degree of solvation ((PhenQ)[Fe_2(Clan)$_3$]·2.7DMF by TGA compared to (PhenQ)[Fe_2(Clan)$_3$]·3.7DMF by elemental analysis). All physical property measurements were undertaken using a single batch of sample having the composition (PhenQ)[Fe_2(Clan)$_3$]·3.7DMF (**3.1^{Cl}b**). Recent investigations of similar porous honeycomb tetraoxolene frameworks have similarly noted batch-to-batch variation in the degree of solvation by elemental analyses.[15]

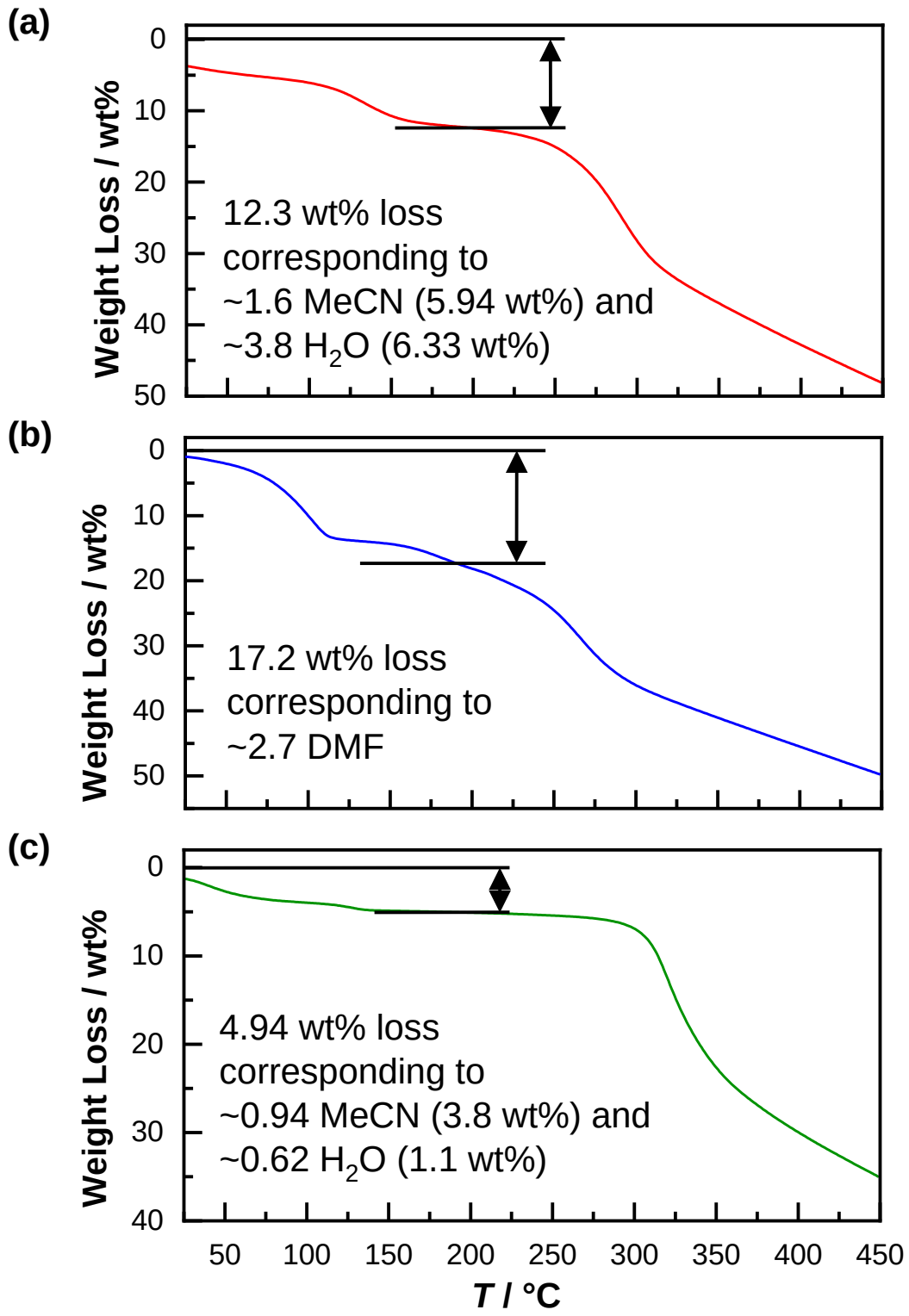


Figure 3.16 Thermogravimetric analyses of (a, red) **3.1^{Cl}a**, (b, blue) **3.1^{Cl}b** and (c, green) **3.2** at a scan rate of 5 °C min^{-1} in a flow of N_2. Non-zero mass loss at 25 °C ascribed to release of volatile MeCN into the N_2 stream during balance stabilisation period at the beginning of the measurement run.

3.2.4 ^{57}Fe Mössbauer Spectroscopy

Validation of the crystallographic Fe oxidation state assignment was performed using ^{57}Fe Mössbauer spectroscopy. Measurement over a large temperature range also confirmed the absence of thermally induced valence tautomerism, albeit in the DMF solvate i.e. **3.1^{Cl}b** only. The spectrum of **3.1^{Cl}b** at 294 K consists of a quadrupole doublet, with a satisfactory parameter set giving an isomer shift of δ = 0.58 mm s^{-1} and a quadrupole splitting ΔE_Q = 1.13 mm s^{-1} (Figure 3.17 and Table 3.3). The isomer shift value is unambiguously assigned as Fe^{III}_{HS} residing in an octahedral environment,[46, 47] with both isomer shift and quadrupole splitting values in agreement with other reported Fe^{III}–tetraoxolene compounds.[10, 11, 27, 30] Upon cooling to 5.8 K, the spectrum transforms to a strong sextet, with a fit to the data giving an isomer shift of δ = 0.61 mm s^{-1} and a quadrupole splitting ΔE_Q = 1.03 mm s^{-1}, which are similarly consistent with Fe^{III}_{HS} in an octahedral environment. Transformation of the spectrum to a sextet at low temperature arises due to spontaneous magnetisation of the sample, which causes Zeeman splitting of the I = 1/2 ground and I = 3/2 excited states of ^{57}Fe into two and four sub-states respectively. Fitting of the data yielded an internal field of B_0 = 47.0 T. These results confirm the Fe oxidation state assignment in **3.1^{Cl}b** as Fe^{III}_{HS}, provide further evidence for the absence of thermally induced valence tautomerism, and provide a significant impetus to study the magnetic properties of **3.1^{Cl}b**, due to the observation of spontaneous magnetisation at low temperature.

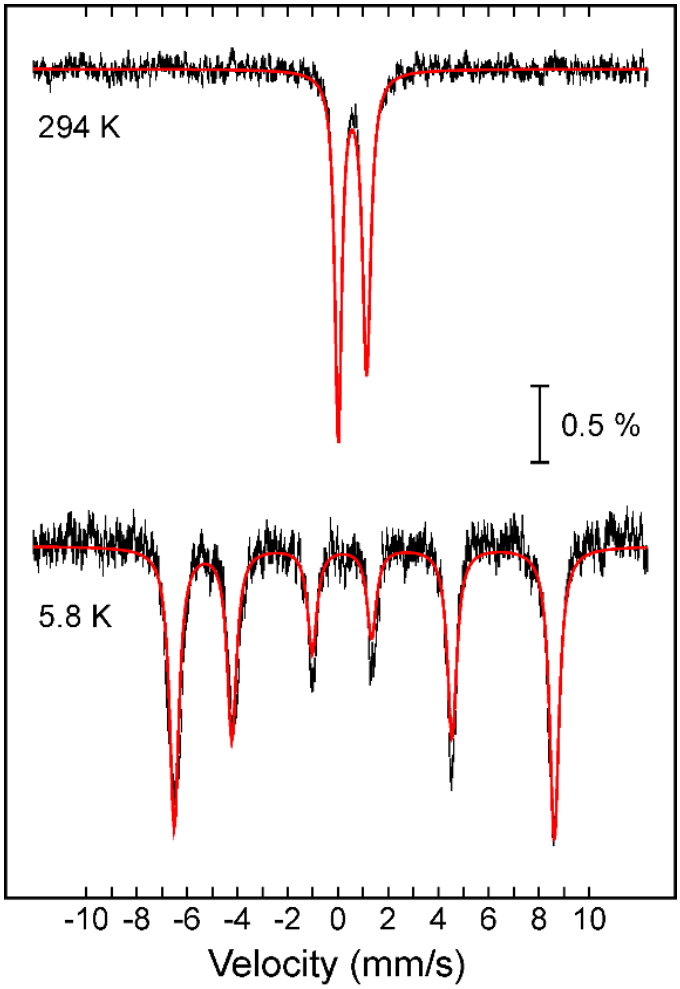


Figure 3.17 ^{57}Fe Mössbauer spectra of **3.1^{Cl}b** at T = 294 K (upper) and T = 5.8 K (lower). The spectra were fit (red) with a quadrupole doublet at T = 294 K and a sextet at T = 5.8 K, representative of Fe^{III}_{HS} and magnetically ordered Fe^{III} respectively. The fitting parameters are given in Table 3.3.

Table 3.3 ^{57}Fe Mössbauer spectral parameters for **3.1^{Cl}b**.

T / K	Species	δ / mm s^{-1}	ΔE_Q / mm s^{-1}	B_0 / T	η / mm s^{-1}	$\Gamma_{L\,(R)}$	I / %
294	Fe^{III}	0.58	1.13	-	-	0.32 (0.40)	100
5.8	Fe^{III}	0.61	1.03	47.0	1	0.45	100

3.2.5 Electronic Spectroscopy

The dark to black colour and metallic lustre of crystals of **3.1^{Cl}b** provided an early indication of the mixed-valence character of the framework (Figure 3.18). Because of this observation, the UV-Visible-Near infrared (UV-Vis-NIR) spectrum of **3.1^{Cl}b** was measured to better understand the presence of any mixed valency. The diffuse-reflectance UV-Vis-NIR spectrum, presented as the Kubelka-Munk transform F(R),

$$\mathrm{F}(R) = \frac{(1-R)^2}{2R} \tag{3.1}$$

where R is the reflectance, of **3.1^{Cl}b** was measured and compared to $(Et_4N)_2[Fe^{III}_2(Clan)_3]\cdot$solvent as reference compound with a redox-inactive cation (Figure 3.19). Although some similarities are observed, there are also notable differences. Like $(Et_4N)_2[Fe^{III}_2(Clan)_3]\cdot$solvent, there are broad absorption bands centred near 17600 and 22500 cm^{-1} in the spectrum of **3.1^{Cl}b**, which are likely due to ligand π–π* and metal-ligand d–π transitions, as for $(Et_4N)_2[Fe^{III}_2(Clan)_3]$ and other mixed-valence Fe–tetraoxolene frameworks.[13, 14, 25] Additionally, an intense, broad absorption band is observed in the NIR region of the spectrum of **3.1^{Cl}b**. Due to the valence pure Fe^{III}_{HS} formulation of **3.1^{Cl}b** assigned from SC-XRD and ^{57}Fe Mössbauer spectroscopic analyses, the NIR band is tentatively attributed to ligand-based IVCT between formal Clan^{2-} and Clan$^{3-\bullet}$ species. which has been proposed in other mixed-valence metal–tetraoxolene frameworks.[10, 13-15, 25] Compared to $(Et_4N)_2[Fe_2(Clan)_3]$, the IVCT band of **3.1^{Cl}b** displays noticeable broadening and shifting of ν_{max} towards higher energy (ν_{max} = 9924 cm^{-1}), as well as some tailing in the low energy NIR region. These differences are due to the differing electronic structures between low symmetry **3.1^{Cl}b** and high symmetry $(Et_4N)_2[Fe_2(Clan)_3]$. The shift of the IVCT band to higher energy possibly reflects an increased barrier to energy transfer from the fully localised **L$_1$** Clan$^{3-\bullet}$ state to the delocalised **L$_2$** Clan^{2-} state, due to charge transfer interactions of **L$_1$** with PhenQ^{2+}.

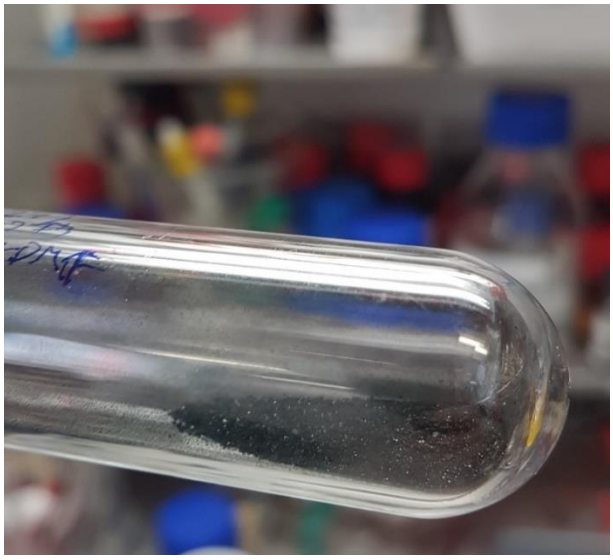


Figure 3.18 Digital photograph of a sample of **3.1^{Cl}b** showing the dark-to-black colour of the crystals.

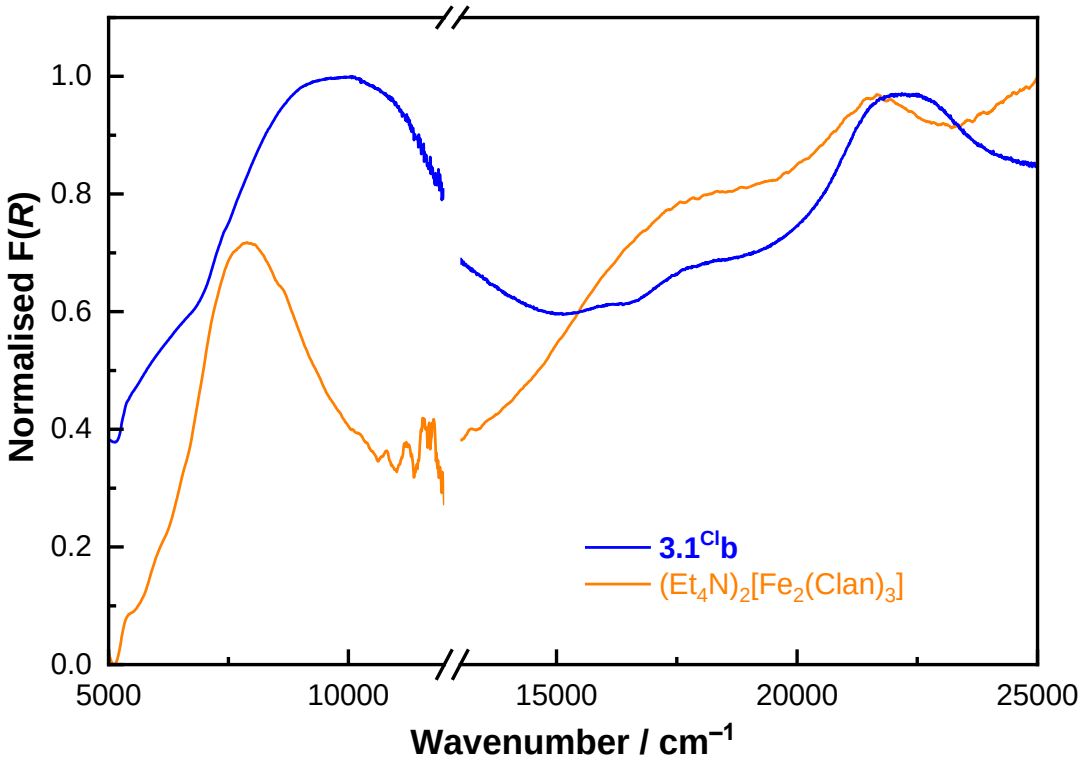


Figure 3.19 Normalised diffuse-reflectance UV-Vis-NIR spectra of **3.1^{Cl}b** (blue) and $(Et_4N)_2[Fe_2(Clan)_3]$ (orange).[14] Each spectrum is normalised to the maximum absorbance set to F(R) = 1. The break in the spectrum corresponds to the NIR detector change over.

The optical band gap (E_g) for **3.1^{Cl}b** was estimated using Tauc analysis[48, 49] upon the experimental UV-Vis-NIR spectrum, yielding an optical band gap of E_g = 0.81 eV (Figure 3.20). This value is within the range expected for a semiconductor and provides additional supporting evidence that **3.1^{Cl}b** is likely to be electrically conductive. The estimated E_g value for **3.1^{Cl}b** is also in good agreement with E_g values reported for the 2D $(Et_4N)_2[Fe_2(Fan)_3]$ and $(Et_4N)_2[Fe_2(Clan)_3]$ frameworks (0.74 eV and 0.79 eV respectively)[14, 25], and the 3D (10,3)-*a* $(^nBu_4N)_2(Fe_2(Fan)_3]$ and $(^nBu_4N)_2(Fe_2(dhbq)_3]$ frameworks (0.67 eV and 0.7 eV respectively).[10, 13] While the partial localisation of Clan$^{3-\bullet}$ ligands in **3.1^{Cl}b** could be expected to cause greater charge localisation and may account for the slighter higher E_g for **3.1^{Cl}b** compared to the aforementioned high symmetry networks, it is salient to remember that optical band gaps do not directly correspond to electronic band gaps.

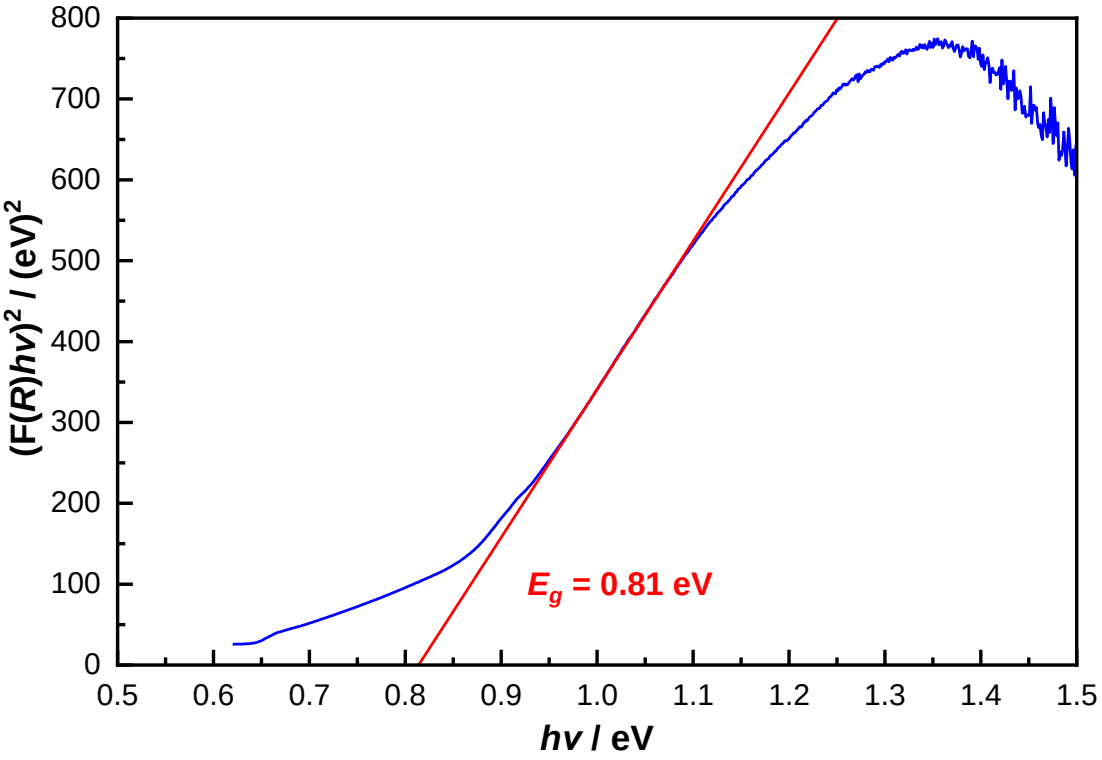


Figure 3.20 Tauc plot of the diffuse-reflectance UV-Vis-NIR data for **3.1^{Cl}b** showing the corresponding optical band gap (E_g).

Analysis of the NIR manifold, tentatively ascribed to ligand-based IVCT, provides further insight into the electronic structure of **3.1^{Cl}b**. Deconvolution of the UV-Vis-NIR spectrum reveals three significant underlying Gaussian bands centred at ν_{max} = 5629, 8544 and 11720 cm^{-1}, with a fourth weaker component at ν_{max} = 10700 cm^{-1} (Figure 3.21); a similar analysis for the NIR manifold of $(Et_4N)_2[Fe_2(Clan)_3]$ is given in Table 3.4. Most significantly, additional underlying Gaussian absorption bands are observed in the NIR manifold of **3.1^{Cl}b** compared to $(Et_4N)_2[Fe_2(Clan)_3]$, which may indicate the presence of multiple CT interactions. This could be accounted for by the presence of localised (**L$_1$**) and delocalised (**L$_2$**) Clan$^{3-\bullet}$ states in **3.1^{Cl}b**, which could be expected to have different activation energies for IVCT due to CT and Coulombic stabilisation of **L$_1$** via stacking with PhenQ^{2+}. The origin of this phenomenon is the subject of future computational study. A theoretical model to relate IVCT to the activation energy for electron transfer has been developed by Hush,[50, 51] which compares the experimental bandwidths at half-height ($\Delta\nu_{1/2}$) to those predicted ($\Delta\nu_{1/2}°$). Following this analysis, the Robin and Day classification of the mixed-valence system,[52] can be estimated using the Γ parameter,[53]

$$\Gamma = 1 - \frac{\Delta\nu_{1/2}}{\Delta\nu_{1/2}^{\circ}} \tag{3.2}$$

From this value, the Robin and Day classification can be determined as: $0 < |\Gamma| < 0.1$ for weakly-coupled Class II systems; $0.1 < |\Gamma| < 0.5$ for moderately-coupled Class II systems; $|\Gamma| \approx 0.5$ at the transition between Class II and Class III; and $0.5 < |\Gamma|$ for Class III systems. The values calculated for the Gaussian bands tentatively ascribed to IVCT suggest that **3.1^{Cl}b** is a weakly-to-moderately coupled Class II material, like the related honeycomb $(Et_4N)_2[Fe_2(Fan)_3]$ and $(Et_4N)_2[Fe_2(Clan)_3]$ frameworks.[14, 25]

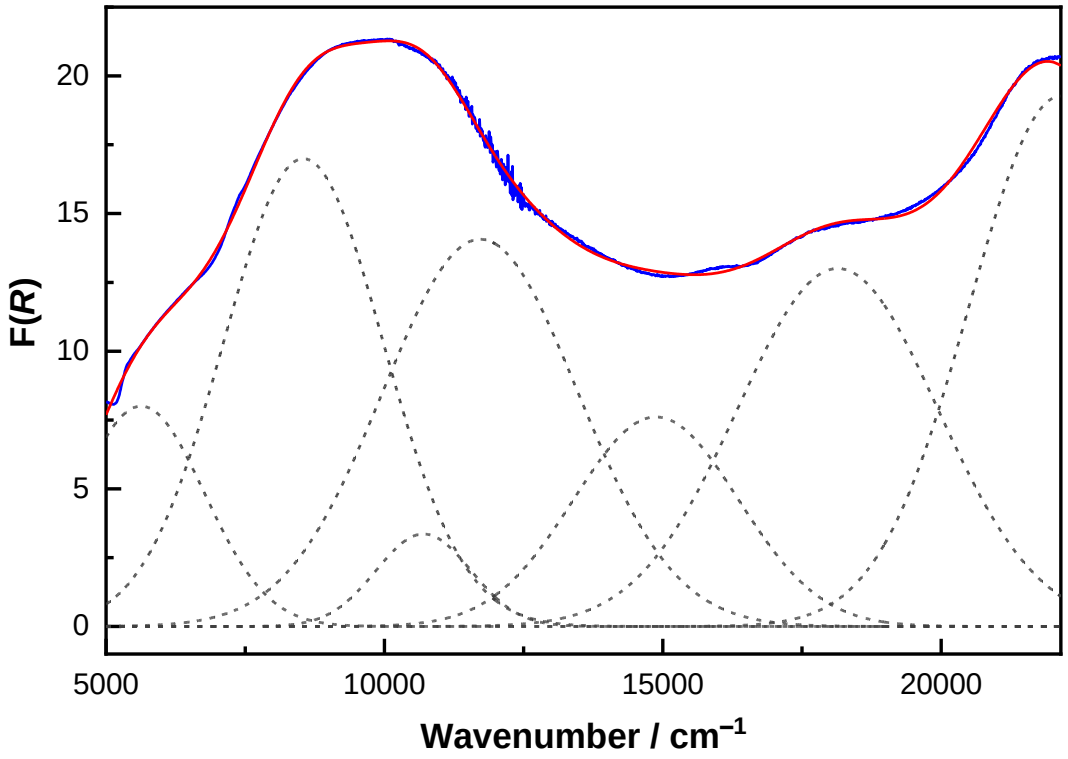


Figure 3.21 Deconvolution of the diffuse-reflectance UV-Vis-NIR spectrum of **3.1^{Cl}b** (blue) with the underlying Gaussian bands from the deconvolution (grey dotted lines) and the associated curvefit (red).

Table 3.4 Spectral data of the deconvoluted diffuse-reflectance spectrum of **3.1^{Cl}b** in comparison with the published data for $(Et_4N)_2[Fe_2(Clan)_3]$.[14] The theoretical predictions for the bandwidths at half-height ($\Delta\nu_{1/2}°$) are provided for the NIR bands which have been tentatively ascribed to IVCT transitions (in bold).

Compound	ν_{max} / cm^{-1}	F(R)$_{max}$ / a.u.	$\Delta\nu_{1/2}$ / cm^{-1}	$\Delta\nu_{1/2}°$ / cm^{-1} [a]	$\lvert\Gamma\rvert$ [b]
3.1^{Cl}b	**5629**	**8.00**	**2677**	**3605**	**0.26**
	8544	**17.0**	**3382**	**4442**	**0.24**
	10700	**3.36**	**2001**	**4972**	**0.60**
	11720	**14.1**	**4120**	**5203**	**0.21**
	14877	7.61	3483	5862	0.41
	18141	13.0	4245	6473	
$(Et_4N)_2[Fe_2(Clan)_3]$	**7445**	**5.68**	**3290**	**4147**	**0.21**
	10075	2.98	2560		
	11390	1.52	1348		
	12890	1.57	1790		
	18577	11.7	6588		

[a] $\Delta\nu_{1/2}° = [2310(\nu_{max})]^{1/2}$ at 298 K.[50, 51]

[b] $\Gamma = 1-(\Delta\nu_{1/2}/\Delta\nu_{1/2}°)$.[53]

3.2.6 Electrochemistry

The presence of multiple possibly interacting redox-active components in **3.1^{Cl}b** prompted analysis of the dc electrochemical behaviour. This was performed by making a paste of **3.1^{Cl}b** in the electrolyte solution of 0.1 M $(Et_4N)PF_6$/MeCN, which was then immobilised on a glassy carbon working electrode as described previously.[13] Cyclic voltammetry was performed over 50–1000 mV s^{-1} scan rates to a maximum of three

cycles (Figure 3.22). Cathodic cycling of the potential revealed two major quasi-reversible processes at E_1 = −0.74 V vs. Fc/Fc^+ (**R_{II}**) and E_2 ca. −1.6 V vs. Fc/Fc^+ (**R_{III}**), with a slight shoulder at −0.5 V vs. Fc/Fc^+ (**R_I**). As expected, based upon the size of Et_4N^+ hindered diffusion of the countercations in the framework channels (either into during cathodic processes, or out of during anodic processes) influences the voltametric behaviour of the framework. This conclusion is supported by narrowing of peak potential widths with increasing scan numbers, particularly at slow scan rates (Figure 3.22a & b), suggestive of an increasingly reversible character of the process at higher scan numbers. This is likely due to slow diffusion of Et_4N^+ in the framework channels, compared to the voltametric time scale. Thus even during anodic cycling, the channels may remain partially occupied with Et_4N^+, with the excess charge in the framework compensated for by diffusion of excess relatively more mobile PF_6^- counteranions into the framework. Moreover, broadening and shifting of the peak potentials to larger absolute values at higher scan rates is consistent with a hindered diffusion regime of countercations in the framework. The presence of three possibly interacting redox-active components in **3.1^{Cl}b**, namely Fe, can^{n-} and PhenQ^{m+}, in comparison to previous studies on metal–tetraoxolene frameworks containing only one[54] or two[7, 8, 10, 13, 34] electroactive components, somewhat complicates precise assignment of the processes.

$PhenQ^{2+}$ undergoes a reversible reduction ($PhenQ^{2+}/PhenQ^{+\bullet}$) at E_1 = −0.43 V vs. Fc/Fc^+ and a second irreversible reduction (presumably $PhenQ^{+\bullet}/PhenQ^0$) at E_2 = −0.82 V vs. Fc/Fc^+ as demonstrated by polarographic measurements on $(PhenQ)(BF_4)_2$.[55] Consequently, **R_I** at −0.5 V vs. Fc/Fc^+ is possibly due to the $PhenQ^{2+}/PhenQ^{+\bullet}$ couple. It is interesting to note that cation reduction (and presumably oxidation upon anodic cycling) does not compromise framework integrity, as suggested by the reversible electrochemical behaviour exhibited by immobilised **3.1^{Cl}b** over several cycles for the entire potential range. Despite a reduced Coulombic interaction between $PhenQ^{+\bullet}$ (generated in situ by reduction of $PhenQ^{2+}$) and the framework, favourable CT interactions between $PhenQ^{+\bullet}$ and framework may offset this reduced Coulombic interaction, thus stabilising the structure. Upon reduction, pyridinium radical cations, and by extension viologen radical cations ($V^{+\bullet}$), are known to dimerise and spin-pair in solution according to:[56-58]

$$2V^{+\bullet} \underset{}{\overset{K_D}{\rightleftharpoons}} (V)_2^{2+} \quad (3.3)$$

Similar dimerisation phenomena have also been observed both in the solid-state and solution, for a range of other neutral, cationic and anionic radicals, including the chloranil semiquinonoid radical anion ($Cl_4BQ^{-\bullet}$).[59] In the solid-state, a key characteristic of these radical dimers is the close co-facial contact between species, at distances significantly shorter than the van der Waals radius of the constituent atoms, but at distances greater than σ-bonds.[59] This also holds true in the solid-state structure of the methyl viologen radical cation [($MeV^{+\bullet}$)PF_6] in which spin-pairing of the $MeV^{+\bullet}$ leads to bulk diamagnetism.[42] Given the alternating co-facial stacking arrangement of $PhenQ^{2+}$ and $Clan^{3-\bullet}$ in **3.1^{Cl}b**, these species are predisposed to radical dimerisation upon reduction of $PhenQ^{2+}$ to $PhenQ^{+\bullet}$. Therefore, the energetic gain provided by spin pairing of electrochemically generated $PhenQ^{+\bullet}$ and extant $Clan^{3-\bullet}$ may thus offset the reduced Coulombic interaction between anionic network and $PhenQ^{2+}$ which would occur upon $PhenQ^{2+}$ reduction, maintaining the integrity of the framework. Future *in situ* electrochemical–P-XRD and EPR spectroelectrochemical studies may provide a more complete understanding of this process and quantify the structural transformations which occur upon reduction.

The process **R$_{II}$** at E_1 = −0.74 V vs. Fc/Fc^+ is assigned to reduction of $Clan^{2-}$ to $Clan^{3-\bullet}$ ligands. This assignment is supported by several previous chemical and voltammetric studies conducted on the related network $(Me_2NH_2)_2[Fe_2(Clan)_3]$. Using cobaltocene ($CoCp_2$, $E°$ = −1.31 V vs. Fc/Fc^+) to reduce $(Me_2NH_2)_2[Fe^{III}{}_2(Clan^{2.67-})_3]\cdot 6DMF\cdot 2H_2O$ to $(CoCp_2)_{1.43}(Me_2NH_2)_{1.57}[Fe_2(Clan^{3-\bullet})_3]\cdot$ 4.9DMF, Harris and co-workers concluded the redox processes were ligand-centred only, as minimal difference in the ^{57}Fe Mössbauer spectra between the as-synthesised and reduced sample were observed, with both spectra well parameterised by values consistent with $Fe^{III}{}_{HS}$.[12] More recently, the electrochemical behaviour of $(Me_2NH_2)_2[Fe^{III}{}_2(Clan^{2.67-})_3]$ was investigated by Long and co-workers using a lithium ion battery (LIB) technique. In this work, a cathodic process at $E_{1/2}$ = 2.71 V vs. Li/Li^+ (−0.73 V vs. Fc/Fc^+) was similarly ascribed to the $Clan^{2-}/Clan^{3-\bullet}$ couple.[34] Given the chemical and topological similarity between **3.1^{Cl}b** and $(Me_2NH_2)_2[Fe^{III}{}_2(Clan^{2.67-})_3]$ it is reasonable to conclude the cathodic process at E_1 = −0.74 V vs. Fc/Fc^+ for **3.1^{Cl}b**, is also due to the $Clan^{2-}/Clan^{3-\bullet}$ couple.

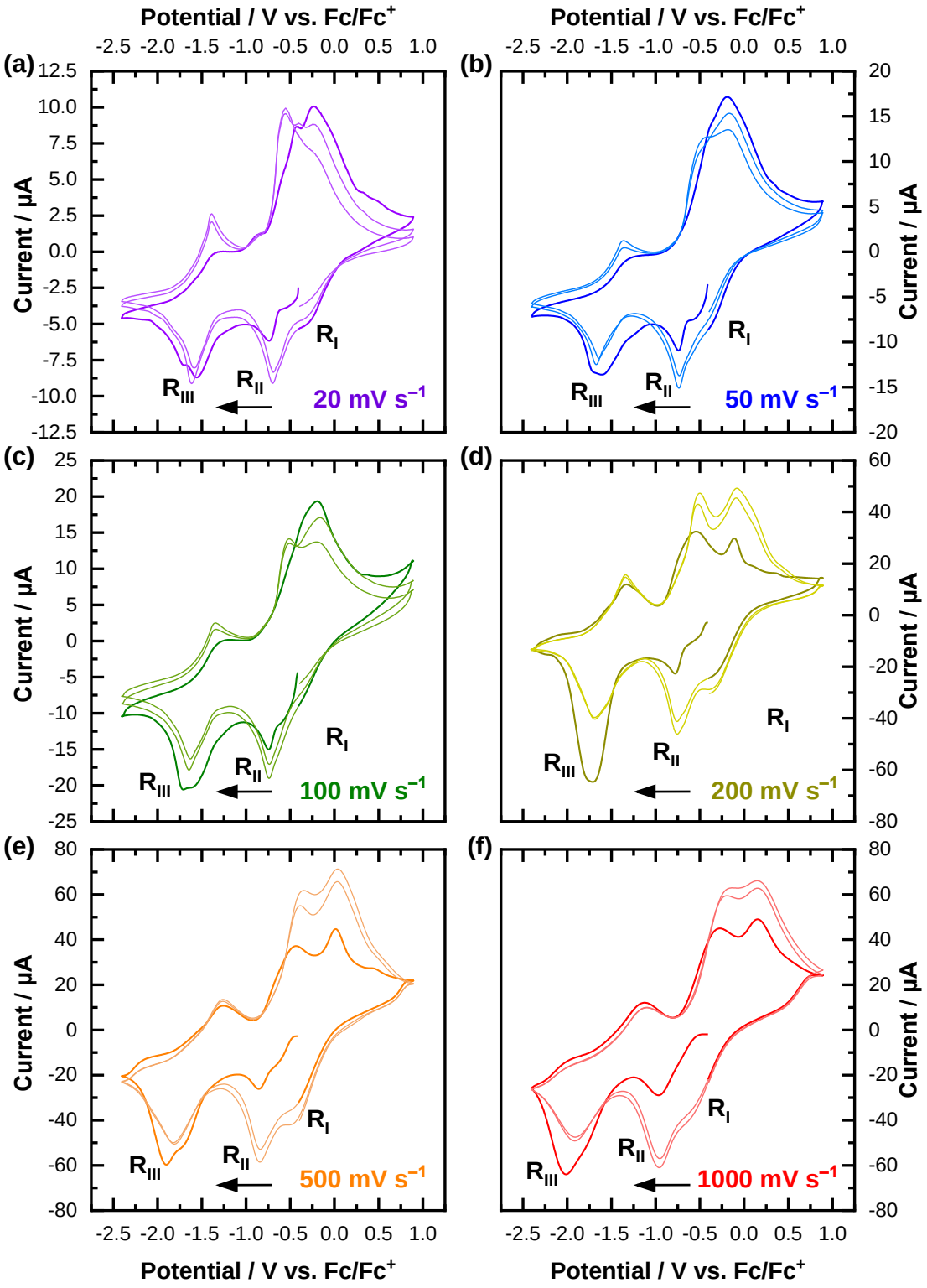


Figure 3.22 Cyclic voltammograms of solid **3.1^{Cl}b** in 0.1 M $(Et_4N)PF_6$/MeCN at (a) 20 mV s^{-1} (purple), (b) 50 mV s^{-1} (blue), (c) 100 mV s^{-1} (green), (d) 200 mV s^{-1} (yellow), (e) 500 mV s^{-1} (orange), and (f) 1000 mV s^{-1} (red). Arrows indicate the direction of the forward scan. First scan shown in bold, subsequent scans shown in fine line.

It is more challenging to draw definitive insights into **R_{III}** at E_2 ca. −1.6 V vs. Fc/Fc^+ in **3.1^{Cl}b**. Long and co-workers performed chemical reduction of the 3D framework $(Bu_4N)_2(Fe_2(dhbq)_3]$ using stoichiometric sodium naphthalenide ($E°$ = −3.10 V vs. Fc/Fc^+)[60] to yield the reduced framework of approximate composition $Na_{3.2}(Bu_4N)_{1.8}[Fe_2(dhbq)_3]$.[10] The nature of the redox processes were determined by *ex situ* ^{57}Fe Mössbauer spectroscopy, with the spectra of the reduced framework adequately described by parameters consistent with Fe^{III}_{HS}. The redox processes were therefore concluded to be exclusively ligand centred. Moreover, *in situ* slow scan voltammetric experiments using a LIB system revealed the framework had a capacity of 3.7 electrons per unit formula i.e. was capable of being reduced to $Li_{3.7}(Bu_4N)_2[Fe_2(dhbq)_3]$, due only to reduction of approximately $(dhbq^{2.67-})_3$ to $(dhbq^{4-})_3$. At least for Fe–dhbq frameworks, these experiments indicate the Fe^{III}/Fe^{II} couple does not play a significant role in the electrochemical behaviour, even at strong reducing potentials i.e. −3.10 V vs. Fc/Fc^+. Contrastingly, more recent voltammetric and ^{57}Fe Mössbauer spectroscopy studies by the same group on $(Me_2NH_2)_2[Fe_2(Clan)_3]\cdot y$DMF have demonstrated involvement of the Fe^{III}/Fe^{II} couple at strong cathodic potentials. In this case, slow scan voltammetry using a LIB battery system showed the as-synthesis framework could be reduced to approximately $Li_6(Me_2NH_2)_2[Fe_2(Clan)_3]\cdot y$DMF, indicating a charge capacity of 6 electrons per unit formula. Given an average ligand charge of 2.67− in the pristine framework, such a charge capacity requires full involvement of the $Clan^{2-}/Clan^{3-\bullet}/Clan^{4-}$ couple in addition to the Fe^{III}/Fe^{II} couple. Importantly, involvement of the Fe^{III}/Fe^{II} in the reductive chemistry of $(Me_2NH_2)_2[Fe_2(Clan)_3]\cdot y$DMF was supported by *ex situ* ^{57}Fe Mössbauer spectroscopy, which revealed significant localised high-spin Fe^{II} character was introduced following electrochemical reduction of the pristine framework. Given the closely matched network topology between **3.1^{Cl}b** and $(Me_2NH_2)_2[Fe_2(Clan)_3]\cdot y$DMF, the observed cathodic process E_2 ca. −1.6 V vs. Fc/Fc^+ in **3.1^{Cl}b** probably involves both the $Clan^{2-}/Clan^{3-\bullet}/Clan^{4-}$ and Fe^{III}/Fe^{II} couples.

3.2.7 Magnetism

Considering the structural similarity of other Fe–tetraoxolene coordination polymers exhibiting interesting magnetic behaviour, we were prompted to study the magnetic properties of **3.1^{Cl}b**. These properties were examined using a range of static and dynamic susceptibility techniques. The temperature dependence of the molar

magnetic susceptibility-temperature product ($\chi_M T$) was measured over 300 to 2 K in two different dc fields (Figure 3.23). At 300 K, the experimental value of $\chi_M T$ is 12.9 cm^3 K mol^{-1}, which is greater than predicted (9.50 cm^3 K mol^{-1}) for a set of two magnetically isolated Fe^{III}_{HS} centres (S = 5/2, g = 2.0) and two $Clan^{3-\bullet}$ ligands (S = 1/2, g =2.0). This behaviour is commonly observed in related 2D honeycomb Fe–tetraoxolene systems,[11, 12, 27, 28] and is attributed to long-range coupling even at 300 K. Upon cooling to 100 K, $\chi_M T$ remains field independent and slowly increases with cooling. Further cooling below 100 K causes $\chi_M T$ to increase dramatically, reaching 327 cm^3 K mol^{-1} at 1 kOe and 78 cm^3 K mol^{-1} at 10 kOe, indicative of strong Fe^{III}–radical coupling leading to magnetic ordering in **3.1^{Cl}b**. Like $(Bu_4N)_2[Fe^{III}_2(dhbq)_3]$,[10] **3.1^{Cl}b** exhibits a marked deviation from Curie-Weiss behaviour below 250 K (Figure 3.24). By performing Curie-Weiss fitting, $\chi_M = C/(T-\Theta)$, of the data between 250–300 K, a Weiss constant Θ = 140 K and Curie constant C = 7.0 cm^3 mol K^{-1} were determined, which are close to those observed for $(Bu_4N)_2[Fe^{III}_2(dhbq)_3]$. The positive Θ value indicates at high temperature, the predominant magnetic interaction is ferromagnetic (FM), whereas at low temperature, net ferrimagnetic (FiM) behaviour dominates.

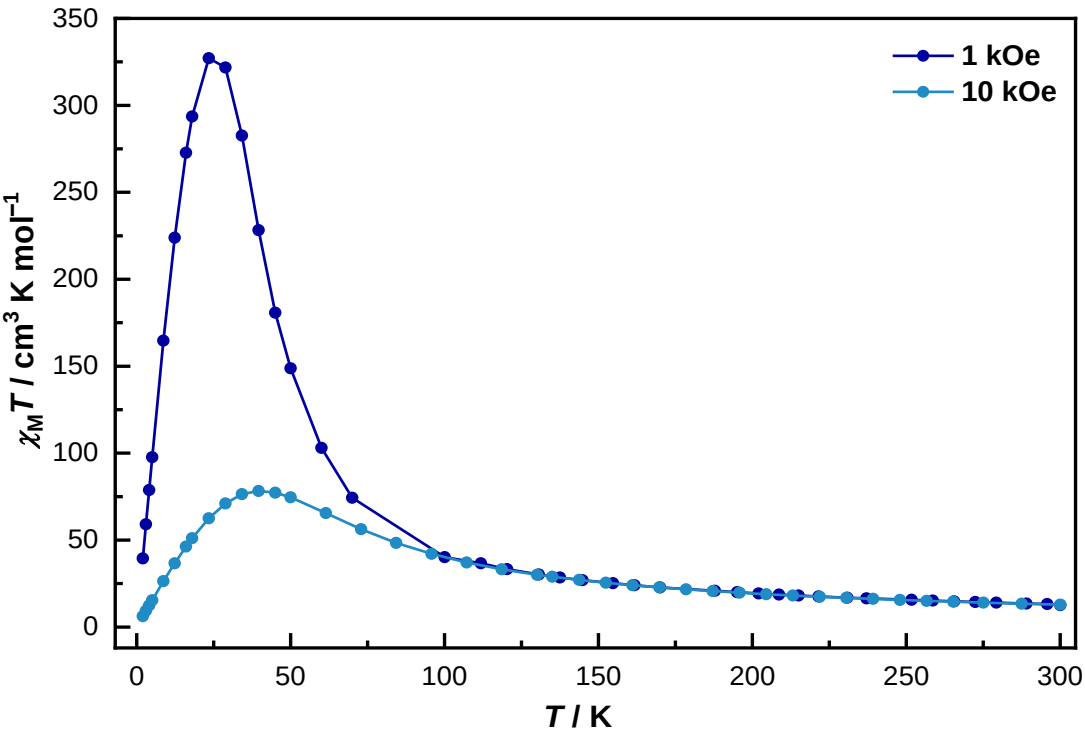


Figure 3.23 Temperature dependence of the dc magnetic susceptibility temperature product ($\chi_M T$) of **3.1^{Cl}b** collected in 1 kOe (dark blue) and 10 kOe (pale blue) applied dc field. Solid lines guide the eye.

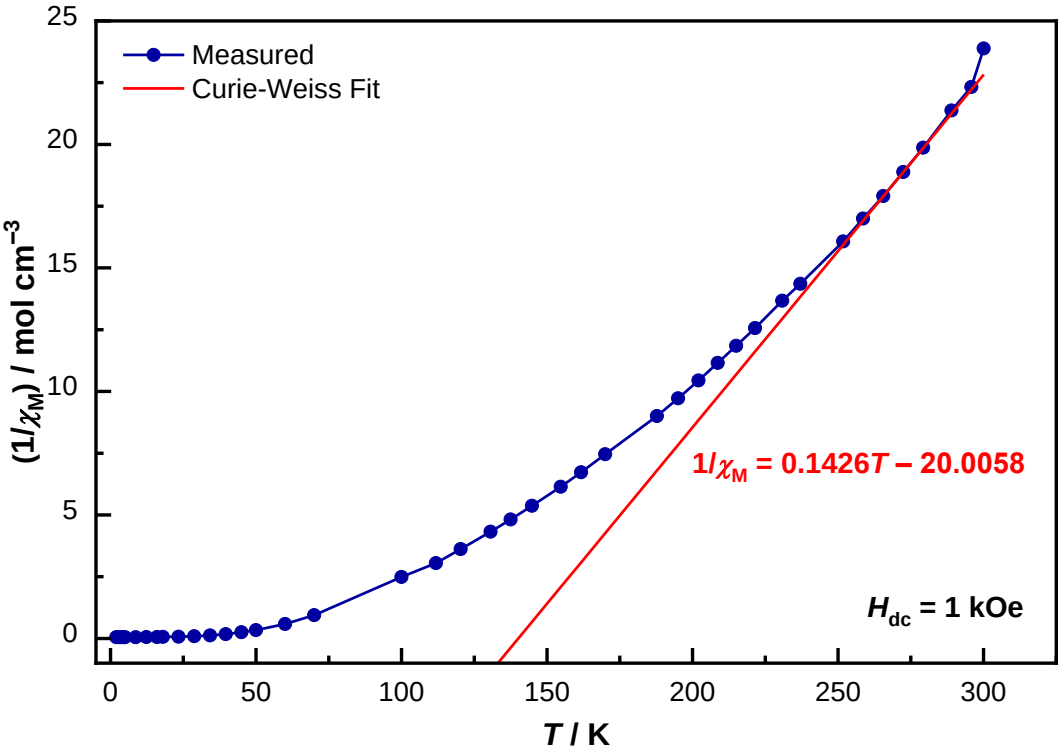


Figure 3.24 Inverse magnetic susceptibility ($1/\chi_M$) versus T for **3.1^{Cl}b** measured in an applied dc field (H_{dc}) of 1 kOe. Solid lines guide the eye. Curie-Weiss fit (red) in the region T = 250–300 K, for calculation of the Weiss constant (Θ).

As indicated by ^{57}Fe Mössbauer spectroscopy, **3.1^{Cl}b** undergoes spontaneous magnetic ordering at low temperature (Section 3.2.4), the presence of which is commonly determined using field-cooled (FC) and zero field-cooled (ZFC) dc susceptibility measurements (Figure 3.25). Bifurcation of the FC and ZFC curves below 40 K confirms that **3.1^{Cl}b** undergoes spontaneous ordering.

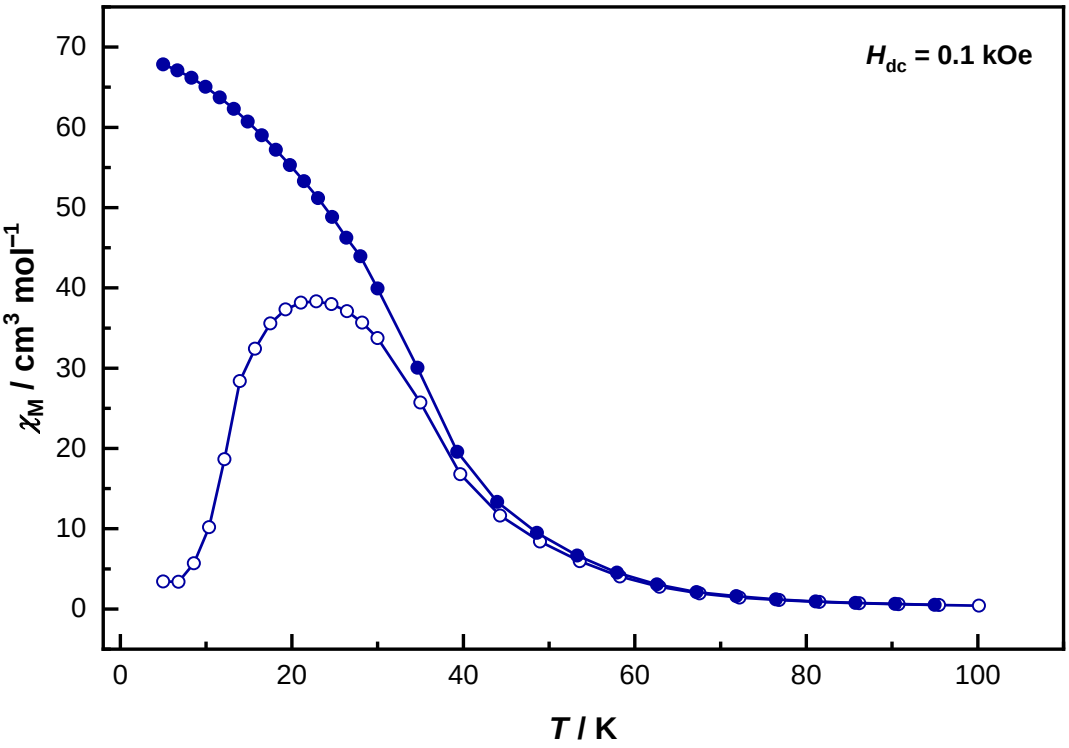


Figure 3.25 Variable-temperature field cooled (FC, closed circles) and zero-field cooled (ZFC, open circles) dc magnetic susceptibility for **3.1^{Cl}b** measured under an applied dc field (H_{dc}) of 0.1 kOe. Solid lines guide the eye.

The precise value of the ordering temperature (T_c) was determined from dynamic susceptibility measurements in zero applied dc field (H_{dc} = 0 Oe) over a range of temperatures. The initial measurements conducted by sweeping over a wide temperature range 2–80 K, reveal a sharp frequency independent peak centred at 30 K for the in-phase ac susceptibility (χ_M'), with non-zero out-of-phase susceptibility (χ_M'') observed as well (Figure 3.26). These results demonstrate that spontaneous ordering in **3.1^{Cl}b** occurs around 30 K consistent with FC and ZFC measurements. By remeasuring the ac susceptibility over a narrower temperature range (15–37 K), the ordering temperature was precisely measured as T_c = 31 K, as evidenced by the peak in χ_M' (Figure 3.27). For $(Me_2NH_2)_2[Fe_2(Clan)_3]\cdot 6DMF\cdot 2H_2O$, there is a slight frequency dependence in maximum χ_M', attributed to glassy magnetic behaviour due to the frustrated magnetic interactions between the two delocalised $Clan^{3-\bullet}$ ligands and Fe^{III}_{HS} centres. In contrast, the χ_M' peak for **3.1^{Cl}b** is frequency independent, suggestive of an absence of glassy magnetic behaviour. This probably arises from the partial

localisation of $Clan^{3-\bullet}$ as $\mathbf{L_1}$ in **3.1^{Cl}b**, in combination with the lower monoclinic symmetry of **3.1^{Cl}b** (compared to trigonally symmetric $(Me_2NH_2)_2[Fe_2(Clan)_3]\cdot 6DMF\cdot 2H_2O$) causing less frustrated magnetic interactions between Fe^{III}_{HS} and the radical ligands. Comparing T_c of **3.1^{Cl}b** to the related 2D honeycomb Fe–tetraoxolene frameworks $(Me_2NH_2)_2[Fe^{III}_2(Clan)_3]\cdot 6DMF\cdot 2H_2O$ (T_c = 80 K) and the reduced analogue $(CoCp_2)_{1.43}(Me_2NH_2)_{1.57}[Fe_2(Clan)_3]\cdot 4.9DMF$ (T_c = 105 K), the decreased value for **3.1^{Cl}b** may stem from less favourable Fe^{III}–radical ligand coupling, due to distortions in the coordination sphere around the Fe^{III} centres in **3.1^{Cl}b**. Importantly, upon desolvation $(Me_2NH_2)_2[Fe^{III}_2(Clan)_3]\cdot 6DMF\cdot 2H_2O$ undergoes a similar geometric distortion as observed in **3.1^{Cl}b**, with a concomitant reduction in ordering temperature to T_c = 26 K, which was ascribed to less favourable Fe^{III}–radical ligand coupling producing a decreased T_c value.

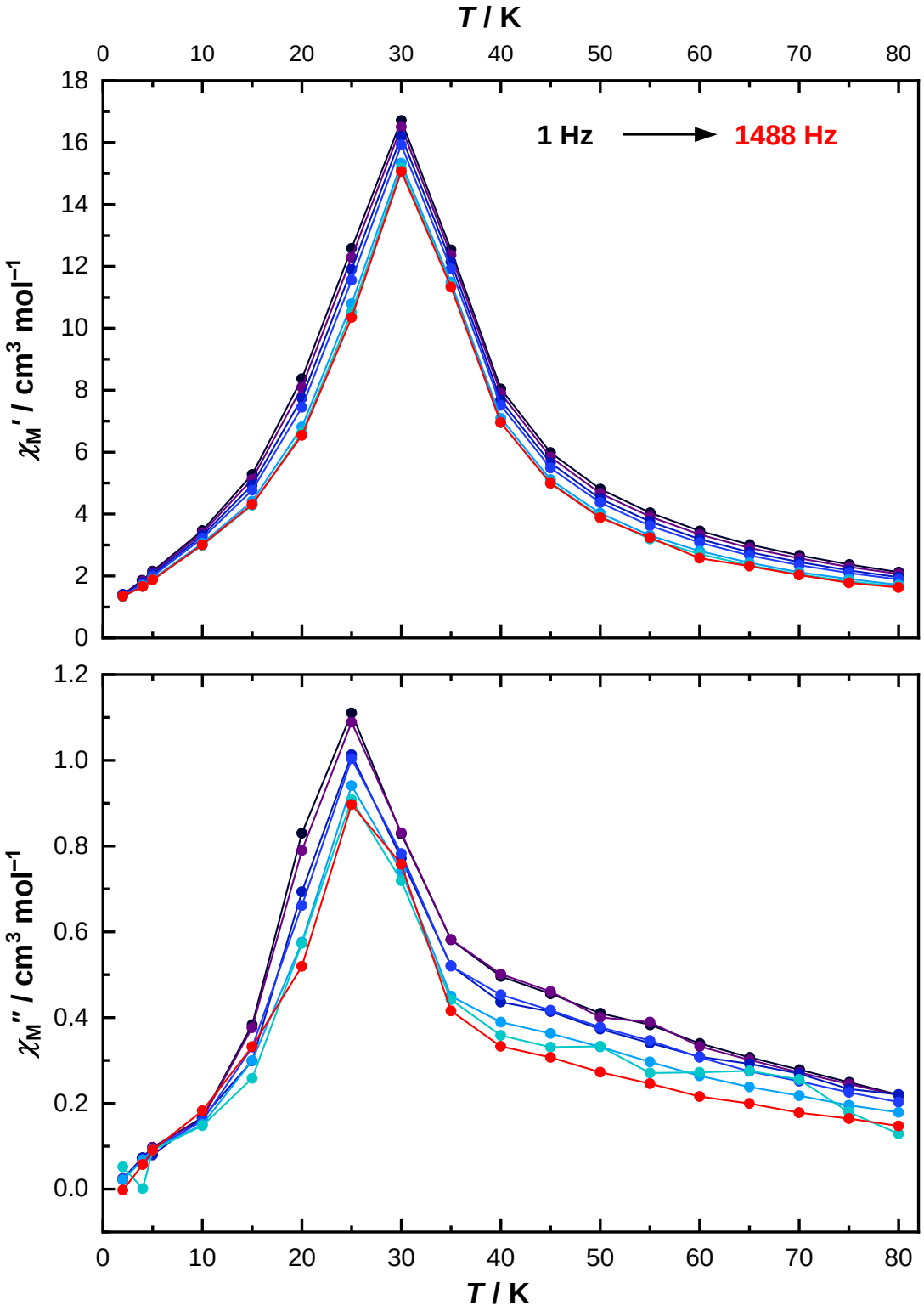


Figure 3.26 Temperature dependence of the in-phase (χ_M') and out-of-phase (χ_M'') ac susceptibility of **3.1^{Cl}b** collected in 0 Oe applied dc field over the range T = 1.8–80 K. Solid lines guide the eye.

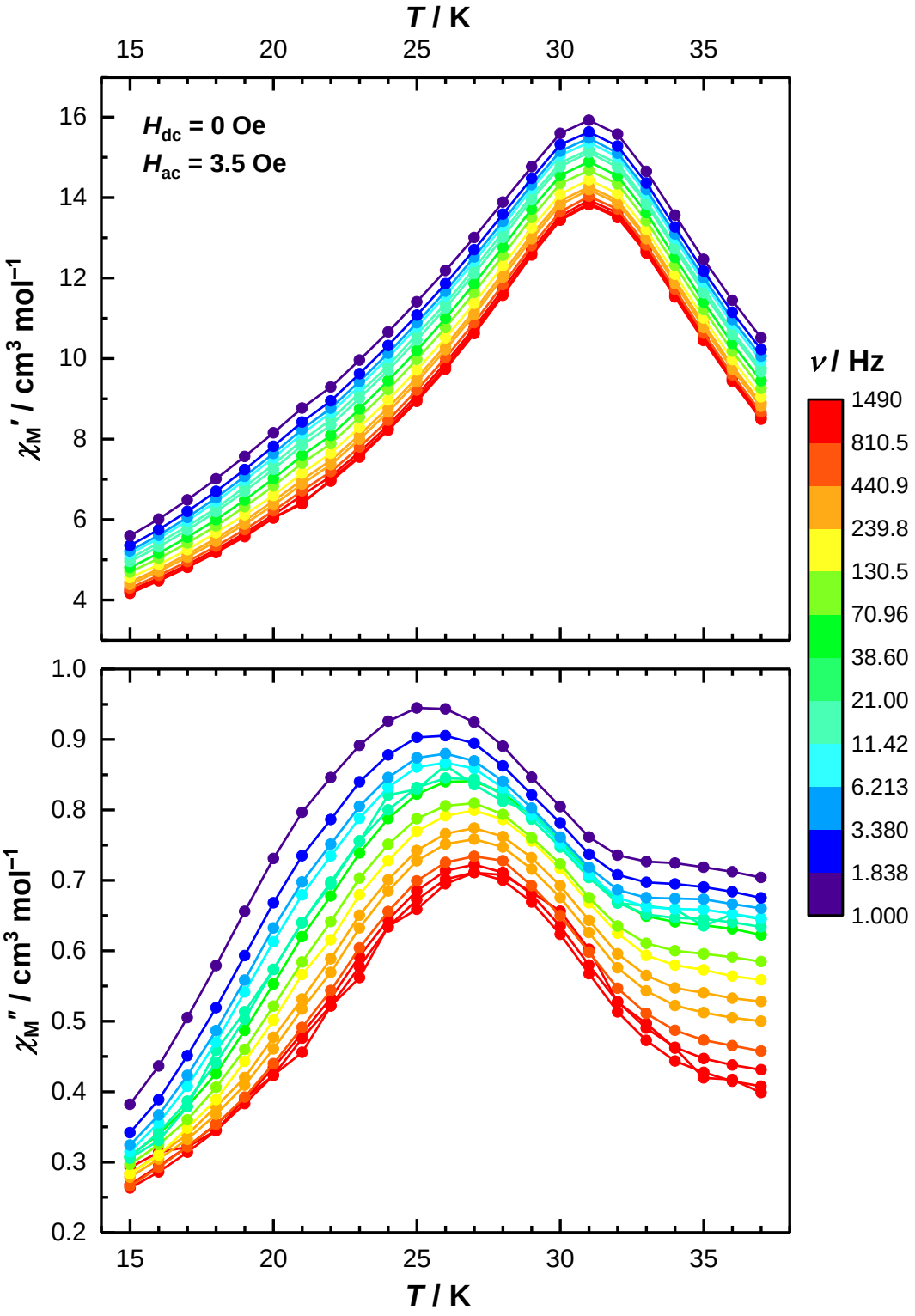


Figure 3.27 Temperature dependence of the in-phase (χ_M') and out-of-phase (χ_M'') ac susceptibility of **3.1^{Cl}b** collected in 0 Oe applied dc field over the range T = 15–37 K. Solid lines guide the eye.

To better understand the magnetic interactions in **3.1^{Cl}b**, low temperature dc magnetisation isotherms were measured (Figure 3.28). The presence of closely spaced low-lying energy levels is demonstrated by superposition of the magnetisation isotherms in the low temperature 2–5.5 K region. For the 2 K isotherm, the magnetisation (M) reaches a maximum value of 8.0 $N_A\mu_B$, which is exactly the value expected for antiferromagnetic (AFM) coupling between two Fe^{III}_{HS} centres (S = 5/2, g = 2.0) and two radical ligands (S = 1/2, g = 2.0), giving an S = 4 Fe_2 repeating unit. Additionally, low temperature magnetic hysteresis measurements were conducted up to a static field of H_{dc} = 50 kOe (Figure 3.29), due to the presence of spontaneous ordering in **3.1^{Cl}b**. Interestingly, despite the relatively high ordering temperature of T_c = 31 K, open hysteresis loops were only observed at 2 K, demonstrating **3.1^{Cl}b** is a permanent porous magnet at low temperature. Gratifyingly, the coercive field of H_c = 2401 Oe compares quite favourably to those observed for $(Me_2NH_2)_2[Fe_2(Clan)_3]\cdot 6DMF\cdot 2H_2O$ and (H_c = 2630 Oe at 1.8 K)[11] and $(^nPr_4N)_2[Fe_2(Clan)_3]\cdot 5$acetone ($H_c$ = 629 Oe at 1.8 K).[27]

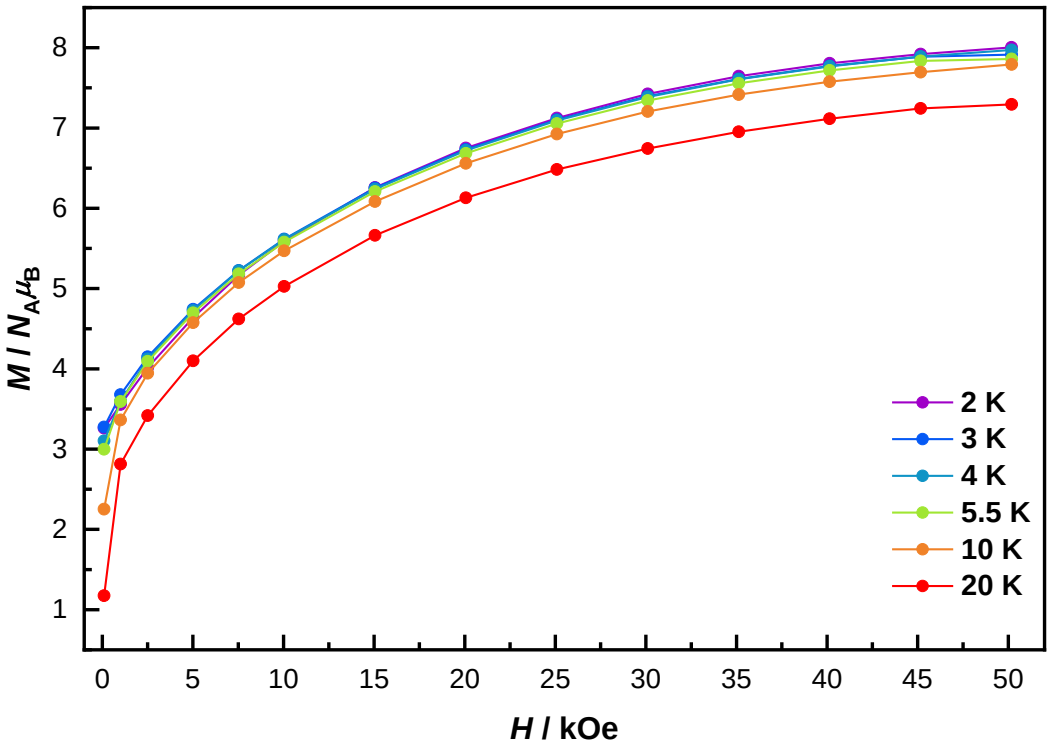


Figure 3.28 Magnetisation isotherms of **3.1^{Cl}b** measured in the range T = 2–20 K. Solid lines guide the eye.

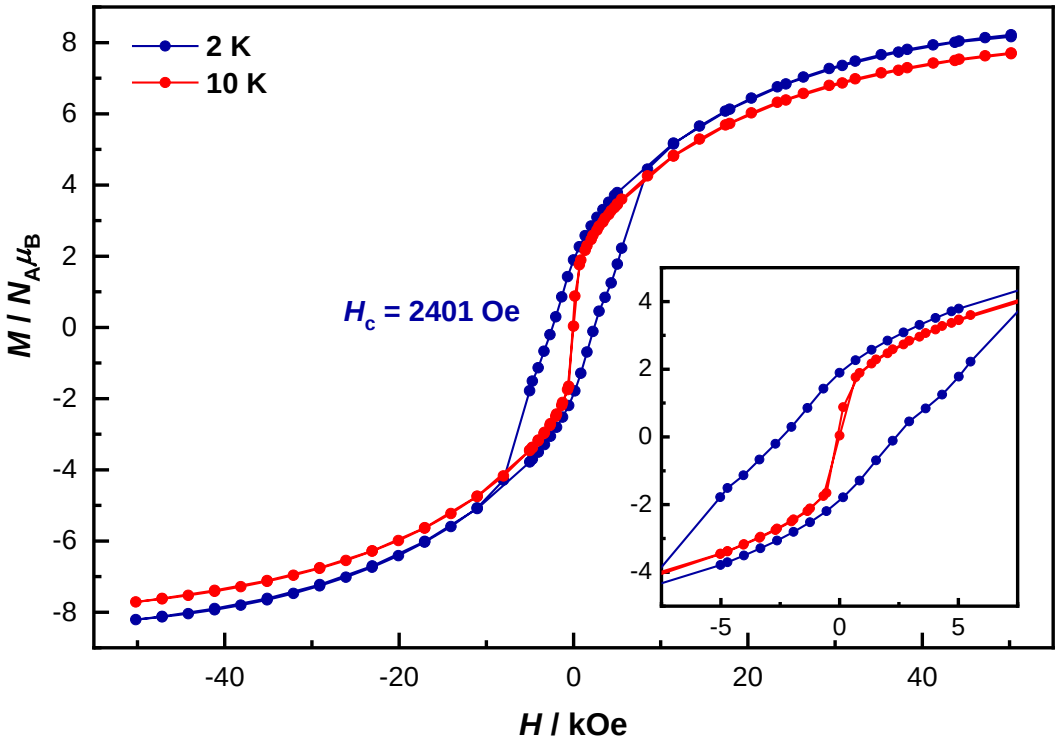


Figure 3.29 Field dependence of the magnetisation of **3.1^{Cl}b**. Inset shows expansion around the hysteresis loops. Solid lines guide the eye.

3.2.8 Electrical Conductivity

Motivated by the presence of IVCT in **3.1^{Cl}b** suggested by electronic spectroscopy, the temperature dependence of the transport properties of **3.1^{Cl}b** was studied. Independent pressed pellet devices were first assembled in a dinitrogen-filled glovebox using a two-point screw cell, and subsequently tested for Ohmic behaviour. Four concordant devices exhibited Ohmic behaviour over the potential range −0.55 to 0.55 V, with the average ambient temperature conductivity equal to σ = 5.6(4) × 10^{-4} S cm^{-1}, and the premier device reaching σ = 6.9(3) × 10^{-4} S cm^{-1} (Table B.1). Unsurprisingly, the values lie somewhat lower than those measured for other semiconductor Fe–tetraoxolene frameworks, which likely arises due to several factors. **3.1^{Cl}b** has relatively lower symmetry and greater extent of radical localisation (Clan$^{3-\bullet}$ and Clan$^{2.5-}$), in contrast to previously reported compounds which exhibit complete delocalisation of the radical ligand valence,[10, 12, 13, 25] or Fe^{II}/Fe^{III} valence.[17, 18] Moreover, pressed pellet measurements are well known to underestimate the intrinsic electrical conductivity, due to the predominance of grain boundary resistance

in the measured pressed pellet resistivity,[61, 62] combined with the highly anisotropic character of the electrical conductivity in 2D layered Fe–tetraoxolene frameworks. Specifically, single crystal measurements conducted perpendicular or parallel to the plane of the anionic sheets reveal conductivity values several orders magnitude different, with unsurprisingly a larger conductivity in the plane of the anionic sheet.[17, 18, 28] This is an especially pertinent factor considering the differences in crystal habit between **3.1^{Cl}b** and other layered Fe–tetraoxolene frameworks. Due to the hexagonal habit exhibited by many honeycomb Fe–tetraoxolene frameworks, there is likely significant preferred orientation of the crystals in the (001) plane, which is equivalent to the plane of the anionic sheet i.e. the highest conductivity direction. In comparison, the block-shaped crystals of **3.1^{Cl}b**, reduces the tendency towards preferred orientation of the crystals in the (001) direction, such that the measured conductivity values for **3.1^{Cl}b** perhaps more closely resemble an average of the parallel and perpendicular conductivity values, while those measured for other layered honeycomb frameworks lie closer to the in-plane conductivity.

Subsequently, variable-temperature conductivity measurements on the four independent pressed pellet devices were performed over the range 300–230 K to better understand the transport properties of **3.1^{Cl}b**. A slight drop in conductivity was observed upon removal from the glovebox, probably due to the slightly higher ambient temperature in the glovebox. Importantly, the devices remained Ohmic when isolated within a thermostated sample container (representative current-bias plot for the premier device given in Figure 3.30).

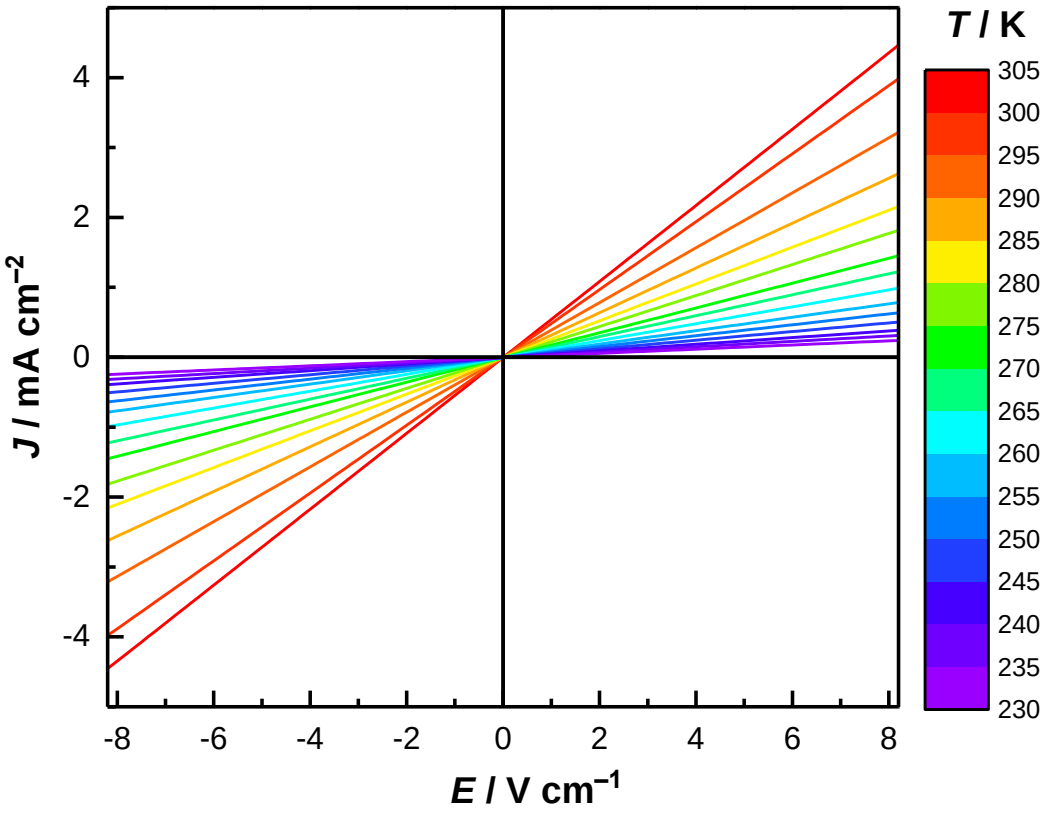


Figure 3.30 Representative variable-temperature current-bias (*i*-*v*) plot for the premier two-point pressed pellet device of **3.1^{Cl}b** (Device 3). Data were measured over the range −0.55 to 0.55 V in 0.01 V steps.

The measured conductivity values range from 3.5(1) × 10^{-4} S cm^{-1} to 5.4(2) × 10^{-4} S cm^{-1} at 300 K. Cooling the devices revealed decreased conductivity values at lower temperatures, consistent with thermally-activated semiconductor behaviour, similarly to other mixed-valence Fe–tetraoxolene frameworks.[10, 12, 13, 25, 28] Fitting of experimental data with the Arrhenius model gives activation energies (E_a) 0.249(2)–0.253(3) eV for the four independent devices (Figure 3.31 for the premier device; Figure B.1 for other devices), which are in good agreement with those calculated for $(Me_2NH_2)_2[Fe_2(Clan)_3]\cdot 6DMF\cdot 2H_2O$ (E_a = 0.26(1) eV) and the desolvated analogue (E_a = 0.19(1) eV).[12]

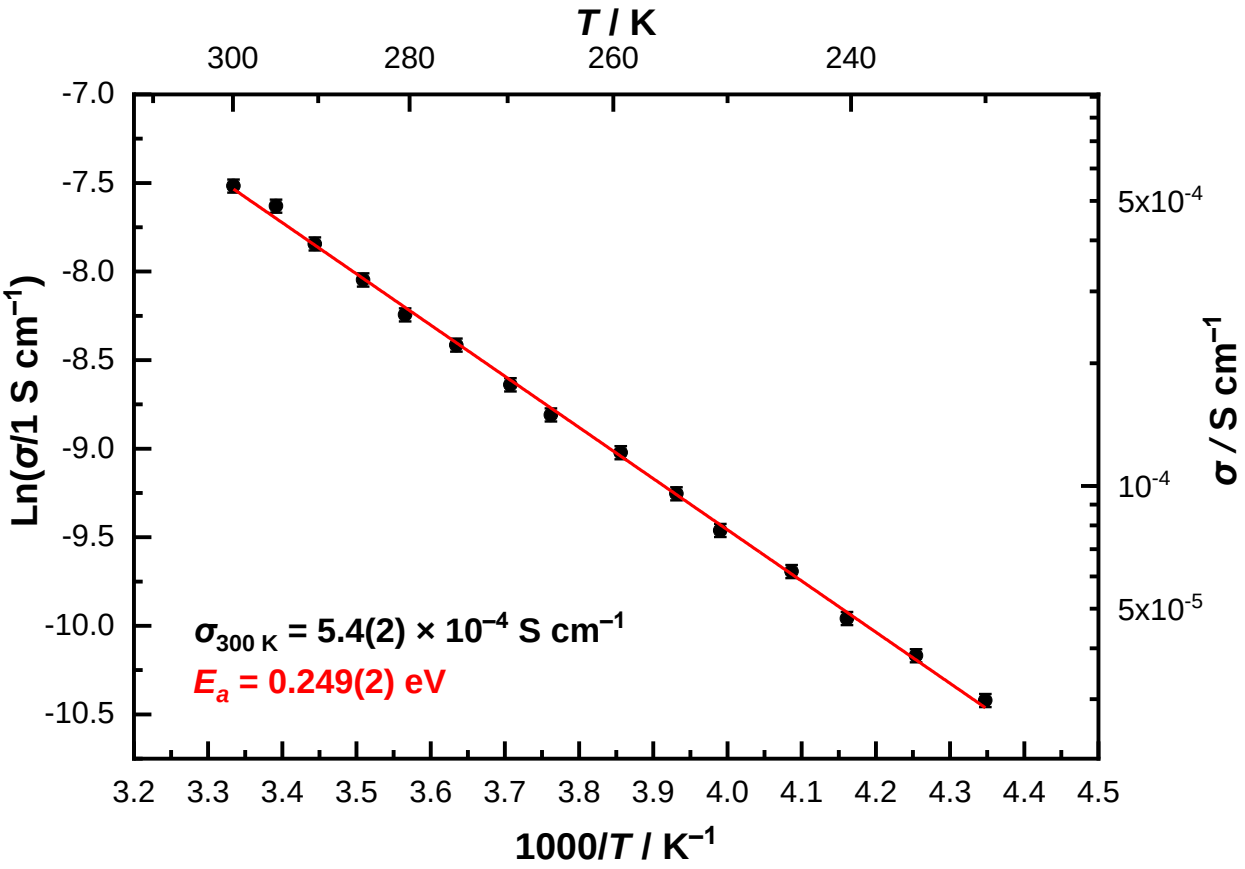


Figure 3.31 Arrhenius plot of the temperature dependence for the electrical conductivity for the premier two-point pressed pellet device of **3.1^{Cl}b** (Device 3). Experimental data (black) and line of best fit (red). Errors bars are ±s.u. Where not visible, error bars lie within the data point.

3.3 Conclusion

Several conclusions can be drawn from the above results. Firstly, SC-XRD measurements demonstrated the redox-active PhenQ^{2+} cation can serve as a countercation in a family of isomorphous 2D honeycomb metal–tetraoxolene frameworks. For the Fe frameworks, the isostructural nature between the three compounds synthesised from fluor-, chlor- and brom-anilate offers the promise of future systematic studies to elucidate the impact of ligand substituents on material properties. Due to time constraints and difficulties in obtaining phase pure samples of the **3.1^{F}** and **3.1^{Br}**, the influence of bridging ligand substituents on the physical properties was not examined. Analogous to other Fe–tetraoxolene frameworks, *in situ*

electron transfer from Fe^{II} to the bridging ligands produces the Fe^{III} frameworks **3.1^{Cl}a**, **3.1^{F}** and **3.1^{Br}** containing the bridging tetraoxolene ligands in multiple valence states. However, in contrast to previously reported compounds, strong CT interactions between electron deficient $PhenQ^{2+}$ and anionic framework causes partial localisation of the $Clan^{3-\bullet}$ valence state in the Fe compounds. For **3.1^{Cl}b**, this produces significant changes to the UV-Vis-NIR spectrum compared to analogous anionic frameworks containing only redox-inactive cations. This likely results from a lower degree of electron delocalisation in **3.1^{Cl}b** caused by partial localisation of the $Clan^{3-\bullet}$ valence state. Despite the strong CT interactions between $PhenQ^{2+}$ and the network in **3.1^{Cl}b**, the electroactivity of the material is not adversely affected, evinced by the quasi-reversible behaviour. The electrochemical behaviour of **3.1^{Cl}b** is in fact richer, arising from the presence of three interacting redox-active species, affording access to new framework redox states. Permanent magnetisation due to spontaneous magnetic ordering at T_c = 31 K in **3.1^{Cl}b** was revealed using a combination of static and dynamic magnetic susceptibility measurements. As expected, spontaneous ordering in **3.1^{Cl}b** arises from AFM coupling between Fe^{III}_{HS} and radical $Clan^{3-\bullet}$ ligands, affording a net FiM material. Thermally activated semiconductor behaviour was demonstrated by temperature dependant electrical conductivity measurements, giving a conductivity of $\sigma_{295\,K} = 4.9 \times 10^{-4}$ S cm^{-1} (E_a = 0.249(2) eV) for the premier device. Long-range charge transport giving rise to electrical conductivity is due to intervalence CT between $Clan^{2-}$ and $Clan^{3-\bullet}$ valence states, as suggested by UV-Vis-NIR spectroscopic data. In combination, these results further reinforce the conclusion that Fe–tetraoxolene frameworks are especially promising candidates as porous, electrically conductive, and magnetic materials. In addition, they demonstrate that redox-active cations are readily incorporated into these materials, where they play both a structure directing role, as well as influencing the valence distribution and material properties by participating in CT interactions between framework and cation.

3.4 Experimental

3.4.1 General Considerations

Unless overwise specified, all manipulations were performed under an atmosphere of dry dinitrogen (N_2) using standard Schlenk techniques or using a Vacuum Atmospheres glovebox. 3,6-Difluoro-1,2,45-tetrahydroxybenzene (H_4Fan) and

3,6-dichloro-1,2,4,5-tetrahydroxybenzene (H_4Clan) were synthesised as described in Chapter 2. For crystallisation of (PhenQ)[Fe_2(Clan)$_3$]·*y*MeCN·zH_2O (**3.1^{Cl}a**) and (PhenQ)[Zn_2(Clan)$_3$]·*y*MeCN·zH_2O (**3.2**), acetonitrile (MeCN) was used without further purification. For solvent exchange on **3.1^{Cl}a** to form (PhenQ)[Fe_2(Clan)$_3$]·*y*DMF (**3.1^{Cl}b**), MeCN and *N*,*N*-dimethylformamide (DMF) were dried twice sequentially over activated 3 Å and 4 Å molecular sieves respectively then stored under an atmosphere of dry N_2. Immediately before use, dry DMF and MeCN were degassed by three freeze-pump-thaw cycles.

3.4.2 Ligand Synthesis

3.4.2.1 3,6-Dibromo-2,5-dihydroxy-1,4-benzoquinone (H_2Bran)

H_2Bran was synthesised using a modified literature procedure,[63] from 2,3,5,6-tetrabromo-1,4-quinone (Br_4BQ) which was obtained using a modified literature procedure.[64, 65] Hydroquinone (27.53 g, 250 mmol) was added to a three-neck round bottom flask fitted with a pressure equalised dropping funnel and reflux condenser topped with a gas outlet tube lead to the hood via a NaOH trap. The hydroquinone was dissolved in glacial AcOH (350 mL) and the reaction was placed in a thermostated oil bath (40 °C) with stirring. Br_2 (92 mL, 1.45 mol) was charged into the dropping funnel, then added dropwise to the stirring reaction over 30 min. The dropping funnel was rinsed into the stirring reaction with AcOH (2 × 50 mL), then charged with conc. HNO_3 (92 mL, 1.45 mol) which was then added dropwise to the reaction over 30 min. The reaction was heated to 60 °C with stirring for 4 hrs, causing vigorous evolution of Br_2 vapour, then cooled to r.t. and stirred overnight. The cooled reaction was poured into stirring H_2O (2.5 L), rising the reaction flask with additional H_2O (2 × 200 mL). The precipitated yellow powder was isolated by suction filtration (Por. 3 frit), then washed with H_2O (1 L) by resuspension with stirring and sonication, followed by 95% MeOH (500 mL). The product was isolated by suction filtration, dried overnight at 100 °C, yielding Br_4BQ as a canary yellow powder which was used without further purification (99.84 g, 94.3%).

Sodium hydroxide (24.00 g, 600 mmol) was dissolved in H_2O (800 mL) then cooled in an ice-water bath to <5 °C. Br_4BQ (25.42 g, 60 mmol) was added portionwise to the vigorously stirring reaction over 10 min, causing a gradual colour change from brown to red. Stirring with cooling was continued a further 30 min., then the reaction

was heated to 70 °C and stirred 90 min. Sodium chloride (52.60 g, 900 mmol) was added to the reaction. Upon dissolution of all NaCl, stirring was ceased and the reaction was cooled slowly to r.t., causing precipitation of a reddish-purple microcrystalline solid. The product was isolated by suction filtration (Por. 3 frit) and washed on the frit with 10% w/v NaOH solution (100 mL), then EtOH (2 × 100 mL). The product was then dried at 100 °C overnight, yielding 15.98 g chocolate-brown product. An additional crop was obtained by cooling the reaction filtrate to 4 °C overnight, which was isolated from the supernatent by suction filtration, washed on the frit with 10% w/v NaOH solution (50 mL), then EtOH (2 × 50 mL) then dried at 100 °C overnight. Combined yield of 16.45 g chocolate-brown Na_2Bran.

Na_2Bran (16.45 g, 48.1 mmol) was suspended in H_2O (500 mL) then heated to 60 °C forming a deep magenta solution, then filtered to remove trace insoluble material. Conc. HCl (160 mL) was added to the stirring filtrate, causing precipitation of a microcrystalline red solid. Stirring was stopped and the reaction cooled slowly to r.t. The product was isolated by suction filtration, dried by suction on the frit, then overnight in vacuo over KOH followed by heating at 100 °C overnight. The crude product was then dissolved in boiling glacial AcOH (260 mL) then hot filtered to remove traces of insoluble brown residue. The filtration was concentrated by boiling (ca. 200 mL) then cooled slowly to rt. causing crystallisation of orange-red scales of the AcOH solvate. The product was isolated by suction filtration (Por. 3 frit), washed on the frit with glacial AcOH (2 × 25 mL), then dried by suction. The product was then washed with cold (−20 °C) toluene (2 × 50 mL), dried by suction, then dried *in vacuo* at 100 °C over KOH yielding the title compound as orange-scales (11.52 g, 64.5% from Br_4BQ).

3.4.2.2 3,6-Dibromo-1,2,4,5-tetrahydroxybenzene (H_4Bran)

H_4Bran was synthesised by reduction of H_2Bran using sodium dithionite. Attempted reduction using Sn/HCl as for the synthesis of H_4Fan and H_4Clan led instead to decomposition of the reaction to a deep brown solution from which no product crystallised. In air, H_2Bran (2.979 g, 10 mmol) was suspended in H_2O (35 mL) with stirring. To the red-purple suspension, sodium dithionite (6.616 g, 38 mmol) was added in one portion, causing an immediate bleaching of solution and precipitation of fine white crystals. The reaction was stirred 30 min. at r.t., then degassed by N_2

bubbling, and cooled to 4 °C overnight. The white product was isolated by suction filtration (Por. 3 frit), washing on the frit with ice-cold degassed H_2O (2 × 20 mL). The product was dried *in vacuo* over KOH, yielding the title compound as a faintly pink solid (1.913 g, 63.8%).

3.4.3 Cation Synthesis

3.4.3.1 5,6-Dihydropyrazino[1,2,3,4-lmn][1,10]phenanthrolinediium dibromide ([PhenQ]Br$_2$)

[PhenQ]Br_2 was synthesized according to a modified literature procedure.[55, 66] 1,10-Phenanthroline (10.813 g, 60 mmol, dried using toluene/H_2O azeotrope) was added to an oven dried round-bottom flask fitted with a reflux condenser and a $CaCl_2$ guard tube, then dissolved in 1,2-dibromoethane (300 mL). The reaction was placed in a thermostated oil bath (140 °C) and heated with stirring for 16 hrs. The reaction was then cooled to r.t., and the precipitated yellow-orange powder isolated by suction filtration, rinsing the reaction flask with acetone (150 mL). The product was washed on the frit with additional acetone (2 × 200 mL) then dried by suction. The yellow crude (21.07 g) was dissolved in the minimum of boiling 80% EtOH (ca. 340 mL), treated with decolorizing charcoal and then hot filtered. The filtrate was cooled to r.t. and stored at −20 °C overnight. The crystallized product was isolated by suction filtration, washing with ice-cold EtOH (2 × 50 mL), acetone (2 × 50 mL) then Et_2O (2 × 50 mL). The product was dried *in vacuo* over P_2O_5, yielding the title compound as orange-brown rods (14.14 g, 64.0%). ^{1}H-NMR (400 MHz, D_2O): δ_H 9.64 (d, J_{AB} = 5.8 Hz, 2H, Ar-***H***2,9), 9.54 (d, J_{AB} = 8.5 Hz, 2H, Ar-***H***4,7), 8.72 (s, 2H, C***H***=C***H***), 8.61 (dd, J_{AB} = 5.8, 8.5 Hz, 2H, Ar-***H***3,6), 5.73 (s, 4H, C***H***$_2$). ^{13}C{^{1}H}-NMR (100 MHz, D_2O): δ_C 149.2, 148.8, 132.5, 130.6, 129.7, 128.2, 53.0. FT-IR (ATR, cm^{-1}): 2934 (w, br), 1635 (w), 1591 (m), 1556 (m), 1499 (w), 1474 (m), 1449 (w), 1418 (m), 1395 (w), 1360 (w), 1340 (w), 1241 (w), 1224 (w), 1151 (w), 1121 (w), 1030 (w), 1010 (w), 935 (m), 866 (s), 769 (w), 713 (m), 695 (s).

3.4.3.2 5,6-Dihydropyrazino[1,2,3,4-lmn][1,10]phenanthrolinediium dinitrate ([PhenQ](NO$_3$)$_2$)

[PhenQ]Br$_2$ was converted to [PhenQ](NO$_3$)$_2$ using anion exchange chromatography. IRA-400(Cl) anion exchange resin (150 mL, 210 meq.) was cleaned by heating (60 °C) in H$_2$O (300 mL) for 30 min. The supernatant was decanted, the resin rinsed with additional H$_2$O (3 × 300 mL) then swollen overnight in 1 M NaOH solution (500 mL). The supernatant was then decanted, and the resin was resuspended in 1 M NaOH (500 mL) before being transferred to a column and eluted with additional 1 M NaOH solution (750 mL) until the eluate was strongly basic. The resin was then eluted with H$_2$O (500 mL) until the eluate was ca. pH 7, then converted to the NO_3^- form by eluting with 1 M HNO$_3$ (1000 mL) until the eluate was strongly acidic, followed by H$_2$O (1000 mL) until the eluate was ca. pH 7. A solution of (PhenQ)Br$_2$ (3.70 g, 10 mmol) in H$_2$O (25 mL) was loaded onto the column, which was then eluted with H$_2$O, collecting 100 mL fractions. Product fractions (tested by monitoring development of intense red colour when an aliquot was added to aqueous sodium dithionite solution; tested negative to AgNO$_3$) were combined and concentrated to dryness at reduced pressure (60 mbar, 50 °C) to a crystalline brownish-orange solid. The product was dried *in vacuo* over P$_2$O$_5$ yielding the title compound as brownish-red crystals (2.97 g, 88.9%). FT-IR (ATR, cm^{-1}): 3042 (w), 3009 (w), 1753 (w), 1637 (w), 1622 (w), 1595 (m), 1557 (m), 1500 (m), 1478 (w), 1448 (w), 1431 (w), 1334 (s, NO_3^- ν_{N-O}), 1320 (s, NO_3^- ν_{N-O}), 1232 (m), 1205 (m), 1173 (w), 1123 (w), 1033 (w), 1009 (w), 937 (m), 863 (s), 825 (m, NO_3^- γ_{N-O}), 770 (w), 716 (m), 702 (s), 617 (w).

3.4.4 Coordination Polymer Synthesis

3.4.4.1 (PhenQ)[Fe$_2$(Clan)$_3$]·yMeCN·zH$_2$O (3.1^{Cl}a)

In air, a solution of (NH$_4$)$_2$Fe^{II}(SO$_4$)$_2$·6H$_2$O (78.43 mg, 0.2 mmol) and [PhenQ]Br$_2$ (148.0 mg, 0.4 mmol) in H$_2$O (4 mL) was carefully layered below a solution of H$_4$Clan (63.3 mg, 0.3 mmol) in MeCN (10 mL) in a soda glass vial (OD = 25 mm), with a buffer layer of 1:1 v/v MeCN/H$_2$O (4 mL) containing LiOAc·2H$_2$O (10.2 mg, 0.1 mmol). For bulk synthesis of **3.1^{Cl}a**, 6 reactions were conducted in parallel. Black parallelepiped crystals with a metallic blue-green lustre suitable for X-ray diffraction

were visible on the vial walls within two days, in addition to a flocculant brown-green powder on the vial bottom. After 7 days, the reactions were transferred to a N_2-filled glovebox for workup. Under N_2, the brown powder was carefully aspirated from the vials in ca. 4 mL mother liquor, then the crystalline product resuspended in the remaining mother liquor, which was then transferred to deoxygenated 2:1 v/v MeCN/H_2O (25 mL total for 6 reactions conducted in parallel). Additional brown powder was removed from the black crystalline product by decanting the supernatant liquid and washing with deoxygenated 2:1 v/v MeCN/H_2O (3 × 50 mL) then deoxygenated MeCN (3 × 50 mL) by resuspension of the crystalline product, sedimentation and decantation of the supernatant. The product was soaked overnight in dry, deoxygenated MeCN (15 mL), then isolated by suction filtration in an N_2-purged glove bag and washed on the frit with MeCN (2 × 10 mL). The yield was not determined due to instability of **3.1a** to solvent loss. For physical property characterisation, the DMF solvate **3.1Clb** was utilised. FT-IR (ATR, cm^{-1}): 3008 (w, br), 2653 (w, br), 1460 (s), 1450 (w), 1439 (w), 1425 (w), 1351 (m), 1238 (w), 1169 (w), 1029 (m), 1002 (m), 901 (w), 843 (s), 771 (w), 713 (w), 695 (m), 604 (m), 573 (m), 480 (s).

3.4.4.2 (PhenQ)[Fe_2(Clan)$_3$]·yDMF (3.1^{Cl}b)

Crystallization of **3.1^{Cl}a** was performed exactly as for **3.1^{Cl}b**, except the workup procedure was modified to handle the product under more rigorously anaerobic conditions. After 7 days of diffusion, the reaction vials were transferred to a N_2-purged glove bag. Under N_2, the brown flocculant powder was carefully decanted from the vials in ca. 4 mL mother liquor, then the crystalline product was dislodged from the vial walls and resuspended in the remaining mother liquor, which was then transferred to deoxygenated 2:1 v/v MeCN/H_2O (25 mL total for 11 reactions conducted in parallel). Additional brown powder was removed from the black crystalline product by decanting the supernatant liquid and resuspending in 2:1 v/v MeCN/H_2O (3 × 100 mL). The product was suspended in 2:1 v/v MeCN/H_2O (30 mL) then transferred to a 2-neck Schlenk tube fitted with a septum and Schlenk cap. The sealed Schlenk tube was removed from the glove bag then attached to a Schlenk line and placed under a dry N_2 atmosphere. The supernatant liquid was decanted by cannula transfer under N_2, and the crystalline product washed by resuspension in dry, deoxygenated MeCN (3 × 20 mL), sedimentation of the product and decantation of the

supernatant liquid by cannula transfer. The product was resuspended in degassed MeCN (20 mL), then soaked overnight (12 hrs.). The supernatant liquid was removed by cannula transfer under N_2, and the product washed with dry, degassed DMF (3 × 20 mL) as above.

The solvent was exchanged by soaking the product overnight in DMF (20 mL), followed by washing with DMF (20 mL), as above. The DMF soaking-wash process was repeated five times total. The black crystalline product was isolated by suction filtration in a flame-dried Schlenk frit under N_2 (Figure 3.32), using dry, deoxygenated DMF (3 × 20 mL) to transfer adherent solids in the Schlenk tube and wash the product on the frit. The solid was then dried *in vacuo* on the frit to a free-flowing crystalline solid. The product on the Schlenk frit was then transferred to a N_2-filled glovebox then transferred into a tared, flame-dried Schlenk tube for storage, yielding **3.1a** as black crystals with a faint blueish-green metallic lustre (529 mg, 39.7% based upon H_4Clan). FT-IR (ATR, cm^{-1}): 3078 (w, br), 3002 (w, br), 2921 (w), 1649 (s, DMF $\nu_{C=O}$), 1466 (s), 1431 (w), 1414 (w), 1390 (w), 1359 (m), 1280 (w), 1252 (w), 1237 (w), 1089 (m), 1031 (m), 1008 (w), 845 (s), 769 (w), 713 (w), 697 (m), 658 (m), 607 (m), 573 (m), 478 (s). Anal. Calcd. for $(C_{14}H_{12}N_2)(Fe_2Cl_6O_{12}C_{18})\cdot 3.7(C_3H_7NO)$: C, 42.74%; H, 3.15%, N, 6.59%. Found: C, 42.85%; H, 3.15%; N, 6.53%.

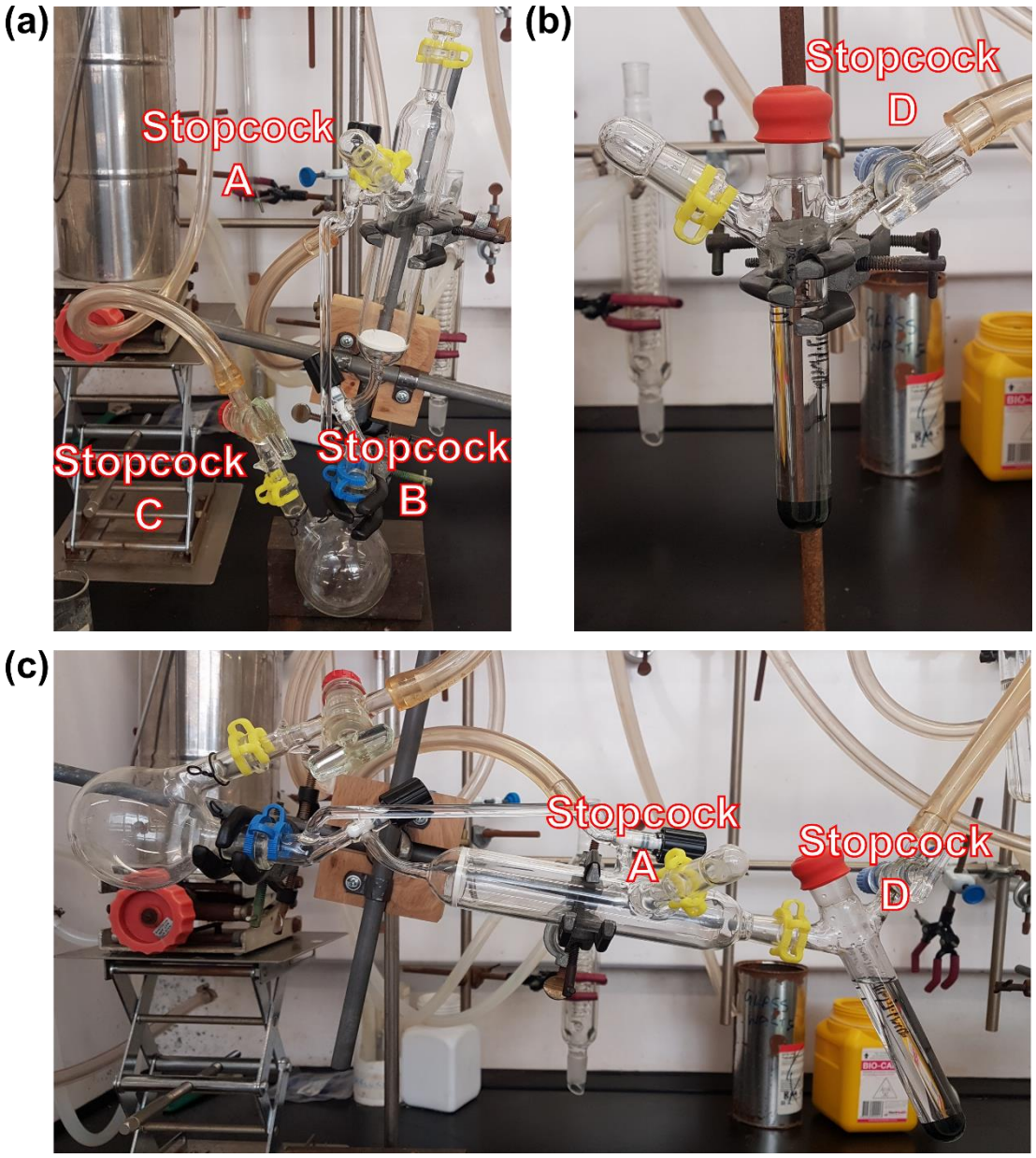


Figure 3.32 Schlenk filtration procedure for isolation of **3.1^{Cl}b** under inert atmosphere conditions. (a) Flame-dried Schlenk frit and receiver flask under dry N_2 atmosphere. After degassing the apparatus, Stopcock B is closed, and Stopcocks A & C are opened to N_2. (b) Two-neck Schlenk tube fitted with septum used for solvent exchange on as-synthesized **3.1^{Cl}a** to yield **3.1^{Cl}b**. Schlenk tube contains **3.1^{Cl}b** (black solid) suspended in dry, deoxygenated DMF. (c) With Stopcocks A & D open to N_2, the Schlenk frit and two-neck Schlenk tube are joined with a brisk current of N_2 flowing from the opened joints.

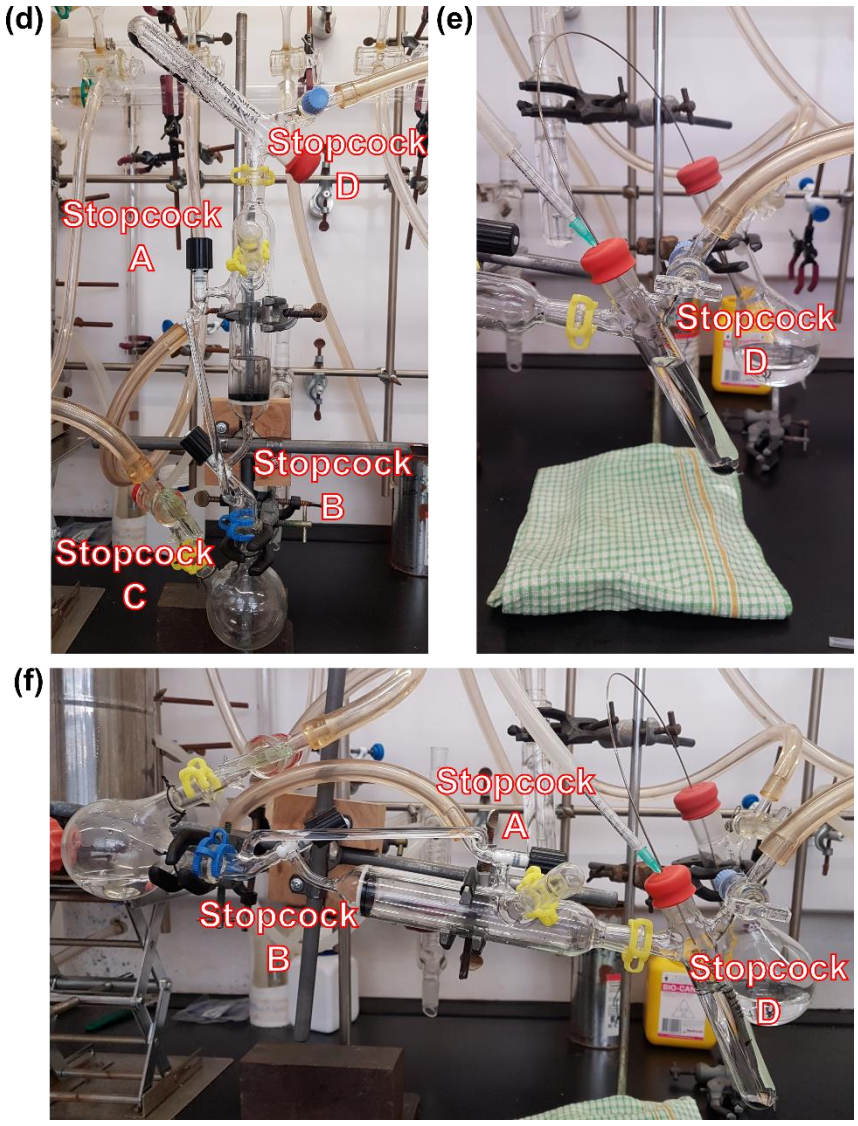


Figure 3.32(cont.) (d) With Stopcock B closed and Stopcocks A & D open to N_2, transfer of the solid **3.1^{Cl}b** from the Schlenk tube onto the frit is accomplished by rotating the apparatus. Note, adherent solid in Schlenk tube. The solid is isolated by placing the receiver flask under static vacuum: with Stopcock B closed, dynamic vacuum is briefly applied to the receiver flask through Stopcock C, which is then closed. With Stopcocks A & D open to N_2, Stopcock B is slowly opened, causing suction of the solvent into the receiver flask. (e & f) Washing of the product on the frit and transfer of adherent solids in the two-neck tube is performed by cannula transfer of dry, deoxygenated DMF with stopcocks A, B & D closed; the apparatus is vented via mineral oil bubbler. Stopcocks A & D are then opened to N_2 and the cannula removed. Washing of product on the frit and transfer of adherent solids is accomplished by repeating (d). Cannula transfer of fresh solvent and washing is performed three times total.

*3.4.4.3 (PhenQ)[Fe$_2$(Fan)$_3$] y*MeCN·z*H$_2$O (3.1^F)*

Crystallisation of **3.1^F** was performed similarly to **3.1^{Cl}a** with some modifications. While use of MeCN as the solvent lead to crystallisation of the desired product, the yield and crystal quality was severely reduced compared to acetone. In air, a solution of $Fe^{II}Cl_2 \cdot 4H_2O$ (19.9 mg, 0.1 mmol), $LiOAc \cdot 2H_2O$ (10.2 mg, 0.1 mmol) and $(PhenQ)Br_2$ (73.6 mg, 0.2 mmol) in H_2O (2 mL) was carefully layered below a solution of H_4Fan (26.7 mg, 0.15 mmol) in acetone (5 mL) in a soda glass vial (OD = 20 mm), with a buffer layer of 1:1 v/v acetone/H_2O (2 mL). Black plate crystals with an intense metallic blue lustre suitable for X-ray diffraction were visible on the vial walls within two days, in addition to a greenish-brown powder on the vial bottom. For SC-XRD, crystals were transferred immediately from the mother liquor to a cryoprotective oil (see Section 3.4.5). Attempts to workup the reactions analogously to **3.1^{Cl}a**, or convert the crystalline product **3.1^F** to a DMF solvate as for **3.1^{Cl}b** lead to decomposition to an unidentified product.

*3.4.4.4 (PhenQ)[Fe$_2$(Bran)$_3$] y*MeCN·z*H$_2$O (3.1^{Br})*

In air, a solution of $(NH_4)_2Fe^{II}(SO_4)_2 \cdot 6H_2O$ (19.6 mg, 0.05 mmol), $LiOAc \cdot 2H_2O$ (1.02 mg, 0.01 mmol) and $(PhenQ)Br_2$ (37.0 mg, 0.1 mmol) in H_2O (2 mL) was carefully layered below a solution of H_4Bran (22.5 mg, 0.075 mmol) in MeCN (5 mL) in a soda glass vial (OD = 20 mm), with a buffer layer of 1:1 v/v MeOH/H_2O. Black parallelepiped crystals with a faint metallic blue-green lustre suitable for X-ray diffraction were visible on the vial walls within two days. For SC-XRD, crystals were transferred immediately from the mother liquor to a cryoprotective oil (see Section 3.4.5). Phase-pure bulk product could not be obtained due to co-crystallisation of a trisbromanilatoferrate(III) salt ($(PhenQ)_3[Fe(bran)_3]_2 \cdot yH_2O$, **3.3**).

*3.4.4.5 (PhenQ)[Zn$_2$(Clan)$_3$]·y*MeCN·z*H$_2$O (3.2)*

Crystallization of **3.2** was performed similarly to **3.1a** using $Zn^{II}(NO_3)_2 \cdot 6H_2O$ and $[PhenQ](NO_3)_2$ with workup in air. Use of $[PhenQ]Br_2$ lead to crystallization of **3.2** contaminated with a copious white solid, presumably a tetrabromidozincate(II) species. Workup and isolation of the crystalline solids was performed without protection from air. In air, a solution of $Zn^{II}(NO_3)_2 \cdot 6H_2O$ (59.5 mg, 0.2 mmol), $[PhenQ](NO_3)_2$ (132.9 mg, 0.4 mmol) and $LiOAc \cdot 2H_2O$ (10.2 mg, 0.1 mmol) in

H_2O (4 mL) was carefully layered below a solution of H_4Clan (63.30 mg, 0.3 mmol) in MeCN (10 mL) in a soda glass vial (OD = 25 mm), with a buffer layer of 1:1 v/v MeCN/H_2O (4 mL). Two reactions were performed in parallel to produce bulk product. Brownish-maroon plate crystals suitable for SC-XRD were visible on the vial walls within two days, in addition to a fine precipitate on the vial bottom. After 7 days, the crystalline product was dislodged from the vial walls and the crystalline product allowed to sediment. The supernatant liquid was carefully decanted, and the combined products washed by resuspending in 2:1 v/v MeCN/H_2O (3 × 20 mL), sedimentation of the crystalline solids and decantation of the supernatant. The product was then washed with MeCN (3 × 20 mL) using a similar procedure, then isolated by suction filtration, washing on the frit with additional MeCN (20 mL), then dried by suction to a free-flowing solid to yield **3.2** as a brownish-maroon powder (31.2 mg, 15.5% based upon H_4Clan). FT-IR (ATR, cm^{-1}): 3392 (w, br), 3072 (w), 3056 (w), 3004 (w), 1629 (w), 1592 (w) 1474 (s), 1375 (s), 1295 (w), 1256 (w), 1173 (w), 1122 (w), 1033 (w), 996 (m), 938 (m), 845 (s), 769 (m), 713 (m), 697 (s), 602 (m), 575 (s), 480 (s). Anal. Calcd. for $(C_{14}H_{12}N_2)(Zn_2Cl_6O_{12}C_{18})\cdot 0.3(C_2H_3N)\cdot 1.8(H_2O)$: C, 38.97%; H, 1.66%, N, 3.21%. Found: C, 38.99%; H, 1.46%; N, 3.25%.

3.4.5 Single-Crystal X-ray Diffraction (SC-XRD)

3.4.5.1 General Considerations

Crystals were transferred directly from the crystallisation mother liquor into an oil-based cryoprotectant to prevent solvent loss. The crystals were then transferred to nylon loops for measurement of crystallographic data. Crystallographic data collection and processing using laboratory sources was performed as described in Chapter 7.

3.4.5.2 (PhenQ)[M_2(Xan)$_3$]·solvent (M = Fe, X = F, Cl, Br; M = Zn, X = Cl)

Crystals of **3.1^{Cl}a**, **3.1^{F}**, **3.1^{Br}**, **3.1^{Cl}b** and **3.2** were removed from the mother liquor and immediately coated with an oil-based cryoprotectant to prevent solvent loss. The crystals were mounted on nylon loops for measurement of crystallographic data using Cu-Kα (λ = 1.54184 Å) radiation on either a Rigaku XtaLAB Synergy-S diffractometer (**3.1^{Cl}a**, **3.1^{F}**, **3.1^{Cl}b**, **3.2**, (PhenQ)Br_2) or an Oxford Diffraction SuperNova diffractometer (**3.1^{Br}**): **3.1^{Cl}a** (Table 3.5), **3.1^{F}**, **3.1^{Br}**, **3.1^{Cl}b** (Table 3.6) and **3.2**

(Table 3.7). Examination of the electron density difference (F_O–F_C) maps revealed the presence of significant positive electron density within the one-dimensional channels of the compounds. This was attributed to severely disordered solvents (MeCN and H_2O for **3.1^{Cl}a, 3.1^{Br}** and **3.2**; acetone and H_2O for **3.1^{F}**; DMF for **3.1^{Cl}b**) which could not be modelled satisfactorily. The scattering contribution of the disordered solvent was accounted for using the SQUEEZE[40] routine in PLATON.[41] The solvation in the channels was then estimated from the electron count determined by SQUEEZE and the molar composition of solvent used during crystallisation. The empirical formulae for **3.1^{Cl}a**, **3.1^{Cl}b**, **3.1^{F}**, **3.1^{Br}** and **3.2** include the estimated solvation. Unless otherwise noted, the thermal and positional parameters for non-hydrogen atoms in the asymmetric unit were refined anisotropically. Hydrogen atoms were placed at calculated positions using suitable riding models and refined using isotropic displacement parameters derived from their parent atoms. In **3.1^{Cl}a**, **3.1^{Cl}b**, **3.1^{F}**, **3.1^{Br}** and **3.2**, the $PhenQ^{2+}$ cation resides on an inversion centre and mirror plane perpendicular to [010] and is thus disordered over two symmetry equivalent positions. The C13A and N13B atoms reside upon symmetry equivalent positions and were refined using EADP and EXYZ restraints. The C13A–C15A (single bond), N13B–C15B (single bond), C13A–C13A′ (double) and C15B–C15B′ (single bond) bond distances in **3.2** were refined using DFIX restraints derived from the equivalent bond distances in $(PhenQ)Br_2$ (Figure 3.8a), in which the cation was unambiguously in the $PhenQ^{2+}$ valence state. In **3.1^{Cl}a**, **3.1^{Cl}b**, **3.1^{F}** and **3.1^{Br}**, the C–C and C–N bond lengths in the pyridinium rings were first compared to the equivalent bond lengths in $(PhenQ)Br_2$ and **3.2** to confirm the cation was in the $PhenQ^{2+}$ valence state. Subsequently, C13A–C15A (single bond), N13B–C15B (single bond), C13A–C13A′ (double) and C15B–C15B′ (single bond) bond distances were refined using the same DFIX restraints as in **3.2**. Crystallographic data and details of the data collections are given in Table 3.5 and Table 3.6.

3.4.5.3 5,6-Dihydropyrazino[1,2,3,4-lmn][1,10]phenanthrolinediium dibromide

Crystallographic data were measured using Cu-Kα (λ = 1.54184 Å) radiation (Table 3.7) on an orange-brown rod removed from the 80% v/v EtOH recrystallisation mother liquor and transferred immediately to a cryoprotective oil.

Table 3.5 Crystallographic data of (PhenQ)[$Fe_2(Clan)_3$]·4.25MeCN·6.3H_2O (**3.1^{Cl}a**) measured at several temperatures.

***T* / K**	**100**	**120**	**140**
Empirical formula	$C_{20.25}H_{18.68}N_{3.13}O_{9.15}Cl_3Fe$	$C_{20.25}H_{18.68}N_{3.13}O_{9.15}Cl_3Fe$	$C_{20.25}H_{18.68}N_{3.13}O_{9.15}Cl_3Fe$
Formula weight	614.41	614.41	614.41
Habit	Block	Block	Block
Crystal system	Monoclinic	Monoclinic	Monoclinic
Space group	*C*2/*m*	*C*2/*m*	*C*2/*m*
a / Å	13.1251(3)	13.1358(2)	13.1493(2)
b / Å	24.2830(6)	24.2759(5)	24.2588(5)
c / Å	8.4943(2)	8.5142(2)	8.5331(2)
α / °	90	90	90
β / °	101.541(2)	101.524(2)	101.485(2)
γ / °	90	90	90
V / Å^3	2652.54(11)	2660.30(9)	2667.44(9)
Z	4	4	4
ρ_{calc} / g cm^{-3}	1.539	1.534	1.530
μ / mm^{-1}	7.823	7.800	7.779
F_{000}	1249.0	1249.0	1249.0
Crystal size / mm^3	0.191 × 0.175 × 0.151	0.191 × 0.175 × 0.151	0.191 × 0.175 × 0.151
Radiation	Cu Kα (λ = 1.54184 Å)	Cu Kα (λ = 1.54184 Å)	Cu Kα (λ = 1.54184 Å)
2θ range / °	7.28 to 148.94	7.282 to 148.878	7.288 to 148.994
Index ranges	$-16 \le h \le 13$ $-26 \le k \le 30$ $-10 \le l \le 10$	$-16 \le h \le 13$ $-26 \le k \le 30$ $-10 \le l \le 10$	$-16 \le h \le 13$ $-26 \le k \le 30$ $-10 \le l \le 10$
Total/independent reflections	13377/2768 [R_{int} = 0.0417, R_{sigma} = 0.0244]	13429/2775 [R_{int} = 0.0413, R_{sigma} = 0.0246]	13427/2786 [R_{int} = 0.0441 R_{sigma} = 0.0249]
Data/restraints/ parameters	2768/89/132	2775/89/132	2786/91/132
Goodness-of-fit on F^2	1.075	1.081	1.095
Final *R* indexes [$I \ge 2\sigma(I)$]	R_1 = 0.0457, wR_2 = 0.1433	R_1 = 0.0454, wR_2 = 0.1440	R_1 = 0.0455, wR_2 = 0.1426
Final *R* indexes [all data]	R_1 = 0.0470, wR_2 = 0.1446	R_1 = 0.0469, wR_2 = 0.1455	R_1 = 0.0470, wR_2 = 0.1443
Largest diff. peak/hole / e Å^{-3}	0.44/−0.83	0.45/−0.81	0.41/−0.81

NB: The empirical formula and F_{000} include the contribution from disordered MeCN and H_2O molecules in the channels of **3.1^{Cl}a**.

Table 3.5(cont.) Crystallographic data of (PhenQ)[$Fe_2(Clan)_3$]·4.25MeCN·6.3H_2O (**3.1^{Cl}a**) measured at several temperatures.

***T* / K**	**160**	**180**	**200**
Empirical formula	$C_{20.25}H_{18.68}N_{3.13}O_{9.15}Cl_3Fe$	$C_{20.25}H_{18.68}N_{3.13}O_{9.15}Cl_3Fe$	$C_{20.25}H_{18.68}N_{3.13}O_{9.15}Cl_3Fe$
Formula weight	614.41	614.41	614.41
Habit	Block	Block	Block
Crystal system	Monoclinic	Monoclinic	Monoclinic
Space group	*C*2/*m*	*C*2/*m*	*C*2/*m*
a / Å	13.1668(2)	13.1854(2)	13.2064(2)
b / Å	24.2424(4)	24.2230(4)	24.1996(4)
c / Å	8.5559(2)	8.58290(10)	8.6108(2)
α / °	90	90	90
β / °	101.457(2)	101.449(2)	101.449(2)
γ / °	90	90	90
V / Å^3	2676.58(9)	2686.74(7)	2697.16(9)
Z	4	4	4
ρ_{calc} / g cm^{-3}	1.525	1.519	1.513
μ / mm^{-1}	7.752	7.723	7.693
F_{000}	1249.0	1249.0	1249.0
Crystal size / mm^3	0.191 × 0.175 × 0.151	0.191 × 0.175 × 0.151	0.191 × 0.175 × 0.151
Radiation	Cu Kα (λ = 1.54184 Å)	Cu Kα (λ = 1.54184 Å)	Cu Kα (λ = 1.54184 Å)
2θ range / °	7.294 to 148.984	7.298 to 149.002	7.306 to 148.994
Index ranges	$-16 \le h \le 13$ $-26 \le k \le 30$ $-10 \le l \le 10$	$-16 \le h \le 13$ $-26 \le k \le 30$ $-10 \le l \le 10$	$-16 \le h \le 13$ $-26 \le k \le 30$ $-10 \le l \le 10$
Total/independent reflections	13508/2794 [R_{int} = 0.0428, R_{sigma} = 0.0255]	13567/2796 [R_{int} = 0.0500, R_{sigma} = 0.0285]	13694/2807 [R_{int} = 0.0551, R_{sigma} = 0.0315]
Data/restraints/ parameters	2794/89/132	2796/89/132	2807/89/132
Goodness-of-fit on F^2	1.069	1.095	1.104
Final *R* indexes [$I \ge 2\sigma(I)$]	R_1 = 0.0463, wR_2 = 0.1464	R_1 = 0.0480, wR_2 = 0.1541	R_1 = 0.0486, wR_2 = 0.1568
Final *R* indexes [all data]	R_1 = 0.0477, wR_2 = 0.1482	R_1 = 0.0494, wR_2 = 0.1559	R_1 = 0.0504, wR_2 = 0.159
Largest diff. peak/hole / e Å^{-3}	0.51/−0.79	0.56/−0.84	0.60/−0.77

NB: The empirical formula and F_{000} include the contribution from disordered MeCN and H_2O molecules in the channels of **3.1^{Cl}a**.

Table 3.5(cont.) Crystallographic data of (PhenQ)[$Fe_2(Clan)_3$]·4.25MeCN·6.3H_2O (**3.1^{Cl}a**) measured at several temperatures.

***T* / K**	**220**	**240**	**260**
Empirical formula	$C_{20.25}H_{18.68}N_{3.13}O_{9.15}Cl_3Fe$	$C_{20.25}H_{18.68}N_{3.13}O_{9.15}Cl_3Fe$	$C_{20.25}H_{18.68}N_{3.13}O_{9.15}Cl_3Fe$
Formula weight	614.41	614.41	614.41
Habit	Block	Block	Block
Crystal system	Monoclinic	Monoclinic	Monoclinic
Space group	*C*2/*m*	*C*2/*m*	*C*2/*m*
a / Å	13.2270(2)	13.2545(2)	13.2757(5)
b / Å	24.1863(3)	24.1592(4)	24.1385(7)
c / Å	8.6448(2)	8.6860(2)	8.7049(3)
α / °	90	90	90
β / °	101.431(2)	101.426(2)	101.389(4)
γ / °	90	90	90
V / Å^3	2710.72(8)	2726.29(9)	2734.60(16)
Z	4	4	4
ρ_{calc} / g cm^{-3}	1.506	1.497	1.492
μ / mm^{-1}	7.655	7.611	7.588
F_{000}	1249.0	1249.0	1249.0
Crystal size / mm^3	0.191 × 0.175 × 0.151	0.191 × 0.175 × 0.151	0.191 × 0.175 × 0.151
Radiation	Cu Kα (λ = 1.54184 Å)	Cu Kα (λ = 1.54184 Å)	Cu Kα (λ = 1.54184 Å)
2θ range / °	7.31 to 149.008	7.318 to 148.808	7.324 to 149
Index ranges	$-16 \le h \le 13$ $-26 \le k \le 30$ $-10 \le l \le 10$	$-16 \le h \le 13$ $-26 \le k \le 30$ $-10 \le l \le 10$	$-16 \le h \le 13$ $-26 \le k \le 30$ $-10 \le l \le 10$
Total/independent reflections	13762/2818 [R_{int} = 0.0621, R_{sigma} = 0.0340]	13818/2839 [R_{int} = 0.0617, R_{sigma} = 0.0344]	13800/2846 [R_{int} = 0.0645, R_{sigma} = 0.0361]
Data/restraints/ parameters	2818/89/132	2839/89/132	2846/89/132
Goodness-of-fit on F^2	1.101	1.092	1.060
Final *R* indexes [$I \ge 2\sigma(I)$]	R_1 = 0.0511, wR_2 = 0.1599	R_1 = 0.0523, wR_2 = 0.1651	R_1 = 0.0542, wR_2 = 0.1675
Final *R* indexes [all data]	R_1 = 0.0535, wR_2 = 0.1632	R_1 = 0.0552, wR_2 = 0.1690	R_1 = 0.0582, wR_2 = 0.1724
Largest diff. peak/hole / e Å^{-3}	0.58/−0.74	0.62/−0.71	0.70/−0.66

NB: The empirical formula and F_{000} include the contribution from disordered MeCN and H_2O molecules in the channels of **3.1^{Cl}a**.

Table 3.6 Crystallographic data of **3.1^{F}**, **3.1^{Br}** and **3.1^{Cl}b**.

Compound	(PhenQ)[Fe_2(Fan)$_3$] ·4.25(Acetone)· 8.6H_2O (**3.1^{F}**)	(PhenQ)[Fe_2(Bran)$_3$] ·4.5MeCN· 5.85H_2O (**3.1^{Br}**)	(PhenQ)[Fe_2(Clan)$_3$] ·4.4DMF (**3.1^{Cl}b**)
Empirical formula	$C_{22.38}H_{27.5}NO_{12.5}F_3Fe$	$C_{20.5}H_{18.6}N_{3.25}O_{8.93}FeBr_3$	$C_{22.6}H_{21.4}N_{3.2}O_{8.2}Cl_3Fe$
Formula weight	623.30	748.87	631.23
Habit	Plate	Plate	Plate
T / K	100.00(10)	130.01(1)	240.00(10)
Crystal system	Monoclinic	Monoclinic	Monoclinic
Space group	*C*2/*m*	*C*2/*m*	*C*2/*m*
a / Å	13.4932(2)	13.1430(17)	13.3813(4)
b / Å	23.5814(3)	24.345(3)	23.8969(4)
c / Å	8.78110(10)	8.7292(13)	8.7982(2)
α / °	90	90	90
β / °	102.811(2)	100.907(15)	100.210(3)
γ / °	90	90	90
V / Å^3	2724.49(7)	2742.6(6)	2768.86(12)
Z	4	4	4
ρ_{calc} / g cm^{-3}	1.520	1.814	1.514
μ / mm^{-1}	5.211	9.995	7.485
F_{000}	1287.0	1467.0	1288.0
Crystal size / mm^3	0.308 × 0.198 × 0.057	0.22 × 0.108 × 0.077	0.213 × 0.124 × 0.044
Radiation	Cu Kα (λ = 1.54184 Å)	Cu Kα (λ = 1.54184 Å)	Cu Kα (λ = 1.54184 Å)
2θ range / °	7.26 to 148.778	10.32 to 140.144	7.398 to 148.984
Index ranges	$-16 \le h \le 16$ $-29 \le k \le 17$ $-11 \le l \le 10$	$-15 \le h \le 15$ $-29 \le k \le 27$ $-10 \le l \le 10$	$-16 \le h \le 15$ $-14 \le k \le 29$ $-10 \le l \le 10$
Total/independent reflections	14384/2849 [R_{int} = 0.0245, R_{sigma} = 0.0152]	2818/2818 [R_{int} = ?, R_{sigma} = 0.0267]	12015/2906 [R_{int} = 0.0289, R_{sigma} = 0.0254]
Data/restraints/ parameters	2849/94/132	2818/89/133	2906/89/132
Goodness-of-fit on F^2	1.090	1.054	1.085
Final R indexes [$I \ge 2\sigma$ (I)]	R_1 = 0.0425, wR_2 = 0.1359	R_1 = 0.0501, wR_2 = 0.1247	R_1 = 0.0366, wR_2 = 0.1084
Final R indexes [all data]	R_1 = 0.0457, wR_2 = 0.1386	R_1 = 0.0568, wR_2 = 0.1278	R_1 = 0.0409, wR_2 = 0.1113
Largest diff. peak/hole/ e Å^{-3}	0.36/−0.29	0.97/−0.72	0.36/−0.23

NB: The empirical formulas and F_{000} include the contribution of disordered solvents in the channels of **3.1^{F}**, **3.1^{Br}** and **3.1^{Cl}b**.

Table 3.7 Crystallographic data of **3.2** and [PhenQ]Br_2.

Compound	(PhenQ)[Zn_2(Clan)$_3$]·4.5MeCN·6.5H_2O (**3.2**)	[PhenQ]Br_2
Empirical formula	$C_{20.5}H_{19.25}N_{3.25}O_{9.25}Cl_3Zn$	$C_{14}H_{12}N_2Br_2$
Formula weight	630.86	368.08
Habit	Plate	Rod
T / K	99.9(5)	99.99(10)
Crystal system	Monoclinic	Triclinic
Space group	*C*2/*m*	*P*−1
a / Å	13.3133(2)	7.5127(2)
b / Å	24.3499(4)	8.0997(3)
c / Å	8.49560(10)	11.1124(4)
α / °	90	104.027(3)
β / °	101.916(2)	102.584(2)
γ / °	90	93.101(2)
V / Å^3	2694.74(7)	636.18(4)
Z	4	2
ρ_{calc} / g cm^{-3}	1.555	1.921
μ / mm^{-1}	4.48	7.926
F_{000}	1280.0	360.0
Crystal size / mm^3	0.214 × 0.142 × 0.034	0.327 × 0.078 × 0.067
Radiation	Cu Kα (λ = 1.54184 Å)	Cu Kα (λ = 1.54184 Å)
2θ range / °	7.26 to 148.998	8.446 to 150.554
Index ranges	$-16 \le h \le 10$ $-30 \le k \le 30$ $-10 \le l \le 10$	$-9 \le h \le 8$ $-10 \le k \le 10$ $-13 \le l \le 13$
Total/independent reflections	14431/2821 [R_{int} = 0.0248, R_{sigma} = 0.0160]	13193/2612 [R_{int} = 0.0278, R_{sigma} = 0.0173]
Data/restraints/ parameters	2821/89/132	2612/0/163
Goodness-of-fit on F^2	1.081	1.102
Final R indexes [$I \ge 2\sigma(I)$]	R_1 = 0.0543, wR_2 = 0.1871	R_1 = 0.0199, wR_2 = 0.0503
Final R indexes [all data]	R_1 = 0.0556, wR_2 = 0.1884	R_1 = 0.0203, wR_2 = 0.0505
Largest diff. peak/hole/ e Å^{-3}	0.57/−1.22	0.34/−0.45

NB: The empirical formula and F_{000} of **3.2** includes the contribution of disordered MeCN and H_2O molecules in the channels.

3.4.6 Powder X-ray Diffraction (P-XRD)

P-XRD data were measured using synchrotron (**3.1^{Cl}a**) or laboratory instrumentation (**3.1^{Cl}b**, **3.2**) as described in Chapter 7. P-XRD data were measured at 250 K for **3.1^{Cl}a** and **3.2** (MeCN slurry), and at 100 and 240 K for **3.1^{Cl}b** (isolated compound). In air, samples of **3.1^{Cl}a** or **3.2** suspended in MeCN were gently ground, then transferred as a slurry to a borosilicate capillary (OD = 0.7 mm) which was then flame sealed. In a N_2-filled glovebox, the isolated compound **3.1^{Cl}b** was gently ground, then transferred to a borosilicate capillary (OD = 0.5 mm). The capillary was then sealed with an electric arc lighter and wax, before being transferred out of the glovebox for measurement.

3.5 References

[1] R. Murase, C. F. Leong, D. M. D'Alessandro, *Inorg. Chem.* **2017**, *56*, 14373-14382.

[2] D. M. D'Alessandro, J. R. R. Kanga, J. S. Caddy, *Aust. J. Chem.* **2011**, *64*, 718-722.

[3] T. B. Faust, D. M. D'Alessandro, *RSC Adv.* **2014**, *4*, 17498-17512.

[4] A. E. Thorarinsdottir, T. D. Harris, *Chem. Rev.* **2020**, *120*, 8716-8789.

[5] L. S. Xie, G. Skorupskii, M. Dincă, *Chem. Rev.* **2020**, *120*, 8536-8580.

[6] M. L. Mercuri, F. Congiu, G. Concas, S. A. Sahadevan, *Magnetochemistry* **2017**, *3*, 17.

[7] K. Taniguchi, J. Chen, Y. Sekine, H. Miyasaka, *Chem. Mater.* **2017**, *29*, 10053-10059.

[8] J. Chen, K. Taniguchi, Y. Sekine, H. Miyasaka, *J. Magn. Magn. Mater.* **2020**, *494*, 165818.

[9] L. Liu, J. A. DeGayner, L. Sun, D. Z. Zee, T. D. Harris, *Chem. Sci.* **2019**, *10*, 4652-4661.

[10] L. E. Darago, M. L. Aubrey, C. J. Yu, M. I. Gonzalez, J. R. Long, *J. Am. Chem. Soc.* **2015**, *137*, 15703-15711.

[11] I.-R. Jeon, B. Negru, R. P. Van Duyne, T. D. Harris, *J. Am. Chem. Soc.* **2015**, *137*, 15699-15702.

[12] J. A. DeGayner, I.-R. Jeon, L. Sun, M. Dincă, T. D. Harris, *J. Am. Chem. Soc.* **2017**, *139*, 4175-4184.

[13] R. Murase, B. F. Abrahams, D. M. D'Alessandro, C. G. Davies, T. A. Hudson, G. N. L. Jameson, B. Moubaraki, K. S. Murray, R. Robson, A. L. Sutton, *Inorg. Chem.* **2017**, *56*, 9025-9035.

[14] C. J. Kingsbury, B. F. Abrahams, D. M. D'Alessandro, T. A. Hudson, R. Murase, R. Robson, K. F. White, *Cryst. Growth Des.* **2017**, *17*, 1465-1470.

[15] M. E. Ziebel, L. E. Darago, J. R. Long, *J. Am. Chem. Soc.* **2018**, *140*, 3040-3051.

[16] G. V. Shilov, Z. K. Nikitina, N. S. Ovanesyan, S. M. Aldoshin, V. D. Makhaev, *Russ. Chem. Bull.* **2011**, *60*, 1209-1219.

[17] S. Benmansour, A. Abhervé, P. Gómez-Claramunt, C. Vallés-García, C. J. Gómez-García, *ACS Appl. Mater. Interfaces* **2017**, *9*, 26210-26218.

[18] S. A. Sahadevan, A. Abhervé, N. Monni, C. Sáenz de Pipaón, J. R. Galán-Mascarós, J. C. Waerenborgh, B. J. C. Vieira, P. Auban-Senzier, S. Pillet, E.-E. Bendeif, P. Alemany, E. Canadell, M. L. Mercuri, N. Avarvari, *J. Am. Chem. Soc.* **2018**, *140*, 12611-12621.

[19] K. S. Min, A. L. Rheingold, A. DiPasquale, J. S. Miller, *Inorg. Chem.* **2006**, *45*, 6135-6137.

[20] K. S. Min, A. G. DiPasquale, J. A. Golen, A. L. Rheingold, J. S. Miller, *J. Am. Chem. Soc.* **2007**, *129*, 2360-2368.

[21] P. Zhang, M. Perfetti, M. Kern, P. P. Hallmen, L. Ungur, S. Lenz, M. R. Ringenberg, W. Frey, H. Stoll, G. Rauhut, J. van Slageren, *Chem. Sci.* **2018**, *9*, 1221-1230.

[22] W. R. Reed, M. A. Dunstan, R. W. Gable, W. Phonsri, K. S. Murray, R. A. Mole, C. Boskovic, *Dalton Trans.* **2019**, *48*, 15635-15645.

[23] A. E. Thorarinsdottir, R. Bjornsson, T. D. Harris, *Inorg. Chem.* **2020**, *59*, 4634-4649.

[24] P. Dechambenoit, J. R. Long, *Chem. Soc. Rev.* **2011**, *40*, 3249-3265.

[25] R. Murase, C. J. Commons, T. A. Hudson, G. N. L. Jameson, C. D. Ling, K. S. Murray, W. Phonsri, R. Robson, Q. Xia, B. F. Abrahams, D. M. D'Alessandro, *Inorg. Chem.* **2020**, *59*, 3619-3630.

[26] J. A. DeGayner, K. Wang, T. D. Harris, *J. Am. Chem. Soc.* **2018**, *140*, 6550-6553.

[27] J. Chen, Y. Sekine, Y. Komatsumaru, S. Hayami, H. Miyasaka, *Angew. Chem. Int. Ed.* **2018**, *57*, 12043-12047.

[28] J. Chen, Y. Sekine, A. Okazawa, H. Sato, W. Kosaka, H. Miyasaka, *Chem. Sci.* **2020**, *11*, 3610-3618.

[29] Y. Sekine, J. Chen, N. Eguchi, H. Miyasaka, *Chem. Commun.* **2020**.

[30] K. Nagayoshi, M. K. Kabir, H. Tobita, K. Honda, M. Kawahara, M. Katada, K. Adachi, H. Nishikawa, I. Ikemoto, H. Kumagai, Y. Hosokoshi, K. Inoue, S. Kitagawa, S. Kawata, *J. Am. Chem. Soc.* **2003**, *125*, 221-232.

[31] M. Atzori, F. Pop, P. Auban-Senzier, C. J. Gómez-García, E. Canadell, F. Artizzu, A. Serpe, P. Deplano, N. Avarvari, M. L. Mercuri, *Inorg. Chem.* **2014**, *53*, 7028-7039.

[32] M. Atzori, F. Pop, P. Auban-Senzier, R. Clérac, E. Canadell, M. L. Mercuri, N. Avarvari, *Inorg. Chem.* **2015**, *54*, 3643-3653.

[33] S. A. Sahadevan, A. Abhervé, N. Monni, P. Auban-Senzier, J. Cano, F. Lloret, M. Julve, H. Cui, R. Kato, E. Canadell, M. L. Mercuri, N. Avarvari, *Inorg. Chem.* **2019**, *58*, 15359-15370.

[34] M. E. Ziebel, C. A. Gaggioli, A. B. Turkiewicz, W. Ryu, L. Gagliardi, J. R. Long, *J. Am. Chem. Soc.* **2020**, *142*, 2653-2664.

[35] B. F. Abrahams, T. A. Hudson, L. J. McCormick, R. Robson, *Cryst. Growth Des.* **2011**, *11*, 2717-2720.

[36] S. Alvarez, D. Avnir, M. Llunell, M. Pinsky, *New J. Chem.* **2002**, *26*, 996-1009.

[37] M. Llunell, D. Casanova, J. Cicera, P. Alemany, S. Alvarez, *SHAPE, Version 2.1*, Universitat de Barcelona, Barcelona, Spain, **2013**.

[38] P. Li, J. M. Maier, E. C. Vik, C. J. Yehl, B. E. Dial, A. E. Rickher, M. D. Smith, P. J. Pellechia, K. D. Shimizu, *Angew. Chem. Int. Ed.* **2017**, *56*, 7209-7212.

[39] T. J. Mooibroek, P. Gamez, J. Reedijk, *CrystEngComm* **2008**, *10*, 1501-1515.

[40] A. L. Spek, *Acta Crystallogr. C* **2015**, *71*, 9-18.

[41] A. L. Spek, *Acta Crystallogr. D* **2009**, *65*, 148-155.

[42] T. M. Bockman, J. K. Kochi, *J. Org. Chem.* **1990**, *55*, 4127-4135.

[43] W. W. Porter, III, T. P. Vaid, *J. Org. Chem.* **2005**, *70*, 5028-5035.

[44] G. Férey, C. Serre, *Chem. Soc. Rev.* **2009**, *38*, 1380-1399.

[45] O. V. Dolomanov, L. J. Bourhis, R. J. Gildea, J. A. K. Howard, H. Puschmann, *J. Appl. Crystallogr.* **2009**, *42*, 339-341.

[46] V. A. Grillo, G. R. Hanson, D. Wang, T. W. Hambley, L. R. Gahan, K. S. Murray, B. Moubaraki, C. J. Hawkins, *Inorg. Chem.* **1996**, *35*, 3568-3576.

[47] N. N. Greenwood, T. C. Gibb, *Mössbauer Spectroscopy*, Chapman and Hall, London, UK, **1971**.

[48] J. Tauc, *Mater. Res. Bull.* **1968**, *3*, 37-46.

[49] S. Kasap, C. Koughia, J. Singh, H. Ruda, S. O'Leary, in *Springer Handbook of Electronic and Photonic Materials* (Eds.: S. Kasap, P. Capper), Springer, New York, NY, **2006**.

[50] N. S. Hush, in *Prog. Inorg. Chem., Vol. 8* (Ed.: F. A. Cotton), Interscience Publishers, New York, NY, **1967**.

[51] N. S. Hush, *Electrochim. Acta* **1968**, *13*, 1005-1023.

[52] M. B. Robin, P. Day, in *Advances in Inorganic Chemistry and Radiochemistry, Vol. 10* (Eds.: H. J. Emeléus, A. G. Sharpe), Academic Press, London, UK, **1968**.

[53] B. S. Brunschwig, C. Creutz, N. Sutin, *Chem. Soc. Rev.* **2002**, *31*, 168-184.

[54] B. F. Abrahams, A. M. Bond, T. H. Le, L. J. McCormick, A. Nafady, R. Robson, N. Vo, *Chem. Commun.* **2012**, *48*, 11422-11424.

[55] S. Hünig, J. Groβ, E. F. Lier, H. Quast, *Liebigs Ann. Chem.* **1973**, *1973*, 339-358.

[56] A. G. Evans, J. C. Evans, M. W. Baker, *J. Chem. Soc., Perkin Trans. 2* **1977**, 1787-1789.

[57] P. M. S. Monk, N. M. Hodgkinson, S. A. Ramzan, *Dyes and Pigments* **1999**, *43*, 207-217.

[58] M. R. Geraskina, A. S. Dutton, M. J. Juetten, S. A. Wood, A. H. Winter, *Angew. Chem. Int. Ed.* **2017**, *56*, 9435-9439.

[59] J.-M. Lü, S. V. Rosokha, J. K. Kochi, *J. Am. Chem. Soc.* **2003**, *125*, 12161-12171.

[60] N. G. Connelly, W. E. Geiger, *Chem. Rev.* **1996**, *96*, 877-910.

[61] L. Sun, M. G. Campbell, M. Dincă, *Angew. Chem. Int. Ed.* **2016**, *55*, 3566-3579.

[62] J.-H. Dou, L. Sun, Y. Ge, W. Li, C. H. Hendon, J. Li, S. Gul, J. Yano, E. A. Stach, M. Dincă, *J. Am. Chem. Soc.* **2017**, *139*, 13608-13611.

[63] J. Stenhouse, *J. Chem. Soc.* **1870**, *23*, 6-14.

[64] H. A. Torrey, W. H. Hunter, *J. Am. Chem. Soc.* **1912**, *34*, 702-716.

[65] C. L. Jackson, E. K. Bolton, *J. Am. Chem. Soc.* **1914**, *36*, 301-308.

[66] L. A. Summers, *Tetrahedron* **1968**, *24*, 5433-5437.

This page intentionally left blank

Chapter 4 Influence of Structural Transformations Upon the Properties of Mixed-Valence Iron–Fluoranilate Coordination Polymers

4.1 Introduction 247

4.1.1 Mixed-Valence Fluoranilate Coordination Polymers 247

4.1.2 Chapter Aim 250

4.2 Results and Discussion 250

4.2.1 Synthesis and Structure Description 250

4.2.2 Variable-Temperature Single-Crystal X-ray Diffraction 264

4.2.3 Solvent Exchange and Structural Transformations 267

4.2.4 ^{57}Fe Mössbauer Spectroscopy 282

4.2.5 Electronic Spectroscopy 289

4.2.6 Electrochemistry 297

4.2.7 Electrical Conductivity 305

4.3 Conclusion 309

4.4 Experimental 311

4.4.1 General Considerations 311

4.4.2 (MeV)[$Fe_2(Fan)_3$]·*y*MeCN (*mP* **4.1a** and *aP* **4.1a**) 311

4.4.3 (MeV)[$Fe_2(Fan)_3$]·2.7DMF (**4.1b**) 313

4.4.4 Single-Crystal X-ray Diffraction 313

4.4.5 Powder X-ray Diffraction 322

4.5 References 322

This page intentionally left blank

4.1 Introduction

4.1.1 Mixed-Valence Fluoranilate Coordination Polymers

From the mid-20th century, the importance of organofluorine compounds has grown in the fields of materials science, and medicinal- and agro-chemistry.[1-3] The unique and favourable physicochemical properties engendered by incorporating fluorine, compared to other halogens, is due to the high electronegativity, low polarizability and small size of F atoms.[4] Organofluorine compounds also have an important role in crystal engineering. Although C–F compounds are somewhat paradoxically weak H-bond acceptors,[4-6] replacement of H with F atoms can alter the electron density distribution in the crystal building blocks, thereby changing the supramolecular interactions between components modifying the structure packing.[7]

Whereas chloranilic, bromanilic and iodanilic acids (H_2Clan, H_2Bran and H_2Ian respectively) were first described in the late 19th and early 20th Centuries,[8, 9] the fluorine-substituted tetraoxolene, fluoranilic acid (H_2Fan), was not reported until 1960.[10] This possibly arises from the challenging solid-phase synthesis of the precursor 2,3,5,6-tetrafluoro-1,4-benzoquinone (fluoranil, F_4BQ),[11] compared to the straightforward synthesis of the other 2,3,5,6-tetrahalo-1,4-benzoquinones. Surprisingly, H_2Fan is a weaker acid than H_2Clan or H_2Bran, as shown by the ca. 0.7 unit higher pK_{a1} for H_2Fan,[10] despite the higher electronegativity of F compared to Cl and Br. This subtle difference can have a notable impact on the physical property of H_2Fan compounds compared to other tetraoxolene-containing compounds. Horiuchi and co-workers have extensively studied ferroelectricity in co-crystals of H_2Xan (X = F, Cl, Br, I) with pyridyl-type proton acceptors.[12-14] The reaction of H_2Clan or H_2Bran with phenazine (phz) gives neutral centrosymmetric co-crystals of (phz)(H_2Clan) and (phz)(H_2Bran).[12] Upon cooling, a phase transition to a polar space group occurs, due to an incipient proton transfer to a semi-ionic ($phzH^+$)($HXan^-$) form.[13, 14] This symmetry-breaking transition causes the compounds to exhibit temperature-dependant dielectric phase transitions and ferroelectric behaviour. Although the F substituted analogue (phz)(H_2Fan) exhibits the same room-temperature centrosymmetric structure as (phz)(H_2Clan) and (phz)(H_2Bran), it does not exhibit any dielectric phase transitions or ferroelectricity upon cooling. This was ascribed to the weaker acidity of H_2Fan inhibiting the incipient proton transfer to the polar semi-ionic

structure, necessary for ferroelectric behaviour.[13] Similarly, co-crystallisation of 2,3-di(2-pyridyl)pyrazine (dppyz) with H_2Xan (X = F, Cl, Br) yields the neutral (dpphz)(H_2Fan) compound, and proton-transferred ionic ($dpphzH^+$)($HXan^-$) (X = Cl, Br) compounds.[14] Room-temperature ferroelectricity was observed in ($dpphzH^+$)($HXan^-$) (X = Cl, Br), whereas neutral (dpphz)(H_2Fan) required application of an external hydrostatic pressure to induce proton-transfer and ferroelectric behaviour.

The properties of Fe–fluoranilate frameworks can also deviate from their chlor- or bromanilate cousins due to slight structural differences. Murase *et al.* recently investigated the structure and properties of two mixed-valence Fe–fluoranilate frameworks and compared them to other Fe–tetraoxolene analogues.[15, 16] Whereas the 3D (10,3)-*a* frameworks (^{n}Bu$_4$N)$_2$[Mn$_2$(Clan)$_3$],[17] and mixed-valence (^{n}Bu$_4$N)$_2$[Fe$_2$(dhbq)$_3$] exhibit cubic symmetry,[18] the mixed-valence (^{n}Bu$_4$N)$_2$[Fe$_2$(Fan)$_3$] framework and the diamagnetic analogue (^{n}Bu$_4$N)$_2$[Zn$_2$(Fan)$_3$] crystallise with only trigonal symmetry.[15] The symmetry reduction in the fluoranilate compounds is due to slight distortions to the M···M···M angles and M···M distances, which appears to impact upon the magnetic and conductive properties. The observed magnetic susceptibility-temperature product ($\chi_M T$ = 10.9 cm^3 K mol^{-1}) of (^{n}Bu$_4$N)$_2$[Fe$_2$(dhbq)$_3$], is higher than the expected value of $\chi_M T$ = 9.5 cm^3 K mol^{-1} for a non-interacting 2 × Fe^{III}_{HS} (S = 5/2) and 2 × $dhbq^{3-\bullet}$ (S = 1/2) spin set.[18] This behaviour is indicative of strong room-temperature metal–radical coupling in (^{n}Bu$_4$N)$_2$[Fe$_2$(dhbq)$_3$]. In contrast, the room-temperature metal–radical coupling in (^{n}Bu$_4$N)$_2$[Fe$_2$(Fan)$_3$] is weaker than in (^{n}Bu$_4$N)$_2$[Fe$_2$(dhbq)$_3$]. This was evinced by the room-temperature $\chi_M T$ = 8.2 cm^3 K mol^{-1}, which is lower than expected for either a $[Fe^{III}_2(Fan^{2.67-})_3]^{2-}$ formulation, or the putative $[Fe^{II}_{0.5}Fe^{III}_{1.5}(Fan^{2-})_{1.5}(Fan^{3-\bullet})_{1.5}]^{2-}$ valence formulation proposed.[15]

A recent investigation of (Et$_4$N)$_2$[Fe$_2$(Fan)$_3$]·solvent has revealed intrinsic Fe-based mixed valency,[16] which has not been observed in other Fe–tetraoxolene frameworks. In contrast to the (10,3)-*a* metal–tetraoxolene frameworks, the 2D honeycomb frameworks (Et$_4$N)$_2$[Fe$_2$(Xan)$_3$]·solvent (X = F, Cl) are isostructural, with delocalised $[Fe^{III}_2(Xan^{2.67-})_3]^{2-}$ ligand charge-state distributions, as indicated by single-crystal X-ray diffraction (SC-XRD) analyses. Intriguingly, ^{57}Fe Mössbauer spectroscopy revealed (Et$_4$N)$_2$[Fe$_2$(Fan)$_3$] exhibits a spectrum consistent with Fe^{II}/Fe^{III}

mixed valency, which contrasts with SC-XRD data which suggests a pure high-spin Fe^{III} (Fe^{III}_{HS}) population. At 293 K, the relative proportions of $Fe^{II}_{HS}/Fe^{III}_{HS}$ are ca. 1:3, with a ca. 1:4 ratio of $Fe^{II}_{HS}/Fe^{III}_{HS}$ at 100 K. The Fe^{II}_{HS} character could be indicative of a fast thermally-activated $[Fe^{III}_2(Fan^{2.67-})_3]^{2-} \leftrightarrow [Fe^{II}Fe^{III}(Fan^{2.33-})_3]^{2-}$ valence state fluctuation. Apparent valence trapping by ^{57}Fe Mössbauer spectroscopy suggests it is slow on this time scale (ca. 10^{-8} s relaxation time for the ^{57}Fe nucleus) but fast compared to the crystallographic time-scale. The authors proposed that slow magnetisation relaxation, which has not been observed in other compounds with delocalised $[Fe^{III}_2(Xan^{2.67-})_3]^{2-}$ ligand charge-state distributions, possibly arose due to the intrinsic Fe^{II}/Fe^{III} mixed valency in $(Et_4N)_2[Fe_2(Fan)_3]$. Moreover, since Fe^{II}/Fe^{III} mixed-valency has not been observed in other layered Fe–chloranilate frameworks,[19, 20] unless subject to post-synthetic reduction,[21] the importance of further exploring the structure and properties of mixed-valence Fe–fluoranilate frameworks is highlighted. Indeed, Miyasaka and co-workers have recently shown the valence tautomeric transition temperature ($T_{1/2}$) in the ligand-charge ordered 2D $(^nPr_4N)_2[Fe_2(Clan)_3]$ framework, is readily and finely modulated by 'alloying' either $Bran^{n-}$ or Fan^{n-} ligands into the structure.[22]

More recently, $(Me_2NH_2)_2[Fe_2(Clan)_3]$ and $(Et_4N)_2[Fe_2(Fan)_3]$ have recently shown promise as lithium-ion battery (LIB) cathode materials, because the compounds can be cycled between multiple redox states leading to high charge capacities .[16, 21] Improving the gravimetric charge capacity and energy density are important goals in battery research. Substituting Cl atoms in Fe–chloranilate frameworks with lighter F substituents will reduce the formula mass of the compound and could be a facile method towards higher gravimetric charge capacities for these compounds. As shown in Chapter 3, incorporation of a viologen-like cation into **3.1^{Cl}b** afforded access to additional framework redox states, which could further increase the charge capacity of an Fe–tetraoxolene framework as a LIB cathode. Therefore, F for Cl substitution, combined with the introduction of redox-active cations may possibly be an effective method to improve the gravimetric charge capacity and energy density of LIB battery cathodes.

4.1.2 Chapter Aim

In Chapters 2 and 3, we demonstrated that the coordination chemistry of Fan^{n-} in combination with viologen cations is less predictable than $Clan^{n-}$, typically leading to different structures when the syntheses were performed under the same conditions used for the metal–chloranilate coordination polymers. This led to the successful synthesis of two novel mixed-valence Fe–fluoranilate frameworks, **2.7** and **3.1^{F}a** containing viologen-like cations, offering the potential to further examine the structure and properties of other Fe–fluoranilate frameworks. Chapter 4 details the synthesis of two related mixed-valence Fe–fluoranilate frameworks containing methyl viologen (MeV^{m+}) cations (MeV)[Fe_2(Fan)$_3$]·solvent (solvent = MeCN, DMF). The initial goal of this work was to synthesise an isostructural family of (MeV)[Fe_2(Xan)$_3$] (X = F, Cl, Br) compounds to systematically determine the impact of ligand substituents on the conductive, magnetic and electrochemical properties of the frameworks. These studies were also aimed at extending the insights gained in Chapter 3 about how interactions between π-electron deficient cations and anionic mixed-valence networks could modulate the physical properties of the compounds. Detailed structural analyses of the two (MeV)[Fe_2(Fan)$_3$] compounds are presented, to elucidate the presence of any phase transitions arising from guest solvent exchange. Following this, spectroscopic, electrochemical, and electrical conductivity measurements are described, which further reinforce the notion that subtle changes in the structure of Fe–tetraoxolene frameworks can have substantial effects on the resultant physical properties.

4.2 Results and Discussion

4.2.1 Synthesis and Structure Description

A sample of (MeV)[Fe_2(Fan)$_3$]·*y*MeCN·*z*H_2O (**4.1a**) was synthesised by carefully layering an aqueous solution of $Fe^{II}Cl_2$·4H_2O, MeV(OTs)$_2$ and LiOAc·2H_2O below an acetonitrile (MeCN) solution of the reduced form of fluoranilic acid, 3,6-difluoro-1,2,4,5-tetrahydroxybenzene (H_4Fan), with a buffer layer of 1:1 v/v MeCN/H_2O. Slow aerial oxidation of the reduced H_4Fan form to the active H_2Fan form, in combination with slow diffusion reactions proved a facile method for producing single-crystal X-ray diffraction (SC-XRD) quality samples. The product formed on the vial walls within two days, as elongated blocky black crystals with a brilliant electric-blue

metallic lustre, which were collected after seven days. Synthesis of bulk samples of **4.1a** was readily achieved by performing multiple diffusion reactions in parallel and combining the crystallised products during workup. The structure of **4.1a** was solved by SC-XRD with a satisfactory refinement found in the monoclinic $P2_1/c$ space group; the compound is herein referred to as *mP* **4.1a**. The asymmetric unit contains two crystallographically inequivalent Fe centres (Fe1 and Fe2), three unique Fan^{n-} ligands (**L_1**, **L_2** and **L_3**), and one MeV^{m+} cation. The asymmetric unit also contains a combination of two ordered and one disordered MeCN molecules, and regions of electron density ascribed to severely disordered MeCN molecules. The severely disordered solvent molecules could not satisfactorily be modelled, so their scattering contribution was accounted for using the SQUEEZE[23] routine in PLATON.[24] The total solvation of *mP* **4.1a** is therefore estimated as $(MeV)[Fe_2(Fan)_3]\cdot 5.3MeCN$.

Each Fe centre in *mP* **4.1a** resides in a slightly distorted octahedral coordination environment, bound to six O donor atoms of three bridging Fan^{n-} ligands, which are linked to three other Fe centres. Two-dimensional (2D) honeycomb (6,3) sheets of composition $[Fe_2(Fan)_3]^{x-}$ are formed by linking every Fe centre of a given configuration (Δ or Λ) to three Fe centres of opposite configuration (Λ or Δ) (Figure 4.1). The anionic sheets are stacked parallel to the crystallographic *c* axis, with the sheet-to-sheet spacing (measured between the mean plane through the Fe centres) equal to 7.150 Å.

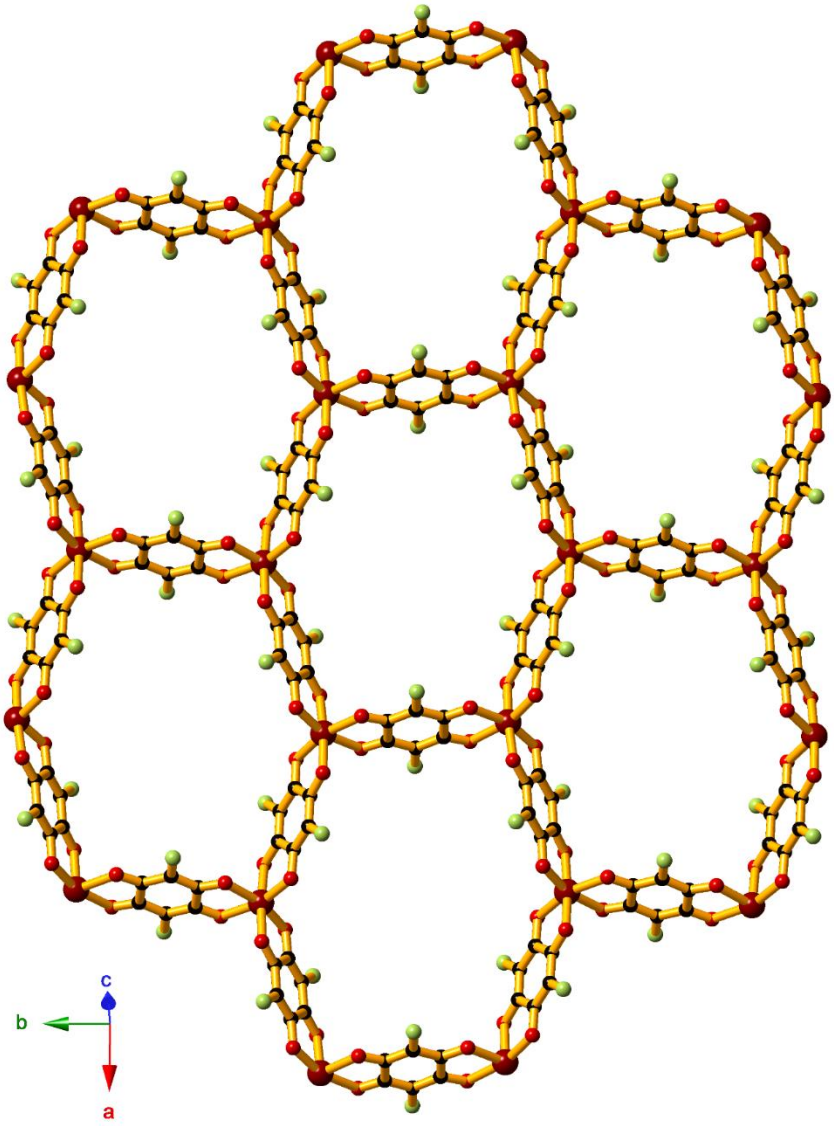


Figure 4.1 The anionic $[Fe_2(Fan)_3]^{x-}$ (6,3) honeycomb sheet in *mP* **4.1a** viewed almost down the crystallographic *c* axis. Maroon = Fe, pale green = F, red = O, black = C.

The Fe···Fe···Fe angles in *mP* **4.1a** deviate significantly from the ideal hexagonal geometry of 120°, with angles of 105.97(1)°, 113.42(1)° and 140.57(1)°. The anionic sheet therefore appears sheared in the *ab* plane. For a row of hexagonal channels parallel to the crystallographic *a* axis, the adjacent rows of hexagonal channels are inclined in the opposite direction in the *ab* plane (Figure 4.2).

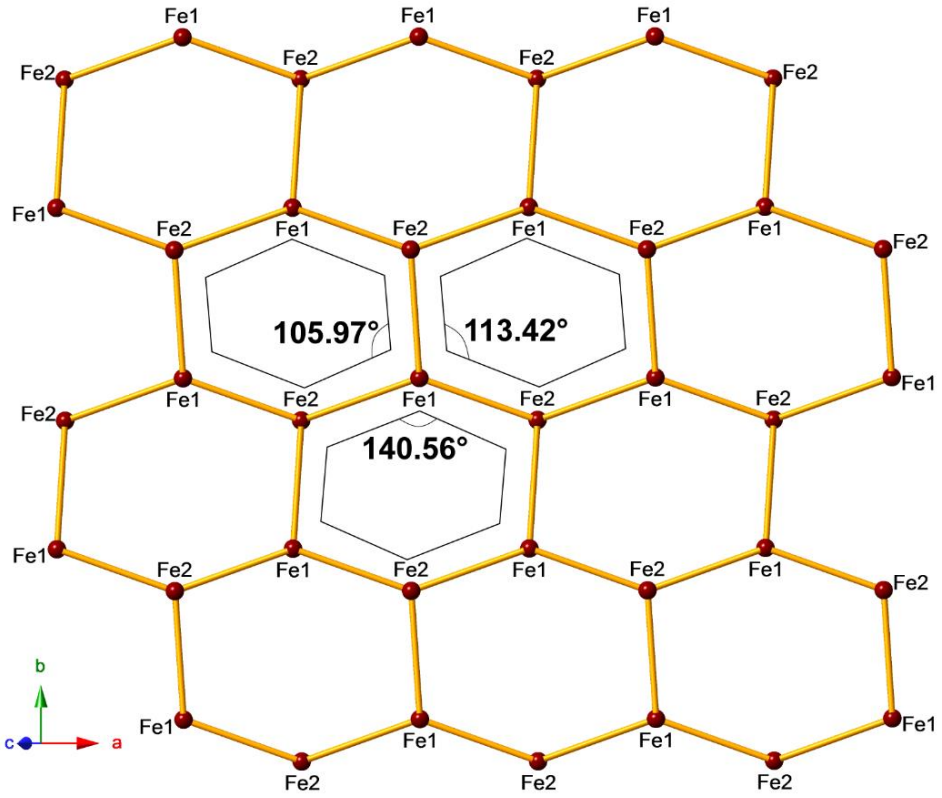


Figure 4.2 The Fe···Fe···Fe angles in the anionic $[Fe_2(Fan)_3]^{x-}$ (6,3) honeycomb sheets of *mP* **4.1a** viewed along the crystallographic *c* axis. Maroon = Fe.

The anionic sheets in *mP* **4.1a** stack in an offset ABAB pattern (Figure 4.3), in contrast to compounds **3.1^{Cl}a** and **3.2**, in which AAAA stacking of the anionic $[M_2(Clan)_3]^{2-}$ sheets is promoted by $PhenQ^{2+}$ cations sandwiched between sheets. This arrangement likely arises as charge balancing MeV^{m+} cations are situated adjacent to Fe2, at a vertex of the hexagonal channel of the anionic sheet (Figure 4.4). Interestingly, the location of MeV^{m+} cations within the hexagonal voids in *mP* **4.1a** also contrasts strongly with the structure of **2.2a**, in which MeV^{2+} cations interleave the anionic $[Mn_2(Clan)_3]^{2-}$ sheets (see Section 2.2.1.1). Although differences in ionic radius between Mn and Fe probably play a role, it also highlights the sensitivity of cation-network interactions to halogen substitution. Significant torsion around the central C–C bond in the MeV^{m+} molecules is observed, due to face-to-face contact between the two pyridinium rings of MeV^{m+} with $\mathbf{L_1}$ and $\mathbf{L_2}$. The face-to-face contact suggests a significant charge-transfer (CT) interaction between the π-electron rich anionic network and the π-electron deficient MeV^{m+} cation.

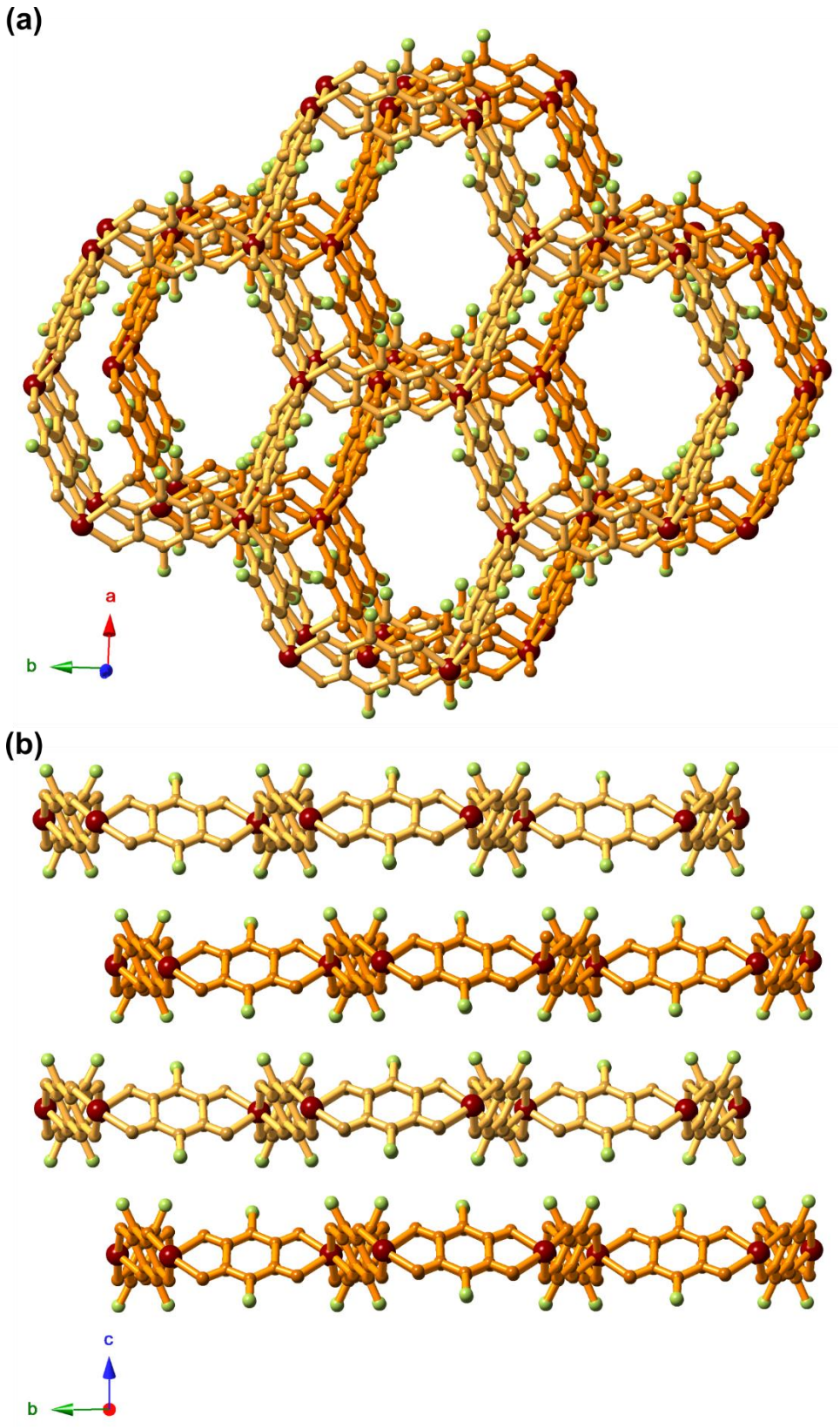


Figure 4.3 ABAB stacking of the anionic $[Fe_2(Fan)_3]^{x-}$ A (tan) and B (orange) sheets in *mP* **4.1a** viewed (a) down the *c* axis (b) along the *a* axis. Maroon = Fe, pale green = F.

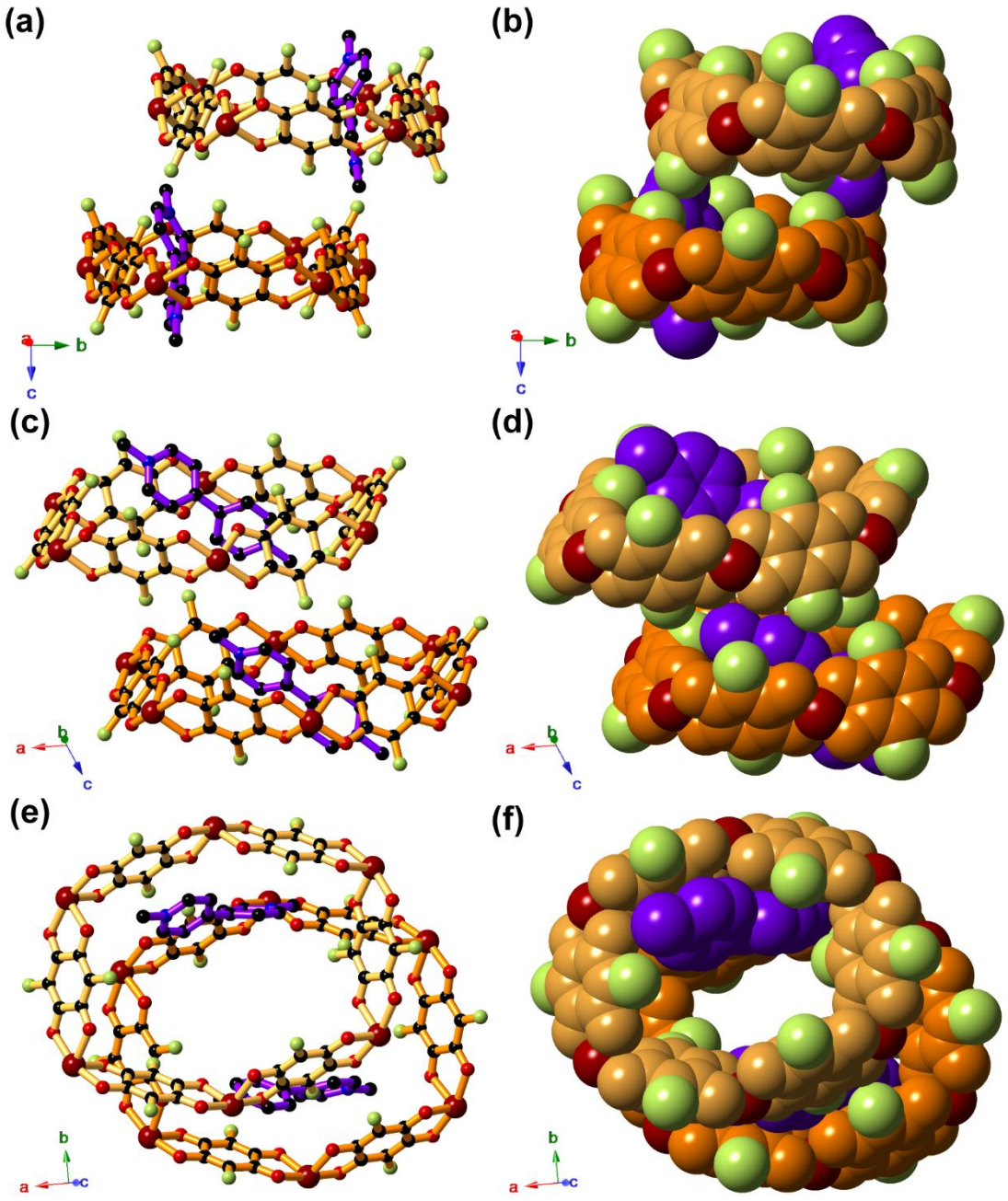


Figure 4.4 Ball-and-stick (a, c, e) and spacefilling (b, d, f) representations of the interactions of the MeV^{m+} cation (purple) with the anionic $[Fe_2(Fan)_3]^{x-}$ sheets above (tan) and below (orange) in *mP* **4.1a**. Views along the crystallographic (a, b) *a* axis and (c, d) *b* axis. (e, f) View just off the crystallographic *c* axis showing MeV^{m+} cations lining the walls of the hexagonal channel. Ordered and disordered MeCN in channels not shown for clarity. Maroon = Fe, pale green = F, red = O, blue = N and black = C.

Despite location of the MeV^{m+} cations within the hexagonal voids of the sheets, spacious channels lined with MeV^{m+} cations are still formed, by stacking of the anionic sheets (Figure 4.5). The framework void spaces in *mP* **4.1a** are filled with ordered and disordered MeCN molecules, and comprise ca. 37% of the unit cell volume, compared with ca. 43% for **2.5**, 46% for **2.6**, 43% for **2.7**, and 44% for **3.1^{Cl}a**. The framework voids in *mP* **4.1a** which form along the crystallographic *c* axis, also interconnect with adjacent hexagonal channels in the *ac* plane. This arrangement produces a 2D void gallery, oriented perpendicularly to the plane of the anionic sheets (Figure 4.6). This contrasts with the strictly 1D framework void channels which are found in **3.1^{X}** (X = F, Cl, Br) and **3.2**, or other porous 2D metal–tetraoxolene coordination polymers,[16, 19, 20, 25-27] such as $(Me_2NH_2)_2[Fe_2(Clan)_3]$ or $(Et_4N)_2[M_2(Xan)_3]$ (M = Fe, Zn; X = F, Cl).

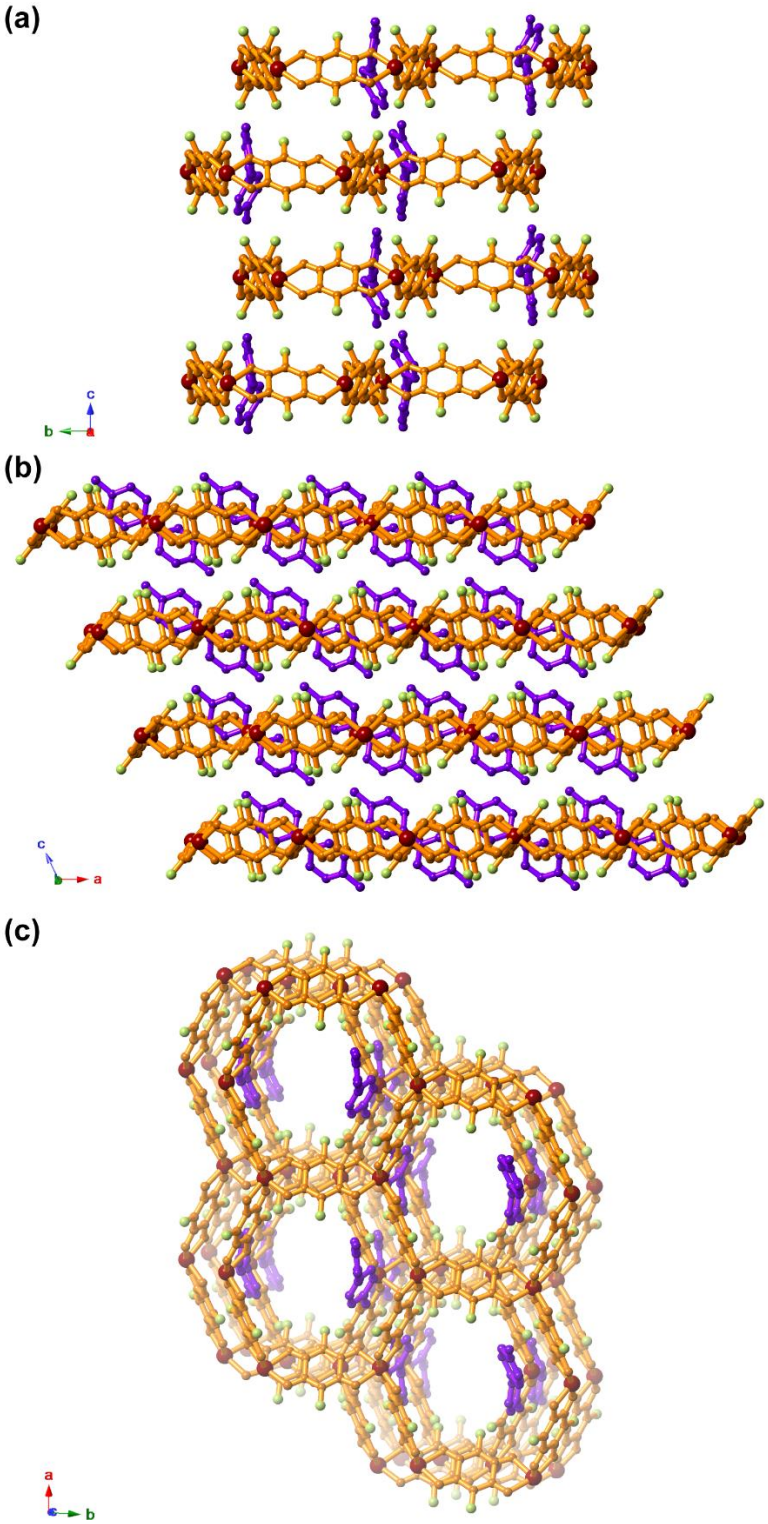


Figure 4.5 Packing of the anionic $[Fe_2(Fan)_3]^{x-}$ sheets (orange) with MeV^{m+} cations (purple) in *mP* **4.1a**. Views along the crystallographic (a) *a* axis and (b) *b* axis. (c) View just off crystallographic *c* axis showing hexagonal channels lined with MeV^{m+} cations. Maroon = Fe, pale green = F. H atoms and MeCN in channels not shown for clarity.

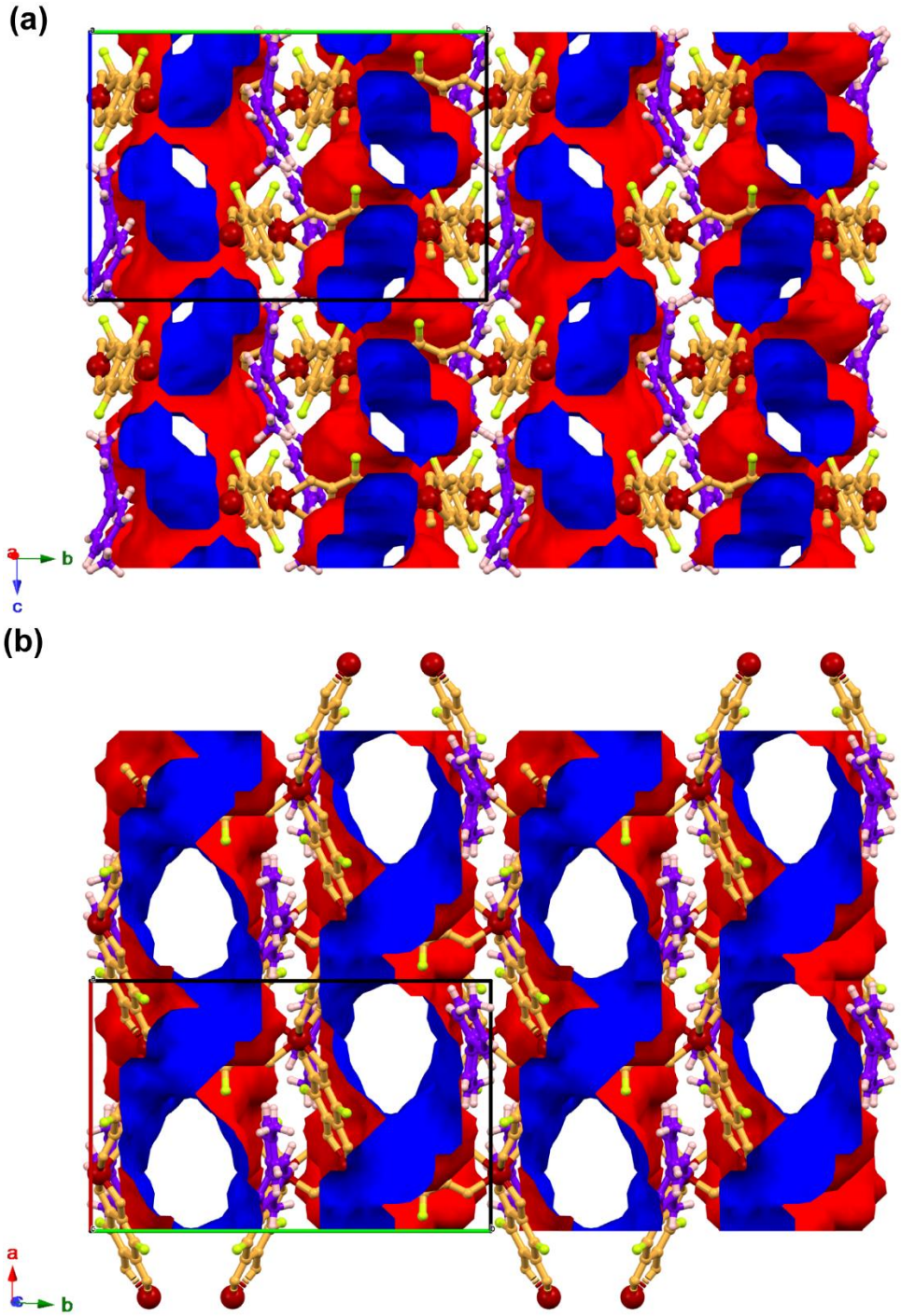


Figure 4.6 The calculated solvent-accessible void space in *mP* **4.1a** viewed along the crystallographic (a) *a* axis, and (b) *c* axis. Void facing surface shown in blue. The void volume (ca. 1646 Å^3) comprises ca. 37% of the unit cell volume (4403.84 Å^3) and is filled with ordered and disordered MeCN molecules. Void volume was calculated with a probe radius of 1.2 Å and an approximate grid spacing of 0.7 Å, using Mercury Version 2020.2.[28] Maroon = Fe, pale green = F, pink = H, tan = Fan^{n-}, purple = MeV^{m+}.

The shift of the Fe coordination environment from ideal octahedral was quantified using the Continuous Shape Measure (CShM) parameters[29, 30] (Table 4.1). A number greater than zero indicates the degree of distortion away from the possible idealised coordination geometries. A similar analysis of the Fe coordination geometry in other Fe–fluoranilate compounds reported in this thesis or in literature is also presented Table 4.1.

Table 4.1 Analysis of the possible coordination geometries quantified using the CShM parameters for the two Fe sites in *mP* **4.1a**, and other Fe–fluoranilate frameworks reported in this thesis and literature.

		Coordination Geometry (Symmetry)					
Compound	**Site**	**HP-6 (D_{6h})**	**PPY-6 (C_{5v})**	**OC-6 (O_h)**	**TPR-6 (D_{3h})**	**JPPY-6 (C_{5v})**	**Ref.**
mP **4.1a**	Fe1	32.350	24.365	**1.327**	10.926	28.034	This work
	Fe2	32.681	23.784	**1.432**	10.682	27.373	
$(Et_4N)_2[Fe_2(Fan)_3]$	Fe1	33.018	24.269	**1.487**	9.885	28.156	[16]
$(^nBu_4N)_2[Fe_2(Fan)_3]$	Fe1	29.563	24.817	**1.166**	12.877	28.824	[15]
	Fe2	28.937	26.606	**1.035**	13.131	30.440	
(PhenQ)$[Fe_2(Fan)_3]$ (**3.1^F**)	Fe1	32.641	24.888	**1.185**	10.641	28.738	This work
(PDiQ)$[Fe_2(Fan)_3]$ (**2.7**)	Fe1	32.542	24.303	**1.281**	10.545	28.078	This work

HP-6: Hexagon; PPY-6: Pentagonal pyramid; OC-6: Octahedron; TPR-6: Trigonal prism; JPPY-6: Johnson pentagonal pyramid J2

These analyses indicate that while both Fe1 and Fe2 sites reside in octahedral environments, there is a greater distortion away from the ideal octahedral geometry particularly when compared to (^{n}Bu$_4$N)$_2$[Fe$_2$(Fan)$_3$],[15] **2.7** (Chapter 2) or **3.1^{F}** (Chapter 3). Only the 2D framework (Et$_4$N)$_2$[Fe$_2$(Fan)$_3$]·5(acetone)[16] exhibits a similarly large distortion away from idealised octahedral environment. Therefore *mP* **4.1a** may exhibit some magnetic or conductive properties in common with (Et$_4$N)$_2$[Fe$_2$(Fan)$_3$]·5(acetone) arising from the unique Fe environments.

The crystallographic Fe, cation and ligand oxidation states were assigned by examining the characteristic Fe–O ($d_{Fe–O}$), C–C ($d_{C–C}$), and C–O ($d_{C–O}$, for ligand) or C–N ($d_{C–N}$, for cation) bond lengths. Although a diamagnetic Zn^{II} analogue of *mP* **4.1a** could not be synthesised (analogous reactions using Mn^{II} or Cd^{II} formed only the 1D ladders as described in Chapter 2), there are several indicators that support a ligand charge-ordered (MeV^{2+})[Fe$^{III}_2$(Fan$^{2–}$)(Fan$^{3–\bullet}$)$_2$] valence formulation. At 100 K, there is significant torsion (ca. 43°) between the two rings of the MeV^{m+} moieties in *mP* **4.1a**, in addition to a central (C41–C44) $d_{C–C}$ of 1.486(3) Å, which is consistent with a single bond expected in MeV^{2+}.[31, 32] The $d_{C–C}$ and $d_{C–N}$ values in the ring also correspond well to those observed in MeV^{2+},[31, 32] showing no evidence of either a semiquinonoid or quinonoid structure expected for MeV$^{+\bullet}$ or MeV^{0} respectively. These observations strongly indicate that MeV^{m+} in *mP* **4.1a** exists in the MeV^{2+} state. Charge neutrality of the framework therefore requires a network charge of [Fe$_2$(Fan)$_3$]$^{2–}$, similarly to other mixed-valence Fe–tetraoxolene frameworks reported in literature[15, 16, 18-20, 27] or this thesis.

Although fewer metal–fluoranilate coordination compounds have been reported in literature, compared to chloranilate, the ligand bond lengths are still diagnostic of oxidation state, due to the similar redox behaviour within the tetraoxolene family of ligands.[33] Each Fe1 and Fe2 site in *mP* **4.1a** is coordinated to three crystallographically unique ligands, **L$_1$**, **L$_2$** and **L$_3$** (Figure 4.7). The mean ligand $d_{C–O}$ values in *mP* **4.1a** are 1.298(1), 1.298(4) and 1.262(3) Å for **L$_1$**, **L$_2$** and **L$_3$** respectively. The corresponding diagnostic (within the five-membered chelate ring) mean $d_{C–C}$ values are 1.470(4) (C2–C3 and C5–C6), 1.472(2) (C14–C15 and C17–C18) and 1.529(4) Å (C26–C27 and C29–C30) Å for **L$_1$**, **L$_2$** and **L$_3$** respectively (Figure 4.7). The stark disparity of $d_{C–O}$ and $d_{C–C}$ for **L$_1$** and **L$_2$**, compared to **L$_3$**, strongly indicates **L$_3$** exists in a different valence state to **L$_1$** and **L$_2$**. The $d_{C–O}$ and $d_{C–C}$ values for **L$_3$** fall

within the range expected for $Clan^{2-}$ ($d_{C–O}$ = 1.248–1.272 Å; $d_{C–C}$ = 1.506–1.551 Å), and also correspond closely to $d_{C–O}$ and $d_{C–C}$ values in $(^{n}Bu_4N)_2[Zn_2(Fan)_3]$ and $(Et_4N)_2[Zn_2(Fan)_3]$·solvent. **L_3** is therefore in the Fan^{2-} valence state. To date, compounds unambiguously containing $Fan^{3-\bullet}$ have not been reported in the Cambridge Structural Database (CSD), however for **L_1** and **L_2**, $d_{C–O}$ and $d_{C–C}$ values lie within the ranges expected for $Clan^{3-\bullet}$, suggesting **L_1** and **L_2** are in the $Fan^{3-\bullet}$ state. Additionally, elongation of $d_{C–O}$ and shortening of $d_{C–C}$ in both **L_1** and **L_2** is apparent, when compared to the values in $(^{n}Bu_4N)_2[Fe_2(Fan)_3]$ and $(Et_4N)_2[Fe_2(Fan)_3]$·5(acetone). Since both compounds contain valence delocalised $Fan^{2.67-}$ ligands, this indicates **L_1** and **L_2** in *mP* **4.1a** exist in a more reduced state i.e. $Fan^{3-\bullet}$ than in $(^{n}Bu_4N)_2[Fe_2(Fan)_3]$ or $(Et_4N)_2[Fe_2(Fan)_3]$·5(acetone). The mean $d_{Fe–O}$ values are 2.0299(7) Å and 2.0251(4) Å for Fe1 and Fe2 respectively, with corresponding bond-valence sum (BVS) values[34] of 2.90 and 2.94, both of which are consistent with high-spin Fe^{III} (Fe^{III}_{HS}), as expected. These values though are slightly longer than observed in $(Et_4N)_2[Fe_2(Fan)_3]$·5(acetone), in which the Fe centre exhibited a BVS value of 2.97.[16] Interestingly, the mean $d_{Fe–O}$ between Fe and **L_3** are elongated to 2.0902(3) Å compared to **L_1** and **L_2** (1.9971(40) and 1.9953(44) Å respectively), also causing an increased Fe–Fe distance across **L_3** (7.9576(6) Å) compared to across **L_1** (7.7545(5) Å) and **L_2** (7.7698(5) Å). This probably results from weaker Coulombic interaction between Fe^{III} and Fan^{2-} (**L_3**), compared to Fe^{III} and $Fan^{3-\bullet}$ (**L_1** and **L_2**). For $(^{n}Pr_4N)_2[Fe_2(Clan)_3]$·2(acetone)·$H_2O$, Miyasaka and co-workers have also observed similar elongation of Fe–O bonds between Fe^{III} and $Clan^{2-}$, and increased Fe–Fe distances across $Clan^{2-}$ compared to $Clan^{3-\bullet}$, suggesting this behaviour is common to the ligand charge-ordered mixed-valence tetraoxolene frameworks. Importantly, this combination of findings all point towards a valence-localised $(MeV^{2+})[Fe^{III}_2(Fan^{2-})(Fan^{3-\bullet})_2]$ formulation of *mP* **4.1a**.

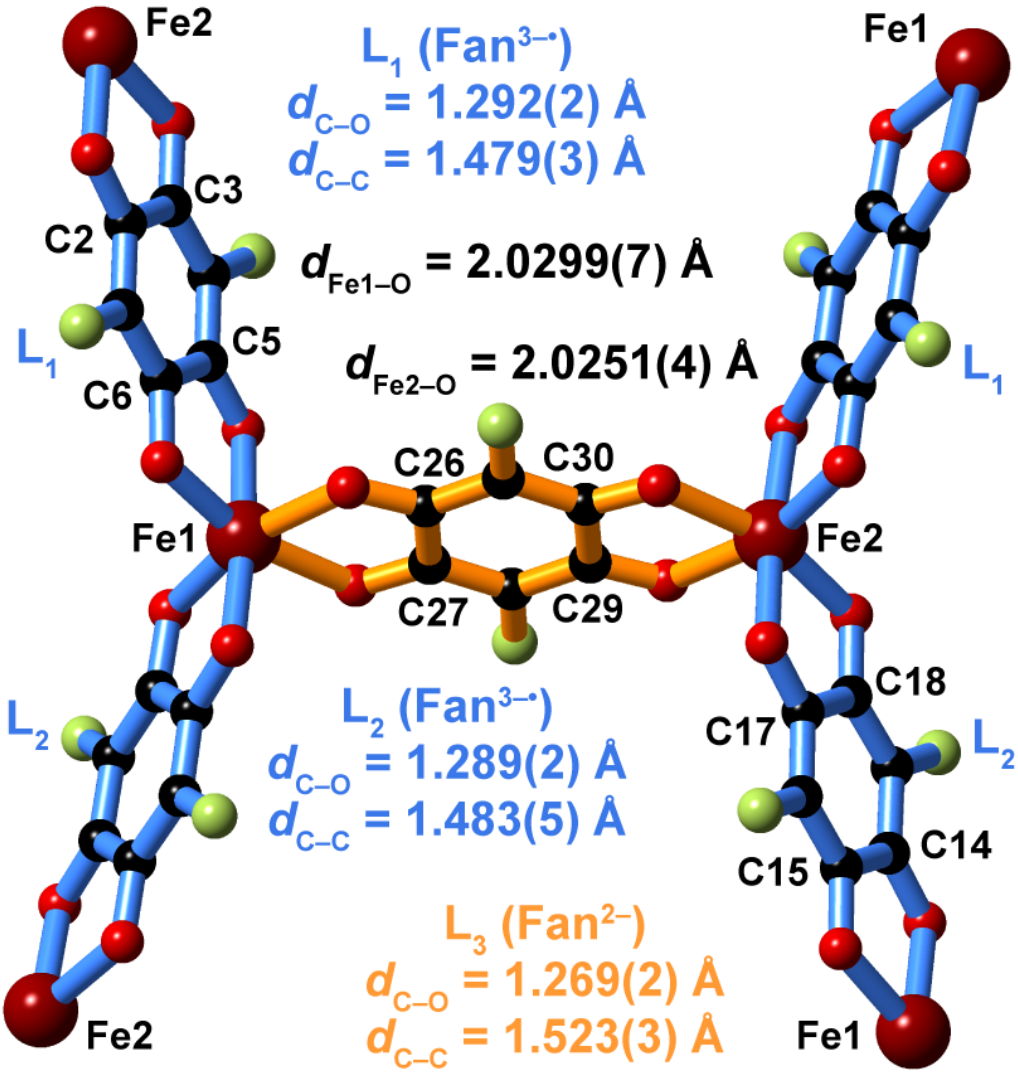


Figure 4.7 Coordination environment and characteristic Fan^{n-} bond lengths around Fe1 and Fe2 in *mP* **4.1a** at T = 100 K. The stated characteristic $d_{C–C}$ values are the mean of the crystallographically independent bond lengths i.e. for $\mathbf{L_1}$: C2–C3 and C5–C6; for $\mathbf{L_2}$: C14–C15 and C17–C18; for $\mathbf{L_3}$: C26–C27 and C29–C30.

In a similar fashion to $(^{n}Pr_4N)_2[Fe_2(Clan)_3]\cdot 2(acetone)\cdot H_2O$, the ligand charge ordering produces anionic $[Fe_2(Fan)_3]^{2-}$ honeycomb sheets comprised of pseudo-1D $\{Fe^{III}–Fan^{3-\bullet}\}_\infty$ chains knitted together with diamagnetic $\mathbf{L_3}$ Fan^{2-} ligands (Figure 4.8). This structure of paramagnetic pseudo-1D chains therefore means *mP* **4.1a** could exhibit single-chain magnetism similarly to ligand-charge order $(^{n}Pr_4N)_2[Fe_2(Clan)_3]\cdot 2(acetone)\cdot H_2O$.[35] Considering the location of MeV^{2+} cations

resting snugly against **L**$_1$ and **L**$_2$, charge localisation at these ligand sites probably results from CT interactions between electron-rich Fan$^{3-\bullet}$ ligands, and electron-deficient MeV^{2+} cations. This is in addition to favourable Coulombic interaction between the highly charged species. This structural disparity observed between *mP* **4.1a** and the 1D fluoranilate ladder compounds **2.3**$_{\mathbf{Mn}}$ and **2.3**$_{\mathbf{Cd}}$ likely arises due to presence of π-electron rich Fan$^{3-\bullet}$ in *mP* **4.1a**, which can engage in strong CT and Coulombic interactions with π-electron deficient MeV^{2+} cations. In contrast, the relatively π-electron poor nature and lower charge of Fan^{2-} in **2.3**$_{\mathbf{Mn}}$ and **2.3**$_{\mathbf{Cd}}$ does not provide a significant driving force for cation-network interaction, causing MeV^{2+} cations to pack between the layers of 1D $[M_2(Fan)_3(H_2O)_2]^{2-}$ ladders in **2.3**$_{\mathbf{Mn}}$ and **2.3**$_{\mathbf{Cd}}$.

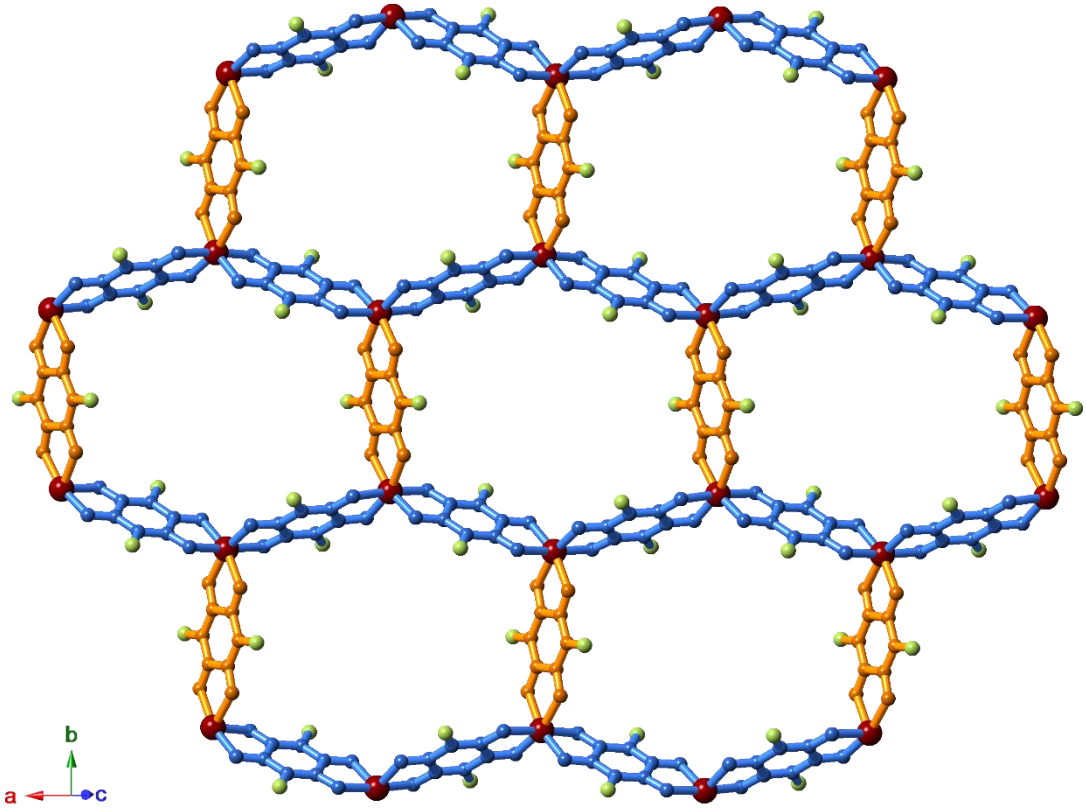


Figure 4.8 Arrangement of **L**$_1$, **L**$_2$ (pale blue, Fan$^{3-\bullet}$) and **L**$_3$ (tan, Fan^{2-}) ligands giving paramagnetic pseudo-1D $\{Fe^{III}–Fan^{3-\bullet}\}_\infty$ chains, bridged by diamagnetic **L**$_3$ ligands, forming the anionic $[Fe_2(Fan)_3]^{2-}$ sheets in *mP* **4.1a**. Maroon = Fe, pale green = F.

4.2.2 Variable-Temperature Single-Crystal X-ray Diffraction

The recent observations of thermally-induced valence tautomerism in the compounds $(Me_4N)_2[FeCl_2(Clan)]$,[36] solvated and desolvated $(^nPr_4N)_2[Fe_2(Clan)_3]$,[35, 37] and $(^nPr_4N)_2[Fe_2(Xan)_3]$ (where X = alloys of Cl and Br, or Cl and F),[22] all of which exhibit ligand-charge ordered structures, aroused the possibility of similar behaviour in *mP* **4.1a**. To study how the MeV^{2+} cation could influence any valence tautomeric processes in *mP* **4.1a**, the temperature dependence of ligand, Fe and cation bond lengths was investigated by SC-XRD. As expected, *in situ* heating from 100 K to 240 K caused thermal expansion of the unit cell (Figure 4.9). This process also caused slight changes in the anionic sheet geometry, and slightly increased the sheet-to-sheet spacing from ca. 7.14 Å to 7.25 Å. Interestingly, the increased sheet-to-sheet spacing in *mP* **4.1a** is less pronounced than in **3.1^{Cl}a**. This is despite the presence of only weak non-covalent interactions between $[Fe_2(Fan)_3]^{2-}$ sheets in *mP* **4.1a**, compared to the strong Coulombic interactions undoubtedly present between the $PhenQ^{2+}$ cations interlaced with $[Fe_2(Clan)_3]^{2-}$ sheets in **3.1^{Cl}a**.

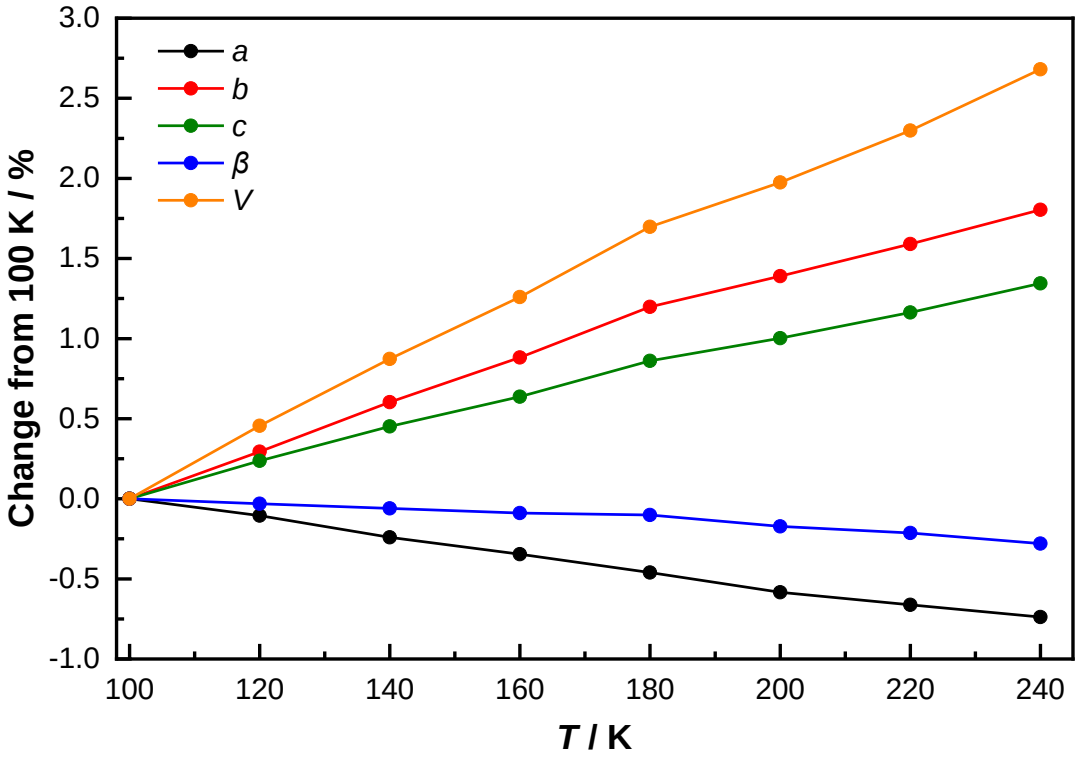


Figure 4.9 Temperature dependence of the cell parameters (*a*, *b*, *c*, *β*, *V*) as measured by SC-XRD for *mP* **4.1a**. All values normalised to those observed at *T* = 100 K.

The temperature-dependant ligand $d_{C–O}$ and diagnostic $d_{C–C}$ values are plotted in Figure 4.10. As for **3.1^{Cl}a**, no significant thermal variation of ligand $d_{C–O}$ or $d_{C–C}$ values was observed. Over the entire temperature range of study, $\mathbf{L_1}$ and $\mathbf{L_2}$ remained in the $Fan^{3-\bullet}$ valence state, as indicated by the longer C–O and shorter C–C bond lengths than in Fan^{2-}, consistent with a semiquinonoid character. The $\mathbf{L_3}$ ligand correspondingly remained in the Fan^{2-} valence state, as evinced by an insignificant variation in mean $d_{C–O}$ or diagnostic $d_{C–C}$. In addition, $d_{Fe–O}$ only varied between 2.0299(4)–2.0251(6) Å for Fe1 and 2.0246(6)–2.0267(5) Å for Fe2, both of which agree with a Fe^{III}_{HS} formulation. These results indicate thermally-induced valence tautomerism is absent in the temperature range 100–240 K. Although it is tempting to attribute this solely to the presence of MeV^{2+}, it is impossible to rule out the presence of valence-tautomerism at a higher temperature. Recent studies on $(^nPr_4N)_2[Fe_2(Clan)_3]$ have shown the valence tautomeric transition temperature ($T_{1/2}$) can be increased from 237 K to above 300 K by desolvation-induced structure transformation. Additionally, it is not possible to decouple the relative importance of ligand substituent electronegativity on promoting valence tautomerism. In fact, recent work published after this study was completed has shown significant decreases or increases of $T_{1/2}$ can be achieved by alloying either bromanilate or fluoranilate ligands respectively, into the $(^nPr_4N)_2[Fe_2(Clan)_3]$ framework.[22] Most significantly, an abrupt increase in magnetic susceptibility (indicative of a valence tautomeric transition) disappeared at ca. 42% Fan^{n-} substitution for $Clan^{n-}$, thereby demonstrating the significant influence of ligand substituents on framework electronic structure. Future computational study is required to better understand how cation-framework interactions impact on this process.

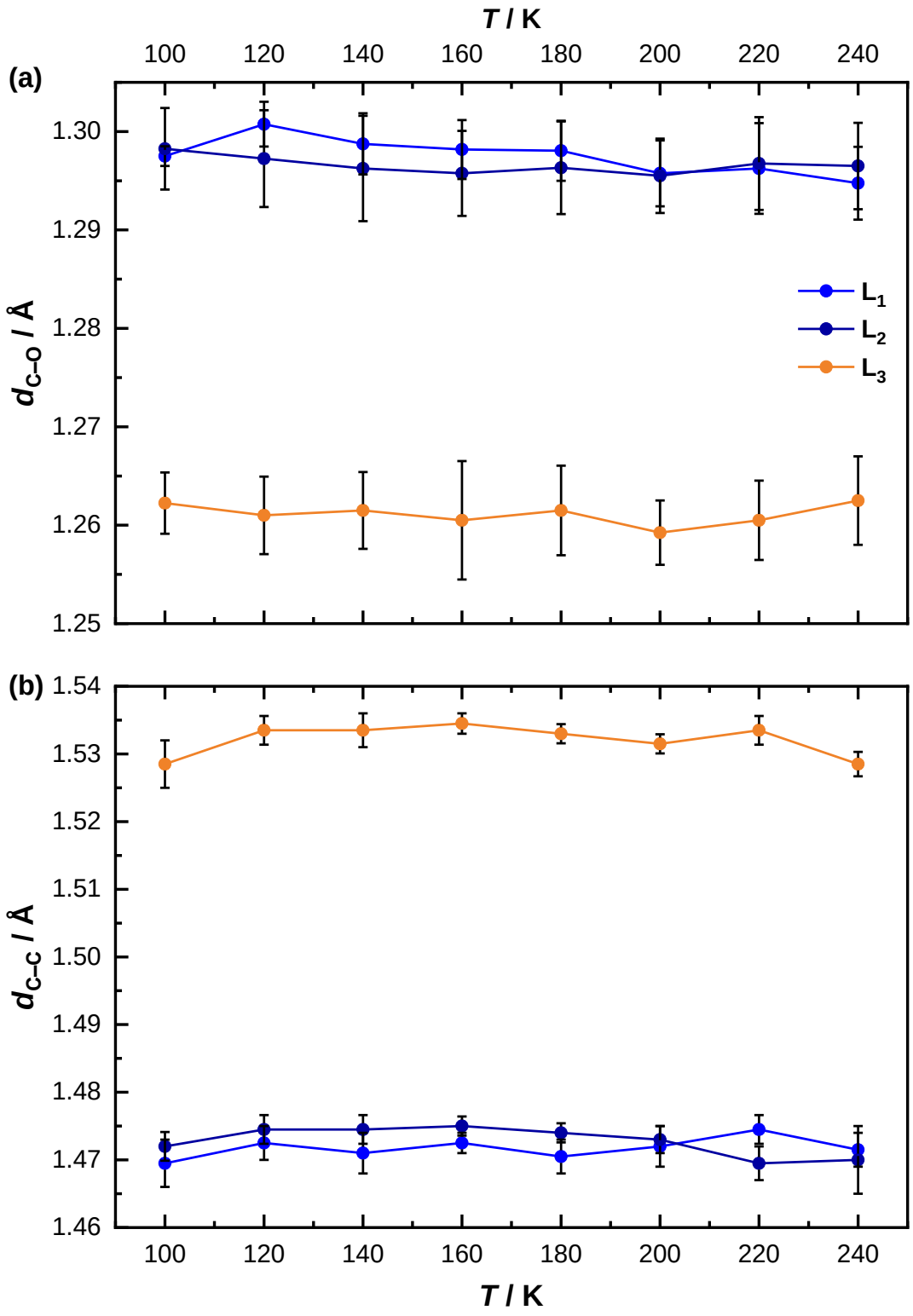


Figure 4.10 Temperature dependence of the characteristic (a) $d_{C–O}$ and (b) $d_{C–C}$ values in *mP* **4.1a** as measured by SC-XRD. Error bars are ± s.u.

4.2.3 Solvent Exchange and Structural Transformations

Structural transformations are commonly observed in layered Fe–tetraoxolene frameworks upon changes in solvation state. Even slight structural distortions can have profound impacts upon the physical properties.[19, 20, 37] Studies of the changes in structure and physical properties upon changing the guest solvation state were therefore undertaken for the (MeV)[$Fe_2(Fan)_3$] framework. Solvent exchange on as-synthesised *mP* **4.1a,** (MeV)[$Fe_2(Fan)_3$]·5.3MeCN, was achieved by soaking crystals in anhydrous, deoxygenated MeCN to yield the isolated MeCN solvate (MeV)[$Fe_2(Fan)_3$]·*y*MeCN (**4.1a**), or DMF to yield the isolated DMF solvate (MeV)[$Fe_2(Fan)_3$]·*y*DMF (**4.1b**). The phase purity of an as-synthesised bulk batch of *mP* **4.1a** was measured by P-XRD, conducted as an slurry in MeCN to maintain the solvation state of the as-synthesised compound (Figure 4.11).

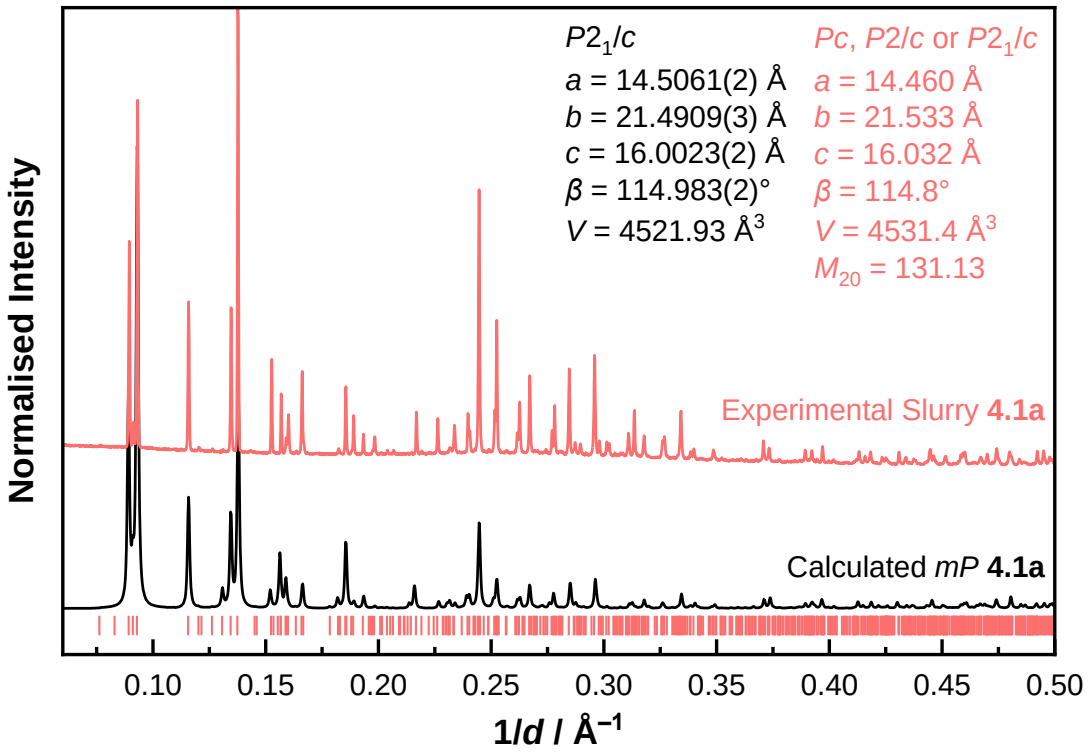
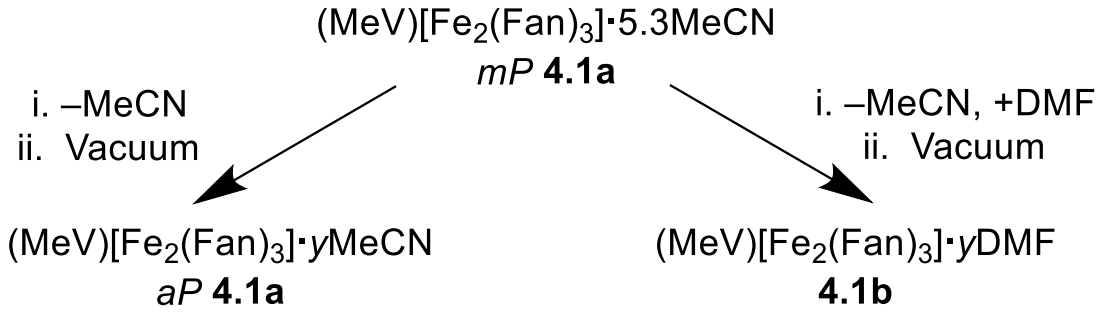


Figure 4.11 Synchrotron P-XRD (λ = 0.58835 Å) pattern of an MeCN slurry of bulk *mP* **4.1a** (pale red, T = 250 K) and calculated pattern from SC-XRD of *mP* **4.1a** (black, T = 240 K). Tick marks (pale red) indicate the positions of the allowed reflections for the unit cell indexed from the experimental P-XRD pattern.

Excellent agreement between the experimental P-XRD pattern (Figure 4.11, pale red) and the calculated pattern from SC-XRD (Figure 4.11, black) is observed, confirming the as-synthesised bulk sample comprises only the desired *mP* **4.1a** phase. Following the solvent exchange process, samples of *mP* **4.1a** and **4.1b** were isolated by Schlenk filtration in a dry dinitrogen (N_2) atmosphere as described in Chapter 3, then transferred to a N_2-filled glovebox for storage and intricate solid manipulations (Scheme 4.1). This process requires application of vacuum to the samples of *mP* **4.1a** and **4.1b** isolated on a Schlenk frit, raising the possibility that partial desolvation of the compounds could occur. Following isolation of *mP* **4.1a**, the P-XRD pattern of isolated powder (Figure 4.12, dark red) shows significant disparities to both the experimental patterns of *mP* **4.1a** in an MeCN slurry (Figure 4.12, pale red), and the pattern calculated from the SC-XRD structure of *mP* **4.1a** (Figure 4.12, black).



Scheme 4.1 Solvent exchange and isolation procedure performed upon as-synthesised (MeV)[Fe_2(Fan)$_3$]·5.3 (*mP* **4.1a**) yielding *aP* **4.1a** and **4.1b**.

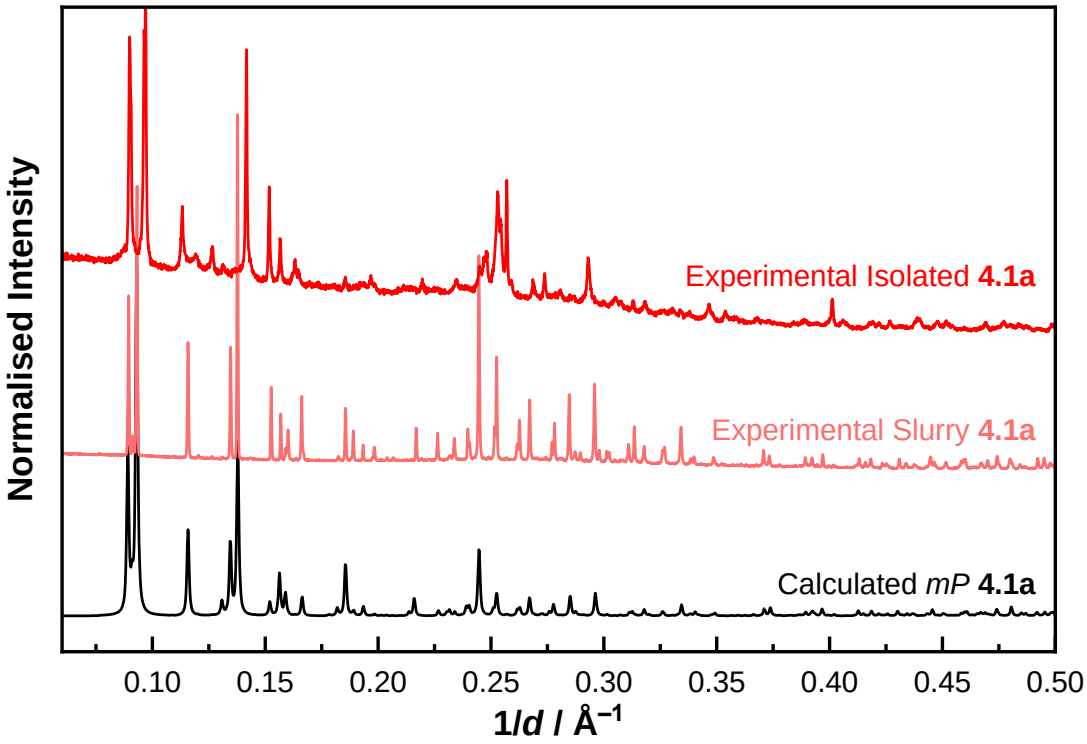


Figure 4.12 Synchrotron P-XRD (λ = 0.58835 Å) pattern of isolated (MeV)[Fe_2(Fan)$_3$]·*y*MeCN (**4.1a**, dark red, T = 100 K), an MeCN slurry of bulk *mP* **4.1a** (pale red, T = 250 K), and calculated pattern from SC-XRD of *mP* **4.1a** (black, T = 240 K).

Indexing the experimental P-XRD pattern for isolated **4.1a** afforded a triclinic unit cell of either *P*1 or *P*−1 symmetry, of almost halved unit cell volume compared to *mP* **4.1a** (Figure 4.13). Further insight into the desolvation-induced structural transformations was obtained from SC-XRD analysis on isolated crystals of **4.1a**. Gratifyingly, single crystal character was maintained in the desolvated sample, although significant twinning and reduced reflection intensity were observed compared to an as-synthesised single crystal of *mP* **4.1a**. A satisfactory structure refinement of the partially desolvated phase of **4.1a** was found in the triclinic *P*−1 space group; the isolated compound is herein referred to as *aP* **4.1a** (Table 4.9). Furthermore, good agreement between the unit cell parameters obtained using P-XRD and SC-XRD is seen, providing an indication of a clean structural transformation from bulk *mP* **4.1a** to bulk *aP* **4.1a** arising due to desolvation (Figure 4.13).

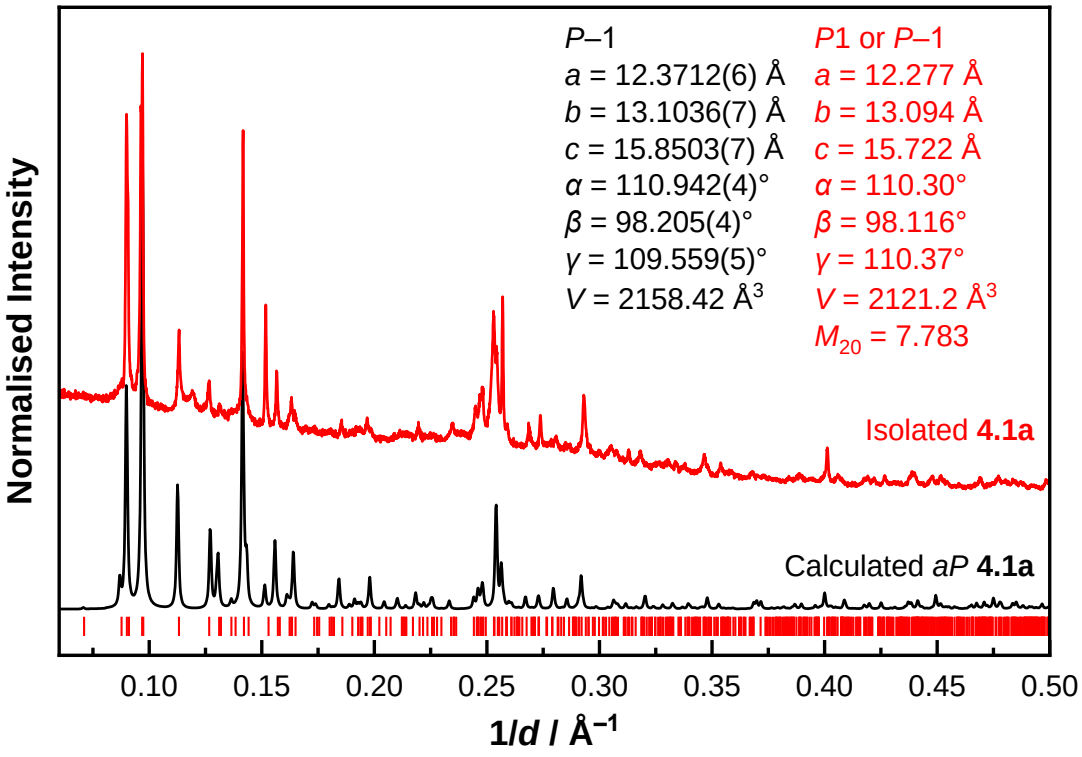


Figure 4.13 Synchrotron P-XRD (λ = 0.58835 Å) pattern of isolated (MeV)[Fe_2(Fan)$_3$]·*y*MeCN (**4.1a**, dark red, T = 100 K) and calculated pattern from SC-XRD of *aP* **4.1a** (black, T = 100 K). Tick marks (red) indicate the positions of the allowed reflections for the unit cell indexed from the experimental P-XRD pattern.

Like the *mP* **4.1a** phase, the asymmetric unit of *aP* **4.1a** contains two Fe centres (Fe1 and Fe2), three crystallographically unique Fan^{n-} ligands (**L$_1$**, **L$_2$** and **L$_3$**), and one MeV^{m+} cation. The framework voids also contain one ordered MeCN molecule, and regions of electron density ascribed to severely disordered MeCN molecules. These disordered solvent molecules could not be modelled satisfactorily, so their scattering contribution was accounted for using the SQUEEZE[23] routine of PLATON.[24] This procedure allowed the degree of solvation to be estimated as (MeV)[Fe_2(Fan)$_3$]·4.8MeCN, which is unsurprisingly lower than the as-synthesised *mP* **4.1a** compound viz. (MeV)[Fe_2(Fan)$_3$]·5.3MeCN. The Fe centres in *aP* **4.1a** also reside in slightly distorted octahedral environments, bound to six O donors of three bridging Fan^{n-} ligands. This arrangement forms anionic (6,3) honeycomb sheets of composition [Fe_2(Fan)^3]$^{x-}$ as with *mP* **4.1a**. The anionic [Fe_2(Fan)$_3$]$^{x-}$ sheets in *aP* **4.1a**

also stack parallel to the crystallographic *c* axis in an offset ABAB manner, with a slight asymmetry in the sheet-to-sheet spacing of 6.959 and 7.188 Å. Most significantly, the partial desolvation process induces changes in the anionic sheet geometry and Fe coordination environments. The Fe···Fe···Fe angles of the anionic sheets change to 104.00(1)°, 112.88(1)° and 143.12(1)° in *aP* **4.1a**. All hexagonal voids within an anionic sheet also incline in the same direction in the *ab* plane, in contrast to *mP* **4.1a** (Figure 4.14). The distortion to the coordination environment around the Fe centres was again quantified using CShM parameters, with the results presented in Table 4.2.

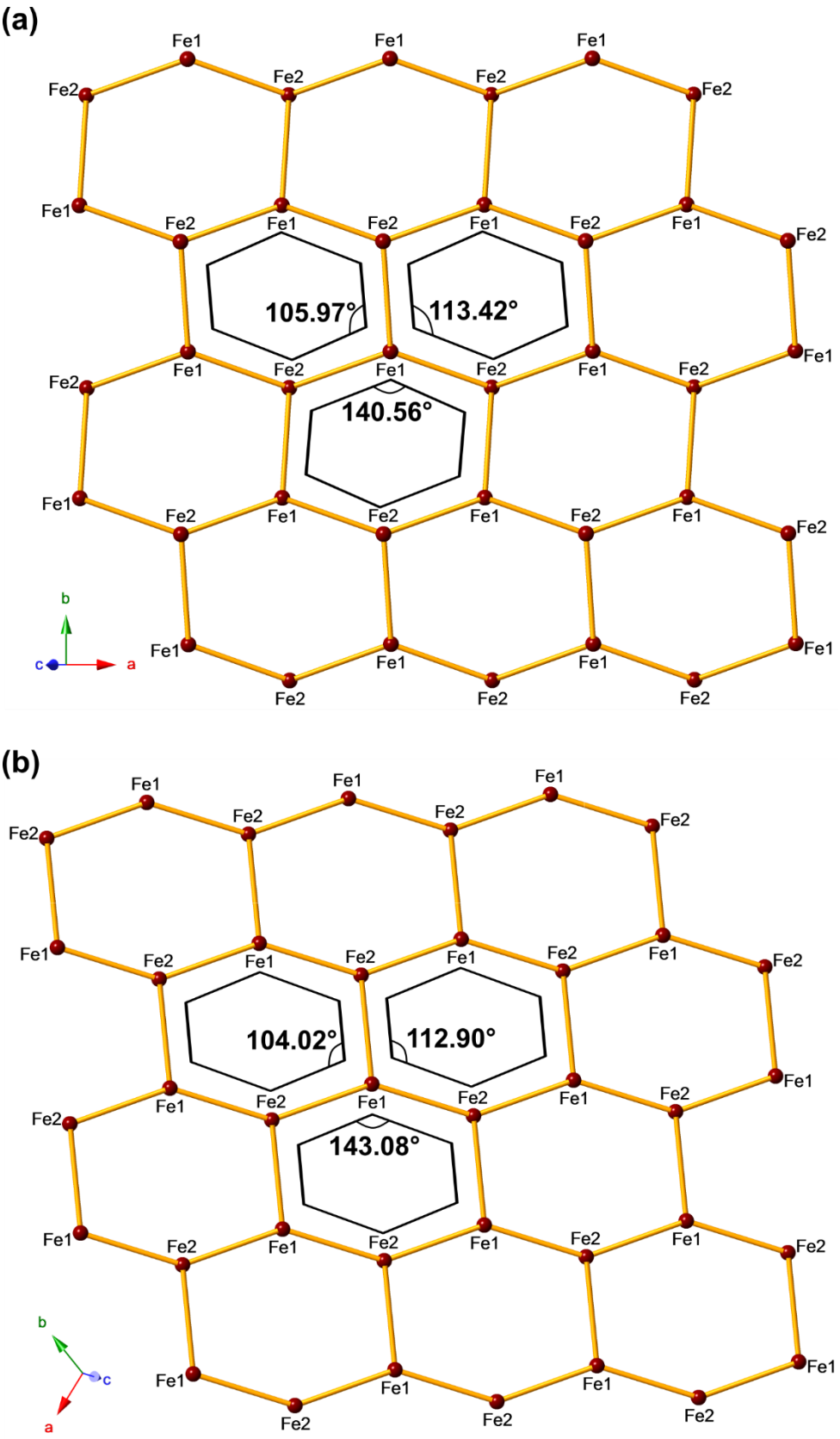


Figure 4.14 Anionic $[Fe_2(Fan)_3]^{2-}$ sheet geometry and Fe···Fe···Fe angles in (a) *mP* **4.1a** and (b) *aP* **4.1a**. Maroon = Fe.

Table 4.2 CShM analyses of the possible coordination geometries of the two Fe sites in the as-synthesised primitive monoclinic (*mP*) phase and isolated primitive triclinic (*aP*) phases of **4.1a**.

Phase	Site	Coordination Geometry (Symmetry)				
		HP-6 (D_{6h})	**PPY-6 (C_{5v})**	**OC-6 (O_h)**	**TPR-6 (D_{3h})**	**JPPY-6 (C_{5v})**
mP **4.1a**	Fe1	32.350	24.365	**1.327**	10.926	28.034
	Fe2	32.681	23.784	**1.432**	10.682	27.373
aP **4.1a**	Fe1	32.115	24.137	**1.370**	11.155	27.854
	Fe2	32.626	23.634	**1.448**	10.654	27.191

HP-6: Hexagon; PPY-6: Pentagonal pyramid; OC-6: Octahedron; TPR-6: Trigonal prism; JPPY-6: Johnson pentagonal pyramid J2

As for *mP* **4.1a**, slight distortion from perfect octahedral coordination geometry for both Fe sites was observed in *aP* **4.1a**. This is especially apparent for Fe2 sites, which lie adjacent to the MeV^{m+} cations residing in the hexagonal channels. Surprisingly though, the magnitude of distortion from perfect octahedral geometry for both Fe sites in the two solvates remain similar in magnitude, despite the differences in anionic sheet geometry. The charge-ordered $(MeV^{2+})[Fe^{III}_2(Fan^{2-})(Fan^{3-\bullet})_2]$ formulation of *mP* **4.1a** is maintained in *aP* **4.1a**, evinced by diagnostic ligand and cation bond lengths, in addition to d_{Fe-O} values. While there is slight shortening of the central (C41–C44) d_{C-C} in MeV^{2+} to 1.477(7) Å in *aP* **4.1a**, it is still consistent with MeV^{2+}.[31] In addition, there is a very small degree of bond length alternation in the two pyridinium rings of the MeV^{m+} cations, although the magnitude is not nearly as pronounced as in $MeV^{+\bullet}$.[31, 32] Both these factors are indicative of MeV^{2+} in *aP* **4.1a**. For $\mathbf{L_1}$ and $\mathbf{L_2}$, the mean d_{C-O} values are 1.300(3) and 1.301(2) Å respectively, with corresponding diagnostic d_{C-C} of 1.460(4) and 1.469(5) Å. These values point towards $\mathbf{L_1}$ and $\mathbf{L_2}$ maintaining the $Fan^{3-\bullet}$ valence state in *aP* **4.1a**. On the other hand, the mean d_{C-O} and d_{C-C} values are 1.265(3) Å and 1.526(4) Å in $\mathbf{L_3}$, both of which agree with a Fan^{2-} valence state. The d_{Fe-O} values for Fe1 and Fe2 are 2.028(19) and 2.026(17) Å, with BVS values of

2.92 and 2.93, all of which agree well with Fe^{III}_{HS}. There is also a marked difference in Fe–Fe distances across $\mathbf{L_1}$ or $\mathbf{L_2}$, compared to $\mathbf{L_3}$, as well as disparity in the mean $d_{Fe–O}$ values to $\mathbf{L_3}$ (2.088(6) Å), compared to $\mathbf{L_1}$ or $\mathbf{L_2}$ (1.997(3) and 1.996(4) Å respectively). Both these are likely the result of weaker Coulombic interactions between Fe^{III} and $Fan^{2–}$, which parallels a similar observation in *mP* **4.1a**. These combinations of factors therefore all support a charge-ordered $(MeV^{2+})[Fe^{III}_2(Fan^{2–})(Fan^{3–\bullet})_2]$ formulation for *aP* **4.1a**.

Solvent exchange on the as-synthesised *mP* **4.1a** to the DMF solvate $(MeV)[Fe_2(Fan)_3]\cdot y$DMF (**4.1b**) was evidenced by a combination of ATR FT-IR spectroscopy, SC- and P-XRD, TGA and elemental analysis. The ATR FT-IR spectra of isolated *aP* **4.1a** and **4.1b** are presented in Figure 4.15. Replacement of guest MeCN with DMF in the channels, was indicated by disappearance of a weak absorption at ν = 2249 cm^{-1} (Figure 4.15, †), ascribed to the $\nu_{C\equiv N}$ of MeCN, and appearance of an intense, sharp absorption ν = 1666 cm^{-1} due to the $\nu_{C=O}$ of DMF (Figure 4.15, ‡). A moderate absorption at ν = 1094 cm^{-1} due to in-plane CH_3 rocking in DMF is also observed (Figure 4.15, *).[38, 39]

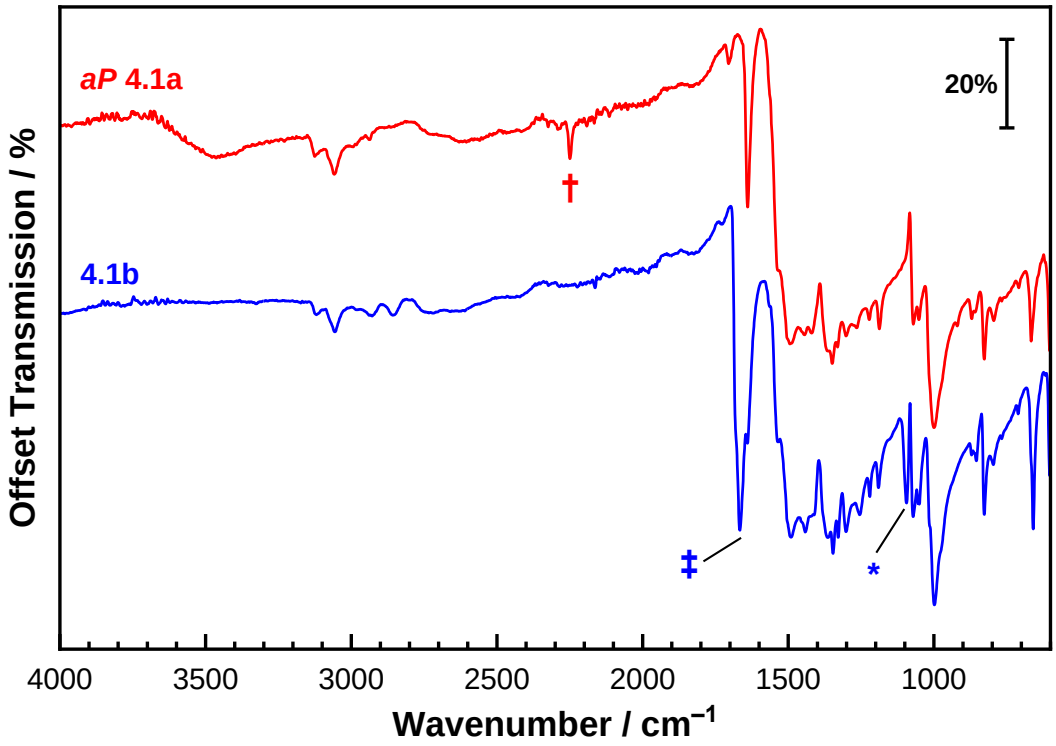


Figure 4.15 ATR FT-IR spectra of (MeV)[Fe_2(Fan)$_3$]·*y*MeCN (*aP* **4.1a**, red) and (MeV)[Fe_2(Fan)$_3$]·*y*DMF (**4.1b**, blue) collected at room temperature in air, showing $\nu_{C\equiv N}$ mode of MeCN (†), and DMF $\nu_{C=O}$ (‡) and in-plane CH_3 rocking (*).

Structural transformations arising from the guest solvent exchange were also followed by a combination of X-ray diffraction techniques. Despite the harsh treatment of crystals of **4.1b**, sufficient crystallinity was maintained to allow structure determination by SC-XRD. A satisfactory structure refinement reveals **4.1b** possesses similar unit cell dimensions as *mP* **4.1a** (Table 4.8 for *mP* **4.1a** and Table 4.9 for **4.1b**) but with a *C*-centred monoclinic cell. The structure refinement was performed in the monoclinic space group *C*2/*c*, in contrast to *P*2$_1$/*c* for *mP* **4.1a**, and *P*−1 for *aP* **4.1a**. Whereas the asymmetric unit of *mP* **4.1a** and *aP* **4.1a** contain three crystallographically independent ligands, the asymmetric unit of **4.1b** contains only two inequivalent Fan^{n-} ligands, $\mathbf{L_4}$ and $\mathbf{L_5}$ in a 2:1 ratio. Like *mP* **4.1a** and *aP* **4.1a**, there are two inequivalent Fe sites, Fe1 and Fe2 present in **4.1b**. Fe1 and Fe2 are situated upon a two-fold axis in **4.1b**, in contrast to the MeCN solvates, in which the Fe sites do not reside on special positions. Charge-balancing MeV^{m+} cations in **4.1b**

are situated in the hexagonal channels nestled against Fe2, as in *mP* **4.1a** and *aP* **4.1a**, so unsurprisingly the Fe···Fe···Fe angles are notably distorted from 120°. The Fe coordination geometry at the Fe2 site is also distorted due to the location of MeV^{m+} cation in the hexagonal void. The magnitude of this distortion is similar across the three compounds and reflects the interaction of MeV^{m+} with the framework at this site. The magnitude of distortion to the Fe coordination environments was quantified using CShM parameters (Table 4.3).

Table 4.3 CShM analyses of the possible coordination geometries of the two Fe sites in **4.1b**.

Site	Coordination Geometry (Symmetry)				
	HP-6 (D_{6h})	**PPY-6 (C_{5v})**	**OC-6 (O_h)**	**TPR-6 (D_{3h})**	**JPPY-6 (C_{5v})**
Fe1	32.249	24.249	**1.270**	11.038	28.042
Fe2	32.703	23.502	**1.459**	10.632	27.207

HP-6: Hexagon; PPY-6: Pentagonal pyramid; OC-6: Octahedron; TPR-6: Trigonal prism; JPPY-6: Johnson pentagonal pyramid J2

The higher symmetry structure results from significant changes to the anionic $[Fe_2(Fan)_3]^{2-}$ sheet geometry and Fe···Fe···Fe angles in **4.1b** (Figure 4.16). This is likely due to the differing molecular volume and shapes of the guest MeCN and DMF molecules present in the channels of the two solvates. Similar distortion or 'breathing' phenomena are common in porous coordination polymers,[40-42] and similar guest-induced structure transformations have also been observed in $(Me_2NH_2)_2[Fe_2(Clan)_3]\cdot 6DMF\cdot 2H_2O$,[19, 20] and **3.1^{Cl}a** and **3.1^{Cl}b**.

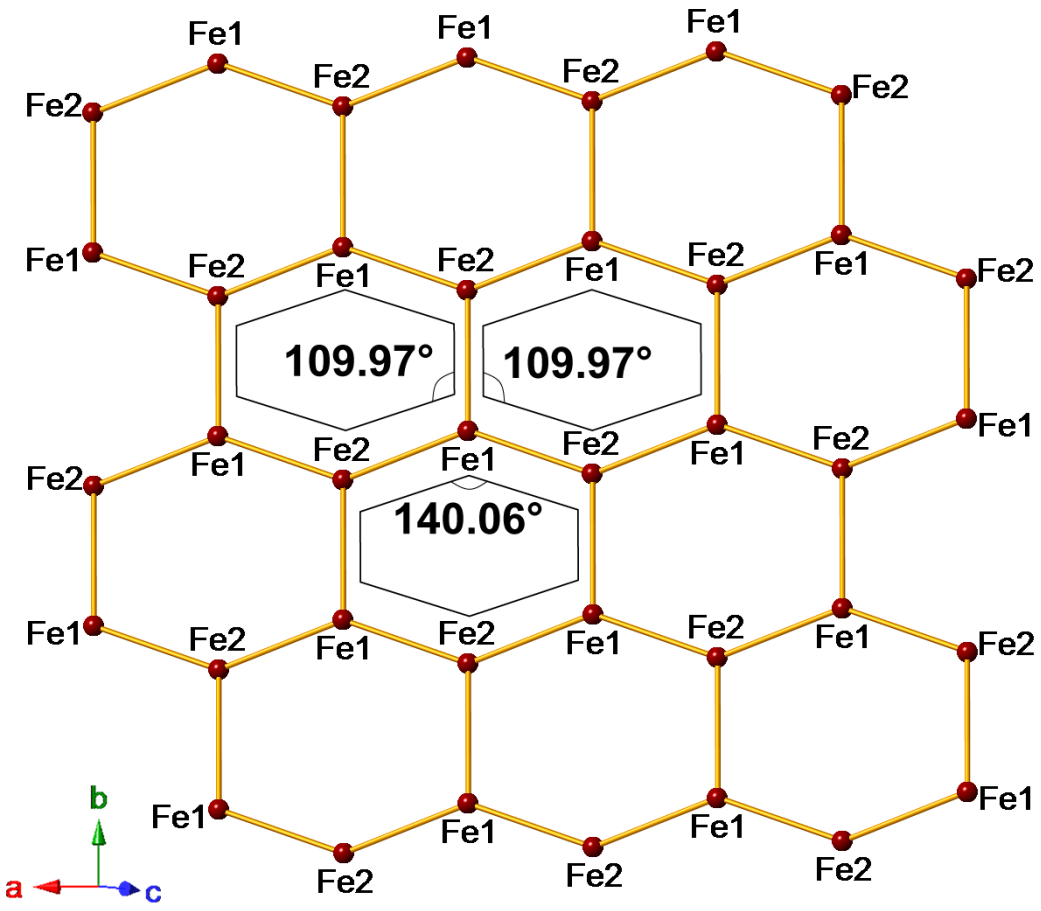


Figure 4.16 The anionic $[Fe_2(Fan)_3]^{x-}$ sheet geometry and Fe···Fe···Fe angles in **4.1b**. Maroon = Fe.

The characteristic ligand $d_{C–O}$ and $d_{C–C}$, and $d_{Fe–O}$ values all indicate that **4.1b** maintains the same ligand-charge ordered $(MeV^{2+})[Fe^{III}_2(Fan^{2-})(Fan^{3-\bullet})_2]$ state as *mP* **4.1a** and *aP* **4.1a**. For MeV^{m+} in **4.1b**, there are no significant differences between $d_{C–C}$ and $d_{C–N}$ values, compared to the equivalent bonds in MeV^{2+} of *mP* **4.1a** or $MeV(BF_4)_2$.[43] Moreover, the central (C23–C23′) $d_{C–C}$ value of 1.484(4) Å is consistent with MeV^{2+}. For $\mathbf{L_4}$, the mean $d_{C–O}$ and $d_{C–C}$ values of 1.295(2) Å and 1.476(3) Å are indicative of the $Fan^{3-\bullet}$ valence state. On the other hand, the mean $d_{C–O}$ and $d_{C–C}$ values of 1.266(2) and 1.525(2) Å in $\mathbf{L_5}$ are consistent with the Fan^{2-} state. In addition, $d_{Fe–O}$ values of 2.027(17) and 2.025(17) Å for Fe1 and Fe2, and BVS values of 2.93 and 2.94 respectively, agree with a Fe^{III}_{HS} oxidation state. In a similar manner to as-synthesised *mP* **4.1a**, the mean $d_{Fe–O}$ values between Fe and $\mathbf{L_4}$ (1.997(6) Å) are markedly different to those between Fe and $\mathbf{L_5}$ (2.083(2) Å), likely a

result of weaker Coulombic interaction between Fe^{III}_{HS} and Fan^{2-} (**L**$_5$) compared to Fe^{III}_{HS} and $Fan^{3-\bullet}$ (**L**$_4$). This is coupled with a commensurate disparity in Fe–Fe distance across **L**$_4$ compared to **L**$_5$, which significantly distorts the honeycomb sheet geometry. This also parallels in similar observation in **2.5**, **2.6** and **2.7** (Chapter 2). Examination of the electron density difference (F_O–F_C, where F_O and F_C are the observed and calculated structure factors for the model) maps for **4.1b** reveals large regions of unassigned electron density that was attributed to guest DMF molecules. These regions exhibited different shapes and electron counts compared to those in *mP* **4.1a**, providing further indication of the guest exchange process. Modelling of this electron density with DMF molecules was attempted, however a satisfactory solvent model could not be achieved, due to severe disorder of the DMF molecules about the 2_1 axis and *c*-glide plane. The scattering contribution of this electron density was accounted for using the SQUEEZE[23] routine of PLATON,[24] affording an estimated solvation of (MeV)[Fe_2(Fan)$_3$]·3.8DMF. Solvation exclusively by DMF was justified as the FT-IR spectrum did not show any absorbances attributable to MeCN in **4.1b** (Figure 4.15).

Synchrotron P-XRD reveals the framework is robust and that the solvent exchange proceeds with retention of crystallinity. The experimental pattern of a bulk sample is satisfactorily indexed with a monoclinic unit cell of equivalent cell dimensions as those measured by SC-XRD of **4.1b** (Figure 4.17, blue). Comparison of the experimental P-XRD pattern with that calculated from the SC-XRD structure (Figure 4.17, black) also reveals excellent agreement between the observed and calculated peak positions. There are however some differences in the ratios of reflection intensity between the calculated and experimental patterns, possibly arising from preferred orientation effects. Nevertheless, these analyses clearly demonstrate conversion from as-synthesised *mP* **4.1a** to **4.1b** proceeds cleanly, giving only a phase-pure product of known composition.

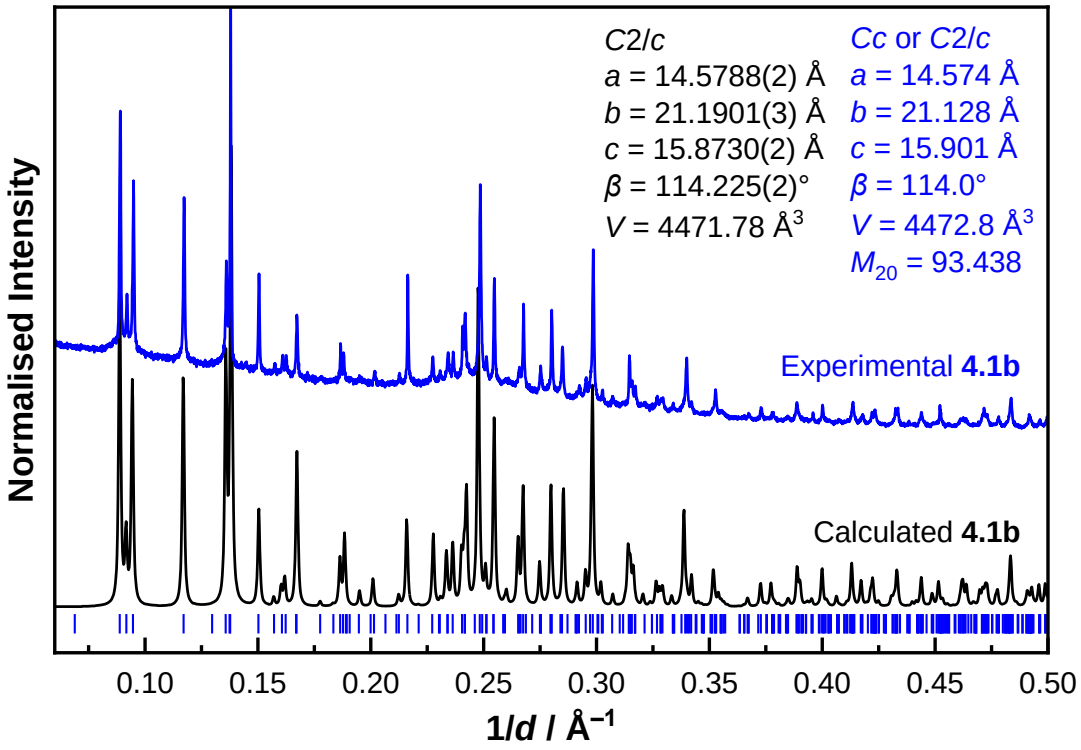


Figure 4.17 Synchrotron P-XRD (λ = 0.58835 Å) pattern of isolated **4.1b** (blue, T = 100 K) and calculated pattern from SC-XRD of **4.1b** (black, T = 100 K). Tick marks (blue) indicate the positions of the allowed reflections for the unit cell indexed from the experimental P-XRD pattern.

Finally, thermogravimetric analysis (TGA) and combustion analysis were utilised to confirm exchange of the guest solvent molecules. TGA demonstrates differences in the percentage content of volatile solvent between *aP* **4.1a** and **4.1b**, in addition to slight differences in the temperature range over which these solvents are lost (Figure 4.18). For *aP* **4.1a**, the volatile solvent comprises ca. 16.6 wt% of the sample, corresponding to ca. 4 MeCN molecules per formula unit i.e. (MeV)[Fe_2(Fan)$_3$]·4MeCN. This value is in reasonable agreement with that estimated from SC-XRD i.e. (MeV)[Fe_2(Fan)$_3$]·4.8MeCN, with the discrepancy probably due to slight solvent loss in the time period between the two measurements. Interestingly, the mass loss proceeds up to ca. 190 °C, which is significantly above the boiling point of MeCN (b.p. 83 °C). Given the propensity of the **4.1** family of compounds to undergo sizable structural distortions upon changes in solvation, it is possible for the void spaces in *aP* **4.1a** to become partially occluded during solvent loss. Consequently,

evaporation of some guest MeCN may require additional energy to further transform the structure to the equilibrium solvent-free structure. While every precaution was taken to ensure minimal solvent loss before TGA, by placing a sample of *aP* **4.1a** in the instrument immediately before measurement after brief handling in air, it is not possible to rule out partial replacement of some guest MeCN with atmospheric H_2O. This could also cause some mass loss to proceed above the boiling point of MeCN.

A similar analysis of **4.1b** reveals a volatile solvent content of 18.2 wt%, consistent with 2.5 DMF molecules per formula unit, with the mass loss proceeding up to ca. 210 °C. In contrast to *aP* **4.1a**, the mass loss proceeds in two indistinct steps, as evidenced by two distinct minima in the rate of mass loss traces (Figure 4.18b, green). As with the MeCN solvate, desolvation proceeding above the boiling point of the solvent possibly reflects entrapment of solvent due to a structural transformation which occludes the channels in **4.1b**. Combustion analyses (see Experimental, Section 4.4.2 and 4.4.3) also show clear differences in the elemental composition between *aP* **4.1a** and **4.1b**, in particular N content, supporting the different fraction and identity of guest solvents between the two compounds. In summary, these results demonstrate the successful formation and characterisation of two differently solvated Fe–tetraoxolene compounds with equivalent framework compositions.

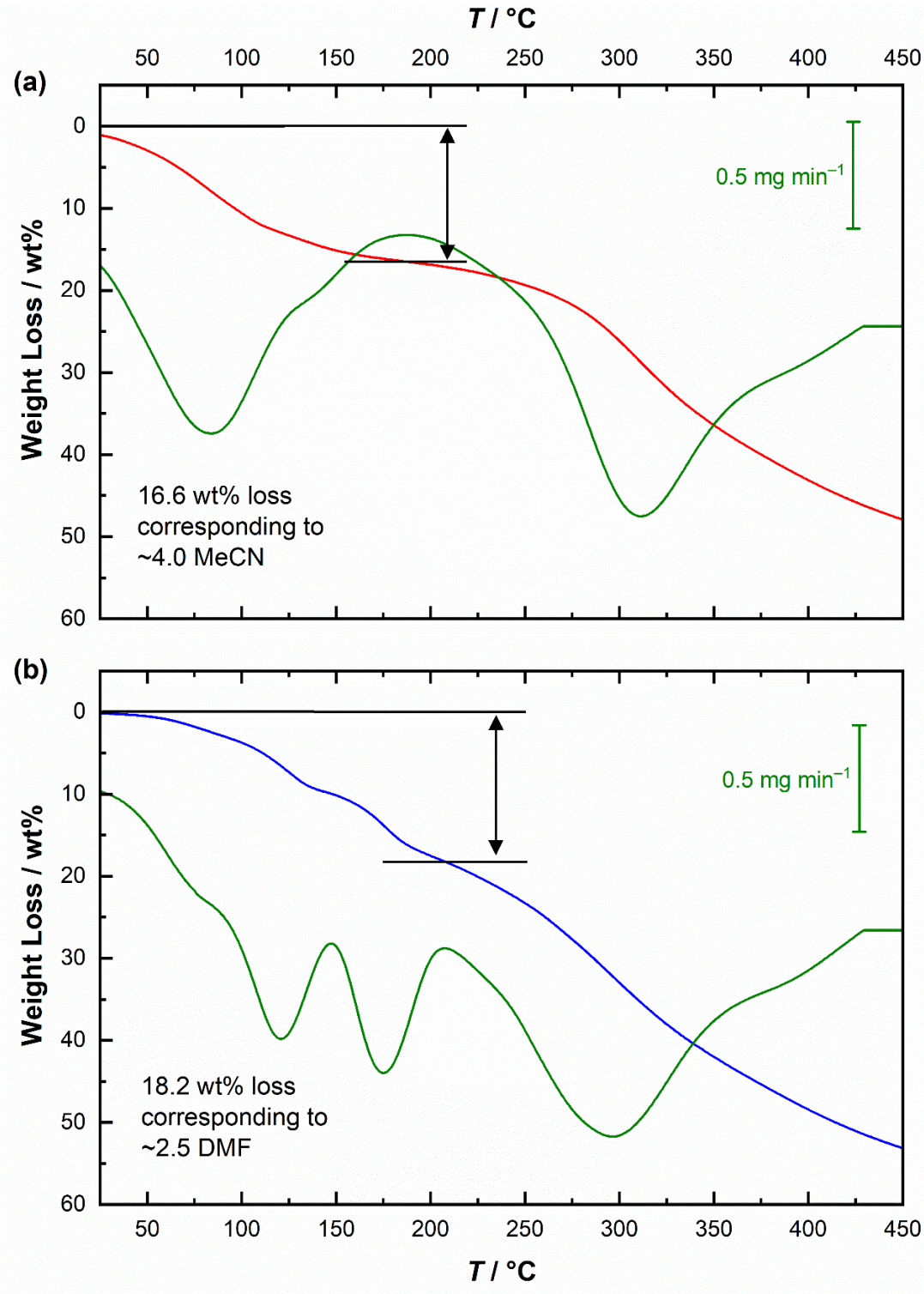


Figure 4.18 Thermogravimetric analyses of (a, red) *aP* **4.1a**, (b, blue) **4.1b** and corresponding rates of mass loss (green) at a scan rate of 5 °C min^{-1} in a flow of N_2. Non-zero mass loss for *aP* **4.1a** ascribed to release of volatile MeCN into the N_2 stream during the balance stabilisation period at the beginning of the measurement run.

4.2.4 ^{57}Fe Mössbauer Spectroscopy

Insight into the temperature-dependence of the Fe valence state in a*P* **4.1a** and **4.1b** was afforded by ^{57}Fe Mössbauer spectroscopy. The spectrum of a*P* **4.1a** at 293 K comprises two underlying quadrupole doublets (Figure 4.19, upper). Fitting the experimental spectrum yields an isomer shift of δ = 0.50 mm s^{-1} and a quadrupole splitting ΔE_Q = 1.02 mm s^{-1} for the first site, and δ = 1.17 mm s^{-1} and ΔE_Q = 1.50 mm s^{-1} for the second site, with an intensity ratio of ca. 2:1 for the two sites (Table 4.4). The parameter set for the first site is consistent with Fe^{III}_{HS} in an octahedral environment,[44] and matches well to parameters obtained for other Fe^{III}–tetraoxolene frameworks.[15, 16, 18-20, 36] The high δ value for the second site is unambiguously attributed to high-spin Fe^{II} (Fe^{II}_{HS}) also in an octahedral environment.[45] Given the putative valence-pure Fe^{III}_{HS} formulation as suggested by SC-XRD, the presence of an Fe^{II}_{HS} site is surprising. However, Fe-based mixed valency in *aP* **4.1a** parallels a similar observation of valence-trapped Fe^{II}_{HS} and Fe^{III}_{HS} sites in $(Et_4N)_2[Fe_2(Fan)_3]\cdot 5(acetone)$, in spite of the valence-pure Fe^{III}_{HS} formulation as suggested by SC-XRD.[16] The 2:1 ratio of Fe^{III}/Fe^{II} in *aP* **4.1a** as indicated by ^{57}Fe Mössbauer spectroscopy, in contrast to the 1:1 ratio of Fe1:Fe2 sites by SC-XRD, suggests the different valence Fe sites do not correspond directly to the crystallographic Fe1 or Fe2 sites. Instead it represents a structure which is valence-trapped on the ^{57}Fe Mössbauer timescale (ca. 10^{-7} s excited state lifetime)[44, 46] but delocalised on the crystallographic timescale (seconds to minutes for collection of a reflection).

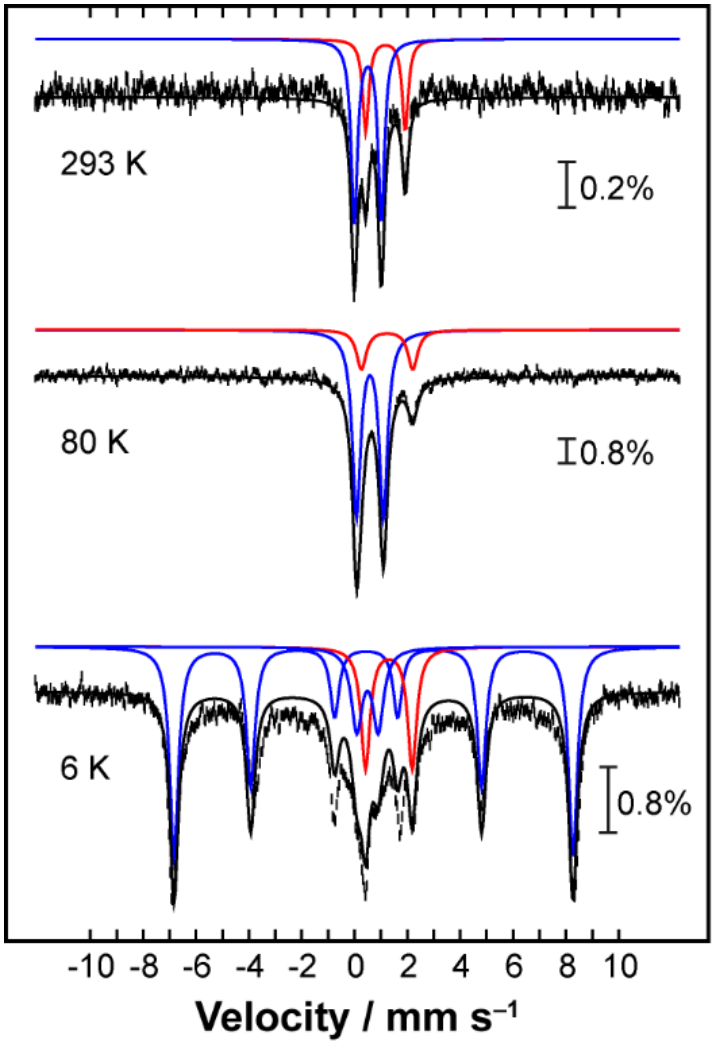


Figure 4.19 ^{57}Fe Mössbauer spectra of *aP* **4.1a** measured at T = 293 K (upper), T = 80 K (middle) and T = 6 K (lower). The fitted spectra correspond to Fe^{III} (blue) and Fe^{II} (red) sites. The fitting parameters are given in Table 4.4.

Table 4.4 Fitted ^{57}Fe Mössbauer spectral parameters for *aP* **4.1a**.

***T* / K**	**Species**	**δ / mm s^{-1}**	**ΔE_Q / mm s^{-1}**	**B_0 / T**	**$\Gamma_{L\,(R)}$**	***I* / %**
293	Fe^{III}	0.50	1.02	-	0.30	67
	Fe^{II}	1.17	1.50	-	0.28	33
80	Fe^{III}	0.58	1.02	-	0.39	80
	Fe^{II}	1.23	1.95	-	0.45	20
6	Fe^{III} magnetic	0.58	0.28	47.0	0.4	65
	Fe^{III}	0.49	0.81	-	0.5	16
	Fe^{II}	1.30	1.80	-	0.41	19

The valence-trapped Fe^{II}/Fe^{III} sites in *aP* **4.1a** at room temperature also present an interesting contrast to the Fe valence population in the honeycomb framework $(TAG)[Fe^{II}Fe^{III}(ClCNan^{2-})_3]$ (TAG^+ = tris(amino)guanidinium, $ClCNan^{2-}$ = 3-chloro-6-cyano-2,5-dihydroxy-1,4-benzoquinone, chlorocyanoanilate). The room temperature spectrum of this compound consists of a single quadrupole doublet with δ = 0.74 mm s^{-1}, which is intermediate between $Fe^{II}{}_{HS}$ and $Fe^{III}{}_{HS}$, indicating a completely valence delocalised structure i.e. $Fe^{2.5+}$ on the ^{57}Fe Mössbauer timescale.[47] Additionally, for both *aP* **4.1a** and $(Et_4N)_2[Fe_2(Fan)_3]\cdot 5(acetone)$, the Fe^{II} sites exhibit lower values of ΔE_Q compared to either: the localised Fe^{II} sites in the $Li_x(Me_2NH_2)_2[Fe_2(Clan)_3]$ framework following reduction of the pristine Fe^{III} framework (Fe^{II} ΔE_Q > 2.5 mm s^{-1});[21] or the low temperature Fe^{II} sites of $(TAG)[Fe^{II}Fe^{III}(ClCNan^{2-})_3]$ framework (Fe^{II} ΔE_Q > 2.4 mm s^{-1}).[47] On the other hand, the ΔE_Q for the $Fe^{II}{}_{HS}$ site in *aP* **4.1a** agree closely with those determined for $Fe^{II}{}_{HS}$ sites in the 1D strip coordination polymers $[Fe^{II}(Clan)(H_2O)_2](phz)$ (phz = phenazine, ΔE_Q = 1.46 mm s^{-1})[45] and $[Fe^{II}(dhbq)(H_2O)_2]$ (ΔE_Q = 1.47 mm s^{-1}),[48, 49] and are slightly larger than the ΔE_Q values for the $Fe^{II}{}_{HS}$ sites in the high temperature phases of solvated and desolvated $(^nPr_4N)_2[Fe_2(Clan)_3]$ (0.89 mm s^{-1} and 1.152 mm s^{-1} respectively).[35, 37] For the 1D strip compounds, the lower ΔE_Q values

were ascribed to tetragonal distortion of the octahedral Fe^{II}_{HS} environment, giving relatively high D_{4h} symmetry of the FeO_6 octahedron. This is compared to the C_{2v} or lower symmetry of the FeO_6 octahedron in the 1D zig-zag compound $[Fe^{II}(Clan)(H_2O)_2](H_2O)$ resulting in a higher ΔE_Q of 2.53 mm s^{-1}.[45] These factors suggest a different symmetry about the transient $Fe^{II}O_6$ octahedron in *aP* **4.1a**, compared to the $Fe^{II}O_6$ octahedra in $(TAG)[Fe^{II}Fe^{III}(ClCNan^{2-})_3]$ or $Li_x(Me_2NH_2)_2[Fe_2(Clan)_3]$. These differences in Fe coordination geometry may give rise to markedly different properties.

The spectrum of *aP* **4.1a** at 80 K is similarly comprised of two underlying quadrupole doublets, with a parameter set of δ = 0.58 mm s^{-1} and ΔE_Q = 1.02 mm s^{-1} for the Fe^{III}_{HS} site, and δ = 1.23 mm s^{-1} and ΔE_Q = 1.95 mm s^{-1} for the Fe^{II}_{HS} site. Cooling also causes the intensity ratio of these sites to change to ca. 4:1 Fe^{III}/Fe^{II}. The reduced proportion of Fe^{II}_{HS} at 80 K compared to 293 K suggests the Fe^{II}_{HS} valence state is higher in energy than the Fe^{III}_{HS} state, and that electron transfer between $Fan^{3-\bullet}$ and Fe^{III}_{HS} to give Fe^{II}_{HS} is thermally activated. Again, the relatively small ΔE_Q values for the Fe^{II}_{HS} site contrast with those in $Li_x(Me_2NH_2)_2[Fe_2(Clan)_3]$ or $(TAG)[Fe^{II}Fe^{III}(ClCNan)_3]$, but agree well with ΔE_Q values of Fe^{II}_{HS} in $(Et_4N)_2[Fe_2(Fan)_3]\cdot 5(acetone)$. The behaviour of *aP* **4.1a** upon cooling to 6 K presents an interesting contrast to the behaviour of other mixed-valence Fe–tetraoxolene frameworks. The spectrum consists of several absorbances which were fitted with an underlying sextet, and two quadrupole doublets. As with the 293 and 80 K spectra, the two underlying quadrupole doublets, with a parameter set of δ = 0.49 mm s^{-1} and ΔE_Q = 0.81 mm s^{-1} for the first site, and δ = 1.30 mm s^{-1} and ΔE_Q = 1.80 mm s^{-1} for the second site, correspond to Fe^{III}_{HS} and Fe^{II}_{HS} respectively. The presence of a sextet is consistent with Fe^{III}_{HS} residing in a magnetic environment, with an internal field parameter B_0 = 47.0 T. This behaviour results from spontaneous magnetisation in the sample, and parallels the low-temperature spontaneous magnetisation of other Fe–tetraoxolene frameworks such as $\mathbf{3.1^{Cl}b}$ in Chapter 3, or $(Me_2NH_2)_2[Fe_2(Clan)_3]\cdot 6DMF\cdot 2H_2O$.[19, 20] The presence of unmagnetised Fe^{III}_{HS} is surprising. We hypothesise this behaviour may reflect that the Fe^{III}_{HS} sub-spectra at 293 and 80 K describe two indistinguishable Fe^{III}_{HS} sites, Fe^{III}_A and Fe^{III}_B, only one of which is involved with electron transfer between $Fan^{3-\bullet}$ producing the Fe^{II}_{HS} site. While this electron transfer process is slow on the ^{57}Fe Mössbauer timescale, it may

be sufficiently fast to prevent long-range ordering of these Fe^{III}_{HS} sites, as the transient formation of Fe^{II}_{HS} requires oxidation of $Fan^{3-\bullet}$ to Fan^{2-}. This valence fluctuation process could cause (anti)ferromagnetic direct coupling between Fe^{III}_{HS} and $Fan^{3-\bullet}$ to be somewhat inhibited, preventing long-range ordering in small domains of the compound. Further studies on the magnetic behaviour of *aP* **4.1a** are ongoing.

Comparison of the ^{57}Fe Mössbauer spectra of *aP* **4.1a** and **4.1b** reveals a dramatic contrast, despite SC-XRD analyses suggesting that both *aP* **4.1a** and **4.1b** contain valence-pure Fe^{III}_{HS} populations. At 295 K, the spectrum of **4.1b** comprises a single quadrupole doublet, parameterised by δ = 0.489 mm s^{-1} and ΔE_Q = 1.016 mm s^{-1} (Figure 4.20 and Table 4.5). These values are consistent with Fe^{III}_{HS} in an octahedral environment,[44, 50] and also closely match δ and ΔE_Q values observed in molecular Fe^{III}–tetraoxolene compounds,[51] and mixed-valence Fe^{III}–tetraoxolene frameworks.[15, 16, 18-20, 35] Upon cooling to 5.8 K, the spectrum of **4.1b** transforms to a sextet, which is satisfactorily fit by the parameter set δ = 0.6 mm s^{-1} and ΔE_Q = 0.28 mm s^{-1}. Like the 295 K spectrum, these values are consistent with Fe^{III}_{HS} residing in an octahedral coordination geometry.[44, 50] The sextet spectrum indicates that the Fe^{III}_{HS} exists in a magnetic environment, resulting from spontaneous magnetic ordering of **4.1b**. As SC-XRD analysis of **4.1b** was conducted only at 100 K, the presence of thermally-induced valence tautomerism cannot be assessed on this basis alone. However, the ambient- and low-temperature ^{57}Fe Mössbauer spectra of **4.1b** provide a good indication that thermally-induced valence tautomerism, from a $[Fe^{III}_2(Fan^{2-})(Fan^{3-\bullet})_2]^{2-}$ to a $[Fe^{II}Fe^{III}(Fan^{2-})_2(Fan^{3-\bullet})]^{2-}$ valence distribution, is absent in **4.1b** between 6 and 295 K. Considering MeV^{2+} cations are located snugly against $Fan^{3-\bullet}$ ligands in **4.1b**, the absence of valence tautomerism likely arises due to strong Coulombic interaction between the cations and the anionic network. This is coupled with strong CT between the π-electron rich $Fan^{3-\bullet}$ ligands and π-electron deficient MeV^{2+} cation, acting to increase the energy barrier for electron transfer to ligand to metal.

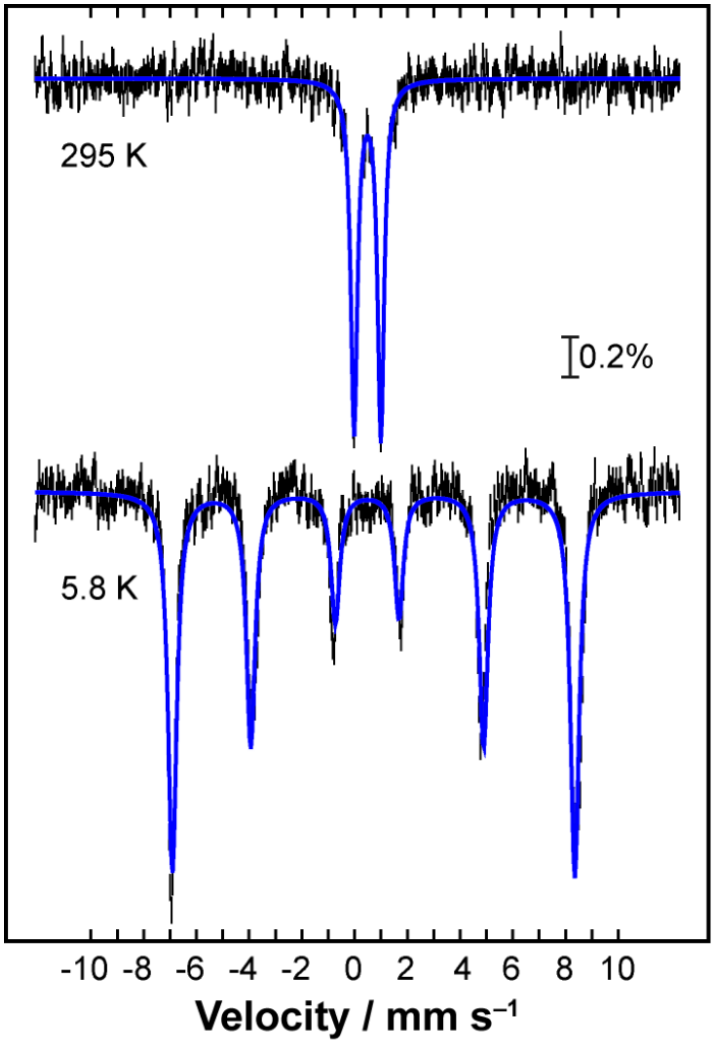


Figure 4.20 ^{57}Fe Mössbauer spectra of **4.1b** in an eicosane matrix measured at T = 295 K (upper) and T = 5.8 K (lower). The experimental spectra (black) were fitted (blue) with a quadrupole doublet at 295 K and a sextet at 5.8 K. The fitting parameters are given in Table 4.5.

Table 4.5 Fitted ^{57}Fe Mössbauer spectral parameters for **4.1b**.

T / K	Species	δ / mm s^{-1}	ΔE_Q / mm s^{-1}	B_0 / T	$\Gamma_{L\,(R)}$	I / %
295	Fe^{III}	0.489	1.016	-	0.304 (0.299)	100
5.8	Fe^{III} magnetic	0.6	0.28	48.0	0.4	100

The valence-pure Fe^{III}_{HS} population in **4.1b** as indicated by ^{57}Fe Mössbauer spectroscopy is in good agreement with the formulation suggested by SC-XRD analyses. This contrasts with *aP* **4.1a**, in which there is a discrepancy between SC-XRD and ^{57}Fe Mössbauer spectroscopic measurements. While the structures of *mP* **4.1a** and **4.1b** both contain two crystallographically inequivalent Fe sites in a 1:1 ratio, the presence of only one distinct Fe^{III}_{HS} site in the ^{57}Fe Mössbauer spectra of **4.1b** suggests crystallographic Fe1 and Fe2 in **4.1b** are spectroscopically indistinguishable on the ^{57}Fe Mössbauer timescale. Moreover as the δ value is perfectly consistent with Fe^{III}_{HS}, putative Fe^{II}/Fe^{III} mixed valency in **4.1b** cannot be valence-detrapped on the ^{57}Fe Mössbauer timescale, as an intermediate isomer shift value would be observed i.e. $\delta \approx 0.7$ mm s^{-1}.[47, 52, 53] While trapped Fe^{II}/Fe^{III} mixed valency has recently been observed in $(Et_4N)_2[Fe_2(Fan)_3]\cdot 5(acetone)$,[16] the origin of this behaviour was not explored in that work. Moreover, to the best of the candidate's knowledge, no demonstration of the guest responsiveness of Fe valence state in Fe–tetraoxolene frameworks has been reported to date.

The origin of the different Fe valence populations between *a* **4.1a** and **4.1b** is not immediately apparent. The $d_{Fe–O}$ or BVS values for Fe1 and Fe2 in *aP* **4.1a** and **4.1b** are not markedly different, and thus do not provide any crystallographic evidence of Fe^{II}/Fe^{III} mixed valency. However, there is a slight difference in the octahedral Fe environment between the different solvates, as noted in Section 4.2.3. For spin-crossover (SCO) Fe^{II} compounds, empirical relationships have been noted between the degree of octahedral distortion and the light-induced excited spin-state trapping (LIESST) transition temperature (T_{LIESST}),[54] or the extent of torsional freedom about Fe^{II} and the $^5T_2 \rightarrow {}^1A_1$ relaxation rate.[55] This demonstrates the sensitivity of electron rearrangement process, SCO in this case, to slight changes in Fe coordination environment. Additionally, the rates of electron transfer between Fe^{II} and Fe^{III} sites, in either mixed-valence trinuclear carboxylate clusters $[Fe_3O(O_2CR)_6L_3]$,[56-58] or mixed-valence biferrocenium cations,[59] are particularly sensitive to the local environments about the Fe centres, resulting from changes in solvation or crystal packing effects. Consequently, Fe^{II}/Fe^{III} mixed valency in $(MeV)[Fe_2(Fan)_3]$, arising from electron transfer between Fe^{III} and $Fan^{3-\bullet}$, could conceivably be influenced by slight distortions to the Fe coordination environment, accounting for the different behaviour between *aP* **4.1a** and **4.1b**. These changes in electronic structure may therefore cause significant

variation in properties such as magnetism or conductivity between the solvates, therefore hinting the (MeV)[$Fe_2(Fan)_3$] compounds could be a useful component of a framework-based guest sensor.

4.2.5 Electronic Spectroscopy

The difference in the Fe valence existing between *aP* **4.1a** and **4.1b**, in addition to the ligand-based mixed valency, prompted measurement of the diffuse-reflectance UV-Visible-Near infrared (UV-Vis-NIR) spectra to better understand how MeV^{2+} cations impacted upon the electronic structures of the networks. As with **3.1^{Cl}b**, the black colour and metallic lustre of crystals of *aP* **4.1a** and **4.1b** visually suggests mixed valency occurs in the frameworks. The diffuse-reflectance UV-Vis-NIR spectra of *aP* **4.1a** and **4.1b** are given in Figure 4.21 as the Kubelka-Munk transform, F(*R*), and are also compared to the spectrum of $(Et_4N)_2[Fe_2(Fan)_3]\cdot 5(acetone)$,[16] as a reference compound, which contains only redox-inactive Et_4N^+ cations. In a similar manner to the differences between **3.1^{Cl}b** and $(Et_4N)_2[Fe_2(Clan)_3]\cdot$solvent, *aP* **4.1a** and **4.1b**, exhibit markedly different electronic spectra compared to $(Et_4N)_2[Fe_2(Fan)_3]\cdot 5(acetone)$, in addition to notable disparities between the two solvates. The spectra exhibit intense absorption bands in the UV (ν_{max} ca. 24000 cm^{-1} and 23000 cm^{-1} for *aP* **4.1a** and **4.1b** respectively) and visible (ν_{max} ca. 17500 cm^{-1}) regions, ascribed to π–π^* and *d*–π transitions respectively. These UV and visible absorptions similar features in the spectrum of $(Et_4N)_2[Fe_2(Fan)_3]\cdot 5(acetone)$. The presence of an intense absorption in the NIR region in the spectra of *aP* **4.1a** and **4.1b** is expected, based upon the presence of ligand-centred mixed valency presumably resulting in intervalence charge transfer (IVCT). However, the peak positions and intensity of these absorptions in NIR region of the spectra are starkly different for the three compounds.

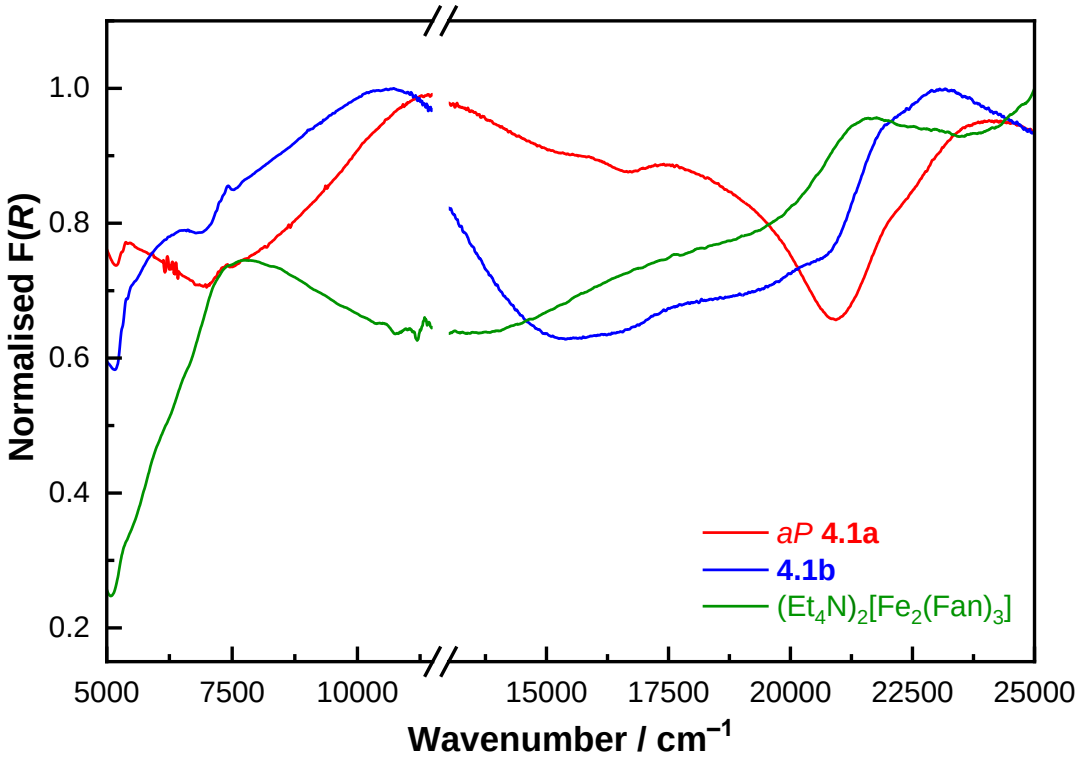


Figure 4.21 Normalised diffuse-reflectance UV-Vis-NIR spectra of *aP* **4.1a** (red), **4.1b** (blue) and $(Et_4N)_2[Fe_2(Fan)_3]$ (teal). Each spectrum is normalised to the maximum absorbance set to F(*R*) = 1. The break in the spectrum corresponds to the NIR detector change over.

There is a marked hypsochromic shift of the NIR ν_{max} for both aP **4.1a** and **4.1b**, compared to the IVCT band in $(Et_4N)_2[Fe_2(Fan)_3]\cdot 5(acetone)$,[16] which parallels the hypsochromic shift of IVCT band in **3.1^{Cl}b**, compared to $(Et_4N)_2[Fe_2(Clan)_3]\cdot solvent$[27] (Section 3.2.5). In **3.1^{Cl}b**, this was attributed to the electron-deficient $PhenQ^{2+}$ cation impacting upon the anionic network electronic structure, because of CT and Coulombic interactions between stacked $PhenQ^{2+}$ and $Clan^{3-\bullet}$ moieties. Similarly, MeV^{2+} nestled against $\mathbf{L_1}$ and $\mathbf{L_2}$ ($Fan^{3-\bullet}$) in *aP* **4.1a**, and $\mathbf{L_5}$ ($Fan^{3-\bullet}$) in **4.1b,** likely increases the energy barrier to electron hopping to the Fan^{2-} site, due to the strong CT and Coulombic interactions between MeV^{2+} cations and the anionic network. This could explain the shift to higher energy for the IVCT band in *aP* **4.1a** and **4.1b**.

The low energy side of this absorption band presents an interesting contrast between the compounds. Whereas F(*R*) for both $(Et_4N)_2[Fe_2(Fan)_3]\cdot 5(acetone)$ and

4.1b fall away towards 5000 cm^{-1}, *aP* **4.1a** is still strongly absorbing in this region, with an additional asymmetric absorption at ν_{max} ca. 5400 cm^{-1} clearly visible; this absorption also appears to extend deep into the near and mid-IR region below the detector cut-off at 5000 cm^{-1}. This band shape with a low energy cut-off is reminiscent of that predicted for a Robin-Day Class III compound.[60] This possibly arises from the Fe^{II}/Fe^{III} mixed valency in *aP* **4.1a**, in combination with ligand-centred mixed valency in *aP* **4.1a.** This feature is likely not observed in the spectrum of **4.1b**, due to the absence of Fe^{II}/Fe^{III} mixed valency. Interestingly, similarly asymmetric absorptions were not observed for $(Et_4N)_2[Fe_2(Fan)_3]\cdot 5(acetone)$, despite the presence of Fe^{II}/Fe^{III} mixed valency.[16] Ziebel *et al.* observed similar asymmetric absorptions with low energy cut-offs in the UV-Vis-NIR spectrum of mixed-valence $(Me_2NH_2)_2[V_2(Clan)_3]$.[39] The authors suggested a fully charge-transferred $[V^{III}_2(Clan^{2-})(Clan^{3-\bullet})_2]^{2-}$ formulation was therefore an inaccurate description of the electronic structure. Consequently, the compound was argued to possess some electron delocalisation between V and $Clan^{n-}$ valence states, and was therefore classified as a Robin-Day Class III material.[39] Similar NIR absorption profiles have also been observed in UV-Vis-NIR spectrum of the $Fe^{III}_2(BDP)_3$ (BDP^{2-} = 1,4-benzenedipyrazolate) framework, upon introduction of Fe^{II}/Fe^{III} mixed valency by chemical reduction.[61] The guest-dependant electronic spectra of *aP* **4.1a** and **4.1b** suggest that marked changes in electronic structure for the $(MeV)[Fe_2(Fan)_3]$ framework can be achieved by changing solvation or guest content, which may provide a facile method in future to switch the properties of this material.

Additional insight into the differences in electronic structure between *aP* **4.1a** and **4.1b** was also provided by deconvolution of the diffuse-reflectance UV-Vis-NIR spectra. The NIR manifold of *aP* **4.1a**, which is attributed to either Fe- or ligand-based IVCT, comprises two significant underlying Gaussian bands at ν_{max} = 5223 and 9887 cm^{-1}, with additional weaker components at ν_{max} = 7743 and 11695 cm^{-1} (Figure 4.22a & Table 4.6). The NIR region of the spectrum of **4.1b** is similarly composed of two intense underlying Gaussian bands at ν_{max} = 5644 and 9709 cm^{-1}, and two weaker bands at ν_{max} = 7626 and 12825 cm^{-1} (Figure 4.22b & Table 4.6). In contrast, the manifold ascribed to IVCT for $(Et_4N)_2[Fe_2(Fan)_3]\cdot 5(acetone)$ consists of a single intense absorption at ν_{max} = 7728 cm^{-1}, with weaker underlying bands at ca. 10000 and 12500 cm^{-1}.[16] The presence of additional underlying bands in the NIR spectra of

aP **4.1a** and **4.1b**, parallels the observations in Section 3.2.5 regarding the presence of multiple underlying Gaussian bands for the NIR manifold of **3.1^{Cl}b**. Like **3.1^{Cl}b**, multiple possible CT interactions of varying activation energies, including ligand-ligand, cation-ligand and metal-ligand, could occur in *aP* **4.1a** and **4.1b**, due to the presence of redox-active MeV^{2+}, rather than the exclusive ligand-ligand CT in $(Et_4N)_2[Fe_2(Fan)_3]\cdot 5(acetone)$.

As described in Section 3.2.5, the theoretical model developed by Hush can be used to link IVCT to the activation energy for electron transfer,[62, 63] which following calculation of the Γ parameter,[60] allows assignment of the Robin-Day classification of the mixed-valence system.[64] The Robin-Day classification can be determined as: $0 < |\Gamma| < 0.1$ for weakly-coupled Class II systems; $0.1 < |\Gamma| < 0.5$ for moderately-coupled Class II systems; $|\Gamma| \approx 0.5$ at the transition between Class II and Class III; and $|\Gamma| > 0.5$ for Class III systems. For **4.1b**, the Γ values calculated for the underlying Gaussian bands suggests that the compound is a weakly-to-moderately coupled Class II material, similarly to the (6,3) frameworks **3.1^{Cl}b**, $(Et_4N)_2[Fe_2(Fan)_3]$ and $(Et_4N)_2[Fe_2(Clan)_3]$.[16, 27] On the other hand, the two more intense NIR bands for *aP* **4.1a** are only weakly coupled, whereas the bands at ν_{max} = 7743 and 11695 cm^{-1} appear near the border of the Class III regime, which could indicate the mechanisms of IVCT in *aP* **4.1a** and **4.1b** differ, presumably due to differences in Fe valency between the compounds. The rationale for the weak coupling observed for the low energy band at ca. 5200 cm^{-1} for *aP* **4.1a**, compared to the stronger coupling suggested for equivalent bands in **3.1^{Cl}b** and **4.1b** is not obvious. Given the uniquely asymmetric absorption profile exhibit by *aP* **4.1a** in this low-energy region, suggestive of a Robin-Day Class III system, additional non-Gaussian absorption bands may be required to model the experimental spectrum more accurately.

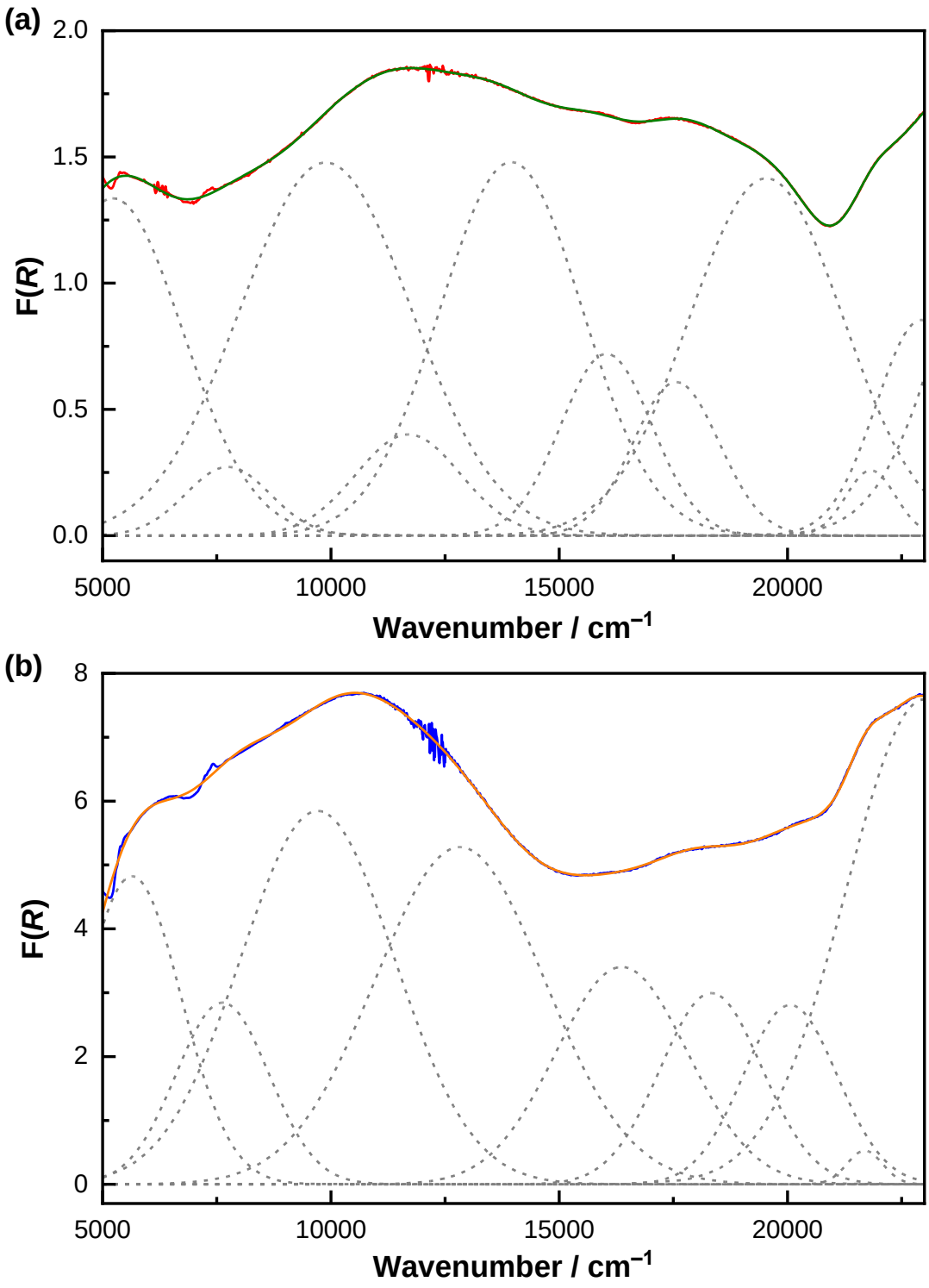


Figure 4.22 Deconvolution of the diffuse-reflectance UV-Vis-NIR spectra of (a) *aP* **4.1a** showing experimental spectrum (red) and curvefit (green), (b) **4.1b** showing experimental spectrum (blue) and curvefit (orange), with the underlying Gaussian bands from the deconvolution (grey dotted lines).

Table 4.6 Spectra data of the deconvolution diffuse-reflectance UV-Vis-NIR spectra of *aP* **4.1a** and **4.1b**. The theoretical predictions for the bandwidths at half-height ($\Delta\nu_{1/2}°$) are provided for the NIR bands which have been tentatively ascribed to IVCT transitions (in bold).

Compound	ν_{max} / **cm^{-1}**	**F(R)$_{max}$ / a.u.**	$\Delta\nu_{1/2}$ / **cm^{-1}**	$\Delta\nu_{1/2}°$ / **cm^{-1}** [(a)]	**$\lvert\Gamma\rvert$** [(b)]
aP **4.1a**	**5223**	**1.34**	**3612**	**3473**	**0.04**
	7743	**0.27**	**2180**	**4229**	**0.48**
	9887	**1.48**	**4424**	**4779**	**0.07**
	11695	**0.40**	**2702**	**5198**	**0.52**
	13949	1.48	3674	5676	
	16034	0.72	2358	6086	
	17561	0.61	2221	6369	
	19537	1.42	3987	6718	
	21824	0.26	1280	7100	
4.1b	**5644**	**4.82**	**2546**	**3611**	**0.29**
	7626	**2.84**	**2399**	**4197**	**0.43**
	9707	**5.85**	**3962**	**4735**	**0.16**
	12825	**5.28**	**4368**	**5443**	**0.20**
	16370	3.40	3398	6149	
	18330	2.99	2627	6507	
	20059	2.81	2429	6807	

(a) $\Delta\nu_{1/2}° = [2310(\nu_{max})]^{1/2}$ at 298 K.[62, 63]

(b) $\left|\Gamma\right| = \left|1-(\Delta\nu_{1/2}/\Delta\nu_{1/2}°)\right|$.[60]

The optical band gap (E_g) for the compounds was subsequently estimated by Tauc analysis[65, 66] upon the experimental spectra of *aP* **4.1a** and **4.1b** (Figure 4.23). This yielded E_g values of 0.73 and 0.69 eV for *aP* **4.1a** and **4.1b** respectively. These values lie in the range expected for semiconductor materials, which provided a further impetus to study the electrical conductivity. The optical band gaps calculated also closely match those estimated for 2D honeycomb $(Et_4N)_2[Fe_2(Fan)_3]$ (0.74 eV)[16] and 3D (10,3)-*a* $(^nBu_4N)_2[Fe_2(Fan)_3]$ (0.67 eV),[15] which are lower than isostructural chloranilate analogues. As previously noted,[16] the lower optical band gaps afforded by fluoranilate ligands may reflect better redox matching between Fe and fluoranilate, compared to Fe and chloranilate. Although the origin for the differences in spectra between *aP* **4.1a** and **4.1b** are not immediately clear, future computational study could prove insightful. Analogously to the results in Chapter 3, these findings clearly demonstrate using redox-active MeV^{2+} countercations perturbs the electronic structure of the tetraoxolene networks, compared to mixed-valence Fe–fluoranilate coordination polymers which contain only redox-inactive countercations.

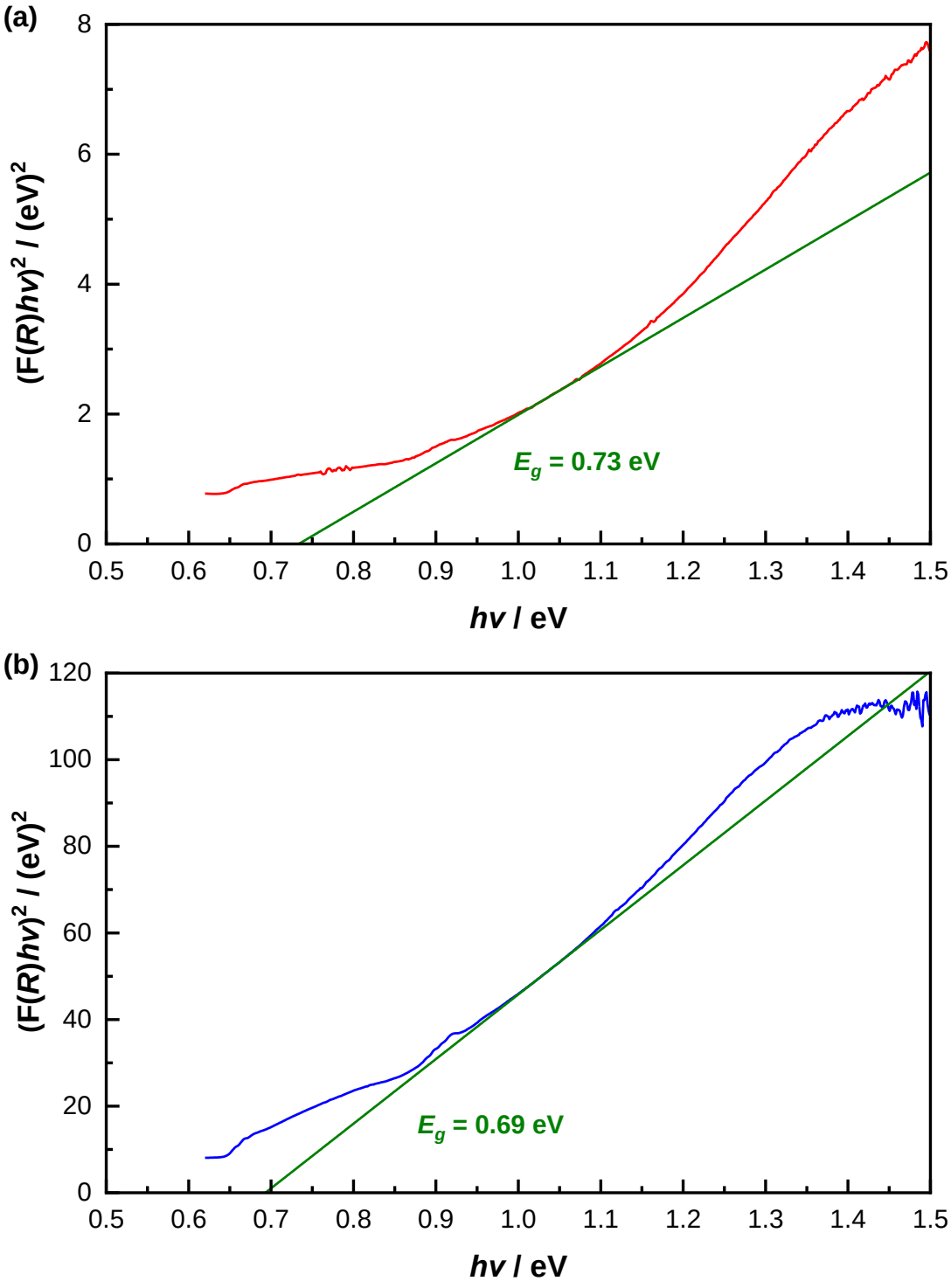


Figure 4.23 Tauc analysis on the experimental UV-Vis-NIR data of (a) *aP* **4.1a** (red) and (b) **4.1b** (blue) showing estimation of the corresponding optical band gaps (E_g, green).

4.2.6 Electrochemistry

Fe–tetraoxolene frameworks such $(Et_4N)_2[Fe_2(Fan)_3]$,[16] or $(Me_2NH_2)_2[Fe_2(Clan)_3]$,[21] exhibit a rich and reversible electrochemical response due to the interaction between the Fe and tetraoxolene couples. Therefore, dc cyclic voltammetry on *aP* **4.1a** was subsequently investigated to understand how the additional redox-active component, namely MeV^{2+}, would influence the electrochemical behaviour. As with **3.1^{Cl}b**, we also hypothesised that incorporating redox-active MeV^{2+} cations into a mixed-valence anionic Fe–fluoranilate framework, would provide additional framework redox states compared to $(^nBu_4N)_2[Fe_2(Fan)_3]$,[15] or $(Et_4N)_2[Fe_2(Fan)_3]$.[16] Dc cyclic voltammetry on *aP* **4.1a** was performed by making a paste of the compounds, which were then immobilised on a glassy carbon electrode, as described previously.[15, 67] Given that framework reduction and oxidation processes require influx and efflux of countercations, the cyclic voltammetry experiments were first performed with 0.5 M $LiBF_4$/MeCN electrolyte. It was expected that the smaller size of Li^+ cations compared to Et_4N^+ or Bu_4N^+ would allow facile counterion movement through the framework, leading to more reversible electrochemical behaviour. For *aP* **4.1a** with 0.5 M $LiBF_4$/MeCN electrolyte, cyclic voltammetry was performed between 20–200 mV s^{-1} scan rates to a maximum of five cycles (Figure 4.24). Upon cycling cathodically, three significant quasi-reversible redox processes are observed at E_1 ca. −0.36 V vs. Fc/Fc^+ (**R$_I$**), E_2 ca. −0.64 V vs. Fc/Fc^+ (**R$_{II}$**), and E_3 ca. −1.1 V vs. Fc/Fc^+ (**R$_{III}$**). As expected, the relative reversibility of these processes, as well as the peak potentials and peak potential widths show significant scan rate dependence. The cathodic shift of peak potential, and peak broadening at higher scan rates is suggestive of hindered counterion ion in the framework pores, as observed previously.[15, 67] Upon framework reduction at slower scan rates, the rate of diffusion of solvated countercations into the framework pores is more closely matched to the voltammetric time scale, therefore the redox processes occur with greater reversibility. Contrastingly, at higher scan rates, an over potential is required to effect diffusion of the solvated counterions through the pores at the voltammetric time scale, causing peak shift and broadening. Narrowing of the peak widths at higher scan numbers provides further evidence of the hindered diffusion of counterions, as observed in **3.1^{Cl}b**.

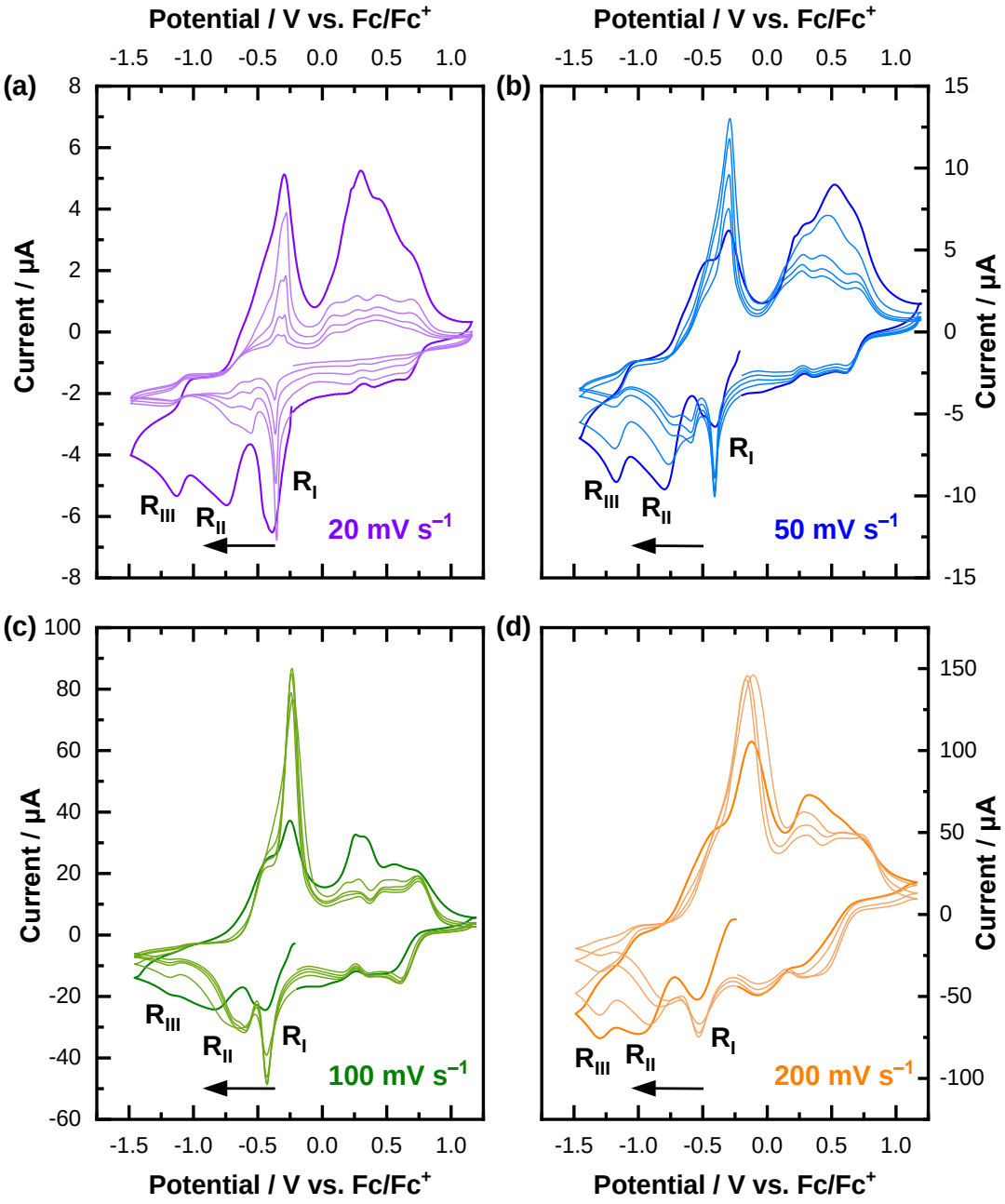


Figure 4.24 Cyclic voltammograms of solid *aP* **4.1a** in 0.5 M $LiBF_4$/MeCN at (a) 20 mV s^{-1} (purple), (b) 50 mV s^{-1} (blue), (c) 100 mV s^{-1} (green), and (d) 200 mV s^{-1} (orange). Arrows indicate the direction of the forward scan. First scan shown in bold, subsequent scans indicated by fine pastel traces.

The behaviour of *aP* **4.1a** at cathodic potentials (relative to Fc/Fc^+) contrasts to the response of of $(Et_4N)_2[Fe_2(Fan)_3]\cdot 5(acetone)$, which only exhibits two quasi-reversible processes at −0.44 V vs. Fc/Fc^+ and −0.73 V vs. Fc/Fc^+.[16] These waves were

tentatively assigned as the $Fan^{2-}/Fan^{3-\bullet}$ and $Fan^{3-\bullet}/Fan^{4-}$ couples, based on previous voltammetric studies on H_2Fan.[15] The potentials of $\mathbf{R_{II}}$ and $\mathbf{R_{III}}$ in *aP* **4.1a** more closely match the redox couples of $Clan^{2-}/Clan^{3-\bullet}$ and $Clan^{3-\bullet}/Clan^{4-}$ in $\mathbf{3.1^{Cl}b}$ and $(Me_2NH_2)_2[Fe_2(Clan)_3]$.[21] This suggests that $\mathbf{R_{II}}$ and $\mathbf{R_{III}}$ may be network-based ligand reductions, with the possible involvement of the Fe^{III}/Fe^{II} couple in $\mathbf{R_{III}}$, similar to $(Me_2NH_2)_2[Fe_2(Clan)_3]$.[21] Compared to $(Et_4N)_2[Fe_2(Fan)_3]\cdot 5(acetone)$, the additional well-defined cathodic process ($\mathbf{R_I}$) in *aP* **4.1a**, indicates that incorporating MeV^{2+} into *aP* **4.1a** affords additional framework redox states as desired. There is some variability in the reported potential for the $MeV^{2+}/MeV^{+\bullet}$ couple ($E_{1/2} = -0.789$ V vs. Fc/Fc^+ by cyclic voltammetry;[31] $E_{1/2} = -0.824$ V vs. Fc/Fc+ by polarography;[68, 69] $E_{1/2} = -0.684$ V vs. Fc/Fc^+ by cyclic voltammetry[70]) so that definitive assignment of $\mathbf{R_I}$ as a MeV^{2+}-centred process is challenging.

Upon higher cyclic numbers, peak-width narrowing of $\mathbf{R_I}$ is significantly more pronounced than $\mathbf{R_{II}}$ and $\mathbf{R_{III}}$, suggesting that the redox processes involved in $\mathbf{R_I}$ are of a different nature to $\mathbf{R_{II}}$ and $\mathbf{R_{III}}$. Because *aP* **4.1a** is electrically conductive (*vide infra*), network reduction or oxidation processes may result in charge-carrier migration from unreduced or oxidised material distant from the framework-electrode interface. Consequently, the measured redox waves could be influenced by a combination of counterion diffusion in the pores of the framework, and charge-carrier hopping into electrochemically active regions of the material. The rate of carrier migration is increased at higher electric field strength, as evidenced by the higher current density at higher electric field strength (see Section 4.2.7), thereby causing the waves of $\mathbf{R_{II}}$ and $\mathbf{R_{III}}$ to be broadened. As MeV^{2+} in *aP* **4.1a** are located within the hexagonal voids, rather than sandwiched between the anionic sheets by Coulombic interactions, changes in MeV^{2+} redox state may not require significant structural distortion to accommodate the formed $MeV^{+\bullet}$ species. Therefore MeV^{2+} redox processes likely occur in isolation from framework electrochemical processes, being influenced only be the diffusion of counterions, so that MeV^{2+} redox processes will be more solution-like accounting for the narrowed peak width for $\mathbf{R_I}$.

The waves at anodic potentials are less reversible, evidenced by the absence of return reduction waves upon cycling back to less positive potentials. This contrasts with $\mathbf{3.1^{Cl}b}$ and $(Et_4N)_2[Fe_2(Fan)_3]\cdot 5(acetone)$, in which the redox waves at anodic potentials are quasi-reversible. In these compounds, $PhenQ^{2+}$ and Et_4N^+ strongly

stabilise stacking of the anionic $[Fe_2(Xan)_3]^{x-}$ sheets by Coulombic interactions. In contrast, MeV^{2+} located within the hexagonal framework voids in *aP* **4.1a** means the predominant $[Fe_2(Fan)_3]^{x-}$ intersheet interactions are only weaker non-covalent bonding. Anion insertion between the anionic sheets upon framework oxidation may further weaken the intersheet interactions causing sheet exfoliation and loss of reversibility following the return reduction wave. Ziebel *et al.* observed reduced charge capacity in lithium-ion batteries (LIB) devices fabricated using $(Me_2NH_2)_2[Fe_2(Clan)_3]$ cathodes if the devices underwent an initial LIB charge cycle (i.e. framework oxidation) prior to discharge.[21] This was ascribed to layer exfoliation and increased anion insertion on the initial charge cycle destabilising the structure. Notably, both *aP* **4.1a** and $(Me_2NH_2)_2[Fe_2(Clan)_3]$ have cations located within the network voids with only weaker non-covalent intersheet interactions, so similar anion-insertion induced structural rearrangements could be operational in *aP* **4.1a**.

The electrochemical behaviour of porous metal–tetraoxolene frameworks is both counter-anion and cation dependant.[16, 21, 67] Ziebel *et al.* noted the discharge capacity of $(Me_2NH_2)_2[Fe_2(Clan)_3]$ LIB devices depends on both the relative anion and cation size,[21] suggesting that both anions and cations are the mobile species in the framework pores, and that the relative mobilities of both species influence device performance. This is in stark contrast to dense oxide-based cathodes eg. $LiCoO_2$ in which alkali metal cations are the only mobile ionic species. Cyclic voltammetry on *aP* **4.1a** between 20–500 mV s^{-1} using 0.1 M $(Et_4N)PF_6$/MeCN electrolyte (Figure 4.25) unsurprisingly leads to notably different behaviour than experiments conducted using small Li^+-based electrolyte. While framework reduction and the accompanying Li^+ insertion likely only leads to small structural distortions,[21] the larger bulk of Et_4N^+ may cause more significant structural distortion upon insertion, leading to a different electrochemical response. Generally, there are two significant quasi-reversible redox processes ($\mathbf{R_I}$ and $\mathbf{R_{II}}$) observed using $(Et_4N)PF_6$, compared to the three processes observed using $LiBF_4$ electrolyte. Similarly, there is a notable cathodic shift of peak potential at faster scan rates, again suggestive of hindered ion diffusion in the framework voids.

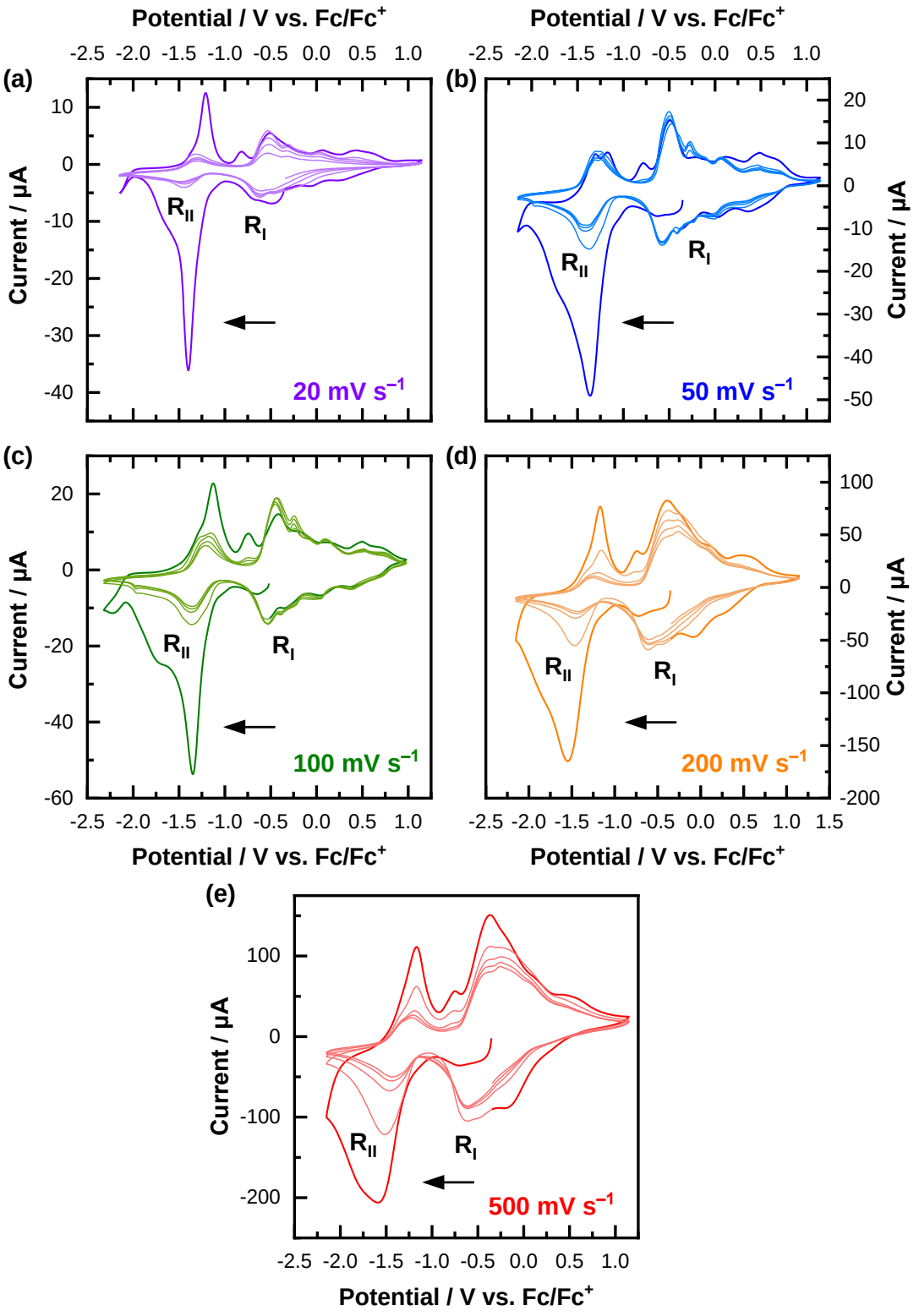
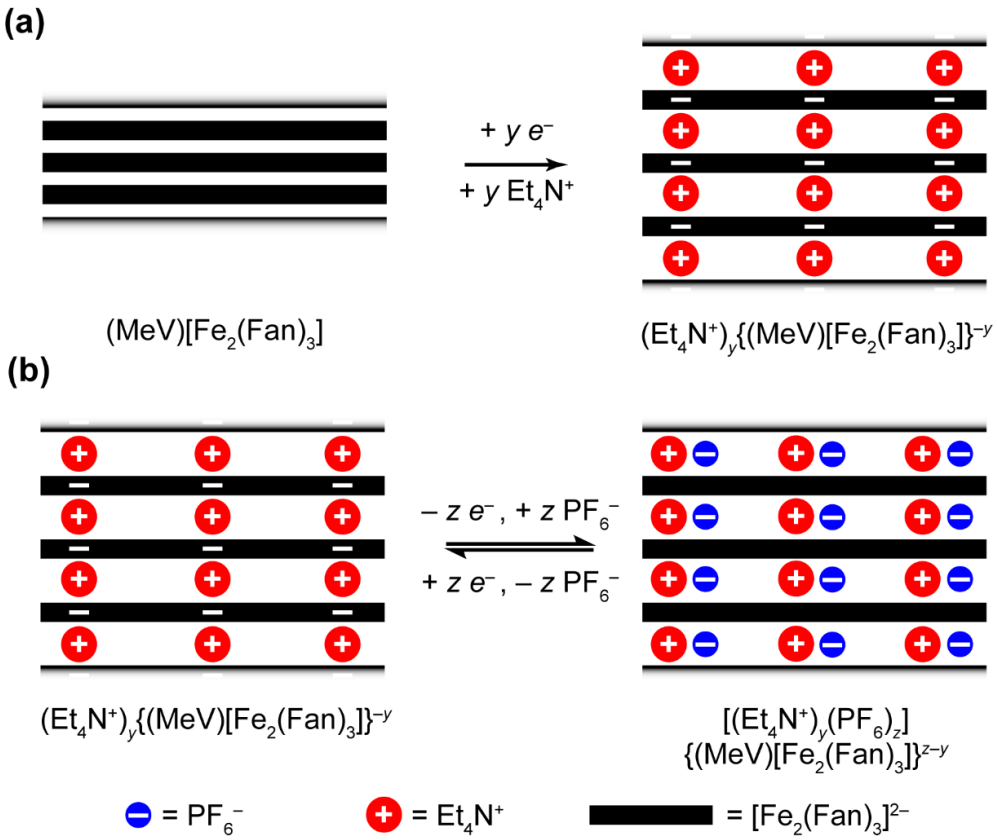


Figure 4.25 Cyclic voltammograms of solid *aP* **4.1a** in 0.1 M $(Et_4N)PF_6$/MeCN at (a) 20 mV s^{-1} (purple), (b) 50 mV s^{-1} (blue), (c) 100 mV s^{-1} (green), (d) 200 mV s^{-1} (orange), and (e) 500 mV s^{-1} (red). Arrows indicate the direction of the forward scan. First scan shown in bold, subsequent scans shown in fine line.

Comparison between the two electrolytes studies also reveals a cathodic shift of peak potential using $(Et_4N)PF_6$ electrolyte, which suggests a greater driving force required to insert Et_4N^+ and PF_6^- into the framework compared to Li^+ and BF_4^-. A similar cathodic shift of peak potential was observed in the 2D honeycomb framework $(Ph_3MeP)_2[Cd_2(dhbq)_3]$ using electrolytes of increasing steric bulk ($LiClO_4$ through to $(^nBu_4N)Br$), which was attributed to the increased hinderance to ion diffusion into the layered structure for bulky cations.[67] Because of these shifts in peak potential, it is not possible to definitively attribute the redox waves to either cation or framework processes, though by comparison with **3.1^{Cl}b** (for which electrochemical experiments were conducted with $(Et_4N)PF_6$, Section 3.2.6) $\mathbf{R_I}$ and $\mathbf{R_{II}}$ are tentatively ascribed to the $Fan^{2-}/Fan^{3-\bullet}$ and $Fan^{3-\bullet}/Fan^{4-}$ couples, with some possible involvement of the Fe^{III}/Fe^{II} couple, giving the similar $E_{1/2}$ values. In contrast to **3.1^{Cl}b**, and *aP* **4.1a** measured using $LiBF_4$, the initial response of *aP* **4.1a** in $(Et_4N)PF_6$ on cycling cathodically differs notably from subsequent cycles, particularly for cathodic processes. We ascribe this to a cycle-dependant change-over in pore mobile ionic species from cations to anions, the possibility of which has been noted earlier for $(Me_2NH_2)_2[Fe_2(Clan)_3]$.[21]

While the traditional view of framework reduction, requires counter-ion (cation) diffusion into the pores to compensate the increased framework negative charge, by analogy with carbon-based supercapacitor materials,[71] two other ion diffusion mechanisms are possible:[21] ion exchange in which framework reduction is accompanied by exchange between anions in the pores and cations in the bulk electrolyte; or alternatively desorption of anions from the pores. The initial framework reduction requires insertion of Et_4N^+ cations into the framework voids to balance the increased framework negative charge (Scheme 4.2a), as there is likely limited PF_6^- in the framework voids which would otherwise allow anion desorption to compensate the more negative framework charge. Because of their steric bulk, positive charge, and ability to participate in extensive non-covalent C–H···O bonding, these Et_4N^+ cations will interact strongly with the framework, similarly to the cation-network interactions in $(Et_4N)_2[Fe_2(Xan)_3]$ (X = F, Cl).[16, 27] This could form the hybrid $(Et_4N)_y\{(MeV)[Fe_2(Fan)_3]\}^{y-}$ ($y > 0$) reduced structure. Given the ability of Et_4N^+ cations to 'glue' anionic $[Fe_2(Xan)_3]^{x-}$ sheets together, framework reoxidation (i.e. making the framework more positive) then possibly involves diffusion of mobile PF_6^-

anions into the framework voids to counteract the increasingly positive framework charge, rather than deinsertion of bulky, strongly interacting Et_4N^+ (Scheme 4.2b, forward reaction). Compared to the initial cathodic wave, the current flow is less upon the initial reoxidation because of increased diffusion hinderance of PF_6^- in the pores due to partial occlusion by Et_4N^+. We hypothesise that Et_4N^+ is retained in the framework for repeated cathodic and anodic cycles, as although the $[Fe_2(Fan)_3]^{x-}$ network becomes more positively charged upon oxidation, the O donor atoms probably retain a significant partial negative charge regardless of network redox state. This is due to: coordination bonding between Fan^{n-} and Fe^{III} causing polarisation of the ligand C–O bonds; and higher electronegativity of O and F compared to C, both of which could participate in Coulombic interactions with inserted Et_4N^+ cations. Following the initial reduction-induced Et_4N^+ insertion, the current response remains approximately constant (with some decrease in response due to loss of *aP* **4.1a** from the electrode) for subsequent cycles. This is because redox processes now only requires desorption and adsorption of mobile PF_6^- anions in the framework voids (Scheme 4.2b, forward and back reactions), which is likely to involve only relatively minor structural transformations.



Scheme 4.2 Proposed ion insertion processes operating during cyclic voltammetry of *aP* **4.1a** in 0.1 M $(Et_4N)PF_6$/MeCN. (a) Initial cation insertion process upon first cathodic cycle. (b) Subsequent PF_6^- absorption and desorption processes upon framework oxidation and reduction processes respectively. MeV^{2+} not shown for clarity.

We hypothesise the more dramatic cycle dependant behaviour of *aP* **4.1a** compared to **3.1^{Cl}b** even when both are measured using $(Et_4N)PF_6$ probably reflects the differences in structure and stability of the two compounds. In **3.1^{Cl}b**, $PhenQ^{2+}$ cations sandwiched between the anionic $[Fe_2(Clan)_3]^{x-}$ sheets stabilises the sheet stacking by Coulombic interactions, and leads to a spacious sheet-to-sheet of spacing ca. 8.5 Å. Because $PhenQ^{2+}$ cations are sandwiched between the anionic $[Fe_2(Clan)_3]^{2-}$ layers in **3.1^{Cl}b**, the cations do not occlude the framework voids allow more facile ion diffusion. Consequently, the initial insertion of Et_4N^+ during reduction of **3.1^{Cl}b** possibly only leads to minor structure transformations. On the other hand, MeV^{m+} in *aP* **4.1a** located within the network voids, reduce the pore dimensions and sheet-to-sheet spacing (ca. 7.2 Å). These factors may both hinder ion diffusion into the framework upon

electrochemical cycling, and result in more significant structural distortions upon Et_4N^+ insertion during the initial framework reduction. Nevertheless, the fascinating and varied electrochemical behaviour of *aP* **4.1a** provides a significant impetus to perform future combined electrochemical–P-XRD experiments to better understand *in situ* the structural behaviour of *aP* **4.1a** under electrochemical cycling. These insights could prove critical in optimising the performance of Fe–fluoranilate frameworks as LIB cathodes.

4.2.7 Electrical Conductivity

Both *aP* **4.1a** and **4.1b** were expected to be electrically conductive, by analogy with **3.1^{Cl}b** and other mixed-valence metal–tetraoxolene frameworks reported in literature, arising from the ligand-based mixed valency. Moreover, the differences in Fe valency between the two compounds warranted a detailed comparison, to better understand the influence that the variation in electronic structure would have upon the electrical conductivity. Therefore two-point pressed pellet devices of *aP* **4.1a** and **4.1b** were assembled in a N_2-filled glovebox and the transport properties measured. For *aP* **4.1a**, four independent devices all exhibited the desired Ohmic behaviour over a potential window of −0.40 to 0.40 V. The mean ambient temperature (ca. T = 305 K in the glovebox) conductivity for the four devices was σ = 1.0(2) × 10^{-3} S cm^{-1}, with the premier device reaching σ = 1.6(1) × 10^{-3} S cm^{-1} (Table B.2). These values, though modest compared to other mixed-valence tetraoxolene frameworks, such as (^{n}Bu$_4$N)$_2$[Fe$_2$(dhbq)$_3$] (σ = 0.16 S cm^{-1}),[18] (Me_2NH_2)$_2$[Fe$_2$(Clan)$_3$]·6DMF·2H_2O (σ = 1.4(7) × 10^{-2} S cm^{-1}),[20] [Me_2NH_2)$_2$[V_2(Clan)$_3$]·6.4DMF (σ = 0.45(3) S cm^{-1}) and (Et_4N)$_2$[Fe$_2$(Fan)$_3$]·5(acetone) (σ = 1.8 × 10^{-2} S cm^{-1}),[16] are still reasonably high. The measured conductivity of *aP* **4.1a** is somewhat surprising given the ligand-charge ordered [Fe^{III}_2(Fan^{2-})($Fan^{3-\bullet}$)$_2$]$^{2-}$ sheet structure of *aP* **4.1a**. Desolvated (^{n}Pr$_4$N)$_2$[Fe$_2$(Clan)$_3$], which exhibits an analogous ligand-charge ordered [Fe^{III}_2($Clan^{2-}$)($Clan^{3-\bullet}$)$_2$]$^{2-}$ sheet structure as *aP* **4.1a**, is less conductive.[37] Single crystal measurements, which ideally eliminate the effect of grain boundary resistance present in pressed pellet measurements, revealed that (^{n}Pr$_4$N)$_2$[Fe$_2$(Clan)$_3$] exhibits an ambient temperature conductivity of only σ = 2.6 × 10^{-4} S cm^{-1} when measured parallel to the pseudo-1D {Fe^{III}–$Clan^{3-\bullet}$}$_\infty$ chain direction. When measured within the plane of the anionic sheet but perpendicular to the {Fe^{III}–$Clan^{3-\bullet}$}$_\infty$ chains, the conductivity falls to σ = 1.0 × 10^{-4} S cm^{-1}. It decreases to σ = 4.1 × 10^{-8} S cm^{-1} when

measured perpendicular to the anionic $[Fe_2(Clan)_3]^{2-}$ sheets, as carrier hopping is less facile across the large sheet-to-sheet distance. Given the predominance of grain boundary resistance in pressed pellet measurements, the observed conductivity of *aP* **4.1a** than single-crystals of $(^nPr_4N)_2[Fe_2(Clan)_3]$ is more surprising.

Fe^{II}/Fe^{III} mixed valency in *aP* **4.1a**, which is not present in $(^nPr_4N)_2[Fe_2(Clan)_3]$ at ambient temperature,[37] may play a role in increasing the electrical conductivity of *aP* **4.1a** relative to$(^nPr_4N)_2[Fe_2(Clan)_3]$. By providing additional sites for charge-carriers to occupy, the Fe^{II}/Fe^{III} mixed valency possibly reduces the energy barrier to charge transport, thereby increasing the electrical conductivity in *aP* **4.1a**. Comparison of the conductivity between the isostructural honeycomb $(Et_4N)_2[Fe_2(Fan)_3]\cdot 5(acetone)$ and $(Et_4N)_2[Fe_2(Clan)_3]\cdot$solvent frameworks is instructive. For the fluoranilate compound, the pressed pellet conductivity is $\sigma_{300\ K} = 1.8 \times 10^{-2}$ S cm^{-1}, whereas isostructural chloranilate compound exhibits a lower pressed pellet conductivity of $\sigma_{300\ K} = 2.2 \times 10^{-3}$ S cm^{-1}.[16] Similarly to *aP* **4.1a**, Fe^{II}/Fe^{III} mixed valency was indicated in $(Et_4N)_2[Fe_2(Fan)_3]\cdot 5(acetone)$ at both 293 and 100 K by ^{57}Fe Mössbauer spectroscopy.[16] Although ^{57}Fe Mössbauer spectroscopy on $(Et_4N)_2[Fe_2(Clan)_3]\cdot$solvent has not been reported,[27] by analogy with the $(Me_2NH_2)_2[Fe_2(Clan)_3]\cdot 6DMF\cdot 2H_2O$ and **3.1^{Cl}b**, $(Et_4N)_2[Fe_2(Clan)_3]\cdot$solvent probably contains a valence-pure Fe^{III}_{HS} population.

The ambient temperature conductivity of **4.1b** is relatively modest. The mean value for four independent devices was $\sigma = 1.5(1) \times 10^{-5}$ S cm^{-1}, with the premier device reaching $\sigma = 1.8(1) \times 10^{-5}$ S cm^{-1} (Table B.3). Considering the highly anisotropic electrical conductivity which exists in layered tetraoxolene frameworks,[37, 47, 72] in addition to the ligand charge-ordered sheet structure in **4.1b**, these relatively low powder conductivity values are expected. Of interest though, is the marked difference in conductivity between *aP* **4.1a** and **4.1b**, despite their almost identical ligand charge-ordered structures. Better insight into the differences arising between these compounds was achieved by measuring the temperature dependence of the electrical conductivity of pressed pellet devices. As desired, all devices remained Ohmic in the potential window −0.55 to 0.55 V, for the entire temperature range; for *aP* **4.1a**, 300–220 K (representative current-bias plot for the premier device given in Figure 4.26a); for **4.1b** a narrower temperature range of 300–240 K was used due to the lower conductivity of **4.1b** (representative current-bias plot for the premier device given in Figure 4.26b).

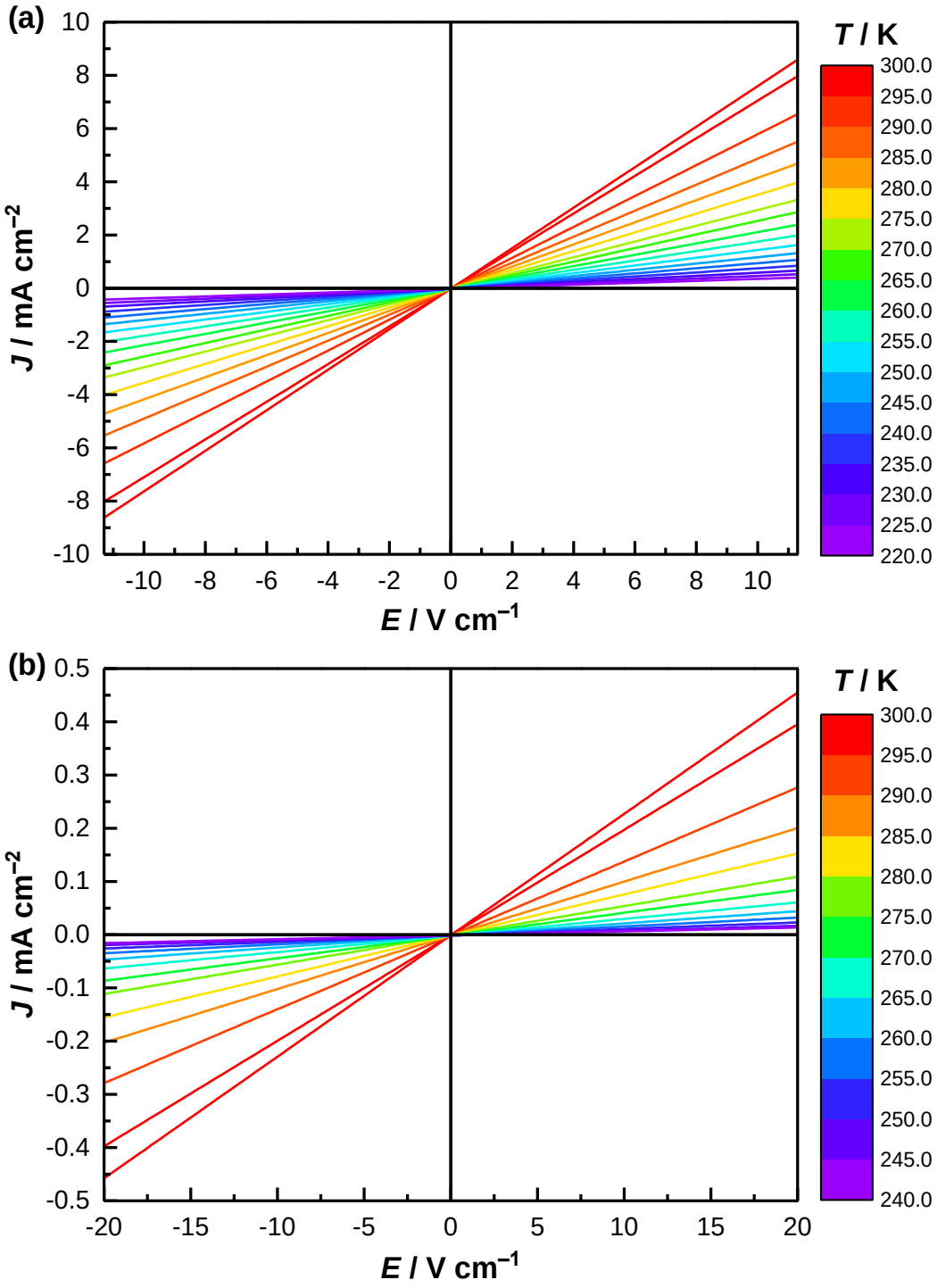


Figure 4.26 Representative variable-temperature current-bias (*i*-*v*) plots for the premier two-point pressed pellet devices of (a) *aP* **4.1a** (Device 4) and (b) **4.1b** (Device 2). Data were measured over the potential range −0.55 to 0.55 V in 0.01 V steps.

At 300 K, the conductivity of four independent devices of *aP* **4.1a** ranged from 5.6(2) × 10^{-4} S cm^{-1} to 7.6(3) × 10^{-4} S cm^{-1}, while for the devices of **4.1b** the conductivity varied from 1.5(1) × 10^{-5} S cm^{-1} to 2.3(1) × 10^{-5} S cm^{-1}. For devices of both compounds, cooling reduced the electrical conductivity, consistent with thermally-activated semiconductor behaviour, expected due to their similarity with other mixed-valence Fe–tetraoxolene frameworks.[15, 16, 18, 20, 37, 39] Fitting the experimental data using the Arrhenius model to determine the activation energy (E_a) reveals another interesting contrast between the two compounds. For the more conductive MeCN solvate *aP* **4.1a**, E_a values for the four devices varied from 0.218(2)–0.234(2) eV (Figure 4.27, red for the premier device; Figure B.2) for the remaining devices). On the other hand, E_a values for devices of **4.1b** were larger, ranging from 0.376(6)–0.414(6) eV (Figure 4.27, blue for the premier device; Figure B.3 for the remaining devices).

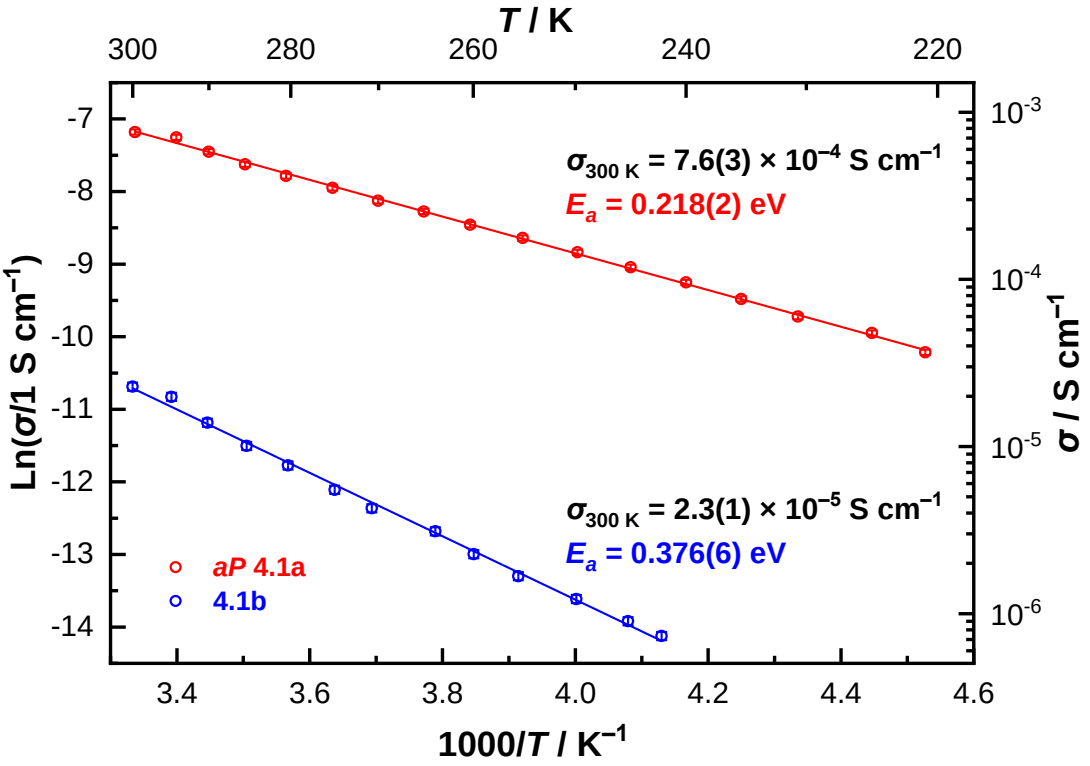


Figure 4.27 Arrhenius plot of the temperature dependence of the electrical conductivity for the premier two-point devices of *aP* **4.1a** (red, Device 4) and **4.1b** (blue, Device 3). Experimental data (open circles) and lines of best fit. Error bars are ± s.u. Where not visible, error bars lie within the data point.

For *aP* **4.1a**, the calculated E_a values are close to those determined for **3.1^{Cl}b** (Chapter 3, 0.249–0.253 eV), $(Me_2NH_2)_2[Fe_2(Clan)_3]\cdot 6DMF\cdot 2H_2O$ (E_a = 0.26(1) eV) and the desolvated analogue (E_a = 0.19(1) eV),[20] though are higher than that of 2D honeycomb $(Et_4N)_2[Fe_2(Fan)_3]\cdot 5(acetone)$ (E_a = 6.2 × 10^{-2} eV),[16] and 3D $(^nBu_4N)_2[Fe_2(Fan)_3]$ (E_a = 0.122 eV). In contrast, the higher E_a values for devices of **4.1b** are expected, in light of the ligand-charged ordered $[Fe^{III}_2(Fan^{2-})(Fan^{3-\bullet})_2]^{2-}$ network structure, which would be expected to have lower carrier mobility and therefore lower conductivity. Indeed, single crystal measurements on $(^nPr_4N)_2[Fe_2(Clan)_3]$ revealed an E_a of ca. 0.43 eV when measured parallel to the $\{Fe^{III}–Clan^{3-\bullet}\}_\infty$ chains, demonstrating the correlation between increased valence state localisation, and an increased energy barrier to carrier hopping between different valence sites. The notable differences in electrical conductivity and activation energy between *aP* **4.1a** and **4.1b** may arise from differences in electronic structure and Fe valency between the two compounds. Both ^{57}Fe Mössbauer and UV-Vis-NIR spectra suggest different electronics structures between the two compounds. While both compounds exhibit broad, intense absorbances in the NIR region, attributed to IVCT between Fan^{2-} and $Fan^{3-\bullet}$ valence states, only *aP* **4.1a** exhibits an additional asymmetric absorbance at low energy (ca. 5200 cm^{-1}). This absorption possibly arises from the Fe^{II}/Fe^{III} mixed valency in *aP* **4.1a** which is absent in **4.1b**. Work is currently underway to compute possible variations in electronic band structure between *aP* **4.1a** and **4.1b**, and therefore gain insight into the origin of this behaviour. Importantly, the guest-responsive Fe mixed valency could be used to produce compounds with switchable magnetism or electrical conductivity.

4.3 Conclusion

A mixed-valence Fe–fluoranilate coordination polymer *mP* **4.1a** was successfully synthesised and structurally characterised. As expected, the *in situ* electron transfer reaction between Fe^{II} and Fan^{2-} afforded a mixed-valence Fe^{III} framework containing radical $Fan^{3-\bullet}$ ligands. Close interaction of the π-electron poor MeV^{2+} cations with the anionic $[Fe_2(Fan)_3]^{2-}$ network plays an important role in localising the ligand valence state giving a charge-ordered $(MeV^{2+})[Fe^{III}_2(Fan^{2-})(Fan^{3-\bullet})_2]$ valence formulation. A similar localisation of at least one $Xan^{3-\bullet}$ state was also observed in the mixed-valence coordination polymers reported in Chapter 2 (**2.5** and **2.6**) and Chapter 3

(**3.1^{X}**, X = F, Cl, Br), further reinforcing that CT interactions between π-electron poor viologen cations and the anionic tetraoxolene framework can promote (partial) ligand charge ordering. Structural comparisons of (MeV)[Fe_2(Fan)$_3$]·solvent with the MeV^{2+}-containing coordination polymers presented in Chapter 2, and the **3.1^{X}** family presented in Chapter 3 lead to interesting conclusions. The templating role of $PhenQ^{2+}$ in producing the **3.1^{X}** family is clear, with similar interactions between the cations and the framework, irrespective of the metal or ligand substituents. On the other hand, the structural disparity observed when using MeV^{2+} countercations, illustrates the templating role of this cation is more subdued. These results highlight the delicate and somewhat capricious interplay between metal, ligand, and cation interactions upon the resultant anionic network structure.

The porous nature of as-synthesised *mP* **4.1a** was demonstrated by both the partial removal of the guest solvent upon isolation, and exchange with a less volatile solvent. Solvent movement, in and out of pores leads to slight structural distortions and the generation of two new compounds, *aP* **4.1a** and **4.1b**, which were characterised by SC- and P-XRD analyses. The transformations observed in the (MeV)[Fe_2(Fan)$_3$] family contrast to the 2D honeycomb (PhenQ)[Fe_2(Clan)$_3$] compounds presented in Chapter 3, which do not undergo notable structure distortion upon guest exchange. Surprisingly, the slight differences in network geometry between *aP* **4.1a** and **4.1b** cause dramatic differences in the spectroscopic and physical properties of the two compounds. ^{57}Fe Mössbauer spectroscopy revealed *aP* **4.1a** contains intrinsic Fe^{II}/Fe^{III} mixed valency, whereas the guest exchanged compound **4.1b** is valence-pure Fe^{III}.

The presence of Fe-based mixed valency in *aP* **4.1a** also results in notable changes to the electronic structure of the network, as shown by differences in the UV-Vis-NIR spectra of *aP* **4.1a** and **4.1b**. As intended, incorporation of redox-active MeV^{2+} cations as counterions for the framework allowed access to additional framework redox states. Markedly cation-dependant electrochemical behaviour was also observed, hinting that future *in situ* voltammetric-P-XRD studies using LIB devices could provide insight into the electrochemical behaviour of these porous electroactive materials. Finally, more facile charge-transport in *aP* **4.1a** arising from a combination of ligand- and Fe-based mixed valency, was evidenced by the higher electrical conductivity of *aP* **4.1a** ($\sigma_{300\ K}$ = 7.6(3) × 10^{-4} S cm^{-1}, E_a = 0.218(2) eV), compared to the Fe^{III} valence-pure **4.1b** compound which only exhibits ligand-based mixed valency

($\sigma_{300\ K}$ = 2.3(1) × 10^{-5} S cm^{-1}, E_a = 0.376(6) eV). Critically, *aP* **4.1a** represents the first example of guest-induced switching of Fe valency, and only the second example of intrinsic Fe-based mixed valency in combination with ligand-based mixed valency, in Fe–tetraoxolene coordination polymers. Considering this seemingly unique property, these investigations provide a significant impetus to further examine the chemistry mixed-valence fluoranilate frameworks, as they may possess interesting and novel physical properties not accessible in mixed-valence chloranilate frameworks.

4.4 Experimental

4.4.1 General Considerations

Unless overwise specified, all manipulations were performed under an atmosphere of dry dinitrogen (N_2) using standard Schlenk techniques or using a Vacuum Atmospheres glovebox. For crystallization of (MeV)[Fe_2(Fan)$_3$]·6MeCN (*mP* **4.1a**) acetonitrile (MeCN) was used without further purification. For post-synthetic washing and solvent-exchange on as-synthesised *mP* **4.1a** to give (MeV)[Fe_2(Clan)$_3$]·3.7MeCN (*aP* **4.1a**) and (MeV)[Fe_2(Clan)$_3$]·2.7DMF (**4.1b**), MeCN and *N*,*N*-dimethylformamide (DMF) were dried twice sequentially over activated 3 Å and 4 Å molecular sieves respectively, then stored under an atmosphere of dry N_2. Immediately before use, anhydrous DMF and MeCN were degassed by three freeze-pump-thaw cycles. Nujol was dried and deoxygenated by stirring over molten Na metal *in vacuo*, then stored in a N_2-filled glovebox over Na sand. 3,6-Difluoro-1,2,4,5-tetrahydroxybenzene (H_4Fan) and *N*,*N*′-dimethyl-4,4′-bipyridinium di(4-toluenesulfonate) (MeV(OTs)$_2$) were synthesised as described in Chapter 2 (Section 2.4). General spectroscopic and physical characterisation was performed as described in Chapter 7.

4.4.2 (MeV)[Fe_2(Fan)$_3$]·*y*MeCN (*mP* 4.1a and *aP* 4.1a)

In air, a solution of $Fe^{II}Cl_2$·4H_2O (39.8 mg, 0.2 mmol), LiOAc·2H_2O (10.2 mg, 0.1 mmol) and MeV(OTs)$_2$ (211.5 mg, 0.4 mmol) in H_2O (4 mL) was carefully layered below a solution of H_4fan (53.4 mg, 0.3 mmol) in MeCN (10 mL) in a soda glass vial (OD = 25 mm), with a buffer layer of 1:1 v/v MeCN/H_2O (4 mL). Black elongated blocks with a metallic blue lustre suitable for X-ray diffraction were visible on the vial walls within two days, in addition to a greenish powder on the vial bottom. For

mP **4.1a**, single crystals were transferred immediately from the mother liquor to a cryoprotective oil (see Section 4.4.4); attempted isolation leads to conversion to *aP* **4.1a**. For bulk synthesis of *aP* **4.1a**, 19 reactions were conducted in parallel. After 7 days, the reactions were transferred to an N_2-purged glovebag for workup. Under N_2, the greenish powder was carefully aspirated from the vials in ca. 4 mL mother liquor, then the black crystalline product dislodged from the vial walls and suspended in the mother liquor. The combined mother liquors were transferred into deoxygenated 2:1 v/v MeCN/H_2O (25 mL). Additional green powder was removed from the crystalline product by decanting the supernatant liquid, then washing with deoxygenated 2:1 v/v MeCN/H_2O (3 × 100 mL) by resuspension of the crystalline product, sedimentation of the heavier crystalline product and decantation of the supernatant liquid. The product was then suspended in deoxygenated 2:1 v/v MeCN/H_2O (20 mL) and transferred to a two-neck Schlenk tube. The Schlenk tube was fitted with a Schlenk cap and rubber septum, then removed from the glovebag and placed under an atmosphere of dry N_2 on a Schlenk line. The suspension was briefly (<5 s) sonicated to breakup larger aggregates, then the supernatant liquid decanted by cannula transfer under dry N_2. The crystalline product was washed with dry, deoxygenated MeCN (3 × 20 mL) by resuspension then sedimentation of the heavier crystalline product, followed by decantation of the supernatant liquid by cannula transfer. The guest solvent was exchanged by soaking in dry, deoxygenated MeCN (20 mL) overnight (12 hrs), followed by decantation of the supernatant by cannula transfer and washing of the product with dry, deoxygenated MeCN (2 × 10 mL) as above. This soaking-washing procedure was repeated five times total. The black crystalline product was isolated by suction filtration in a flame-dried Schlenk frit under N_2, using dry, deoxygenated MeCN (3 × 20 mL) to transfer adherent solids from the Schlenk tube and wash the product on the frit (see Chapter 3, Figure 3.32). The product was then dried *in vacuo* on the frit to a free flowing crystalline solid. The product on the Schlenk frit was pumped into an N_2-filled glovebox then transferred to a tared, flame-dried Schlenk tube for storage, yielding *aP* **4.1a** as black crystals with a brilliant blueish-green metallic lustre (375 mg, 20.3% based upon H_4Fan). FT-IR (ATR, cm^{-1}): 3476 (br w), 3058 (w), 2249 (w), 1707 (w), 1640 (m), 1494 (m), 1349 (m), 1187 (w), 1071 (w), 1000 (s), 870 (w), 827 (m), 666 (m). Anal. Calcd. for $(C_{12}H_{14}N_2)(Fe_2F_6O_{12}C_{18})\cdot 3.7(C_2H_3N)$: C, 46.22%; H, 2.60%; N, 8.22%. Found: C, 46.03%; H, 2.67%; N, 8.22%.

4.4.3 (MeV)[$Fe_2(Fan)_3$]·2.7DMF (4.1b)

Crystallisation and isolation of **4.1b** was performed analogously to *aP* **4.1a**. 19 reactions were conducted in parallel. Following soaking of the black crystalline product once in dry, deoxygenated MeCN (20 mL) as described above, the supernatant liquid was decanted by cannula transfer under dry N_2, and the product washed with dry, deoxygenated DMF (3 × 20 mL) as described previously. The crystalline black product was resuspended in dry, deoxygenated DMF (20 mL) and soaked overnight (12 hrs.) following by washing of the product with DMF (2 × 10 mL) as described for *aP* **4.1a**; this soaking-washing procedure was similarly repeated five times total. The product was isolated by suction filtration in a flame-dried Schlenk frit under N_2, using dry, deoxygenated DMF (3 × 20 mL) to transfer adherent solids from the Schlenk tube and wash the product on the frit. The product on the frit was transferred to an N_2-filled glovebox, then transferred to a tared, flame-dried Schlenk tube for storage, yielding **4.1b** as black crystals with a brilliant blueish-green metallic lustre (489 mg, 25.3% based upon H_4Fan). FT-IR (ATR, cm^{-1}): 3056 (w), 1666 (s), 1640 (m), 1490 (m), 1441 (w), 1346 (m), 1329 (w), 1302 (w), 1255 (w), 1220 (w), 1190 (w), 1094 (m), 1071 (w), 1050 (w), 999 (s), 827 (m), 659 (m). Anal. Calcd. for $(C_{12}H_{14}N_2)(Fe_2F_6O_{12}C_{18})\cdot 2.7(C_3H_7NO)$: C, 44.98%; H, 3.26%; N, 6.47%. Found: C, 45.21%; H, 3.27%; N, 6.32%.

4.4.4 Single-Crystal X-ray Diffraction

4.4.4.1 General Considerations

Following isolation as described below, crystals were coated with an oil-based cryoprotectant to prevent solvent loss, then transferred to nylon loops for measurement of crystallographic data. Crystallographic data collection and processing using laboratory sources was performed as described in Chapter 7.

4.4.4.2 (MeV)[Fe$_2$(Fan)$_3$]·5.3MeCN (mP 4.1a)

As-synthesised crystals of *mP* **4.1a** were cold mounted using dry ice to preserve the solvation state. The crystals were removed directly from the mother liquor, and rapidly transferred to pre-cooled oil-based cryoprotectant, before mounting on nylon loops for measurement of crystallographic data (Table 4.8). Between 160–240 K, rigid bond restraints were applied using the RIGU instruction to all non-hydrogen atoms in the MeV^{2+} molecule in the asymmetric unit. Disagreeable reflections (Table 4.7) were excluded from the refinement using the OMIT instruction. Disagreeable reflections are considered as those with,

$$\sqrt{\frac{wD_{hkl}{}^2}{\langle wD^2 \rangle}} > 10 \tag{4.1}$$

where w is given by the weighting formula, D_{hkl} for a given reflection is determined by,

$$D_{hkl} = F_O{}^2 - F_C{}^2 \tag{4.2}$$

where F_O and F_C are the observed and calculated structure factors respectively, and $\langle wD^2 \rangle$ is the average over all reflections.

Table 4.7 Disagreeable reflections omitted from the structure refinements of *mP* **4.1a** at various temperatures.

***T* / K**	**Omitted Reflections**
100	N/A
120	(−13 1 2), (−12 0 4), (−12 0 2)
140	(−17 1 8), (−15 1 6), (−12 0 4)
160	N/A
180	N/A
200	(−4 7 4), (5 1 0)
220	N/A
240	(−2 1 4) (−2 5 3), (−1 4 6), (0 5 5), (4 6 1)

Inspection of the electron density difference (F_O−F_C) maps revealed the presence of significant positive electron density within the voids in the structure. This was attributed to a combination of well-ordered and disordered MeCN molecules (5.3 MeCN molecules per formula unit total). Over the entire temperature range (100–240 K), two MeCN molecules per formula unit were readily modelled; rigid bond restraints were applied to all non-hydrogen atoms in these molecules using the RIGU instruction, with additional similarity restraints applied non-hydrogen atoms in both molecules from 140 K and above using the SIMU instruction. Above 200 K, additional interatomic distance restraints of 1.137 Å (C≡N 1,2 distance), 1.456 Å (C–CH_3 1,2 distance) and 2.593 Å (N···CH_3 1,3 distance) were applied using the DFIX instruction for one of these MeCN sites.

Between 100–160 K, one MeCN per formula unit could be modelled as disordered over two positions. The total occupancy of this molecule was fixed at one, and the occupancy of each site allowed to refine against each other. Rigid bond and similarity restraints on all non-hydrogen atoms for both positions of this molecule were applied using RIGU and SIMU instructions, respectively. The EADP instruction was utilised to constrain the atomic displacement parameters for each pair of equivalent atoms in the two parts to be equal. At 140 and 160 K, additional interatomic distance restraints of 1.137 Å (C≡N 1,2 distance), 1.456 Å (C–CH_3 1,2 distance) and 2.593 Å (N···CH_3 1,3 distance) were applied using the DFIX instruction, for both positions. At 180 K, disorder of the MeCN molecule became too severe to be satisfactorily modelled.

The remaining regions of residual positive electron density were ascribed to severely disordered MeCN molecules, with the scattering contribution of these disordered molecules accounted for using the SQUEEZE[23] routine in PLATON.[24] The remaining solvation in the voids (100–160 K, 2.3 MeCN per formula unit; 180–240 K, 3.3 MeCN per formula unit) was then estimated from the electron count determined by SQUEEZE, assuming it comprised solely MeCN.

Table 4.8 Crystallographic data for the primitive monoclinic phase of (MeV)[$Fe_2(Fan)_3$]·5.3MeCN (*mP* **4.1a**) measured at several temperatures.

***T* / K**	**100**	**120**	**140**
Empirical formula	$C_{40.6}H_{29.9}N_{7.3}O_{12}F_6Fe_2$	$C_{40.6}H_{29.9}N_{7.3}O_{12}F_6Fe_2$	$C_{40.6}H_{29.9}N_{7.3}O_{12}F_6Fe_2$
Formula weight	1037.72	1037.72	1037.72
Habit	Block	Block	Block
Crystal system	Monoclinic	Monoclinic	Monoclinic
Space group	$P2_1/c$	$P2_1/c$	$P2_1/c$
a / Å	14.61400(10)	14.5986(2)	14.5789(2)
b / Å	21.1101(2)	21.1723(3)	21.2375(3)
c / Å	15.79000(10)	15.8274(2)	15.8614(2)
α / °	90	90	90
β / °	115.3050(10)	115.269(2)	115.236(2)
γ / °	90	90	90
V / Å^3	4403.84(7)	4423.93(12)	4442.29(12)
Z	4	4	4
ρ_{calc} / g cm^{-3}	1.565	1.558	1.552
μ / mm^{-1}	6.137	6.109	6.084
F_{000}	2106.0	2106.0	2106.0
Crystal size / mm^3	0.317 × 0.191 × 0.178	0.317 × 0.191 × 0.178	0.317 × 0.191 × 0.178
Radiation	Cu Kα (λ = 1.54184 Å)	Cu Kα (λ = 1.54184 Å)	Cu Kα (λ = 1.54184 Å)
2θ range	6.69 to 157.492	6.696 to 157.25	6.702 to 157.638
Index ranges	$-14 \le h \le 18$ $-26 \le k \le 26$ $-20 \le l \le 20$	$-17 \le h \le 18$ $-26 \le k \le 26$ $-19 \le l \le 20$	$-18 \le h \le 17$ $-26 \le k \le 26$ $-20 \le l \le 19$
Total/independent reflections	43484/9419 [R_{int} = 0.0312, R_{sigma} = 0.0226]	45646/9426 [R_{int} = 0.0368, R_{sigma} = 0.0265]	45550/9457 [R_{int} = 0.0356, R_{sigma} = 0.0273]
Data/restraints/ parameters	9419/78/566	9426/78/566	9457/99/566
Goodness-of-fit on F^2	1.067	1.049	1.053
Final R indexes [$I \ge 2\sigma(I)$]	R_1 = 0.0328, wR_2 = 0.0933	R_1 = 0.0416, wR_2 = 0.1199	R_1 = 0.0412, wR_2 = 0.1214
Final R indexes [all data]	R_1 = 0.0354, wR_2 = 0.0950	R_1 = 0.0472, wR_2 = 0.1239	R_1 = 0.0471, wR_2 = 0.1254
Largest diff. peak/hole / e Å^{-3}	0.46/−0.41	0.52/−0.46	0.51/−0.51

NB: The empirical formula and F_{000} values include the contribution of 2.3 disordered MeCN molecules in the channels of *mP* **4.1a**.

Table 4.8(cont.) Crystallographic data for the primitive monoclinic phase of (MeV)[$Fe_2(Fan)_3$]·5.3MeCN (*mP* **4.1a**) measured at several temperatures.

***T* / K**	**160**	**180**	**200**
Empirical formula	$C_{40.6}H_{29.9}N_{7.3}O_{12}F_6Fe_2$[a]	$C_{40.6}H_{29.9}N_{7.3}O_{12}F_6Fe_2$[b]	$C_{40.6}H_{29.9}N_{7.3}O_{12}F_6Fe_2$[b]
Formula weight	1037.72	1037.72	1037.72
Habit	Block	Block	Block
Crystal system	Monoclinic	Monoclinic	Monoclinic
Space group	$P2_1/c$	$P2_1/c$	$P2_1/c$
a / Å	14.56345(14)	14.5467(2)	14.5287(2)
b / Å	21.2963(2)	21.3630(2)	21.4035(2)
c / Å	15.89071(16)	15.9260(2)	15.9483(2)
α / °	90	90	90
β / °	115.2022(12)	115.188(2)	115.1060(10)
γ / °	90	90	90
V / Å^3	4459.32(9)	4478.59(11)	4490.82(10)
Z	4	4	4
ρ_{calc} / g cm^{-3}	1.546	1.539	1.535
μ / mm^{-1}	6.061	6.035	6.018
F_{000}	2106.0[a]	2106.0[b]	2106.0[b]
Crystal size / mm^3	0.317 × 0.191 × 0.178	0.317 × 0.191 × 0.178	0.317 × 0.191 × 0.178
Radiation	Cu Kα (λ = 1.54184 Å)	Cu Kα (λ = 1.54184 Å)	Cu Kα (λ = 1.54184 Å)
2θ range	6.708 to 157.352	6.714 to 156.974	6.718 to 157.694
Index ranges	$-18 \le h \le 17$ $-26 \le k \le 27$ $-20 \le l \le 19$	$-18 \le h \le 17$ $-26 \le k \le 27$ $-20 \le l \le 19$	$-18 \le h \le 17$ $-27 \le k \le 27$ $-20 \le l \le 19$
Total/independent reflections	46258/9505 [R_{int} = 0.0348, R_{sigma} = 0.0252]	46587/9542 [R_{int} = 0.0352, R_{sigma} = 0.0246]	46895/9588 [R_{int} = 0.0373, R_{sigma} = 0.0263]
Data/restraints/ parameters	9505/213/566	9542/150/527	9588/153/527
Goodness-of-fit on F^2	1.074	1.061	1.064
Final R indexes [$I \ge 2\sigma(I)$]	R_1 = 0.0390, wR_2 = 0.1152	R_1 = 0.0385, wR_2 = 0.1141	R_1 = 0.0392, wR_2 = 0.1162
Final R indexes [all data]	R_1 = 0.0437, wR_2 = 0.1184	R_1 = 0.0435, wR_2 = 0.1173	R_1 = 0.0451, wR_2 = 0.1201
Largest diff. peak/hole / e Å^{-3}	0.48/−0.44	0.49/−0.42	0.42/−0.44

NB: The empirical formula and F_{000} values include the contribution of [a]: 2.3 or [b]: 3.3 disordered MeCN molecules in the channels of *mP* **4.1a**.

Table 4.8(cont.) Crystallographic data for the primitive monoclinic phase of (MeV)[Fe_2(Fan)$_3$]·5.3MeCN (*mP* **4.1a**) measured at several temperatures.

***T* / K**	**220**	**240**
Empirical formula	$C_{40.6}H_{29.9}N_{7.3}O_{12}F_6Fe_2$	$C_{40.6}H_{29.9}N_{7.3}O_{12}F_6Fe_2$
Formula weight	1037.72	1037.72
Habit	Block	Block
Crystal system	Monoclinic	Monoclinic
Space group	$P2_1/c$	$P2_1/c$
a / Å	14.51720(10)	14.5061(2)
b / Å	21.4459(2)	21.4909(3)
c / Å	15.9737(2)	16.0023(2)
α / °	90	90
β / °	115.0590(10)	114.983(2)
γ / °	90	90
V / Å^3	4505.05(8)	4521.92(12)
Z	4	4
ρ_{calc} / g cm^{-3}	1.530	1.524
μ / mm^{-1}	5.999	5.977
F_{000}	2106.0	2106.0
Crystal size / mm^3	0.317 × 0.191 × 0.178	0.317 × 0.191 × 0.178
Radiation	Cu Kα (λ = 1.54184 Å)	Cu Kα (λ = 1.54184 Å)
2θ range	6.722 to 157.242	6.722 to 157.278
Index ranges	$-17 \le h \le 18$ $-27 \le k \le 27$ $-19 \le l \le 20$	$-17 \le h \le 18$ $-27 \le k \le 27$ $-19 \le l \le 20$
Total/independent reflections	47023/9609 [R_{int} = 0.0417, R_{sigma} = 0.0276]	46837/9635 [R_{int} = 0.0368, R_{sigma} = 0.0276]
Data/restraints/ parameters	9609/138/527	9635/153/527
Goodness-of-fit on F^2	1.062	1.070
Final R indexes [$I \ge 2\sigma$ (I)]	R_1 = 0.0457, wR_2 = 0.1370	R_1 = 0.0406, wR_2 = 0.1255
Final R indexes [all data]	R_1 = 0.0529, wR_2 = 0.1425	R_1 = 0.0486, wR_2 = 0.1306
Largest diff. peak/hole / e Å^{-3}	0.69/−0.59	0.39/−0.43

NB: The empirical formula and F_{000} values include the contribution of 3.3 disordered MeCN molecules in the channels of *mP* **4.1a**.

4.4.4.3 (MeV)[Fe$_2$(Fan)$_3$]·4.8MeCN (aP 4.1a)

In an N_2-filled glovebox, isolated crystals of *aP* **4.1a** were suspended in anhydrous, deoxygenated Nujol to protect the crystals from exposure to atmospheric oxygen outside the glovebox. The suspension was passed out of the glovebox, and the crystals immediately transferred into an oil-based cryoprotectant before mounting on nylon loops for measurement of crystallographic data (Table 4.9). Analysis of the reflection data using CrysAlisPRO revealed the presence of a two-component overlapping twin in the crystal. Data reduction and multi-scan absorption corrections upon both twin components were performed using CrysAlis PRO to produce a HKLF5 dataset with contributions from both twin components. The structure was solved using the separated data of only one twin component using SHELXT, with subsequent structure refinements performed using the twin HKLF5 dataset and the BASF instruction. Rigid bond restraints were applied to all non-hydrogen atoms in the structure using the RIGU instruction. Inspection of the electron density difference (F_O–F_C) maps revealed the presence of significant positive electron density within the voids in the structure. Part of this residual electron density was readily modelled as one well ordered MeCN molecule per formula unit. The remaining residual electron density, attributed to severely disordered MeCN molecules, which could not satisfactorily be modelled. The scattering contribution of the disordered solvent was accounted for using the SQUEEZE[23] routine in PLATON.[24] The remaining solvation in voids of 3.8 MeCN per formula unit (4.8 MeCN per formula unit total) was then estimated from the electron count determined by SQUEEZE, assuming it comprised solely MeCN. The absence of guest H_2O was justified by use of extensive soaking of as-synthesised material in anhydrous MeCN following crystallisation, in addition to handling of the isolated sample under anhydrous, anaerobic conditions (see Section 4.4.2).

4.4.4.4 (MeV)[Fe$_2$(Fan)$_3$]·3.8DMF (4.1b)

In an N_2-filled glovebox, isolated crystals of **4.1b** were suspended in anhydrous, deoxygenated Nujol to protect the crystals from exposure to atmospheric oxygen outside the glovebox. The suspension was passed out of the glovebox, and the crystals immediately transferred into an oil-based cryoprotectant before mounting on nylon loops for measurement of crystallographic data (Table 4.9). Rigid bond restraints were applied to all non-hydrogen ligand atoms in the structure using the RIGU instruction.

Inspection of the electron density difference ($F_O - F_C$) maps revealed the presence of significant positive electron density within the voids in the structure. While the form of these regions closely resembled the shape of DMF molecules, satisfactory modelling of this solvent was prevented by severe multi-part disorder around sites of 2/*m* and 2-fold rotational symmetry. The scattering contribution of this disordered solvent was accounted for using the SQUEEZE[23] routine in PLATON.[24] The solvation in the voids was then estimated from the electron count determined by SQUEEZE, assuming it comprised solely DMF (3.8 DMF per formula unit). The absence of guest H_2O and MeCN was justified by use of extensive soaking of as-synthesised material in anhydrous MeCN then DMF following crystallisation, in addition to handling of the isolated sample under anhydrous, anaerobic conditions (see Section 4.4.3). The absence of a large absorption around ν = 3500 cm^{-1} attributed to H_2O, or a weak absorption around ν = 2250 cm^{-1} attributed to $\nu_{C\equiv N}$ of MeCN in the FT-IR spectrum of **4.1b** (Figure 4.15) validates this assumption.

Table 4.9 Crystallographic data for *aP* **4.1a** and **4.1b**.

Compound	(MeV)[$Fe_2(Fan)_3$]·4.8MeCN (*aP* **4.1a**)	(MeV)[$Fe_2(Fan)_3$]·3.8DMF (**4.1b**)
Empirical formula	$C_{39.6}H_{28.4}N_{6.8}O_{12}F_6Fe_2$	$C_{20.7}H_{20.3}N_{2.9}O_{7.9}F_3Fe$
Formula weight	1017.19	548.95
Habit	Irregular plate	Plank
T / K	100.00(1)	100.00(10)
Crystal system	Triclinic	Monoclinic
Space group	$P\bar{1}$	$C2/c$
a / Å	12.3712(6)	14.5788(2)
b / Å	13.1036(7)	21.1901(2)
c / Å	15.8503(7)	15.8730(2)
α / °	110.942(4)	90
β / °	98.205(4)	114.225(2)
γ / °	109.559(5)	90
V / Å^3	2158.4(2)	4471.78(11)
Z	2	8
ρ_{calc} / g cm^{-3}	1.565	1.631
μ / mm^{-1}	6.244	6.131
F_{000}	1031.0	2248.0
Crystal size / mm^3	0.347 × 0.189 × 0.098	0.176 × 0.058 × 0.034
Radiation	Cu Kα (λ = 1.54184 Å)	Cu Kα (λ = 1.54184 Å)
2θ range	6.256 to 143.846	7.85 to 156.044
Index ranges	$-13 \le h \le 15$ $-16 \le k \le 14$ $-19 \le l \le 19$	$-17 \le h \le 18$ $-26 \le k \le 24$ $-19 \le l \le 20$
Total/independent reflections	16009/16009 [R_{int} = 0.054, R_{sigma} = 0.0113]	33811/4751 [R_{int} = 0.0355, R_{sigma} = 0.0199]
Data/restraints/ parameters	16009/384/500	4751/165/237
Goodness-of-fit on F^2	1.035	1.109
Final R indexes [$I \ge 2\sigma(I)$]	R_1 = 0.0614, wR_2 = 0.1783	R_1 = 0.0473, wR_2 = 0.1434
Final R indexes [all data]	R_1 = 0.0721, wR_2 = 0.1887	R_1 = 0.0503, wR_2 = 0.1456
Largest diff. peak/hole / e Å^{-3}	0.73/−0.42	0.32/−0.67

NB: The empirical formula and F_{000} values include the contribution of 3.8 disordered MeCN molecules in *aP* **4.1a** and 3.8 disordered DMF in of **4.1b**.

4.4.5 Powder X-ray Diffraction

The P-XRD data were collected using the PD beamline at the Australian Synchrotron,[73] as described in Chapter 7. P-XRD data were measured at 250 K for *mP* **4.1a** (MeCN slurry), and 100 K for *aP* **4.1a** and **4.1b**. In air, a sample of as-synthesised *mP* **4.1a** was transferred from the mother liquor and washed with 2:1 v/v MeCN/H_2O (3 × 20 mL) then MeCN (3 × 20 mL) to remove amorphous by-products. The crystalline product was gently ground under MeCN then transferred as a slurry to a borosilicate capillary (OD = 0.7 mm) which was then flame sealed. In a N_2-filled glovebox, the isolated compounds *aP* **4.1a** and **4.1b** were gently ground, then transferred to borosilicate capillaries (OD = 0.5 mm). The capillaries were then sealed with an electric arc lighter and wax, before being transferred out of the glovebox for measurement.

4.5 References

[1] W. R. Dolbier, *J. Fluorine Chem.* **2005**, *126*, 157-163.

[2] M. Pagliaro, R. Ciriminna, *J. Mater. Chem.* **2005**, *15*, 4981-4991.

[3] J. Wang, M. Sánchez-Roselló, J. L. Aceña, C. del Pozo, A. E. Sorochinsky, S. Fustero, V. A. Soloshonok, H. Liu, *Chem. Rev.* **2014**, *114*, 2432-2506.

[4] L. Shimoni, J. P. Glusker, *Struct. Chem.* **1994**, *5*, 383-397.

[5] J. D. Dunitz, R. Taylor, *Chem. Eur. J.* **1997**, *3*, 89-98.

[6] J. D. Dunitz, *ChemBioChem* **2004**, *5*, 614-621.

[7] K. Reichenbächer, H. I. Süss, J. Hulliger, *Chem. Soc. Rev.* **2005**, *34*, 22-30.

[8] J. Stenhouse, *J. Chem. Soc.* **1870**, *23*, 6-14.

[9] H. A. Torrey, W. H. Hunter, *J. Am. Chem. Soc.* **1912**, *34*, 702-716.

[10] K. Wallenfels, K. Friedrich, *Chem. Ber.* **1960**, *93*, 3070-3082.

[11] K. Wallenfels, W. Draber, *Chem. Ber.* **1957**, *90*, 2819-2832.

[12] S. Horiuchi, F. Ishii, R. Kumai, Y. Okimoto, H. Tachibana, N. Nagaosa, Y. Tokura, *Nat. Mater.* **2005**, *4*, 163-166.

[13] S. Horiuchi, R. Kumai, Y. Tokura, *J. Mater. Chem.* **2009**, *19*, 4421-4434.

[14] S. Horiuchi, R. Kumai, Y. Tokura, *J. Am. Chem. Soc.* **2013**, *135*, 4492-4500.

[15] R. Murase, B. F. Abrahams, D. M. D'Alessandro, C. G. Davies, T. A. Hudson, G. N. L. Jameson, B. Moubaraki, K. S. Murray, R. Robson, A. L. Sutton, *Inorg. Chem.* **2017**, *56*, 9025-9035.

[16] R. Murase, C. J. Commons, T. A. Hudson, G. N. L. Jameson, C. D. Ling, K. S. Murray, W. Phonsri, R. Robson, Q. Xia, B. F. Abrahams, D. M. D'Alessandro, *Inorg. Chem.* **2020**, *59*, 3619-3630.

[17] B. F. Abrahams, T. A. Hudson, L. J. McCormick, R. Robson, *Cryst. Growth Des.* **2011**, *11*, 2717-2720.

[18] L. E. Darago, M. L. Aubrey, C. J. Yu, M. I. Gonzalez, J. R. Long, *J. Am. Chem. Soc.* **2015**, *137*, 15703-15711.

[19] I.-R. Jeon, B. Negru, R. P. Van Duyne, T. D. Harris, *J. Am. Chem. Soc.* **2015**, *137*, 15699-15702.

[20] J. A. DeGayner, I.-R. Jeon, L. Sun, M. Dincă, T. D. Harris, *J. Am. Chem. Soc.* **2017**, *139*, 4175-4184.

[21] M. E. Ziebel, C. A. Gaggioli, A. B. Turkiewicz, W. Ryu, L. Gagliardi, J. R. Long, *J. Am. Chem. Soc.* **2020**, *142*, 2653-2664.

[22] Y. Sekine, J. Chen, N. Eguchi, H. Miyasaka, *Chem. Commun.* **2020**.

[23] A. L. Spek, *Acta Crystallogr. C* **2015**, *71*, 9-18.

[24] A. L. Spek, *Acta Crystallogr. D* **2009**, *65*, 148-155.

[25] L. Liu, L. Li, J. A. DeGayner, P. H. Winegar, Y. Fang, T. D. Harris, *J. Am. Chem. Soc.* **2018**, *140*, 11444-11453.

[26] C. J. Kingsbury, B. F. Abrahams, J. E. Auckett, H. Chevreau, A. D. Dharma, S. Duyker, Q. He, C. Hua, T. A. Hudson, K. S. Murray, W. Phonsri, V. K. Peterson, R. Robson, K. F. White, *Chem. Eur. J.* **2019**, *25*, 5222-5234.

[27] C. J. Kingsbury, B. F. Abrahams, D. M. D'Alessandro, T. A. Hudson, R. Murase, R. Robson, K. F. White, *Cryst. Growth Des.* **2017**, *17*, 1465-1470.

[28] C. F. Macrae, P. R. Edgington, P. McCabe, E. Pidcock, G. P. Shields, R. Taylor, M. Towler, J. van de Streek, *J. Appl. Crystallogr.* **2006**, *39*, 453-457.

[29] S. Alvarez, *Chem. Rev.* **2015**, *115*, 13447-13483.

[30] S. Alvarez, D. Avnir, M. Llunell, M. Pinsky, *New J. Chem.* **2002**, *26*, 996-1009.

[31] T. M. Bockman, J. K. Kochi, *J. Org. Chem.* **1990**, *55*, 4127-4135.

[32] N. Leblanc, N. Mercier, O. Toma, A. H. Kassiba, L. Zorina, P. Auban-Senzier, C. Pasquier, *Chem. Commun.* **2013**, *49*, 10272-10274.

[33] M. L. Mercuri, F. Congiu, G. Concas, S. A. Sahadevan, *Magnetochemistry* **2017**, *3*, 17.

[34] O. C. Gagne, F. C. Hawthorne, *Acta Crystallogr. B* **2015**, *71*, 562-578.

[35] J. Chen, Y. Sekine, Y. Komatsumaru, S. Hayami, H. Miyasaka, *Angew. Chem. Int. Ed.* **2018**, *57*, 12043-12047.

[36] J. A. DeGayner, K. Wang, T. D. Harris, *J. Am. Chem. Soc.* **2018**, *140*, 6550-6553.

[37] J. Chen, Y. Sekine, A. Okazawa, H. Sato, W. Kosaka, H. Miyasaka, *Chem. Sci.* **2020**, *11*, 3610-3618.

[38] A. Shastri, A. K. Das, S. Krishnakumar, P. J. Singh, B. N. R. Sekhar, *The Journal of Chemical Physics* **2017**, *147*, 224305.

[39] M. E. Ziebel, L. E. Darago, J. R. Long, *J. Am. Chem. Soc.* **2018**, *140*, 3040-3051.

[40] C. Serre, F. Millange, C. Thouvenot, M. Noguès, G. Marsolier, D. Louër, G. Férey, *J. Am. Chem. Soc.* **2002**, *124*, 13519-13526.

[41] G. Férey, C. Serre, *Chem. Soc. Rev.* **2009**, *38*, 1380-1399.

[42] D. N. Dybtsev, H. Chun, K. Kim, *Angew. Chem. Int. Ed.* **2004**, *43*, 5033-5036.

[43] F. Yang, J.-C. Deng, Z.-G. Li, J.-W. Xu, *Acta Crystallogr. E* **2008**, *64*, o253.

[44] N. N. Greenwood, T. C. Gibb, *Mössbauer Spectroscopy*, Chapman and Hall, London, UK, **1971**.

[45] S. Kawata, S. Kitagawa, H. Kumagai, T. Ishiyama, K. Honda, H. Tobita, K. Adachi, M. Katada, *Chem. Mater.* **1998**, *10*, 3902-3912.

[46] P. Gütlich, E. Bill, A. X. Trautwein, *Mössbauer Spectroscopy and Transition Metal Chemistry*, Springer-Verlag, Berlin, Germany, **2011**.

[47] S. A. Sahadevan, A. Abhervé, N. Monni, C. Sáenz de Pipaón, J. R. Galán-Mascarós, J. C. Waerenborgh, B. J. C. Vieira, P. Auban-Senzier, S. Pillet, E.-E. Bendeif, P. Alemany, E. Canadell, M. L. Mercuri, N. Avarvari, *J. Am. Chem. Soc.* **2018**, *140*, 12611-12621.

[48] J. T. Wrobleski, D. B. Brown, *Inorg. Chem.* **1979**, *18*, 2738-2749.

[49] J. T. Wrobleski, D. B. Brown, *Inorg. Chem.* **1979**, *18*, 498-504.

[50] V. A. Grillo, G. R. Hanson, D. Wang, T. W. Hambley, L. R. Gahan, K. S. Murray, B. Moubaraki, C. J. Hawkins, *Inorg. Chem.* **1996**, *35*, 3568-3576.

[51] K. Nagayoshi, M. K. Kabir, H. Tobita, K. Honda, M. Kawahara, M. Katada, K. Adachi, H. Nishikawa, I. Ikemoto, H. Kumagai, Y. Hosokoshi, K. Inoue, S. Kitagawa, S. Kawata, *J. Am. Chem. Soc.* **2003**, *125*, 221-232.

[52] T. Manago, S. Hayami, H. Oshio, S. Osaki, H. Hasuyama, R. H. Herber, Y. Maeda, *J. Chem. Soc., Dalton Trans.* **1999**, 1001-1012.

[53] G. V. Shilov, Z. K. Nikitina, N. S. Ovanesyan, S. M. Aldoshin, V. D. Makhaev, *Russ. Chem. Bull.* **2011**, *60*, 1209-1219.

[54] M. Marchivie, P. Guionneau, J.-F. Letard, D. Chasseau, *Acta Crystallogr. B* **2005**, *61*, 25-28.

[55] J. K. McCusker, A. L. Rheingold, D. N. Hendrickson, *Inorg. Chem.* **1996**, *35*, 2100-2112.

[56] S. M. Oh, D. N. Hendrickson, K. L. Hassett, R. E. Davis, *J. Am. Chem. Soc.* **1985**, *107*, 8009-8018.

[57] T. Sato, F. Ambe, K. Endo, M. Katada, H. Maeda, T. Nakamoto, H. Sano, *J. Am. Chem. Soc.* **1996**, *118*, 3450-3458.

[58] S. Onaka, Y. Sakai, T. Ozeki, T. Nakamoto, Y. Kobayashi, M. Takahashi, R. Ogiso, T. Takayama, M. Shiotsuka, *Dalton Trans.* **2014**, *43*, 6711-6719.

[59] R. J. Webb, T. Y. Dong, C. G. Pierpont, S. R. Boone, R. K. Chadha, D. N. Hendrickson, *J. Am. Chem. Soc.* **1991**, *113*, 4806-4812.

[60] B. S. Brunschwig, C. Creutz, N. Sutin, *Chem. Soc. Rev.* **2002**, *31*, 168-184.

[61] M. L. Aubrey, B. M. Wiers, S. C. Andrews, T. Sakurai, S. E. Reyes-Lillo, S. M. Hamed, C.-J. Yu, L. E. Darago, J. A. Mason, J.-O. Baeg, F. Grandjean, G. J. Long, S. Seki, J. B. Neaton, P. Yang, J. R. Long, *Nat. Mater.* **2018**, *17*, 625-632.

[62] N. S. Hush, in *Prog. Inorg. Chem., Vol. 8* (Ed.: F. A. Cotton), Interscience Publishers, New York, NY, **1967**.

[63] N. S. Hush, *Electrochim. Acta* **1968**, *13*, 1005-1023.

[64] M. B. Robin, P. Day, in *Advances in Inorganic Chemistry and Radiochemistry, Vol. 10* (Eds.: H. J. Emeléus, A. G. Sharpe), Academic Press, London, UK, **1968**.

[65] J. Tauc, *Mater. Res. Bull.* **1968**, *3*, 37-46.

[66] S. Kasap, C. Koughia, J. Singh, H. Ruda, S. O'Leary, in *Springer Handbook of Electronic and Photonic Materials* (Eds.: S. Kasap, P. Capper), Springer, New York, NY, **2006**.

[67] B. F. Abrahams, A. M. Bond, T. H. Le, L. J. McCormick, A. Nafady, R. Robson, N. Vo, *Chem. Commun.* **2012**, *48*, 11422-11424.

[68] S. Hünig, J. Groβ, E. F. Lier, H. Quast, *Liebigs Ann. Chem.* **1973**, *1973*, 339-358.

[69] S. Hünig, J. Groβ, W. Schenk, *Liebigs Ann. Chem.* **1973**, *1973*, 324-338.

[70] S. Hünig, W. Schenk, *Liebigs Ann. Chem.* **1979**, *1979*, 1523-1533.

[71] A. C. Forse, C. Merlet, J. M. Griffin, C. P. Grey, *J. Am. Chem. Soc.* **2016**, *138*, 5731-5744.

[72] S. Benmansour, A. Abhervé, P. Gómez-Claramunt, C. Vallés-García, C. J. Gómez-García, *ACS Appl. Mater. Interfaces* **2017**, *9*, 26210-26218.

[73] K. S. Wallwork, B. J. Kennedy, D. Wang, *AIP Conference Proceedings* **2007**, *879*, 879-882.

This page intentionally left blank

Chapter 5 Structural Transformations and Properties of a Methyl Viologen Containing Mixed-Valence Iron–Chloranilate Framework

5.1 Introduction 329

5.1.1 Impact of Tetraoxolene Ligand Substituents 329

5.1.2 Chapter Aim 331

5.2 Results and Discussion 332

5.2.1 Synthesis and Structure Description 332

5.2.2 Crystallographic Determination of Oxidation States 338

5.2.3 Variable-Temperature Single-Crystal X-ray Diffraction 341

5.2.4 Structural Transformations 344

5.2.5 ^{57}Fe Mössbauer Spectroscopy 356

5.2.6 Electronic Spectroscopy 358

5.2.7 Electrochemistry 366

5.2.8 Electrical Conductivity 372

5.3 Conclusion 377

5.4 Experimental 379

5.4.1 General Considerations 379

5.4.2 (MeV)[$Fe_2(Clan)_3$]·*y*MeCN (**5.1**, *y* =6; **5.2**, *y* = 1.3) 379

5.4.3 Single-Crystal X-ray Diffraction 381

5.4.4 Powder X-ray Diffraction (P-XRD) 387

5.5 References 387

This page intentionally left blank

5.1 Introduction

5.1.1 Impact of Tetraoxolene Ligand Substituents

One attractive quality of tetraoxolene ligands with respect to their use in functional coordination polymers, is the presence of 3,6-substituents, as variation of these substituents offers the potential to modulate the material properties.[1] Early work on tetraoxolene-bridged dicopper(II) complexes demonstrated that the strength of ferromagnetic (FM) coupling between $S = 1/2$ Cu^{II} centres, was subtly influenced by the relative electron-donating or -withdrawing nature of the substituents on the diamagnetic Xan^{2-} ligands.[2] This behaviour is also apparent when the Xan^{2-} form is incorporated into metal–tetraoxolene coordination polymers, which in turn affects bulk magnetic properties such as long-range ordering. As highlighted in Chapter 1, Atzori *et al.* demonstrated the ferrimagnetic (FiM) ordering temperature (T_c) could be tailored between 5.5–11 K, in an isostructural family of 2D layered coordination polymers $(^{n}Bu_4N)[Mn^{II}Cr^{III}(Xan)_3]$ (X = H, Cl, Br, I).[3] Similarly, the degree of electron delocalisation in the mixed-valence 2D frameworks $[(H_3O)(H_2O)(phz)_3][Fe^{II}Fe^{III}(Xan)_3]$ (X = Cl, Br) was influenced by the halogen substituent present on the diamagnetic Xan^{2-} ligands. The more electron-withdrawing Cl substituent allowed a greater degree of Fe^{II}/Fe^{III} valence delocalisation, increasing the higher electrical conductivity compared to the bromanilate compound.[4]

Systematic investigation into the role of ligand substituents in modulating the degree of magnetic or electronic communication mediated by the paramagnetic trianion $Xan^{3-\bullet}$ form has been conspicuously absent. In contrast to extensive studies on the diamagnetic Xan^{2-} form, recent literature studying the influence of $Xan^{3-\bullet}$ ligand substituents on the degree of magnetic and electronic communication is somewhat contradictory. Thorarinsdottir *et al.* reported the synthesis of a family of diiron(II) complexes containing bridging tetraoxolene ligands, to develop structure-property relationships between the strength of magnetic coupling and ligand substituents.[5] In the diiron(II) complexes $[\{(Me_3tpa)Fe^{II}\}_2(Xan)]$ (Me_3tpa = tris(6-methyl-2-pyridylmethyl)amine; X = OMe, Cl, NO_2, SMe_2^+) in the quinonoid-bridged Xan^{n-} form (n = 2 for OMe, Cl, NO_2; n = 0 for SMe_2^+), replacement of electron-donating OMe with electron-withdrawing SMe_2^+ groups, caused a 0.64 V anodic shift of the ligand-centred quinonoid-to-semiquinonoid redox process. The strongly

electron-withdrawing SMe_2^+ and NO_2 substituents also caused slightly weaker FM coupling between the Fe^{II} centres, compared to the OMe and Cl substituted complexes. Reduction of the complexes, transforming the bridging ligands to the semiquinoinoid radical $Xan^{n-\bullet}$ forms (n = 3, X = OMe, Cl, NO_2; n = 1, X = SMe_2^+), resulted in strong direct antiferromagnetic (AFM) coupling between the S = 2 Fe^{II} centres and the S = 1/2 bridging ligands. Somewhat surprisingly though, the strength of magnetic coupling was largely insensitive to the identity of the ligand substituents, with the exchange constants only varying between $J_M = -57(10)$ cm^{-1} for electron-donating X = OMe, and $J_M = -65(8)$ cm^{-1} for electron-withdrawing SMe_2^+ substituents. Density functional theory (DFT) calculations give insight into why the magnetic coupling is insensitive to the nature of the ligand substituents. These calculations showed that for the radical-bridged complexes, insignificant spin density resided on the ligand 3- and 6- positions, with minimal orbital contribution from the substituent groups. This consequently caused the insensitivity of degree of metal–radical coupling to the identity of the ligand substituents. The authors however noted that the secondary functionality such as electrical conductivity or photophysical properties might be influenced by the identity of the ligand substituents.

Despite the insensitivity of metal–radical coupling to ligand substituents in molecular compounds, there is still an effect in mixed-valence Fe–tetraoxolene frameworks. Sekine *et al.* synthesised a family of isostructural layered honeycomb $(^nPr_4N)_2[Fe_2(Clan)_3]\cdot$solvent frameworks, containing tuneable proportions of 'alloyed' fluor- or bromanilate ligands (Fan^{n-} and $Bran^{n-}$ respectively), to develop magnetic structure property relationships.[6] As highlighted previously, the $(^nPr_4N)_2[Fe_2(Clan)_3]\cdot$solvent family of compounds exhibits single chain magnetism, due to the low-temperature ligand charge-ordered $[Fe^{III}_2(Clan^{2-})(Clan^{3-\bullet})_2]^{2-}$ formulation,[7] in addition to thermally-induced valence tautomerism. Alloying up-to 65% bromanilate, or 42% fluoranilate ligands into $(^nPr_4N)_2[Fe_2(Clan)_3]$ gave isostructural frameworks as evinced by P-XRD analyses, with higher proportions of Fan^{n-} or $Bran^{n-}$ leading to structure transformations. Interestingly, the strength of AFM metal–radical coupling was not strongly impacted by the halogen substituent, which parallels the aforementioned work by Thorarinsdottir *et al*. In contrast, the valence-tautomeric transition temperature ($T_{1/2a}$) of the 2D frameworks was effectively tailored by the proportions of Fan^{n-} or $Bran^{n-}$ ligands 'alloyed' into the network. For

the solvated compounds, the relatively less electron-withdrawing Br substituent shifted the valence tautomeric transition, from $T_{1/2a}$ = 237 K for $(^{n}Pr_4N)_2[Fe_2(Clan)_3]\cdot$solvent to $T_{1/2a}$ = 184 K for the 65% alloyed bromanilate compound $(^{n}Pr_4N)_2[Fe_2(Clan)_{1.05}(Bran)_{1.95}]\cdot$solvent. Conversely, incorporation of fluoranilate into the frameworks increased $T_{1/2a}$ up to 270 K for the 31% alloyed compound $(n Pr_4N)_2[Fe_2(Clan)_{2.07}(Fan)_{0.93}]\cdot$solvent, with the valence tautomeric transition also becoming less distinct at higher fluoranilate content. The desolvated compounds also exhibited an analogous variation of the two-step valence tautomeric transition temperatures ($T_{1/2b}$ and $T_{1/2c}$), with increasing bromanilate content shifting the transition to lower temperature, and inclusion of fluoranilate shifting the transition to higher temperature. In Chapter 4 it was also highlighted that the layered (6,3) coordination polymer $(Et_4N)_2[Fe_2(Fan)_3]$,[8] exhibits markedly different spectroscopic and physical properties than the isostructural $(Et_4N)_2[Fe_2(Clan)_3]$ compound.[9] These results highlight that although the strength of metal–radical interaction in tetraoxolene-bridged systems are largely insensitive to the ligand substituents, even minor variations in these parameters can manifest as substantial changes in the physical properties of the frameworks material. Consequently, systematic studies on isostructural families of mixed-valence tetraoxolene coordination polymers, are still of considerable importance, to uncover robust and versatile methods to tailor the physiochemical properties of the framework materials.

5.1.2 Chapter Aim

Encouraged by the results presented in Chapter 3, demonstrating $PhenQ^{2+}$ templated an isostructural family of anionic Fe–tetraoxolene coordination polymers $(PhenQ)[Fe_2(Xan)_3]\cdot$solvent (X = F, Cl, Br), we first sought to synthesise chloranilate analogues of the layered 2D $(MeV)[Fe_2(Fan)_3]\cdot$solvent coordination polymers described in Chapter 4. This chapter was first aimed at gaining structural insight into the sensitivity of cation-framework interactions to ligand substituents, by further comparison to fluor- and chloranilate coordination chemistry. Additionally, the results presented in Chapter 4 provided a significant impetus to understand the origin of the guest-induced switching of Fe valency. Namely if this intrinsic Fe^{II}/Fe^{III} mixed valency was uniquely engendered in by fluoranilate ligands; or alternatively, if charge-transfer (CT) interactions between π-electron deficient *N*,*N*′-dimethyl-4,4′-pyridinium (MeV^{2+}) cations and the anionic Fe–tetraoxolene networks, gave rise to a rapid valence

fluctuations and therefore Fe^{II}/Fe^{III} mixed valency. Towards these goals of understanding potential disparities in fluor- and chloranilate coordination chemistry, this chapter describes the synthesis of a MeV^{2+} containing mixed-valence Fe–chloranilate coordination polymer (MeV)[Fe_2(Clan)$_3$]·6MeCN. In line with the studies on fluoranilate presented in Chapter 2, the mixed-valence Fe–chloranilate coordination polymer (MeV)[Fe_2(Clan)$_3$]·6MeCN is not isostructural to the (MeV)[Fe_2(Fan)$_3$]·solvent compounds, further highlighting the structurally divergent nature of fluoranilate coordination polymers. Extended single crystal (SC-XRD) and powder X-ray diffraction (P-XRD) experiments revealed the as-synthesised compound (MeV)[Fe_2(Clan)$_3$]·6MeCN undergoes a dramatic structure transformation upon isolation, yielding a second mixed-valence Fe–chloranilate framework (MeV)[Fe_2(Clan)$_3$]·*y*MeCN. Subsequent spectroscopic, electrochemical and electrical conductivity measurements were performed on this compound, to better understand how the unique structure of the isolated compound gave rise to unexpected physical properties.

5.2 Results and Discussion

5.2.1 Synthesis and Structure Description

The coordination polymer (MeV)[Fe_2(Clan)$_3$]·6MeCN (**5.1**) was synthesised by carefully layering an aqueous solution of $Fe^{II}Cl_2$·4H_2O, MeV(OTs)$_2$ and LiOAc·2H_2O below an acetonitrile (MeCN) solution of the reduced form of chloranilic acid, 3,6-dichloro-1,2,4,5-tetrahydroxybenzene (H_4Clan), with a buffer layer of 1:1 v/v MeCN/H_2O. As with all other coordination polymers synthesised in this work, slow diffusion reactions, coupled with slow aerial oxidation of the H_4Xan form to the active H_2Xan form, was the most successful route to produce crystals amenable to single-crystal X-ray diffraction (SC-XRD). Black, elongated block crystals with a brilliant blueish-green metallic lustre were visible on the vial walls within two days. The crystalline product was harvested after five days. Bulk samples of **5.1** were obtained by performing numerous diffusion reactions in parallel, with the crystallised products combined for purification and workup. The structure of **5.1** was determined using SC-XRD, with a satisfactory structure refinement found in the triclinic $P\bar{1}$ space group. With some exceptions in Fe–O ($d_{Fe–O}$) and ligand C–O and C–C bond lengths ($d_{C–O}$ and $d_{C–C}$ respectively), **5.1** is isostructural to (MeV)[Mn_2(Clan)$_3$]·6MeCN (**2.2a**)

described in Chapter 2, rather than the (MeV)[$Fe_2(Fan)_3$] family of compounds described in Chapter 4.

The asymmetric unit of **5.1** comprises one crystallographically unique Fe centre, three unique $Clan^{n-}$ ligands (**L_1**, **L_2** and **L_3**) and one MeV^{m+} cation each residing on inversion centres, and three well ordered MeCN molecules. Every Fe centre resides in a slightly distorted octahedral coordination environment, coordinated to six O donor atoms of three bis-bidentate $Clan^{n-}$ ligands. The distortion away from perfect octahedral geometry was quantified using Continuous Shape Measure (CShM)[10, 11] parameters (Table 5.1). The $Clan^{n-}$ ligands bridge each Fe centre to three other Fe centres, giving an anionic network composition of $[Fe_2(Clan)_3]^{x-}$. Each Fe centre of a given configuration (Δ or Λ) links to three centres of opposite configuration (Λ or Δ), affording an anionic network with the familiar (6,3) honeycomb sheet topology (Figure 5.1a). Given the low triclinic symmetry of **5.1**, there is unsurprisingly significant distortion of the network away from perfect hexagonal geometry, with Fe···Fe···Fe angles of 113.34°, 115.48° and 131.14°. The mean planes of the anionic $[Fe_2(Clan)_3]^{x-}$ sheets (defined as through the Fe centres) are parallel with the (111) plane, which is inclined by an angle of 74.04° to the (001) plane i.e. *ab* plane. The planes of the anionic $[Fe_2(Clan)_3]^{x-}$ sheets are therefore inclined from the crystallographic *c* axis, in contrast to the **3.1^{X}** and **4.1** series of compounds in which the planes of the anionic $[Fe_2(Xan)_3]^{2-}$ sheets lie perpendicular to the crystallographic *c* axis. When **5.1** is viewed down the crystallographic *a* axis, the configuration of all Fe centres in a column parallel to the *a* axis is all Δ or Λ, so the sheet stacking is AAAA, with a sheet-to-sheet spacing of 7.268 Å (Figure 5.1b).

Table 5.1 Analysis of the possible Fe coordination geometries in (MeV)[$Fe_2(Clan)_3$]·6MeCN (**5.1**) quantified using CShM parameters.

Site	Coordination Geometry (Symmetry)				
	HP-6 (D_{6h})	**PPY-6 (C_{5v})**	**OC-6 (O_h)**	**TPR-6 (D_{3h})**	**JPPY-6 (C_{5v})**
Fe1	33.611	21.770	**1.961**	9.188	25.577

HP-6: Hexagon; PPY-6: Pentagonal pyramid; OC-6: Octahedron; TPR-6: Trigonal prism; JPPY-6: Johnson pentagonal pyramid J2

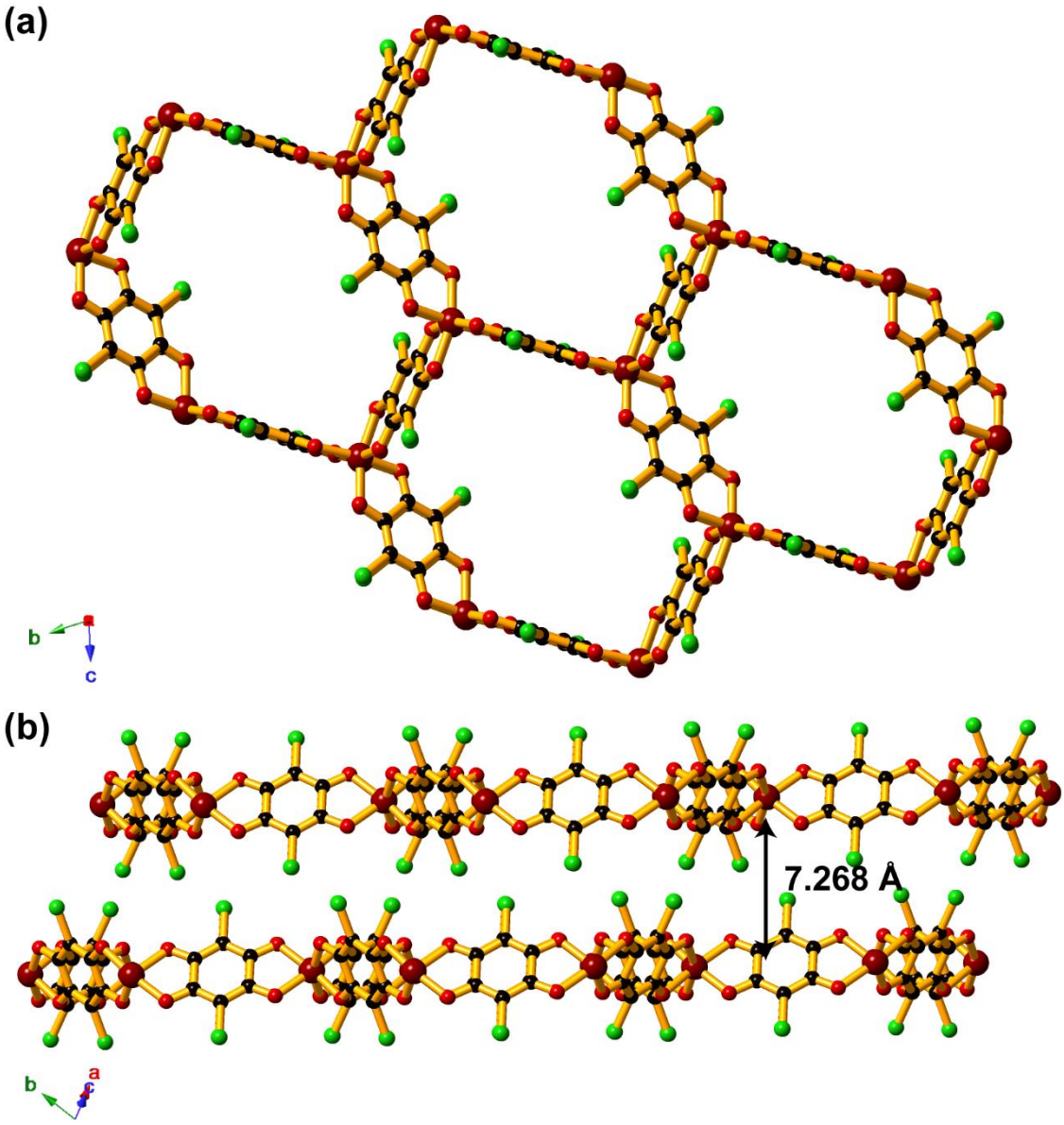


Figure 5.1 The anionic $[Fe_2(Clan)_3]^{x-}$ (6,3) honeycomb sheets in **5.1** viewed (a) down the crystallographic *a* axis and (b) along the plane of the anionic sheets parallel to the crystallographic (111) plane. Maroon = Fe, green = Cl, red = O, and black = C.

Charge-balancing MeV^{m+} cations are situated between these anionic sheets, sandwiched between $\mathbf{L_1}$ ligands in the sheets above and below (Figure 5.2). Like the **3.1**$^{\mathbf{X}}$ family, the location of the cation probably results from a combination of Coulombic and charge-transfer (CT) interactions between the electron-deficient MeV^{m+} cations and the anionic $[Fe_2(Clan)_3]^{x-}$ sheets, in addition to favourable shape complementarity.

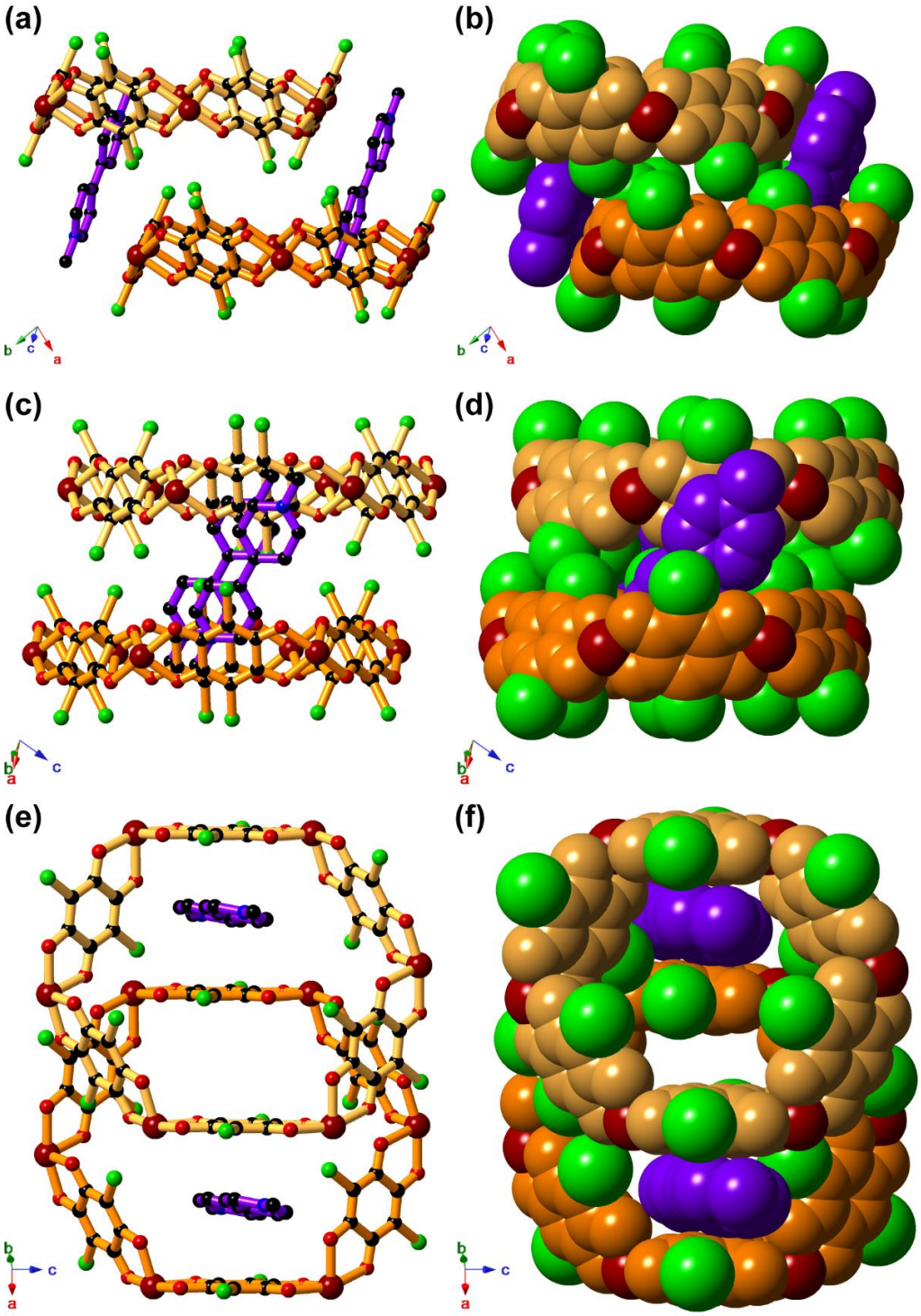


Figure 5.2 Ball-and-stick (a, c, e) and spacefilling (b, d, f) representations of the interactions of the MeV^{m+} cations (purple) with the anionic $[Fe_2(Clan)_3]^{x-}$ sheets above (tan) and below (orange) in **5.1**. Views along the (a–d) crystallographic (111) plane and along (e, f) one-dimensional channels. Maroon = Fe, green = Cl, red = O, blue = N, and black = C. H atoms and ordered MeCN in channels not shown for clarity.

There are also short C–H···O interatomic contacts ($d_{H\cdots O}$ = 2.315 and 2.488 Å) between the H3, H3′, H5, H5′ hydrogen atoms of MeV^{m+} and coordinated O atoms of **L₃** ligands above and below which help pin the cation in place (Figure 5.3). The location of MeV^{m+} in **5.1** contrasts strongly with the location of MeV^{2+} in the **4.1** family of compounds. For the **4.1** family, MeV^{2+} cations reside completely within the distorted hexagonal cavity of the honeycomb $[Fe_2(Fan)_3]^{2-}$ sheets, resulting in only weak non-covalent intersheet interactions. This disparity possibly arises from the different sizes of F versus Cl substituents in **4.1** and **5.1** respectively. Notably, there are significant C–F···F–C close contacts resulting from anionic sheet stacking in *mP* **4.1a** ($d_{F\cdots F}$ = 2.721 and 2.830 Å). These contacts could be incompatible with the larger atomic radius of Cl, so that (MeV)$[Fe_2(Clan)_3]$ cannot adopt the same sheet stacking and cation packing arrangement as the **4.1** family. The location of MeV^{m+} cations between the $[Fe_2(Clan)_3]^{x-}$ sheets gives the initial impression that spacious channels are formed when viewed down the crystallographic *a* or *b* axis (Figure 5.4). However, these framework voids are filled with six highly ordered MeCN molecules per formula unit, which completely occlude the channels. The ordering of MeCN within the channels suggests this solvent plays an important role in templating the structure.

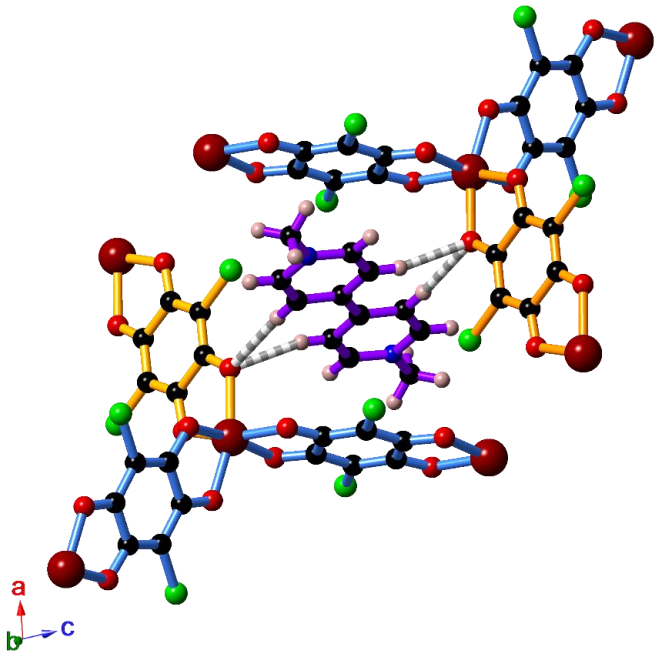


Figure 5.3 C–H···O interactions (dashed grey) between MeV^{m+} (purple) and **L₃** (yellow) in anionic $[Fe_2(Clan)_3]^{x-}$ sheets above and below. **L₁** and **L₂** in pale blue. Maroon = Fe, green = Cl, red = O, blue = N, black = C, and pale pink = H.

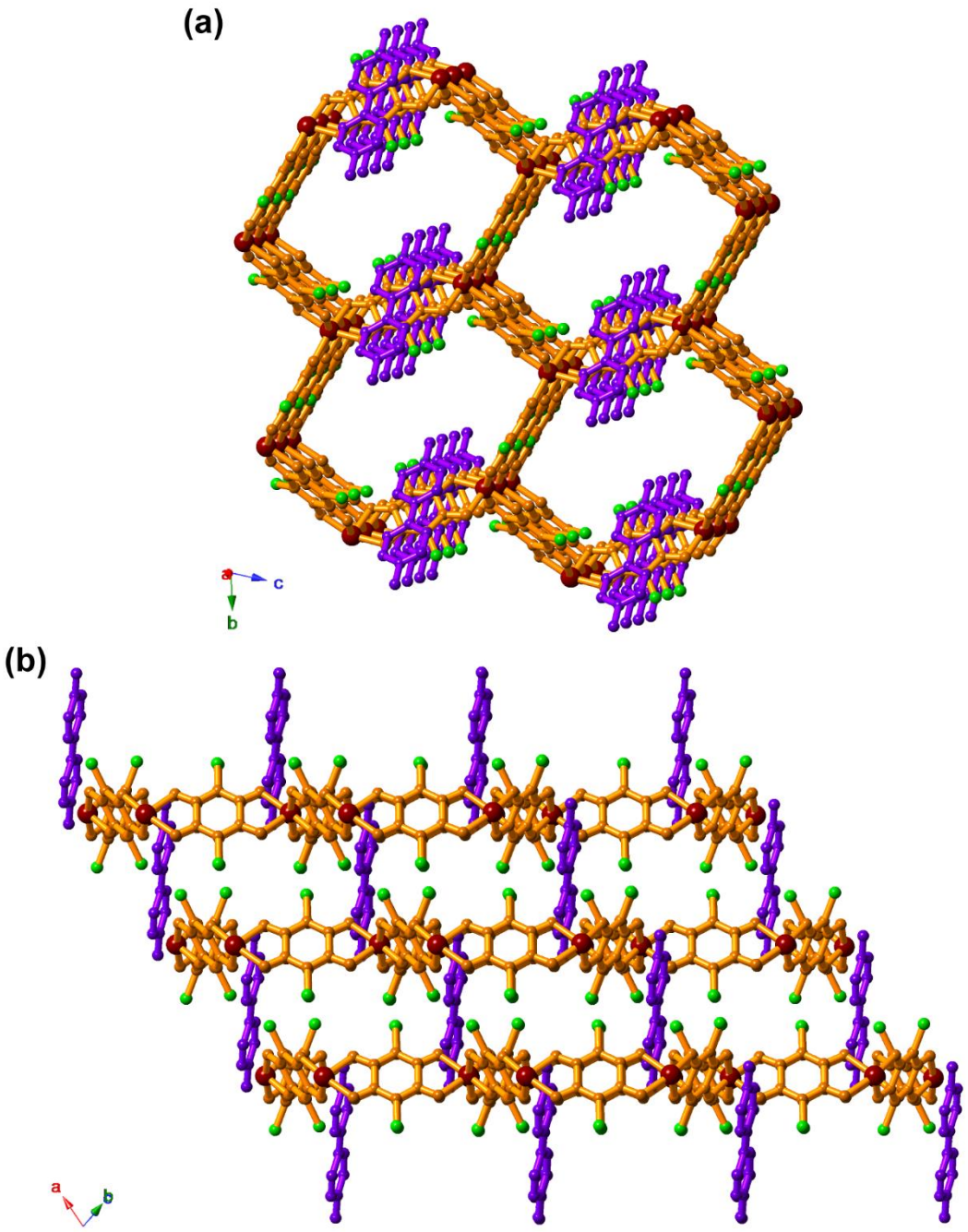


Figure 5.4 Alternating stacking of MeV^{m+} (purple) with $\mathbf{L_1}$ ligands in the anionic $[Fe_2(Clan)_3]^{x-}$ sheets (orange) in **5.1**. View down the (a) crystallographic *a* axis showing hexagonal channels and AAAA stacking. (b) View in the plane of the anionic $[Fe_2(Clan)_3]^{x-}$ sheets. Maroon = Fe, and green = Cl. H atoms and ordered MeCN in channels not shown for clarity.

5.2.2 Crystallographic Determination of Oxidation States

The oxidation states of Fe, Clan^{n-} and MeV^{m+} in **5.1** were determined from mean Fe–O ($d_{Fe–O}$), mean diagnostic ligand ($d_{C–O}$ and $d_{C–C}$) and cation ($d_{C–C}$ and $d_{C–N}$) bond lengths, as with the **3.1^{X}** and **4.1** families of compounds. Although the isostructural Mn compound (**2.2a**) is not diamagnetic, previous analysis showed the ligands and cation to exist unambiguously in the Clan^{2-} and MeV^{2+} oxidation states respectively, allowing **2.2a** to be used as a $[M^{II}_2(Clan^{2-})_3]^{2-}$ reference. To date, all attempts to produce a diamagnetic Zn^{II} analogue of **5.1** have proven unsuccessful, with analogous attempts using Cd^{II} yielding only the diamondoid **2.1$_{Cd}$** coordination polymer described in Chapter 2. For **5.1**, there are several points of evidence supporting a ligand charge-ordered $(MeV^{2+})[Fe^{III}_2(Clan^{2-})(Clan^{3-\bullet})_2]$ formulation, in contrast to the $(MeV^{2+})[Mn^{II}_2(Clan^{2-})_3]$ formulation for **2.2a**. At 100 K, $d_{C–C}$ and $d_{C–N}$ values for the MeV^{m+} cations in **5.1** closely match those of the MeV^{2+} cations in **2.2a**, in addition to MeV^{2+} in various salts.[12, 13] In **5.1**, there is no evidence of bond length alternation in the pyridinium rings, which would otherwise suggest semiquinonoid character consistent with the MeV$^{+\bullet}$ oxidation state.[14, 15] In particular, the central C–C bond is well known to be diagnostic of oxidation state in viologens.[14-16] In **5.1**, this central $d_{C–C}$ (C23–C23′) value is 1.483(4) Å, consistent with that observed in MeV^{2+}.[12, 13] These factors allow the network charge state to be formulated as $[Fe_2(Clan)_3]^{2-}$.

The mean ligand $d_{C–O}$ values in **5.1** are 1.292(2) Å and 1.289(2) Å for **L$_1$** and **L$_2$** respectively (Figure 5.5). The corresponding characteristic $d_{C–C}$ values across the five-membered chelate rings (C2–C4′ for **L$_1$**; C8–C10′ for **L$_2$**;) are 1.479(3) Å for **L$_1$**, and 1.483(3) Å for **L$_2$**. Comparison of these $d_{C–O}$ and $d_{C–C}$ values with those observed in **2.2a** and other metal–chloranilate compounds (see Appendix A), strongly suggests that **L$_1$** exists in the Clan$^{3-\bullet}$ state (expected bond length ranges: $d_{C–O}$ = 1.291–1.316 Å; $d_{C–C}$ = 1.431–1.473 Å). The values for **L$_2$** fall just outside these expected ranges, though this deviation is only minor, so that **L$_2$** is similarly present in the Clan$^{3-\bullet}$ valence state. For **L$_3$**, the $d_{C–O}$ and $d_{C–C}$ (C14–C16′) values are 1.269(2) Å and 1.523(3) Å respectively. Therefore, **L$_3$** unambiguously exists in the oxidised Clan^{2-} state, as the values fall within the expected bond lengths ranges for Clan^{2-} ($d_{C–O}$ = 1.248–1.272 Å; $d_{C–C}$ = 1.506–1.551 Å; Appendix A). The network consequently exhibits ligand-centred mixed valency and possesses a ligand charge-ordered structure, due to the inequivalence of **L$_1$**, **L$_2$** and **L$_3$**.

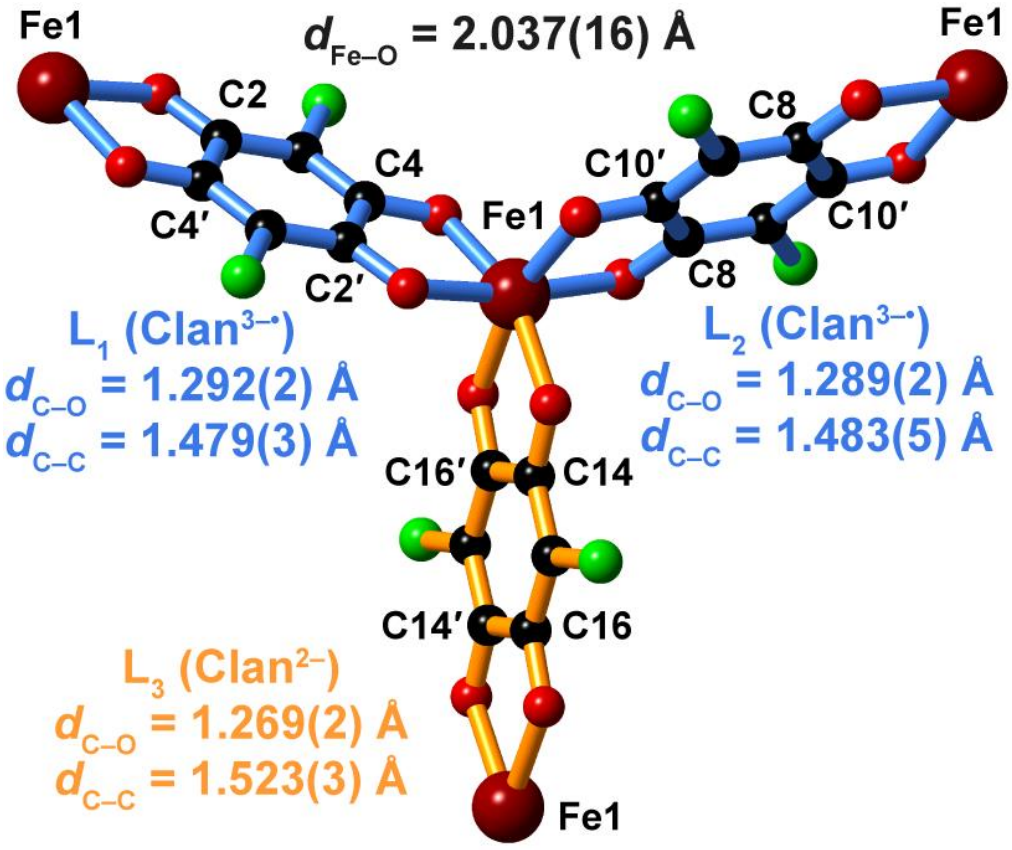


Figure 5.5 Characteristic Clan^{n-} bond lengths and coordination environment around Fe in **5.1** at T = 100 K.

As with other mixed-valence Fe–tetraoxolene frameworks reported in this thesis and in the literature, ligand-centred mixed valency arises due to spontaneous electron transfer from Fe^{II} to $Clan^{2-}$, affording Fe^{III} and $Clan^{3-\bullet}$ states. At 100 K, the mean d_{Fe-O} values are 2.010(4), 2.011(3) and 2.091(12) Å for **L₁**, **L₂** and **L₃** respective, with an overall mean d_{Fe-O} = 2.037(16) Å. The mean d_{Fe-O} value is reasonably consistent with that expected for high-spin Fe^{III} (Fe^{III}_{HS}) and also those observed in other mixed-valence Fe^{III}–tetraoxolene frameworks (Table A.4). Elongation of Fe–O bonds between Fe and **L₃**, compared to Fe and **L₁** or **L₂**, probably arises due to weaker Coulombic interaction between Fe^{III}_{HS} and $Clan^{2-}$, compared to Fe^{III} and $Clan^{3-\bullet}$. Similar elongation of these bonds between Fe^{III}_{HS} and Xan^{2-} was noted in Chapter 4 for the **4.1** family, and has also been observed in $(^{n}Pr_4N)_2[Fe_2(Clan)_3]$.[7, 17] The Fe–Fe distance is also commensurately elongated across **L₃** to 7.9926(5) Å, compared to Fe–Fe distances across **L₁** and **L₂** of 7.8500(5) and 7.8463(3) Å respectively. Similar

behaviour has been observed in the **4.1** family, $(^{n}Pr_4N)_2[Fe_2(Clan)_3]$,[7, 17] and $(Me_4N)_2[FeCl_2(Clan)]$.[18] This likely arises due to different Coulombic interaction strength between Fe^{III}_{HS} and the different ligand charge states.[7] This combination of factors all reinforce the idea that the framework exhibits a charge-ordered $(MeV^{2+})[Fe^{III}_2(Clan^{2-})(Clan^{3-\bullet})_2]$ formulation, similar to the low temperature charge-ordered state of $(^{n}Pr_4N)_2[Fe^{III}_2(Clan^{2-})(Clan^{3-\bullet})_2]$.[7, 17] As with this compound, the anionic honeycomb $[Fe_2(Clan)_3]^{2-}$ sheets in **5.1** are formed from paramagnetic pseudo-1D $\{Fe^{III}–Clan^{3-\bullet}\}_\infty$ chains knitted together with diamagnetic $Clan^{2-}$ (**L₃**) ligands (Figure 5.6). Localisation of at least one ligand valence state (**L₁**) possibly arises due to strong CT interaction between electron-deficient MeV^{2+} and electron-rich **L₁** ($Clan^{3-\bullet}$), promoted by the alternating stacking of these components together. The CT interaction is also supplemented by attractive Coulombic interactions, which are stronger between $Clan^{3-\bullet}$ and MeV^{2+} than putative $Clan^{2-}$ and MeV^{2+}, which aid to localise $Clan^{3-\bullet}$.

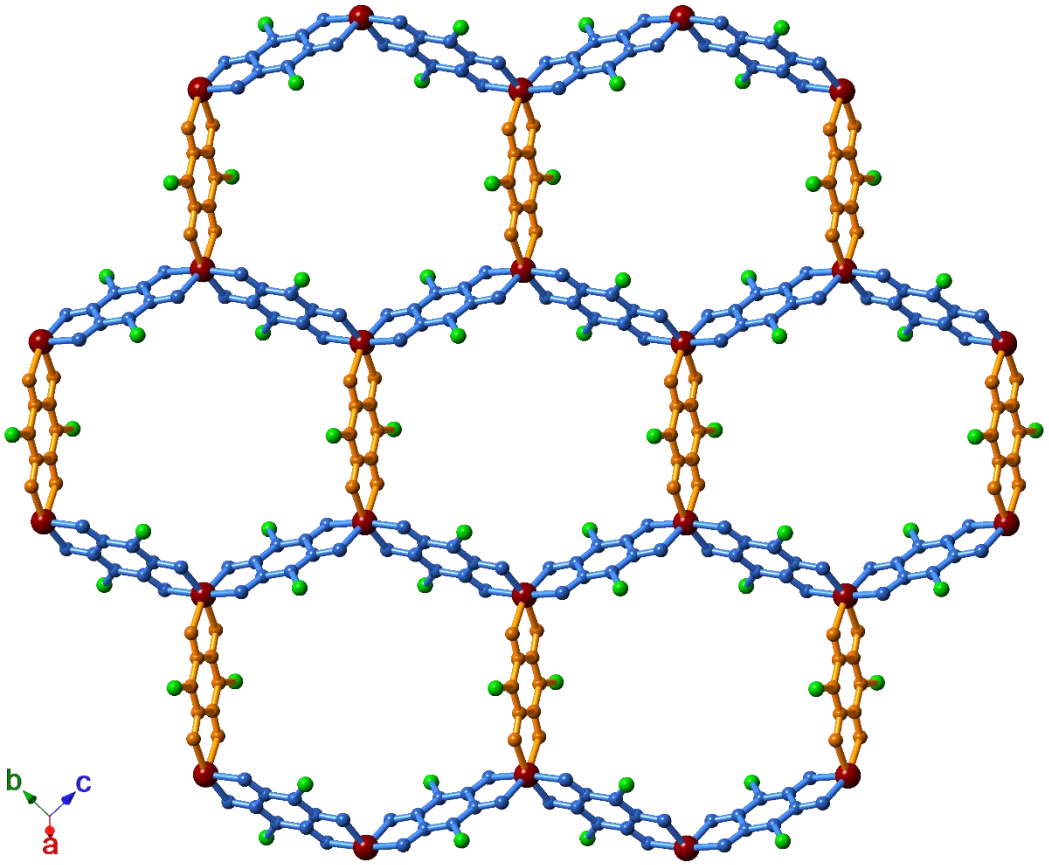


Figure 5.6 Arrangement of **L₁**, **L₂** (pale blue, $Clan^{3-\bullet}$) and **L₃** (tan, $Clan^{2-}$) ligands forming pseudo-1D $\{Fe^{III}–Clan^{3-\bullet}\}_\infty$ chains bridged by **L₃** producing the anionic $[Fe_2(Clan)_3]^{2-}$ sheets in **5.1**. Maroon = Fe, green = Cl.

5.2.3 Variable-Temperature Single-Crystal X-ray Diffraction

Given the identical ligand charge-ordered $[Fe^{III}_2(Clan^{2-})(Clan^{3-\bullet})_2]^{2-}$ formulations for **5.1** and $(^nPr_4N)_2[Fe_2(Clan)_3]\cdot 2(Acetone)\cdot H_2O$,[7] we were intrigued by the possibility that **5.1** could exhibit thermally-induced valence tautomerism. To date, this behaviour has only been observed in Fe–tetraoxolene coordination polymers exhibiting valence localised $Xan^{3-\bullet}$ states,[7, 17, 18] though the origin of this behaviour is not well understood compared to valence tautomerism in Mn– or Co–dioxolene complexes.[19, 20] Variable-temperature SC-XRD was performed by warming the sample from 100 K to 260 K to investigate the presence of thermally-induced valence tautomerism. Thermal variation of the unit cell parameters demonstrates the expected expansion of the unit cell upon warming (Figure 5.7).

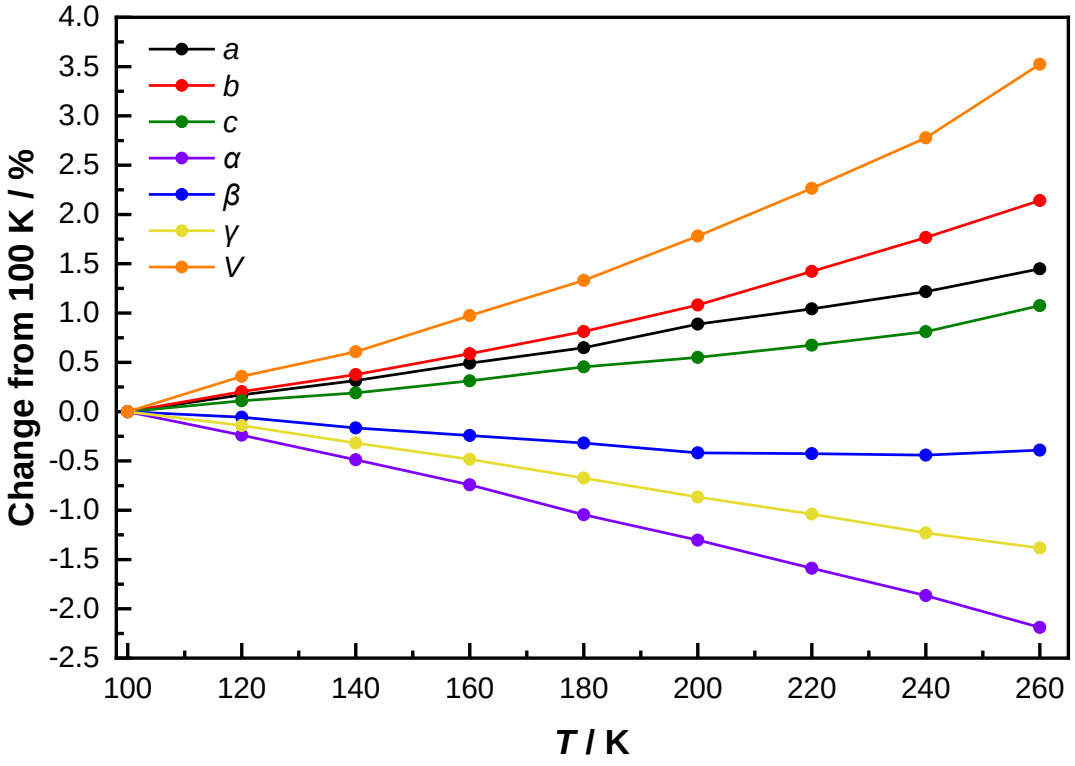


Figure 5.7 Temperature dependence of the unit cell parameters (*a*, *b*, *c*, *α*, *β*, *γ* and *V*) as measured by SC-XRD for **5.1**. All values are normalised to those observed at T = 100 K.

From 100–260 K, $d_{C–O}$ values in **L₁** range from 1.285–1.294 Å, with the $d_{C–C}$ values varying in the range 1.475–1.484 Å (Figure 5.8). Although some values lie just outside the expected ranges of $d_{C–O}$ = 1.291–1.316 Å and $d_{C–C}$ = 1.431–1.473 Å for $Clan^{3–\bullet}$ ligands, the deviation from the expected values is small, suggesting that **L₁** remains in the $Clan^{3–\bullet}$ state over the entire temperature range. This is expected, arising from the intimate face-to-face interaction between electron-deficient MeV^{2+} and more electron-rich **L₁** $Clan^{3–\bullet}$ ligand. This CT interaction possibly limits thermally-induced electron transfer from **L₁**, by a combination of energetically favourable CT and Coulombic interactions stabilising the **L₁** site in the $Clan^{3–\bullet}$ valence state. Thermal variation of the **L₃** bond lengths is similarly minimal, with $d_{C–O}$ values in the range 1.267–1.271 Å, and $d_{C–C}$ varying between 1.515–1.523 Å. These values are within the ranges of $d_{C–O}$ = 1.248–1.272 Å and $d_{C–C}$ = 1.506–1.551 Å expected for the $Clan^{2–}$ state, demonstrating no thermally-induced valence state change of **L₃**. This is expected, as thermally-induced valence tautomerism in Fe–dioxolene or Fe–tetraoxolene compounds occurs only from the low temperature $\{Fe^{III}–Diox^{2–}\}$ or $\{Fe^{III}–Clan^{3–\bullet}\}$ states, to $\{Fe^{II}–Diox^{–\bullet}\}$ or $\{Fe^{II}–Clan^{2–}\}$ states at high temperature,[7, 17, 18, 21] rather than $\{Fe^{III}–Clan^{2–}\}$ to $\{Fe^{II}–Clan^{–\bullet}\}$. In contrast to **L₁** and **L₃**, the temperature dependence of $d_{C–O}$ and $d_{C–C}$ values for **L₂** is less instructive of oxidation state. Between 100–260 K, the $d_{C–O}$ values decrease from 1.290(2) Å to 1.278(6) Å, while $d_{C–C}$ increased from 1.482(3) Å to 1.502(9) Å. This appears to indicate a transition of **L₂** from the $Clan^{3–\bullet}$ to a state intermediate between $Clan^{3–\bullet}$ and $Clan^{2–}$, presumably by electron transfer to a Fe^{III} site. This behaviour is also supported by elongation of $d_{Fe–O}$ from 2.038(14) Å at 100 K to 2.053(9) at 260 K, with corresponding bond valence sum (BVS) values of 2.84 and 2.71 at 100 K and 260 K respectively.

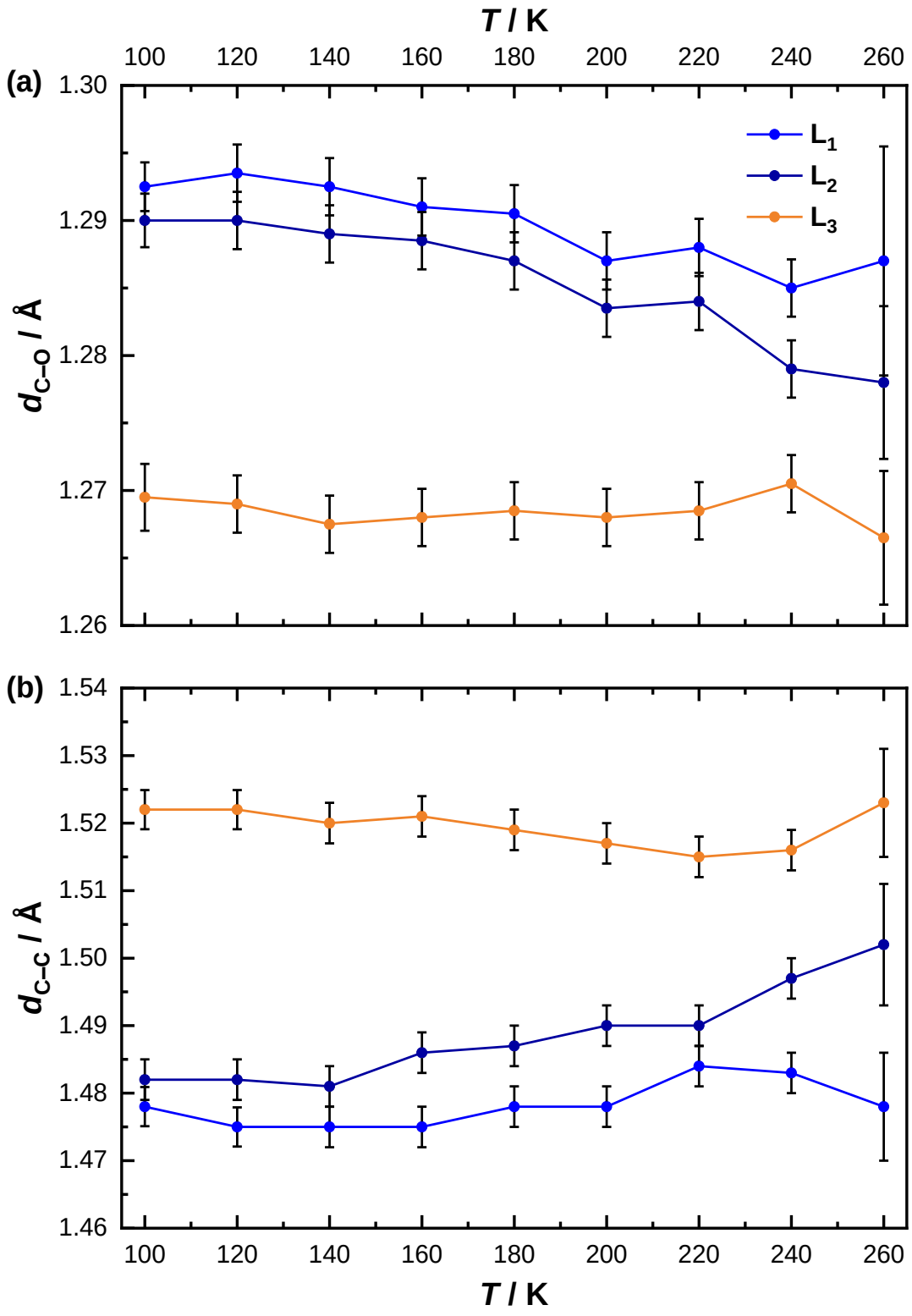


Figure 5.8 Temperature dependence of the characteristic ligand (a) $d_{C–O}$ and (b) $d_{C–C}$ values in **5.1** as measured by SC-XRD. Error bars are ± s.u.

The apparent gradual variation of $\mathbf{L_2}$ valence state contrasts with the sharp thermally-induced valence tautomerism observed in $(^{n}Pr_4N)_2[Fe_2(Clan)_3]\cdot 2(Acetone)\cdot H_2O$,[7] or $(Me_4N)_2[FeCl_2(Clan)]$.[18] In both these compounds, the valence tautomeric transition from the $\{Fe^{III}–Clan^{3-\bullet}\}$ to $\{Fe^{II}–Clan^{2-}\}$ states occurred over a narrow 20 K window, observed via SC-XRD and static magnetic susceptibility measurements,[7] or Raman and ^{57}Fe Mössbauer spectroscopy.[18] Miyasaka and co-workers recently demonstrated that the valence tautomeric transition temperature $T_{1/2}$ = 236 K for $(^{n}Pr_4N)_2[Fe_2(Clan)_3]\cdot 2(Acetone)\cdot H_2O$ increased to $T_{1/2}$ = 317 K upon desolvation.[17] The desolvated compound also transitioned through an intermediate partially charge-ordered $(^{n}Pr_4N)_2[Fe^{2.5}{}_2(Clan^{2-})(Clan^{2.5-})_2]$ state. This behaviour was ascribed to modification of the Coulombic interactions between anionic network and the $^{n}Pr_4N^{+}$ cations upon desolvation, which altered the relative stability of the $(^{n}Pr_4N)_2[Fe^{III}{}_2(Clan^{2-})(Clan^{3-\bullet})_2]$ and $(^{n}Pr_4N)_2[Fe^{II}Fe^{III}(Clan^{2-})_2(Clan^{3-\bullet})]$ tautomers. Despite the ambiguity of a valence tautomeric transition in **5.1**, these results further reinforce the conclusions drawn for **2.5**, $\mathbf{3.1^{Cl}a}$ and *mP* **4.1a**, namely that CT and Coulombic interactions imparted by π-electron deficient cations enforce stable localisation of the $Xan^{3-\bullet}$ valence state.

5.2.4 Structural Transformations

5.2.4.1 Structure Identification

The phase purity of a bulk sample of **5.1** was investigated by synchrotron P-XRD analysis (Figure 5.9). The P-XRD pattern was first measured as a slurry in MeCN, to maintain the solvation state of the framework, as desolvation-induced structural distortions are well known in similar compounds, such as $(Me_2NH_2)_2[Fe_2(Clan)_3]$,[22, 23] $(^{n}Pr_4N)_2[Fe_2(Clan)_3]$,[17] $\mathbf{3.1^{Cl}a}$ and the **4.1** family. Gratifyingly, excellent agreement between the experimental and calculated P-XRD patterns is observed, with the experimental pattern satisfactorily indexed with unit cell parameters matching those determined by SC-XRD. The differences between the relative reflection intensities between the calculated and experimental patterns is probably due to minor preferred orientation effects in the P-XRD sample. Nevertheless, these results demonstrate bulk **5.1** contains only the single expected crystalline phase.

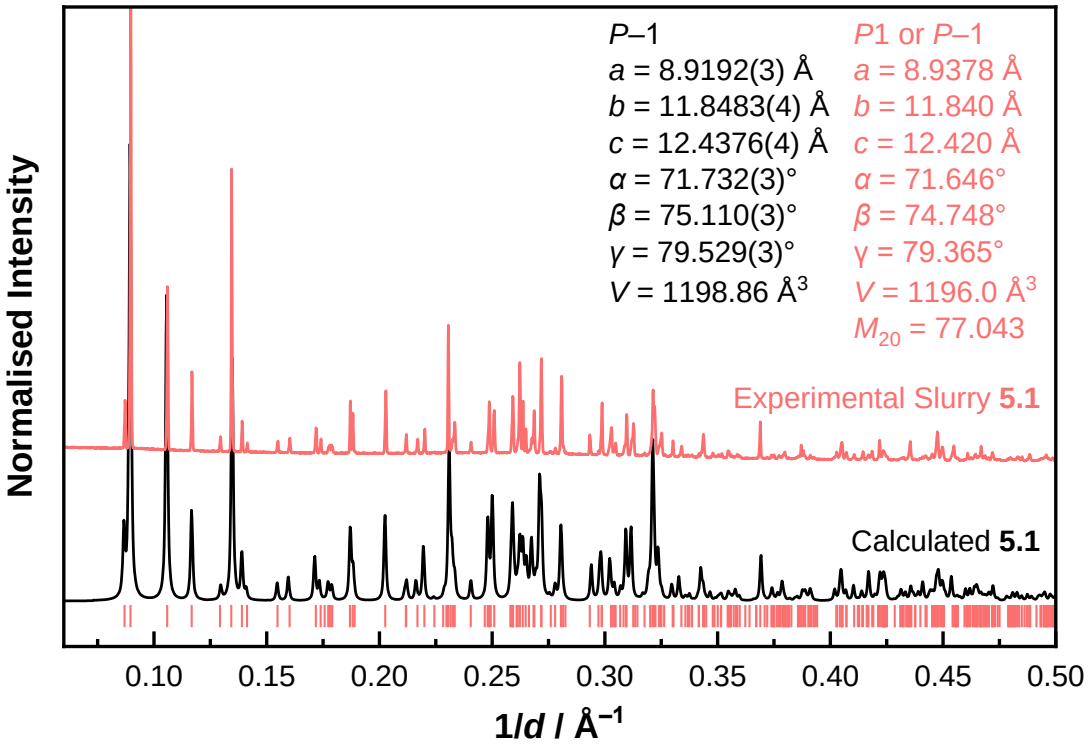


Figure 5.9 Synchrotron P-XRD (λ = 0.58835 Å) pattern of an MeCN slurry of bulk **5.1** (pale red, T = 250 K), and calculated pattern (black, T = 240 K) from SC-XRD of **5.1**. Tick marks (pale red) indicate the positions of the allowed reflections of the unit cell indexed from the experimental P-XRD pattern.

As with other Fe–tetraoxolene frameworks reported in this thesis that were handled under inert atmosphere conditions, we envisaged workup and isolation of **5.1** could cause framework desolvation. Specifically, placing an isolated sample of **5.1** under static vacuum in a Schlenk frit, before transfer into a N_2-filled glovebox could cause partial desolvation, putatively generating a new phase as observed for the transition of *mP* **4.1a** to *aP* **4.1a**. Desolvation in Fe–tetraoxolene frameworks is known to cause geometric distortion[22, 23] and phase transitions,[17] which impact upon the electronic structure and physical properties. Insight into any structural transition is therefore essential in understanding framework properties. Comparing the synchrotron P-XRD pattern of isolated **5.1** following transfer into an N_2-filled glovebox, with the synchrotron P-XRD pattern of **5.1** as an MeCN slurry reveals stark differences (Figure 5.10). This is particularly apparent at low 1/*d* values, where additional peaks are observed in the P-XRD pattern of the isolated **5.1** (Figure 5.10, red). Despite the

different measurement temperatures used for slurry and isolated P-XRD samples of **5.1**, the disparity between the P-XRD patterns cannot be ascribed to thermally-induced variation of the unit cell parameters. Variable-temperature SC-XRD measurements revealed only minor changes (< 5%) to the unit cell parameters of **5.1** between 100–260 K (Figure 5.7), which are inconsistent with the marked changes in Bragg reflection positions observed in the P-XRD pattern of isolated **5.1** (Figure 5.10). This unambiguously indicates that as-synthesised **5.1** undergoes a structural transformation upon isolation and putative solvent loss; the isolated compound is subsequently referred to as **5.2**.

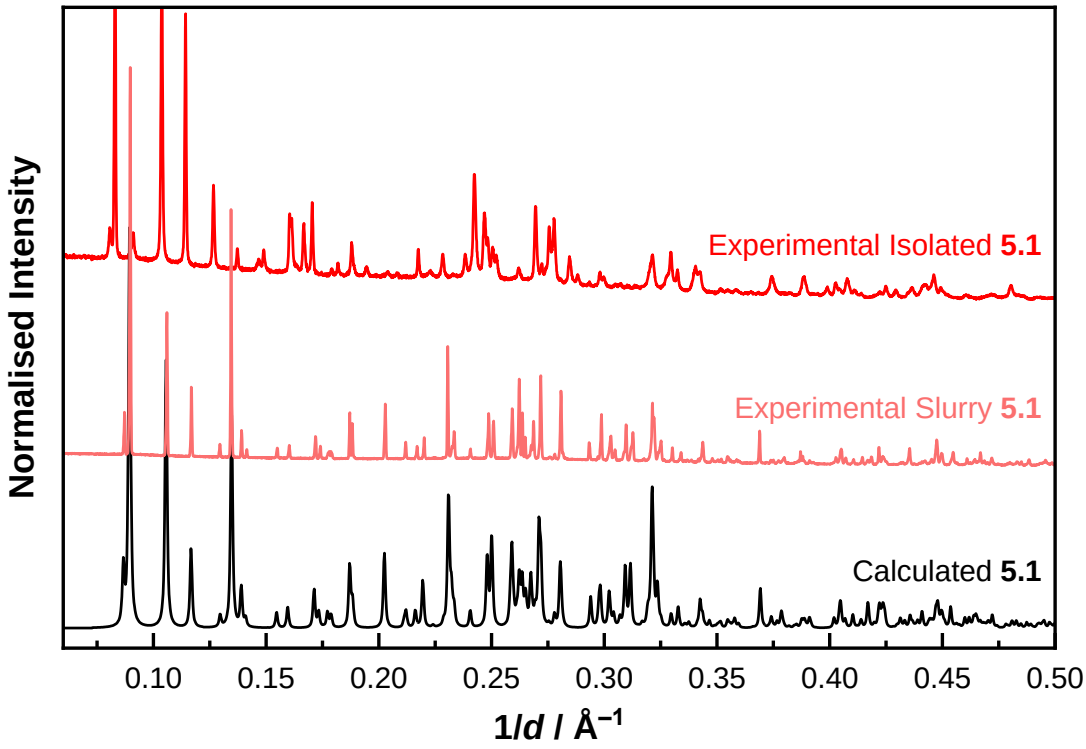


Figure 5.10 Synchrotron P-XRD (λ = 0.58835 Å) pattern of isolated bulk **5.1** (**5.2**, red, T = 100 K), MeCN slurry of bulk **5.1** (pale red, T = 250 K), and calculated pattern (black, T = 240 K) from SC-XRD of as-synthesised **5.1**.

Further analysis of the P-XRD data was undertaken to better understand this transformation. The experimental P-XRD pattern of **5.2** was satisfactorily indexed with a triclinic cell of almost doubled volume compared to the as-synthesised unit cell volume (1955.2 Å^3 for **5.2**, compared to 1196.0 Å^3 for as-synthesised **5.1**). The unit cell lengths and angles were also markedly altered. Remarkably though, sufficient

crystallinity was observed in isolated crystals of **5.2** to allow SC-XRD analysis, despite the single crystals having been severely 'mistreated' by isolation and partial desolvation. Like isolated crystals of *aP* **4.1a**, the isolated crystals of **5.2** were severely twinned and exhibited significantly reduced reflection intensity, so that variable-temperature SC-XRD data sets were less than ideal using laboratory source instrumentation. Moreover, synchrotron instrumentation was not used, as the low triclinic symmetry of **5.2** would limit the data completeness obtainable using the Australian Synchrotron MX1 and MX2 beamlines. Nevertheless, following data collection using laboratory source instrumentation, a satisfactory structure refinement of **5.2** was found in the triclinic *P*−1 space group (Table 5.6), with the measured unit cell parameters closely matching the parameters determined from the experimental P-XRD pattern of bulk **5.2** (Figure 5.11). Additionally, no extraneous peaks were observed in the experimental P-XRD pattern, demonstrating transformation of as-synthesised **5.1** to **5.2**, remarkably with retention of crystallinity.

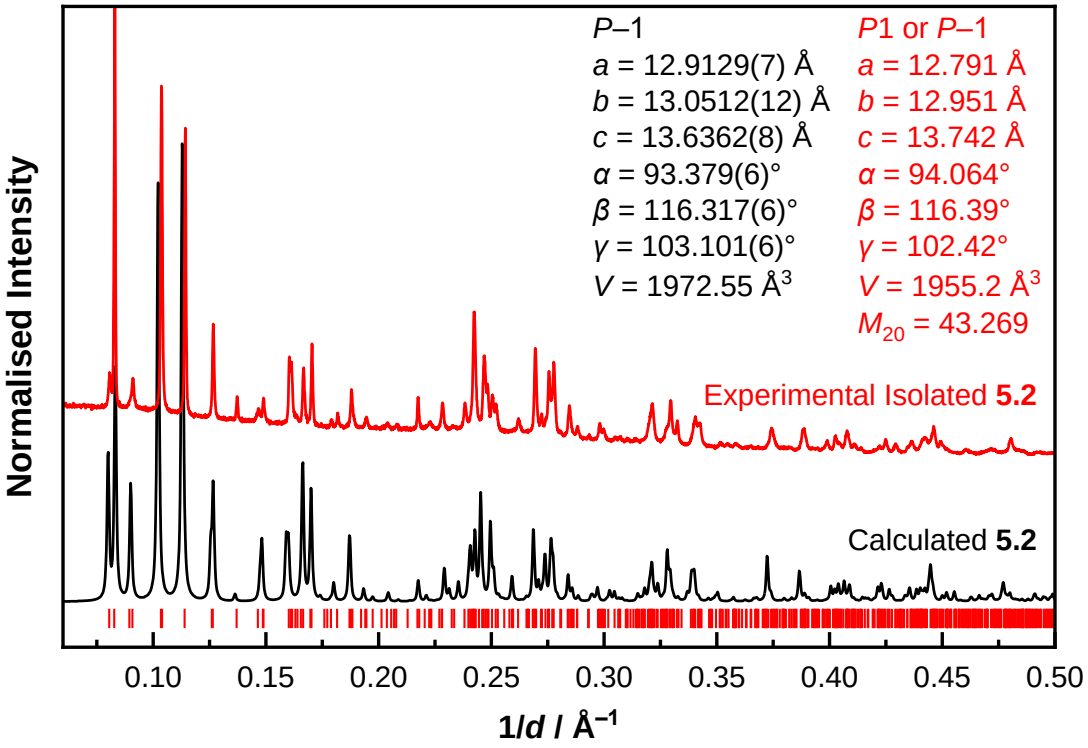


Figure 5.11 Synchrotron P-XRD (λ = 0.58835 Å) pattern of **5.2** (isolated **5.1**) (red, T = 100 K), and calculated pattern (black, T = 100 K) from SC-XRD of **5.2**. Tick marks (red) indicate the positions of the allowed reflections of the unit cell indexed from the experimental P-XRD pattern.

5.2.4.2 Structure Description

The significantly enlarged unit cell volume of **5.2**, is consistent with an asymmetric unit of twice the size of **5.1**. This is confirmed by comparing the contents of the asymmetric units between as-synthesised **5.1** and **5.2**. The asymmetric unit of as-synthesised **5.1** contains one unique Fe centre, and three unique Clan^{n-} ligands (**L$_1$**, **L$_2$** and **L$_3$**), each located on a centre of inversion and one MeV^{2+} cation situated on a centre of inversion; three well ordered MeCN molecules. In contrast, the asymmetric unit of **5.2** contains two unique Fe centres (Fe1 and Fe2), six unique Clan^{n-} ligands (**L$_1$**, **L$_2$**, **L$_3$**, **L$_4$**, **L$_5$**, **L$_6$**) each located on inversion centres, in addition to a MeV^{m+} cation placed on a general position. The structure of **5.2** maintains the same (6,3) honeycomb sheet topology as **5.1**, with each Fe centre coordinated to six O donor atoms of bridging bis-bidentate Clan^{n-} ligands. In contrast to **5.1** which contains only one type of anionic honeycomb [Fe$_2$(Clan)$_3$]$^{2-}$ layer, there are two different types of anionic honeycomb [Fe$_2$(Clan)$_3$]$^{x-}$ layers in **5.2**. In these two types of layers, Fe1 centres of Λ or Δ configuration are bridged by **L$_1$**, **L$_2$** and **L$_3$** only to Fe1 centres of Δ or Λ configuration. Fe2 are similarly only bridged to other Fe2 centres via **L$_4$**, **L$_5$** and **L$_6$**, thereby forming separate Fe1 and Fe2 layers. The anionic [Fe$_2$(Clan)$_3$]$^{x-}$ sheets are both parallel to the the crystallographic (010) plane, with a significantly reduced sheet-to-sheet spacing of 6.253 Å, compared to 7.267 Å in **5.1**.

The starkest difference between as-synthesised **5.1** and **5.2**, is the location of charge-balancing MeV^{m+} cations. In **5.1**, MeV^{m+} cations are located sandwiched between the anionic [Fe$_2$(Clan)$_3$]$^{2-}$ layers above and below (Figure 5.2), forming alternating stacks of MeV^{2+} and Clan$^{3-\bullet}$ (**L$_1$**) (Figure 5.4). By contrast, MeV^{m+} cations in **5.2** reside exclusively within the hexagonal cavity of the Fe2 anionic sheets, nestled near the vertex formed by an Fe2 centre, with each pyridinium ring of MeV^{m+} oriented towards **L$_4$** and **L$_5$** in the Fe2 layers (Figure 5.12). The hexagonal voids of the Fe1 anionic layers do not contain MeV^{m+} cations, and instead contain severely disordered MeCN solvent (*vide infra*). The location and orientation of MeV^{m+} in the hexagonal cavities of the Fe2 sheets is like that in *mP* or *aP* **4.1a**, and **4.1b**. Despite this, **5.2** is not isostructural with these compounds; in *mP* and *aP* **4.1a**, and **4.1b**, each hexagonal void contains only one MeV^{2+} molecule, whereas each hexagonal void in Fe2 layers of **5.2** is packed with two MeV^{m+} cations (Figure 5.12e & f). The long axis of MeV^{m+} in **5.2** is more inclined to the mean Fe2 plane (42.58°), compared to the inclination of

MeV^{2+} to the mean Fe plane in *aP* **4.1a** and **4.1b** (38.51°). Consequently, MeV^{m+} cations in **5.2** intrude slightly into hexagonal voids in the anionic sheets above and below (Figure 5.12a & c). The two MeV^{m+} cations are also pinned in position at either end by a line of three Cl atoms from $\mathbf{L_4}$, $\mathbf{L_5}$ and $\mathbf{L_6}$ in the Fe2 anionic layers (Figure 5.12e & f). The void space between the two MeV^{m+} molecules then forms a slot in which Cl atoms from $\mathbf{L_1}$ in the Fe1 anionic layers sit. Considering the locations of MeV^{m+} in **5.1** and **5.2**, the partial removal of MeCN from the framework voids allows MeV^{m+} cations to slip from their location sandwiched between two anionic sheets for **5.1**, to end up residing within the hexagonal channel of the Fe2 anionic sheet (Figure 5.13), as these hexagonal voids are no longer completely occupied by MeCN as in **5.1**. This dramatic structure rearrangement is probably allowed by the malleable conformation of MeV^{m+} about the central C–C bond. In **5.1**, the torsion between the pyridinium rings about the central C–C bond is only 0.4°, whereas in **5.2**, the inter-ring torsion about the central C–C axis is 44.4°.

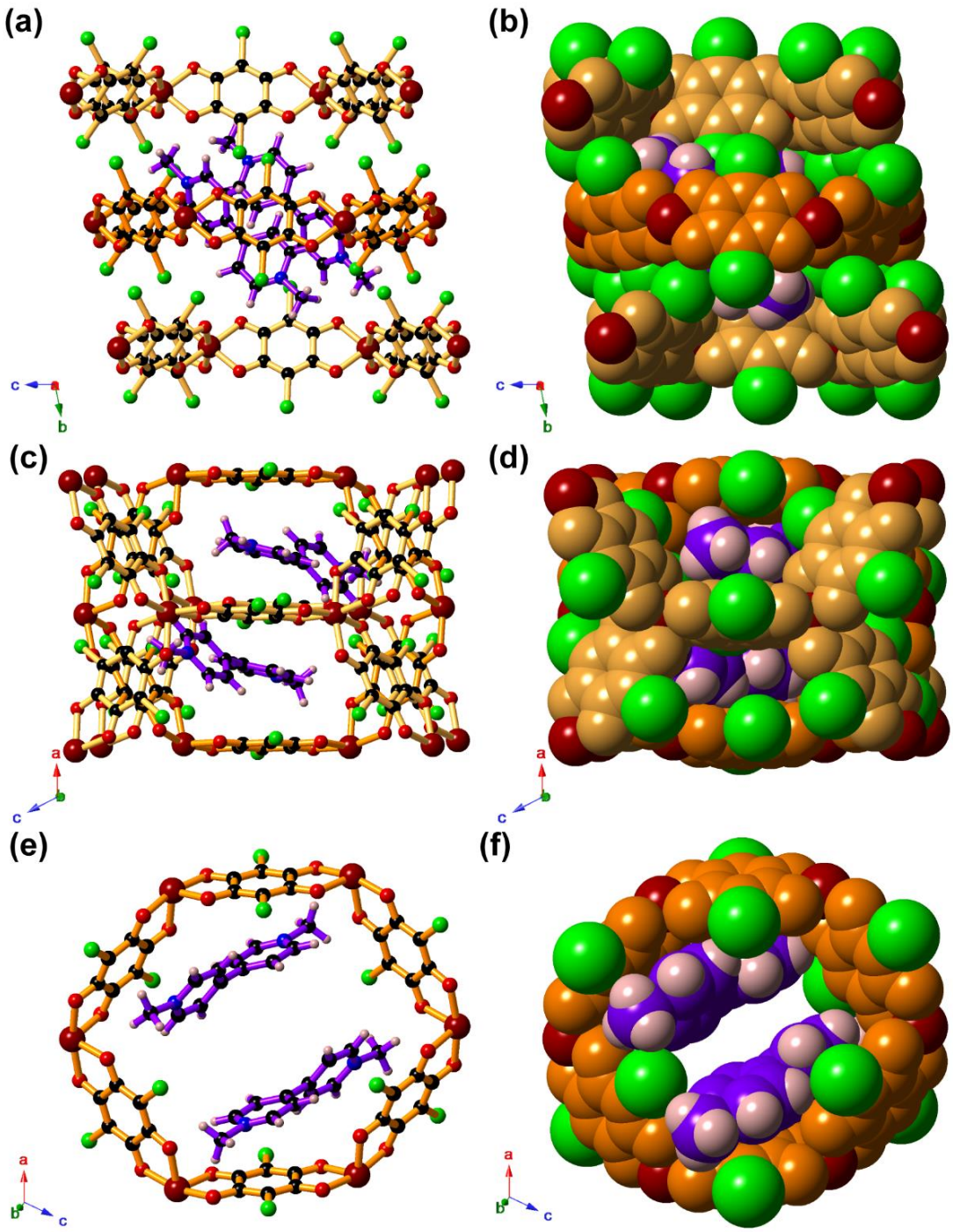


Figure 5.12 Ball-and-stick (a, c, e) and spacefilling (b, d, f) representations of the interactions of the MeV^{m+} cation (purple) with the Fe1 (tan) and Fe2 (orange) anionic $[Fe_2(Clan)_3]^{x-}$ layers in **5.2**. Views along the (a, b) crystallographic *a* axis and (c, d) *b* axis. (e, f) View of MeV^{m+} packing into the hexagonal void of the Fe2 anionic sheet. Maroon = Fe, green = Cl, red = O, blue = N, black = C, and pale pink = H.

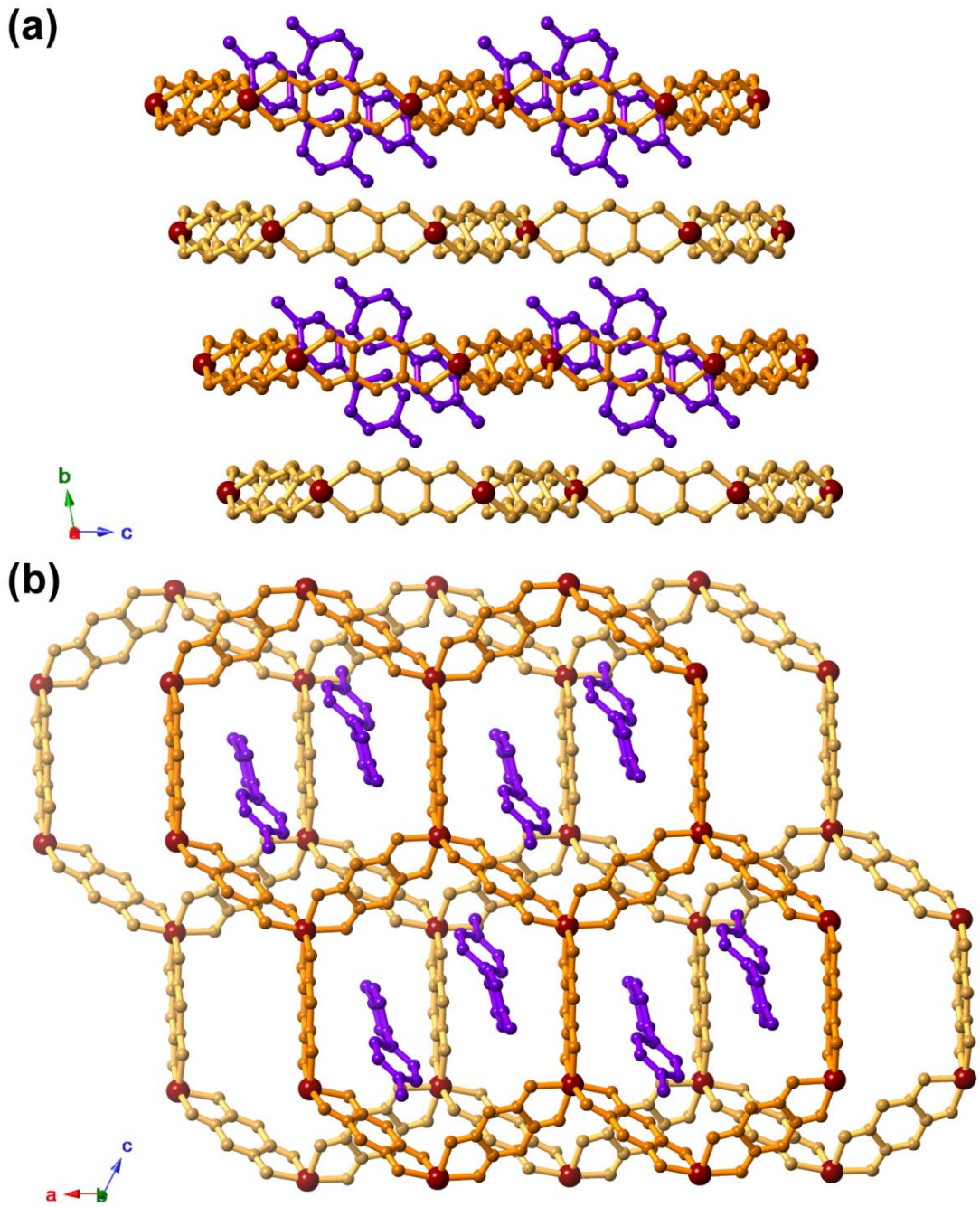


Figure 5.13 Stacking of the Fe1 (tan) and Fe2 (orange) anionic $[Fe_2(Clan)_3]^{x-}$ sheets, and location of the MeV^{m+} (purple) cations in **5.2**. View along the crystallographic (a) *a* axis and (b) *b* axis. Maroon = Fe. H and Cl atoms not shown for clarity.

Despite the location of MeV^{2+} cations nestled against the Fe2 centres, there is markedly less distortion from perfect hexagonal geometry in either the Fe1 or Fe2 anionic sheets, compared to the anionic sheets in **4.1a** or **5.1**. In **5.2**, the Fe···Fe···Fe angles are 110.86(2)°, 121.60(2)° and 127.51(2)° in the Fe1 anionic sheets, and 110.88(2)°, 120.34(2)° and 128.56(2)° in the Fe2 sheets; the largest angle in the Fe2 sheets unsurprisingly occurs at the Fe2 vertex closest to the MeV^{m+} cations. This contrasts with Fe···Fe···Fe angles of 104.00(1)°, 112.88(1)° and 143.12(1)° in *aP* **4.1a**. The structural transformation to **5.2** also causes a significant change to the coordination geometry about Fe1 and Fe2 compared to that in **5.1**, which was quantified using CShM parameters (Table 5.2).[10, 11, 24] For both Fe1 and Fe2, the coordination geometry moves towards perfect octahedral. The Fe2 sites exhibit a greater degree of geometric distortion than Fe1 sites because MeV^{m+} cations reside within the channels of the Fe2 anionic sheets, nestled against Fe2 centres.

Table 5.2 CShM analyses of the possible coordination geometries of the Fe sites in **5.1** and **5.2**.

Phase	Site	Coordination Geometry (Symmetry)				
		HP-6 (D_{6h})	**PPY-6** (C_{5v})	**OC-6** (O_h)	**TPR-6** (D_{3h})	**JPPY-6** (C_{5v})
5.1	Fe1	33.611	21.770	**1.961**	9.188	25.577
5.2	Fe1	31.195	23.610	**1.338**	11.433	27.381
	Fe2	32.145	22.079	**1.665**	10.704	25.792

HP-6: Hexagon; PPY-6: Pentagonal pyramid; OC-6: Octahedron; TPR-6: Trigonal prism; JPPY-6: Johnson pentagonal pyramid J2

Following refinement of the framework structure, inspection of the electron density difference (F_O–F_C) maps revealed significant residual positive electron density in the network voids. This was attributed to severely disordered MeCN solvent molecules, which could not be modelled satisfactorily. The scattering contribution of this disordered solvent was accounted for using the SQUEEZE[25] routine in PLATON.[26] The solvation in the voids was then estimated from the electron count determined by

SQUEEZE, assuming it comprised solely MeCN (2.7 MeCN per formula unit). Solvation exclusively by MeCN was justified by several considerations. The as-synthesised compound **5.1** crystallises with six MeCN per formula unit, despite crystallisation in a 2:1 v/v MeCN/H_2O solvent system. This solvation is maintained when the compound is placed exclusively in MeCN following workup by 2:1 v/v MeCN/H_2O and MeCN solvent washing, as demonstrated by P-XRD data (Figure 5.9). During workup, the crystalline product is maintained under rigorously anaerobic and anhydrous conditions, and washed only with anhydrous solvents, either using standard Schlenk techniques, or an N_2-filled glovebox with a closely monitored atmospheric moisture level of ca. 1 ppmv H_2O. Lastly, the ATR FT-IR spectrum of **5.2** does not show any intense broad absorptions in the region attributed to H_2O (ca. 3500 cm^{-1}), but does show an absorption ascribed to $\nu_{C\equiv N}$ of MeCN at ν = 2247 cm^{-1} (Figure 5.14, †).

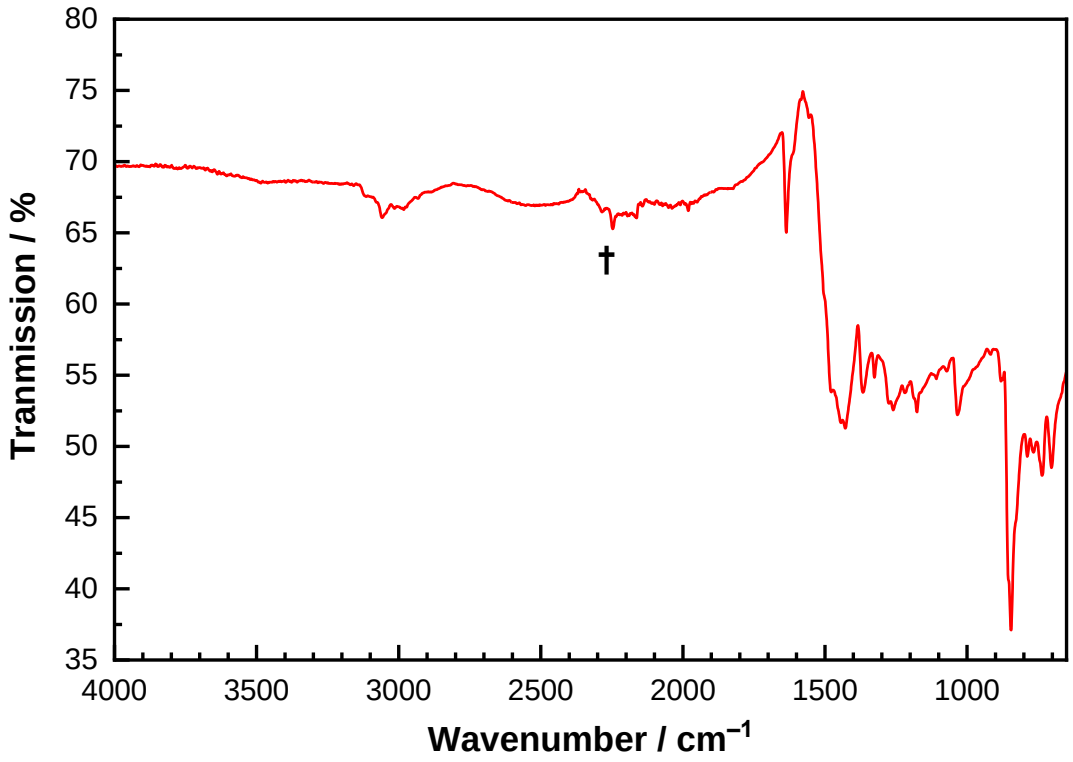


Figure 5.14 ATR FT-IR spectrum of **5.2** collected at room temperature in air.

5.2.4.3 Crystallographic Determination of Oxidation States

Due to severe twinning and sub-optimal diffraction quality (R_1 = 0.0973, wR_2 = 0.2852, for $I>4\sigma(I)$) exhibited by isolated crystals of **5.2**, the resultant C–C bond length precision (0.0108 Å) in **5.2** is less than for **5.1**. Therefore, definitive assignment of crystallographic Fe, $Clan^{n-}$ and MeV^{m+} oxidation states is more challenging in **5.2** compared to **5.1**. Nevertheless, there are several factors which suggest that **5.2** maintains the same charge-ordered $(MeV^{2+})[Fe^{III}_2(Clan^{2-})(Clan^{3-\bullet})_2]$ formulation as **5.1**. Comparison of $d_{C–C}$ and $d_{C–N}$ values for MeV^{m+} cations in **5.2**, with $d_{C–C}$ and $d_{C–N}$ values for structures containing MeV^{2+} or $MeV^{+\bullet}$,[13-15] tentatively suggest MeV^{m+} remains in the MeV^{2+} valence state in **5.2**. Charge neutrality therefore requires a network charge of $[Fe_2(Clan)_3]^{2-}$. The average $d_{Fe–O}$ values for Fe1 and Fe2 are 2.020(8) and 2.018(10) Å respectively, both of which lie within the expected range of Fe^{III}_{HS}, particularly those observed in mixed-valence Fe^{III}–tetraoxolene frameworks (Table A.4).[7-9, 17, 22, 23, 27, 28] The presence of Fe^{III}_{HS} in both Fe1 and Fe2 layers, in combination with the $[Fe^{III}_2(Clan)_3]^{2-}$ network charge, therefore requires a 2:1 ratio of $Clan^{3-\bullet}$ to $Clan^{2-}$ valence states in both types of sheets, though assignment of ligand charged-ordering in each type of layer is less definitive than in **5.1**.

Within the Fe2 anionic layers, the Fe–Fe distances across **L$_4$**, **L$_5$** and **L$_6$** are 7.762(1), 7.802(2) and 7.917(2) Å respectively. This disparity is consistent with similar observations in the **4.1** family of compounds and **5.1**, namely an increased Fe–Fe distance across $Clan^{2-}$. This is attributed to the weaker Coulombic interaction between $Clan^{2-}$ and Fe^{III}_{HS}, compared to $Clan^{3-\bullet}$ and Fe^{III}_{HS}. In addition, there is a commensurate elongation of mean $d_{Fe–O}$ for **L$_6$** (2.053(4) Å) compared to **L$_4$** and **L$_5$** (2.005(7) and 1.998(4) Å respectively), which parallels the behaviour in **5.1** and $(n\text{Pr}_4\text{N})_2[Fe_2(Clan)_3]$.[7, 17] Examination of average ligand $d_{C–O}$ and $d_{C–C}$ values is less instructive. The $d_{C–O}$ values are 1.280(9), 1.277(6) and 1.269(6) Å for **L$_4$**, **L$_5$** and **L$_6$** respectively, with $d_{C–C}$ values across the five-membered chelate ring of 1.490(9), 1.473(10) and 1.492(9) Å for **L$_4$**, **L$_5$** and **L$_6$** respectively. It is immediately obvious that these values do not all fall consistently within or between the expected ranges of $d_{C–O}$ = 1.248–1.272 Å and $d_{C–C}$ = 1.506–1.551 Å for $Clan^{2-}$, and $d_{C–O}$ = 1.291–1.316 Å and $d_{C–C}$ = 1.431–1.473 Å for $Clan^{3-\bullet}$, so unambiguous assignment of oxidation state is difficult. However, both elongation of the C–C bonds, and shorting of C–O bonds in **L$_6$** compared to **L$_4$** and **L$_5$**, suggest that **L$_6$** is present in

less reduced state compared to **L₄** and **L₅**. Coupled with lengthened Fe–O bonds between Fe2 and **L₆**, and elongation of the Fe–Fe distance across **L₆**, we can tentatively surmise that **L₆** is in the $Clan^{2-}$ state, and **L₄** and **L₅** likely exist as $Clan^{3-\bullet}$, to maintain charge neutrality in **5.2**. Moreover, as MeV^{2+} lies near an Fe2 vertex nestled against **L₄** and **L₅**, these ligands are more likely to maintain a higher $Clan^{3-\bullet}$ charge state than **L₆**, due to CT and Coulombic interaction with the MeV^{2+} cations.

Assignment of ligand valence distribution in the Fe1 layers is more ambiguous than in the Fe2 layers. Across **L₁**, **L₂** and **L₃**, the Fe–Fe distances are 7.788(2), 7.835(2) and 7.844(1) Å respectively, with mean $d_{Fe–O}$ values of 1.995(4), 2.021(4) and 2.044(4) Å for **L₁**, **L₂** and **L₃** respectively. There is evidently less disparity between these values compared to the Fe–Fe distances across **L₄**, **L₅** and **L₆**, which may reflect a degree of radical ligand delocalisation, particularly between **L₂** and **L₃**. Importantly though, this parameter is not as sensitive to ligand oxidation state as either $d_{C–O}$ or $d_{C–C}$ values, as evidenced in **5.1** (see Section 5.2.2). As in the Fe2 layer, the ligand $d_{C–O}$ and $d_{C–C}$ values are not definitive with respect to the assignment of ligand oxidation state. The mean $d_{C–O}$ values for **L₁**, **L₂** and **L₃** are 1.284(6), 1.272(6) and 1.263(6) Å respectively, and the corresponding diagnostic $d_{C–C}$ values are 1.482(10), 1.497(10) and 1.519(10) Å. The values for **L₃** lie within the ranges of $d_{C–O}$ = 1.248–1.272 Å and $d_{C–C}$ = 1.506–1.551 Å expected for $Clan^{2-}$. This suggests that **L₃** exists as $Clan^{2-}$, which is supported by elongated Fe–O bonds between Fe1 and **L₃**, and the lengthened Fe–Fe distance relative to **L₁** and **L₂**. The presence of one putative $Clan^{2-}$ is expected based upon the $[Fe^{III}_2(Clan)_3]^{2-}$ network charge, to maintain charge neutrality in **5.2**. Consequently, this requires that **L₁** and **L₂** exist as $Clan^{3-\bullet}$. Although the corresponding $d_{C–O}$ and $d_{C–C}$ values for **L₁** and **L₂** lie between those expected for either $Clan^{2-}$ or $Clan^{3-\bullet}$, the elongation of ligand C–O bonds, and shortening of diagnostic C–C bonds compared to **L₃**, tentatively indicates that **L₁** and **L₂** exist in a more reduced state than **L₃**, putatively $Clan^{3-\bullet}$. This assignment is further supported by the previously noted shortening of Fe–O bond lengths and Fe–Fe distances across **L₁** and **L₂** relative to **L₃**.

These observations suggest that both Fe1 and Fe2 layers exhibit the same $[Fe^{III}_2(Clan^{2-})(Clan^{3-\bullet})_2]^{2-}$ ligand charge-ordered structure as the anionic $[Fe_2(Clan)_3]^{2-}$ layers in as-synthesised **5.1**. However, given the reduced Coulombic and CT interactions between the MeV^{2+} cations and the network in the Fe1 layers relative to the Fe2 layers, this strict charge-ordered formulation has the caveat that it

may not necessarily be indicative of the true electronic structure. Therefore, the magnetic interactions between Fe^{III}_{HS} and $Clan^{3-\bullet}$ ligands may be more complicated than expected based upon a strict ligand charge-ordered $[Fe^{III}_2(Clan^{2-})(Clan^{3-\bullet})_2]^{2-}$ formulation. Moreover, the different coordination geometries in the Fe1 and Fe2 sheets, and different CT and Coulombic interactions experienced by each type of anionic sheet, may give rise to disparate magnetic interactions and charge transport in each type of anionic layer, affording a material with novel or different physical properties behaviour compared to $(^{n}Pr_4N)_2[Fe_2(Clan)_3]$.

5.2.5 ^{57}Fe Mössbauer Spectroscopy

As with other mixed-valence Fe–tetraoxolene frameworks reported in this thesis, ^{57}Fe Mössbauer spectroscopy was employed to better understand the temperature dependence of Fe oxidation states. This preliminary measurement was conducted on an MeCN slurry of **5.1**, which was isolated immediately before the measurement; planned measurements on the isolated framework **5.2** have been delayed due to the current COVID19 pandemic situation. The spectrum of **5.1** at 293 K consists of a broad doublet composed of two underlying quadrupole doublets from spectroscopically inequivalent Fe sites (Figure 5.15, upper). Fitting of these absorbances gives an isomer shift δ = 0.60 mm s^{-1}, and a quadrupole splitting of ΔE_Q = 1.06 mm s^{-1} for Site A, and δ = 0.69 mm s^{-1} and ΔE_Q = 1.37 mm s^{-1} for Site B (Table 5.3). Although **5.1** contains only one crystallographically unique Fe site, the presence of two distinct spectroscopic Fe sites may reflect partial conversion of **5.1** to **5.2** following isolation, producing the two crystallographically unique Fe sites observed in **5.2**. Interestingly though, the intensity ratio I of these two sites does not match the 1:1 ratio of Fe1:Fe2 sites in **5.2**, possibly indicating a structural fluctuation observable only on the ^{57}Fe Mössbauer timescale (^{57}Fe excited state lifetime ca. 10^{-7} s [29, 30]). Nevertheless, the δ values are readily attributed to Fe^{III}_{HS} coordinated to O donor atoms in an octahedral environment,[29, 31] and agree well with values reported for other Fe^{III}–tetraoxolene coordination polymers.[7, 18, 22, 23, 27]

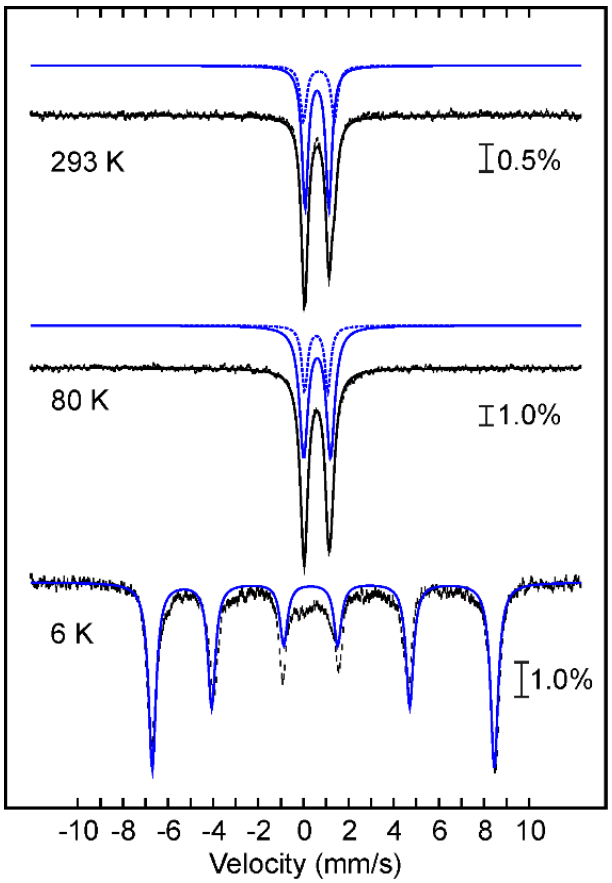


Figure 5.15 ^{57}Fe Mössbauer spectra of **5.1** collected immediately following isolation from an MeCN slurry at T = 293 K (upper), T = 80 K (middle) and T = 6 K (lower).

Table 5.3 Fitted ^{57}Fe Mössbauer spectral parameters for **5.1** measured immediately following isolating from an MeCN slurry.

T / K	Species	δ / mm s^{-1}	ΔE_Q / mm s^{-1}	B_0 / T	$\Gamma_{L\,(R)}$	I / %
293	Fe^{III} A	0.60	1.06	-	0.33	72
	Fe^{III} B	0.69	1.37	-	0.33	28
80	Fe^{III} A	0.61	1.19	-	0.45	75
	Fe^{III} B	0.57	1.03	-	0.31	25
6	Fe^{III} magnetic	0.60	0.56	47.2	0.40	100

While the ΔE_Q value for Site A closely matches values observed in other Fe–tetraoxolene frameworks, the observed ΔE_Q for Site B is slightly larger than previously observed in these frameworks e.g. $(Me_2NH_2)_2[Fe^{III}_2(Clan)_3]$ (ΔE_Q = 1.059 mm s^{-1}), $(Cp_2Co)_{1.43}(Me_2NH_2)_{1.57}[Fe^{III}_2(Clan)_3]$ (ΔE_Q = 1.018 mm s^{-1}) and **3.1^{Cl}b** (ΔE_Q = 1.13 mm s^{-1}). The ΔE_Q for Site B is however close to values observed in $(^nPr_4N)_2[Fe_2(Clan)_3]$ (ΔE_Q = 1.213 mm s^{-1} for the solvated, and ΔE_Q = 1.228 mm s^{-1} for the desolvated compounds) and $(Bu_4N)_2[Fe_2(dhbq)_3]$ (ΔE_Q = 1.279 mm s^{-1}). The higher ΔE_Q value for Site B is still consistent with Fe^{III}_{HS}, and likely reflects a greater ligand field asymmetry around Site B,[31] caused by the relatively large distortion of the Fe coordination geometry away from perfect octahedral (Table 5.2). At 80 K, the spectrum is similarly comprised of two underlying quadrupole doublets from inequivalent Fe sites (Figure 5.15, middle). The fitting parameters are δ = 0.61 mm s^{-1} and ΔE_Q = 1.19 mm s^{-1} for Site A, and δ = 0.57 mm s^{-1} and ΔE_Q = 1.03 mm s^{-1} for Site B, which are again completely consistent with Fe^{III}_{HS}, in agreement with SC-XRD experiments. The pure Fe^{III}_{HS} populations at 293 K and 80 K demonstrate that **5.1** does not undergo thermally-induced valence tautomerism. While the spectroscopic Fe^{III}_{HS} state at 80 K agrees well with the low temperature SC-XRD structure, the absence of valence tautomerism indicated by ^{57}Fe Mössbauer spectroscopy contrasts with the crystallographic results. This discrepancy probably results from different time-scales between the ^{57}Fe Mössbauer spectroscopic and crystallographic measurements. Upon cooling to 6 K, the spectrum transforms to a sextet attributed to a single Fe site, with a fit to the data giving values of δ = 0.60 mm s^{-1} and ΔE_Q = 0.56 mm s^{-1}, with an internal field parameter of B_0 = 47.2 T. These values are consistent with Fe^{III}_{HS} residing in a magnetic environment, as observed in the low temperature spectrum of **3.1^{Cl}b**. This qualitatively demonstrates **5.1** undergoes spontaneous magnetic ordering between 80 and 6 K, thus providing a significant motivation for future magnetic studies.

5.2.6 Electronic Spectroscopy

The presence of ligand-centred mixed valency in **5.2** was indicated by SC-XRD analyses, in addition to the black colour and metallic lustre of the crystals, like the other mixed-valence Fe–tetraoxolene frameworks reported in this thesis. Intervalence charge transfer (IVCT) can be a preliminary indicator of long-range charge transport, therefore diffuse-reflectance UV-Vis-NIR spectroscopy was used to further study the electronic structure of **5.2**. The UV-Vis-NIR spectrum of **5.2** (Figure 5.16, red) is

compared to the spectrum of the (6,3) honeycomb coordination polymers **3.1^{Cl}b** (Figure 5.16, blue) and $(Et_4N)_2[Fe_2(Clan)_3]$ (Figure 5.16, green).[9] The partially ligand charge-ordered $[Fe^{III}_2(Clan^{2.5-})_2(Clan^{3-\bullet})]^{2-}$ compound **3.1^{Cl}b** is used to understand the impact on the electronic structure of increased valence localisation in **5.2**. On the other hand, $(Et_4N)_2[Fe_2(Clan)_3]$ represents a reference which contains only redox inactive Et_4N^+ cations, and which exhibits a delocalied $[Fe^{III}_2(Clan^{2.67-})_3]^{2-}$ formulation. This comparison also provides insight of how the electron deficient MeV^{2+} cations in **5.2** impact the electronic structure. Although there are some common features between the spectra of **5.2**, **3.1^{Cl}b** and $(Et_4N)_2[Fe_2(Clan)_3]$, there are also noticeable differences.

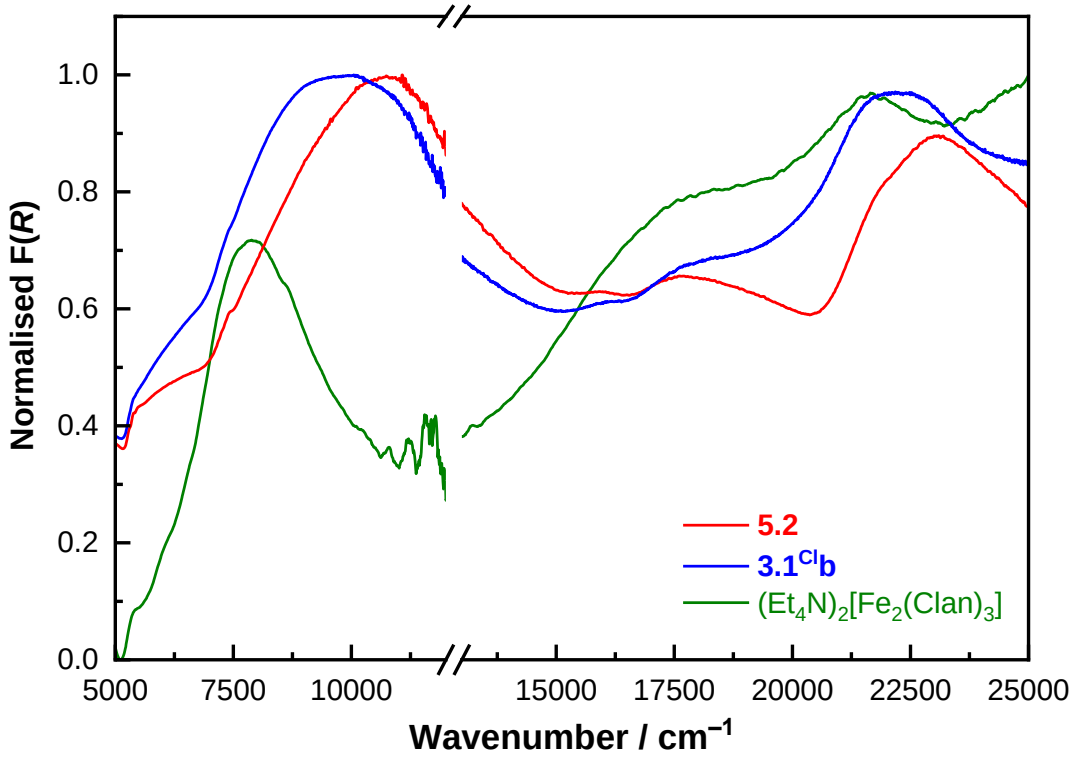


Figure 5.16 Normalised diffuse-reflectance UV-Vis-NIR spectra of **5.2** (red), **3.1^{Cl}b** (blue), and $(Et_4N)_2[Fe_2(Clan)_3]$·solvent (green).[9] Each spectrum normalised to the maximum absorbance set at F(R) = 1. The break in the spectra corresponds to the NIR-Vis detector change-over.

The spectrum of **5.2** exhibits intense absorptions in the visible region at ν_{max} ca. 23000 cm^{-1} and ca. 17500 cm^{-1}, as with the spectra of **3.1^{Cl}b** and $(Et_4N)_2[Fe_2(Clan)_3]$. These features are common to all Fe–tetraoxolene frameworks reported in this thesis and are attributed to ligand π–π^* and metal-ligand d–π transitions, respectively. IVCT in **5.2**, is indicated by the intense absorption in the NIR region, which is also observed in the spectrum of mixed-valence **3.1^{Cl}b** and $(Et_4N)_2[Fe_2(Clan)_3]$. IVCT has also been rationalised in other mixed-valence metal–tetraoxolene frameworks by similar observations.[8, 9, 27, 28, 32, 33] Given that ^{57}Fe Mössbauer spectroscopy indicates that **5.1** contains a valence-pure population of Fe^{III}_{HS}, which is presumably also true for **5.2**, the IVCT process therefore likely arises from electron transfer between the localised $Clan^{2-}$ and $Clan^{3-\bullet}$ states in **5.2**.

Although **5.2** and $(Et_4N)_2[Fe_2(Clan)_3]$ both exhibit ligand-based IVCT, the NIR ν_{max} of **5.2** is noticeably broadened and shifted to higher energy, compared to the NIR absorption of $(Et_4N)_2[Fe_2(Clan)_3]$. The NIR ν_{max} of **5.2** also undergoes a hypsochromic shift relative to **3.1^{Cl}b**, suggesting that the increased ligand charge localisation in **5.2** impacts upon the electronic structure. However, **5.2** is still strongly absorbing in the ca. 7000 cm^{-1} region like **3.1^{Cl}b** and $(Et_4N)_2[Fe_2(Clan)_3]$. A low energy tail is also observed for **5.2**, which is absent in the $(Et_4N)_2[Fe_2(Clan)_3]$ spectrum. Critically, the NIR bands in **3.1^{Cl}b**, and *aP* **4.1a** and **4.1b** are also broadened and hypsochromically shifted when compared to $(Et_4N)_2[Fe_2(Clan)_3]$ (see Section 3.2.5) and $(Et_4N)_2[Fe_2(Fan)_3]$ (see Section 4.2.5) respectively. As for **3.1^{Cl}b**, *aP* **4.1a** and **4.1b**, the NIR band broadening and shifting in **5.2** suggests that the IVCT interactions have been significantly modified by incorporating redox-active cations. In the case of **3.1^{Cl}b**, broadening of the NIR manifold arises because it is comprised of several underlying Gaussian peaks (see Section 3.2.5). These energetically inequivalent underlying bands in **3.1^{Cl}b** arose due to the multiple possible CT interactions between all the chemically and crystallographically inequivalent redox-active species. This contrasts with the NIR manifold of $(Et_4N)_2[Fe_2(Clan)_3]$, which was readily deconvoluted to a single underlying Gaussian band.[9] The ligands in trigonally symmetric $(Et_4N)_2[Fe_2(Clan)_3]$ are chemically and crystallographically equivalent, and all exhibit the same non-integer valence state of $Clan^{2.67-}$. Consequently, the activation energy to IVCT between any three equivalent ligand sites would be equal, causing only a single observable NIR absorption band. The triclinic structure of **5.2** presents a

stark contrast, as all the ligands (**L_1**–**L_6**) in **5.2** are crystallographically inequivalent. Therefore, the activation energy to electron transfer from each $Clan^{3-\bullet}$ to $Clan^{2-}$ site will be inequivalent, owing to the different Coulombic interactions at each ligand site. Additionally, the profile of the low energy NIR tail in **5.2** is also different to the asymmetric low energy absorption observed in *aP* **4.1a**, that was tentatively ascribed to a Robin-Day Class III IVCT between Fe^{II} and Fe^{III}. This suggests that the low energy NIR tailing in **5.2** has a different origin than in *aP* **4.1a**, and probably involves IVCT between $Clan^{3-\bullet}$ and $Clan^{2-}$ as observed in other mixed-valence Fe–tetraoxolene frameworks.

To gain insight into the spectral differences between **5.2** and the related 2D honeycomb Fe–chloranilate compounds, deconvolution of the NIR manifold of **5.2** was performed using an approach similar to that employed for the spectra of **3.1^{Cl}b**, *aP* **4.1a** and **4.1b**. Deconvolution of the diffuse-reflectance UV-Vis-NIR spectrum of **5.2** indicates there are three underlying Gaussian bands centred at ν_{max} = 5473, 8688 and 11223 cm^{-1} in the NIR region (Figure 5.17). A similar analysis performed on the spectrum of $(Et_4N)_2[Fe_2(Clan)_3]$ and **3.1^{Cl}b** (NIR bands only; see Section 3.2.5 for full analysis) is presented in Table 5.4. The additional underlying Gaussian bands in the spectrum of **5.2** compared to $(Et_4N)_2[Fe_2(Clan)_3]$ is expected, based upon the proposed energetically inequivalent CT interactions in **5.2**. Critically, **3.1^{Cl}b**, *aP* **4.1a** and **4.1b** all exhibit notably broad IVCT manifolds, which arises from multiple underlying Gaussian components in the NIR region. The underlying NIR absorptions for **5.2** are also centred at similar energies to the underlying Gaussian bands for **3.1^{Cl}b**, *aP* **4.1a** and **4.1b**, which presumably results from localisation of the $Xan^{3-\bullet}$ state in all the compounds. Determination of the extent of localisation of valent states according to the Robin-Day classification[34] for the IVCT processes in **5.2** was achieved using the theoretical method described by Hush.[35, 36] The Γ parameter[37] was calculated using a method analogous to that employed in the analysis of **3.1^{Cl}b**, *aP* **4.1a** and **4.1b**. The value determined for the Γ parameter, allows assignment within the Robin-Day classification as follows: $0 < |\Gamma| < 0.1$ for weakly-coupled Class II systems; $0.1 < |\Gamma| < 0.5$ for moderately-coupled Class II systems; $|\Gamma| \approx 0.5$ at the transition between Class II and Class III; and $|\Gamma| > 0.5$ for Class III systems. The calculated Γ values suggest the NIR bands ascribed to IVCT in **5.2** are weakly-to-moderately coupled Class II systems,

like those in the structurally similar 2D honeycomb frameworks **3.1^{Cl}b** and $(Et_4N)_2[Fe_2(Clan)_3]$.[9]

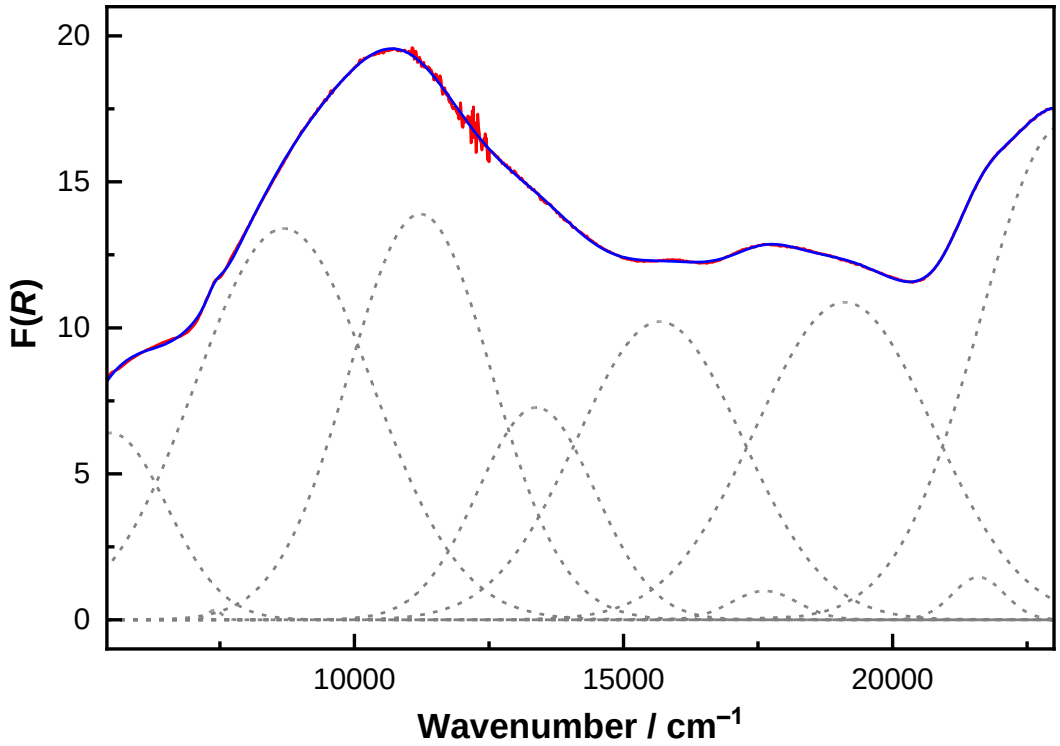


Figure 5.17 Deconvolution of the diffuse-reflectance UV-Vis-NIR spectrum of **5.2** (red) with the underlying Gaussian bands from the deconvolution (grey dotted lines) and the associated curvefit (blue).

Table 5.4 Spectral data of the deconvoluted diffuse-reflectance UV-Vis-NIR spectrum of **5.2**, in comparison with the published data for **3.1^{Cl}b** (Section 3.2.5) and $(Et_4N)_2[Fe_2(Clan)_3]$.[9] The theoretical predictions for the bandwidths at half-height ($\Delta\nu_{1/2}°$) are provided for the NIR bands which have been tentatively ascribed to IVCT transitions (in bold).

Compound	ν_{max} / cm^{-1}	F(R)$_{max}$ / a.u.	$\Delta\nu_{1/2}$ / cm^{-1}	$\Delta\nu_{1/2}°$ / cm^{-1} (a)	$\lvert\Gamma\rvert$ (b)
5.2	**5473**	**6.40**	**2456**	**3556**	**0.31**
	8688	**13.4**	**3855**	**4480**	**0.14**
	11223	**13.9**	**3134**	**5092**	**0.38**
	13382	7.27	2561	5560	
	15675	10.2	3631	6017	
	17619	0.99	1451	6380	
	19112	10.9	3879	6644	
3.1^{Cl}b	**5629**	**8.00**	**2677**	**3605**	**0.26**
	8544	**17.0**	**3382**	**4442**	**0.24**
	10700	**3.36**	**2001**	**4972**	**0.60**
	11720	**14.1**	**4120**	**5203**	**0.21**
$(Et_4N)_2[Fe_2(Clan)_3]$	**7445**	**5.68**	**3290**	**4147**	**0.21**
	10075	**2.98**	**2560**	**4824**	**0.53**
	11390	1.52	1348		
	128900	1.57	1790		
	18577	11.7	6588		

(a) $\Delta\nu_{1/2}° = [2310(\nu_{max})]^{1/2}$ at 298 K.[35, 36]

(b) $|\Gamma| = |1-(\Delta\nu_{1/2}/\Delta\nu_{1/2}°)|$.[37]

Compared to **3.1^{Cl}b** and $(Et_4N)_2[Fe_2(Clan)_3]$, the strongest NIR bands for **5.2** show a greater disparity in the degree of electron delocalisation, indicated by the values of the Γ parameters for each band. This suggests the electronic structure of **5.2** may differ notably from that of either **3.1^{Cl}b** or $(Et_4N)_2[Fe_2(Clan)_3]$. We hypothesise this arises because **5.2** contains two types of anionic $[Fe_2(Clan)_3]^{2-}$ layers, which engage in different Coulombic and CT interactions with MeV^{2+} countercations. The ligands in the Fe1 anionic layers (**L$_1$**–**L$_3$**) do not engage in CT interactions with MeV^{2+} cations, and experience weaker Coulombic interactions with these cations, arising from the relatively large separation distance between Fe1 anionic layers and MeV^{2+}. Because there are fewer competing interactions which would stabilise the $Clan^{3-\bullet}$ valence state at a given ligand site, IVCT between **L$_1$**, **L$_2$** and **L$_3$** probably has a relatively lower activation energy, compared to ligand-based IVCT between **L$_4$**, **L$_5$** and **L$_6$** in the Fe2 layers. The more facile IVCT in the Fe1 layers is also suggested by comparison of the Fe–Fe distances across the ligands, although these distances are not as definitive of ligand oxidation state as $d_{C–O}$ and $d_{C–C}$ values. Comparison of the Fe–Fe distances across the $Clan^{n-}$ ligands for the Fe1 layers compared to the Fe2 layers, reveals a more even distribution of Fe–Fe distances in the Fe1 layers (see Section 5.2.4.3). This hints that on the spectroscopic time scale, the fully ligand-charge ordered $[Fe^{III}_2(Clan^{2-})(Clan^{3-\bullet})_2]^{2-}$ formulation is not a totally accurate representation of the electronic structure in the Fe1 anionic layers. Instead, the electronic structure may be influenced by contributions from partially charge-ordered or disordered formulations i.e. $[Fe^{III}_2(Clan^{2.5-})_2(Clan^{3-\bullet})]^{2-}$ or $[Fe^{III}_2(Clan^{2.67-})_3]^{2-}$, in addition to a major contribution from the $[Fe^{III}_2(Clan^{2-})(Clan^{3-\bullet})_2]^{2-}$ charge-ordered formulation. Future computational analysis could provide insight into this proposition.

Finally, an estimation of the optical band gap (E_g) for **5.2** was provided by Tauc analysis[38, 39] on the experimental UV-Vis-NIR spectrum, affording an optical band gap of E_g = 0.86 eV (Figure 5.18). The estimated E_g value falls within the range expected for semiconductor materials, suggesting that **5.2** should exhibit electrical conductivity in line with other mixed-valence Fe–tetraoxolene frameworks. The calculated E_g value also closely matches E_g values estimated for the (6,3) honeycomb frameworks **3.1^{Cl}b** (Chapter 3, 0.81 eV) and $(Et_4N)_2[Fe_2(Clan)_3]$ (0.79 eV),[9] although the E_g value for **5.2** is slightly higher than observed for the 3D (10,3)-*a* frameworks

(^{n}Bu$_4$N)$_2$(Fe$_2$(Fan)$_3$] and (^{n}Bu$_4$N)$_2$(Fe$_2$(dhbq)$_3$] (0.67 eV and 0.7 eV respectively).[27, 28] The slightly higher E_g value for **5.2** compared to other mixed-valence Fe^{III}–chloranilate frameworks, may result from localisation of the ligand valence states, such that optical excitation of IVCT is less favoured energetically. A slightly increased E_g for **3.1^{Cl}b**, relative to (Et$_4$N)$_2$[Fe$_2$(Clan)$_3$] was also observed, that was attributed to partial ligand charge localisation causing less facile IVCT. However optical band gaps do not always directly correlate with the electronic band gap,[39] so it is difficult to make predictions about the expected electrical conductivity of **5.2** relative to the other frameworks using this comparison alone. In summary, these results continue the theme developed throughout this thesis, that introducing CT interactions between mixed-valence tetraoxolene networks and π-electron deficient viologen countercations consistently influences the electronic structures and spectroscopic properties of these materials.

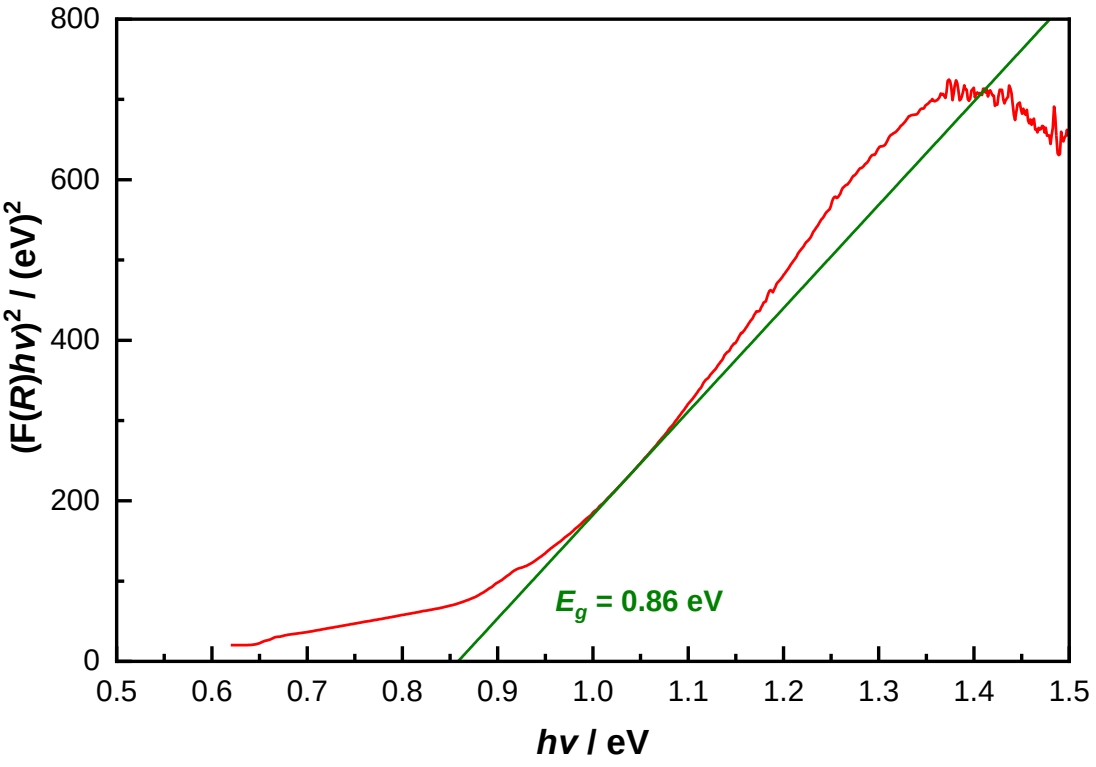


Figure 5.18 Tauc analysis on the experimental UV-Vis-NIR data of **5.2** (red) showing estimation of the optical band gap (E_g, green).

5.2.7 Electrochemistry

The electrochemical behaviour of **5.2** was studied by dc cyclic voltammetry on a paste of the compound immobilised on a glassy carbon electrode, as for the other electrochemical studies in this work. We were particularly interested in studying how the densely packed structure of **5.2** could affect the electrochemical properties, especially compared to the porous compounds **3.1^{Cl}b** and *aP* **4.1a**. Given the dense packing in **5.2**, cyclic voltammetry was performed using only 0.5 M $LiBF_4$/MeCN electrolyte, to allow more facile ion diffusion in the structure, compared to bulky organic electrolytes such as $(Et_4N)PF_6$ or $(^nBu_4N)PF_6$. Cyclic voltammetric experiments were performed at scan rates between 20–200 mV s^{-1} for a maximum of five cycles, over both a wide anodic and cathodic potential range (Figure 5.19, ca. −1.4 to 1.2 V vs Fc/Fc^+), and subsequently an exclusively cathodic potential window (Figure 5.20, ca. −1.4 to −0.2 V vs Fc/Fc^+). Measurement over two potential windows was necessary, arising from the irreversible response upon framework oxidation (*vide infra*), in contrast to **3.1^{Cl}b** and *aP* **4.1a**, which exhibit greater stability over a wide potential range. For the wide range window, cathodic cycling reveals the presence of two significant quasi-reversible redox waves at E_1 ca. −0.67 V vs. Fc/Fc^+ (**R_I**) and E_2 ca. −1.12 V vs. Fc/Fc^+ (**R_{II}**), with a slight shoulder at E_3 ca. – 0.48 V vs. Fc/Fc^+ (Figure 5.19). As with **3.1^{Cl}b** and *aP* **4.1a** (see Section 3.2.6 and 4.2.6), there is a slight cathodic shift of peak potentials at higher scan rates, as well as broadening of the redox waves, indicative of hindered ion diffusion. Upon switching to positive potential, a large irreversible anodic wave at ca. 0.4 V vs. Fc/Fc^+ is observed. Notably, no return wave for this process is seen upon cycling back to cathodic potentials. Moreover, there is a dramatic drop in current response, particularly at slower scan rates. This is attributed to loss of material from the electrode, and also to electrochemically-induced irreversible structure transformation (*vide infra*). At 20 mV s^{-1} scan rate (Figure 5.19a), the loss of current response is so severe that subsequent cycles did not reveal any significant current flow, despite repeated attempts with freshly immobilised sample, so only one cycle is presented.

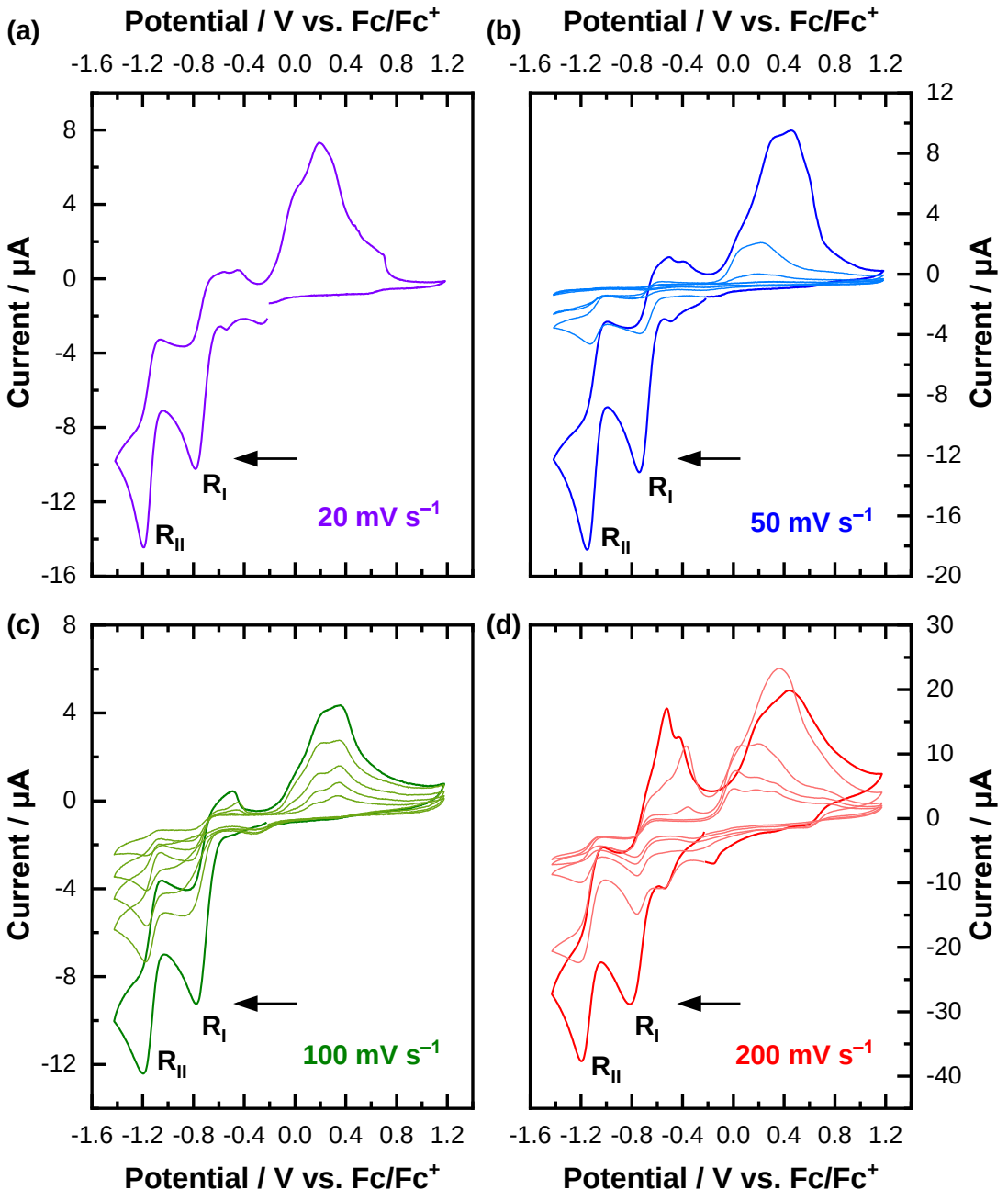


Figure 5.19 Cyclic voltammograms of solid **5.2** in 0.5 M $LiBF_4$/MeCN at (a) 20 mV s^{-1} (purple), (b) 50 mV s^{-1} (blue), (c) 100 mV s^{-1} (green), and (d) 200 mV s^{-1} (red). Arrows indicate the direction of the forward scan. First scan shown in bold, subsequent scans shown in fine pastel line. NB: Excessive loss of material was observed upon subsequent cycles at 20 mV s^{-1}.

The two quasi-reversible processes at E_1 ca. −0.67 V vs. Fc/Fc^+ (**R_I**), and ca. −1.12 V vs. Fc/Fc^+ (**R_{II}**) nicely parallels the behaviour observed in numerous redox-active tetraoxolene frameworks. For the 2D honeycomb framework (^{n}Bu$_4$N)[$Mn^{II}Cr^{III}$(Clan)$_3$], electrochemical studies using a lithium-ion battery (LIB) device demonstrated the $Clan^{2-}/Clan^{3-\bullet}$ reduction occurs at ca. 2.6 V vs. Li/Li^+ (ca. −0.84 V vs. Fc/Fc^+), which corresponds reasonably well to the potential of **R_I**. Moreover, in the potential range 2.2 to 3.4 V vs. Li/Li^+ (ca. −1.24 to 0 V vs. Fc/Fc+), no additional redox processes were observed for (^{n}Bu$_4$N)[$Mn^{II}Cr^{III}$(Clan)$_3$], supporting the conclusion this process is ligand based. Similarly, the reversible $Clan^{2-}/Clan^{3-\bullet}$ reduction couple in mixed-valence (Me$_2$NH$_2$)$_2$[Fe$_2$(Clan)$_3$] was observed at 2.71 V vs. Li/Li^+ (ca. −0.73 V vs. Fc/Fc^+) using a LIB device, allowing **R_I** to be assigned as the expected $Clan^{2-}/Clan^{3-\bullet}$ couple. The second cathodic process **R_{II}** at −1.12 V vs Fc/Fc^+ corresponds well to the reversible reduction at 2.35 V vs. Li/Li^+ (ca. −1.1 V vs. Fc/Fc^+) in (Me$_2$NH$_2$)$_2$[Fe$_2$(Clan)$_3$],[33] and reasonably well to the quasi-reversible process at ca. −1.51 V vs. Fc/Fc^+ in **3.1^{Cl}b**. This process is tentatively ascribed to reduction of $Clan^{3-\bullet}$ to $Clan^{4-}$, with some possible involvement of the Fe^{III}/Fe^{II} couple, analogously to (Me$_2$NH$_2$)$_2$[Fe$_2$(Clan)$_3$].[33] For this compound, electrochemical experiments revealed a capacity of 6 electrons per unit formula, which requires both ligand- and metal-centred redox processes to occur i.e. (Me$_2$NH$_2$)$_2$[Fe^{III}_2($Clan^{2.67-}$)$_3$] to (Me$_2$NH$_2$)$_2$[Fe^{II}_2($Clan^{4-}$)$_3$]. Additionally, *ex situ* ^{57}Fe Mössbauer spectroscopy confirmed the presence of Fe^{II}_{HS} upon reduction, indicating simultaneous involvement of ligand and metal redox processes during framework reduction. Although spectroscopic measurements on **5.2** have not been performed, due to the comparable anionic honeycomb sheet structures between (Me$_2$NH$_2$)$_2$[Fe$_2$(Clan)$_3$] and **5.2**, involvement of ligand- and metal-based couples in the **R_{II}** process is feasible. The more cathodic potential for the $Clan^{3-\bullet}/Clan^{4-}$ couple in **3.1^{Cl}b** compared to **5.2**, is likely due to use of more sterically bulky (Et$_4$N)PF$_6$ electrolyte used in the study of **3.1^{Cl}b**. For both *aP* **4.1a** (Section 4.2.6) and (Ph$_3$MeP)$_2$[Cd$_2$(dhbq)$_3$],[40] a cation size-dependant redox potential is observed. This occurs due to the greater electrochemical driving force necessary to sufficiently transform the structures to accommodate intercalation of bulkier countercations between the anionic layers during reduction.

The oxidation processes of **5.2** at anodic potentials relative to Fc/Fc^{+} are largely irreversible, as indicated by the absence of a return wave and dramatic loss of current response for subsequent cycle numbers. This is particularly true at low scan rates (Figure 5.19a & b), and contrasts quite sharply with the reversible oxidation processes observed in both **3.1^{Cl}b** and $(Me_2NH_2)_2[Fe_2(Clan)_3]$.[33] We hypothesise the disparate network-to-cation packing interactions between the aforementioned compounds and **5.2** (see Section 3.2.1), are the likely cause of this different electrochemical behaviour. Long and co-workers have noted the traditional view of ion transport in layered framework materials may differ significantly from the ion transport processes in classical layered oxide-based LIB cathodes.[33] Notably, the LIB discharge capacity was dependant on both anion and cation size, suggesting that both counteranions and -cations are inserted and deinserted during electrochemical cycling upon $(Me_2NH_2)_2[Fe_2(Clan)_3]$. This behaviour contrasts that of layered oxide cathodes, such as $LiCoO_2$, in which Li^{+} insertion during LIB discharging (cathode reduction), and Li^{+} deinsertion during LIB charging (cathode oxidation), are the major ionic transport process. While *ex situ* P-XRD studies of layered metal-tetraoxolene frameworks in LIB systems revealed these compounds are stable to framework reduction (battery discharge),[8, 33, 41, 42] these structural studies have been confined to relatively cathodic potentials i.e. below the potential of the as-synthesised framework. Relatively less is known about putative structural transformations accompanying framework oxidation at potentials more anodic than the resting potential of the framework i.e. battery charging above ca. 3.0 V vs Li/Li^{+}.

As for $(Me_2NH_2)_2[Fe_2(Clan)_3]$, and proposed for *aP* **4.1a**, ion transport during framework oxidation above the native $(MeV^{2+})[Fe^{III}_2(Clan^{2-})(Clan^{3-\bullet})_2]$ state of **5.2** could proceed via two distinct pathways: deinsertion of bulky MeV^{2+} cations from the structure; or insertion of small, mobile BF_4^{-} anions into the structure, to counteract the increasing network positive charge. Some structural plasticity and movement of MeV^{2+} cations is undoubtedly possible, as evidenced by the transformation from **5.1** to **5.2**. However, considering the interactions (Coulombic, CT and steric) between MeV^{2+} and the anionic network that would need to be overcome to achieve movement of MeV^{2+}, deinsertion of MeV^{2+} from the structure seems unlikely. By contrast BF_4^{-} is smaller and only exhibits Coulombic interaction with the framework, therefore framework oxidation probably accompanied by insertion of mobile, solvated BF_4^{-}

anions into the structure to maintain overall electrical neutrality, rather than deinsertion of MeV^{2+}. The lack of continuous solvent-filled channels in **5.2** also means that insertion of solvated anions into the structure likely occurs by intercalation of the anionic $[Fe_2(Clan)_3]^{x-}$ sheets. Insertion of BF_4^- anions between the anionic sheets could destabilise the relatively weak intersheet Coulombic interactions, causing sheet exfoliation and loss of long-range stacking order. Significantly, Ziebel *et al.* noted reduced discharge capacity in LIB devices using $(Me_2NH_2)_2[Fe_2(Clan)_3]$ cathodes, when the batteries were initially charged to 4.2 V vs. Li/Li^+ (ca. 0.75 V vs. Fc/Fc^+, framework oxidation), compared to devices which underwent an initial discharge to 1.8 V vs. Li/Li^+ (ca. −1.65 V vs. Fc/Fc^+, framework reduction) then charge cycle to 4.2 V vs. Li/Li^+. The drop in performance was attributed to enhanced anion insertion on the first charge cycle, leading to exfoliation of the oxidised putative neutral $[Fe^{III}_2(Clan^{2-})_3]$ sheets, and loss of long-range stacking order and structure collapse.

The reversibility of the framework reduction processes was further assessed by performing dc cyclic voltammetry on **5.2** over a strictly cathodic potential window (−1.4 to −0.2 V vs. Fc/Fc^+). These measurements were made with scan rates between 20–200 mV s^{-1} for a maximum of five cycles (Figure 5.20). As expected, the two quasi-reversible reduction processes, $\mathbf{R_I}$ at ca. −0.67 V vs. Fc/Fc^+ and $\mathbf{R_{II}}$ at ca. −1.12 V vs. Fc/Fc^+, are retained from the studies over a broader potential window (Figure 5.19). As with the initial electrochemical experiments, narrowing of the peak potential widths at slower scan rates indicates that hindered ion diffusion still influences the electrochemical response of **5.2**. However, in stark contrast to the experiments conducted over a wide potential window, cycling over a strict cathodic window largely maintains the current response and reversibility for subsequent electrochemical cycles, even at slow scan rates. We attribute the slight loss of current response to a small loss of material from the electrode during the experiment. The more stable response over multiple cycles is possibly a consequence of ion insertion and deinsertion in the framework being largely confined to movement of Li^+, rather than insertion of BF_4^- hypothesised during oxidation of **5.2**.

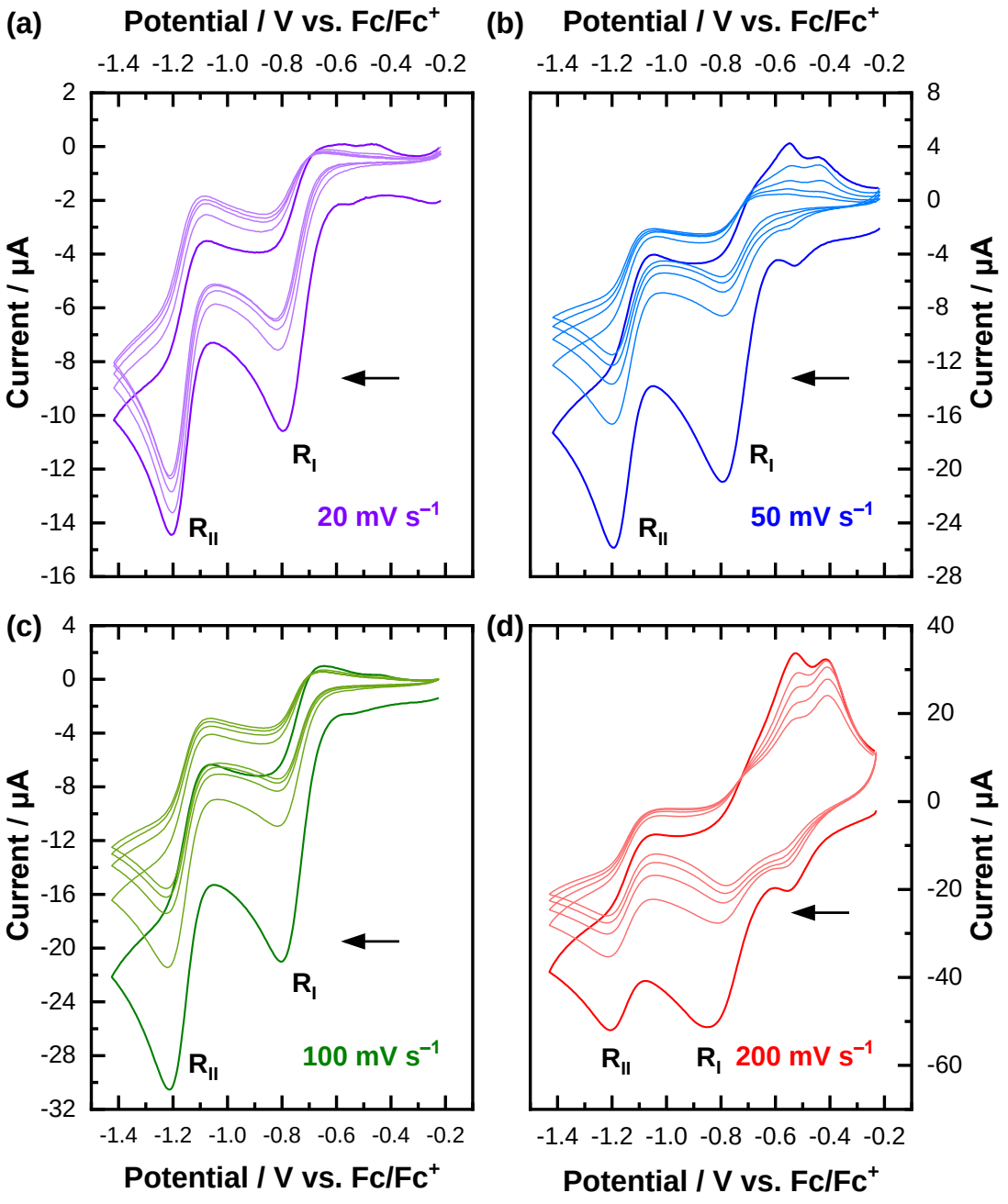


Figure 5.20 Narrow-range cyclic voltammograms (ca. −1.4 to −0.2 V vs. Fc/Fc^+) of solid **5.2** in 0.5 M $LiBF_4$/MeCN at (a) 20 mV s^{-1} (purple), (b) 50 mV s^{-1} (blue), (c) 100 mV s^{-1} (green), and (d) 200 mV s^{-1} (red). Arrows indicate the direction of the forward scan. First scan shown in bold, subsequent scans shown in fine pastel line.

The shoulder at ca. −0.5 V vs. Fc/Fc^{+}, which is particularly prominent at 200 mV s^{-1} scan rate, is tentatively attributed to the $MeV^{2+}/MeV^{+\bullet}$ couple. This is based upon the position of the $MeV^{2+}/MeV^{+\bullet}$ couple in *aP* **4.1a**, and redox potential of $MeV^{2+}/MeV^{+\bullet}$ in solution.[14, 43-45] The reason for the increased prominence of this process, and more reversible return wave at higher scan rates is not immediately obvious (Figure 5.19d). This may reflect different time scales between electrochemically-induced ion diffusion in the framework, and any structural transformations required to accommodate putative $MeV^{+\bullet}$ cations. The addition of framework redox states due to incorporation of MeV^{2+} in **5.2** is less clear, in contrast to **3.1^{Cl}b**, in which incorporation of redox-active $PhenQ^{2+}$ cations into the structure clearly affords additional framework redox states. Future slow-scan voltammetric and *in situ* LIB voltammetric–P-XRD studies could provide significant insight into the electrochemical processes in **5.2**. In particular, whether both tetraoxolene network and cation redox states are electrochemically active, and the nature of the structural transformations which take place at each redox state. Compared to *aP* **4.1a**, in which MeV^{2+} redox states are accessible, the different behaviour of **5.2**, despite the ostensibly equivalent $(MeV)[Fe_2(Xan)_3]$ compositions of both compounds, highlights the intimate relationship between overall structure and properties. Given the delicate balance between cation and network on the structure, there is significant scope to uncover a diverse range of electroactive framework materials.

5.2.8 Electrical Conductivity

Lastly, electrical conductivity in **5.2** was studied, in line with the presence of ligand-centred IVCT as suggested by electronic spectroscopy, and structural similarity with other semiconductive Fe–tetraoxolene frameworks. The electrical transport properties of crystalline powders of **5.2** were assessed using two-point pressed pellet devices assembled in a dinitrogen-filled glovebox. Four independent devices were all Ohmic over the potential range −0.25 to 0.25 V, exhibiting a mean ambient temperature (ca. T = 305 K in the glovebox) conductivity of $\sigma = 5.0(2) \times 10^{-3}$ S cm^{-1}, and with the premier device reaching $5.8(2) \times 10^{-3}$ S cm^{-1} (Table B.4). While these values fall short of those achieved by recent high symmetry mixed-valence Fe–tetraoxolene frameworks such as $(^{n}Bu_4N)_2[Fe_2(dhbq)_3]$ (σ = 0.16 S cm^{-1}, cubic symmetry),[27] $(Me_2NH_2)_2[Fe_2(Clan)_3]\cdot 6DMF\cdot 2H_2O$ ($\sigma = 1.4(7) \times 10^{-2}$ S cm^{-1}, trigonal symmetry)[23], $[(H_3O)(H_2O)(phenazine)_3][Fe_2(Clan)_3]$ ($\sigma = 3.0 \times 10^{-2}$ S cm^{-1},

trigonal symmetry),[4] and $(Et_4N)_2[Fe_2(Fan)_3]\cdot 5(acetone)$ (σ = 1.8 × 10^{-2} S cm^{-1}, trigonal symmetry),[8] they are surprisingly high considering the low triclinic symmetry and ligand charge-ordered structure of **5.2**. Indeed, single-crystal measurements on desolvated $(^nPr_4N)_2[Fe_2(Clan)_3]$, which exhibits a similar ligand-charge ordered $[Fe^{III}_2(Clan^{2-})(Clan^{3-\bullet})_2]^{2-}$ sheet formulation as **5.2**, revealed a room-temperature conductivity of only $\sigma_{//c}$ = 2.6 × 10^{-4} S cm^{-1}, when measured along the highest conductivity axis parallel to the $\{Fe^{III}–Clan^{3-\bullet}\}_\infty$ chains.[17] The conductivity fell to $\sigma_{\perp c}$ = 1.0 × 10^{-4} S cm^{-1} when measured perpendicular to the $\{Fe^{III}–Clan^{3-\bullet}\}_\infty$ chains in the plane of the sheet, and further decreased to $\sigma_{\perp s}$ = 4.1 × 10^{-8} S cm^{-1}, when measured perpendicular to the anionic $[Fe_2(Clan)_3]^{2-}$ sheets. Additionally, single-crystal conductivity measurements on the 2D honeycomb framework $(TAG)[Fe^{II}Fe^{III}(CNClan^{2-})_3]\cdot(solvent)$ (TAG = triaminoguanidinium) which exhibits trigonal symmetry, revealed an intrasheet conductivity only as high as $\sigma_{//s}$ = 2.0 × 10^{-3} S cm^{-1}.[46] Given the: low triclinic symmetry of **5.2**; highly anisotropic conductivity exhibited by 2D layered metal–tetraoxolene materials; and the dominance of grain boundary resistance in the measured conductivity of powder samples in pressed pellet devices,[47, 48] the conductivity values displayed by pressed pellet devices of **5.2** seem even more surprising.

Further insights into the transport properties of **5.2** were obtained by measuring the temperature dependence of the electrical conductivity in the pressed pellet devices over the range 295–215 K. As with the other compounds described in this thesis, a slight drop in conductivity was observed upon removing the pressed pellet devices from the inert atmosphere glovebox. However importantly, all devices remained Ohmic over the entire temperature range of study (representative current-bias, *i*-*v* plot for the premier device given in Figure 5.21). At 295 K, the measured conductivities of four independent pressed pellet devices ranged from 2.3(1) × 10^{-3} S cm^{-1}, to 3.4(1) × 10^{-3} S cm^{-1}. Upon cooling, the conductivity of the devices decreased, consistent with the expected thermally-activated semiconductor behaviour, as observed for other mixed-valence metal–tetraoxolene frameworks.[4, 8, 23, 27, 28, 46]

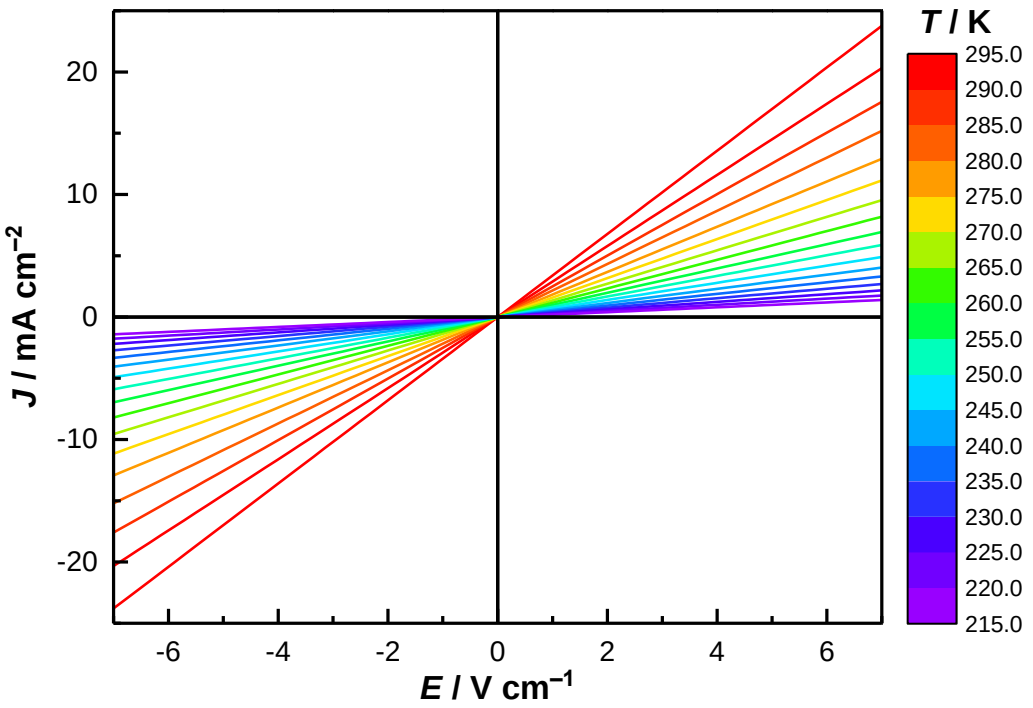


Figure 5.21 Representative variable-temperature current-bias (*i*-*v*) plot for the premier two-point pressed pellet device of **5.2** (Device 3). Data were measured over the range −0.35 to −0.35 V in 0.01 V steps.

An Arrhenius fit to the experimental data gives activation energies (E_a) varying in the range 0.186(1) to 0.195(1) eV for the four independent devices (Figure 5.22 for the premier device; Figure B.4 for the other devices). The calculated E_a values for devices of **5.2** are surprisingly similar to high symmetry Fe–tetraoxolene frameworks with fully delocalised ligand or metal valence states, such as $(Me_2NH_2)_2[Fe_2(Clan)_3]$·solvent ($E_a$ = 0.26(1) eV for solvated, E_a = 0.19(1) eV for desolvated),[23] or (TAG)[$Fe^{II}Fe^{III}$(CNClan)$_3$] (E_a = 0.15 eV). Additionally, the E_a values for **5.2** are lower than those calculated for compounds with a similar ligand-charge ordered $[Fe^{III}_2(Xan^{2-})(Xan^{3-\bullet})_2]^{2-}$ formulation as **5.2**, such as $(^nPr_4N)_2[Fe_2(Clan)_3]$ (E_a = 0.44 eV for single crystal), *aP* **4.1a** and **4.1b** (Section 4.2.7; E_a = 0.218(2) eV and E_a = 0.376(6) eV respectively), or partially charge-ordered **3.1^{Cl}b** (Section 3.2.8; E_a = 0.249(2) eV). The higher electrical conductivity and lower E_a for **5.2**, compared to these compounds, and suggests the electronic band structure in **5.2** is different to these compounds, despite the putative equivalent ligand charge-ordered $[Fe_2(Xan^{2-})(Xan^{3-\bullet})_2]^{2-}$ formulations.

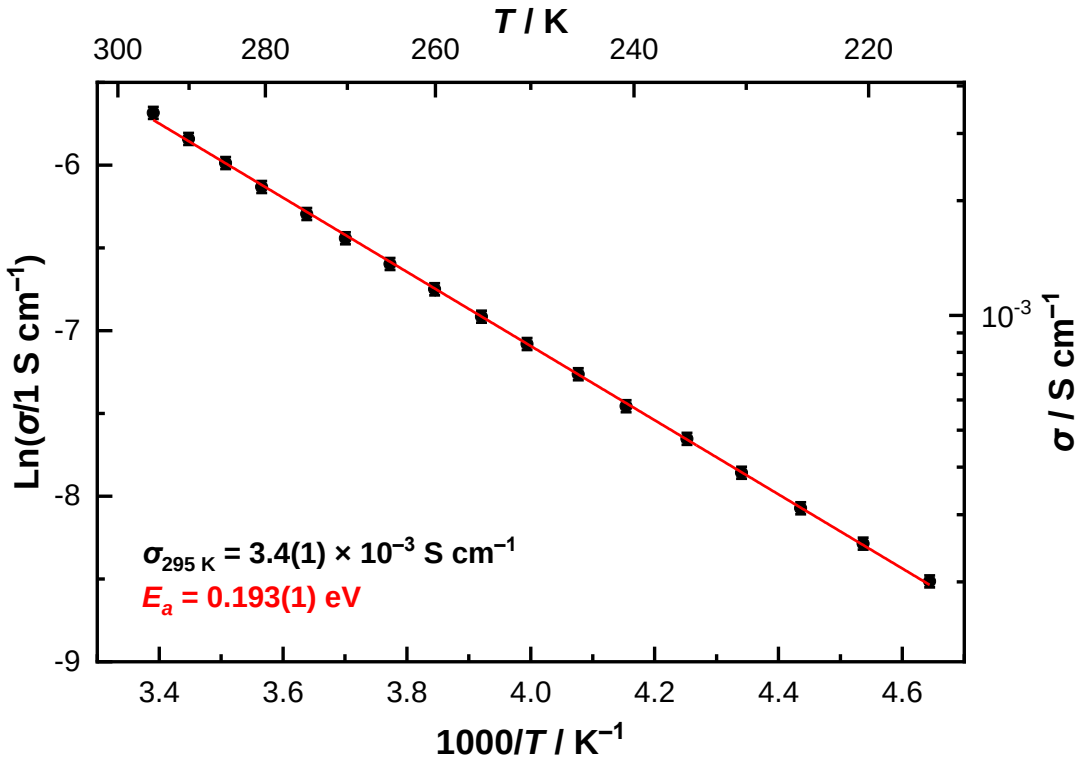


Figure 5.22 Arrhenius plot of the temperature dependence of the electrical conductivity for the premier two-point pressed pellet device of **5.2** (Device 3). Experimental data (black) and line of best fit (blue). Error bars are ± s.u. Where not visible, error bars lie within the data point.

Several structural considerations may account for the unexpectedly high electrical conductivity and low E_a of **5.2**, compared to the aforementioned Fe–tetraoxolene frameworks with complete or partial ligand charge ordering. The Coulombic interactions between anionic $[Fe_2(Clan)_3]^{2-}$ sheets and cations are markedly different between $(^nPr_4N)_2[Fe_2(Clan)_3]$ and **5.2** (Figure 5.23). For the former, every anionic layer is equidistant from the $^nPr_4N^+$ cations located between the anionic layers. Consequently, charge carriers (either holes or electrons) within every $[Fe_2(Clan)_3]^{2-}$ layer will experience an equivalent Coulombic interaction, which in turn would influence the probability of carrier hopping, and therefore carrier mobility and electrical conductivity. In contrast, MeV^{2+} cations are sited exclusively within the hexagonal cavity of the Fe2 anionic sheets in **5.2**. This would result in disparate Coulombic interactions experienced by charge carriers in Fe1 compared to Fe2 sheets, which may increase the carrier mobility in the Fe1 anionic sheets relative to the Fe2

sheets. Given CT interactions of viologen cations with the anionic tetraoxolene networks localises the $Xan^{3-\bullet}$ state over a large temperature range, reducing any network–cation interaction for a given layer could allow more facile charge transport within that layer.

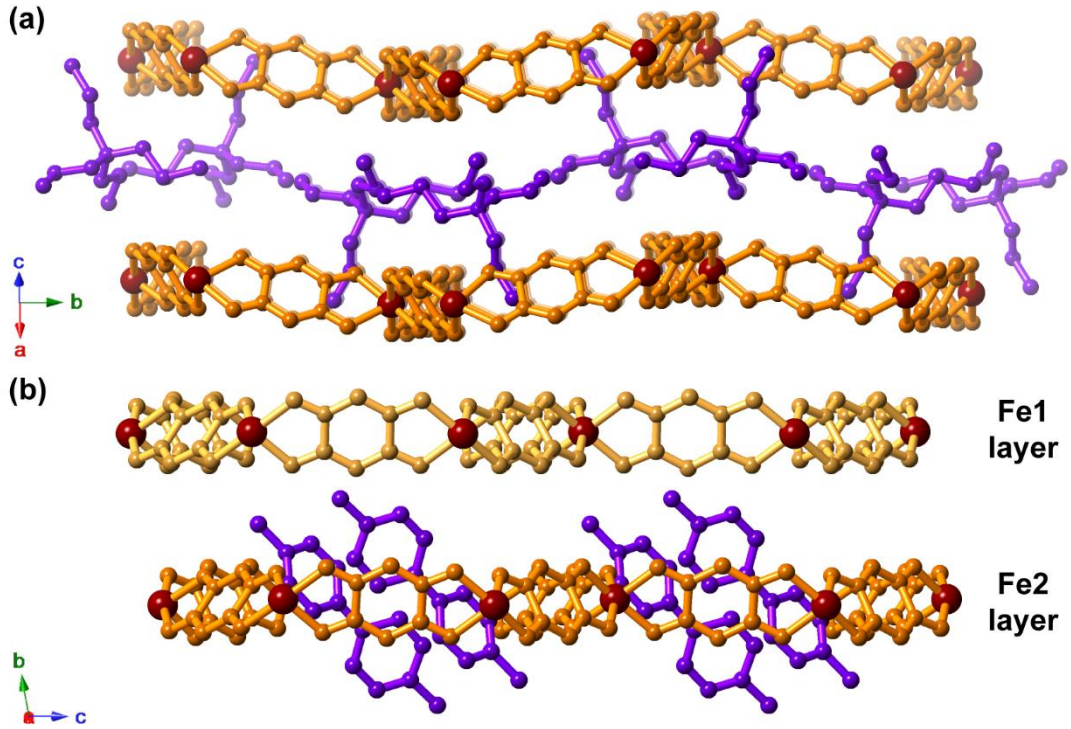


Figure 5.23 Interlayer Coulombic interactions between cations (purple) and anionic $[Fe_2(Clan)_3]^{2-}$ sheets (tan and orange) in $(^nPr_4N)_2[Fe_2(Clan)_3]$ and (b) **5.2**. Maroon = Fe. Cl not shown for clarity.

Secondly, there is significant corrugation of the anionic $[Fe_2(Clan)_3]^{2-}$ sheets in $(^nPr_4N)_2[Fe_2(Clan)_3]$ (Figure 5.23a), compared to the planar Fe1 or Fe2 anionic $[Fe_2(Clan)_3]^{2-}$ in **5.2**. Distortions to the sheet geometry, and hence the Fe coordination environment in $(^nPr_4N)_2[Fe_2(Clan)_3]$, may cause less efficient metal–ligand orbital overlap, and therefore a lower carrier mobility and electrical conductivity within the plane of the anionic sheets. Desolvation of $(Me_2NH_2)_2[Fe_2(Clan)_3]\cdot 6DMF\cdot 2H_2O$ induces a slight geometric layer distortion, causing the electrical conductivity to decrease from $\sigma_{RT} = 1.4(7) \times 10^{-2}$ S cm^{-1} to $\sigma_{RT} = 1.0(3) \times 10^{-3}$ S cm^{-1} for the desolvated framework,[23] which illustrates slight network geometry distortions may impact upon intrasheet change transport. Finally, **5.2** also exhibits a dramatically

reduced sheet-to-sheet spacing of 6.253 Å, compared to 8.903 Å in (^{n}Pr$_4$N)$_2$[Fe$_2$(Clan)$_3$]. Although the electrical conductivity is typically several orders of magnitude lower perpendicular to the plane of the anionic sheets,[4, 17, 46] reducing the distance over which intersheet carrier hopping occurs could also facilitate a higher charge mobility and therefore increased overall pressed-pellet conductivity. Critically, these results highlight that for topologically similar Fe–chloranilate compounds, the electrical conductivity is not solely dependent on the ligand substituents and degree of ligand-charge ordering. Rather, there is delicate balance between the measured properties of the mixed-valence frameworks, and a combination of network–cation interactions and structure packing, in addition to the degree of electron delocalisation between the different ligand valence states.

5.3 Conclusion

In this chapter, a novel mixed-valence Fe–chloranilate coordination polymer **5.1** was successfully obtained and characterised structurally. As desired, spontaneous electron transfer from the Fe^{II} precursor and $Clan^{2-}$ ligand, afforded a framework containing Fe^{III} and intrinsic ligand-centred mixed valency. Detailed analysis of the structure revealed the as-synthesised compound exhibited a ligand charged-order (MeV^{2+})[Fe^{III}_2($Clan^{2-}$)($Clan^{3-\bullet}$)$_2$] valence formulation, resulting from strong Coulombic and CT interactions between the π-electron poor MeV^{2+} cations and the anionic [Fe$_2$(Clan)$_3$]$^{2-}$ network. Critically, this drives home the theme put forth throughout this thesis, that using viologen cations reliably enforces localisation of the $Xan^{3-\bullet}$ valence state, and is therefore a robust strategy to produced ligand charge-ordered mixed-valence Fe–tetraoxolene frameworks. On the other hand, the structural disparity observed between the (MeV)[Fe$_2$(Fan)$_3$] compounds and **5.1**, demonstrates the contrasting nature of fluoranilate coordination chemistry, which is apparently more sensitive to subtle supramolecular interactions. This disparity also suggests that MeV^{2+} cations play a more malleable templating role, compared to $PhenQ^{2+}$ cations in the **3.1^{X}** family of compounds, arising from the conformational flexibility.

In contrast to the **3.1^{X}** or **4.1** family of compounds, which exhibit only minor geometric distortions to the networks upon changes in solvation, isolation of as-synthesised **5.1** caused a dramatic structural transformation to a new phase **5.2**. This transition was followed by SC- and P-XRD, revealing the partially-desolvated isolated

phase **5.2** exhibits a unique ABAB layered structure, in which two types of anionic $[Fe_2(Clan)_3]^{2-}$ layers participate in different interactions with the MeV^{2+} cations. The CT interactions between MeV^{2+} and the anionic network also modifies the UV-Vis-NIR spectrum of **5.2**, similarly to other viologen-containing mixed-valence compounds reported in this thesis. This behaviour provides further evidence that use of viologen countercations is an effective method to influence the electronic structure of Fe–tetraoxolene frameworks. The ABAB layered structure of **5.2** gives rise to somewhat unexpected physical properties. While MeV^{2+} in **5.2** remains redox-active, the absence of strong intersheet Coulombic interactions destabilises the structure to anodic electrochemical processes, in contrast to **3.1^{Cl}b** which was stable to anionic and cathodic processes. Finally, transport measurements on **5.2** revealed the compound exhibits thermally-activated semiconductor behaviour, which was ascribed to IVCT between the different ligand valence states. The premier pressed-pellet device reached $\sigma_{295\ K}$ = 3.4(1) × 10^{-3} S cm^{-1}, which is surprisingly high and comparable to the electrical conductivities exhibited by Fe–tetraoxolene frameworks with completely delocalised ligand valence formulations. Moreover, the activation energy (E_a = 0.193(1) eV) is surprisingly lower than Fe^{III}–chloranilate frameworks with similar ligand charge-ordered $[Fe^{III}_2(Clan^{2-})(Clan^{3-\bullet})_2]^{2-}$ valence formulations. These findings are suggestive of more facile charge-transport in **5.2**, than in Fe–chloranilate compounds with analogous ligand charge-ordered valence formations such as $(^nPr_4N)_2[Fe_2(Clan)_3]$. The relatively more facile charge-transport in **5.2** was attributed to the asymmetric Coulombic interactions between MeV^{2+} and by the two types of anionic $[Fe_2(Clan)_3]^{2-}$ layers, which has not previously been observed in Fe–tetraoxolene coordination polymers.

In summary, these results demonstrate that although the resultant structures and transformations engendered by viologen cations are sometimes unpredictable, these cations can still be recruited for the synthesis of spectroscopically and electrically interesting mixed-valence tetraoxolene frameworks. Moreover, they provide significant motivation to further explore the range of mixed-valence tetraoxolene materials containing viologen cations, to uncover functional compounds with unexpected and tantalising synergies of physical properties, arising from their unique structures compared to frameworks containing only redox-inactive cations.

5.4 Experimental

5.4.1 General Considerations

Unless overwise specified, all manipulations were performed under an atmosphere of dry dinitrogen (N_2) using standard Schlenk techniques or using a Vacuum Atmospheres glovebox. For crystallization of (MeV)[Fe_2(Clan)$_3$]·6MeCN (**5.1**), acetonitrile (MeCN) was used without further purification. For post-synthetic solvent washing on as-synthesised **5.1** to give (MeV)[Fe_2(Clan)$_3$]·1.3MeCN (**5.2**), MeCN was dried twice sequentially over activated 3 Å molecular sieves, then stored under an atmosphere of dry N_2. Immediately before use, anhydrous MeCN was degassed by three freeze-pump-thaw cycles. Nujol was dried and deoxygenated by stirring over molten Na metal *in vacuo*, then stored in a N_2-filled glovebox over Na sand. 3,6-Dichloro-1,2,4,5-tetrahydroxybenzene (H_4Clan) and *N*,*N*′-dimethyl-4,4′-bipyridinium di(4-toluenesulfonate) (MeV(OTs)$_2$) were synthesised as described in Chapter 2 (Sections 2.4.2.3 and 2.4.3.1 respectively). General spectroscopic and physical characterisation was performed as described in Chapter 7.

5.4.2 (MeV)[Fe_2(Clan)$_3$]·*y*MeCN (5.1, *y* =6; 5.2, *y* = 1.3)

In air, a solution of $Fe^{II}Cl_2$·4H_2O (39.8 mg, 0.2 mmol), LiOAc·2H_2O (10.2 mg, 0.1 mmol) and MeV(OTs)$_2$ (211.5 mg, 0.4 mmol) in H_2O (4 mL) was carefully layered below a solution of H_4Clan (63.3 mg, 0.3 mmol) in MeCN (10 mL) in a soda glass vial (OD = 25 mm), with a buffer layer of 1:1 v/v MeCN/H_2O (4 mL). Black elongated blocks with a metallic blue lustre suitable for SC-XRD were visible on the vial walls within two days, in addition to a greenish powder on the vial bottom. For (MeV)[Fe_2(Clan)$_3$]·6MeCN (**5.1**), single crystals were transferred immediately from the mother liquor to a cryoprotective oil (see Section 0); attempted isolation of the **5.1** phase leads to conversion to (MeV)[Fe_2(Clan)$_3$]·*y*MeCN (**5.2**) during workup.

For bulk synthesis of **5.2**, 20 reactions were conducted in parallel using equivalent conditions as for crystallisation of **5.1**. After 5 days, the reactions were transferred to an N_2-purged glovebag for workup. Under N_2, the greenish powder was carefully aspirated from the vials in ca. 4 mL mother liquor. The black crystalline product was then dislodged from the vial walls and suspended in the remaining mother liquor. The combined mother liquors were added to deoxygenated 2:1 v/v MeCN/H_2O (25 mL).

Additional green powder was removed from the crystalline product by decanting the supernatant liquid, then washing with deoxygenated 2:1 v/v MeCN/H_2O (3 × 100 mL) by resuspension of the crystalline product, sedimentation of the heavier crystalline product and decantation of the supernatant liquid. The crystalline product was then suspended in deoxygenated 2:1 v/v MeCN/H_2O (20 mL) and transferred to a two-neck Schlenk tube. The Schlenk tube was fitted with a Schlenk cap and rubber septum, then removed from the glovebag and placed under an atmosphere of dry N_2 on a Schlenk line. The suspension was briefly (<5 s) sonicated to breakup larger aggregates, then the supernatant liquid decanted by cannula transfer under dry N_2. The crystalline product was washed with dry, deoxygenated MeCN (3 × 20 mL) by resuspension of the crystalline product, sedimentation of the crystals, then decantation of the supernatant liquid by cannula transfer. Adventitious H_2O of crystallisation was removed by soaking in dry, deoxygenated MeCN (20 mL) overnight (12 hrs), followed by decantation of the supernatant by cannula transfer and washing of the product with dry, deoxygenated MeCN (2 × 10 mL) as described above. This soaking-washing procedure was repeated five times total. The black crystalline product was isolated by suction filtration in a flame-dried Schlenk frit under N_2, using dry, deoxygenated MeCN (3 × 20 mL) to transfer adherent solids from the Schlenk tube and wash the product on the frit (Figure 3.32). The product was then dried *in vacuo* on the frit to a free-flowing crystalline solid. The product on the Schlenk frit was moved into an N_2-filled glovebox, then transferred to a tared, flame-dried Schlenk tube for storage, yielding **5.2** as black crystals with a brilliant blueish-green metallic lustre (544 mg, 28.0% based upon H_4Clan). FT-IR (ATR, cm^{-1}): 3059 (w), 2247 (w), 1636 (m), 1428 (m), 1366 (m), 1323 (w), 1258 (w), 1176 (w) 1034 (w), 845 (s), 790 (w), 736 (w), 703 (w). Anal. Calcd. for $(C_{12}H_{14}N_2)(Fe_2Cl_6O_{12}C_{18})\cdot 1.3(C_2H_3N)$: C, 40.27%; H, 1.86%; N, 4.71%. Found: C, 40.72%; H, 1.85%; N, 4.71%.

5.4.3 Single-Crystal X-ray Diffraction

5.4.3.1 (MeV)[Fe$_2$(Clan)$_3$]·6MeCN (5.1)

Crystals of **5.1** were removed directly from the mother liquor and immediately coated with an oil-based cryoprotectant to prevent solvent loss, then mounted on nylon loops for measurement of crystallographic data(Table 5.5). Data were measured using Cu-Kα (λ = 1.54184 Å) radiation on a Rigaku XtaLAB Synergy-S diffractometer as described in Chapter 7. At all temperatures, rigid bond restraints using the RIGU instruction were applied to MeCN solvent molecules in the asymmetric unit. Similarity restraints using the SIMU instruction were applied to MeCN solvent molecules at 160 K and above. From 180–240 K, two-part positional disorder of one MeCN molecule was observed. The total occupancy of this molecule was set at one, and the occupancy of each site allowed to refine against each other. The atomic displacement parameters for each pair of equivalent atoms in the two parts were constrained to be equal using the EADP instruction. This solvent disorder could not be satisfactorily modelled at 260 K, so the putatively disordered MeCN molecule was modelled in a single position with enlarged atomic displacement parameters.

From 140 K, rigid bond restraints were applied to the atoms in **L$_3$** (O13 through Cl18) using the RIGU instruction; at 260 K, these rigid bond restraints were extended to all atoms (excluding Fe) in the asymmetric unit. Between 200–240 K, data beyond d = 0.82 Å were excluded from the refinement, while at 260 K, data beyond d = 0.837 Å were excluded from the refinement, using the SHEL instruction. The disagreeable reflections (1 1 3) (180–260 K) and (1 2 4) (200–240 K) were also excluded from the refinement using the OMIT instruction.

Table 5.5 Crystallographic data for (MeV)[$Fe_2(Clan)_3$]·6MeCN (**5.1**) measured at several temperatures.

***T* / K**	**100**	**120**	**140**
Empirical formula	$C_{21}H_{16}N_4O_6Cl_3Fe$	$C_{21}H_{16}N_4O_6Cl_3Fe$	$C_{21}H_{16}N_4O_6Cl_3Fe$
Formula weight	582.58	582.58	582.58
Habit	Trapezoid	Trapezoid	Trapezoid
Crystal system	Triclinic	Triclinic	Triclinic
Space group	*P*−1	*P*−1	*P*−1
a / Å	8.8120(2)	8.8270(2)	8.8398(2)
b / Å	11.6427(3)	11.6663(3)	11.6865(3)
c / Å	12.3376(3)	12.3511(3)	12.3611(3)
α / °	73.096(2)	72.921(2)	72.739(2)
β / °	75.443(2)	75.400(2)	75.318(2)
γ / °	80.519(2)	80.405(2)	80.262(2)
V / Å^3	1166.46(5)	1170.63(5)	1173.54(5)
Z	2	2	2
ρ_{calc} / g cm^{-3}	1.659	1.653	1.649
μ / mm^{-1}	8.767	8.736	8.715
F_{000}	590.0	590.0	590.0
Crystal size / mm^3	0.305 × 0.119 × 0.064	0.305 × 0.119 × 0.064	0.305 × 0.119 × 0.064
Radiation	Cu Kα (λ = 1.54184 Å)	Cu Kα (λ = 1.54184 Å)	Cu Kα (λ = 1.54184 Å)
2θ range	7.67 to 156.932	7.668 to 157.454	7.67 to 157.49
Index ranges	$-10 \le h \le 11$ $-14 \le k \le 14$ $-13 \le l \le 15$	$-10 \le h \le 11$ $-14 \le k \le 14$ $-13 \le l \le 15$	$-10 \le h \le 11$ $-14 \le k \le 14$ $-13 \le l \le 15$
Total/independent reflections	24142/4933 [R_{int} = 0.0473, R_{sigma} = 0.0288]	24316/4958 [R_{int} = 0.0472, R_{sigma} = 0.0288]	24356/4973 [R_{int} = 0.0504, R_{sigma} = 0.0298]
Data/restraints/ parameters	4933/27/320	4958/27/320	4973/54/320
Goodness-of-fit on F^2	1.048	1.057	1.067
Final *R* indexes [$I \ge 2\sigma(I)$]	R_1 = 0.0372, wR_2 = 0.1046	R_1 = 0.0369, wR_2 = 0.1047	R_1 = 0.0379, wR_2 = 0.1082
Final *R* indexes [all data]	R_1 = 0.0391, wR_2 = 0.1057	R_1 = 0.0388, wR_2 = 0.1059	R_1 = 0.0401, wR_2 = 0.1095
Largest diff. peak/hole / e Å^{-3}	0.50/−0.55	0.46/−0.48	0.42/−0.50

Table 5.5(cont.) Crystallographic data for (MeV)[$Fe_2(Clan)_3$]·6MeCN (**5.1**) measured at several temperatures.

***T* / K**	**160**	**180**	**200**
Empirical formula	$C_{21}H_{16}N_4O_6Cl_3Fe$	$C_{21}H_{16}N_4O_6Cl_3Fe$	$C_{21}H_{16}N_4O_6Cl_3Fe$
Formula weight	582.58	582.58	582.58
Habit	Trapezoid	Trapezoid	Trapezoid
Crystal system	Triclinic	Triclinic	Triclinic
Space group	*P*−1	*P*−1	*P*−1
a / Å	8.8553(2)	8.8691(3)	8.8903(3)
b / Å	11.7111(3)	11.7373(4)	11.7687(4)
c / Å	12.3762(3)	12.3936(4)	12.4055(5)
α / °	72.553(2)	72.331(3)	72.143(4)
β / °	75.261(2)	75.202(3)	75.128(3)
γ / °	80.130(2)	79.976(3)	79.821(3)
V / Å^3	1177.83(5)	1181.99(7)	1187.24(8)
Z	2	2	2
ρ_{calc} / g cm^{-3}	1.643	1.637	1.630
μ / mm^{-1}	8.683	8.652	8.614
F_{000}	590.0	590.0	590.0
Crystal size / mm^3	0.305 × 0.119 × 0.064	0.305 × 0.119 × 0.064	0.305 × 0.119 × 0.064
Radiation	Cu Kα (λ = 1.54184 Å)	Cu Kα (λ = 1.54184 Å)	Cu Kα (λ = 1.54184 Å)
2θ range	7.668 to 157.284	7.668 to 157.614	7.668 to 140.078
Index ranges	$-10 \le h \le 11$ $-14 \le k \le 14$ $-13 \le l \le 15$	$-10 \le h \le 11$ $-14 \le k \le 14$ $-13 \le l \le 15$	$-10 \le h \le 10$ $-14 \le k \le 14$ $-13 \le l \le 15$
Total/independent reflections	24513/4980 [R_{int} = 0.0500, R_{sigma} = 0.0297]	24595/4992 [R_{int} = 0.0518, R_{sigma} = 0.0307	23735/4505 [R_{int} = 0.0496, R_{sigma} = 0.0299]
Data/restraints/ parameters	4980/60/320	4992/111/331	4505/111/331
Goodness-of-fit on F^2	1.063	1.053	1.049
Final *R* indexes [$I \ge 2\sigma(I)$]	R_1 = 0.0377, wR_2 = 0.1076	R_1 = 0.0377, wR_2 = 0.1068	R_1 = 0.0350, wR_2 = 0.1011
Final *R* indexes [all data]	R_1 = 0.0402, wR_2 = 0.1091	R_1 = 0.0405, wR_2 = 0.1084	R_1 = 0.0378, wR_2 = 0.1026
Largest diff. peak/hole / e Å^{-3}	0.44/−0.50	0.39/−0.49	0.38/−0.40

Table 5.5(cont.) Crystallographic data for (MeV)[Fe_2(Clan)$_3$]·6MeCN (**5.1**) measured at several temperatures.

***T* / K**	**220**	**240**	**260**
Empirical formula	$C_{21}H_{16}N_4O_6Cl_3Fe$	$C_{21}H_{16}N_4O_6Cl_3Fe$	$C_{21}H_{16}N_4O_6Cl_3Fe$
Formula weight	582.58	582.58	582.58
Habit	Trapezoid	Trapezoid	Trapezoid
Crystal system	Triclinic	Triclinic	Triclinic
Space group	*P*−1	*P*−1	*P*−1
a / Å	8.9039(2)	8.9192(3)	8.9397(2)
b / Å	11.8084(3)	11.8483(4)	11.8921(3)
c / Å	12.4208(3)	12.4376(4)	12.4702(2)
α / °	71.935(2)	71.732(3)	71.4967(18)
β / °	75.122(2)	75.110(3)	75.148(2)
γ / °	79.682(2)	79.529(3)	79.405(2)
V / Å^3	1192.88(5)	1198.86(7)	1207.57(5)
Z	2	2	2
ρ_{calc} / g cm^{-3}	1.622	1.614	1.602
μ / mm^{-1}	8.573	8.530	8.469
F_{000}	590.0	590.0	590.0
Crystal size / mm^3	0.305 × 0.119 × 0.064	0.305 × 0.119 × 0.064	0.305 × 0.119 × 0.064
Radiation	Cu Kα (λ = 1.54184 Å)	Cu Kα (λ = 1.54184 Å)	Cu Kα (λ = 1.54184 Å)
2θ range	7.666 to 140.15	7.664 to 140.15	7.65 to 134.11
Index ranges	$-10 \le h \le 10$ $-14 \le k \le 14$ $-13 \le l \le 15$	$-10 \le h \le 10$ $-14 \le k \le 14$ $-13 \le l \le 15$	$-10 \le h \le 10$ $-14 \le k \le 14$ $-13 \le l \le 14$
Total/independent reflections	23837/4528 [R_{int} = 0.0491, R_{sigma} = 0.0304]	23895/4552 [R_{int} = 0.0565, R_{sigma} = 0.0340]	22642/4304 [R_{int} = 0.0576, R_{sigma} = 0.0379]
Data/restraints/ parameters	4528/111/331	4552/111/331	4304/189/320
Goodness-of-fit on F^2	1.046	1.043	1.233
Final *R* indexes [$I \ge 2\sigma(I)$]	R_1 = 0.0359, wR_2 = 0.1038	R_1 = 0.0388, wR_2 = 0.1108	R_1 = 0.0644, wR_2 = 0.1727
Final *R* indexes [all data]	R_1 = 0.0389, wR_2 = 0.1055	R_1 = 0.0427, wR_2 = 0.1131	R_1 = 0.0935, wR_2 = 0.2556
Largest diff. peak/hole / e Å^{-3}	0.37/−0.39	0.38/−0.41	0.88/−1.18

5.4.3.2 (MeV)[Fe$_2$(Clan)$_3$]·2.7MeCN (5.2)

In an N_2-filled glovebox, isolated crystals of **5.2** were suspended in anhydrous, deoxygenated Nujol to protect the crystals from exposure to aerial dioxygen outside the glovebox. The suspension was passed out of the glovebox, and the crystals immediately transferred to an oil-based cryoprotectant, before mounting on nylon loops for measurement of crystallographic data (Table 5.6). Data were measured using Cu-Kα (λ = 1.54184 Å) radiation on a Rigaku XtaLAB Synergy-S diffractometer as described in Chapter 7. Analysis of the reflection data using CrysAlisPRO revealed the presence of a three-component twin in the crystal. Data reduction, multi-scan and Gaussian absorption corrections of all twin components were performed using CrysAlis PRO to produce a HKLF5 dataset with contributions from all twin components. The structure was solved using only one twin component with SHELXT, with subsequent structure refinements performed using the HKLF5 dataset and the BASF instruction. Due to poor quality, data beyond d = 0.837 Å were excluded from the refinement, in addition to a disagreeable reflection (−2 2 2). Rigid bond restraints were applied to all non-hydrogen atoms (except Fe) in the structure using the RIGU instruction. Inspection of the electron density difference (F_O−F_C) maps revealed the presence of significant positive electron density within the voids in the structure. This was attributed to severely disordered MeCN molecules which could not be modelled satisfactorily. The scattering contribution of the disordered solvent was accounted for using the SQUEEZE[25] routine in PLATON.[26] The solvation in the framework voids was then estimated from the electron count determined by SQUEEZE, assuming it comprised solely MeCN (2.7 MeCN per formula unit). The absence of guest H_2O was justified by use of extensive soaking of as-synthesised material in anhydrous MeCN following crystallisation, in addition to handling of the isolated sample under anhydrous, anaerobic conditions (see Section 5.4.2). The absence of a large absorbance around 3500 cm^{-1} attributed to H_2O, and presence of a $\nu_{C\equiv N}$ = 2247 cm^{-1} attributed to MeCN, in the FT-IR spectrum of isolated **5.2** validates this assumption (Figure 5.14).

Table 5.6 Crystallographic data for **5.2**.

Compound	(MeV)[Fe_2(Clan)$_3$]·2.7MeCN (**5.2**)
Empirical formula	$C_{35.4}H_{22.1}N_{4.7}O_{12}Cl_6Fe_2$
Formula weight	1029.68
Habit	Trapezoid
T / K	100.00(1)
Crystal system	Triclinic
Space group	$P\bar{1}$
a / Å	12.9129(7)
b / Å	13.0512(12)
c / Å	13.6362(8)
α / °	93.379(6)
β / °	116.317(6)
γ / °	103.101(6)
V / Å^3	1972.6(3)
Z	2
ρ_{calc} / g cm^{-3}	1.734
μ / mm^{-1}	10.250
F_{000}	1035.0
Crystal size / mm^3	0.431 × 0.139 × 0.06
Radiation	Cu Kα (λ = 1.54184 Å)
2θ range	134.156
Index ranges	$-12 \le h \le 15$ $-15 \le k \le 15$ $-16 \le l \le 16$
Total/independent reflections	9347/9347 [R_{int} = 0.091, R_{sigma} = 0.0141]
Data/restraints/ parameters	9347/267/473
Goodness-of-fit on F^2	1.047
Final R indexes [$I \ge 2\sigma(I)$]	R_1 = 0.0973, wR_2 = 0.2852
Final R indexes [all data]	R_1 = 0.1155, wR_2 = 0.3076
Largest diff. peak/hole / e Å^{-3}	1.22/−0.73

NB: The empirical formula and calculated F_{000} values include the contribution of 2.7 disordered MeCN molecules in the channels of **5.2**.

5.4.4 Powder X-ray Diffraction (P-XRD)

P-XRD measurements were performed using the PD beamline at the Australian Synchrotron,[49] as described in Chapter 7. The sample temperature was controlled using an Oxford Cryostream 700 at 250 K for **5.1** and 100 K for **5.2**. In air, a sample of as-synthesised **5.1** was transferred from the mother liquor and washed with 2:1 MeCN/H_2O (3 × 20 mL), then MeCN (3 × 20 mL) to remove amorphous by-products. The crystalline product was gently ground under MeCN then transferred as a slurry to a borosilicate capillary (OD = 0.7 mm), which was then flame sealed. In a N_2-filled glovebox, isolated **5.2** was gently ground with an agate mortar and pestle, then transferred to a borosilicate capillary (OD = 0.5 mm). The capillary was then sealed with an electric arc lighter and wax before being transferred out of the glovebox for measurement of P-XRD data.

5.5 References

[1] M. L. Mercuri, F. Congiu, G. Concas, S. A. Sahadevan, *Magnetochemistry* **2017**, *3*, 17.

[2] F. Tinti, M. Verdaguer, O. Kahn, J. M. Savariault, *Inorg. Chem.* **1987**, *26*, 2380-2384.

[3] M. Atzori, S. Benmansour, G. Mínguez Espallargas, M. Clemente-León, A. Abhervé, P. Gómez-Claramunt, E. Coronado, F. Artizzu, E. Sessini, P. Deplano, A. Serpe, M. L. Mercuri, C. J. Gómez García, *Inorg. Chem.* **2013**, *52*, 10031-10040.

[4] S. Benmansour, A. Abhervé, P. Gómez-Claramunt, C. Vallés-García, C. J. Gómez-García, *ACS Appl. Mater. Interfaces* **2017**, *9*, 26210-26218.

[5] A. E. Thorarinsdottir, R. Bjornsson, T. D. Harris, *Inorg. Chem.* **2020**, *59*, 4634-4649.

[6] Y. Sekine, J. Chen, N. Eguchi, H. Miyasaka, *Chem. Commun.* **2020**.

[7] J. Chen, Y. Sekine, Y. Komatsumaru, S. Hayami, H. Miyasaka, *Angew. Chem. Int. Ed.* **2018**, *57*, 12043-12047.

[8] R. Murase, C. J. Commons, T. A. Hudson, G. N. L. Jameson, C. D. Ling, K. S. Murray, W. Phonsri, R. Robson, Q. Xia, B. F. Abrahams, D. M. D'Alessandro, *Inorg. Chem.* **2020**, *59*, 3619-3630.

[9] C. J. Kingsbury, B. F. Abrahams, D. M. D'Alessandro, T. A. Hudson, R. Murase, R. Robson, K. F. White, *Cryst. Growth Des.* **2017**, *17*, 1465-1470.

[10] S. Alvarez, D. Avnir, M. Llunell, M. Pinsky, *New J. Chem.* **2002**, *26*, 996-1009.

[11] S. Alvarez, *Chem. Rev.* **2015**, *115*, 13447-13483.

[12] F. Huang, K. A. Switek, L. N. Zakharov, F. R. Fronczek, C. Slebodnick, M. Lam, J. A. Golen, W. S. Bryant, P. E. Mason, A. L. Rheingold, M. Ashraf-Khorassani, H. W. Gibson, *J. Org. Chem.* **2005**, *70*, 3231-3241.

[13] F. Yang, J.-C. Deng, Z.-G. Li, J.-W. Xu, *Acta Crystallogr. E* **2008**, *64*, o253.

[14] T. M. Bockman, J. K. Kochi, *J. Org. Chem.* **1990**, *55*, 4127-4135.

[15] N. Leblanc, N. Mercier, O. Toma, A. H. Kassiba, L. Zorina, P. Auban-Senzier, C. Pasquier, *Chem. Commun.* **2013**, *49*, 10272-10274.

[16] W. W. Porter, III, T. P. Vaid, *J. Org. Chem.* **2005**, *70*, 5028-5035.

[17] J. Chen, Y. Sekine, A. Okazawa, H. Sato, W. Kosaka, H. Miyasaka, *Chem. Sci.* **2020**, *11*, 3610-3618.

[18] J. A. DeGayner, K. Wang, T. D. Harris, *J. Am. Chem. Soc.* **2018**, *140*, 6550-6553.

[19] C. G. Pierpont, *Coord. Chem. Rev.* **2001**, *216-217*, 99-125.

[20] T. Tezgerevska, K. G. Alley, C. Boskovic, *Coord. Chem. Rev.* **2014**, *268*, 23-40.

[21] N. Shaikh, S. Goswami, A. Panja, X.-Y. Wang, S. Gao, R. J. Butcher, P. Banerjee, *Inorg. Chem.* **2004**, *43*, 5908-5918.

[22] I.-R. Jeon, B. Negru, R. P. Van Duyne, T. D. Harris, *J. Am. Chem. Soc.* **2015**, *137*, 15699-15702.

[23] J. A. DeGayner, I.-R. Jeon, L. Sun, M. Dincă, T. D. Harris, *J. Am. Chem. Soc.* **2017**, *139*, 4175-4184.

[24] M. Llunell, D. Casanova, J. Cicera, P. Alemany, S. Alvarez, *SHAPE, Version 2.1*, Universitat de Barcelona, Barcelona, Spain, **2013**.

[25] A. L. Spek, *Acta Crystallogr. C* **2015**, *71*, 9-18.

[26] A. L. Spek, *Acta Crystallogr. D* **2009**, *65*, 148-155.

[27] L. E. Darago, M. L. Aubrey, C. J. Yu, M. I. Gonzalez, J. R. Long, *J. Am. Chem. Soc.* **2015**, *137*, 15703-15711.

[28] R. Murase, B. F. Abrahams, D. M. D'Alessandro, C. G. Davies, T. A. Hudson, G. N. L. Jameson, B. Moubaraki, K. S. Murray, R. Robson, A. L. Sutton, *Inorg. Chem.* **2017**, *56*, 9025-9035.

[29] N. N. Greenwood, T. C. Gibb, *Mössbauer Spectroscopy*, Chapman and Hall, London, UK, **1971**.

[30] P. Gütlich, E. Bill, A. X. Trautwein, *Mössbauer Spectroscopy and Transition Metal Chemistry*, Springer-Verlag, Berlin, Germany, **2011**.

[31] V. A. Grillo, G. R. Hanson, D. Wang, T. W. Hambley, L. R. Gahan, K. S. Murray, B. Moubaraki, C. J. Hawkins, *Inorg. Chem.* **1996**, *35*, 3568-3576.

[32] M. E. Ziebel, L. E. Darago, J. R. Long, *J. Am. Chem. Soc.* **2018**, *140*, 3040-3051.

[33] M. E. Ziebel, C. A. Gaggioli, A. B. Turkiewicz, W. Ryu, L. Gagliardi, J. R. Long, *J. Am. Chem. Soc.* **2020**, *142*, 2653-2664.

[34] M. B. Robin, P. Day, in *Advances in Inorganic Chemistry and Radiochemistry, Vol. 10* (Eds.: H. J. Emeléus, A. G. Sharpe), Academic Press, London, UK, **1968**.

[35] N. S. Hush, in *Prog. Inorg. Chem., Vol. 8* (Ed.: F. A. Cotton), Interscience Publishers, New York, NY, **1967**.

[36] N. S. Hush, *Electrochim. Acta* **1968**, *13*, 1005-1023.

[37] B. S. Brunschwig, C. Creutz, N. Sutin, *Chem. Soc. Rev.* **2002**, *31*, 168-184.

[38] J. Tauc, *Mater. Res. Bull.* **1968**, *3*, 37-46.

[39] S. Kasap, C. Koughia, J. Singh, H. Ruda, S. O'Leary, in *Springer Handbook of Electronic and Photonic Materials* (Eds.: S. Kasap, P. Capper), Springer, New York, NY, **2006**.

[40] B. F. Abrahams, A. M. Bond, T. H. Le, L. J. McCormick, A. Nafady, R. Robson, N. Vo, *Chem. Commun.* **2012**, *48*, 11422-11424.

[41] K. Taniguchi, J. Chen, Y. Sekine, H. Miyasaka, *Chem. Mater.* **2017**, *29*, 10053-10059.

[42] J. Chen, K. Taniguchi, Y. Sekine, H. Miyasaka, *J. Magn. Magn. Mater.* **2020**, *494*, 165818.

[43] S. Hünig, J. Groβ, E. F. Lier, H. Quast, *Liebigs Ann. Chem.* **1973**, *1973*, 339-358.

[44] S. Hünig, J. Groβ, W. Schenk, *Liebigs Ann. Chem.* **1973**, *1973*, 324-338.

[45] S. Hünig, W. Schenk, *Liebigs Ann. Chem.* **1979**, *1979*, 1523-1533.

[46] S. A. Sahadevan, A. Abhervé, N. Monni, C. Sáenz de Pipaón, J. R. Galán-Mascarós, J. C. Waerenborgh, B. J. C. Vieira, P. Auban-Senzier, S. Pillet, E.-E. Bendeif, P. Alemany, E. Canadell, M. L. Mercuri, N. Avarvari, *J. Am. Chem. Soc.* **2018**, *140*, 12611-12621.

[47] L. Sun, M. G. Campbell, M. Dincă, *Angew. Chem. Int. Ed.* **2016**, *55*, 3566-3579.

[48] J.-H. Dou, L. Sun, Y. Ge, W. Li, C. H. Hendon, J. Li, S. Gul, J. Yano, E. A. Stach, M. Dincă, *J. Am. Chem. Soc.* **2017**, *139*, 13608-13611.

[49] K. S. Wallwork, B. J. Kennedy, D. Wang, *AIP Conference Proceedings* **2007**, *879*, 879-882.

This page intentionally left blank

Chapter 6 Conclusion

6.1 Thesis Summary 393

6.2 Future Work.....401

6.3 References 406

This page intentionally left blank

6.1 Thesis Summary

This thesis has described a structurally diverse range of anionic metal–tetraoxolene coordination polymers containing viologen-like countercations, and explored the magnetic, electrochemical, and conductive properties of several of these compounds.

Chapter 2 examined how several 4,4′- and 2,2′-bipyridyl derived viologens (RV^{2+} and RQ^{2+} respectively) influenced the topology and geometry of fluoranilate and chloranilate coordination polymers. Redox-inactive ammonium or phosphonium species have commonly been used as counterions for anionic tetraoxolene coordination polymers. Compared to these cations, we expected the structure-directing role of RV^{2+} and RQ^{2+} cations would be more complicated, because they can engage in charge-transfer (CT) interactions with π-electron rich species, in addition to Coulombic, C–H···O and steric interactions. Use of a small range of viologen countercations yielded a structurally diverse range of 1-, 2- and 3D anionic tetraoxolene coordination polymers. The combination of *N*,*N*′-dimethyl-4,4′-bipyridinium (MeV^{2+}) cations and chloranilate ($Clan^{2-}$), with either Mn^{II} or Cd^{II} yielded the dense 3D diamondoid networks $(MeV)[M(Clan)_2]$ (M = Mn^{II}, Cd^{II}). Varying the solvent used during synthesis also afforded the 2D honeycomb network $(MeV)[Mn_2(Clan)_3]\cdot 6MeCN$. In contrast, when fluoranilate (Fan^{2-}) ligands were employed, ladder-type 1D coordination polymers of composition $(MeV)[M_2(Fan)_3(H_2O)_2]$ (M = Mn^{II}, Cd^{II}) were generated. These results clearly demonstrate the somewhat unpredictable role that MeV^{2+} cations play in templating tetraoxolene networks. When using divalent metal species and ligands in the quinonoid dianionic Xan^{2-} state, as in aforementioned examples, the viologen countercations only interact with the anionic tetraoxolene networks by steric, Coulombic and C–H···O associations. The relatively electron-poor character of Xan^{2-} ligands in these coordination polymers inhibits donor-acceptor CT interactions between anionic tetraoxolene networks and viologen countercations. Although the types of interactions between the countercations, either redox-active viologens or redox-inactive alkylammonium cations, and the anionic tetraoxolene networks are similar, the largely planar shape and defined interaction geometry of viologen cations gives rise to the structural diversity. Additionally, the resultant coordination polymer topologies obtained were strongly dependant on the precise synthetic conditions employed,

suggesting the interplay between ligands, metals, cations, and solvents is more delicate with viologen cations, than with alkylammonium countercations.

When used as countercations for mixed-valence Fe–tetraoxolene frameworks, the structure directing role of viologen cations is more complicated. Reacting the 2,2′-bipyridine-derived viologen cations dipyrido[1,2-*a*:2′,1′-*c*]pyrazinediium ($PDiQ^{2+}$), and 6,7-dihydrodipyrido[1,2-*a*:2′,1′-*c*]pyrazinediium (DiQ^{2+}), with Fe^{II} and $Clan^{2-}$ ligands, afforded the mixed-valence 3D (10,3)-*b* frameworks (PDiQ)[$Fe_2(Clan)_3$]·solvent (**2.5**) and (DiQ)[$Fe_2(Clan)_3$]·solvent (**2.6**). Ligand-based mixed valency in these compounds arose due to a spontaneous electron transfer between Fe^{II} and $Clan^{2-}$, as has been observed in other Fe–tetraoxolene frameworks, producing Fe^{III} and $Clan^{3-\bullet}$ states. Additionally, the planar geometry and π-electron deficient character of the $PDiQ^{2+}$ and DiQ^{2+} cations allowed them to engage in strong CT interactions with the mixed-valence networks, giving ligand charge-ordered network formulations. These CT interactions, in addition to enhanced Coulombic interactions, consistently localise the $Xan^{3-\bullet}$ state and cause $[Fe^{III}_2(Clan^{2-})(Clan^{3-\bullet})_2]^{2-}$ ligand charge ordering, when viologens are employed as countercations. Interestingly, use of Fan^{2-} ligands in combination with Fe^{II} and $PDiQ^{2+}$ afforded a mixed-valence 2D (6,3) coordination polymer (PDiQ)[$Fe^{III}_2(Fan)_3$]·solvent, rather than the desired (10,3)-*b* network, further highlighting the structurally divergent nature of fluor- and chloranilate coordination polymers. Despite $PDiQ^{2+}$ only engaging in Coulombic and C–H···O associations with the anionic $[Fe_2(Fan)_3]^{2-}$ network, localisation of the $Fan^{3-\bullet}$ state and ligand charge-ordering was still observed in this compound. These results suggest that using viologen countercations could be a versatile method to induce charge-state localisation in these mixed-valence frameworks, which may be useful in modulating material properties that are influenced by the degree of valence delocalisation.

Detailed structural investigations for an isostructural family of 2D mixed-valence frameworks (PhenQ)[$Fe_2(Xan)_3$] (**3.1^{X}**, $PhenQ^{2+}$ = 5,6-dihydropyrazino[1,2,3,4-*lmn*][1,10]-phenanthrolinediium; X = F, Cl, Br) were reported in Chapter 3. Additionally, comprehensive physical properties measurements were undertaken on the DMF-solvated compound **3.1^{Cl}b**, to elucidate how the $PhenQ^{2+}$ cation impacted upon the conductive, electroactive and magnetic behaviour of the compound. Considering the structural disparity displayed between fluor- and chloranilate

coordination polymers reported in Chapter 2, the ability to obtain a mixed-valence Fe–fluoranilate framework **3.1^{F}**, that was isostructural to the MeCN-solvated Fe–chloranilate compound **3.1^{Cl}a**, was somewhat surprising. The isostructural nature of the **3.1^{X}** family is probably due to the favourable shape complementarity between $PhenQ^{2+}$ and the interlayer space between $[Fe_2(Xan)_3]^{2-}$ sheets, coupled with the low conformational flexibility of $PhenQ^{2+}$ cations. Consequently, $PhenQ^{2+}$ cations may be more effective at dictating the resultant network topology, despite slight perturbations to the supramolecular interactions arising from differences in ligand halogen substituents. Like the mixed-valence compounds **2.5** and **2.6** described in Chapter 2, the Coulombic and CT interactions between $PhenQ^{2+}$ and the anionic $[Fe_2(Xan)_3]^{2-}$ networks are responsible for localisation of the $Xan^{3-\bullet}$ state in the **3.1^{X}** family. It is therefore clear that introducing CT interactions between viologens and mixed-valence tetraoxolene networks is an effective strategy to enforce at least partial localisation of the $Xan^{3-\bullet}$ state. The partial ligand charge-ordering exhibited by **3.1^{Cl}b** causes notable differences in the spectroscopic properties and therefore electronic structure, compared to $(Et_4N)_2[Fe_2(Clan)_3]$ which contains only redox-inactive cations such as. Additionally, inclusion of redox-active $PhenQ^{2+}$ countercations in **3.1^{Cl}b** gives access to new framework redox states, without compromising the desirable magnetic and conductive properties. These additional redox states could conceivably be exploited to produce switchable magnetic or conductive behaviour, by perturbing the electronic structure of these materials. Alternatively, these additional framework redox states could prove useful in increasing the gravimetric charge capacity and energy density of anionic tetraoxolene frameworks when employed as lithium-ion battery (LIB) cathodes.

Chapters 4 and 5 reported the attempted synthesis of an isostructural family of mixed-valence Fe–fluoranilate (Chapter 4) and Fe–chloranilate (Chapter 5) frameworks using MeV^{2+} countercations. Consistent with the variations witnessed with fluor- and chloranilate networks described in Chapter 2, the mixed-valence compounds $(MeV)[Fe_2(Fan)_3]\cdot$solvent and $(MeV)[Fe_2(Clan)_3]\cdot$solvent described in Chapter 4 and 5 respectively, are not isostructural. The structural disparity between the fluor- and chloranilate compounds is consistent with the observations presented in Chapter 2, that the supramolecular interactions which occur during assembly are delicately balanced. Regardless of these factors, for both the $(MeV)[Fe_2(Fan)_3]\cdot$solvent

and (MeV)[$Fe_2(Clan)_3$]·solvent frameworks, CT and Coulombic interactions between the π-electron deficient MeV^{2+} cations and anionic tetraoxolene networks caused localisation of the $Xan^{3-\bullet}$ state, producing ligand charge-ordered $[Fe_2(Xan^{2-})(Xan^{3-\bullet})_2]^{2-}$ formulations.

Detailed structure and property investigations into the mixed-valence (MeV)[$Fe_2(Fan)_3$]·solvent frameworks, *mP* **4.1a**, *aP* **4.1a** and **4.1b** were the focus of Chapter 4. In comparison to the mixed-valence **3.1^{X}** frameworks, the network geometry of the **4.1** family is more plastic to changes in solvation, allowing the distinct solvates *aP* **4.1a** and **4.1b** to be isolated. Despite both compounds showing equivalent 2D (6,3) network topologies and only slight disparities between their structures, dramatic differences in their spectroscopic and physical properties are observed. ^{57}Fe Mössbauer spectroscopy revealed the DMF solvate **4.1b** contains valence-pure Fe^{III} centres. By contrast, the isolated MeCN solvate *aP* **4.1a** exhibits intrinsic Fe^{II}/Fe^{III} mixed valency, in addition to the ligand-centred mixed valency present in both *aP* **4.1a** and **4.1b**. The different Fe valences between the compounds leads to a notable disparity in their electronic structures, suggestive of more facile intervalence charge-transfer (IVCT) in *aP* **4.1a** leading to a higher electrical conductivity than **4.1b**. The presence of Fe-based mixed valency in *aP* **4.1a**, presumably reflects a valence fluctuation that occurs more rapidly than the crystallographic time scale, and highlights the importance of multiple characterisation techniques to fully understand the structure and properties of these materials. Moreover, since this behaviour is thus far unique to mixed-valence Fe–fluoranilate systems, it underscores the importance of further systematic investigations into the spectroscopic and physical properties of mixed-valence Fe–fluoranilate frameworks.

Chapter 5 exclusively described the synthesis, structure and properties of a mixed-valence framework (MeV)[$Fe_2(Clan)_3$]·6MeCN (**5.1**) and the isolated compound (MeV)[$Fe_2(Clan)_3$]·*y*MeCN (**5.2**). While **5.1**, and the **3.1^{Cl}** and **4.1** families of frameworks all exhibit 2D (6,3) network topologies, the structural stability varies significantly upon isolation of crystalline material. A combination of single-crystal and powder X-ray diffraction analyses showed that **5.1** undergoes a dramatic structure transformation to the partially desolvated compound **5.2**. The ABAB $[Fe_2(Clan)_3]^{2-}$ layer stacking structure, arises from repositioning of MeV^{2+} cations. This also produces a unique packing arrangement in which MeV^{2+} cations only engage in strong

interactions with only one type of anionic layer. This packing arrangement seems to destabilise the overall structure to repeated Li^+ insertion-deinsertion possibly limiting use of 5.2 as a LIB battery cathode. On the other hand, **5.2** exhibits a higher-than-expected electrical conductivity based upon the ligand charge-ordered structure, in fact approaching the values measured for mixed-valence tetraoxolene frameworks with completely delocalised ligand valence states. A definitive cause for this higher-than-expected conductivity and more facile charge transport is not immediately apparent but is hypothesised to result from the disparate interactions between each type of anionic $[Fe_2(Clan)_3]^{2-}$ layer and the MeV^{2+} cations. In combination, these results demonstrate the observed electrochemical and transport behaviour of mixed-valence tetraoxolene frameworks is not solely dictated by the presence of redox-active species and relative degrees of electron delocalisation within the anionic layers. Rather, these properties are also influenced by the overall packing arrangement of cations and the mixed-valence tetraoxolene network.

Although these results are wide and varied, several consistent themes emerge from this work. This thesis first set out to determine if viologens could act as countercations for anionic tetraoxolene coordination polymers, and if they can predictably influence the network structure and topology. Gratifyingly, the structures obtained clearly demonstrate viologens are successfully incorporated as countercations in these anionic networks. On the other hand, the structural diversity of the coordination polymers obtained, highlights the unpredictability of packing interactions and network geometry obtained using viologen countercations. Evidently, the supramolecular interactions which occur between metals, ligands, viologen cations and solvents are more sensitive and capricious than when redox-inactive ammonium or phosphonium cations are employed. In particular, the greater range of 1-, 2- and 3D structures obtained using MeV^{2+} highlights the weaker structure-directing role of this cation compared to $PhenQ^{2+}$, DiQ^{2+} or $PDiQ^{2+}$ cations. The relative conformational flexibility amongst the viologen cations is likely an important factor which influences the structural diversity. Since the pyridinium C–H bonds of viologens exist in defined geometries, the C–H···O interactions these cations engage in are strongly directional, causing the resultant supramolecular associations to be sensitive to cation geometry. The greater diversity of structures obtained using MeV^{2+} cations likely arises because it can undergo variable torsion of the pyridinium rings about the central C–C bond, as

observed in MeV^{2+} salts and the coordination polymers presented in this work (Table 6.1). The more malleable conformation of MeV^{2+} countercations allows them to be accommodated into a variety of supramolecular environments, formed by diverse anionic network topologies and geometries. In contrast, DiQ^{2+}, $PDiQ^{2+}$ and $PhenQ^{2+}$ cations exhibit less conformational flexibility (Table 6.1), because the *N*,*N*′-ethylene and -ethine bridges of these cations limit the torsion of the pyridinium rings about the 2,2′-bipyridyl-like central C–C bond. These cations will therefore act as more rigid supramolecular building blocks that can pack into a more limited range of supramolecular , compared to MeV^{2+} and presumably other 4,4′-bipyridine derived viologens.

Table 6.1 Inter-ring torsions exhibited by viologen cations, in selected salts reported in literature, and tetraoxolene coordination polymers in this thesis.

Compound	Viologen	Inter-ring Torsion / °	Dimen. & Topology	Ref.
$MeV(PF_6)_2$	MeV^{2+}	0.1	N/A	[1]
2.1$_{Mn}$	MeV^{2+}	39.4	3D diamondoid	This work
2.1$_{Cd}$	MeV^{2+}	39.7	3D diamondoid	This work
2.2a	MeV^{2+}	0.4	2D (6,3)	This work
2.3$_{Mn}$	MeV^{2+}	18.2	1D ladder	This work
2.3$_{Cd}$	MeV^{2+}	16.1	1D ladder	This work
mP **4.1a**	MeV^{2+}	43.0	2D (6,3)	This work
aP **4.1a**	MeV^{2+}	37.7	2D (6,3)	This work
4.1b	MeV^{2+}	37.5	2D (6,3)	This work
5.1	MeV^{2+}	0.4	2D (6,3)	This work
5.2	MeV^{2+}	44.4	2D (6,3)	This work
$PDiQ(PF_6)_2$	$PDiQ^{2+}$	4.1	N/A	This work
2.5	$PDiQ^{2+}$	1.67	3D (10,3)-*b*	This work
2.7	$PDiQ^{2+}$	0.0	2D (6,3)	This work
$DiQ(PF_6)_2$	DiQ^{2+}	19.0	N/A	[2]
2.6	DiQ^{2+}	17.9	3D (10,3)-*b*	This work
$(PhenQ)Br_2$	$PhenQ^{2+}$	6.1	N/A	This work
3.1^{F}	$PhenQ^{2+}$	1.7	2D (6,3)	This work
3.1^{Cl}b	$PhenQ^{2+}$	1.9	2D (6,3)	This work
3.1^{Br}	$PhenQ^{2+}$	1.5	2D (6,3)	This work

Mixed valency features in all the Fe–tetraoxolene network materials described in this thesis, with the resulting structure dependent upon the identity of the viologen, ligand, and the degree of solvation (Table 6.2). Except for **2.7**, the viologen cations engage in strong CT and Coulombic interactions with the anionic Fe–tetraoxolene networks, consistently localising the $Xan^{3-\bullet}$ state at the site of this association. This predictable ordering of ligand valence states also has a significant impact upon the electronic structure of the compounds, demonstrating the hitherto unused strategy of using cation–framework CT interactions to alter the physical properties.

Table 6.2 Mixed-valence Fe–tetraoxolene frameworks reported in this thesis.

Compound	Cation	Fe Valence	Ligand Charge Distribution	Dimen. & Topology
2.5	$PDiQ^{2+}$	$Fe^{III\ (a)}$	$[Fe_2(Clan^{2-})(Clan^{3-\bullet})_2]^{2-}$	3D (10,3)-*b*
2.6	DiQ^{2+}	$Fe^{III\ (a)}$	$[Fe_2(Clan^{2-})(Clan^{3-\bullet})_2]^{2-}$	3D (10,3)-*b*
2.7	$PDiQ^{2+}$	$Fe^{III\ (a)}$	$[Fe_2(Fan^{2-})(Fan^{3-\bullet})_2]^{2-}$	2D (6,3)
3.1^{F}	$PhenQ^{2+}$	$Fe^{III\ (a)}$	$[Fe_2(Fan^{2.5-})_2(Fan^{3-\bullet})]^{2-}$	2D (6,3)
3.1^{Cl}a	$PhenQ^{2+}$	$Fe^{III\ (a)}$	$[Fe_2(Clan^{2.5-})_2(Clan^{3-\bullet})]^{2-}$	2D (6,3)
3.1^{Cl}b	$PhenQ^{2+}$	$Fe^{III\ (a, b)}$	$[Fe_2(Clan^{2.5-})_2(Clan^{3-\bullet})]^{2-}$	2D (6,3)
3.1^{Br}	$PhenQ^{2+}$	$Fe^{III\ (a)}$	$[Fe_2(Bran^{2.5-})_2(Bran^{3-\bullet})]^{2-}$	2D (6,3)
mP **4.1a**	MeV^{2+}	$Fe^{III\ (a)}$	$[Fe_2(Fan^{2-})(Fan^{3-\bullet})_2]^{2-}$	2D (6,3)
aP **4.1a**	MeV^{2+}	$Fe^{III\ (a)}$ $Fe^{2.67\ (b)}$	$[Fe_2(Fan^{2-})(Fan^{3-\bullet})_2]^{2-}$	2D (6,3)
4.1b	MeV^{2+}	$Fe^{III\ (a, b)}$	$[Fe_2(Fan^{2-})(Fan^{3-\bullet})_2]^{2-}$	2D (6,3)
5.1	MeV^{2+}	$Fe^{III\ (a, b)}$	$[Fe_2(Clan^{2-})(Clan^{3-\bullet})_2]^{2-}$	2D (6,3)
5.2	MeV^{2+}	$Fe^{III\ (a)}$	$[Fe_2(Clan^{2-})(Clan^{3-\bullet})_2]^{2-}$	2D (6,3)

(a) Determined by SC-XRD analysis

(b) Determined by ^{57}Fe Mössbauer spectroscopy

Although synthesis of isostructural families of tetraoxolene coordination polymers was a major aim of this work, which would allow systematic structure-property investigations, the desired families of compounds could not be synthesised for reasons which are not immediately apparent. In particular, the fluoranilate coordination polymers structures obtained typically always differed significantly from chloranilate coordination polymers synthesised under equivalent conditions. Consequently, it was not possible to perform the intended systematic structure-property investigations by simply varying the ligand substituents. On the other hand, since the chemistry of fluoranilate coordination polymers is largely unexplored, there is considerable scope to uncover novel materials with potentially interesting structures or properties. Additionally, given the almost limitless possibility to vary the chemistry and structure of viologen cations, a host of diverse and interesting, yet undiscovered anionic tetraoxolene frameworks undoubtedly abounds. Since the redox properties of viologens are readily controlled, opportunities also arise to tailor the properties of tetraoxolene networks by exploiting the interactions between all the redox-active components. These explorations will likely reveal a fertile field of novel materials that possess a tantalising synergy of porosity, electroactivity, switchable magnetic ordering, and electrical conductivity.

6.2 Future Work

Despite uncovering the role of viologen countercations in modulating the charge state distribution of mixed-valence tetraoxolene networks, there are several areas of merit for further investigation, to better understand the opportunities and possible limitations arising from this strategy.

- **Magnetic Investigations**

In Chapter 2, the mixed-valence 3D (10,3)-*b* frameworks **2.5** and **2.6** were described, which to the best of the candidate's knowledge, are the first reported examples of tetraoxolene frameworks which exhibit this network topology. For bimetallic $[M^{II}M^{III}(ox)_3]^-$ oxalate networks, the 2D layered (6,3) networks undergo spontaneous magnetic ordering at significantly higher temperatures than the 3D (10,3)-*a* networks;[3] analogous behaviour is also seen in ferrimagnetic (FiM) mixed-valence (6,3) and (10,3)-*a* Fe–tetraoxolene networks.[4-7] A handful of homo- and heterometallic (10,3)-*b* oxalate networks have been reported,[8-11] however possible

long-range ordering in (10,3)-*b* $[M^{II}M^{III}(ox)_3]^-$ networks has not reported or compared to that of (6,3) and (10,3)-*a* $[M^{II}M^{III}(ox)_3]^-$ networks. Therefore, it is difficult to infer what magnetic behaviour mixed-valence (10,3)-*b* tetraoxolene frameworks might be expected compared to the FiM (6,3) and (10,3)-*a* Fe–tetraoxolene frameworks. Magnetic investigations on **2.5** and **2.6** could reveal if porous and stable 3D tetraoxolene frameworks can exhibit magnetic ordering at comparable temperatures to the 2D (6,3) networks, or alternatively if this framework topology gives rise to novel magnetic behaviour.

In Chapters 4 and 5, a range of mixed-valence 2D Fe–tetraoxolene frameworks were described. ^{57}Fe Mössbauer spectroscopy revealed the compounds *aP* **4.1a**, **4.1b** and **5.1** all undergo spontaneous magnetic ordering upon cooling. Despite strong metal–radical coupling occurring in these compounds, long-range magnetic ordering is somewhat surprising. Since the anionic layers are constructed from FiM pseudo-1D $\{Fe^{III}–Xan^{3-\bullet}\}_\infty$ chains, the compounds are expected to exhibit single-chain magnetism, analogously to $(^nPr_4N)_2[Fe_2(Clan)_3]$ but which does not spontaneously order.[12, 13] The compounds *aP* **4.1a**, **4.1b** and **5.1** are therefore worthy of magnetic characterisation to determine whether single-chain magnetism and magnetic ordering can coexist in these compounds, or if these two magnetic behaviours occur in different temperature regimes. Additionally, the presence of unmagnetised Fe^{II} and Fe^{III} sites in *aP* **4.1a** may give rise to interesting magnetic behaviour not previously observed in Fe–tetraoxolene coordination polymers, or allow guest-responsive magnetic state switching upon conversion to a valence-pure Fe^{III} form like **4.1b**.

Although the utility of the metal–radical approach in producing magnetic tetraoxolene frameworks is firmly established, a more detailed microscopic picture of how these compounds spontaneously order has not been demonstrated. Powder neutron diffraction is commonly used to understand the ordering behaviour of traditional inorganic magnetic compounds, though it has seldom been employed to elucidate the magnetic structure of coordination polymers.[14-17] In the mixed-valence 2D layered frameworks, strong direct antiferromagnetic coupling between paramagnetic metals and radicals ligands gives intrasheet FiM ordering.[5, 7] However the nature of the intersheet magnetic interactions is more ambiguous, and has only been inferred from bulk magnetic measurements.[5] Neutron diffraction investigations on metal–tetraoxolene frameworks could uncover the precise nature of the ferro- and

antiferromagnetic interactions in these compounds which give rise to spontaneous long-range ordering. These experiments could prove especially exciting for the 3D (10,3)-*b* frameworks **2.5** and **2.6**, as the magnetic ordering behaviour of metal–tetraoxolene frameworks with this topology is unknown. More complete knowledge of the magnetic interactions in these compounds could facilitate design and synthesis of porous materials which spontaneously order at higher, technologically useful temperatures.

- **Electrochemical and Lithium-Ion Battery Studies**

The voltammetric investigations described in Chapters 3, 4 and 5 clearly demonstrate additional framework redox states are engendered using redox-active viologens as countercations. 2D Fe–tetraoxolene frameworks are possible candidates as lithium-ion battery (LIB) cathodes,[18, 19] because accessing the multiple metal- and ligand-based redox processes can increase the cathode charge capacity, compared to inorganic cathodes such as $LiCoO_2$.[19] Since viologen countercations can introduce additional framework redox states, it is important to determine whether using these cations, instead of redox-inactive cations, is an effective method to further increase the charge capacity of metal–tetraoxolene LIB cathodes.

The structural distortions which occur during charge and discharge cycles can influence the long-term stability of LIB cathodes. In Chapter 4, the electrochemical behaviour of *aP* **4.1a** exhibited profound electrolyte size dependence, suggesting putative structural distortions directly impact the electrochemical response. Nevertheless, detailed insight into the nature of the structural transformations in metal–tetraoxolene frameworks upon electrochemical cycling is lacking. For conventional inorganic battery materials, *in situ* and *in operando* electrochemical–powder X-ray diffraction (P-XRD) techniques have helped uncover the structural processes which occur on battery charge and discharge.[20] Similar experiments conducted on metal–tetraoxolene LIB cathodes could prove especially interesting, given the greater structural flexibility of these compounds compared to inorganic cathode materials. Of particular interest would be voltammetric and *in situ* electrochemical–P-XRD experiments on the (10,3)-*b* networks **2.5** and **2.6**. Battery cathodes manufactured from oxides with 3D topologies, such as $LiMn_2O_4$ spinel compounds,[21] have attracted significant attention.[22] Compared to more conventional layered cathode materials

such as $LiCoO_2$ or $LiNiO_2$, 3D oxide cathodes allow greater charge-discharge rates due to higher Li^+ conductivity, and can have greater long-term structural stability.[23] Due to their porous 3D structure, the (10,3)-*b* compounds **2.5** and **2.6** as LIB cathodes similarly could exhibit better long-term electrochemical performance, compared to 2D layered Fe–tetraoxolene frameworks such as $(Et_4N)_2[Fe_2(Fan)_3]$[18] or $(Me_2NH_2)_2[Fe_2(Clan)_3]$.[19] This is because the 3D (10,3)-*b* networks cannot undergo layer exfoliation and loss of ordering due to Li^+ insertion during LIB discharge cycles, which may occur in the 2D Fe–tetraoxolene framework LIB cathodes.[19]

- **Redox Interactions Between Viologens and Ligands**

For all the as-synthesised coordination polymers reported in this thesis, the viologen countercations exist exclusively in the oxidised dication RV^{2+} or RQ^{2+} state. However, the ability of viologen cations in the radical cation state ($RV^{+\bullet}$ or $RQ^{+\bullet}$) to influence the structure and topology of tetraoxolene coordination polymers remains unknown. Secondly, the possible effect that redox reactions between oxidised viologens and reduced ligands, has upon the structure is unexplored. A relatively simple modification to the synthetic approach utilised in the candidate's research group may yield interesting new materials. In contrast to literature methods which begin with the quinonoid dianion Xan^{2-} form of the ligands,[4-5, 12, 24-30] the strategy employed by the candidate's research group and in this thesis, has been to allow slow aerial oxidation of the aromatic tetraoxolene tetraanion (Xan^{4-}), to the Xan^{2-} state, which then coordinates to M^{II} species.[18, 31-33] In our hands, this procedure leads to improved crystal quality, which is critical for single-crystal X-ray diffraction analyses. Interestingly, RV^{2+} or RQ^{2+} species could be sufficiently strongly oxidising to react with aromatic Xan^{4-}, so that if crystallisation reactions were conducted in the absence of aerial dioxygen (O_2), $RV^{+\bullet}$ or $RQ^{+\bullet}$, and either $Xan^{3-\bullet}$ or Xan^{2-} species could be produced, depending on the reaction stoichiometry.

The possibility of such a redox reaction became apparent during early synthetic trials to synthesise Mn^{II} coordination polymers using RV^{2+} and H_4Clan under unoptimised conditions. For several of these reactions with various RV^{2+} cations, an intense royal blue colour was observed in solution near the boundary of the two solvent layers; this blue colour was discharged immediately upon exposure to aerial O_2. $RV^{+\bullet}$ species commonly exhibit an intense blue colour in solution, depending on the

N-quaternary groups,[34] so the presence of a strong blue colour in solution and the air sensitive nature immediately suggested the presence of $RV^{+\bullet}$ in solution. In one case, a 2D coordination polymer was obtained which exhibited a $(BnV^{2+})(BnV^{+\bullet})[Mn^{II}_2(Clan^{2-})_2(Clan^{3-\bullet})]$ (BnV^{m+} = *N*,*N*′-dibenzyl-4,4′-bipyridinium) valence state distribution; this compound was not reported in this thesis due to challenges associated with reliably producing sufficient quantities of the material. The radical $BnV^{+\bullet}$ and $Clan^{3-\bullet}$ species in the compound presumably therefore resulted from a spontaneous electron transfer between BnV^{2+} and $Clan^{4-}$. Preliminary crystallographic investigations also revealed this redox reaction is reasonably general in nature; a series of highly air-sensitive radical cation salts of approximate composition $(RV^{+\bullet})_2(Clan^{2-})$ or $(RQ^{+\bullet})_2(Clan^{2-})$ were obtained when metals and aerial O_2 was excluded from the crystallisation reactions. The absence of $Clan^{3-\bullet}$ in these radical cation salts suggests coordination to metal centres is required to stabilise the $Xan^{3-\bullet}$ state, in line with studies on radical tetraoxolene-bridged diiron and dichromium complexes.[35]

Since the production of bridging radical $Xan^{3-\bullet}$ species using this approach does not require M^{II} species capable of reduced Xan^{2-}, the Xan^{4-}/RV^{2+} redox reaction could prove a novel method to incorporate the paramagnetic $Xan^{3-\bullet}$ form into coordination polymers assembled from redox-inactive metals. Due to their typically large *S* values, paramagnetic Ln^{III} species are of particular interest, as porous Ln^{III}–tetraoxolene coordination polymers containing paramagnetic $Xan^{3-\bullet}$ ligands could exhibit very large magnetic moments or high magnetic ordering temperatures. While studies on dinuclear Ln^{III} complexes containing bridging $Xan^{3-\bullet}$ ligands revealed direct metal–radical coupling does occur,[36, 37] the magnetic behaviour of Ln^{III}–tetraoxolene coordination containing $Xan^{3-\bullet}$ ligands is totally unexplored. Therefore, significant scope exists to investigate the structural chemistry and magnetic properties of $Xan^{3-\bullet}$ containing Ln^{III}–tetraoxolene coordination polymers, obtained using viologens as *in situ* oxidising agents for the Xan^{4-} precursor.

6.3 References

[1] F. Huang, K. A. Switek, L. N. Zakharov, F. R. Fronczek, C. Slebodnick, M. Lam, J. A. Golen, W. S. Bryant, P. E. Mason, A. L. Rheingold, M. Ashraf-Khorassani, H. W. Gibson, *J. Org. Chem.* **2005**, *70*, 3231-3241.

[2] F. Huang, C. Slebodnick, K. A. Switek, H. W. Gibson, *Tetrahedron* **2007**, *63*, 2829-2839.

[3] R. S. Fishman, M. Clemente-León, E. Coronado, *Inorg. Chem.* **2009**, *48*, 3039-3046.

[4] L. E. Darago, M. L. Aubrey, C. J. Yu, M. I. Gonzalez, J. R. Long, *J. Am. Chem. Soc.* **2015**, *137*, 15703-15711.

[5] I.-R. Jeon, B. Negru, R. P. Van Duyne, T. D. Harris, *J. Am. Chem. Soc.* **2015**, *137*, 15699-15702.

[6] R. Murase, B. F. Abrahams, D. M. D'Alessandro, C. G. Davies, T. A. Hudson, G. N. L. Jameson, B. Moubaraki, K. S. Murray, R. Robson, A. L. Sutton, *Inorg. Chem.* **2017**, *56*, 9025-9035.

[7] J. A. DeGayner, I.-R. Jeon, L. Sun, M. Dincă, T. D. Harris, *J. Am. Chem. Soc.* **2017**, *139*, 4175-4184.

[8] M. R. Sundberg, R. Kivekäs, J. K. Koskimies, *J. Chem. Soc., Chem. Commun.* **1991**, 526-527.

[9] H.-Y. Shen, W.-M. Bu, D.-Z. Liao, Z.-H. Jiang, S.-P. Yan, G.-L. Wang, *Inorg. Chem.* **2000**, *39*, 2239-2242.

[10] B. Zhang, Y. Zhang, D. Zhu, *Dalton Trans.* **2012**, *41*, 8509-8511.

[11] B. Zhang, P. J. Baker, Y. Zhang, D. Wang, Z. Wang, S. Su, D. Zhu, F. L. Pratt, *J. Am. Chem. Soc.* **2018**, *140*, 122-125.

[12] J. Chen, Y. Sekine, Y. Komatsumaru, S. Hayami, H. Miyasaka, *Angew. Chem. Int. Ed.* **2018**, *57*, 12043-12047.

[13] J. Chen, Y. Sekine, A. Okazawa, H. Sato, W. Kosaka, H. Miyasaka, *Chem. Sci.* **2020**, *11*, 3610-3618.

[14] R. A. Mole, J. A. Stride, P. F. Henry, M. Hoelzel, A. Senyshyn, A. Alberola, C. J. Gómez Garcia, P. R. Raithby, P. T. Wood, *Inorg. Chem.* **2011**, *50*, 2246-2251.

[15] R. A. Mole, M. A. Nadeem, J. A. Stride, V. K. Peterson, P. T. Wood, *Inorg. Chem.* **2013**, *52*, 13462-13468.

[16] J. M. M. Lawler, P. Manuel, A. L. Thompson, P. J. Saines, *Dalton Trans.* **2015**, *44*, 11613-11620.

[17] P. J. Saines, N. C. Bristowe, *Dalton Trans.* **2018**, *47*, 13257-13280.

[18] R. Murase, C. J. Commons, T. A. Hudson, G. N. L. Jameson, C. D. Ling, K. S. Murray, W. Phonsri, R. Robson, Q. Xia, B. F. Abrahams, D. M. D'Alessandro, *Inorg. Chem.* **2020**, *59*, 3619-3630.

[19] M. E. Ziebel, C. A. Gaggioli, A. B. Turkiewicz, W. Ryu, L. Gagliardi, J. R. Long, *J. Am. Chem. Soc.* **2020**, *142*, 2653-2664.

[20] Q. Gu, J. A. Kimpton, H. E. A. Brand, Z. Wang, S. Chou, *Adv. Energy Mater.* **2017**, *7*, 1602831.

[21] M. M. Thackeray, *Prog. Solid State Chem.* **1997**, *25*, 1-71.

[22] A. Kraytsberg, Y. Ein-Eli, *Adv. Energy Mater.* **2012**, *2*, 922-939.

[23] A. Manthiram, *Nat. Comm.* **2020**, *11*, 1550.

[24] S. Kawata, S. Kitagawa, M. Kondo, I. Furuchi, M. Munakata, *Angew. Chem. Int. Ed. Engl.* **1994**, *33*, 1759-1761.

[25] S. Kawata, S. Kitagawa, H. Kumagai, T. Ishiyama, K. Honda, H. Tobita, K. Adachi, M. Katada, *Chem. Mater.* **1998**, *10*, 3902-3912.

[26] H. Kumagai, S. Kawata, S. Kitagawa, *Inorg. Chim. Acta* **2002**, *337*, 387-392.

[27] M. Atzori, S. Benmansour, G. Mínguez Espallargas, M. Clemente-León, A. Abhervé, P. Gómez-Claramunt, E. Coronado, F. Artizzu, E. Sessini, P. Deplano, A. Serpe, M. L. Mercuri, C. J. Gómez García, *Inorg. Chem.* **2013**, *52*, 10031-10040.

[28] M. E. Ziebel, L. E. Darago, J. R. Long, *J. Am. Chem. Soc.* **2018**, *140*, 3040-3051.

[29] S. Benmansour, I. Pérez-Herráez, C. Cerezo-Navarrete, G. López-Martínez, C. Martínez Hernández, C. J. Gómez-García, *Dalton Trans.* **2018**, *47*, 6729-6741.

[30] K. A. Collins, R. J. Saballos, M. S. Fataftah, D. Puggioni, J. M. Rondinelli, D. E. Freedman, *Chem. Sci.* **2020**, *11*, 5922-5928.

[31] B. F. Abrahams, T. A. Hudson, L. J. McCormick, R. Robson, *Cryst. Growth Des.* **2011**, *11*, 2717-2720.

[32] C. J. Kingsbury, B. F. Abrahams, D. M. D'Alessandro, T. A. Hudson, R. Murase, R. Robson, K. F. White, *Cryst. Growth Des.* **2017**, *17*, 1465-1470.

[33] C. J. Kingsbury, B. F. Abrahams, J. E. Auckett, H. Chevreau, A. D. Dharma, S. Duyker, Q. He, C. Hua, T. A. Hudson, K. S. Murray, W. Phonsri, V. K. Peterson, R. Robson, K. F. White, *Chem. Eur. J.* **2019**, *25*, 5222-5234.

[34] C. L. Bird, A. T. Kuhn, *Chem. Soc. Rev.* **1981**, *10*, 49-82.

[35] A. Dei, D. Gatteschi, L. Pardi, U. Russo, *Inorg. Chem.* **1991**, *30*, 2589-2594.

[36] P. Zhang, M. Perfetti, M. Kern, P. P. Hallmen, L. Ungur, S. Lenz, M. R. Ringenberg, W. Frey, H. Stoll, G. Rauhut, J. van Slageren, *Chem. Sci.* **2018**, *9*, 1221-1230.

[37] W. R. Reed, M. A. Dunstan, R. W. Gable, W. Phonsri, K. S. Murray, R. A. Mole, C. Boskovic, *Dalton Trans.* **2019**, *48*, 15635-15645.

This page intentionally left blank

Chapter 7 Experimental Methods

7.1 Single Crystal X-ray Diffraction (SC-XRD) 411

7.1.1 Laboratory Instrumentation 411
7.1.2 Synchrotron Instrumentation 411
7.1.3 Structure Solution and Refinement 412
7.1.4 Crystallographic Terminology 412

7.2 Powder X-ray Diffraction (P-XRD) 414

7.2.1 Laboratory Instrumentation 414
7.2.2 Synchrotron Instrumentation 414

7.3 Elemental Analysis 414

7.4 Spectroscopic Methods 415

7.4.1 Nuclear Magnetic Resonance (NMR) Spectroscopy 415
7.4.2 Infrared Spectroscopy 415
7.4.3 Electronic Spectroscopy 415
7.4.4 ^{57}Fe Mössbauer Spectroscopy 416

7.5 Thermogravimetric Analysis (TGA) 417

7.6 Electrochemistry 417

7.7 Magnetometry 417

7.8 Electrical Conductivity 418

7.8.1 Terminology 418
7.8.2 Experimental 419

7.9 References 420

This page intentionally left blank

7.1 Single Crystal X-ray Diffraction (SC-XRD)

7.1.1 Laboratory Instrumentation

Crystallographic data were measured as noted using a Rigaku XtaLAB Synergy-S diffractometer equipped with graphite monochromated Cu-Kα (λ = 1.54184 Å) or Mo-Kα (λ = 0.71073 Å) microfocus sources and a HyPix-6000 E detector, and an Oxford Diffraction Cryostream 800. Alternatively, crystallographic data were measured using an Oxford Diffraction SuperNova diffractometer equipped with a graphite monochromated Cu-Kα (λ = 1.54184 Å) microfocus source, Atlas CCD detector, and an Oxford Diffraction Cryostream 700. Data reduction, multi-scan and Gaussian absorption corrections were performed using CrysAlis PRO.[1]

7.1.2 Synchrotron Instrumentation

Crystallographic data were measured using the MX1 or MX2 beamlines of the Australian Synchrotron with monochromatic synchrotron radiation (λ = 0.71073 Å) as noted,[2-3] with control of the beamline and endstation equipment achieved using the Blu-Ice GUI interface.[4] Data collection using the MX1 beamline was achieved using a SmarGon goniometer to conduct four independent ω scans with frames collected every 0.1° in ω:

- ω = 0–360°, φ = 0°, χ = 0°
- ω = 150–390°, φ = 0°, χ = 57.47°
- ω = 150–390°, φ = 90°, χ = 57.47°
- ω = 150–390°, φ = 180°, χ = 57.47°

Frame scaling and merging was performed using the WebGUI interface Autoprocessing routine using XDS and XSCALE.[5] Data collection using the MX2 beamline was achieved using a single φ scan (φ = 0–360°, κ = 0°, ω = 0°), with frames collected every 0.1° in φ. Unit cell indexing and refinement, data reduction and absorption corrections were performed using XDS.[5] The sample temperature was controlled at 100 K using an Oxford Diffraction Cryostream 700.

7.1.3 Structure Solution and Refinement

The structures were solved with SHELXT using intrinsic phasing,[6] then refined using the SHELXL2018 package with least squares minimization on F^2,[7] through the ShelXle[8] and OLEX2[9] graphical user interfaces. Unless otherwise noted, the thermal and positional parameters for non-hydrogen atoms in the asymmetric unit were refined anisotropically. Hydrogen atoms were placed at calculated positions using suitable riding models and refined using isotropic displacement parameters derived from their parent atoms.

7.1.4 Crystallographic Terminology

Statistical parameters for evaluation of crystallographic data were generated using SHELXL of the SHELX2018 package,[7] and are defined by the following equations:

The agreement index for merging of equivalent observed reflections (F_O) based upon F^2 is given by,

$$R_{\text{int}} = \frac{\sum \left| F_O^{\,2} - F_O^{\,2}(mean) \right|}{\sum F_O^{\,2}} \tag{7.1}$$

Where $F_O^2(mean)$ is the mean observed structure factor for a given set of equivalent reflections.

The agreement index based the F_O and calculated (F_C) structure factors based on F is given by,

$$R_1 = \frac{\sum \left| |F_O| - |F_C| \right|}{\sum |F_O|} \tag{7.2}$$

the agreement index between F_O and F_C based upon F^2 obtained during least-squares refinement is given by,

$$wR_2 = \left(\frac{\sum w(F_O^{\,2} - F_C^{\,2})^2}{\sum w(F_O^{\,2})^2} \right)^{\frac{1}{2}} \tag{7.3}$$

where the weighting scheme *w* is given by,

$$w = \frac{1}{\sigma^2({F_O}^2) + (AP)^2 + BP} \tag{7.4}$$

$$P = \frac{2{F_C}^2 + \max({F_C}^2, 0)}{3} \tag{7.5}$$

and *A* and *B* are fitting parameters of the weighting scheme.

The Goodness of Fit (*GooF*) based upon F^2 is given by,

$$GooF = S = \left(\frac{\sum w\left({F_O}^2 - {F_C}^2\right)^2}{n - p} \right)^{\frac{1}{2}} \tag{7.6}$$

where *n* and *p* are the number of reflections and parameters respectively.

The isotropic atomic displacement parameter (Debye-Waller factor) is given by,

$$f_{DW} = \exp\left(-8\pi^2 \left\langle u^2 \right\rangle \frac{\sin^2\theta}{\lambda^2} \right) \tag{7.7}$$

where $\langle u^2 \rangle$ (Å^2) is the mean-squared atomic displacement from the equilibrium position.[10]

The anisotropic atomic displacement parameter (ADP) is given by,

$$\begin{aligned} f_{ADP} = \exp[-2\pi^2 (&h^2 a^{*2} U_{11} + k^2 b^{*2} U_{22} + l^2 c^{*2} U_{33} + \\ &2hka^* b^* U_{12} + 2hla^* b^* U_{13} + 2klb^* c^* U_{23})] \end{aligned} \tag{7.8}$$

where *h*, *k* and *l* are the Miller indices, a^*, b^* and c^* (Å^{-1}) are the reciprocal unit cell lengths, and U_{ij} (Å^2) are the components of the atomic displacement tensor **U**,

$$\mathbf{U} = \begin{pmatrix} U_{11} & U_{12} & U_{13} \\ U_{12} & U_{22} & U_{23} \\ U_{13} & U_{32} & U_{33} \end{pmatrix} \tag{7.9}$$

noting that $U_{ij} = U_{ji}$.[10]

7.2 Powder X-ray Diffraction (P-XRD)

7.2.1 Laboratory Instrumentation

P-XRD measurements were performed on samples contained in borosilicate capillaries using a Rigaku XtaLAB Synergy-S diffractometer equipped with a graphite monochromated Cu-Kα (λ = 1.54184 Å) microfocus source and a HyPix-6000 E detector. The temperature was controlled using an Oxford Diffraction Cryostream 800, and data processing were performed using CrysAlis PRO.[1]

7.2.2 Synchrotron Instrumentation

P-XRD measurements were performed on samples contained in borosilicate capillaries using the PD beamline at the Australian Synchrotron.[11] The experiments were undertaken using monochromatic synchrotron radiation (λ = 0.58835 Å or 0.77457 Å as indicated), which was refined against a NIST SRM LaB_6-660c standard using the GSAS-II interface.[12] Data were collected using the Mythen microstrip detector[13] from 3–83° (λ = 0.77457 Å) or 2–76.8° (λ = 0.58835 Å) in 2θ, with the sample temperature maintained using an Oxford Cryostream 700. To cover the gaps between detector modules, two datasets were collected with the detector set 0.5° apart and then merged to a single dataset using PDViPeR (https://www.ansto.gov.au/user-access/instruments/australian-synchrotron-beamlines/powder-diffraction/pdviper).
Indexing of P-XRD data were performed using CONOGRAPH graphical user interface.[14]

7.3 Elemental Analysis

Elemental analysis (CHN) was performed at the Campbell Microanalytical Laboratory, University of Otago. For transport of air-sensitive compounds (**3.1^{Cl}b**, *aP* **4.1a**, **4.1b**, **5.2**), samples were added to flame-dried ampoules in an N_2-filled glovebox. The ampoules were fitted with a sealable adapter, then brought out of the glovebox. The adapter was purged with dry N_2 on a Schlenk line by 3× evacuate-backfill cycles, then the ampoule was flame-sealed under 1 atm of dry N_2.

7.4 Spectroscopic Methods

7.4.1 Nuclear Magnetic Resonance (NMR) Spectroscopy

Proton (^{1}H) and proton-decoupled carbon-13 (^{13}C{^{1}H}) NMR spectroscopy was performed using a Varian Unity spectrometer operating at 400 and 100 MHz respectively. All spectra were acquired at 25 °C. Proton (δ_H) and carbon-13 (δ_C) chemical shift values are reported in parts per million (ppm) downfield of external tetramethylsilane, in the form: δ_H (multiplicity, J_{AB}, integration, assignment). ^{1}H- and ^{13}C{^{1}H}-NMR spectra were referenced to residual ^{1}H signals in the deuterated solvents, and the ^{13}C solvent signal respectively, except for spectra acquired in D_2O which were referenced to the ^{1}H and ^{13}C signals of acetone (internal standard, δ_H 2.22; δ_C 215.94).

7.4.2 Infrared Spectroscopy

Attenuated total internal reflectance (ATR) Fourier-transform infrared (FT-IR) spectra were recorded in air under ambient conditions using a Perkin Elmer Spotlight 100 spectrometer fitted with a ZnSe Universal ATR accessory, or a Bruker Alpha spectrometer fitted with a diamond ATR accessory. FT-IR spectra as KBr discs were measured on a Bruker Tensor 27 FTIR spectrometer.

7.4.3 Electronic Spectroscopy

Diffuse reflectance UV-Visible-Near IR (UV-Vis-NIR) spectra were collected using an Agilent CARY5000 spectrometer fitted with a Harrick Praying Mantis™ diffuse reflectance accessory using Varian WinUV software V3.0. The samples were finely ground in an Ar-filled glovebox then placed in a Harrick Praying Mantis™ high temperature reaction chamber which was sealed before being transferred out of the glovebox for measurement. Spectra were collected in the range 5000–25000 cm^{-1} and referenced to a $BaSO_4$ background.

Diffuse reflectance UV-Vis-NIR spectra are presented as the Kubelka-Munk transform,

$$F(R) = \frac{(1-R)^2}{2R} \tag{7.10}$$

where R (-) is the measured reflectance. The diffuse reflectance spectra were deconvoluted using the curve-fitting subroutine implemented within the GRAMS32 commercial software package. The following procedure was employed for the analysis of spectral data. The positions of the underlying components were estimated by examining the first- and second-order derivatives of the bands as a guide to the energies of the major components. The energies of the major components were subsequently fixed, and the spectral deconvolution procedure performed to obtain the parameters for the band intensities and bandwidths. The fixed parameters were successively removed as the fit was iteratively refined. Deconvolution was performed with the minimum number of components required to obtain convergence of the fitting procedure. The band manifold was approximated by multiple Gaussian-shaped components. Based on the reproducibility of the parameters obtained from the deconvolutions, the uncertainties in the energies (ν_{max}), intensities $\{F(R)_{max}\}$ and bandwidths ($\Delta\nu_{1/2}$) were estimated as ± 10 cm^{-1}, 0.001 × 10^3 and ± 10 cm^{-1}, respectively.

7.4.4 ^{57}Fe Mössbauer Spectroscopy

^{57}Fe Mössbauer spectra were measured between 5.8–295 K as noted using a Science Engineering & Education Co. spectrometer (Minneapolis, MN) with a ^{57}Co-Rh source, equipped with a closed cycle refrigerator from Janis Research Co. (Woburn, MA) and Sumitomo Heavy Industries, Ltd. (Tokyo, Japan). Data were collected in constant acceleration mode in transmission geometry with a small magnetic field (47 mT) applied parallel to the γ-rays. The zero velocity of the spectrum was calibrated to the centroid of the room temperature spectrum of a 25 μm α-Fe foil. The spectra were analysed using WMOSS Mössbauer Spectral Analysis Software (www.wmoss.org). For measurement of isolated air-sensitive compounds (**3.1^{Cl}b**, **4.1b**), in an N_2-filled glovebox, a small quantity (ca. 30 mg) of the compound was added to a machined polyethene sample cup, which was covered with molten anhydrous, deoxygenated eicosane. Once solidified, the sample cup was transferred to

a dried Schlenk tube for transportation to the spectrometer, before insertion of the sample cup by brief handling in air. For spectra measured following isolation from slurries in MeCN (*aP* **4.1a**, **5.1**), in air, a slurry of the compound was added to a polythene sample cup, the solvent was carefully decanted then the sample cup was transferred immediately to the spectrometer.

7.5 Thermogravimetric Analysis (TGA)

Thermogravimetric analysis (TGA) was performed using a Mettler Toledo TGA/SDTA851e between 25 °C and 450 °C using a heating rate of 5 °C min^{-1} in a flow of N_2. For TGA on air-sensitive samples (**3.1^{Cl}b**, *aP* **4.1a**, **4.1b**, **5.2**), the compounds were transferred from an N_2-filled glovebox immediately before commencement of the measurement.

7.6 Electrochemistry

Cyclic voltammetric measurements on solid samples were performed using an eDAQ potentiostat interfaced to an eDAQ 401 e-corder. Dry N_2 was bubbled through solutions of 0.1 M $(Et_4N)PF_6$/MeCN or 0.5 M $LiBF_4$/MeCN prior to experiments. The cyclic voltammograms were recorded using a polished glassy carbon working electrode (D = 1 mm), a Pt wire counter electrode and a leakless Ag/AgCl reference electrode ($(Et_4N)PF_6$/MeCN) or a Ag wire quasi-reference electrode ($LiBF_4$/MeCN). The quasi-reference electrodes were calibrated to an internal ferrocene/ferrocenium (Fc/Fc^+) couple. The sample was mounted in air to the working electrode by dipping the electrode into a paste comprising gently ground compound in the supporting electrolyte for $(Et_4N)PF_6$/MeCN, or pure MeCN for $LiBF_4$/MeCN.

7.7 Magnetometry

Magnetic measurements on **3.1^{Cl}b** were performed on an accurately weighed sample placed in a calibrated gelatin capsule and restrained in an eicosane matrix. The sealed capsule was held in the centre of a soda straw and the latter fixed to the sample rod. Data were collected using a Quantum Design MPMS-XL SQUID magnetometer. Dc magnetic susceptibility data were collected between 2–300 K in applied dc fields (H_{dc}) of 1 and 10 kOe. Magnetisation isotherms were measured at a rate of 1 kOe $step^{-1}$ from 0–1 kOe, 2.5 kOe $step^{-1}$ from 1–10 kOe and 5 kOe $step^{-1}$ from 10–50 kOe.

Magnetic hysteresis measurements were performed using a rate of 680 Oe step^{-1} from −5 to 5 kOe, and 3000 Oe step^{-1} between −50 to −5 kOe and 5 to 50 kOe. Ac susceptibility measurements were collected in an applied ac field H_{ac} = 3.5 Oe, oscillating between 1–1488 Hz. The characteristic ordering temperature (T_c) was estimated as the temperature at which the in-phase ac susceptibility (χ_M') is maximum.

7.8 Electrical Conductivity

7.8.1 Terminology

Ohm's Law defines that the voltage drop (v / V) across a conducting material is directly proportional to the current flow (i / A) and resistance (r / Ω) of the material:

$$v = ir \tag{7.11}$$

As R depends on the length of the material (L / cm) and cross-sectional area (A_{cross} / cm^2), the relative ease of current flow through a material is typically given as the specific resistivity (ρ / Ω cm),

$$\rho = r\frac{A_{cross}}{L} \tag{7.12}$$

which is independent of material geometry allowing dissimilar materials to be easily compared based upon the ease at which they allow current flow.

The conductivity (σ / Ω^{-1} cm^{-1} or more commonly S cm^{-1}) of a material is the inverse of ρ,

$$\sigma = \frac{1}{\rho} \tag{7.13}$$

which also allows Ohm's Law to be reformulated,

$$\begin{aligned} v &= \frac{i}{\sigma}\left(\frac{L}{A_{cross}}\right) \\ \sigma\left(\frac{v}{L}\right) &= \frac{i}{A_{cross}} \\ \sigma E &= J \end{aligned} \tag{7.14}$$

where E (V cm^{-1}) is the electric field strength, and J (A cm^{-2}) is the current density.

For thermally-activated semiconductor behaviour, the activation energy (E_a, eV) is determined using the Arrhenius relationship,

$$\sigma = \sigma_0 \exp\left(\frac{-E_a}{k_B T}\right) \quad (7.15)$$

where σ_0 (S cm−1) is the pre-exponential, taken as 1 S cm^{-1}, k_B (8.617333 × 10^{-5} eV K^{-1}) is the Boltzmann constant, and T (K) is temperature.

7.8.2 Experimental

Ambient and variable-temperature electrical conductivity measurements were performed in pressed-pellet two-electrode screw cells similar to those described previously (Figure 7.1).[15, 16] In an N_2-filled glovebox, four independent screw cells for each compound (**3.1^{Cl}b**, *aP* **4.1a**, **4.1b**, **5.2**) were constructed by placing two copper dies (D = 3.0 mm) polished to a mirror finish, into a snugly fitting borosilicate tube (ID = 3.0 mm). The tube was then held within a 3D printed PLA cell holder, and the copper dies compressed by two brass screws threaded through the cell holder. The blank cell length was measured using a calliper, then the empty cells were disassembled, and a sample of each compound placed into the glass tube. The copper dies were then reinserted to the borosilicate tubes, and the pressed pellets formed *in situ* under anaerobic conditions by tightening the brass screws in the PLA sample holder. The sample thickness was then measured using a calliper.

REDACTED THIRD PARTY COPYRIGHT MATERIAL

Figure 7.1 (Top) components of two-electrode electrical conductivity screw cell. (Bottom) Assembled two electrode screw cell containing sample (black) pressed between copper dies, held in PLA cell holder. NB: Not to scale. Reproduced with permission from Ref. [17]. Copyright © 2020 American Chemical Society.

For ambient temperature conductivity measurements within the glovebox, the brass screws were connected by alligator clip-equipped copper wires to an Ossila X100 (Sheffield, UK) source-measure unit (SMU) interfaced to home-built software. The sample cells were shielded from light, and all current-voltage (*i*-*v*) curves checked for linearity measured potential window, maximum ± 0.55 V, to confirm Ohmic behaviour. For variable-temperature electrical conductivity measurements, the screw cells were sealed with dry, deoxygenated sealing wax to ensure an airtight seal. The cells were then removed from the glovebox and placed into a home-built thermostated N_2-purged sample chamber, allowing variable-temperature measurements on two cells in parallel. The temperature was controlled to ±1 K in the range 220–300 K in 5 K steps, by regulating the flowrate of cold and hot dry N_2 gas into the sample chamber. The screw cells were connected to the SMU via alligator clip-equipped copper cables and BNC cables, and current-bias (*i*-*v*) curves were measured over the potential window, maximum ± 0.55 V in 0.01 V steps. The resulting linear *i*-*v* curves (confirming Ohmic behaviour) were fitted with Ohm's law (Equation (7.14)) to determine the conductivity, with the temperature dependence of the conductivity modelled using an Arrhenius relationship (Equation (7.15)). Details of the independent devices and measured transport properties for each compound are contained in Appendix B.

7.9 References

[1] Agilent, *CrysAlis PRO*, Agilent Technologies Ltd, Yarnton, Oxfordshire, England, **2014**.

[2] N. P. Cowieson, D. Aragao, M. Clift, D. J. Ericsson, C. Gee, S. J. Harrop, N. Mudie, S. Panjikar, J. R. Price, A. Riboldi-Tunnicliffe, R. Williamson, T. Caradoc-Davies, *J. Synchrotron Rad.* **2015**, *22*, 187-190.

[3] D. Aragao, J. Aishima, H. Cherukuvada, R. Clarken, M. Clift, N. P. Cowieson, D. J. Ericsson, C. L. Gee, S. Macedo, N. Mudie, S. Panjikar, J. R. Price, A. Riboldi-Tunnicliffe, R. Rostan, R. Williamson, T. T. Caradoc-Davies, *J. Synchrotron Rad.* **2018**, *25*, 885-891.

[4] T. M. McPhillips, S. E. McPhillips, H.-J. Chiu, A. E. Cohen, A. M. Deacon, P. J. Ellis, E. Garman, A. Gonzalez, N. K. Sauter, R. P. Phizackerley, S. M. Soltis, P. Kuhn, *J. Synchrotron Rad.* **2002**, *9*, 401-406.

[5] W. Kabsch, *Acta Crystallogr. D* **2010**, *66*, 125-132.

[6] G. Sheldrick, *Acta Crystallogr. A* **2015**, *71*, 3-8.

[7] G. Sheldrick, *Acta Crystallogr. C* **2015**, *71*, 3-8.

[8] C. B. Hübschle, G. M. Sheldrick, B. Dittrich, *J. Appl. Crystallogr.* **2011**, *44*, 1281-1284.

[9] O. V. Dolomanov, L. J. Bourhis, R. J. Gildea, J. A. K. Howard, H. Puschmann, *J. Appl. Crystallogr.* **2009**, *42*, 339-341.

[10] K. N. Trueblood, H.-B. Burgi, H. Burzlaff, J. D. Dunitz, C. M. Gramaccioli, H. H. Schulz, U. Shmueli, S. C. Abrahams, *Acta Crystallogr. A* **1996**, *52*, 770-781.

[11] K. S. Wallwork, B. J. Kennedy, D. Wang, *AIP Conference Proceedings* **2007**, *879*, 879-882.

[12] B. H. Toby, R. B. Von Dreele, *J. Appl. Crystallogr.* **2013**, *46*, 544-549.

[13] B. Schmitt, C. Brönnimann, E. F. Eikenberry, F. Gozzo, C. Hörmann, R. Horisberger, B. Patterson, *Nucl. Instrum. Methods Phys. Res. A* **2003**, *501*, 267-272.

[14] R. Oishi-Tomiyasu, *J. Appl. Crystallogr.* **2014**, *47*, 593-598.

[15] L. E. Darago, M. L. Aubrey, C. J. Yu, M. I. Gonzalez, J. R. Long, *J. Am. Chem. Soc.* **2015**, *137*, 15703-15711.

[16] L. Sun, C. H. Hendon, M. A. Minier, A. Walsh, M. Dincă, *J. Am. Chem. Soc.* **2015**, *137*, 6164-6167.

[17] M. P. van Koeverden, B. F. Abrahams, D. M. D'Alessandro, P. W. Doheny, C. Hua, T. A. Hudson, G. N. L. Jameson, K. S. Murray, W. Phonsri, R. Robson, A. L. Sutton, *Chem. Mater.* **2020**, *32*, 7551-7563.

This page intentionally left blank

Appendix A Tetraoxolene Bond Length Analysis

A.1 Procedure for Bond Length Analysis A3

A.2 Distributions of Bond Lengths A6

A.3 Tabulations of Bond Lengths for *M*–Clan^{n-} Compounds A7

A.4 Tabulations of Bond Lengths in Fe–Clan^{n-} Compounds A28

A.5 Ligand Abbreviations A32

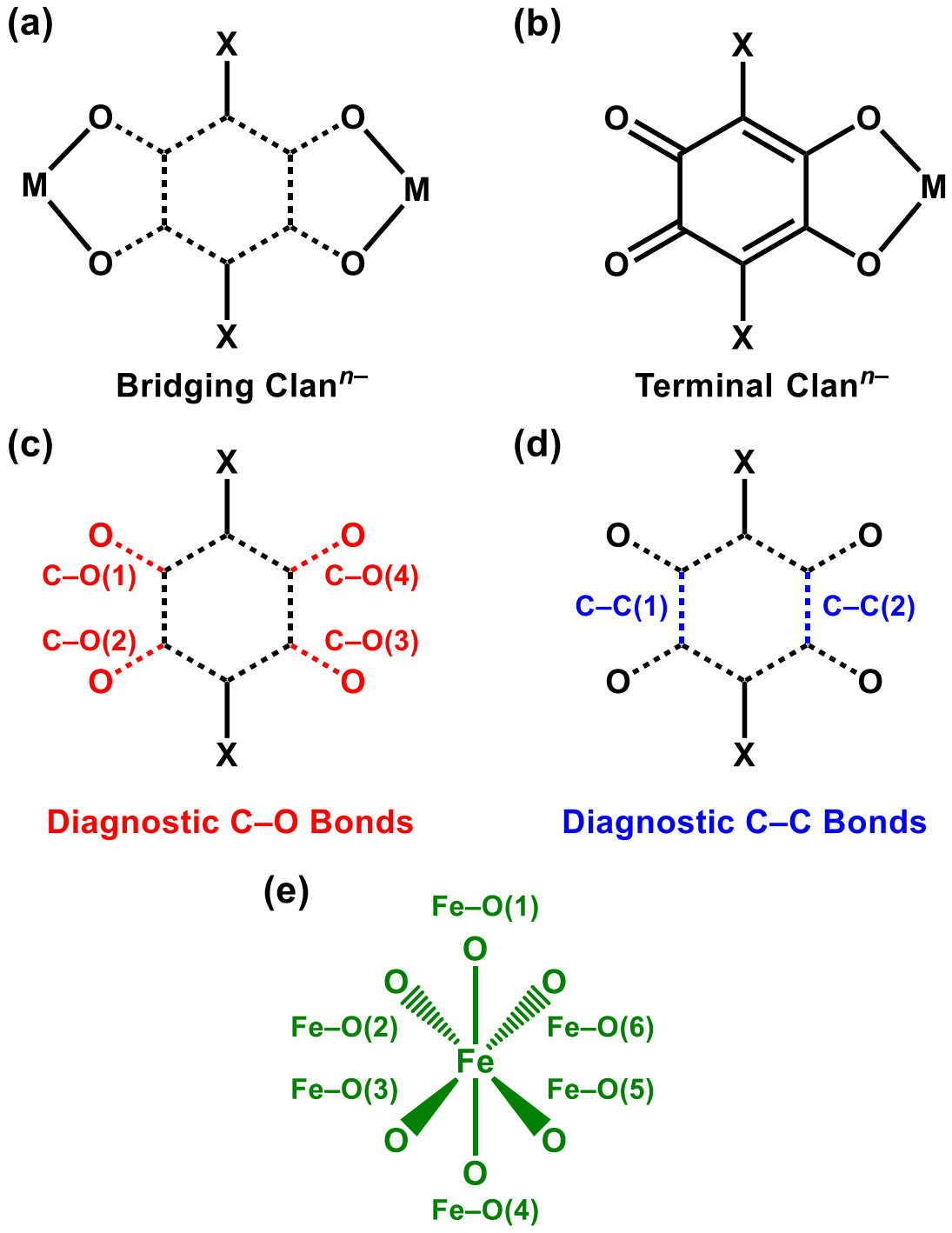
A.6 References A35

This page intentionally left blank

A.1 Procedure for Bond Length Analysis

Analysis and tabulation of the mean C–O and diagnostic C–C bond lengths ($d_{C–O}$ and $d_{C–C}$ respectively) in *M*–Clan$^{n–}$ compounds was performed by extracting crystallographic data published in the Cambridge Crystallographic Database (CSD) as of 29th July 2019. For analysis of Fe–O bond lengths ($d_{Fe–O}$), in addition to $d_{C–O}$ and $d_{C–C}$ values for Fe–Clan$^{n–}$ compounds, the data was extracted as of 9th March 2021 and is tabulated separately. The analyses were only performed on structures containing at least one bridging Clan$^{n–}$ ligand (μ-Clan, Scheme A.1a) coordinated to at least one d-, f- or p- block metal centre. Where the *M*–Clan$^{n–}$ compounds contain both terminal (Scheme A.1b) and bridging coordination modes, the $d_{C–O}$ and $d_{C–C}$ values are presented separately and noted as distinct coordination modes. Structures which exhibited R_1 values greater than 0.1 were excluded from the analysis to avoid bias from poorly refined crystallographic models. The Clan$^{n–}$ valence state, either Clan$^{2–}$, Clan$^{3–\bullet}$ or Clan$^{4–}$ as assigned by considering the valence states of the metals, counteranions and-cations, and other ligands in the compound.

The tabulated $d_{C–O}$ and $d_{C–C}$ values represent the mean of the unique bond lengths (C–O(1) through C–O(4), Scheme A.1c; and C–C(1) and C–C(2), Scheme A.1d respectively) for each crystallographic distinct Clan$^{n–}$ moiety in the compound. Compounds with more than one crystallographically distinct Clan$^{n–}$ ligand have their mean $d_{C–O}$ and $d_{C–C}$ values tabulated for each unique ligand. Similarly, $d_{Fe–O}$ values presented are the mean of the unique Fe–O bond lengths (Fe–O(1) through Fe–O(6), Scheme A.1e), with the mean $d_{Fe–O}$ values for each crystallographically unique Fe centres noted separately. Where error values are presented, they are the standard deviation of the mean $d_{C–O}$, $d_{C–C}$ and $d_{Fe–O}$ values in each distinct Clan$^{n–}$ species or Fe centre in the compounds. If no error values are given, then the C–O (C–O(1) through C–O(4)), C–C (C–C(1) and C–C(2)) or Fe–O (Fe–O(1) through Fe–O(6)) bonds in the compound are crystallographically equivalent.



Scheme A.1 (a) Bridging and (b) terminal coordination modes of Clan^{n-} ligands. Crystallographically unique (c) C–O, (d) diagnostic C–C, and (e) Fe–O bond used to determine mean $d_{C–O}$, $d_{C–C}$ and $d_{Fe–O}$ values for *M*–Clan^{n-} and Fe–Clan^{n-} compounds published within the CSD.

For the Clan^{2-} state, analysis of the distribution of unfiltered mean $d_{C–O}$ and $d_{C–C}$ values (Figure A.1), revealed several outlying $d_{C–O}$ and $d_{C–C}$ values; these compounds were subsequently filtered from the analyses and tabulations (Table A.1) of $d_{C–O}$ and $d_{C–C}$ values to prevent biasing the data. For the Clan$^{3-\bullet}$ or Clan^{4-}, there is an insufficient quantity of data to perform such filtering, so all extracted mean $d_{C–O}$ and $d_{C–C}$ bond length data are tabulated; Clan$^{3-\bullet}$ (Table A.2) and Clan^{4-} (Table A.3). Similarly, the extracted $d_{C–O}$, $d_{C–C}$ and $d_{Fe–O}$ data for Fe–Clan^{n-} compounds have not been filtered to remove statistical outliers, so that all the bond length data is tabulated (Table A.4). These analyses demonstrated the expected bond length ranges for Clan^{2-} are $d_{C–O}$ = 1.248–1.272 Å, and $d_{C–C}$ = 1.506–1.551 Å, while for Clan$^{3-\bullet}$, the expected bond length values are $d_{C–O}$ = 1.291–1.316 Å, and $d_{C–C}$ = 1.431–1.473 Å.

A.2 Distributions of Bond Lengths

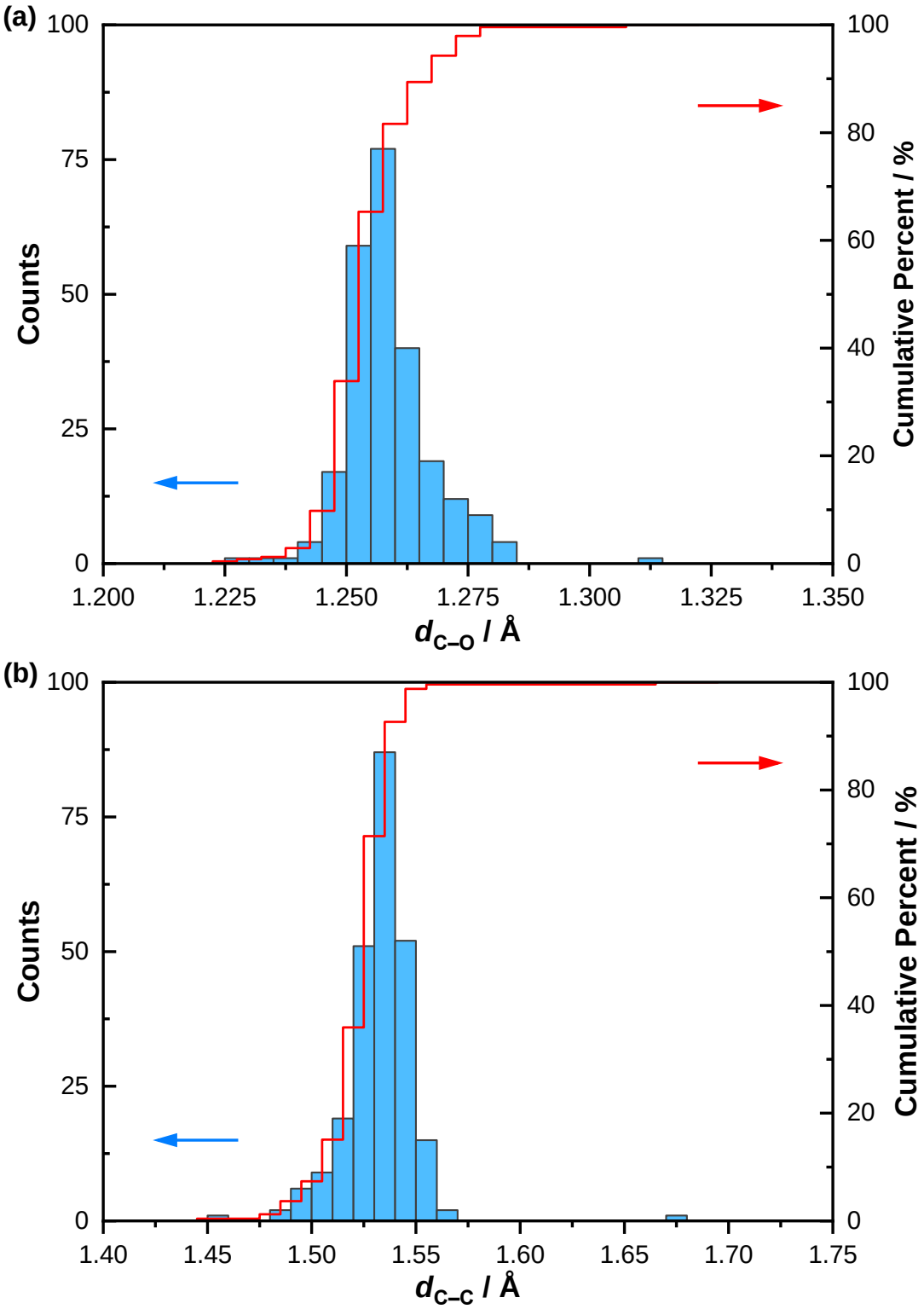


Figure A.1 Unfiltered distributions of unique crystallographic (a) d_{C-O} (bin size 0.005 Å) and (b) diagnostic d_{C-C} (bin size 0.01 Å) values for *M*–Clan^{2-} reported to date.

A.3 Tabulations of Bond Lengths for *M*–Clan^{n-} Compounds

Table A.1 Average $d_{C–O}$ and diagnostic $d_{C–C}$ values of Clan^{n-} moieties in *M*–Clan^{2-} compounds reported to date.

Compound	CCDC Ref. Code	Average $d_{C–O}$ / Å	Average $d_{C–C}$ / Å	Clan^{n-} Charge State	Dimen.	R_1	Ref.
$[Cu^{II}_2(pmdeta)_2(\mu\text{-Clan})](BPh_4)_2$	PMECAC	1.250(7)	1.543	2−	0	6.1	[1]
$[Ni^{II}_2(tren)_2(\mu\text{-Clan})](BPh_4)_2$	CATRNI	1.258(7)	1.536	2−	0	5.9	[1]
$[Cu^{II}_2(\mu\text{-tpy})_2(\mu\text{-Clan})](PF_6)_2$	FUWWUP	1.255(1)	1.535	2−	0	5.4	[2]
$[Rh^{I}_2(cod)_2(\mu\text{-Clan})]$	LAHSES	1.270(13)	1.520	2−	0	6.24	[3]
$[Cu^{II}_2(\mu\text{-2,2′-bpy})_2(meoh)_2(\mu\text{-Clan})](PF_6)_2$	WIDBAM	1.262(1)	1.520	2−	0	3.26	[4]
$[Rh^{III}_2(CO)_2Me_2I_2(\mu\text{-Clan})]$	TENVUD	1.268(1)	1.522	2−	0	4.09	[5]
$[Mn^{II}_2(tpa)_2(\mu\text{-Clan})](ClO_4)_2$	GIVTIO	1.256(1); 1.252(1)	1.525; 1.542	2−	0	5.55	[6]
$[Cu^{II}_2(Me_3tacn)_2(\mu\text{-Clan})](ClO_4)_2$	QABCEB	1.260(9)	1.531	2−	0	5.21	[7]
$[Fe^{III}_2(H_2O)_2(Clan)_2(\mu\text{-Clan})]\cdot 4H_2O$	QOCHEV	1.260(6); 1.257(33)[a]	1.530; 1.530(2)[a]	2−	0	4.54	[8]

[a] Terminal mono-coordinating

Table A.1(cont.) Average $d_{C–O}$ and diagnostic $d_{C–C}$ values of Clan$^{n–}$ moieties in M–Clan$^{2–}$ compounds reported to date.

Compound	CCDC Ref. Code	Average $d_{C–O}$ / Å	Average $d_{C–C}$ / Å	Clan$^{n–}$ Charge State	Dimen.	R_1	Ref.
$[Sc^{III}_2(H_2O)_6(Clan)_2(\mu\text{-Clan})]\cdot 10H_2O$	MOBBEK	1.272(16); 1.251(7);[b] 1.264(16)[b]	1.522(14); 1.543(5);[b] 1.530(23)[b]	2−	0	5.6	[9]
$[Zn^{II}_4(\mu\text{-LPy})(\mu\text{-Clan})_2](ClO_4)_2\cdot 4MeCN$	EGATEL	1.245(4); 1.254(4)	1.533(5); 1.524(9)	2−	0	6	[10]
$[Yb^{III}_2(HBpz_3)_4(\mu\text{-Clan})]\cdot 3CH_2Cl_2$	OBIBEH	1.251(2)	1.537	2−	0	3.15	[11]
$[Cu^{II}_2(tpy)_2(dmso)_2(\mu\text{-Clan})]$ $[Cu^{II}(Clan)_2(dmso)_2]$	ERAQIX	1.257(2); 1.251(25)[b]	1.530; 1.522(11)[b]	2−	0	6.39	[12]
$[Os^{II}_2(pap)_2(PPh_3)_4(\mu\text{-Clan})](ClO_4)_2$	XALFEW	1.279(3)	1.502	2−	0	4.57	[13]
$[Co^{II}_2(tpa)_2(\mu\text{-Clan})](BF_4)_2\cdot 2MeOH$	REMREH	1.256(1)	1.528	2−	0	5.45	[14]
$[Co^{III}_2(tpa)_2(\mu\text{-Clan})](BF_4)_4\cdot MeCN$	NIBKAL	1.263(12)	1.507	2−	0	6.41	[15]
$[Fe^{II}_2(tpa)_2(\mu\text{-Clan})](BF_4)_2\cdot 2MeOH$	NIBKEP	1.261(10)	1.528	2−	0	4.64	[15]
$[Fe^{II}_2(tpa)_2(\mu\text{-Clan})](BF_4)_2\cdot 2MeOH$	NIBKEP01	1.258(8)	1.536	2−	0	7.81	[16]
$[Ir^{III}_2Cp^{*}_2Cl_2(\mu\text{-Clan})]\cdot 2CH_2Cl_2$	YOHQIW	1.271(6)	1.516	2−	0	2.77	[17]

[b] Terminal mono-coordinating

Table A.1(cont.) Average $d_{C–O}$ and diagnostic $d_{C–C}$ values of Clan$^{n–}$ moieties in M–Clan$^{2–}$ compounds reported to date.

Compound	CCDC Ref. Code	Average $d_{C–O}$ / Å	Average $d_{C–C}$ / Å	Clan$^{n–}$ Charge State	Dimen.	R_1	Ref.
$[Ir^{III}_2Cp^*_2(Br\text{-}ppy)_2(\mu\text{-}Clan)](CF_3SO_3)_2\cdot CH_2Cl_2$	YOHQOC	1.259(15)	1.511(14)	2−	0	8.61	[17]
$[Ir^{III}_4Cp^*_4(\mu\text{-}pyz)_2(\mu\text{-}Clan)_2](CF_3SO_3)_4\cdot PhMe\cdot CH_2Cl_2\cdot 1.5MeOH\cdot H_2O$	YOHQUI	1.265(14); 1.280(10)	1.543(2); 1.526(4)	2−	0	6.51	[17]
$[Ir^{III}_4Cp^*_4(\mu\text{-}4,4'\text{-}bpy)_2(\mu\text{-}Clan)_2](CF_3SO_3)_4\cdot PhMe$	YOHRAP	1.265(9); 1.269(15)	1.522(21); 1.532(22)	2−	0	5.66	[17]
$[Ir^{III}_4Cp^*_4(\mu\text{-}4,4'\text{-}bpe)_2(\mu\text{-}Clan)_2](CF_3SO_3)_4$	YOHRET	1.257(6)	1.497(8)	2−	0	5.9	[17]
$[Re^{I}_4(CO)_{12}(\mu\text{-}4,4'\text{-}bpy)_2(\mu\text{-}Clan)_2]\cdot$ mesitylene	DOMDOZ	1.268(9)	1.522(10)	2−	0	6.3	[18]
$[Cu^{II}_2\{(Meim)_2\text{-}prop\}_2Cl_2(\mu\text{-}Clan)]\cdot 8MeCN\cdot 2H_2O$	EFETUF	1.261(2)	1.530	2−	0	2.99	[19]
$[Rh^{III}_2Cp^*_4(\mu\text{-}4,4'\text{-}bpy)_2(\mu\text{-}Clan)_2](CF_3SO_3)_4$	EGAQOT	1.263(14)	1.520(13)	2−	0	9.64	[20]
$[Ru^{III}_2(Cy)_4(\mu\text{-}4,4'\text{-}bpy)_2(\mu\text{-}Clan)_2](CF_3SO_3)_4\cdot 2PhMe\cdot 2H_2O$	EGAQUZ	1.266(11)	1.499(7)	2−	0	6.19	[20]
$[Ru^{III}_4(Cy)_4(\mu\text{-}4,4'\text{-}bpe)_2(\mu\text{-}Clan)_2](CF_3SO_3)_4$	EGARAG	1.255(16)	1.510(4)	2−	0	6.26	[20]
$[Ru^{III}_4(C_6Me_6)_4(\mu\text{-}4,4'\text{-}bpe)_2(\mu\text{-}Clan)_2](CF_3SO_3)_4\cdot 2Et_2O\cdot 2Acetone$	IHIGIQ	1.267(5)	1.514(2)	2−	0	3.19	[21]

Table A.1(cont.) Average $d_{C–O}$ and diagnostic $d_{C–C}$ values of Clan$^{n–}$ moieties in M–Clan$^{2–}$ compounds reported to date.

Compound	CCDC Ref. Code	Average $d_{C–O}$ / Å	Average $d_{C–C}$ / Å	Clan$^{n–}$ Charge State	Dimen.	R_1	Ref.
$[(V^{IV}O)_2Cl_2(2,2'\text{-bpy})_2(\mu\text{-Clan})]$	SONYIE	1.260(1)	1.525	2−	0	4.46	[22]
$[Re^{I}_4(CO)^{12}(\mu\text{-TXyBim})(\mu\text{-Clan})_2]$	EHUREF	1.277(13)	1.505(8)	2−	0	5.07	[23]
$[Cu^{II}_2(tpa)_2(\mu\text{-Clan})](ClO_4)_2\cdot 4MeOH$	MIRTIS	1.260(20)	1.538	2−	0	3.72	[24]
$[Re^{I}_2(CO)_6(\mu\text{-dppOb})(\mu\text{-Clan})]\cdot PhMe$	QIJQOR	1.261(8)	1.500(9)	2−	0	7.9	[25]
$[Re^{I}_6(CO)_{18}\{\mu\text{-(SMeBim)}_3\text{-Mes}\}_2(\mu\text{-Clan})_2]\cdot 4PhMe$	TENDIB	1.270(15); 1.269(10)	1.502; 1.535(7)	2−	0	5.2	[26]
$[Re^{I}_2(CO)_6(\mu\text{-BXyTBim})(\mu\text{-Clan})]$	FOVXUL	1.265(2)	1.507	2−	0	6.27	[27]
$[Rh^{III}_4Cp^{*}_4(\mu\text{-}\{Rh^{III}Cp^{*}(pdt)\}_2(\mu\text{-Clan})_2](CF_3SO_3)_4\cdot 2MeOH\cdot Et_2O$	MOSSOE	1.264(12)	1.533(5)	2−	0	6.04	[28]
$[Ir^{III}_4Cp^{*}_4(\mu\text{-}\{Ir^{III}Cp^{*}(pdt)\}_2(\mu\text{-Clan})_2](CF_3SO_3)_4\cdot 2MeOH\cdot Et_2O$	MOSSUK	1.275(12)	1.506(8)	2−	0	5.66	[28]
$(4,4'\text{-bpyH}_2)[Cu^{II}_2(Clan)_2(H_2O)_2(\mu\text{-Clan})]\cdot 2H_2O$	UQUYUC	1.261; 1.258(25)[c]	1.522; 1.530(24)[c]	2−	0	3.56	[29]
$[Rh^{III}_2Cp^{*}_2(H_2O)_2(\mu\text{-Clan})](CF_3SO_3)_2$	AWUSIW	1.261(2)	1.516	2−	0	4.11	[30]

[c] Terminal mono-coordinating

Table A.1(cont.) Average $d_{C–O}$ and diagnostic $d_{C–C}$ values of Clan$^{n–}$ moieties in M–Clan$^{2–}$ compounds reported to date.

Compound	CCDC Ref. Code	Average $d_{C–O}$ / Å	Average $d_{C–C}$ / Å	Clan$^{n–}$ Charge State	Dimen.	R_1	Ref.
$[Rh^{III}_8Ag^{I}_2Cp^{*}_8(meoh)_4(CF_3SO_3)_2(\mu\text{-pym})_4(\mu\text{-Clan})_4](CF_3SO_3)_4\cdot 2H_2O$	AWUSUI	1.259(11); 1.256(3)	1.535(7); 1.530(9)	2−	0	6.58	[30]
$[Rh^{III}_8Ag^{I}_2Cp^{*}_8(\mu\text{-pym})_4(\mu\text{-Clan})_4](CF_3SO_3)_6\cdot p\text{-xylene}\cdot 12MeOH\cdot 4H_2O$	AWUTIX	1.271(6); 1.261(5)	1.514(5); 1.521(5)	2−	0	5.9	[30]
$[Rh^{III}_4Cp^{*}_4(\mu\text{-4-pbdy})_2(\mu\text{-Clan})_2](CF_3SO_3)_4\cdot 0.67{}^{i}Pr_2O$	KEFZUT	1.257(15); 1.261(7); 1.263(4)	1.518(4); 1.521(2); 1.515(22)	2−	0	9.74	[31]
$[Ir^{III}_4Cp^{*}_4(\mu\text{-4-pbdy})_2(\mu\text{-Clan})_2](CF_3SO_3)_4$	KEGBAC	1.280(23); 1.268(5); 1.272(24)	1.540(1); 1.498(32); 1.513(10)	2−	0	8.93	[31]
$[Rh^{III}_8Pd^{II}_2Cp^{*}_8(\mu\text{-pyz})_2(\mu\text{-4,4′-bpyOHama})_4(\mu\text{-Clan})_2](CF_3SO_3)_4(NO_3)_4\cdot 12MeOH\cdot 2Et_2O\cdot 12H_2O$	MEKCOX	1.270(12)	1.523(6)	2−	0	6.44	[32]
$[Ni^{II}_2(py)_6Cl_2(\mu\text{-Clan})]$	PAXFUS	1.253(1); 1.255(2)	1.534; 1.534	2−	0	3.26	[33]
$[Mn^{II}_2(py)_6Cl_2(\mu\text{-Clan})]$	PAXGAZ	1.249; 1.250(1)	1.539; 1.542	2−	0	3.28	[33]
$[Dy^{III}_2(HBpz_3)_4(\mu\text{-Clan})]\cdot 2CH_2Cl_2$	DEKTOF	1.257(2)	1.538	2−	0	3.35	[34]

Table A.1(cont.) Average $d_{C–O}$ and diagnostic $d_{C–C}$ values of Clan$^{n–}$ moieties in M–Clan$^{2–}$ compounds reported to date.

Compound	CCDC Ref. Code	Average $d_{C–O}$ / Å	Average $d_{C–C}$ / Å	Clan$^{n–}$ Charge State	Dimen.	R_1	Ref.
$[Dy^{III}_2(HBpz_3)_4(\mu\text{-Clan})]\cdot 2CH_2Cl_2$	DEKTOF01	1.255(8)	1.551	2−	0	3.99	[35]
$[Dy^{III}_2(HBpz_3)_4(\mu\text{-Clan})]\cdot 2CH_2Cl_2$	DEKTOF02	1.261(4)	1.536	2−	0	3.88	[36]
$[Y^{III}_2(HBpz_3)_4(\mu\text{-Clan})]\cdot 2CH_2Cl_2$	DEKTUL	1.233(15)	1.516	2−	0	4.54	[34]
$[Y^{III}_2(HBpz_3)_4(\mu\text{-Clan})]\cdot 2CH_2Cl_2$	DEKTUL01	1.248(1)	1.540	2−	0	4.78	[35]
$[Y^{III}_2(HBpz_3)_4(\mu\text{-Clan})]\cdot 2$Acetone	DEKVAT	1.255(3)	1.539	2−	0	3.38	[34]
$[Re^{I}_2(CO)_6(POPh_3)(\mu\text{-Clan})]$	GIHFEL	1.273(4)	1.496	2−	0	5.16	[37]
$[Re^{I}_2(CO)_6(POPh_3)(\mu\text{-Clan})]$	GIHFEL01	1.275(4)	1.493	2−	0	4.97	[38]
$[Ir^{III}_4Cp^{*}_4(\mu\text{-}\{Ir^{III}Cp^{*}(dapz)\})_2(\mu\text{-Clan})_2](CF_3SO_3)_4\cdot 6MeOH\cdot H_2O$	GIBSOC	1.265(14)	1.511(16)	2−	0	5.39	[39]
$[Ir^{III}_4Cp^{*}_4(\mu\text{-}\{Ir^{III}Cp^{*}Cl(dhqox)\})_2(\mu\text{-Clan})_2](CF_3SO_3)_2\cdot 4MeOH$	GIBSUI	1.258(6)	1.520(11)	2−	0	3.23	[39]
$[Re^{I}_2(CO)_6(\mu\text{-BPNim})(\mu\text{-Clan})]\cdot$PhMe	JEWJUT	1.259(9)	1.549	2−	0	5.15	[40]
$[Tb^{III}_2(HBpz_3)_4(\mu\text{-Clan})]\cdot 2CH_2Cl_2$	LEPNIG	1.255(1)	1.535	2−	0	4.05	[35]
$[Gd^{III}_2(HBpz_3)_4(\mu\text{-Clan})]\cdot 2CH_2Cl_2$	LEPNOM	1.226(8)	1.532	2−	0	9.33	[35]
$[Gd^{III}_2(HBpz_3)_4(\mu\text{-Clan})]\cdot 2CH_2Cl_2$	LEPNOM01	1.260(1)	1.537	2−	0	3.31	[36]

Table A.1(cont.) Average $d_{C–O}$ and diagnostic $d_{C–C}$ values of Clan$^{n–}$ moieties in M–Clan$^{2–}$ compounds reported to date.

Compound	CCDC Ref. Code	Average $d_{C–O}$ / Å	Average $d_{C–C}$ / Å	Clan$^{n–}$ Charge State	Dimen.	R_1	Ref.
$[Rh^{III}_4Cp^*_4(\mu\text{-}\{Cu^{II}_2(\mu\text{-}^t\text{Buacac}_2\text{-py})_2\})_2(\mu\text{-Clan})_2](CF_3SO_3)_4\cdot$Corannulene$\cdot 9MeOH\cdot 7H_2O$	VETLAK	1.260(11); 1.255(5)	1.520(5); 1.528(1)	2−	0	5.98	[41]
$[Ir^{III}_4Cp^*_4(\mu\text{-3-pbdy})_2(\mu\text{-Clan})_2](CF_3SO_3)_4\cdot 11MeOH\cdot 5H_2O$	WIGFIE	1.278(37); 1.313(50)	1.490(15); 1.538(40)	2−	0	7.37	[42]
$[Re^{I}_2(CO)_6(\mu\text{-BPOPh}_2\text{-7-TH})(\mu\text{-Clan})]$	VIKSUG	1.283(10)	1.489(16)	2−	0	5.64	[43]
$[Ir^{III}_4Cp^*_4(\mu\text{-bpyeyan})_2(\mu\text{-Clan})_2](CF_3SO_3)_4\cdot 4^i\text{Pr}_2O\cdot 5MeOH\cdot 5H_2O$	BOFSUN	1.275(20); 1.284(26); 1.259(16); 1.271(13)	1.508(9); 1.505(15); 1.481(12); 1.528(6)	2−	0	9.7	[44]
$[Fe^{II}_2(Me_3tpa)_2(\mu\text{-Clan})](BF_4)_2\cdot 0.7H_2O$	LUNHIO	1.254(16)	1.532	2−	0	9.18	[45]
$[Cu^{II}(H_2O)_2(\mu\text{-Clan})]\cdot H_2O$	VOMNAM	1.266(18)	1.530(1)	2−	1	4.8	[46]
$[Cu^{II}(meoh)_2(\mu\text{-Clan})]$	HESKIZ	1.260(2)	1.530	2−	1	2.9	[47]
$[Cu^{II}(dcmb)(\mu\text{-Clan})]$	NACKEH	1.253(16)	1.537	2−	1	3.05	[48]
$[Mn^{II}(2,2'\text{-bpy})(\mu\text{-Clan})]$	RAZJIL	1.254(3); 1.255(2)	1.540; 1.544	2−	1	3.57	[49]
$[Cu^{II}(H_2O)_2(\mu\text{-Clan})]\cdot$phz	TINPOV	1.258(17)	1.532	2−	1	2.7	[50]

Table A.1(cont.) Average $d_{C–O}$ and diagnostic $d_{C–C}$ values of Clan$^{n–}$ moieties in M–Clan$^{2–}$ compounds reported to date.

Compound	CCDC Ref. Code	Average $d_{C–O}$ / Å	Average $d_{C–C}$ / Å	Clan$^{n–}$ Charge State	Dimen.	R_1	Ref.
[Cu^{II}(H$_2$O)(μ-Clan)·ohphz	TINQAI	1.272	1.559	2−	1	3.4	[50]
[Fe^{II}(H$_2$O)$_2$(μ-Clan)]·H$_2$O	KIQJID	1.257(1)	1.523	2−	1	4.5	[51]
[Fe^{II}(H$_2$O)$_2$(μ-Clan)]·H$_2$O	KIQJID01	1.259	1.53	2−	1	3.15	[8]
[Co^{II}(H$_2$O)$_2$(μ-Clan)]·H$_2$O	KIQJOJ	1.258(1)	1.523	2−	1	2.7	[51]
[Mn^{II}(H$_2$O)$_2$(μ-Clan)]·H$_2$O	KIQJUP	1.257(5)	1.527	2−	1	4.5	[51]
[Mn^{II}(H$_2$O)$_2$(μ-Clan)]·H$_2$O	KIQJUP02	1.260(3)	1.537	2−	1	0.99	[52]
[Fe^{II}(H$_2$O)$_2$(μ-Clan)]·phz	KIQKAW	1.262(13)	1.522	2−	1	2.3	[51]
[Co^{II}(H$_2$O)$_2$(μ-Clan)]·phz	KIQKEA	1.256(8)	1.537	2−	1	3.1	[51]
[Mn^{II}(H$_2$O)$_2$(μ-Clan)]·phz	KIQKIE	1.258(5)	1.534	2−	1	3	[51]
[Cd^{II}(H$_2$O)$_2$(μ-Clan)]·H$_2$O	QOCHAR	1.254(2)	1.543	2−	1	2.43	[8]
[Mn^{II}(tpy)(μ-Clan)]	NEHZAB	1.253(3); 1.254(1)	1.535; 1.535	2−	1	5.15	[53]
[Cu$^{II}_2$(tpy)$_2$(μ-Clan)][Cu^{II}(Clan)$_2$]	ERAQET	1.244(29); 1.248(32)[d]	1.550; 1.540(23)[d]	2−	1	6.28	[12]

[d] Terminal mono-coordinating

Table A.1(cont.) Average $d_{C–O}$ and diagnostic $d_{C–C}$ values of Clan$^{n–}$ moieties in M–Clan$^{2–}$ compounds reported to date.

Compound	CCDC Ref. Code	Average $d_{C–O}$ / Å	Average $d_{C–C}$ / Å	Clan$^{n–}$ Charge State	Dimen.	R_1	Ref.
[Cd^{II}(1,10-phen)(μ-Clan)]	FAHPIO	1.250(7); 1.248	1.540; 1.542	2−	1	4.56	[54]
[Sn^{IV}Me$_2$(dmso)(μ-Clan)]·DMSO	URUJIB	1.253(1)	1.530(7)	2−	1	4.27	[55]
[Sn^{IV}*n*Bu$_2$(dmso)(μ-Clan)]	URUJOH	1.253(4); 1.250(9)	1.519; 1.534	2−	1	5.08	[55]
[Sn^{IV}Ph$_2$(dmso)(μ-Clan)]·DMSO	URUJUN	1.259(6)	1.527(6)	2−	1	1.96	[55]
[U^{VI}O$_2$(H$_2$O)(μ-Clan)]·bpym·4H$_2$O	GEPZOS	1.268(11); 1.275(1)	1.527; 1.540	2−	1	3.4	[56]
[Mn^{II}(2,2′-bpy)(μ-Clan)]·2EtOH	LERTOT	1.257(2)	1.543(2)	2−	1	3.7	[57]
[Fe^{II}(tren(imid)$_3$)]$_2$[Mn^{II}Cr^{III}Cl$_2$(Clan)(μ-Clan)$_2$]Cl·MeOH·3CH$_2$Cl$_2$·0.5MeCN	HOWHUY	1.264(20); 1.258(23); 1.256(29)	1.518(12); 1.537(15); 1.533(20)	2−	1	8.12	[58]
[Mn^{II}(etoh)$_2$(μ-Clan)]	NIXSAQ	1.260(5)	1.541	2−	1	3.23	[59]
[Cu^{II}(imid)$_2$(μ-Clan)]	UQUTEH	1.251(6); 1.252(4)	1.536; 1.536(4)	2−	1	3.53	[29]
[Cu^{II}(etoh)$_2$(μ-Clan)]	UQUYOW	1.257(2)	1.546(2)	2−	1	4.79	[29]
[Cu^{II}(mecn)(μ-Clan)]	UQUZAJ	1.264(4)	1.526(2)	2−	1	4.44	[29]

Table A.1(cont.) Average $d_{C–O}$ and diagnostic $d_{C–C}$ values of Clan$^{n–}$ moieties in *M*–Clan$^{2–}$ compounds reported to date.

Compound	CCDC Ref. Code	Average $d_{C–O}$ / Å	Average $d_{C–C}$ / Å	Clan$^{n–}$ Charge State	Dimen.	R_1	Ref.
$[Cu^{II}(H_2O)_2(\mu\text{-Clan})]$	UQUZEN	1.263(11)	1.533	2−	1	7.3	[29]
$(2,2'\text{-bpyH})_2[Mn^{II}_2(\mu\text{-Clan})_3(H_2O)_2]\cdot 2H_2O$	PAXGED	1.257(5);[e] 1.251(15)[f]	1.535;[e] 1.529(10)[f]	2−	1[g]	4.55	[33]
$[Mn^{II}(1,10\text{-phen})(\mu\text{-Clan})]\cdot EtOH$	PAXHAA	1.253(3); 1.250(1)	1.540; 1.531	2−	1	5.51	[33]
$[Co^{II}(2,2'\text{-bpy})(\mu\text{-Clan})]\cdot EtOH$	PAXHEE	1.256(2)	1.531	2−	1	4.37	[33]
$[Mn^{II}(4\text{-ppy})_2(\mu\text{-Clan})]$	TAZSEV	1.253(11)	1.546	2−	1	7.11	[60]
$[Zn^{II}(py)_2(\mu\text{-Clan})]\cdot$Acetone	TAZVEY	1.252(5); 1.259(1)	1.537; 1.559	2−	1	5.15	[61]
$[Cd^{II}(meoh)_2(\mu\text{-Clan})]$	TEBCOV	1.256(11)	1.549	2−	1	3.64	[62]
$[Mn^{II}(tpa)(\mu\text{-Clan})]\cdot MeOH$	BEPJAK	1.249(2); 1.254(3)	1.541; 1.539	2−	1	5.55	[63]
$(Me_4N)_2[Fe^{II}Cl_2(\mu\text{-Clan})]$	VEXGOX[h]	1.256(11)	1.523	2−	1	7.27	[64]

[e] Bridging bis-bidendate

[f] Bridging mono- and bi-dendate

[g] 1D ladder-like chain

[h] Structure at T = 250 K

Table A.1(cont.) Average $d_{C–O}$ and diagnostic $d_{C–C}$ values of Clan$^{n–}$ moieties in M–Clan$^{2–}$ compounds reported to date.

Compound	CCDC Ref. Code	Average $d_{C–O}$ / Å	Average $d_{C–C}$ / Å	Clan$^{n–}$ Charge State	Dimen.	R_1	Ref.
$[Pr^{III}_2(etoh)_6(\mu\text{-Clan})_3]\cdot 2EtOH$	CAZZAE	1.248; 1.251(1); 1.239(13)	1.527; 1.530; 1.522	2−	2	2.5	[65]
$[Ca^{II}(H_2O)_2(\mu\text{-}H_2O)(\mu\text{-Clan})]\cdot H_2O$	FIYKUT	1.255(2)	1.536	2−	2	3.07	[66]
$[Y^{III}_2(H_2O)_6(\mu\text{-Clan})_3]\cdot 6.6H_2O$	GASMUI	1.254(13); 1.252(1); 1.256(1)	1.524; 1.536; 1.536	2−	2	4.45	[67]
$[Cu^{II}(\mu\text{-pyz})(\mu\text{-Clan})]$	HESKEV	1.257(24)	1.537	2−	2	2	[47]
$[Mn^{II}_2(H_2O)_2(\mu\text{-2,2′-bpym})(\mu\text{-Clan})_2]\cdot 2EtOH\cdot 2H_2O$	NEHZEF	1.251(4); 1.253(4)	1.535; 1.539	2−	2	4.01	[53]
$[Co^{II}(\mu\text{-pyz})(\mu\text{-Clan})]$	HUHPAB	1.263(5)	1.534	2−	2	4.69	[68]
$[Mn^{II}(\mu\text{-pyz})(\mu\text{-Clan})]$	HUHPEF	1.255(6)	1.536	2−	2	2.15	[68]
$[La^{III}_2(H_2O)_4(\mu\text{-}H_2O)_2(\mu\text{-Clan})_3]\cdot 7H_2O$	MIZYAV	1.252(5); 1.262(1)	1.531(4); 1.525	2−	2	3.98	[9]
$[Pr^{III}_2(H_2O)_6(\mu\text{-Clan})_3]\cdot 12H_2O$	MIZYID	1.256(1); 1.254(13); 1.261	1.527; 1.550; 1.544	2−	2	8.42	[9]

Table A.1(cont.) Average $d_{C–O}$ and diagnostic $d_{C–C}$ values of Clan$^{n–}$ moieties in *M*–Clan$^{2–}$ compounds reported to date.

Compound	CCDC Ref. Code	Average $d_{C–O}$ / Å	Average $d_{C–C}$ / Å	Clan$^{n–}$ Charge State	Dimen.	R_1	Ref.
$[Tb^{III}_2(H_2O)_6(\mu\text{-Clan})_3]\cdot 12H_2O$	MIZYUP	1.257(9); 1.255(9); 1.258(10)	1.529; 1.519; 1.529	2−	2	4.82	[9]
$[Ce^{III}_2(H_2O)_6(\mu\text{-Clan})_3]\cdot 12H_2O$	MIZZAW	1.254(3); 1.262	1.532; 1.534	2−	2	3.4	[9]
$[Ce^{III}_2(H_2O)_6(\mu\text{-Clan})_3]\cdot 12H_2O$	MIZZAW01	1.258(11); 1.250(8); 1.255(4)	1.530; 1.533; 1.538	2−	2	3.68	[9]
$[Y^{III}_2(H_2O)_6(\mu\text{-Clan})_3]\cdot 10H_2O$	MIZZEA	1.253(16); 1.253(5); 1.256(1)	1.528; 1.533; 1.529	2−	2	3.96	[9]
$[Gd^{III}_2(H_2O)_6(\mu\text{-Clan})_3]\cdot 10H_2O$	MIZZIE	1.253(16); 1.256(3); 1.256(1)	1.530; 1.530; 1.518	2−	2	2.35	[9]
$(H_3O)_2(phz)_3[Cu^{II}_2(\mu\text{-Clan})_3]\cdot 2Acetone\cdot 2H_2O$	SAJBEL	1.248	1.537	2−	2	5.22	[69]
$(H_3O)_2(phz)_3[Cu^{II}_2(\mu\text{-Clan})_3]$	SAJBIP	1.253	1.531	2−	2	4.72	[69]
$(H_3O)_2(phz)_3[Cd^{II}_2(\mu\text{-Clan})_3]\cdot 2Acetone\cdot 2H_2O$	SAJBOV	1.247	1.540	2−	2	4.77	[69]
$(H_3O)_2(phz)_3[Zn^{II}_2(\mu\text{-Clan})_3]\cdot 2Acetone\cdot 2H_2O$	SAJBUB	1.249	1.546	2−	2	5.98	[69]

Table A.1(cont.) Average $d_{C–O}$ and diagnostic $d_{C–C}$ values of Clan$^{n–}$ moieties in M–Clan$^{2–}$ compounds reported to date.

Compound	CCDC Ref. Code	Average $d_{C–O}$ / Å	Average $d_{C–C}$ / Å	Clan$^{n–}$ Charge State	Dimen.	R_1	Ref.
$(H_3O)_2(phz)_3[Co^{II}_2(\mu\text{-Clan})_3]\cdot 2Acetone\cdot 2H_2O$	SAJCAI	1.259	1.526	2−	2	6.69	[69]
$(Et_4N)_2[Ca^{II}Sn^{IV}(\mu\text{-Clan})_4]$	BAKBAS	1.257(17)	1.539(16)	2−	2	1.82	[70]
$(Et_4N)_2[Ca^{II}Sn^{IV}(\mu\text{-Clan})_4]\cdot CS_2$	BAKBEW	1.253(21)	1.539(14)	2−	2	3.64	[70]
$(Et_4N)_2[Ca^{II}Sn^{IV}(\mu\text{-Clan})_4]\cdot 2MeCN\cdot 0.5H_2O$	BAKBIA	1.261(22)	1.531(17)	2−	2	3.55	[70]
$(Et_4N)_2[Ca^{II}Sn^{IV}(\mu\text{-Clan})_4]\cdot 2Acetone\cdot 2H_2O$	BAKBOG	1.259(21)	1.543(13)	2−	2	2.87	[70]
$(H_3O)_2(phz)_3[Mn^{II}_2(\mu\text{-Clan})_3]\cdot 2Acetone\cdot 2H_2O$	VEQDUS[i]	1.253	1.545	2−	2	5.66	[71]
$(H_3O)_2(phz)_3[Mn^{II}_2(\mu\text{-Clan})_3]\cdot 2Acetone\cdot 2H_2O$	VEQDUS01[j]	1.252	1.541	2−	2	4.94	[71]
$(H_3O)_2(phz)_3[Mn^{II}_2(\mu\text{-Clan})_3]\cdot 2Acetone\cdot 2H_2O$	VEQDUS02[k]	1.259	1.537	2−	2	4.86	[71]
$[Eu^{III}_2(H_2O)_2(2,2'\text{-bpym})_2(\mu\text{-Clan})_3]\cdot 4EtOH$	GEPZUY	1.257(4); 1.258(7); 1.258(1)	1.540; 1.535; 1.551	2−	2	2.55	[72]

[i] Structure at room temperature (T = 283–303 K)
[j] Structure at T = 200 K
[k] Structure at T = 150 K

Table A.1(cont.) Average $d_{C–O}$ and diagnostic $d_{C–C}$ values of Clan$^{n–}$ moieties in *M*–Clan$^{2–}$ compounds reported to date.

Compound	CCDC Ref. Code	Average $d_{C–O}$ / Å	Average $d_{C–C}$ / Å	Clan$^{n–}$ Charge State	Dimen.	R_1	Ref.
$[Gd^{III}_2(H_2O)_6(\mu\text{-Clan})_3]\cdot 2EtOH$	GEQBAH	1.271; 1.243(10)	1.543; 1.550	2−	2	6.64	[73]
$[Gd^{III}_2(H_2O)_6(\mu\text{-Clan})_3]\cdot 2(2,2'\text{-bpym})\cdot 6H_2O$	GEQBEL	1.253(7); 1.252(2)	1.528(6); 1.553	2−	2	2.79	[74]
$(H_3O)(phz)_3[Mn^{II}Cr^{III}(\mu\text{-Clan})_3]$	MIRFEA	1.277(20)	1.459(23)	2−	2	5.59	[75]
$[Fe^{III}(sal_2\text{-trien})][Mn^{II}Cr^{III}(\mu\text{-Clan})_3]\cdot 5MeCN\cdot MeOH\cdot 0.5CH_2Cl_2\cdot 0.5H_2O$	HOWHAE	1.259(18); 1.262(7)	1.547; 1.527(16)	2−	2	9.35	[58]
$[Fe^{III}(acac_2\text{-trien})][Mn^{II}Cr^{III}(\mu\text{-Clan})_3]\cdot 2MeCN$	MUMKUC	1.266(22); 1.269(15)	1.530(11); 1.529(13)	2−	2	4.41	[76]
$(EtPh_3P)_2[KFe^{III}(\mu\text{-Clan})3]\cdot 2DMF$	QUJJOW	1.255(23); 1.263(25); 1.257(21)	1.544(19); 1.553(12); 1.540(9)	2−	2	5.79	[77]
$(H_3O)(phz)_3[Fe^{II}Fe^{III}(\mu\text{-Clan})_3]\cdot 13H_2O$	QEFPOJ	1.268	1.529	2−	2	3.81	[78]
$(Et_3NH)[Mn^{II}Cr^{III}(\mu\text{-Clan})_3]$	SEQCID	1.264(27)	1.527(15)	2−	2	6.89	[79]
$(Et_4N)_2[Zn^{II}_2(\mu\text{-Clan})_3]\cdot 24H_2O$	XARDEC	1.249	1.543	2−	2	6.88	[80]

Table A.1(cont.) Average $d_{C–O}$ and diagnostic $d_{C–C}$ values of Clan$^{n–}$ moieties in M–Clan$^{2–}$ compounds reported to date.

Compound	CCDC Ref. Code	Average $d_{C–O}$ / Å	Average $d_{C–C}$ / Å	Clan$^{n–}$ Charge State	Dimen.	R_1	Ref.
$[Er^{III}_2(H_2O)_6(\mu\text{-Clan})_3]\cdot 10H_2O$	NIGNEZ	1.253(17); 1.266(15); 1.271(2)	1.537; 1.521; 1.535	2–	2	4.95	[81]
$[Er^{III}_2(dmac)_4(\mu\text{-Clan})_3]$	NIGNOJ	1.254(18); 1.250(32); 1.260(8)	1.533(35); 1.554(6); 1.567(23)	2–	2	6.19	[81]
$[Er^{III}_2(fm)_6(\mu\text{-Clan})_3]\cdot 4FM\cdot 2H_2O$	NIGNUP	1.252(12); 1.253(2); 1.259(16)	1.539; 1.540; 1.540	2–	2	3.41	[81]
$[Er^{III}_2(dmf)_6(\mu\text{-Clan})_3]$	NIGPAX	1.251(4); 1.250(1)	1.540; 1.553(2)	2–	2	4.04	[81]
$[Er^{III}_2(dmso)_4(\mu\text{-Clan})_3]\cdot 2DMSO\cdot 2H_2O$	NIGQIG	1.262(10); 1.254(1); 1.258(18)	1.530; 1.541; 1.547	2–	2	4.08	[81]
$(Et_4N)_2[Mn^{II}_2(\mu\text{-Clan})_3]\cdot x$DMF	NIHQED	1.254	1.555	2–	2	6.8	[82]
$(Et_4N)_2[Co^{II}_2(\mu\text{-Clan})_3]\cdot x$DMF	NIHQUT	1.275	1.537	2–	2	7.89	[83]

Table A.1(cont.) Average $d_{C–O}$ and diagnostic $d_{C–C}$ values of Clan$^{n–}$ moieties in M–Clan$^{2–}$ compounds reported to date.

Compound	CCDC Ref. Code	Average $d_{C–O}$ / Å	Average $d_{C–C}$ / Å	Clan$^{n–}$ Charge State	Dimen.	R_1	Ref.
(^{n}Pr$_4$N)$_2$[Fe$^{III}_2$(μ-Clan)$_3$]·2Acetone·H$_2$O	SIQPIU[l]	1.259(3)	1.536(2)	2−	2	4.44	[84]
(^{n}Pr$_4$N)$_2$[Fe^{II}Fe^{III}(μ-Clan)$_3$]·2Acetone·H$_2$O	SIQPIU01[m]	1.258(2); 1.266(2)	1.530(2); 1.518(5)	2−	2	5.98	[84]
Na(Me$_4$N)[Mn$^{II}_2$(μ-Clan)$_3$]·5.5THF·MeCN	CIXNUV	1.249	1.516	2−	2	13.05	[82]
(Me$_4$N)$_2$[Mn$^{II}_2$(μ-Clan)$_3$]·3.2Et$_2$O	CIXPEH	1.248	1.538	2−	2	7.5	[82]
(Et$_4$N)[Bi^{III}(μ-Clan)$_2$]·1.5Acetone	QOFBEV	1.243	1.560	2−	2	4.42	[85]
(Me$_4$N)[Sc^{III}(μ-Clan)$_2$]	QOFBIZ	1.248	1.529	2−	2	6.8	[85]
(Et$_4$N)[Y^{III}(μ-Clan)$_2$]	QOFBOF	1.258	1.528	2−	2	17.35	[85]
(Et$_4$N)[Y^{III}(μ-Clan)$_2$]·1.87I$_2$	QOFBUL	1.259	1.514	2−	2	5.28	[85]
(Et$_4$N)[Y^{III}(μ-Clan)$_2$]·0.91Br$_2$	QOFCAS	1.255	1.552	2−	2	6.88	[85]
(Et$_4$N)[Dy^{III}(μ-Clan)$_2$]·1.5Acetone	QOFCEW	1.259	1.544	2−	2	3.3	[85]
(Et$_4$N)[Sc^{III}(μ-Clan)$_2$]·Acetone	QOFMUW	1.260	1.547	2−	2	5.67	[85]
(Et$_4$N)[Gd^{III}(μ-Clan)$_2$]·Acetone	QOFNAD	1.254	1.541	2−	2	2.98	[85]
(Et$_4$N)[Yb^{III}(μ-Clan)$_2$]·Acetone	QOFNEH	1.247	1.545	2−	2	2.87	[85]

[l] Structure at T = 100 K

[m] Structure at T = 241 K

Table A.1(cont.) Average $d_{C–O}$ and diagnostic $d_{C–C}$ values of Clan$^{n–}$ moieties in M–Clan$^{2–}$ compounds reported to date.

Compound	CCDC Ref. Code	Average $d_{C–O}$ / Å	Average $d_{C–C}$ / Å	Clan$^{n–}$ Charge State	Dimen.	R_1	Ref.
$(Et_4N)[In^{III}(\mu\text{-Clan})_2]\cdot 1.5$Acetone	QOFNIL	1.259	1.549	2−	2	3.69	[85]
$(Et_4N)[Er^{III}(\mu\text{-Clan})_2]\cdot$Acetone	QOFNOR	1.252	1.547	2−	2	2.9	[85]
$(Et_4N)[Y^{III}(\mu\text{-Clan})_2]\cdot$Acetone	QOFNUX	1.254	1.545	2−	2	2.21	[85]
$(Et_4N)[Tb^{III}(\mu\text{-Clan})_2]\cdot 1.5$Acetone	QOFPAF	1.248	1.542	2−	2	4.56	[85]
$(Et_4N)[Lu^{III}(\mu\text{-Clan})_2]\cdot 1.5$Acetone	QOFPEJ	1.254	1.553	2−	2	2.91	[85]
$(Et_4N)[Ho^{III}(\mu\text{-Clan})_2]\cdot 1.5$Acetone	QOFPIN	1.255	1.541	2−	2	2.95	[85]
$(^n Pr_4N)_2[Fe^{III}_2(\mu\text{-Clan})_3]$	LUDNUW[n]	1.257(5)	1.534	2−	2	4.13	[86]
$(^n Pr_4N)_2[Fe^{III}_2(\mu\text{-Clan})_3]$	LUDNUW01[o]	1.260(2)	1.536	2−	2	6.39	[86]
$(^n Pr_4N)_2[Fe^{2.5}_2(\mu\text{-Clan})_3]$	LUDNUW02[p]	1.254(10)	1.541	2−	2	6.99	[86]
$(^n Pr_4N)_2[Fe^{II}_2(\mu\text{-Clan})_3]$	LUDNUW03[q]	1.258(19); 1.252(2)	1.539; 1.535(6)	2−	2	7.43	[86]
$[Ag^{I}_2(\mu\text{-Clan})]$	RORQOE	1.243(4)	1.553	2−	3	2.3	[87]

[n] Structure at T = 103 K
[o] Structure at T = 300 K
[p] Structure at T = 330 K
[q] Structure at T = 380 K

Table A.1(cont.) Average $d_{C–O}$ and diagnostic $d_{C–C}$ values of Clan$^{n–}$ moieties in M–Clan$^{2–}$ compounds reported to date.

Compound	CCDC Ref. Code	Average $d_{C–O}$ / Å	Average $d_{C–C}$ / Å	Clan$^{n–}$ Charge State	Dimen.	R_1	Ref.
$(H_3O)[Y^{III}(\mu\text{-Clan})_2]\cdot 8MeOH$	MOBBIO	1.264(17)	1.547	2−	3	8.08	[9]
$[Th^{IV}(H_2O)_2(\mu\text{-Clan})_2]\cdot 4H_2O$	MOBBOU	1.256(13); 1.263(9)	1.512; 1.524	2−	3	4.85	[9]
$(^{n}Bu_4N)_2[Mn^{II}(\mu\text{-Clan})_3]\cdot 8MeOH$	OWIVEW	1.252	1.679	2−	3	9.54	[88]
$(MeEt_3N)[Na(dmf)][NaFe^{III}(\mu\text{-Clan})_3]$	QUJKOX	1.258(23); 1.258(26); 1.258(25)	1.534(18); 1.535(19); 1.539(20)	2−	3	4.13	[77]
$[Zn^{II}(bix)(\mu\text{-Clan})]\cdot 2H_2O$	TEBDIQ	1.248(16); 1.253(2)	1.547; 1.544	2−	3	4.38	[89]
$[Zn^{II}(4,4'\text{-bpy})(\mu\text{-Clan})]$	TEBDUC	1.252(1)	1.544	2−	3	5.62	[90]

Table A.2 Average $d_{C–O}$ and diagnostic $d_{C–C}$ values of Clan$^{n–}$ moieties in *M*–Clan$^{2.67–}$ and *M*–Clan$^{3–\bullet}$ compounds reported to date.

Compound	CCDC Ref. Code	Average C–O / Å	Average C–C / Å	Clan$^{n–}$ Charge State	Dimen.	R_1	Ref.
$(^n\text{Pr}_4\text{N})_2[\text{Fe}^{2.5}{}_2(\mu\text{-Clan})_3]$	LUDNUW02[r]	1.271(5)	1.504(10)	2.5−	2	6.99	[86]
$(\text{Me}_2\text{NH}_2)_2[\text{Fe}^{\text{III}}{}_2(\mu\text{-Clan})_3]\cdot 6\text{DMF}\cdot 2\text{H}_2\text{O}$	ZACDAL	1.280	1.48	2.67−	2	9.54	[91]
$(\text{Et}_4\text{N})_2[\text{Fe}^{\text{III}}{}_2(\mu\text{-Clan})_3]\cdot 20\text{H}_2\text{O}$	XARDIG	1.284	1.491	2.67−	2	5.31	[80]
$(\text{Me}_2\text{NH}_2)_4[\text{Fe}^{2.67}{}_3(\mu\text{-Clan})_3(\text{SO}_4)_2]$	FUHNII	1.245(10)	1.519	2.67−	2	4.7	[92]
$[\text{Co}_2(\text{triphos})_2(\mu\text{-Clan})](\text{BF}_4)_2\cdot 2\text{Acetone}$	RAFKOY	1.316(5)	1.441	3−	0	5.05	[93]
$[\text{Co}_2(\text{triphos})_2(\mu\text{-Clan})]_2(\text{Co}^{\text{II}}\text{Cl}_4)\cdot 1.6\text{Et}_2\text{O}\cdot\text{MeOH}$	FAYMOH	1.312	1.452	3−	0	7.03	[94]
$[\text{Co}^{\text{II}}{}_2(\text{tpa})_2(\mu\text{-Clan})]\text{BF}_4\cdot 2\text{Et}_2\text{O}$	REMRIL	1.293(11)	1.473	3−	0	4.69	[14]
$[\text{Co}^{\text{III}}{}_2(\text{tpa})_2(\mu\text{-Clan})](\text{BF}_4)_3\cdot 4\text{MeCN}$	NIBJUE	1.312(5)	1.457	3−	0	4.36	[15]
$[\text{Fe}^{\text{II}}{}_2(\text{Me}_3\text{tpa})_2(\mu\text{-Clan})](\text{BF}_4)\cdot 0.5\text{Et}_2\text{O}$	LUNJAI	1.293(11)	1.468(6)	3−	0	5.96	[45]
$(\text{Me}_4\text{N})_2[\text{Fe}^{\text{III}}\text{Cl}_2(\mu\text{-Clan})]$	VEXGOX01[s]	1.291(6)	1.466	3−	1	6.53	[64]
$(\text{CoCp}_2)_{1.43}(\text{Me}_2\text{NH}_2)_{1.57}[\text{Fe}^{\text{III}}{}_2(\mu\text{-Clan})_3]\cdot 4.9\text{DMF}$	GEFKAG	1.297	1.431	3−	2	12.22	[95]

[r] Structure at T = 330 K
[s] Structure at T = 100 K

Table A.2(cont.) Average $d_{C–O}$ and diagnostic $d_{C–C}$ values of Clan$^{n–}$ moieties in M–Clan$^{2.67–}$ and M–Clan$^{3–\bullet}$ compounds reported to date.

Compound	CCDC Ref. Code	Average C–O / Å	Average C–C / Å	Clan$^{n–}$ Charge State	Dimen.	R_1	Ref.
(^{n}Pr$_4$N)$_2$[Fe$^{III}_2$(μ-Clan)$_3$]·2Acetone·H$_2$O	SIQPIU[t]	1.297(2); 1.293(3)	1.468(3); 1.472	3−	2	4.44	[84]
(^{n}Pr$_4$N)$_2$[Fe^{II}Fe^{III}(μ-Clan)$_3$]·2Acetone·H$_2$O	SIQPIU01[u]	1.294(3)	1.469	3−	2	5.98	[84]
Na$_3$(Me$_4$N)$_2$[Mn$^{II}_2$(μ-Clan)$_3$]·3.9THF	CIXPAD	1.290	1.408	3−	2	15.3	[82]
(^{n}Pr$_4$N)$_2$[Fe$^{III}_2$(μ-Clan)$_3$]	LUDNUW[v]	1.293(4)	1.476(2)	3−	2	4.13	[86]
(^{n}Pr$_4$N)$_2$[Fe$^{III}_2$(μ-Clan)$_3$]	LUDNUW01[w]	1.286(4)	1.475(3)	3−	2	6.39	[86]

[t] Structure at T = 103 K
[u] Structure at T = 241 K
[v] Structure at T = 103 K
[w] Structure at T = 300 K

Table A.3 Average $d_{C–O}$ and diagnostic $d_{C–C}$ values of Clan$^{n–}$ moieties in *M*–Clan$^{4–}$ compounds reported to date.

Compound	CCDC Ref. Code	Average C–O / Å	Average C–C / Å	Clan$^{n–}$ Charge State	Dimen.	R_1	Ref.
$[Os^{II}_2(CO)_4(PPh_3)_4(\mu\text{-Clan})]$	XALFAS	1.305(4)	1.447	4−	0	4.37	[13]
$[Ga^{III}_2(tren)_2(\mu\text{-Clan})](BPh_4)_2\cdot 2MeOH$	GIDTIX	1.362(14)	1.398	4−	0	4.65	[96]
$[Ga^{III}Cr^{III}(tren)_2(\mu\text{-Clan})](BPh_4)_2\cdot 2MeOH$	GIDTOD	1.360(11)	1.405	4−	0	4.26	[96]
$[Cr^{III}_2(tren)_2(\mu\text{-Clan})](BPh_4)_2\cdot 2MeOH$	GIHHUB	1.357(8)	1.403	4−	0	6.74	[96]

A.4 Tabulations of Bond Lengths in Fe–Clan^{n-} Compounds

Table A.4 Average $d_{Fe–O}$, and $d_{C–O}$ and diagnostic $d_{C–C}$ values of Clan^{n-} moieties of Fe–Clan^{n-} compounds reported to date.

Compound	CCDC Ref. Code	Average $d_{Fe–O}$ / Å	Average $d_{C–O}$ / Å	Average $d_{C–C}$ / Å	Clan^{n-} Charge State	Dimen.	R_1	Ref.
$[Fe^{III}_2(H_2O)_4(Clan)_2(\mu\text{-Clan})]\cdot 4H_2O$	QOCHEV	2.012(29)	1.260(6); 1.257(33)[x]	1.530; 1.530(2)x	2−	0	4.54	[8]
$[Fe^{II}_2(tpa)_2(\mu\text{-Clan})](BF_4)_2\cdot 2MeOH$	NIBKEP	2.138(75)	1.261(10)	1.528	2−	0	4.64	[15]
$[Fe^{II}_2(tpa)_2(\mu\text{-Clan})](BF_4)_2\cdot 2MeOH$	NIBKEP01	2.136(75)	1.258(8)	1.536	2−	0	7.81	[16]
$[Fe^{II}_2(Me_3tpa)_2(\mu\text{-Clan})](BF_4)_2\cdot 0.7H_2O$	LUNHIO	2.119(69)	1.254(16)	1.532	2−	0	9.18	[45]
$[Fe^{II}_2(Me_3tpa)_2(\mu\text{-Clan})](BF_4)\cdot 0.5Et_2O$	LUNJAI	2.060(70)	1.293(11)	1.468(6)	3−	0	5.96	[45]
$[Fe^{II}(H_2O)_2(\mu\text{-Clan})]\cdot H_2O$	KIQJID	2.138(15)	1.257(1)	1.523	2−	1	4.5	[51]
$[Fe^{II}(H_2O)_2(\mu\text{-Clan})]\cdot H_2O$	KIQJID01	2.140(18)	1.259	1.53	2−	1	3.15	[8]
$[Fe^{II}(H_2O)_2(\mu\text{-Clan})]\cdot phz$	KIQKAW	2.141(8)	1.262(13)	1.522	2−	1	2.3	[51]
$(Me_4N)_2[Fe^{II}Cl_2(\mu\text{-Clan})]$	VEXGOX[y]	2.140(44)	1.256(11)	1.523	2−	1	7.27	[64]
$(Me_4N)_2[Fe^{III}Cl_2(\mu\text{-Clan})]$	VEXGOX01[z]	2.027(26)	1.291(6)	1.466	3−	1	6.53	[64]

[x] Terminal mono-coordinating

[y] Structure at T = 250 K

[z] Structure at T = 100 K

Table A.4(cont.) Average $d_{Fe–O}$, and $d_{C–O}$ and diagnostic $d_{C–C}$ values of Clan$^{n–}$ moieties of Fe–Clan$^{n–}$ compounds reported to date.

Compound	CCDC Ref. Code	Average $d_{Fe–O}$ / Å	Average $d_{C–O}$ / Å	Average $d_{C–C}$ / Å	Clan$^{n–}$ Charge State	Dimen.	R_1	Ref.
$(EtPh_3P)_2[KFe^{III}(\mu\text{-Clan})_3]\cdot 2DMF$	QUJJOW	2.054(25)	1.255(23); 1.263(25); 1.257(21)	1.544(19); 1.553(12); 1.540(9)	2−	2	5.79	[77]
$(H_3O)(phz)_3[Fe^{II}Fe^{III}(\mu\text{-Clan})_3]\cdot 13H_2O$	QEFPOJ	2.063(2)	1.268	1.529	2−	2	3.81	[78]
$(^nPr_4N)_2[Fe^{III}_2(\mu\text{-Clan})_3]\cdot 2Acetone\cdot H_2O$	SIQPIU[aa]	2.029(42); 2.020(40)	1.259(3) 1.297(2); 1.293(3)	1.536(2) 1.468(3); 1.472	2− 3−	2	4.44	[84]
$(^nPr_4N)_2[Fe^{II}Fe^{III}(\mu\text{-Clan})_3]\cdot 2Acetone\cdot H_2O$	SIQPIU01[bb]	2.091(11); 2.024(35)	1.258(2); 1.266(2) 1.294(3)	1.530(2); 1.518(5) 1.469	2− 3−	2	5.98	[84]
$(MeEt_3N)[Na(dmf)][NaFe^{III}(\mu\text{-Clan})_3]$	QUJKOX	2.011(15)	1.258(23); 1.258(26); 1.258(25)	1.534(18); 1.535(19); 1.539(20)	2−	3	4.13	[77]

[aa] Structure at T = 103 K
[bb] Structure at T = 241 K

Table A.4(cont.) Average $d_{Fe–O}$, and $d_{C–O}$ and diagnostic $d_{C–C}$ values of Clan$^{n–}$ moieties of Fe–Clan$^{n–}$ compounds reported to date.

Compound	CCDC Ref. Code	Average $d_{Fe–O}$ / Å	Average $d_{C–O}$ / Å	Average $d_{C–C}$ / Å	Clan$^{n–}$ Charge State	Dimen.	R_1	Ref.
(^{n}Pr$_4$N)$_2$[Fe$^{III}_2$(μ-Clan)$_3$]	LUDNUW[cc]	2.019(45)	1.257(5) 1.293(4)	1.534 1.476(2)	2− 3−	2	4.13	[86]
(^{n}Pr$_4$N)$_2$[Fe$^{III}_2$(μ-Clan)$_3$]	LUDNUW01[dd]	2.027(43)	1.260(2) 1.286(4)	1.536 1.475(3)	2− 3−	2	6.39	[86]
(^{n}Pr$_4$N)$_2$[Fe$^{2.5}_2$(μ-Clan)$_3$]	LUDNUW02[ee]	2.058(22)	1.254(10) 1.271(5)	1.541 1.504(10)	2− 2.5−	2	6.99	[86]
(^{n}Pr$_4$N)$_2$[Fe$^{II}_2$(μ-Clan)$_3$]	LUDNUW03[ff]	2.096(9)	1.258(19); 1.252(2)	1.539; 1.535(6)	2−	2	7.43	[86]
(Me$_2$NH$_2$)$_2$[Fe$^{III}_2$(μ-Clan)$_3$]·6DMF·2H$_2$O	ZACDAL	2.020(3)	1.280	1.48	2.67−	2	9.54	[91]
(Et$_4$N)$_2$[Fe$^{III}_2$(μ-Clan)$_3$]·20H$_2$O	XARDIG	2.019	1.284	1.491	2.67−	2	5.31	[80]
(Me$_2$NH$_2$)$_4$[Fe$^{2.67}_3$(μ-Clan)$_3$(SO$_4$)$_2$][gg]	FUHNII	2.031(21)	1.245(10)	1.519	2.67−	2	4.7	[92]

[cc] Structure at T = 103 K
[dd] Structure at T = 300 K
[ee] Structure at T = 330 K
[ff] Structure at T = 380 K
[gg] Fe valence state estimated from ^{57}Fe Mössbauer spectroscopy

Table A.4(cont.) Average $d_{Fe–O}$, and $d_{C–O}$ and diagnostic $d_{C–C}$ values of Clan$^{n–}$ moieties of Fe–Clan$^{n–}$ compounds reported to date.

Compound	CCDC Ref. Code	Average $d_{Fe–O}$ / Å	Average $d_{C–O}$ / Å	Average $d_{C–C}$ / Å	Clan$^{n–}$ Charge State	Dimen.	R_1	Ref.
$(CoCp_2)_{1.43}(Me_2NH_2)_{1.57}[Fe^{III}_2(\mu\text{-Clan})_3]\cdot$ 4.9DMF	GEFKAG	2.028(5)	1.297	1.431	3−	2	12.22	[95]

A.5 Ligand Abbreviations

Table A.5 Ligand abbreviations used in Table A.1 through Table A.4.

Abbreviation	Ligand
$(Meim)_2$-prop	3,3-bis(1-methylimidazol-2-yl)propionate
$(SMeBim)_3$-Mes	1,3,5-tri(2-methylthiobenzimidazol-1-ylmethyl)-2,4,6-trimethylbenzene
2,2′-bpy	2,2′-bipyridine
2,2′-bpym	2,2′-bipyrimidine
3-pbdy	1,4-bis(3-pyridyl)butadiyne
4,4′-bpday	1,4-bis(4-pyridyl)but-1,3-diyne
4,4′-bpe	(E)-1,2-bis(4-pyridyl)ethene
4,4′-bpy	4,4′-bipyridine
4,4′-bpyOHama	4,4′-bypyridine-2-hydroxamic acid
4-pbdy	1,4-bis(4-pyridyl)butadiyne
4-ppy	4-phenylpyridine
$acac_2$-trien:	4,15-dimethyl-5,8,11,14-tetraazaoctadeca-2,4,14,16-tetraene-2,17-diol
bix	1,4-bis(imidazol-1-ylmethyl)benzene
BPNim	bis(4-(naphtho[2,3-d]imidazol-1-ylmethyl)phenyl)methane
$BPOPh_2$-7-TH	1,1'-(7,8-dipropyldithieno[3,2-*e*:3',2'-*e*']benzo[1,2-*b*:4,3-*b*'] bis[1]benzothiophene-2,13-diyl)bis[1,1-diphenylphosphine oxide]
bpyeyan	1,5-bis[2-(4-pyridyl)ethynyl]anthracene
Br-ppy	4-(4-bromophenyl)pyridine
BXyTBim	1,1'-[1,4-phenylenebis(methylene)]bis[2-(2-thienyl)-1*H*-benzimidazole]
C_6Me_6	hexamethylbenzene
Clan	3,6-dichloro-2,5-dihydroxy-1,4-benzoquinone (chloranilate)
cod	1,4-cyclooctadiene
Cp^*	pentamethylcyclopentadienyl
Cy	cymeme

Table A.5(cont.) Ligand abbreviations used in **Table A.1** through **Table A.4**.

Abbreviation	Ligand
dapz	2,3-diaminopyrazine
dcmb	3,3′-dicarboxymethyl-2,2′-bipyridine
dhqox	2,3-dihydroxy-quinoxaline
dmac	*N*,*N*-dimethylacetamide
dmf	*N*,*N*-dimethylformamide
dppOb	1,1'-(1,4-butanediyl)bis[1,1-diphenylphosphine oxide]
fm	formamide
$HBpz_3$	hydrotris(1-pyrazolyl)borate
L_{Py}	19,39-dimethyl-3,15,23,35-tetrakis(2-pyridinylmethyl)-6,9,12,26,29,32-hexaoxa-3,15,23,35-tetraazatricyclo[35.3.1.$1^{17,21}$]dotetraconta-1(41),17,19,21(42),37,39-hexaene-41,42-diol
Me_3tacn	1,4,7-trimethyl-1,4,7-triazacyclononane
Me_3tpa	tris(6-methyl-2-pyridylmethyl)amine
ohphz	octahydrophenazine
pap	2-(phenylazo)pyridine
pdt	pyrazine-2,3-dithiolate
phz	phenazine
pmdeta	*N*,*N*,*N*′,*N*″,*N*″-pentamethyldiethylenetriamine
$POPh_3$	triphenylphosphine oxide
PPh_3	triphenylphosphine
py	pyridine
pym	pyrimidine
pyz	pyrazine
sal_2-trien:	bis(salicylidene)-*N*,*N*‴-triethylenetetramine
$^tBuacac_2$-py	3,5-bis(4,4-dimethyl-1,3-pentadione)pyridine
tdmpmb	1,2,4,5-tetrakis(dimethoxyphosphorylmethyl)benzene
tpa	tris(2-pyridylmethyl)amine

Table A.5(cont.) Ligand abbreviations used in **Table A.1** through **Table A.4**.

Abbreviation	Ligand
tpy	2,2':6',2"-terpyridine
tren	tris(2-aminoethyl)amine
tren(imid)	tris{[2-{(imidazole-4-yl) methylidene}amino]ethyl}amine
trisphos	1,1,1-tris(diphenylphosphinomethyl)ethane
TXyBim	1,2,4,5-tetrakis(5,6-dimethylbenzimidazol-1-ylmethyl)benzene

A.6 References

[1] C. G. Pierpont, L. C. Francesconi, D. N. Hendrickson, *Inorg. Chem.* **1977**, *16*, 2367-2376.

[2] J. V. Folgado, R. Ibanez, E. Coronado, D. Beltran, J. M. Savariault, J. Galy, *Inorg. Chem.* **1988**, *27*, 19-26.

[3] M. A. Calvo, A. M. Manotti Lanfredi, L. A. Oro, M. T. Pinillos, C. Tejel, A. Tiripicchio, F. Ugozzoli, *Inorg. Chem.* **1993**, *32*, 1147-1152.

[4] C. Fujii, M. Mitsumi, M. Kodera, K.-I. Motoda, M. Ohba, N. Matsumoto, H. Okawa, *Polyhedron* **1994**, *13*, 933-938.

[5] A. Elduque, Y. Garcés, L. A. Oro, M. T. Pinillos, A. Tiripicchio, F. Ugozzoli, *J. Chem. Soc., Dalton Trans.* **1996**, 2155-2158.

[6] D. F. Xiang, C. Y. Duan, X. S. Tan, Y. J. Liu, W. X. Tang, *Polyhedron* **1998**, *17*, 2647-2653.

[7] S. Gallert, T. Weyhermüller, K. Wieghardt, P. Chaudhuri, *Inorg. Chim. Acta* **1998**, *274*, 111-114.

[8] B. F. Abrahams, K. D. Lu, B. Moubaraki, K. S. Murray, R. Robson, *J. Chem. Soc., Dalton Trans.* **2000**, 1793-1797.

[9] B. F. Abrahams, J. Coleiro, K. Ha, B. F. Hoskins, S. D. Orchard, R. Robson, *J. Chem. Soc., Dalton Trans.* **2002**, 1586-1594.

[10] A. Yoshino, H. Matsudaira, E. Asato, M. Koikawa, T. Shiga, M. Ohba, H. Okawa, *Chem. Commun.* **2002**, 1258-1259.

[11] M. Abdus Subhan, R. Kawahata, H. Nakata, A. Fuyuhiro, T. Tsukuda, S. Kaizaki, *Inorg. Chim. Acta* **2004**, *357*, 3139-3146.

[12] M. Kawahara, M. K. Kabir, K. Yamada, K. Adachi, H. Kumagai, Y. Narumi, K. Kindo, S. Kitagawa, S. Kawata, *Inorg. Chem.* **2004**, *43*, 92-100.

[13] P. Gupta, A. Das, F. Basuli, A. Castineiras, W. S. Sheldrick, H. Mayer-Figge, S. Bhattacharya, *Inorg. Chem.* **2005**, *44*, 2081-2088.

[14] K. S. Min, A. L. Rheingold, A. DiPasquale, J. S. Miller, *Inorg. Chem.* **2006**, *45*, 6135-6137.

[15] K. S. Min, A. G. DiPasquale, J. A. Golen, A. L. Rheingold, J. S. Miller, *J. Am. Chem. Soc.* **2007**, *129*, 2360-2368.

[16] A. L. Rheingold, J. S. Miller, *CSD Communication* **2019**.

[17] Y.-F. Han, Y.-J. Lin, W.-G. Jia, G.-X. Jin, *Organometallics* **2008**, *27*, 4088-4097.

[18] R.-T. Liao, W.-C. Yang, P. Thanasekaran, C.-C. Tsai, M. Sathiyendiran, Y.-H. Liu, T. Rajendran, H.-M. Lin, T.-W. Tseng, K.-L. Lu, *Chem. Commun.* **2008**, 3175-3177.

[19] P. C. A. Bruijnincx, M. Viciano-Chumillas, M. Lutz, A. L. Spek, J. Reedijk, G. van Koten, R. J. M. Klein Gebbink, *Chem. Eur. J.* **2008**, *14*, 5567-5576.

[20] Y.-F. Han, W.-G. Jia, Y.-J. Lin, G.-X. Jin, *Organometallics* **2008**, *27*, 5002-5008.

[21] B. Therrien, *Eur. J. Inorg. Chem.* **2009**, 2445-2453.

[22] P. B. Chatterjee, K. Bhattacharya, N. Kundu, K.-Y. Choi, R. Clérac, M. Chaudhury, *Inorg. Chem.* **2009**, *48*, 804-806.

[23] C.-H. Chuang, M. Sathiyendiran, Y.-H. Tseng, J.-Y. Wu, K.-C. Hsu, C.-H. Hung, Y.-S. Wen, K.-L. Lu, *Organometallics* **2010**, *29*, 283-285.

[24] D. Schweinfurth, M. M. Khusniyarov, D. Bubrin, S. Hohloch, C.-Y. Su, B. Sarkar, *Inorg. Chem.* **2013**, *52*, 10332-10339.

[25] B. Shankar, P. Elumalai, R. Shanmugam, V. Singh, D. T. Masram, M. Sathiyendiran, *Inorg. Chem.* **2013**, *52*, 10217-10219.

[26] P. Rajakannu, P. Elumalai, F. Hussain, M. Sathiyendiran, *J. Organomet. Chem.* **2013**, *725*, 1-4.

[27] P. Rajakannu, S. M. Mobin, M. Sathiyendiran, *J. Organomet. Chem.* **2014**, *771*, 68-77.

[28] J.-J. Liu, Y.-J. Lin, G.-X. Jin, *Dalton Trans.* **2015**, *44*, 10281-10288.

[29] M. Jurić, K. Molčanov, D. Žilić, B. Kojić-Prodić, *RSC Adv.* **2016**, *6*, 62785-62796.

[30] W.-Y. Zhang, Y.-J. Lin, Y.-F. Han, G.-X. Jin, *J. Am. Chem. Soc.* **2016**, *138*, 10700-10707.

[31] Y. Lu, Y.-X. Deng, Y.-J. Lin, Y.-F. Han, L.-H. Weng, Z.-H. Li, G.-X. Jin, *Chem* **2017**, *3*, 110-121.

[32] Y.-Y. Zhang, W.-X. Gao, Y.-J. Lin, L.-W. Mi, G.-X. Jin, *Chem. Eur. J.* **2017**, *23*, 11133-11140.

[33] L. Androš Dubraja, K. Molčanov, D. Žilić, B. Kojić-Prodić, E. Wenger, *New J. Chem.* **2017**, *41*, 6785-6794.

[34] M. A. Dunstan, E. Rousset, M.-E. Boulon, R. W. Gable, L. Sorace, C. Boskovic, *Dalton Trans.* **2017**, *46*, 13756-13767.

[35] P. Zhang, M. Perfetti, M. Kern, P. P. Hallmen, L. Ungur, S. Lenz, M. R. Ringenberg, W. Frey, H. Stoll, G. Rauhut, J. van Slageren, *Chem. Sci.* **2018**, *9*, 1221-1230.

[36] R. Ishikawa, S. Michiwaki, T. Noda, K. Katoh, M. Yamashita, K. Matsubara, S. Kawata, *Inorganics* **2018**, *6*, 7.

[37] R. Arumugam, B. Shankar, R. Shanmugam, T. Arumuganathan, M. Sathiyendiran, *Dalton Trans.* **2018**, *47*, 13894-13901.

[38] A. chemarumugam, *CSD Communication* **2018**.

[39] L.-L. Dang, Y.-J. Lin, G.-X. Jin, *Dalton Trans.* **2018**, *47*, 6378-6385.

[40] M. Bhol, B. Shankar, M. Sathiyendiran, *Dalton Trans.* **2018**, *47*, 4494-4500.

[41] Q.-J. Fan, Y.-J. Lin, F. E. Hahn, G.-X. Jin, *Dalton Trans.* **2018**, *47*, 2240-2246.

[42] Y.-X. Deng, H.-N. Zhang, Y.-J. Lin, G.-X. Jin, *J. Coord. Chem.* **2018**, *71*, 1959-1970.

[43] E. Q. Procopio, D. Dova, S. Cauteruccio, A. Forni, E. Licandro, M. Panigati, *ACS Omega* **2018**, *3*, 11649-11654.

[44] W.-L. Shan, Y.-J. Lin, F. E. Hahn, G.-X. Jin, *Angew. Chem. Int. Ed.* **2019**, *58*, 5882-5886.

[45] A. E. Thorarinsdottir, R. Bjornsson, T. D. Harris, *Inorg. Chem.* **2020**, *59*, 4634-4649.

[46] S. Cueto, H.-P. Straumann, P. Rys, W. Petter, V. Gramlich, F. S. Rys, *Acta Crystallogr. C* **1992**, *48*, 458-460.

[47] S. Kawata, S. Kitagawa, M. Kondo, I. Furuchi, M. Munakata, *Angew. Chem. Int. Ed. Engl.* **1994**, *33*, 1759-1761.

[48] S. Decurtins, H. W. Schmalle, L.-M. Zheng, J. Ensling, *Inorg. Chim. Acta* **1996**, *244*, 165-170.

[49] L.-M. Zheng, H. W. Schmalle, R. Huber, S. Decurtins, *Polyhedron* **1996**, *15*, 4399-4405.

[50] S. Kawata, S. Kitagawa, H. Kumagai, C. Kudo, H. Kamesaki, T. Ishiyama, R. Suzuki, M. Kondo, M. Katada, *Inorg. Chem.* **1996**, *35*, 4449-4461.

[51] S. Kawata, S. Kitagawa, H. Kumagai, T. Ishiyama, K. Honda, H. Tobita, K. Adachi, M. Katada, *Chem. Mater.* **1998**, *10*, 3902-3912.

[52] V. Vuković, K. Molčanov, C. Jelsch, E. Wenger, A. Krawczuk, M. Jurić, L. Androš Dubraja, B. Kojić-Prodić, *Cryst. Growth Des.* **2019**, *19*, 2802-2810.

[53] M. K. Kabir, M. Kawahara, H. Kumagai, K. Adachi, S. Kawata, T. Ishii, S. Kitagawa, *Polyhedron* **2001**, *20*, 1417-1422.

[54] A. Michaelides, C. D. Papadimitriou, J. C. Plakatouras, S. Skoulika, P. G. Veltsistas, *Polyhedron* **2004**, *23*, 2587-2593.

[55] V. Barba, J. Zaragoza, H. Höpfl, N. Farfán, H. I. Beltrán, L. S. Zamudio-Rivera, *J. Organomet. Chem.* **2011**, *696*, 1949-1956.

[56] G. Zucchi, P. Thuery, M. Ephritikhine, *CSD Communication* **2012**.

[57] Y. Nishimura, A. Himegi, A. Fuyuhiro, S. Hayami, S. Kawata, *Acta Crystallogr. E* **2013**, *69*, m119-m120.

[58] A. Abhervé, M. Clemente-León, E. Coronado, C. J. Gómez-García, M. Verneret, *Inorg. Chem.* **2014**, *53*, 12014-12026.

[59] S. Tanaka, A. Himegi, T. Ohishi, A. Fuyuhiro, S. Kawata, *Acta Crystallogr. E* **2014**, *70*, m90-m91.

[60] C. J. Kingsbury, B. F. Abrahams, R. Robson, *CSD Communication* **2017**.

[61] C. J. Kingsbury, K. F. White, B. F. Abrahams, R. Robson, *CSD Communication* **2017**.

[62] C. J. Kingsbury, B. F. Abrahams, R. Robson, *CSD Communication* **2017**.

[63] A. N. Simonson, C. M. Kareis, N. S. Ovanesyan, D. O. Baumann, A. L. Rheingold, A. M. Arif, J. S. Miller, *Polyhedron* **2018**, *139*, 215-221.

[64] J. A. DeGayner, K. Wang, T. D. Harris, *J. Am. Chem. Soc.* **2018**, *140*, 6550-6553.

[65] P. E. Riley, S. F. Haddad, K. N. Raymond, *Inorg. Chem.* **1983**, *22*, 3090-3096.

[66] C. Robl, A. Weiss, *Mater. Res. Bull.* **1987**, *22*, 497-504.

[67] C. Robl, *Mater. Res. Bull.* **1987**, *22*, 1483-1491.

[68] H. Kumagai, S. Kawata, S. Kitagawa, *Inorg. Chim. Acta* **2002**, *337*, 387-392.

[69] T.-T. Luo, Y.-H. Liu, H.-L. Tsai, C.-C. Su, C.-H. Ueng, K.-L. Lu, *Eur. J. Inorg. Chem.* **2004**, *2004*, 4253-4258.

[70] B. F. Abrahams, M. J. Grannas, T. A. Hudson, S. A. Hughes, N. H. Pranoto, R. Robson, *Dalton Trans.* **2011**, *40*, 12242-12247.

[71] G. V. Shilov, Z. K. Nikitina, N. S. Ovanesyan, S. M. Aldoshin, V. D. Makhaev, *Russ. Chem. Bull.* **2011**, *60*, 1209-1219.

[72] G. Zucchi, P. Thuery, M. Ephritikhine, *CSD Communication* **2012**.

[73] G. Zucchi, P. Thuery, M. Ephritikhine, *CSD Communication* **2012**.

[74] G. Zucchi, P. Thuery, M. Ephritikhine, *CSD Communication* **2012**.

[75] M. Atzori, S. Benmansour, G. Mínguez Espallargas, M. Clemente-León, A. Abhervé, P. Gómez-Claramunt, E. Coronado, F. Artizzu, E. Sessini, P. Deplano, A. Serpe, M. L. Mercuri, C. J. Gómez García, *Inorg. Chem.* **2013**, *52*, 10031-10040.

[76] A. Abhervé, S. Mañas-Valero, M. Clemente-León, E. Coronado, *Chem. Sci.* **2015**, *6*, 4665-4673.

[77] S. Benmansour, C. Vallés-García, P. Gómez-Claramunt, G. Mínguez Espallargas, C. J. Gómez-García, *Inorg. Chem.* **2015**, *54*, 5410-5418.

[78] S. Benmansour, A. Abhervé, P. Gómez-Claramunt, C. Vallés-García, C. J. Gómez-García, *ACS Appl. Mater. Interfaces* **2017**, *9*, 26210-26218.

[79] M. Palacios-Corella, A. Fernández-Espejo, M. Bazaga-García, E. R. Losilla, A. Cabeza, M. Clemente-León, E. Coronado, *Inorg. Chem.* **2017**, *56*, 13865-13877.

[80] C. J. Kingsbury, B. F. Abrahams, D. M. D'Alessandro, T. A. Hudson, R. Murase, R. Robson, K. F. White, *Cryst. Growth Des.* **2017**, *17*, 1465-1470.

[81] S. Benmansour, I. Pérez-Herráez, C. Cerezo-Navarrete, G. López-Martínez, C. Martínez Hernández, C. J. Gómez-García, *Dalton Trans.* **2018**, *47*, 6729-6741.

[82] L. Liu, J. A. DeGayner, L. Sun, D. Z. Zee, T. D. Harris, *Chem. Sci.* **2019**, *10*, 4652-4661.

[83] L. Liu, L. Li, J. A. DeGayner, P. H. Winegar, Y. Fang, T. D. Harris, *J. Am. Chem. Soc.* **2018**, *140*, 11444-11453.

[84] J. Chen, Y. Sekine, Y. Komatsumaru, S. Hayami, H. Miyasaka, *Angew. Chem. Int. Ed.* **2018**, *57*, 12043-12047.

[85] C. J. Kingsbury, B. F. Abrahams, J. E. Auckett, H. Chevreau, A. D. Dharma, S. Duyker, Q. He, C. Hua, T. A. Hudson, K. S. Murray, W. Phonsri, V. K. Peterson, R. Robson, K. F. White, *Chem. Eur. J.* **2019**, *25*, 5222-5234.

[86] J. Chen, Y. Sekine, A. Okazawa, H. Sato, W. Kosaka, H. Miyasaka, *Chem. Sci.* **2020**, *11*, 3610-3618.

[87] W. Frenzer, R. Wartchow, H. Bode, *Z. Kristallogr. Cryst. Mater.* **1997**, *212*, 237.

[88] B. F. Abrahams, T. A. Hudson, L. J. McCormick, R. Robson, *Cryst. Growth Des.* **2011**, *11*, 2717-2720.

[89] C. J. Kingsbury, B. F. Abrahams, R. Robson, *CSD Communication* **2017**.

[90] C. J. Kingsbury, B. F. Abrahams, R. Robson, *CSD Communication* **2017**.

[91] I.-R. Jeon, B. Negru, R. P. Van Duyne, T. D. Harris, *J. Am. Chem. Soc.* **2015**, *137*, 15699-15702.

[92] M. E. Ziebel, C. A. Gaggioli, A. B. Turkiewicz, W. Ryu, L. Gagliardi, J. R. Long, *J. Am. Chem. Soc.* **2020**, *142*, 2653-2664.

[93] K. Heinze, G. Huttner, L. Zsolnai, A. Jacobi, P. Schober, *Chem. Eur. J.* **1997**, *3*, 732-743.

[94] K. Heinze, G. Huttner, O. Walter, *Eur. J. Inorg. Chem.* **1999**, *1999*, 593-600.

[95] J. A. DeGayner, I.-R. Jeon, L. Sun, M. Dincă, T. D. Harris, *J. Am. Chem. Soc.* **2017**, *139*, 4175-4184.

[96] D. Guo, J. K. McCusker, *Inorg. Chem.* **2007**, *46*, 3257-3274.

This page intentionally left blank

Appendix B Electrical Conductivity Data

B.1 Cell Dimensions and Transport Properties B3

B.2 Variable-Temperature Transport Properties B5

This page intentionally left blank

B.1 Cell Dimensions and Transport Properties

Table B.1 Pellet thickness and measured transport properties of four independent two-point pressed pellet devices of **3.1^{Cl}b**.

	Pellet Thickness / cm	Resistance @ Ambient T^a / Ω	Conductivity @ Ambient T^a / S cm^{-1}	Resistance @ 300 K^b / Ω	Conductivity @ 300 K^b / S cm^{-1}	Activation Energy (E_a) / eV
Device 1	0.112(2)	2801.7(7)	$5.6(2) \times 10^{-4}$	3761.8(3)	$4.2(1) \times 10^{-4}$	0.253(2)
Device 2	0.052(1)	1599(2)	$4.6(1) \times 10^{-4}$	2095.6(3)	$3.5(1) \times 10^{-4}$	0.250(2)
Device 3	0.066(2)	1345.4(3)	$6.9(3) \times 10^{-4}$	1717.9(2)	$5.4(2) \times 10^{-4}$	0.249(2)
Device 4	0.066(1)	1753.6(3)	$5.3(2) \times 10^{-4}$	2133.4(1)	$4.8(1) \times 10^{-4}$	0.253(3)

Table B.2 Pellet thickness and measured transport properties of four independent two-point pressed pellet devices of *aP* **4.1a**.

	Pellet Thickness / cm	Resistance @ Ambient T^a / Ω	Conductivity @ Ambient T^a / S cm^{-1}	Resistance @ 300 K^b / Ω	Conductivity @ 300 K^b / S cm^{-1}	Activation Energy (E_a) / eV
Device 1	0.033(1)	525.8(2)	$8.9(3) \times 10^{-4}$	836.6(1)	$5.6(2) \times 10^{-4}$	0.229(2)
Device 2	0.050(1)	480.4(1)	$1.5(1) \times 10^{-4}$	961.2(1)	$7.4(2) \times 10^{-4}$	0.219(2)
Device 3	0.027(1)	237.0(1)	$1.6(1) \times 10^{-3}$	512.0(1)	$7.5(4) \times 10^{-4}$	0.235(2)
Device 4	0.047(1)	460.5(1)	$1.3(1) \times 10^{-3}$	877.5(1)	$7.6(3) \times 10^{-4}$	0.218(2)

[a]: Measured in a two-point screw cell in N_2-filled glovebox at ambient *T* ca. 305 K.

[b]: Measured in a two-point screw cell contained in a home-built thermostatted N_2-purged sample chamber.

Table B.3 Pellet thickness and measured transport properties of four independent two-point pressed pellet devices of **4.1b**.

	Pellet Thickness / cm	**Resistance @ Ambient T^a / Ω**	**Conductivity @ Ambient T^a / S cm^{-1}**	**Resistance @ 300 K^b / Ω**	**Conductivity @ 300 K^b / S cm^{-1}**	**Activation Energy (E_a) / eV**
Device 1	0.038(1)	30731(30)	$1.8(1) \times 10^{-5}$	32891(1)	$1.5(1) \times 10^{-5}$	0.414(6)
Device 2	0.027(1)	14060(6)	$2.7(2) \times 10^{-5}$	16429(1)	$2.3(1) \times 10^{-5}$	0.376(6)
Device 3	0.037(1)	32151(32)	$1.6(1) \times 10^{-5}$	35470(1)	$1.5(1) \times 10^{-5}$	0.398(6)
Device 4	0.027(1)	21291(15)	$1.7(1) \times 10^{-5}$	25033(1)	$1.5(1) \times 10^{-5}$	0.385(8)

Table B.4 Pellet thickness and measured transport properties of four independent two-point pressed pellet devices of **5.2**.

	Pellet Thickness / cm	**Resistance @ Ambient T^a / Ω**	**Conductivity @ Ambient T^a / S cm^{-1}**	**Resistance @ 295 K^b / Ω**	**Conductivity @ 295 K^b / S cm^{-1}**	**Activation Energy (E_a) / eV**
Device 1	0.052(1)	160.1(1)	$4.6(2) \times 10^{-3}$	276.2(1)	$2.7(1) \times 10^{-3}$	0.190(1)
Device 2	0.048(1)	139.2(1)	$4.9(2) \times 10^{-3}$	295.4(1)	$2.3(1) \times 10^{-3}$	0.195(1)
Device 3	0.045(1)	110.9(1)	$5.8(2) \times 10^{-3}$	188.4(1)	$3.4(1) \times 10^{-3}$	0.193(1)
Device 4	0.049(1)	143.2(1)	$4.8(2) \times 10^{-3}$	254.4(1)	$2.7(1) \times 10^{-3}$	0.186(1)

[a]: Measured in a two-point screw cell in N_2-filled glovebox at ambient T ca. 305 K.

[b]: Measured in a two-point screw cell contained in a home-built thermostatted N_2-purged sample chamber.

B.2 Variable-Temperature Transport Properties

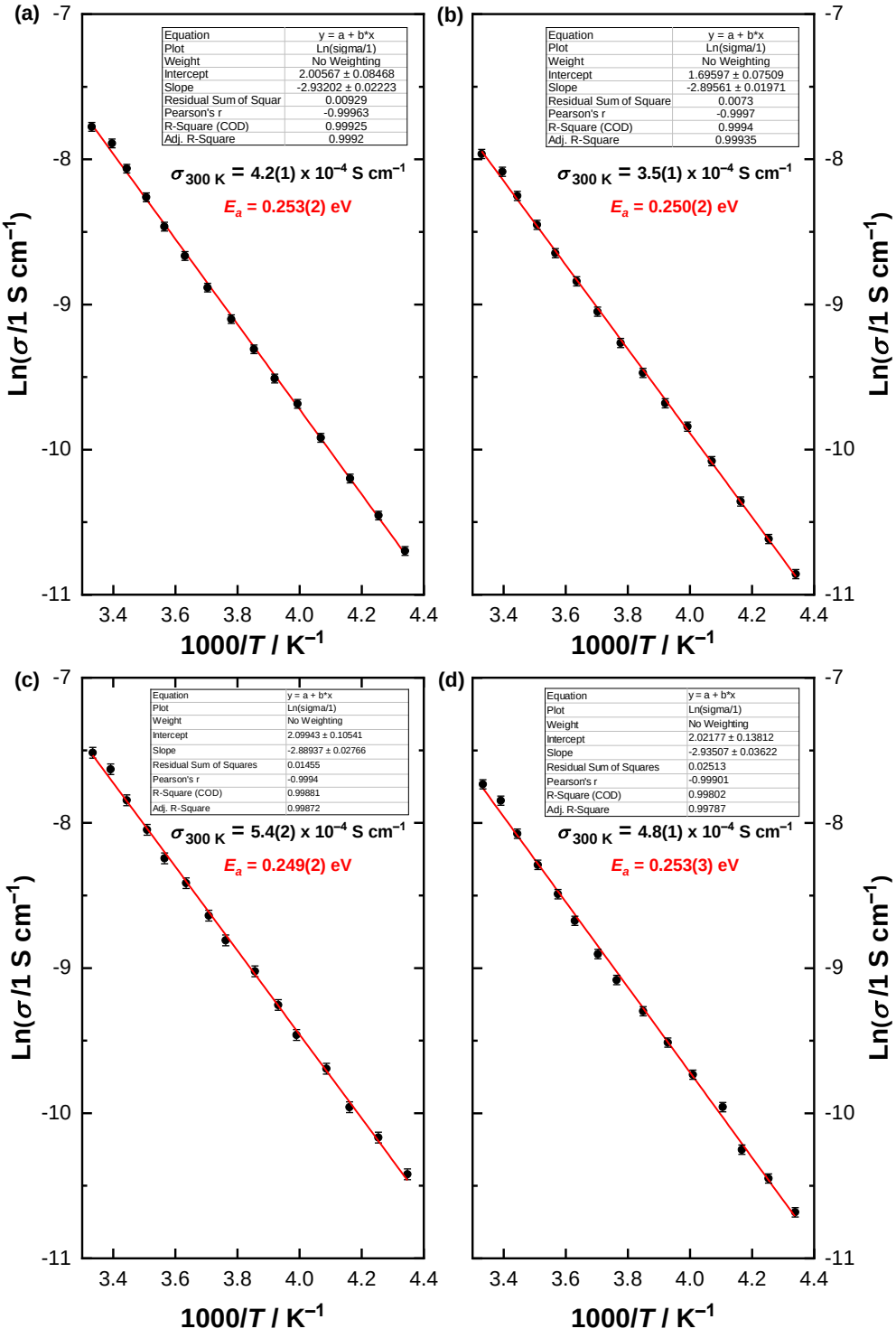


Figure B.1 (a–d) Arrhenius fits of the variable-temperature electrical conductivity for **3.1^{Cl}b** in four independent pressed pellet devices. Experimental data in black circles, lines of best fit in red. Error bars are ± s.u. Where not visible, error bars lie within the data points.

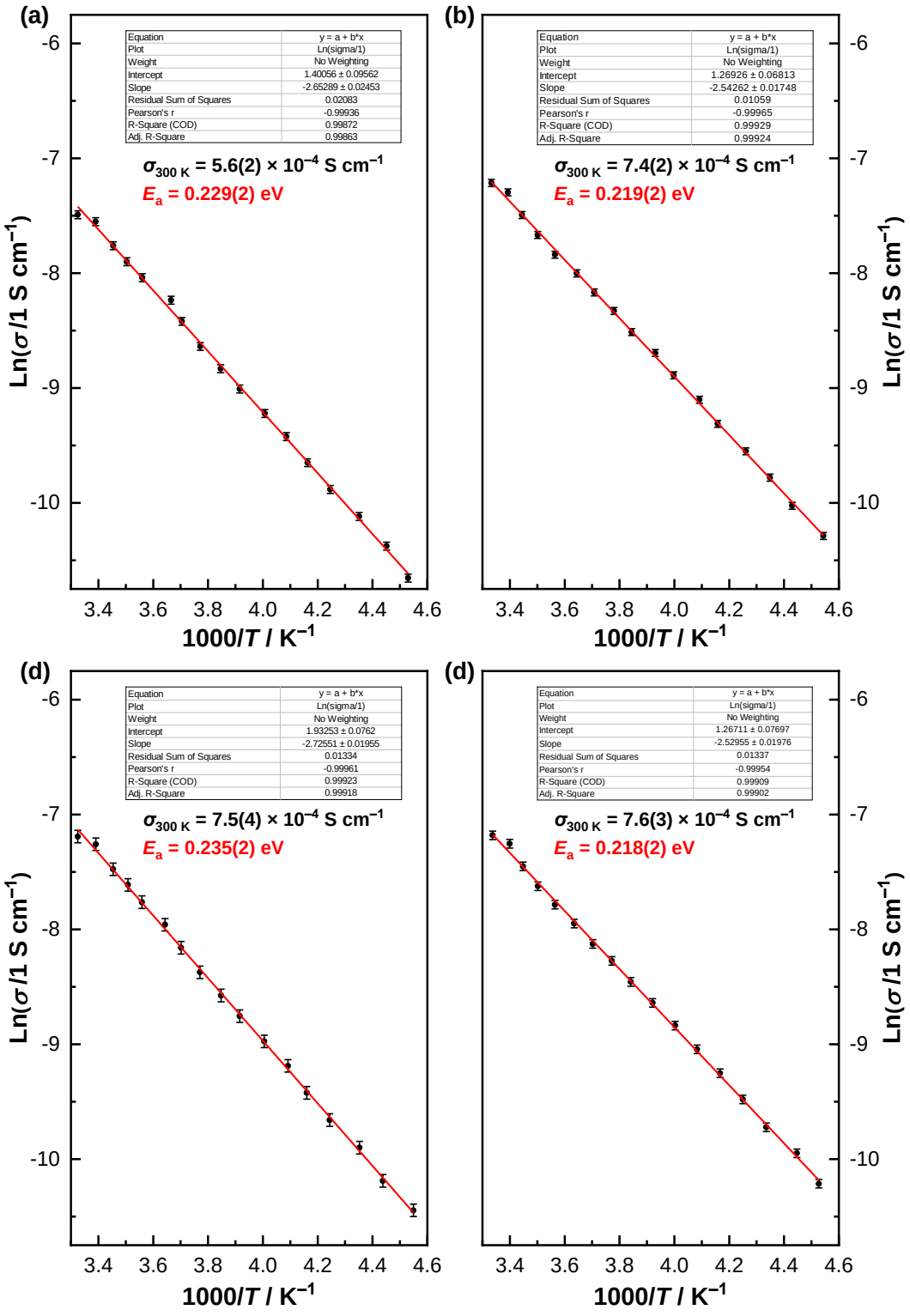


Figure B.2 (a–d) Arrhenius fits of the variable-temperature electrical conductivity for *aP* **4.1a** in four independent pressed pellet devices. Experimental data in black circles, lines of best fit in red. Error bars are ± s.u. Where not visible, error bars lie within the data points.

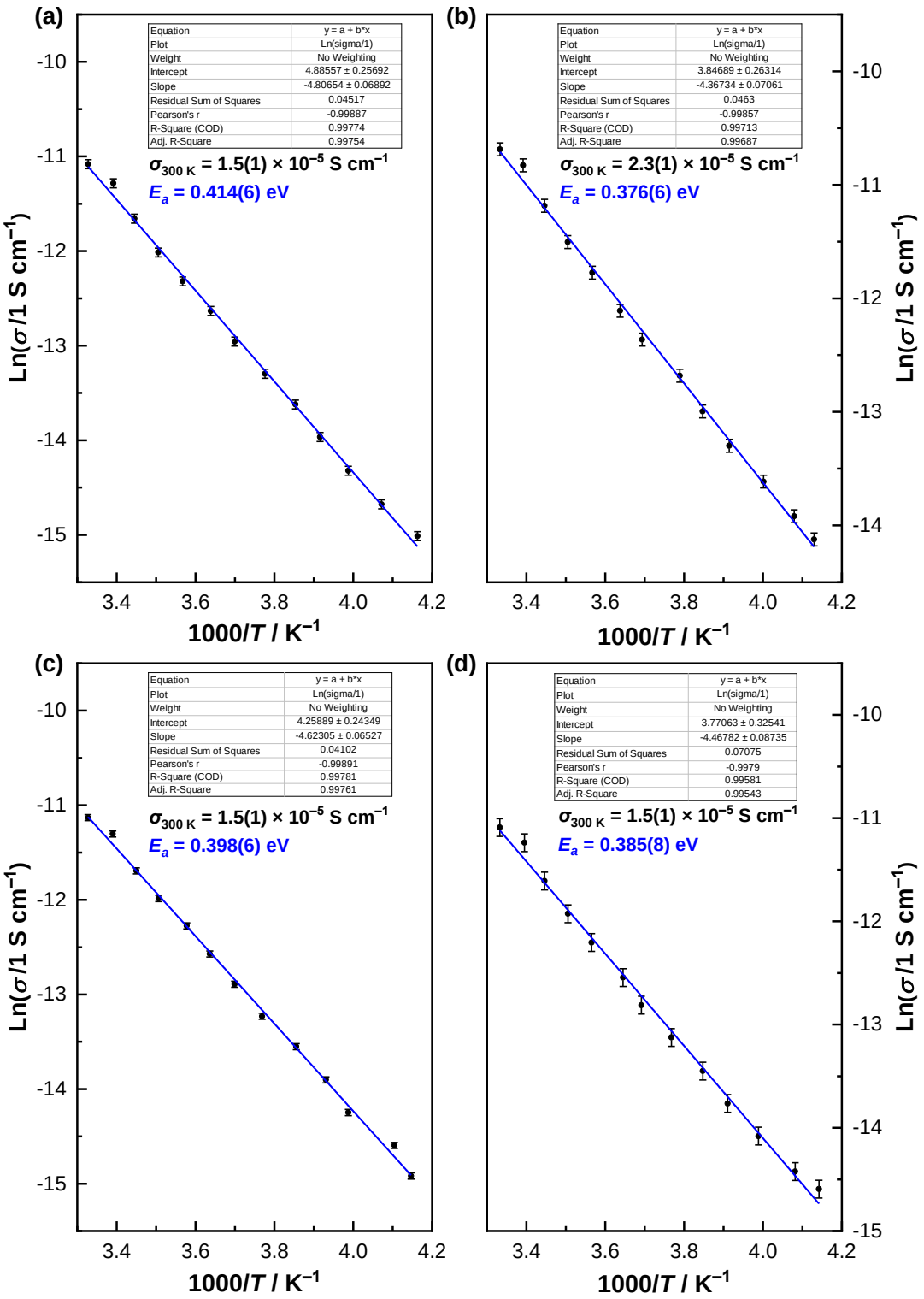


Figure B.3 (a–d) Arrhenius fits of the variable-temperature electrical conductivity for **4.1b** in four independent pressed pellet devices. Experimental data in black circles, lines of best fit in blue. Error bars are ± s.u. Where not visible, error bars lie within the data points.

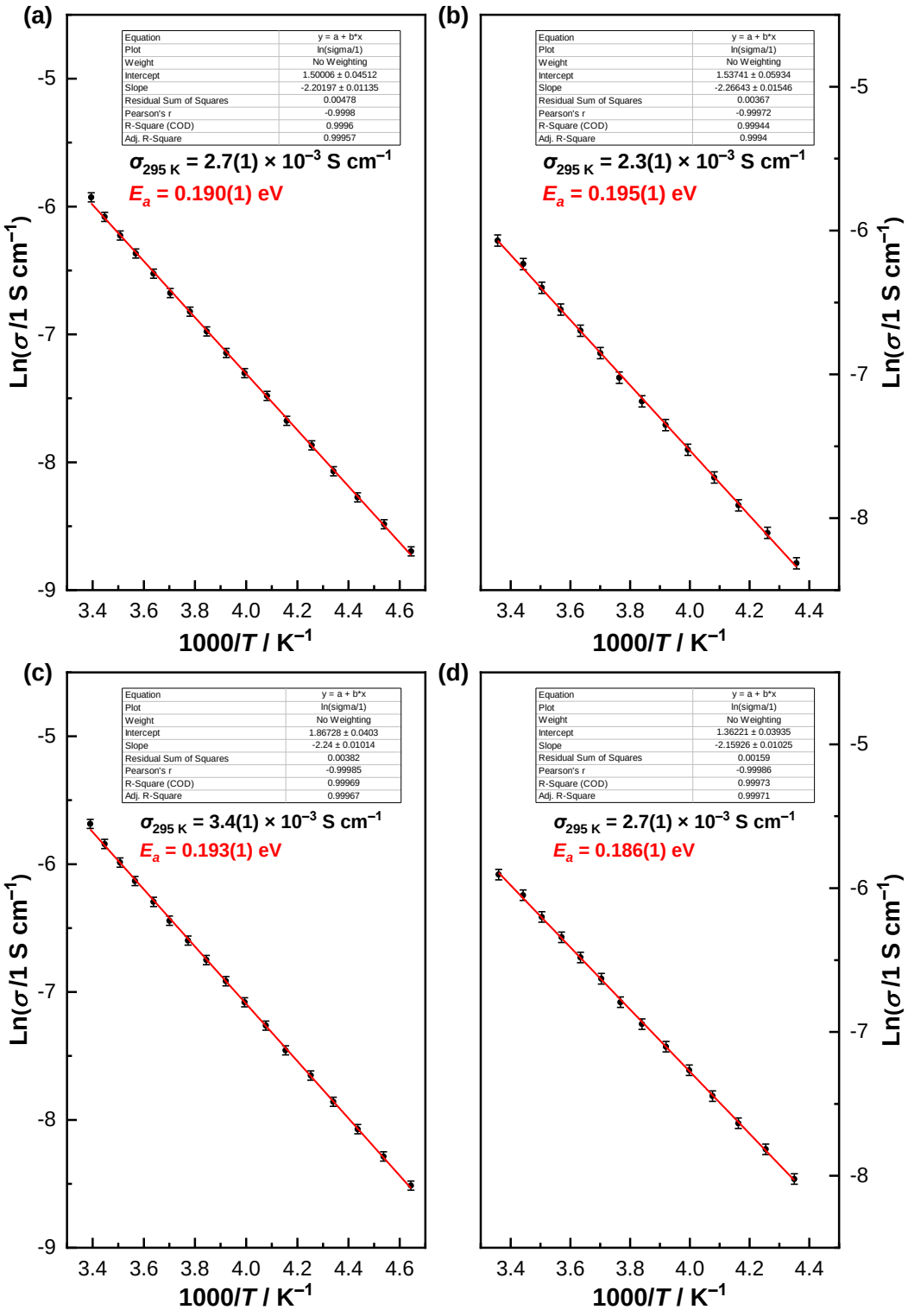


Figure B.4 (a–d) Arrhenius fits of the variable-temperature electrical conductivity for **5.2** in four independent pressed pellet devices. Experimental data in black circles, lines of best fit in red. Error bars are ± s.u. Where not visible, error bars lie within the data points.

This page intentionally left blank

This page intentionally left blank

CHEMISTRY OF MATERIALS

pubs.acs.org/cm Article

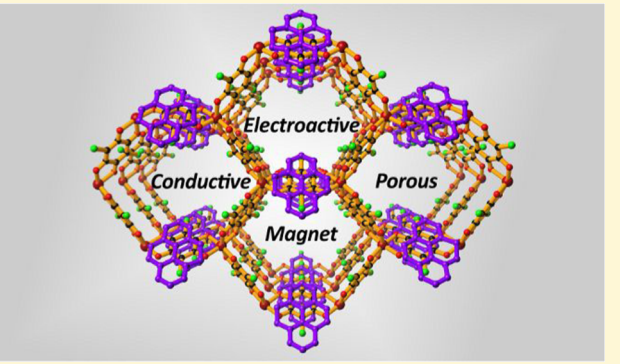
Tuning Charge-State Localization in a Semiconductive Iron(III)–Chloranilate Framework Magnet Using a Redox-Active Cation

Martin P. van Koeverden, Brendan F. Abrahams,* Deanna M. D'Alessandro, Patrick W. Doheny, Carol Hua, Timothy A. Hudson, Guy N. L. Jameson, Keith S. Murray, Wasinee Phonsri, Richard Robson, and Ashley L. Sutton

Cite This: https://dx.doi.org/10.1021/acs.chemmater.0c03132 Read Online

ACCESS | Metrics & More | Article Recommendations | Supporting Information

ABSTRACT: The elucidation of mechanisms to modulate the properties of multifunctional electroactive, conductive, and magnetic porous materials is desirable to aid their future application. The synthesis and characterization of a two-dimensional (2D) mixed-valence metal–tetraoxolene coordination polymer containing a redox-active dication, $(PhenQ)[Fe_2(Clan)_3]\cdot$solvent (**1**; $Clan^{n-}$ = deprotonated 3,6-dichloro-2,5-dihydroxy-1,4-benzoquinone; $PhenQ^{2+}$ = 5,6-dihydropyrazino[1,2,3,4-*lmn*][1,10]-phenanthrolindiium), are reported. The $PhenQ^{2+}$ cation in **1** introduces additional accessible framework redox states and effectively directs the localization of ligand valence states. Static and dynamic magnetic susceptibility measurements demonstrated that the dimethylformamide (DMF) solvate, **1b**, undergoes spontaneous magnetization below T_c = 31 K, with variable-temperature electrical conductivity measurements revealing that **1b** is a modest semiconductor with a conductivity of $\sigma_{295K} = 4.9 \times 10^{-4}$ S cm^{-1} (E_a = 0.249(2) eV). In concert, these results demonstrate that introducing noncovalent interactions between anionic metal–tetraoxolene frameworks and redox-active cations is an effective method to alter the electronic structure and properties of these porous frameworks. Moreover, they forecast the synthesis of new anionic metal–tetraoxolene compounds with diverse electronic and magnetic properties using this hitherto unused strategy.



INTRODUCTION

Coordination polymers and metal–organic frameworks (MOFs) exhibiting combinations of electrical conductivity, electroactivity, magnetic ordering, and porosity have attracted significant fundamental and applied attention in recent years.[1−8] Compared to many nonporous inorganic (semi)-conductors, conductivity in these materials can be modulated using interactions between the framework and guest species within the pores[9] or, in some cases, can be introduced in an otherwise nonconductive framework.[10] These materials therefore have diverse potential applications in sensing and as components in (opto)electronic and energy conversion devices.[11,12] However, the electrically insulating nature of many porous coordination polymers limits their use in these applications. For typical materials, the use of redox-inactive metal species coordinated via hard donor atoms such as O and N to large redox-inactive ligands inhibits long-range charge transport, producing highly insulating materials.[1,5] These factors also significantly reduce any coupling interactions between paramagnetic metal centers, thereby preventing long-range magnetic ordering.

A versatile route toward electrically conductive frameworks is by incorporating electroactive metals and/or ligands in multiple formal oxidation states, producing mixed-valence frameworks. Mixed valency produces low-energy pathways for long-range charge transport, resulting in electrically conductive materials.[6,13] For example, although lacking porosity, single crystals of the coordination polymer $Cu(Me_2DCNQI)_2$ (Me_2DCNQI = 2,5-dimethyl-*N*,*N*′-dicyanoquinodiimine) exhibit metallic conductivity up to 5×10^5 S cm^{-1} at 3.5 K.[14] The metallicity arises from the combination of $Cu^{I/II}$ mixed valency coupled with effective pπ–d orbital overlap with the mixed-valence $DCNQI^{0/-\bullet}$ ligands.[15−17] More recently, metal-centered mixed valency has been used to control the electrical conductivity in porous Fe–azolate frameworks. While the as-synthesized materials (containing either valence pure Fe^{II} or Fe^{III} centers) are poor semiconductors or insulators, the introduction of Fe-centered mixed valency, by either oxidative[18−20] or reductive[21] doping, produces up to 8 orders

Received: July 30, 2020
Revised: August 5, 2020
Published: August 5, 2020

ACS Publications © XXXX American Chemical Society

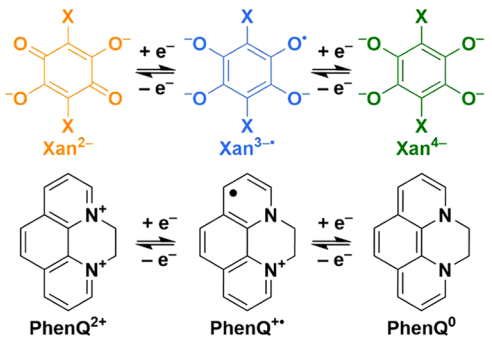
of magnitude enhancement in electrical conductivity over the pristine valence pure frameworks.

The synthesis of frameworks with ligand-centered mixed valency is another particularly effective method to produce porous materials exhibiting both spontaneous ordering and electrical conductivity. A low-energy pathway for charge transport is provided by the multiple ligand valence states,[13] with long-range magnetic ordering promoted due to significantly enhanced spin exchange between the paramagnetic metal centers, mediated by the radical ligands.[3,22] The deprotonated forms of the tetraoxolenes, 2,5-dihydroxy-1,4-benzoquinone (H_2dhbq; Scheme 1, X = H), and the 3,6-disubstituted analogues (termed anilic acids, H_2Xan, Scheme 1, X = F, Cl, Br, I, NO_2, CN, etc.) are promising ligands in this regard.[23] Following the pioneering work of Robl and co-workers,[24,25] a diverse range of one-dimensional (1D), two-dimensional (2D), and three-dimensional (3D) coordination polymers has been synthesized using this ligand family.[26−29] The presence of 3,6-disubstitution allows the degree of electronic communication between the metal centers to be varied,[30] enabling tuning of properties such as the magnetic ordering temperature.[31] Tetraoxolenes also exhibit three readily accessible redox states: a quinonoid dianion (Xan^{2-}), a paramagnetic semiquinonoid trianion ($Xan^{3-\bullet}$), and an aromatic tetraanion (Xan^{4-}) (Scheme 1, upper).[32−36] The Xan^{2-} and Xan^{4-} states mediate weak metal−metal interaction via superexchange,[32,35] with the $Xan^{3-\bullet}$ state allowing strong exchange typically via antiferromagnetic coupling between the paramagnetic ligand and metal centers.[33,34,37,38] Importantly, the reversible redox activity of tetraoxolene ligands is maintained when incorporated into coordination polymers;[39] thus, the redox state of the frameworks and, therefore, the material's properties can be switched by voltammetric[40−42] or chemical[43,44] methods. These characteristics have led to the generation of tetraoxolene coordination polymers exhibiting electrical conductivity[43,45−51] and interesting magnetic properties, such as spontaneous ordering[43,52] and slow relaxation.[48,50,53]

The countercation in anionic tetraoxolene frameworks plays an important role in dictating the resulting network topology and geometry, similarly to metal−oxalate networks.[23,54] In spite of the redox activity of tetraoxolene frameworks, electroactive cations have rarely been incorporated into anionic metal−tetraoxolene compounds,[55−58] with current studies on extended porous mixed-valence tetraoxolene frameworks utilizing exclusively redox-inert cations.[42,43,45,47,49−53,59,60] Interestingly, ferromagnetic, metallic materials result when electroactive tetrachalcogenofulvalene-based radical cations are introduced into bimetallic anionic oxalate networks.[61,62] We therefore envisaged that the inclusion of redox-active cations into mixed-valence tetraoxolene frameworks could be a fruitful strategy to introduce new or perhaps modulate the existing properties of these materials, by virtue of the interplay between all electroactive components. Quaternized bipyridinium cations, commonly termed viologens, are another class of cationic electroactive molecules, which have been widely utilized in functional materials[63,64] such as electrochromic devices,[65,66] molecular switches,[67−69] and organic batteries.[70,71] Like tetraoxolenes, they commonly exist in three accessible redox states: an oxidized aromatic dication, a one-electron reduced semiquinonoid radical cation, and a quinonoid neutral species.[72] Moreover, the π-electron-deficient character and often planar molecular geometry of viologens also promote charge-transfer interactions with π-electron-rich molecules.

Herein, we present investigations on a semiconducting, redox-active 2D honeycomb Fe^{III}-chloranilate framework magnet incorporating a viologen cation, namely, 5,6-dihydropyrazino[1,2,3,4-*lmn*][1,10]-phenanthrolindiium ($PhenQ^{2+}$, Scheme 1, bottom). Notably, the charge-transfer interactions of $PhenQ^{2+}$ with the anionic network effectively control the localization of ligand valence states. The redox activity of $PhenQ^{2+}$ in the material is maintained, affording additional framework redox states, without destroying the desirable magnetic and electrically conductive properties.

Scheme 1. Redox States of the Tetraoxolene Ligands (Anilic Acids, X = H, F, Cl, Br, I; Cl in This Work, $Clan^{n-}$) (Upper) and of the Dication 5,6-Dihydropyrazino[1,2,3,4-*lmn*][1,10]-phenanthrolindiium ($PhenQ^{2+}$) (Bottom)[a]



[a]Single canonical forms of the paramagnetic radical species ($Xan^{3-\bullet}$ and $PhenQ^{+\bullet}$) are shown.

RESULTS AND DISCUSSION

$(PhenQ)[Fe_2(Clan)_3]\cdot y MeCN\cdot z H_2O$ (**1a**) was synthesized by layering an aqueous solution of $(NH_4)_2Fe^{II}(SO_4)_2\cdot 6H_2O$ and $(PhenQ)Br_2$ below a MeCN solution of the reduced form of H_2Clan, 3,6-dichloro-1,2,4,5-tetrahydroxybenzene (H_4Clan), with a buffer layer of 1:1 v/v MeCN−H_2O containing LiOAc. Black block crystals with a metallic blue-green luster appeared upon diffusion over 7 days. An analogous reaction using $Zn^{II}(NO_3)_2\cdot 6H_2O$ and $PhenQ(NO_3)_2$ yielded single crystals of the isostructural Zn^{II} compound, $(PhenQ)[Zn_2(Clan)_3]\cdot y MeCN\cdot z H_2O$ (**2**). The structures of **1a** and **2** were determined by single crystal X-ray diffraction (SC-XRD) in the monoclinic $C2/m$ space group (Tables S1 and S2, respectively). Each Fe center lies upon a twofold axis and resides in a slightly distorted octahedral coordination environment, bound to six O donor atoms of three bridging $Clan^{n-}$ ligands. Every Fe center (either Δ or Λ configuration) is linked via the bridging $Clan^{n-}$ ligands to three Fe centers of opposite configuration, resulting in a two-dimensional (6,3) honeycomb sheet structure $[Fe_2(Clan)_3]^{x-}$ (Figure 1a). The anionic sheets are stacked parallel to the crystallographic c-axis, with the sheet-to-sheet spacing corresponding to the length of the c-axis (see Figure 1b, 8.4943(2) Å, for **1a**). The phase purity of bulk samples was confirmed by powder X-ray diffraction (P-XRD) (Figures S3 and S4). Interestingly, slight changes in the cell dimensions, notably the c-axis length, were observed in bulk samples of both **1a** and **2**. This behavior has previously been observed in $(Me_2NH_2)_2[Fe_2(Clan)_3]$,[42] and likely arises from c-axis disorder or changes to the sheet-to-sheet spacing

https://dx.doi.org/10.1021/acs.chemmater.0c03132
Chem. Mater. XXXX, XXX, XXX−XXX

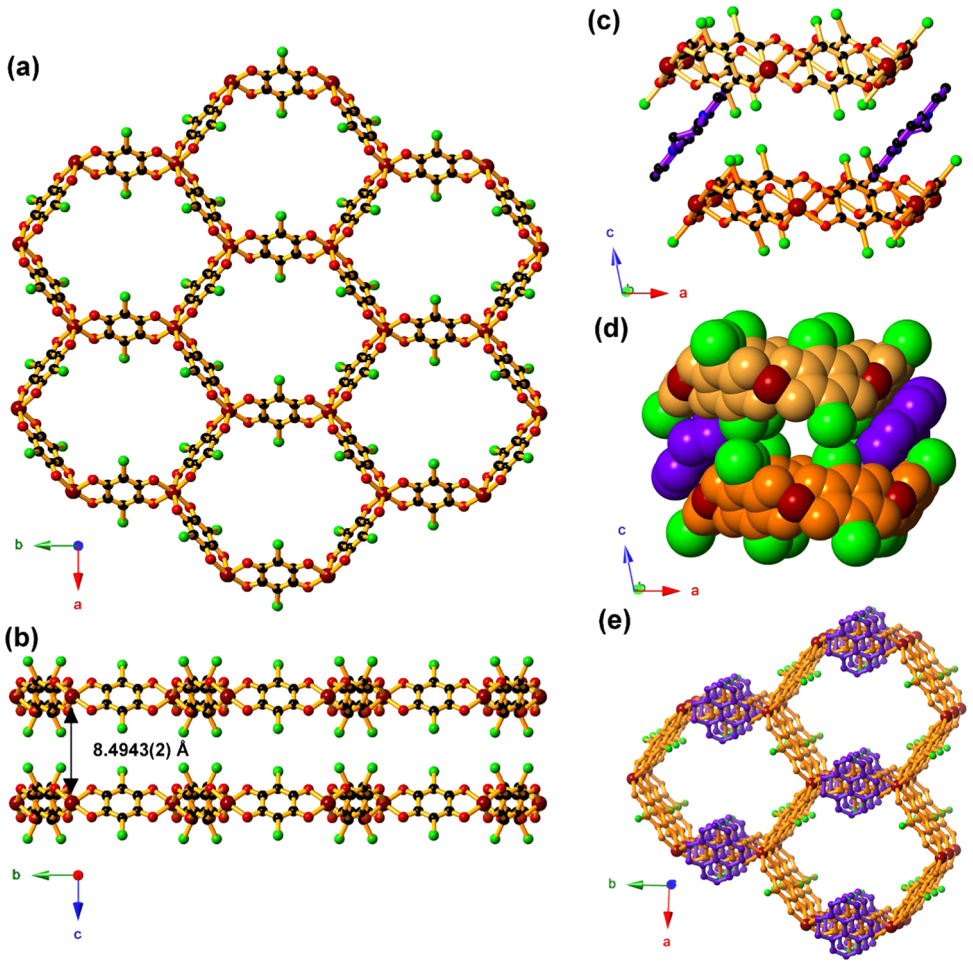


Figure 1. X-ray crystal structures of **1a**. The anionic $[Fe_2(Clan)_3]^{x-}$ (6,3) honeycomb sheets viewed (a) along the crystallographic *c*-axis and (b) down the *a*-axis. (c) Ball-and-stick representation showing $PhenQ^{m+}$ (purple bonds) sandwiched between anionic $[Fe_2(Clan)_3]^{x-}$ sheets above (pale brown bonds) and below (orange bonds). (d) Space-filling representation showing $PhenQ^{m+}$ (purple) sandwiched between anionic $[Fe_2(Clan)_3]^{x-}$ sheets above (pale brown) and below (orange). (e) Alternating stacking of $PhenQ^{m+}$ (purple) with ligands in the $[Fe_2(Clan)_3]^{x-}$ sheets resulting in AAAA stacking and spacious one-dimensional channels. Disordered MeCN and H_2O in channels are not shown for clarity. Maroon = Fe, green = Cl, red = O, blue = N, and black = C.

resulting from minor changes in solvation between single crystal and bulk powder samples.

Charge-balancing $PhenQ^{m+}$ cations are located between the anionic sheets and are snugly sandwiched between two $Clan^{n-}$ ligands from the sheets above and below (Figures 1c,d and S5). The interaction between the ligand and the cation likely arises from the favorable shape complementarity, in addition to strong $\pi-\pi$ interactions between the electron-deficient $PhenQ^{m+}$ cations and anionic $Clan^{n-}$ ligands, which are as close as 3.22 Å (for C···Cl). When viewed along the *c*-axis, this arrangement produces an alternating stack of $PhenQ^{m+}$ and $Clan^{n-}$, enforcing an AAAA stacking of anionic sheets, in which the configuration of every Fe center in a column of Fe centers parallel to the *c*-axis has the same handedness, either all Δ or Λ (Figures 1e and S6). This sheet stacking also produces spacious one-dimensional channels oriented parallel to the *c*-axis and inclined ca. 11° from the normal to the *ab*-plane. The partial intrusion of the $PhenQ^{m+}$ cations into the channels results in a distortion away from the hexagonal cross-section commonly featured in honeycomb $[M_2(Clan)_3]^{x-}$ networks.[44,52,59] The channels occupy ca. 1153 $Å^3$ in the unit cell and comprise ca. 43% of the unit cell volume (2652 $Å^3$), and are filled with highly disordered MeCN and H_2O solvent molecules (Figure S7).

The oxidation states of Fe, $Clan^{n-}$, and $PhenQ^{m+}$ in **1a** were elucidated by examining characteristic bond lengths, using the Zn^{II} compound, **2**, as a reference in which the ligands and cations are unambiguous in the $Clan^{2-}$ and $PhenQ^{2+}$ oxidation states (vide infra). The asymmetric unit of **1a** contains a single Fe center and two crystallographically unique $Clan^{n-}$ ligands in a 1:2 ratio ($\mathbf{L_1}$ and $\mathbf{L_2}$, respectively) (Figure 2); this arrangement is also observed in **2** (Figure S8). The anionic honeycomb sheets are consequently formed from the adjacent $[Fe-\mathbf{L_2}]_\infty$ or $[Zn-\mathbf{L_2}]_\infty$ chains, bridged by $\mathbf{L_1}$ in the direction of the *b*-axis (Figure S9). For **2**, at 100 K, the mean C−O bond lengths in $\mathbf{L_1}$ and $\mathbf{L_2}$ were 1.256(4) and 1.253(6) Å, respectively, with C−C bond lengths across the five-membered chelate ring of 1.533(4) and 1.547(6) Å for $\mathbf{L_1}$ and $\mathbf{L_2}$, respectively. These correspond to values expected for $Clan^{2-}$ ligands in metal−chloranilate compounds (C−O: 1.248−1.272 Å; C−C: 1.506−1.551 Å; 95% confidence interval) (Table S3), allowing the anionic sheets in **2** to be unambiguously formulated as $[Zn_2^{II}(Clan^{2-})_3]^{2-}$. Maintenance of charge neutrality thus requires $PhenQ^{m+}$ to exist in the dicationic state; thus, **2** is formulated as $(PhenQ^{2+})[Zn_2^{II}(Clan^{2-})_3]\cdot$

https://dx.doi.org/10.1021/acs.chemmater.0c03132
Chem. Mater. XXXX, XXX, XXX−XXX

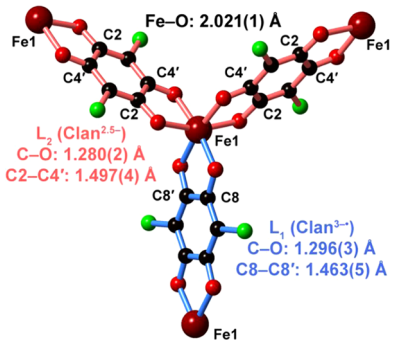


Figure 2. Coordination environment around Fe centers in **1a**, and diagnostic bond lengths at 100 K. $\mathbf{L_1}$ ($Clan^{3-\bullet}$) and $\mathbf{L_2}$ ($Clan^{2.5-}$) forms are highlighted with blue and pale red bonds, respectively. Maroon = Fe, green = Cl, red = O, and black = C.

solvent. Crystallographic C−C and C−N bond lengths are known to be diagnostic of the oxidation state in viologen-like compounds due to transformation from an aromatic to semiquinonoid structure upon one-electron reduction.[73,74] Comparison of the C−C and C−N bond lengths in $PhenQ^{m+}$ between **2** and $(PhenQ^{2+})Br_2$ does not reveal significant differences and are therefore supportive of an aromatic, dicationic character for $PhenQ^{m+}$ in **2** (Figure S10a,b).

A similar comparison of C−C and C−N bond lengths between compound **2** and **1a** (Figure S10b,c) indicates that $PhenQ^{m+}$ exists in **1a** in the dicationic aromatic valence state. Consequently, the anionic network in **1a** is also formulated as $[Fe_2(Clan)_3]^{2-}$. At 100 K, the Fe−O bond lengths in **1a** range from 2.006(2) Å ($\mathbf{L_1}$) to 2.025(2) and 2.030(2) Å ($\mathbf{L_2}$), which correspond closely to those observed for other Fe−tetraoxolene coordination polymers containing high-spin Fe^{III} (Fe_{HS}^{III}) (Table S6).[45,46,52] The mean C−O bond length in $\mathbf{L_1}$ is 1.296(3) Å, with a C−C bond length across the five-membered chelate ring (C8−C8′) of 1.463(5) Å, which matches values expected for coordinated $Clan^{3-\bullet}$ ligands (C−O: 1.291−1.316 Å; C−C: 1.431−1.473 Å, Table S4). In contrast, C−O and C−C bond lengths (1.280(2) and 1.497(4) Å, respectively) for $\mathbf{L_2}$ are intermediate between those displayed by the diamagnetic $Clan^{2-}$ or radical $Clan^{3-\bullet}$ forms (Tables S3 and S4). Given that the Fe centers exist as Fe_{HS}^{III}; $\mathbf{L_1}$ is present in the $Clan^{3-\bullet}$ state; and $PhenQ^{m+}$ exists in the dicationic oxidation state ($PhenQ^{2+}$, vide supra), electrical neutrality in **1a** requires $\mathbf{L_2}$ to possess an average charge of 2.5− per ligand, i.e., $(PhenQ^{2+})[Fe_2^{III}(\mathbf{L_2})_2{}^{5-}\mathbf{L_1}^{3-\bullet}]$.

Control over the extent of valence state localization is critical in designing functional tetraoxolene frameworks, as the extent of delocalization directly influences properties such as conductivity and magnetic ordering or slow relaxation. At the two extremes are complete localization of ligand valence states, i.e., only integer ligand oxidation states[48,51,53] and complete delocalization, i.e., only noninteger ligand oxidation states.[43,45,46,50,52,59] **1a** is present between these two extremes, containing both valence localized ($\mathbf{L_1}$) and delocalized ($\mathbf{L_2}$) states, and we were interested in investigating the effect this would have on the properties of the material. This partial charge ordering in **1a** probably arises from the charge-transfer interactions between the π-electron-poor $PhenQ^{2+}$ cation and the anionic network. Additionally, variable-temperature SC-XRD measurements conducted over the range of 100−260 K (Figure S11 displays thermal variation of the cell parameters) reveal minimal thermal variation in ligand C−O and C−C bond lengths (Figure S12), indicating that **1a** maintains the partially charge-ordered ($PhenQ^{2+}$)-$[Fe_2^{III}(Clan^{2.5-})_2(Clan^{3-\bullet})]$ state. This is in stark contrast to other Fe−tetraoxolene polymers, which exhibit thermally induced valence tautomerism in this temperature range between a $[Fe^{III}-Clan^{3-\bullet}]$ state at $T < T_{1/2}$ to a $[Fe^{II}-Clan^{2-}]$ form at $T > T_{1/2}$.[48,53] This contrasting behavior may arise from strong $\pi-\pi$ interaction between electron-poor $PhenQ^{2+}$ and electron-rich $\mathbf{L_1}$, coupled with Coulombic stabilization of the $PhenQ^{2+}/Clan^{3-\bullet}$ pair relative to a $PhenQ^{2+}/Clan^{2-}$ pair. These factors together both likely increase the energy barrier to the thermally induced electron transfer from $\mathbf{L_1}$ to Fe^{III}. The presence of the valence delocalized $\mathbf{L_2}$ state, formally $[(Clan^{2-})(Clan^{3-\bullet})]$, may also suggest a very low-energy barrier to the electron transfer between the two crystallographically equivalent $\mathbf{L_2}$ ligands, such that the thermally induced electron transfer to Fe^{III} is energetically unfavorable. Future computational studies may provide insight into this proposition.

Upon removal from the mother liquor and exposure to the atmosphere, solvent located in the channels of **1a** was readily lost from the crystals, as observed by thermogravimetric analysis (TGA, Figure S13a). The facile solvent loss from the one-dimensional channels could complicate the analysis of physical property data, as structural distortions have occurred in similar frameworks upon changes in the guest solvation state, with concomitant changes in conductivity and magnetic ordering temperature.[51,52] Indeed, conductivity studies attempted using **1a** showed anomalous time dependence during the measurements. This was ascribed to a continuous solvent loss, resulting in a concomitant unquantifiable change to framework geometry during the experiment. Therefore, crystals of **1a** were transformed via solvent exchange to the dimethylformamide (DMF) solvate $(PhenQ)[Fe_2(Clan)_3]\cdot y$DMF (**1b**), observed by a combination of single-crystal X-ray diffraction (Table S2) and spectroscopic and physical techniques (see the Supporting Information for extended discussion). The solvent exchange process provided a facile demonstration of the porous nature of the framework and greatly improved the stability of **1b** to desolvation compared to **1a** (Figure S13a,b); therefore, all further investigations were performed using **1b**.

The Fe_{HS}^{III} oxidation state assignment was validated by measuring the ^{57}Fe Mössbauer spectra of **1b** in an eicosane matrix (see the Experimental Section). At 294 K, the spectrum of **1b** exhibits a quadrupole doublet, and a fit to the data gives an isomer shift of δ = 0.58 mm s^{-1} and a quadrupole splitting ΔE_Q = 1.13 mm s^{-1} (Figure 3 and Table S9). The δ value is consistent with the previously reported Fe^{III}−tetraoxolene coordination polymers[45,52,53,55] and unambiguously describes Fe_{HS}^{III} residing in an octahedral environment,[75,76] also further confirming the absence of thermally induced valence tautomerism. At 5.8 K, a strong sextet is observed with an isomer shift of δ = 0.61 mm s^{-1} and a quadrupole splitting ΔE_Q = 1.03 mm s^{-1}, with an internal field B_0 = 47.0 T, indicating that **1b** undergoes spontaneous magnetization.[43]

UV−visible (vis)−near-infrared (NIR) was used to investigate the presence of intervalence charge transfer (IVCT) in **1b** and determine the effect of incorporating $PhenQ^{2+}$ on the electronic spectrum. $(Et_4N)_2[Fe_2^{III}(Clan)_3]\cdot$solvent[59] was used as a reference compound as it contains only redox-inactive cations. As with $(Et_4N)_2[Fe_2^{III}(Clan)_3]$, **1b** shows broad absorption bands around ca. 17 600 and 22 500 cm^{-1}, ascribed to $\pi-\pi^*$ and d−π transitions (Figure 4). A broad, intense

https://dx.doi.org/10.1021/acs.chemmater.0c03132
Chem. Mater. XXXX, XXX, XXX−XXX

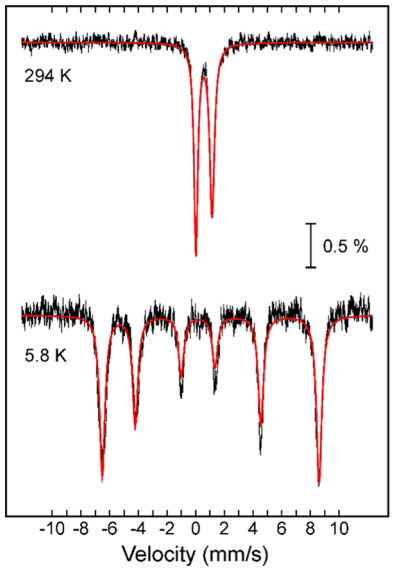


Figure 3. ^{57}Fe Mössbauer spectra of **1b** at 294 K (upper) and 5.8 K (lower). The spectra were fitted (red) with a quadrupole doublet at 294 K and a sextet at 5.8 K representative of high-spin Fe^{III} and magnetically ordered Fe^{III}, respectively. The fitting parameters are given in Table S9.

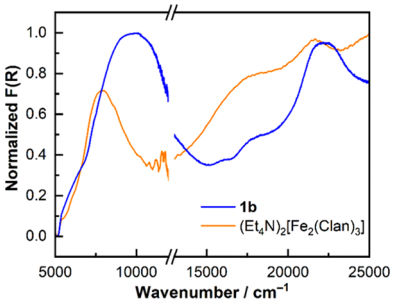


Figure 4. Normalized diffuse reflectance spectra of **1b** (blue) and $(Et_4N)_2[Fe_2(Clan)_3]$ (orange). The break in the spectrum corresponds to the NIR−vis detector change-over.

absorbance band is also observed in the NIR region of **1b**. Given that both SC-XRD and ^{57}Fe Mössbauer spectroscopy analyses confirm a valence pure Fe_{HS}^{III} formulation in **1b**, the NIR band is tentatively attributed to the ligand-based IVCT between $Clan^{2-}$ and $Clan^{3-\bullet}$ species, similar to other Fe^{III}−tetraoxolene frameworks.[45,46,59] However, in stark contrast to the previously reported mixed-valence Fe^{III}−tetraoxolene compounds, the IVCT band of **1b** exhibits a noticeable broadening and a shift of ν_{max} toward higher energy (ν_{max} = 9924 cm^{-1}); in addition to a low-energy tail in the NIR region. These differences likely arise from the contrasting electronic structures of low symmetry **1b**, which possesses a partial charge-ordered state, and in higher symmetry Fe^{III}−tetraoxolene frameworks in which there is full delocalization of the charge state. Additionally, the NIR absorbance band is notably absent in the diffuse reflectance spectrum of **2**, consistent with the absence of IVCT expected due to **2** containing only $Clan^{2-}$ ligands (Figure S18). The optical band gaps (E_g) of **1b** and **2** were estimated as 0.81 and 1.83 eV, respectively, following Tauc analysis of the experimental data (Figures S19 and S20).[77,78] The E_g value for **1b** lies close to that of the previously reported Fe^{III}−tetraoxolene frameworks, namely, E_g = 0.74 and 0.79 eV for the 2D honeycomb $(Et_4N)_2[Fe_2(Fan)_3]$ and $(Et_4N)_2[Fe_2(Clan)_3]$ frameworks, respectively,[50,59] and E_g = 0.67 and 0.7 eV for the 3D (10,3)-*a* $(Bu_4N)_2(Fe_2(Fan)_3]$ and $(Bu_4N)_2(Fe_2(dhbq)_3]$ frameworks, respectively.[45,46] Although it is tempting to ascribe the higher E_g value in **1b** to the partial localization of radical ligands, which would cause a lower degree of electron delocalization, compared to $(Et_4N)_2[Fe_2(Fan)_3]$, $(Et_4N)_2[Fe_2(Clan)_3]$, $(Bu_4N)_2(Fe_2(Fan)_3]$, and $(Bu_4N)_2(Fe_2(dhbq)_3]$, it is pertinent to note that optical band gaps do not directly represent the electronic band gap. However, the similar E_g values amongst the family of Fe^{III}−tetraoxolene frameworks provide some preliminary indication that the electrical conductivity of **1b** may be comparable to the previously reported compounds.

An analysis of the NIR manifold of **1b** indicates the presence of three major underlying Gaussian components at 5629, 8544, and 11 720 cm^{-1}, and a fourth lower intensity component at 10 700 cm^{-1} (Figure S21 and Table S10). Considering the relationship between IVCT and the activation barrier to electron transfer theoretically described by Hush,[79,80] the experimental bandwidths at half-height ($\Delta\nu_{1/2}$) were compared with those calculated using the Γ parameter, where $\Gamma = 1 - (\Delta\nu_{1/2})/(\Delta\nu_{1/2}^{\circ})$.[81] This can offer insight into the class of a mixed-valence system within the Robin and Day classification scheme:[82] $0 < |\Gamma| < 0.1$ for weakly coupled class II systems; $0.1 < |\Gamma| < 0.5$ for moderately coupled class II systems; $|\Gamma| \approx 0.5$ at the transition between class II and class III; and $|\Gamma| > 0.5$ for class III systems. The calculated $|\Gamma|$ values (Table S10) suggest that **1b** lies in the moderately to weakly coupled class II regime, as also noted for the closely related $(Et_4N)_2[Fe_2(Fan)_3]$ and $(Et_4N)_2[Fe_2(Clan)_3]$ systems.[50,59]

Further study of the metal, ligand, and cation oxidation states was also attempted using X-band electron paramagnetic resonance (EPR) spectroscopy. The spectrum of **1b** consists of a strong, very broad signal with no obvious underlying component attributed to an organic radical (Figure S22). This contrasts with the EPR spectrum of mixed-valence $(Bu_4N)_2[Fe_2(Fan)_3]$, which consists of a radical signal readily ascribed to the radical $Fan^{3-\bullet}$ ligands.[46] This difference likely results from the significant room-temperature exchange coupling between Fe_{HS}^{III} and $Clan^{3-\bullet}$, which exists in **1b** (as evinced by dc magnetic susceptibility measurements, vide infra), compared to the room-temperature isolated spin formulation of $(Bu_4N)_2[Fe_2(Fan)_3]$. The spectrum of **2** interestingly exhibits a signal consistent with an organic radical in an axial environment (Figure S23, g_z = 2.0069; $g_{x,y}$ = 2.0042). The incorporation of the trace organic radical in **2** despite the expected diamagnetic formulation is proposed to arise from a redox interaction between $PhenQ^{2+}$ and $Clan^{4-}$, producing trace $Clan^{3-\bullet}$ during synthesis. The absence of any NIR absorbance in the UV−vis−NIR spectrum of **2** is consistent with the absence of detectable IVCT, demonstrating only trace incorporation of $Clan^{3-\bullet}$ into **2**.

The dc electrochemistry of **1b** as a solid was studied using 0.1 M $(Et_4N)PF_6$/MeCN as the electrolyte, by immobilizing a paste of **1b** on a glassy carbon electrode as described previously.[46] Cyclic voltammetry (CV) reveals the presence of two broad quasi-reversible processes upon cycling cathodically, with the first major process observed at E_1 = −0.74 V vs Fc/Fc^+ with a slight shoulder around −0.5 V vs Fc/Fc^+ and a broader second major process at E_2 ca. −1.6 V vs Fc/Fc^+ (Figures 5 and S20). Notably, narrowing of the peak widths is observed with the increasing cycle number, which is likely due

https://dx.doi.org/10.1021/acs.chemmater.0c03132
Chem. Mater. XXXX, XXX, XXX−XXX

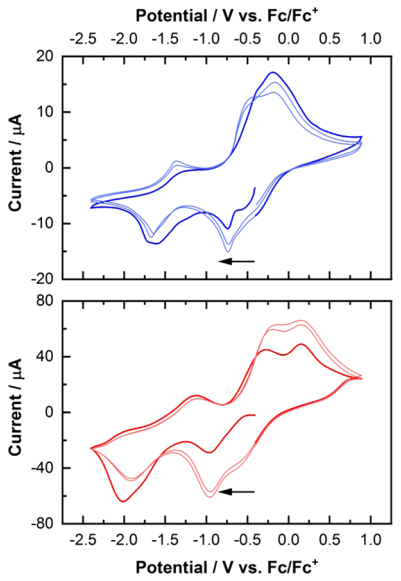


Figure 5. Cyclic voltammograms on solid **1b** in 0.1 M $(Et_4N)PF_6$/MeCN at 50 mV s^{-1} (upper, blue) and 1000 mV s^{-1} (lower, red). Arrows indicate the direction of the forward scan. The first scan is shown in bold, and subsequent scans are shown in a fine line.

to slow diffusion of the Et_4N^+ countercations within the pores of the framework compared to the voltammetric timescale so that the electrochemical process becomes increasingly reversible with higher cycle numbers. Further evidence of this hindered diffusion regime is the cathodic shift and broadening of the peaks upon measurement at higher scan rates (Figures 5 (bottom) and S24).

In contrast to previous electrochemical studies on metal–tetraoxolene frameworks, which are limited to one[39] or two[40−42,45,46] possible electroactive components, the involvement of up to three electroactive species in **1b** complicates the interpretation of the voltammograms. Polarographic measurements have previously shown that the $PhenQ^{2+}$ cation (as the $(PhenQ)(BF_4)_2$ salt) undergoes a reversible reduction ($PhenQ^{2+}/PhenQ^{+\bullet}$) at $E_1 = -0.43$ V vs Fc/Fc^+ and a second irreversible reduction (presumably $PhenQ^{+\bullet}/PhenQ^0$) at $E_2 = -0.82$ V vs Fc/Fc^+.[83] In **1b**, the shoulder at −0.5 V vs Fc/Fc^+ is most readily attributed to the $PhenQ^{2+}/PhenQ^{+\bullet}$ couple, confirming that the introduction of an electroactive cation provides access to additional framework redox states. The first major process at $E_1 = -0.74$ V vs Fc/Fc^+ is tentatively assigned to the reduction of $Clan^{2-}$ to $Clan^{3-\bullet}$ ligands, as supported by previous ^{57}Fe Mössbauer spectroscopic and electrochemical studies on the redox chemistry of $(Me_2NH_2)_2[Fe_2(Clan)_3]\cdot y$DMF.[42,43]

Assignment of the process at E_2 ca. −1.6 V vs Fc/Fc^+ in **1b** is more challenging, and probably involves a combination of $Clan^{3-\bullet}/Clan^{4-}$ and Fe^{III}/Fe^{II} couples, as supported by recent electrochemical and ^{57}Fe Mössbauer studies on $(Me_2NH_2)_2[Fe_2(Clan)_3]\cdot y$DMF.[42] Slow scan voltammetry of this material demonstrated a charge capacity of six electrons per formula unit, i.e., reduction to $Li_6(Me_2NH_2)_2[Fe_2(Clan)_3]\cdot y$DMF, consistent with full involvement of the $Clan^{2-}/Clan^{3-\bullet}/Clan^{4-}$ and Fe^{III}/Fe^{II} couples. This was supported by ex situ ^{57}Fe Mössbauer spectroscopy, which demonstrated the introduction of a significant localized high-spin Fe^{II} character upon framework reduction. The closely matching layered honeycomb structures between **1b** and $(Me_2NH_2)_2[Fe_2(Clan)_3]\cdot y$DMF suggest that the combination of ligand- and metal-centered redox processes could play a role in the electrochemical behavior of **1b** at strongly reducing potentials.

The magnetic properties of **1b** were probed using a combination of static and dynamic magnetic susceptibility measurements. At 300 K, the dc magnetic susceptibility–temperature product, $\chi_M T$ is 12.9 cm^3 K mol^{-1} (Figure 6a),

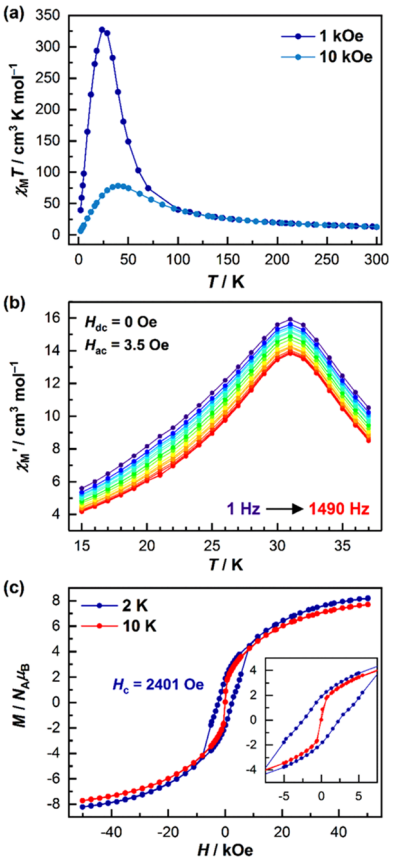


Figure 6. (a) Variable-temperature dc susceptibility of **1b** collected in an applied field of 1 kOe (dark blue) and 10 kOe (pale blue). Solid lines guide the eye. (b) Temperature dependence of the in-phase ac susceptibility of **1b** collected in 0 Oe applied dc field for the determination of the ordering temperature (T_c). (c) Field dependence of the magnetization for **1b**. The inset shows the expansion of the hysteresis loops.

greater than the value of 9.50 cm^3 K mol^{-1} expected for a noninteracting set of two Fe_{HS}^{III} centers ($S = 5/2$) and two $Clan^{3-\bullet}$ ligands ($S = 1/2$). This is ascribed to long-range magnetic coupling, as has been observed previously.[52,53] Between 300 and 100 K, $\chi_M T$ remains field independent and gradually increases upon cooling. Below 100 K, $\chi_M T$ increases significantly, reaching a value of 327 cm^3 K mol^{-1} at 1 kOe and 78 cm^3 K mol^{-1} at 10 kOe, indicative of strong Fe^{III}-radical coupling. A marked deviation from Curie–Weiss behavior in **1b** is observed below 250 K, similar to the previously reported $(Bu_4N)_2[Fe_2^{III}(dhbq)_3]$ (Figure S25).[45] A Curie–Weiss fit, $\chi_M = C/(T - \theta)$, in the region 250–300 K reveals a Weiss constant of $\theta = 140$ K and a Curie constant of $C = 7.0$ cm^3 K mol^{-1}. As with $(Bu_4N)_2[Fe_2(dhbq)_3]$, the positive Weiss constant indicates that ferromagnetic coupling predominates at high temperatures, whereas at lower temperatures, the

https://dx.doi.org/10.1021/acs.chemmater.0c03132
Chem. Mater. XXXX, XXX, XXX−XXX

dominant interaction is a net ferrimagnetic coupling, as evidenced by the gradual increase in magnetization (Figure S26), typical of ferrimagnetic materials.

Field-cooled (FC) and zero-field-cooled (ZFC) dc susceptibility measurements show bifurcation below 30 K (Figure S27), indicative of spontaneous magnetization of the sample, in agreement with the low-temperature ^{57}Fe Mössbauer spectroscopy data. The lower ordering temperature (T_c) of **1b** compared to $(Me_2NH_2)_2[Fe_2^{III}(Clan)_3]\cdot 6DMF\cdot 2H_2O$ (T_c = 80 K),[52] possibly results from distortions to the Fe coordination sphere, associated with the lower symmetry in **1b** (Figure S14). Notably, the desolvated $(Me_2NH_2)_2[Fe_2^{III}(Clan)_3]$ compound exhibited a significantly reduced T_c of 26 K, compared to the DMF solvate, concomitant with the distortion of the framework geometry due to desolvation.[52] This framework distortion was proposed to cause less favorable Fe^{III}-radical coupling, compared to the solvated analogue, resulting in a reduced T_c. The accurate determination of T_c was achieved by investigating the temperature dependence of the ac susceptibility in the zero applied dc field. A sharp frequency-independent peak is observed in the in-phase (χ_M') and out-of-phase (χ_M'') susceptibilities, indicating an ordering temperature of T_c = 31 K (Figures S28, 6b, and S29). The frequency invariancy of maximum χ_M' for **1b** contrasts with the slight frequency-dependent χ_M' maximum observed for $(Me_2NH_2)_2[Fe_2(Clan)_3]\cdot 6DMF\cdot 2H_2O$, which was attributed to the glassy magnetic behavior due to frustrated magnetic interactions.[52] The absence of glassy behavior in **1b** possibly arises from the lower symmetry and partial ligand valence state localization, leading to less frustration of the magnetic interactions in **1b**. Low-temperature magnetization isotherms up to 50 kOe indicate that the low-lying energy levels are closely spaced (Figure S30). At 2 K, the data reaches a maximum of 8.0 $N_A\mu_B$, which matches the expected value of 8.0 $N_A\mu_B$ for the S = 4 Fe_2 repeating unit (two S = 5/2 Fe_{HS}^{III} centers antiferromagnetically coupling to two S = 1/2 $Clan^{3-\bullet}$ radical ligands). Low-temperature magnetic hysteresis measurements up to H_{dc} = 50 kOe reveal the presence of open hysteresis loops at 2 K, with a coercive field of H_c = 2401 Oe (Figure 6c). The presence of open hysteresis loops is consistent with the presence of spontaneous ordering below T_c = 31 K. The H_c of **1b** compares favorably to $(Me_2NH_2)_2[Fe_2^{III}(Clan)_3]\cdot 6DMF\cdot 2H_2O$, which exhibits an intrinsic coercivity H_c = 2630 Oe at 1.8 K,[52] and $(^nPr_4N)_2[Fe_2(Clan)_3]\cdot 2(acetone)$ with H_c = 629 Oe at 1.8 K.[53]

Finally, the electrical transport properties of **1b** were investigated due to the mixed-valence nature and semiconductor behavior suggested by electronic spectroscopy. Initial resistivity measurements on pressed pellets of **1b** were performed in a dinitrogen-filled glovebox using four independent two-point screw cell devices. The average ambient temperature conductivity of the four devices was $5.6(4)\times 10^{-4}$ S cm^{-1} with the premier device reaching $6.9(3)\times 10^{-4}$ S cm^{-1} and with all devices exhibiting ohmic behavior over the range of −0.55 to 0.55 V (see Table S11 for full details). Notably, these values fall short of recently reported Fe−tetraoxolene systems, possibly arising from the lower symmetry and a greater extent of localized ligand charge in **1b** ($Clan^{3-\bullet}$ and $Clan^{2.5-}$) compared to the frameworks with either fully delocalized $dhbq^{2.67-}$ or $Xan^{2.67-}$ valence states,[43,45,46] or fully delocalized $Fe^{II/III}$ states.[49,60] Importantly, these measurements are likely to significantly underestimate the intrinsic electronic conductivity of **1b**. This is probably due to the combination of the dominance of grain boundary resistance in pressed pellet measurements,[84] in addition to the highly anisotropic nature of the electrical conductivity in the layered 2D Fe−tetraoxolene frameworks, observed when the conductivity is measured parallel or perpendicular to the plane of the anionic 2D sheets (typically several orders of magnitude).[49,51,60]

To further elucidate the nature of the electron transport process, variable-temperature resistivity measurements in the range of 300−230 K were performed on four independent pressed pellet devices of **1b** using two-point screw cells (representative temperature-dependent I−V plots for the premier device are shown in Figure S31). At 300 K, the measured conductivity ranges from $3.5(1)\times 10^{-4}$ to $5.4(2)\times 10^{-4}$ S cm^{-1}, and over the entire temperature range, all devices exhibit typical thermally activated semiconductor behavior. Arrhenius fitting of the transport data affords activation energies (E_a) of 0.249(2)−0.253(3) eV (Figure S32), which are comparable to similar layered Fe^{III}−chloranilate compounds measured in pressed pellet devices.[43]

CONCLUSIONS

The successful incorporation of an electroactive viologen cation into an anionic mixed-valence Fe^{III}−tetraoxolene framework has advanced the ability of mixed-valence tetraoxolene frameworks to concomitantly possess electrical conductivity, magnetic ordering, and porosity. The 2D honeycomb Fe^{III} framework $(PhenQ)[Fe_2(Clan)_3]\cdot$solvent exhibits partial localization of the ligand valence states due to strong charge-transfer interactions between the electron-poor redox-active cation and the anionic framework. These interactions lead to notable changes in the spectroscopic properties of the material compared to analogous anionic frameworks containing only redox-inactive cations but do not compromise the electroactivity of the resultant framework, as evidenced by the reversible electrochemical processes. The compound is a permanent magnet with an ordering temperature of T_c = 31 K and displays semiconductor behavior with a conductivity of $\sigma_{295K} = 4.9\times 10^{-4}$ S cm^{-1} (E_a = 0.249(2) eV) for the premier device. This is consistent with the presence of IVCT between the oxidized and reduced forms of the ligand, likely responsible for the long-range charge transport in the framework. Further investigations are currently underway to examine the structure-directing effect of other redox-active viologen-based cations on metal−tetraoxolene frameworks and the effect that cation−framework interactions have on the resultant electrical and magnetic properties. Given the extraordinary richness of redox, structural, and supramolecular chemistry displayed by viologen-based cations, there is a considerable scope to synthesize novel families of multifunctional porous materials exhibiting a tantalizing synergy of electrical conductivity, redox activity, and magnetic ordering by incorporating these cations into mixed-valence tetraoxolene frameworks.

EXPERIMENTAL SECTION

General. Unless overwise specified, all manipulations were performed under an atmosphere of dry dinitrogen (N_2) using standard Schlenk techniques or using a Vacuum Atmosphere glovebox. For the crystallization of $(PhenQ)[Fe_2(Clan)_3]\cdot y$MeCN$\cdot zH_2$O (**1a**) and $(PhenQ)[Zn_2(Clan)_3]\cdot y$MeCN$\cdot zH_2$O (**2**), acetonitrile (MeCN) was used without further purification. For solvent exchange on **1a** to form $(PhenQ)[Fe_2(Clan)_3]\cdot y$DMF (**1b**), MeCN

https://dx.doi.org/10.1021/acs.chemmater.0c03132
Chem. Mater. XXXX, XXX, XXX−XXX

and *N*,*N*-dimethylformamide (DMF) were dried twice sequentially over activated 3 and 4 Å molecular sieves, respectively, and then stored under an atmosphere of dry N_2. Immediately before use, dry DMF and MeCN were degassed by three freeze−pump−thaw cycles. Elemental analyses (CHN) of **1b** and **2** were performed at the Campbell Microanalytical Laboratory, University of Otago. For transport, a sample of **1b** was added to a flame-dried ampoule in a N_2-filled glovebox, which was fitted with a sealable adapter. The ampoule was removed from the glovebox, purged on a Schlenk line, and then flame-sealed under 1 atm of dry N_2. Attenuated total internal reflectance (ATR) Fourier-transform infrared (FT-IR) spectra were recorded in air under ambient conditions using either a Bruker *α* spectrometer fitted with a diamond ATR accessory or a PerkinElmer Spotlight 100 spectrometer fitted with a ZnSe Universal ATR accessory. 3,6-Dichloro-1,2,4,5-tetrahydroxybenzene (H_4Clan)[59] and 5,6-dihydropyrazino[1,2,3,4-*lmn*][1,10]phenanthrolindiium dibromide ([PhenQ]Br_2)[83,85] were synthesized according to the modified literature procedures.

Synthesis of (PhenQ)[Fe_2(Clan)$_3$]·*y*MeCN·*z*H_2O (1a). In air, a solution of $(NH_4)_2Fe^{II}(SO_4)_2{\cdot}6H_2O$ (78.43 mg, 0.2 mmol) and (PhenQ)Br_2 (148.0 mg, 0.4 mmol) in H_2O (4 mL) was carefully layered below a solution of H_4Clan (63.3 mg, 0.3 mmol) in MeCN (10 mL) in a soda glass vial (OD = 25 mm), with a buffer layer of 1:1 v/v MeCN/H_2O (4 mL) containing LiOAc·$2H_2O$ (10.2 mg, 0.1 mmol). For the bulk synthesis of **1a**, six reactions were conducted in parallel and the products were combined during workup. Black parallelepiped crystals with a metallic blue-green luster were visible on the vial walls within 2 days, in addition to a flocculant brown-green powder on the vial bottom. After 7 days, the reactions were transferred to a N_2-purged glovebag. The brown powder was carefully decanted from the vials in ca. 4 mL mother liquor, and then the crystalline product was resuspended in the remaining mother liquor, which was then transferred to deoxygenated 2:1 v/v MeCN/H_2O (a total of 25 mL for six crystallizations). Additional brown powder was removed from the crystalline product by decanting the supernatant liquid and washing with deoxygenated 2:1 v/v MeCN/H_2O (3 × 50 mL) and then with deoxygenated MeCN (3 × 50 mL) by resuspension of the crystalline product, sedimentation of the heavier crystalline product, and decantation of the supernatant. The crystalline product was soaked overnight in dry, deoxygenated MeCN (15 mL), then isolated by suction filtration in a glovebag, and washed on the frit with MeCN (2 × 10 mL). The yield was not determined due to the instability of **1a** to solvent loss. For physical property characterization, **1b** was utilized. FT-IR (ATR, cm^{-1}): 3008 (w, br); 2653 (w, br); 1460 (s); 1450 (w); 1439 (w); 1425 (w); 1351 (m); 1238 (w); 1169 (w); 1029 (m); 1002 (m); 901 (w); 843 (s); 771 (w); 713 (w); 695 (m); 604 (m); 573 (m); 480 (s).

Synthesis of (PhenQ)[Fe_2(Clan)$_3$]·*y*DMF (1b). Crystallization of **1b** was performed analogously to **1a** using a modified workup procedure. For the bulk synthesis of **1b**, 11 reactions were conducted in parallel and the products were combined during workup. After 7 days of diffusion, the reaction vials were transferred to a N_2-purged glovebag. The brown flocculant powder was carefully decanted from the vials in ca. 4 mL mother liquor, and then the crystalline product was resuspended in the mother liquor, which was then transferred to deoxygenated 2:1 v/v MeCN/H_2O (a total of 25 mL for 11 reactions conducted in parallel). Additional brown powder was removed from the black crystalline product by decanting the supernatant liquid and resuspending in 2:1 v/v MeCN/H_2O (3 × 100 mL). The product was suspended in 2:1 v/v MeCN/H_2O (30 mL) and then transferred to a two-neck Schlenk tube fitted with a septum and Schlenk cap. The sealed Schlenk tube was then attached to a Schlenk line, and the supernatant liquid was decanted by cannula transfer under dry N_2. The crystalline product was washed by resuspension in dry, deoxygenated MeCN (3 × 20 mL), sedimentation of the product, and decantation of the supernatant liquid by cannula transfer. The product (**1a**) was resuspended in degassed MeCN (20 mL) and then soaked overnight (12 h). The supernatant liquid was removed by cannula transfer under N_2, and the product was washed with dry, degassed DMF (3 × 20 mL) as above. The solvent was exchanged by soaking the product overnight in DMF (20 mL, 12 h), followed by washing with DMF (20 mL), as above. The DMF soaking−washing process was repeated five times in total. The black crystalline product was isolated by suction filtration in a flame-dried Schlenk frit under N_2 (Figure S1), using dry, deoxygenated DMF (3 × 20 mL) to transfer adherent solids in the Schlenk tube and wash the solids on the frit. The product was dried in vacuo on the frit to a free-flowing crystalline solid, then transferred to a N_2-filled glovebox before storage in a tared, flame-dried Schlenk tube, yielding **1b** as black crystals with a faint blueish-green metallic luster (529 mg, 39.7% based on H_4Clan). FT-IR (ATR, cm^{-1}): 3078 (w, br), 3002 (w, br); 2921 (w); 1649 (s, DMF $\nu_{C=O}$); 1466 (s); 1431 (w); 1414 (w); 1390 (w); 1359 (m); 1280 (w); 1252 (w); 1237 (w); 1089 (m); 1031 (m); 1008 (w); 845 (s); 769 (w); 713 (w); 697 (m); 658 (m); 607 (m); 573 (m); 478 (s). Anal. calcd. for $(C_{14}H_{12}N_2)(Fe_2Cl_6O_{12}C_{18})\cdot 3.69(C_3H_7NO)$: C, 42.73%; H, 3.15%, N, 6.58%. Found: C, 42.85%; H, 3.15%: N, 6.53%.

Single-Crystal X-ray Diffraction (SC-XRD). Crystals of **1a**, **1b**, **2**, and (PhenQ)Br_2 suitable for X-ray diffraction were removed from the mother liquor and immediately coated with an oil-based cryoprotectant to prevent solvent loss. The crystals were mounted on nylon loops, and then crystallographic data were measured using a Rigaku XtaLAB Synergy-S diffractometer equipped with a Cu K*α* (*λ* = 1.54148 Å) microfocus source, graphite monochromator, HyPix-6000 E detector, and an Oxford Diffraction Cryostream 800. Data reduction and multiscan absorption corrections were performed using CrysAlis PRO.[86] The structures were solved with SHELXT using intrinsic phasing[87] and then refined using the SHELXL2018 package using least-squares minimization on F^2,[88] using the ShelXle[89] and OLEX2[90] graphical user interfaces. For **1a**, **1b**, and **2**, the examination of the electron density difference ($F_O - F_C$) maps revealed the presence of significant positive electron density within the one-dimensional channels. This was attributed to severely disordered solvents (MeCN and H_2O for **1a** and **2**; DMF for **1b**), which could not be modeled satisfactorily. The scattering contribution of the disordered solvent was accounted for using the SQUEEZE[91] routine in PLATON.[92] The solvation in the channels was then estimated from the electron count determined by SQUEEZE and the molar composition of solvent used during crystallization. The empirical formulae for **1a**, **1b**, and **2** include the estimated solvation. Unless otherwise noted, the thermal and positional parameters for nonhydrogen atoms in the asymmetric unit were refined anisotropically. Hydrogen atoms were placed at calculated positions using suitable riding models and refined using isotropic displacement parameters derived from their parent atoms. In **1a**, **1b**, and **2**, the $PhenQ^{2+}$ cation resides on a site of 2/*m* symmetry and is thus disordered over two symmetry equivalent positions. The C13A and N13B atoms reside upon symmetry equivalent positions and were refined using EADP and EXYZ restraints. The C13A−C15A (single bond), N13B−C15B (single bond), C13A−C13A′ (double bond), and C15B−C15B′ (single bond) bond distances in **2** were refined using DFIX restraints derived from the equivalent bond distances in (PhenQ)Br_2 (Figure S10a), in which the cation was unambiguously in the $PhenQ^{2+}$ valence state. In **1a** and **1b**, the C−C and C−N bond lengths in the pyridinium rings were first compared to the equivalent bond lengths in (PhenQ)Br_2 and **2** to confirm that the cation was in the $PhenQ^{2+}$ valence state. Subsequently, C13A−C15A (single bond), N13B−C15B (single bond), C13A−C13A′ (double bond), and C15B−C15B′ (single bond) bond distances were refined using the same DFIX restraints as in **2**. Crystallographic data and details of the data collections are given in Tables S1 and S2. The CIF files have been deposited with the Cambridge Structural Database (CCDC reference numbers 1994067−1994078) and can be obtained free of charge via www.ccdc.cam.ac.uk/conts/retrieving.html (or from the Cambridge Crystallographic Data Center, 12 Union Road, Cambridge CB2 1EZ, U.K.; fax: (+44) 1223-336-033; or deposit@ccdc.cam.ac.uk).

Powder X-ray Diffraction (P-XRD). In air, **1a** was gently ground as a slurry in MeCN and then transferred to a borosilicate capillary (OD = 0.7 mm), which was then flame-sealed. The P-XRD pattern was

https://dx.doi.org/10.1021/acs.chemmater.0c03132
Chem. Mater. XXXX, XXX, XXX−XXX

collected using the PD beamline at the Australian Synchrotron.[93] The experiments were undertaken with a wavelength of λ = 0.774574 Å, which was refined against a combined diamond-NIST SRM LaB6-660c standard using the GSAS-II interface.[94] Data were collected using the Mythen microstrip detector[95] from 3 to 83° in 2θ. To cover the gaps between the detector modules, two datasets were collected with the detector set 0.5° apart and then merged to a single dataset using PDViPeR (https://www.ansto.gov.au/user-access/instruments/australian-synchrotron-beamlines/powder-diffraction/pdviper). The sample temperature was controlled using an Oxford Cryostream 700 set at T = 250 K. In a N_2-filled glovebox, compound **1b** was gently ground and then transferred to a borosilicate capillary (OD = 0.3 mm), which was then sealed with an electric arc lighter. The P-XRD pattern was measured using a Rigaku diffraction XtaLAB Synergy-S diffractometer using Cu Kα radiation (λ = 1.54184 Å). The sample temperature was controlled using an Oxford Cryostream 800 set at T = 100 or 240 K. Compound **2** was gently ground as a slurry in MeCN and then loaded into a borosilicate capillary (OD = 0.7 mm), which was then flame-sealed. The P-XRD pattern was measured using a Rigaku Diffraction XtaLAB Synergy-S diffractometer using Cu Kα radiation (λ = 1.54184 Å). The sample temperature was controlled using an Oxford Cryostream 800 set at T = 250 K.

^{57}Fe Mössbauer Spectroscopy. In a N_2-filled glovebox, a sample of **1b** was added to a machined polythene sample cup and then covered with molten dry, deoxygenated eicosane. Once solidified, the sample cup was transferred to a dried Schlenk tube for transport to the spectrometer before insertion into the spectrometer by brief handling in air. ^{57}Fe Mössbauer spectra were measured at 5.8 and 294 K using a Science Engineering & Education Co. spectrometer (Minneapolis, MN) with a ^{57}Co-Rh source equipped with a closed-cycle refrigerator from Janis Research Co. (Woburn, MA) and Sumitomo Heavy Industries, Ltd. (Tokyo, Japan). Data were collected in constant acceleration mode in transmission geometry with a small magnetic field (47 mT) applied parallel to the γ-rays. The zero velocity of the spectrum was calibrated to the centroid of the room-temperature spectrum of a 25 μm α-Fe foil. The spectra were analyzed using WMOSS Mössbauer Spectral Analysis Software (www.wmoss.org).

Electronic Spectroscopy. Diffuse reflectance UV−visible−near-IR (UV−vis−NIR) spectra of **1b** and $(Et_4N)_2[Fe_2(Clan)_3]$ were collected using an Agilent CARY5000 spectrometer fitted with a Harrick Praying Mantis diffuse reflectance accessory using Varian WinUV software v3.0. The samples were finely ground in air and then measured. Spectra were collected in the range of 5000−25 000 cm^{-1} and are presented as the Kubelka−Munk transform, where $F(R) = (1 - R)^2/2R$ and are referenced to a $BaSO_4$ background. The diffuse reflectance spectrum for **1b** was deconvoluted using the curve-fitting subroutine implemented within the GRAMS32 commercial software package. The following procedure was employed for the analysis of the spectral data. The positions of the underlying components were estimated by examining the first- and second-order derivatives of the bands as a guide to the energies of the major components. The energies of the major components were subsequently fixed, and the spectral deconvolution procedure was performed to obtain the parameters for the band intensities and bandwidths. The fixed parameters were successively removed as the fit was iteratively refined. Deconvolution was performed with the minimum number of components required to obtain the convergence of the fitting procedure. The band manifold was approximated by multiple Gaussian-shaped components. Based on the reproducibility of the parameters obtained from the deconvolutions, the uncertainties in the energies (ν_{max}), intensities {$F(R)_{max}$}, and bandwidths ($\Delta\nu_{1/2}$) were estimated as ±10 cm^{-1}, 0.001 × 10^3, and ±10 cm^{-1}, respectively.

EPR Spectroscopy. Continuous-wave X-band EPR spectroscopy of **1b** and **2** was performed using a Bruker EMXnano spectrometer. Solid-state samples of **1b** and **2** were added to quartz tubes under an atmosphere of dry N_2 and air, respectively, and then sealed. The microwave power and attenuation were tuned to prevent signal saturation, and the spectra were acquired using a modulation amplitude of 2 G. All data and reported g-values are field corrected according to a strong pitch reference.

Electrochemistry. Electrochemical measurements on **1b** were performed using an eDAQ potentiostat interfaced to an eDAQ 401 e-corder. Dry N_2 was bubbled through solutions of 0.1 M $(Et_4N)PF_6$/MeCN prior to experiments. The cyclic voltammograms were recorded using a polished glassy carbon working electrode (D = 1 mm), a Pt wire counter electrode, and a leakless Ag/AgCl reference electrode calibrated to the ferrocene/ferrocenium (Fc/Fc^+) couple. The sample was mounted to the working electrode by dipping the electrode into a paste comprising gently ground compound **1b** in the supporting electrolyte.

Magnetic Measurements. Magnetic measurements on **1b** were performed on an accurately weighed sample placed in a calibrated gelatin capsule and restrained in an eicosane matrix. The sealed capsule was held in the center of a soda straw, and the latter was fixed to the sample rod. Data was collected using a Quantum Design MPMS-XL superconducting quantum interference device (SQUID) magnetometer. dc magnetic susceptibility data were collected between 2 and 300 K in applied dc fields of 1 and 10 kOe. Magnetization isotherms were measured at a rate of 1 kOe step^{-1} from 0 to 1 kOe, 2.5 kOe step^{-1} from 1 to 10 kOe, and 5 kOe step^{-1} from 10 to 50 kOe. Magnetic hysteresis measurements were performed using a rate of 680 Oe step^{-1} from −5 to 5 kOe and 3000 Oe step^{-1} between −50 to −5 kOe and 5 to 50 kOe. ac susceptibility measurements were performed in an applied ac field of 3.5 Oe, oscillating between 1 and 1488 Hz. The characteristic ordering temperature (T_c) was estimated as the temperature at which the in-phase ac susceptibility (χ_M') is maximum.

Variable-Temperature Electrical Conductivity. Variable-temperature electrical conductivity measurements on **1b** were conducted using two-electrode screw cells (Figure S2) similar to those described previously.[45,96] In a N_2-filled glovebox, the screw cells were constructed by placing two copper dies (D = 3.0 mm) polished to a mirror finish, into a snugly fitting borosilicate tube (ID = 3.0 mm). The tube was then held within a 3D printed polylactic acid (PLA) cell holder, and the copper dies compressed by two brass screws threaded through the cell holder. The blank cell length was measured using a caliper, then the cells were disassembled, and a sample of compound **1b** was placed into the glass tube. The pressed pellets were formed in situ under anaerobic conditions by compressing the sample between the polished copper dies by tightening the brass screws in the PLA sample holder. The sample thickness was then measured using a caliper. The conductivity cells were sealed with dry, deoxygenated sealing wax to ensure an airtight seal, then removed from the glovebox and placed into a home-built thermostated N_2-purged sample chamber allowing variable-temperature measurements on two cells in parallel. The temperature was controlled to ±1 K in the range of 220−300 K in 5 K steps by regulating the flow rate of cold and hot dry N_2 gas into the sample chamber. The conductivity cells were connected to an Ossila X100 (Sheffield, U.K.) source-measure unit (SMU) interfaced with home-built software via alligator clip-equipped copper cables and BNC cables. The $I-V$ curves were measured over the potential window ±0.55 V in 0.01 V steps, and the resulting linear curves (confirming ohmic behavior) were fitted with Ohm's law

$$J = \sigma E \quad (1)$$

where J (A cm^{-2}) is the current density, E (V cm^{-1}) is the electrical field strength, and σ (S cm^{-1}) is the conductivity. The temperature dependence of the conductivity was subsequently modeled using the Arrhenius equation

$$\sigma = \sigma_0 \exp\left(\frac{E_a}{k_B T}\right) \quad (2)$$

where σ_0 (S cm^{-1}) is pre-exponential, E_a (eV) is the activation energy, k_B (8.617333 × 10^{-5} eV K^{-1}) is the Boltzmann constant, and T (K) is the temperature.

https://dx.doi.org/10.1021/acs.chemmater.0c03132
Chem. Mater. XXXX, XXX, XXX−XXX

■ ASSOCIATED CONTENT

Supporting Information

The Supporting Information is available free of charge at https://pubs.acs.org/doi/10.1021/acs.chemmater.0c03132.

Additional synthetic and experimental details, crystallographic tables, P-XRD, additional figures, FT-IR, TGA, ^{57}Fe Mössbauer parameters, UV−vis−NIR, EPR, CV, static and dynamic magnetic susceptibility plots, *I*−*V* curves and Arrhenius fits (PDF)

Crystallographic data for reported structures **1a**, **1b**, **2**, and (PhenQ)Br_2 (ZIP)

■ AUTHOR INFORMATION

Corresponding Author

Brendan F. Abrahams − *School of Chemistry, The University of Melbourne, Parkville, VIC 3010, Australia;* orcid.org/0000-0003-2957-860X; Email: bfa@unimelb.edu.au

Authors

Martin P. van Koeverden − *School of Chemistry, The University of Melbourne, Parkville, VIC 3010, Australia;* orcid.org/0000-0002-7339-5168

Deanna M. D'Alessandro − *School of Chemistry, The University of Sydney, Sydney, NSW 2006, Australia;* orcid.org/0000-0002-1497-2543

Patrick W. Doheny − *School of Chemistry, The University of Sydney, Sydney, NSW 2006, Australia;* orcid.org/0000-0003-1705-8850

Carol Hua − *School of Chemistry, The University of Melbourne, Parkville, VIC 3010, Australia;* orcid.org/0000-0002-4207-9963

Timothy A. Hudson − *School of Chemistry, The University of Melbourne, Parkville, VIC 3010, Australia*

Guy N. L. Jameson − *School of Chemistry, The University of Melbourne, Parkville, VIC 3010, Australia; Bio21 Molecular Science and Biotechnology Institute, Parkville, VIC 3010, Australia;* orcid.org/0000-0001-9416-699X

Keith S. Murray − *School of Chemistry, Monash University, Clayton, VIC 3800, Australia*

Wasinee Phonsri − *School of Chemistry, Monash University, Clayton, VIC 3800, Australia*

Richard Robson − *School of Chemistry, The University of Melbourne, Parkville, VIC 3010, Australia*

Ashley L. Sutton − *School of Chemistry, The University of Melbourne, Parkville, VIC 3010, Australia*

Complete contact information is available at: https://pubs.acs.org/10.1021/acs.chemmater.0c03132

Author Contributions

This manuscript was written through contributions of all authors.

Notes

The authors declare no competing financial interest.

■ ACKNOWLEDGMENTS

The authors gratefully acknowledge the support of the Australian Research Council (DP180101413, DP170100034, FT170100283). Preliminary variable-temperature SC-XRD experiments were undertaken on the MX1 beamline, and part of this research was undertaken on the powder diffraction beamline at the Australian Synchrotron, part of ANSTO. This research was supported by the use of the EPR spectroscopy facilities provided by the Sydney Analytical Core Facility at the University of Sydney. Dr. Stephen P. Best is gratefully acknowledged for helpful discussions and furnishing access to an inert atmosphere glovebox.

■ REFERENCES

(1) Sun, L.; Campbell, M. G.; Dincă, M. Electrically Conductive Porous Metal−Organic Frameworks. *Angew. Chem., Int. Ed.* **2016**, *55*, 3566−3579.

(2) Givaja, G.; Amo-Ochoa, P.; Gómez-García, C. J.; Zamora, F. Electrical Conductive Coordination Polymers. *Chem. Soc. Rev.* **2012**, *41*, 115−147.

(3) Dechambenoit, P.; Long, J. R. Microporous Magnets. *Chem. Soc. Rev.* **2011**, *40*, 3249−3265.

(4) D'Alessandro, D. M. Exploiting Redox Activity in Metal−Organic Frameworks: Concepts, Trends and Perspectives. *Chem. Commun.* **2016**, *52*, 8957−8971.

(5) D'Alessandro, D. M.; Kanga, J. R. R.; Caddy, J. S. Towards Conducting Metal-Organic Frameworks. *Aust. J. Chem.* **2011**, *64*, 718−722.

(6) Leong, C. F.; Usov, P. M.; D'Alessandro, D. M. Intrinsically Conducting Metal−Organic Frameworks. *MRS Bull.* **2016**, *41*, 858−864.

(7) Thorarinsdottir, A. E.; Harris, T. D. Metal−Organic Framework Magnets. *Chem. Rev.* **2020**, DOI: 10.1021/acs.chemrev.9b00666.

(8) Xie, L. S.; Skorupskii, G.; Dincă, M. Electrically Conductive Metal−Organic Frameworks. *Chem. Rev.* **2020**, DOI: 10.1021/acs.chemrev.9b00766.

(9) Allendorf, M. D.; Foster, M. E.; Léonard, F.; Stavila, V.; Feng, P. L.; Doty, F. P.; Leong, K.; Ma, E. Y.; Johnston, S. R.; Talin, A. A. Guest-Induced Emergent Properties in Metal−Organic Frameworks. *J. Phys. Chem. Lett.* **2015**, *6*, 1182−1195.

(10) Talin, A. A.; Centrone, A.; Ford, A. C.; Foster, M. E.; Stavila, V.; Haney, P.; Kinney, R. A.; Szalai, V.; El Gabaly, F.; Yoon, H. P.; Léonard, F.; Allendorf, M. D. Tunable Electrical Conductivity in Metal-Organic Framework Thin-Film Devices. *Science* **2014**, *343*, 66−69.

(11) Allendorf, M. D.; Schwartzberg, A.; Stavila, V.; Talin, A. A. A Roadmap to Implementing Metal−Organic Frameworks in Electronic Devices: Challenges and Critical Directions. *Chem. − Eur. J.* **2011**, *17*, 11372−11388.

(12) Stavila, V.; Talin, A. A.; Allendorf, M. D. MOF-Based Electronic and Opto-Electronic Devices. *Chem. Soc. Rev.* **2014**, *43*, 5994−6010.

(13) Murase, R.; Leong, C. F.; D'Alessandro, D. M. Mixed Valency as a Strategy for Achieving Charge Delocalization in Semiconducting and Conducting Framework Materials. *Inorg. Chem.* **2017**, *56*, 14373−14382.

(14) Aumüller, A.; Erk, P.; Klebe, G.; Hünig, S.; von Schütz, J. U.; Werner, H.-P. A Radical Anion Salt of 2,5-Dimethyl-*N*,*N*′-dicyanoquinonediimine with Extremely High Electrical Conductivity. *Angew. Chem., Int. Ed.* **1986**, *25*, 740−741.

(15) Kobayashi, A.; Kato, R.; Kobayashi, H.; Mori, T.; Inokuchi, H. The Organic π-Electron Metal System with Interaction through Mixed-Valence Metal Cation: Electronic and Structural Properties of Radical Salts of Dicyano-quinodiimine, $(DMe\text{-}DCNQI)_2Cu$ and $(MeCl\text{-}DCNQI)_2Cu$. *Solid State Commun.* **1987**, *64*, 45−51.

(16) Inoue, I. H.; Kakizaki, A.; Namatame, H.; Fujimori, A.; Kobayashi, A.; Kato, R.; Kobayashi, H. Copper Valence Fluctuation in the Organic Conductor (Dimethyl-*N*,*N*′-dicyanoquinonediimine)$_2$Cu Studied by X-ray Photoemission Spectroscopy. *Phys. Rev. B* **1992**, *45*, 5828−5833.

(17) von Schuetz, J. U.; Bauer, D.; Hünig, S.; Sinzger, K.; Wolf, H. C. Copper(2+) States as Mediators for Metallic Conductivity in DCNQI Radical Anion Salts. *J. Phys. Chem. A.* **1993**, *97*, 12030−12033.

(18) Gándara, F.; Uribe-Romo, F. J.; Britt, D. K.; Furukawa, H.; Lei, L.; Cheng, R.; Duan, X.; O'Keeffe, M.; Yaghi, O. M. Porous,

Conductive Metal-Triazolates and Their Structural Elucidation by the Charge-Flipping Method. *Chem. − Eur. J.* **2012**, *18*, 10595−10601.
(19) Park, J. G.; Aubrey, M. L.; Oktawiec, J.; Chakarawet, K.; Darago, L. E.; Grandjean, F.; Long, G. J.; Long, J. R. , Charge Delocalization and Bulk Electronic Conductivity in the Mixed-Valence Metal−Organic Framework Fe(1,2,3-Triazolate)2(Bf4)X. *J. Am. Chem. Soc.* **2018**, *140*, 8526−8534.
(20) Xie, L. S.; Sun, L.; Wan, R.; Park, S. S.; DeGayner, J. A.; Hendon, C. H.; Dincă, M. Tunable Mixed-Valence Doping toward Record Electrical Conductivity in a Three-Dimensional Metal−Organic Framework. *J. Am. Chem. Soc.* **2018**, *140*, 7411−7414.
(21) Aubrey, M. L.; Wiers, B. M.; Andrews, S. C.; Sakurai, T.; Reyes-Lillo, S. E.; Hamed, S. M.; Yu, C.-J.; Darago, L. E.; Mason, J. A.; Baeg, J.-O.; Grandjean, F.; Long, G. J.; Seki, S.; Neaton, J. B.; Yang, P.; Long, J. R. Electron Delocalization and Charge Mobility as a Function of Reduction in a Metal−Organic Framework. *Nat. Mater.* **2018**, *17*, 625−632.
(22) Faust, T. B.; D'Alessandro, D. M. Radicals in Metal-Organic Frameworks. *RSC Adv.* **2014**, *4*, 17498−17512.
(23) Mercuri, M. L.; Congiu, F.; Concas, G.; Sahadevan, S. A. Recent Advances on Anilato-Based Molecular Materials with Magnetic and/or Conducting Properties. *Magnetochemistry* **2017**, *3*, No. 17.
(24) Weiss, A.; Riegler, E.; Robl, C. Polymeric 2,5-Dihydroxy-1,4-benzoquinone Transition Metal Complexes $Na_2(H_2O)_{24}[M_2(C_6H_2O_4)_3]$ (M = Mn^{2+}, Cd^{2+}). *Z. Naturforsch., B: J. Chem. Sci.* **1986**, *41*, 1501.
(25) Robl, C. Complexes with Substituted 2,5-Dihydroxy-P-Benzoquinones: The Inclusion Compounds $[Y(H_2O)_3]_2(C_6Cl_2O_4)_3 \cdot 6.6H_2O$ and $[Y(H_2O)_3]_2(C_6Br_2O_4)3 \cdot 6H_2O$. *Mater. Res. Bull.* **1987**, *22*, 1483−1491.
(26) Kitagawa, S.; Kawata, S. Coordination Compounds of 1,4-Dihydroxybenzoquinone and Its Homologues. Structures and Properties. *Coord. Chem. Rev.* **2002**, *224*, 11−34.
(27) Kawata, S.; Kitagawa, S.; Kondo, M.; Furuchi, I.; Munakata, M. Two-Dimensional Sheets of Tetragonal Copper(II) Lattices: X-ray Crystal Structure and Magnetic Properties of $[Cu(C_6O_4Cl_2)(C_4H_4N_2)]_n$. *Angew. Chem., Int. Ed.* **1994**, *33*, 1759−1761.
(28) Abrahams, B. F.; Lu, K. D.; Moubaraki, B.; Murray, K. S.; Robson, R. X-ray Diffraction and Magnetic Studies on a Series of Isostructural Divalent Metal Chloranilates with Zigzag Polymeric Chain Structures and on a Dinuclear Iron(III) Chloranilate. *J. Chem. Soc., Dalton Trans.* **2000**, 1793−1797.
(29) Abrahams, B. F.; Coleiro, J.; Ha, K.; Hoskins, B. F.; Orchard, S. D.; Robson, R. Dihydroxybenzoquinone and Chloranilic Acid Derivatives of Rare Earth Metals. *J. Chem. Soc., Dalton Trans.* **2002**, 1586−1594.
(30) Tinti, F.; Verdaguer, M.; Kahn, O.; Savariault, J. M. Interaction between Copper(II) Ions Separated by 7.6 Å. Crystal Structure and Magnetic Properties of (μ-Iodanilato)bis[(*N*,*N*,*N*′,*N*′-tetramethylethylenediamine)copper(II)] Diperchlorate. *Inorg. Chem.* **1987**, *26*, 2380−2384.
(31) Atzori, M.; Benmansour, S.; Mínguez Espallargas, G.; Clemente-León, M.; Abhervé, A.; Gómez-Claramunt, P.; Coronado, E.; Artizzu, F.; Sessini, E.; Deplano, P.; Serpe, A.; Mercuri, M. L.; Gómez García, C. J. A Family of Layered Chiral Porous Magnets Exhibiting Tunable Ordering Temperatures. *Inorg. Chem.* **2013**, *52*, 10031−10040.
(32) Dei, A.; Gatteschi, D.; Pardi, L.; Russo, U. Tetraoxolene Radical Stabilization by the Interaction with Transition-Metal Ions. *Inorg. Chem.* **1991**, *30*, 2589−2594.
(33) Min, K. S.; Rheingold, A. L.; DiPasquale, A.; Miller, J. S. Characterization of the Chloranilate(•3−) π Radical as a Strong Spin-Coupling Bridging Ligand. *Inorg. Chem.* **2006**, *45*, 6135−6137.
(34) Min, K. S.; DiPasquale, A. G.; Golen, J. A.; Rheingold, A. L.; Miller, J. S. Synthesis, Structure, and Magnetic Properties of Valence Ambiguous Dinuclear Antiferromagnetically Coupled Cobalt and Ferromagnetically Coupled Iron Complexes Containing the Chloranilate(2−) and the Significantly Stronger Coupling Chloranilate(•3−) Radical Trianion. *J. Am. Chem. Soc.* **2007**, *129*, 2360−2368.
(35) Guo, D.; McCusker, J. K. Spin Exchange Effects on the Physicochemical Properties of Tetraoxolene-Bridged Bimetallic Complexes. *Inorg. Chem.* **2007**, *46*, 3257−3274.
(36) Nakabayashi, K.; Ohkoshi, S.-i. Monometallic Lanthanoid Assembly Showing Ferromagnetism with a Curie Temperature of 11 K. *Inorg. Chem.* **2009**, *48*, 8647−8649.
(37) Zhang, P.; Perfetti, M.; Kern, M.; Hallmen, P. P.; Ungur, L.; Lenz, S.; Ringenberg, M. R.; Frey, W.; Stoll, H.; Rauhut, G.; van Slageren, J. Exchange Coupling and Single Molecule Magnetism in Redox-Active Tetraoxolene-Bridged Dilanthanide Complexes. *Chem. Sci.* **2018**, *9*, 1221−1230.
(38) Reed, W. R.; Dunstan, M. A.; Gable, R. W.; Phonsri, W.; Murray, K. S.; Mole, R. A.; Boskovic, C. Tetraoxolene-Bridged Rare-Earth Complexes: A Radical-Bridged Dinuclear Dy Single-Molecule Magnet. *Dalton Trans.* **2019**, *48*, 15635−15645.
(39) Abrahams, B. F.; Bond, A. M.; Le, T. H.; McCormick, L. J.; Nafady, A.; Robson, R.; Vo, N. Voltammetric Reduction and Re-Oxidation of Solid Coordination Polymers of Dihydroxybenzoquinone. *Chem. Commun.* **2012**, *48*, 11422−11424.
(40) Taniguchi, K.; Chen, J.; Sekine, Y.; Miyasaka, H. Magnetic Phase Switching in a Tetraoxolene-Bridged Honeycomb Ferrimagnet Using a Lithium Ion Battery System. *Chem. Mater.* **2017**, *29*, 10053−10059.
(41) Chen, J.; Taniguchi, K.; Sekine, Y.; Miyasaka, H. Electrochemical Development of Magnetic Long-Range Correlations with T_c = 128 K in a Tetraoxolene-Bridged Fe-Based Framework. *J. Magn. Magn. Mater.* **2020**, *494*, No. 165818.
(42) Ziebel, M. E.; Gaggioli, C. A.; Turkiewicz, A. B.; Ryu, W.; Gagliardi, L.; Long, J. R. Effects of Covalency on Anionic Redox Chemistry in Semiquinoid-Based Metal−Organic Frameworks. *J. Am. Chem. Soc.* **2020**, *142*, 2653−2664.
(43) DeGayner, J. A.; Jeon, I.-R.; Sun, L.; Dincă, M.; Harris, T. D. 2D Conductive Iron-Quinoid Magnets Ordering up to T_c = 105 K via Heterogenous Redox Chemistry. *J. Am. Chem. Soc.* **2017**, *139*, 4175−4184.
(44) Liu, L.; DeGayner, J. A.; Sun, L.; Zee, D. Z.; Harris, T. D. Reversible Redox Switching of Magnetic Order and Electrical Conductivity in a 2D Manganese Benzoquinoid Framework. *Chem. Sci.* **2019**, *10*, 4652−4661.
(45) Darago, L. E.; Aubrey, M. L.; Yu, C. J.; Gonzalez, M. I.; Long, J. R. Electronic Conductivity, Ferrimagnetic Ordering, and Reductive Insertion Mediated by Organic Mixed-Valence in a Ferric Semiquinoid Metal−Organic Framework. *J. Am. Chem. Soc.* **2015**, *137*, 15703−15711.
(46) Murase, R.; Abrahams, B. F.; D'Alessandro, D. M.; Davies, C. G.; Hudson, T. A.; Jameson, G. N. L.; Moubaraki, B.; Murray, K. S.; Robson, R.; Sutton, A. L. Mixed Valency in a 3D Semiconducting Iron−Fluoranilate Coordination Polymer. *Inorg. Chem.* **2017**, *56*, 9025−9035.
(47) Ziebel, M. E.; Darago, L. E.; Long, J. R. Control of Electronic Structure and Conductivity in Two-Dimensional Metal−Semiquinoid Frameworks of Titanium, Vanadium, and Chromium. *J. Am. Chem. Soc.* **2018**, *140*, 3040−3051.
(48) DeGayner, J. A.; Wang, K.; Harris, T. D. A Ferric Semiquinoid Single-Chain Magnet Via Thermally-Switchable Metal−Ligand Electron Transfer. *J. Am. Chem. Soc.* **2018**, *140*, 6550−6553.
(49) Sahadevan, S. A.; Abhervé, A.; Monni, N.; Sáenz de Pipaón, C.; Galán-Mascarós, J. R.; Waerenborgh, J. C.; Vieira, B. J. C.; Auban-Senzier, P.; Pillet, S.; Bendeif, E.-E.; Alemany, P.; Canadell, E.; Mercuri, M. L.; Avarvari, N. Conducting Anilate-Based Mixed-Valence Fe(II)Fe(III) Coordination Polymer: Small-Polaron Hopping Model for Oxalate-Type Fe(II)Fe(III) 2D Networks. *J. Am. Chem. Soc.* **2018**, *140*, 12611−12621.
(50) Murase, R.; Commons, C. J.; Hudson, T. A.; Jameson, G. N. L.; Ling, C. D.; Murray, K. S.; Phonsri, W.; Robson, R.; Xia, Q.; Abrahams, B. F.; D'Alessandro, D. M. Effects of Mixed Valency in an Fe-Based Framework: Coexistence of Slow Magnetic Relaxation,

https://dx.doi.org/10.1021/acs.chemmater.0c03132
Chem. Mater. XXXX, XXX, XXX−XXX

Semiconductivity, and Redox Activity. *Inorg. Chem.* **2020**, *59*, 3619−3630.
(51) Chen, J.; Sekine, Y.; Okazawa, A.; Sato, H.; Kosaka, W.; Miyasaka, H. Chameleonic Layered Metal−Organic Frameworks with Variable Charge-Ordered States Triggered by Temperature and Guest Molecules. *Chem. Sci.* **2020**, *11*, 3610−3618.
(52) Jeon, I.-R.; Negru, B.; Van Duyne, R. P.; Harris, T. D. A 2d Semiquinone Radical-Containing Microporous Magnet with Solvent-Induced Switching from T_c = 26 to 80 K. *J. Am. Chem. Soc.* **2015**, *137*, 15699−15702.
(53) Chen, J.; Sekine, Y.; Komatsumaru, Y.; Hayami, S.; Miyasaka, H. Thermally Induced Valence Tautomeric Transition in a Two-Dimensional Fe-Tetraoxolene Honeycomb Network. *Angew. Chem., Int. Ed.* **2018**, *57*, 12043−12047.
(54) Clemente-León, M.; Coronado, E.; Martí-Gastaldo, C.; Romero, F. M. Multifunctionality in Hybrid Magnetic Materials Based on Bimetallic Oxalate Complexes. *Chem. Soc. Rev.* **2011**, *40*, 473−497.
(55) Nagayoshi, K.; Kabir, M. K.; Tobita, H.; Honda, K.; Kawahara, M.; Katada, M.; Adachi, K.; Nishikawa, H.; Ikemoto, I.; Kumagai, H.; Hosokoshi, Y.; Inoue, K.; Kitagawa, S.; Kawata, S. Design of Novel Inorganic−Organic Hybrid Materials Based on Iron-Chloranilate Mononuclear Complexes: Characteristics of Hydrogen-Bond-Supported Layers toward the Intercalation of Guests. *J. Am. Chem. Soc.* **2003**, *125*, 221−232.
(56) Atzori, M.; Pop, F.; Auban-Senzier, P.; Gómez-García, C. J.; Canadell, E.; Artizzu, F.; Serpe, A.; Deplano, P.; Avarvari, N.; Mercuri, M. L. Structural Diversity and Physical Properties of Paramagnetic Molecular Conductors Based on Bis(ethylenedithio)-detrathiafulvalene (BEDT-TTF) and the Tris(chloranilato)ferrate-(III) Complex. *Inorg. Chem.* **2014**, *53*, 7028−7039.
(57) Atzori, M.; Pop, F.; Auban-Senzier, P.; Clérac, R.; Canadell, E.; Mercuri, M. L.; Avarvari, N. Complete Series of Chiral Paramagnetic Molecular Conductors Based on Tetramethyl-bis(ethylenedithio)-tetrathiafulvalene (TM-BEDT-TTF) and Chloranilate-Bridged Heterobimetallic Honeycomb Layers. *Inorg. Chem.* **2015**, *54*, 3643−3653.
(58) Sahadevan, S. A.; Abhervé, A.; Monni, N.; Auban-Senzier, P.; Cano, J.; Lloret, F.; Julve, M.; Cui, H.; Kato, R.; Canadell, E.; Mercuri, M. L.; Avarvari, N. Magnetic Molecular Conductors Based on Bis(ethylenedithio)tetrathiafulvalene (BEDT-TTF) and the Tris-(chlorocyananilato)ferrate(III) Complex. *Inorg. Chem.* **2019**, *58*, 15359−15370.
(59) Kingsbury, C. J.; Abrahams, B. F.; D'Alessandro, D. M.; Hudson, T. A.; Murase, R.; Robson, R.; White, K. F. Role of NEt_4^+ in Orienting and Locking Together $[M_2lig_3]^{2-}$ (6,3) Sheets (H_2lig = Chloranilic or Fluoranilic Acid) to Generate Spacious Channels Perpendicular to the Sheets. *Cryst. Growth Des.* **2017**, *17*, 1465−1470.
(60) Benmansour, S.; Abhervé, A.; Gómez-Claramunt, P.; Vallés-García, C.; Gómez-García, C. J. Nanosheets of Two-Dimensional Magnetic and Conducting Fe(II)/Fe(III) Mixed-Valence Metal−Organic Frameworks. *ACS Appl. Mater. Interfaces* **2017**, *9*, 26210−26218.
(61) Coronado, E.; Galán-Mascarós, J. R.; Gómez-García, C. J.; Laukhin, V. Coexistence of Ferromagnetism and Metallic Conductivity in a Molecule-Based Layered Compound. *Nature* **2000**, *408*, 447−449.
(62) Alberola, A.; Coronado, E.; Galán-Mascarós, J. R.; Giménez-Saiz, C.; Gómez-García, C. J. A Molecular Metal Ferromagnet from the Organic Donor Bis(ethylenedithio)tetraselenafulvalene and Bimetallic Oxalate Complexes. *J. Am. Chem. Soc.* **2003**, *125*, 10774−10775.
(63) Striepe, L.; Baumgartner, T. Viologens and Their Application as Functional Materials. *Chem. − Eur. J.* **2017**, *23*, 16924−16940.
(64) Ding, J.; Zheng, C.; Wang, L.; Lu, C.; Zhang, B.; Chen, Y.; Li, M.; Zhai, G.; Zhuang, X. Viologen-Inspired Functional Materials: Synthetic Strategies and Applications. *J. Mater. Chem. A* **2019**, *7*, 23337−23360.
(65) Mortimer, R. J. Organic Electrochromic Materials. *Electrochim. Acta* **1999**, *44*, 2971−2981.
(66) Madasamy, K.; Velayutham, D.; Suryanarayanan, V.; Kathiresan, M.; Ho, K.-C. Viologen-Based Electrochromic Materials and Devices. *J. Mater. Chem. C* **2019**, *7*, 4622−4637.
(67) Sun, J.; Wu, Y.; Wang, Y.; Liu, Z.; Cheng, C.; Hartlieb, K. J.; Wasielewski, M. R.; Stoddart, J. F. An Electrochromic Tristable Molecular Switch. *J. Am. Chem. Soc.* **2015**, *137*, 13484−13487.
(68) Ashton, P. R.; Balzani, V.; Becher, J.; Credi, A.; Fyfe, M. C. T.; Mattersteig, G.; Menzer, S.; Nielsen, M. B.; Raymo, F. M.; Stoddart, J. F.; Venturi, M.; Williams, D. J. A Three-Pole Supramolecular Switch. *J. Am. Chem. Soc.* **1999**, *121*, 3951−3957.
(69) Gittins, D. I.; Bethell, D.; Schiffrin, D. J.; Nichols, R. J. A Nanometre-Scale Electronic Switch Consisting of a Metal Cluster and Redox-Addressable Groups. *Nature* **2000**, *408*, 67−69.
(70) Luo, J.; Hu, B.; Debruler, C.; Liu, T. L. A Π-Conjugation Extended Viologen as a Two-Electron Storage Anolyte for Total Organic Aqueous Redox Flow Batteries. *Angew. Chem., Int. Ed.* **2018**, *57*, 231−235.
(71) Liu, T.; Wei, X.; Nie, Z.; Sprenkle, V.; Wang, W. A Total Organic Aqueous Redox Flow Battery Employing a Low Cost and Sustainable Methyl Viologen Anolyte and 4-HO-TEMPO Catholyte. *Adv. Energy Mater.* **2016**, *6*, No. 1501449.
(72) Bird, C. L.; Kuhn, A. T. Electrochemistry of the Viologens. *Chem. Soc. Rev.* **1981**, *10*, 49−82.
(73) Bockman, T. M.; Kochi, J. K. Isolation and Oxidation-Reduction of Methylviologen Cation Radicals. Novel Disproportionation in Charge-Transfer Salts by X-ray Crystallography. *J. Org. Chem.* **1990**, *55*, 4127−4135.
(74) Porter, W. W., III; Vaid, T. P. Isolation and Characterization of Phenyl Viologen as a Radical Cation and Neutral Molecule. *J. Org. Chem.* **2005**, *70*, 5028−5035.
(75) Grillo, V. A.; Hanson, G. R.; Wang, D.; Hambley, T. W.; Gahan, L. R.; Murray, K. S.; Moubaraki, B.; Hawkins, C. J. Synthesis, X-Ray Structural Determination, and Magnetic Susceptibility, Mössbauer, and EPR Studies of $(Ph_4P)_2[Fe_2(Cat)_4(H_2O)_2]\cdot 6H_2O$, a Catecholato-Bridged Dimer of Iron(III). *Inorg. Chem.* **1996**, *35*, 3568−3576.
(76) Greenwood, N. N.; Gibb, T. C. *Mössbauer Spectroscopy*; Chapman and Hall: London, 1971.
(77) Tauc, J. Optical Properties and Electronic Structure of Amorphous Ge and Si. *Mater. Res. Bull.* **1968**, *3*, 37−46.
(78) Kasap, S.; Koughia, C.; Singh, J.; Ruda, H.; O'Leary, S. Optical Properties of Electronic Materials: Fundamentals and Characterization. In *Springer Handbook of Electronic and Photonic Materials*; Kasap, S.; Capper, P., Eds.; Springer: New York, NY, 2006.
(79) Hush, N. S. Intervalence-Transfer Absorption. Part 2. Theoretical Considerations and Spectroscopic Data. In *Progress in Inorganic Chemistry*; Cotton, F. A., Ed.; Interscience Publishers: New York, NY, 1967; Vol. *8*.
(80) Hush, N. S. Homogeneous and Heterogeneous Optical and Thermal Electron Transfer. *Electrochim. Acta* **1968**, *13*, 1005−1023.
(81) Brunschwig, B. S.; Creutz, C.; Sutin, N. Optical Transitions of Symmetrical Mixed-Valence Systems in the Class II−III Transition Regime. *Chem. Soc. Rev.* **2002**, *31*, 168−184.
(82) Robin, M. B.; Day, P. Mixed Valence Chemistry—a Survey and Classification. In *Advances in Inorganic Chemistry and Radiochemistry*; Emeléus, H. J.; Sharpe, A. G., Eds.; Academic Press, 1968; Vol. *10*.
(83) Hünig, S.; Groβ, J.; Lier, E. F.; Quast, H. Two-Step Redox Systems, XII - Synthesis and Polarography of Quaternary Salts Derived from Phenanthrolines, 2,7-Diazapyrene and from Diazoniapentaphenes. *Liebigs Ann. Chem.* **1973**, *1973*, 339−358.
(84) Dou, J.-H.; Sun, L.; Ge, Y.; Li, W.; Hendon, C. H.; Li, J.; Gul, S.; Yano, J.; Stach, E. A.; Dincă, M. Signature of Metallic Behavior in the Metal−Organic Frameworks M_3(hexaiminobenzene)$_2$ (M = Ni, Cu). *J. Am. Chem. Soc.* **2017**, *139*, 13608−13611.
(85) Summers, L. A. Chemical Constitution and Activity of Bipyridylium Herbicides-II: Diquaternary Salts of 1,10-Phenanthroline. *Tetrahedron* **1968**, *24*, 5433−5437.
(86) Llunell, M.; Casanova, D.; Cicera, J.; Alemany, P.; Alvarez, S. *SHAPE*, version 2.1; Universitat de Barcelona: Barcelona, Spain, 2013.

https://dx.doi.org/10.1021/acs.chemmater.0c03132
Chem. Mater. XXXX, XXX, XXX−XXX

(87) Sheldrick, G. SHELXT - Integrated Space-Group and Crystal-Structure Determination. *Acta Crystallogr. A* **2015**, *71*, 3−8.
(88) Sheldrick, G. Crystal Structure Refinement with SHELXL. *Acta Crystallogr., Sect. C: Struct. Chem.* **2015**, *71*, 3−8.
(89) Hübschle, C. B.; Sheldrick, G. M.; Dittrich, B. ShelXle: A Qt Graphical User Interface for SHELXL. *J. Appl. Crystallogr.* **2011**, *44*, 1281−1284.
(90) Dolomanov, O. V.; Bourhis, L. J.; Gildea, R. J.; Howard, J. A. K.; Puschmann, H. OLEX2: A Complete Structure Solution, Refinement and Analysis Program. *J. Appl. Crystallogr.* **2009**, *42*, 339−341.
(91) Spek, A. L. PLATON SQUEEZE: A Tool for the Calculation of the Disordered Solvent Contribution to the Calculated Structure Factors. *Acta Crystallogr., Sect. C: Struct. Chem.* **2015**, *71*, 9−18.
(92) Spek, A. L. Structure Validation in Chemical Crystallography. *Acta Crystallogr., Sect. D: Biol. Crystallogr.* **2009**, *65*, 148−155.
(93) Wallwork, K. S.; Kennedy, B. J.; Wang, D. The High Resolution Powder Diffraction Beamline for the Australian Synchrotron. *AIP Conf. Proc.* **2007**, *879*, 879−882.
(94) Toby, B. H.; Von Dreele, R. B. GSAS-II: The Genesis of a Modern Open-Source All Purpose Crystallography Software Package. *J. Appl. Crystallogr.* **2013**, *46*, 544−549.
(95) Schmitt, B.; Brönnimann, C.; Eikenberry, E. F.; Gozzo, F.; Hörmann, C.; Horisberger, R.; Patterson, B. Mythen Detector System. *Nucl. Instrum. Methods Phys. Res., Sect. A* **2003**, *501*, 267−272.
(96) Sun, L.; Hendon, C. H.; Minier, M. A.; Walsh, A.; Dincă, M. Million-Fold Electrical Conductivity Enhancement in Fe_2(DEBDC) Versus Mn_2(DEBDC) (E = S, O). *J. Am. Chem. Soc.* **2015**, *137*, 6164−6167.

https://dx.doi.org/10.1021/acs.chemmater.0c03132
Chem. Mater. XXXX, XXX, XXX−XXX

Supporting Information for:

Tuning Charge-State Localization in a Semiconductive Iron(III)–Chloranilate Framework Magnet Using A Redox Active Cation

Martin P. van Koeverden,[†] Brendan F. Abrahams,[*,†] Deanna M. D'Alessandro,[‡] Patrick W. Doheny,[‡] Carol Hua,[†] Timothy A. Hudson,[†] Guy N. L. Jameson,[†,#] Keith S. Murray,[§] Wasinee Phonsri,[§] Richard Robson,[†] and Ashley L. Sutton[†]

*Email: bfa@unimelb.edu.au

[†] School of Chemistry, The University of Melbourne, Parkville, Victoria 3010, Australia
[‡] School of Chemistry, The University of Sydney, Sydney, New South Wales 2006, Australia
[#] Bio21 Molecular Science and Biotechnology Institute, Parkville, Victoria 3010, Australia
[§] School of Chemistry, Monash University, Clayton, Victoria 3800, Australia

Table of Contents

Experimental S3

Figure S1 Schlenk filtration procedure S5

Figure S2 Components of two-electrode screw cell S8

Table S1 Crystallographic data of **1a** S9

Table S2 Crystallographic data of **1b**, **2** and (PhenQ)Br_2 S12

Table S3 Average C–O and C−C bond lengths of $Clan^{n-}$ moieties in M−$Clan^{2-}$ compounds reported to date. S13

Table S4 Average C–O and C−C bond lengths of $Clan^{n-}$ moieties in M−$Clan^{2.67-}$ and M−$Clan^{3-\bullet}$ compounds reported to date. S21

Table S5 Average C–O and C−C bond lengths of $Clan^{n-}$ moieties in M−$Clan^{4-}$ compounds reported to date. S21

Table S6 Average Fe–O, and C–O and C–C bond lengths of $Clan^{n-}$ moieties in Fe–$Clan^{n-}$ compound reported to date. S22

Table S7 Ligand abbreviations used in **Table S3** through **Table S6** S24

Figure S3 Synchrotron P-XRD diffraction pattern of bulk **1a** S26

Figure S4 P-XRD diffraction patterns of bulk **2** S27

Figure S5 Interaction of the $PhenQ^{m+}$ cation with the anionic $[Fe_2(Clan)_3]^{x-}$framework S28

Figure S6 Alternating stacking of $PhenQ^{m+}$ with ligands in the $[Fe_2(Clan)_3]^{x-}$ sheets S29

Figure S7 Solvent-accessible void space in **1a** S30

Figure S8 Coordination environment Fe in **1a** and Zn in **2** S31

Figure S9 Arrangement of $\mathbf{L_1}$ and $\mathbf{L_2}$ ligands in anionic $[Fe_2(Clan)_3]^{2-}$ sheets S32

Figure S10 Bond lengths in $PhenQ^{2+}$ moieties S33

Figure S11 Temperature dependence of the cell parameters for **1a** S34

Figure S12 Temperature dependence of the average C–O and C–C bond lengths in **1a** S35
Extended Discussion on Solvent Exchange S36
Table S8 Analysis of the possible Fe coordination geometries in 1a and 1b S37
Figure S13 TGA of **1a**, **1b** and **2** S38
Figure S14 The Fe–Fe angles in the $[Fe_2(Clan)_3]^{2-}$ sheets S39
Figure S15 P-XRD diffraction patterns of bulk **1b** S40
Figure S16 Electron density difference ($F_O - F_C$) maps S41
Figure S17 ATR FT–IR spectra of **1a**, **1b** and **2** S44
Table S9 ^{57}Fe Mössbauer spectral parameters for **1b** S45
Figure S18 Diffuse reflectance UV-Vis-NIR spectrum of S46
Figure S19 Tauc analysis from UV-Vis-NIR spectrum of **1b** S47
Figure S20 Tauc analysis from UV-Vis-NIR spectrum of **2** S48
Figure S21 Deconvolution of diffuse reflectance UV-Vis-NIR spectrum of **1b** S49
Table S10 Spectral data for the deconvoluted spectrum of **1b** S50
Figure S22 X-band EPR spectrum of **1b** at room temperature S51
Figure S23 X-band EPR spectrum of **2** at room temperature S52
Figure S24 Solid-state cyclic voltammograms of **1b** S53
Figure S25 Inverse magnetic susceptibility ($1/\chi_M$) versus T for **1b** S54
Figure S26 Variable-temperature field-cooled magnetization of **1b** S55
Figure S27 Variable-temperature zero-field cooled and field-cooled dc magnetic susceptibility for **1b** S56
Figure S28 Variable-temperature ac magnetic susceptibility for **1b** S57
Figure S29 Temperature dependence of the out-of-phase ac susceptibility for **1b** S58
Figure S30 Magnetization isotherms of **1b** S59
Table S11 Measured transport properties of **1b** S60
Figure S31 Representative variable temperature current-bias plot for **1b** S61
Figure S32 Arrhenius fits of the variable temperature electrical conductivity for **1b** S62
References S63

Experimental

General Considerations

Unless overwise specified, all manipulations were performed under an atmosphere of dry dinitrogen (N_2) using standard Schlenk techniques or using a Vacuum Atmospheres glovebox. For crystallisation of (PhenQ)[Fe_2(Clan)$_3$]·yMeCN·$z$$H_2O$ (**1a**) and (PhenQ)[Zn_2(Clan)$_3$]·yMeCN·$z$$H_2O$ (**2**), acetonitrile (MeCN) was used without further purification. For solvent exchange on **1a** to form (PhenQ)[Fe_2(Clan)$_3$]·yDMF (**1b**), MeCN and *N*,*N*-dimethylformamide (DMF) were dried twice sequentially over activated 3 Å and 4 Å molecular sieves respectively then stored under at atmosphere of dry N_2. Immediately before use, dry DMF and MeCN were degassed by three freeze-pump-thaw cycles. Proton (^{1}H) and proton-decoupled carbon-13 (^{13}C{^{1}H}) NMR spectroscopy was performed using a Varian Unity spectrometer operating at 400 and 100 MHz respectively. All spectra were acquired at 25 °C. Proton (δ_H) and carbon-13 (δ_C) chemical shift values are reported in parts per million (ppm) downfield of external tetramethylsilane. ^{1}H- and ^{13}C{^{1}H}-NMR spectra were referenced to residual ^{1}H signals in the deuterated solvents and the solvent signal respectively, except for spectra acquired in D_2O which were referenced to the ^{1}H and ^{13}C signals of acetone (internal standard, δ_H 2.22; δ_C 215.94). Thermogravimetric analysis (TGA) was performed using a Mettler Toledo TGA/SDTA851e between 25 °C and 450 °C using a heating rate of 5 °C min^{-1} in a flow of N_2. Attenuated total internal reflectance (ATR) Fourier-transform infrared (FT-IR) spectra were recorded in air under ambient conditions using either a Bruker Alpha spectrometer fitted with a diamond ATR accessory, or a Perkin Elmer Spotlight 100 spectrometer fitted with a ZnSe Universal ATR accessory. Elemental analyses (CHN) of **1b** and **2** were performed at the Campbell Microanalytical Laboratory, University of Otago. For transport, a sample of **1b** was added to a dried ampoule in an N_2-filled glovebox, which was fitted with a sealable adapter. The ampoule was removed from the glovebox, purged on a Schlenk line, then flame-sealed under 1 atm of dry N_2.

3,6-Dichloro-1,2,4,5-tetrahydroxybenzene (H_4Clan)

H_4Clan was synthesised using a modified literature procedure.[1] In air, chloranilic acid (H_2Clan, 6.270 g, 30 mmol) was suspended in concentrated HCl (150 mL) then heated to 100 °C with stirring. Mossy tin (4.271 g, 36 mg-atom) was added portion wise over 5 minutes to the stirring red-orange suspension, causing gas evolution, and gradual bleaching of the solution. After 20 min., the clear pale-yellow reaction solution was hot filtered through glass fibre paper to remove traces of an insoluble tan residue and unreacted Sn, rinsing the reaction flask with additional hot concentrated HCl (2 × 20 mL). The clear filtrate was transferred to a flask fitted with a septum, purged with N_2 then cooled to rt. then 4 °C overnight. The product crystallised as white needles, which were isolated by suction filtration. The product was washed with ice-cold concentrated HCl (3 × 25 mL), then sucked dry and washed with ice-cold $CHCl_3$ (2 × 25 mL). The solid was dried *in vacuo* over KOH then P_2O_5, yielding the title compound as white to pale-tan needles (3.8505 g, 61.1%). The product is stable over several months when stored under dry N_2 at 4 °C. ^{13}C{^{1}H}-NMR (100 MHz, d_6-Acetone): δ_C 137.3, 110.5. FT-IR (ATR, cm^{-1}): 3281 (s, br); 1632 (w); 1541 (w); 1466 (s); 1327 (m); 1288 (m); 1148 (s); 961 (s); 920 (m); 861 (m); 821 (s); 713 (m); 608 (m).

5,6-Dihydropyrazino[1,2,3,4-*lmn*][1,10]phenanthrolindiium dibromide ([PhenQ]Br_2)

[PhenQ]Br_2 was synthesised according to a modified literature procedure.[2, 3] 1,10-Phenanthroline (10.813 g, 60 mmol, dried using toluene/H_2O azeotrope) was added to an oven dried round-bottom flask fitted with a reflux condenser and a $CaCl_2$ guard tube, then dissolved in 1,2-dibromoethane (300 mL). The reaction was placed in a thermostated oil bath (140 °C) and heated with stirring for 16 hrs. The reaction was then cooled to rt., and the precipitated yellow-orange powder isolated by suction filtration, rinsing the reaction flask with acetone (150 mL). The product was washed on the frit with additional acetone (2 × 200 mL) then dried by suction. The yellow crude (21.0681 g) was dissolved in the minimum of boiling 80% EtOH (ca. 340 mL), treated with decolourising charcoal then hot filtered. The filtrate was cooled to rt. then stored at −20 °C overnight, then the crystallised product was isolated by suction filtration, washing with ice-cold EtOH (2 × 50 mL), acetone (2 × 50 mL) then Et_2O (2 × 50 mL). The product was dried *in vacuo* over P_2O_5, yielding the title compound as orange-brown rods (14.14 g, 64.0 %). ^{1}H-NMR (400 MHz, D_2O): δ_H 9.64 (d, *J* = 5.8 Hz, 2H, Ar-***H***2,9), 9.54 (d, *J* = 8.5 Hz, 2H, Ar-***H***4,7), 8.72 (s, 2H, C***H***=C***H***), 8.61 (dd, J = 5.8, 8.5 Hz, 2H, Ar-***H***3,6), 5.73 (s, 4H, C***H***$_2$). ^{13}C{^{1}H}-NMR (100 MHz, D_2O): δ_C 149.2, 148.8, 132.5, 130.6, 129.7, 128.2, 53.0. FT-IR (ATR, cm^{-1}): 2934 (w, br); 1635 (w); 1591 (m) 1556 (m); 1499 (w); 1474 (m); 1449 (w); 1418 (m); 1395 (w); 1360 (w); 1340 (w); 1241 (w); 1224 (w); 1151 (w); 1121 (w); 1030 (w); 1010 (w); 935 (m); 866 (s); 769 (w); 713 (m); 695 (s).

5,6-Dihydropyrazino[1,2,3,4-*lmn*][1,10]phenanthrolindiium dinitrate ([PhenQ]$(NO_3)_2$)

[PhenQ]Br_2 was converted to [PhenQ]$(NO_3)_2$ using anion exchange chromatography. IRA-400(Cl) anion exchange resin (150 mL, 210 meq.) was cleaned by heating (60 °C) in H_2O (300 mL) for 30 min. The supernatant was decanted, the resin rinsed with additional H_2O (3 × 300 mL) then swollen overnight in 1 M NaOH solution (500 mL). The supernatant was then decanted, and the resin was resuspended in 1 M NaOH (500 mL) then transferred to a column and eluted with additional 1 M NaOH solution (750 mL) until the eluate was strongly basic. The resin was then eluted with H_2O (500 mL) until the eluate was ca. pH 7, then converted to the NO_3^- form by eluting with 1 M HNO_3 (1000 mL) until then the eluate was strongly acidic, followed by H_2O (1000 mL) until the eluate was ca. pH 7. A solution of [PhenQ]Br_2 (3.70 g, 10 mmol) in H_2O (25 mL) was loaded onto the column, which was then eluted with H_2O, collecting 100 mL fractions. Product fractions (tested by monitoring development of intense red colour when an aliquot was added to aqueous sodium dithionite solution; tested negative to $AgNO_3$) were combined and concentrated to dryness at reduced pressure (60 mbar, 50 °C) to a crystalline brownish-orange solid. The product was dried *in vacuo* over P_2O_5 yielding the title compound as brownish-red crystals (2.97 g, 88.9 %). FT-IR (ATR, cm^{-1}): 3042 (w); 3009 (w); 1753 (w); 1637 (w); 1622 (w); 1595 (m); 1557 (m); 1500 (m); 1478 (w); 1448 (w); 1431 (w); 1334 (s, NO_3^- ν_{N-O}); 1320 (s, NO_3^- ν_{N-O}); 1232 (m); 1205 (m); 1173 (w); 1123 (w); 1033 (w); 1009 (w); 937 (m); 863 (s); 825 (m, NO_3^- γ_{N-O}); 770 (w); 716 (m); 702 (s); 617 (w).

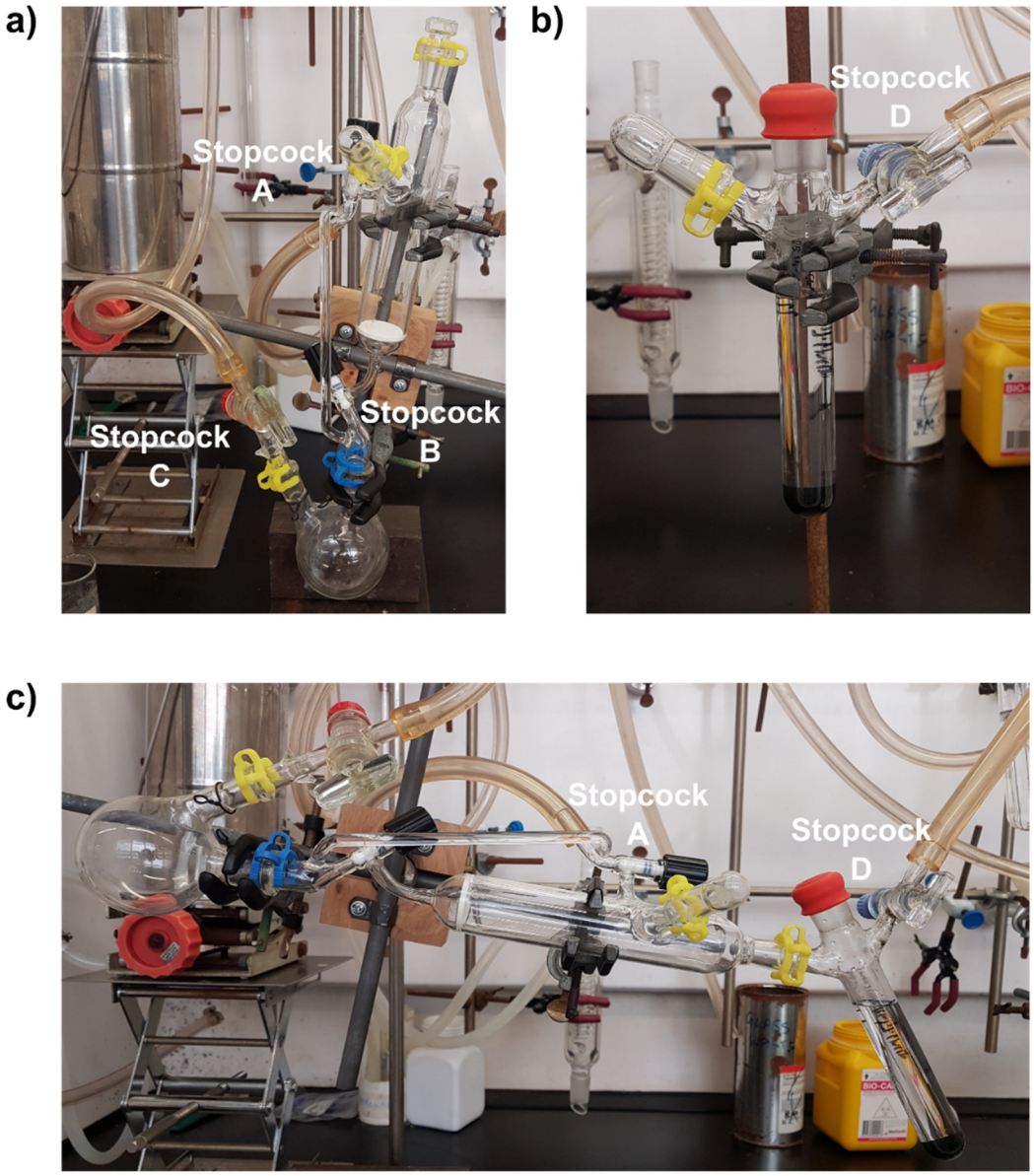


Figure S1 Schlenk filtration procedure for isolation of **1b** under inert atmosphere conditions. a) Flame-dried Schlenk frit and receiver flask under dry N_2 atmosphere. After degassing the apparatus, Stopcock B is closed, and Stopcocks A & C are opened to N_2. b) Two-neck Schlenk tube fitted with septum used for solvent exchange on as-synthesised **1a** to yield **1b**. Schlenk tube contains **1b** (black solid) suspended in dry, deoxygenated DMF. c) With Stopcocks A & D open to N_2, the Schlenk frit and two-neck Schlenk tube are joined with a brisk current of N_2 flowing from the opened joints.

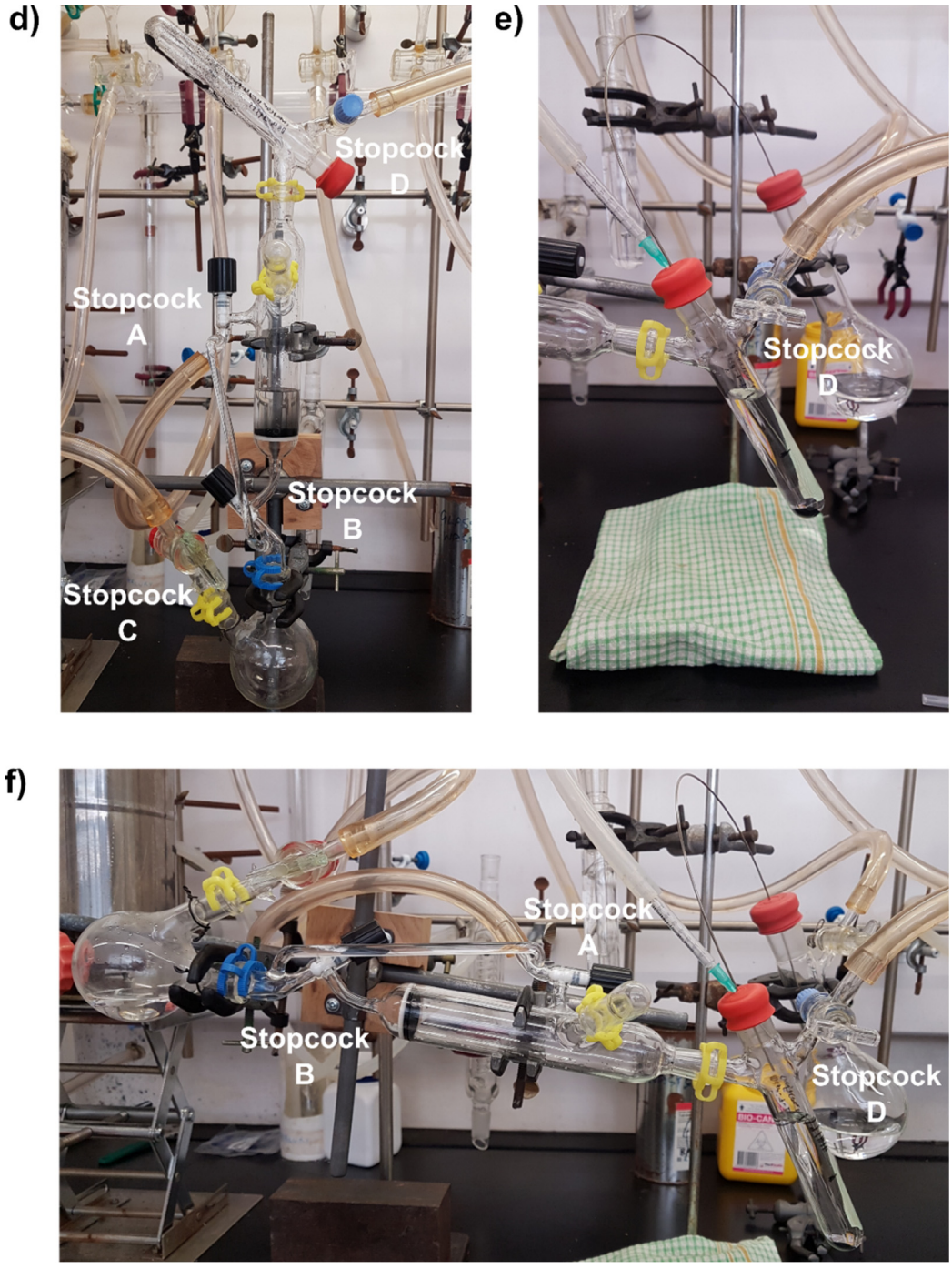


Figure S1(cont.) d) With Stopcock B closed and Stopcocks A & D open to N_2, transfer of the solid **1b** from the Schlenk tube onto the frit is accomplished by rotating the apparatus. Note, adherent solid in Schlenk tube. The solid is isolated by placing the receiver flask under static vacuum: with Stopcock B closed, dynamic vacuum is briefly applied to the receiver flask through Stopcock C, which is then closed. With Stopcocks A & D open to N_2, Stopcock B is slowly opened, causing suction of the solvent into the receiver flask. e) and f) Washing of the product on the frit and transfer of adherent solids in the two-neck tube is performed by cannula transfer of dry, deoxygenated DMF with stopcocks A, B & D closed; the apparatus is vented via mineral oil bubbler. Stopcocks A & D are then opened to N_2 and the cannula removed. Washing of product on the frit and transfer of adherent solids is accomplished by repeating d). Cannula transfer of fresh solvent and washing is performed three times total.

(PhenQ)[Zn_2(Clan)$_3$]·*y*MeCN·*z*H_2O (2)

Crystallisation of **2** was performed similarly to **1a** using $Zn^{II}(NO_3)_2·6H_2O$ and $[PhenQ](NO_3)_2$ with workup in air. Use of $[PhenQ]Br_2$ lead to crystallisation of **2** contaminated with a copious white solid, presumably a tetrabromidozincate(II) species. Workup and isolation of the crystalline solids was performed without protection from air. In brief, in air, a solution of $Zn^{II}(NO_3)_2·6H_2O$ (59.5 mg, 0.2 mmol), $[PhenQ](NO_3)_2$ (132.9 mg, 0.4 mmol) and $LiOAc·2H_2O$ (10.2 mg, 0.1 mmol) in H_2O (4 mL) was carefully layered below a solution of H_4Clan (63.30 mg, 0.3 mmol) in MeCN (10 mL) in a soda glass vial (OD = 25 mm), with a buffer layer of 1:1 v/v MeCN/H_2O (4 mL). Two reactions were performed in parallel to produce bulk product. Brownish-maroon plate crystals suitable for SC-XRD were visible on the vial walls within two days, in addition to a fine precipitate on the vial bottom. After 7 days, the crystalline product was dislodged from the vial walls and the crystalline product allowed to sediment. The supernatant liquid was carefully decanted, and the combined products washed by resuspending in 2:1 v/v MeCN/H_2O (3 × 20 mL), sedimentation of the crystalline solids and decantation of the supernatant. The product was then washed with MeCN (3 × 20 mL) using a similar procedure, then isolated by suction filtration, washing on the frit with additional MeCN (20 mL), then dried by suction to a free-flowing solid to yield **2** as a brownish-maroon powder (31.2 mg, 15.5 % based upon H_4Clan). FT–IR (ATR, cm^{-1}): 3392 (w, br), 3072 (w); 3056 (w), 3004 (w), 1629 (w); 1592 (w) 1474 (s); 1375 (s); 1295 (w); 1256 (w); 1173 (w); 1122 (w); 1033 (w); 996 (m); 938 (m); 845 (s); 769 (m); 713 (m); 697 (s); 602 (m); 575 (s); 480 (s). Anal. Calcd. for $(C_{14}H_{12}N_2)(Zn_2Cl_6O_{12}C_{18})·0.34(C_2H_3N)·1.82(H_2O)$: C, 38.99 %; H, 1.67 %, N, 3.25 %. Found: C, 38.99 %; H, 1.46 %: N, 3.25 %.

Bond Length Analysis

Tabulation of the range of C–O, C–C and Fe–O bond lengths in *M*–Clan^{n-} compounds was performed by analysis of crystallographic data published within the Cambridge Crystallographic Database (CSD) as of 29th July 2019. Only structures which contained at least one bridging Clan^{n-} ligand, and coordination of a bridging Clan^{n-} to at least one transition metal were considered in the analysis; for structures which contain both bridging and terminal Clan^{n-} ligands, their respective C–O and C–C bond lengths have been tabulated separately. Structures which exhibited R_1 values greater than 0.1 were excluded from the analysis to avoid bias from poorly refined crystallographic models. The data were then classified based upon the Clan^{n-} valence state, either Clan^{2-} (Table S3), Clan$^{3-\bullet}$ (Table S4) or Clan^{4-} (Table S5) by considering the valence states of the metals and other ligands in the compound, then sorted according to the dimensionality of the compound. Where error values on C–O, C–C and Fe–O bond lengths are given, these represent the standard deviation of averaged crystallographically inequivalent bonds in each Clan^{n-} species in the compounds; were no error values are given, this is an indication the respective C–O, C–C and Fe–O bonds in the compound ae crystallographically equivalent.

Variable Temperature Electrical Conductivity

In an N_2-filled glovebox, the screw cells (Figure S2) were constructed by placing two copper dies (*D* = 3.0 mm) polished to a mirror finish, into a snugly fitting borosilicate tube (ID = 3.0 mm). The tube was then held within a 3D printed PLA cell holder, and the copper dies compressed by two brass screws threaded through the cell holder. The blank cell length was

measured using a calliper, then the cells disassembled and a sample of compound **1b** placed into the glass tube. The pressed pellets were formed *in situ* under anaerobic conditions by compressing the sample between the polished copper dies by tightening the brass screws in the PLA sample holder. The sample thickness was then measured using a calliper.

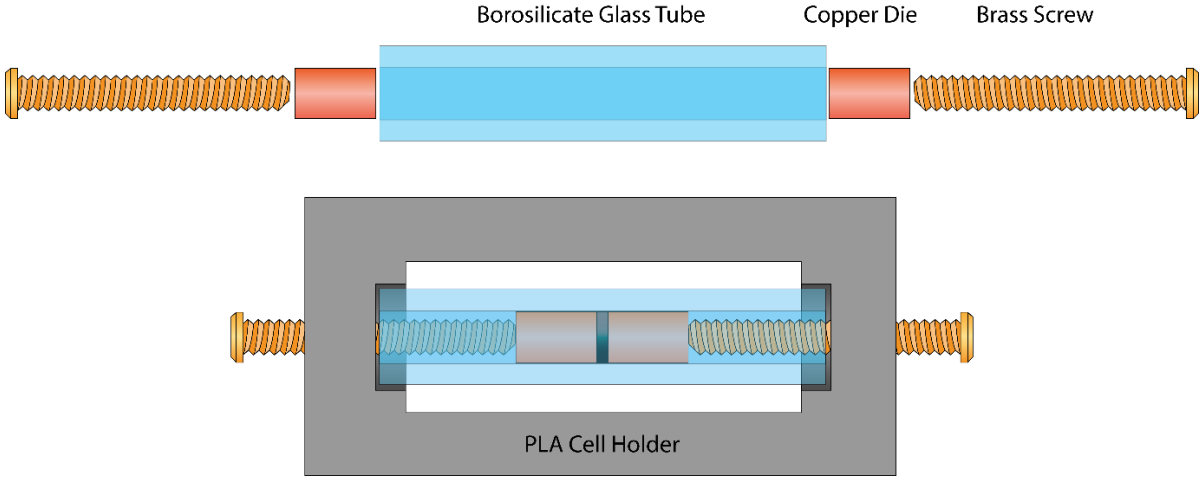


Figure S2 (Top) components of two-electrode screw cell. (Bottom) Assembled two electrode screw cell containing sample (black, **1b**) pressed between copper dies, held in PLA cell holder. NB: Not to scale.

For ambient temperature conductivity measurements within the glovebox, the brass screws were connected by alligator clip-equipped copper wires to an Ossila X100 (Sheffield, UK) source-measure unit (SMU) interfaced to home-built software. The sample cells were shielded from light, and all current-voltage (*I*-*V*) curves measured were Ohmic over the potential window ± 0.55 V. For variable temperature electrical conductivity measurements, the screw cells were sealed with dry, deoxygenated sealing wax to ensure an airtight seal. The cells were then removed from the glovebox and placed into a home-built thermostated N_2-purged sample chamber allowing variable temperature measurements on two cells in parallel. The temperature was controlled to ± 1 K in the range 220–300 K in 5 K steps by regulating the flowrate of cold and hot dry N_2 gas into the sample chamber. The screw cells were connected to the SMU via alligator clip-equipped copper cables and BNC cables, and *I*-*V* curves were measured over the potential window ± 0.55 V in 0.01 V steps. The resulting linear *I*-*V* curves (confirming Ohmic behaviour) were fitted with Ohm's law,

$$J = \sigma E \tag{1}$$

where J (A cm^{-2}) is the current density, E (V cm^{-1}) is the electric field strength, and σ (S cm^{-1}) is the sample conductivity. The temperature dependence of the conductivity was modelled using the Arrhenius equation,

$$\sigma = \sigma_0 \exp\left(\frac{E_a}{\mathrm{k}_B T}\right) \tag{2}$$

were σ_0 (S cm^{-1}) is the pre-exponential, E_a (eV) is the activation energy, k_B (8.617333 × 10^{-5} eV K^{-1}) is the Boltzmann constant, and T (K) is temperature.

Table S1 Crystallographic data of **1a** measured at several temperatures.

T **/ K**	**100**	**120**	**140**
Empirical formula	$C_{20.25}H_{18.68}N_{3.13}O_{9.15}Cl_3Fe$	$C_{20.25}H_{18.68}N_{3.13}O_{9.15}Cl_3Fe$	$C_{20.25}H_{18.68}N_{3.13}O_{9.15}Cl_3Fe$
Formula weight	614.41	614.41	614.41
Habit	Block	Block	Block
Crystal system	Monoclinic	Monoclinic	Monoclinic
Space group	*C*2/*m*	*C*2/*m*	*C*2/*m*
a / Å	13.1251(3)	13.1358(2)	13.1493(2)
b / Å	24.2830(6)	24.2759(5)	24.2588(5)
c / Å	8.4943(2)	8.5142(2)	8.5331(2)
α / °	90	90	90
β / °	101.541(2)	101.524(2)	101.485(2)
γ / °	90	90	90
V / Å^3	2652.54(11)	2660.30(9)	2667.44(9)
Z	4	4	4
ρ_{calc} / g cm^{-3}	1.539	1.534	1.530
μ / mm^{-1}	7.823	7.800	7.779
F_{000}	1249.0	1249.0	1249.0
Crystal size / mm^3	0.191 × 0.175 × 0.151	0.191 × 0.175 × 0.151	0.191 × 0.175 × 0.151
Radiation	Cu Kα (λ = 1.54184 Å)	Cu Kα (λ = 1.54184 Å)	Cu Kα (λ = 1.54184 Å)
2θ range	7.28 to 148.94	7.282 to 148.878	7.288 to 148.994
Index ranges	$-16 \le h \le 13$ $-26 \le k \le 30$ $-10 \le l \le 10$	$-16 \le h \le 13$ $-26 \le k \le 30$ $-10 \le l \le 10$	$-16 \le h \le 13$ $-26 \le k \le 30$ $-10 \le l \le 10$
Total/independent reflections	13377/2768 [R_{int} = 0.0417, R_{sigma} = 0.0244]	13429/2775 [R_{int} = 0.0413, R_{sigma} = 0.0246]	13427/2786 [R_{int} = 0.0441 R_{sigma} = 0.0249]
Data/restraints/ parameters	2768/89/132	2775/89/132	2786/91/132
Goodness-of-fit on F^2	1.075	1.081	1.095
Final *R* indexes [$I \ge 2\sigma(I)$]	R_1 = 0.0457, wR_2 = 0.1433	R_1 = 0.0454, wR_2 = 0.1440	R_1 = 0.0455, wR_2 = 0.1426
Final *R* indexes [all data]	R_1 = 0.0470, wR_2 = 0.1446	R_1 = 0.0469, wR_2 = 0.1455	R_1 = 0.0470, wR_2 = 0.1443
Largest diff. peak/hole / e Å^{-3}	0.44/−0.83	0.45/−0.81	0.41/−0.81

$R_1 = \sum \| F_O | - | F_C \| / \sum | F_O | ; wR_2 = \left[\sum w(F_O^2 - F_C^2)^2 / \sum w(F_O^2)^2 \right]^{1/2} ; w = 1 \Big/ \left[\sigma^2 \left(F_O^2 \right) + (\mathbf{A}P)^2 + \mathbf{B}P \right]$

$; P = \left(\left(F_O^2, 0 \right)_{\max} + 2F_C^2 \right) \Big/ 3$

NB: The empirical formula includes the contribution of disordered MeCN and H_2O molecules in the channels of **1a**.

Table S1 (cont.) Crystallographic data of **1a** measured at several temperatures.

T **/ K**	**160**	**180**	**200**
Empirical formula	$C_{20.25}H_{18.68}N_{3.13}O_{9.15}Cl_3Fe$	$C_{20.25}H_{18.68}N_{3.13}O_{9.15}Cl_3Fe$	$C_{20.25}H_{18.68}N_{3.13}O_{9.15}Cl_3Fe$
Formula weight	614.41	614.41	614.41
Habit	Block	Block	Block
Crystal system	Monoclinic	Monoclinic	Monoclinic
Space group	*C*2/*m*	*C*2/*m*	*C*2/*m*
a / Å	13.1668(2)	13.1854(2)	13.2064(2)
b / Å	24.2424(4)	24.2230(4)	24.1996(4)
c / Å	8.5559(2)	8.58290(10)	8.6108(2)
α / °	90	90	90
β / °	101.457(2)	101.449(2)	101.449(2)
γ / °	90	90	90
V / Å^3	2676.58(9)	2686.74(7)	2697.16(9)
Z	4	4	4
ρ_{calc} / g cm^{-3}	1.525	1.519	1.513
μ / mm^{-1}	7.752	7.723	7.693
F_{000}	1249.0	1249.0	1249.0
Crystal size / mm^3	0.191 × 0.175 × 0.151	0.191 × 0.175 × 0.151	0.191 × 0.175 × 0.151
Radiation	Cu Kα (λ = 1.54184 Å)	Cu Kα (λ = 1.54184 Å)	Cu Kα (λ = 1.54184 Å)
2θ range	7.294 to 148.984	7.298 to 149.002	7.306 to 148.994
Index ranges	$-16 \le h \le 13$ $-26 \le k \le 30$ $-10 \le l \le 10$	$-16 \le h \le 13$ $-26 \le k \le 30$ $-10 \le l \le 10$	$-16 \le h \le 13$ $-26 \le k \le 30$ $-10 \le l \le 10$
Total/independent reflections	13508/2794 [R_{int} = 0.0428, R_{sigma} = 0.0255]	13567/2796 [R_{int} = 0.0500, R_{sigma} = 0.0285]	13694/2807 [R_{int} = 0.0551, R_{sigma} = 0.0315]
Data/restraints/ parameters	2794/89/132	2796/89/132	2807/89/132
Goodness-of-fit on F^2	1.069	1.095	1.104
Final *R* indexes [$I \ge 2\sigma(I)$]	R_1 = 0.0463, wR_2 = 0.1464	R_1 = 0.0480, wR_2 = 0.1541	R_1 = 0.0486, wR_2 = 0.1568
Final *R* indexes [all data]	R_1 = 0.0477, wR_2 = 0.1482	R_1 = 0.0494, wR_2 = 0.1559	R_1 = 0.0504, wR_2 = 0.159
Largest diff. peak/hole / e Å^{-3}	0.51/−0.79	0.56/−0.84	0.60/−0.77

$R_1 = \sum \| F_O | - | F_C \| / \sum | F_O | ; wR_2 = \left[\sum w(F_O^2 - F_C^2)^2 / \sum w(F_O^2)^2 \right]^{1/2} ; w = 1 \Big/ \left[\sigma^2 \left(F_O^2 \right) + (\mathbf{A}P)^2 + \mathbf{B}P \right]$

$; P = \left(\left(F_O^2, 0 \right)_{\max} + 2F_C^2 \right) \Big/ 3$

NB: The empirical formula includes the contribution of disordered MeCN and H_2O molecules in the channels of **1a**.

Table S1 (cont.) Crystallographic data of **1a** measured at several temperatures.

T **/ K**	**220**	**240**	**260**
Empirical formula	$C_{20.25}H_{18.68}N_{3.13}O_{9.15}Cl_3Fe$	$C_{20.25}H_{18.68}N_{3.13}O_{9.15}Cl_3Fe$	$C_{20.25}H_{18.68}N_{3.13}O_{9.15}Cl_3Fe$
Formula weight	614.41	614.41	614.41
Habit	Block	Block	Block
Crystal system	Monoclinic	Monoclinic	Monoclinic
Space group	*C*2/*m*	*C*2/*m*	*C*2/*m*
a / Å	13.2270(2)	13.2545(2)	13.2757(5)
b / Å	24.1863(3)	24.1592(4)	24.1385(7)
c / Å	8.6448(2)	8.6860(2)	8.7049(3)
α / °	90	90	90
β / °	101.431(2)	101.426(2)	101.389(4)
γ / °	90	90	90
V / Å^3	2710.72(8)	2726.29(9)	2734.60(16)
Z	4	4	4
ρ_{calc} / g cm^{-3}	1.506	1.497	1.492
μ / mm^{-1}	7.655	7.611	7.588
F_{000}	1249.0	1249.0	1249.0
Crystal size / mm^3	0.191 × 0.175 × 0.151	0.191 × 0.175 × 0.151	0.191 × 0.175 × 0.151
Radiation	Cu Kα (λ = 1.54184 Å)	Cu Kα (λ = 1.54184 Å)	Cu Kα (λ = 1.54184 Å)
2θ range	7.31 to 149.008	7.318 to 148.808	7.324 to 149
Index ranges	$-16 \le h \le 13$ $-26 \le k \le 30$ $-10 \le l \le 10$	$-16 \le h \le 13$ $-26 \le k \le 30$ $-10 \le l \le 10$	$-16 \le h \le 13$ $-26 \le k \le 30$ $-10 \le l \le 10$
Total/independent reflections	13762/2818 [R_{int} = 0.0621, R_{sigma} = 0.0340]	13818/2839 [R_{int} = 0.0617, R_{sigma} = 0.0344]	13800/2846 [R_{int} = 0.0645, R_{sigma} = 0.0361]
Data/restraints/ parameters	2818/89/132	2839/89/132	2846/89/132
Goodness-of-fit on F^2	1.101	1.092	1.060
Final *R* indexes [$I \ge 2\sigma(I)$]	R_1 = 0.0511, wR_2 = 0.1599	R_1 = 0.0523, wR_2 = 0.1651	R_1 = 0.0542, wR_2 = 0.1675
Final *R* indexes [all data]	R_1 = 0.0535, wR_2 = 0.1632	R_1 = 0.0552, wR_2 = 0.1690	R_1 = 0.0582, wR_2 = 0.1724
Largest diff. peak/hole / e Å^{-3}	0.58/−0.74	0.62/−0.71	0.70/−0.66

$R_1 = \sum \| F_O | - | F_C \| / \sum | F_O | ; wR_2 = \left[\sum w(F_O^2 - F_C^2)^2 / \sum w(F_O^2)^2 \right]^{1/2} ; w = 1 \Big/ \left[\sigma^2 \left(F_O^2 \right) + (\mathbf{A}P)^2 + \mathbf{B}P \right]$

$; P = \left(\left(F_O^2, 0 \right)_{\max} + 2F_C^2 \right) \Big/ 3$

NB: The empirical formula includes the contribution of disordered MeCN and H_2O molecules in the channels of **1a**.

Table S2 Crystallographic data of **1b**, **2** and (PhenQ)Br_2.

Compound	(PhenQ)[Fe_2(Clan)$_3$]·4.4DMF (**1b**)	(PhenQ)[Zn_2(Clan)$_3$]·4.5MeCN·6.5H_2O (**2**)	(PhenQ)Br_2
Empirical formula	$C_{22.6}H_{21.4}N_{3.2}O_{8.2}Cl_3Fe$	$C_{20.5}H_{19.25}N_{3.25}O_{9.25}Cl_3Zn$	$C_{14}H_{12}N_2Br_2$
Formula weight	631.23	630.86	368.08
Habit	Plate	Plate	Rod
T / K	240.00(10)	99.9(5)	99.99(10)
Crystal system	Monoclinic	Monoclinic	Triclinic
Space group	$C2/m$	$C2/m$	$P\bar{1}$
a / Å	13.3813(4)	13.3133(2)	7.5127(2)
b / Å	23.8969(4)	24.3499(4)	8.0997(3)
c / Å	8.7982(2)	8.49560(10)	11.1124(4)
α / °	90	90	104.027(3)
β / °	100.210(3)	101.916(2)	102.584(2)
γ / °	90	90	93.101(2)
V / Å^3	2768.86(12)	2694.74(7)	636.18(4)
Z	4	4	2
ρ_{calc} / g cm^{-3}	1.514	1.555	1.921
μ / mm^{-1}	7.485	4.48	7.926
F_{000}	1288.0	1280.0	360.0
Crystal size / mm^3	0.213 × 0.124 × 0.044	0.214 × 0.142 × 0.034	0.327 × 0.078 × 0.067
Radiation	Cu Kα (λ = 1.54184 Å)	Cu Kα (λ = 1.54184 Å)	Cu Kα (λ = 1.54184 Å)
2θ range	7.398 to 148.984	7.26 to 148.998	8.446 to 150.554
Index ranges	$-16 \le h \le 15$ $-14 \le k \le 29$ $-10 \le l \le 10$	$-16 \le h \le 10$ $-30 \le k \le 30$ $-10 \le l \le 10$	$-9 \le h \le 8$ $-10 \le k \le 10$ $-13 \le l \le 13$
Total/independent reflections	12015/2906 [R_{int} = 0.0289, R_{sigma} = 0.0254]	14431/2821 [R_{int} = 0.0248, R_{sigma} = 0.0160]	13193/2612 [R_{int} = 0.0278, R_{sigma} = 0.0173]
Data/restraints/ parameters	2906/89/132	2821/89/132	2612/0/163
Goodness-of-fit on F^2	1.085	1.081	1.102
Final R indexes [$I \ge 2\sigma(I)$]	R_1 = 0.0366, wR_2 = 0.1084	R_1 = 0.0543, wR_2 = 0.1871	R_1 = 0.0199, wR_2 = 0.0503
Final R indexes [all data]	R_1 = 0.0409, wR_2 = 0.1113	R_1 = 0.0556, wR_2 = 0.1884	R_1 = 0.0203, wR_2 = 0.0505
Largest diff. peak/hole/ e Å^{-3}	0.36/-0.23	0.57/−1.22	0.34/−0.45

$R_1 = \sum \| F_o | - | F_c \| / \sum | F_o | ; wR_2 = \left[\sum w(F_o^2 - F_c^2)^2 / \sum w(F_o^2)^2 \right]^{1/2} ; w = 1 \Big/ \left[\sigma^2 \left(F_o^2 \right) + (\mathbf{A}P)^2 + \mathbf{B}P \right]$

$; P = \left(\left(F_o^2, 0 \right)_{\max} + 2F_c^2 \right) \Big/ 3$

NB: The empirical formulas includes the contribution of disordered DMF in the channels of **1b** and MeCN and H_2O molecules in the channels of **2**.

Table S3 Average C–O and C−C bond lengths of Clan^{n-} moieties in *M*−Clan^{2-} compounds reported to date.

Compound	CCDC Ref. Code	Average C–O / Å	Average C–C / Å	Clan^{n-} Charge State	Dimen.	R_1	Ref.
$[Cu^{II}_2(pmdeta)_2(\mu\text{-Clan})](BPh_4)_2$	PMECAC	1.250(7)	1.543	2−	0	6.1	4
$[Ni^{II}_2(tren)_2(\mu\text{-Clan})](BPh_4)_2$	CATRNI	1.258(7)	1.536	2−	0	5.9	4
$[\mu\text{-tpy})_2(\mu\text{-Clan})](PF_6)_2$	FUWWUP	1.255(1)	1.535	2−	0	5.4	5
$[Rh^{I}_2(cod)_2(\mu\text{-Clan})]$	LAHSES	1.270(13)	1.520	2−	0	6.24	6
$[\mu 2,2'\text{-bpy})_2(\mu\text{-Clan})](PF_6)_2$	WIDBAM	1.262(1)	1.520	2−	0	3.26	7
$[Rh^{III}_2(CO)_2Me_2I_2(\mu\text{-Clan})]$	TENVUD	1.268(1)	1.522	2−	0	4.09	8
$[Mn^{II}_2(tpa)_2(\mu\text{-Clan})](ClO_4)_2$	GIVTIO	1.256(1); 1.252(1)	1.525; 1.542	2−	0	5.55	9
$[Cu^{II}_2(Me_3tacn)_2(\mu\text{-Clan})](ClO_4)_2$	QABCEB	1.260(9)	1.531	2−	0	5.21	10
$[Fe^{III}_2(H_2O)_2(Clan)_2(\mu\text{-Clan})]\cdot 4H2O$	QOCHEV	1.260(6); 1.257(33)[a]	1.530; 1.530(2)[a]	2−	0	4.54	11
$[Sc^{III}_2(H_2O)_6(Clan)_2(\mu\text{-Clan})]\cdot 10H2O$	MOBBEK	1.272(16); 1.251(7);[a] 1.264(16)[a]	1.522(14); 1.543(5);[a] 1.530(23)[a]	2−	0	5.6	12
$[Zn^{II}_4(\mu\text{-LPy})(\mu\text{-Clan})_2](ClO_4)_2\cdot 4MeCN$	EGATEL	1.245(4); 1.254(4)	1.533(5); 1.524(9)	2−	0	6	13
$[Yb^{III}_2(HBpz_3)_4(\mu\text{-Clan})]\cdot 3CH_2Cl_2$	OBIBEH	1.251(2)	1.537	2−	0	3.15	14
$[Cu^{II}_2(tpy)_2(dmso)_2(\mu\text{-Clan})]$ $[Cu^{II}(Clan)_2(dmso)_2]$	ERAQIX	1.257(2); 1.251(25)[a]	1.530; 1.522(11)[a]	2−	0	6.39	15
$[Os^{II}_2(pap)_2(PPh_3)_4(\mu\text{-Clan})](ClO_4)_2$	XALFEW	1.279(3)	1.502	2−	0	4.57	16
$[Co^{II}_2(tpa)_2(\mu\text{-Clan})](BF_4)_2\cdot 2MeOH$	REMREH	1.256(1)	1.528	2−	0	5.45	17
$[Co^{III}_2(tpa)_2(\mu\text{-Clan})](BF_4)_4\cdot MeCN$	NIBKAL	1.263(12)	1.507	2−	0	6.41	18
$[Fe^{II}_2(tpa)_2(\mu\text{-Clan})](BF_4)_2\cdot 2MeOH$	NIBKEP	1.261(10)	1.528	2−	0	4.64	18
$[Ir^{III}_2Cp^{*}_2Cl_2(\mu\text{-Clan})]\cdot 2CH_2Cl_2$	YOHQIW	1.271(6)	1.516	2−	0	2.77	19
$[Ir^{III}_2Cp^{*}_2(Br\text{-ppy})_2(\mu\text{-Clan})]$ $(CF_3SO_3)_2\cdot CH_2Cl_2$	YOHQOC	1.259(15)	1.511(14)	2−	0	8.61	19
$[Ir^{III}_4Cp^{*}_4(\mu\text{-pyz})_2(\mu\text{-Clan})_2]$ $(CF_3SO_3)_4\cdot PhMe\cdot CH_2Cl_2\cdot 1.5MeOH\cdot H_2O$	YOHQUI	1.265(14); 1.280(10)	1.543(2); 1.526(4)	2−	0	6.51	19
$[Ir^{III}_4Cp^{*}_4(\mu\text{-}4,4'\text{-bpy})_2(\mu\text{-Clan})_2]$ $(CF_3SO_3)_4\cdot PhMe$	YOHRAP	1.265(9); 1.269(15)	1.522(21); 1.532(22)	2−	0	5.66	19
$[Ir^{III}_4Cp^{*}_4(\mu\text{-}4,4'\text{-bpe})_2(\mu\text{-Clan})_2]$ $(CF_3SO_3)_4$	YOHRET	1.257(6)	1.497(8)	2−	0	5.9	19
$[Re^{I}_4(CO)_{12}(\mu\text{-}4,4'\text{-bpy})_2(\mu\text{-Clan})_2]\cdot$ mesitylene	DOMDOZ	1.268(9)	1.522(10)	2−	0	6.3	20

[a] Terminal mono-coordinating

Table S3(cont.) Average C–O and C–C bond lengths of Clan^{n-} moieties in *M*–Clan^{2-} compounds reported to date.

Compound	CCDC Ref. Code	Average C–O / Å	Average C–C / Å	Clan^{n-} Charge State	Dimen.	R_1	Ref.
$[Cu^{II}_2\{(Meim)_2\text{-prop}\}_2Cl_2(\mu\text{-Clan})]\cdot 8MeCN\cdot 2H_2O$	EFETUF	1.261(2)	1.530	2−	0	2.99	21
$[Rh^{III}_2Cp^*_4(\mu\text{-}4,4'\text{-bpy})_2(\mu\text{-Clan})_2](CF_3SO_3)_4$	EGAQOT	1.263(14)	1.520(13)	2−	0	9.64	22
$[Ru^{III}_2(Cy)_4(\mu\text{-}4,4'\text{-bpy})_2(\mu\text{-Clan})_2](CF_3SO_3)_4\cdot 2PhMe\cdot 2H_2O$	EGAQUZ	1.266(11)	1.499(7)	2−	0	6.19	22
$[Ru^{III}_4(Cy)_4(\mu\text{-}4,4'\text{-bpe})_2(\mu\text{-Clan})_2](CF_3SO_3)_4$	EGARAG	1.255(16)	1.510(4)	2−	0	6.26	22
$[Ru^{III}_4(C_6Me_6)_4(\mu\text{-}4,4'\text{-bpe})_2(\mu\text{-Clan})_2](CF_3SO_3)_4\cdot 2Et_2O\cdot 2Acetone$	IHIGIQ	1.267(5)	1.514(2)	2−	0	3.19	23
$[(V^{IV}O)_2Cl_2(2,2'\text{-bpy})_2(\mu\text{-Clan})]$	SONYIE	1.260(1)	1.525	2−	0	4.46	24
$[Re^{I}_4(CO)^{12}(\mu\text{-TXyBim})(\mu\text{-Clan})_2]$	EHUREF	1.277(13)	1.505(8)	2−	0	5.07	25
$[Cu^{II}_2(tpa)_2(\mu\text{-Clan})](ClO_4)_2\cdot 4MeOH$	MIRTIS	1.260(20)	1.538	2−	0	3.72	26
$[Re^{I}_2(CO)_6(\mu\text{-dppOb})(\mu\text{-Clan})]\cdot PhMe$	QIJQOR	1.261(8)	1.500(9)	2−	0	7.9	27
$[Re^{I}_6(CO)_{18}\{\mu\text{-}(SMeBim)_3\text{-Mes}\}_2(\mu\text{-Clan})_2]\cdot 4PhMe$	TENDIB	1.270(15); 1.269(10)	1.502; 1.535(7)	2−	0	5.2	28
$[Re^{I}_2(CO)_6(\mu\text{-BXyTBim})(\mu\text{-Clan})]$	FOVXUL	1.265(2)	1.507	2−	0	6.27	29
$[Rh^{III}_4Cp^*_4(\mu\text{-}\{Rh^{III}Cp^*(pdt)\}_2(\mu\text{-Clan})_2](CF_3SO_3)_4\cdot 2MeOH\cdot Et_2O$	MOSSOE	1.264(12)	1.533(5)	2−	0	6.04	30
$[Ir^{III}_4Cp^*_4(\mu\text{-}\{Ir^{III}Cp^*(pdt)\}_2(\mu\text{-Clan})_2](CF_3SO_3)_4\cdot 2MeOH\cdot Et_2O$	MOSSUK	1.275(12)	1.506(8)	2−	0	5.66	30
$(4,4'\text{-bpyH}_2)[Cu^{II}_2(Clan)_2(H_2O)_2(\mu\text{-Clan})]\cdot 2H_2O$	UQUYUC	1.261; 1.258(25)[b]	1.522; 1.530(24)[b]	2−	0	3.56	31
$[Rh^{III}_2Cp^*_2(H_2O)_2(\mu\text{-Clan})](CF_3SO_3)_2$	AWUSIW	1.261(2)	1.516	2−	0	4.11	32
$[Rh^{III}_8Ag^{I}_2Cp^*_8(meoh)_4(CF_3SO_3)_2(\mu\text{-pym})_4(\mu\text{-Clan})_4](CF_3SO_3)_4\cdot 2H_2O$	AWUSUI	1.259(11); 1.256(3)	1.535(7); 1.530(9)	2−	0	6.58	32
$[Rh^{III}_8Ag^{I}_2Cp^*_8(\mu\text{-pym})_4(\mu\text{-Clan})_4](CF_3SO_3)_6\cdot p\text{-xylene}\cdot 12MeOH\cdot 4H_2O$	AWUTIX	1.271(6); 1.261(5)	1.514(5); 1.521(5)	2−	0	5.9	32
$[Rh^{III}_4Cp^*_4(\mu\text{-4-pbdy})_2(\mu\text{-Clan})_2](CF_3SO_3)_4\cdot 0.67{}^{i}Pr_2O$	KEFZUT	1.257(15); 1.261(7); 1.263(4)	1.518(4); 1.521(2); 1.515(22)	2−	0	9.74	33
$[Ir^{III}_4Cp^*_4(\mu\text{-4-pbdy})_2(\mu\text{-Clan})_2](CF_3SO_3)_4$	KEGBAC	1.280(23); 1.268(5); 1.272(24)	1.540(1); 1.498(32); 1.513(10)	2−	0	8.93	33
$[Rh^{III}_8Pd^{II}_2Cp^*_8(\mu\text{-pyz})_2(\mu\text{-}4,4'\text{-bpyOHama})_4(\mu\text{-Clan})_2](CF_3SO_3)_4(NO_3)_4\cdot 12MeOH\cdot 2Et_2O\cdot 12H_2O$	MEKCOX	1.270(12)	1.523(6)	2−	0	6.44	34

[b] Terminal mono-coordinating

Table S3(cont.) Average C–O and C–C bond lengths of Clan^{n-} moieties in *M*–Clan^{2-} compounds reported to date.

Compound	CCDC Ref. Code	Average C–O / Å	Average C–C / Å	Clan^{n-} Charge State	Dimen.	R_1	Ref.
$[Ni^{II}_2(py)_6Cl_2(\mu\text{-Clan})]$	PAXFUS	1.253(1); 1.255(2)	1.534; 1.534	2−	0	3.26	35
$[Mn^{II}_2(py)_6Cl_2(\mu\text{-Clan})]$	PAXGAZ	1.249; 1.250(1)	1.539; 1.542	2−	0	3.28	35
$[Dy^{III}_2(HBpz_3)_4(\mu\text{-Clan})]\cdot 2CH_2Cl_2$	DEKTOF	1.257(2)	1.538	2−	0	3.35	36
$[Dy^{III}_2(HBpz_3)_4(\mu\text{-Clan})]\cdot 2CH_2Cl_2$	DEKTOF01	1.255(8)	1.551	2−	0	3.99	37
$[Dy^{III}_2(HBpz_3)_4(\mu\text{-Clan})]\cdot 2CH_2Cl_2$	DEKTOF02	1.261(4)	1.536	2−	0	3.88	38
$[Y^{III}_2(HBpz_3)_4(\mu\text{-Clan})]\cdot 2CH_2Cl_2$	DEKTUL	1.233(15)	1.516	2−	0	4.54	36
$[Y^{III}_2(HBpz_3)_4(\mu\text{-Clan})]\cdot 2CH_2Cl_2$	DEKTUL01	1.248(1)	1.540	2−	0	4.78	37
$[Y^{III}_2(HBpz_3)_4(\mu\text{-Clan})]\cdot 2$Acetone	DEKVAT	1.255(3)	1.539	2−	0	3.38	36
$[Re^{I}_2(CO)_6(POPh_3)(\mu\text{-Clan})]$	GIHFEL	1.273(4)	1.496	2−	0	5.16	39
$[Re^{I}_2(CO)_6(POPh_3)(\mu\text{-Clan})]$	GIHFEL01	1.275(4)	1.493	2−	0	4.97	40
$[Ir^{III}_4Cp^{*}_4(\mu\text{-}\{Ir^{III}Cp^{*}(dapz)\})_2(\mu\text{-Clan})_2](CF_3SO_3)_4\cdot 6MeOH\cdot H_2O$	GIBSOC	1.265(14)	1.511(16)	2−	0	5.39	41
$[Ir^{III}_4Cp^{*}_4(\mu\text{-}\{Ir^{III}Cp^{*}Cl(dhqox)\})_2(\mu\text{-Clan})_2](CF_3SO_3)_2\cdot 4MeOH$	GIBSUI	1.258(6)	1.520(11)	2−	0	3.23	41
$[Re^{I}_2(CO)_6(\mu\text{-BPNim})(\mu\text{-Clan})]\cdot$PhMe	JEWJUT	1.259(9)	1.549	2−	0	5.15	42
$[Tb^{III}_2(HBpz_3)_4(\mu\text{-Clan})]\cdot 2CH_2Cl_2$	LEPNIG	1.255(1)	1.535	2−	0	4.05	37
$[Gd^{III}_2(HBpz_3)_4(\mu\text{-Clan})]\cdot 2CH_2Cl_2$	LEPNOM	1.226(8)	1.532	2−	0	9.33	37
$[Gd^{III}_2(HBpz_3)_4(\mu\text{-Clan})]\cdot 2CH_2Cl_2$	LEPNOM01	1.260(1)	1.537	2−	0	3.31	38
$[Rh^{III}_4Cp^{*}_4(\mu\text{-}\{Cu^{II}_2(\mu\text{-}^{t}Buacac_2\text{-py})_2\})_2(\mu\text{-Clan})_2](CF_3SO_3)_4\cdot$Corannulene$\cdot 9MeOH\cdot 7H_2O$	VETLAK	1.260(11); 1.255(5)	1.520(5); 1.528(1)	2−	0	5.98	43
$[Ir^{III}_4Cp^{*}_4(\mu\text{-3-pbdy})_2(\mu\text{-Clan})_2](CF_3SO_3)_4\cdot 11MeOH\cdot 5H_2O$	WIGFIE	1.278(37); 1.313(50)	1.490(15); 1.538(40)	2−	0	7.37	44
$[Re^{I}_2(CO)_6(\mu\text{-BPOPh}_2\text{-7-TH})(\mu\text{-Clan})]$	VIKSUG	1.283(10)	1.489(16)	2−	0	5.64	45
$[Ir^{III}_4Cp^{*}_4(\mu\text{-bpyeyan})_2(\mu\text{-Clan})_2](CF_3SO_3)_4\cdot 4^{i}Pr_2O\cdot 5MeOH\cdot 5H_2O$	BOFSUN	1.275(20); 1.284(26); 1.259(16); 1.271(13)	1.508(9); 1.505(15); 1.481(12); 1.528(6)	2−	0	9.7	46
$[Cu^{II}(H_2O)_2(\mu\text{-Clan})]\cdot H_2O$	VOMNAM	1.266(18)	1.530(1)	2−	1	4.8	47
$[Cu^{II}(meoh)_2(\mu\text{-Clan})]$	HESKIZ	1.260(2)	1.530	2−	1	2.9	48
$[Cu^{II}(dcmb)(\mu\text{-Clan})]$	NACKEH	1.253(16)	1.537	2−	1	3.05	49
$[Mn^{II}(2,2'\text{-bpy})(\mu\text{-Clan})]$	RAZJIL	1.254(3); 1.255(2)	1.540; 1.544	2−	1	3.57	50

Table S3(cont.) Average C–O and C–C bond lengths of Clan^{n-} moieties in *M*–Clan^{2-} compounds reported to date.

Compound	CCDC Ref. Code	Average C–O / Å	Average C–C / Å	Clan^{n-} Charge State	Dimen.	R_1	Ref.
$[Cu^{II}(H_2O)_2(\mu\text{-Clan})]\cdot phz$	TINPOV	1.258(17)	1.532	2−	1	2.7	51
$[Cu^{II}(H_2O)(\mu\text{-Clan})\cdot ohphz$	TINQAI	1.272	1.559	2−	1	3.4	51
$[Fe^{II}(H_2O)_2(\mu\text{-Clan})]\cdot H_2O$	KIQJID	1.257(1)	1.523	2−	1	4.5	52
$[Fe^{II}(H_2O)_2(\mu\text{-Clan})]\cdot H_2O$	KIQJID01	1.259	1.53	2−	1	3.15	11
$[Co^{II}(H_2O)_2(\mu\text{-Clan})]\cdot H_2O$	KIQJOJ	1.258(1)	1.523	2−	1	2.7	52
$[Mn^{II}(H_2O)_2(\mu\text{-Clan})]\cdot H_2O$	KIQJUP	1.257(5)	1.527	2−	1	4.5	52
$[Mn^{II}(H_2O)_2(\mu\text{-Clan})]\cdot H_2O$	KIQJUP02	1.260(3)	1.537	2−	1	0.99	53
$[Fe^{II}(H_2O)_2(\mu\text{-Clan})]\cdot phz$	KIQKAW	1.262(13)	1.522	2−	1	2.3	52
$[Co^{II}(H_2O)_2(\mu\text{-Clan})]\cdot phz$	KIQKEA	1.256(8)	1.537	2−	1	3.1	52
$[Mn^{II}(H_2O)_2(\mu\text{-Clan})]\cdot phz$	KIQKIE	1.258(5)	1.534	2−	1	3	52
$[Cd^{II}(H_2O)_2(\mu\text{-Clan})]\cdot H_2O$	QOCHAR	1.254(2)	1.543	2−	1	2.43	11
$[Mn^{II}(tpy)(\mu\text{-Clan})]$	NEHZAB	1.253(3); 1.254(1)	1.535; 1.535	2−	1	5.15	54
$[Cu^{II}_2(tpy)_2(\mu\text{-Clan})][Cu^{II}(Clan)_2]$	ERAQET	1.244(29); 1.248(32)[c]	1.550; 1.540(23)[c]	2−	1	6.28	15
$[Cd^{II}(1,10\text{-phen})(\mu\text{-Clan})]$	FAHPIO	1.250(7); 1.248	1.540; 1.542	2−	1	4.56	55
$[Sn^{IV}Me_2(dmso)(\mu\text{-Clan})]\cdot DMSO$	URUJIB	1.253(1)	1.530(7)	2−	1	4.27	56
$[Sn^{IV}nBu_2(dmso)(\mu\text{-Clan})]$	URUJOH	1.253(4); 1.250(9)	1.519; 1.534	2−	1	5.08	56
$[Sn^{IV}Ph_2(dmso)(\mu\text{-Clan})]\cdot DMSO$	URUJUN	1.259(6)	1.527(6)	2−	1	1.96	56
$[U^{VI}O_2(H_2O)(\mu\text{-Clan})]\cdot bpym\cdot 4H_2O$	GEPZOS	1.268(11); 1.275(1)	1.527; 1.540	2−	1	3.4	57
$[Mn^{II}(2,2'\text{-bpy})(\mu\text{-Clan})]\cdot 2EtOH$	LERTOT	1.257(2)	1.543(2)	2−	1	3.7	58
$[Fe^{II}(tren(imid)_3)]_2[Mn^{II}Cr^{III}Cl_2(Clan)(\mu\text{-Clan})_2]Cl\cdot MeOH\cdot 3CH_2Cl_2\cdot 0.5MeCN$	HOWHUY	1.264(20); 1.258(23); 1.256(29)	1.518(12); 1.537(15); 1.533(20)	2−	1	8.12	59
$[Mn^{II}(etoh)_2(\mu\text{-Clan})]$	NIXSAQ	1.260(5)	1.541	2−	1	3.23	60
$[Cu^{II}(imid)_2(\mu\text{-Clan})]$	UQUTEH	1.251(6); 1.252(4)	1.536; 1.536(4)	2−	1	3.53	31
$[Cu^{II}(etoh)_2(\mu\text{-Clan})]$	UQUYOW	1.257(2)	1.546(2)	2−	1	4.79	31
$[Cu^{II}(mecn)(\mu\text{-Clan})]$	UQUZAJ	1.264(4)	1.526(2)	2−	1	4.44	31
$[Cu^{II}(H_2O)_2(\mu\text{-Clan})]$	UQUZEN	1.263(11)	1.533	2−	1	7.3	31

[c] Terminal mono-coordinating

Table S3(cont.) Average C–O and C–C bond lengths of Clan^{n-} moieties in *M*–Clan^{2-} compounds reported to date.

Compound	CCDC Ref. Code	Average C–O / Å	Average C–C / Å	Clan^{n-} Charge State	Dimen.	R_1	Ref.
(4,4′-bpyH)$_2$[Mn$^{II}_2$(μ-Clan)$_3$]·2H$_2$O	PAXGED	1.257(5);[d] 1.251(15)[e]	1.535;[d] 1.529(10)[e]	2−	1[f]	4.55	35
[Mn^{II}(1,10-phen)(μ-Clan)]·EtOH	PAXHAA	1.253(3); 1.250(1)	1.540; 1.531	2−	1	5.51	35
[Co^{II}(2,2'-bpy)(μ-Clan)]·EtOH	PAXHEE	1.256(2)	1.531	2−	1	4.37	35
[Mn^{II}(4-ppy)$_2$(μ-Clan)]	TAZSEV	1.253(11)	1.546	2−	1	7.11	61
[Zn^{II}(py)$_2$(μ-Clan)]·Acetone	TAZVEY	1.252(5); 1.259(1)	1.537; 1.559	2−	1	5.15	62
[Cd^{II}(meoh)$_2$(μ-Clan)]	TEBCOV	1.256(11)	1.549	2−	1	3.64	63
[Mn^{II}(tpa)(μ-Clan)]·MeOH	BEPJAK	1.249(2); 1.254(3)	1.541; 1.539	2−	1	5.55	64
(Me$_4$N)$_2$[Fe^{II}Cl$_2$(μ-Clan)]	VEXGOX[g]	1.256(11)	1.523	2−	1	7.27	65
[Pr$^{III}_2$(etoh)$_6$(μ-Clan)$_3$]·2EtOH	CAZZAE	1.248; 1.251(1); 1.239(13)	1.527; 1.530; 1.522	2−	2	2.5	66
[Ca^{II}(H$_2$O)$_2$(μ-H$_2$O)(μ-Clan)]·H$_2$O	FIYKUT	1.255(2)	1.536	2−	2	3.07	67
[Y$^{III}_2$(H$_2$O)$_6$(μ-Clan)$_3$]·6.6H$_2$O	GASMUI	1.254(13); 1.252(1); 1.256(1)	1.524; 1.536; 1.536	2−	2	4.45	68
[Cu^{II}(μ-pyz)(μ-Clan)]	HESKEV	1.257(24)	1.537	2−	2	2	48
[Mn$^{II}_2$(H$_2$O)$_2$(μ-2,2′-bpym)(μ-Clan)$_2$]· 2EtOH·2H$_2$O	NEHZEF	1.251(4); 1.253(4)	1.535; 1.539	2−	2	4.01	54
[Co^{II}(μ-pyz)(μ-Clan)]	HUHPAB	1.263(5)	1.534	2−	2	4.69	69
[Mn^{II}(μ-pyz)(μ-Clan)]	HUHPEF	1.255(6)	1.536	2−	2	2.15	69
[La$^{III}_2$(H$_2$O)$_4$(μ-H$_2$O)$_2$(μ-Clan)$_3$]·7H$_2$O	MIZYAV	1.252(5); 1.262(1)	1.531(4); 1.525	2−	2	3.98	12
[Pr$^{III}_2$(H$_2$O)$_6$(μ-Clan)$_3$]·12H$_2$O	MIZYID	1.256(1); 1.254(13); 1.261	1.527; 1.550; 1.544	2−	2	8.42	12
[Tb$^{III}_2$(H$_2$O)$_6$(μ-Clan)$_3$]·12H$_2$O	MIZYUP	1.257(9); 1.255(9); 1.258(10)	1.529; 1.519; 1.529	2−	2	4.82	12
[Ce$^{III}_2$(H$_2$O)$_6$(μ-Clan)$_3$]·12H$_2$O	MIZZAW	1.254(3); 1.262	1.532; 1.534	2−	2	3.4	12

[d] Bridging bis-bidendate
[e] Bridging mono- and bi-dendate
[f] 1D ladder-like chain
[g] Structure at T = 250 K

Table S3(cont.) Average C–O and C–C bond lengths of Clan^{n-} moieties in *M*–Clan^{2-} compounds reported to date.

Compound	CCDC Ref. Code	Average C–O / Å	Average C–C / Å	Clan^{n-} Charge State	Dimen.	R_1	Ref.
$[Ce^{III}_2(H_2O)_6(\mu\text{-Clan})_3]\cdot 12H_2O$	MIZZAW01	1.258(11); 1.250(8); 1.255(4)	1.530; 1.533; 1.538	2−	2	3.68	12
$[Y^{III}_2(H_2O)_6(\mu\text{-Clan})_3]\cdot 10H_2O$	MIZZEA	1.253(16); 1.253(5); 1.256(1)	1.528; 1.533; 1.529	2−	2	3.96	12
$[Gd^{III}_2(H_2O)_6(\mu\text{-Clan})_3]\cdot 10H_2O$	MIZZIE	1.253(16); 1.256(3); 1.256(1)	1.530; 1.530; 1.518	2−	2	2.35	12
$(H_3O)_2(phz)_3[Cu^{II}_2(\mu\text{-Clan})_3]\cdot$ 2Acetone$\cdot 2H_2O$	SAJBEL	1.248	1.537	2−	2	5.22	70
$(H_3O)_2(phz)_3[Cu^{II}_2(\mu\text{-Clan})_3]$	SAJBIP	1.253	1.531	2−	2	4.72	70
$(H_3O)_2(phz)_3[Cd^{II}_2(\mu\text{-Clan})_3]\cdot$ 2Acetone$\cdot 2H_2O$	SAJBOV	1.247	1.540	2−	2	4.77	70
$(H_3O)_2(phz)_3[Zn^{II}_2(\mu\text{-Clan})_3]\cdot$ 2Acetone$\cdot 2H_2O$	SAJBUB	1.249	1.546	2−	2	5.98	70
$(H_3O)_2(phz)_3[Co^{II}_2(\mu\text{-Clan})_3]\cdot$ 2Acetone$\cdot 2H_2O$	SAJCAI	1.259	1.526	2−	2	6.69	70
$(Et_4N)_2[Ca^{II}Sn^{IV}(\mu\text{-Clan})_4]$	BAKBAS	1.257(17)	1.539(16)	2−	2	1.82	71
$(Et_4N)_2[Ca^{II}Sn^{IV}(\mu\text{-Clan})_4]\cdot CS_2$	BAKBEW	1.253(21)	1.539(14)	2−	2	3.64	71
$(Et_4N)_2[Ca^{II}Sn^{IV}(\mu\text{-Clan})_4]\cdot$ 2MeCN$\cdot 0.5H_2O$	BAKBIA	1.261(22)	1.531(17)	2−	2	3.55	71
$(Et_4N)_2[Ca^{II}Sn^{IV}(\mu\text{-Clan})_4]\cdot$ 2Acetone$\cdot 2H_2O$	BAKBOG	1.259(21)	1.543(13)	2−	2	2.87	71
$(H_3O)_2(phz)_3[Mn^{II}_2(\mu\text{-Clan})_3]\cdot$ 2Acetone$\cdot 2H_2O$	VEQDUS[h]	1.253	1.545	2−	2	5.66	72
$(H_3O)_2(phz)_3[Mn^{II}_2(\mu\text{-Clan})_3]\cdot$ 2Acetone$\cdot 2H_2O$	VEQDUS01[i]	1.252	1.541	2−	2	4.94	72
$(H_3O)_2(phz)_3[Mn^{II}_2(\mu\text{-Clan})_3]\cdot$ 2Acetone$\cdot 2H_2O$	VEQDUS02[j]	1.259	1.537	2−	2	4.86	72
$[Eu^{III}_2(H_2O)_2(2,2'\text{-bpym})_2(\mu\text{-Clan})_3]\cdot$ 4EtOH	GEPZUY	1.257(4); 1.258(7); 1.258(1)	1.540; 1.535; 1.551	2−	2	2.55	73
$[Gd^{III}_2(H_2O)_6(\mu\text{-Clan})_3]\cdot 2EtOH$	GEQBAH	1.271; 1.243(10)	1.543; 1.550	2−	2	6.64	74
$[Gd^{III}_2(H_2O)_6(\mu\text{-Clan})_3]\cdot 2(2,2'\text{-bpym})\cdot$ $6H_2O$	GEQBEL	1.253(7); 1.252(2)	1.528(6); 1.553	2−	2	2.79	75

[h] Structure at room temperature (T = 283–303 K)

[i] Structure at T = 200 K

[j] Structure at T = 150 K

Table S3(cont.) Average C–O and C−C bond lengths of Clan^{n-} moieties in *M*−Clan^{2-} compounds reported to date.

Compound	CCDC Ref. Code	Average C–O / Å	Average C–C / Å	Clan^{n-} Charge State	Dimen.	R_1	Ref.
$(H_3O)(phz)_3[Mn^{II}Cr^{III}(\mu\text{-Clan})_3]$	MIRFEA	1.277(20)	1.459(23)	2−	2	5.59	76
$[Fe^{III}(sal_2\text{-trien})][Mn^{II}Cr^{III}(\mu\text{-Clan})_3]\cdot 5MeCN\cdot MeOH\cdot 0.5CH_2Cl_2\cdot 0.5H_2O$	HOWHAE	1.259(18); 1.262(7)	1.547; 1.527(16)	2−	2	9.35	59
$[Fe^{III}(acac_2\text{-trien})][Mn^{II}Cr^{III}(\mu\text{-Clan})_3]\cdot 2MeCN$	MUMKUC	1.266(22); 1.269(15)	1.530(11); 1.529(13)	2−	2	4.41	77
$(EtPh_3P)_2[KFe^{III}(\mu\text{-Clan})3]\cdot 2DMF$	QUJJOW	1.255(23); 1.263(25); 1.257(21)	1.544(19); 1.553(12); 1.540(9)	2−	2	5.79	78
$(H_3O)(phz)_3[Fe^{II}Fe^{III}(\mu\text{-Clan})_3]\cdot 13H_2O$	QEFPOJ	1.268	1.529	2−	2	3.81	79
$(Et_3NH)[Mn^{II}Cr^{III}(\mu\text{-Clan})_3]$	SEQCID	1.264(27)	1.527(15)	2−	2	6.89	80
$(Et_4N)_2[Zn^{II}_2(\mu\text{-Clan})_3]\cdot 24H_2O$	XARDEC	1.249	1.543	2−	2	6.88	1
$[Er^{III}_2(H_2O)_6(\mu\text{-Clan})_3]\cdot 10H_2O$	NIGNEZ	1.253(17); 1.266(15); 1.271(2)	1.537; 1.521; 1.535	2−	2	4.95	81
$[Er^{III}_2(dmac)_4(\mu\text{-Clan})_3]$	NIGNOJ	1.254(18); 1.250(32); 1.260(8)	1.533(35); 1.554(6); 1.567(23)	2−	2	6.19	81
$[Er^{III}_2(fm)_6(\mu\text{-Clan})_3]\cdot 4FM\cdot 2H_2O$	NIGNUP	1.252(12); 1.253(2); 1.259(16)	1.539; 1.540; 1.540	2−	2	3.41	81
$[Er^{III}_2(dmf)_6(\mu\text{-Clan})_3]$	NIGPAX	1.251(4); 1.250(1)	1.540; 1.553(2)	2−	2	4.04	81
$[Er^{III}_2(dmso)_4(\mu\text{-Clan})_3]\cdot 2DMSO\cdot 2H_2O$	NIGQIG	1.262(10); 1.254(1); 1.258(18)	1.530; 1.541; 1.547	2−	2	4.08	81
$(Et_4N)_2[Mn^{II}_2(\mu\text{-Clan})_3]\cdot x$DMF	NIHQED	1.254	1.555	2−	2	6.8	82
$(Et_4N)_2[Co^{II}_2(\mu\text{-Clan})_3]\cdot x$DMF	NIHQUT	1.275	1.537	2−	2	7.89	83
$(^nPr_4N)_2[Fe^{III}_2(\mu\text{-Clan})_3]\cdot 2Acetone\cdot H_2O$	SIQPIU[k]	1.259(3)	1.536(2)	2−	2	4.44	84
$(^nPr_4N)_2[Fe^{II}Fe^{III}(\mu\text{-Clan})_3]\cdot 2Acetone\cdot H_2O$	SIQPIU01[l]	1.258(2); 1.266(2)	1.530(2); 1.518(5)	2−	2	5.98	84
$Na(Me_4N)[Mn^{II}_2(\mu\text{-Clan})_3]\cdot 5.5THF\cdot MeCN$	CIXNUV	1.249	1.516	2−	2	13.05	82
$(Me_4N)_2[Mn^{II}_2(\mu\text{-Clan})_3]\cdot 3.2Et_2O$	CIXPEH	1.248	1.538	2−	2	7.5	82
$(Et_4N)[Bi^{III}(\mu\text{-Clan})_2]\cdot 1.5Acetone$	QOFBEV	1.243	1.560	2−	2	4.42	85
$(Me_4N)[Sc^{III}(\mu\text{-Clan})_2]$	QOFBIZ	1.248	1.529	2−	2	6.8	85

[k] Structure at $T = 100$ K

Table S3(cont.) Average C–O and C−C bond lengths of Clan^{n-} moieties in *M*−Clan^{2-} compounds reported to date.

Compound	CCDC Ref. Code	Average C–O / Å	Average C–C / Å	Clan^{n-} Charge State	Dimen.	R_1	Ref.
$(Et_4N)[Y^{III}(\mu\text{-Clan})_2]$	QOFBOF	1.258	1.528	2−	2	17.35	85
$(Et_4N)[Y^{III}(\mu\text{-Clan})_2]\cdot 1.87I_2$	QOFBUL	1.259	1.514	2−	2	5.28	85
$(Et_4N)[Y^{III}(\mu\text{-Clan})_2]\cdot 0.91Br_2$	QOFCAS	1.255	1.552	2−	2	6.88	85
$(Et_4N)[Dy^{III}(\mu\text{-Clan})_2]\cdot$1.5Acetone	QOFCEW	1.259	1.544	2−	2	3.3	85
$(Et_4N)[Sc^{III}(\mu\text{-Clan})_2]\cdot$Acetone	QOFMUW	1.260	1.547	2−	2	5.67	85
$(Et_4N)[Gd^{III}(\mu\text{-Clan})_2]\cdot$Acetone	QOFNAD	1.254	1.541	2−	2	2.98	85
$(Et_4N)[Yb^{III}(\mu\text{-Clan})_2]\cdot$Acetone	QOFNEH	1.247	1.545	2−	2	2.87	85
$(Et_4N)[In^{III}(\mu\text{-Clan})_2]\cdot$1.5Acetone	QOFNIL	1.259	1.549	2−	2	3.69	85
$(Et_4N)[Er^{III}(\mu\text{-Clan})_2]\cdot$Acetone	QOFNOR	1.252	1.547	2−	2	2.9	85
$(Et_4N)[Y^{III}(\mu\text{-Clan})_2]\cdot$Acetone	QOFNUX	1.254	1.545	2−	2	2.21	85
$(Et_4N)[Tb^{III}(\mu\text{-Clan})_2]\cdot$1.5Acetone	QOFPAF	1.248	1.542	2−	2	4.56	85
$(Et_4N)[Lu^{III}(\mu\text{-Clan})_2]\cdot$1.5Acetone	QOFPEJ	1.254	1.553	2−	2	2.91	85
$(Et_4N)[Ho^{III}(\mu\text{-Clan})_2]\cdot$1.5Acetone	QOFPIN	1.255	1.541	2−	2	2.95	85
$[Ag^{I}_2(\mu\text{-Clan})]$	RORQOE	1.243(4)	1.553	2−	3	2.3	86
$(H_3O)[Y^{III}(\mu\text{-Clan})_2]\cdot$8MeOH	MOBBIO	1.264(17)	1.547	2−	3	8.08	12
$[Th^{IV}(H_2O)_2(\mu\text{-Clan})_2]\cdot 4H_2O$	MOBBOU	1.256(13); 1.263(9)	1.512; 1.524	2−	3	4.85	12
$(^{n}Bu_4N)_2[Mn^{II}(\mu\text{-Clan})_3]\cdot$8MeOH	OWIVEW	1.252	1.679	2−	3	9.54	87
$(MeEt_3N)[Na(dmf)][NaFe^{III}(\mu\text{-Clan})_3]$	QUJKOX	1.258(23); 1.258(26); 1.258(25)	1.534(18); 1.535(19); 1.539(20)	2−	3	4.13	78
$[Zn^{II}(bix)(\mu\text{-Clan})]\cdot 2H_2O$	TEBDIQ	1.248(16); 1.253(2)	1.547; 1.544	2−	3	4.38	88
$[Zn^{II}(4,4'\text{-bpy})(\mu\text{-Clan})]$	TEBDUC	1.252(1)	1.544	2−	3	5.62	89

[1] Structure at T = 241 K

Table S4 Average C–O and C−C bond lengths of Clan^{n-} moieties in *M*−Clan$^{2.67-}$ and *M*−Clan$^{3-\bullet}$ compounds reported to date.

Compound	CCDC Ref. Code	Average C–O / Å	Average C–C / Å	Clan^{n-} Charge State	Dimen.	R_1	Ref.
$(Me_2NH_2)_2[Fe^{III}_2(\mu\text{-Clan})_3]\cdot 6DMF\cdot 2H_2O$	ZACDAL	1.280	1.48	2.67−	2	9.54	90
$(Et_4N)_2[Fe^{III}_2(\mu\text{-Clan})_3]\cdot 20H_2O$	XARDIG	1.284	1.491	2.67−	2	5.31	1
$[Co_2(triphos)_2(\mu\text{-Clan})](BF_4)_2\cdot 2$Acetone	RAFKOY	1.316(5)	1.441	3−	0	5.05	91
$[Co_2(triphos)_2(\mu\text{-Clan})]_2(Co^{II}Cl_4)\cdot 1.6Et_2O\cdot$MeOH	FAYMOH	1.312	1.452	3−	0	7.03	92
$[Co^{II}_2(tpa)_2(\mu\text{-Clan})]BF_4\cdot 2Et_2O$	REMRIL	1.293(11)	1.473	3−	0	4.69	17
$[Co^{III}_2(tpa)_2(\mu\text{-Clan})](BF_4)_3\cdot 4$MeCN	NIBJUE	1.312(5)	1.457	3−	0	4.36	18
$(Me_4N)_2[Fe^{III}Cl_2(\mu\text{-Clan})]$	VEXGOX01[m]	1.291(6)	1.466	3−	1	6.53	65
$(Cp_2Co)_{1.43}(Me_2NH_2)_{1.57}[Fe^{III}_2(\mu\text{-Clan})_3]\cdot 4.9$DMF	GEFKAG	1.297	1.431	3−	2	12.22	93
$(^n Pr_4N)_2[Fe^{III}_2(\mu\text{-Clan})_3]\cdot 2$Acetone$\cdot H_2O$	SIQPIU[n]	1.297(2); 1.293(3)	1.468(3); 1.472	3−	2	4.44	84
$(^n Pr_4N)_2[Fe^{III}_2(\mu\text{-Clan})_3]\cdot 2$Acetone$\cdot H_2O$	SIQPIU01[o]	1.294(3)	1.469	3−	2	5.98	84
$Na_3(Me_4N)_2[Mn^{II}_2(\mu\text{-Clan})_3]\cdot 3.9$THF	CIXPAD	1.290	1.408	3−	2	15.3	82

Table S5 Average C–O and C−C bond lengths of Clan^{n-} moieties in *M*−Clan^{4-} compounds reported to date.

Compound	CCDC Ref. Code	Average C–O / Å	Average C–C / Å	Clan^{n-} Charge State	Dimen.	R_1	Ref.
$[Os^{II}_2(CO)_4(PPh_3)_4(\mu\text{-Clan})]$	XALFAS	1.305(4)	1.447	4−	0	4.37	16
$[Ga^{III}_2(tren)_2(\mu\text{-Clan})](BPh_4)_2\cdot 2$MeOH	GIDTIX	1.362(14)	1.398	4−	0	4.65	94
$[Ga^{III}Cr^{III}(tren)_2(\mu\text{-Clan})](BPh_4)_2\cdot 2$MeOH	GIDTOD	1.360(11)	1.405	4−	0	4.26	94
$[Cr^{III}_2(tren)_2(\mu\text{-Clan})](BPh_4)_2\cdot 2$MeOH	GIHHUB	1.357(8)	1.403	4−	0	6.74	94

[m] Structure at T = 100 K
[n] Structure at T = 103 K
[o] Structure at T = 241 K

Table S6 Average Fe–O, and C–O and C–C bond lengths of Clan^{n-} moieties in Fe–Clan^{n-} compound reported to date.

Compound	CCDC Ref. Code	Average Fe–O / Å	Average C–O / Å	Average C–C / Å	Clan^{n-} Charge State	Dimen.	R_1	Ref.
$[Fe^{III}_2(H_2O)_4(Clan)_2(\mu\text{-Clan})]\cdot 4H_2O$	QOCHEV	2.012(29)	1.260(6); 1.257(33)[p]	1.530; 1.530(2)[p]	2−	0	4.54	11
$[Fe^{II}_2(tpa)_2(\mu\text{-Clan})](BF_4)_2\cdot 2MeOH$	NIBKEP	2.138(75)	1.261(10)	1.528	2−	0	4.64	18
$[Fe^{II}(H_2O)_2(\mu\text{-Clan})]\cdot H_2O$	KIQJID	2.138(15)	1.257(1)	1.523	2−	1	4.5	52
$[Fe^{II}(H_2O)_2(\mu\text{-Clan})]\cdot H_2O$	KIQJID01	2.140(18)	1.259	1.53	2−	1	3.15	11
$[Fe^{II}(H_2O)_2(\mu\text{-Clan})]\cdot phz$	KIQKAW	2.141(8)	1.262(13)	1.522	2−	1	2.3	52
$(Me_4N)_2[Fe^{II}Cl_2(\mu\text{-Clan})]$	VEXGOX[q]	2.140(44)	1.256(11)	1.523	2−	1	7.27	65
$(Me_4N)_2[Fe^{III}Cl_2(\mu\text{-Clan})]$	VEXGOX01[r]	2.027(26)	1.291(6)	1.466	3−	1	6.53	65
$(EtPh_3P)_2[KFe^{III}(\mu\text{-Clan})_3]\cdot 2DMF$	QUJJOW	2.054(25)	1.255(23); 1.263(25); 1.257(21)	1.544(19); 1.553(12); 1.540(9)	2−	2	5.79	78
$(H_3O)(phz)_3[Fe^{II}Fe^{III}(\mu\text{-Clan})_3]\cdot 13H_2O$	QEFPOJ	2.063(2)	1.268	1.529	2−	2	3.81	79

[p] Terminal mono-coordinating

[q] Structure at T = 250 K

[r] Structure at T = 100 K

Table S6(cont.) Average Fe–O, and C–O and C–C bond lengths of Clan^{n-} moieties in Fe–Clan^{n-} compounds reported to date.

Compound	CCDC Ref. Code	Average Fe–O / Å	Average C–O / Å	Average C–C / Å	Clan^{n-} Charge State	Dimen.	R_1	Ref.
(^{n}Pr$_4$N)$_2$[Fe$^{III}_2$(μ-Clan)$_3$]·2Acetone·H$_2$O	SIQPIU[s]	2.029(42); 2.020(40)	1.259(3) 1.297(2); 1.293(3)	1.536(2) 1.468(3); 1.472	2− 3−	2	4.44	84
(^{n}Pr$_4$N)$_2$[Fe^{II}Fe^{III}(μ-Clan)$_3$]·2Acetone·H$_2$O	SIQPIU01[t]	2.091(11); 2.024(35)	1.258(2); 1.266(2) 1.294(3)	1.530(2); 1.518(5) 1.469	2− 3−	2	5.98	84
(MeEt$_3$N)[Na(dmf)][NaFe^{III}(μ-Clan)$_3$]	QUJKOX	2.011(15)	1.258(23); 1.258(26); 1.258(25)	1.534(18); 1.535(19); 1.539(20)	2−	3	4.13	78
(Me$_2$NH$_2$)$_2$[Fe$^{III}_2$(μ-Clan)$_3$]·6DMF·2H$_2$O	ZACDAL	2.020(3)	1.280	1.48	2.67−	2	9.54	90
(Et$_4$N)$_2$[Fe$^{III}_2$(μ-Clan)$_3$]·20H$_2$O	XARDIG	2.019	1.284	1.491	2.67−	2	5.31	1
(Cp$_2$Co)$_{1.43}$(Me$_2$NH$_2$)$_{1.57}$[Fe$^{III}_2$(μ-Clan)$_3$]·4.9DMF	GEFKAG	2.028(5)	1.297	1.431	3−	2	12.22	93

[s] Structure at T = 103 K

[t] Structure at T = 241 K

Table S7 Ligand abbreviations used in **Table S3** through **Table S6**.

Abbreviation	Ligand
$(Meim)_2$-prop	3,3-bis(1-methylimidazol-2-yl)propionate
$(SMeBim)_3$-Mes	1,3,5-tri(2-methylthiobenzimidazol-1-ylmethyl)-2,4,6-trimethylbenzene
2,2′-bpy	2,2′-bipyridine
2,2′-bpym	2,2′-bipyrimidine
3-pbdy	1,4-bis(3-pyridyl)butadiyne
4,4′-bpday	1,4-bis(4-pyridyl)but-1,3-diyne
4,4′-bpe	(E)-1,2-bis(4-pyridyl)ethene
4,4′-bpy	4,4′-bipyridine
4,4′-bpyOHama	4,4′-bypyridine-2-hydroxamic acid
4-pbdy	1,4-bis(4-pyridyl)butadiyne
4-ppy	4-phenylpyridine
$acac_2$-trien:	4,15-dimethyl-5,8,11,14-tetraazaoctadeca-2,4,14,16-tetraene-2,17-diol
bix	1,4-bis(imidazol-1-ylmethyl)benzene
BPNim	bis(4-(naphtho[2,3-d]imidazol-1-ylmethyl)phenyl)methane
$BPOPh_2$-7-TH	1,1'-(7,8-dipropyldithieno[3,2-*e*:3',2'-*e*']benzo[1,2-*b*:4,3-*b*'] bis[1]benzothiophene-2,13-diyl)bis[1,1-diphenylphosphine oxide]
bpyeyan	1,5-bis[2-(4-pyridyl)ethynyl]anthracene
Br-ppy	4-(4-bromophenyl)pyridine
BXyTBim	1,1'-[1,4-phenylenebis(methylene)]bis[2-(2-thienyl)-1*H*-benzimidazole]
C_6Me_6	hexamethylbenzene
Clan	3,6-dichloro-2,5-dihydroxy-1,4-benzoquinone (chloranilate)
cod	1,4-cyclooctadiene
Cp^*	pentamethylcyclopentadienyl
Cy	cymeme
dapz	2,3-diaminopyrazine
dcmb	3,3′-dicarboxymethyl-2,2′-bipyridine
dhqox	2,3-dihydroxy-quinoxaline
dmac	*N*,*N*-dimethylacetamide
dmf	*N*,*N*-dimethylformamide
dppOb	1,1'-(1,4-butanediyl)bis[1,1-diphenylphosphine oxide]
fm	formamide
$HBpz_3$	hydrotris(1-pyrazolyl)borate
L_{Py}	19,39-dimethyl-3,15,23,35-tetrakis(2-pyridinylmethyl)-6,9,12,26,29,32-hexaoxa-3,15,23,35-tetraazatricyclo[35.3.1.$1^{17,21}$]dotetraconta-1(41),17,19,21(42),37,39-hexaene-41,42-diol
Me_3tacn	1,4,7-trimethyl-1,4,7-triazacyclononane
ohphz	octahydrophenazine

Table S7(cont.) Ligand abbreviations used in **Table S3** through **Table S6**.

Abbreviation	Ligand
pap	2-(phenylazo)pyridine
pdt	pyrazine-2,3-dithiolate
phz	phenazine
pmdeta	*N*,*N*,*N*′,*N*″,*N*″-pentamethyldiethylenetriamine
$POPh_3$	triphenylphosphine oxide
PPh_3	triphenylphosphine
py	pyridine
pym	pyrimidine
pyz	pyrazine
sal_2-trien:	bis(salicylidene)-*N*,*N*‴-triethylenetetramine
^{t}Buacac$_2$-py	3,5-bis(4,4-dimethyl-1,3-pentadione)pyridine
tdmpmb	1,2,4,5-tetrakis(dimethoxyphosphorylmethyl)benzene
tpa	tris(2-pyridylmethyl)amine
tpy	2,2':6',2''-terpyridine
tren	tris(2-aminoethyl)amine
tren(imid)	tris{[2-{(imidazole-4-yl) methylidene}amino]ethyl}amine
trisphos	1,1,1-tris(diphenylphosphinomethyl)ethane
TXyBim	1,2,4,5-tetrakis(5,6-dimethylbenzimidazol-1-ylmethyl)benzene

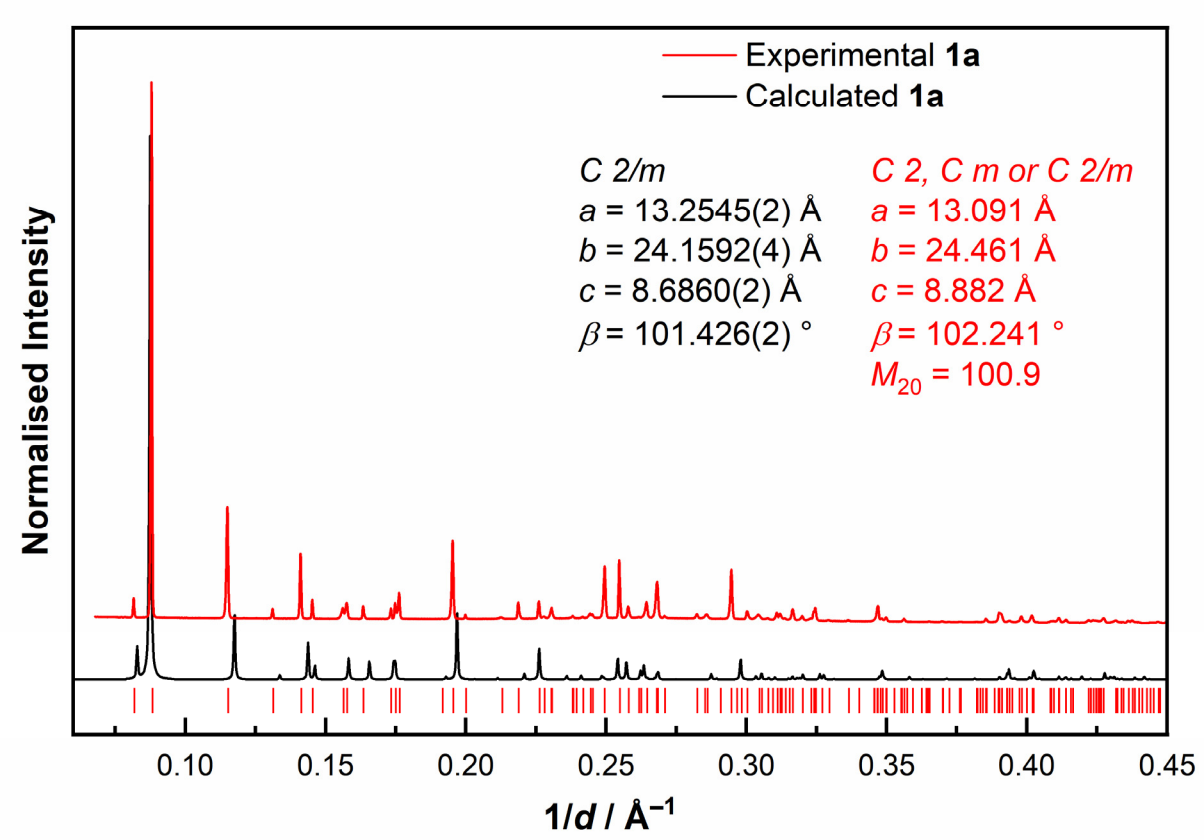


Figure S3 Synchrotron P-XRD diffraction pattern of bulk **1a** (red, T = 250 K) and calculated pattern (black, T = 240 K) from SC-XRD data of **1a**. NB: Experimental 2θ values from synchrotron radiation (λ = 0.774929 Å) have been converted to 1/d values to simplify comparison between P-XRD patterns measured using lab source Cu Kα radiation (λ = 1.54148 Å). Tick marks show the positions of the calculated reflections from the indexed pattern (red).

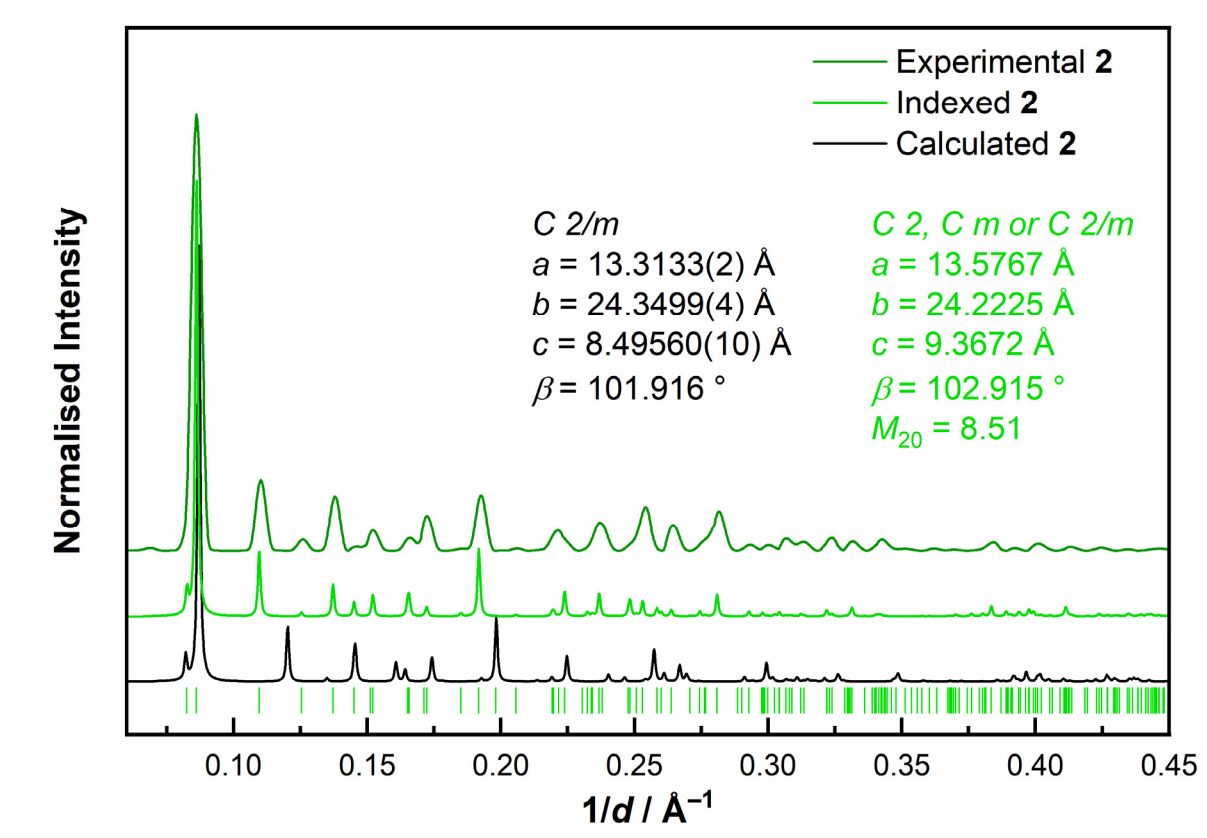


Figure S4 P-XRD diffraction patterns of bulk **2** (dark green, T = 250 K), calculated pattern **2** from indexed experimental P-XRD (pale green) and calculated pattern (black, T = 100 K) from SC-XRD of **2**. NB: Experimental 2θ values from lab source Cu Kα radiation (λ = 1.54148 Å) have been converted to 1/d values to simplify comparison between P-XRD measured using synchrotron radiation (λ = 0.774929 Å). Tick marks show the positions of the calculated reflections from the indexed pattern (pale green).

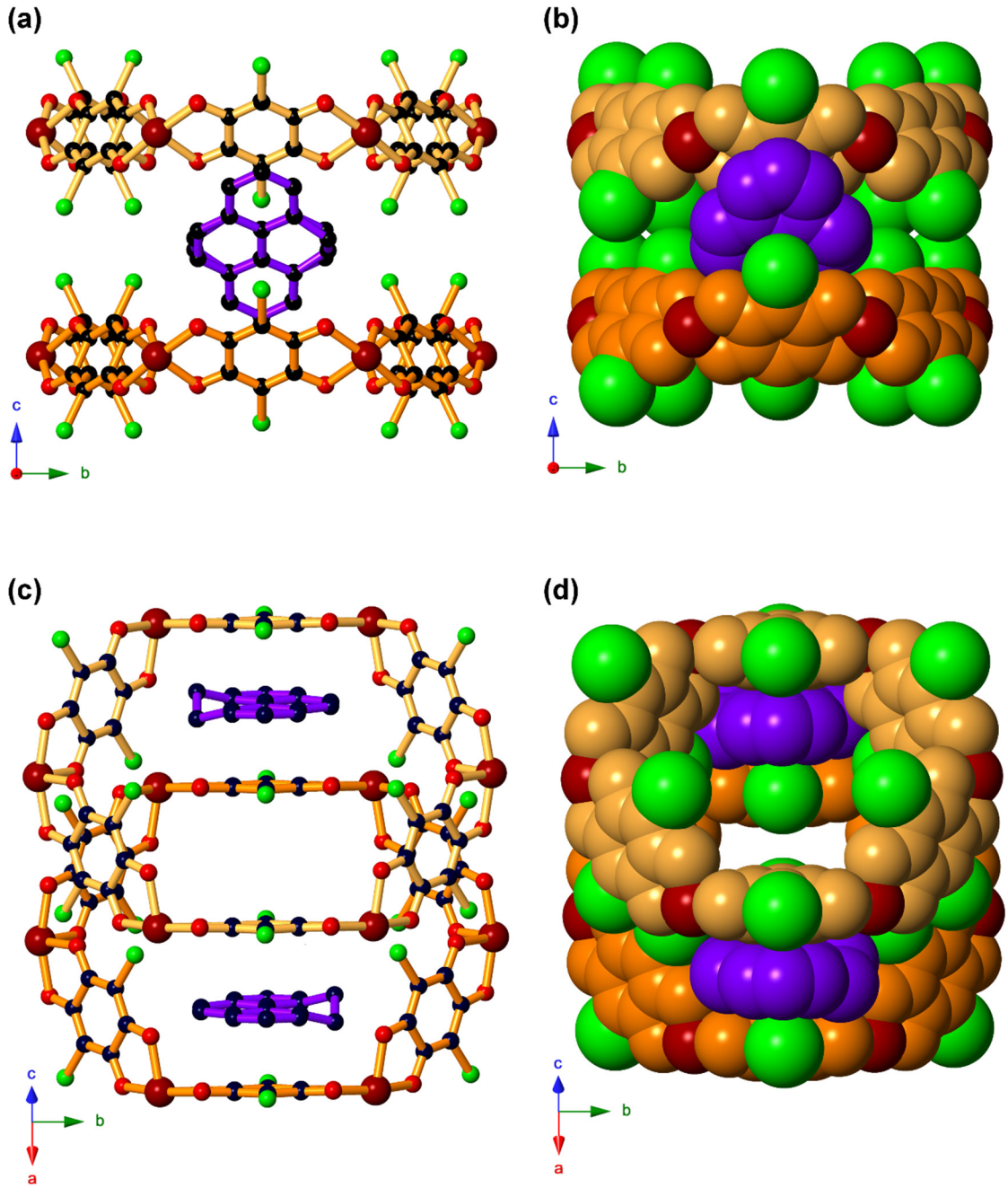


Figure S5 Alternative views of the interaction of the PhenQ^{m+} cation with the anionic $[Fe_2(Clan)_3]^{x-}$ framework in **1a**. (a) Ball-and-stick and (b) spacefilling representations viewed along the crystallographic *a* axis, showing PhenQ^{m+} (a, purple bonds; b, purple atoms) sandwiched between anionic sheets above (pale brown) and below (orange). Maroon = Fe, green = Cl, red = O, blue = N, and black = C. (c) Ball-and-stick and (d) spacefilling representations viewed along the one-dimensional channels, showing PhenQ^{m+} (c, purple bonds; d, purple atoms) sandwiched between anionic sheets above (pale brown) and below (orange). Maroon = Fe, green = Cl, red = O, blue = N, and black = C.

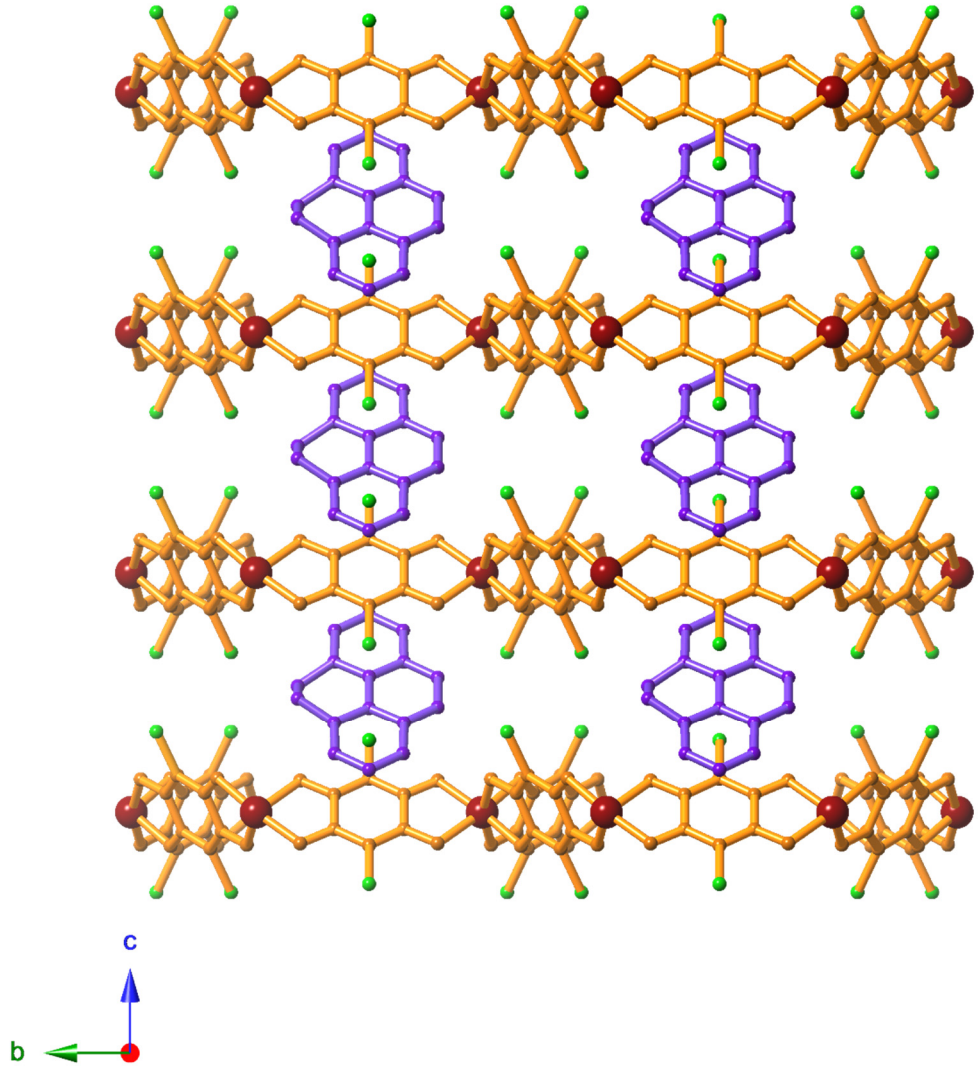


Figure S6 View along the crystallographic *a* axis showing alternating stacking of PhenQ^{m+} (purple) with ligands in the $[Fe_2(Clan)_3]^{x-}$ sheets in **1a** giving AAAA stacking of the sheets. Disordered MeCN and H_2O in channels not shown for clarity. Maroon = Fe, green = Cl.

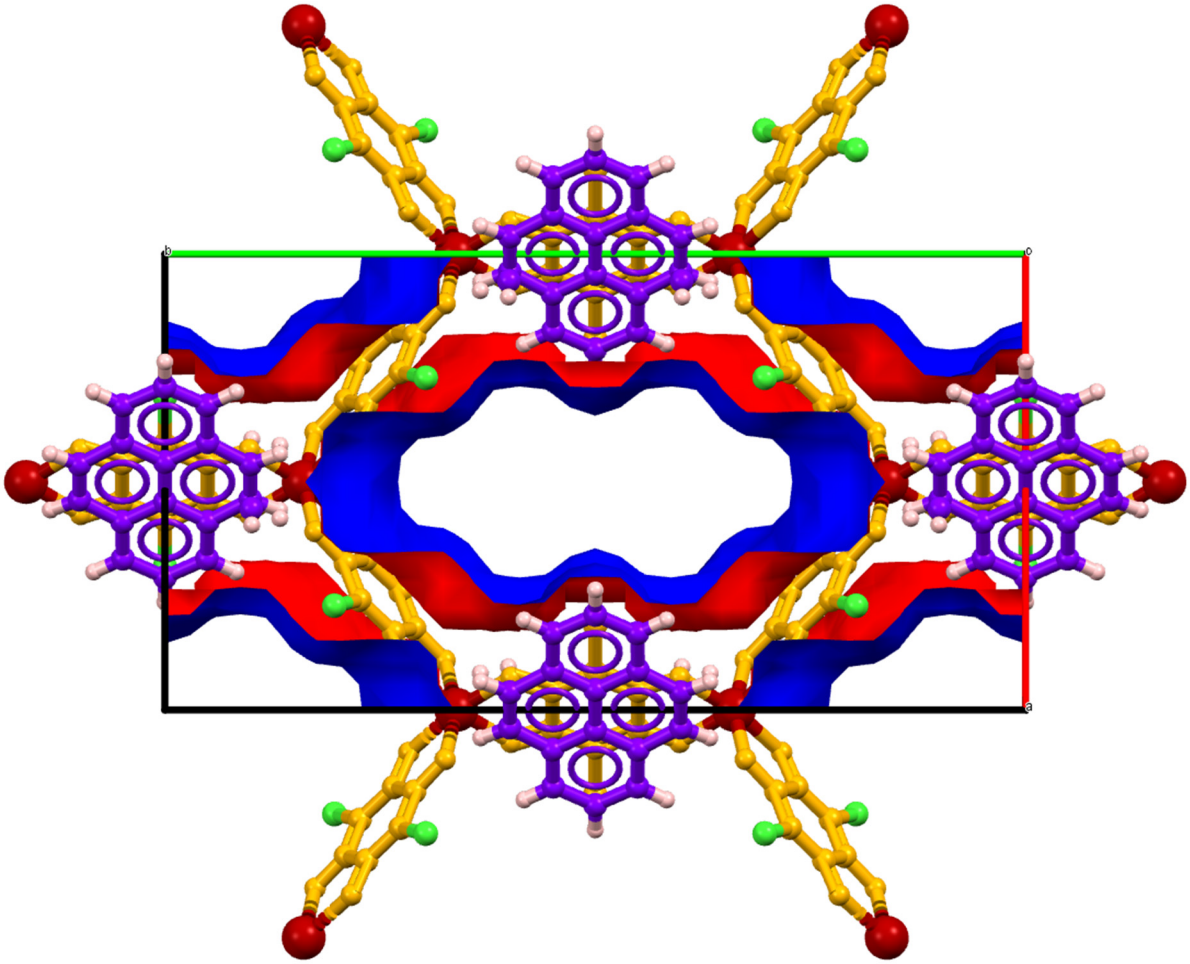


Figure S7 View along the crystallographic *c* axis showing calculated solvent-accessible void space in **1a**. Void facing surface shown in blue. The void volume (1155 $Å^3$) comprises ca. 43% of the unit cell volume (2652.54 $Å^3$) and is filled with highly disordered MeCN and H_2O molecules. The void volume was calculated with a probe radius of 1.2 Å and an approximate grid spacing of 0.7 Å, using Mercury. Maroon = Fe, green = Cl, pink = H, orange = $Clan^{n-}$, purple = $PhenQ^{2+}$.

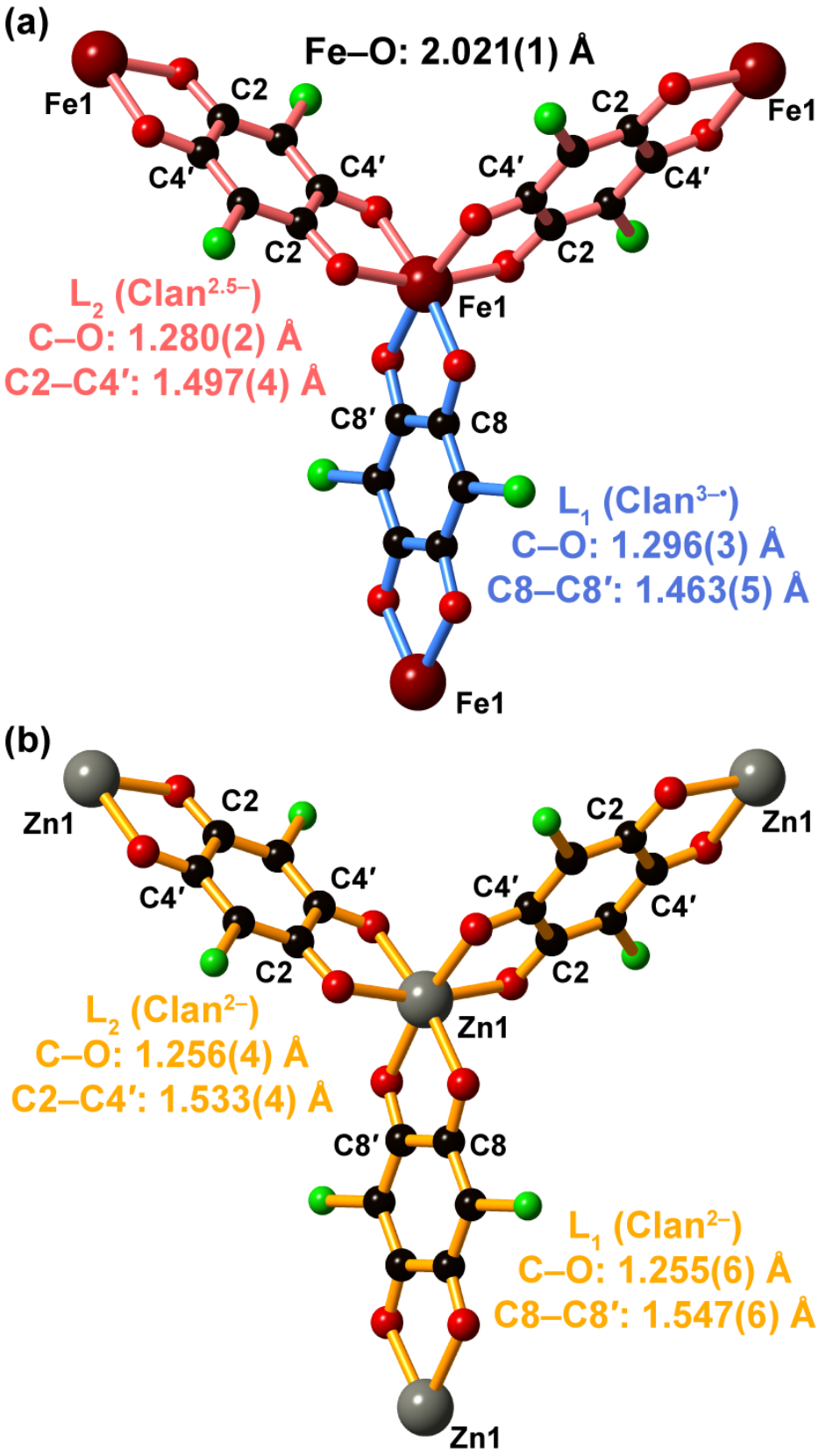


Figure S8 Coordination environment and characteristic Clan^{n-} bond lengths around (a) Fe in **1a** and (b) Zn in **2** at T = 100 K.

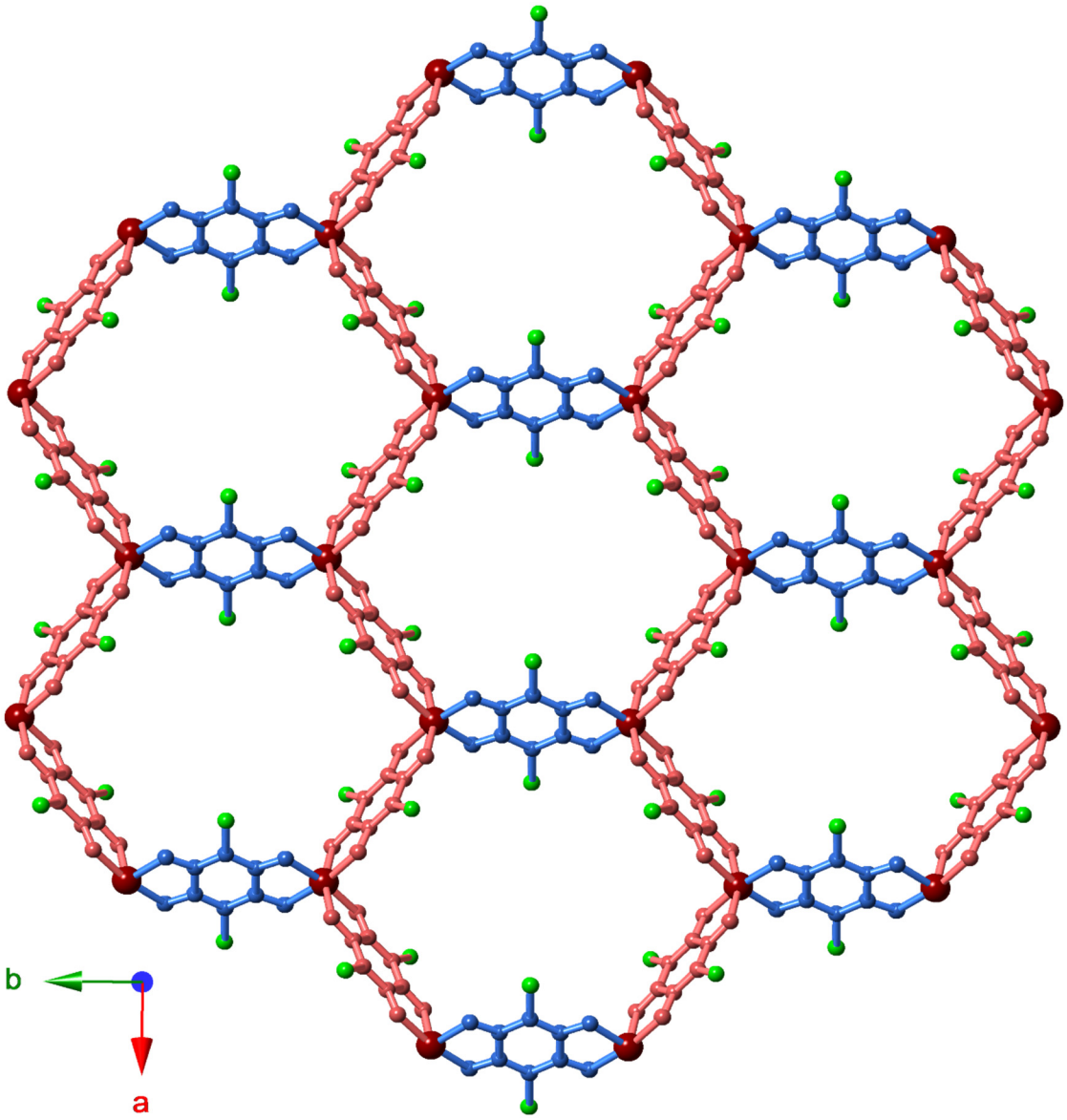


Figure S9 Arrangement of $\mathbf{L_1}$ (blue, $Clan^{3-\bullet}$) and $\mathbf{L_2}$ (pink, $Clan^{2.5-}$) ligands in **1a** giving $[Fe–\mathbf{L_2}]_\infty$ chains bridged by $\mathbf{L_1}$, which produces the anionic $[Fe_2(Clan)_3]^{2-}$ sheets. Maroon = Fe, green = Cl. An equivalent arrangement of L_1 and L_2 is replicated in the Zn^{II} compound **2**, however both $\mathbf{L_1}$ and $\mathbf{L_2}$ are in the $Clan^{2-}$ valence state in **2**.

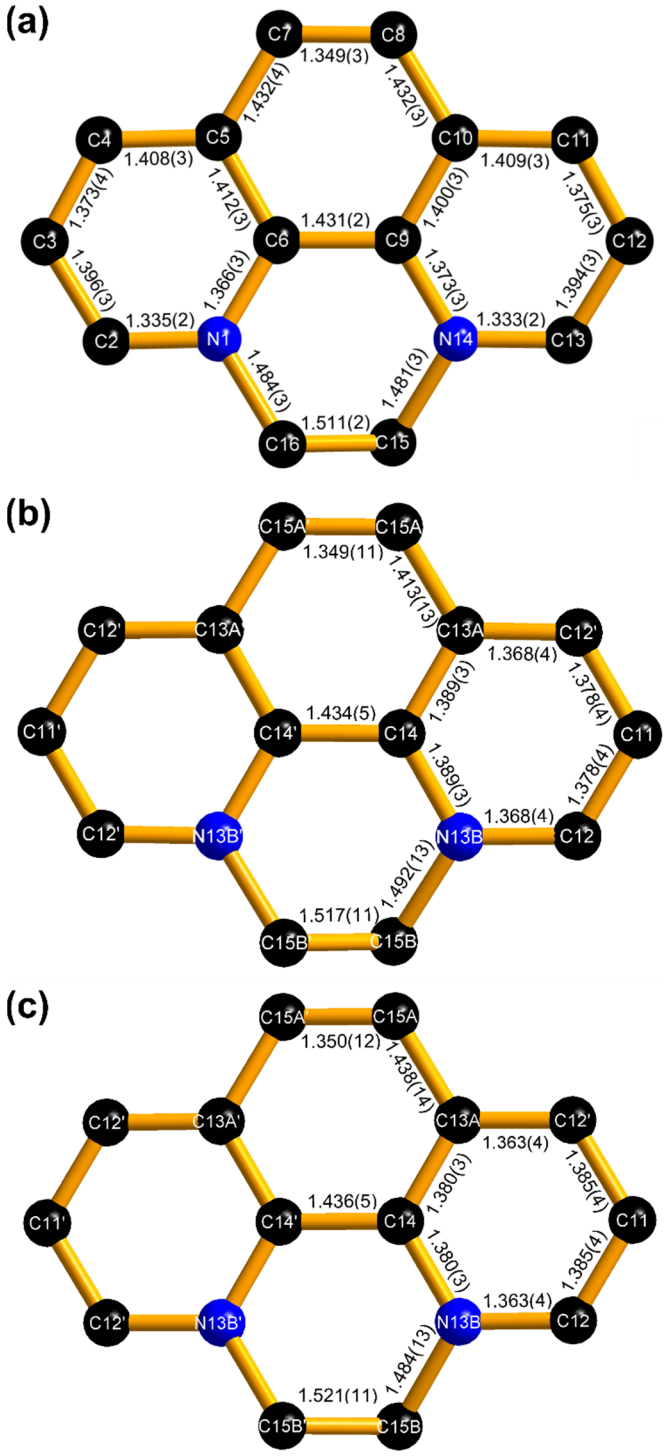


Figure S10 Bond lengths in $PhenQ^{2+}$ moieties in (a) $(PhenQ^{2+})Br_2$, (b) **1a** and (c) **2**. NB: The location of $PhenQ^{2+}$ on two special positions (inversion centre on the C14–C14′ bond, and mirror plane bisecting the molecule) results in crystallographic disorder over two symmetry related positions in **1a** and **2**. Consequently, the C13A and N13B positions have 50% occupancy by C13A and N13B respectively. Thus, the observed C–C and C–N bonds to these atoms are the average of the crystallographically unique C–C and C–N bonds observed in $(PhenQ^{2+})Br_2$. Blue = N, black = C.

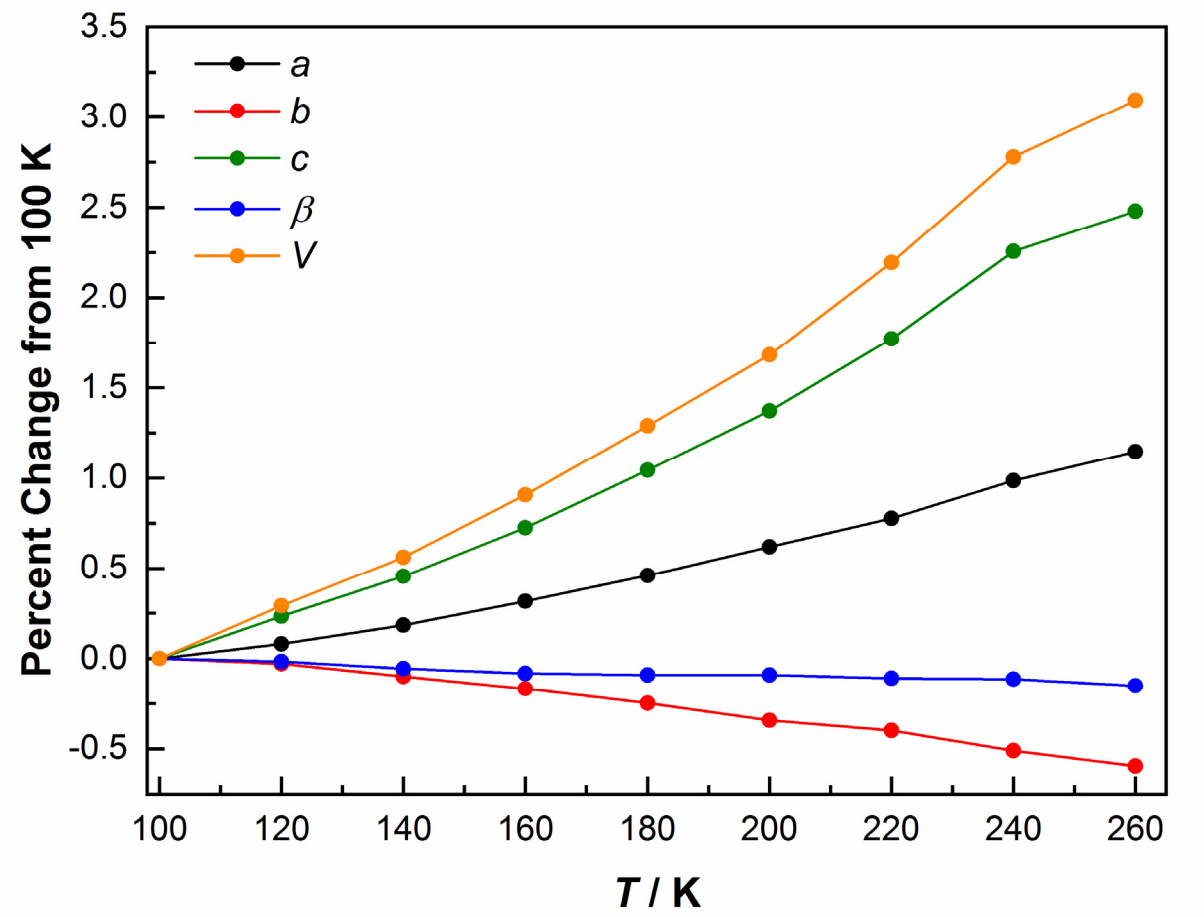


Figure S11 Temperature dependence of the cell parameters (a, b, c, β and V) as measured by SC-XRD for **1a**, where all values are normalised to those observed at T = 100 K.

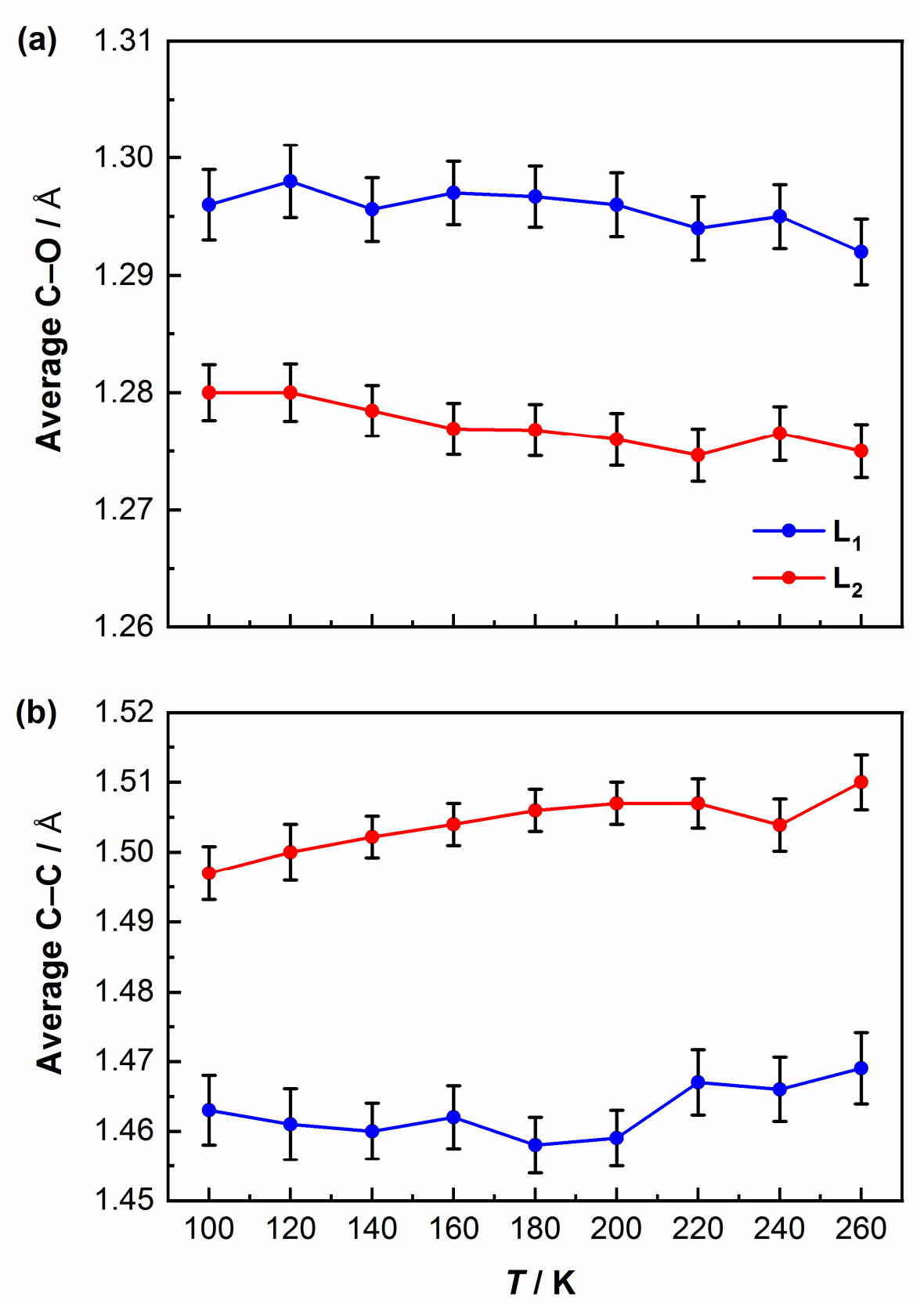


Figure S12 Temperature dependence of the average Clan^{n-} (a) C–O and (b) diagnostic C–C (C8–C8′ for $\mathbf{L_1}$; C2–C4′ for $\mathbf{L_2}$) bond lengths in 1a as measured by SC-XRD. Error bars are ± s.u.

Extended Discussion on Solvent Exchange in 1a and 1b

Single crystal character was preserved upon solvent exchange to **1b**, although the diffraction quality was reduced compared to **1a**, precluding variable-temperature SC-XRD. The structure of the DMF solvate, compound **1b**, was determined by SC-XRD and was revealed to possess the same monoclinic *C2/m* symmetry as **1a**, with slight changes in the cell parameters, most notably the crystallographic *c* axis, with a corresponding increase in the interlayer spacing (8.6860(2) Å in **1a**, 8.7982(2) Å in **1b**; Table S1 & S2). These changes were accompanied by a concomitant distortion of the hexagonal channels towards a perfect hexagon in **1b** (Figure S14), in addition to very slight changes in the metal coordination geometry which were quantified using the SHAPE parameter (Table S8).[95] Examination of the electron density difference ($F_O - F_C$) maps of **1a** and **1b** revealed a significant disparity between the two solvates (Figure S15). In contrast to **1a**, in which the one-dimensional channels were occupied by electron density which could not satisfactorily be modelled as ordered MeCN and H_2O solvent (Figure S15a, c, e), the electron density difference map of **1b** clearly displayed regions of electron density which corresponded closely to DMF solvent, corresponding to approximately four DMF molecules per formula unit i.e. (PhenQ)[Fe_2(Clan)$_3$]·4DMF (Figure S15b, d, f). Full modelling of the guest solvent was not possible due to residual disorder which could not be modelled, so again the SQUEEZE[96] routine of PLATON[97] was used to account for the scattering contribution of ordered and disordered guest solvent, allowing an estimation of the degree of solvation as (PhenQ)[Fe_2(Clan)$_3$]·4.4DMF. P-XRD confirmed the absence of decomposition following the solvent exchange process and indicated that bulk **1b** was phase pure (Figure S15). Similarly to **1a** and **2**, slight changes in unit cell parameters were observed, probably resulting from slight changes in solvation between single crystals of **1b** and the isolated bulk product. Introduction of DMF into the channels in **1b** was also observed by FT-IR, as evidenced by appearance of an intense band at 1649 cm^{-1} ascribed to $\nu_{C=O}$ of DMF (Figure S16), in addition to TGA and elemental analyses (Figure S13 and Experimental). Notably, some discrepancy between the degree of solvation calculated by TGA and elemental analyses was observed, however we ascribed this to batch-to-batch variation in the degree of solvation ((PhenQ)[Fe_2(Clan)$_3$]·2.7DMF by TGA compared to (PhenQ)[Fe_2(Clan)$_3$]·3.69DMF by elemental analysis). All physical property measurements were undertaken using a single batch of sample having the composition (PhenQ)[Fe_2(Clan)$_3$]·3.69DMF (**1b**). Recent investigations of similar porous honeycomb tetraoxolene frameworks have similarly noted batch-to-batch variation in the degree of solvation by elemental analyses.[98]

Table S8 Analysis of the possible Fe coordination geometries in **1a** and **1b** at 240 K quantified using the SHAPE parameter.

	Coordination Geometry (Symmetry)				
Compound	**HP-6 (D_{6h})**	**PPY-6 (C_{5v})**	**OC-6 (O_h)**	**TPR-6 (D_{3h})**	**JPPY-6 (C_{5v})**
1a	32.234	23.281	**1.461**	10.541	27.233
1b	32.170	23.356	**1.408**	10.672	27.290

HP-6: Hexagon; PPY-6: Pentagonal pyramid; OC-6: Octahedron; TPR-6: Trigonal prism; JPPY-6: Johnson pentagonal pyramid J2

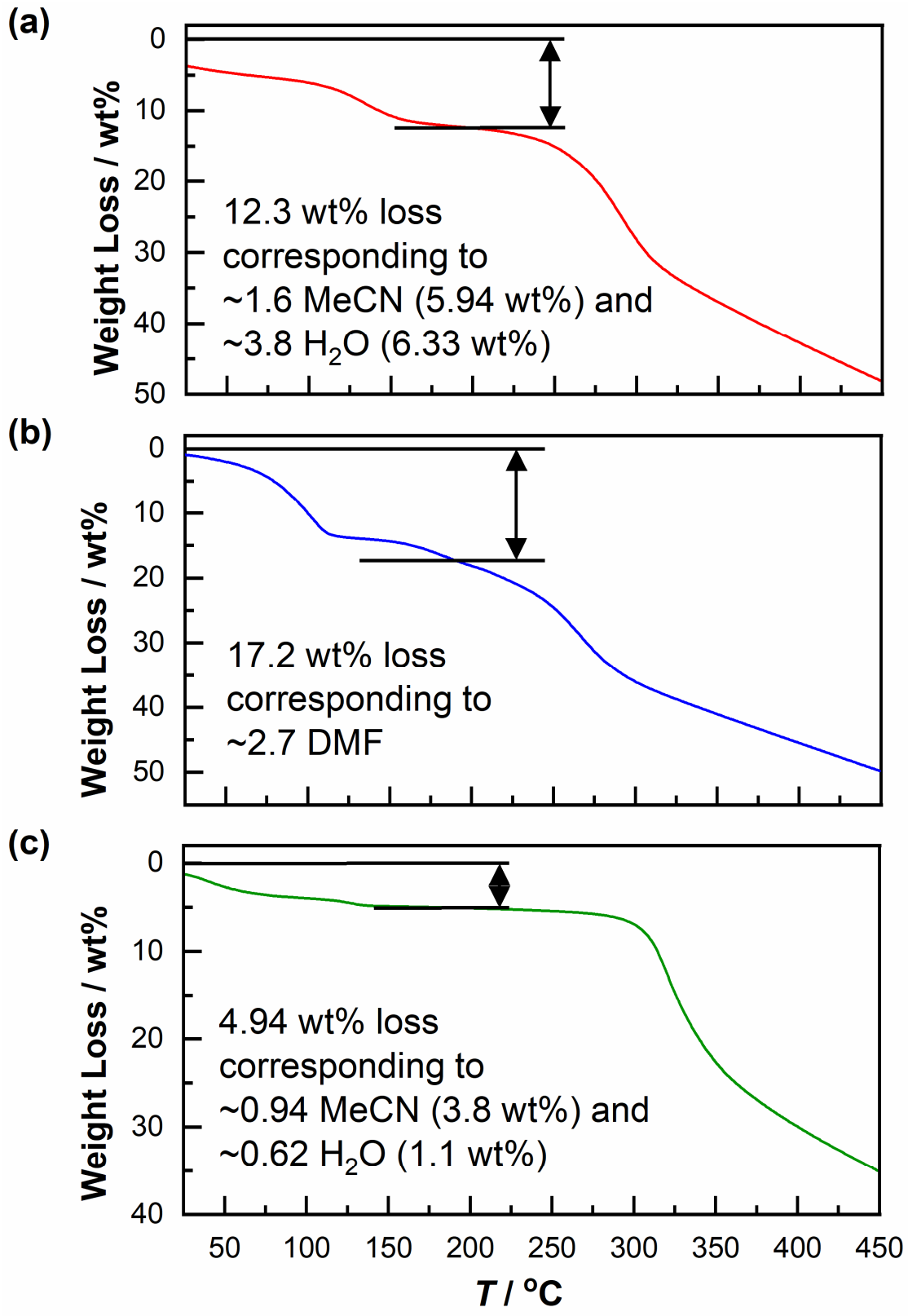


Figure S13 TGA of (a, red) **1a**, (b, blue) **1b** and (c, green) **2** at a scan rate of 5 °C min^{-1} in a flow of N_2. Non-zero mass loss at 25 °C ascribed to release of volatile MeCN in N_2 flow during temperature equilibration period at beginning of measurement run.

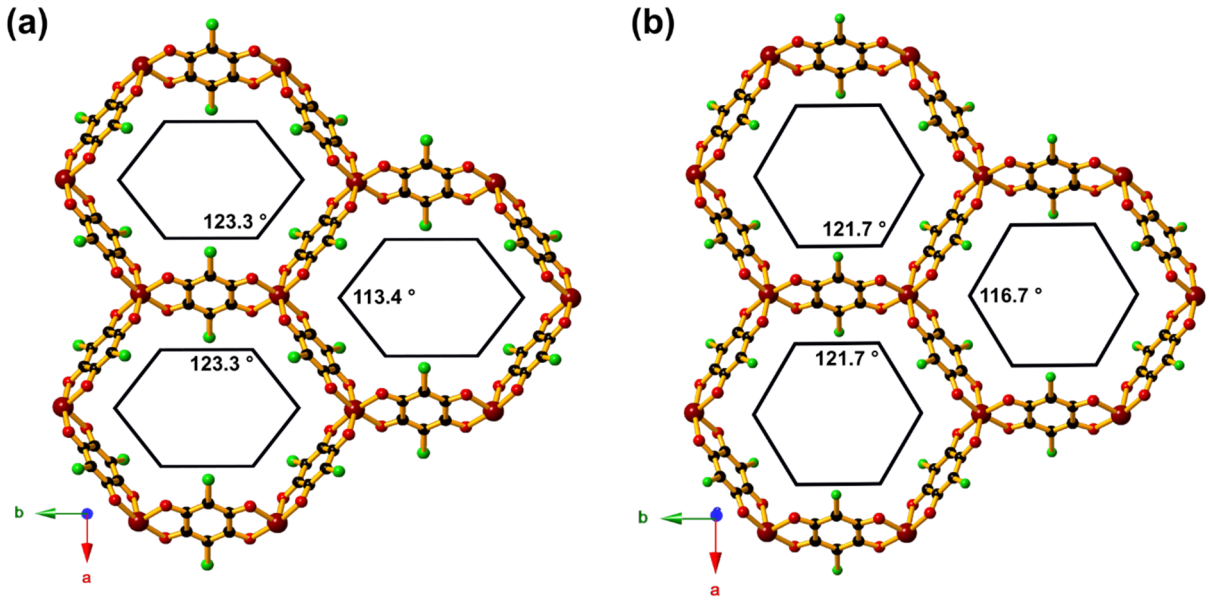


Figure S14 The Fe–Fe angles in the $[Fe_2(Clan)_3]^{2-}$ sheets for (a) MeCN solvate **1a** and (b) DMF solvate **1b**

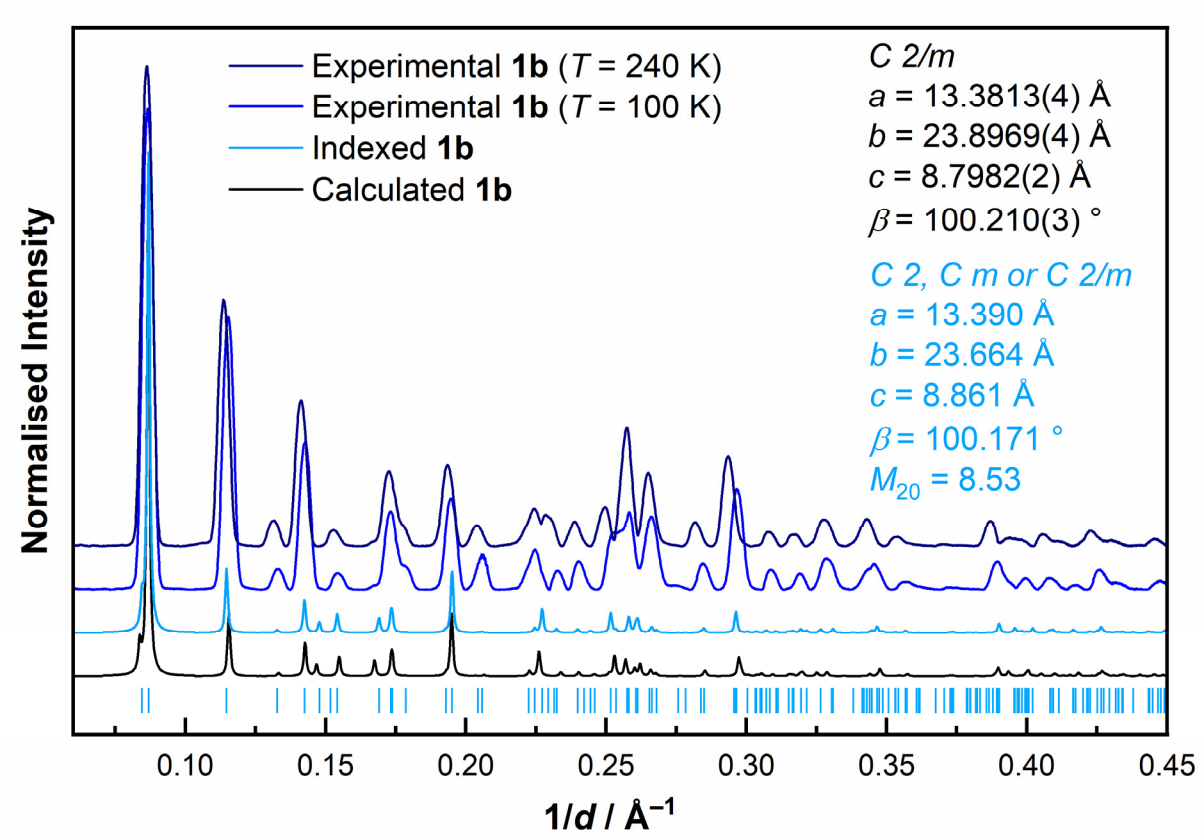


Figure S15 P-XRD diffraction patterns of bulk **1b** (navy, $T = 240$ K), bulk **1b** (royal blue, $T = 100$ K), calculated **1b** from indexed experimental P-XRD (pale blue) and calculated pattern (black, $T = 240$ K) from SC-XRD of **1a**. NB: Experimental 2θ values from lab source Cu Kα radiation (λ = 1.54148 Å) have been converted to $1/d$ values to simplify comparison between P-XRD measured using synchrotron radiation ($\lambda = 0.774929$ Å). Tick marks show the positions of the calculated reflections from the indexed pattern (pale blue).

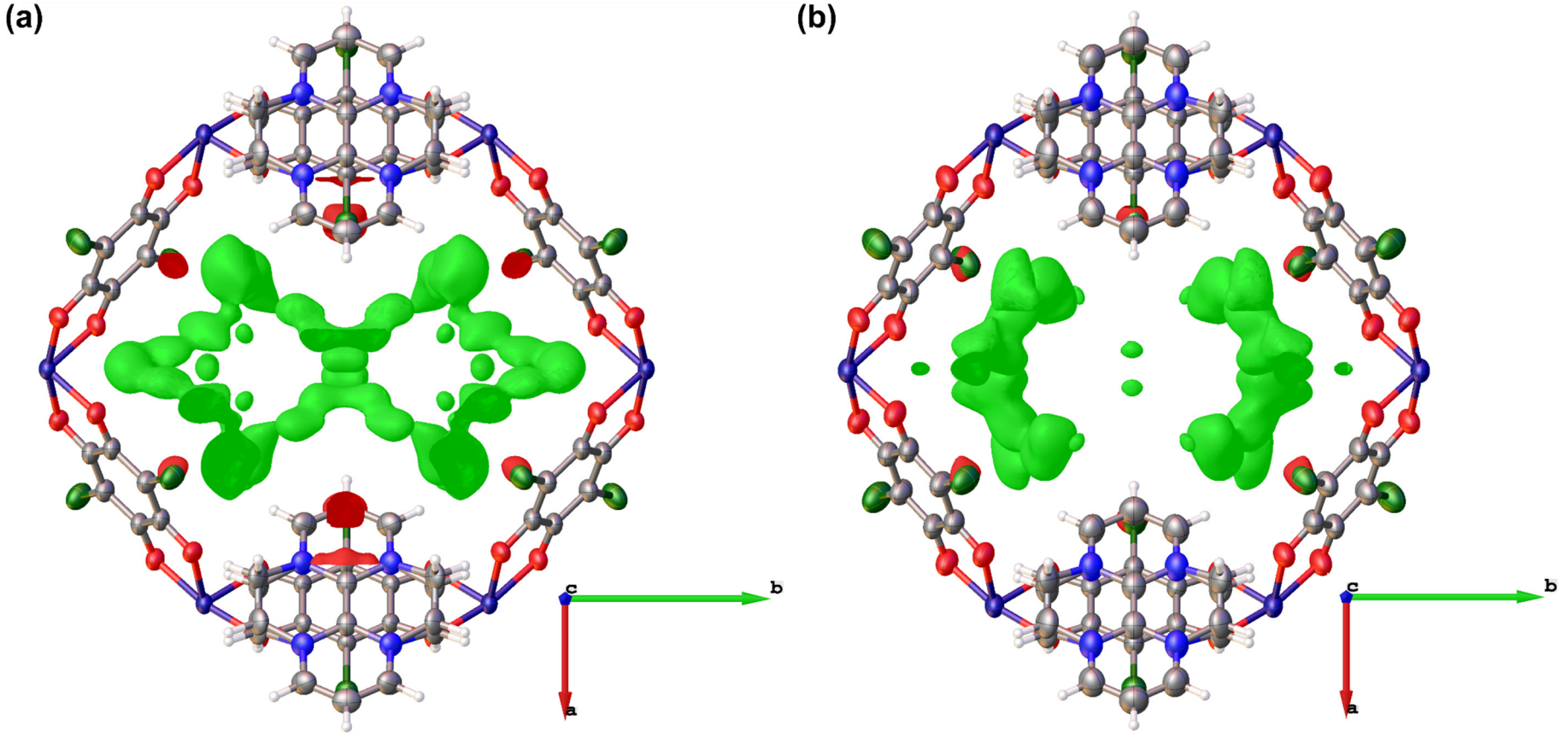


Figure S16 Electron density difference ($Fo - Fc$) maps viewed along crystallographic *c* axis for (a) **1a** and (b) **1b**. Maps plotted at a level of 1.4 e Å^{-3} and a resolution of 0.1 Å using the *OLEX2* graphical user interface.[99]

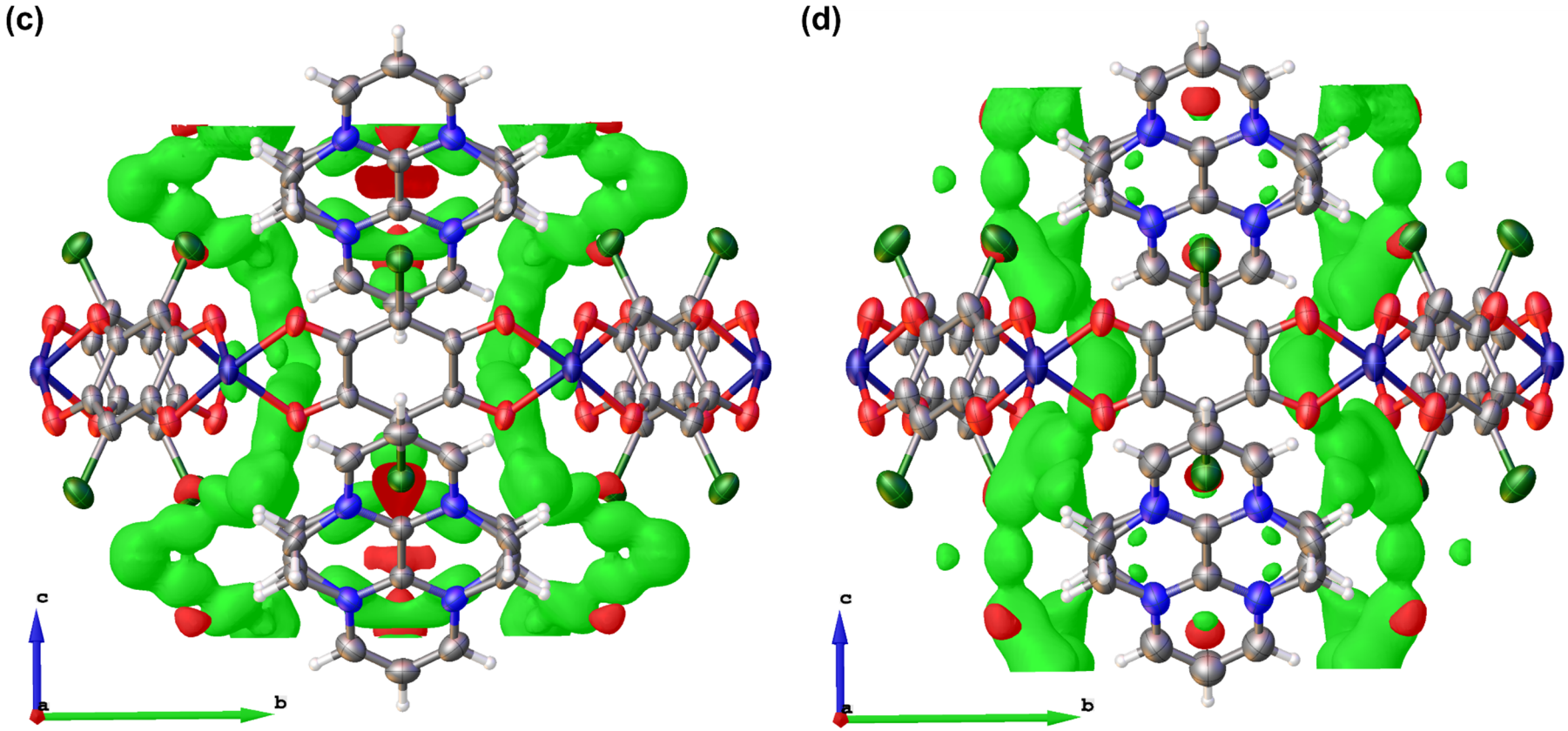


Figure S16(cont.) Electron density difference ($F_O - F_C$) maps viewed along crystallographic *a* axis for (c) **1a** and (d) **1b**. Maps plotted at a level of 1.4 e Å^{-3} and a resolution of 0.1 Å using the *OLEX2* graphical user interface.[99]

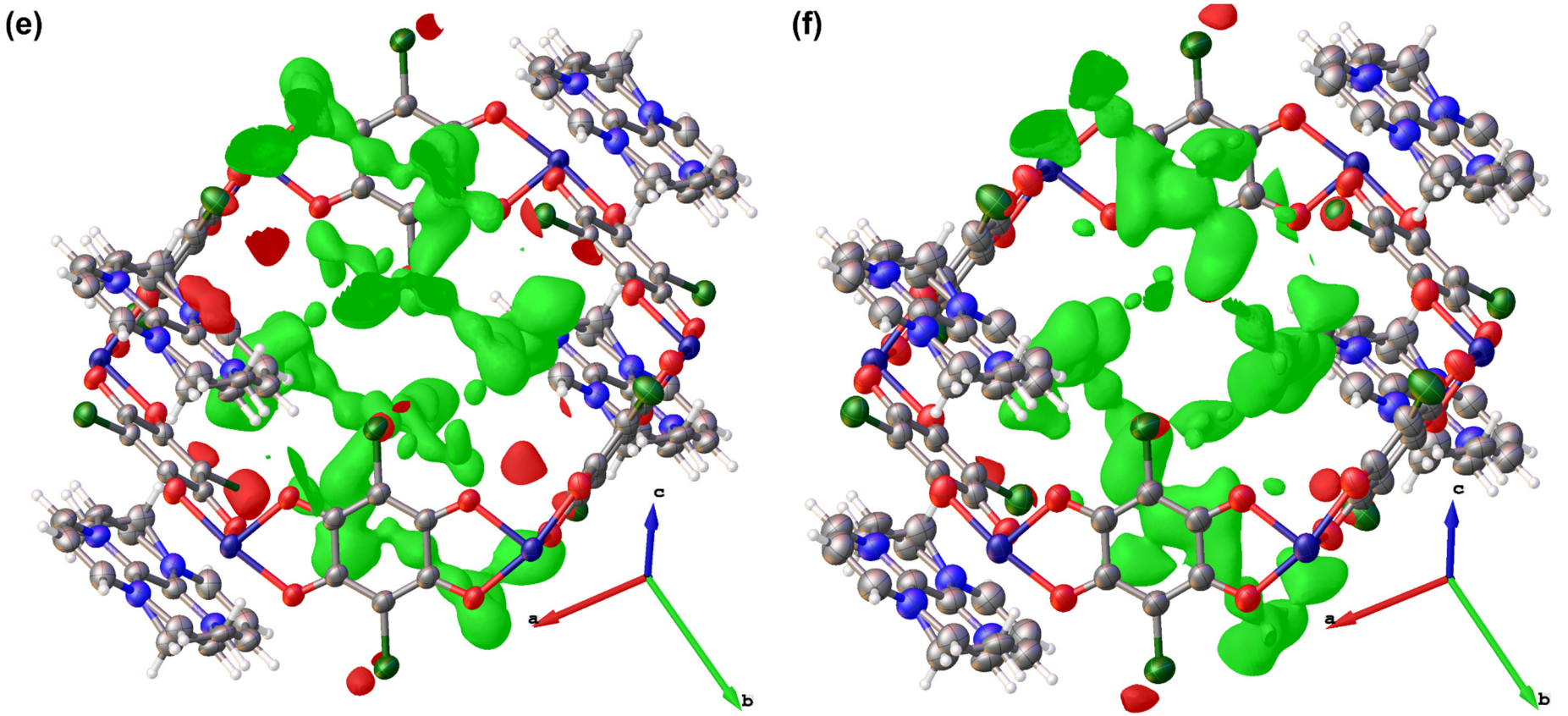


Figure S16(cont.) Electron density difference ($Fo - Fc$) maps oblique to 1D channels for (e) **1a** and (f) **1b**. Maps plotted at a level of 1.4 e Å^{-3} and a resolution of 0.1 Å using the *OLEX2* graphical user interface.[99]

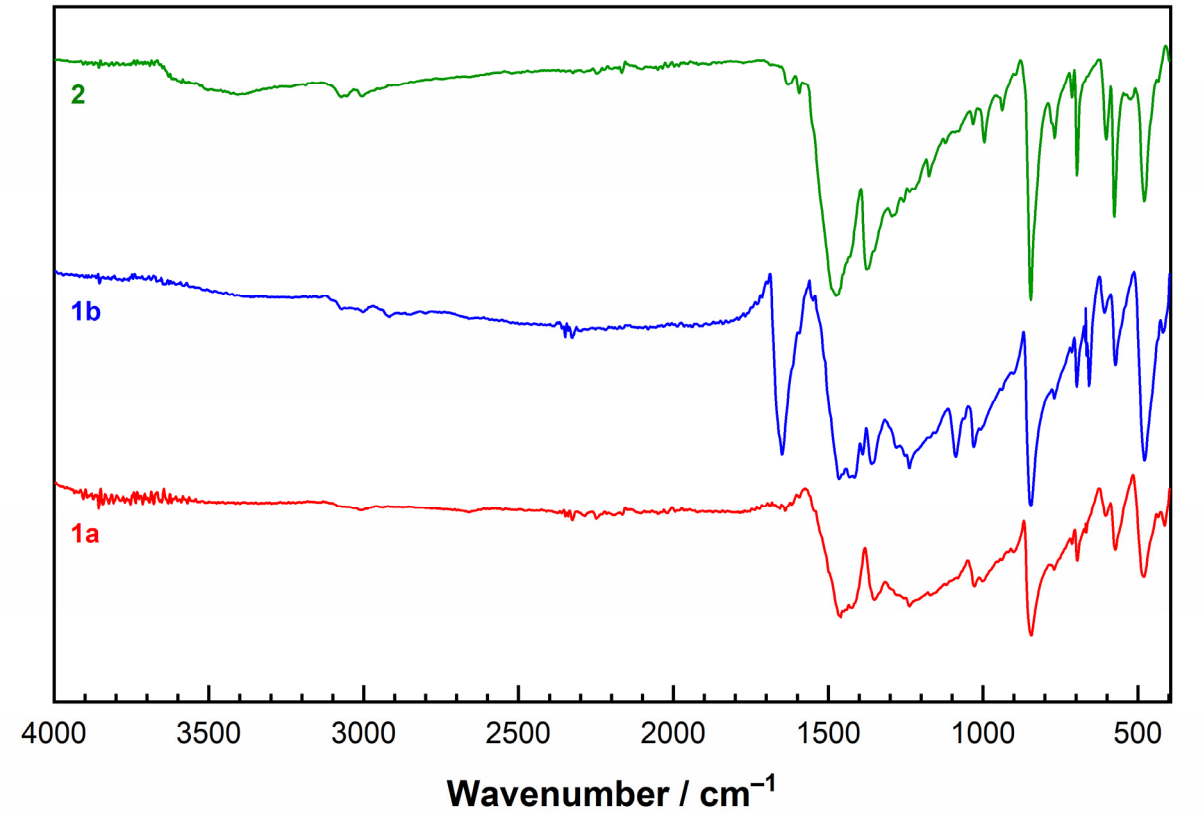


Figure S17 ATR FT–IR spectra of **1a** (red), **1b** (blue) and **2** (green) collected at room temperature. Note the appearance of the DMF $\nu_{C=O}$ at ν = 1649 cm^{-1} upon exchange of the guest solvent from MeCN and H_2O in **1a**, to DMF in **1b**.

Table S9 ^{57}Fe Mössbauer spectral parameters for **1b** measured at 294 and 5.8 K.

T / K	Species	δ / mm s^{-1}	ΔE_Q / mm s^{-1}	B_0 / T	η / mm s^{-1}	$\Gamma_{L\,(R)}$	I / %
294	Fe^{III}	0.58	1.13	-	-	0.32 (0.40)	100
5.8	Fe^{III}	0.61	1.03	47.0	1	0.45	100

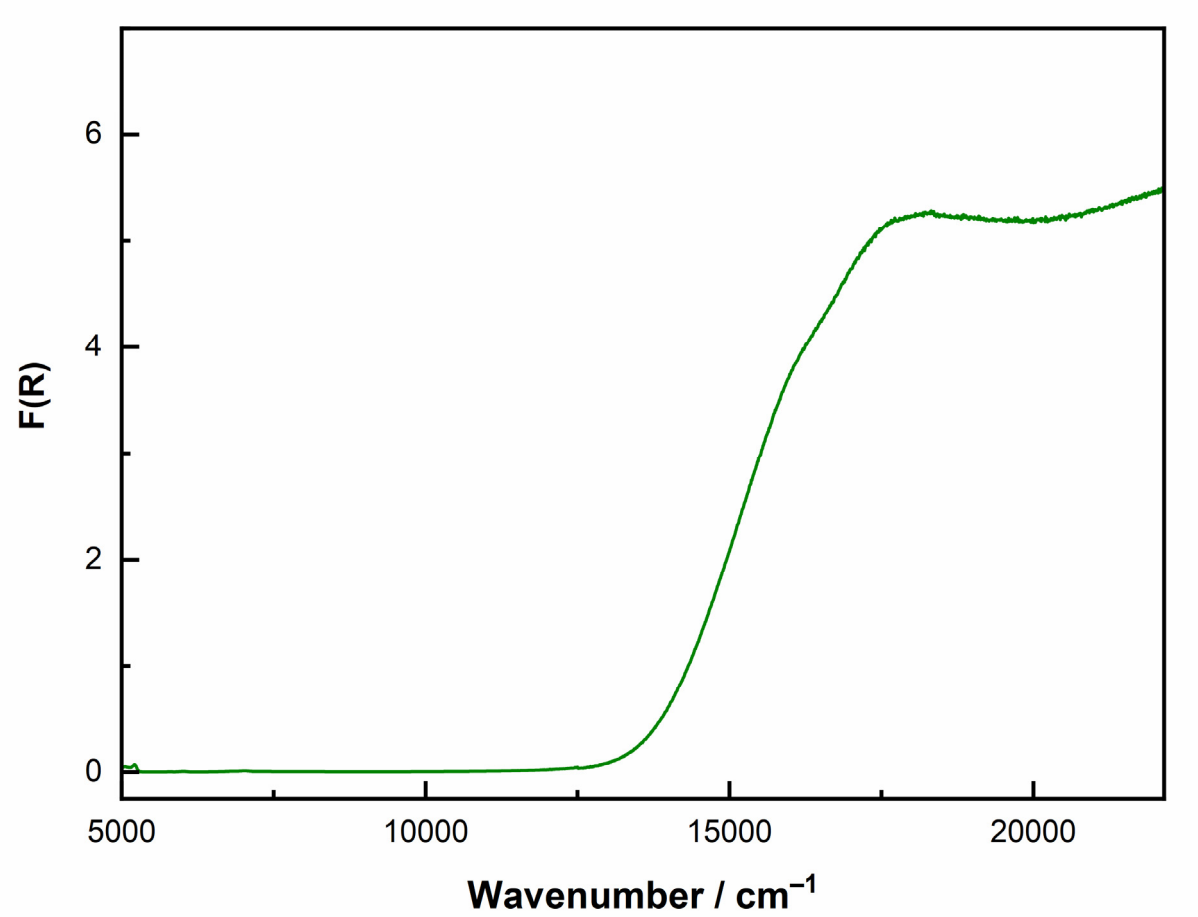


Figure S18 Diffuse reflectane UV-Vis-NIR spectrum of **2** (green).

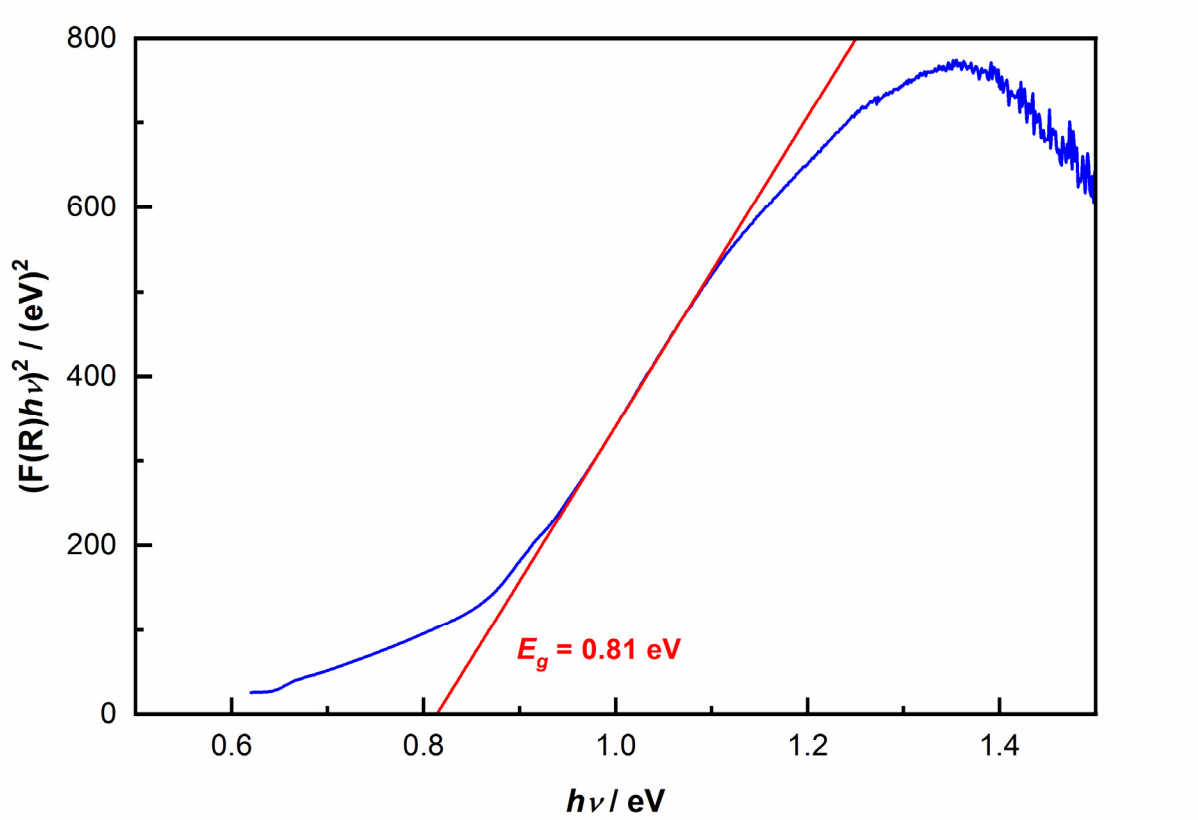


Figure S19 Tauc analysis from UV-Vis-NIR spectrum of **1b**. The tangent line (red) is used to estimate the optical band gap (E_g).

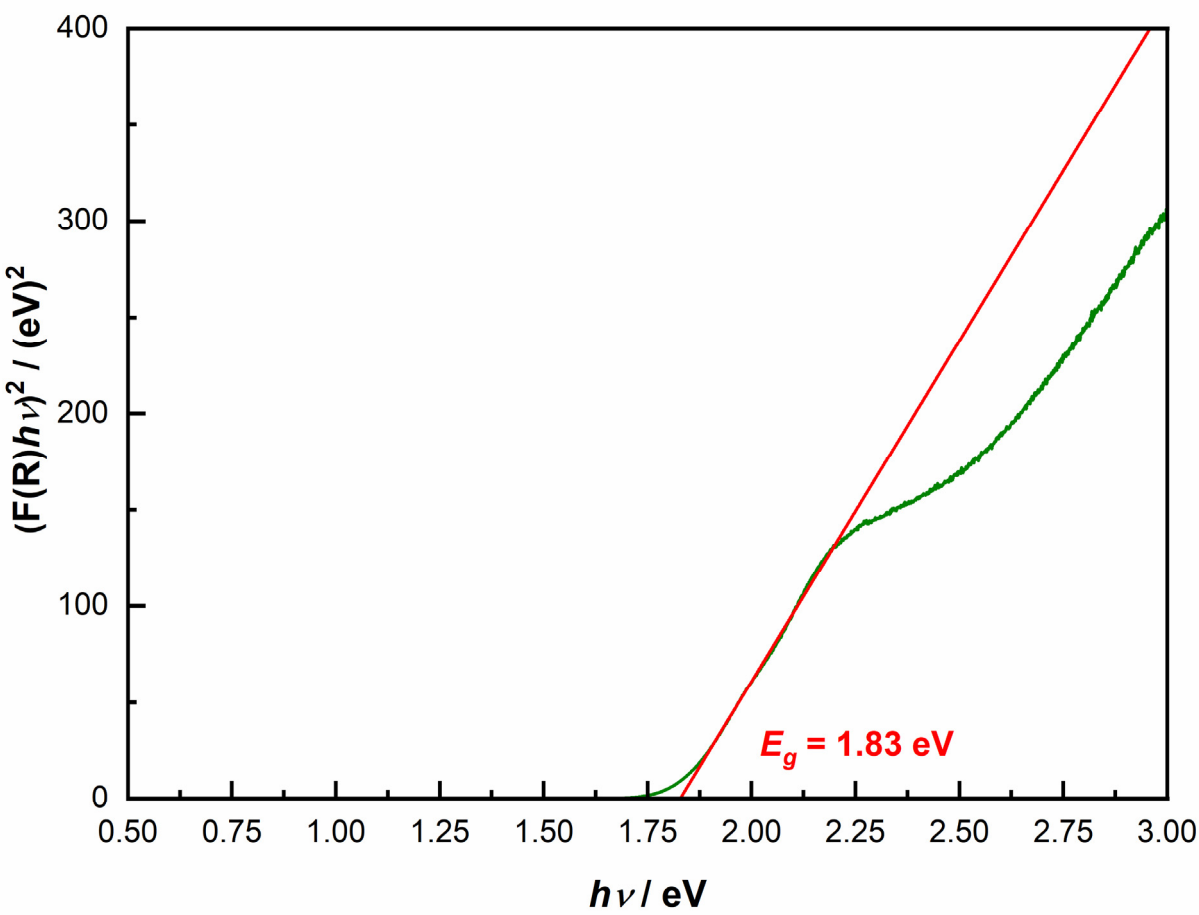


Figure S20 Tauc analysis from UV-Vis-NIR spectrum of **2**. The tangent line (red) is used to estimate the optical band gap (E_g).

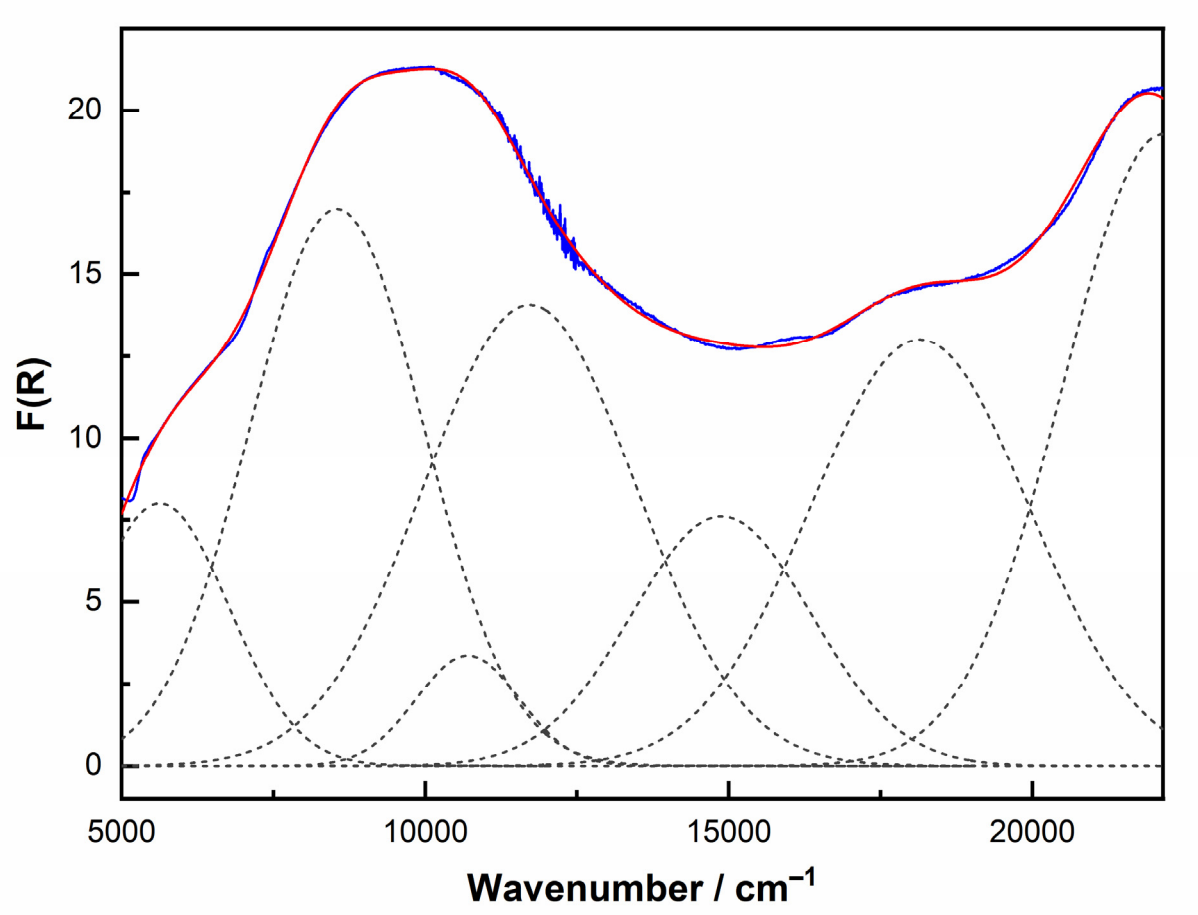


Figure S21 Deconvolution of diffuse reflectance UV-Vis-NIR spectrum of **1b** (blue) with the underlying Gaussian bands obtained from the deconvolution (grey dotted lines) and the associated curvefit (red).

Table S10 Spectral data of the deconvoluted diffuse reflectance spectra of **1b** in comparison with the published data for $(Et_4N)_2[Fe_2(Clan)_3]$.[1] The theoretical predictions for the bandwidth at half-height are provided for the near-infrared bands which has been tentatively ascribed to Intervalence Charge Transfer (IVCT) transitions (in bold).

	ν_{max} / cm^{-1}	$F(R)_{max}$ / a.u.	$\Delta\nu_{1/2}$ / cm^{-1}	$\Delta\nu_{1/2}°$ / cm^{-1} [a]	$\lvert\Gamma\rvert$ [b]
1b	**5629**	**8.00**	**2677**	**3605**	**0.26**
	8544	**17.0**	**3382**	**4442**	**0.24**
	10700	**3.36**	**2001**	**4972**	**0.60**
	11720	**14.1**	**4120**	**5203**	**0.21**
	14877	7.61	3483	5862	0.41
	18141	13.0	4245	6473	
$(Et_4N)_2[Fe_2(Clan)_3]$	**7445**	**5.68**	**3290**	**4147**	**0.21**
	10075	2.98	2560		
	11390	1.52	1348		
	128900	1.57	1790		
	18577	11.7	6588		

[a] $\Delta\nu_{1/2}° = [2310(\nu_{max})]^{1/2}$ at 298 K.[100, 101]

[b] $\Gamma = 1 - (\Delta\nu_{1/2} / \Delta\nu_{1/2}°)$.[102]

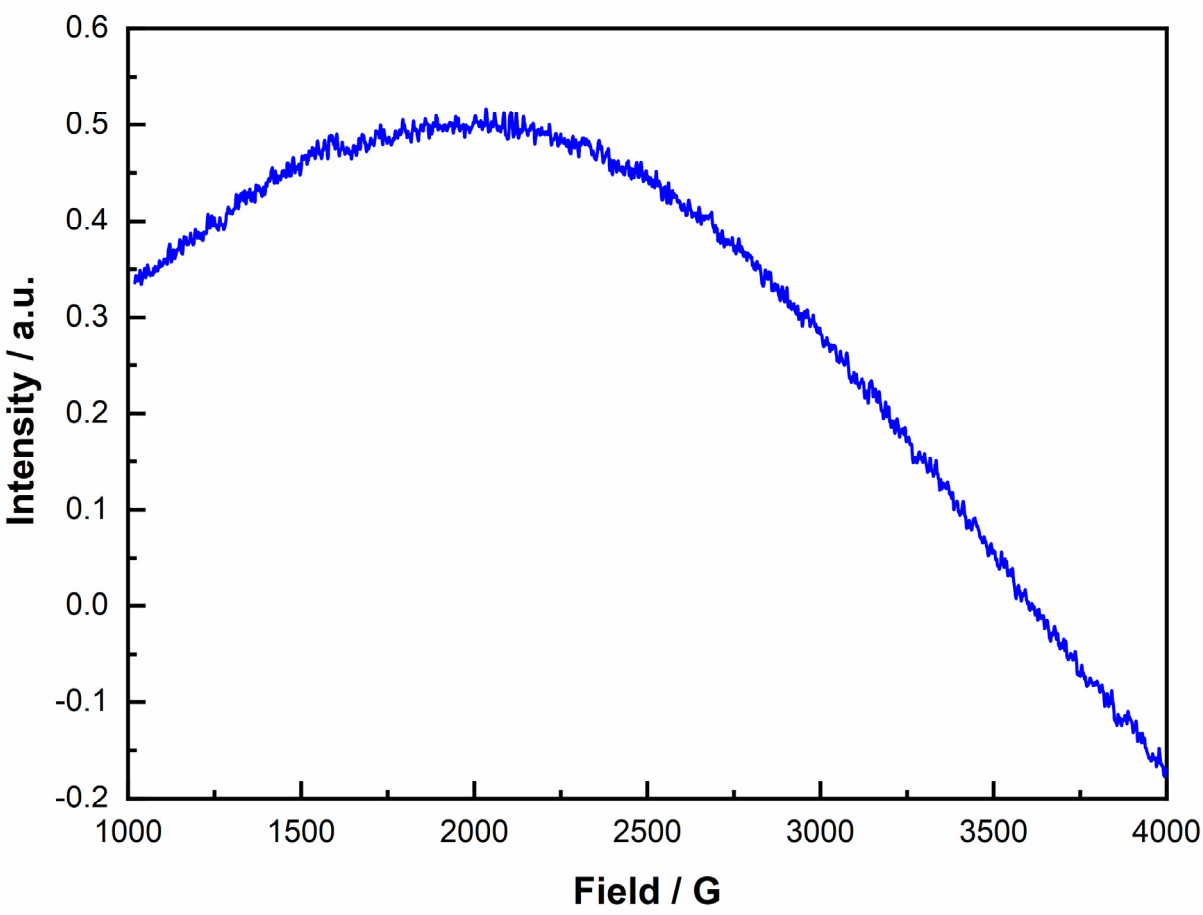


Figure S22 X-band EPR spectrum of **1b** in the solid-state measured at room temperature.

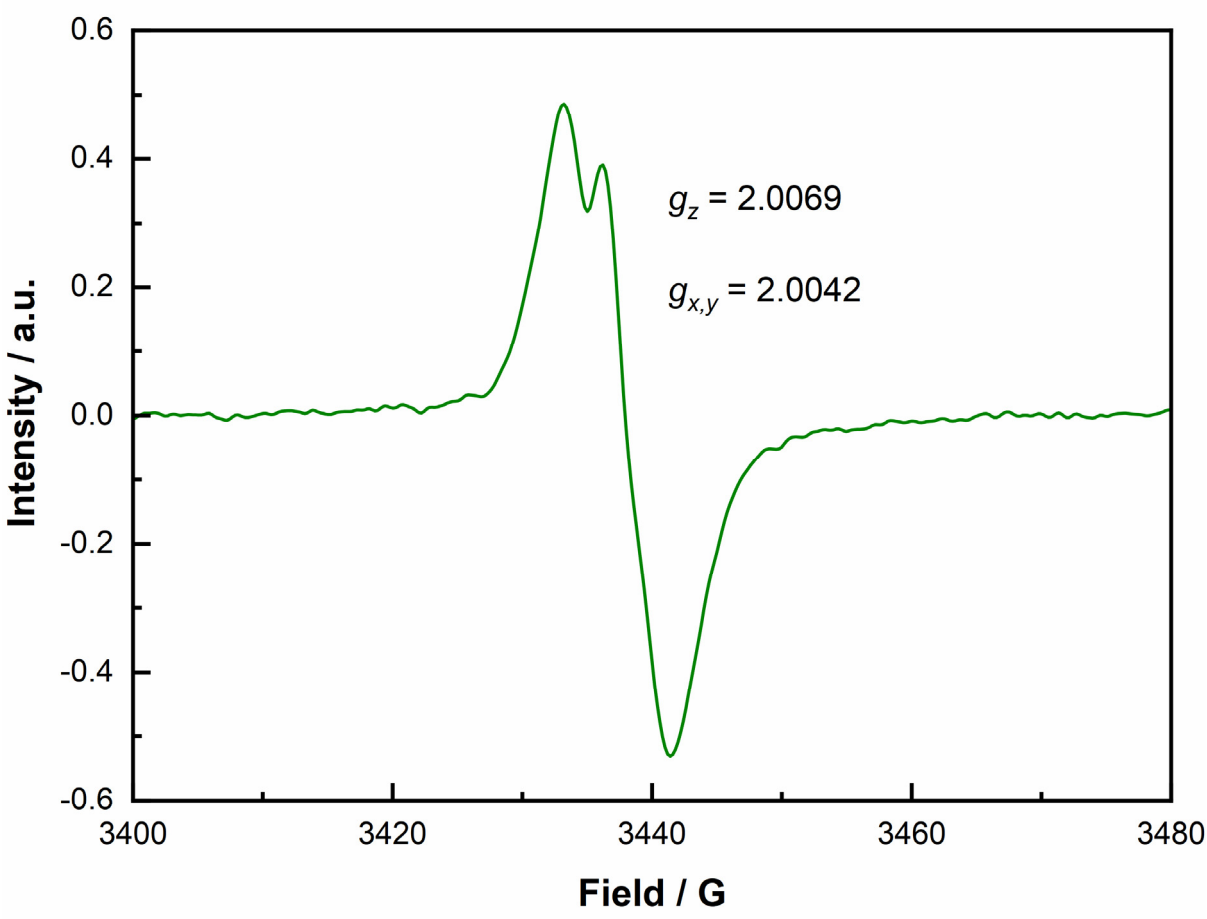


Figure S23 X-band EPR spectrum of **2** in the solid-state measured at room temperature. The observed radical signal is consistent with an organic radical in an axial environment.

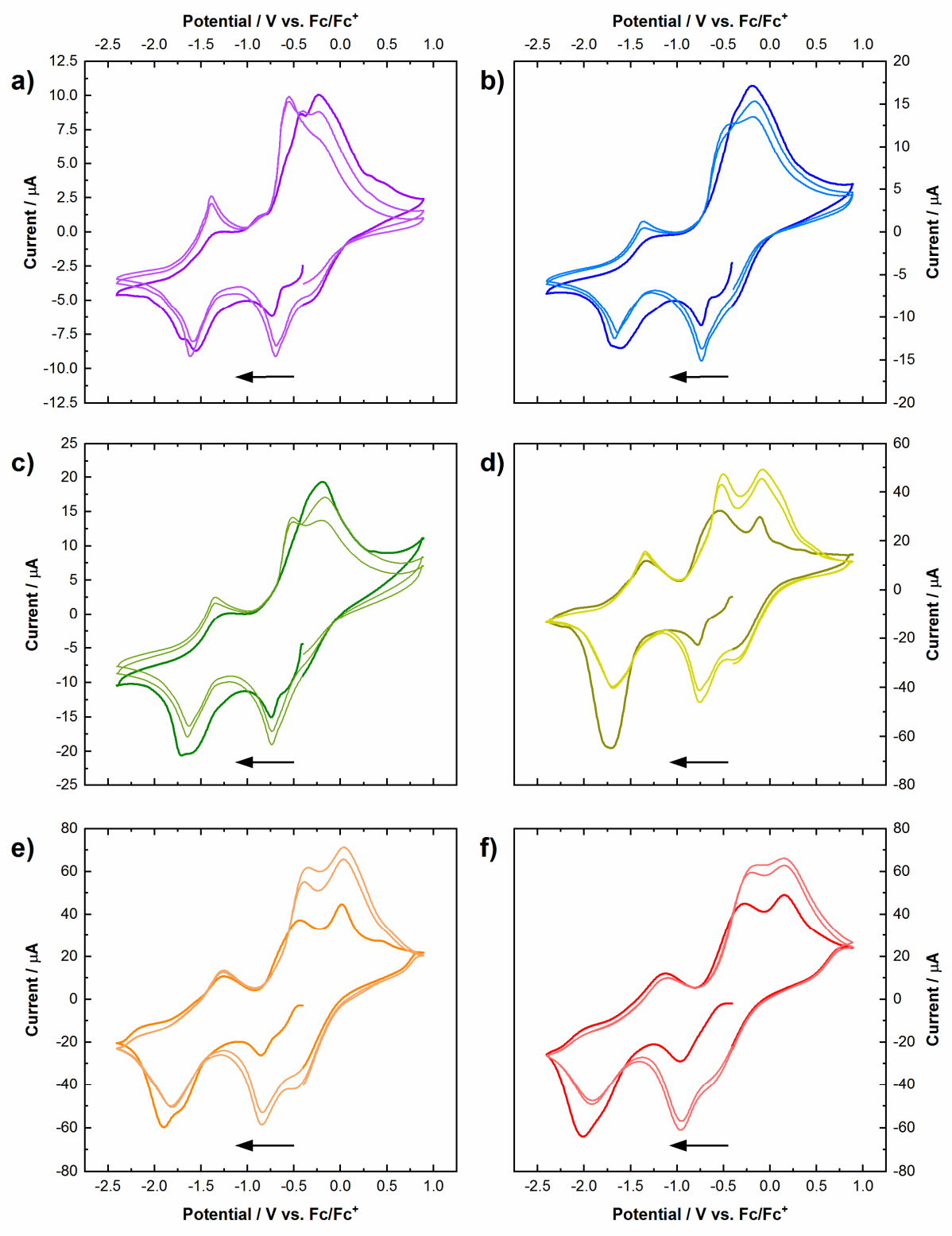


Figure S24 Solid-state cyclic voltammograms of **1b** in 0.1 M $(Et_4N)PF_6$/MeCN at a) 20 mV s^{-1} (purple), b) 50 mV s^{-1} (blue), c) 100 mV s^{-1} (green), d) 200 mV s^{-1} (yellow), e) 500 mV s^{-1} (orange), and f) 1000 mV s^{-1} (red). Arrows indicate the direction of the forward scan. First scan shown in bold, subsequent scans shown in fine line.

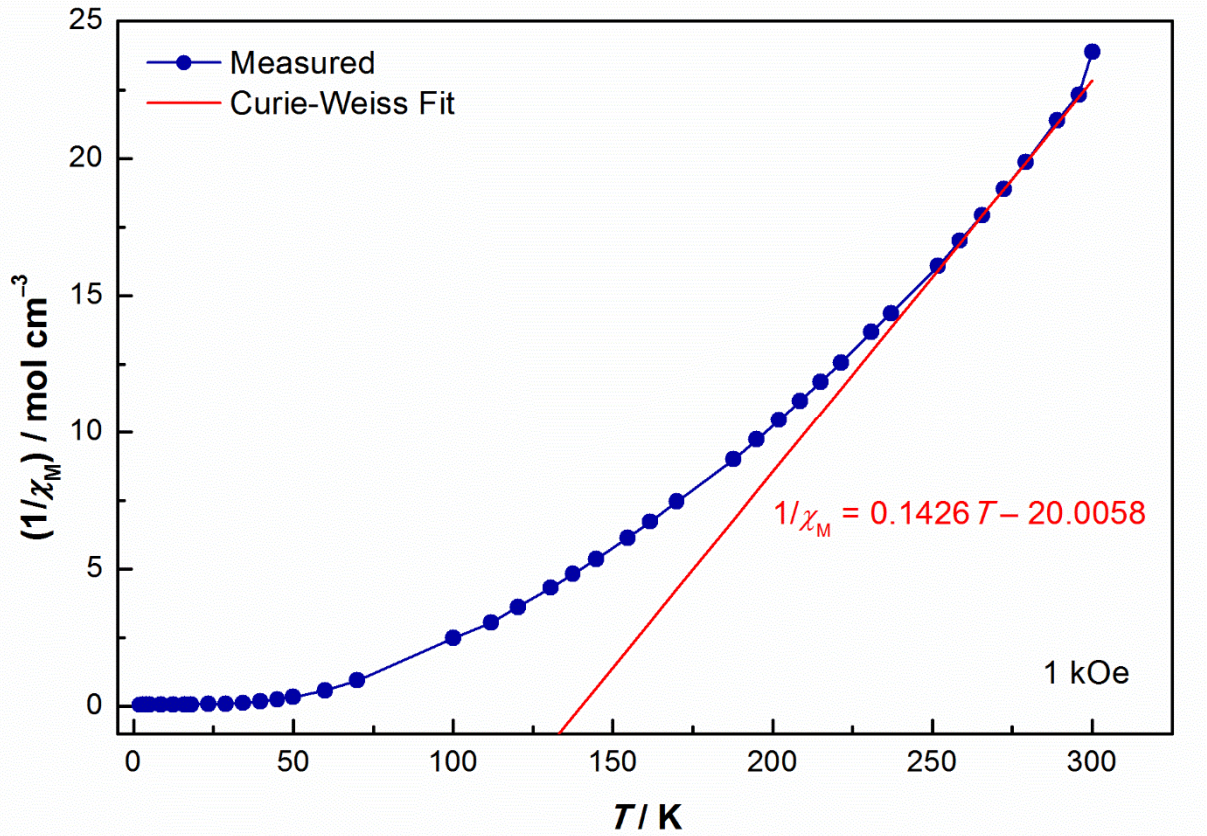


Figure S25 Inverse magnetic susceptibility ($1/\chi_M$) versus T for **1b** (blue) measured in an applied dc field of 1 kOe; solid line to guide the eye. Curie-Weiss fit (red) to the data in the region T = 250–300 K, and the corresponding equation for the line of fit, shown in red.

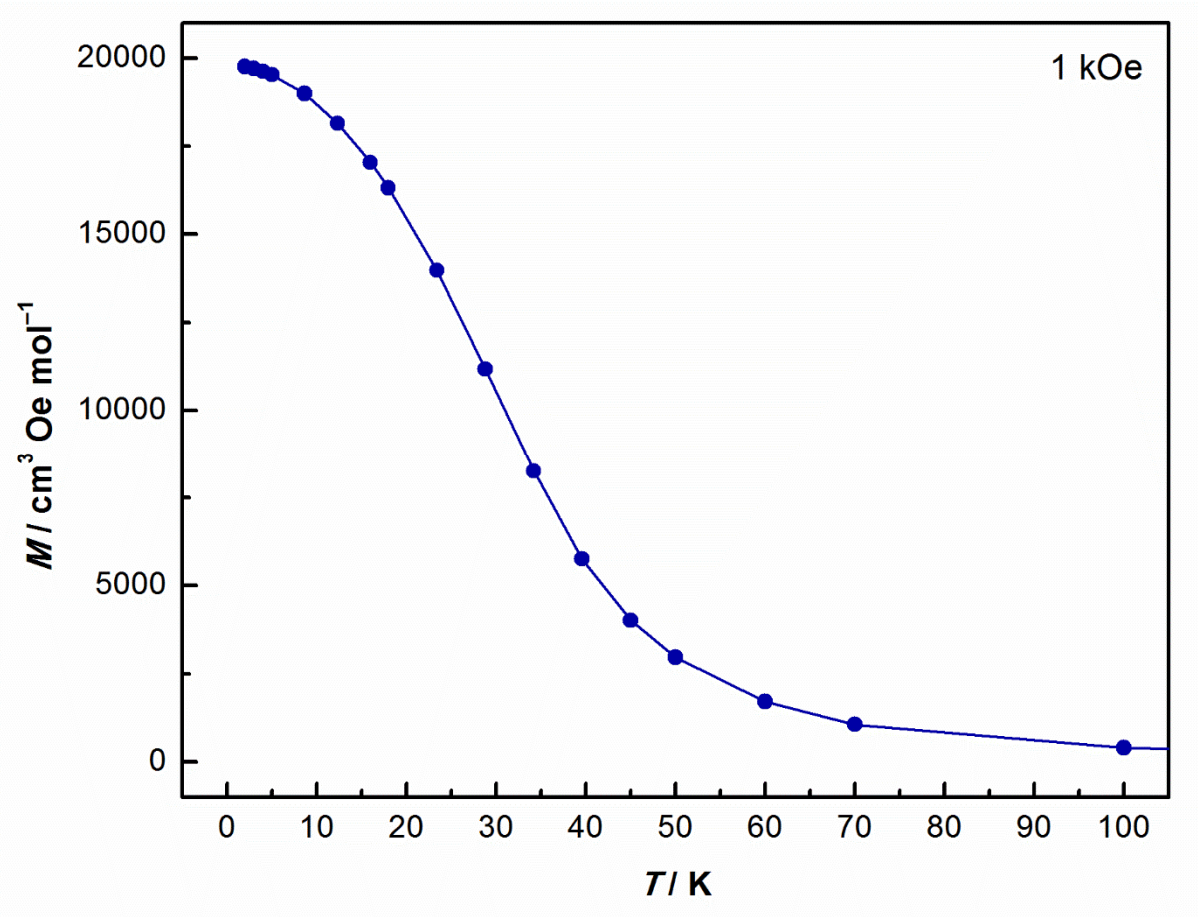


Figure S26 Variable-temperature field-cooled magnetisation of **1b** in an applied dc field of 1 kOe.

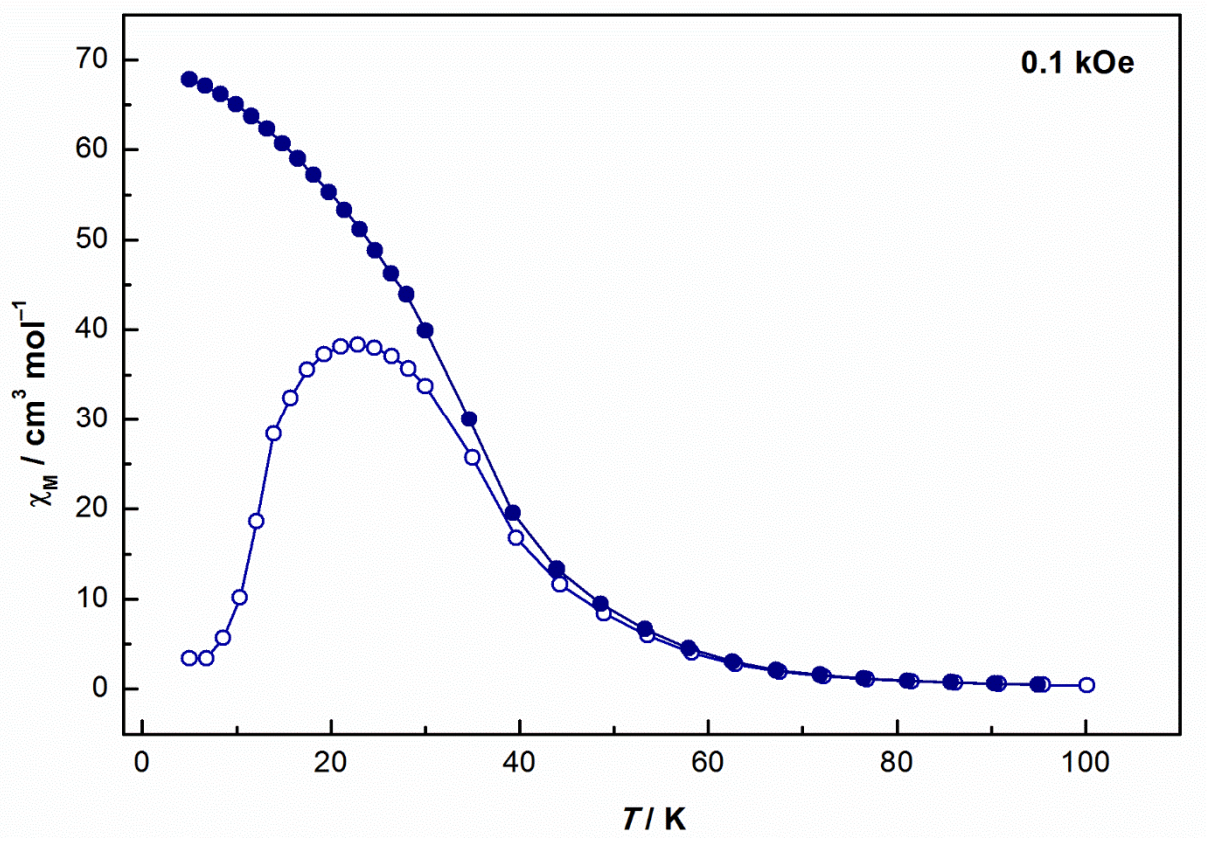


Figure S27 Variable-temperature zero-field cooled (ZFC, open circles) and field-cooled (FC, closed circles) dc magnetic susceptibility for **1b** under an applied dc field of 0.1 kOe.

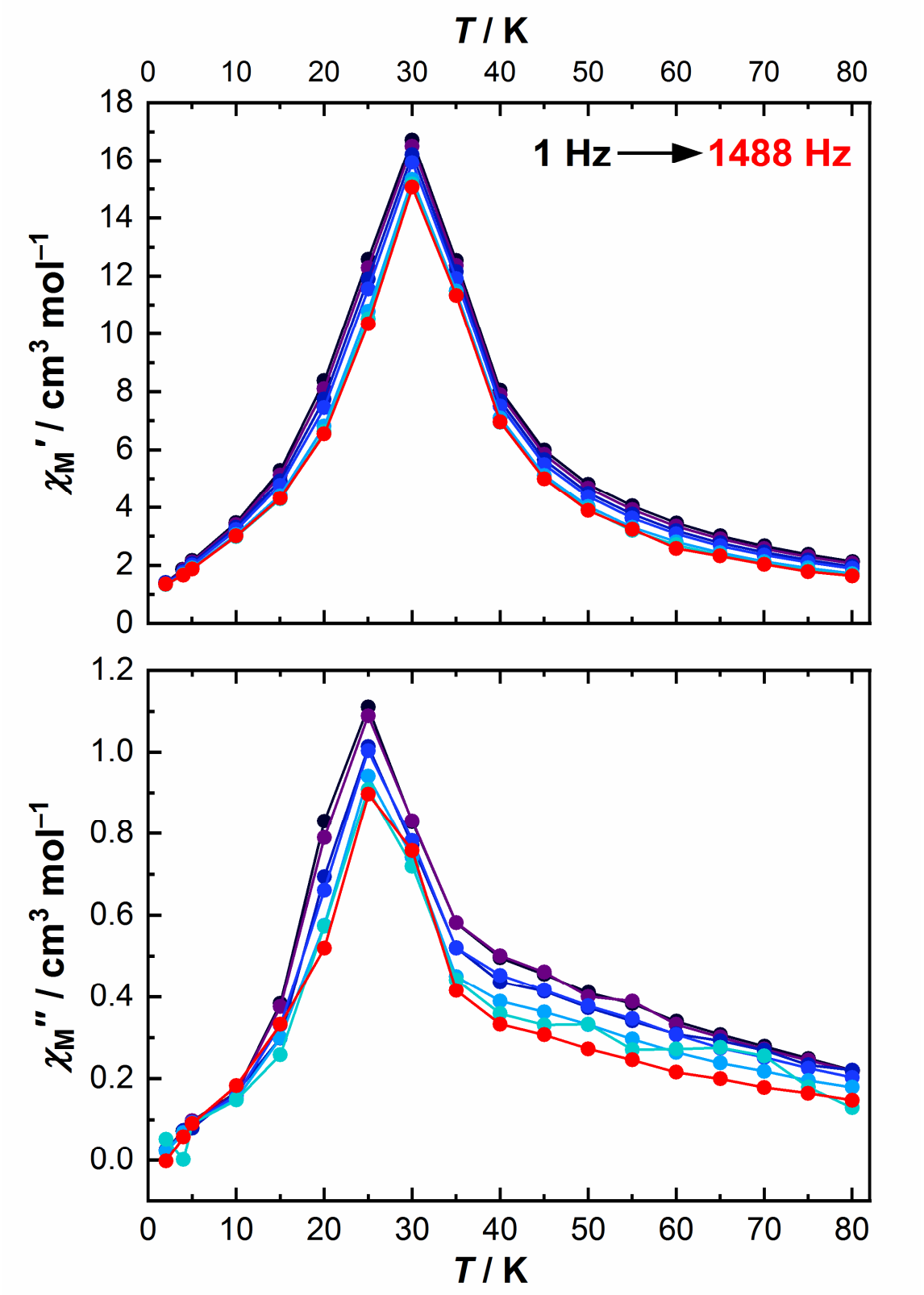


Figure S28 Variable-temperature ac magnetic susceptibility for **1b** collected under zero applied dc field in the temperature range 2–80 K and in the frequency range 1 (black) to 1488 (red) Hz. Lines are to guide the eye.

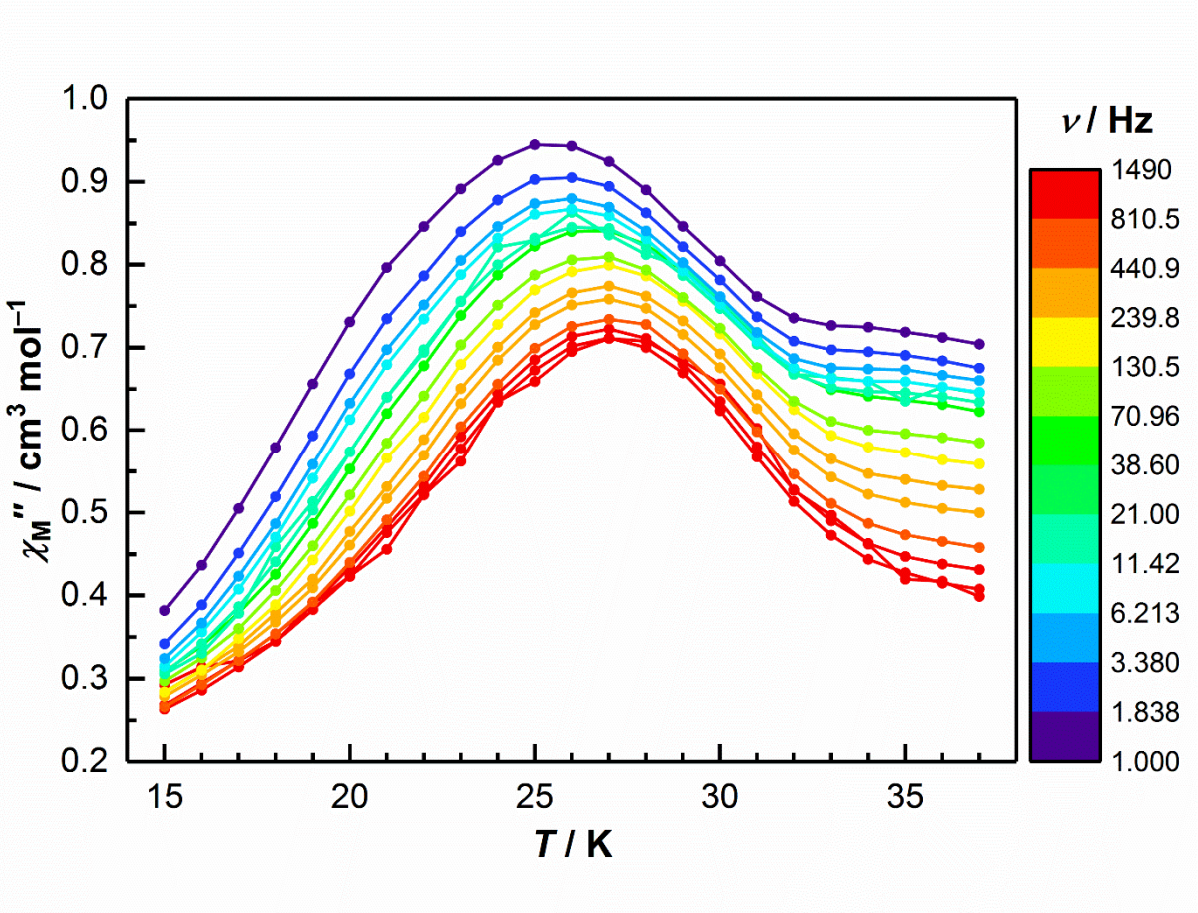


Figure S29 Temperature dependence of the out-of-phase ac susceptibility (χ_M'') for 1b collected in 0 Oe applied dc field for determination of the ordering temperature (T_N). Solid lines guide the eye.

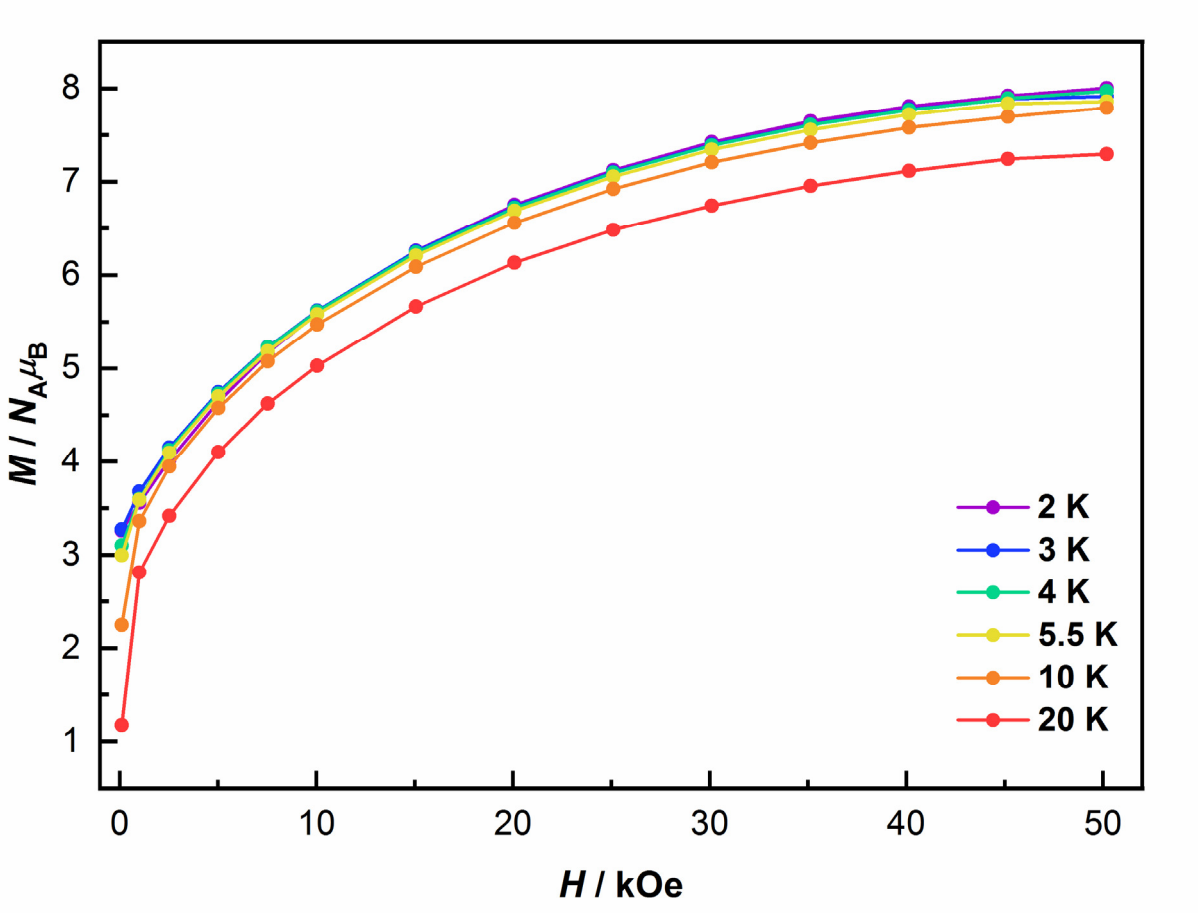


Figure S30 Magnetisation isotherms of **1b** measured in the range T = 2–20 K. Solid lines guide the eye.

Table S11 Pellet thickness and measured transport properties of **1b** for four independent two-point pressed pellet devices.

	Pellet Thickness / cm	**Resistance @ Ambient T^a / Ω**	**Conductivity @ Ambient T^a / S cm^{-1}**	**Resistance @ 300 K^b / Ω**	**Conductivity @ 300 K^b / S cm^{-1}**	**Activation Energy (E_a) / eV**
Device 1	0.112(2)	2801.7(7)	$5.6(2) \times 10^{-4}$	3761.8(3)	$4.2(1) \times 10^{-4}$	0.253(2)
Device 2	0.0515(1)	1599(2)	$4.6(1) \times 10^{-4}$	2095.6(3)	$3.5(1) \times 10^{-4}$	0.250(2)
Device 3	0.066(2)	1345.4(3)	$6.9(3) \times 10^{-4}$	1717.9(2)	$5.4(2) \times 10^{-4}$	0.249(2)
Device 4	0.066(1)	1753.6(3)	$5.3(2) \times 10^{-4}$	2133.4(1)	$4.8(1) \times 10^{-4}$	0.253(3)

[a]: Measured in a two-point screw cell in N_2-filled glovebox at ambient T ca. 305 K.

[b]: Measured in a two-point screw cell contained in a home-built thermostated N_2-purged sample chamber.

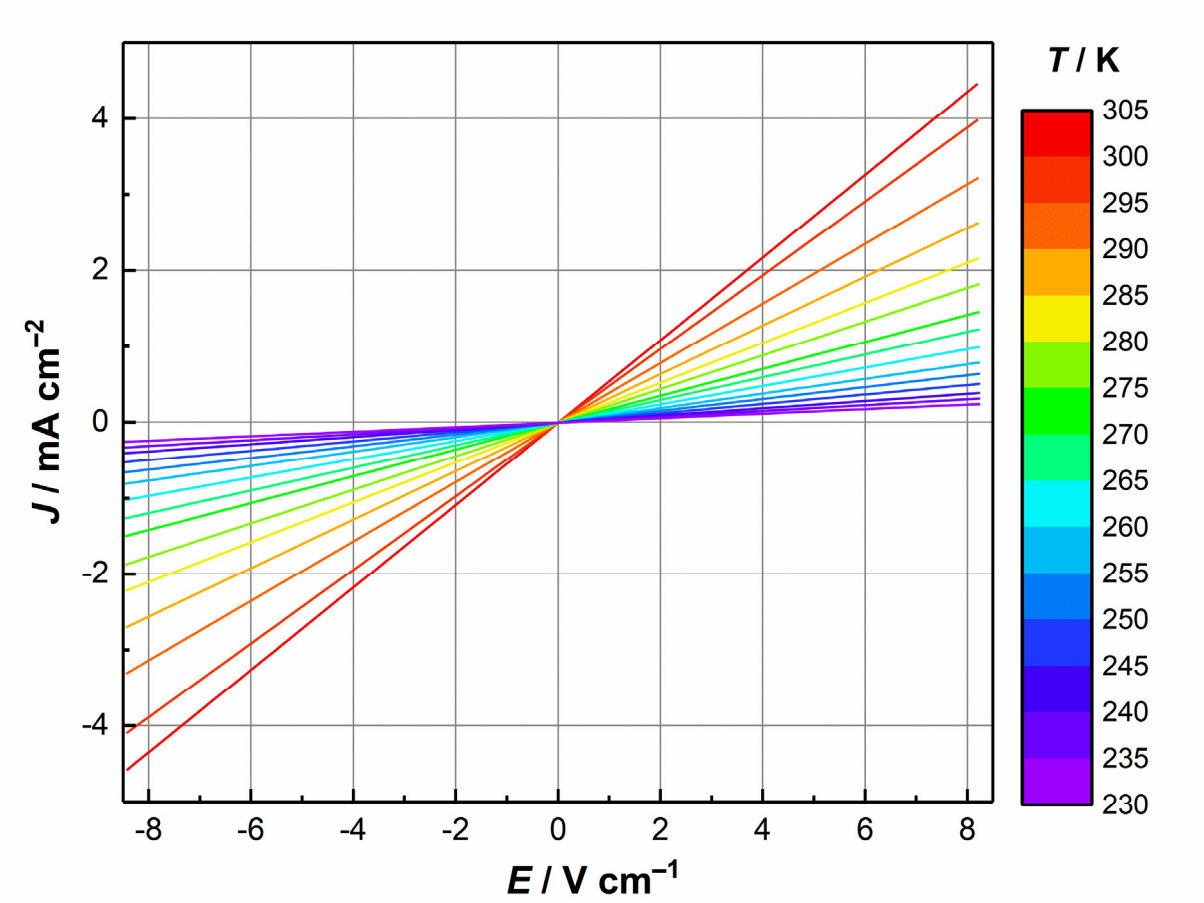


Figure S31 Representative variable temperature current-bias plot for the premier two-point pressed pellet device of **1b** (Device 3). Data were measured over the range −0.55 to 0.55 V in 0.01 V steps.

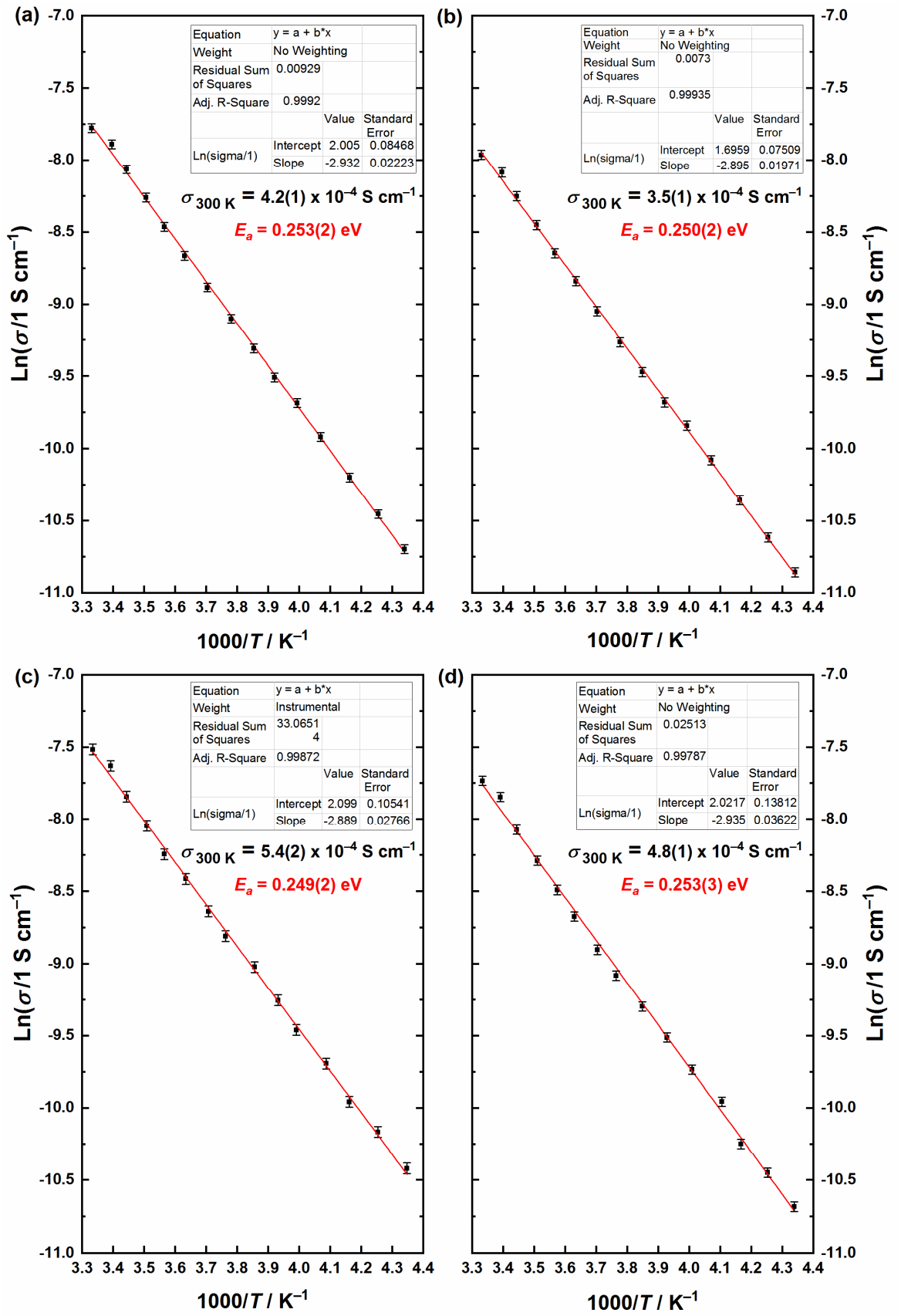


Figure S32 Arrhenius fits of the variable temperature electrical conductivity for **1b** in four independent devices (a–d). Experiment data in black squares, lines of best fit in red. Error bars are ± s.u. Where not visible, error bars lie within the data points.

References

1. Kingsbury, C. J.; Abrahams, B. F.; D'Alessandro, D. M.; Hudson, T. A.; Murase, R.; Robson, R.; White, K. F., *Cryst. Growth Des.* **2017,** 17, 1465-1470.

2. Summers, L. A., *Tetrahedron* **1968,** 24, 5433-5437.

3. Hünig, S.; Groβ, J.; Lier, E. F.; Quast, H., *Liebigs Ann. Chem.* **1973,** 1973, 339-358.

4. Pierpont, C. G.; Francesconi, L. C.; Hendrickson, D. N., *Inorg. Chem.* **1977,** 16, 2367-2376.

5. Folgado, J. V.; Ibanez, R.; Coronado, E.; Beltran, D.; Savariault, J. M.; Galy, J., *Inorg. Chem.* **1988,** 27, 19-26.

6. Calvo, M. A.; Manotti Lanfredi, A. M.; Oro, L. A.; Pinillos, M. T.; Tejel, C.; Tiripicchio, A.; Ugozzoli, F., *Inorg. Chem.* **1993,** 32, 1147-1152.

7. Fujii, C.; Mitsumi, M.; Kodera, M.; Motoda, K.-I.; Ohba, M.; Matsumoto, N.; Okawa, H., *Polyhedron* **1994,** 13, 933-938.

8. Elduque, A.; Garcés, Y.; Oro, L. A.; Pinillos, M. T.; Tiripicchio, A.; Ugozzoli, F., *J. Chem. Soc., Dalton Trans.* **1996**, 2155-2158.

9. Xiang, D. F.; Duan, C. Y.; Tan, X. S.; Liu, Y. J.; Tang, W. X., *Polyhedron* **1998,** 17, 2647-2653.

10. Gallert, S.; Weyhermüller, T.; Wieghardt, K.; Chaudhuri, P., *Inorg. Chim. Acta* **1998,** 274, 111-114.

11. Abrahams, B. F.; Lu, K. D.; Moubaraki, B.; Murray, K. S.; Robson, R., *J. Chem. Soc., Dalton Trans.* **2000**, 1793-1797.

12. Abrahams, B. F.; Coleiro, J.; Ha, K.; Hoskins, B. F.; Orchard, S. D.; Robson, R., *J. Chem. Soc., Dalton Trans.* **2002**, 1586-1594.

13. Yoshino, A.; Matsudaira, H.; Asato, E.; Koikawa, M.; Shiga, T.; Ohba, M.; Okawa, H., *Chem. Commun.* **2002**, 1258-1259.

14. Abdus Subhan, M.; Kawahata, R.; Nakata, H.; Fuyuhiro, A.; Tsukuda, T.; Kaizaki, S., *Inorg. Chim. Acta* **2004,** 357, 3139-3146.

15. Kawahara, M.; Kabir, M. K.; Yamada, K.; Adachi, K.; Kumagai, H.; Narumi, Y.; Kindo, K.; Kitagawa, S.; Kawata, S., *Inorg. Chem.* **2004,** 43, 92-100.

16. Gupta, P.; Das, A.; Basuli, F.; Castineiras, A.; Sheldrick, W. S.; Mayer-Figge, H.; Bhattacharya, S., *Inorg. Chem.* **2005,** 44, 2081-2088.

17. Min, K. S.; Rheingold, A. L.; DiPasquale, A.; Miller, J. S., *Inorg. Chem.* **2006,** 45, 6135-6137.

18. Min, K. S.; DiPasquale, A. G.; Golen, J. A.; Rheingold, A. L.; Miller, J. S., *J. Am. Chem. Soc.* **2007,** 129, 2360-2368.

19. Han, Y.-F.; Lin, Y.-J.; Jia, W.-G.; Jin, G.-X., *Organometallics* **2008,** 27, 4088-4097.

20. Liao, R.-T.; Yang, W.-C.; Thanasekaran, P.; Tsai, C.-C.; Sathiyendiran, M.; Liu, Y.-H.; Rajendran, T.; Lin, H.-M.; Tseng, T.-W.; Lu, K.-L., *Chem. Commun.* **2008**, 3175-3177.

21. Bruijnincx, P. C. A.; Viciano-Chumillas, M.; Lutz, M.; Spek, A. L.; Reedijk, J.; van Koten, G.; Klein Gebbink, R. J. M., *Chem. Eur. J.* **2008,** 14, 5567-5576.

22. Han, Y.-F.; Jia, W.-G.; Lin, Y.-J.; Jin, G.-X., *Organometallics* **2008,** 27, 5002-5008.

23. Therrien, B., *Eur. J. Inorg. Chem.* **2009**, 2445-2453.

24. Chatterjee, P. B.; Bhattacharya, K.; Kundu, N.; Choi, K.-Y.; Clérac, R.; Chaudhury, M., *Inorg. Chem.* **2009,** 48, 804-806.

25. Chuang, C.-H.; Sathiyendiran, M.; Tseng, Y.-H.; Wu, J.-Y.; Hsu, K.-C.; Hung, C.-H.; Wen, Y.-S.; Lu, K.-L., *Organometallics* **2010,** 29, 283-285.

26. Schweinfurth, D.; Khusniyarov, M. M.; Bubrin, D.; Hohloch, S.; Su, C.-Y.; Sarkar, B., *Inorg. Chem.* **2013,** 52, 10332-10339.

27. Shankar, B.; Elumalai, P.; Shanmugam, R.; Singh, V.; Masram, D. T.; Sathiyendiran, M., *Inorg. Chem.* **2013,** 52, 10217-10219.

28. Rajakannu, P.; Elumalai, P.; Hussain, F.; Sathiyendiran, M., *J. Organomet. Chem.* **2013,** 725, 1-4.

29. Rajakannu, P.; Mobin, S. M.; Sathiyendiran, M., *J. Organomet. Chem.* **2014,** 771, 68-77.

30. Liu, J.-J.; Lin, Y.-J.; Jin, G.-X., *Dalton Trans.* **2015,** 44, 10281-10288.

31. Jurić, M.; Molčanov, K.; Žilić, D.; Kojić-Prodić, B., *RSC Adv.* **2016,** 6, 62785-62796.

32. Zhang, W.-Y.; Lin, Y.-J.; Han, Y.-F.; Jin, G.-X., *J. Am. Chem. Soc.* **2016,** 138, 10700-10707.

33. Lu, Y.; Deng, Y.-X.; Lin, Y.-J.; Han, Y.-F.; Weng, L.-H.; Li, Z.-H.; Jin, G.-X., *Chem* **2017,** 3, 110-121.

34. Zhang, Y.-Y.; Gao, W.-X.; Lin, Y.-J.; Mi, L.-W.; Jin, G.-X., *Chem. Eur. J.* **2017,** 23, 11133-11140.

35. Androš Dubraja, L.; Molčanov, K.; Žilić, D.; Kojić-Prodić, B.; Wenger, E., *New J. Chem.* **2017,** 41, 6785-6794.

36. Dunstan, M. A.; Rousset, E.; Boulon, M.-E.; Gable, R. W.; Sorace, L.; Boskovic, C., *Dalton Trans.* **2017,** 46, 13756-13767.

37. Zhang, P.; Perfetti, M.; Kern, M.; Hallmen, P. P.; Ungur, L.; Lenz, S.; Ringenberg, M. R.; Frey, W.; Stoll, H.; Rauhut, G.; van Slageren, J., *Chem. Sci.* **2018,** 9, 1221-1230.

38. Ishikawa, R.; Michiwaki, S.; Noda, T.; Katoh, K.; Yamashita, M.; Matsubara, K.; Kawata, S., *Inorganics* **2018,** 6, 7.

39. Arumugam, R.; Shankar, B.; Shanmugam, R.; Arumuganathan, T.; Sathiyendiran, M., *Dalton Trans.* **2018,** 47, 13894-13901.

40. chemarumugam, A., *CSD Communication* **2018**.

41. Dang, L.-L.; Lin, Y.-J.; Jin, G.-X., *Dalton Trans.* **2018,** 47, 6378-6385.

42. Bhol, M.; Shankar, B.; Sathiyendiran, M., *Dalton Trans.* **2018,** 47, 4494-4500.

43. Fan, Q.-J.; Lin, Y.-J.; Hahn, F. E.; Jin, G.-X., *Dalton Trans.* **2018,** 47, 2240-2246.

44. Deng, Y.-X.; Zhang, H.-N.; Lin, Y.-J.; Jin, G.-X., *J. Coord. Chem.* **2018,** 71, 1959-1970.

45. Procopio, E. Q.; Dova, D.; Cauteruccio, S.; Forni, A.; Licandro, E.; Panigati, M., *ACS Omega* **2018,** 3, 11649-11654.

46. Shan, W.-L.; Lin, Y.-J.; Hahn, F. E.; Jin, G.-X., *Angew. Chem. Int. Ed.* **2019,** 58, 5882-5886.

47. Cueto, S.; Straumann, H.-P.; Rys, P.; Petter, W.; Gramlich, V.; Rys, F. S., *Acta Crystallogr. C* **1992,** 48, 458-460.

48. Kawata, S.; Kitagawa, S.; Kondo, M.; Furuchi, I.; Munakata, M., *Angew. Chem. Int. Ed. Engl.* **1994,** 33, 1759-1761.

49. Decurtins, S.; Schmalle, H. W.; Zheng, L.-M.; Ensling, J., *Inorg. Chim. Acta* **1996,** 244, 165-170.

50. Zheng, L.-M.; Schmalle, H. W.; Huber, R.; Decurtins, S., *Polyhedron* **1996,** 15, 4399-4405.

51. Kawata, S.; Kitagawa, S.; Kumagai, H.; Kudo, C.; Kamesaki, H.; Ishiyama, T.; Suzuki, R.; Kondo, M.; Katada, M., *Inorg. Chem.* **1996,** 35, 4449-4461.

52. Kawata, S.; Kitagawa, S.; Kumagai, H.; Ishiyama, T.; Honda, K.; Tobita, H.; Adachi, K.; Katada, M., *Chem. Mater.* **1998,** 10, 3902-3912.

53. Vuković, V.; Molčanov, K.; Jelsch, C.; Wenger, E.; Krawczuk, A.; Jurić, M.; Androš Dubraja, L.; Kojić-Prodić, B., *Cryst. Growth Des.* **2019,** 19, 2802-2810.

54. Kabir, M. K.; Kawahara, M.; Kumagai, H.; Adachi, K.; Kawata, S.; Ishii, T.; Kitagawa, S., *Polyhedron* **2001,** 20, 1417-1422.

55. Michaelides, A.; Papadimitriou, C. D.; Plakatouras, J. C.; Skoulika, S.; Veltsistas, P. G., *Polyhedron* **2004,** 23, 2587-2593.

56. Barba, V.; Zaragoza, J.; Höpfl, H.; Farfán, N.; Beltrán, H. I.; Zamudio-Rivera, L. S., *J. Organomet. Chem.* **2011,** 696, 1949-1956.

57. Zucchi, G.; Thuery, P.; Ephritikhine, M., *CSD Communication* **2012**.

58. Nishimura, Y.; Himegi, A.; Fuyuhiro, A.; Hayami, S.; Kawata, S., *Acta Crystallogr. E* **2013,** 69, m119-m120.

59. Abhervé, A.; Clemente-León, M.; Coronado, E.; Gómez-García, C. J.; Verneret, M., *Inorg. Chem.* **2014,** 53, 12014-12026.

60. Tanaka, S.; Himegi, A.; Ohishi, T.; Fuyuhiro, A.; Kawata, S., *Acta Crystallogr. E* **2014,** 70, m90-m91.

61. Kingsbury, C. J.; Abrahams, B. F.; Robson, R., *CSD Communication* **2017**.

62. Kingsbury, C. J.; White, K. F.; Abrahams, B. F.; Robson, R., *CSD Communication* **2017**.

63. Kingsbury, C. J.; Abrahams, B. F.; Robson, R., *CSD Communication* **2017**.

64. Simonson, A. N.; Kareis, C. M.; Ovanesyan, N. S.; Baumann, D. O.; Rheingold, A. L.; Arif, A. M.; Miller, J. S., *Polyhedron* **2018,** 139, 215-221.

65. DeGayner, J. A.; Wang, K.; Harris, T. D., *J. Am. Chem. Soc.* **2018,** 140, 6550-6553.

66. Riley, P. E.; Haddad, S. F.; Raymond, K. N., *Inorg. Chem.* **1983,** 22, 3090-3096.

67. Robl, C.; Weiss, A., *Mater. Res. Bull.* **1987,** 22, 497-504.

68. Robl, C., *Mater. Res. Bull.* **1987,** 22, 1483-1491.

69. Kumagai, H.; Kawata, S.; Kitagawa, S., *Inorg. Chim. Acta* **2002,** 337, 387-392.

70. Luo, T.-T.; Liu, Y.-H.; Tsai, H.-L.; Su, C.-C.; Ueng, C.-H.; Lu, K.-L., *Eur. J. Inorg. Chem.* **2004,** 2004, 4253-4258.

71. Abrahams, B. F.; Grannas, M. J.; Hudson, T. A.; Hughes, S. A.; Pranoto, N. H.; Robson, R., *Dalton Trans.* **2011,** 40, 12242-12247.

72. Shilov, G. V.; Nikitina, Z. K.; Ovanesyan, N. S.; Aldoshin, S. M.; Makhaev, V. D., *Russ. Chem. Bull.* **2011,** 60, 1209-1219.

73. Zucchi, G.; Thuery, P.; Ephritikhine, M., *CSD Communication* **2012**.

74. Zucchi, G.; Thuery, P.; Ephritikhine, M., *CSD Communication* **2012**.

75. Zucchi, G.; Thuery, P.; Ephritikhine, M., *CSD Communication* **2012**.

76. Atzori, M.; Benmansour, S.; Mínguez Espallargas, G.; Clemente-León, M.; Abhervé, A.; Gómez-Claramunt, P.; Coronado, E.; Artizzu, F.; Sessini, E.; Deplano, P.; Serpe, A.; Mercuri, M. L.; Gómez García, C. J., *Inorg. Chem.* **2013,** 52, 10031-10040.

77. Abhervé, A.; Mañas-Valero, S.; Clemente-León, M.; Coronado, E., *Chem. Sci.* **2015,** 6, 4665-4673.

78. Benmansour, S.; Vallés-García, C.; Gómez-Claramunt, P.; Mínguez Espallargas, G.; Gómez-García, C. J., *Inorg. Chem.* **2015,** 54, 5410-5418.

79. Benmansour, S.; Abhervé, A.; Gómez-Claramunt, P.; Vallés-García, C.; Gómez-García, C. J., *ACS Appl. Mater. Interfaces* **2017,** 9, 26210-26218.

80. Palacios-Corella, M.; Fernández-Espejo, A.; Bazaga-García, M.; Losilla, E. R.; Cabeza, A.; Clemente-León, M.; Coronado, E., *Inorg. Chem.* **2017,** 56, 13865-13877.

81. Benmansour, S.; Pérez-Herráez, I.; Cerezo-Navarrete, C.; López-Martínez, G.; Martínez Hernández, C.; Gómez-García, C. J., *Dalton Trans.* **2018,** 47, 6729-6741.

82. Liu, L.; DeGayner, J. A.; Sun, L.; Zee, D. Z.; Harris, T. D., *Chem. Sci.* **2019,** 10, 4652-4661.

83. Liu, L.; Li, L.; DeGayner, J. A.; Winegar, P. H.; Fang, Y.; Harris, T. D., *J. Am. Chem. Soc.* **2018,** 140, 11444-11453.

84. Chen, J.; Sekine, Y.; Komatsumaru, Y.; Hayami, S.; Miyasaka, H., *Angew. Chem. Int. Ed.* **2018,** 57, 12043-12047.

85. Kingsbury, C. J.; Abrahams, B. F.; Auckett, J. E.; Chevreau, H.; Dharma, A. D.; Duyker, S.; He, Q.; Hua, C.; Hudson, T. A.; Murray, K. S.; Phonsri, W.; Peterson, V. K.; Robson, R.; White, K. F., *Chem. Eur. J.* **2019,** 25, 5222-5234.

86. Frenzer, W.; Wartchow, R.; Bode, H., *Z. Kristallogr. Cryst. Mater.* **1997,** 212, 237.

87. Abrahams, B. F.; Hudson, T. A.; McCormick, L. J.; Robson, R., *Cryst. Growth Des.* **2011,** 11, 2717-2720.

88. Kingsbury, C. J.; Abrahams, B. F.; Robson, R., *CSD Communication* **2017**.

89. Kingsbury, C. J.; Abrahams, B. F.; Robson, R., *CSD Communication* **2017**.

90. Jeon, I.-R.; Negru, B.; Van Duyne, R. P.; Harris, T. D., *J. Am. Chem. Soc.* **2015,** 137, 15699-15702.

91. Heinze, K.; Huttner, G.; Zsolnai, L.; Jacobi, A.; Schober, P., *Chem. Eur. J.* **1997,** 3, 732-743.

92. Heinze, K.; Huttner, G.; Walter, O., *Eur. J. Inorg. Chem.* **1999,** 1999, 593-600.

93. DeGayner, J. A.; Jeon, I.-R.; Sun, L.; Dincă, M.; Harris, T. D., *J. Am. Chem. Soc.* **2017,** 139, 4175-4184.

94. Guo, D.; McCusker, J. K., *Inorg. Chem.* **2007,** 46, 3257-3274.

95. Llunell, M.; Casanova, D.; Cicera, J.; Alemany, P.; Alvarez, S., *Shape, Version 2.1*. Universitat de Barcelona: Barcelona, Spain, 2013.

96. Spek, A. L., *Acta Crystallogr. C* **2015,** 71, 9-18.

97. Spek, A. L., *Acta Crystallogr. D* **2009,** 65, 148-155.

98. Ziebel, M. E.; Darago, L. E.; Long, J. R., *J. Am. Chem. Soc.* **2018,** 140, 3040-3051.

99. Dolomanov, O. V.; Bourhis, L. J.; Gildea, R. J.; Howard, J. A. K.; Puschmann, H., *J. Appl. Crystallogr.* **2009,** 42, 339-341.

100. Hush, N. S., Intervalence-Transfer Absorption. Part 2. Theoretical Considerations and Spectroscopic Data. In *Prog. Inorg. Chem.*, Cotton, F. A., Ed. Interscience Publishers: New York, NY, 1967; Vol. 8.

101. Hush, N. S., *Electrochim. Acta* **1968,** 13, 1005-1023.

102. Brunschwig, B. S.; Creutz, C.; Sutin, N., *Chem. Soc. Rev.* **2002,** 31, 168-184.